5th MASHCON

International Conference on Ship Manoeuvring in Shallow and Confined Water with non-exclusive focus on manoeuvring in waves, wind and current

Conference Proceedings

19 - 23 May 2019
Ostend, Belgium

Flanders Hydraulics Research
Flanders State of the Art
MARITIME TECHNOLOGY GHENT UNIVERSITY
GHENT UNIVERSITY

Conference Proceedings

5th MASHCON
International Conference on Ship Manoeuvring in Shallow and Confined Water
with non-exclusive focus on
manoeuvring in waves, wind and current

19 - 23 May 2019, Ostend, Belgium

Editors

Maxim Candries, Evert Lataire (Maritime Technology Division, Ghent University)

Katrien Eloot, Guillaume Delefortrie (Flanders Hydraulics Research)

Published by:
Knowledge Centre Manoeuvring in Shallow and Confined Water
(Maritime Technology Division, Ghent University and Flanders Hydraulics Research)
info@shallowwater.be
www.shallowwater.be

Organisation

Members of the International Scientific Committee

Dr. Carl-Uwe Böttner	Federal Waterways Engineering and Research Institute (BAW), Germany
Dr. Larry Daggett	Waterway Simulation Technology, USA
Prof. Guillaume Delefortrie	Flanders Hydraulics Research, Belgium
Dr. Jonathan Duffy	Australian Maritime College, Australia
Prof. Bettar Ould el Moctar	ISMT, University of Duisburg Essen, Germany
Dr. Katrien Eloot	Flanders Hydraulics Research, Belgium
Prof. Yoshitaka Furukawa	Department of Marine Systems Engineering, Kyushu University, Japan
Dr. Tim Gourlay	Perth Hydro Pty Ltd, Australia
Prof. Alexander Härting	Department of Maritime Studies, Jade University Elsfleth, Germany
Prof. Katsuro Kijima	Nagasaki Institute of Applied Science, Japan
Prof. Yonghwan Kim	Department of Naval Architecture and Ocean Engineering, Seoul National University, Republic of Korea
Prof. Nikolai Kornev	Faculty of Mechanical Engineering and Marine Technology, University of Rostock, Germany
Prof. Evert Lataire	Maritime Technology Division, Ghent University, Belgium
Prof. Bjørnar Pettersen	Norwegian University of Science and Technology, Norway
Mr. Frans Quadvlieg	MARIN, The Netherlands
Mr. Marc Steinwand	Schiffbau-Versuchsanstalt Potsdam GmbH, Germany
Prof. Marc Vantorre	Maritime Technology Division, Ghent University, Belgium
Assoc. Prof. Michael Woodward	Australian Maritime College, Australia
Prof. Hironori Yasukawa	Department of Transportation and Environmental Systems, Hiroshima University, Japan
Prof. Zao-Jian Zou	School of Naval Architecture, Ocean and Civil Engineering, Shanghai Jiao Tong University, China

Review Coordination

Dr. Maxim Candries	Maritime Technology Division, Ghent University, Belgium

Organising Committee

Dr. Maxim Candries	Maritime Technology Division, Ghent University, Belgium
Prof. Evert Lataire	Maritime Technology Division, Ghent University, Belgium
Mrs. Ellen Vyncke	Maritime Technology Division, Ghent University, Belgium
Dr. Katrien Eloot	Flanders Hydraulics Research, Belgium
Prof. Guillaume Delefortrie	Flanders Hydraulics Research, Belgium
Mrs. Viki Kruyniers	Flanders Hydraulics Research, Belgium

Lay-out

Mr. Yvan Machiels	Flanders Hydraulics Research, Belgium

Table of Contents

Preface

For several reasons, the 5th International Conference on Ship Manoeuvring in Shallow and Confined Water has a somewhat special character. First of all, it is the last time the MASHCON conferences can be counted on the fingers of one hand. Moreover, we can celebrate the 10th anniversary of the first edition, which took place in Antwerp in May 2009. Apparently, organising a conference dedicated to hydrodynamic aspects of ship manoeuvring in areas with horizontal and/or vertical restrictions was not a bad idea after all. The event gradually increased in size to reach a kind of steady-state, with around 40 presentations and some 100 participants – a suitable size for a conference in a niche domain of ship hydrodynamics and nautical science. But also the reputation of the event has grown, and MASHCON apparently has found its place in the conference landscape.

The 5th MASHCON is also special because of its venue. MASHCON is an initiative of the Knowledge Centre Manoeuvring in Shallow and Confined Water, which is based on a long-term cooperation between Flanders Hydraulics Research, and the Maritime Technology Division of Ghent University. This Knowledge Centre was created to consolidate, extend and disseminate knowledge on the mentioned topic, and one of the ways to do so is indeed organising conferences. We intend to create a habit to organise every other conference abroad, and stay at home in between, which so far resulted in MASHCON editions in Antwerp (2009), Trondheim (2011), Ghent (2013) and Hamburg (2016). The selection of Antwerp and Ghent, home cities of the two organising partners of the Knowledge Centre, was rather straightforward, but the present location requires some clarification. Ostend was selected as the venue because in 2016, the Flemish Government decided for a major investment in the development of Flanders Maritime Laboratory, a unique research facility which, after completion, will contain a towing tank for manoeuvres in shallow water and a coastal and ocean basin. Just a few days before this Conference, the buildings were inaugurated, opening the way for the installation of the experimental equipment in the coming years.

A last reason why the 5th MASHCON is different from other editions is a personal one: my name is no longer mentioned in the conference proceedings as one of the editors. This is a direct consequence of my own decision to retire on the 1st of February of this year. I would like to take my last opportunity to address you in a MASHCON preface to emphasize the importance of events like this one. Nowadays the benefits of scientific conferences and symposia are often questioned, referring to the convenience of internet connections for transfer of information and personal contacts on the one hand and the time and money consuming nature of attending such meetings on the other. In the academic world, participating to conferences is in some research groups even discouraged because of the – in my personal opinion often mistakenly – lower rating of conference papers compared to journal papers. From my own experience, I can only testify that participation to conferences offering the opportunity to present the results of research in several stages of development to an audience with a similar focus definitely has an encouraging, stimulating, inspiring effect, irrespective the phase of your career. Contacts and confrontation with colleagues from all over the world allow to put your own research and methodology into another perspective, and often international co-operations are initiated at such meetings. This is not only the case for dedicated conference cycles, but also for participation to working groups and committees of international organisations such as the International Towing Tank Conference (ITTC) and the World Association for Waterborne Transport Infrastructure (PIANC).

Conferences are excellent platforms of exchange of information, experiences, ideas and opinions, provided that the quality of the contributions is high and the scope is relevant and consistent. I am confident that the 5th MASHCON conference fulfils these requirements and I am very hopeful about the future.

Marc Vantorre

Organising Institutions

Maritime Technology Division, Ghent University

Tech Lane Ghent Science Park Campus Ardoyen 60

9052 Ghent, Belgium

www.maritiem.ugent.be

Flanders Hydraulics Research

Berchemlei 115, 2140 Antwerp , Belgium

http://www.watlab.be/en

Sponsor

CVBA Brabo

Noorderlaan 21, Haven 28,

2030 Antwerp, Belgium

http://www.brabo.com/nl

Agency for Maritime & Coastal Services

Koning Albert II-laan 20, bus 5

1000 Brussel

www.agentschapmdk.be

5th MASHCON

International Conference on Ship Manoeuvring in Shallow and Confined Water

with non-exclusive focus on manoeuvring in waves, wind and current.

19 – 23 May 2019

Thermae Palace, Ostend, Belgium

CONFERENCE PROGRAMME

19 MAY 2019 (SUNDAY)

18:00 - 20:00	**Registration + Welcome Reception**

20 MAY 2019 (MONDAY)

08:00 - 09:00	**Registration**
09:00 - 09:15	**Opening address by Prof. Frank Mostaert**
09:15 – 10:00	**Invited Keynote Speech by Prof. Marc Vantorre**
	SESSION 1 – Confined water effects (Chair: Prof. Marc Vantorre)
10:00 – 10:25	*Maneuvering Hydrodynamic Derivatives and Course Stability of a Ship Close to A Bank (WWC023)* Hironori Yasukawa Department of Transportation and Environmental Systems, Hiroshima University, Japan
10:25 - 10:50	*Calibrating and measuring wakes and drag forces of inland vessels in confined water in a towing tank (WWC059)* Clément Caplier, Guillaume Gomit, Germain Rousseaux, Damien Calluaud, Ludovic Chatellier and Laurent David Pprime Institute, CNRS, University of Poitiers, ISAE-ENSMA, France
10:50 - 11:15	**Refreshment break**

	SESSION 2 – Wind, waves and/or current - Benchmark data (Chair: Prof. Bettar Ould el Moctar)	**SESSION 3 – Full-scale measurements** (Chair: Dr. Carl-Uwe Böttner)
11:15 - 11:40	*Sailing in shallow water waves with the DTC container carrier: Open model test data for validation purposes (WWC001)* Thibaut Van Zwijnsvoorde, Manases Tello Ruiz, Guillaume Delefortrie and Evert Lataire Flanders Hydraulics Research, Belgium ; Maritime Technology Division, Ghent University, Belgium	*Full scale measurement of ship motions to validate strip theory (WWC015)* Butteur Mulumba Ntamba Ntamba, Bernhard Schwarz-Röhr, Chen Zhang and Alexander Härting Cape Peninsula University of Technology, South Africa ; Jade Hochschule, Germany ; Ghent University, Belgium ; Universität Oldenburg, Germany
11:40 - 12:05	*Benchmarking of DIFFRAC, FATIMA, HydroSTAR, MOSES, NEMOH, OCTOPUS, PDStrip, RAPID, SEAWAY, SlenderFlow and WAMIT against measured vertical motions of the Duisburg Test Case container ship in shallow water (WWC006)* Tim Gourlay, Evert Lataire, Guillaume Delefortrie, Luca Donatini, Manases Tello Ruiz, Daniel Veen, Tim Bunnik, Reint Dallinga Perth Hydro, Australia ; Maritime Technology Division, Ghent University, Belgium ; Flanders Hydraulics Research, Belgium ; Bentley Systems, Australia ; MARIN, The Netherlands	*Estimation of the center of rotation for a ship in real sea state environment (WWC016)* Chen Zhang, Alexander Härting, Butteur Mulumba Ntamba Ntamba and Bernhard Schwarz-Röhr Jade Hochschule, Germany ; Cape Peninsula University of Technology, South Africa ; Universität Oldenburg, Germany ; Ghent University, Belgium
12:05 - 12:30	*Uncertainty quantification of hydrodynamic forces on the DTC model in shallow water waves using CFD and non-intrusive polynomial chaos method (WWC021)* Li Xia, Shuai Yuan, Zao-Jian Zou and Lu Zou School of Naval Architecture, Ocean and Civil Engineering, Shanghai Jiao Tong University, China ; State Key Laboratory of Ocean Engineering, Shanghai Jiao Tong University, China	*Verification of RAOs in sea trials (WWC017)* Bernhard Schwarz-Röhr, Alexander Härting, Marc Mansuy, Marc Vantorre, Jeroen Verwilligen, Butteur Ntamba Ntamba and Chen Zhang Jade Hochschule, Germany ; Cape Peninsula University of Technology, South Africa ; Universität Oldenburg, Germany ; Maritime Technology Division, Ghent University, Belgium ; Flanders Hydraulics Research, Belgium
12:30 - 13:30	**Lunch**	

	SESSION 4 – Wind, waves and/or current (Chair: Mr. Frans Quadvlieg)	**SESSION 5 – Full-scale measurements** (Chair: Prof. Alexander Härting)
13:30 - 13:55	*Predicting manoeuvring capabilities of a DTMB Ship in CFD with dynamically controlled surfaces (WWC045)* Inno Gatin, Vuko Vukčević and Hrvoje Jasak Faculty of Mechanical Engineering and Naval Architecture, University of Zagreb, Croatia	*Application of novel system identification methodology for finding roll damping and restoring parameters by using the measured response at sea (WWC043)* Mohammadreza Javanmardi, Chris Hens, Jack Bucher and Gregory Hibbert OMC International, Melbourne, Australia
13:55 - 14:20	*Simulation of the effect of installed power minimisation on ship motion (WWC046)* Emmanuel Irimagha, Zhiqiang Hu, Richard Birmingham, and Michael Woodward Newcastle University, UK ; University of Tasmania, Australia	*Sea trials for determination of manoeuvring characteristics in shallow water conditions (WWC032)* Hanne Jansch and Carl-Uwe Böttner Federal Waterways Engineering and Research Institute (BAW), Germany

14:20 - 14:45	*Parameter estimation for a ship's roll response model in shallow water using an intelligent machine learning method (WWC051)* Changyuan Chen, Manases Tello Ruiz, Guillaume Delefortrie, Tianlong Mei, Evert Lataire and Marc Vantorre Ghent University, Belgium ; Flanders Research Hydraulics, Belgium ; Shanghai Jiao Tong University, China	*Full-scale measurements of vertical motions on ultra large container vessels in Scheldt estuary (WWC036)* Jeroen Verwilligen, Katrien Eloot, Marc Mansuy and Marc Vantorre Flanders Hydraulics Research, Belgium ; Maritime Technology Division, Ghent University, Belgium
14:45 – 15:00	**Refreshment break**	

	SESSION 6 – Wind, waves and/or current Benchmark data (Chair: Prof. Yonghwan Kim)	**SESSION 7 – Simulators** (Chair: Prof. Yoshitaka Furukawa)
15:00 – 15:25	*CFD-based numerical prediction of vertical motions and resistance for DTC container carrier in shallow water waves (WWC022)* Shuai Yuan, Li Xia, Zao-Jian Zou and Lu Zou School of Naval Architecture, Ocean and Civil Engineering, Shanghai Jiao Tong University, China ; State Key Laboratory of Ocean Engineering, Shanghai Jiao Tong University, China	*Description of hydro/meteo data in ship manoeuvring simulators: a survey on the state of the art (WWC031)* Luca Donatini, Marc Vantorre, Jeroen Verwilligen and Guillaume Delefortrie Maritime Technology Division, Ghent University, Belgium ; Flanders Hydraulics Research, Belgium
15:25 – 15:50	*Free running maneuvering tests of the DTC hull in calm water and regular waves with focus on uncertainty analysis based on repetition tests (WWC018)* Øyvind Rabliås and Trygve Kristiansen Dept. of Marine Technology, Norwegian University of Science and Technology, Norway ; SINTEF Ocean, Norway	*On the assessment of ship squat and wave motions for large containerships in shallow water in a real time maneuvering simulator (WWC042)* Eduardo A. Tannuri Universidade de São Paulo, São Paulo, Brazil
15:50 - 16:15	**Refreshment break**	

	SESSION 8 - Wind, waves and/or current Benchmark data (Chair: Prof. Zao-Jian Zou)	**SESSION 9 – Shallow water effects** (Chair: Dr. Katrien Eloot)
16:15 - 16:40	*Numerical assessment of added resistance in waves of the DTC container ship in finite water depths (WWC055)* Ivana Martić, Guillermo Chillcce, Manases Tello Ruiz, Jorge Ramirez, Nastia Degiuli and Bettar Ould El Moctar Faculty of Mechanical Engineering and Naval Architecture, University of Zagreb, Croatia ; Institute of Ship Technology, Ocean Engineering and Transport Systems (ISMT), the University of Duisburg-Essen, Germany ; Maritime Technology Division, Ghent University, Belgium ; Knud e Hansen A/S, Denmark	*Analysis of the flow conditions between the bottoms of the ship and of the waterway (WWC033)* Carl-Uwe Böttner, Pascal Anschau and Ivan Shevchuk Federal Waterways Engineering and Research Institute (BAW), Germany ; Schiffbau-Versuchsanstalt Potsdam, Germany ; Institute for Fluid Dynamics and Ship Theory, Hamburg University of Technology, Germany
16:40 – 17:05	*RANS evaluation of the DTC's vertical motion sailing in finite water depth waves (WWC056)* Guillermo Chillcce, Ivana Martić, , Manases Tello Ruiz, Jorge Ramirez, Nastia Degiuli and Bettar Ould El Moctar	*A nautical approach to the effect of ship parameters on wave impact on the intertidal river bank in the bend of Bath (WWC008)* Abed Benmestoura, Deirdre Luyckx, Peter Bueken and Stijn Temmerman

	Institute of Ship Technology, Ocean Engineering and Transport Systems (ISMT), the University of Duisburg-Essen, Germany ; Faculty of Mechanical Engineering and Naval Architecture, University of Zagreb, Croatia ; Maritime Technology Division, Ghent University, Belgium ; Knud e Hansen A/S, Denmark	Antwerp Maritime Academy, Belgium ; Department of Biology, University of Antwerp, Belgium
17:05 - 17:30	*A modular mathematical approach to predict the maneuvering ability of Duisburg Test Case in regular waves (WWC039)* Omer Kemal Kinaci, Omer Faruk Sukas and Sakir Bal Faculty of Naval Architecture and Ocean Engineering, Istanbul Technical University, Turkey	*Numerical investigation of scale effects on squat in shallow water (WWC035)* Ivan Shevchuk, Carl-Uwe Böttner and Nikolai Kornev Technical University Hamburg, Germany ; Federal Waterways Engineering and Research Institute (BAW), Germany ; University of Rostock, Germany

19:00 - 21:00	**Barbecue**

21 MAY 2019 (TUESDAY)

8:00 – 09:00	**Registration**
	MARC VANTORRE HONOURING SYMPOSIUM
09:00 – 09:45	**Invited Keynote Speech by Prof. Andrés Cura-Hochbaum**
	MARC VANTORRE HONOURING SYMPOSIUM – Pt. 1 (Chair: Prof. Andrés Cura-Hochbaum)
09:45 – 10:10	*Investigation of the nominal and effective propeller inflow for a family of inland waterway vessels (WWC009)* Benjamin Friedhoff, Katja Hoyern, Sven List and Matthias Tenzer Development Centre for Ship Technology and Transport Systems (DST), Germany
10:10 – 10:35	*Robustness and quality of squat predictions in shallow water conditions based on RANS-calculations (WWC014)* Jonas Bechthold and Marko Kastens Federal Waterways Engineering and Research Institute (BAW), Germany
10:35 – 10:50	**Refreshment break**
10:50 – 11:35	**Invited Keynote Speech by Dr. Vicky Stratigaki**
	MARC VANTORRE HONOURING SYMPOSIUM – Pt. 2 (Chair: Dr. Vicky Stratigaki)
11:35 – 12:00	*Shallow-water effects in ship model testing and at full scale (WWC010)* Hoyte C. Raven MARIN, The Netherlands
12:00 – 12:25	*Simulation study of approach manoeuvre in lightering and reverse lightering operations (WWC025)* Masaaki Sano and Hironori Yasukawa Department of Transportation and Environmental Systems, Hiroshima University, Japan
12:25 - 13:30	**Lunch**

	SESSION 10 – Wind, waves and/or current (Chair: Prof. Yonghwan Kim)	**SESSION 11 – Shallow and confined water** (Chair: Prof. Guillaume Delefortrie)
13:30 – 13:55	*An experimental study on the captive model test of KCS in regular waves (WWC037)* Hujae Choi, Dong Jin Kim, Yeon Gyu Kim, Dong Jin Yeo, Kunhang Yun and Gyeong Jung Lee Korea Research Institute of Ships and Ocean Engineering (KRISO), Rep. of Korea	*Shallow water power correction for high-speed vessels (WWC002)* Jan Richter, Lars-Uve Schrader, Oliver Reinholz Hamburg Ship Model Basin (HSVA), Germany
13:55 - 14:20	*The influence of wave drift forces coefficients in the assessment of navigable areas of ports and harbours exposed to high waves. Effect of vessel speed and wave spectrum considered (WWC012)* Raul Redondo, Juan Carlos Carmona and Raul Atienza Siport 21, Spain	*Shallow water effects on ship-generated waves (WWC011)* Qingsong Zeng, Cornel Thill and Robert Hekkenberg Maritime and Transport Technology, Delft University of Technology, The Netherlands
14:20 - 14:45	*Numerical and experimental study on the wave–body interaction problem with the effect of forward speed and finite water depth in regular waves (WWC064)*	*Coupling dynamic mooring analysis with sailing vessel effects for the estimation of mooring loads. A case study (WWC052)* Damián Villaverde Vega, Bart Verheyen and Francisco Aracil

	Tianlong Mei, Guillaume Delefortrie, Manases Tello Ruiz, Changyuan Chen, Evert Lataire, Marc Vantorre and Zaojian Zou School of Naval Architecture, Ocean and Civil Engineering, Shanghai Jiao Tong University, China ; Maritime Technology Division, Ghent University, Belgium ; Flanders Hydraulics Research, Belgium ; State Key Laboratory of Ocean Engineering, Shanghai Jiao Tong University, China	IMDC, Belgium
14:45 - 15:10	*Study on the maneuvering simulation of a ship with wave effect in regular waves (WWC019)* Yeon-Gyu Kim, Dong Jin Yeo, Dong-Jin Kim, Kunhang Yun, Gyeong-Joong Lee, Bo-Woo Nam and Min-Guk Seo Korea Research Institute of Ships and Ocean Engineering (KRISO), Rep. of Korea	*Manoeuvring simulation models for inland ships (WWC061)* Frans Quadvlieg, Chris Willemsen, Wytze de Boer and Guido Oud MARIN, The Netherlands
15:10 - 15:35	**Refreshment break**	

	SESSION 12 - Shallow water effects (Chair: Dr. Tim Gourlay)	**SESSION 13 – Ship – ship interaction** (Chair: Prof. Yoshitaka Furukawa)
15:35 - 16:00	*The naval battle of Actium and the myth of the ship-holder : The effect of bathymetry (WWC007)* Johan Fourdrinoy, Clément Caplier, Yann Devaux, Germain Rousseaux, Areti Gianni, Ierotheos Zacharias, Isabelle Jouteur, Paul Martin, Julien Dambrine, Madalina Petcu and Morgan Pierre CNRS – Université de Poitiers – ISAE-ENSMA, Institut Pprime, France ; University of Patras, Greece ; Université de Poitiers, Forellis, France ; Université de Montpellier, France ; Université de Poitiers, Laboratoire de Mathématiques et Applications, France	*Detailed assessment of navigable areas for encounter manoeuvres by means of numerical models and real time manoeuvring simulation (WWC013)* Lourdes Pecharroman, Raul Atienza, Carlos Cal, Raul Redondo and Miguel de Ros Siport 21, Spain
16:00 - 16:25	*Numerical study on the effect of operating water depth on the turning maneuver of a container ship (WWC020)* Akhil Balagopalan and P Krishnankutty Department of Ocean Engineering, Indian Institute of Technology Madras, India	*Transient response of a moored vessel induced by a passing ship (WWC003)* Liang Li and Zhi-Ming Yuan Department of Naval Architecture, Ocean and Marine Engineering, University of Strathclyde, UK
16:25 - 16:50	*Shallow water surge resistance identification for inland vessels (WWC034)* Arne Eggers, Gerben Peeters, Peter Slaets and Maarten Vanierschot Mechanical Engineering Technology Cluster TC , KU Leuven, Belgium	*An economical algorithm for computation of ship to ship interaction forces in real time (WWC004)* Grigory Vilenskiy SimTech Ltd., Russia

19:30 – 23:00	**Conference Dinner**

22 MAY 2019 (WEDNESDAY)

09:00 – 12:00	**Technical visit of the Towing Tank for Manoeuvres in Shallow Water**
12:30 – 13:30	**Lunch**
13:30 – 14:15	**Invited Keynote Speech by Prof. Hironori Yasukawa**
	SESSION 14 – Wind, waves and/or current (Chair: Prof. Hironori Yasukawa)
14:15 – 14:40	*Initial and steady turning characteristics of KRISO container ship (KCS) in regular waves (WWC065)* Dong Jin Kim, Kunhang Yun, Dong Jin Yeo, Yeon Gyu Kim Korea Research Institute of Ships & Ocean Engineering (KRISO), Rep. of Korea
14:40 - 15:05	*Real-time estimation of the ship maneuverable range in wind (WWC050)* Toshio Iseki Tokyo University of Marine Science and Technology Japan
15:05 - 15:20	**Refreshment break**
	SESSION 15 – Numerical modelling (Chair: Prof. Evert Lataire)
15:20 - 15:55	*Numerical modelling of the muddy layer effect on ship squat and resistance (WWC060)* Sami Kaidi, Mohamed Ali, Emmanuel Lefrançois and Hassan Smaoui CEREMA-DtecEMF, France ; Sorbonne universités, Université de technologie de Compiègne, laboratoire Roberval, France
15:55 - 16:20	*Estimation of mathematical model for ship maneuvering in waves based on estimation-before-modeling technique (WWC058)* MyungJun Jeon, Hyeon Kyu Yoon and Dong Jin Kim Changwon National University, Korea ; Korea Research Institute of Ships & Ocean Engineering, Rep. of Korea
16:20 – 16:55	*Prediction of ship-lock interaction by using a modified potential flow solver (WWC005)* Zhiming Yuan Department of Naval Architecture, Ocean and Marine Engineering, University of Strathclyde, UK
16:55 – 17:00	**Closing Words by Prof. Evert Lataire**

23 MAY 2019 (THURSDAY)

09:00 – 13:00	**Optional excursion:** **Technical visit to the Port of Zeebrugge**

NUMERICAL STUDY ON THE EFFECT OF OPERATING WATER DEPTH ON THE TURNING MANEUVER OF A CONTAINER SHIP

Akhil Balagopalan and **P. Krishnankuttty**,
Department of Ocean Engineering, Indian Institute of Technology Madras, India

NUMERICAL STUDY ON THE EFFECT OF OPERATING WATER DEPTH ON THE TURNING MANEUVER OF A CONTAINER SHIP

Akhil Balagopalan and **P Krishnankuttty,** Department of Ocean Engineering, Indian Institute of Technology Madras, India

SUMMARY

In shallow water, the flow around a ship modifies considerably and the hydrodynamic derivatives appearing in the ships maneuvering equations of motion also changes. Vessels operating in such lower water depth regions become sluggish and also respond poorly to the use of control surfaces. This paper aims to study the shallow water effects on maneuvering performance of a container ship by simulating standard turning circle test. PMM tests are conducted for different water depths ranging from very shallow (h/T=1.2) to deep water (h/T>3) conditions using a commercial CFD package. Free running model test is also conducted in a maneuvering basin to validate the numerical simulations.

NOMENCLATURE

a_H	Rudder force increase factor
A_R	Profile area of the rudder (m^2)
B	Breadth (m)
C_B	Block coefficient
C_M	Midship area coefficient
D	Depth (m)
D_P	Diameter of the propeller
F_N	Rudder normal force
H_R	Rudder span length
K_T	Open water thrust coefficient
I_Z	Moment of inertia in Z direction
L_{BP}	Length between perpendiculars (m)
L_{WL}	Length of waterline (m)
m	Mass of the ship (kg)
N_H	Yaw moment acting on ship hull
N_P	Yaw moment due to propeller
N_R	Yaw moment due to rudder
N_v	Derivative of yaw moment with respect to yaw rate
N_{rrr}	Third order coupled hydrodynamic derivative of yaw moment with respect to yaw rate
$N_{\dot{r}}$	Derivative of yaw moment with respect to yaw acceleration
N_v	Derivative of yaw moment with respect to sway velocity
$N_{\dot{v}}$	Derivative of yaw moment with respect to sway acceleration
N_{vrr}	Third order cross coupled hydrodynamic derivative of yaw moment with respect to sway velocity and yaw rate
N_{vvr}	Third order cross coupled hydrodynamic derivative of yaw moment with respect to sway velocity and yaw rate
N_{vvv}	Third order coupled hydrodynamic derivative of yaw moment with respect to sway velocity
r	Yaw rate (rad/s)
$\dot{r}$	Yaw acceleration (rad/s^2)
S	Wetted surface area (m^2)
$t^{'}$	Non dimensional time
t_P	Thrust deduction factor
T	Draft of the ship (m)
T_P	Propeller thrust
U_m	Model speed (m/s)
u_R	Longitudinal rudder inflow velocity
$\dot{u}$	Surge acceleration (m/s^2)
v	Sway velocity (m/s)
v_R	Lateral rudder inflow velocity
$\dot{v}$	Sway acceleration (m/s^2)
$X_{\dot{u}}$	Hydrodynamic derivative in surge with respect to surge acceleration
x_R	Longitudinal position of rudder (m)
X_H	Surge force acting on ship hull
X_P	Surge force due to propeller
X_R	Surge force due to rudder
X_{rr}	Second order hydrodynamic derivative of surge force due to sway yaw rate
X_{uu}	Second order hydrodynamic derivative of surge force due to surge velocity
X_{vv}	Second order hydrodynamic derivative of surge force due to sway velocity
X_{vr}	Second order coupled hydrodynamic derivative of surge force due to sway velocity and yaw rate
Y_H	Sway force acting on the hull
Y_P	Sway force due to propeller
Y_R	Sway force due to rudder
Y_r	Hydrodynamic derivative of sway force with respect to yaw rate
Y_{rrr}	Third order coupled hydrodynamic derivative of sway force with respect to yaw rate
$Y_{\dot{r}}$	Hydrodynamic derivative of sway force with respect to yaw acceleration
Y_v	Hydrodynamic derivative of sway force with respect to sway velocity
$Y_{\dot{v}}$	Hydrodynamic derivative of sway force with respect to sway acceleration

Y_{vrr}	Third order cross coupled hydrodynamic derivative of sway force with respect to sway velocity and yaw rate
Y_{vvr}	Third order cross coupled hydrodynamic derivative of sway force with respect to sway velocity and yaw rate
Y_{vvv}	Third order coupled hydrodynamic derivative of sway force with respect to sway velocity
Ψ	yaw angle (degree)
α_R	effective inflow angle to rudder
β	Drift angle (degree)
δ	Rudder angle (degree)
λ	Aspect ratio of the rudder
ω_P	Wake fraction
ρ	Density of water (kg/m^3)

1 INTRODUCTION

Correct determination of hydrodynamic derivatives appearing in the maneuvering equations of motion of a marine vehicle is essential for the accurate prediction of its maneuvering performance. Solution of these equations leads to the simulation of the ship motions in the horizontal plane for a surface ship and thus help in understanding its course stability, turning ability, rudder effectiveness and ship responsiveness. The hydrodynamic derivatives are usually determined experimentally using Planar Motion Mechanism (PMM) setup which is attached to the towing carriage in a towing tank. Standard definitive maneuvers such as turning circle and zig-zag are simulated using the estimated hydrodynamic derivatives. Even though experimental methods are more reliable, these facilities are rare and often prohibitively expensive. More viable option, primarily during the early stages of the ship design, is to determine these derivatives numerically. Most of the ship maneuvering studies and regulations are in deep water conditions, whereas the ship maneuvering performance is much worse in shallow waters and its controllability is difficult. In shallow waters, the flow around the vessel changes, vessel becomes sluggish and hence it influences the maneuvering performance of the vessel.

Esso Osaka test program by Crane *et.al* (1979) is a classic benchmark experimental test in which shallow water effects on maneuvering of a tanker ship are examined at full scale. Shallow water simulations are normally conducted at model scales. PMM experimental test in shallow water for *Esso Osaka* in a model scale by Bogdanov *et.al* (1987) has given good result when compared with that of the full scale test. PMM experiments are used for shallow water studies by various researchers such as Fabbri *et al.* (2005), Yeo et *al.*(2013) etc. and Delefortrie and Vantorre (2007) developed a mathematical model for shallow water conditions covering various range of water depths. RANSE based CFD solvers are widely used nowadays to study the water depth effects on ships maneuverability [Sakamoto *et al.* (2007); S. L. Toxopeus *et al.* (2013)]. SIMMAN 2008 & 2014 workshops provided benchmark examples for the prediction capabilities of different ship manoeuvring simulation methods through systematic quantitative comparisons and validation against EFD data for tanker - KVLCC, container ship -KCS, and surface combatant-5415.

An attempt is made in this paper to study the shallow water effects on the manoeuvring performance of a vessel using numerical Planar Motion Mechanism (PMM) test. KRISO Container Ship (KCS), a benchmark example used by different research groups, is taken for the present study. Planar Motion Mechanism (PMM) tests are performed in a numerical environment using commercial CFD package Star CCM+. Guidelines for the numerical studies are followed as prescribed by ITTC. These numerical tests are conducted in both deep water (h/T>3) and in shallow water conditions (h/T=1.2, 1.5, 2). Effects of water depth on the ship maneuvering characteristics are evaluated by simulating turning circle trajectory. Experimental free running test was also conducted in deep water condition in a maneuvering basin.

2 MATHEMATICAL MODEL

2.1 COORDINATE SYSTEM

The coordinate system used for the present work is shown in Fig. 1. Right handed coordinate system is used for representing earth fixed (EX_0, EY_0) as well as ship fixed (x, y) coordinate systems. Origin of the ship fixed coordinate system is located at the center of gravity of the ship O.

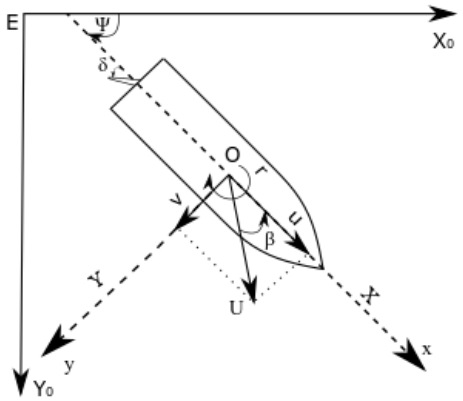

Figure 1. Coordinate System

2.2 EQUATIONS OF MOTION

The mathematical model used for the present study is based on the Maneuvering Modelling Group (MMG) model [Ogawa *et al.* (1977)] described in the Bulletin of Society of Naval Architecture of Japan in 1977. The present study considers the motion of vessel in horizontal plane and roll effects are not taken into consideration.

Maneuvering equations of motion of a surface ship in horizontal plane is represented by the following equations.

$$(m - X_{\dot{u}})\dot{u} - (m - Y_{\dot{v}})vr = X_H + X_P + X_R \quad (1)$$

$$(m - Y_{\dot{v}})\dot{v} + (m - X_{\dot{u}})ur - Y_{\dot{r}}\dot{r} = Y_H + Y_P + Y_R \quad (2)$$

$$(I_Z - N_{\dot{r}})\dot{r} + N_{\dot{v}}\dot{v} = N_H + N_P + N_R \quad (3)$$

X_H, Y_H, N_H represents the hydrodynamic force and moments acting on the hull in surge, sway and yaw motions. X_P, Y_P, X_R and Y_R represents the forces induced by the propeller and rudder in surge and sway directions. N_P and N_R represents the moments induced by the propeller and rudder respectively.

X_H, Y_H and N_H are represented as a function of coupled and nonlinear hull derivatives as follows.

$$X_H = X_{\dot{u}}\dot{u} + Y_{\dot{v}}vr + X_{|u|u}\,u|u| + X_{vr}vr + X_{vv}v^2 + X_{rr}r^2 \quad (4)$$

$$Y_H = X_{\dot{u}}ur + Y_{\dot{v}}\dot{v} + Y_{\dot{r}}\dot{r} + Y_v v + Y_r r + Y_{vvv}v^3 + Y_{rrr}r^3 + Y_{vvr}v^2 r + Y_{vrr}vr^2 \quad (5)$$

$$N_H = N_{\dot{v}}\dot{v} + N_{\dot{r}}\dot{r} + N_v v + N_r r + N_{vvv}v^3 + N_{rrr}r^3 + N_{vvr}v^2 r + N_{vrr}vr^2 \quad (6)$$

Rudder and propeller forces are calculated using the following equations [7-10]

$$X_R = -(1-t_R)\,F_N \sin\delta \quad (7)$$

$$Y_R = -(1+a_H)\,F_N \cos\delta \quad (8)$$

$$N_R = -(1+a_H)\,x_H\,F_N \cos\delta \quad (9)$$

$$X_P = (1-t_P)\,T_P \quad (10)$$

F_N is the rudder normal force, a_H is rudder force increase factor, x_H is the longitudinal coordinate of the lateral force in steering, t_p is thrust deduction factor and T_P is the thrust produced by the propeller

2.3 SHALLOW WATER COMPENSATION FOR RUDDER AND PROPELLER EFFECTS

Wake fraction correction due to the variation in water depth is generally applied by the formulae proposed by Yasukawa (1998) but is applicable for ships with high block coefficients. So empirical formulas proposed by Osman Md Amin et al. (2008) is used in this paper for wake fraction correction and thrust deduction fraction. Shallow water compensation for longitudinal and lateral inflow velocity to rudder is given using the formulae's proposed by Kobayashi (1995).

3 NUMERICAL STUDY

3.1 SHIP MODEL

Figure 2.KCS Model

KCS (KRISO Container Ship) model, a benchmark container ship which is being used by various research organizations around the world, is taken for the present study (Fig.2). Model scale ratio of 1:75.5 is selected by considering the limitations of Towing Tank facility available at IIT Madras, India and also to match with the scale used by NMRI, Japan, thus making the comparison of the results and/or validation of the present study straight forward. Main particulars of the vessel and model details are given in Table 1.

Table 1. Particulars of the ship

Main Particulars	Full Scale	Model (1:75.5)
L_{bp} (m)	230	3.0464
L_{wl} (m)	232.5	3.0791
B (m)	32.2	0.4265
D (m)	19	0.2517
T (m)	10.8	0.1430
Displacement (m^3)	52030	0.1209
Wetted surface area (m^2)	9530	1.6719
C_b	0.651	0.651
C_m	0.985	0.985

3.2 COMPUTATIONAL DOMAIN AND BOUNDARY CONDITIONS

RANSE based commercial CFD package Star CCM+ is used for the present work. Different computational domains are created based on water depth conditions. Fluid domain dimensions are selected based on ITTC Standards and are given in Table 2. Boundary conditions for the deep water domain are as follows- inlet as velocity inlet, outlet as pressure outlet and slip wall conditions at sides, bottom and top. No slip wall conditions is applied at the hull surface. For the shallow water cases, bottom is given a no slip wall condition to capture the relative velocity effect happening between the hull and sea bed. Wave damping option is enabled on the side walls to avoid the wave reflections. SST k-ω (Menter,1993) turbulence model which is a variance of k-ω turbulence model being used by researchers (Simonsen *et al.,*2012; Shenoi *et al.,*2014) for similar maneuvering problems is selected for the present study. Volume of Fluid (VOF) model is enabled to capture the free surface effect at the air water interface. Three dimensional segregated implicit unsteady method used as flow solver. Governing equations were solved with a time interval of 0.01s.

Table 2. Computational domains

Direction	h/T=1.2	h/T=1.5	h/T=2	Deep (h/T=32)
Forward	2 L_{bp}	2 L_{bp}	2 L_{bp}	2 L_{bp}
Aft	3 L_{bp}	3 L_{bp}	3 L_{bp}	3 L_{bp}
Side	3 L_{bp}	3 L_{bp}	3 L_{bp}	3 L_{bp}
Deck to top	1.5 L_{bp}	1.5 L_{bp}	1.5L_{bp}	1.5 L_{bp}
Keel to bottom	0.00938 L_{bp}	0.0.234 L_{bp}	0.0469 L_{bp}	1.5 L_{bp}

3.3 SELECTION OF GRID AND DEPENDENCY STUDY

Unstructured trimmed hexahedral mesh is generated with near wall prismatic layers. Separate volumetric blocks with refined mesh density is created at bow, stern and at free surface. Mesh generated around the ship model is given in Fig.3 & Fig. 4.

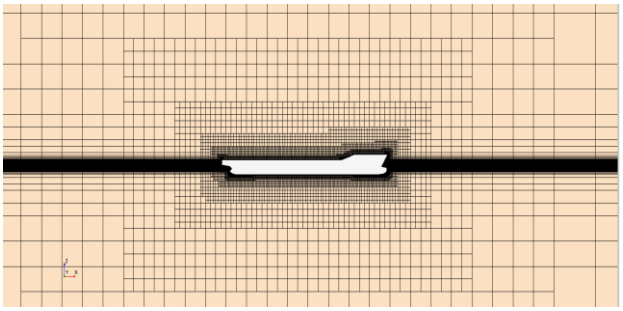

Figure 3. Mesh configuration around the vessel

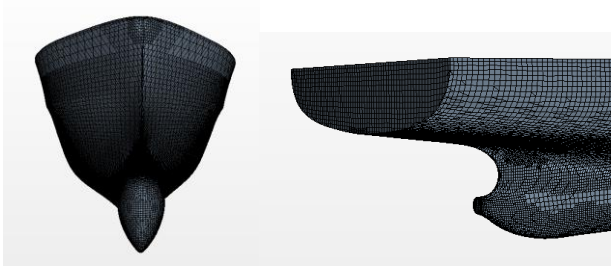

Figure 4. Mesh configuration at bow and stern

Grid dependence study has been carried out to ensure that the numerical results are not affected by the base size/no of cells. Three different meshes (fine, medium and coarse) are created based on the grid refinement ratio of $\sqrt{2}$ to analyse the grid dependency. Straight line test is conducted at a drift angle of 15 degrees for all the three meshes. Total hydrodynamic force acting on the vessel in x, y direction and the moment in z direction are estimated by giving an inflow velocity of 1.1m/s. Grid independence test results for 15^0 straight line test is given in Table 3.

Table 3. Straight line test results

Grid	No of cells (millions)	X'	Y'	N'
Coarse	1.13	-0.002468	0.005048	0.001844
Medium	1.81	-0.002440	0.004991	0.001782
Fine	2.46	-0.002441	0.004997	0.001794

Forces and moments are non-dimensionalised by using the following relations.

$$X' = \frac{X}{0.5\rho L_{bp}{}^2 U^2} \tag{11}$$

$$Y' = \frac{Y}{0.5\rho L_{bp}{}^2 U^2} \tag{12}$$

$$N' = \frac{N}{0.5\rho L_{bp}{}^3 U^2} \tag{13}$$

Grid convergence ratio R_G is estimated by using the following relation

$$R_G = \varepsilon_{21}/\varepsilon_{32} \tag{14}$$

Where ε_{32} is the change in result from coarse to medium grid for the forces *X', Y'* and moment *Z'* and ε_{21} is the change in result from medium grid to fine grid for the forces *X', Y'* and moment *Z'*. Oscillatory convergence is obtained from the drift angle test with R_G values -0.2778, -0.1043, -0.1875 for forces *X', Y'* and moment *Z'* respectively. Change in results ranges from 1.14% to 3.15% from coarse to medium and less than 0.65% for medium to fine.

It can be seen from the analysis that the change in grid from medium to fine doesn't have much influence on the solution result and moreover increases the computational time also. Hence it was decided to go with medium meshing for the further numerical analysis.

3.4 PMM SIMULATIONS

Pure sway, pure yaw and combined modes of operations in Planar Motion Mechanism are simulated numerically. Maximum sway amplitude of oscillation in all the three modes are kept as 0.3m. Frequency of oscillation in pure sway mode is taken as 0.628 *rad/s*, following ITTC guidelines (IITC2011; Vantorre *et al.,*1997). In pure yaw mode and in combined mode, 0.785 *rad/s* is considered for the numerical simulation (IITC2011; Vantorre *et al*.,1997) For the present study, drift angle of 3 degree is given in the combined mode of PMM oscillation.

3.5 DETERMINATION OF HYDRODYNAMIC DERIVATIVES

Time history of surge force, sway force and yaw moments acting at the center of gravity of the vessel for all the three modes of PMM motion (pure sway, pure yaw and yaw

with drift) are calculated from CFD. These hydrodynamic forces and moments are fitted into Fourier series and the hydrodynamic derivatives are found out by equating the Fourier coefficients with the corresponding derivatives appearing in the mathematical model given in equations [4-6].

4 FREE RUNNING EXPERIMENTAL TEST

Free running model test is conducted at Seakeeping and Manoeuvring Basin (SMB) facility available at Naval Science and Technical Laboratory (NSTL), India. Loading conditions and moment of inertias are scaled down suitably and the dynamic similarity between the model and prototype is maintained throughout the experiment as mentioned by ITTC (ITTC Recommended Procedures and Guidelines). Standard 35 degree turning circle test (Fig. 5) is conducted at model self-propulsion point corresponding to the speed of 1.4 m/s which is 98% of the service speed of the model.

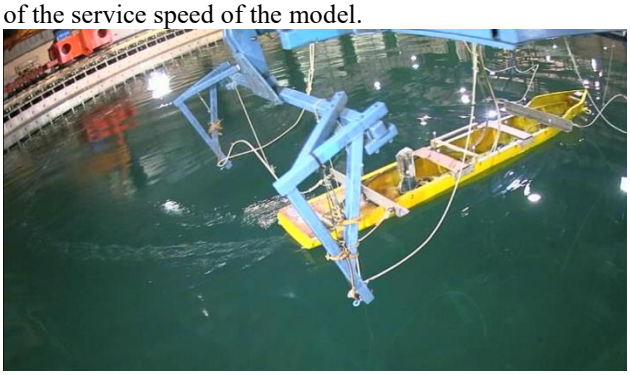

Fig. 5 Turning circle experimental test

5 RESULTS AND DISCUSSION

5.1 DEEP WATER CASE

Numerical simulation of planar motion mechanism has been carried out, hydrodynamic derivatives are estimated and turning characteristic of KCS container ship is simulated for 35 degree turning circle by solving the equations of motions. Numerical simulations are conducted for an inlet velocity of 1.4 m/s. Fig. 6 shows the comparison between numerical PMM generated turning circle and the experimental free running turning circle for deep water condition.

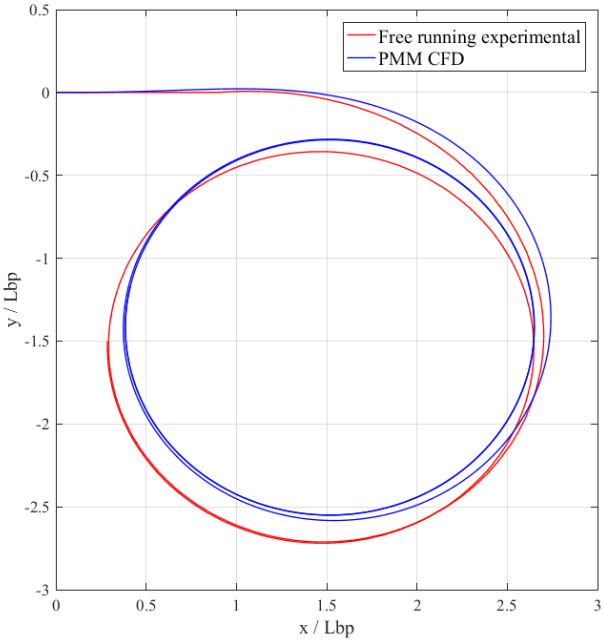

Figure 6. Turning circle trajectory for deep water

Numerical and experimental test results are showing a good match in general for the deep water condition. Major turning particulars are listed in Table 2. It is observed that the tactical diameter is having a 5.1% variation between CFD and experimental values. Steady turning radius has a very close match between CFD and experimental readings. Variation is about 3.64 % for advance.

Table 4. Numerical and experimental turning parameters for deep water condition

Parameter	CFD PMM	Free running experimental
Tactical diameter	2.585 L_{bp}	2.71 L_{bp}
Advance	2.754 L_{bp}	2.85 L_{bp}
Steady turning radius	1.145 L_{bp}	1.175 L_{bp}

5.2 SHALLOW WATER CASE

PMM simulations are conducted for three different water depth conditions ranging from very shallow to medium ie. h/T=1.2, 1.5 and 2. Inlet velocity in shallow water simulations are reduced to 0.55 m/s by considering the excessive sinkage and trim occurs due to the bottom contraints. Hydrodynamic reaction forces and moments acting on the vessel are estimated numerically in all the three modes of PMM oscaillations. Tests are repeated for all the three water depth conditions. These forces and moments obtained are used to find out the hydodynamic derivatives appearing in the equations of motion using Fourier series representation. Estimated hydrodynamic derivatives are input into the equations of motion and sloved it numerically and turning trajectories are simulated for 35 degree turn. Simulated turning trajectoires for different water depth conditions are plotted in Figure 7.

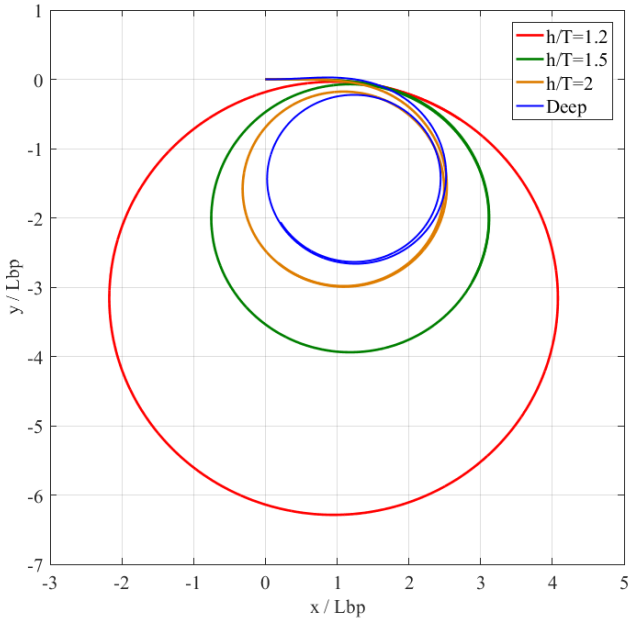

Figure 7. Turning circle trajectory for different water depth.

It can be observed from the turning circle trajectory that the turning parameters such as tactical diameter, advance and steady turning radius increases significantly with decrease in under keel clearance. Comparison of the major turning parameters for the vessel in different water depth conditions in terms of vessel length (L_{bp}) are given in Figures 8,9 and 10.

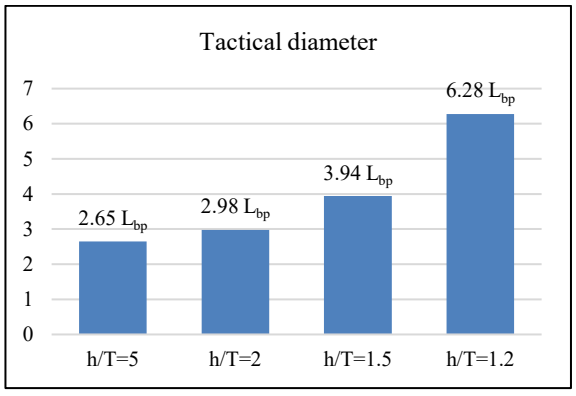

Figure 8. Tactical diameter

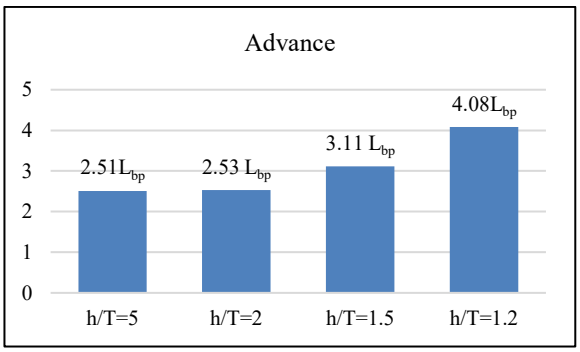

Figure 9. Advance

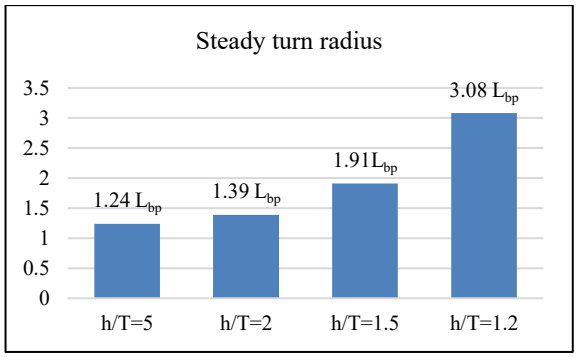

Figure 10. Steady turning radius

Tactical diameter has increased 137% when the water depth changes from deep to very shallow condition (h//T=1.2). Steady turning radius also follows the same trend and increases 148% when compared to deep water case. Advance has a relatively moderate effect on water depth and has increased 62%. Substantial increment for the turning parameters are followed by the reduction in yaw rate and speed loss. Rate at which the vessel is taking turn for the same aproach speed in differernt water depth conditions are plotted in Figure 11 and the corresponding speed loss is plotted in Figure 12.

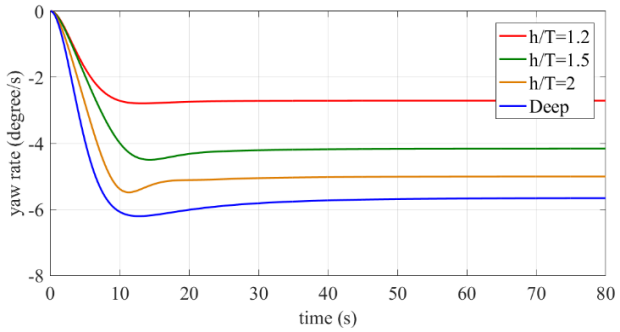

Figure 11. Rate of turn

Rate of turn decreses substantially corresponding to the change in water depth. Vesel which becomes steady with a turning rate of 5.7 degree/s in deep water has a steady turn rate of 2.7 degree/s for a depth of 1.2 times draft. Yaw rate gradually reduces when the vesel moves from deep to shallow water conditon. For 1.5T and 2T water depth the corresponding turning rates are 4.1degree/s and 5 degree/s. Speed loss in turning reduces with decrease in water depth. Vessel with an aproach speed of 0.55 m/s becomes steady at 0.34 m/s in deep water attains a steady speed of 0.45 m/s in 1.2T water depth condition, a marginal decrement in speed loss of about 32%. 1.5T and 2T water depth also reduces the speed loss by 23% and 11% respectively.

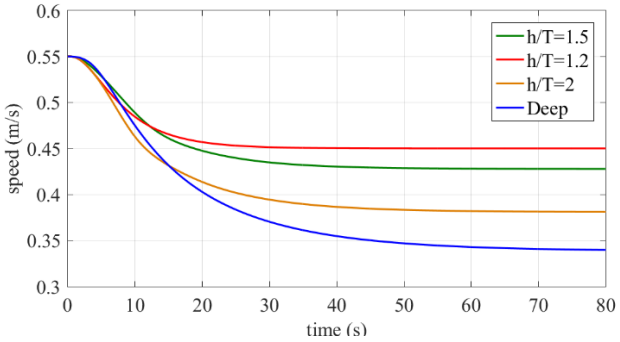

Figure 12. Speed loss in turning

Angle between the ships central axis and the tangent to its path in turning, called drift angle reduces with decrese in water depth (Figure 13). Increase in lateral forces and moments associated with the decrease in water depth will tend to reduce the drift angle of the vessel. Vessel in deep water with a steady drift angle of 4 degree reduces to 0.5 degree in 1.2T. Drift angle in 1.5T and 2T are 1 degree and 3 degree respectively.

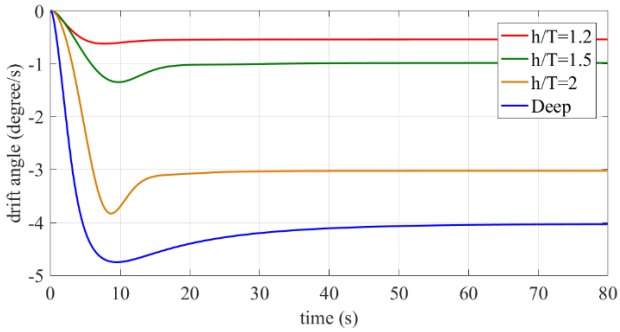

Figure 13. Drift angle

6 CONCLUSION

In the present study numerical simulation of planar motion mechanism is carried out for different water depths, hydrodynamic derivatives are estimated and standard 35 degree turning circle test of a container ship is simulated by solving the equations of motion. A detailed study of turning trajectory, speed loss in turning, yaw rate and drift angle are listed for all the water depth conditions. Free running turning circle experimental test which is conducted in the maneuvering basin gives a close match to that of the deep water numerical test. Even though the deep water numerical studies are validated experimentally, shallow water cases should also be verified to confirm its validity. Present numerical study is a part of the ongoing shallow water maneuvering research work at IIT Madras, India. Shallow water numerical results will be verified using the experimental techniques as a part of the project.

7 REFERENCES

Bogdanov, P, Vassilev, P, Lefterova, M, Milanov, , 1987 “Esso Osaka” tanker manoeuvrability investigations in deep and shallow water, using PMM, International Shipbuilding Progress, vol. 34, no. 390, pp. 30-39.

Crane, C.L., jr., 1979a, Maneuvering Trials of the 278,000 DWT Esso Osaka in Shallow and Deep Water, Transactions of the SNAME, Vol. 87, pp. 251-283.

Delefortrie, G., M. Vantorre, 2007. Modeling the maneuvering behaviour of container carriers in shallow water. Journal of Ship Research, 51(4), pp.287-296

Fabbri, L., Benedetti, L., Bouscasse, B., F. La Gala and C. Lugni, 2005. An experimental maneuverability study on the effect of water depth for blunt ships. A research report submitted to INSEAN (The Italian Ship Model Basin), Italy.

ITTC, 2002. Full scale measurements manoeuvrability full scale manoeuvring trials procedure. ITTC Recommended Procedures 7.5-04-02-01. Proceedings of 23th International Towing Tank Conference, 8-14 September, Venice, Italy.

ITTC, 2011a. Practical Guidelines for ship CFD application. ITTC Recommended Procedures and Guidelines 7.5-03-02-03. Proceedings of 26th International Towing Tank Conference, August 28-September 3, Rio de Janeiro, Brazil.

ITTC, 2011b. Guidelines on use of RANS tools for maneuverability prediction. ITTC Recommended Procedures and Guidelines 7.5-03-04-01. Proceedings of 26th International Towing Tank Conference, August 28-September 3, Rio de Janeiro, Brazil

Kobayashi, E, 1995. The development of practical simulation system to evaluate ship maneuverability in shallow water, Proceedings PRADS95, pp. 1.712-1.723.

Menter, F.R., 1993. Zonal Two Equation k-ω turbulence models for aerodynamic flows". AIAA Paper. 93-2906

Ogawa A, Koyama T, Kijima K., 1977. MMG report-I, on the mathematical model of ship maneuvering. Bull Soc naval Archit. Jpn. 575:22-28

Sakamoto, N., Wilson, R. V., Stern, F., 2007. Reynolds-Averaged Navier-Stokes simulations for high-speed wigley hull in deep and shallow water. Journal of Ship Research, 51(3), pp.187-203.

SIMMAN, 2014. Workshop on Verification and Validation of Ship Manoeuvring Simulation Methods. www.SIMMAN2014.dk

Simonsen, C.D., Otzen, J.F., Klimt, C., Larsen L., Stern, F., 2012. Maneuvering predictions in the early design phase using CFD generated PMM data. Proceedings of 29th Symposium on Naval Hydrodynamics, August 26-31, Gothenburg, Sweden.

Shenoi R., Krishnankutty, P., Selvam, R. P., 2014. Study of manoeuvrability of container ship by static and dynamic simulations using RANSE based solver. Journal of Ships and Offshore Structures. http://dx.doi.org/10.1080/17445302.2014.987439

Toxopeus, S. L., Simonsen, C. D., Guilmineau, E., Visonneau, M., Xing, T., Stern, F. , 2013. Investigation of water depth and basin wall effects on KVLCC2 in manoeuvring motion using viscous-flow calculations. J Mar Sci Technol , DOI 10.1007/s00773-013-0221-6

Vantorre, M., Eloot, K., 1997. Requirements for standard harmonic captive manoeuvring tests. Proceedings of 4th IFAC Conference on Manoeuvring and Control of Marine Craft: MCMC'97, September 10-12, Brijuni, Croatia, pp. 93-98.

Yasukawa, H., 1998. Computation of effective rudder forces of a ship in shallow water, Symposium of forces acting on a maneuvering vessel (MAN98), Val de Reuil, pp 125-133.

Yeo, D., Yun, K., Kim, Y., Kim, S., 2013. Benchmark HPMM tests for KCS in shallow water. Proceedings of 3rd International Conference on ship Manoeuvring in Shallow and Confined Waters, Ghent, Belgium, pp.249-255.

8 AUTHORS BIOGRAPHY

Akhil Balagopalan is a naval architect and PhD research scholar in the Department of Ocean Engineering, IIT Madras, India. His research topic includes experimental and numerical techniques in maneuvering of ships with an emphasis on shallow water effects.

P Krishnankutty, naval architect, senior professor in the Department of Ocean Engineering, IIT Madras India. His major fields of interest are ship maneuvering and motions, ocean wave structure interaction, ship to ship hydrodynamic interactions and biomimetic propulsion systems.

ROBUSTNESS AND QUALITY OF SQUAT PREDICTIONS IN SHALLOW WATER CONDITIONS BASED ON RANS-CALCULATIONS

Jonas Bechthold and **Marko Kastens**,
Federal Waterways Engineering and Research Institute, Hamburg, Germany

ROBUSTNESS AND QUALITY OF SQUAT PREDICTIONS IN SHALLOW WATER CONDITIONS BASED ON RANS-CALCULATIONS

Jonas Bechthold and **Marko Kastens,** Federal Waterways Engineering and Research Institute, Hamburg, Germany

SUMMARY

Estimating ship squat is necessary to maintain safe navigation in the approach channel. The trim pattern of ships in shallow and restricted water can vary from trim bow down to stern down or variable trim orientation in dependence of the speed. The sinkage and trim pattern of three Postpanmax container ships in shallow and confined water are predicted by using a RANSE based CFD method, and the developed CFD setup is applied to the DTC container ship of the 5th MASHCON 2019. The predicted results are compared with the model test data to analyze the robustness of the CFD method and the quality of squat prediction. The presented RANS method is robust and the quality of the predicted squat values is better than 20 % deviation. When both CFD and EFD share the same model setup, the prediction deviation is less than 10 %.

NOMENCLATURE

A_{ms}	Underwater midship section area (m²)
A_c	Underwater section area of the channel (m²)
B	Beam (m)
B_S	Bias (-)
c_B	Block coefficient (-)
c_p	Pressure coefficient (-)
F_h	Depth Froude number (-)
g	Gravitational acceleration (m/s²)
h	Water depth (m)
L_{PP}	Length between perpendiculars (m)
λ	Scale factor (-)
S	Blockage factor (-)
S_{Bow}	Squat at bow position (m)
S_{CoG}	Sinkage at ship's center of gravity (m)
S_{Stern}	Squat at stern position (m)
T	Draft (m)
V	Ship speed (m/s)
∇	Displacement (m³)
Q	Quality score (-)

BAW	Federal Waterways Engineering and Research Institute
CoG	Ship's center of gravity
DTC	Duisburg Test Case
PPM	Postpanmax container ship
UKC	Under keel clearance
WSV	Waterways and shipping administration

1 INTRODUCTION

The prediction of squat for ships in extreme shallow water conditions is important to maintain safe navigation in channels and harbors. When large squat occurs at small under keel clearance (UKC), the ship can encounter grounding. This can damage both the ship and the waterway infrastructure. Ship dimensions have continued to grow in the last years. Harbors, such as the port of Hamburg together with federal authorities, have to adapt the navigation channel to provide unobstructed and safe access to the port. Predicting squat in advance is vital for this task.

The Federal Waterways Engineering and Research Institute (BAW) provides engineering consultancy work for the waterways and shipping administration (WSV) in Germany. This includes simulations of ship hydrodynamics in shallow water for the design of waterways. In this context, squat is an important parameter to estimate the dimensions of navigational channels.

In the past, physical model tests were conducted for this task. RANSE based CFD simulations can be used if these models are validated with experimental data to maintain the reliability of the results. For the used CFD model it is important to cover a wide range of ships and geometrical setups to ensure the robustness of the method. In this study, the robustness of the developed setup is presented by simulating trim and sinkage for ships with different trim and sinkage patterns.

Assessing the quality and uncertainty of predicted results is important for the engineering consultancy work. In particular, the reliability of trim predictions has not been investigated extensively. The accuracy of sinkage and trim predictions in this study is evaluated by a comparison between model test data and computed results of CFD simulations.

Additionally, the developed setup is used to calculate sinkage and trim for the 5th MASHCON 2019 benchmark case, in which the DTC (Duisburg Test Case) is experimentally tested. Results of simulations and model tests are presented and compared with each other.

2 STATE OF THE ART OF SQUAT CALCULATION

When entering shallow water, the flow field around the ship changes. The flow velocity around the hull and between the channel floor and keel increases, which causes a dynamic sinkage and trim of the ship. Sinkage combined with the trim angle determines the maximum occurring squat either at the bow or the stern of the ship.

This maximum squat is important for the design of waterways.

For waterways, three different channel conditions exist: Unrestricted channels with no lateral boundaries, confined or restricted channels with an underwater trench, or canals, which have emergent banks at the side, often represented as a single slope. In canals, the strongest influence of the geometrical boundaries on the sinkage and trim is observed. Therefore, this paper focusses on ships in canals.

Several parameters influence ship squat: Water depth h to draft T ratio (h/T), blockage factor S, ship speed V as well as the underwater hull shape of the ship with the associated block coefficient c_B. Decreasing water depth leads to increased flow velocity around the hull with larger squat. To describe the influence of geometrical boundaries on squat, the blockage factor S is used. It is defined as the ratio of the underwater section area of the channel A_c to the underwater midship section area A_{ms} as $S = A_c/A_{ms}$.

A large number of different methods exists to calculate squat. These are mainly dependent on some of the parameters given above. In the following, a brief overview of the methods to estimate ship squat is presented.

2.1 PHYSICAL MODEL TESTS

Physical model tests have a long history in the marine industry. Several marine towing tank facilities exist all over the world and are still extensively used. Model testing of ships in shallow water are conducted by different institutions.

Model tests of the KCS (Kriso Container Ship) were carried out at the Development Center for Ship Technology and Transport Systems (DST) in Duisburg as presented by Mucha and el Moctar (2014) and for the DTC presented by Mucha et al. (2014).

Flanders Hydraulic Research conducted tests of the KVLCC2 hull in shallow water with different canal width and different side wall distances as presented in Lataire et al. (2012). As another example, the DTC has been extensively tested in shallow water and waves for the 5th MASHCON 2019 benchmark (van Zwijnsvoorde et al. (2019)).

The BAW in Hamburg conducted model test of different ships in shallow water. Examples for sinkage and trim measurements of a containership (DTC) are given by Uliczka (2010). A general overview of different ships and squat measurements can be found in Gourlay et al. (2015), which includes two Postpanmax container ships tested at BAW.

Model tests can be used to determine forces, moments, sinkage and trim and ship induced loads in shallow water. Measurements of local flow patterns are difficult and might disturb the flow field. In contrast to this, CFD simulations allow a deeper insight into the flow field at any positions without disturbing it. CFD simulations are time consuming but more flexible in changing the model setup compared to model tests.

Nevertheless, model tests are still of huge importance for the validation of CFD simulations to ensure quality and reliability of the results.

2.2 EMPIRICAL FORMULAE AND ANALYTICAL METHODS

The following selection of equations for squat is well known and often cited:

- ICORELS (1980)
- Barrass (1979)
- Yoshimura (1986)
- Römisch (1989)

These squat formulae are either limited to certain types of channels (unrestricted, channel and canal) and/or are only valid for a certain range of parameters such as h/T, c_B or depth-Froude-number F_h. Predicting squat with these equations for different ships with varying dimensions in varying channel geometries can lead to inaccurate results.

Some formulae only give results for the bow squat, others only the maximum squat, independent of the position, at which the maximum squat occurs. A change of the trim orientation dependent of the ship's speed is not considered within these formulae. Examples of different squat values calculated by formulae for the same parameters are given for a bulk carrier in Demirbilek and Sargent (1999) and for different ships in Briggs et al. (2009). These results are also compared with experimental data.

Besides empirical formulae, methods based on slender body theory exist to calculate squat. As an example, Gourlay et al. (2015) investigated trim and sinkage of different container ships with slender body theory. It was found that slender body theory underpredicts the sinkage in narrow and/or restricted channels. Today's large ships, with lengths of up to 400 m, beams over 60 m and increased drafts are beyond the limits of slender bodies.

Accurate and robust squat predictions for all ships and channel geometries are difficult to obtain with empirical formulae and analytical methods without using corrections.

2.3 COMPUTATIONAL FLUID DYNAMICS

There are methods based on potential theory, which can be used to calculate squat in shallow and confined water. Low computational power requirements for these methods allow fast simulation times.

In the investigation of Gourlay et al. (2015), the results for sinkage of a Rankine source method showed better agreement with experimental data in comparison to slender body theory. As another example, Mucha et al. (2016) found a boundary element method (GL Rankine) to be able to predict midship sinkage at low moderate speed with good accuracy. Three ships were investigated with larger deviations to experiments found at higher depth Froude numbers, especially for trim predictions.

RANSE based simulations used for squat predictions are more time consuming but take into account the viscous effects. Increased computational power and parallelization have led to shorter simulation times so that RANS simulations have become more feasible in the past years. Setup and numerical settings for simulations of ship motions in shallow water are still difficult compared to deep water simulations: the small gap between ship and the channel floor is a source of numerical instability and can cause simulations to be aborted.

In the following, an overview of latest RANS based investigations of trim and sinkage for ships in shallow water is presented. Latest developments in CFD, recommendations and validation aspects are presented.

Jachowski (2008) investigated ship squat of the KCS for different speeds and h/T ratios down to 1.2 using Ansys FLUENT. Squat was compared with several empirical formulae and good agreement was found. Trim was not considered and no dynamic mesh motion was used.

Tezdogan et al. (2016) presented the squat and resistance of the DTC advancing through a canal with STAR-CCM+ and compared the results with experimental data of Uliczka (2010). DFBI Translation & Rotation method was used, which moves the whole computational domain. A comparison was made only for sinkage at Center of Gravity (CoG), which was within 10 % of the experiments, whereas the trim was not evaluated.

Mucha et al. (2016) studied the resistance and squat of three ships. The DTC, KCS and KVLCC2 were simulated with a RANS method and the results were compared with experimental data. Trim predictions had larger deviations to experiments than the midship sinkage. Therefore, further validation of trim predictions is important.

Liu et al. (2017) used STAR-CCM+ to investigate the hydrodynamic forces and squat in confined waters for two ships (KVLCC2 and KCS). Sinkage and resistance results of the CFD simulations are presented and compared to experimental data. A promising agreement for sinkage was found. The trim has not been analyzed and validated with experimental data.

A comprehensive study of the DTC is done by Terziev et al. (2018) by investigating the DTC in a stepped channel at h/T =1.3. The DFBI Rotation and Translation technique of STAR-CCM+ was used, where the whole computational domain follows the body motion. Sinkage and trim have been compared to results from slender body theory, in which some disagreement between the Slender-Body theory and CFD results was found in particular for larger speeds. A comparison with experiments has not been made. For larger trim angles, the free water surface was pierced by the domain boundaries. The authors suggest using overset mesh to overcome this but also mentioned the possible collision of the overset mesh with the channel bottom at small UKC.

For small h/T ratios, Shevchuk et al. (2016) investigated the flow field in the gap between ship hull and river bottom with URANS and hybrid LES-URANS simulations. The boundary layer was found to grow on both the ship hull and channel bottom. This leads to remarkably viscous effects, which are neglected in potential theory. The conducted hybrid LES-URANS simulations, which are more costly, showed the existence of flow separation structures for small h/T ratios, nevertheless, in comparison to pure URANS simulations, a change of mean dynamic sinkage and trim was not found for the hybrid simulations.

Several investigations of RANS simulations covered the calculation of trim and sinkage in shallow water. The main focus of the validations was predominantly on sinkage at CoG, which can be accurately predicted with RANS simulations. Validation of trim has not been conducted extensively, which is necessary to ensure improved reliability and quality of squat predictions with CFD simulations.

3 NUMERICAL INVESTIGATION OF SHIP SQUAT IN EXTREME SHALLOW WATER

In this investigation RANS simulations are used to predict trim and sinkage of ships in extreme shallow water with a water depth to draft ratio h/T of less than 1.2. At this water depth, a significant influence of the channel bottom on trim and sinkage is observed.

Results of sinkage and trim for ships in shallow water at different speed V and water depth h can be compared by using the depth Froude number F_h. It is defined as

$$F_h = \frac{V}{\sqrt{gh}}, \quad (1)$$

where g is the gravitational acceleration. It expresses the relation between ship speed and maximum wave velocity in shallow water. Additionally, sinkage and trim are influenced by the blockage factor S. With decreasing blockage factor, the influence of lateral boundaries (e.g. slopes, banks) and horizontal boundaries (channel bottom) increases and leads to increased squat.

In the following test cases, blockage factor S and depth Froude number F_h are varied to study the influence of these parameters on sinkage and trim.

3.1 INVESTIGATED SHIPS AND CHANNEL CONFIGURATIONS

Three different ships are used in this study: PPM55, PPM52 and PPM40. All ships are Postpanmax (PPM) container ships, with a beam of 40 to 55 meters. Main dimensions and channel parameters are given in Table 1. All simulations are conducted at a model scale of $\lambda = 40$ or $\lambda = 60$. The drafts are defined for even keel condition.

Table 1. Main dimensions of the numerical ship fleet

Ship	PPM55	PPM52	PPM40
L_{PP} (m)	360.0	347.0	320.0
T (m)	16.0	13.5	14.5
B (m)	55.0	52.0	40.0
∇ (m³)	215965	155927	134108
c_B (-)	0.68	0.64	0.72
h (m)	18.0	15.8	16.5
UKC (m)	2.0	2.3	2.0
h/T (-)	1.125	1.170	1.138
λ (-)	40	60	40

All ships have been developed for model tests conducted at BAW for different investigations. These three ships were chosen due to the different trim pattern with either stern down trim, bow down trim or variable trim dependent on the ship speed. Experimental results of all ships are available for validation.

In Figure 1 the cross-sections of the three ships are presented. More details on ship data and exemplary model test results for these ships are presented in Uliczka et al. (2004) and Gourlay et al. (2015).

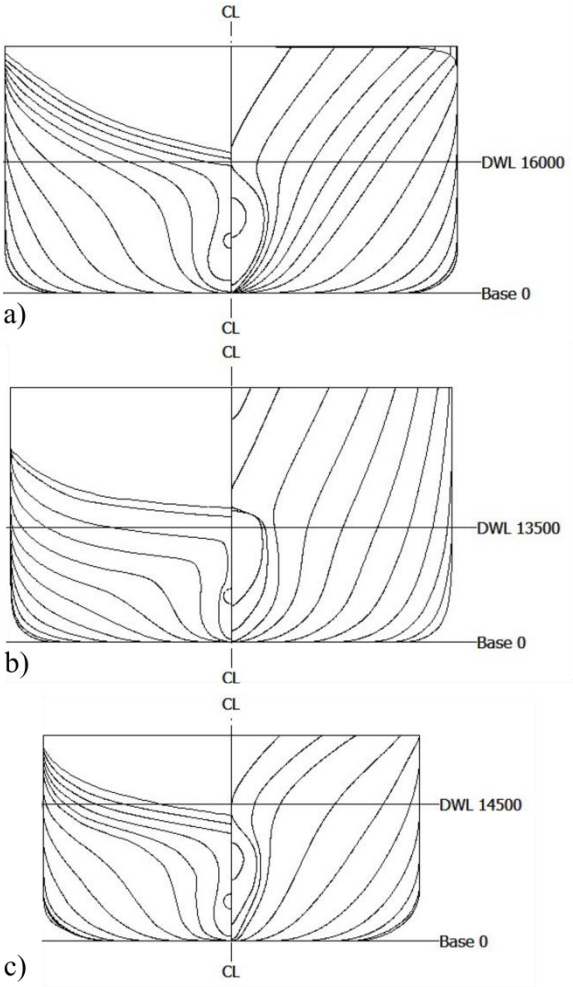

Figure 1. Cross-sections of the investigated ships: a) PPM55, b) PPM52 and c) PPM40

Figure 2 shows the channel setups for all three ships.

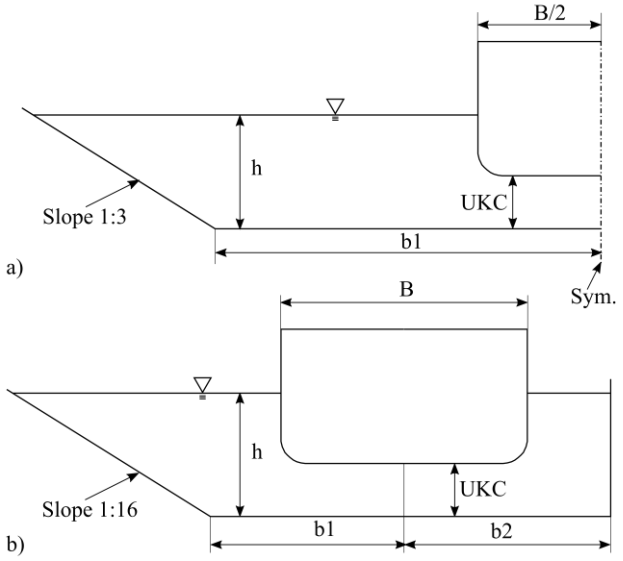

Figure 2. Channel setup for a) PPP55 and PPM40 and b) PPM52 (not at scale)

In this study the blockage factor S is varied by increasing the bottom-slope distance b1. Four blockage factors S are studied for PPM50 and PPM40 and one single blockage factor for PPM52. In the following, cases with different blockage factors are named as follows:

- A1 to A4 for PPM55
- B1 to B4 for PPM40
- C1 for PPM52

The test matrix with the investigated ship speed range V, blockage factors S and associated bottom slope distances b1 is presented in Table 2. 74 simulations are conducted in total for all nine test cases and different speeds.

Table 2. Test matrix for all three ships: blockage factor S, channel parameters (b1, b2) and investigated ship speed range V (all dimensions in model scale)

Case	Ship	S (-)	b1 (m)	b2 (m)	V (m/s)
A1	PPM55	10	5.4	-	[0.6, 1.2]
A2		15	8.4	-	
A3		20	11.4	-	
A4		25	14.4	-	
B1	PPM40	14	5.4	-	[0.6, 1.3]
B2		21	8.4	-	
B3		28	11.4	-	
B4		35	14.4	-	
C1	PPM52	11	4.6	1.20	[0.57, 0.90]

3.2 COMPUTATIONAL DOMAIN AND MESH

The presented channel geometry is built as a computational domain. In
Figure **3**, the computational domain with its boundaries is shown exemplary for the PPM40.

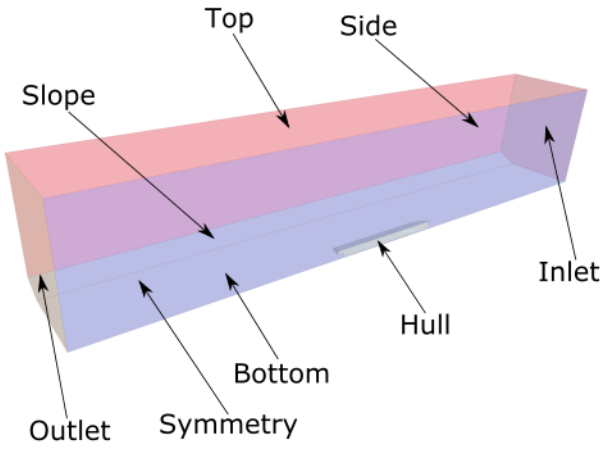

Figure 3. Computational domain with used boundaries

The following boundary conditions are used for the simulations:

- Inlet: velocity inlet
- Outlet: pressure outlet
- Top: velocity inlet
- Side: velocity inlet
- Slope: slip-wall
- Bottom: slip-wall
- Hull: no-slip wall
- Symmetry: symmetry plane

The inlet is placed about 2 L_{PP} in front of the ship and the outlet is placed 1.5 L_{PP} aft of the ship. A height of 1.0 L_{PP} is used from the water surface to the top of the domain. A slip wall condition is used on the bottom and slope to ensure a horizontally gradient free water level.

The internal mesh generator of STAR-CCM+ is used. All domains are meshed using the surface remesher, prism layer mesher and the trimmed cell mesher. The trimmed cells consist of mainly hexahedral cells to capture a sharp interface between water and air. Prism layers are used to discretize the boundary layer on the ship hull, with the cell size much smaller in normal direction to the body as in tangential direction. All meshes are created based on a predefined base size, which is defined as a fraction of the ship length L_{PP}. This results in comparable mesh sizes for all three ships.
Figure **4** shows an exemplary mesh of the PPM40 consisting of 2.58 million volume cells.

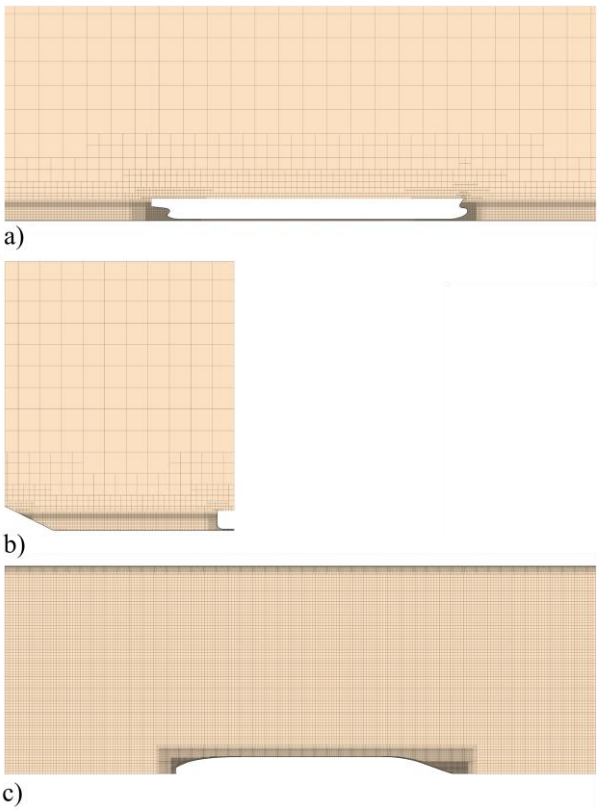

Figure 4. Exemplary mesh for PPM40: a) longitudinal cut, b) transversal cut and c) horizontal cut

Refinement blocks with volumetric controls are placed at the free water surface with low vertical cell size, at the

bow and stern and at close proximity around the hull with small isotropic cell size. A small vertical cell size is used to accurately discretize the gap between ship hull and channel bottom.

3.3 NUMERICAL METHOD

The numerical method used by STAR-CCM+ is the Finite-Volume-Method (FVM), which solves the RANS equations for incompressible fluids in the integral form. Further details of numerical fluid dynamics are given in the book of Ferziger and Perić (2002). A SIMPLE algorithm (Semi-Implicit Method for Pressure Linked Equations) is used to link the continuity equation to the momentum equations. Convective terms in the RANS equations are discretized using a second order upwind scheme. All integrals are approximated using the midpoint rule, which is of second order accuracy.

For capturing the free water surface, the Volume of Fluid (VoF) method is implemented (Hirt and Nichols (1981)). The convective transport of volume fraction is discretized with the High Resolution Interface Capturing (HRIC) scheme of Muzaferija et al. (1998). The transient term of the equations is discretized by a first order implicit unsteady method and the time step size is always set to fulfill a Courant number smaller than one. For turbulence closure, the k-ω SST-Menter turbulence model with all y^+ wall treatment is used. In this study, the y^+ values are always forced to be in the range of $30 < y^+ < 80$ throughout all simulations by setting an appropriate near wall thickness y at the wall.

DFBI-Morphing (Dynamic Fluid Body Interaction) is used for the ship's sinkage and trim motions. The method moves mesh vertices according to the dynamic trim and sinkage motions of the ship. This is done in order to avoid piercing of the free water surface by the moving domain boundaries, which follow the body motion, and to avoid gradients of the still water level when DFBI Translation and Rotation is used instead.

3.4 REALIZATION AND METHOD OF ANALYSIS

At the beginning of the simulation, the ship motions are fixed for 70 s. Thereafter the fluid forces are ramped up for 30 s to minimize strong initial motions of the ship. Each velocity is simulated for 400 s to ensure convergence.

Initially, the flow velocity is increased with larger increments, when the squat is small. At higher velocities, smaller increments are used to avoid the grounding of the ship. A momentum source term is used when the fluid velocity is increased during the simulation to avoid the creation of an unwanted gravity wave. Sinkage and trim are evaluated by calculating the mean of the last 100 s for each velocity. The squat is also evaluated at two positions (bow and stern), which correspond to the squat measurement positions in the experiments.
Most of the simulations are conducted on 32 to 96 cores, depending on the number of cells of the mesh. The runtime for one velocity (400 s of simulation time) is in the range of a few days.

4 RESULTS

To get an initial assessment of the reliability of the CFD model results, convergence and mesh studies are shown first.

4.1 SINKAGE AND TRIM CONVERGENCE

For case A1 (PPM55 with S = 10) Figure 5 presents the time series of sinkage at CoG, trim and ship speed.

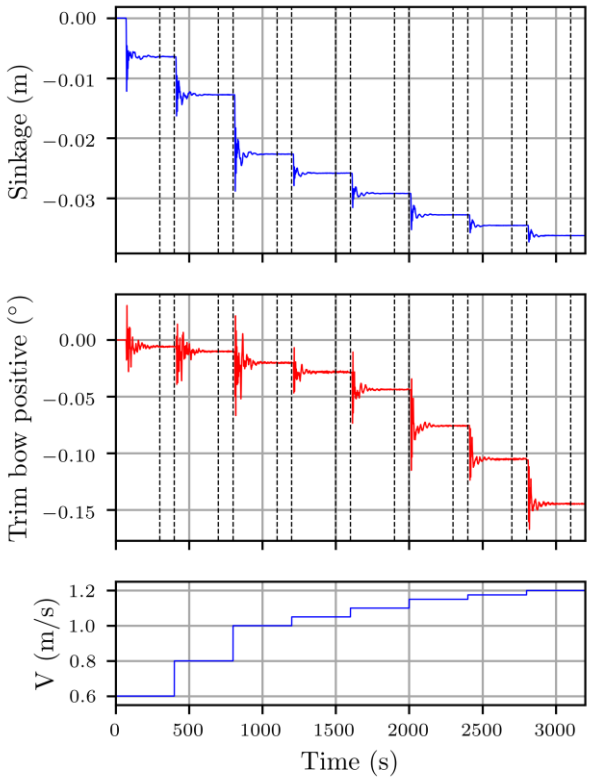

Figure 5. Case A1 - time series of sinkage at CoG, trim and ship speed V, consisting of eight different speed sections.

Converged sinkage and trim are observed initially after approximately 200 s until the flow velocity is increased. At higher speed, the motion also converges within this time interval. The dashed lines mark the evaluation intervals for the calculation of mean values of sinkage and trim used later. In these evaluation intervals, a low noise level throughout all velocities is observed. The relative standard deviation is less than 4 % for trim and less than 1 % for sinkage and squat at bow and stern.

4.2 MESH UNCERTAINTY

All meshes used in this paper are built with a similar base size, which is dependent on the ship length L_{PP}. Mesh uncertainty for sinkage at CoG is evaluated here by simulations with three refined meshes, exemplary for case A1. A refinement factor of r = $\sqrt{2}$ is used and applied on the mesh base size. This results in 0.84 to 3.96 million volume cells as presented in Table 3.

Table 3. Parameters of the mesh uncertainty study for Case A1 with three refined meshes and a refinement factor of $r_{21} = r_{32} = \sqrt{2}$

Mesh i	Base Size h_i (m)	No. of cells 10^6 (-)
1	0.148	3.96
2	0.210	1.71
3	0.297	0.84

The uncertainty analysis and calculation of the grid convergence index is done according to the guidelines of Celik et al. (2008). Figure 6 shows the grid convergence index GCI_{fine}^{21} of the sinkage at CoG. GCI_{fine}^{21} decreases from about five percent at the lowest speed to less than one percent at higher speed. This represents an acceptable mesh uncertainty for the following investigations. Therefore, the results in this study are always given for the medium size mesh.

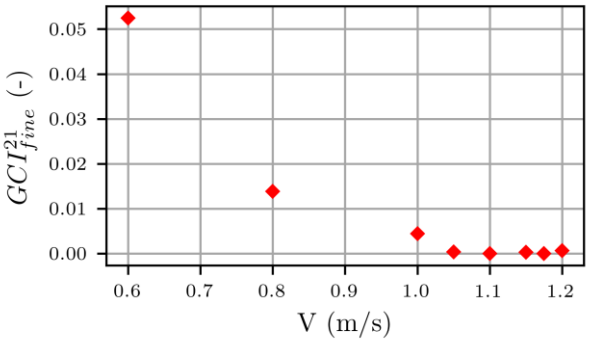

Figure 6. Case A1 - grid convergence index for sinkage at CoG

4.3 SINKAGE AND TRIM FOR DIFFERENT SHIPS

Nondimensional sinkage at CoG and trim for the three investigated ships and the smallest blockage factor S are compared in Figure 7.

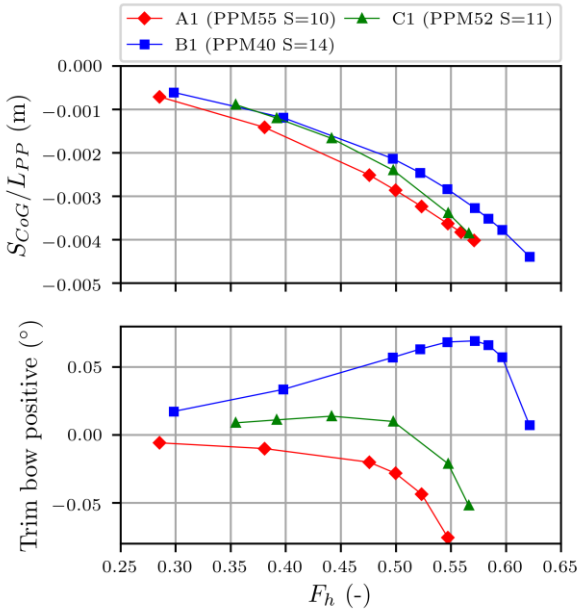

Figure 7. Nondimensional sinkage and trim for all three ships with the smallest blockage factor

The sinkage increases for all ships at higher speed, but despite similar blockage factors (e.g. for A1 and C1) differences in squat increase at higher speed. Variations in sinkage are less dominant than variations in trim.

For all three ships, the variations in trim are significant with different trim pattern in dependence of the ship speed. Trim either to the bow or to the stern is present for A1 and B1, whereas for case C1 the slight bow down trim changes to stern down trim at higher velocity.

The change of trim for case C1 is visualized in Figure 8, which shows the distribution of the pressure coefficient c_p at two depth-Froude numbers. At F_h = 0.39 the ship trims slightly bow down, whereas at F_h = 0.57, the higher low pressure area at the aft part of the ship leads to a stern down trim.

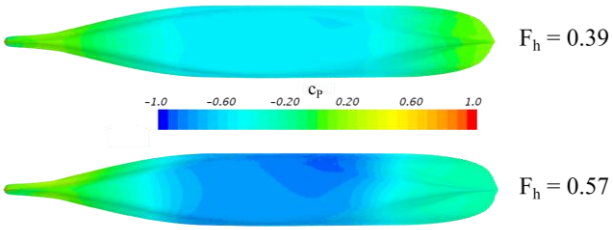

Figure 8. Pressure coefficient distribution for case C1 at two depth Froude numbers

4.4 INFLUENCE OF THE BLOCKAGE FACTOR

The influence of the blockage factor S is evaluated for PPM55 (Figure 9) and PPM40 (Figure 10). Smaller blockage factors lead to larger sinkage for both ships. This dependence is stronger at higher speed. At low speed, the trim is not dependent of the blockage factor up to F_h = 0.4

for PPM55 and up to $F_h = 0.55$ for PPM40. Above these speeds, there is a stronger influence of the blockage factor on the trim, particularly for the smallest blockage factors (A1 and B1). Following this, sinkage and trim are strongly influenced by the blockage factor. Larger differences between both ships are observed at higher depth Froude numbers ($F_h > 0.5$).

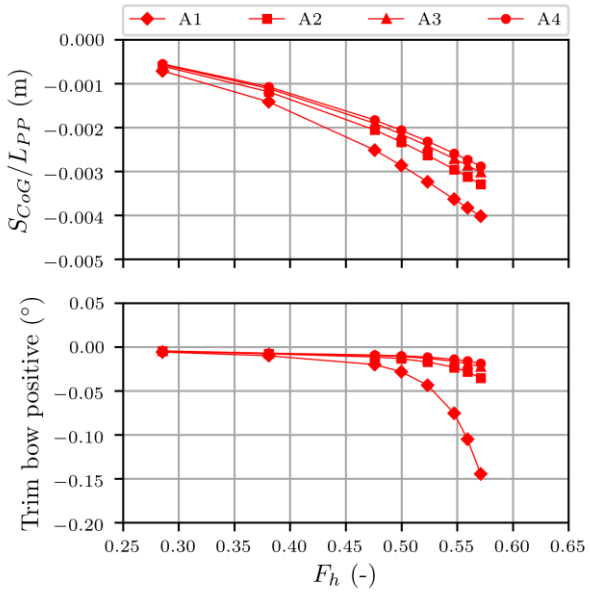

Figure 9. Nondimensional sinkage and trim for cases A (PPM55)

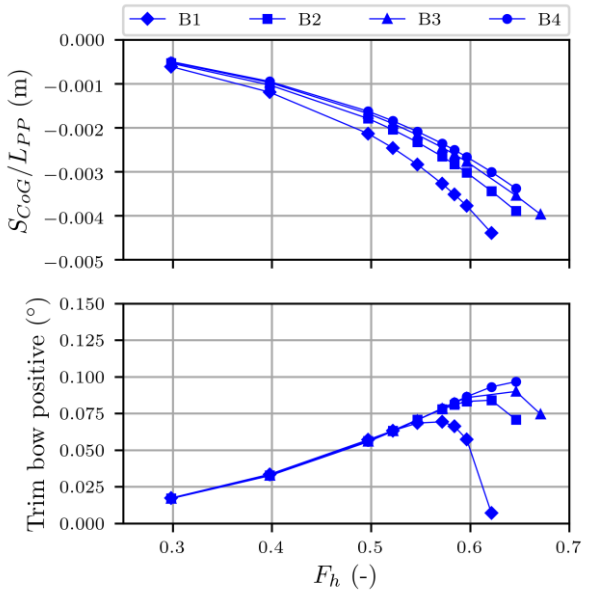

Figure 10. Nondimensional sinkage and trim for cases B (PPM40)

4.5 VALIDATION FOR CASE A1

Squat predictions at bow and stern for case A1 are presented in Figure 11, in which CFD simulations and experimental fluid dynamics (EFD) results are compared.

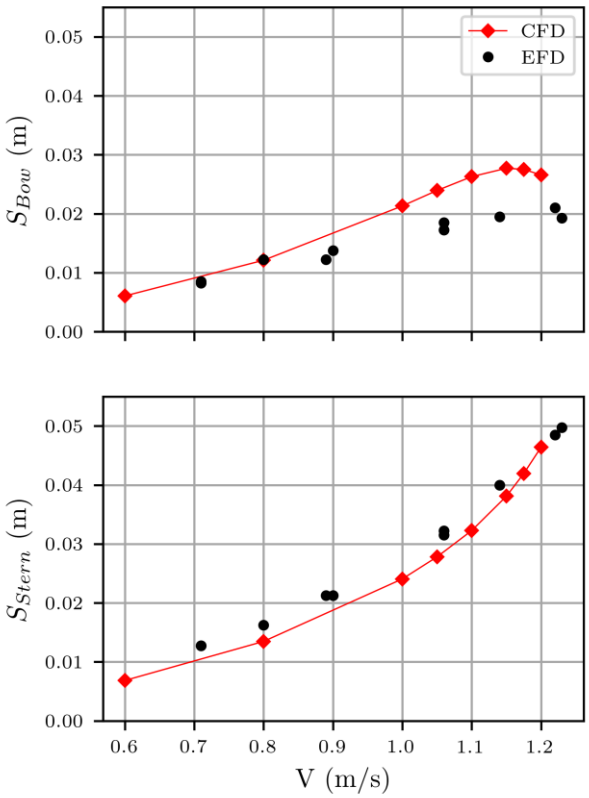

Figure 11. Case A1 - squat at bow and stern for CFD and EFD

Deviations of bow squat are smaller at low speed, whereas bow squat is overpredicted by CFD at higher speed. Overpredicted bow squat at higher speed might be caused by the two different setups: CFD simulations are conducted without propeller whereas the EFD tests include propeller. The predicted stern squat by CFD is slightly underpredicted.

A different perspective on the results can be made by comparing sinkage and trim (Figure 12). The sinkage is in good agreement with the experiments with a slight overprediction at higher speed, whereas the trim angle of the CFD simulations is significantly larger. Larger deviations in squat at higher speed (Figure 11) can be explained by the inaccurately predicted trim angle, while the sinkage is more accurately predicted.

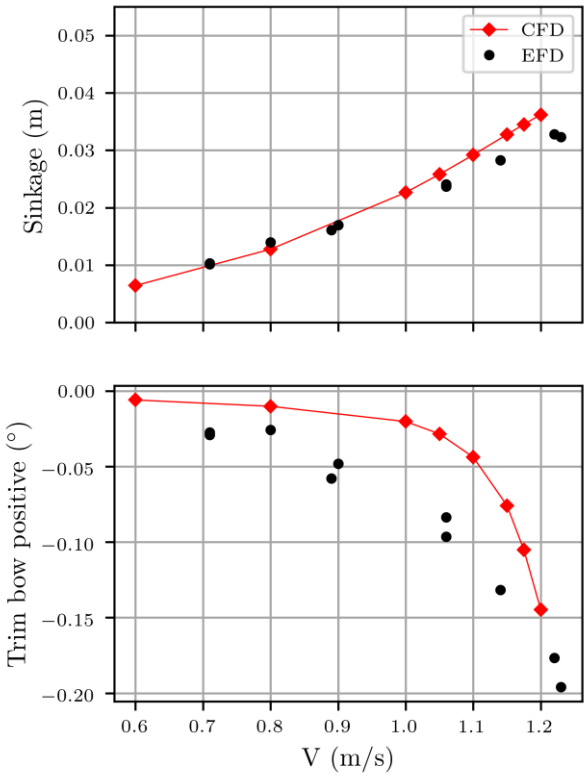

Figure 12. Case A1 - sinkage and trim for CFD and EFD

4.6 EVALUATION OF QUALITY

The quality of predicted sinkage at CoG, squat at bow and stern and trim is investigated by comparing the predicted values with experimental data. A quality score Q is defined as the square root of the mean of all squared single deviations i = 1...n between CFD and EFD as

$$Q = \sqrt{\frac{1}{n}\sum_{i=1}^{n}\left(\frac{X_{EFD,i}-X_{CFD,i}}{X_{EFD,i}}\right)^2}. \quad (2)$$

Normalization by the EFD values has the advantage that the score can be interpreted as a percentage value. As an example, a score of 0.09 means 9 % deviation of the CFD results compared to EFD. Therefore, a small quality score Q means small deviations of CFD compared to EFD. To calculate the quality score of a value X, the numerical results are linearly interpolated to the measured speed of the experiments. Interpolation is only done for speeds within the conducted velocity range of the simulations.

To detect a systematic deviation, the tendency or bias B_S of the deviations is calculated with

$$B_S = \sum_{i=1}^{n} sgn(X_{EFD,i} - X_{CFD,i}). \quad (3)$$

The following example illustrates the interpretation of the bias parameter B_S: -8/8 means that all eight single differences out of n = 8 velocities are negative – a systematic overprediction. Values of 8/8 means a systematic underprediction and values of -4/8 can be interpreted as an unsystematic deviation.

In Table 4, the quality score Q and bias B_S are presented for all investigated test cases. Altogether 69 experimental results for squat are compared with the results of the CFD simulations.

The quality score of all squat predictions at bow and stern is below 20 % except for case A1 at the bow and C1 at the stern. A quality score of less than 20 % for squat is an acceptable limit, since the experimental results also possess uncertainties, particularly at higher speed, as discussed later.

Compared to squat, the quality score of the trim predictions is significantly larger with more than 64 %. Due to angle relation between trim and squat at bow and stern with quantitatively small absolute angles, large deviations in trim do not lead to deviations of the same magnitude for bow and stern squat. Therefore, the quality score of squat at bow and stern is more important from a practical point of view.

Table 4. Quality score Q and bias B_S of squat at bow, stern, CoG and trim for all cases

	Quality score Q (-)				Bias B_S (-)			
Case	**S_{Bow}**	**S_{Stern}**	**S_{CoG}**	**Trim**	**S_{Bow}**	**S_{Stern}**	**S_{CoG}**	**Trim**
A1	0.28	0.13	0.09	0.66	-6/8	8/8	-2/8	-8/8
A2	0.09	0.14	0.05	0.64	-6/8	8/8	4/8	-8/8
A3	0.15	0.18	0.08	0.73	-4/8	8/8	2/8	-8/8
A4	0.20	0.14	0.06	0.74	-4/5	5/5	1/5	-5/5
B1	0.19	0.13	0.13	2.18	-8/8	0/8	-6/8	-8/8
B2	0.05	0.13	0.05	1.11	-4/6	6/6	6/6	-6/6
B3	0.07	0.12	0.06	1.03	-8/8	6/8	2/8	-8/8
B4	0.13	0.16	0.09	0.90	-4/6	4/6	2/6	-6/6
C1	0.09	0.39	0.25	1.01	2/12	12/12	12/12	-12/12
				Sum	-42/69	57/69	9/69	**-69/69**

Throughout all cases and all velocities the bias for trim is negative (-69/69). Negative bias means, the predicted trim of the simulations is systematically more bow down or larger than in the experiments.

By calculating the full scale values for squat at bow and stern, the absolute deviation in squat is between -0.32 m and 0.33 m, if test case C1 is not included, otherwise the upper limit is 1.0 m. With increasing speed, the deviations also increase slightly. The absolute error for trim, is between -0.12 ° and -0.007° for all simulations, which is relatively small.

Uncertainties of the simulations have been investigated and discussed before. However, the measurements also include uncertainties which must be considered. To exemplify, the variations of the experiments are investigated for test case C1. In Figure 13, sinkage and trim are presented for both CFD and EFD with minimum and maximum values inside the evaluation interval presented as bars.

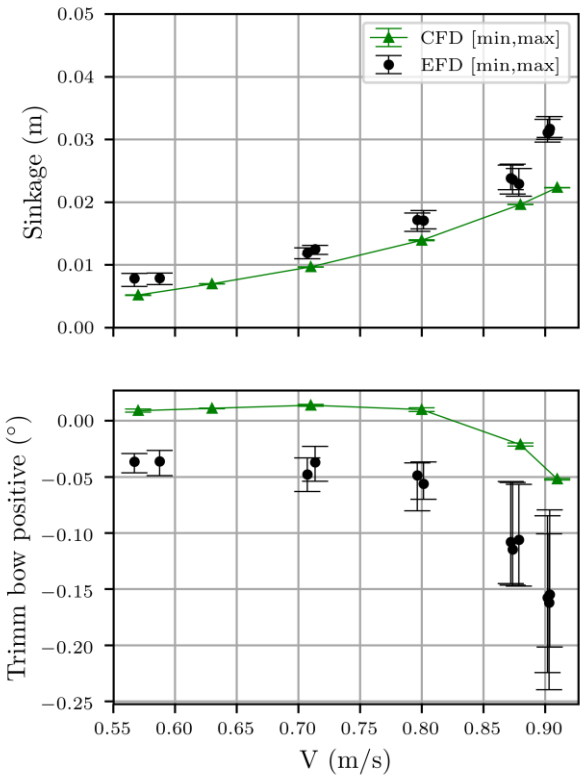

Figure 13. Case C1 - sinkage and trim with minimum and maximum values for EFD and CFD

Variations of the CFD simulations are significantly smaller as for the EFD model tests. Particularly variations of trim are higher at higher speed. Due to the limited length of the towing tank, the ship model's motions possess less time to converge in contrast to the CFD model. Since the trim angles of the CFD simulations do not lie inside the variation range of the experiments, the predicted trim angle is systematically different.

The systematic deviation of the trim angle might be caused by the different setups: All CFD simulations in this study are conducted without propeller, whereas all experiments are conducted with self-propelled ships.

5 APPLICATION OF METHOD FOR MASHCON BENCHMARK DATA (DTC)

Furthermore, the developed setup is used for the provided DTC benchmark data of the 5th MASHCON 2019. Since the main focus of this MASCHON is on maneuvering in currents and waves this paper focus only on the test cases without waves. Due to the low squat values for the first benchmark case C1, only the two remaining still water cases are considered, named here as DTC-C2 DTC-C3.

In the provided benchmark data by van Zwijnsvoorde et al. (2019), the DTC is experimentally tested in shallow water and waves at a model scale of 89.11 in a laterally restricted canal. Main dimensions of the DTC and the test case parameters are presented in Table 5.

Table 5. Main dimensions of DTC at model scale and test case parameters

L_{PP} (m)	3.984
T (m)	0.163
B (m)	0.572
c_B (-)	0.661

Case	h/T (-)	V (m/s)	S (-)
DTC-C2	2.0	0.872	29.8
DTC-C3	1.2	0.327	24.8

Figure 14 and Figure 15 show the measured sinkage at CoG and squat at bow and stern position for both cases. The original time signal is filtered to eliminate the noise. In both cases the ship trims bow down with DTC-C3 having a smaller squat. Resulting values for S_{Bow}, S_{Stern} and S_{CoG} are extracted by calculating the mean in the dotted time intervals (50 - 70 s and 100 - 140 s).

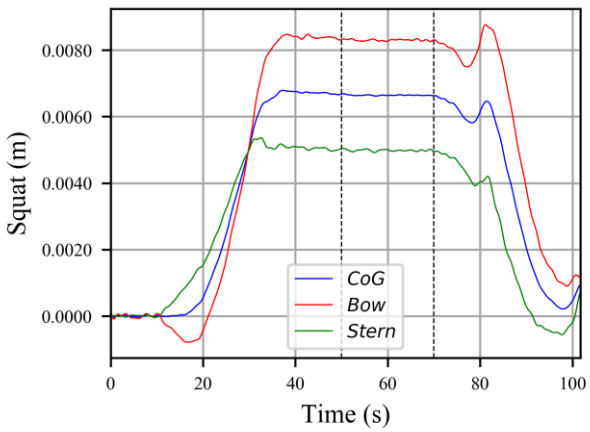

Figure 14. Benchmark case DTC-C2 - sinkage at CoG and squat at bow and stern position from experiments

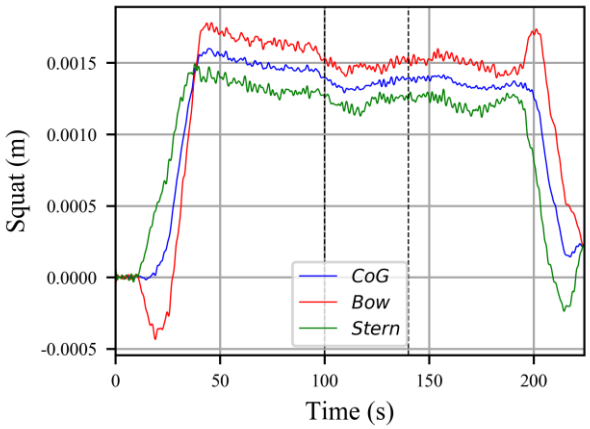

Figure 15. Benchmark case DTC-C3 - sinkage at CoG and squat at bow and stern position from experiments

Simulations for these two test cases are set up with similar numerical settings and mesh to maintain comparability to the results presented before. The volume mesh consists of 1.71 million cells for DTC-C2 and 2.58 million cells for DTC-C3. In contrast to the previous results both methods – EFD and CFD - have the same setup without propeller.

Figure 16 shows the convergence plot of the CFD simulation of sinkage and trim. Converged motions are observed after 200 s and the mean values are calculated in the dotted time interval (300 to 400 s).

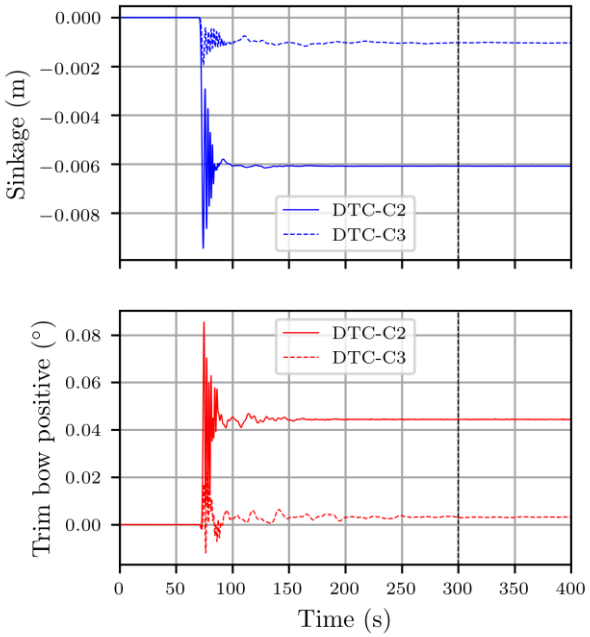

Figure 16. Benchmark case DTC-C2 and DTC-C3 - CFD results for sinkage at CoG and trim

A comparison of predicted and measured sinkage, squat at bow and stern, trim as well as the quality score is presented in Table 6. For DTC-C2 the quality score of sinkage and squat is below 9 % and less than 7 % for trim.

For DTC-C3 the predicted sinkage and squat at both positions is underpredicted, with a higher quality score of less than 24 %. The quality score of the trim angle is smaller compared to the PPM container ship simulations with only 14.5 %. Since the sinkage and squat values are very low in this case with a maximum of 1.5 mm, the absolute deviations in squat are acceptable.

Table 6. Results of EFD and CFD for DTC benchmark cases C2 and C3

Case		EFD (m,°)	CFD (m,°)	Q (-)
DTC-C2	S_{CoG}	0.0066	0.0061	0.084
	S_{Bow}	0.0083	0.0077	0.078
	S_{Stern}	0.0045	0.0046	0.084
	Trim	0.0477	0.0444	0.069
DTC-C3	S_{CoG}	0.0014	0.0010	0.230
	S_{Bow}	0.0015	0.0012	0.223
	S_{Stern}	0.0012	0.0010	0.238
	Trim	0.0037	0.0031	0.145

In contrast to the simulation results of the three PPM ships presented before, trim deviations are much smaller, with a maximum quality score of 14.5 % (DTC-C3) compared to a minimum quality score of 64 % (A2).

The systematic overprediction of trim is not observed for this benchmark, which emphasizes the assumption of the systematic trim deviation being caused by the different setups of CFD and EFD.

6 CONCLUSIONS

The ability of RANS simulations to conduct squat predictions in laterally confined shallow water was shown. Robustness of the method was shown by the ability to simulate sinkage and trim for three different PPM container ships with different trim patterns. Different channel configurations and varying blockage factors led to different trim and sinkage patterns.

To quantify the accuracy of the CFD simulations, a quality score was introduced and calculated for the results of 69 experiments in total. Furthermore, the bias of deviations between EFD and CFD was presented to investigate the nature of deviations - systematic or not.

The overall deviation of squat predictions for all investigated ships was found to be less than 20 % or between -0.32 m and 0.33 m in full scale, with two exceptions. In comparison to squat, trim showed a systematic deviation (overprediction) between simulations and experiments, but the angle deviations were relatively small with values between -0.12 ° and -0.007 °.

Systematic trim deviations might be caused by the different setup of CFD simulations and EFD model tests: the CFD simulations do not include a propeller, whereas

the ships are self-propelled in the experiments. This result was emphasized by the simulation results of the 5th MASHCON 2019 benchmark. A fair agreement between numerical results and the experiments was found due to the similar setup with both ships being towed without a propeller. In contrast to the PPM container ship simulations before, the trim angle was more accurately predicted.

When considering and focusing on a quality parameter of CFD simulations, the accuracy of the measurements with the experimental model setup constrains should not be ignored. Considering this, a quality score of 10 to 20 % seems an appropriate value.

In further research work, improved predictions of squat by CFD can be expected by including a propeller model – either a virtual disc or a geometrically resolved propeller. Furthermore, the influence of the propeller can be quantified as well as the effort required by implementing both proposed methods in the simulations.

7 REFERENCES

Barrass, C. B. (1979). Phenomena of ship squat. in: *International Shipbuilding Progress* 26. DOI: 10.3233/ISP-1979-2629403.

Briggs, M. J., Vantorre, M., Uliczka, K., Debaillon, P. (2009). Prediction of squat for underkeel clearance. in: *Handbook of coastal and ocean engineering (Ed. YC Kum)*.

Celik, I. B., Ghia, U., Roache, P. J. (2008). Procedure for estimation and reporting of uncertainty due to discretization in CFD applications. in: *J. Fluids Eng.* 130 (7).

Demirbilek, Z., Sargent, F. (1999). Deep-draft coastal navigation entrance channel practice. Coastal Engineering Technical Note I-63.

Ferziger, J. H., Perić, M. (2002). Computational Methods for Fluid Dynamics. Berlin, Heidelberg: Springer Berlin Heidelberg.

Gourlay, T., Ha, J. H., Mucha, P., Uliczka, K. (2015). Sinkage and Trim of Modern Container Ships in Shallow Water. In : Australasian Coasts & Ports Conference 2015: 22nd Australasian Coastal and Ocean Engineering Conference and the 15th Australasian Port and Harbour Conference.

Hirt, C. W., Nichols, B. D. (1981). Volume of fluid (VOF) method for the dynamics of free boundaries. in: *Journal of computational physics* 39 (1), pp. 201–225.

ICORELS (1980). Report of Working Group IV. International Comission for the Reception of Large Ships (PIANC Bulletin No. 35, Supplement (1980)).

Jachowski, J. (2008). Assessment of ship squat in shallow water using CFD. in: *Archives of Civil and Mechanical Engineering* 8 (1), pp. 27–36. DOI: 10.1016/S1644-9665(12)60264-7.

Lataire, E., Vantorre, M., Delefortrie, G. (2012). A prediction method for squat in restricted and unrestricted rectangular fairways. in: *Ocean Engineering* 55, pp. 71–80. DOI: 10.1016/j.oceaneng.2012.07.009.

Liu, Y., Zou, L., Zou, Z. J., Lu, T. C., Liu, J. X. (2017). Numerical Predictions of Hydrodynamic Forces and Squat of Ships in Confined Waters. In : The 8th International Conference on Computational Methods.

Mucha, P., Deng, G., Gourlay, T., el Moctar, O. (2016). Validation Studies on Numerical Prediction of Ship Squat and Resistance in Shallow Water. in: *4th MASHCON International Conference on Ship Manoeuvring in Shallow and Confined Water. DOI:* 10.18451/978-3-939230-38-0_16.

Mucha, P., el Moctar, O., Böttner, C.-U. (2014). Technical Note. PreSquat – Workshop on Numerical Prediction of Ship Squat in Restricted Waters. in: *Ship Technology Research* 61 (3), pp. 162–165. DOI: 10.1179/str.2014.61.3.004.

Mucha, P., el Moctar, O. (2014). Numerical Prediction of Resistance and Squat for a Containership in Shallow Water. In : Proceedings of the 17th Numerical Towing Tank Symposium. Sweden.

Muzaferija, S., Peric, M., Sames, P., Schellin, T. (1998). A Two-Fluid Navier-Stokes Solver to Simulate Water Entry. In : Proceeding of the 22nd symposium of naval hydrodynamics. Washington, DC.

Römisch, K. (Ed.) (1989). Empfehlungen zur Bemessung von Hafeneinfahrten: Technische Universität Dresden (Band 1 Wasserbauliche Mitteilungen).

Shevchuk, I., Böttner, C. U., Kornev, N. (2016). Numerical analysis of the flow in the gap between the ship hull and the fairway bottom in extremely shallow water. In : 4th MASHCON - International Conference on Ship Manoeuvring in Shallow and Confined Water with Special Focus on Ship Bottom Interaction.

Terziev, M., Tezdogan, T., Oguz, E., Gourlay, T., Demirel, Y. K., Incecik, A. (2018). Numerical investigation of the behaviour and performance of ships advancing through restricted shallow waters. in: *Journal of Fluids and Structures* 76.

Tezdogan, T., Incecik, A., Turan, O. (2016). A numerical investigation of the squat and resistance of ships advancing through a canal using CFD. in: *Journal of Marine Science and Technology* 21. DOI: 10.1007/s00773-015-0334-1.

Uliczka, K., Kondziella, B., Flügge, G. (2004). Dynamisches Fahrverhalten sehr großer Containerschiffe in seitlich begrenztem extremen Flachwasser. in: *HANSA 141*.

Uliczka, K. (2010). Fahrdynamisches Verhalten eines großen Containerschiffs in seiten- und tiefenbegrenztem Fahrwasser. Bundesanstalt für Wasserbau, Hamburg.

Van Zwijnsvoorde, T., Tello Ruiz, M., Delefortrie, G., Lataire, E. (2019). Sailing in shallow water waves with the DTC container carrier: open model test data for validation purposes. In : 5th MASHCON International Conference on Ship Manoeuvring in Shallow and Confined Water. Belgium, pp. 1–10.

Yoshimura, Y. (1986). Mathematical model for the manoeuvring ship motion in shallow water. in: *Journal of the Kansai society of naval architects* (200).

8 AUTHORS BIOGRAPHY

Jonas Bechthold is working at Federal Waterways Engineering and Research Institute in Hamburg since 2017. He is responsible for CFD simulations in the field of interaction between ship and waterway focusing on ship dynamics.

Marko Kastens is a Senior Research Fellow at Federal Waterways Engineering and Research Institute in Hamburg since 2003. He is responsible for consulting the authorities as well as scientific research in the area of interaction between ship and waterway.

A NAUTICAL APPROACH TO THE EFFECT OF SHIP PARAMETERS ON WAVE IMPACT ON THE AN INTERTIDAL RIVER BANK IN THE BEND OF BATH

Abed Benmestoura, Deirdre Luyckx and **Peter Bueken**,
Antwerp Maritime Academy, Belgium

Stijn Timmerman,
Department of Biology, University of Antwerp, Belgium

A NAUTICAL APPROACH TO THE EFFECT OF SHIP PARAMETERS ON WAVE IMPACT ON THE AN INTERTIDAL RIVER BANK IN THE BEND OF BATH

Abed Benmestoura, Deirdre Luyckx and **Peter Bueken,** Antwerp Maritime Academy, Belgium
Stijn Timmerman, Department of Biology, University of Antwerp, Belgium

SUMMARY

This research aims to examine which ship parameters influence the height of ship generated waves that trigger river bank erosion. All types of river bank materials are reported to erode when ship induced primary wave height exceeds the threshold of 35 cm. The current work tries to identify factors that can be controlled by navigators in order to diminish river bank erosion. Data of ship passages were collected using a wave sensor positioned in a location where wave action is an important constraint for settlement, growth and survival of vegetation. A statistical model was used to predict the mean wave height of the primary wave based on ship characteristics. The result indicates that besides ship speed, volume and distance also affect primary wave height. However, speed reduction is highly recommended for reducing wave height and minimizing erosion potential when the vessel sails close to the shoreline.

NOMENCLATURE

AIS	Automatic Identification System
b	Channel width (m)
B	Width (m)
D	Draft (m)
g	Acceleration due to gravity (m/s^2)
GMT	Greenwich Mean Time
h	Channel depth (m)
H	Primary wave height (cm)
Heading E	Course steered by the ship to the East
Heading W	Course steered by the ship to the West
IMO	International Maritime Organization
L	Length (m)
vol	Ship volume (1000 m^3)
v	Ship speed (knots)
VTS	Vessel traffic system

1 INTRODUCTION

Dense shipping traffic in a restricted waterway produces a specific wave climate of ship-induced waves, in addition to the natural wave action. The impact of passing vessels in coastal waterways on erosion and sedimentation of river banks has repeatedly been discussed from different perspectives. Studies on ship generated waves have been carried out on many different sites in the world, including the Waikato River, New Zealand (McConchie and Toleman, 2003), the Kenai River, Alaska (Dorova and Moore, 1997), the Gordon River, Tasmania (Nanson et al., 1994), the Venice Lagoon, Italy (Rapaglia et al., 2015, 2011), the Scheldt estuary, the Netherlands (Schroevers et al., 2011) and the Göta River, Sweden (Larson et al., 2017). The models, predicting primary wave height as a function of ship properties, presented in literature are often site-specific.

Schoellhamer (1996) explained the height of primary waves as a function of the Froude number $Fr = v/\sqrt{gh}$ (with v expressed in m/s) and width and draft of the vessel. In a study at Hillsborough Bay, Florida, he found a significant positive association between primary wave height and $Fr^{2.4}S^{1.6}$, where $S = BD/bh$. Kriebel and Seelig (2005) performed a study at Chesapeake Bay, Maryland, and identify the speed of the vessel, its distance to the measurement location and the length of the vessel as the primary factors influencing wave height. Schroevers et al. (2011) studied primary wave height in the Scheldt estuary, the Netherlands, and present an exponential relationship between primary wave height and the product of length and speed of the vessel.

The current study is also performed in the Scheldt estuary (SW Netherlands and Belgium), a tidal river estuary which is a major coastal waterway in Europe. Being the only direct route from the Port of Antwerp (Belgium) to the sea, it is an important shipping route with dense shipping traffic. The Scheldt estuary is characterized by restricted waterways with some sharp bends. This study focuses on ship induced waves at a location far away from the waterway, close to the transition to natural marsh vegetation which is periodically submerged at high tide and emergent at low tide. This position was selected as wave action is an important constraint for settlement, growth and survival of vegetation (Callaghan et al., 2010; Silinski et al., 2015). Natural marsh vegetation provides important functions, such as protection of dikes from direct wave impacts and erosion (Gedan et al., 2011; Heuner et al., 2015; Möller et al., 2014), and creation of natural habitats (Barbier et al., 2011).

Primary ship-induced waves are long period waves, as opposed to short period wind waves. Silinski et al. (2015) studied how pioneer plants of tidal marshes respond to ship-induced wave action and report that survival strategies of seedlings as well as adult plants have a high chance of failing when exposed to ship-induced waves at water levels of at least 20 cm. According to a study performed in the Gordon River (Nanson et al., 1994) erosion may already be initiated at small wave heights (3-4 cm). Further,

most unconsolidated materials may be removed from the base of river banks and transported into the river when the wave height reaches 5-10 cm. The erosion rate slowly increases for wave heights of 25 cm, and becomes more significant when wave height attains 35 cm. Above this wave height threshold, most consolidated and unconsolidated bank materials are reported to erode (Nanson et al., 1994). Nanson et al. (1994) also identify primary wave height as the most simple wave characteristic for the prediction of erosion potential. Based on this observation, other wave characteristics such as wave period were not addressed in the present study.

Primary wave heights of ship-induced waves exceeding the threshold of 35 cm are thus considered as indicators of potential damage to the intertidal mudflat caused by erosion and by limiting tidal marsh vegetation settlement. The primary aim of this research is to establish a predictive model of the height of primary ship waves in the bend of Bath, on the selected location far from the waterway. This question will be assessed from a nautical point of view. The effect on mean primary wave height of ship parameters such as length, width, draft, speed and distance to the shore will be identified, focusing on factors that can be controlled by navigators in order to diminish the impact of passing vessels on the river bank.

2 MATERIAL AND METHODS

During an 18 month field measurement campaign (May 2012 until December 2013), wave heights were registered on the intertidal mudflat of Rilland (The Netherlands) in the bend of Bath, a narrow river section in the Scheldt estuary, see Figure 2. Water depth in the channel at the measurement location varies between approximately 14 m and 19.5 m and depends on the tide. Three pressure sensors were installed at the study site at different distances from the river edge: at 590 m (SN0001), at 540 m (SN0003) and at 335 m (SN0004). The positions of the devices are indicated in Figure 3. During low tide, the sensors fell dry, during high tide they were submerged. For the current research, the data of sensor SN0001 were investigated, which is located furthest away from the waterway, close to the transition to natural marsh vegetation which is periodically submerged at high tide and emergent at low tide. This position is of particular interest as wave action is an important constraint for settlement, growth and survival of vegetation (Callaghan et al., 2010; Silinski et al., 2015).

The pressure sensor used in the study is of type PTX 1830, manufactured by GE Sensing & Inspection, Leicester, UK, see Figure 1. The device continuously measures the water pressure at a frequency of 16 Hz. The pressure signal was converted into water height by means of linear wave theory, thus correcting for depth attenuation (Ellis et al., 2006).

Figure 1. The pressure sensors (PTX 1830) used to collect data of ship passages

Registered wave heights were combined and synchronized with AIS (Automatic Identification System) data on passing ships. AIS data available for this study involve ship dimensions (length L, width B and draft D), ship name and IMO number, as well as selected geographical positions in the bend of Bath and Greenwich Mean Time of passage at these positions. Average speed v was calculated by using the time interval and the distance between two registered AIS positions. Distance between the sailing line and the measuring location was approximated by means of interpolation and extrapolation, based on a piecewise linear track between registered positions.

During the entire measurement campaign, data for almost 10,000 ship passages were gathered. The data were provided by the Vessel Traffic Service (VTS) and consist of passages of cargo vessels, tankers, other types of seagoing vessels and inland vessels. However, many of those ship passages are not of interest for the current study, which aims at seagoing vessels with a minimum length of 150 m. Firstly, data on inland vessels navigating in the secondary navigational channel were not retained. Secondly, the bend of Bath is a busy waterway and often seagoing ships sail close to one another, which causes their wave patterns to interfere. In order to eliminate interference of waves generated by different ships, only isolated ship passages were selected for analysis. A ship passage was considered to be isolated when no other vessels passed the sensors through the main navigational channel within an interval of 15 minutes before and 15 minutes after the considered ship. After selection of isolated passages, a data base of 235 ship passages was obtained. This data base will be used to assess models for primary ship waves from literature (Schoellhamer, 1996; Kriebel and Seelig, 2005; Schroevers et al., 2011), and to establish an alternative predictive model for the situation in the bend of Bath in particular.

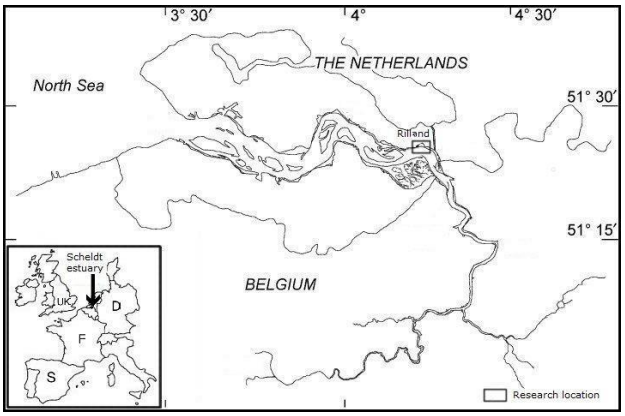

Figure 2. Research location

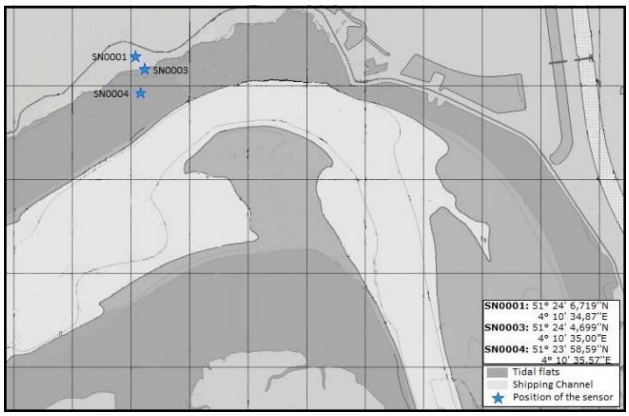

Figure 3. Position of the pressure sensors near the mudflat of Rilland (The Netherlands)

3 RESULTS

For the isolated ship passages, the influence of ship characteristics on wave height of the primary wave was investigated. The dimensions of the vessels (length L, width B and draft D) are significantly and positively correlated to the primary wave height, see Table 1. There is also a significant positive association between speed of the vessel and primary wave height, while the distance of the vessel to the measurement location is significantly negatively associated with primary wave height (Table 1).

Table 1. Pearson's product-moment correlation of ship parameters with primary wave height H

parameter	r	p	df
L	0.65	<0.001	233
B	0.64	<0.001	233
D	0.47	<0.001	233
v	0.24	<0.001	233
v^2	0.23	0.0003	233
MinDist	-0.18	0.005	233

The data from the measurement campaign in the bend of Bath are found to be consistent with primary wave height models known from literature. A positive association was found between primary wave height and $Fr^{2.4}S^{1.6}$, where $S = BD/bh$ (r=0.50, p<0.001, df=233), thus confirming Schoellhamer's model (1996). Kriebel and Seelig (2005) propose a model which explains $g.H$ as a function of $v^a(MinDist/L)^b$, for some exponents a and b. For the data in the bend of Bath, $a = 1.10$ and $b = -1.47$ were found, giving a significant positive association (r=0.72, p<0.001, df=233). The exponential relationship between primary wave height and $L.v$ proposed by Schroevers et al. (2011) was also confirmed by the current study (r=0.69, p<0.001, df=233). However, in all three cases the models from literature leave a considerable part of the spread in the data unexplained. Therefore, an alternative model is proposed, which explains primary wave height as a function of ship dimensions, ship speed and an indication of the distance between vessel and shore.

According to Table 1, ship dimensions and ship speed are important factors influencing the height of primary waves. As the three main dimensions of a ship are correlated, they are summarized in one single parameter, the volume expressed in 10^3 m³, being the product of length, width and draft: $vol = L.B.D/1000$. This product is a very rough approximation of the underwater volume of the ship, not taking into account the exact hull design. Ship speed and the interaction between speed and volume were also added to the model as significant predictors for primary wave height, see Table 3. Concerning the ship speed it was tested whether the square of ship speed v^2 can improve the model. The correlation between v^2 and primary wave height is strong though not as strong as the correlation between v and primary wave height, see Table 1. Moreover, adding $v^2$to the model or replacing v by v^2did not improve its predictive power. As such, plain ship speed v was retained as a predictor for primary wave height in the final model.

The distance between the sailing vessel and the measurement location cannot be determined accurately for our data set. It can be approximately calculated, which results in an estimate that is not very precise. As an alternative to distance, heading, which is the course steered by the vessel, was tested as a predictor for primary wave height. In the bend of Bath, vessels either sail towards the port of Antwerp (heading E), or towards Flushing and the North Sea (heading W). For safety reasons, vessels should maintain a distance of approximately 1/3 of the channel width to oncoming traffic. By doing so, vessels will navigate at close distance to the buoy line: close to the red buoy line when heading W and close to the green buoy line when heading E. In the bend of Bath, the red buoy line is often at short distance from the river bank. Vessels heading E sail on the other side of the waterway, so further away from the river bank (Pilot Association Antwerp, 2016).

In the bend of Bath, tidal currents are an important factor. Inbound currents occur before high tide whereas outbound currents occur after high tide. As such vessels heading E before high tide and vessels heading W after high tide sail with the tidal current; in other cases the vessels sail against the tidal current. The distribution of heading with respect

to tidal current was investigated for the selected passages, results can be found in Table 2. Heading and direction of tidal current are not correlated for the considered passages (Pearson's chi-squared test p = 1, df=1). Hence the variable heading is not confounded with the direction of the tidal current and it mainly classifies ships according to their distance to the shore.

Table 2. Heading with respect to tidal current

	with current	against current
heading E	55	51
heading W	68	61

By increasing the r squared value from 0.59 to 0.71, the variable heading which allows only two values (E and W) appears to be a better predictor for mean primary wave height than distance to the measurement location, which only increases the r squared value to 0.61. Therefore, heading is retained as a final predictor in the model. As such, it is found that mean primary wave height can be modelled as follows for the considered ship passages in the bend of Bath:

$$H = -13.57 + 1.14v + 0.0145v * vol + 8.31 headingW. \quad (1)$$

Primary wave height H is expressed in cm, ship speed v is expressed in knots and volume vol in 10^3 m³. The variable $headingW$ is a dummy variable which equals 1 for vessels sailing towards Flushing (West), and equals 0 for vessels sailing towards Antwerp (East). All predictors in this model are statistically significant at the 0.00001 level; the model has an r squared value of 0.71 and thus explains more than 70% of all variation in the data. An overview of coefficients and their 95% confidence intervals can be found in Table 3. The remaining variation in the data may be due to other factors, like meteorological conditions such as wind, or the (tidal) current and exact water depth at the time and position of the passing vessel

Table 3. Coefficients of regression model (1), with 95% confidence intervals

predictor	estimate	95% CI
v	1.141	[0.76; 1.52]
v.vol	0.0145	[0.0131; 0.0159]
headingW	8.309	[6.619; 10.000]

The regression model (1) which was calculated for the data on primary wave height reveals the most important factors influencing mean primary wave height of ship generated waves in the bend of Bath. For every knot increase of vessel speed, the mean primary wave height is expected to increase with 1.14 cm. However, if ship volume increases, the effect of speed on mean primary wave height becomes more important, which is expressed by the significant interaction term of speed v with volume. Finally, mean primary wave height is on average 8.31 cm higher for vessels heading to the North Sea than for vessels heading to the port of Antwerp. A graphical representation of model (1) can be found in Figure 4 and Figure 5.

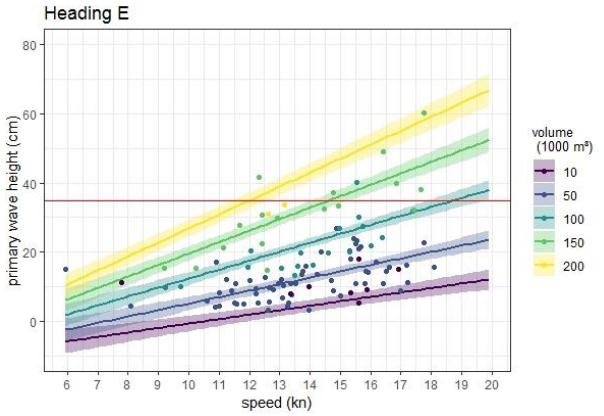

Figure 4. Mean height of primary ship waves at sensor SN0001, for vessels heading E. Dots represent observed primary wave heights. Lines represent predicted mean primary wave height with 95% confidence band as a function of speed in knots, for vessels with different volumes. The red horizontal line represents the threshold of 35 cm.

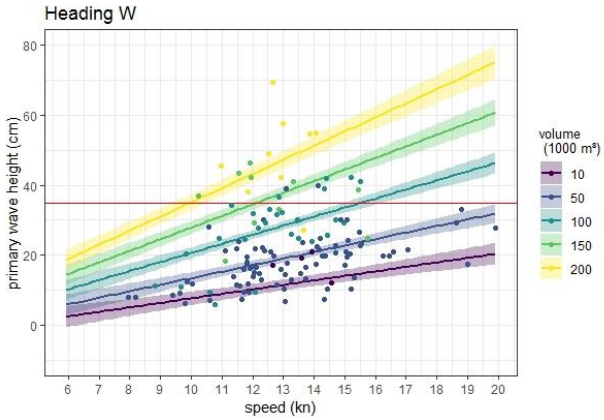

Figure 5. Mean height of primary ship waves at sensor SN0001, for vessels heading W. Dots represent observed primary wave heights. Lines represent predicted mean primary wave height with 95% confidence band as a function of speed in knots, for vessels with different volumes. The red horizontal line represents the threshold of 35 cm.

4 DISCUSSION

When comparing Figure 4 and Figure 5, the heading of the vessel stands out as an important factor influencing mean primary wave height. For ships heading E, towards Antwerp, many observations show wave heights between 10 cm and 20 cm and only a minority of events gave rise to wave heights greater than 35 cm. For ships heading W, towards the North Sea, reported primary wave heights at sensor SN0001 are considerably higher, with an important number of events surpassing the threshold of 35 cm. This

is an immediate consequence of navigating regulations, as ships heading W must sail close to the red buoys line, and hence close to the pressure sensor. For ships heading E this distance is larger, as they are required to navigate close to the green buoys line which is located further away from the river bank.

Apart from heading, the combination of ship speed and ship volume has an important effect on mean primary wave height. With increasing ship volume, the volume of displaced water increases, resulting in general in higher primary waves. This effect becomes more important when ship speed increases, as more energy is transferred to the ship generated waves. The importance of ship speed and ship dimensions was also identified by Schoellhamer (1996), Kriebel and Seelig (2005) and Schroevers et al. (2011). When compared to those results from literature, regression model (1) differs in that it combines the three main dimensions of a vessel into a single parameter (the volume), instead of considering the effect of one or more individual ship dimensions. Model (1) also describes how the effect of speed changes according to the volume of the ship. By adding heading as a third variable, it focuses on easily interpretable and clear factors that are known to navigators in the bend of Bath. By interpretation of regression model (1), practical guidelines to navigators can be formulated concerning speed reduction in order to diminish mudflat erosion. Those guidelines differ for ships heading E and ships heading W.

For ships heading E, Figure 4reveals that primary waves of 35 cm or more, which are reported to induce erosion for all types of soils (Nanson et al., 1994), will on average only be reached by large vessels with a volume of 100,000 m³ and above, at relatively high speeds. In the considered data base, primary wave heights of 35 cm and more were recorded for only 7 vessels heading E. According to model (1), mean primary wave height for vessels of 200,000 m³ and above exceeds 35 cm when speed is at least 12 to 12.5 knots. For vessels of 150,000 m³ the critical speed increases to approximately 15 knots. According to the Pilot Association Antwerp, there is no speed limit on the Scheldt estuary. The effective speed of vessels depends on conditions such as ship traffic and weather. Most vessels spontaneously reduce speed when approaching sharp bends such as the bend of Bath. However, to keep up with sailing schedule and tide, fast vessels such as container vessels can reach high speeds that may exceed 16 knots.

When heading W, the situation is different. In this case the speeds giving rise to mean primary wave heights of 35 cm and above are considerably lower for all vessels. For vessels of 100,000 m³, mean primary wave height exceeds 35 cm at a speed of approximately 16 knots. When volume increases to 150,000 m³, the critical speed is already reached at 12-12.5 knots, while the critical speed for vessels of 200,000 m³ is only approximately 10 knots.

To summarize (see Table 4) small vessels with a volume of at most 100,000 m³ will hardly ever generate primary waves exceeding the threshold of 35 cm when heading E. For course W, they should navigate at speeds lower than 15.5 knots, which is the case for all vessels in this category in the data base under investigation.

Larger vessels with a volume of 150,000 m³ reach the critical speed for erosion at 14.5 knots when heading E and already at 12 knots when heading W.

Vessels with a volume of 200,000 m³ and above should maintain speeds lower than 12 knots when heading E, and lower than 10 knots when heading W. In the data base under investigation, almost all vessels in this class were sailing at speeds above this threshold when heading W.

Table 4. Critical ship speed at which mudflat erosion is likely to occur

Heading (East / West)	Volume (m³)	Critical Speed (kn)
East	100,000	/
	150,000	14.5 kn
	200,000	12.0 kn
West	100,000	15.5 kn
	150,000	12.0 kn
	200,000	10.0 kn

The presented results only apply to the location of sensor SN0001, see Figure 2, far away from the waterway. Waves have already been distorted after travelling over the mudflat when arriving at the sensor. On other locations closer to the waterway, the effect of ship parameters on wave height may be different, although similar results are expected. However, the critical speed is suspected to be higher for locations closer to the waterway. This issue can be verified in future research. Nevertheless, the measurement location under research, close to the transition to natural marsh vegetation, is a valuable location for assessing erosion potential of ship-induced waves, since wave action is an important constraint for settlement, growth and survival of natural marsh vegetation that is not present closer to the waterway.

5 CONCLUSIONS

In this paper, data on ship generated waves recorded in a field campaign (2012-2013) in the bend of Bath were analyzed. The study intended to assess the relationship between the height of the primary wave generated by seagoing vessels and ship characteristics, on a location far from the waterway.

For the specific situation of the bend of Bath, vessel volume, speed and heading emerged as the most important vessel-related predictors for the primary wave height. Mean primary wave height increases as both volume and speed increase, where the effect of increasing speed is more important for larger vessels. Heading E or W is an indicator of how close to the shore the ship is navigating and as such also influences mean primary wave height of

waves when they reach the intertidal mudflat. It is preferred over exact distance to the shore, as it is an easy and straightforward element for navigators when deciding at what speed they can pass in the bend of Bath, and as the use of distance instead of heading does not improve the statistical model proposed.

Based on the statistical model, practical recommendations towards navigators in the bend of Bath can be formulated. Ship speed stands out as the obvious parameter controllable by navigators that has a clear impact on erosion potential of ship-induced waves, as has been summarized in Table 4. Overall, it can be concluded that for ships heading E, towards the port of Antwerp, a speed reduction is less important than for ships heading W, towards the North Sea. When heading W, speed reduction is strongly recommended for reducing mean primary wave height and thus erosion potential. The larger the volume of the vessel, the smaller the recommended maximum speed in the bend of Bath for vessels heading W. For large vessels, another option for reducing the erosion potential on the mudflat is sailing in the middle of the waterway, which is only possible in the absence of other shipping traffic. Given the density of traffic in the bend of Bath, this is often not possible and speed appears to be the only controllable factor for reducing wave height and as such erosion effects on the intertidal mudflat.

This research has thrown up many questions in need of further investigation. Apart from ship speed, other factors that are controlled by navigators may influence primary wave height. Further experimental investigations are needed to estimate the effect of maneuvers performed by the navigator on wave height in restricted river sections.

6 ACKNOWLEDGEMENTS

This work was performed within the framework of a Doctoral research on waves generated by vessels and their impact on river banks and was sponsored by the Antwerp Maritime Academy (Antwerp, Belgium). Part of this work was also supported by the BOF (research fund) of the University of Antwerp.

The authors would like to thank the reviewers for their valuable comments and suggestions for improvement of the paper.

7 REFERENCES

Barbier, E.B., Hacker, S.D., Kennedy, C., Koch, E.W., Stier, A.C., Silliman, B.R., 2011. The value of estuarine and coastal ecosystem services. Ecological monographs 81, 169–193.

Callaghan, D.P., Bouma, T.J., Klaassen, P., Van der Wal, D., Stive, M.J.F., Herman, P.M.J., 2010. Hydrodynamic forcing on salt-marsh development: Distinguishing the relative importance of waves and tidal flows. Estuarine, Coastal and Shelf Science 89, 73–88.

Dorova, J., Moore, G., 1997. Effects of boat wakes on streambank erosion, Kenai River. Alaska. Technical Report 97-4105, US Geological Survey, Anchorage, Alaska, prepared in cooperation with the Alaska Department of Fish and Game.

Ellis, J.T., Sherman, D.J., Bauer, B.O., 2006. Depth compensation for pressure transducer measurements of boat wakes. Journal of Coastal Research 488–492.

Gedan, K.B., Kirwan, M.L., Wolanski, E., Barbier, E.B., Silliman, B.R., 2011. The present and future role of coastal wetland vegetation in protecting shorelines: answering recent challenges to the paradigm. Climatic Change 106, 7–29.

Heuner, M., Silinski, A., Schoelynck, J., Bouma, T.J., Puijalon, S., Troch, P., Fuchs, E., Schröder, B., Schröder, U., Meire, P., Temmerman, S., 2015. Ecosystem Engineering by Plants on Wave-Exposed Intertidal Flats Is Governed by Relationships between Effect and Response Traits. PLOS ONE 10, e0138086. https://doi.org/10.1371/journal.pone.0138086

Kriebel, D.L., Seelig, W.N., 2005. An empirical model for ship-generated waves, in: Ocean Waves Measurement and Analysis. Presented at the 5th Int. Symposium Waves, IAHR Secretariat, Madrid, Spain.

Larson, M., Almström, B., Göransson, G., Hanson, H., Danielsson, P., 2017. Sediment movement induced by ship-generated waves in restricted waterways, in: Proceedings of Coastal Dynamics 2017. Presented at the Coastal Dynamics 2017, Coastal Dynamics 2017, Helsingør, Denmark, pp. 300–311.

McConchie, J., Toleman, I., 2003. Boat wakes as a cause of riverbank erosion: a case study from the Waikato River, New Zealand. Journal of Hydrology (New Zealand) 163–179.

Möller, I., Kudella, M., Rupprecht, F., Spencer, T., Paul, M., Van Wesenbeeck, B.K., Wolters, G., Jensen, K., Bouma, T.J., Miranda-Lange, M., 2014. Wave attenuation over coastal salt marshes under storm surge conditions. Nature Geoscience 7, 727–731.

Nanson, G.C., Von Krusenstierna, A., Bryant, E.A., Renilson, M.R., 1994. Experimental measurements of river-bank erosion caused by boat-generated waves on the gordon river, Tasmania. River Research and Applications 9, 1–14.

Rapaglia, J., Zaggia, L., Parnell, K., Lorenzetti, G., Vafeidis, A.T., 2015. Ship-wake induced sediment remobilization: Effects and proposed management strategies for the Venice Lagoon. Ocean & Coastal Management 110, 1–11. https://doi.org/10.1016/j.ocecoaman.2015.03.002

Rapaglia, J., Zaggia, L., Ricklefs, K., Gelinas, M., Bokuniewicz, H., 2011. Characteristics of ships' depression waves and associated sediment resuspension in Venice Lagoon, Italy. Journal of Marine Systems, Elsevier 85, 45–56. https://doi.org/10.1016/j.jmarsys.2010.11.005

Schoellhamer, D.H., 1996. Anthropogenic Sediment Resuspension Mechanisms in a Shallow Microtidal Estuary. Estuarine, Coastal and Shelf Science 43, 533–548. https://doi.org/10.1006/ecss.1996.0086

Schroevers, M., Huisman, B.J.A., van der Wal, M., Terwindt, J., 2011. Measuring ship induced waves and currents on a tidal flat in the Western Scheldt Estuary, in: Current, Waves and Turbulence Measurements (CWTM). Presented at the 2011 IEEE/OES 10th, IEEE, Monterey, CA, pp. 123–129. https://doi.org/10.1109/CWTM.2011.5759539

Silinski, A., Heuner, M., Schoelynck, J., Puijalon, S., Schröder, U., Fuchs, E., Troch, P., Bouma, T.J., Meire, P., Temmerman, S., 2015. Effects of Wind Waves versus Ship Waves on Tidal Marsh Plants: A Flume Study on Different Life Stages of Scirpus maritimus. PLOS ONE 10, e0118687. https://doi.org/10.1371/journal.pone.0118687

8 AUTHORS BIOGRAPHY

Abed Benmestoura holds the current position of lecturer and research associate at Antwerp Maritime Academy (AMA), Belgium. In the frame work of his PhD research he investigates the impact of ship induced waves on river banks.

Deirdre Luyckx obtained a PhD in Mathematics at Ghent University and holds the current position of Professor at Antwerp Maritime Academy (AMA), Belgium. She is responsible for teaching mathematics, physics and statistics and provides support to statistical aspects of research at AMA. Het current interests include data analysis and visualization, with applications in a maritime context.

Peter Bueken obtained a PhD in Mathematics from the University of Leuven and holds the current position of Professor at the Maritime Academy of Antwerp (AMA), Belgium. He started teaching mathematics, data analysis and computer science at Antwerp Maritime Academy in 1999. His current interests include database management and programming web applications.

Stijn Temmerman is a Professor of Earth Sciences at the Department of Biology, University of Antwerp, Belgium. He is teaching and coordinating research projects on coastal, estuarine and river system dynamics. His experience includes interactions between waves, tidal flow, sediment transport, geomorphology and organisms living in intertidal areas, and how these bio-physical interactions drive the response of coastal and estuarine ecosystems to global change and human impacts.

ANALYSIS OF THE FLOW CONDITIONS BETWEEN THE BOTTOMS OF THE SHIP AND OF THE WATERWAY

Carl-Uwe Böttner,
Federal Waterways Engineering and Research Institute, Hamburg, Germany

Pascal Anschau,
Schiffbau-Versuchsanstalt Potsdam, Germany

Ivan Shevchuk,
Institute for Fluid Dynamics and Ship Theory, Hamburg University of Technology, Germany

ANALYSIS OF THE FLOW CONDITIONS BETWEEN THE BOTTOMS OF THE SHIP AND OF THE WATERWAY

Carl-Uwe Böttner, Federal Waterways Engineering and Research Institute, Hamburg, Germany
Pascal Anschau, Schiffbau-Versuchsanstalt Potsdam, Germany
Ivan Shevchuk, Institute for Fluid Dynamics and Ship Theory, Hamburg University of Technology, Germany

SUMMARY

A physical model test was performed, to which a scaled model (1:40) was designed and constructed to carry two Laser Doppler Velocimetry sensors and provide optical access at different locations along the hull to detect the stream close to bottom of the hull and resolving the boundary layer flow at the hull. The measurement campaign was conducted in a shallow water towing tank and included a range of water depths and ship speeds such that the influence of each became analysable. The purpose of the experiment is to provide validation data to further corroborate a numerical approach and to gain deeper insight in the flow conditions in the gap flow underneath the vessel in very shallow water. In addition the extension of the effect of propulsion on the dynamic sinkage and trim in very shallow water was checked. Even though for one particular ship design and restricted to model scale 1:40, the results are regarded a valuable basis for further investigations on this phenomenon.

NOMENCLATURE

B	ship beam (m)
h	water depth (m)
L	length of the towing tank (m)
L_{PP}	length between perpendiculars (m)
T	draught of the ship (m)
V	speed (m/s)
$V_{Full\ Scale}$	speed through water, full scale (kn)
W	width of the towing tank
λ	model scale (-)
∇	displacement (m^3)

1 INTRODUCTION

Through years of experimental tests in model scale to predict ship induced wave loads on bank protection in channels and waterways at Federal Waterways Engineering and Research Institute (BAW), a comprehensive collection of squat measurements had grown, allowing drawing some principal and systematic conclusions on the squat effect in shallow and restricted waters. One was the observation of a significant increase of the trim angle when water depth to draught ratio is decreased to less than h/T = 1.3. Change in the flow regime was suspected to be responsible for this effect.

Basically the squat phenomenon is a pure Bernoulli-effect and driven by local pressure conditions. Therefore it is tempting to apply potential flow approach to calculate the squat to be expected. The advantages to other computational fluid dynamics approaches are evident: at very low computational cost a similar useful result is obtained in an extremely short time. Modern Panel codes, solving potential flow equations for arbitrary shaped bodies like ship hulls, get the solutions in parts of a second up to some minutes CPU-Time.

Unfortunately for very shallow water conditions, which apply to water depth to draught ratios h/T < 1.3, the potential flow solutions for squat get inaccurate and show a big difference to the measurement data in towing tank (Böttner et al., 2011). One plausible explanation is that the basic assumption of potential flows, the negligibility of viscous effects in the flow is no longer valid. This appears self-evident, besides it is unclear why and how viscous effects appear on the scene. Considering the dimensions of the gap, a ship of a draught of 12 m still has more than 3 m under keel clearance at h/T < 1.3, it is not obvious how viscous boundary layers gain influence in the flow regime.

Initiated by these findings or possibly better said educated guesses, further research has been performed to validate the presumption and to identify the underlying mechanisms. Obviously, there are two aspects to be further investigated. First the possible influence of boundary layers wherefore the boundary layers and the viscous turbulence needs to be measured and calculated. And in continuation second whether this applies for full scale as well or is a phenomenon restricted to the conditions in model scale. The experiments reported here aim at the first aspect; the investigation of full scale flow conditions is reserved for numerical approaches.

To strengthen the assumption and gain deeper insight in the first aspect, computational fluid dynamics simulations with viscosity have been performed by solving unsteady Reynolds Averaged Navier-Stokes Equations (U-RANSE). Even though the model scale is 1:40, the pure dimensions are nevertheless challenging for numerical calculation, especially if the boundary layers are to be scrutinized. A quite elaborate investigation using the RANSE solver package OpenFOAM (Greenshield and Weller, 2019) was performed, which revealed boundary layers growing along the hull length stream downwards at both walls, the hull of the vessel as well as the floor of the towing tank and unify in the last third of the hull if speed

through water of the ship is high enough (Shevchuk et al., 2016).
The numerical results are strongly sensitive on the numerical and physical boundary conditions set. This situation is very often the impetus for validation through experimental data gained from according suitable experimental set-ups.

Therefore an experimental measurement campaign in the physical model was planned and launched. The aim was to determine the flow conditions in the close vicinity of the bottom of the hull and to resolve the boundary layer flow, if possible. The experimental set-up, the measurements and the results are introduced in the following chapters.

To answer the second aspect, the applicability of the results in the physical model to the natural conditions in scale 1:1, another numerical fluid dynamics investigation has been initiated. Obviously measurements at real ships sailing in the waterways and channels are practically very complicated if not impossible. But also in the virtual world of fluid dynamics simulations flow around a ship is one of the most demanding and challenging tasks, since the highest Reynolds-Numbers (range of Billions) of technical flows do occur here.

2 OPTICAL FLOW MEASUREMENTS IN TOWING TANK

2.1 EXPERIMENTAL SET-UP

Laser Doppler Velocimetry (LDV) is an optical flow velocity detection technique, where the Doppler-shift of reflected phase interference pattern is evaluated.

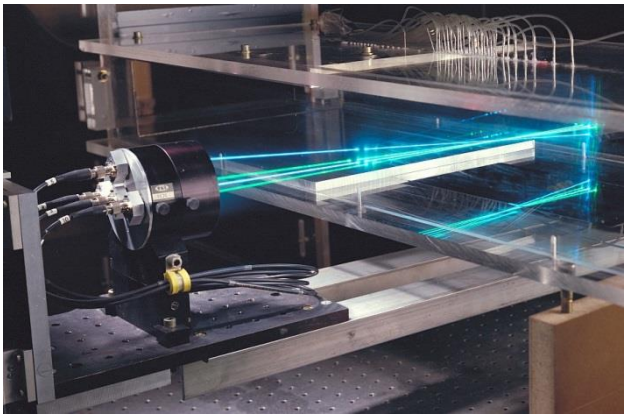

Figure 1. 2D-LDV where two different wave lengths are generated and oriented 90°, each of them is split and slightly shifted so that four beams are finally focussed by lenses and the backscatter is analysed. (Foto: Wikipedia)

A coherent laser beam is split in two parts and the angle under which the two half beams are focussed in the control volume and permeate each other let them interfere and generate a set of straight fringes. The focal length of the lenses determines the size of the control volume. The interference pattern moves with a characteristic speed, which is subject to Doppler shift when reflected by a particle passing the control volume. The moving direction of the interference pattern gives the orientation of the detected speed component. For 2D-measurements a second beam in another, distinguishable wave length and oriented so, that the pattern moves rectangular to the first one is required, as in **Figure 1**, where a green and a blue coherent laser beam is focussed in the same control volume with a 90° shifted orientation.

Figure 2.A 1D and a 2D-LDV mounted on the model of a 14000 TEU Containership to detect the near wall flow conditions. (Foto: SVA-P)

A model of 14000 TEU Container ship (cf. Table 1) was designed and constructed especially to the needs of LDV measurements through the hull. To get insight in the flow conditions, 7 small windows were included (**Figure 3**) three along the longitudinal centre, two at the chine, and two in the aft section upstream of the propeller disc to get an idea of the propeller inflow and its changing depending on the propeller load. The model was fitted with propeller and rudder and the experiments have been performed in self-propulsion mode, i.e. model propulsion condition, no friction correction applied.

Table 1. Dimensions of the model ship

14000 TEU Container Carrier – M1628S001			
Length btw. Perpendiculars	L_{PP}	[m]	8.68
Beam	B	[m]	1.3
Draught	T	[m]	0.4
Displacement	∇	[m^3]	3.0127
Scale	λ	[–]	40

The towing tank tests were performed at Duisburg Towing Tank, which provides the required shallow water conditions. The tank dimensions at Duisburg are listed in Table 2. This facility also offers optical access from below by a window in the floor quite in the middle of the tank. This is used for wake measurements by particle imaging velocimetry, which was decided not to be used together with LDVs, to avoid any possible damages by pumping laser

light of high intensity into the highly amplified photonic detectors.

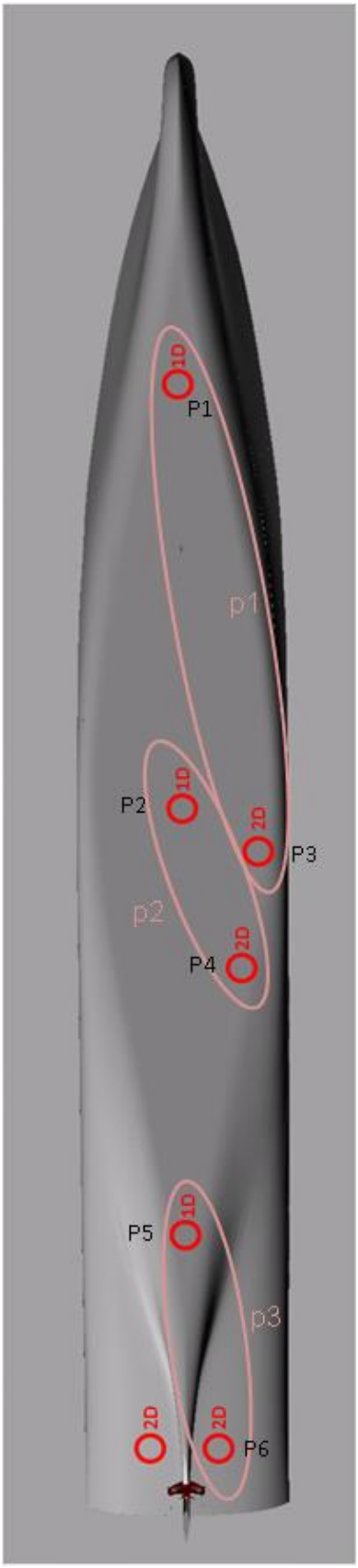

Figure 3. Positions of windows for LDV measurement

The mounting of the LDVs, visible partly in **Figure 2**, was designed such, that always two positions were occupied at the same time and two LDVs were in use. The LDVs had to be moved from one position to the next, therefore according weights could be shifted opposite to guarantee trim and ballast constant during the entire measurement campaign.

Table 2. Dimensions of the towing tank

Shallow Water Tank at DST, Duisburg, Germany			
Length	L	[m]	200
Width	W	[m]	10
Depth	h	[m]	0 - 1.2
Carriage speed, max	V_{max}	[m/s]	6.5

The LDVs were mounted on traverses fitted with stepping motors for precise positioning in vertical direction. Initial position was always at the outer edge of the window, such that the control volume just started to provide valid signals. From that position always when given minimum number of valid detections, the control volume was moved 5 mm further, away from hull towards the flow regime of the boundary layer.

2.2 EXPERIMENTS

Different speeds and different water depths were chosen (Table 3) in order to cover a significant range of conditions and to see possible transition regimes.

Table 3. Speeds and under keel clearances

Water depths			
	h/T	Depth [m]	UKC [m]
h1	1.5	0.6	0.2
h2	1.25	0.5	0.1
h3	1.15	0.46	0.06

Speeds		
Speed	Full Scale [kn]	Model [m/s]
V1	8	0.65
V2	10	0.81
V3	12	0.98
V4	14	1.14

Additionally the dynamic sinkage and trim were detected for comparison with results from other similar experiments. In shallow water experiments squat is one of the effects of interest.

There is a permanent discussion on the influence of the propeller and propeller load on dynamic sinkage and trim in shallow water conditions. Therefore some additional test runs for comparison were included, with fixed propeller (rotationally fixed) and with propeller dismantled (as in resistance towing test). Obviously the comparison is valid only for this particular ship design, but regarded

helpful to get a more general insight in this phenomenon later when suitable data from other designs might eventually become available.

3 RESULTS

The main purpose of the experiments was to detect the flow conditions in the boundary layer at the bottom of the hull. This was initiated by the lack of data to validate the numerical findings presented in 2016 (Shevchuk et al., 2016).

3.1 BOUNDARY LAYER AMIDSHIPS CENTRE HULL

An interesting finding of the numerical investigation was a unification of the two boundary layers in the gap flow between the bottoms of the hull and the waterway. In the simulations this occurred basically in the centre and the aft third of the hull bottom plate. Therefore this experimental campaign was arranged to confirm the numerical findings. In the centre line of the hull there are the windows at position P1, P2 and P5, see **Figure 3**.

P1 is at the front part, as forward as possible to get optical access. P2 is positioned close to the main frame in the middle of the bottom plate and P5 is in the aft area, where the bottom plate is still plain enough to accommodate a window for optical flow measurements.

The experimental results in **Figure 4** to **Figure 7**indicate that the boundary layer could be resolved. The speed close to the hull is quite comparable for all of the four velocities. As well, an increase of the boundary layer flow speed with growing distance to the hull up to the ship speed can be observed in positions P2, P3 and P4 (**Figure 4** to **Figure 7**).

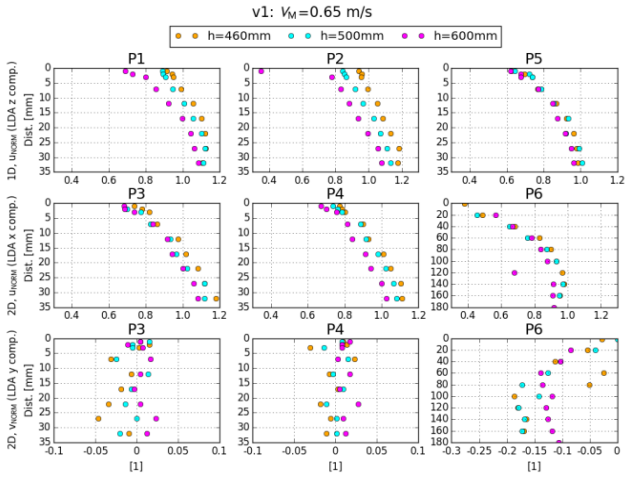

Figure 4. Boundary layer at the hull at different under keel clearances (h/T = 1.5; 1.25; 1.15) and positions (Figure 3), 8 kn in full scale.

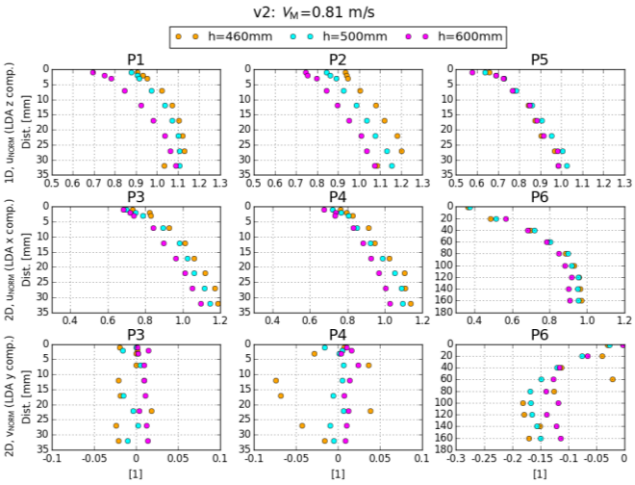

Figure 5. Boundary layer at the hull at different under keel clearances (h/T = 1.5; 1.25; 1.15) and positions (Figure 3), 10 kn in full scale.

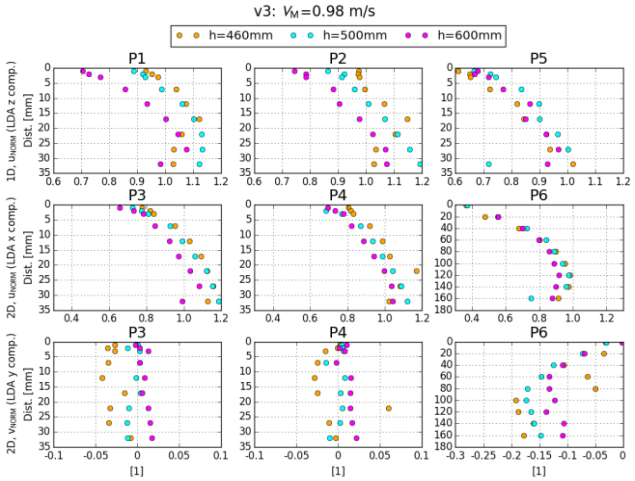

Figure 6. Boundary layer at the hull at different under keel clearances (h/T = 1.5; 1.25; 1.15) and positions (Figure 3), 12 kn in full scale.

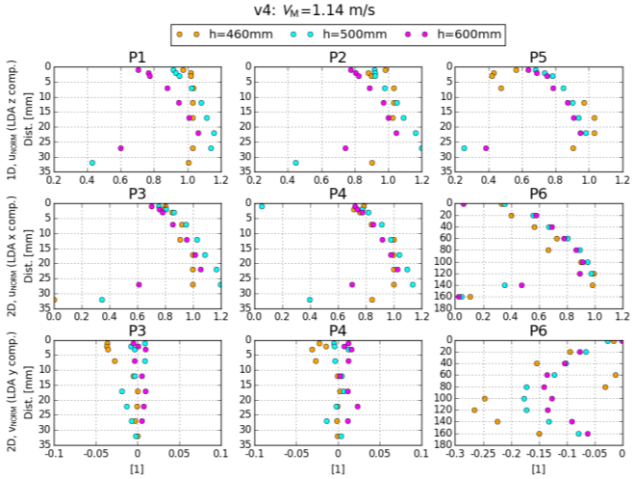

Figure 7. Boundary layer at the hull at different under keel clearances (h/T = 1.5; 1.25; 1.15) and positions (Figure 3), 14 kn in full scale.

3.2 BOUNDARY LAYER AT CHINE

Next to the central flow at the bottom of the hull, the flow conditions and its direction at the chine was of interest. Especially if there is some flow directed upwards around the chine and possibly some chine vortex generated. The windows at positions P3 and P4 (**Figure 3**) were designed as close to the chine as possible to still provide sufficient access for optical measurement techniques like LDV.

To gain insight in potentially twisted and or sheared flow conditions if upwards flow partially occurred, the 2D-LDV detectors were applied at these positions. In **Figure 4** to **Figure 7** there are for the particular positions P3, P4 and P6 two graphs each, showing component in direction of ship speed and traversal flow speed component.

There was no upstream effect detected, the orthogonal flow component detected is varying around the mean value 0 m/s (**Figure 4** to **Figure 7**) at P3 and P4 is for all of the 4 speeds and all of the under keel clearances investigated. The longitudinal component in the boundary layer is comparable to what has been observed at central positions P1 and P2 and is coherent with the overall figure suggested by the experimental results.

3.3 GROWTH OF THE BOUNDARY LAYER

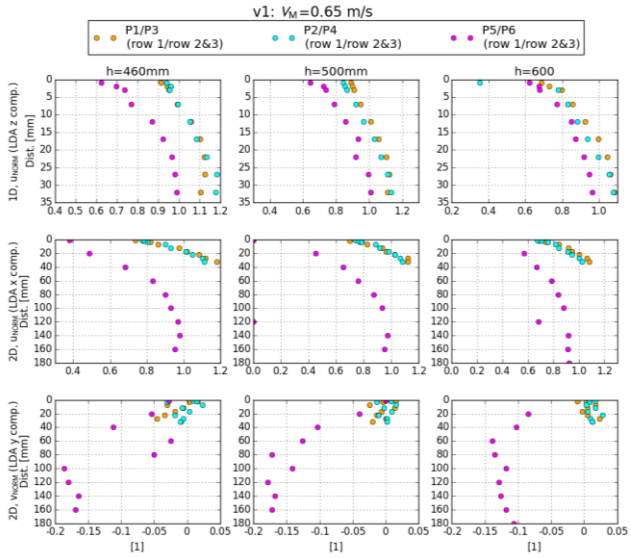

Figure 8. Boundary layer along the hull from bow (yellow) over midship (turquoise) to aft (pink) at different under keel clearances (h/T = 1.5; 1.25; 1.15) 8 kn in full scale.

The numerical findings are indicatively affirmed by the experimental results. In **Figure 8** to **Figure 11** the flow speeds are plotted for one speed and one water depth in one plot. The boundary layer increases for all speeds and all h/T-ratios at the aft region. According the assumed unification of the boundary layers, the boundary layer flow in P5 is almost constant over the range of velocities investigated (**Figure 8** to **Figure 11**). Additionally the width of the gap has an impact. As becomes obvious in each top row in **Figure 8** to **Figure 11**, where the 1D-LDV measurements along the centre are plotted, decreasing gap width induces increasing alternation of boundary layer at the aft ship. From the lowest width (water depth h = 460 mm) to the highest investigated (water depth h = 600 mm) the difference of the boundary layer from bow to aft decreases with increasing gap width or water depth.

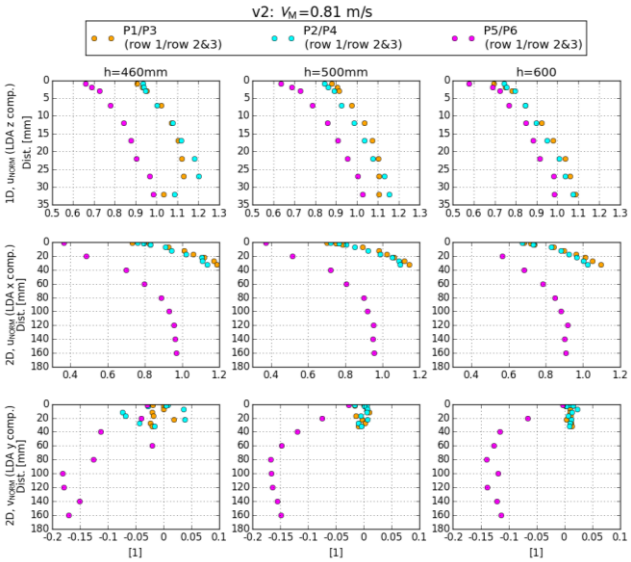

Figure 9. Boundary layer along the hull from bow (yellow) over midship (turquoise) to aft (pink) at different under keel clearances (h/T = 1.5; 1.25; 1.15) 10 kn in full scale.

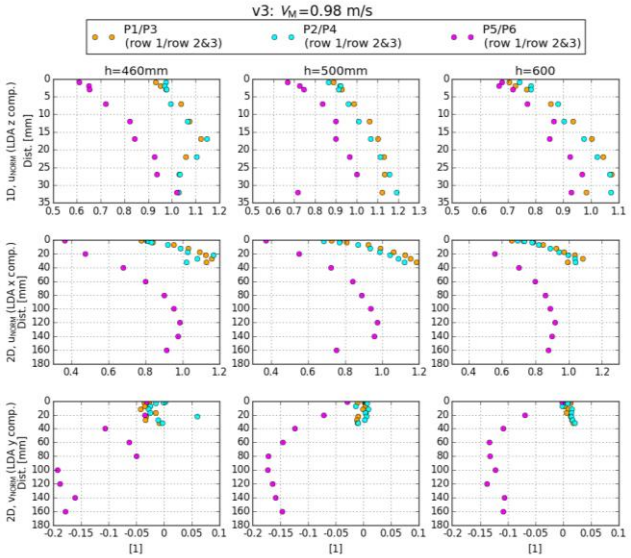

Figure 10. Boundary layer along the hull from bow (yellow) over midship (turquoise) to aft (pink) at different under keel clearances (h/T = 1.5; 1.25; 1.15) 12 kn in full scale.

In the second and third row, the results for the 2D-LDV measurements at Position P6 are plotted in pink color. At this position, which is located in the aft ship close to water line, bigger stepping was applied to detect variations in wake and inflow conditions to the propeller.

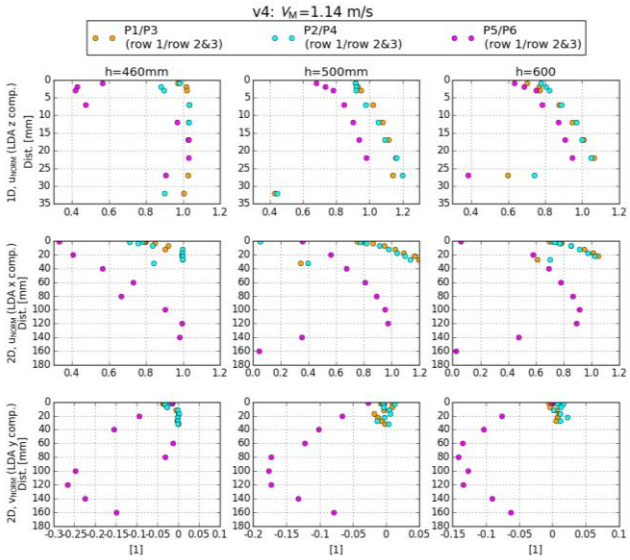

Figure 11. Boundary layer along the hull from bow (yellow) over midship (turquoise) to aft (pink) at different under keel clearances (h/T = 1.5; 1.25; 1.15) 14 kn in full scale.

3.4 INFLUENCE OF PROPELLER ON SQUAT

As already mentioned, there is an ongoing debate on the actual influence of the propeller induced pressure distribution on the dynamic sinkage and trim of the aft section. Especially in very shallow water, i.e. h/T < 1.3, where a considerable increase of the resistance is noticed and the propeller is opposed to increased load and torque, the propulsion induced pressure field is suspected of further reducing under keel clearance at the stern and changing trim angle. Regularly there is a significant change in trim observed in comparison to Squat in moderate shallow water conditions. Another well-known shallow water effect is an increase of resistance resulting in a higher loaded propeller working at higher torque. There is no doubt that this effect leads to a more prominent pressure field in the in- and outflow region of the propeller disc. From literature it is well known, that the pressure field induced by the propeller under load alters the flow conditions in the aft ship area. This is limited to the vicinity of the propeller's position and might be considered reaching no further upstream than up to 10 times propeller disc diameter (Vladimir Krasilnikov, 2014). The dominant interaction of the propeller's pressure field and the hull is by vibration induction when the tip pressure peaks pass by the aft ship above the propeller and induce noise and vibrations in the hull (Su et al., 2017; SVA Potsdam, 2015). What isn't that obvious is to reckon quantitatively the degree of propeller's influence on squat in very shallow water.

At the premises of BAW, there is no towing carriage in the test facility available since unnecessary for civil engineering waterway investigations. Therefore, all squat data at the basin of BAW are gained from physical model tests at the model self-propulsion condition solely. The physical model test campaign presented herein was performed at Duisburg Towing Tank, which offers a towing carriage and was regarded as a valuable opportunity checking the propellers influence to this particular ship at least, well knowing that this is additionally restricted to model scale.

Table 5. Squat with and without Propulsion

Speed = 0.98 m/s (12 kn in full scale) and h/T = 1.15

Value	Unit	Self-Propelled	No Propeller
Sink_Bow	[mm]	25.03	27.7
Sink_Stern	[mm]	18.63	17.9
Trim	[°]	0.048	0.074

A comparison of squat with and without propulsion at similar draft, speed and water depth conditions is shown in Table 5. In case "Self-Propelled" the carriage follows the vessel which is hold captive in heading and yaw, but free to move in all of the remaining modes. "No Propeller" is realized by towing the model with the carriage at the given speed; the propeller has been dismantled and was replaced by a cap covering the hub.

The flow detections at position P6 were included to investigate potential change of propeller inflow regime due to shallow water conditions. Comparing **Figure 4** to **Figure 7** as well as in **Figure 8** to **Figure 11**, there was no influence of the under keel clearance on the flow observed in this position. Apparently there is none or only minor blocking effect on the wake by small under keel clearance. Removing the propeller has an effect and the propeller's contribution to the wake entirely on radial components becomes visible in **Figure 12**.

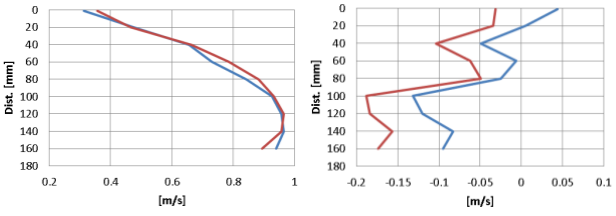

Figure 12. Flow conditions in position P6 in front of the propeller disc: with (red) and without (blue) Propeller mounted. Longitudinal (u-comp.) left and orthogonal (v-comp.) right, h/T = 1.15, V_M = 0.98 m/s

To investigate the alternation of the flow conditions by a either loaded or standing propeller, as it occurs while manoeuvring in harbours for instance, in another series some runs were repeated with the propeller fixed in rotation and the ship towed by the carriage. The blockage by the non-rotating propeller has a prominent effect on the

flow. The stopped propeller generates a backwater upstream which results in reverse flow direction (**Figure 13**, left). Less surprisingly, radial component of flow in front of the propeller more or less vanishes for propellers stopped (**Figure 13**, right).

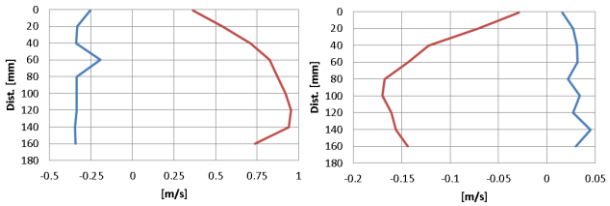

Figure 13. Flow conditions in position P6 in front of the propeller disc: rotating (red) and fixed (blue) Propeller mounted. Longitudinal (u-comp.) left and orthogonal (v-comp.) right, h/T = 1.25, V_M = 0.98 m/s

4 VALIDATION OF NUMERICAL RESULTS

Basically the purpose of the physical model test campaign was to provide data for validation of numerical fluid dynamics results and findings with another ship model and already presented at the 4th MASHCON (Shevchuk et al., 2016). A short citation of the publication shall be included here:

"[…] The most interesting results were obtained for the velocity distribution in the gap between the ship and the channel bottom.

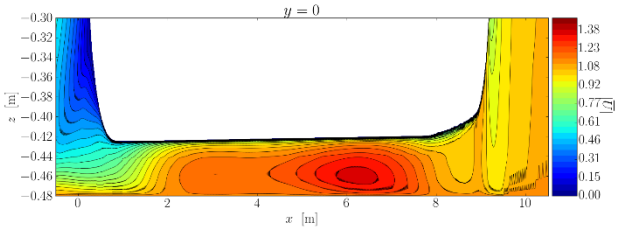

Figure 14: Velocity magnitude distribution at the middle line plane of PPM55 at h/T=1.15, U=1.13m/s

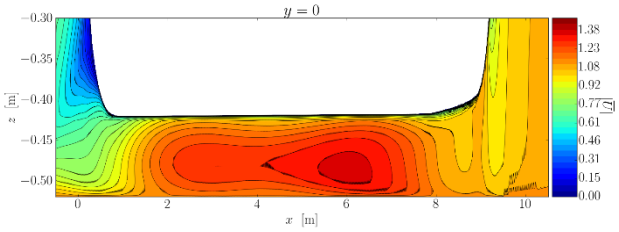

Figure 15: Velocity magnitude distribution at the middle line plane of PPM55 at h/T=1.3, U=1.13m/s

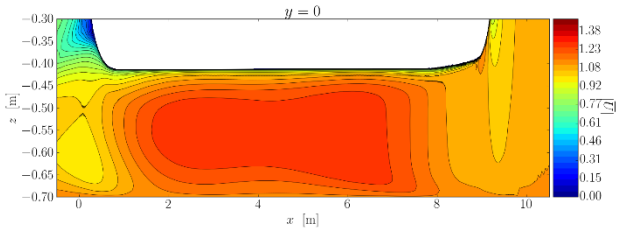

Figure 16: Velocity magnitude distribution at the middle line plane of PPM55 at h/T=1.75

In the Figure 14, Figure 15and Figure 16 one can see the distribution of the velocity magnitude at the middle line plane at different depths at the speed of 1.13 m/s. In the presented figures the following phenomenon can be observed. At h/T = 1.75 one can distinguish two separate boundary layers growing in the gap: one on the bottom and one on the ship hull. As h/T decreases, these two get united so that there is no region, for which it could be stated that the viscous effects are negligible there. […]"

This particular numerical approach was applied to the ship model PPM52, which was built to accommodate Laser Doppler Velocimetry. The squat predictions and the flow condition close to the hull's wall and the tank's wall was the criteria for the numerical approach to prove validity. The Reynolds Averaged Navier-Stokes Equations were solved using OpenFOAM (Greenshield and Weller, 2019), the equations were solved with second order accuracy on a numerical grid of 23 to 25 Million control volumes, required to achieve non-dimensional wall distances smaller than one ($y^+ < 1$), allowing resolving the boundary layer completely without near wall modelling.

The agreement of the numerical and the experimental values is shown exemplary at a vessel's speed of 10 kn in full scale for different depth to draft ratios (h/T). The h/T ratios vary from 1.5 over 1.25 down to 1.15 (**Figure 17** to **Figure 19**). The RANSE simulation agrees well with the experimental findings discussed in 3.3. The boundary layer is extended in wall orthogonal direction with decreasing water depth and under keel clearance.

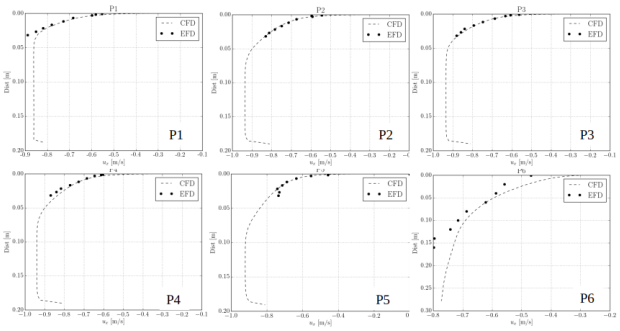

Figure 17. Comparison of numerical results and experimental data at six positions and vessel speed of 0.81 m/s (model scale) and depth to draft ratio (h/T) of 1.5

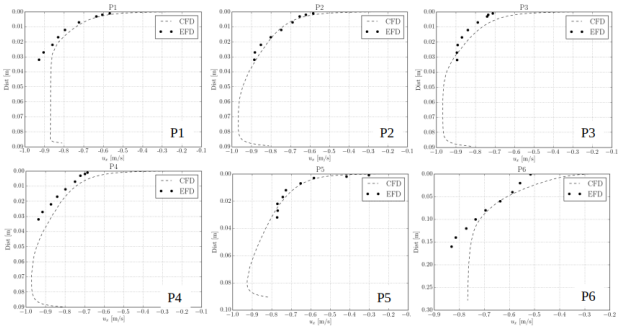

Figure 18. Comparison of numerical results and experimental data at six positions and vessel speed of 0.81 m/s (model scale) and depth to draft ratio (h/T) of 1.25

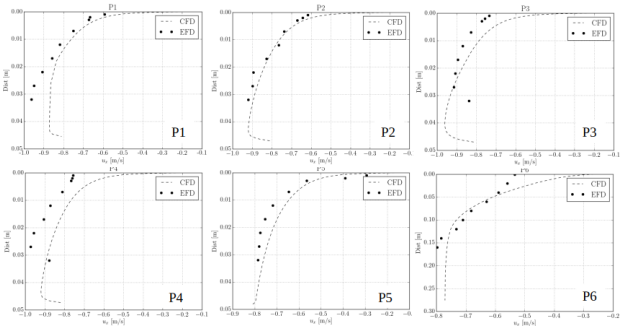

Figure 19. Comparison of numerical results and experimental data at six positions and vessel speed of 0.81 m/s (model scale) and depth to draft ratio (h/T) of 1.15

5 CONCLUSIONS

A model in scale 1:40 has been constructed for optical access to boundary layer flow conditions. Laser Doppler Velocimetry could be successfully applied and revealed the flow regime in the gap between the bottom of the hull and the towing tank floor. The two aims of the physical model measurements campaign were successfully reached: first to provide insight in the flow conditions close to the hull and second to provide data for evaluation and validation of numerical modelling approaches. Additionally the qualitative and quantitative contribution of the loaded propeller to the dynamic sinkage and trim in very shallow water was tested and approved.

The results are encouraging for further investigation of the phenomenon of squat in terms of scale effect. The propeller obviously gains impact on squat at very shallow water, but up o now, the evidence is in model scale only. Scaled model tests are well-known for higher wake numbers and more prominent wake than the same geometry at full scale. This is one of the challenges when predicting required propulsion and determining the proper self-propulsion point in full scale from propulsion tests in a towing tank in model scale. Accordingly, a less prominent impact of the propeller is expected in full scale. To which extend is subject of ongoing work.

6 REFERENCES

Böttner, C.-U., Heimann, J. and Uliczka, K., 2011. Numerical prediction of Squat of large Container Carriers on Waterways, in: Marine CFD 2011: 22-23 March, 2011, London, UK

Greenshield, C, and Weller, H., 2019. OpenFOAM and the OpenFOAM Foundation, available at: https://openfoam.org/.

Krasilnikov, V., 2014. Numerical Modeling of Ship-Propeller Interaction under Self-Propulsion Condition, in: Star Global Conference, Vienna, Austria.

Shevchuk, I., Böttner, C.-U. and Kornev, N., 2016. Numerical analysis of the flow in the gap between the ship hull and the fairway bottom in extremely shallow water, in: Proceedings of the 4th International Conference on Ship Manoeuvring in Shallow and Confined Water with Special Focus on Ship Bottom Interaction. Bundesanstalt für Wasserbau, Hamburg, Germany, pp. 37–42. https://doi.org/10.18451/978-3-939230-38-0.

Su, Y., Kim, S., Du, W., et al., 2017. Prediction of the Propeller-induced Hull Pressure Fluctuation via a Potential-based Method: Study of the Rudder Effect and the Effect from Different Wake Alignment Methods, in: Fifth International Symposium on Marine Propulsion: SMP'17.

SVA Potsdam, 2015. Pressure Fluctuation Measurement. available at: https://www.sva-potsdam.de/en/pressure-fluctuation-measurement/.

7 AUTHORS BIOGRAPHY

Carl-Uwe Böttner currently works as a research engineer with the Federal Waterways Engineering and Research Institute (BAW) in Hamburg on the fields of ship dynamics and ship handling simulation. He is responsible for consulting the authorities in terms of ship handling simulation.

Pascal Anschau currently works as a senior research engineer with Potsdam Towing Tank (SVA Potsdam). He is mainly responsible for computational fluid dynamics simulations and analysis of ship hydrodynamics. He studied Naval Architecture at Technical University of Berlin and holds a Diploma degree.

Ivan Shevchuk Works at TU Hamburg at the Institute for Fluid Dynamics and Ship Theory as a research engineer on the field of computational fluid dynamics. He holds a diploma and a PhD degree on Naval Architecture.

CALIBRATING AND MEASURING WAKES AND DRAG FORCES OF INLAND VESSELS IN CONFINED WATER IN A TOWING TANK

Clément Caplier, Guillaume Gomit, Germain Rousseaux, Damien Calluaud, Ludovic Chatellier and **Laurent David**,
Pprime Institute, CNRS - University of Poitiers - ISAE-ENSMA, France.

CALIBRATING AND MEASURING WAKES AND DRAG FORCES OF INLAND VESSELS IN CONFINED WATER IN A TOWING TANK.

Clément Caplier, Guillaume Gomit, Germain Rousseaux, Damien Calluaud, Ludovic Chatellier and **Laurent David,** Pprime Institute, CNRS - University of Poitiers - ISAE-ENSMA, France.

SUMMARY

This paper gives a review of the experimental methods developed in the towing tank of the Pprime Institute of the University of Poitiers, France, for the characterization of ship wakes and drag forces in confined waters. Different waterway configurations in calm water and in the presence of a current are reproduced in the experimental facility and small scale ship models of different block coefficients are considered. Stereoscopic optical methods have been developed in the laboratory for the measurement of the free surface deformation around the ship. The full wake generated by the ship is fully characterized and its hydraulic and undulatory properties are analyzed in both real space and spectral domain. In addition, a system for the measurement of the ship drag force has been set up and visualizations of the wakes have been performed in parallel with a high-speed camera, to relate the ship resistance crisis with its visual footprint in the wake.

NOMENCLATURE

α_b	Banks inclination angle (°)
A_{FFT}	Normalized amplitude of the Fast Fourier Transform of the ship wake (-)
A_1	Normalized amplitude of the transverse waves in calm water (-)
A_2	Normalized amplitude of the transverse waves in counter-current (-)
B	Beam (width) of the ship hull (m)
C_b	Block coefficient of the ship hull (-)
C_d	Drag coefficient of the ship hull (-)
D	Draft of the ship hull (m)
F_{h1}	Critical Froude number (sub.→trans.) (-)
F_{h2}	Critical Froude number (trans.→sup.) (-)
$F_{h,s}$	Froude-depth number of the ship (-)
$F_{L,s}$	Froude-length number of the ship (-)
F_X	Axial component of ship resistance (N)
g	Gravitational acceleration (m.s^{-2})
H	Height of the ship hull (m)
h	Water depth (m)
h_b	Height of the inclined bank (m)
h_{bottom}	Height of the double bottom (m)
I	Expanded uncertainty (k=2) of the ship resistance measurement (N)
$k_{x,y}$	Wavenumber along the x (longitudinal) or y (transversal) axis (m^{-1})
L_s	Length of the ship (m)
L_c	Length of the canal (m)
L_1	Normalized length of the wash zone in calm water (-)
L_2	Normalized length of the wash zone in counter-current (-)
$\lambda_{t,1}$	Normalized wavelength of the transverse waves in calm water (-)
$\lambda_{t,2}$	Normalized wavelength of the transverse waves in counter-current (-)
m	Blockage ratio of the waterway (-)
ρ	Density of water (kg/m^3)
S_w	Wetted surface area of the ship (m^2)
U_s	Ship speed (m/s)
u_c	Velocity of the river current (m/s)
u_r	Velocity of the return current (m/s)
W	Large width of the waterway (m)
w	Small width of the waterway (m)
w_b	Width of the inclined bank (m)
X	Longitudinal dimension of the wake (m)
ΔX	Spatial resolution along the X axis (m)
Y	Transversal dimension of the wake (m)
ΔY	Spatial resolution along the Y axis (m)
Z	Vertical dimension of the wake (m)
ΔZ	Spatial resolution along the Z axis (m)

1 INTRODUCTION

When a ship progresses in a confined waterway, such as a river, a canal or an estuary, it faces an increase in the advancing resistance and also experiences various phenomena in the waterway. There is a lowering of the water level, combined with the generation of a return current around the ship hull. The waves generated in its wake interact with the current of the waterway and reflect on the river banks, causing erosion and sediment transport issues. It is necessary to understand experimentally the creation and interaction between these phenomena with respect to the functional and geometrical parameters of the ship and the waterway, in order to prevent their appearance in the waterway, for both economical (reduce fuel consumption) and ecological (reduce bank erosion) reasons. This path of research has been investigated in the past few years by the Hydrodynamic and Environmental Flows team of the Pprime Institute of the University of Poitiers in France. A configuration of confined waterway with a presence of current has been reproduced in the towing tank of the laboratory, and several experimental methods have been developed for the measurement of the ship resistance, the characterization of the return current around the hull, the study of the wave reflections and the full-field characterization of the generated ship wake. In the first part of the paper, the waterway configuration set up in the towing tank of the Pprime Institute is presented and the small scale ship models representative of maritime and river ships are introduced. In the second part, the experimental measurement methods are detailed. Then, the main results of the studies are presented and finally research perspectives will be exposed with the future project of development of the canal.

2 THE TOWING TANK AND THE SHIP MODELS

2.1 THE WATERWAY

Figure 1 represents the cross-section of the towing tank of the Pprime Institute. It is composed of a bottom trapezoidal section of small width w=1.10 m and large width W=1.50 m, and a top rectangular section of same width. The inclination of the banks is α_b=45° and their width and height are w_b=h_b=0.20 m. A double bottom of height h_{bottom}=0.38 m can be installed in the towing tank to reduce the water depth to reproduce a shallow waterway of rectangular cross-section of depth h. The water depth has been set up to h=0.103 m for the experiments. The rail mounted towing trolley carries the ship hull at a speed U_s up to 2.35 $m.s^{-1}$ along the canal of length L_c=20 m. The double-bottom gives also the possibility to generate a current by placing a circulator in the lower section, and two honeycombs structures at the extremities of the canal to laminarize the flow. The current can be generated in both directions with respect to the ship motion (co- or counter-current). The canal is equipped with bottom and lateral windows to perform optical measurements and visualizations.

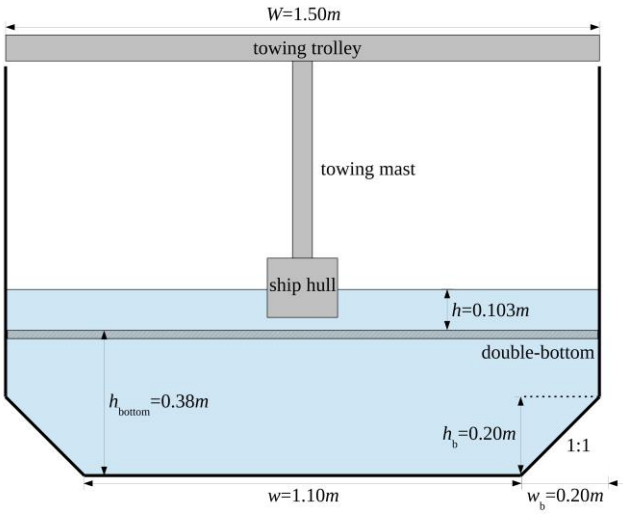

Figure 1. Transversal section of the towing tank.

2.2 THE SMALL SCALE SHIP MODELS

In order to compare the experimental results with numerical calculations of ship wakes and ship resistance, two generic ship hulls of parabolic shape have been considered. They are based on the Wigley (1926) hull form with a rectangular cross-section, mathematically defined by Eq. (1) with n=2 for a classical Wigley hull:

$$y = f(x) = \frac{B}{2}\left[1 - \left(\frac{2x}{L_s}\right)^n\right] \quad (1)$$

As the block coefficient of such a Wigley hull is C_b=0.67, another Wigley-based ship hull with an exponent n=8, giving a block coefficient C_b=0.89, has been considered (Caplier *et al.*, 2016). These two ship hulls noted WH2 and WH8 because of their n-coefficients are then representative of maritime and river ships in terms of block coefficients. The ship hulls dimensions are L_s=1.20 m, B=0.18 m and H=0.15 m, and their draft is set-up to D=0.075 m for the experiments. They are shown on Figure 2. As regards the effects of scale, the ship speeds for the experiments are set high enough to avoid capillary effects (less than 5%). In this range of ship speeds, the effects of the scale on the flow characteristics are limited (Gomit *et al.*, 2015).

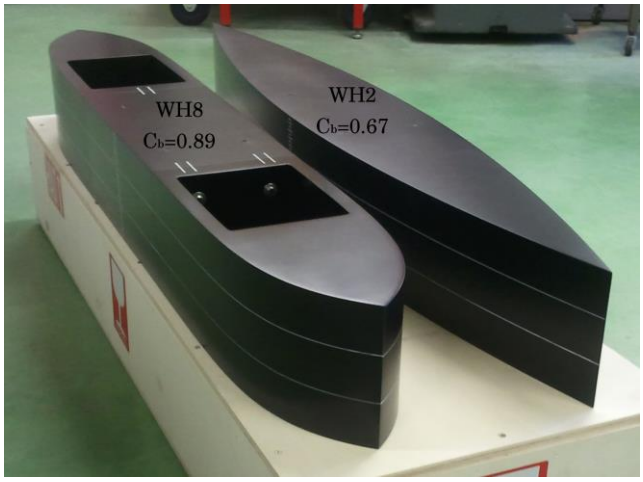

Figure 2. The WH8 and WH2 ship hulls.

3 THE MEASUREMENT AND THE ANALYSIS OF THE SHALLOW WATER SHIP WAKE

3.1 MEASUREMENT OF THE FREE SURFACE DEFORMATION

The free surface deformation is measured with a stereoscopic measurement method, based on the principle of refraction of light rays through the surface of water that is developed in our laboratory (Gomit *et al.*, 2013). The setup is represented on Figure 3. It is composed of two Dantec SpeedSense 1040 cameras that deliver a resolution of 2320x1726 *px,* mounted with Nikkor AF 28 *mm* 1:2.8 lenses. They focus on the same zone with an opposite angle of ±15° with respect to the longitudinal axis of the canal, and ±35° with respect to the vertical axis. The common field covered by the cameras forms a rectangle of dimensions 0.75x0.90 m^2, corresponding to the half width of the canal. The stereoscopic system is calibrated by translating a dotted calibration plate and using a distortion model. A speckle-pattern is placed at the bottom of the canal and its image with the water surface at rest is recorded on the cameras for the reference. Then the ship is launched and the images of the pattern, deformed by the free surface deformations, are recorded on both cameras at a frequency of 10 frames per second with an exposure time of 10 *ms*. Each run is performed three times to check the repeatability of the measurement. The image pairs are then processed with a reconstruction algorithm written in C++ and based on the SLIP library (Tremblais *et al.*, 2010) that computes the free surface deformation at each time-step. Then the whole wake is

reconstructed around the ship hull with a dedicated reconstruction program, with a spatial resolution ΔX=ΔY=10 *mm* and a precision ΔZ=0.1 *mm* on the water level.

3.2 ANALYSIS IN THE REAL SPACE

An example of the wakes measured in calm water and in the presence of a counter-current with the stereo-refraction measurement method are shown on Figure 4 (Caplier *et al.*, 2015a). These wakes are generated by the WH2 hull for a ship speed U_s=0.45 $m.s^{-1}$ and a water depth h=0.103 m, giving a Froude-depth number $F_{h,s}=U_s/(gh)^{1/2}$=0.45 and a Froude-length number $F_{L,s}=U_s/(gL_s)^{1/2}$=0.13. The wake on the bottom of the figure is generated in a calm water configuration, whereas the top one is generated in the presence of a counter-current of velocity u_c=0.20 $m.s^{-1}$, corresponding to an effective Froude-depth number in the referential of the laboratory $F_{h,s}=(U_s+u_c)/(gh)^{1/2}$=0.65 (Caplier *et al.*, 2015a).

A qualitative analysis of these wakes in the real space shows that the transverse wavelength and amplitude are increasing in the presence of the counter-current. The waves generated by the ship in its wake are convected by the current, that results in a widening of the wash zone at the banks of the canal. For a quantitative comparison of the wakes, longitudinal or transverse cuts can be made in the wave fields. Figure 5 represents the longitudinal cuts performed in the calm water and counter-current wakes For the same ship speed, the length of the wash zone increases from 0.9L_s to 2L_s (L_s=1.2 *m* is the ship length) with the counter-current, representing more than a doubling of its length. The transverse waves amplitude and wavelengths at the river banks respectively grows from A_1=0.012h to A_2=0.059h (h=0.103 *m* is the initial water depth), and from $\lambda_{t,1}$=0.1L_s to $\lambda_{t,2}$=0.3L_s, an increase of nearly 500% of the amplitude and 30% of the wavelength.

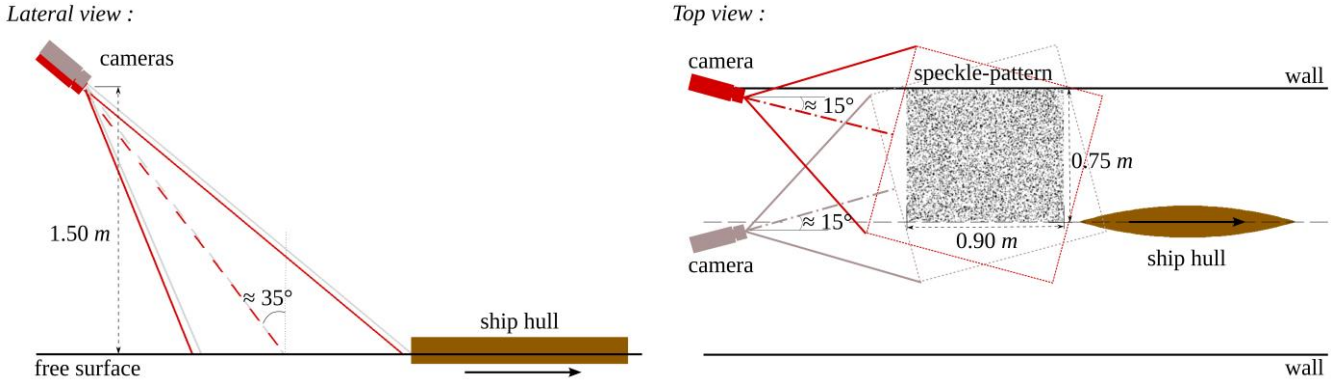

Figure 3. Schematic representation of the experimental setup for the free surface measurement by stereo-refraction.

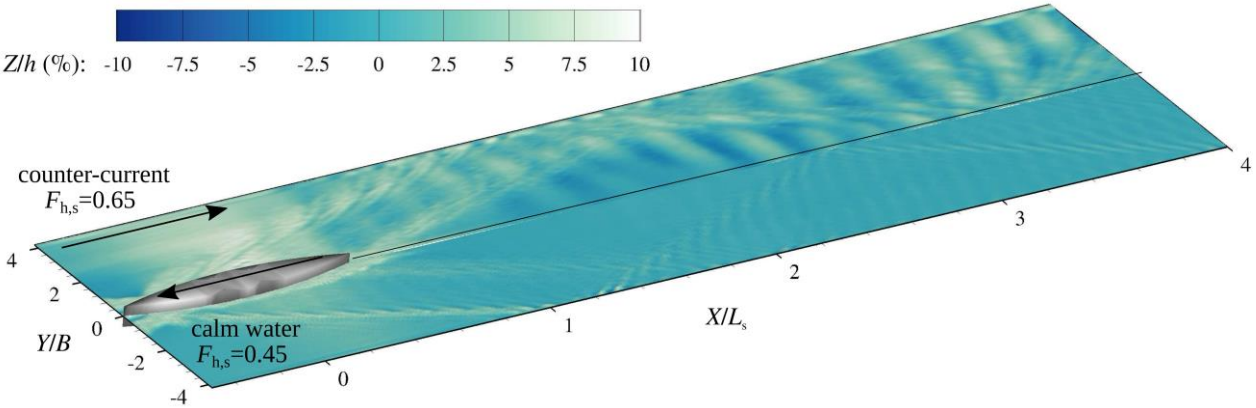

Figure 4. The wakes generated in calm water (bottom) and in the presence of a counter-current (top) by the WH2 hull, measured with the stereorefraction measurement method.

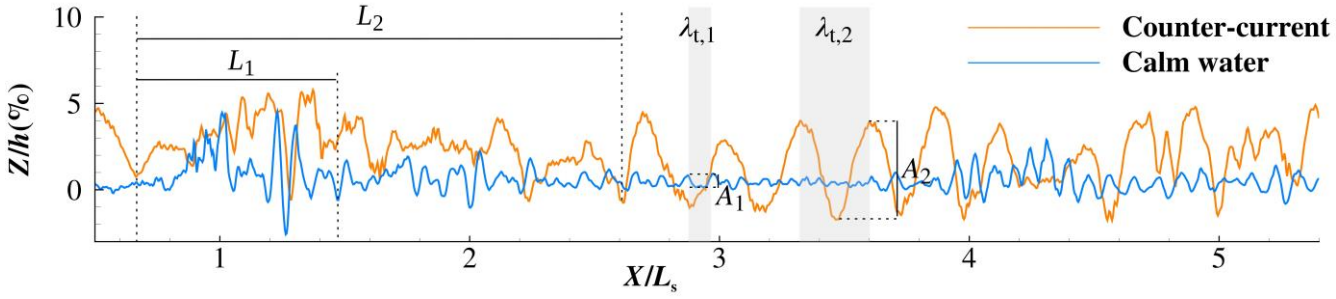

Figure 5. Longitudinal cuts in the wakes generated in calm water and in the presence of a counter-current at a transversal position Y/B=3.5. (L_1 ; A_1 ; $\lambda_{t,1}$) and (L_2 ; A_2 ; $\lambda_{t,2}$) represent respectively the width of the reflection zone, and the amplitude and the wavelength of the transverse waves, in calm water and in counter-current.

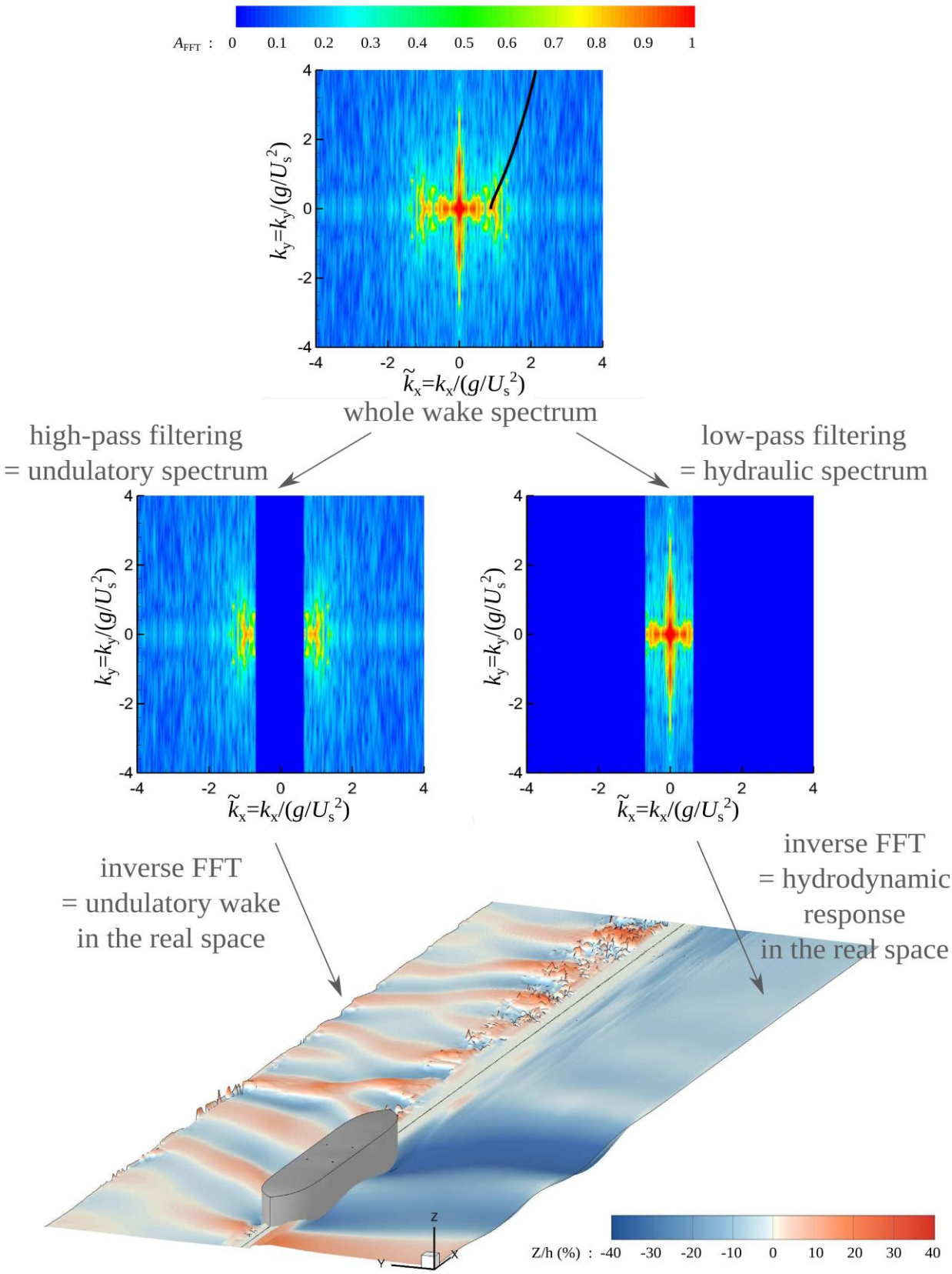

Figure 6 : Spectral analysis of a ship wake. The top figure represents the spectrum of the wake generated by the WH8 hull in a calm and shallow water configuration for a Froude-depth number $F_{h,s}$=0.80 and a Froude-length number $F_{L,s}$=0.23. Then the spectrum is filtered to separate the hydraulic and undulatory components of the wake, which are reconstructed in the real space by computing the inverse bidimensional FFT.

3.3 SPECTRAL ANALYSIS OF SHIP WAKES

The stereo-refraction measurement method gives a full, detailed and fine reconstruction of the ship wake. Then, it is possible to proceed the analysis in the spectral space by computing the bidimensional Fast Fourier Transform (FFT) of the wake. The method has been introduced by (Carusotto and Rousseaux, 2013), developed by (Gomit *et al.*, 2014) for the analysis of ship wakes in deep water and then adapted by (Caplier *et al.,* 2016) for the analysis of ship wakes generated in shallow water.

An example of the spectrum of the wake generated by the WH8 hull, for a ship speed U_s=0.80 $m.s^{-1}$ and a water depth h=0.103 m, giving a Froude-depth number $F_{h,s}=U_s/(gh)^{1/2}$=0.80 and a Froude-length number $F_{L,s}=U_s/(gL_s)^{1/2}$=0.23, is given on the right of Figure 6 (Caplier *et al.,* 2016). The color on the spectrum represents the spectral repartition of the normalized amplitude of the FFT along the different wave lengths and directions in the wake. The high-pass or low-pass filtering of the spectrum and its reconstruction in the real space by computing an inverse bidimensional FFT allows to separate the hydraulic and undulatory components of the wake (Gomit *et al.*, 2014) (Caplier *et al.,* 2016).

3.4 MEASUREMENT OF THE RETURN CURRENT

The stereoscopic system can also be used to measure the return current generated around the hull, by computing the displacements of floating particles placed at the surface of the water. The images of these markers can then be processed by a stereo-PIV algorithm to calculate the flow velocity (Chatellier *et al.*, 2013). The result is given on Figure 7 on which the return current is measured around the WH2 hull for a ship speed U_s=0.70 $m.s^{-1}$ and a water depth h=0.103 m, giving a Froude-depth number $F_{h,s}=U_s/(gh)^{1/2}$=0.70 and a Froude-length number $F_{L,s}=U_s/(gL_s)^{1/2}$=0.20. The return current is calculated in the whole field around the hull, it reaches its maximum of amplitude (30% of the ship speed) at the middle of the hull, and extends along the whole width of the waterway. Then its direction alternates between the crests and troughs of the transverse waves, and its amplitude decreases slowly.

4 THE SHIP RESISTANCE AND ITS VISUAL FOOTPRINT

Resistance trials have been carried out in the towing tank of the Pprime Institute. The measurement of the ship drag force is performed with a Kistler 9272 multi-component dynamometer installed between the ship hull and the towing mast (Figure 8). The six-component piezoelectric sensor measures the axial forces in each direction as well as the torques. The ship resistance is taken as the axial force F_X opposed to the motion of the ship. The maximum measured amplitude is F_X=20 N and the uncertainty is I=0.80 N (Caplier, 2015). Then the non-dimensional drag coefficient C_d can be derived with Equation 2, where S_w is the wetted surface area of the ship:

$$C_d = \frac{F_X}{\frac{1}{2}\rho S_w U_s^2} \quad (2)$$

Figure 9 represents the drag coefficients of the WH2 and WH8 hulls measured in a shallow water configuration (h=0.103 m) at different ship speeds (the Froude-depth number of the ship $F_{h,s}$ is between 0.60 and 1.31, and the Froude-length number of the ship $F_{L,s}$ is between 0.18 and 1.38). The evolution of the ship resistance is bounded by the critical Froude-depth numbers F_{h1} and F_{h2} calculated by Schijf's theory (Schijf, 1949). These critical Froude-depth numbers are calculated by Equations 3 and 4:

$$F_{h1} = \left[2sin\left(\frac{arcsin(1-m)}{3}\right)\right]^{\frac{3}{2}} \quad (3)$$

$$F_{h2} = \left[2sin\left(\frac{\pi-arcsin(1-m)}{3}\right)\right]^{\frac{3}{2}} \quad (3)$$

They depend on the blockage ratio m (cross section of the ship to cross section of the canal). In the present experiments, m=0.0874.

A sudden increase of the drag coefficient is observed for $F_{h,s}$=F_{h1}=0.64 for both hulls. This increase referred as "the resistance crisis" appears at the boundary between the subcritical and the transcritical regime. Finally, there is a decrease of the ship resistance at the entrance in the supercritical regime for $F_{h,s}$=F_{h2}=1.37. Parallel visualizations have been made during the resistance trials, with a high-speed camera Photron Fastcam SA1 of resolution 1024x1024 *px* equipped with a Sigma 28 *mm* F1.8 DG ASP lens (Figure 8). The camera installed on the side of the canal, and captures images of the wave amplitudes at the window during the passage of the ship at a frequency of 125 *fps*. Then a dedicated algorithm assembles the images to give a picture-like representation of the wave amplitudes. Figure 10 represents the visualizations performed during the transition between the subcritical and transcritical regime (Froude-depth number F_h from 0.60 to 0.85 and Froude-length number F_h from 0.19 to 0.22). These visualizations highlight an increase of the transverse wavelength and amplitude at the boundary between the subcritical and transcritical regimes. A wave breaking is also visible on some waves. So when a ship navigates in a confined waterway, it experiences a sudden increase of its fuel consumption, and the waves that it generates grow, break and reflect on the river banks. That process is destructive for the river banks and needs to be investigated in a future work, to prevent its appearance and to design appropriate bank protections.

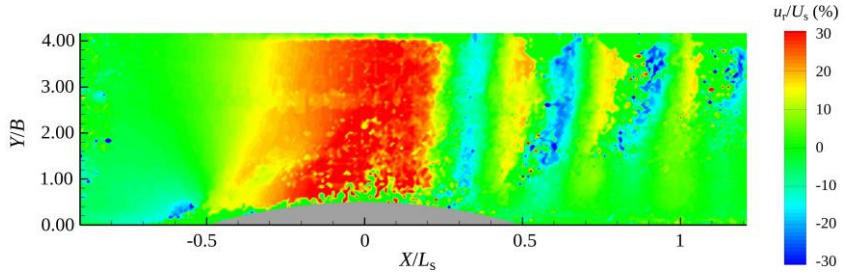

Figure 7. The return current u_r measured around the WH2 hull for a Froude-depth number $F_{h,s}$=0.70 with the stereo-correlation measurement method.

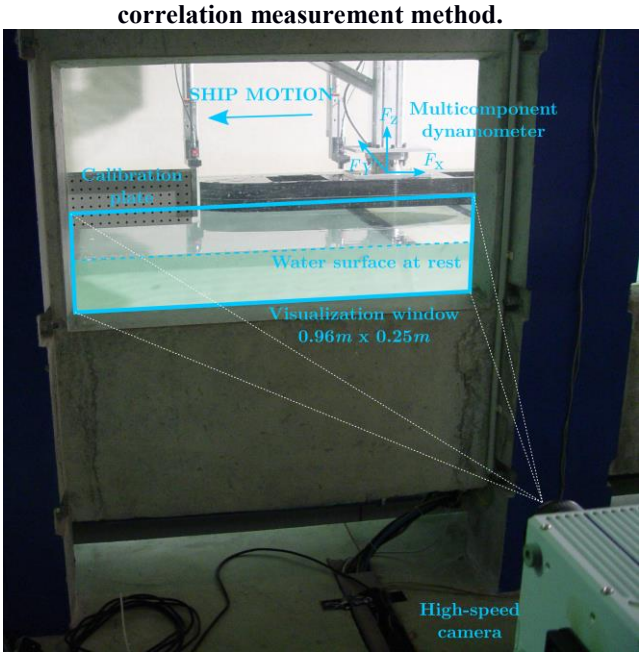

Figure 8. Measurement of the ship resistance with a multi-component dynamometer and lateral visualizations with a high-speed camera.

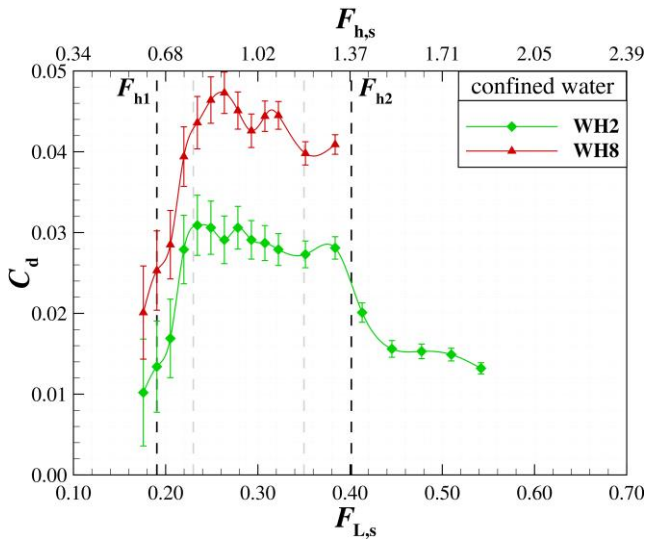

Figure 9. Drag coefficients of the ship hulls measured in a shallow water configuration for different ship speeds. The black dotted lines correspond to the critical Froude numbers F_{h1}=0.64 and F_{h2}=1.37 linked to the blockage of the waterway.

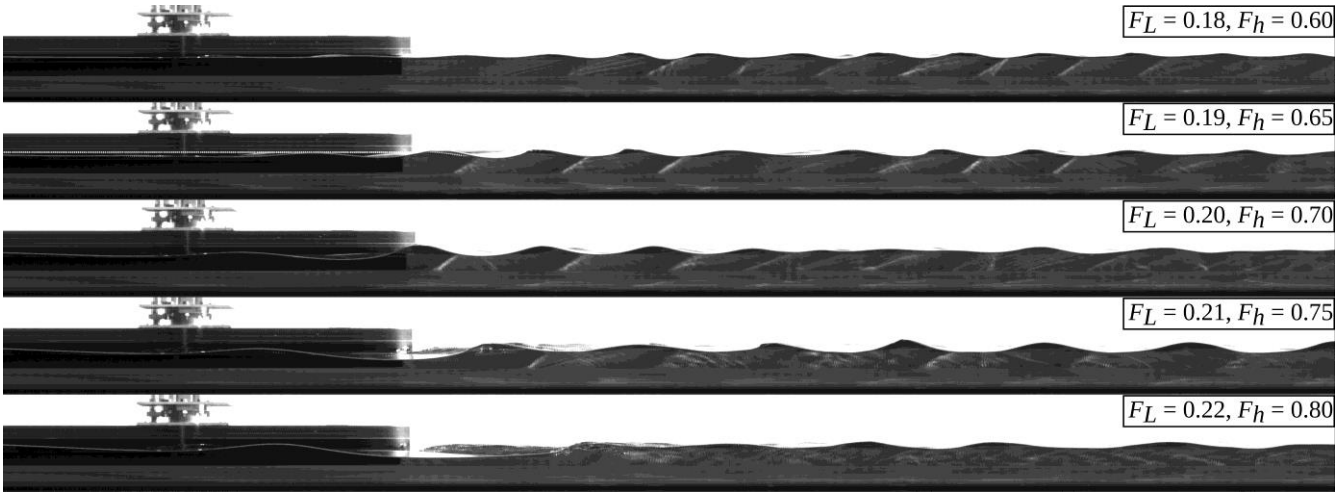

Figure 10. Visualizations of the wave amplitudes generated by the WH8 hull at the window of the canal in a shallow water configuration (h=0.103 m). Ship speed is increasing from the top to the bottom.

5 CONCLUSIONS AND PERSPECTIVES

During the past few years, several experimental studies have been made in the towing tank of the Pprime Institute, to investigate the effects of confinement on ships wakes and drag and to understand interaction between the ship and the waterway. Measurement methods have been developed and adapted for this topic, to obtain a full and detailed measurement of the ship wake and to determine the drag forces applying on the hull. These methods give high quality results that allow to perform a fine analysis of the wave properties in both real and spectral spaces. The hydrodynamic effects appearing in the waterway can also be quantified and analyzed. The comparison of the resistance diagrams with the

visualizations of the wakes allows to identify the visual footprint of the crisis of ship resistance. The towing tank of the Pprime Institute is currently under work, and will be lengthened of one third of its actual length, to reach 30 *m*. The towing carriage and the current generation will also be improved. These great improvements on the facility will open the way to future experimental studies, in order to continue the investigations on this path of research.

6 REFERENCES

Caplier, C., 2015. Etude expérimentale des effets de hauteur d'eau finie, de confinement latéral et de courant sur les sillages et la résistance à l'avancement des navires. (In French). Phd Thesis of the University of Poitiers, France, 2015.

Caplier C., Rousseaux G., Calluaud D., David L., 2015a. The effects of river counter-currents on ships wakes: an experimental approach, in: Proceedings of the AIPCN-SHF congress "Hydrodynamics and simulation applied to inland waterway and port approaches", Meudon, France.

Caplier C., Rousseaux G., Calluaud D., David L., 2015b. An experimental study of the effects of finite water depth and lateral confinement on ships wake and drag, in: Proceedings of the AIPCN-SHF congress "Hydrodynamics and simulation applied to inland waterway and port approaches", Meudon, France.

Caplier C., Rousseaux G., Calluaud D., David L., 2016. Energy distribution in shallow water ship wakes from a spectral analysis of the wave field. Physics of Fluids, 28(10):107104. https://dx.doi.org/10.1063/1.4964923

Carusotto I., Rousseaux G., 2013. The Čerenkov effect revisited: from swimming ducks to zero modes in gravitational analogues. Lecture Notes in Physics Springer, 6:109-144. https://doi.org/10.1007/978-3-319-00266-8_6

Chatellier L., Jarny S., Gibouin F., David L., 2013. A parametric PIV/DIC method for the measurement of free surface flows. Experiments in Fluids, 54(3):1-15. https://doi.org/10.1007/s00348-013-1488-4

Gomit, G. Chatellier, L. Calluaud, D., David, L., 2013. Free surface measurement by stereo-refraction. Experiments in Fluids, 54(6), 1-11. https://doi.org/10.1007/s00348-013-1540-4

Gomit, G. Rousseaux, G. Chatellier, L. Calluaud, D., David, L., 2014. Spectral analysis of ship waves in deep water from accurate measurements of the free surface elevation by optical methods. Physics of Fluids, 26:122101. http://dx.doi.org/10.1063/1.4902415

Gomit, G. Chatellier, L. Calluaud, D., David, L. Fréchou, D. Boucheron, R. Perelman, O. Hubert, C., 2015. Large scale free surface measurement for the analysis of ship waves in a towing tank. Experiments in Fluids, 56(10), 184.

Schijf, J.B., 1949. Protection of embankments and bed in inland and maritime waters, and in overflow or weirs. In: Proceedings of the 17th International Navigation Congress, Lisbon, Portugal.

Tremblais B., David L., 2010. Standard Library for Image Processing software. http://sliplib.prd.fr/

Wigley, W.C.S., 1926. Ship wave resistance. A comparison of mathematical theory with experimental results. Transactions of the Royal Institution of Naval Architects, 1926, 14:124-141.

7 AUTHORS BIOGRAPHY

Clément Caplier holds the current position of Postdoctoral Researcher at the University of Poitiers - Institut Pprime, France. He is specialized in optical measurement techniques for hydrodynamics. His previous experience includes an experimental thesis on the effects of finite water depth, lateral confinement and current on ships wakes and drag.

Guillaume Gomit holds the current position of Assistant Professor at the University of Poitiers - Institut Pprime, France. He obtained his PhD from the University of Poitiers in 2013 for his thesis on the optical measurement of ship waves in towing tanks. His research interests range from experimental hydrodynamic to rheology and transport of cohesive sediments.

Germain Rousseaux holds the current position of Senior Scientist at CNRS. He is a physicist doing interdisciplinary studies. His previous experience includes a PhD thesis on sand ripples formation with specializations on wave-current interactions (wave blocking, tidal bore...) and wake physics. He is interested with wave resistance theory and its applications to wash waves reduction by shapes optimization.

Damien Calluaud holds the current position of Assistant Professor at the University of Poitiers - Institut Pprime, France. He develops some stereoscopic and free surface measurements. His main interests are the ship waves, the bank erosion, the sediment transport and the ecohydraulics.

Ludovic Chatellier holds the current position of Assistant Professor the University of Poitiers - Institut Pprime, France. He is involved in renewable energy, hydrodynamics, ecohydraulics and optical metrology. His previous experience includes free-surface measurements, flow and wake analysis, development of energy harvesters and fish protection devices.

Laurent David is Professor of fluid mechanics in the university of Poitiers. He is at the head of the team HYDEE (Hydrodynamics and Environmental flows). Since twenty years, he develops 2D and 3D optical measurements (TR-PIV, surface and volumic PIV). His research interests are free surface flows, turbulent and unsteady flows, fluid structure interactions and ecohydraulics.

PARAMETER ESTIMATION FOR A SHIP'S ROLL RESPONSE MODEL IN SHALLOW WATER USING AN INTELLIGENT MACHINE LEARNING METHOD

Changyuan Chen and Manases Tello Ruiz,
Ghent University, Belgium

Guillaume Delefortrie,
Flanders Hydraulics Research and Ghent University, Belgium

Tianlong Mei,
Shanghai Jiao Tong University, China

Evert Lataire and Marc Vantorre,
Ghent University, Belgium

PARAMETER ESTIMATION FOR A SHIP'S ROLL RESPONSE MODEL IN SHALLOW WATER USING AN INTELLIGENT MACHINE LEARNING METHOD

Changyuan Chen and **Manases Tello Ruiz,** Ghent University, Belgium
Guillaume Delefortrie, Flanders Hydraulics Research and Ghent University, Belgium
Tianlong Mei, Shanghai Jiao Tong University, China
Evert Lataire and **Marc Vantorre**, Ghent University, Belgium

SUMMARY

In order to accurately identify the ship's roll model parameters in shallow water, and solve the problems of difficult estimating nonlinear damping coefficients by traditional methods, a novel Nonlinear Least Squares - Support Vector Machine (NLS-SVM) is introduced. To illustrate the validity and applicability of the proposed method, simulation data and decay tests data are combined and utilized to estimate unknown parameters and predict the roll motions. Firstly, simulation data is applied in the NLS-SVM model to obtain estimated damping parameters, compared with pre-defined parameters to verify the validity of the proposed method. Subsequently, decay tests data are used in identifying unknown parameters by utilizing traditional models and the new NLS-SVM model, the results illustrate that the intelligent method can improve the accuracy of parametric estimation, and overcome the conventional algorithms' weakness of difficult identification of the nonlinear damping parameter in the roll model. Finally, to show the wide applicability of the proposed model in shallow water, experimental data from various speeds and Under Keel Clearances (UKCs) are applied to identify the damping coefficients. Results reveal the potential of using the NLS-SVM for the problem of the roll motion in shallow water, and the effectiveness and accuracy are verified as well.

Keywords: roll model; shallow water; NLS-SVM; damping parameters; parameter identification

1 INTRODUCTION

Roll motion is one of the most critical responses the ship experiences in her lifespan. An accurate prediction of its development in real scenarios is then deemed necessary so to understand better the ship behavior and to avoid any hazardous conditions (Jiang et al., 2016; Yin et al., 2018). For this purpose, the identification of the roll viscous damping's contribution is of critical interest (Sun and Sun, 2013; Jiang et al., 2017). The most common approach to obtain this component is by means of free roll decay tests and fitting the measured response by conventional methods such as Least Squares (LS) approach. This method, however, when applied in shallow water has some difficulties to provide a clear distinction of the viscous parameters, especially in the nonlinear term. One may argue that other alternatives, available nowadays, can provide better results (especially for the nonlinear damping term).

The paper aims to investigate novel intelligent identification approaches which can be compared and tested against conventional methods. In the present work, the NLS-SVM algorithm will be investigated. Compared with other intelligent approaches, using large samples of data to estimate unknown parameters, NLS-SVM only depends on limited support vectors based on small samples. Besides, the structure risk minimization theory – instead of empirical risk minimization – is adopted by NLS-SVM to solve optimization problems. A global optimization result is obtained, and local optimization issues are avoided. Moreover, high accuracy, time saving and wide applicability performances of NLS-SVM are especially suitable for the identification of damping parameters in shallow water.

To verify the effectiveness, accuracy and applicability of the NLS-SVM parametric estimation model in shallow water, free roll decay tests for a scale model of an Ultra Large Container Vessel (ULCV) at different forward speeds and different UKCs were carried out. Then, simulation and experimental data are used to identify and predict the ship's roll motions. Comparisons between predicted data and original data illustrate the potential of employing the proposed method for the problem of roll motion in shallow water.

2 SHIP ROLL HYDRODYNAMIC MODEL

In a sense, an accurate definition and prediction of damping parameters (especially nonlinear damping coefficients) in the ship roll model is a very necessary task (Hou and Zou, 2016; Hou et al., 2018). On the basis of the rigid body theory (Hou and Zou, 2015), the 1DOF ship roll motion model can be written as (Xing and McCue, 2010):

$$(I_{xx} + A_{44}^{\infty})\ddot{\phi} + B(\dot{\phi}) + C_{44}\phi = 0 \quad (1)$$

where I_{xx} is the mass moment of inertia, A_{44}^{∞} is the added mass moment of inertia (at infinite frequency), B is the moment due to the damping phenomena, C_{44} is the roll restoring coefficient, and ϕ is the roll angle. The single dotted and double dotted variables represent the first and second order derivatives.

The total damping coefficients are divided into a linear ($b_{\dot{\phi}}$), a nonlinear ($b_{\dot{\phi}|\dot{\phi}|}$) (Ikeda et al., 1977; Himeno, 1981), and a potential contribution components in the following form:

$$B(\dot{\phi}) = b_{\dot{\phi}}\dot{\phi} + b_{\dot{\phi}|\dot{\phi}|}\dot{\phi}|\dot{\phi}| + \int_{-\infty}^{+\infty} h_{44}(t-\tau)\dot{\phi}(\tau)d\tau \quad (2)$$

where $\dot{\phi}$ is the roll rate and h_{44} is the impulse response function (IRF). Substituting $B(\dot{\phi})$ into Eq. (1), the final model in the time domain is expressed as follows:

$$(I_{xx} + A_{44}^{\infty})\ddot{\phi} + b_{\dot{\phi}}\dot{\phi} + b_{\dot{\phi}|\dot{\phi}|}\dot{\phi}|\dot{\phi}| + \\ + \int_{-\infty}^{+\infty} h_{44}(t-\tau)\dot{\phi}(\tau)d\tau + C_{44}\phi = 0 \quad (3)$$

3 PARAMETERS ESTIMATION APPROACHE

3.1 PROBLEM STATEMENT

Assuming that a parametric system in state-form is available in the form of:

$$\frac{dX}{dt} = g(X, T, \theta) \quad (4)$$

Where $X = [x_1; x_2; \dots; x_i]$ is the state variable, $\frac{dX}{dt} = \left[\frac{d}{dt}x_1, \frac{d}{dt}x_2, \dots, \frac{d}{dt}x_i\right]^T$ is the derivative of each state variable, $T = [t_1, t_2, \dots, t_i]^T$ is the time variable, $\theta = [\theta_1, \theta_2, \dots, \theta_i]^T$ is an unknown set of parameters (Mehrkanoon et al., 2012).

For the parametric system, the main goal is to identify the unknown parameters θ from observed data $Y = [y_1, y_2, \dots, y_i]^T$at time variable $T = [t_1, t_2, \dots, t_i]^T$.

$$e_i = Y(t_i) - X(t_i), i = 1,2 \cdots n \quad (5)$$

where $e_i = [e_1, e_2, \dots, e_i]^T$is the error between observed data Y and outputs of the estimate state variable X. The final goal is shifted to get the set of unknown parameters by minimizing the error e_i.

3.2 IDENTIFICATION PROCEDURE

Step 1 Obtain sample data

Obtain training samples data $\{(t_i, y_i), i = 1,2, \dots, n\}$, where t_i is the time series, and y_i is the numerical simulation data or experimental data.

Step 2 Approximate the state variable

Estimate the state variable $\hat{X} = [\hat{x}_1, \hat{x}_2, \dots, \hat{x}_i]^T$ based on simulation or experimental data$\{(t_i, y_i), i = 1,2, \cdots n\}$. In the present study, NLS-SVM is adopted to approximate the state variable $\hat{X}$. x_k or the k-th state variable can be obtained by an approximation function of the following form:

$$\hat{x}_k(t) = w_k^T \varphi(t) + b_k \quad (6)$$

where t is the input data (time), $\hat{x}_k$ is the output data, w_k is the weight value, $\varphi(\cdot)$ is the nonlinear function, which maps the input data t to the Euclidean space, b_k is the bias (David et al., 2013; Xu and Guedes Soares, 2016).

To solve the convex optimization issue according to the minimization of structure risk theory, construct and solve the following cost function:

$$\min_{w,b,e} f(w, e) = \frac{1}{2}w^T w + \frac{1}{2}\gamma\|e_i\|_2^2 \quad (7)$$

Subject to

$$y_i = w^T\varphi(t_i) + b + e_i \quad (8)$$

where $i = 1,2, \cdots$, n, γ is penalty factor, e_i is the error.

A lagrangian function is introduced to solve the optimization problem as follows:

$$\mathrm{L}(w, b, e, a) = \frac{1}{2}w^T w + \frac{1}{2}\gamma\|e_i\|_2^2 - \\ \sum_{i=1}^{n} a_i[w^T\varphi(t_i) + b + e_i - y_i] \quad (9)$$

where the coefficients a_i are the Lagrange multipliers. The derivative matrix is obtained by partially differentiating Eq. (9) with respect to w, b, e, a:

$$\begin{bmatrix} K + \gamma^{-1}I_N & 1_N \\ 1_N^T & 0 \end{bmatrix}\begin{bmatrix} a^k \\ b^k \end{bmatrix} = \begin{bmatrix} y^k \\ 0 \end{bmatrix} \quad (10)$$

where $K(t_i, t_j) = \varphi(t_i)\varphi(t_j)$ is the kernel function, I_N is the identity matrix, $1_N = [1; 1; \dots; 1]$, $\alpha^k = [a_1^k; a_2^k; \dots; a_n^k]$.

The regression model is expressed as

$$\hat{x}_k(t) = w_k^T\varphi(t) + b_k = \sum_{i=1}^{n} \alpha_i^k K(t_i, t) + b_k \quad (11)$$

Step 3 Derivatives of the state variable approximation

Approximate the derivatives of the state variable $\frac{d}{dt}\hat{X} = \left[\frac{d}{dt}\hat{x}_1, \frac{d}{dt}\hat{x}_2, \dots, \frac{d}{dt}\hat{x}_n\right]$ by differentiating the approximated model with time.

Differentiation of $\hat{x}_k(t)$ with time, yields:

$$\frac{d}{dt}\hat{x}_k(t) = w_k^T\dot{\varphi}(t) = \\ \sum_{i=1}^{n} \alpha_i^k \ \varphi(t_i)^T\dot{\varphi}(t) \quad (12)$$

According to the Mercer Theorem (Steinwart and Scovel, 2012), the derivatives of the kernel are equal to the derivatives of the feature map. Therefore, the derivatives of the kernel can be obtained in the form of:

$$K_1(t_i, t) = \frac{\partial K(t_i,t)}{\partial t} = \ \varphi(t_i)^T\dot{\varphi}(t) \quad (13)$$

$$\frac{d}{dt}\hat{x}_k(t) = \sum_{i=1}^{n} \alpha_i^k K_1(t_i, t) \quad (14)$$

Step 4 Identification of unknown parameters, and model's prediction

$\hat{x}_k(t)$ and $\frac{d}{dt}\hat{x}_k(t)$ in Eq. (11) and Eq. (14) are the approximated values of the k-th state variable and its derivative. All the state variables $\hat{X}$ and their derivatives $\frac{d}{dt}\hat{X}$ can be obtained by using the above same procedure based on NLS-SVM (RBF kernel). After substituting $\hat{X}$ and $\frac{d}{dt}\hat{X}$ in Eq. (4), the linear or nonlinear algebraic equation with unknown parameters is constructed.

Finally, the unknown parameters can be obtained by solving the optimization problem as:

$$\min_{\theta} \frac{1}{2}\sum_i^n \|e_i\|_2^2 \quad (15)$$

Subject to

$$e_i = \frac{d}{dt}\hat{X}(t_i) - g\left(\hat{X}(t_i), T, \theta\right), i = 1,2, \cdots n \quad (16)$$

4 FREE DECAY TESTS OF ROLL MODEL

4.1 TOWING TANK

Free decay tests were carried out at the Towing Tank for Manoeuvres in Confined Water (co-operation Flanders Hydraulics Research and Ghent University) in Antwerp, Belgium (Delefortrie et al., 2016) . The main dimensions of the towing tank are displayed in Table 1.

Table 1. The main dimensions of the Towing Tank for Manoeuvres in Confined Water.

Item	Value	Units
Total length	87.5	m
Useful length	68.0	m
Width	7.0	m
Maximum water depth	0.50	m
Length of the ship models	3.5-4.5	m

4.2 SHIP MODEL

A 1/90 scale model of Ultra Large Container Vessel (ULCV) was chosen to carry out free roll decay tests (Tello Ruiz, 2018). The main parameters and cross sectional view of the ship model are shown in the Table 2 and Figure 1.

Table 2. ULCV ship model parameters.

Item	Model scale(1/90)		Full scale	
	Value	Units	Value	Units
L_{OA}	4.418	m	397.6	m
L_{PP}	4.191	m	377.2	m
B	0.627	m	56.4	m
D	0.330	m	29.7	m
T_M	0.145	m	13.1	m
m	226.4	kg	165046	ton
C_b	0.6	--	0.6	--

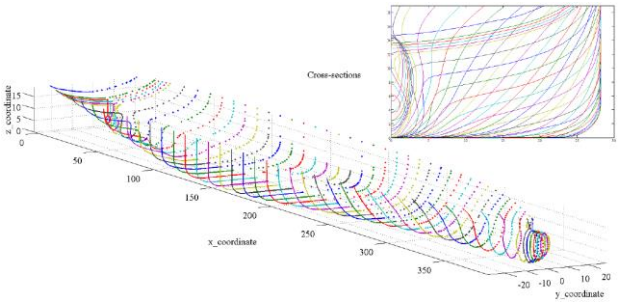

Figure 1. The cross sectional view of the ULCV ship.

4.3 DECAY TESTS

The free decay tests were performed by providing an initial roll angle of the ship model. Then, the ship model was hold at this initial position until the towing carriage reached its desired speed and immediately released by pulling the cord attached to a wooden stick (Tello Ruiz, 2018; Jang et al., 2010; Avalos et al., 2014). A illustration of the model test setup and mechanism is displayed in Figure 2.

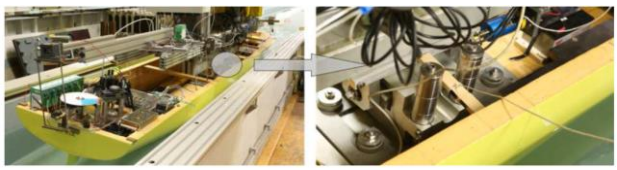

Figure 2. The model test setup and mechanism.

The free decay tests were carried out at different UKCs (from 20% to 190%UKC) and speeds (from 0 kn to 21kn). For the present study, the speeds at 0, 6, 12 knots and the UKCs of 20%, 35%, 190% are selected as study cases. The initial roll angles at the chosen conditions are presented in Table 3.

Table 3. The initial roll angles at different speeds and UKCs.

UKCs	Speeds		
	0kn	6kn	12kn
20%UKC	2.70°	2.71°	2.74°
35%UKC	3.11°	3.27°	1.95°
190%UKC	6.96°	6.45°	6.23°

5 PARAMETER IDENTIFICAION

Taking into consideration of the parameters estimation method in the section 3, the novel NLS-SVM approach is introduced to estimate the linear and nonlinear viscous damping parameters in the nonlinear roll model. The identification process is, in more detail, described in Table 4 and Figure 3.

Table 4. Identification process of the NLS-SVM model.

Parameter identification using NLS-SVM
1. Obtain the roll training sample $\{(t_i, \phi_i), i = 1,2,\cdots,n\}$ based on numerical simulation tests or decay tests. t_i is time series and ϕ_i is roll angles.
2. Estimate the trajectory of the roll angle ϕ (the state variable) by using NLS-SVM model, Eq. (11).
3. Differentiate the NLS-SVM predicting model with respect to time, Eq. (14); And the closed-form approximation for the first ($\dot{\phi}$) and second ($\ddot{\phi}$) derivatives of the state variable are obtained respectively.
4. Identify the linear ($b_{\dot{\phi}}$) and nonlinear ($b_{\dot{\phi}\|\dot{\phi}\|}$) viscous damping coefficients by solving the optimization problem in Eq. (15).
5. Substitute the identified linear and nonlinear viscous damping coefficients in the roll model, Eq. (3). After applying a fourth-order Runge-Kutta approach to solve the ship's roll response equation, the roll motions of the ship are predicted.

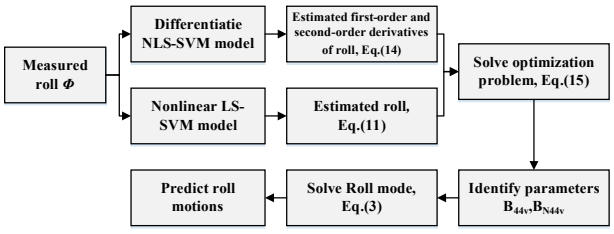

Figure 3. Identification process of NLS-SVM.

In order to verify the effectiveness, accuracy as well as applicability of the NLS-SVM model in shallow water,

three case studies are conducted by using the novel identification method, they are:

Case 1. Validate the effectiveness of the NLS-SVM (5.1)

Case 2. Illustrate the advantages of the NLS-SVM (5.2)

Case 3. Verify the applicability of the NLS-SVM in shallow water (5.3)

These cases are described in detail in the following subsections.

5.1 EFFECTIVENESS OF NLS-SVM MODEL

In this case study, the roll motions with pre-defined linear ($b_{\dot{\phi}}$) and nonlinear ($b_{\dot{\phi}|\dot{\phi}|}$) viscous damping coefficients (Table 5) are selected to simulate a free roll decay test. The pre-defined linear and nonlinear damping parameters are substituted into the roll model, Eq. (3). It is worth noting that other parameters in Eq. (3) are regarded as known values, which can be found in Tello Ruiz (2018). Using a fourth-order Runge-Kutta approach to solve the differential equation the simulated roll angles (samples data) are obtained.

Subsequently, simulated samples data are divided into two sets, the first set as a training sample (blue circles) is used to train the NLS-SVM model and the second set as a test sample (green circles) is selected to test the model. The training results are displayed in Figure 4 (a).

After the NLS-SVM model being trained, unknown damping coefficients are identified by the proposed model and are shown in Table 5. Comparing the identified parameters with the pre-defined parameters, the results show that the relative errors of the linear ($b_{\dot{\phi}}$) and nonlinear ($b_{\dot{\phi}|\dot{\phi}|}$) viscous damping coefficients are about 0.3% and 1.0%, respectively. These very small errors reveal that the NLS-SVM approach can accurately identify unknown parameters and can be well applied in identifying the roll model.

Furthermore, for a better idea of the importance of the method, the identified damping parameters are used to predict the roll motions and are compared against sample data. Satisfactory agreement between predicted values and original values can be found in Figure 4(b), with maximum errors between predicted values and original values of around 0.001. This illustrates the potential of the NLS-SVM as it performs well with high prediction accuracy. Therefore, the novel NLS-SVM algorithm can be applied in identifying the ship roll model.

Table 5. Pre-defined parameters and identified parameters using the NLS-SVM approach.

Parameters	Known	Identified	Error (%)
$b_{\dot{\phi}}$ (10^8)	6.0	6.0171	0.2850
$b_{\dot{\phi}\|\dot{\phi}\|}$ (10^7)	4.0	4.0417	1.0425

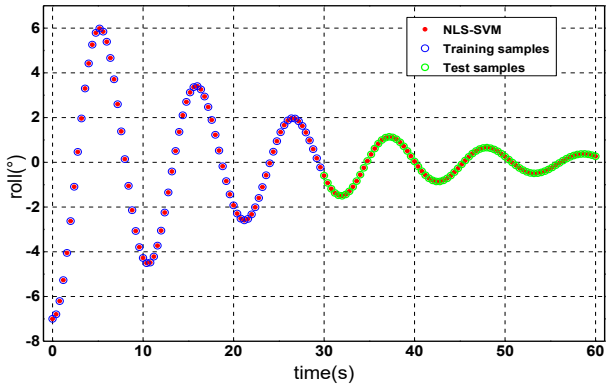

(a) Training results

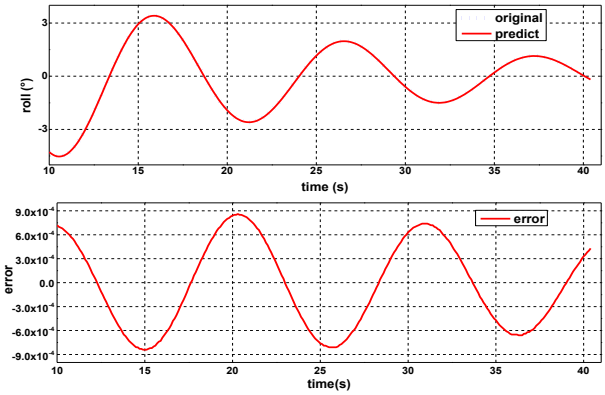

(b) Predicted results and errors

Figure 4. Training and predicted results with pre-defined damping coefficients.

5.2 COMPARISON WITH DIFFERENT IDENTIFICATION METHODS

In order to illustrate the advantages of the NLS-SVM algorithm, traditional methods, such as Nonlinear Least Square (NLS) and Fitting Least Square (FLS) algorithms are selected for comparing and analyzing.

The NLS algorithm has been one of the most common approaches used to identify unknown parameters before intelligent algorithms appeared (Zhu et al., 2017a). The method is described in Figure 5.

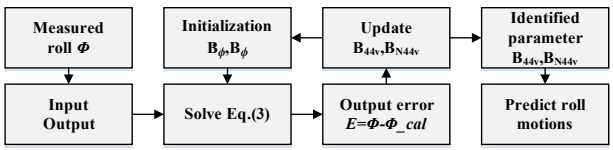

Figure 5. Nonlinear Least Square (NLS) identification method.

Apart from the NLS, the FLS algorithm has also been successfully applied for system identification. The main difference is that in the FLS approach the curve fitting is firstly applied to the initial data, then a basic LS algorithm is applied to identify the unknown parameters. This process is relatively simpler than the direct application

displayed Figure 5, Figure 6 sketches the process for better illustration purposes.

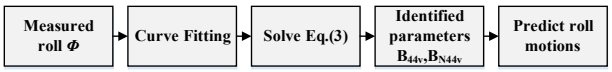

Figure 6. Fitting Least Square (FLS) identification method.

Aiming at comparing and analyzing the performance of the three identified approaches, three evaluation indexes are selected, they are the Mean Absolute Error (MAE), the Root Mean Square Error (RMSE) (Zhu et al., 2017b), and the Computational time (CPU time) (Huang et al., 2018). In machine learning theory, the MAE is employed to assess the performance of the model; the RMSE is utilized to measure the accuracy of the model; the CPU time is represented as time and energy cost (Zhang et al., 2018). The MAE and the RMSE are, respectively given by:

$$\mathrm{MAE} = \frac{\sum_n^{i=1}|\phi_i - \hat{\phi}_i|}{n} \tag{17}$$

$$\mathrm{RMSE} = \sqrt{\frac{\sum_n^{i=1}(\phi_i - \hat{\phi}_i)^2}{n}} \tag{18}$$

In this case study, the decay tests data at the speed of 12 knot and the UKC of 20% are selected to compare and analyze. The parameters identified by the methods described above and their respective comparison can be found in Table 6. From the results, it can be seen that the linear damping coefficient ($b_{\dot{\phi}}$) can be identified by all methods within the same magnitude (10^8). The nonlinear term, however, has some discrepancies, the traditional NLS method estimates a magnitude of $b_{\dot{\phi}|\dot{\phi}|}$ which is around 100 times smaller than other two approaches. The latter, draws the main attention to consider the use of intelligent method, the NLS-SVM, for improving the performance in practice.

Moreover, the MAE is around 0.0405 for the NLS-SVM model, which decreased by 27.9% from 0.0562 for the NLS model and by 17.2% from 0.0489 for the FLS model respectively. For accuracy analysis, the RMSE (0.0502) of the NLSSVM is reduced by 20.6% (0.0632) compared to the NLS model and by 17.4% (0.0608) compared to the FLS model, which demonstrates that the NLS-SVM model's errors are smaller, and the accuracy is higher than traditional methods. Moreover, comparing the CPU times, less time and energy are taken by the proposed model.

$$\mathrm{error} = \phi_{known} - \phi_{pred} \tag{19}$$

Table 6. Comparisons among different methods.

Parameters	Methods		
	NLS	FLS	NLSSVM
$b_{\dot{\phi}}$ (10^8)	3.30	3.43	3.38
$b_{\dot{\phi}\|\dot{\phi}\|}$ (10^7)	0.0493	5.14	3.55
MAE	0.0562	0.0489	0.0405
RMSE	0.0632	0.0608	0.0502
CPU time(s)	97	13	12

Subsequently, the identified linear and nonlinear damping coefficients are employed to predict the ship's roll motions separately. The predicted results and errors (Eq. (19)) are presented in Figure 7(a) and 7(b), respectively. From Figure 7(a), there are small but not significant deviations between the original data and predicted data for the three identification approaches. It is noted that the predicted values by the NLS-SVM method are closer to the original values than the other two approaches. Furthermore, the overall errors of the NLS-SVM model in Figure 7(b) are smaller than that of NLS and FLS methods.

In conclusion, the analyzed results demonstrate that the new NLS-SVM model has better identification performance and time saving ability as well as higher accuracy compared to traditional algorithms. The advantages of the NLS-SVM are validated.

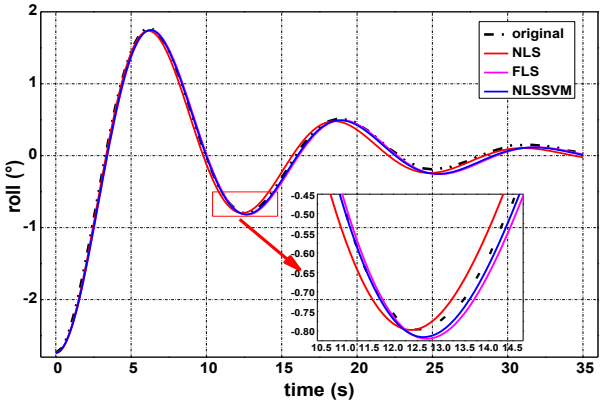

(a) Predicted results

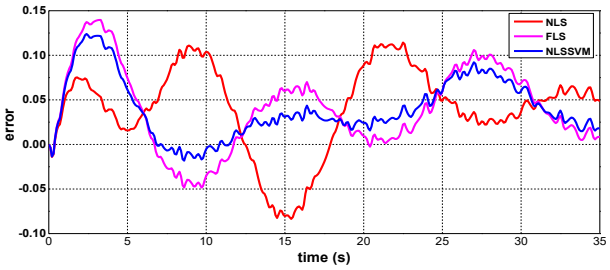

(b) errors

Figure 7. Predicted results and errors among different methods.

5.3 APPLICATIONS ANALYSIS OF NLS-SVM

In this section, the free roll decay tests from various UKCs and speeds are studied. The applicability in shallow water of the NLS-SVM model is illustrated.

5.3.1 Applicability analysis for different UKCs

Considering the effect of water depth on the damping coefficients, three different UKCs (20%, 35% and 190% UKC) at a speed of 6 knots are selected as case studies. After the NLS-SVM model being trained by the decay

tests data in different UKCs, Table 7 presents a quantitative comparison of the identified results. It is noted that the RMSE (the values around 0.022-0.072) and the MAE (around 0.018-0.051) are pretty low, and computational time is very short (10-20s), which verify good generality and applicability of the NLS-SVM model both in shallow water and deep water.

Table 7. Comparisons among different UKC.

Parameters	UKC (6 knot)		
	20% UKC	35% UKC	190% UKC
$b_{\dot{\phi}}$ (10^8)	1.97	1.70	0.95
$b_{\dot{\phi}\lvert\dot{\phi}\rvert}$ (10^7)	3.01	3.26	4.03
MAE	0.0177	0.0124	0.0510
RMSE	0.0223	0.0143	0.0729
CPU time	15	11	18

Substituing the identified parameters in the roll model Eq. (3), ship roll motions are predicted for different UKCs. In Figure 8(a), 8(b) and 8(c), the predicted roll angles agree well with the original values from decay tests for different UKCs. In addition, the maximum errors of different UKCs are about 0.06, 0.02 and 0.2, which are obtained at lower roll angles, and the errors could be a source of the model formulation problem and not of the identification method. The results show that the NLS-SVM method can successfully be used to identify parameters of the roll model in the shallow and deep water with small errors.

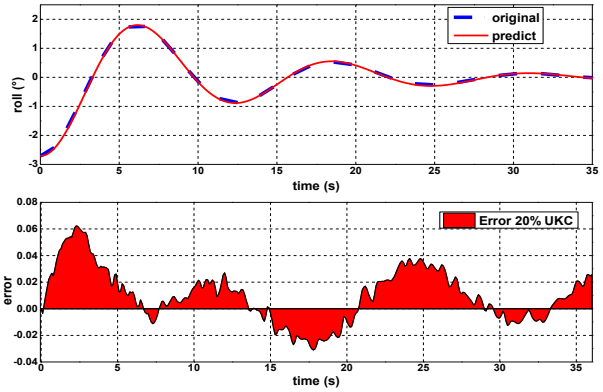

(a) Predicted results and errors for 20% UKC

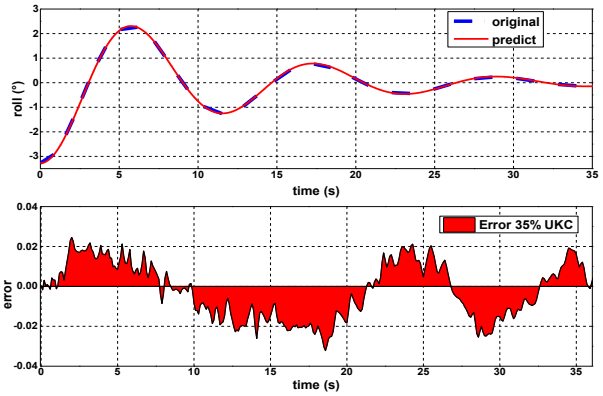

(b) Predicted results and errors for 35% UKC

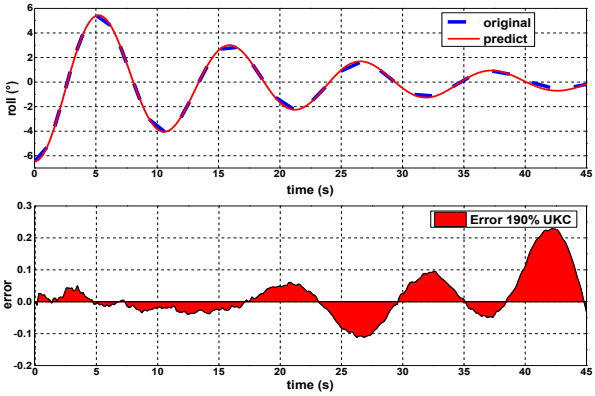

(c) Predicted results and errors for 190% UKC

Figure 8. Predicted results and errors in different UKCs.

5.3.2 Applicability analysis for different speeds

Similarly, the applicability in shallow water (20% UKC) at different speeds is investigated. The experimental data at 0, 6, 12 knots are taken as examples to train the NLS-SVM model and unknown linear and nonlinear damping coefficients at different speeds are estimated. The identified results are shown in Table 8. It can be seen that the three evolution indexes are very small. The RMSE is around 0.0185, 0.0223 and 0.0502 respectively, whose value increase slightly with higher speed. Moreover, the MAE at different speeds is with small values about 0.0185 to 0.0452. For the CPU time, it is equal (15s). After quantitative comparison, it can be concluded that the NLS-SVM model has good applicability in shallow water at different speeds.

Table 8. Comparisons among different speeds.

Parameters	Speed (20% UKC)		
	0kn	6kn	12kn
$b_{\dot{\phi}}$ (10^8)	1.93	1.97	3.38
$b_{\dot{\phi}\lvert\dot{\phi}\rvert}$ (10^7)	2.66	3.01	3.55
MAE	0.0185	0.0177	0.0405
RMSE	0.0185	0.0223	0.0502
CPU Time(s)	15	15	15

Furthermore, the predicted results in shallow water at different speeds are obtained in Figure 9(a), 9(b) and 9(c). It can be seen that the predicted values have satisfactory agreement with the original data at different speeds. The predicted roll angles at a speed of 12kn are a little bit higher than the original ones, but the predicted results are still valid, because the overall errors are very small and the effect on the ship is not significant.

To summarize, the effectiveness and applicabilty of the NLS-SVM approach applied in shallow water at different speeds are verified.

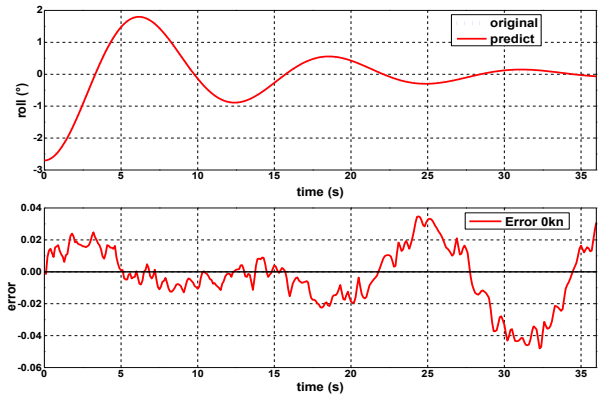

(a) Predicted results and errors at 0kn

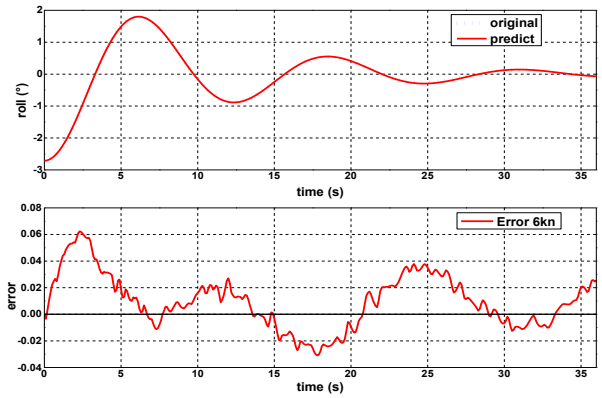

(b) Predicted results and errors at 6kn

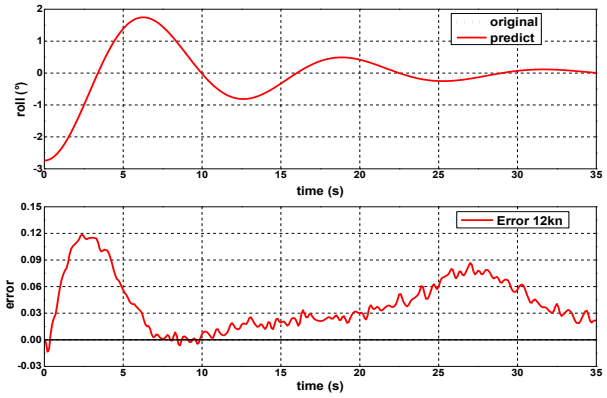

(c) Predicted results and errors at 12kn

Figure 9. Predicted results and errors at different speeds.

6 CONCLUSIONS

In this paper, the novel NLS-SVM parametric identification approach for estimating unknown damping coefficients in shallow water is investigated. Firstly, comparisons between simulation roll angles based on pre-defined damping coefficients and predicted roll angles using estimated damping coefficients presents satisfactory agreement, which illustrate the proposed identification algorithm can be effectively applied in identifying the roll model. Subsequently, comparing traditional identification approaches (NLS and FLS) with intelligent method, the NLS-SVM algorithm can perform better with higher accuracy, and overcome the weakness of conventional methods for identifying nonlinear damping coefficients. Moreover, decay tests data in different UKCs and speeds were prepared for the purpose of demonstrating the shallow water effect in parametric identification based on the NLS-SVM method. The good agreement between decay tests results and predicted results suggests the satisfactory applicability of the proposed algorithm in shallow water. Therefore, the effectiveness, accuracy and applicability of the NLS-SVM model applied in identifying the roll model in shallow water, have been verified by qualitative and quantitative analysis.

Future work includes two aspects: first, other parameters in roll model will be identified and analyzed. In addition, intelligent optimized algorithms will be considered as well as to obtain the best penalty factors and kernel factors of the NLS-SVM model.

7 ACKNOWLEDGEMENTS

This work was supported by the program of China Scholarships Council (201706570007, 201806230196) and Special Research Fund - Cofunding for Chinese candidates holding a CSC-grant (01SC8418).

8 REFERENCES

Avalos, G.O.G., Wanderley, J.B.V., Fernandes, A.C., Oliveira, A.C., 2014. Roll damping decay of a FPSO with bilge keel. Ocean Eng. 87, 111–120.

David, M.S., Dictino, C., Jesus Manuel, D.L.C., Joaquin, A., 2013. Identification of a surface marine vessel using LS-SVM. J. Appl. Math. 2013, 1–11.

Delefortrie, G., Geerts, S., Vantorre, M., 2016. The towing tank for manoeuvres in shallow water. In: Proceedings of 4th MASHCON. Hamburg, Germany, pp. 226–235.

Himeno, Y., 1981. Prediction of ship roll damping – state of the art. Technical Report of Department of Naval Architecture and Marine Engineering. University of Michigan, Michigan, USA.

Hou, X.R., Zou, Z.J., 2015. SVR-based identification of nonlinear roll motion equation for FPSOs in regular waves. Ocean Eng. 109, 531–538.

Hou, X.R., Zou, Z.J., 2016. Parameter identification of nonlinear roll motion equation for floating structures in irregular waves. Appl. Ocean Res. 55, 66–75.

Hou, X.R., Zou, Z.J., Liu, C., 2018. Nonparametric identification of nonlinear ship roll motion by using the motion response in irregular waves. Appl. Ocean Res. 73, 88–99.

Huang, B.G., Zou, Z.J., Ding, W.W., 2018. Online prediction of ship roll motion based on a coarse and fine tuning fixed grid wavelet network. Ocean Eng. 160, 425–437.

Ikeda, Y., Himeno, Y., Tanaka, N., 1977. On eddy making component of roll damping force on naked hull. J. Soc. Nav. Archit. Japan. 1977(142), 54–64.

Jang, T.S., Kwon, S.H., Lee, J.H., 2010. Recovering the functional form of the nonlinear roll damping of ships from a free-roll decay experiment: An inverse formulism. Ocean Eng. 37, 1337–1344.

Jiang, Y., Zhu, R., Miao, G., Yang, C., 2016. Damping prediction of a rolling ship with bilge keel in viscous flow based on numerical simulation. Shipbuild. China. 57(2), 1–12.

Jiang, Y., Zhu, R.C., Fan, J., Ma, C., 2017. Non-parametric identification of nonlinear damping and restoring forces for ship free roll decay in numerical tank. J. Mar. Sci. Technol. 25(4), 404–416.

Mehrkanoon, S., Falck, T., Suykens, J.A.K., 2012. Parameter estimation for time varying dynamical systems using least squares support vector machines. IFAC Proc. Vol. 45(16), 1300–1305.

Steinwart, I., Scovel, C., 2012. Mercer's theorem on general domains: on the interaction between measures, kernels, and RKHSs. Constr. Approx. 35(3), 363–417.

Sun, L.P., Sun, W. Ben, 2013. Parameter identification of the non-linear rolling damping based on PLS regression technique. Adv. Mater. Res. 779(1), 675–679.

Tello Ruiz, M., 2018. Manoeuvring model of a container vessel in coastal waves. Ghent University, Belgium.

Xing, Z., McCue, L., 2010. Modeling ship equations of roll motion using neural networks. Nav. Eng. J. 122(3), 49–60.

Xu, H.T., Guedes Soares, C., 2016. Vector field path following for surface marine vessel and parameter identification based on LS-SVM. Ocean Eng. 113, 151–161.

Yin, J.C., Perakis, A.N., Wang, N., 2018. A real-time ship roll motion prediction using wavelet transform and variable RBF network. Ocean Eng. 160, 10–19.

Zhang, X.K., Zhang, Q., Ren, H.X., Yang, G.P., 2018. Linear reduction of backstepping algorithm based on nonlinear decoration for ship course-keeping control system. Ocean Eng. 147, 1–8.

Zhu, M., Hahn, A., Wen, Y., Bolles, A., 2017a. Comparison and optimization of the parameter identification technique for estimating ship response models. In: 2017 IEEE 3rd International Conference on Control Science and Systems Engineering. Beijing, China, pp. 743–750.

Zhu, M., Hahn, A., Wen, Y.Q., Bolles, A., 2017b. Identification-based simplified model of large container ships using support vector machines and artificial bee colony algorithm. Appl. Ocean Res. 68, 249–261.

9 AUTHORS BIOGRAPHY

Changyuan Chen, a PhD candidate at the Maritime Technology Division, which belongs to the Faculty of Engineering and Architecture of Ghent University. His experience includes research on trajectory controller, intelligent control strategies, machine learning techniques applied to ship hydrodynamics, etc.

Manases Tello Ruiz PhD, Naval Architect and Marine Engineer, is a Research Staff at Ghent University. He has been involved in several (inter-)national projects with main focus on manoeuvring, seakeeping, and wave energy converters. Currently, he is working on ship air pollution and machine learning techniques applied to ship hydrodynamics. At present he is also a member of the ITTC Specialist Committee of Manoeuvring in Waves, at which he has been appointed as secretary.

Guillaume Delefortrie, PhD, naval architect, is expert nautical researcher at Flanders Hydraulics Research and visiting professor at Ghent University. He is in charge of the research in the Towing Tank for Manoeuvres in Confined Water and the development of mathematical models based on model tests. He has been secretary of the 27th and 28th ITTC Manoeuvring Committee and is chairman of the 29th ITTC Manoeuvring Committee.

Tianlong Mei， PhD student at School of Naval Architecture, Ocean and Civil Engineering, Shanghai Jiao Tong University and the division of Maritime Technology at Ghent University. His experience includes numerical studies on wave structure interaction and ship manoeuvring in waves.

Evert Lataire, PhD, naval architect, is currently postdoctoral assistant at the division of Maritime Technology at Ghent University. He has written a PhD on the topic of bank effects mainly based upon model tests carried out in the shallow water towing tank of FHR. His fifteen year experience includes research on ship manoeuvring in shallow and confined water such as ship-ship interaction, ship-bottom interaction and ship-bank interaction.

Marc Vantorre, naval architect, is full senior professor of marine hydrodynamics and head of the Maritime Technology Division at Ghent University, Belgium. His research focuses on ship behaviour in shallow and confined waters, mainly in close co-operation with Flanders Hydraulics Re-search in Antwerp. He is former member of PIANC Working Groups and of the ITTC Manoeuvring Committee.

RANS EVALUATION OF THE DTC'S VERTICAL MOTION SAILING IN FINITE WATER DEPTH WAVES

Guillermo Chillcce,
Institute of Ship Technology, Ocean Engineering and Transport Systems, the University of Duisburg-Essen, Germany

Ivana Martić,
Faculty of Mechanical Engineering and Naval Architecture, University of Zagreb, Croatia

Manases Tello Ruiz,
Maritime Technology Division, Ghent University, Belgium

Jorge Ramirez,
Knud e Hansen A/S, Denmark

Nastia Degiuli,
Faculty of Mechanical Engineering and Naval Architecture, University of Zagreb, Croatia

Ould el Moctar,
Institute of Ship Technology, Ocean Engineering and Transport Systems, the University of Duisburg-Essen, Germany

RANS EVALUATION OF THE DTC'S VERTICAL MOTION SAILING IN FINITE WATER DEPTH WAVES

Guillermo Chillcce, Institute of Ship Technology, Ocean Engineering and Transport Systems, the University of Duisburg-Essen, Germany
Ivana Martić Faculty of Mechanical Engineering and Naval Architecture, University of Zagreb, Croatia
Manases Tello Ruiz, Maritime Technology Division, Ghent University, Belgium
Jorge Ramirez, Knud e Hansen A/S, Denmark
Nastia Degiuli, Faculty of Mechanical Engineering and Naval Architecture, University of Zagreb, Croatia
Ould el Moctar, Institute of Ship Technology, Ocean Engineering and Transport Systems, the University of Duisburg-Essen, Germany

SUMMARY

Ship motions in finite water depth are important not only due to possibly large motions or accelerations but also due to the increased possibility of impact with the seabed or channel's bottom induced by those large motions. In finite depth the phenomena of squat is also present and it is affected due to the wave pressure change. Thus, the combined effect of the ship's periodical motions and the ship's squat could lead to grounding or bottom impacts. A detailed numerical analysis of the DTC containership's motions in waves and two different water depths were carried out. The results show that motion amplitudes can be captured fairly.

NOMENCLATURE

P	Pressure [N/m^2]
ν	Kinematic viscosity [m^2/s]
ρ	Density of water [kg/m^3]
L_{PP}	Ship length between perpendicular [m]
H_W	Wave Height [mm]
H_{max}	Maximum height in time record
f	frequency in time record [1/s]
a0	mean value in time record
A1	first harmonic in time record
A2	second harmonic in time record
h	Water depth [m]
T_W	Wave period [s]
g	gravity acceleration [m/s^2]
Fr	Froude number [-]
AP	After perpendicular [-]
FP	Forward perpendicular [-]
heave	The ship's vertical motion amidships [mm]
trim	Draughts difference between FP and AP to L_{PP} ratio [mm/m]
z_VA	Ship's vertical motion at the AP and the ship's symmetry plane [mm]
z_VF	Ship's vertical motion of the FP at the ship's symmetry plane [mm]
WG4	Wave profile recorded in from of the ship [mm]

1 INTRODUCTION

The ship's vertical motion is one of the most critical responses to be assessed when sailing in finite water depths. Such cases occur, for instance, when a ship is approaching a port. Because of the limited water depth available and the risk of bottom touching, this motion delimits whether or not a ship, at a given draft and speed, can safely access a port. Maximum allowed drafts are then recommended based on the ship's type, ship's speed, and the environmental conditions. Considering the increasing dimensions of ships during the last decades and the already limited depth of harbours and access channels, the regulations on the ship motions became even more restrictive. Thus, accurate estimations of the ship motions are of major interest for port access policies in order to exploit the use of the port itself to its maximum capacity.

When a ship sails in shallow water squat effects will be present, inducing the ship's sinkage and trim. Moreover, in such restrictive water depths the ship can also be subjected to the waves, e.g. in the access channels to the main ports of Belgium (see Vantorre et al., 2008). The combined effect of waves and squats will significantly reduce the under keel clearance (UKC); taking into account that ships already sail in very shallow water (e.g. 15% UKC) conditions, the resulting motions can lead to bottom touching.

The study of the combined effects of waves and shallow water on the ship has been, for instance, conducted numerically and experimentally in Vantorre and Journée (2003). A potential code (based on strip theory) was used to validate the results for the oscillatory motions. The obtained results showed a good agreement with experiments for wave lengths of comparable order to the ship length but showed poor approximations for the shorter wave lengths. With respect to squat, trim and sinkage, an extensive database based on calm water results was generated which was also further used in Vantorre et al., (2008) to determine tidal windows for deep-drafted ships approaching and leaving the Belgian harbours according to probabilistic criteria (see Vantorre et al., 2008).

Experimental studies are regarded as the most accurate means of evaluating the complex fluid behaviour developed around the ship hull. However, in recent years, numerical estimations by means of computational fluid dynamics (CFD) have offered comparable results with a relatively good accuracy. For instance, Sigmund and el Moctar, (2018) analysed the ship motions and added resistance in deep water of four different hull shapes using RANSE-based field methods. The predicted heave and pitch motion showed a deviation of less than 2% with respect to the experiments, showing the capabilities of the RANSE-based method to accurately predict the ship motion in deep water. Wave-induced ship motions in shallow water were studied by Tezdogan et al. (2016). The authors describe a method to simulate a tanker using a RANSE-based solver. A case was analysed where a ship has zero speed at 20% UKC. This case corresponds to a very shallow condition and for a wave with $\lambda/Lpp = 0.53$ results show an over-prediction of heave and under-prediction of pitch for about 19% and 7%, respectively. These large differences demonstrate the challenges that still remain to accurately simulate wave-induced motions in shallow water.

The use of RANSE-based field methods has proven to be an appropriate tool for complex marine phenomena. Wave-induced ship motions can be modelled by overset methods or morphing (grid deformation) methods. Despite the advantages and disadvantages of these methods, both have been used for ship hydrodynamics. In general, the overset method is better when large ship motions are expected and there is enough space to overlap the background mesh and the moving mesh. In contrast morphing is best suited when small motions are expected.

In spite of a fair amount of works found in literature using CFD for the problem of ship motions in waves, one can find only few of them paying attention to the shallow water problem, and from these works, to the authors' best knowledge, none has addressed the case with non-zero forward speed. The present work will investigate the ship's vertical motions of the DTC container ship in shallow water (100% UKC) and very shallow water (20% UKC) under the effect of waves with and without forward speed. The study is based on a RANS solver using volume of fluids to capture the fluid interface. For validation purposes the results will be compared against model tests conducted at the Towing Tank for Manoeuvres in Confined water at Flanders Hydraulics Research (in co-operation with Ghent University and conducted as part of the EU-funded SHOPERA project).

2 NUMERICAL METHOD

The Reynolds Averaged Navier Stokes Equations (RANSE) are used to model the flow around the ship. The equation (1) represents the mass conservation and equation (2) the momentum conservation. The numerical solution is carried out using the Finite Volume Method (FVM) which divides the domain in control volumes. Additionally, the Volume of Fluid (VOF) method is used to capture the interface between air and water. This method uses an additional transport equation of variable α as shown in equation (3). The variable α is the volume fraction and measures the amount of water or air that is contained in a control volume.

$$\frac{\partial}{\partial t}\int_V \rho dV + \int_S \rho(\boldsymbol{v} - \boldsymbol{v_s}) \cdot \boldsymbol{n} dS = 0 \quad (1)$$

$$\frac{\partial}{\partial t}\int_V \rho u_i dV + \int_S \rho u_i(\boldsymbol{v} - \boldsymbol{v_s}) \cdot \boldsymbol{n} dS = \int_S(\tau_{ij}\boldsymbol{i}_j - p\boldsymbol{i}_i) \cdot \boldsymbol{n} dS + \int_V \rho \boldsymbol{g}\boldsymbol{i}_i dV \quad (2)$$

$$\frac{\partial}{\partial t}\int_V \alpha dV + \int_S \alpha(\boldsymbol{v} - \boldsymbol{v_s}) \cdot \boldsymbol{n} dS = 0 \quad (3)$$

In the above equations the integration is carried out over a volume V or over the enclosed surface S with unit vector normal $\boldsymbol{n}$. The fluid velocity is represented by $\boldsymbol{v}$ and $\boldsymbol{v_s}$ represents the control volume's surface velocity. u_i are the velocity components on the Cartesian coordinates. $\boldsymbol{i}_j$ is the unit vector in direction x_j of the Cartesian coordinate. τ_{ij} represents the components of the viscous stress tensor. A detailed description of the numerical methods for RANSE can be found in, e.g., Ferziger and Perić (2012) and Moukalled et al., (2016).

3 SELECTED TEST CASES

The Duisburg Test Case (DTC, see el Moctar et al., 2012) containership is used to investigate the wave-induced ship motions. Experimental tests were carried out during the SHOPERA project (EU-funded project) in the Towing Tank for Manoeuvres in Confined water at Flanders Hydraulics Research in co-operation with Ghent University. Table 1 shows the selected test cases for the present analysis.

Table 1. Test cases

ID	UKC [%]	V [m/s]	Fr [-]	H_W [mm]	T_W [s]
CW2	100	0.327	0.05	62.31	1.38
CW3	100	0.872	0.14	62.35	1.38
CW4	20	0	0	22.21	1.66
CW5	20	0.327	0.05	21.26	1.66

A post-processing analysis of the experimental data has been carried out for further comparison with the numerical estimations. The analysis was performed following the recommendations in Van Zwijnsvoorde et al., (2019) with respect to the selection of the time windows and adopting the approach described in Tello Ruiz et al. (2016) for the analysis of the harmonic signals. In this method the signal is filtered with a band pass filter and further fitted with a least square method up to a third order Fourier expansion with eight unknown parameters, see equation (4).

$$f(t) = a_0 + \sum_{i=1}^{3} a_i \sin(i\omega t) + b_i \cos(i\omega t) \quad (4)$$

In equation (4) a_0 and ω are the mean and the frequency of harmonic signal, respectively; the remaining terms a_i

and b_i are the harmonic components related to the first, second and third order of Fourier series.

4 COMPUTATIONAL PROCEDURE

4.1 WAVE PROPAGATION

From the experimental data it is deduced that waves have a nonlinear behaviour. According to current theories, these waves can be modelled with the Stokes wave theory. Using the main wave parameters, it can be confirmed that they are classified as Stokes waves of second order, as shown in Figure 1, where the experimental values (red dots) have been plotted as a function of the non-dimensional wave height (H/gT^2) versus the non-dimensional depth (h/gT^2). Thus, for a general simulation of the waves a fifth order Stokes theory is used. Note that from the wave's point of view, the studied waves do not represent shallow water waves but rather intermediate depth waves.

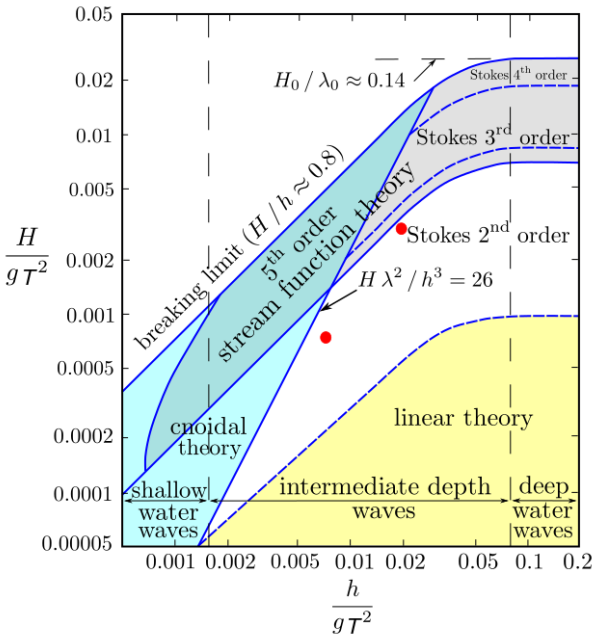

Figure 1. Current wave theories (Méhauté, 1976)**. The red dots represent the experimental waves used in CW2 and CW4 tests. Source: Wikimedia (2019)**

One of the major problems with free surface simulations is related to undesired wave reflection from domain boundaries. For instance, reflexion from the outlet boundary superposes with the incoming waves creating an unrealistic wave pattern. For regular waves simulations two methods can be used to avoid wave reflexion, the wave damping method and the wave forcing method. The first method aims to reduce the wave amplitude to zero; as such, it can be understood as a virtual beach. The second method forces the wave amplitude to be equal as the initial incoming wave amplitude, hence simulating the condition that far from the ship the disturbances disappear and the wave elevation remains the same as the incoming wave. Nevertheless, both methods are numerical techniques that use additional source terms in the momentum equations and volume fraction.

A common practice in numerical simulations for the problem of a ship in waves is the damping method. When considering only waves in the analysis, the reflection coefficient is used to measure the effectiveness of the damping region (see for instance Perić and Abdel-Maksoud, 2017 and Rapuc et al., 2018). In Rapuc et al., (2018) a reflexion coefficient with less than 1% in deep water was achieved under optimum damping parameter selection. A similar analysis in shallow water yields reflexion coefficients less than 3% for the optimum damping parameter.

In order to produce an effective damping, large domains behind the ship were used. The calculation of the length where waves are damped, the damped function, and the damping intensity were mostly related as the user experience. These parameters were studied in detail by Perić and Abdel-Maksoud (2018). The authors proposed an analytical formula to find the optimum damping parameters and the use of a smaller domain in which the damping length is defined and optimized before starting the simulations.

In the present work, the wave damping method with optimum parameters was initially considered in the simulations. In spite of the damping method working appropriately for the larger speed and larger UKC, the method had to be discarded. This was because problems arose due to the ship's low speed and the small wave amplitudes used in the 20% UKC cases. The diffracted waves which propagated in all direction travelled also towards the inlet boundary, disturbing the incoming waves. For such cases, the superposition of the incoming and reflected waves resulted in an irregular wave pattern which needed to be removed. The damping method could not be used in the inlet condition because it is simply not possible to damp only the reflected waves without damping the incoming waves. Instead, the forcing method was preferred. The forcing method was applied in the inlet, side and outlet boundaries up to a distance of 2.4 m as shown in Figure 2. This configuration allows the incoming wave to be constant over the domain and the diffracted waves to be absorbed in the forcing regions.

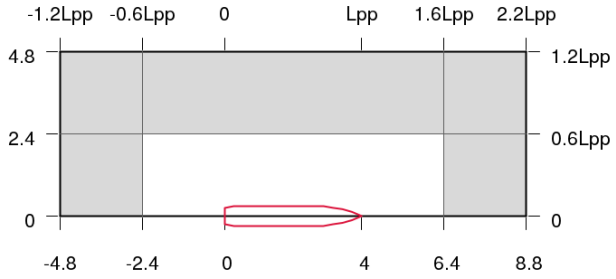

Figure 2. Numerical domain used in the simulation for the forcing method. The grey area is the zone where forcing is applied to absorb the reflected waves.

The discretization of the domain to allow an accurate representation of the waves is another important aspect. Three levels of refinement are used to properly model the kinematic wave energy. This refinement procedure was proposed by Rapuc et al., (2018) and adapted here for the shallow water problem. The main idea is also to accurately capture the velocities of the wave field. This aspect is more important in shallow water because particles at the bottom still have velocity. Therefore, it should be ensured that the velocity is well represented in the whole computational domain. This is accomplished by three refinement levels. The first level of refinement is created to capture the free surface (interface between water and air). It is suggested a minimum of 100 cells per wave length and 20 control volumes per wave height. The other two refinements increase smoothly from the first zone only in the vertical direction.

4.2 SHIP IN HEAD WAVES

The focus is to capture the ship vertical motions induced by waves. The overset mesh technique was used as a first option. However, for the 20% UKC case difficulties arose due to the small space between the ship's bottom and the seabed. The main drawback was the insufficient number of control volumes to interpolate the results between the overset and background mesh. Therefore, a morphing method was selected for all simulations. The major difficulty with morphing technique is to avoid zero or negative volumes. This happens when the body is subjected to large motions. Thus, special care should be taken in the grid topology avoiding large changes in the cell sizes near the body.

Two methods are commonly used to model the inner region of the boundary layer. The selection of the model depends on the Reynolds number. For low values of the Reynolds number the *low y+ wall* treatment resolves the viscous layer. In order to use the *low y+* treatment it is necessary that the first cells near the wall have a $y+$ value less or equal to one. This requirement increases substantially the number of cells required to discretise the entire domain. The *high y+ wall* treatment can be used instead with coarser cells near the wall. The main assumption of this method is that the cells near to the wall lie within the logarithmic-law layer ($y+ >30$). This method does not resolve the viscous sublayer but rather uses wall functions to obtain the boundary conditions for the continuum equation. A third method called *all y+ wall* treatment is provided by STAR-CCM+ for cases where $y+$ less than one or larger than thirty is not possible. The method consists of a hybrid treatment that emulates the *low y+* and *high y+* treatment depending on the size of the cell near the wall. A reasonable result is expected with this method even for $y+$ values between one and thirty.

Six prism layers near the hull were used to model the boundary layer. The first aim was to obtain $y+$ less than one; however, due to the very thin cells near the wall, a problem known as numerical ventilation occurred. Therefore, the all $y+$ value treatment was adopted.
The ship's hull is modelled as a rigid body and as a non-slip wall. The pressure over the ship's hull surface is integrated and those forces are used to calculate the ship motions. This process is automatically carried out by the dynamic fluid body interaction (DFBI) module.

4.3 BOUNDARY CONDITIONS

Boundary conditions define the physical condition of the problem. Six boundary conditions are used to enclose the domain and one boundary condition inside the domain, which corresponds to the hull surface. The inlet condition is used to prescribe the wave velocity. From this boundary waves start to propagate towards the outlet. The outlet is treated as a pressure outlet, taking as reference the pressure of the Stokes wave generated in the inlet condition. A symmetry boundary is imposed at the ship's symmetry plane. Thus, only half of the domain is simulated. On the other side (lateral wall) a non-slip wall is imposed. The top boundary is set to velocity inlet. Thus, the wave's velocity is prescribed there.

The bottom boundary is set as a non-slip wall with a velocity equal to the ship's forward speed. It should be noted that the problem is solved in the inertial coordinate system that travels with a constant ship's forward speed. From this frame of reference, the bottom seems to move opposite to the ship.

Ships sailing at low speed in very shallow conditions are more costly to simulate because smaller control volumes are needed to capture small pressure variation. This means that the number of cells in the domain increases. Furthermore, simulation of small wave height increases the number of cells. The wave height is subdivided by 20 control volumes. Thus, it is no surprise that, in order to accurately capture the pressure around the ship in very shallow water, the number of cells should increase considerably.

5 RESULTS

All computations were carried out at model scale following the experimental configuration. The coordinate system used in the simulation differs from the experiments. For the numerical calculation an orthogonal coordinate system with z-axis pointing upward was used. In contrast, the experiments used an orthogonal system with z-axis pointing downward. The x-axis in both the computations and the experiments points towards the ship's bow. For comparison purposes the computed values were transformed to the frame used in the experiments.

The grid topology for the 20% UKC and the 100% UKC cases are the same, an example of the discretization on the waterplane is given in Figure 3. The domain consisted of 8.9 million control volumes for the 20% UKC cases and 7.6 million control volumes for 100% UKC cases. This

difference is caused by the wave elevation being approximately three times smaller in the 20% UKC case than in the 100% UKC case. Thus, smaller control volumes are needed to capture the wave elevation.

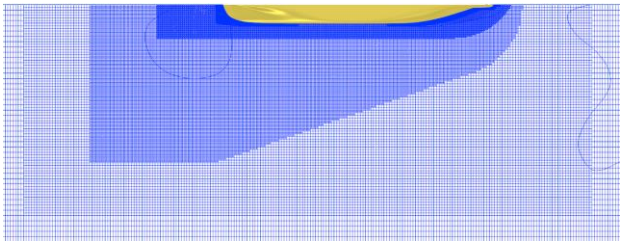

Figure 3. Numerical discretization of the water plane. Hull shape in yellow and control volumes in blue.

Measured vertical motions of the DTC containership are available for the CW3 and CW4 cases. The analysed variables are the wave profile recorder by WG4, the heave motion, as well as the trim and sinkage at the aft (z_VA) and forward (z_VF) perpendiculars. Care should be taken with respect to the definition given in the experiments. For instance, *heave* is defined as the vertical translation at amidships rather than at the centre of gravity (COG). The pitch motion is not given in the experiments, instead the *trim* is provided, which is defined as the difference between the draft at the forward and aft perpendiculars.

5.1 100% UKC TEST CASE

The CW2 and CW3 test cases correspond to shallow water condition with 100% UKC. The wave parameters for both cases are similar with small differences in the wave height (see Table 1). The ship Froude numbers are 0.05 for the CW2 case and 0.14 for the CW3 case.

Challenges have been found at low Froude number when aiming to capture small variations in the fluid domain, requiring significantly smaller control volumes which substantially increase the computational time. This was needed as waves reflected from the ship have small amplitudes and propagate in all directions. Thus, to accurately capture such wave elevations, smaller control volumes were required. This was also the case when tests in waves were considered, especially at low speed where the waves travelling with the ship (steady waves) superpose with the incoming waves (unsteady waves). Therefore, to capture this superposition phenomena smaller control volumes are also needed.

Figure 4 shows the comparison between measured and computed motions of the CW3 case. The results are presented for heave, trim and vertical motions at the aft and forward perpendiculars. Note that the first five seconds of the numerical simulation correspond to the imposed ramp to attain a smooth transition from the initial condition to the periodical motions. These periodical motions are reached at 7.5 seconds, see for instance the heave motion where the harmonic oscillation had been reached, indicating that the numerical simulation has converged.

In Figure 4 one can also observe that the mean values are different from zero, showing that the problem of ship motions in finite depth is a nonlinear problem. These non-zero average values can also be seen in the vertical motions at the forward and after perpendiculars. A closer look at the time series (see Figure 5) shows that the measured heave is always positive meaning that the ship sinks below the mean water free surface. The computed values follow the periodicity of the oscillations when compared to experiments but have around 1.5 mm offset for the heave motion. The vertical motion at the aft perpendicular is better captured numerically than the forward perpendicular. The trim motion depends on the motion values at aft and forward perpendicular. Thus, the deviation observed in the time series arises from the less accurate prediction of the motions at forward perpendicular.

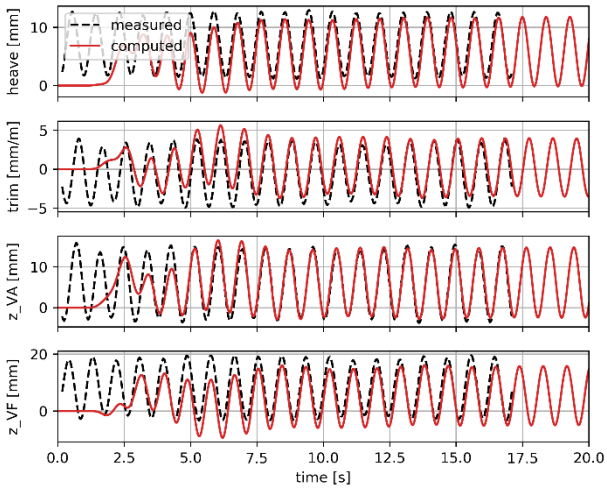

Figure 4. Comparison of the measured and computed motions of DTC containership sailing in head waves at $Fn = 0.14$, $\lambda = 0.55Lpp$ and $H_w = 62.35\,mm$ (CW3 case).

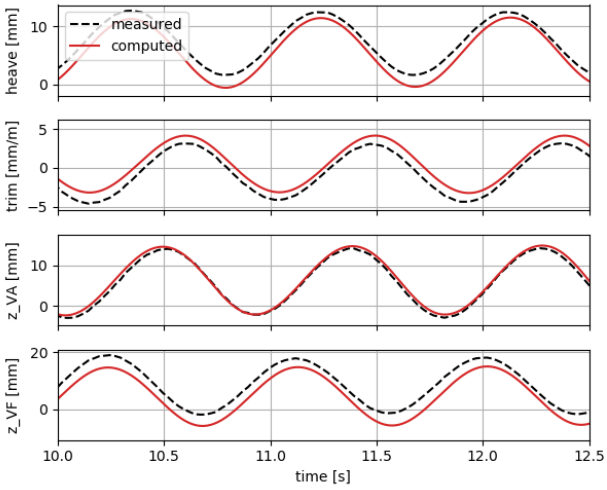

Figure 5. Zoom in on figure 4.

In order to quantify the accuracy of the computed values, a harmonic decomposition of the time records was carried out using equation (4); the results are shown in Table 3.

All first harmonics, with the exception of trim, are within the measured precision uncertainties (see table 8 in Van Zwijnsvoorde et al., 2019). The largest differences are found for the mean values of the heave and forward perpendicular motions. In absolute values, these differences correspond to 1.5 mm and 3 mm respectively. Notice that the precision uncertainty at 100% UKC for heave is 0.7 mm, and for the forward perpendicular motion is 0.8 mm. Therefore, the computed amplitudes are in good correlation with the measured ones.

Figure 6 shows the computed free surface elevation for the CW3 case. The ship Froude number is 0.14. At this speed the ship is faster than the reflected waves, leaving behind the ship's reflected waves. The smooth wave profiles in front of the ship show also that the forcing method, used to avoid wave reflexions from the domain's boundaries, works properly. From Figure 6 one can also confirm that wave elevations have larger absolute values for crests than troughs, which is a common feature of the Stokes waves.

Table 3. Harmonic decomposition of the computed and measured time records of CW3 case.

CW3	H_{max}	f	a0	A1	A2
	mm	1/s	mm	mm	mm
heave comp.	11.95	7.03	5.59	5.97	0.05
heave meas.	11.11	7.05	7.06	5.55	0.04
trim comp.	7.44	7.04	0.23	3.72	0.07
trim meas.	8.09	7.05	-0.60	4.04	0.07
z_VA comp.	16.98	7.04	6.04	8.51	0.17
z_VA meas.	17.63	7.05	5.86	8.80	0.16
z_VF comp	20.89	7.03	5.16	10.42	0.12
z_VF meas.	21.31	7.05	8.26	10.66	0.13

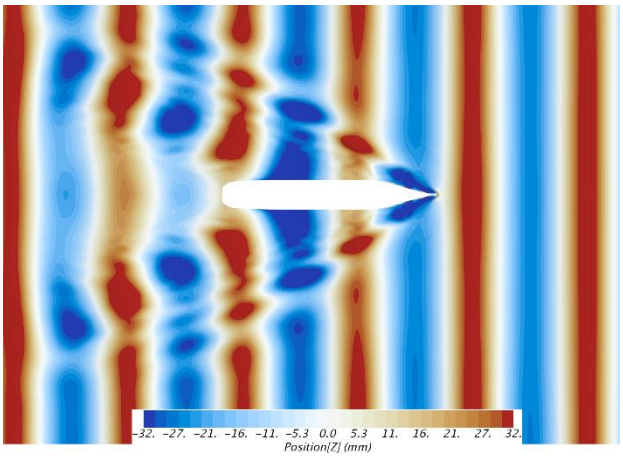

Figure 6. Computed free surface elevation around DTC containership sailing in regular head waves at $Fr = 0.14$, $\lambda = 0.55L_{PP}$ and $H_W = 62.35$ mm (CW3 case).

Figure 7 shows the computed values of the DTC containership sailing in head waves at Froude number of 0.05 (CW2 case). At such low speed it is expected that the major influence of motions comes from waves. This can be observed in the mean values of all motions which are very small compared to the case CW3. For instance, the heave motion oscillates periodically with mean value of 0.5 mm and amplitude of 8.0 mm. The largest mean value is observed for the vertical motion at aft perpendicular with the value of 1.5 mm. In general, these small mean values indicate that the nonlinearities associated with the sinkage and trim have decreased due to the low ship speed. Nonetheless, the first harmonic oscillations amplitudes of all motions have increased. For instance, the amplitude of the vertical motion at forward perpendicular in the CW3 case is 10.42 mm while in the CW2 case the amplitude is 15.11 mm. Therefore, given the same wave amplitude, the ship has larger oscillations at lower speed.

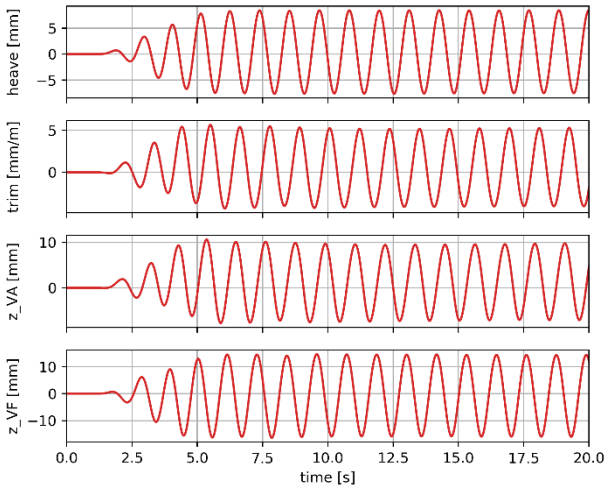

Figure 7. Computed motions of DTC containership sailing in head waves at $Fn = 0.05$, $\lambda = 0.55Lpp$ and $H_w = 62.31$ mm (CW2 case).

5.2 20% UKC TEST CASE

Figure 8 shows the measured and computed values for the wave elevation, the ship motions in heave, the trim and the vertical motions at the aft and forward perpendiculars for the test case CW4. The first plot corresponds to the wave elevation measured at WG4. It is important to notice that the computed wave crests are approximately 18% larger than the experiments whereas wave troughs do not present significant differences. Note that the computed waves were simulated based on the wave records of WG2, provided in Van Zwijnsvoorde et al., (2019). This difference indicates that the wave height in the towing tank decays in the direction of wave propagation, as it was reported in Tello Ruiz, (2018). Recall that the wave gauge WG4 is located at 4.03 m in front of and moving with the ship model whereas wave gauge WG2 is placed at 44 m, at a fixed location, in front of the model. Thus, for simulation purposes it is beneficial to use the wave elevation that approaches the ship. However, such measuring could bring some additional challenges such as avoiding reflected waves from the measurements. Therefore, the results should be analysed carefully.

A larger deviation is observed for the vertical motion values especially for the heave motions were differences in amplitude reach up to 1.38 mm with respect to the measured ones (see table 4). The vertical motions at the aft and forward perpendiculars have a difference of around 0.9 mm and 0.4 mm, respectively, with respect to the measured values. The sources of those differences are in part due to the larger wave height used in the simulations. However, it is also possible that the mesh is still coarse for this very shallow water condition. Further spatial discretization study is needed to verify this case. So far only one mesh with 8.9 million control volumes had been used.

Besides the differences in the wave elevation and possible inaccuracies due to coarse mesh, the precision uncertainty of the measured times series for the case of 20% UKC is larger than for the 100% UKC case. For instance, the precision uncertainty for heave is 1.5 mm and for the vertical motions at the aft and at the forward perpendicular are both around 1.5 mm. Such relatively large precision uncertainty for the small values involved in this very shallow condition distort the relative comparison.

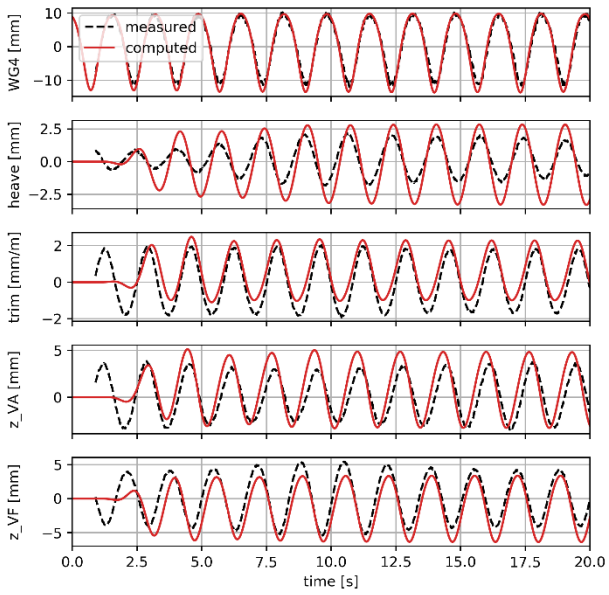

Figure 8. Comparison of the measured and computed motions for the containership sailing in head waves at $Fn = 0$, $\lambda = 0.55Lpp$ and $H_w = 22.21$ mm (CW4 case).

Figure 9 shows the computed free surface elevation for the CW4 case ($Fn = 0$). In contrast to CW3, it is not possible to see a clear wake around the ship. However, it can be observed that the diffracted wave from the ship travels in all directions. Looking carefully at area of the ship's bow, it is possible to observe circular ripples propagating outward from the bow. The diffracted waves next to the hull have a smaller wave length compared to the incoming wave. Thus, those waves represent high frequency waves. However, no high frequency is observed in the time signals, meaning that numerical forcing is absorbing well the diffracted waves.

Table 4. Harmonic decomposition of the computed and measured time records of CW4 case.

CW4	H_{max}	f	a0	A1	A2
	mm	1/s	mm	Mm	mm
heave comp.	5.58	3.80	-0.16	2.75	0.02
heave meas.	2.75	3.77	0.17	1.38	0.03
trim comp.	3.32	3.80	0.55	1.66	0.12
trim meas.	3.52	3.78	-0.02	1.77	0.08
z_VA comp.	7.94	3.82	0.94	3.95	0.22
z_VA meas.	6.14	3.78	0.14	3.06	0.12
z_VF comp	9.45	3.78	-1.26	4.73	0.25
z_VF meas.	8.70	3.77	0.21	4.35	0.19
WG4 comp.	22.97	3.79	0.14	11.26	1.76
WG4 meas.	20.39	3.78	0.30	10.13	1.34

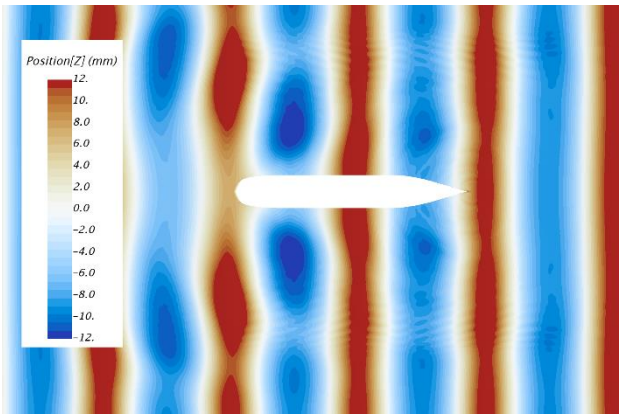

Figure 9. Computed free surface elevation around DTC containership sailing in regular head waves at $Fn = 0$, $\lambda = 0.55Lpp$ and $H_w = 22.21\,mm$ (CW4 case).

When the ship moves in the shallow water condition with a Froude number of 0.05, the vertical motions change drastically. These changes can be seen e.g. in the mean values of heave (see Figure 10) where it increases from -0.16 mm in zero speed case to 1.22 mm in the speed case. Those values seem small, but the amplitudes of heave motions are only around 2.1 mm. It can be also observed that in general the amplitudes of motions have reduced compared to a zero speed case. Therefore, the case with zero speed has smaller mean values but higher amplitude motions when compared with a non-zero speed case. Note that a similar conclusion was reached for the 100% UKC case (see section 5.1).

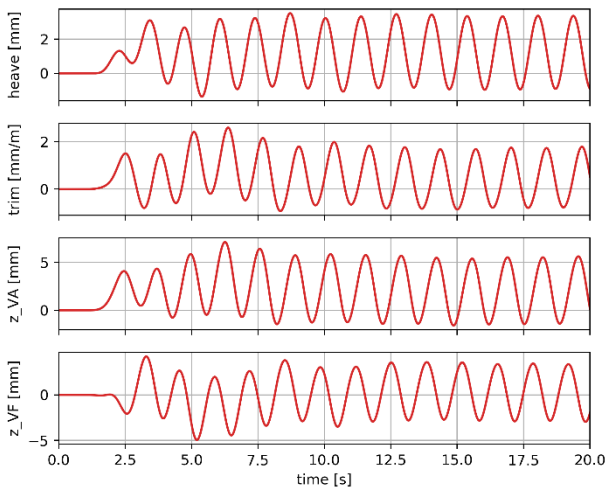

Figure 10. Comparison of the measured and computed motions for the containership sailing in head waves at $Fn = 0$, $\lambda = 0.55Lpp$ and $H_w = 21.26$ mm (CW5 case).

5.3 FINITE INFLUENCE OF DEPTH

In the CW2 and CW5 cases the container ship is sailing in head waves at 0.05 Froude number with a wave length of $0.55L_{PP}$, but with different wave height and wave frequency. The wave frequency differs because of its dependency on the water depth through the dispersion relationship. Nevertheless, some comparison can be made assuming that the motions behave linearly with respect to the wave height amplitude.

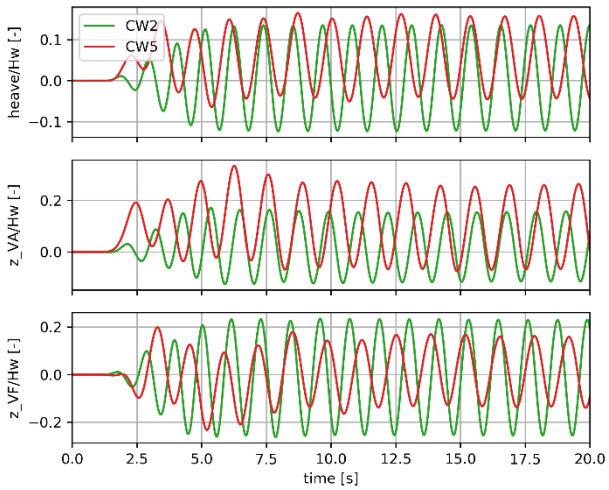

Figure 11. Comparison of the motions of CW2 (100% UKC) and CW5 (20% UKC) at $Fn = 0.05$ and $\lambda = 0.55Lpp$. Non-dimensional values.

Figure 11 shows the heave, and the vertical motions at the aft and forward perpendiculars non-dimensionalised by the wave height. From Figure 11 one can observe larger mean values in 20% UKC (CW5 case), which means that the ship sinks more in 20% UKC. The maximum values of the heave and motion at the aft perpendicular are also larger in 20% UKC than in 100% UKC. This means that when sailing in 20% UKC with the same velocity and wave length, the ship's bottom moves more toward the seabed.

5.4 DISCUSION ON WAVES PROFILE

The numerical simulations of waves were based on Stokes theory which take into account the nonlinearities of the wave due to free surface and bottom conditions. This theory is used to generate values for the wave boundary conditions. Thus, given a wave height and wave period, velocity and pressure computed from the Stokes theory are used on the domain boundaries. The use of analytical wave formulations is important in numerical computations, but usually the wave profiles are not compared with the experimental measured wave profile.

It is common practice to provide wave height and wave period to reproduce the wave properties. Model tests were carried out measuring these two parameters. Depending on the wave generator, the wave velocity profile could be different for the same wave height and period, thus, changing the pressure field under the waves. Therefore, it would be better if also the wave velocity profile could be measured in experiments to avoid inaccurate wave modelling in numerical computations.

6 CONCLUSIONS

A numerical analysis of the DTC container ship motions in head waves at 100% UKC and 20% UKC was carried out. The numerical results at 100% UKC show a good correlation with the corresponding measured values. In general, the difference between computed and analysed values are within the experimental precision uncertainties. The oscillatory amplitudes are well captured by the simulation, but larger relative differences have been found in the mean values, which produces an offset in the time series. This is a sign that the nonlinearities involved in the wave-induced motions in shallow water have not been fully solved yet. Thus, a discretization study is needed.

For the 20% UKC case it was found that the wave elevation in the towing tank decreases in the propagation direction. This aspect becomes more important when small amplitudes are involved because it produces a large relative error. Therefore, for numerical purposes it would be beneficial to have the wave elevation measured as near as possible to the ship.

For a given shallow water condition, 100% or 20% UKC, the increase in ship's forward speed affects vertical motions in two ways. Firstly, the average of the motions increases. Secondly, the amplitude of oscillation reduces. Those results were found when increasing the speed from $Fr = 0.05$ to $Fr = 0.14$ in 100 % UKC and when increasing from $Fr = 0$ to $Fr = 0.05$ in 20% UKC. Regarding the influence of the depth under same speed and wave conditions ($Fr = 0.05$ and $\lambda = 0.55Lpp$), it has been found that the containership sinks more at 20% UKC than at

100% UKC. This can be explained by the fact that the seabed has a larger influence on the pressure around the ship.

Overall, the numerical results have provided a deep insight into the wave-induced motions at shallow water conditions. The numerical results correlate with the measured ones. The small differences found in the harmonics amplitudes are within the precision uncertainties. However, a discretization study is still needed to corroborate some large deviation in the mean values.

7 ACKNOWLEDGEMENTS

This research was partially carried out within the framework of the Innoship project (project number 03SX416B). The authors acknowledge the financial support by the Federal Ministry for Economic Affairs and Energy (Bundesministerium für Wirtschaft und Energie) of Germany. Furthermore, the authors would like to thank the Faculty of Mechanical Engineering and Naval Architecture, University of Zagreb, for funding the licence of the software package STAR-CCM+.

8 REFERENCES

el Moctar, O., Shigunov, V., Zorn, T., 2012. Duisburg Test Case : Post-Panamax Container Ship for Benchmarking. Sh. Technol. Res. J. 59, 50–64.

Ferziger, J.H., Perić, M., 2012. Computational Methods for Fluid Dynamics. Springer-Verlag Berlin Heidelberg. https://doi.org/10.1007/978-3-642-56026-2

Méhauté, B. Le, 1976. An Introduction to Hydrodynamics and Water Waves. Springer Science & Business Media.

Moukalled, F., Mangani, L., Darwish, M., 2016. The Finite Volume Method in Computational Fluid Dynamics An Advanced Introduction with. Springer Science+Business Media. https://doi.org/10.1007/978-3-319-16874-6

Perić, R., Abdel-Maksoud, M., 2018. Analytical prediction of reflection coefficients for wave absorbing layers in flow simulations of regular free-surface waves. Ocean Engineering, Vol. 147, 132–147. https://doi.org/10.1016/j.oceaneng.2017.10.009

Perić, R., Abdel-Maksoud, M., 2017. Predicting the Reflection Coefficients of Wave Damp-ing Zones Before Running the Flow Simulations, in: Proceedings of the 20th Numerical Towing Tank Sympo-Sium (NuTTS2017). Wageningen, the Netherlands.

Rapuc, S., Crepier, P., Jaouen, F., Bunnik, T., Regnier, P., 2018. Towards Guidelines for Consistent Wave Propagation in CFD Simulations, in: Proceedings of NAV 2018: 19th International Confer-Ence on Ship and Maritime Research. https://doi.org/10.3233/978-1-61499-870-9-515

Sigmund, S., el Moctar, O., 2018. Numerical and experimental investigation of added resistance of different ship types in short and long waves. Ocean Eng. 147, 51–67. https://doi.org/10.1016/j.oceaneng.2017.10.010

Tello Ruiz, M., 2018. Manoeuvring model of a container vessel in coastal waves. PhD Thesis, Ghent University.

Tello Ruiz, M., Vantorre, M., Delefortrie, G., 2016. Induced wave forces on a ship manoeuvring in coastal waves. Ocean Eng. 121, 472–491.
Tezdogan, T., Incecik, A., Turan, O., 2016. Full-scale unsteady RANS simulations of vertical ship motions in shallow water. Ocean Eng. 123, 131–145. https://doi.org/10.1016/j.oceaneng.2016.06.047

Van Zwijnsvoorde, T., Tello Ruiz, M., Delefortrie, G., Lataire, E. 2019. Sailing in shallow water waves with the DTC container carrier, in: Proceedings of the 5th International Conference on Ship Manoeuvring in Shallow and Confined Water with non-exclusive focus on Manoeuvring in Waves, Wind and Current. Ostend, Belgium.

Vantorre, M., Journée, J., 2003. Validation of the strip theory code SEAWAY by model tests in very shallow water. Flanders Hydraul. Res. Numer. Model. Colloquium,.

Vantorre, M., Laforce, E., Eloot, K., Richter, J., Verwilligen, J., Lataire, E., 2008. Ship motions in shallow water as the base for a probalistic approach policy, in: Proceedings of the ASME 27th International Conference on Offshore Mechanics and Arctic Engineering - OMAE 2008. pp. 1–10.

Wikimedia (2019) the graphic was retrieved from: https://commons.wikimedia.org/wiki/File:Water_wave_theories.svg

9 AUTHORS BIOGRAPHY

Guillermo Chillcce holds the current position of research assistant at the Institute of Ship Technology, Ocean Engineering and Transport Systems (University of Duisburg-Essen). His area of expertise is seakeeping and manoeuvring analysis by means of boundary element methods and field methods.

Ivana Martić is a doctoral student of Naval Architecture and teaching/research assistant at the Faculty of Mechanical Engineering and Naval Architecture, University of Zagreb. Her area of research includes ship hydrodynamics.

Manases Tello Ruiz PhD, Naval Architect and Marine Engineer, is a Research Staff at Ghent University. He has been involved in several (inter)national projects with main focus on manoeuvring, seakeeping, and wave energy converters. Currently, he is working on ship air pollution and

machine learning techniques applied to ship hydrodynamics. At present he is also a member of the ITTC Specialist Committee of Manoeuvring in Waves, for which he has been appointed as secretary.

Jorge Ramirez holds the current position of naval architect at Knud e Hansen in Denmark. He is responsible for performing different analyses to assist in the design process of a vessel, such as trim optimization, resistance analysis, wind loads and ship propulsion. His previous experience includes research for wave loads on offshore wind turbines, experimental and numerical analysis, wave energy converters.

Nastia Degiuli is a full professor at the Faculty of Mechanical Engineering and Naval Architecture, University of Zagreb and head of the Chair of Ship Hydrodynamics. Her area of expertise involves experimental and numerical ship hydrodynamics.

Ould el Moctar, Prof. Dr.-Ing. is full Professor in Ship Technology and Ocean Engineering at the University of Duisburg-Essen. His publications cover various aspects of hydrodynamics and Fluid-Structure-Interaction. The focus of his research is seakeeping, hydroelasticity, slamming and sloshing, cavitation, manoeuvring and propulsion in waves. He is editor and co-editor of many international journals.

AN EXPERIMENTAL STUDY ON THE CAPTIVE MODEL TEST OF KCS IN REGULAR WAVES

Hujae Choi, Dong Jin Kim, Yeon Gyu Kim, Dong Jin Yeo, Kunhang Yun and **Gyeong Joong Lee**,
Korea Research Institute of Ship and Ocean Engineering, Republic of Korea

AN EXPERIMENTAL STUDY ON THE CAPTIVE MODEL TEST OF KCS IN REGULAR WAVES

Hujae Choi, Dong Jin Kim, Yeon Gyu Kim, Dong Jin Yeo, Kunhang Yun and Gyeong Joong Lee, Korea Research Institute of Ship and Ocean Engineering, Republic of Korea

SUMMARY

In order to investigate maneuvering characteristics of KCS in waves, captive model tests in regular waves were conducted. Purpose of the test is measuring maneuvering hull forces in waves. Model tests were carried out using CPMC (Computerized Planar Motion Carriage) of ocean engineering basin in KRISO (Korea Research Institute of Ships and Ocean engineering). Total 6 degrees-of-freedom motion were fixed by two points supporting captive model test device, which is specially designed for the test. Several static drift tests were conducted in calm sea and in regular waves, varying wave amplitude, length, and direction. Hydrodynamic maneuvering forces in waves and hydrodynamic coefficients related to sway velocity were estimated based on the test results.

NOMENCLATURE

λ	Wave length (m)
H_w	Wave height (m)
χ	Wave direction (˚)
U	Forward velocity (m/s)
ψ	Heading angle (˚)
o-x_0y_0	Earth-fixed coordinate (-)
O-xy	Body-fixed coordinate (-)
β	Drift angle (˚)
u, v	Surge, Sway velocity (m/s)
r	Yaw velocity (˚/s)
u̇, v̇	Surge, Sway acceleration (m/s^2)
ṙ	Yaw acceleration (˚/s^2)
m	Mass of ship (kg)
I_{zz}	Yaw moment of inertia of ship (kg·m^2)
x_G	Position of Center of gravity (m)
m	Mass of model ship (kg)
m	Mass of model ship (kg)
$X_H, Y_H,$	Hydrodynamic surge, sway force acting on hull (N)
N_H	Hydrodynamic yaw moment acting on hull (N·m)
$X_T, Y_T,$	Surge, Sway towing force (N)
N_T	Yaw towing moment (N·m)
$X_0, Y_0,$	Hydrodynamic surge, sway force at zero drift angle (N)
N_0	Hydrodynamic yaw moment at zero drift angle (N·m)
X_{vv}, Y_v, N_v	Hydrodynamic coefficient (-)
F	General force (N)
M	General moment (N·m)
V	General ship velocity (m/s)
F'	Nondimensional general force (-)
M'	Nondimensional general moment (-)
L_{BP}	Length between perpendicular (m)
ρ	Density of water (kg/m^3)

1 INTRODUCTION

Traditionally, maneuvering performance of a ship has been studied in calm water condition through the model test or sea trial. However, necessity for estimation of maneuvering performance of a ship in waves has been grown in that it is associated with the estimation of minimum required horsepower of a ship for keeping maneuverability in adverse weather. Because of this necessity, international studies have been conducted such as SHOPERA (Energy Efficient Safe Ship OPERAtion) project of European Union and JASNAOE project of Japan.

For the investigation of maneuvering performance of a ship in waves, free running model test is the most instinctive way. There are several researches which conducted free running model test.

Ueno et al. (2003) carried out turning tests, zig-zag tests and stopping tests in regular waves to investigate maneuvering performance of a VLCC model in waves. Yasukawa (2006a, 2006b) carried out turning tests in regular and irregular waves with a container ship model, and also conducted numerical analysis of maneuvering simulations in waves and compared both results.

Another way to investigate maneuvering performance of a ship is captive model test. Jeon et al. (2015) carried out PMM model test in waves with a 4600TEU container ship and derived the hydrodynamic coefficients both in calm water and in waves, their method is most similar to this study.

In the SHOPERA project, various experiments were conducted such as seakeeping tests for estimating wave drift forces and moment, turning tests in regular and irregular waves. Target model ship were KVLCC2 and DCT.

Solving the maneuvering of a ship in waves is hard since it has both characteristics of maneuvering and seakeeping in traditional naval architecture. To unifying these heterogeneous characteristics, there have been a lot of researches. Especially estimating maneuvering performance of ship in waves through numerical method. Ottosson and Bystrom (1991) calculated maneuvering in waves by using fixed added mass and damping coefficient. Fang et al. (2005) presented equation of motion of ship

maneuvering in waves using hydrodynamic coefficients depending on encounter frequency. It was upgraded form of Ottosson and Bystrom, but it also didn't consider memory effect by waves. Lee (1992) investigated significance of memory effect in the problem of maneuvering of ship in waves. Bailey et al. (1997) presented the equation of motion considering memory effect by using convolution integral. Fossen (2005) derived it by matrix form and presented the equation in state space representation. Skejic and Faltinsen (2008) compared various theory calculating 2nd order drift force, and presented two-time scale model which separates low frequency motion by maneuvering from high frequency motion by wave incidence. Seo et al. (2011), Seo and Kim (2011), Seo (2016) solved the problem of ship maneuvering in waves using time domain Rankine panel method, and the results were compared with experimental data.

This paper presents captive model test results to investigate the ship maneuvering characteristics in waves. Static drift tests with various drift angles and wave conditions were presented. The model ship is totally bound to the experiment equipment, so that measured hydrodynamic forces and moments do not contain radiation components.

2 MODEL TEST

2.1 TEST FACILITY

Figure 1. Ocean engineering basin of KRISO

Model test was conducted in ocean engineering basin of KRISO as shown in Figure 1. The piston type wave generators are located at the front and left side of the basin, and the wave absorbers are located at each other sides of the basin. Both regular and irregular waves can be generated by the wave generators. The length, breadth and depth of KRISO ocean engineering basin is 56m, 30m and 4.5m respectively. During the tests, model ship meets at least five numbers of wave crest in constant maximum speed after acceleration phase.

2.2 MODEL SHIP

Figure 2. KCS container model ship

KCS container ship was selected as a target ship of experiment. KCS is a representative hull form widely selected to investigate hydrodynamics of container ship. Many researches have been conducted various model tests of KCS, it is easy to compare our test results with other experiment results. The tests were conducted with rudder, but without propeller. Particulars of target ship such as principal dimensions, scale ratio and Froude number are listed in Table 1.

Table 1. Test condition of real and model ship.

Contribution	Real ship	Model ship
Scale ratio	65.90	
L_{BP}	230.0 m	3.49 m
Displacement	52030 m^3	0.1818 m^3
Fn	0.173	
Ship speed	16 knots	1.014 m/s

2.3 TEST EQUIPMENT

2.3 (a) Captive Model Test Device

A two points supporting captive model test device was designed. The model ship is totally fixed by the device in 6 degrees-of-freedom. As a result, model ship cannot make radiation waves during the test. To measure hydrodynamic forces and moments, two load cells were located in each capturing point, and there are hinges to free the installation stresses. Two ultrasonic sensors which can measure incident wave height were attached at the midship of model ship (port and starboard). The pictures of captured model ship and captive model test device are presented in figure 3 and 4.

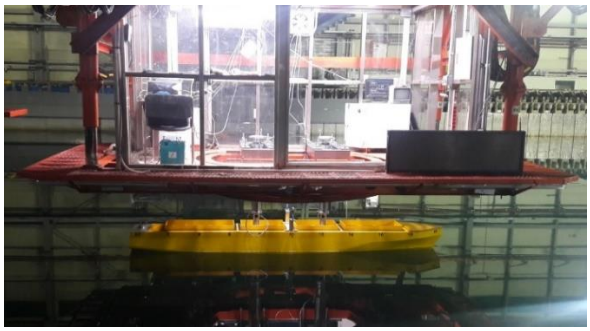

Figure 3. KCS model ship installed with captive model test device

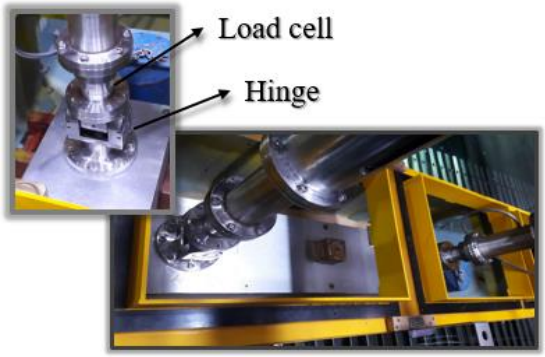

Figure 4. Captive model test device

2.3 (b) Data Acquisition System

While test is conducting, 6 DOF force and moment of model ship, wave height and position of CPMC were measured. In order to measure 6 DOF force and moment, two 6 DOF load cells were used and whole 12 electrical signal outputs were converted to 6 DOF force and moment. NI USB-6289 was used as DAQ devices. Detailed flow chart of data acquisition system is denoted in Figure 4.

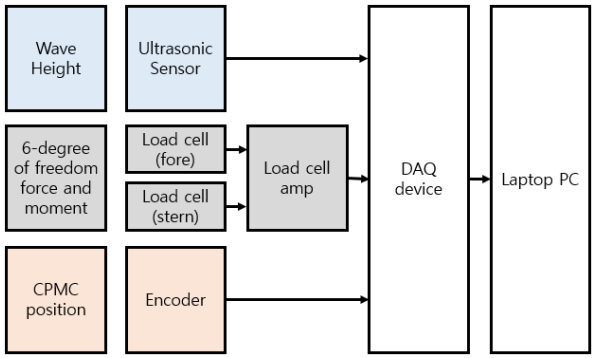

Figure 4. Flow chart of data acquisition system

2.3 (c) Calibration

In order to obtain 6 DOF forces and moments of model ship during the tests, calibration test was conducted. Since two 6 DOF load cells were used, the number of output electrical signal is 12. Converting 12 electrical signals to 6 DOF force and moment, 6 by 12 calibration matrix was needed. Several calibration test cases were designed to endow 6 DOF forces and moments, those can be applied to two load cells, sufficiently. Figure 5. Shows a picture of calibration test set-up using the calibration test device.

Figure 5. Calibration test using calibration test device

2.4 TEST CONDITION

Test conditions for the static test are listed in Table 2. Most of tests in waves were conducted under wave height H_w/L_{BP}=0.02, and the case of H_w/L_{BP} = 0.015 was conducted for some cases in order to investigate influence of wave height in wave exciting force. The depth of basin is 4.5m and the condition of depth is deep water sufficiently.

Table 2. Test conditions

Class	Condition	
	Wave length [λ/L_{BP}]	Drift angle [β (°)]
Static drift	-	0, ±2, ±4, ±6, 9, 12, 18
Head Sea [χ=180°]	0.7	0, 2, 4, 6, 9, 12
	1.2	0, 2, 4, 6, 12
	1.0, 0.5	0, 2, 4, 6
	1.5	0
Beam Sea [χ=90°]	0.7	0, ±2, ±4, ±6, 9, 12, 18
	1.2, 1	0, ±6
	1.5, 0.5	0
Follow Sea [χ=0°]	1.2, 1.0, 0.7, 0.5	0

3 SHIP MANEUVERING MODEL

3.1 COORDINATE SYSTEMS

The coordinate system to describe ship maneuvering model is denoted in Figure 6. The o-x_0y_0 coordinate is the earth-fixed coordinate which is inertial reference frame, and the O-xy coordinate is the body-fixed coordinate which is non-inertial reference frame. The center of body-fixed coordinate is midship of the model ship. The rotation angle between those two coordinates are defined as heading angle, ψ. For the vertical coordinates, z, ϕ, θ

denote heave, roll and pitch motions respectively, and Z, K, M denote heave force, roll and pitch moments respectively.

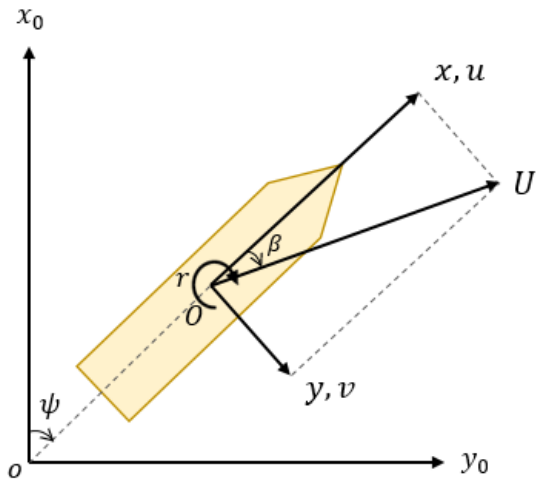

Figure 6. Ship coordinates system

3.2 HYDRODYNAMIC FORCE AND MOMENT MODEL

The horizontal plane 3 DOF motion consisting of surge, sway and yaw was adopted to represent ship maneuvering motion. Equations of motion of 3 DOF motion are represented as follows:

$$\begin{aligned} \mathrm{m}(\dot{u} - \mathrm{v}r - x_G r^2) &= X_H + X_T \\ \mathrm{m}(\dot{v} + \mathrm{u}r - x_G \dot{r}) &= Y_H + Y_T \\ I_{zz}\dot{r} + \mathrm{m}x_G(\dot{v} + \mathrm{u}r) &= N_H + N_T \end{aligned} \quad (1)$$

Where X_H, Y_H, N_H in Equation (1) are hydrodynamic force and moment acting on hull. In this study, the model ship is totally captured by captive model test device. It means that hydrodynamic maneuvering force and moment acting on hull can be considered as superposition of maneuvering hull force in calm water and wave exciting force. It is noted that radiation force caused by ship motion is not included in measurement. This has a tremendous advantage in some respects, when validating CFD calculation results. In this study, mean value of hydrodynamic maneuvering force in waves are considered. When static drift test is being conducted, whole hydrodynamic maneuvering force in waves can be represented as below at small drift angle.

$$\begin{aligned} X_H &= X_0 + X_{vv}v^2 \\ Y_H &= Y_0 + Y_v v \\ N_H &= N_0 + N_v v \end{aligned} \quad (2)$$

Force and moment in Equation (1) and (2) can be nondimensionalized based on the Society of Naval Architects and Marine Engineers(SNAME) definition represented as below

$$F' = \frac{F}{\frac{1}{2}\rho {L_{BP}}^2 V^2}$$
$$M' = \frac{M}{\frac{1}{2}\rho {L_{BP}}^3 V^2} \quad (3)$$

4 TEST RESULTS

Whole tests were carried out at the Froude number of 0.173, which is 16 knots for real ship. Corresponding towing speed is 1.014 m/s. Horizontal forces and moment are presented through nondimensionalization using Equation (3)

4.1 RAW DATA CURVE FITTING

Since the sensor data contain noise, the data were fit by high order sinusoidal curve. The example of curve fitting is shown is figure 7.

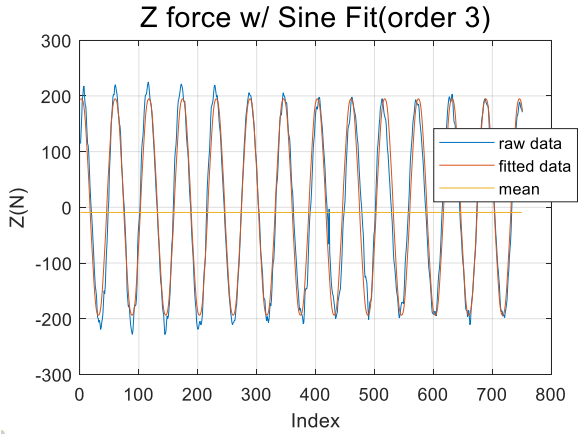

Figure 7. Example of raw data curve fitting

4.2 MEAN WAVE EXCITING FORCE ACCORDING TO WAVE CONDITIONS

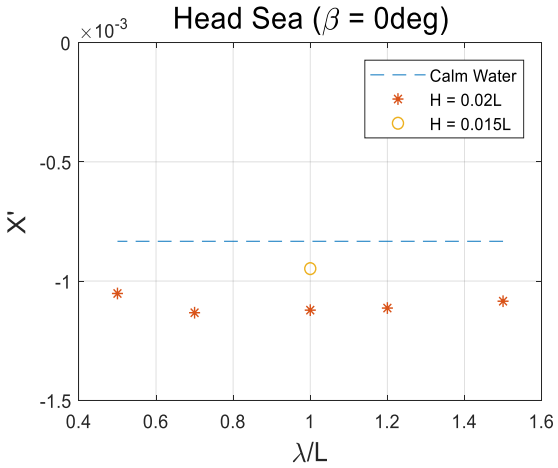

Figure 8. Captive model test results in head sea condition (β = 0°)

Figure 8 represents captive model test results in head sea condition varying wave length and height. The situation of this test is similar to the added resistance test. However, in the sense that the model ship is fully constrained to the device and cannot move freely in heave, roll and pitch, it is expressed in terms of the mean wave exciting force rather than the additional resistance. In this test, wave height of H_w/L_{BP}=0.02 was selected for investigating the effect of wave exciting force. For very few cases, wave height of H_w/L_{BP} =0.015 was conducted in order to investigate the effect of wave height. According to test results of Figure 8, mean wave exciting force component in surge is about 20 ~ 25 % of surge force in calm water test result. When compared by wave length, largest mean wave exciting force was measured at λ/L_{BP}=0.7, followed by 1.0, 1.2, 1.5, 0.5 in turn. The effect of wave height is also seen in the Figure 8.

4.3 STATIC DRIFT TEST

4.3 (a) Static drift test in calm water

Static drift test in calm water was carried out at various drift angles. The linear damping coefficient Y_v and N_v could be derived from the static drift test. Below Figure 9 and 10 represents the result of static drift test along with the results of other tests (Kim et al, 2009).

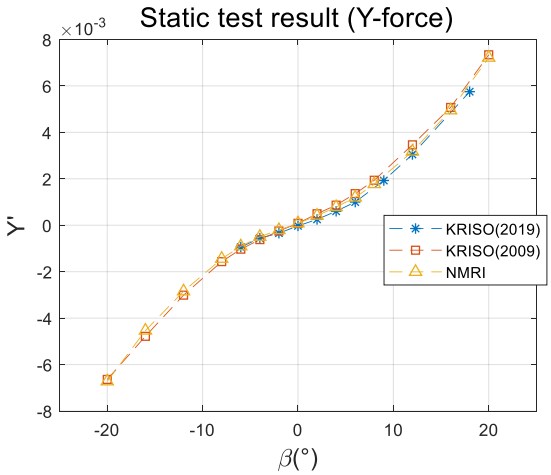

Figure 9. Static drift test result in calm water (sway force)

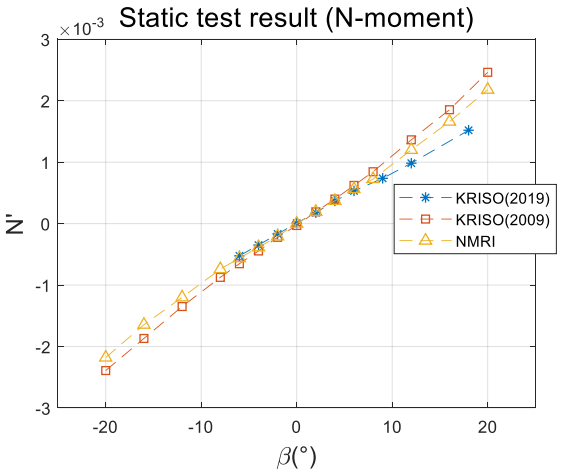

Figure 10. Static drift test result in calm water (yaw moment)

The nondimensionalized result in Y force of this experiment (KRISO2019) is well accordance with the results of previous experiment of KRISO in 2009 (KRISO2009) and NMRI, but it shows quite discrepancy in yaw moment at large angle. The reason for the discrepancy is thought to be propeller presence. Experiments on KRISO2009 and NMRI were carried out during propeller self-propulsion, which made larger rudder normal force. As a result, yaw moment due to the rudder normal force was added to the moment acting on the hull, resulting in larger yaw moment result.

4.3 (b) Static drift tests in waves

Static drift tests in waves were carried out in five wave length conditions listed in Table 3. The nondimensinalized sway force and yaw moment are shown in figures 11~16. The tests were conducted in five wave length conditions at head sea, one wave length condition at beam sea. Wave heights for both head sea and beam sea conditions are the same as H_w/L_{BP}=0.02.

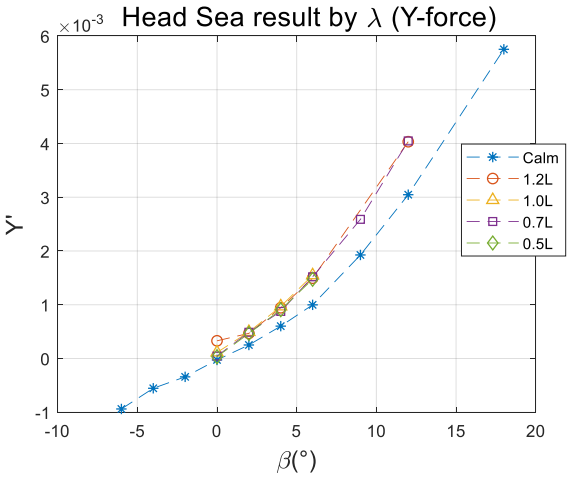

Figure 11. Static drift tests results at head sea (sway force)

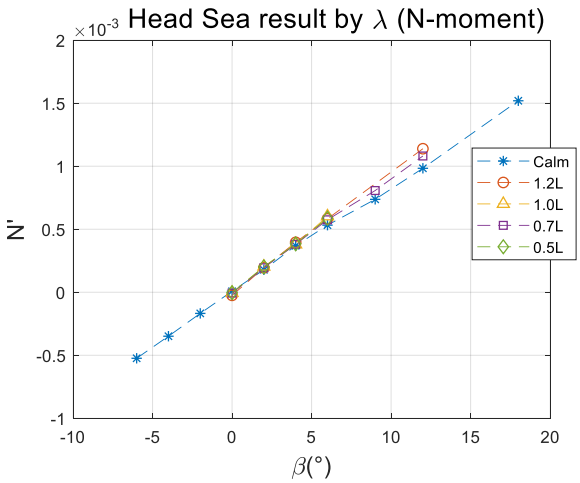

Figure 12. Static drift tests results at head sea (yaw moment)

Figure 11 and 12 present sway force and yaw moment ofstatic drift tests at head sea. The results are also compared with calm water test results. Since the waves acting on a model ship did not generate ship motions, hydrodynamic forces and moments did not have radiation component. It can be noted that the influence of the waves increases as the drift angle increases.

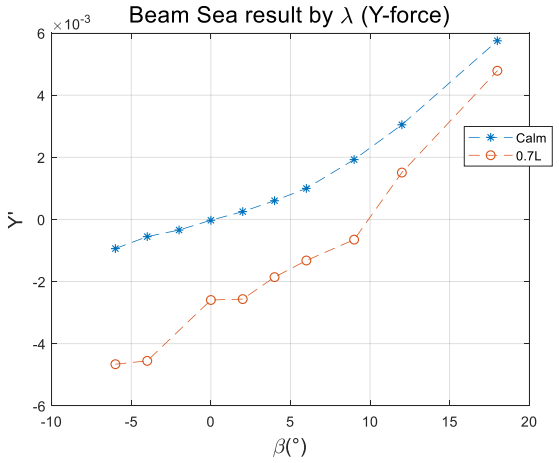

Figure 13. Static drift test result in beam sea (sway force)

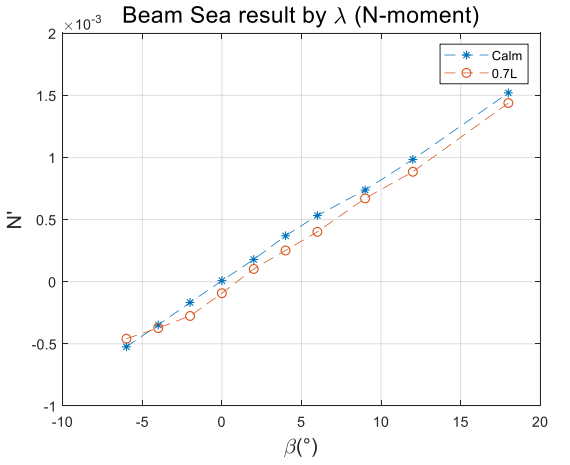

Figure 14. Static drift test result in beam sea (yaw moment)

Figure 13 and 14 present sway force and yaw moment of static drift tests at beam sea. The tests were conducted with wave length of λ/L_{BP}=0.7 and the results were compared with calm water tests results. Since the wave comes to the side of the hull, it can be seen in the Figure 13 that negative sway force is applied to model ship induced by the wave. However, the yaw moment is not significantly different from the calm water result, which can be suspected that the distance between the center of mass and the point of action of the hydrodynamic force is close.

4.4 HYDRODYNAMIC CODEFFICIENTS

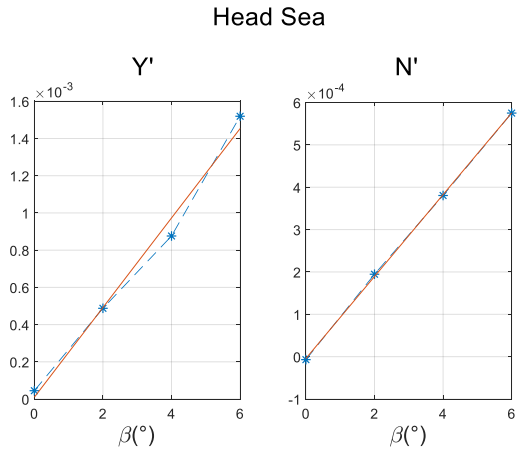

Figure 15. Static drift test result in head sea (in small angle with line fitting)

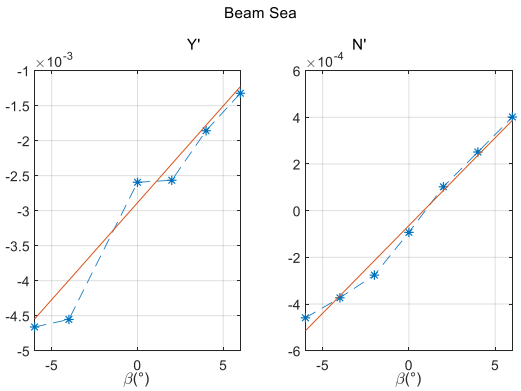

Figure 16. Static drift test result in beam sea (in small angle with line fitting)

Figure 15 and 16 present results of static drift tests in waves at small drift angles. In the Figures, it can be suspected that the hydrodynamic force and moment are proportional to the drift angle in linear way. Linear sway and yaw hydrodynamic coefficients were estimated, and results are listed in Table 3.

Table 3. Hydrodynamic coefficients

Class	λ/L_{BP}	Y_v	N_v
Calm water	-	-8.931E-3	-5.073E-3
Head sea	1.2	-1.139E-2	-5.809E-3
	1.0	-1.372E-2	-5.738E-3
	0.7	-1.381E-2	-5.544E-3
	0.5	-1.367E-2	-5.608E-3
Beam sea	0.7	-1.587E-2	-4.313E-3

5. CONCLUSION

Captive model tests in calm sea and in waves were performed in KRISO ocean engineering basin in order to investigate the effect of wave exciting force of a ship advancing with drift angle. KCS model ship was selected for captive model tests. Through this study, it was possible to investigate the quantitative tendency of mean wave exciting force according to drift angle, wave length, direction and height. In addition, the linearity of the static drift test in waves at small angle was also confirmed, and linear hydrodynamic coefficients were derived.
For the future work, exquisitely designed turning test in waves will be conducted. Through the turning test, it will be possible to obtain hydrodynamic coefficient related to yaw rate. Using this series of experimental results, it is expected to understand the maneuvering performance of ship such as directional stability in waves according to the wave conditions.

5 ACKNOWLEDGEMENTS

This research was supported by a grant from Endowment Project of “Development of the Analysis Technology of Ship’s Integrated Ability of Maneuvering and Seakeeping (3/3)” funded by Korea Research Institute of Ships and Ocean Engineering (PES3010).

6 REFERENCES

Bailey, P.A., Price, W.G., Temarel, P., 1997. A Unified mathematical model describing the manoeuvring of a ship travelling in a seaway. Transactions of the Royal Institution of Naval Architects, 140, pp.131-149.

Fang, M.C., Luo, J.H., Lee, M.L., 2005. A nonlinear mathematical model for ship turning circle simulation in waves. Journal of Ship Research, 49(2), pp.69-79.

Fossen, T.I., 2005. A Nonlinear unified state-space model for ship maneuvering and control in a seaway. International Journal of Bifurcation and Chaos, 19(9), pp.2717-2746.

Jeon, M. J., Lee, D. H., Nguyen, V. M., Yoon, H. K., 2015. Estimation of Hydrodynamic Coefficients in Waves using PMM Test, in Proceedings of the 2nd International Conference on Advanced Engineering – Theory and Applications. Ho Chi Minh City, Vietnam, pp.845-853.

Kim, Y. G., Yeo, D. J., Kim, S. Y., Yun, K. H., Oh, B. I., 2009. Prediction of Maneuverability of KCS by CPMC Captive Model Test. Journal of the Society of Naval Architects of Korea, 46(6), pp. 553-561.

Lee, S.K., 1992. A study on the memory effect of the radiation forces in the maneuvering motion of a ship. Transactions of the Society of Naval Architects of Korea, 29(3), pp.53-58.

Ottosson, P., Bystrom, L., 1991. Simulation of the dynamics of a ship manuvering in waves. Transaction of Society of Naval Architects and Marine Engineers, 99, pp.281-298.

Seo, M.G., Kim, Y., Kim, K.H., 2011. Effects on nonlinear ship motions on ship maneuvering in large amplitude waves. Journal of the Society of Naval Architests of Korea, 48(6), pp.516-527.

Seo, M.G., Kim, Y., 2011. Numerical analysis on ship maneuvering coupled with ship motion in waves. Ocean Engineering, 38, pp.1934-1945.

Seo, M.G., 2016. Study on prediction method for ship operation performance in waves. Ph.D. Thesis. Seoul National University

SHOPERA, 2016. Presentation of benchmark results. SHOPERA Benchmark Workshop, London, 15 April 2016.

Skejic, R., Faltinsen, O.M., 2008. A unified seakeeping and maneuvering analysis of ships in regular waves. Journal of Marine Science and Technology, 13, pp.371-394.

Ueno, M., Nimura, T., Miyazaki, H., 2003. Experimental study on manoeuvring motion of a ship in waves. International Conference on Marine Simulation and Ship Manoeuvrability, Japan, pp.1-7.

Yasukawa, H., 2006a. Simulations of a ship maneuvering in waves (1st report: turning motion). Journal of the Japan Society of Naval Architects and Ocean Engineers, 4, pp.127-136.

Yasukawa, H., 2006b. Simulations of wave-induced motions of a turning ship. Journal of the Japan Society of Naval Architects and Ocean Engineers, 4, pp.117-126.

7 AUTHORS BIOGRAPHY

Hujae Choi holds the current position of junior researcher at Korea Research Institute of Ship and Ocean engineering. He received a bachelor and master degrees of

Engineering in a department of Naval Architecture and Ocean Engineering at Seoul National University. His main interests are maneuvering and control of ship and maritime autonomous surface ship.

Dong Jin Kim is a senior engineer at Korea Research Institute of Ships and Ocean Engineering. He received a bachelor, master, and Ph.D. degrees of Engineering in a department of Naval Architecture and Ocean Engineering at Seoul National University. His major fields are manoeuvring and seakeeping analyses of high speed vessels as well as other surface vehicles.

Yeon Gyu Kim holds the current position of principal researcher at Korea Research Institute of Ships and Ocean Engineering. He is responsible for prediction of manoeuvrability of ships and submersible bodies.

Dong Jin Yeo holds the current position of principal researcher at Korea Research Institute of Ships and Ocean Engineering. He is responsible for identification, performance prediction, and control of ocean vehicles' dynamics. His previous experience includes design of optimal inputs for the identification of ocean vehicles' dynamics, modeling of ocean vehicles' dynamics, etc.

Kunhang Yun holds the current position of senior researcher at Korea Research Institute of Ships and Ocean Engineering. He is responsible for manoeuvring simulation of maritime vehicles and maritime simulator.

Gyeong Joong Lee holds the current position of principal researcher at Korea Research Institute of Ships and Ocean Engineering. His current research field is on the dynamics of marine vehicles, especially on the wave interaction on a surface ship and flooding simulation of a damaged ship.

DESCRIPTION OF HYDRO/METEO DATA IN SHIP MANOEUVRING SIMULATORS: A SURVEY ON THE STATE OF THE ART

Luca Donatini and **Marc Vantorre**,
Maritime Technology Division, Ghent University, Belgium

Jeroen Verwilligen,
Flanders Hydraulics Research, Belgium

Guillaume Delefortrie,
Flanders Hydraulics Research, Belgium and Maritime Technology Division, Ghent University, Belgium

DESCRIPTION OF HYDRO/METEO DATA IN SHIP MANOEUVRING SIMULATORS: A SURVEY ON THE STATE OF THE ART

Luca Donatini and **Marc Vantorre,** Maritime Technology Division, Ghent University, Belgium
Jeroen Verwilligen, Flanders Hydraulics Research, Belgium
Guillaume Delefortrie, Flanders Hydraulics Research, Belgium and Maritime Technology Division, Ghent University, Belgium

SUMMARY

This paper describes the results of a survey performed by the authors to assess how hydro/meteo conditions are presently modelled in ship manoeuvring simulators. A questionnaire regarding current, waves, wind and water levels was sent to a selected list of simulator developers and users. The received answers were thoroughly analysed and are summarized in this paper as an overview of the state of the art in hydro/meteo data for ship simulators at the time of writing. All the results are published in an anonymous form to guarantee a high discretion level to all parties who answered the survey.

1 INTRODUCTION

Ship manoeuvring simulators are nowadays regarded as invaluable tools in both the design of port infrastructures and the training of maritime professionals. The level of realism of simulations increased dramatically in the last decade due to the ever increasing availability of computational power impacting on both mathematical modelling and visual performances.
Manoeuvring simulation software is in a permanent state of development, for different reasons. The evolution of computer hardware nowadays allows to perform calculations in real-time which were absolutely impossible a few decades ago. On the other hand, customers have increasing demands with respect to the complexity of simulations, the realism of both ship behaviour and environmental conditions, and the accuracy and reliability of the results. Because of improved position measurement systems, operations are performed with decreasing margins which also means that both mathematical models for ship manoeuvring and the representation of the meteorological and hydrological conditions have to meet higher standards.
While mathematical models for the manoeuvring behaviour of ships are well documented in literature, an overview concerning hydro/meteo modelling in ship manoeuvring simulators is hard to find in the public domain. In order to determine a strategy for future developments in this respect, Flanders Hydraulics Research (FHR) has commissioned the Maritime Technology Division of Ghent University (UGent) to perform a study to determine an optimal way of representing waves, currents, tides and wind. In the frame of such a study, it is appropriate to examine the state of the art, not only by studying the specialized literature, but also by contacts with other developers, scientists and advanced users who are involved in similar matters. As such, not only a better view will be obtained on the common practice, but exchange of ideas might also lead to a better communication and even co-operation.
In order to investigate the current state of art of hydro/meteo modelling in ship simulators, a questionnaire was sent to a selected list of simulator developers and users. The explicit aim of the questionnaire was the collection of information to be publicly summarized in the form of a scientific publication. The answers from several parties which took the effort to return a filled in questionnaire were collected and analysed, and are summarized in this paper. All the received data are published here in an anonymous way to ensure the appropriate level of confidentiality to all the parties involved.
The information summarized in this paper could benefit the whole community of ship simulator users and developers by making everyone more aware of the present common practices, while also fixing a starting point for future research and improvements.

2 QUESTIONNAIRE

The questionnaire on hydro/meteo modelling was developed by UGent in collaboration with FHR with the aim to collect information about the way current, waves, wind and water levels are presently modelled in ship manoeuvring simulators worldwide. The questionnaire was sent to approximately thirty parties, selected between simulator developers and advanced users. Twelve replies were received in time to be included in this paper.
The questionnaire contains five main sections, investigating different aspects of hydro/meteo modelling:

1. General information
2. Current
3. Waves
4. Wind
5. Water levels

Each of these different sections will be analysed in more detail in a following chapter.

3 GENERAL INFORMATION

The general information section of the questionnaire contains questions about the replying institute and the types of simulators in use. The twelve received replies come from ten different countries, and can be categorized as in the following.

Two replies came from universities, four from public research institutes and six from private companies. For convenience, all will be generally referred as "*institutes*" in the paper. Ten of the replies came from simulator developing institutes and two from simulator users. All of the developer institutes except for one are involved in the development of both the mathematical model and the visual part of simulators. All the developer institutes use their own simulators for design consultancy purposes, eight of them also use simulators for scientific research and five among this eight also for training purposes. On the other hand, the two simulator users mainly use simulators for design/consultancy purposes, with only one of them using simulators also for scientific research.
All replying institutes develop or use simulators based on 6DOF mathematical models. Eleven institutes deal with full mission bridge simulators, while one deals with a part task simulator, composed of a reduced set of nautical instruments and visualization devices. One of the institutes only deals with inland navigation simulations, while the others are mainly focused on confined, coastal or open water simulations.

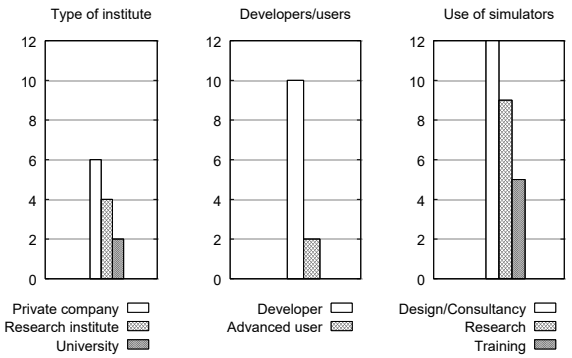

Figure 1. General information.

4 CURRENT

Current fields are present in almost all the environments where a ship operates, due to different physical phenomena. At open sea, surface oceanic currents are induced principally by wind and Coriolis effects. Near the coast, on the other hand, currents are mainly induced by the tidal excursion and by river outlets, due to both the river discharge and the associated density flow. More locally, currents can also be originated by the effects of man-made constructions like locks, weirs and harbours. Examples of such effects are discharges due to lock openings and tidal induced currents at harbour entrances. Due to the ubiquitous presence of current and to the relevant effect it has on the manoeuvring behaviour of ships, it is a very significant parameter to be modelled in order to improve the realism of simulations.

4.1 CURRENT FIELD REPRESENTATION

The questions concerning current field representation investigate how the current field and its space and time variability are modelled in simulators.
Current is represented as a 2D **vector** of horizontal speed by most of the institutes who participated to the survey. Only two institutes out of twelve use a more advanced 3D vector representation of current which includes a vertical speed component.
A **spatial variation** of the current field is modelled by most of the survey participants: only one does not foresee the possibility to deal with a variable current field in the **horizontal** plane. Among the institutes that deal with horizontal variations of the current field, ten implement the possibility of variable grid size, while the remaining one can only manage a fixed grid size on the whole domain. Concerning the interpolation of gridded current field values in the horizontal direction, seven repliers use linear interpolation, one uses upwind interpolation and three use proprietary algorithms which were not disclosed.
The horizontal resolution of the current fields is dependent on several different factors, like the type of application or the resolution of the numerical models providing the results (when used). According to the received replies the horizontal resolution for the current field used in simulators is on average between 20m and 100m. As notable exceptions, one of the replying institutes can go as low as a couple of meters in coastal areas and as high as 500m in offshore areas, while another institute uses a default resolution of less than one meter.
The **vertical variation** of current fields is completely neglected by six repliers. Among the remaining six institutes, four consider such variation in the pre-processing phase, by calculating a depth averaged current field and using this 2D field as the input for the simulator. In these cases, the depth average can be performed based either on the water depth or on the vessel's draft. The depth averaging process can be based on a simple average of the current velocity or on an average of the velocity squared, which leads to more significant averaged values from the point of view of the forces and moments generated by current. The remaining two institutes use a fully 3D current field as a direct input to simulators. One of these two institutes actually implements a depth-averaging procedure in real time during the simulation. For each time step, a draft averaged current velocity is calculated for each of the 2D longitudinal strips in which the ship is discretized. The draft averaging is based on the velocity squared. The last institute discretizes the ship by means of a voxel approach, with a small number of depth layers (usually 3). The current velocity acting on each voxel is calculated through an interpolation of the input 3D current field based on a proprietary algorithm.
Among all six institutes which consider vertical variations of the current field, either in the form of depth averaged or fully 3D current fields, two use an absolute vertical coordinate system, while four can choose between an absolute system and a relative coordinate system based on the local and temporal water depth.

Concerning **time variation** of the current field, eight replying institutes use this feature, one institute does not use the feature even if it is available and three institutes do not provide this functionality. The time intervals for current field updates range between less than a second and a couple of hours. In the last case, a sine function is fitted to the current field values available at the update times. Five institutes adopt linear interpolation in time between the input current fields, two use not disclosed proprietary interpolation algorithms and one does not interpolate.

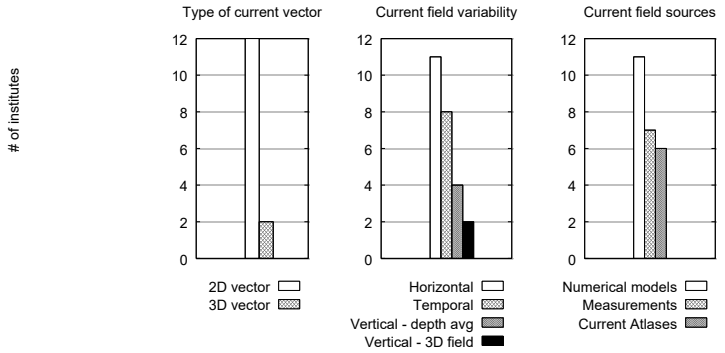

Figure 2. Current field representation.

4.2 SOURCE AND FORMAT OF CURRENT INPUTS

The next sub-section of the questionnaire investigates the **sources** of current field data and the input file formats. Eleven institutes out of twelve have the possibility to get current fields data from dedicated simulations performed with hydraulic software. Only one institute does not foresee this option, while for another one it is the only possible one. Different numerical models are used by different institutes, usually depending on in-house availability or client requests. Seven institutes can directly use current field data coming from measurements, and six can use current atlases and databases. However, at least two institutes pointed out that current measurements, while not being a direct input for the simulator, have a crucial role in the validation and calibration of numerical results.

Concerning the **format** of input files for current fields, it is strictly dependent on the simulator software. The picture coming out from the survey is that there is no recognized standard: proprietary file formats, simple ASCII files, xml files and MATLAB files are some of the possibilities according to the received answers. Most institutes write converters to convert current fields in arbitrary formats to the format which their simulator expects. Two of the replying institutes are currently investigating the possibility to adopt netCDF as an exchange file format. NetCDF is a binary format commonly used in atmospheric and oceanographic simulations to store large amounts of array-oriented data in an organized and self-describing way.

4.3 CURRENT INDUCED FORCES AND MOMENTS

The questionnaire focuses then on how current fields are used to calculate hydrodynamic forces and moments acting on the ship. First of all, the number of **degrees of freedom** which the current effects are accounted for is investigated. Two of the replying institutes consider current effects only in 2DOF: surge and sway. Six institutes consider the current effects in 3DOF, taking also into account yaw. Two institutes consider the effects in 4DOF, adding roll to the picture. Finally, two institutes considers current effects in all 6DOF. One of these two institutes specifies that, due to the modelling of current as a 2D vector (no vertical speed component), the current effects in heave and pitch are due to current induced squat motions.

The most common way to calculate current induced forces and moments, adopted by ten of the replying institutes, is to calculate the mean current speeds and accelerations acting on the vessel in each of the considered DOF. When a horizontal variation of the current field is considered, the mean current speeds are calculated as an average of the sectional current speeds which are interpolated in real time at different positions along the ship length. In the reply where the vertical variation of current is also taken into account, the sectional speeds are in turn obtained by means of a draft averaging procedure for each 2D strip (see previous paragraph). The mean current speed components acting on the hull are combined with the vessel's own speed components to obtain relative speed through water components, which are fed into the manoeuvring model. The current effects on the hull are therefore accounted for by using relative speed components to calculate the hydrodynamic forces and moments. One institute adopts a different approach: the ship is discretized in 20 sections, and current induced forces and moments are calculated for each section using a sectional drag coefficient, which is assumed to be constant along the hull. The contribution of the different sections is integrated along the ship length to produce the total current induced force and moment. Finally, the institute which implements fully 3D current fields models the hull through a voxel approach and calculates current induced pressures acting on each voxel based on Bernoulli equation. The voxel pressures are then integrated to provide current induced forces and moments.

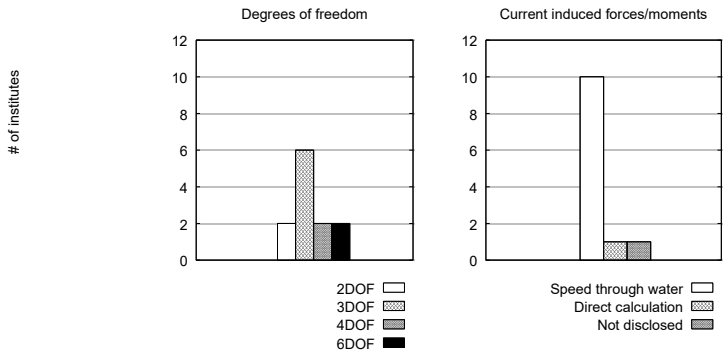

Figure 3. Current induced forces and moments.

4.4 ADDITIONAL FEATURES

Additional current features investigated in the questionnaire are the effects of density stratified fluids and the influence of the ship's presence on the current field in confined water.

Concerning the effects of **stratified fluids**, eleven of the replying institutes do not consider them, while one points out that such effects are taken into account by the hydraulic models which provide the current field input.

Concerning the effects of the **ship on** the **current** field in confined water, only two institutes replied that their simulators are capable of accounting for such an effect. In one case, an additional speed is added to the current speed to represent the speed increase under the hull of the ship due to Venturi effects. Only the longitudinal component of the current velocity is considered in the process. In the other case, the way this effect is accounted for is not disclosed. Among the ten institutes which do not include the effects of the ship on the current field in confined water, seven describe such an effect as highly desirable feature.

5 WAVES

Among the different types of gravity waves occurring on the oceans, wind generated waves are the ones which have the highest impact on ships. In order to be generated, wind waves need two factors: a forcing wind field and a sufficiently large water extension, called fetch, over which the wind can blow. Wind waves are in fact generated locally as very short ripples and can evolve into long waves along the fetch due to the wind which keeps transferring energy to the generated waves. When analysing a local wave climate, a distinction is usually made between the wind sea, which refers to waves generated in place by the local wind field, and swell, which refers to waves generated far away which have propagated to the location of interest.

Wave effects are generally not present in inland waterways, rivers or harbours. When dealing with simulations in these environments, wave effects can usually be neglected. An important exception to this consideration needs to be raised when the conditions occur for internal wave agitation phenomena. When an enclosed basin has reflective boundaries and an open inlet, the external sea waves can penetrate in the basin and keep evolving inside it for a long time due to repeated reflections on the boundaries. The magnitude of this physical process is strongly dependent on both the precise harbour geometry and the detailed characteristics of forcing waves. In certain conditions, the effects of internal wave agitation can be relevant for the ship behaviour.

Wave effects on a ship can be crudely split into two: second order wave effects, which induce mean drift forces acting on time scales comparable to the ones characterizing the manoeuvring dynamics, and first order wave effects, which induce oscillatory motions at higher frequencies. This distinction is at the base of the two time scales approach to the modelling of ship manoeuvring behaviour in waves. According to this approach, the wave induced drift loads influence the manoeuvrability behaviour, and are therefore of major relevance for a ship manoeuvring simulator; the oscillatory motions, on the other hand, are considered independent and are optionally included in simulators mainly to improve realism. In this case, wave effects can be dealt with in the frequency domain resorting to wave spectra and response amplitude operators (RAOs).

A different approach to the problem is based on a unified description of the hydrodynamic problem. This requires a more elaborated mathematical model, where wave effects need to be accounted for in the time domain.

5.1 WAVE FIELD REPRESENTATION

The next section of the questionnaire investigates the description of waves in ship manoeuvring simulators. All replying institutes apart from two include the effect of waves. One of the institutes neglecting waves deals only with inland navigation while the another one deals mainly with confined water and inland navigation. The majority of institutes which include wave effects, nine, model waves in the form of wave spectra. Only one institute adopts a different approach, implementing an internal wave model based on wind inputs and a simplified fetch based formulation. Among the nine institutes which adopt a spectral representation, all can work with uni-directional, frequency dependent wave spectra, and six of them can also work with directional wave spectra. The institute adopting an internal simplified wave model can model different wave systems by setting up different input winds coming from different directions and with different fetches.

Six of the nine institutes dealing with wave spectra take into account a **spatial variability** of such quantity. The **temporal variability** of wave spectra, on the other hand, is neglected by almost all repliers. This can be ascribed to the fact that the time scales of significant changes in wave spectra, usually between 30 minutes and a few hours, are longer than the common duration of a real time simulation. Therefore, the wave climate can be considered as steady during real time simulations. One institute does not disclose information concerning spatial or temporal variations of wave spectra. Among the six institutes

implementing a spatial variability of the wave spectra, three do not interpolate wave data in space, one performs linear interpolation of the wave spectra and two perform linear interpolation of integral parameters like the significant wave height and mean wave direction, reconstructing the directional spectrum based on theoretical spectral formulations and directional spreading functions.
Five of the replying institutes can use the results of wave agitation models (Bousinnesq, mild-slope, …) for describing the wave climate in restricted waters.

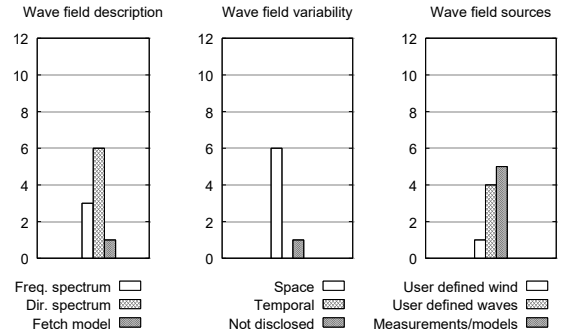

Figure 4. Wave field description.

5.2 SOURCE AND FORMAT OF WAVE INPUTS

Concerning the source of wave data to be used in simulations, three main options were outlined from the received answers: wave measurements, numerical wave models and user defined wave parameters. Five institutes rely mainly on user defined parameters. One of these institutes is the one implementing a simplified fetch based wave model: in this case, the user defined parameters are wind speed, direction and fetch length. For the other four institutes relying on user defined parameters, these are classic integral wave parameters such as significant wave height, mean wave direction and wave period. Such parameters are converted into a spectral representation by the use of theoretical wave spectrums (e.g. JONSWAP, Bretschneider, …) and directional spreading functions (e.g. cos2, cos-2s[1], …).
The remaining five institutes can take wave input data either from wave buoy measurements or from the results of wave models calibrated with measured data coming from buoys or satellites. In most cases, only integral data are obtained from wave models or buoys, and theoretical spectra are fitted to the input wave data. In at least one case, a bi-modal spectrum approach is used, which distinguishes between wind sea and swell. A JONSWAP spectrum describes the wind sea, coupled with a cos-2s spreading function, while the swell is modelled through a uni-directional JONSWAP spectrum (larger peakedness gamma factor) or through a regular wave.

[1] Widely used distribution where the s parameter accounts for the spreading of wave energy around a mean wave direction.

No general indications about common formats for input wave data were found from the received answers.

5.3 WAVE INDUCED FORCES AND MOMENTS

Among the ten institutes which implement waves in simulations, nine consider the wave induced effects on the ship in all 6 **degrees of freedom**, while one only considers the effects in 4 DOF: surge, sway, roll and pitch. Concerning the **wave effects** took into consideration, all ten institutes consider 1st order wave induced oscillatory motions as well as 2nd order mean wave drift forces in the horizontal plane. In one case, first order motions are calculated in 3 DOF (roll, pitch and heave) while second order drift forces and moments are considered in the remaining 3 DOF (surge, sway and yaw). Five institutes also consider time-varying 2nd order wave forces (*slowly-varying*) in the horizontal plane.
Nine institutes have the option to use **Response Amplitude Operators** (RAOs) to calculate oscillatory ship motions in the frequency domain. Frequency domain motions are usually transformed in the time domain by means of Fourier transforms. Two of these nine institutes have the alternative possibility to directly calculate **wave exciting forces and radiation forces** in the time domain and to solve the equations of motion for first order oscillatory motions in real time. This approach allows to consider non-linear Froude-Krylov forces and to achieve a tighter integration between the manoeuvring and seakeeping mathematical models. One of the institutes does not have the option to use RAOs due to wave modelling approach: this is the institute which models waves through an internal fetch based wave model (see previous paragraph), and therefore does not consider wave spectra. In this case, wave forces and moments are calculated only by an integration of non-linear Froude-Krylov forces calculated on the ship hull, which is discretized by means of a voxel approach. None of the replying institutes resorts to an external physical engine for the calculation of wave induced forces and moments.
Seven of the ten institutes which implement waves describe a direct **correlation between the wave pattern used in the mathematical model and the one used in the visualization part.** As for the three exceptions, in one case the match between the two wave patterns is not exact: the same integral parameters (significant wave height, mean wave direction and wave period) are used, but the directional spreading for the visualization part is calculated independently from the one used in the mathematical model. One institute distinguishes between swell and wind sea: for swell there is a direct correlation between the visuals and the mathematical model, while for wind sea the two representations are independent. In the mathematical model wind sea is represented as a spectrum, while in the visualization part it is modelled through an external visualization engine based on the local

wind speed. Finally, one institute reports no direct correlation between the two wave patterns.

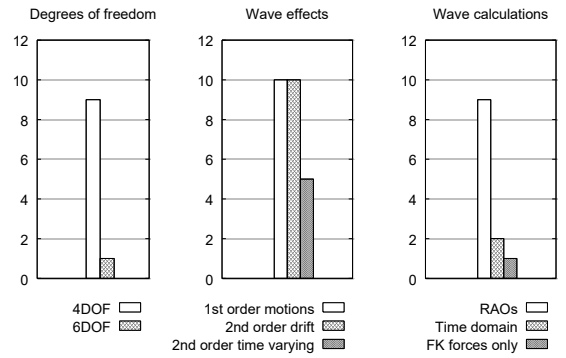

Figure 5. Wave induced forces and moments.

5.4 CURRENT-WAVE INTERACTION

The only additional wave modelling feature investigated in the questionnaire concerns the interaction between current and waves. Three institutes reply that this effect is taken into account in the calculation of wave induced motions. One of them specifies that this is done through the calculation of a wave drift damping which takes into account the influence of waves on drift forces. Another institute points out that the effect of current on the wave field is accounted for in the numerical wave models providing wave data input to the simulator. The last institute does not provide additional details about how this feature is implemented. One institute does not disclose if this feature is implemented or not.

6 WIND

As for current, a ship can be subject to wind in all its operating environments. Wind acts on the upper works of a ship, mainly originating a force in the horizontal plane and a yawing moment. Due to the vertical distance between the point of application of the wind induced force and the point of application of the resisting hydrodynamic force, a heeling moment is also originated. The resulting heeling angle, which can be large, changes the geometry of the hull, and therefore also the manoeuvring behaviour of the ship. The effects of wind on the ship manoeuvring behaviour can be relevant, especially for ships with tall cargo and/or superstructures, like container vessels, cruise ships and car carriers.

6.1 WIND FIELD REPRESENTATION

Concerning the representation of wind fields in simulators, first of all the questionnaire focuses on **turbulent fluctuations** of wind speed and direction in time. Two of the replying institutes assume a constant wind speed, neglecting turbulence fluctuations. Two institutes only consider fluctuations in the wind speed, while all the other eight institutes model turbulent fluctuations of both wind speed and direction.

The questionnaire then investigates the variability of the mean wind fields in space and time. Three institutes do not take the **horizontal variability** of mean wind fields into account, and model a constant mean wind field in space. This is independent from the modelling of turbulent fluctuations described above: despite considering a uniform mean wind field over the simulation domain, two of the institutes which do not model a spatial variability still take into account turbulent wind fluctuations. The other nine institutes take spatial variability of wind fields into consideration. One of them only does so based on the sheltering effects induced by terrain elevation, buildings or other vessels. No additional details concerning typical grid sizes or spatial interpolation techniques for wind fields were made available through the received answers.
Concerning the **vertical variation** of wind fields, only two institutes take it into account, by implementing a vertical wind distribution which affects only the wind speed magnitude. A vertical variation of the wind field is accounted for also by another institute, but only with respect to the effects of wind sheltering by land features or other vessels.
Six institutes out of twelve can model **time variations** of the mean wind field along a simulation. Ten of the replying institutes, on the other hand, foresee the possibility for the simulator operator to adapt the wind fields in real time.

6.2 SOURCE AND FORMAT OF WIND INPUTS

A clear picture about the source of input wind fields used in simulators could not be obtained from the received replies. When constant wind speed and direction are assumed over the simulation domain, their values are usually selected by the simulator operator based on the desired environmental conditions and on experience about the local wind climate of the area to be simulated. On the other hand, when a spatial variability of the mean wind field is foreseen, the spatial distribution is most likely the result of a numerical model. At least two of the replying institutes have the possibility to use wind fields calculated by CFD codes and converted to 2D fields as the input for simulations. The details for such a conversion are not disclosed.
No indications can be derived from the received answers about specific file formats used for providing input wind fields to simulators.

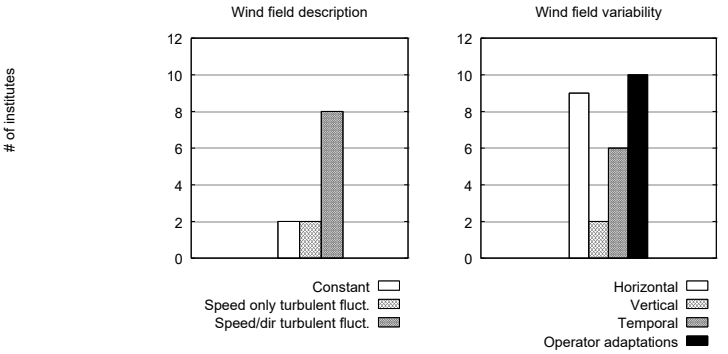

Figure 6. Wind field description.

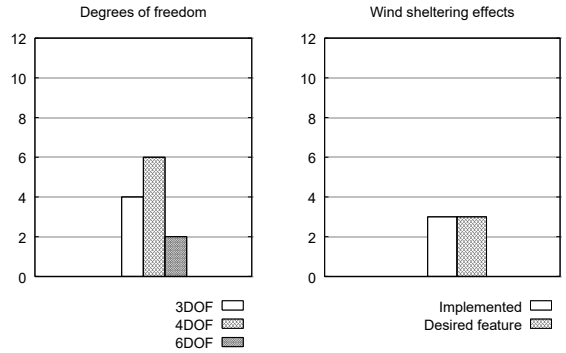

Figure 7. Wind induced forces and moments.

6.3 WIND INDUCED FORCES AND MOMENTS

Six of the replying institutes model wind induced forces and moments in 4 **degrees of freedom**: surge, sway, yaw and roll (heel). Four institutes model wind effects in the horizontal 3 DOF, while two institutes model the effects in all 6 DOF.

Nine institutes take into account the **horizontal variation** of wind speed along the ship length in the calculation of wind induced forces and moments. In at least two cases this is done by interpolating the input wind field at a number of points along the ship length and then calculating an average wind vector. The relative wind vector (taking into account the ship's motion) is then combined with wind coefficients to provide aerodynamic forces and moments. In another case, the ship superstructure is modelled through a voxel approach, and the force exerted by the wind field on each voxel is integrated over the whole superstructure. No additional information was obtained from the remaining three institutes. Two of the replying institutes also take into account the **vertical variability** of the input wind field in the calculation of wind induced forces and moments.

Only three institutes consider the **sheltering effect** of the ship on the input wind field. In one case, the input wind field is modified inside a box which travels with the ship and is reshaped according to the incident wind speed and direction. No information is disclosed by the other two institutes. Among the institutes which do not consider the sheltering effect of the ship on the input wind field, at least three point out that this is a highly desired feature and a topic for further developments.

7 WATER LEVELS

Ocean water levels change due to tidal effects. The magnitude of tidal excursion depends on the geographic location, and is usually higher near to the coast line. Water levels can also change in man-made hydraulic structures such as locks. Due to the large periods of water level changes, a ship does not experience significant forces due to such changes. Therefore, in sufficiently deep water, water level changes have no effect on the manoeuvring behaviour of a ship. However, when the water depth is comparable with the ship's draft, the ship's manoeuvring behaviour is significantly influenced by the under keel clearance (UKC), which is defined as the ratio between the vertical distance from the keel line to the sea bottom and the draft of the vessel. Due to this, the effects of changing water levels need to be taken into account in order to achieve realistic manoeuvring simulations in shallow water.

7.1 WATER LEVELS REPRESENTATION

Regarding the representation of water levels in simulations, two institutes only considers a spatial and temporal constant value for the whole simulation. Nine institutes consider a temporal variation of the water level along the simulation, while five consider spatial variations of the water level over the simulation domain. Four of the institutes which consider a temporal variation also consider spatial variations, while one considers spatial variations only. Four institutes reflect the spatial variations of water levels in the visuals, for example in the evident case of two sides of a lock.

7.2 SOURCE AND FORMAT OF WATER LEVEL INPUTS

Similarly to what happened for wind input, no clear picture can be drawn concerning the source of water levels input. Usually, this information either comes from the same numerical models which provide current field inputs or is set up by simulator operators based on their experience.

Apart from one institute resorting to netCDF (see also 4.2) as the input file format for water levels, no other

information can be derived from the received answers concerning this topic as well.

7.3 ROLE OF WATER LEVELS IN MATHEMATICAL MODEL

The final section of the questionnaire investigates how water levels are accounted for in the mathematical models of simulators. Nine of the replying institutes model the effects of water levels by using different mathematical models for predefined under keel clearance (UKC) values. Usually, the water level at the ship position is interpolated from the input water levels, if needed, and a UKC value is calculated based on the ship's draft. The forces acting on the ship are then calculated according to the mathematical model corresponding to the calculated UKC. One institute adopts a different approach, based on a single mathematical model and direct calculations of corrections to the hydrodynamic forces in confined water. The remaining two institutes did not specify how water levels are taken into account.

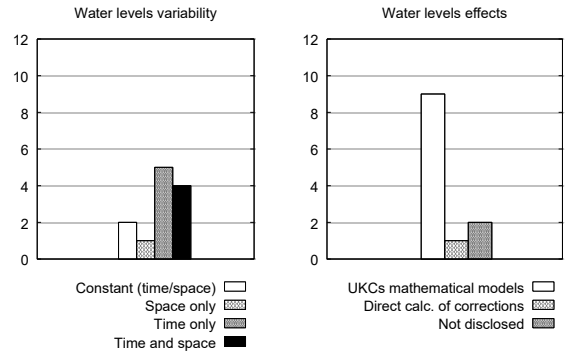

Figure 8. Water levels description and effects.

8 CLOSING REMARKS

Ship manoeuvring simulations have proven to be of great utility for a wide list of applications, which range from the design of port infrastructures to the training of maritime professionals. The usefulness of simulations is tightly linked with the degree of accuracy and realism which can be attained. Current, wind, waves and water levels can all have a large impact on the behaviour of ships. Therefore, the realism of simulations does not only depend on the accuracy of the mathematical models which describe the manoeuvring behaviour of ships, but also, to a great extent, on how the hydro/meteo conditions and their effects on ships are modelled. While mathematical models for the manoeuvring behaviour of ships have been and still are largely discussed in scientific literature, the modelling of hydro/meteo conditions lacks a publicly available reference literature. With the aim to start filling this gap, a survey on the state of the art of hydro/meteo conditions modelling in ship manoeuvring simulators was developed by the authors. A questionnaire focusing on current, waves, wind and water levels was sent to approximately 30 parties, selected between simulators developers and advanced users. Among the recipients, only 12 institutes replied to the survey in time for their answers to be included in this work. The reluctance of a large part of the contacted parties to provide answers on the topic reveals that a description of the implementation of hydro/meteo conditions in a simulator is not considered as an objectively technical and scientific information. While this can be partially understood in the logic of commercial competition, it also prevents the crucial exchange of information needed to push forward the boundaries of simulation accuracy. The results of the survey published in this paper outline some common approaches as well as some consistent differences in how hydro/meteo conditions and their effects on ship behaviour are modelled by different institutes. In the hope of the authors, the present work represents a first step towards a more scientific approach to the modelling of hydro/meteo conditions in ship manoeuvring simulators, and also a possible starting point for collaborations aimed at the common goal to make ship manoeuvring simulations ever more realistic.

9 ACKNOWLEDGEMENTS

The present work is performed in the frame of project WL_2017_06 (Scientific support for the implementation of seakeeping in the ship manoeuvring simulators), granted to Ghent University by Flanders Hydraulics Research, Antwerp (Department of Mobility and Public Works, Flemish Government, Belgium).

The authors wish to thank all institutes who participated to the questionnaire.

10 AUTHORS BIOGRAPHY

Luca Donatini, naval architect, is a PhD student at Ghent University. He is currently working on a project aimed at improving the modelling of hydro/meteo effects in the ship manoeuvring simulator of Flanders Hydraulic Research. His previous experiences encompass seakeeping studies to allow inland vessels on a Belgian sea trajectory and the inclusion of hydro/meteo effects in an open source mooring dynamics code. He also has an extensive experience in atmospheric and spectral wave modelling from global to regional scales.

Marc Vantorre, naval architect, is emeritus professor of marine hydrodynamics and former head of the Maritime Technology Division at Ghent University, Belgium. His research focuses on ship behaviour in shallow and confined waters, mainly in close co-operation with Flanders Hydraulics Research in Antwerp. He is former member of PIANC Working Groups and of the ITTC Manoeuvring Committee..

Jeroen Verwilligen holds the current position of senior expert in nautical research at Flanders Hydraulics Research. He is experienced with simulation studies, nautical accessibility studies and full scale measurements.

He is member of the PIANC MarCom WG 171 on Ship Handling Simulation Dedicated to Channel and Harbour Design.

Guillaume Delefortrie, PhD, naval architect, is expert nautical researcher at Flanders Hydraulics Research and visiting professor at Ghent University. He is in charge of the research in the Towing Tank for Manoeuvres in Confined Water and the development of mathematical models based on model tests. He has been secretary of the 27th and 28th ITTC Manoeuvring Committee and is chairman of the 29th ITTC Manoeuvring Committee.

SHALLOW WATER SURGE RESISTANCE IDENTIFICATION FOR INLAND VESSELS

Arne Eggers,
Mechanical Engineering Technology Cluster TC, Campus Group T Leuven, KU Leuven, Belgium

Gerben Peeters,
SB PhD fellow at FWO, Faculty of Engineering Technology, KU Leuven, Belgium

Peter Slaets and **Maarten Vanierschot**, Mechanical Engineering Technology Cluster TC, Campus Group T Leuven, KU Leuven, Belgium

SHALLOW WATER SURGE RESISTANCE IDENTIFICATION FOR INLAND VESSELS

Arne Eggers Mechanical Engineering Technology Cluster TC, Campus Group T Leuven, KU Leuven, Belgium
Gerben Peeters, SB PhD fellow at FWO, Faculty of Engineering Technology, KU Leuven, Belgium
Peter Slaets and **Maarten Vanierschot,** Mechanical Engineering Technology Cluster TC, Campus Group T Leuven, KU Leuven, Belgium

SUMMARY

Shifting from classical means of transportation, such as road traffic, towards inland shipping and railway transport is a possible answer to the frequent traffic jams and the high level of pollution on Belgian and European roads. Inland shipping has a comparably low environmental impact, in terms of noise and energy consumption, and might become more economical if the vessels are operating under a high level of autonomy. Model based autonomous sailing algorithms can benefit from the knowledge of the vessel's hydrodynamic behavior. In comparison to seagoing vessels, little to none research has been conducted on how to identify inland ships using computation fluid dynamics (CFD), particularly in shallow water. Hence, this research developed a CFD model to predict the resistance forces acting on inland vessels in shallow water. To proof this methodology, a benchmark vessel for seagoing ships, the KVLCC2 hull, has been examined.

NOMENCLATURE

B	Width of the hull (m)
C_B	Block coefficient (-)
Co	Courant Number (-)
Co_{FS}	Courant Number in the free surface (-)
t	Time (s)
T	Draft of the hull (m)
T_{ij}	Viscous stress (Pa)
L_{pp}	Length between perpendiculars of the Hull (m)
g_i	Gravitational constant i=1-3 (m/s^2)
h	Height field (m)
$\bar{p}'$	Time averaged gravity corrected pressure (N/m^2)
$\bar{u}_i$	Time averaged velocity i = 1-3 (m/s)
$\overline{u_i u_j}$	Reynolds stress tensor i,j = 1-3 (Pa)
u_{main}	Ship velocity (m/s)
u^+	Non-dimensional velocity (-)
U	Uncertainty of CFD values (N)
UKC	Under keel clearance (%)
r	Grid refinement ratio (-)
R	Grid convergence ratio (-)
y^+	Non-dimensional wall distance (-)
x_i	Spatial coordinate i = 1-3 (m)
X	Drag Force (N)
ϵ	Difference between CFD and EFD Values (%)
ϵ_{ij}	Difference between grid i and grid j Values (%)
ΔX	Difference in drag force between grids (N)
λ	Scaling factor (-)
μ	Viscosity of mixture (Pa s)
μ_{air}	Viscosity of air (Pa s)
μ_{water}	Viscosity of water (Pa s)
ρ	Density of mixture (kg/m^3)
ρ_{air}	Density of air (kg/m^3)
ρ_{water}	Density of water (kg/m^3)
ϕ	VoF scalar (-)

1 INTRODUCTION

The growing demand for mobility and transportation in the European Union and the world, leads to the development of new concepts and ideas in the transportation sector. As the massive personal and freight transport on roads introduces traffic jams, accidents and pollution, a shift towards a more balanced transportation concept, including railway transport and inland shipping, is natural. As its energy consumption per km/ton is roughly 17% of that of road and 50% of that of railway transport, the environmental impact of inland shipping is considered to be small (European Commission, 2018). Therefore, it is an important part of the European transportation network. However, due to the relatively high need of labor and the tough competition on the transportation market, it is at the moment mostly economical by deploying huge ships with high loading capacities. These larger barges are in many cases only suited for entering deeper channel systems. The more shallow or confined regions, which are often apparent in northern Europe, need to be fed by smaller barges. To serve this need, the European Watertruck+ project aims to build medium and small sized vessels of the European Class (CEMT) type ranging from I to IV ("Watertruck+," 2018). These vessels are applied in modular designed convoys, consisting of self-propelled, non-propelled and push ships, which increases the economic and technical flexibility. A possibility to further improve the economic competitiveness of the CEMT barges is to make them autonomous or semi-autonomous, thus decreasing the need of manual labor. Identification of the hydrodynamic characteristics for these vessels is a necessity to improve modern control algorithms for autonomous sailing ships.
The state-of-the-art measures to identify ship characteristics may be separated into three groups. Firstly, a scale model may be investigated by measuring the forces acting on it in a towing tank by applying experimental fluid dynamic (EFD) (G. Delefortrie, K. Eloot, & F. Mostaert, 2013). EFD applications suffer from the relatively high costs of building a scale model or a real size ship and the

need of a towing tank. This makes it difficult to apply EFD in the early design stage of a vessel to optimize its shape. However, EFD values based on scale models may be scaled to the real size vessel and are known to be very reliable and accurate. Hence, they are often applied as validation proving the methodology of other cheaper methods right. Secondly, regression formulae, which combine different data sets of comparable cases to calculate the best fitting coefficient, may be used (Hans and Zhao, 2017). The method is computationally cheap and produces fast results. Nevertheless, if the available data for the investigated hull is limited or the influence of geometrical changes should be assessed this method becomes difficult to apply reasonably. Thirdly, CFD may be applied to solve the governing physical equations numerically. As such, the geometry is represented by a numerical grid which is able to capture the relevant features. Thus, influences of geometrical changes and other parameters may be predicted. The generated data can also be used to optimize the hydrodynamic shape of the current inland vessels (Rotteveel, Hekkenberg, & van der Ploeg, 2017). However, CFD methodologies are often complex combinations of different state-of-the-art models, performing differently depending on the actual physics involved and the exact set up. Hence, applied CFD has to be validated by data usually based on EFD results where the validation case has to feature the same physical phenomena as the actual identification case.

Ship hulls may be mainly divided into two field of application, inland and seagoing vessels. The latter have been subject of EFD and CFD studies frequently (Guo & Steen, 2011)(SIMMAN, 2014). Benchmarks hulls such as the KVLCC2 or DTC hull have been investigated numerically in open water conducting manoeuvres, such as zig-zag or turning circles (Shigunov, el Moctar, Papanikolaou, Potthoff, & Liu, 2018), in shallow water (Toxopeus, 2013) and in waves (Guo & Steen, 2011). However, only little research has been conducted on the identification inland vessels in general and on the smaller CEMT I and II types, particularly (Rotteveel et al., 2017). This is especially true for shallow water simulations, although inland vessels are facing shallow and restricted water not only in harbors or during docking manoeuvres but most of the time in channels and rivers. Hence, methodologies which predict the flow around CEMT type vessels in open and shallow waters are a necessity to accelerate the optimization of future vessel generations and to enable the development of more automated and autonomous inland vessels.

To close this literature gap, this research developed a CFD based model to identify inland vessels in shallow water. The inland vessel is the CEMT I, which is a basic self-propelled barge of the CEMT type with a high block coefficient ($C_B = 0.95$). As there is little to no EFD data on inland vessels available this research validates its methodology based on the KVLCC2 hull. As stated earlier, plenty of EFD and CFD data on this hull in various conditions are available. Additionally, the KVLCC2 hull features a rather high block coefficient ($C_B = 0.81$) which is close to the usual values of inland ships. However, the KVLCC2 hull is shaped more hydrodynamical, preventing flow detachment, which will most probably occur on the CEMT I's block shaped hull. This might give rise to transient behavior. Furthermore, the KVLCC2 hull is designed to bear an external propeller, while the CEMT I hull features an internal actuation. As it has no external actuation, CEMT I bare hull simulations are expected to show higher alignment with the in-operation flow fields of the vessel. The open source toolbox OpenFOAM (OpenCFD, 2018) solves the governing equations in the computational domain, which is discretized using a hexahedron dominant mesh generated with the open source mesh generation software snappyHexMesh. The turbulent fluctuations were modelled by the frequently applied k-omega SST turbulence model (Menter, 1994). As the wave pattern influences the hull's resistance force the free surface needs to be taken into account. Here, a Volume of Fluid (VoF) method (Hirt & Nichols, 1981) is applied. This paper continues with chapter 2 describing the applied methodology, chapter 3 discussing the results and chapter 4 draws a conclusion.

2 METHODOLOGY

2.1 FLOW MODELING

OpenFOAM solves the Reynolds averaged Navier-Stokes(RANS) equations:

$$\frac{\partial \bar{u}_i}{\partial x_i} = 0, \tag{1}$$

$$\frac{\partial \bar{u}_i}{\partial t} + \bar{u}_j \frac{\partial \bar{u}_i}{\partial x_j} = \frac{1}{\rho}\frac{\partial \bar{p}}{\partial x_i} + \frac{\partial}{\partial x_i}\left(\frac{1}{\rho}T_{ij} - \overline{u_\iota{}' u_j{}'}\right) + g_i. \tag{2}$$

Where $\bar{u}_i$ is the time averaged velocity, t is the time, x_i the spatial coordinate, $\bar{p}$ the time averaged pressure, T_{ij} the viscous stresses, $\overline{u_\iota{}' u_j{}'}$ the Reynolds stresses and g_i the gravitational constant. In the RANS equations the turbulent fluctuations are time averaged to reduce the computational costs. Therefore, the mean flow has to be modelled. This is done by applying the k-omega SST turbulence model, which combines the higher stability of the k-epsilon model with the better wall flow and separation prediction of the original k-omega model. The free surface is modelled by a VoF method which establishes a scalar function ϕ. This function indicates which phase is apparent in a fluid cell, where $\phi = 0$ indicates the presence of air, $\phi = 1$ of water and $0 < \phi < 1$ of the free surface between the two phases. The scalar function is transported passively with the predicted flow field:

$$\frac{\partial \phi}{\partial t} + \bar{u}_j \frac{\partial \phi}{\partial x_j} = 0. \tag{3}$$

Once the flow field and the phase distribution is known the scalar function ϕ may be applied to determine the local flow properties:

$$\rho = \phi\rho_{water} + (1-\phi)\rho_{air}, \tag{4}$$

$$\mu = \phi\mu_{water} + (1-\phi)\mu_{air}. \tag{5}$$

Where ρ is the mixture density, ρ_{water} the water density, ρ_{air} the air density, μ the mixture viscosity, μ_{water} the water viscosity and μ_{air} the air viscosity. The no slip wall boundary conditions in these simulations are handled by the law of the wall, formulated by Spalding in 1961 (Spalding, 1961). This approach computes the velocity in the first grid cell at the wall based on a law which fits experimental data for universal turbulent flows over the complete boundary layer ranging from $y^+ = 0$ to $y^+ = 300$:

$$y^+ = u^+ + 0.1108 \cdot \left(e^{0.4u^+} - 1 - 0.4u^+ - \frac{(0.4u^+)^2}{2!} - \frac{(0.4u^+)^3}{3!}\right). \quad (6)$$

Where u^+ is the non-dimensional velocity and y^+ the non-dimensional wall distance. In comparison to classical wall functions, this approach offers more flexibility and accuracy as also grid points within the viscous sublayer and the buffer layer can be handled and a higher resolution of the boundary layer automatically leads to a more grid independent solution. However, it still benefits from the advantages of wall functions, such as lower cell count and higher convergence rate in the wall boundary layers.

2.2 VESSELS

The methodology is validated by the frequently examined KVLCC2 hull, which combines a high block coefficient ($C_B = 0.81$) with publicly available EFD data for shallow and free water cases. In table 1, where L_{pp} is the length between perpendiculars, B the width, T the draft, C_B the block coefficient and λ the scaling factor, the characteristics of the different vessel are compared. The two hulls show similarities in all characteristics which leads to comparable Froude and Reynolds numbers at the same longitudinal velocities. Figure 1 shows the KVLCC2 and CEMT I hulls in side and top view. As the KVLCC2 hull is a seagoing tanker, its shape is optimized to minimize hydrodynamic resistance forces. Whereas, the primary design goal of the CEMT I is a maximum of payload while keeping the hull's production cost low. Therefore, the block coefficient of the CEMT I is higher and the hull shape features sharp corners which may introduce detachment.

Table 1. Vessel Characteristics

	CEMT I		KVLCC2	
	full size	scale model	full size	scale model
$L_{pp}\ (m)$	38.5	4.81	320	4.27
$B\ (m)$	5.05	0.63	58	0.77
$T\ (m)$	1.8	0.23	20.8	0.28
C_B	0.95	0.95	0.81	0.81
λ	1	8^{-1}	1	75^{-1}

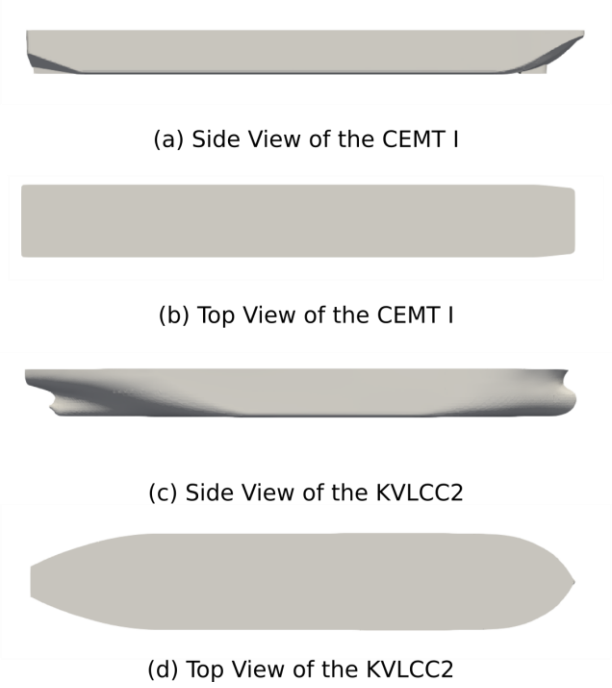

Figure 1. Investigated ship hulls

2.3 CASE SETUP

As no or only minimal transient behavior was observed in transient simulations, all cases converge towards a steady state, which was assumed to be reached if the fluctuations of the drag force drop under a tolerance value. This steady state was achieved in a stable and efficient way by local time stepping (LTS), allowing spatial variations of the time step, only limited by the maximum local Courant number, which is defined by the user for the single phase and the free surface areas differently. This approach allows to separate the time scales around the free surface from the rest of the domain (Jasak, Vukčević, & Christ, 2014). These methods have been applied to seagoing vessels, incorporating different modifications to the algorithm, and are known to be comparable to commercial software in terms of efficiency and robustness (Kim & Park, 2017). The maximum local Courant number was set to Co = 1000 during most of the computations, only reduced to Co = 1 to minimize fluctuations and inaccuracy when determining the final value, while the free surface Courant number was kept at $Co_{FS} = 1$ to assure convergence of the free surface flow. A second order upwind scheme handles the convective term for momentum and a van Leer limited TVD-Scheme the VoF scalar. The LTS scheme implemented in OpenFOAM applies a first order Euler discretization to the time derivatives, which is sufficient as transient behavior is not studied. The computational domain is set up around a body fixed coordinate system. The domain and the physical boundary conditions are depicted in figure 2, where u_{main} is the inlet velocity. Here, the wall velocities of the no slip walls, the hull and the bottom patch, are described. Based on these the velocities in the cells at the wall are set according to equation 6.

The pressure on all walls and the inlet is set by applying a body force corrected zero gradient boundary condition.

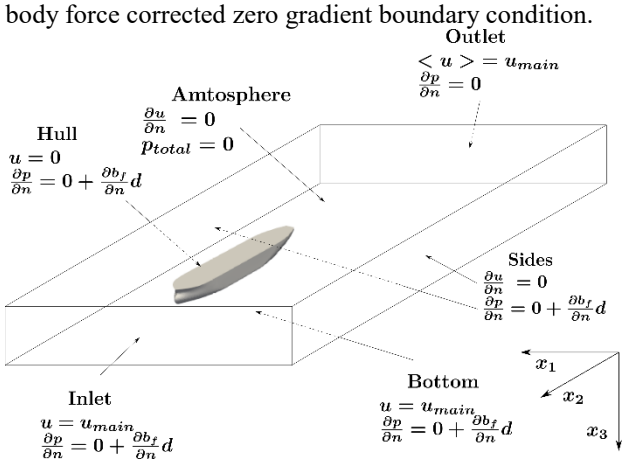

Figure 2. Case setup and boundary conditions

To increase the solver's convergence rate the outlet velocities are set to values which average to u_{main}, together with the imposed inlet velocity this assures conservation of mass for the water phase, over the whole domain. The shallow water setup is described in figure 3, the side walls are placed in sufficient distance to assume their influence neglectable. The bottom is placed based on the experimental data available for the KVLCC2 hull to generate shallow water conditions at 20% and 50% under keel clearance (UKC), while the investigated velocities are orientated at the allowed maximum in local Belgium channel systems ("VisuRIS - Kanaal Leuven-Dijle," 2018).

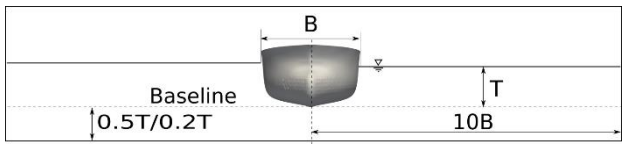

Figure 3. Geometrical shallow water setup

2.4 GRID STUDY

The hexahedra dominated computational meshes were generated by the open source software snappyHexMesh. The cells are clustered around the hull applying six refinement boxes, each of them decreasing the characteristic cell size by factor two. At the no slip boundary conditions, boundary layer cells have been added to resolve the physical boundary layer. An example for the KVLCC2 hull is shown in figure 4. The grid independence study has been conducted for the K50 test case, which is described in table 4, and the grid sizes are described in table 2.

Table 2. Grid characteristics

	coarse	medium	fine
number	3	2	1
cells x10^6	0.78	2.43	6.81

According to the International Towing Tank Conference's guideline the refinement ratio between the different grids in all spatial dimension was set onto a value close to $r = \sqrt{2}$ (ITTC, 2017). The differences between the computations on the grids are shown in table 3. The grid convergence ratio can be calculated:

$$\mathrm{R} = \frac{\epsilon_{1,2}}{\epsilon_{3,2}}. \quad (7)$$

Where R is the grid convergence ratio and ϵ_{ij} the error percentage between grid i and j. As depicted in figure 5, where X is the predicted drag force and ΔX is the difference between the computed drag forces on different grids, the grid convergence is oscillatory and the uncertainties may be estimated:

$$U = \frac{X_{max} - X_{min}}{2}. \quad (8)$$

Where U is the uncertainty and X_{max} and X_{min} the maximum and minimum drag forces predicted on different grids.

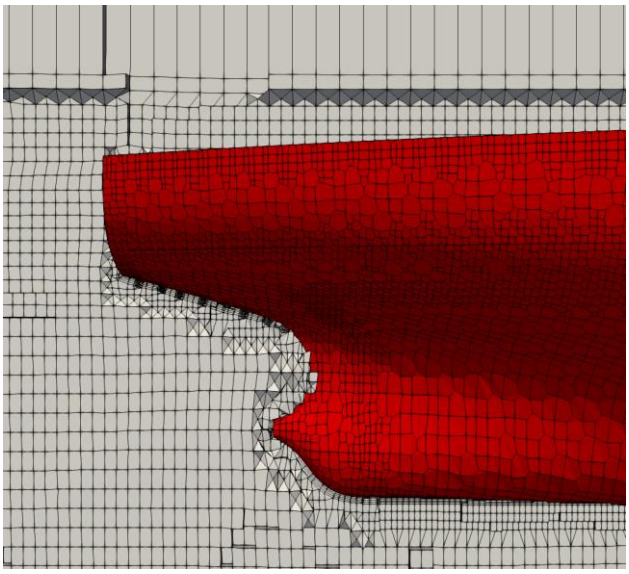

Figure 4. Computational Mesh around the stern of the KVLCC2

The EFD's uncertainty of 0.06N on a 68% confidence interval is in the same order of magnitude as the oscillation of the simulations on different numerical grids (G. Delefortrie et al., 2013). Hence, it may be seen as sufficiently small. The medium grid was selected for the following simulations as it (i) made simulations with reasonable computational costs possible and (ii) featured a low uncertainty based on the conducted grid study.

Table 3. Grid study

	3 to 2	2 to 1
r	1.46	1.41
$\Delta X\ (N)$	0.16	-0.14
$\epsilon(\%)$	5.2	-4.8

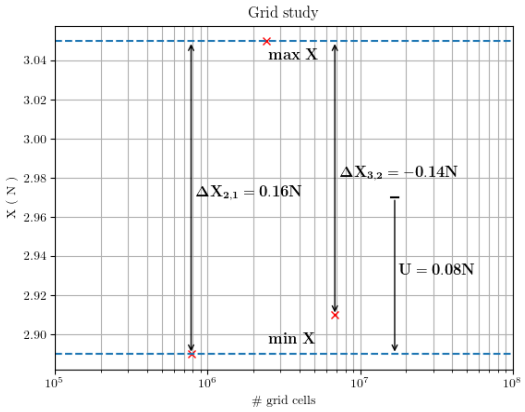

Figure 5. Oscillating grid convergence. Grid convergence Ratio R = -0.92

3 RESULTS

3.1 CFD EFD KVLCC2

Table 4. Test case characteristics, CFD results and error compared to EFD values

	u_{main}	UKC	hull	X (N)	ϵ(%)
K50	0.416	50%	KVLCC2	3.05	-1.4
K20	0.416	20%	KVLCC2	3.6	-0.55
C2.50	0.2	50%	CEMTI	1.31	-
C4.50	0.4	50%	CEMTI	3.96	-
C2.20	0.2	20%	CEMTI	1.7	-
C4.20	0.4	20%	CEMTI	4.4	-

Even though the hull was assumed to be fixed and no sinkage or trim was taken into account, the drag forces could be predicted with a maximum error of $\epsilon = -1.4\%$ for the relevant velocities. Furthermore, all simulations underestimate the drag which is reasonably as the actual sinkage and trim in EFD are increasing the drag force. The computed drag forces for the KVLCC2 and CEMT I hulls are listed in table 4. The values of the KVLCC2 hull are compared to EFD values to validate the methodology. In figure 6 the gravity corrected pressure fields around the KVLCC2 hull is depicted at 50% and 20% UKC. The gravity corrected pressure is defined as the static pressure without the gravity component:

$$\bar{p}' = \bar{p} - \rho g_i h. \tag{9}$$

Where $\bar{p}'$ is the time averaged gravity corrected pressure and h the height field. Removing the gravity component from the pressure field increases the visibility of effects occurring due to ship and wave dynamics as in hydrodynamic applications these are often small compared to gravity. Furthermore, the pressure iso-lines in figure 6 are computed using only the hexahedral cells, as the polygons in the free surface influence the pressure strongly. However, the influence on the wave pattern was found not to have a strong influence on the computed drag, as the results match experimental data. The area under the hull is reduced due to the shallowness of the set-up, introducing a higher resistance. Thus, the pressure at the bow is increased leading to a higher pressure drag. Furthermore, the smaller cross section forces higher velocities below the vessel, increasing the viscous drag component. Both of these effects amplify by lowering the UKC value.

3.2 CFD CEMT I

After validating the methodology on the KVLCC2 hull it could be used to predict the drag forces acting on the CEMT I at multiple velocities. As such, this data was applied to identify the coefficients of the second order single variable polynomial fit for the CEMT I hull:

$$X = X_u u_{main} + X_{uu} u_{main}^2. \tag{10}$$

Where X_U and X_{UU} are the linear and quadratic coefficient. Table 4 shows the drag forces on the CEMT I hull. Due to the same effects described for the KVLCC2 hull, the drag increases while reducing the UKC. Figure 6 compares the surface flow field for the CEMT I and the KVLCC2 hull. Due to the less hydrodynamic shape of the CEMT I hull the flow detaches at the stern creating a low pressure zone, increasing the pressure drag. This becomes visible as well in the comparison of the pressure in the symmetry plane. At the stern of the KVLLC2 hull only little detachment is occurring. Hence, the pressure remains high, while the CEMT I creates a low pressure wake over the full draft of the hull. This implies massive potential for improvement of the CEMT I's shape. However, other constraints such easy manufacturing and high pay load have to be taken into account. To assess the possibility of transient effects due to vortex shedding in the CEMT I's wake, transient simulation have been conducted for the C4.50 and C4.20 cases. Nevertheless, no or only minimal transient effects have been observed.
Figure 7 shows the CEMT I's polynomial fits for different UKCs and open water. These may be used to build control algorithms for the CEMT I.

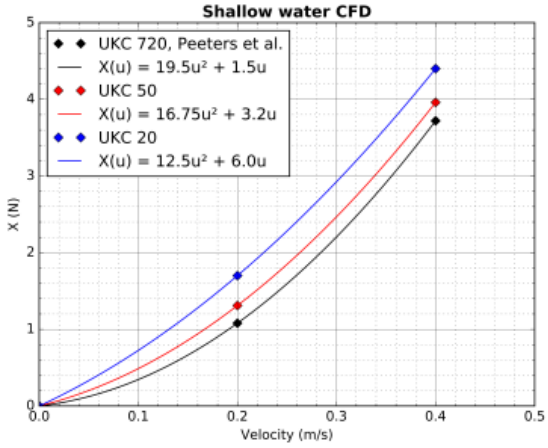

Figure 7. Polynomial fit for the drag forces of the CEMT I hull at different UKCs. UKC 720 values from (Peeters, Eggers, Boonen, Slaets, & Vanierschot, 2018)

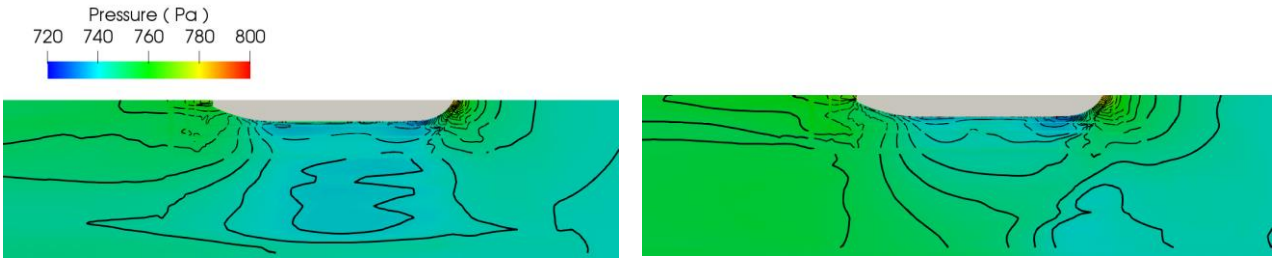

(a) Relative gravity corrected pressure around the KVLCC2 hull at 50% UKC (left), 20% UKC (right) and $u_{main} = 0.416m/s$

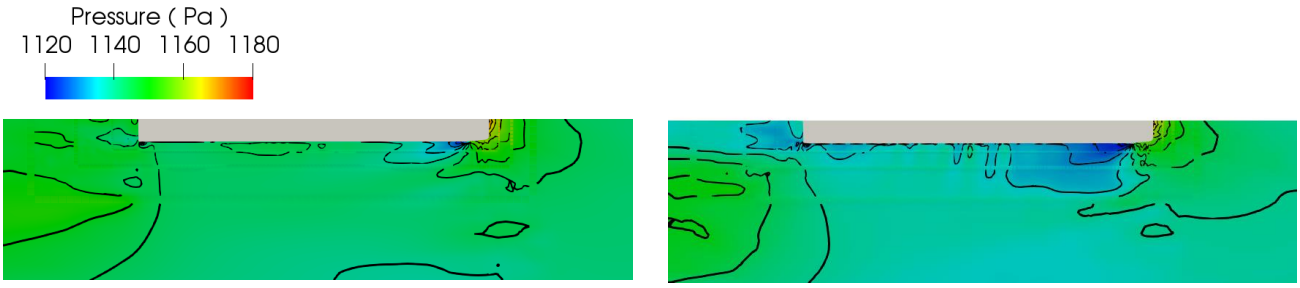

(b) Relative gravity corrected pressure around the CEMT I hull at 50% UKC (left), 20% UKC (right) and $u_{main} = 0.4m/s$

(c) Relative gravity corrected pressure around the KVLCC2 hull at 50% UKC and $u_{main} = 0.416m/s$

(d) Relative gravity corrected pressure around the KVLCC2 hull at 20% UKC and $u_{main} = 0.416m/s$

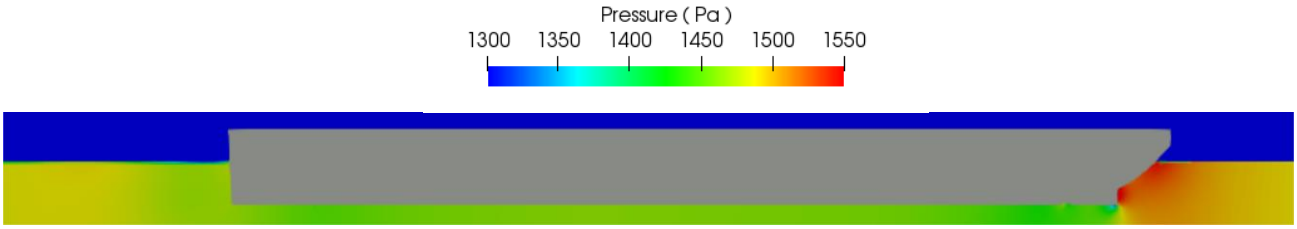

(e) Relative gravity corrected pressure around the CEMT I hull at 50% UKC and $u_{main} = 0.4m/s$

(f) Relative gravity corrected pressure around the CEMT I hull at 20% UKC and $u_{main} = 0.4m/s$

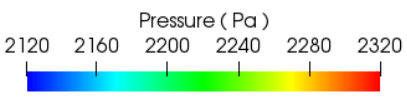

Figure 6. Comparison of relative gravity corrected pressure around the CEMT I and KVLCC2 hull

4 CONCLUSION

OpenFOAM's VoF solver in combination with the LTS scheme offers a robust and efficient tool to predict drag forces on ship hulls with high block coefficients in shallow water. The applied methodology was proven to be working on the KVLCC2 benchmark case. Furthermore, the CEMT I hull got investigated and the derived drag forces were used to identify the coefficients of the second order single variable polynomial fit for the CEMT I hull. This can be used in future research to create algorithms increasing the level of autonomy of the CEMT I ships.

5 ACKNOWLEDGEMNT

The computational resources and services used in this work were provided by the VSC (Flemish Supercomputer Center), funded by the Research Foundation - Flanders (FWO) and the Flemish Government – department EWI. The authors would also like to thank the FWO for funding the research of G. Peeters, project 1S12519N.

6 REFERENCES

European Commission, 2018. Inland waterways - Mobility and Transport - European Commission. Retrieved from /transport/modes/inland_en

Delefortrie, G, Eloot, K., Mostaert, F., 2013. *Execution of Model Tests with KCS and KVLCC2. Version 3_0. WL Rapporten, 00_066*. Flanders Hydraulic Research Antwerp, Belgim.

Guo, B., Steen, S., 2011. Evaluation of added resistance of kvlcc2 in short waves. *Journal of Hydrodynamics, Ser. B*, *23*(6), 709–722. https://doi.org/10.1016/S1001-6058(10)60168-0

Hirt, C. W., Nichols, B. D. , 1981. Volume of fluid (VOF) method for the dynamics of free boundaries. *Journal of Computational Physics*, *39*(1), 201–225. https://doi.org/10.1016/0021-9991(81)90145-5

ITTC, 2017. Uncterainty Analysis in CFD Verification and Validation Methodology and Procedures. Retrieved from: https://www.ittc.info/media/8153/75-03-01-01.pdf

Jasak, H., Vukčević, V., Christ, D., 2014. Rapid Free Surface Simulation for Steady-State Hull Resistance with FVM using OpenFOAM. In *30 Symposium on Naval Hydrodynamics*. Retrieved from: http://bib.irb.hr/datoteka/727067.SteadyNavalHydroSolver002.pdf

Kim, G.-H., Park, S., 2017. Development of a numerical simulation tool for efficient and robust prediction of ship resistance. *International Journal of Naval Architecture and Ocean Engineering*, *9*(5), 537–551. https://doi.org/10.1016/j.ijnaoe.2017.01.003

Liu, J., Hekkenberg, R., Quadvlieg, F., Hopman, H. Zhao, B., 2017. An integrated empirical manoeuvring model for inland vessels. *Ocean Engineering*, *137*, 287–308.

Menter, F. R., 1994. Two-equation eddy-viscosity turbulence models for engineering applications. *AIAA Journal*, *32*(8), 1598–1605. https://doi.org/10.2514/3.12149

OpenCFD, 2018. OpenFOAM® - Official home of The Open Source Computational Fluid Dynamics (CFD) Toolbox. Retrieved on 11/10/2018 from http://www.openfoam.com

Peeters, G., Eggers, A., Boonen, R., Slaets, P., Vanierschot, M., 2018. Surge resistance identification of inland vessels by computational fluid dynamics. In *2018 OCEANS - MTS/IEEE Kobe Techno-Oceans, OCEANS - Kobe 2018*. https://doi.org/10.1109/OCEANSKOBE.2018.8559048

Rotteveel, E., Hekkenberg, R., van der Ploeg, A., 2017. Inland ship stern optimization in shallow water. *Ocean Engineering*, *141*, 555–569. https://doi.org/10.1016/j.oceaneng.2017.06.028

Shigunov, V., el Moctar, O., Papanikolaou, A., Potthoff, R., Liu, S., 2018. International benchmark study on numerical simulation methods for prediction of manoeuvrability of ships in waves. *Ocean Engineering*, *165*, 365–385. https://doi.org/10.1016/j.oceaneng.2018.07.031

SIMMAN, 2014. Retrieved from https://simman2014.dk/

Spalding, D. B., 1961. A Single Formula for the "Law of the Wall." *Journal of Applied Mechanics*, *28*(3), 455–458. https://doi.org/10.1115/1.3641728

Toxopeus, S. L., 2013. Viscous-Flow Calculations for KVLCC2 in Deep and Shallow Water. In L. Eça, E. Oñate, J. García-Espinosa, T. Kvamsdal, & P. Bergan (Eds.), *MARINE 2011, IV International Conference on Computational Methods in Marine Engineering* (Vol. 29, pp. 151–169). Dordrecht: Springer Netherlands. Retrieved from: http://link.springer.com/10.1007/978-94-007-6143-8_9

VisuRIS - Kanaal Leuven-Dijle, 2018. Retrieved on 22/11/2018 from https://www.visuris.be/Leuven-Dijle

Watertruck+. (2018). Retrieved from http://www.watertruckplus.eu

7 AUTHORS BIOGRAFIES

Arne Eggers is a graduate student at the KU Leuven since 2016. Mr. Eggers specializes in CFD for applied hydrodynamics and aerodynamics. Among other projects, he conducted optimization studies of flow based recycling machines, predictions of the hydrodynamic drag on ships,

and aerodynamic drag on cars. Before starting at the KU Leuven, he completed his master's degree in Computational Engineering at the Technical University of Darmstadt. After that, he worked as a researcher in combustion modeling at the Institute for Energy and Power Plants at the Technical University of Darmstadt.

Gerben Peeters is an SB PhD fellow at FWO (Flanders research foundation). He has been conducting research at the Department of Mechanical Engineering of the KU Leuven since December 2015. His interests lie in the fields of mathematical modelling, identification procedures, and control theory. He combines these interest fields in his doctoral study "Towards Autonomous Inland Shipping" which started in January 2017.

Peter Slaets is a professor at KU Leuven in the area of autonomous mobile robotics with a special focus on inland waterway transport and service robots. After finishing his PhD at KU Leuven, department of Mechanical Engineering in 2008, he joined the electromechanical department at Group T university college in Leuven. At campus Group T, he co-founded the intelligent mobility research group covering both technological and managerial aspects. The integration of campus Group T in KU Leuven in 2013 led to a cross-pollination of engineering technology with engineering leading to new opportunities. Currently he is supervising 6 PhD students and coordinator of several research/industrial projects within the domain of autonomous vehicles with a special focus on inland barges. His long term vision is to transform the Flemish waterways (again) to a competitive and sustainable logistic platform that serve as a viable alternative for road transport.

Maarten Vanierschot is a professor at KU Leuven, campus Group T Leuven. He received a Master's degree in Electromechanical Engineering from the KU Leuven, Belgium in 2002 where he also received a PhD in 2007. He obtained a post-doc scholarship from 2007 till 2009, after which, he became an assistant professor at campus Group T. His research focusses on experimental, numerical and theoretical fluid mechanics with an emphasis on large industrial applications including aerodynamics, hydrodynamics and heat- and mass transfer.

THE NAVAL BATTLE OF ACTIUM AND THE MYTH OF THE SHIP-HOLDER: THE EFFECT OF BATHYMETRY

Johan Fourdrinoy, Clément Caplier, Yann Devaux and Germain Rousseaux,
CNRS – Université de Poitiers – ISAEENSMA - Institut Pprime, France

Areti Gianni and Ierotheos Zacharias,
University of Patras, Greece

Isabelle Jouteur,
Université de Poitiers, Forellis France

Paul Martin,
Université de Montpellier, France

Julien Dambrine, Madalina Petcu and Morgan Pierre,
Université de Poitiers, Laboratoire de Mathématiques et Applications, France.

THE NAVAL BATTLE OF ACTIUM AND THE MYTH OF THE SHIP-HOLDER: THE EFFECT OF BATHYMETRY

Johan Fourdrinoy, Clément Caplier, Yann Devaux and **Germain Rousseaux,** CNRS – Université de Poitiers – ISAE-ENSMA - Institut Pprime, France
Areti Gianni and **Ierotheos Zacharias**, University of Patras, Greece
Isabelle Jouteur, Université de Poitiers, Forellis France
Paul Martin, Université de Montpellier, France
Julien Dambrine, Madalina Petcu and **Morgan Pierre,** Université de Poitiers, Laboratoire de Mathématiques et Applications, France.

SUMMARY

A myth of antiquity is explained with modern science in the context of an ancient naval battle. A legend was invoked by the admiral Pliny the Elder to explain the defeat of Antony and Cleopatra against Octavian at the naval battle of Actium. A fish, called echeneis or remora, is said to have the power to stop ships or to delay their motion by adhering to the hull. Naturalists have since studied how the fish sucking-disk with its typical pattern of parallel striae sticks to its host. Here we show the pattern of the free surface measured in a towing tank in the wake of an ancient galley is similar to the striae pattern of the fish. We have measured the bathymetry at the mouth of the Ambracian Gulf that influenced the physical environment of the battle. The computations demonstrate the increase of wave resistance of a galley as a function of the draft to the water depth ratio in shallow water corresponding to the appearance of a particular wake pattern: the echeneidian free surface pattern.

NOMENCLATURE [SUMMARY]

α	Wake angle (°)
$A_n = T/h$	Antonian number
B	Beam (m)
C_F	Friction coefficient (N)
$\mathrm{Fr}_h = U/\sqrt{gh}$	Froude depth number
$\mathrm{Fr}_L = U/\sqrt{gL}$	Length Froude number
g	Gravity of Earth (m/s²)
h	Depth (m)
$k = \sqrt{k_x^2 + k_y^2}$	Wavelength (m^{-1})
k_x	Longitudinal wavelength (m^{-1})
k_y	Transversal wavelength (m^{-1})
L	Length of ship (m)
λ	Linear scale of ship model
ω	Pulse wave (rad/s)
m	Blockage parameter
ν	kinematic viscosity (m²/s)
R_t	Total resistance (N)
R_v	Viscosity resistance (N)
R_w	Wave making resistance (N)
$\mathrm{Re} = VL/\nu$	Reynolds number
ρ	Density of water (kg/m^3)
S	Wetted surface (m²)
σ	Surface tension (kg/s²)
T	Draft (m)
t_W	Water temperature (°C)
V_m	Model speed (m/s)
V_R	Real-scale speed (knots)
UKC_m	Under keel clearance
W	Tank width

1 INTRODUCTION

September 2, 31 BC was a turning point for the ancient world, and an enigma for historians and scientists of all times. That day, the confrontation of Antony and Cleopatra against Octavian took place, near Actium in the Ambracian Gulf, the epilogue of the Civil War between the Western Roman world and the Eastern Oriental world. Antony, with his heavy fleet composed among others of decaremes, faces Octavian and his light fleet composed among others of triremes. Two mysterious anomalies disrupt the unfolding of history: Antony remains inexplicably motionless for three hours at the exit of the Gulf, then, instead of charging forward to break through the opposing lines, he fails to pick up speed. This forced him to adopt combat tactics involving getting close to the enemy in order to board their vessels for which his large boats were ill-suited. The ancient sources which mention these anomalies either give no explanation at all or give explanations which are less than convincing. Everything seems to point to Antony's fleet first having been compelled to remain motionless and then to Antony's having had to choose the least promising combat tactics. The explanation usually given by historians and modern philologists is that Antony expected wind to rise from the land; then, his fleet, having repelled that of Octavian, could sail off covering Cleopatra who stayed in the rear (Antony's rear fleet was a priority, because it was carrying the war booty). In contrast to the use of naval combat, the fleet of Antony had left the masts and sails lying on the deck of the ship - which has not been easy manned on board, but would allow, when the time comes, to prepare masts and sails to escape and to be sure of not being caught by the enemy ships, equipped to fight, that is to say, only with oars. Things did not go as planned: the collapse of Antony's frontline helped the admiral of Octavian, Agrippa, to attack the isolated part of Antony's vessels. In Section 9.1 with supplementary information on Ancient History, the reasons for the long immobility of the fleet of Antony are examined. We have a clue that this immobility was not expected: the surprise of the opponents. As

Octavian certainly knew the plan of Antony and the tactics he would adopt. He is surprised to see him sitting still. Another clue, less pronounced, is Antony's customary haranguing of his board troops and crews by moving along the front of the ship, but he did this on a small boat, and not - as one would have expected - from his flagship. The purpose was indeed to harangue the troops from a dominant position. In a small boat however, the leader is not in a dominant position… (Carter, 1970; Martin, 1995; Lange, 2011; Murray 2012). The explanation of these events are much written about, and (Tarn, 1931) warned us "The true history of Antony and Cleopatra will probably never be known; it is buried too deep beneath the version of the victors". A legend was invoked by Pliny the Elder (Pliny the Elder, 1857) (the naturalist and the admiral of the western Roman navy in the first century) to explain the defeat of Antony and Cleopatra against Octavian. A fish, called echeneis or remora and ship-holder or sucking-fish nowadays, is said to have the power to stop ships or to delay their motion by adhering to the hull (Jouteur, 2009). Some scientists have brought other reasoning and arguments: biofouling; rudder effect turbulent brake; dead-water in deep water… Gudger (Gudger, 1918) even concluded his review of these explanations with the definite statement that "another myth of the ancients is dissipated in thin air".

A research project has been set up to defy this point of view by analysing three new scientific reasons for the difficulties in manoeuvring by analysing the effect of shallow water only, stratification in shallow water and ship squat. In this introducing work on a scientific study of the battle of Actium, this paper focuses exclusively on the first effect. The bathymetry at the mouth of the Ambracian Gulf that influenced the physical environment of the battle has been measured and is described in Section 2. The Section 3 of the papers contains mathematical computations that demonstrate the increase of wave resistance of a galley with a draft of the order of the water depth in shallow water corresponding to the appearance of a so-called "echeneis" free surface pattern.

2 BATTLE'S CONDITIONS

2.1 THE OCEANOGRAPHIC CHARACTERISTICS OF THE AMBRACIAN GULF

"Oceanographic research in the Amvrakikos Gulf in Western Greece, a semi-enclosed embayment isolated from the Ionian Sea by a narrow, shallow sill, has shown that it is characterized by a fjord-like oceanographic regime" (Ferentinos et al, 2010). The entrance of the Ambracian Gulf, i.e. the area where the Actium Battle took place, limits the gulf's communication with the open Ionian Sea. It is a particularly shallow and narrow area (see Section 9.4 with supplementary information on oceanography).

The bathymetric map (Hellenic …, 1982) was used to reconstruct the bathymetry of the area where the Actium battle was held. The map's data were digitized and projected in the WGS 1984 - UTM 34N coordinate system. The map's data combined with bathymetric data, that where recovered during two sampling cruises in September – October 2012 period. Depth measurements were made along 10 transects and 20 points, uniformly distributed in the area of interest.

In order to reconstruct the bathymetry (explained in Section 9.4 with supplementary information on Oceanography) at the gulf's entrance in 31 BC, when the battle occurred, basic modifications to the current map were made. These modifications were based on: a) the relative sea level changes during the last 2000 years and; b) the morphological changes due to human interventions in the area over the last decades. The dredging of a navigational channel during the 1970s, changed the area's bathymetry as well as its hydrodynamics and its sedimentation processes. These changes resulted in morphological structures formation, which were identified and removed during the bathymetry reconstruction. In addition, based on literature and observations data, it was concluded that the average sea level during the battle was 75 cm lower than the current one (Lambeck and Purcell, 2005). This was also considered for the ancient bathymetry reconstruction.

Decaremes, with a draft of 2.5 m, have been limited in their position. Indeed, part of the entrance has a depth of less than 2.5 m

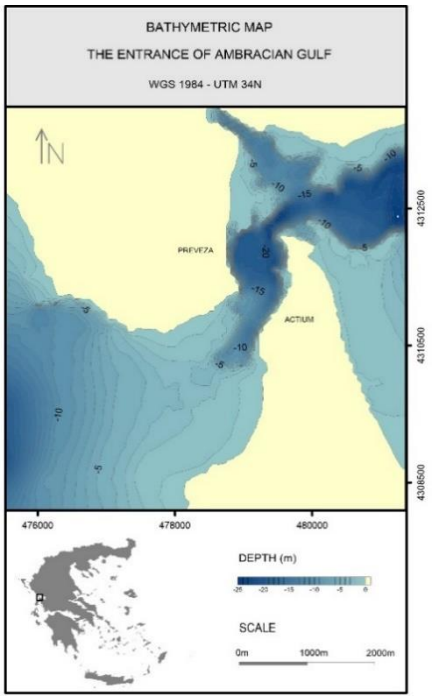

Figure 1. The bathymetric map of the Ambracian Gulf entrance 2000BP.

2.2 RECONSTRUCTION OF AN ANCIENT GALLEY MODEL

Laboratory experiments have been carried out in order to reproduce the assumed configuration of the battle. The water level, vessel's speeds and dimensions have been determined using the aforementioned bathymetry measurements, naval archeo-architecture inputs and historical reports of the battle (see Section 9.1 with

supplementary information on ancient history and Section 9.3 with supplementary information on naval architecture). Both fleets in presence at Actium had very different characteristics with respect to naval architecture. Hence, we decided to take as representative classes of boats for the two fleets: a trireme for Octavian and a decareme for Antony, both featuring the Athlit ram. According to (Murray et al., 2017), the Athlit ram would belong to a class 4. However, because of the reduced size of our warship model in the experiments, differences in the ram's geometry and epoch would be negligible at these scales.

It seems there is a consensus around the naval plans of a trireme with a slight variation depending on the period: the fifth-century BC trireme Olympias has dimensions a little bit smaller than the triremes present during the first century BC Actium battle. Unfortunately, there is no historical evidence for the real dimensions of a decareme. As a matter of fact, the boat classes bigger than 5 were no more built after the battle of Actium, principally because of Antony's defeat.

Figure 2. The small scale model of the Greek galley used in the experiments.

The geometry of the reduced model was based on the hull lines of the trireme Olympias generously provided by the Trireme Trust (Figure 2). At the water line, the ship model is 120 cm long and 13.5 cm wide. The draft is around 3,9 cm, depended of configurations (trireme or decareme), and the T/h ratio. The ram geometry was reverse engineered by (Murray, 2012) and the Institute for Visualization of History. As we use the same model to study the trireme and decareme behaviours, we scale the experiments using scaling laws (Table 1). The Olympias trireme is 32.08 m long, 3.43 m wide, with a 1.05m draft at waterline, and as presented in the main text we suppose that decaremes were twice as big, so the respective scaling-factor for the lengths is 26.73 for the trireme configuration and 53.47 for the decareme one. Considering the bathymetric data presented in the supplementary information on Oceanography, we chose 3 meters as a representative mean water depth at the outlet of the Ambracian Gulf, when corrected for the change in the water level since the battle. Hence, the water height in the towing tank was set to 11.22 cm for the trireme configuration and 5.61 cm for the decareme configuration (so the underkeel clearance is respectively 7.27 cm and 1.68 cm). The model speeds have been Froude depth numberscaled with (water depth) Froude number. Experiments were carried out for the height and length Froude numbers values indicated in the table below. The speed values are given in meter per second for the model and in knots for a real-scale vessel. During the experiments, the water temperature was about 21°C. Calm water resistance tests with a small-scale trireme model had already been carried out in the past by Grekoussis and Loukakis (Grekoussis and Loukakis, 1985, 1986) with a 3.2 m long small-scale model in a water depth of 3 m. The range of the Froude numbers Fr_L was between 0.090 and 0.397, corresponding to Froude depth numbers Fr_h between 0.093 and 0.410. Given these values we can assert that their experiments were performed in deep water conditions and they did not focus on shallow water effects. The choice of the 1.2m length for our small-scale model allows us to explore a wider range of Froude depth numbers (between 0.3 and 1.63), while staying under the limit length Froude number Fr_L=0.5 recently highlighted by (Rabaud and Moisy, 2013; Noblesse et al. 2014) from which the angle of the wake starts to decrease (an effect already present in deep water). Hence the maximum of wave resistance measured corresponding to the appearance of a shallow water wake pattern and not to another phenomenon. In battle conditions, if boats were in compact formation, a lateral confinement effect (as in tank) can be envisaged. There would be interference between the wakes, which will be the subject of a future. The limitations of the reduced model were studied in section 9.6.

Table 1. Significant values for trireme and decareme with reduced and real scales. MS=model scale / RS=real scale.

	Trireme RS	Trireme MS	Decareme RS	Decareme MS
λ (ratio scale)	26.73		53.47	
L (length)	32.08 m	1.2 m	64.15 m	1.2 m
B (beam)	3.6 m	13.5 cm	7.2 m	13.5 cm
T (draft at midship)	1.05 m	3.93 cm	2.10 m	3.93 cm
h (depth)	3 m	11.2 cm	3 m	5.6 cm
UKC (under keel clearance)	1.95 m	7.2 cm	0.9 m	1.68 cm
$A_n = T/h$	0.35	0.35	0.70	0.70
W (tank width)	Min: 5×B=18 m (compact formation)	1.49 m	Min: 5×B=36 m (compact formation)	1.49 m
m (blockage parameter)	0	0.013	0	0.026
V (boat speed)	5 knots	0.50 m. s^{-1}	5 knots	0.35 m. s^{-1}
V (boat speed)	10 knots	1.00 m. s^{-1}	10 knots	0.70 m. s^{-1}

3 PHYSICAL COMPARISON OF TRIREME AND DECAREME CONFIGURATIONS

3.1 MATHEMATICAL COMPUTATIONS OF THE WAVE RESISTANCE OF ANCIENT GALLEYS

From naval architectural data and based on Sretensky's analytical formulation (Sretensky, 1936), it is possible to calculate a prediction of wave making resistance of an ancient galley based on linear theory. Because of the importance of the ships design in the battle of Actium, we took into account the actual shapes of the galleys. Until now, numerical computations of the wave resistance with Sretensky's formula involving real ship hulls were made by using polynomial representation or uniform grids. In our case, the ships exhibit details at different scales. This led us to use meshes with triangular elements, refined in areas of finer details such as the ram at the bow of the ship (see Section 9.5 with supplementary on mathematics). The theoretical predictions of Sretensky require to be in shallow water configuration, without significant hydraulic effects (water level drawdown and return current) (Pompée, 2015). The numerical calculations present in Figure 3, were carried out for trireme or decareme configurations, and by varying the Antonian number $A_n=T/h$. As observed by (Russell, 1839; Inui, 1954), we observe a peak of resistance for $Fr_h = 1$ whose magnitude grows with A_n. To this resistance we can add a viscous resistance due to the friction of the boat with the water. This viscous resistance can be predicted by the (ITTC, 1957) protocol. By adding these two components of resistance (wave and friction), we obtain a total resistance according to the speed, the geometry (decareme or trireme), and the Antonian number (Figure 3). See SI on Mathematics for curves showing viscous and wave contributions for each configuration.

Using the measured bathymetry and the previous computations, and last results, we infer the theoretical wave making resistance of both the trireme and decareme in various points of the mouth of the Ambracian Gulf. The results of our predictions on total resistance are summed up in the two maps shown in the Figure 4. Our maps were computed for two velocities: 7 knots (left figure) and 10.5 knots (right figure), so Fr_h=1 when h=3 m. The latter being typical of a ramming manoeuver whereas the former corresponds to the cruising speed. These maps show in colours R_D/R_T, i.e. the ratio between the total resistance applied to a decareme and the one applied to a trireme in each point of the Ambracian Gulf. Our measured bathymetric data are plotted with line contours (in white), and three particular areas are highlighted: the shallow zone inaccessible for the decareme (in grey), the shallow zone inaccessible for both the trireme and the decareme (in black), and the land (in brown). At the cruising speed of 7 knots, our calculations predict a wave resistance ratio close to 1, almost uniformly on the battlefield, which means that no particular ship has an advantage when its velocity is lower than the ramming velocity (see Section 9.5 with supplementary on mathematics). At this speed, the viscous resistance is the main component of the total resistance. Hence, the factor 4 as explained in the SI which is mostly compensated by the ratio in the number of rowers 605/170=3.56. Thus, the larger wetted surface of a decareme is compensated by a greater rowing power. The trap is a confinement effect, not a simple viscous effect. At the ramming speed of 10.5 knots, the wave resistance ratio is much higher and the R_D/R_T can go up to, forming a bottleneck zone at the entry of the gulf. This result confirms the idea that ramming may have been impossible for Antony's ships in the particular entrance zone of the Ambracian Gulf and hence answers to the second anomaly underlined by the historical reports namely the impossibility to use the ramming tactic.

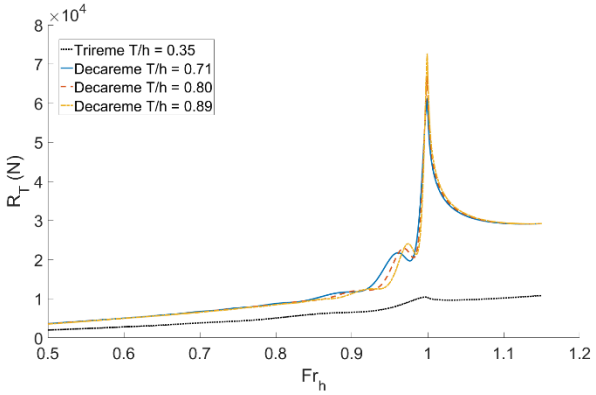

Figure 3. Calculated total resistances, composed by a wave making resistance and a viscous resistance, as a function of Frh for a varying ship draft to depth ratio.

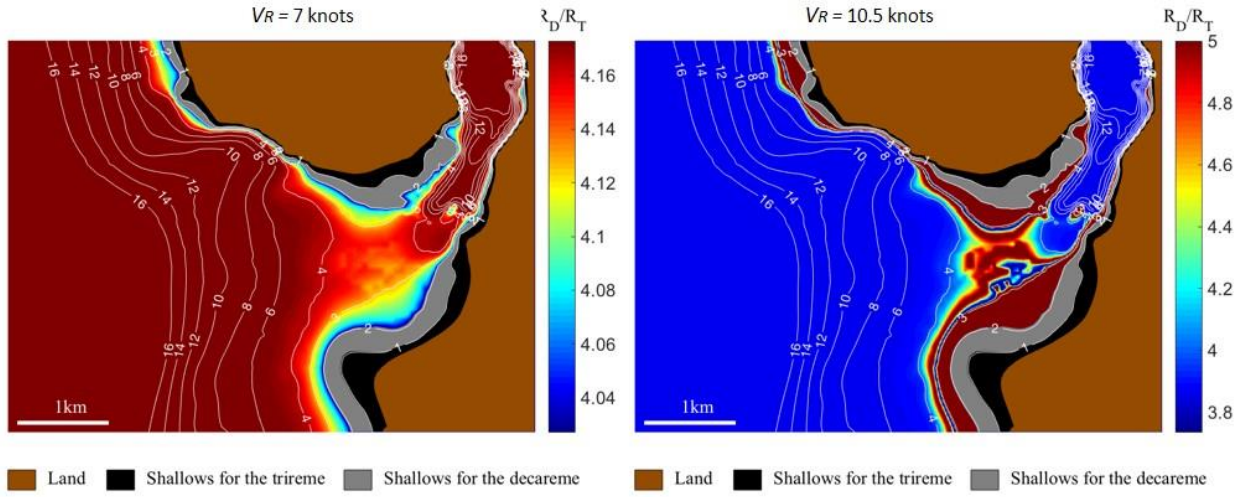

Figure 4. Maps featuring the ancient bathymetry and theoretical predictions of total resistance ratio R_D/R_T for two different velocities: 7 knots (left) and 10.5 knots (right). For the attack speed of 10.5 knots, decareme's resistance R_D is two to ten times larger than the trireme's resistance R_T. The colormap has been limited to 5 to make the results more visible, however, in a small area at the entrance of the channel, the ratio R_D/R_T may increase up to a factor 10 at 10.5 knots (see SI on Mathematics for an unlimited colormap).

3.2 THE SURFACE WAKES OF AN ANCIENT GALLEY

Experiments are carried out in a towing tank 20 m long and 1.49 m wide. The model, placed in the middle of the tank, is fixed to prevent any degree of liberty, and test only the impact of the draft. The top-view of wake is recorded by fast camera at 125 Hz.

The wake pattern of the ship gives a clue on the deep or shallow water configuration. Indeed, in deep water, the usual Kelvin wake pattern, featuring a V shape, has a constant angle at 19.47°. From $\mathrm{Fr_L} \approx 0.5$, the angle should diminish with the Froude number based on the length of the boat. (Rabaud and Moisy, 2013) propose a decrease according to $1/\mathrm{Fr_L}$ while (Noblesse et al., 2014) propose a decrease according to $1/\mathrm{Fr_L}^2$. In shallow water, this angle is dependant of the Froude depth number, reaching a maximum for $\mathrm{Fr}_h = 1$ (Havelock, 1908; Inui, 1936; Soomere, 2009; Ersan and Beji, 2013). On the top views, one observes two V-like wakes at the bow and the stern of the galley. Each wake is composed of a system of divergent and transverse waves, which superimpose and form the so-called cusp waves, defining an envelope corresponding usually to maximum wave heights (Darmon et al., 2013). In addition, a turbulent wake is clearly seen behind the stern of the ship. There is a measure of the wake angle in the spectral domain, from an image of the wake seen from above (Figure 6 and see 9.6.b for the methodology). The dispersion relation:

$$0 = {V_m}^2 {k_x}^2 - \left(gk + \frac{\sigma}{\rho}k^3\right)\tanh(kh)$$

has an inflexion point, where the slope is directly connected to the angle (Carusotto and Rousseaux, 2013; Gomit, et al. 2014; Caplier 2015). The trireme and decareme configurations show the same evolution of the wake angle, corresponding to a shallow water regime (Figure 7). This validates the hypothesis necessary for the use of the Sretensky's formula to be in shallow water in order to compute the wave resistance.

For the decareme, an additional system of quasi-parallel waves of the divergent type appears in addition to the Kelvin wake pattern and superimposes to create another wake pattern starting roughly at Fr_h=0.8 (Figure 8). The amplitude of this additional system of waves increases with respect to the speed of the ship until a Froude depth number of 1.0, where they are the most visible. Past that Froude number, the value of the amplitude decreases with the speed, and the quasi-parallel waves bend toward the stern-wake (Figure 8). The Froude depth number of 0.85 corresponds to the real scale speed around 9-10 knots, which was approximately the attack speed of the galleys. In addition to this "echeneidian" wake-pattern, a double bow wave appears, only in the decareme configuration, with a similar behavior and a maximum amplitude reached for Fr_h=1.15 (Figure 9). The first wave (in green) presents an angle similar to a Mach cone, while the second (in red) does not seem linear. If the boat stops suddenly, the second wave unfolds and is ejected forwards (Figure 10). This behaviour is reminiscent of the shallow wave pattern of the free surface observed a long time ago by the engineer Scott Russell (Russell, 1839) who towed boats in a shallow canal of Scotland. On the contrary, the first wave (in green) remains folded. Thus, the first wave can be another shallow effect (amplified by a horizontal confinement). The second is due to a canal effect, so therefore absent at sea.

The modification of the wake shape is known since then to be related to an enormous increase of wave resistance (Inui, 1954; Kirsch, 1966; Kostyukov, 1968). This typical shallow water wake behind the galley is strikingly similar to the echeneis suction disk (Figure 13) that was reported

to have appeared during the Actium battle when interpreting correctly Pliny's and Octavian's accounts, or as described by Elien (Elien, 1972): "For adhering with its teeth to the extreme stern of the ship driven by a following wind and full sails, just as an unmastered and unbridled horse is held in with a strong rein, so the fish overcomes the most violent onset of the winds and holds the ship as if tied fast to her wharf. [...] But the sailors understand and realize what ails the ship; and it is from this action that the fish has acquired its name, for those who have had experience call it the Ship-holder".

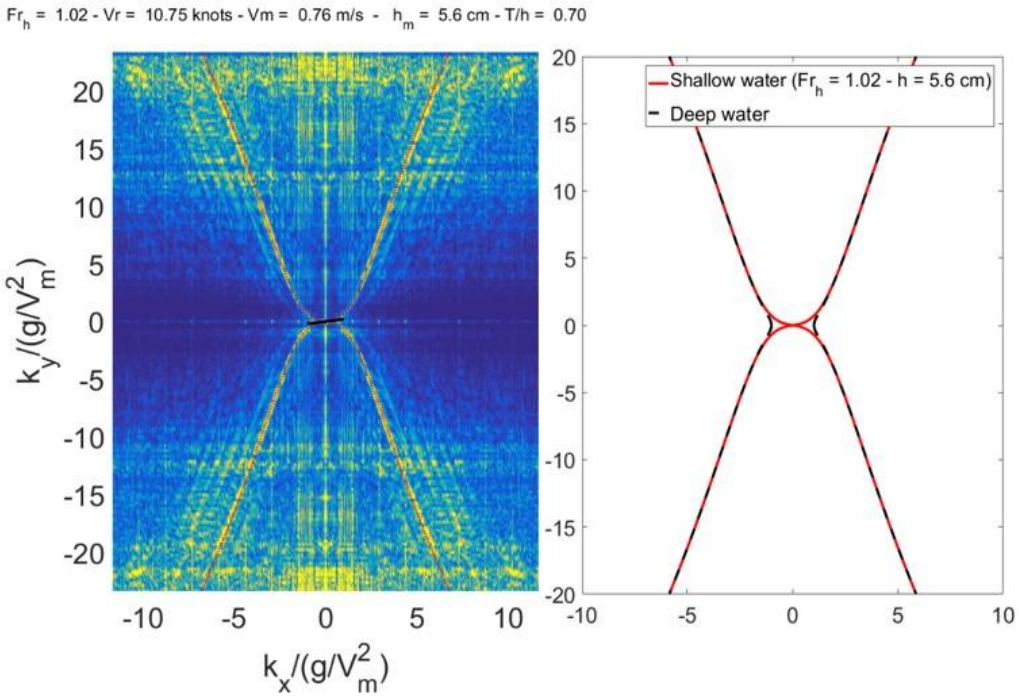

Figure 6. Left: Fast Fourier transform of the surface wake based on simple visualization with an aerial picture, in configuration decareme at Fr_h=1.02. In red, the theoretical dispersion relation; in black the slope at the inflexion point. Right: Theoretical dispersion relation at Fr_h=1.02, in shallow and deep water configurations.

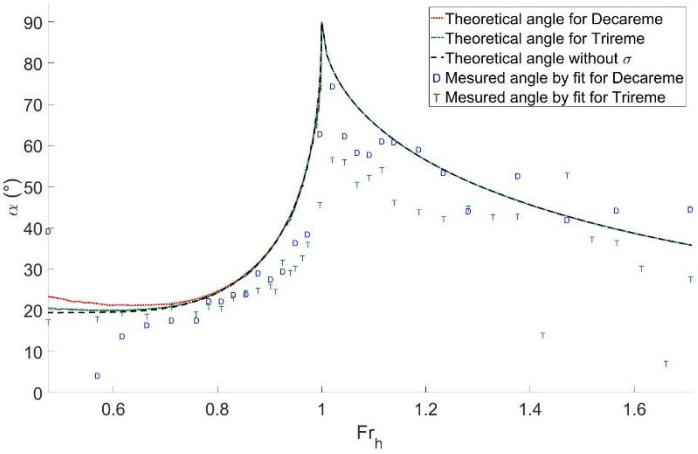

Figure 7. Measured wake angle (Kelvin angle) via spatial FFT, in configurations decareme and trireme, as a function of Fr_h. Green T are measured in trireme configuration and blue D in decareme configuration. Black curve is the theoretical angle's behavior by (Havelock, 1908), valid for linear theory with an idealized point source.

While the dimensionless number Fr_h, which is identical for trireme or decareme, only indicates a shallow water behavior, we use the Antonian number $A_n=T/h$, which drives the effect of strong vertical confinement. By adjusting this number, by increasing the draft, we observe a similar but amplified behavior of the particular wake pattern (Figure 11), as calculated by the formula of Sretensky (Figure 3). It is said that Antony's boats loaded with both sails and war chest (Carter 1970; Martin, 1995; Lange, 2011), which would imply a stronger draft.

In addition to these simple visualizations, the whole wave field behind the boat has been experimentally measured in the towing tank by a stereorefraction method (Caplier, 2015; Gomit, 2013) (Figure 12). This method is based on the calculation of the surface undulations from the apparent deformation of a pattern (roughcast) placed on the bottom of the towing tank. The refraction of light rays at the water-air interface allows, through two cameras, to reconstruct a 3D visualization of the wake. This reconstruction of the free surface deformation due to the

motion of the ship clearly highlights the non-classical wake pattern that has been observed and identified behind the decareme in the experiments. The complexity of the wake pattern would have been impossible to capture with classical intrusive local methods such as resistive or acoustic probes so it was necessary to use this state-of-the-art optical method to measure the whole wake (more information in the SI on Fluid Mechanics).

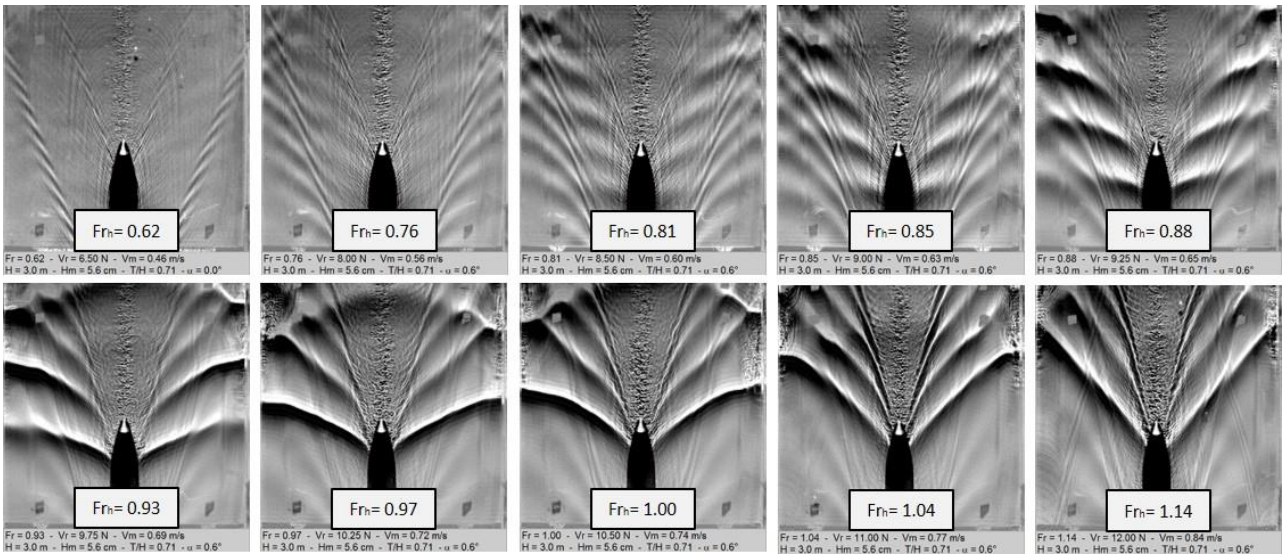

Figure 8. Evolution with Froude depth number of the wake pattern for a decareme configuration. Supplementary to usual Kelvin wake pattern, quasi-parallel waves of the divergent type appear from $Fr_h > 0.8$. The amplitude of this additional system of waves increases with respect to the boat speed until a $Fr_h = 1$. After, the value of the amplitude decreases with the speed, and this parallel waves bend toward the stern wake. The ship has no angle with the horizontal.

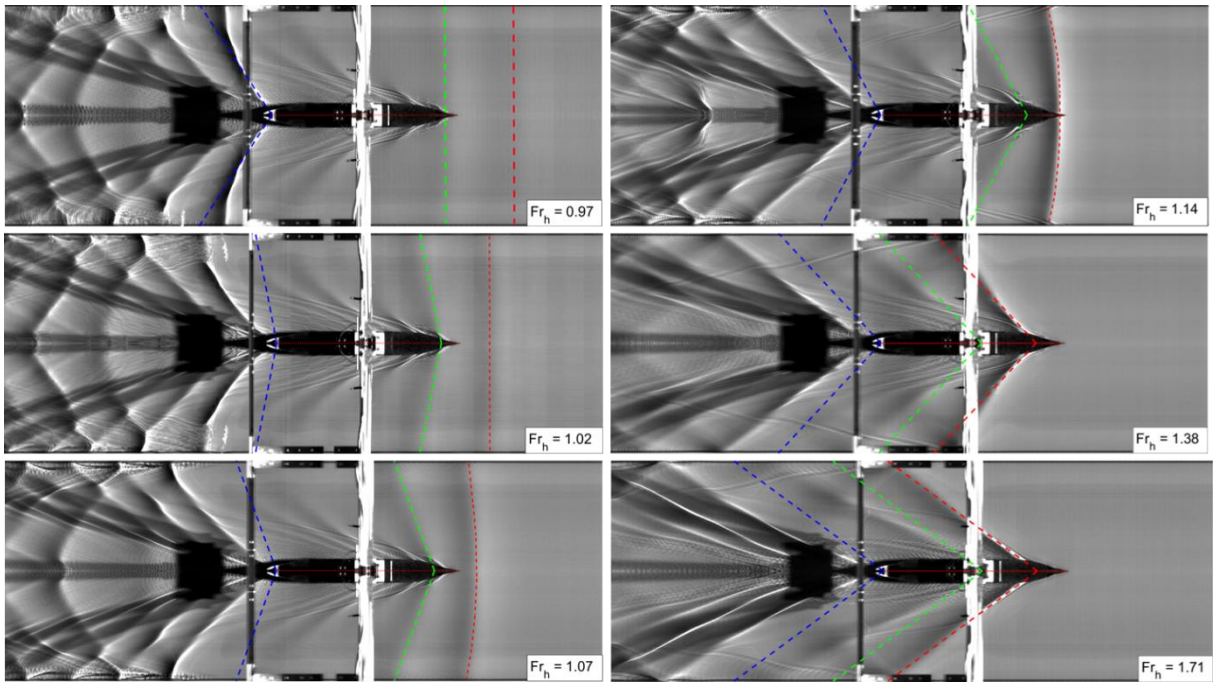

Figure 9. Evolution with Froude depth number of the bow wave for a decareme configuration. A bow wake (in green) appears from a $Fr_h \approx 1$. Its angle decreases according to a Mach angle : $\alpha = \tan^{-1}\left[{Fr_h}^2 - 1\right]^{-1} = \sin^{-1}[Fr_h]^{-1}$. A second bow wave with a bigger amplitude (in red) appears in the front of the first.

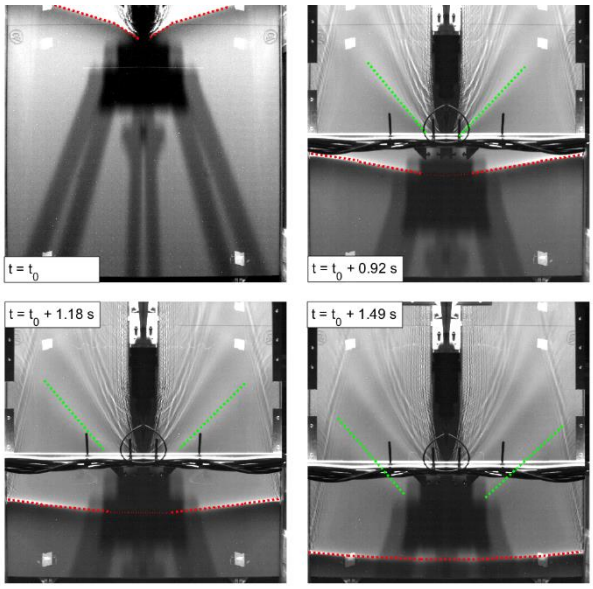

Figure 10. Top-views of bow wave ejections when the boat decelerates before stopping at the end of the run. The first bow wave (in green) keeps its slope and is a purely linear shallow effect. The second bow wave (in red) detaches from the prow and creates a solitonic wave à la Scott Russell (Scott Russell, 1939). The second wave is usually akin to a channel effect (not present in the open sea).

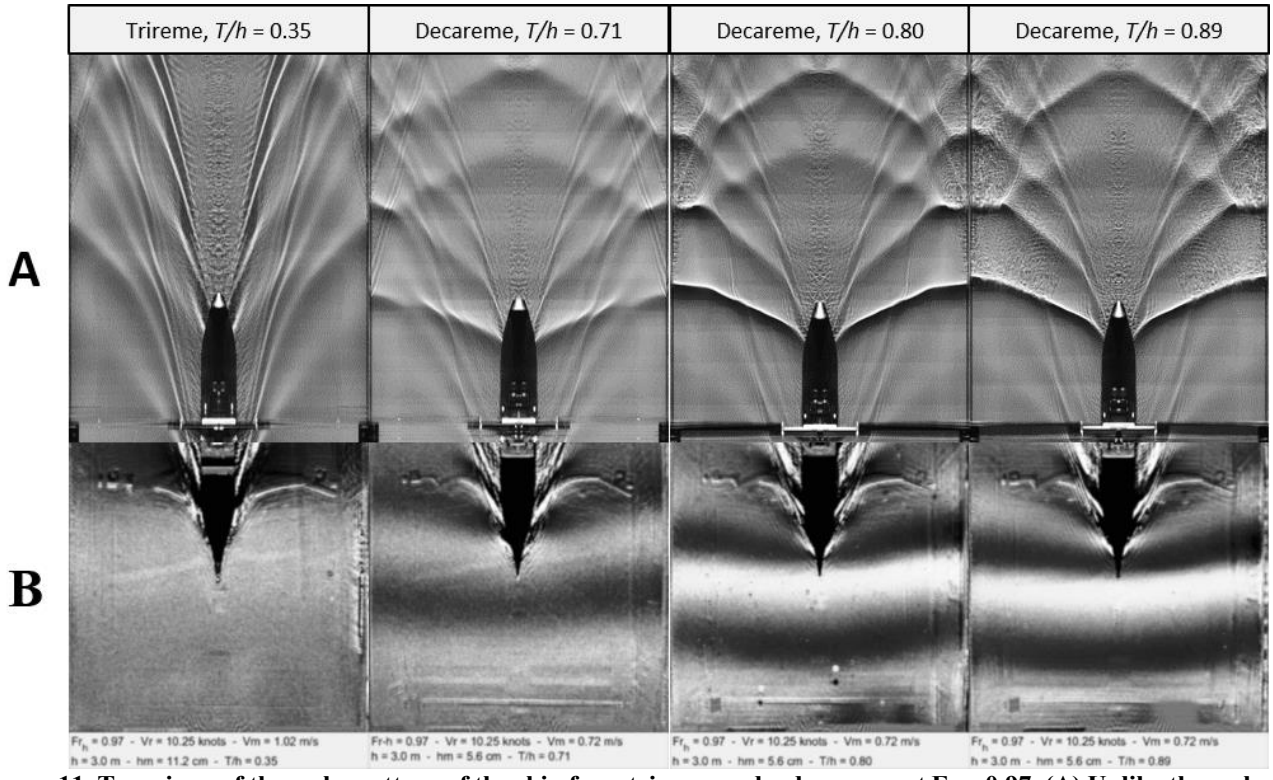

Figure 11. Top-views of the wake pattern of the ship for a trireme and a decareme at Fr_h=0.97. (A) Unlike the wake pattern of the trireme which is similar to the usual Kelvin wake pattern, in decareme configuration we observe the "echeneidian" pattern (quasi-parallel waves of the divergent type) superimposes with the deep water wakes and which create a complex wake pattern. The amplitude of this shallow waters wake increases with T/h. (B) A bow wave appears in decareme configuration (not for a trireme) whose amplitude increases with T/h.

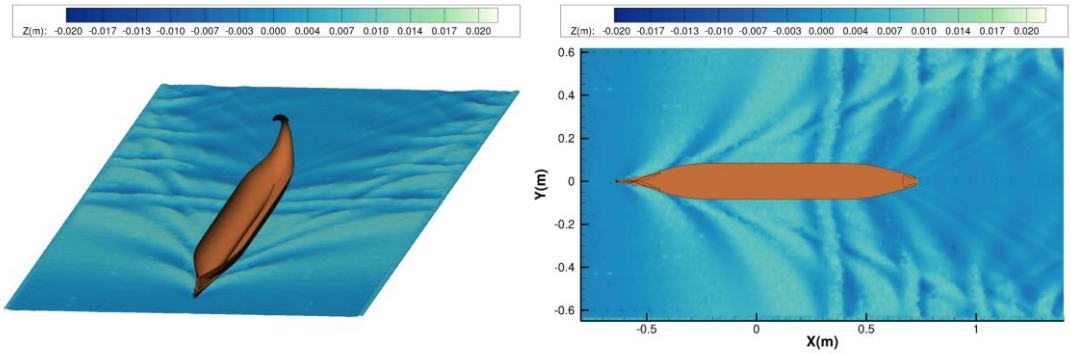

Figure 12.The particular echeneidian wake behind the ship in the decareme configuration at Fr_h=0.85, measured with the stereorefraction method in the towing tank. In this experiment the keel of the boat makes an angle of 0.13 ° with the horizontal (stern sunk) which is equivalent to an increase of an effective draft along the hull.

4 DISCUSSION: THE SCIENTIFIC EXPLANATION OF THE LEGEND OF THE SHIP-HOLDER

According to Albert Günther, "there is scarcely a fish of the existence of which the ancients have been equally certain, and which has so much occupied their imagination... as the Echeneis of the Greeks or Remora of the Latins" (Günther, 1860). With our interdisciplinary approach between human and fundament al sciences, we believe we can explain this famous myth of Antiquity: the battle of Actium, where an echeneis, the small fish which allegedly hampered ships and triggered the interest of historians, writers and poets for twenty centuries. For example, Ovid in his Halieutica, says "The small echeneis is present, wonderful to say, a great hindrance to ships". As we have seen in the introduction, this myth is invoked to explain, e.g., the defeat of Antony and Cleopatra against Octavian at the naval battle of Actium twenty centuries ago. The admiral Pliny the Elder reports: "At the battle of Actium, it is said, a fish of this kind stopped the Pretorian ship of Antony in its course, at the moment that he was hastening from ship to ship to encourage and exhort his men, and so compelled him to leave it and go on board another. Hence it was, that the fleet of Ceasar (Octavian) gained the advantage in the onset, and charged with a redoubled impetuosity" (Pliny the Elder, 1857).

The issue of the origin of the echeneis tale, which is said to have detained Antony, is discussed in Section 9.2 with supplementary information on Linguistics. According to the common opinion, the legend was created by the defenders of Antony and intended to explain the immobility of the flagship, and thus that the fleet did depend on the flagship's moves. For our part, we believe, on the basis of a number of indications contained in the poetic exaltation of the contemporary battle of Actium, that it is one of the themes of Augustan propaganda on this battle, which was exalted as the Principate epiphany. The legend of echeneis is prior to Actium and it was applied to the excitement of the battle, to show that the gods and nature itself were on the "good side", that of Octavian. It is known that Octavian Augustus, after the battle, founded the town of Nicopolis ad Actium; on this forum stood, as in Rome, a forum rostra (one can see the remains today) adorned with the rams of several Antonians ships (Murray, 2012), including probably the flagship of Antony (abandoned by him for a faster one, a quinquereme, at the time of flee). Our hypothesis is that when the ship was lifted from the water in order to recover the rostrum, an echeneis was found attached to the hull and this served to support the activation of the legend. The fish is known to stick to rock or boat in bad weather and the Actium battle happened after four days of storms. Plutarch gives details on the progress of the naval battle: "Caesar (Octavian)… was astonished to see the enemy lying motionless in the narrows; indeed, their ships had the appearance of riding at anchor" (Plutarch, 1988). One of the possible interpretation of the use of the word anchor relies on the legend of the "echeneis" from *echein-* (to hold) and *-naus* (the ship). Pliny the Elder, who was a naturalist and natural philosopher as is well known nowadays but also the Admiral of the fleet of Mycene in the Mediterranean Sea which is less known, gave an explanation for the difficulties that the galleys of Antony had to struggle with during the naval confrontation by invoking the Greek myth. The fish, called echeneis in Greek or remora in Latin is said to have the power to stop ships or to delay ("mora" in Latin) their motion by adhering to its stern. Naturalists have since studied the way in which the haustellum (a sucking-disk with a typical pattern of parallel striae) of the fish exerts an enormous pressure on its host (sharks, turtles, whales, boats, scuba divers, etc.). For Pliny's translator, J. Bostok, the echeneidian myth is "an absurd tradition, no doubt, invented, probably to palliate the disgrace of defeat". But for others, the authority of Pliny the Elder (and subsequent commentators) is such that he would not have relied on such a tale even to protect the reputation of Antony and Cleopatra.

The purpose of this work has been to provide a visual explanation of the legend which corresponds to the naval difficulties met by the Antonian fleet based on scientific clues. Hence, we have displayed for the first time the visual signature of the Ancient myth of the echeneis, which answers the first anomaly noticed by the historians in the introduction and substantiates the legend for the linguists.

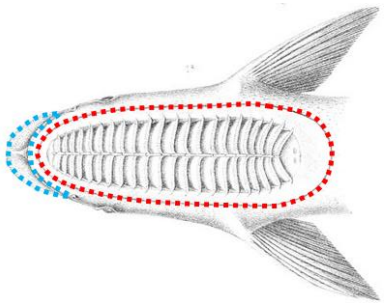

Figure 13. Illustration of Echeneis naucrates (Grandidier, 1885). The lips (blue) can represent the bow waves, and the sucking disk pattern (red) can represent the particular echeneidian wake pattern.

5 CONCLUSIONS

For the first time since twenty centuries, we have shown conclusively that the global pattern of the free surface measured in this work with modern and non-intrusive optical methods in the wake of an ancient galley moving in shallow waters is similar to the pattern of striae on the sucking-disk of the echeneis fish. Hence, the Antonian boats have been influenced by a physical echeneis and not a biological one during the battle of Actium. From the analysis of the resistance charts, we have demonstrated that the Antonian fleet was unable to use the ramming tactics because the wave resistance was increased up to ten times compared to the Octavian fleet. By a strange coincidence (or maybe not a hazard?), several centuries later another naval battle at the same location produces the same astonishment for the final result: Preveza battle in 1538, where the Ottoman forces fought against the Christian navy and, to the general surprise, won. The Ottoman fleet under the command of Barbarossa with the smallest boats albeit considered as inferior, prevailed. Another possible explanation for the boats difficulty in manoeuvres is the dead-water phenomenon, which can be encountered, for example, in the Northern fjords where ice melting creates two water layers of different densities, with a sharp interface between fresh and saline water (see Section 9.4 with supplementary on oceanography and Ekman, 1904; Grue, 2015; 2016; Esmaeilpour, 2017). The resulting wave resistance exerted on moving boats is significantly increased by the generation of internal waves at the interface. Hence, our future goal will be to compute theoretically the wave resistance in a two-layer shallow water basin since the mouth of the Ambracian gulf has a shallow fjord recirculation. In the laboratory experiments, we will measure the wave resistance of ship models (corresponding to the Actium and Preveza battle) moving in our towing tank at different density stratifications. In addition, confinement effects like water level drawdown, return current, ship squat will be examined as well. Thus, we hope to shed light on the History of these two naval battles with the help of Contemporary Science… With respect to the biological remora, it is unable to explain, of course, the drag on the boat (see Beckert et al., 2016 for a recent study on the fluid dynamics of an attached remora) … We anticipate our work will allow a revisit by historians of the events and by linguists of the legend as well as open new perspectives on battles with similar conditions like the one of Preveza in 1538.

6 ACKNOWLEDGEMENTS

This research was funded by the CNRS Interdisciplinary Mission in 2013 (INSIS/INSHS co-funding), by the Poitiers University through two successive two-years funding (ACI UP on Wave Resistance 2013-2014 and ACI Pprime on Actium 2014-2015) and by the Patras University (Inland & Coastal Water Laboratory). The authors are indebted to William Murray and the Institute for Visualization of History for sharing their 3D plans of the Athlit rostrum and those of the temple in Nicopolis. The hull lines of the galley were provided by the Trireme Trust and we thank Doug Pattison for discussions on naval architecture. Christian Oddon from Cabinet Mauric translates the drawn hull lines of John Coates into numerical lines with modern softwares of naval architecture. The reduced model was built by Formes & Volumes in La Rochelle. We thank the services of metrology, computer sciences, electronics and the mechanical workshop of the Pprime Institute in Poitiers for helping in the course of experiments. The support of Michel Briand is gratefully acknowledged. We thank the former and current directors of the Pprime Institute and of the LMA. This work benefited from the support of the project OFHYS of the CNRS 80 Pprime initiative in 2019.

7 REFERENCES

Beckert, M., Flammang, B.E., Anderson, E.J., Nadler, J.H., 2016. Theoretical and computational fluid dynamics of an attached remora (Echeneis naucrates). Zoology 119, 430–438.

Caplier, C., 2015. Etude expérimentale des effets de hauteur d'eau finie, de confinement latéral et de courant sur les sillages et la résistance à l'avancement des navires. Université de Poitiers.

Carlson, D.N., 2002. Caligula's floating palaces-archaeologists and shipwrights resurrect one of the emperor's Sumptuous pleasure boats.

Carter, J.M., 1970. The battle of Actium: the rise & triumph of Augustus Caesar. Hamish Hamilton.

Carusotto, I., Rousseaux, G., 2013. The Cerenkov effect revisited: from swimming ducks to zero modes in gravitational analogues, in: Analogue Gravity Phenomenology. Springer, pp. 109–144.

Chatellier, L., Jarny, S., Gibouin, F., David, L., 2013. A parametric PIV/DIC method for the measurement of free surface flows. Exp. Fluids 54, 1488.

Coates, J.F., 1989. The trireme sails again. Sci. Am. 260, 96–105.

D'Amato, R., Rava, G., 2015. Republican roman warships 509-27 BC, New Vanguard. Bloomsbury Publishing.

Darmon, A., Benzaquen, M., Raphaël, E., 2013. A solution to the Kelvin wake angle controversy. J. Fluid Mech. 73, 8.

Doutreleau, Y., Jodet, L., Laurens, J.-M., 2011. Résistance et propulsion du navire. Ellipses.

Ekman, V.W., 1905. The Norwegian North polar expedition, 1893-1896: scientific results. Longmans, Green and Company.

Ersan, D.B., Beji, S., 2013. Numerical simulation of waves generated by a moving pressure field. Ocean Eng. 59, 231–239.

Esmaeilpour, M., Martin, J.E., Carrica, P.M., 2018. Computational Fluid Dynamics Study of the Dead Water Problem. J. Fluids Eng. 140, 31203.

Ferentinos, G., Papatheodorou, G., Geraga, M., Iatrou, M., Fakiris, E., Christodoulou, D., Dimitriou, E., Koutsikopoulos, C., 2010. Fjord water circulation patterns and dysoxic/anoxic conditions in a Mediterranean semi-enclosed embayment in the Amvrakikos Gulf, Greece. Estuar. Coast. Shelf Sci. 88, 473–481.

Gomit, G., 2013. Développement de techniques de mesure de surfaces libres par moyens optiques: Application à l'analyse de l'écoulement généré par un modèle de bateau en bassin des carènes. Poitiers.

Gomit, G., Chatellier, L., Calluaud, D., David, L., 2013. Free surface measurement by stereo-refraction. Exp. Fluids 54, 1540.

Gomit, G., Rousseaux, G., Chatellier, L., Calluaud, D., David, L., 2014. Spectral analysis of ship waves in deep water from accurate measurements of the free surface elevation by optical methods. Phys. Fluids 26, 122101.

Gotman, A.S., 2002. Study of Michell's integral and influence of viscosity and ship hull form on wave resistance. Ocean. Eng. Int. 6, 74–115.

Grandidier, A., 1885. Illustration of Echeneis naucrates. Hist. la Géographie Madagascar.

Grekoussis, C., Loukakis, T., 1986. AAthenian trireme: calm water resistance tests with ram at trimmed conditions. Rep. No. NAL.

Grekoussis, C., Loukakis, T., 1985. Athenian Trireme Calm Water Resistance Tests Without Ram. Rep. No. NAL.

Grue, J., 2015. Nonlinear dead water resistance at subcritical speed. Phys. Fluids 27, 82103.

Grue, J., Bourgault, D., Galbraith, P.S., 2016. Supercritical dead water: effect of nonlinearity and comparison with observations. J. Fluid Mech. 803, 436–465.

Gudger, E.W., 1918. The myth of the ship-holder: studies in Echeneis or Remora. J. Nat. Hist. 2, 271–307.

Günther, A., 1860. On the history of Echeneis. Ann. Mag. Nat. Hist. 5, 386–402.

Havelock, T.H., 1908. The propagation of groups of waves in dispersive media, with application to waves on water produced by a travelling disturbance. Proc. R. Soc. Lond. A 81, 398–430.

Hellenic navy hydrographic service of prevenza, 1982. Preveza Strait - Bay and Harbour (ca. 1:10.000).

Inui, T., 1954. Wave-making resistance in shallow sea and in restricted water, with special reference to its discontinuities. J. Zosen Kiokai 1954, 1–10.

Inui, T., 1936. On Deformation, Wave Patterns and Resonance Phenomenon of Water Surface due to a Moving Disturbance. Proc. Physico-Mathematical Soc. Japan. 3rd Ser. 18, 60–98.

ITTC57, 1957. Testing and extrapolation methods: propulsion, performance propulsion test.

Jouteur, I., 2009. Monstres et merveilles: Créatures prodigieuses de l'Antiquité. Les Belles lettres.

Kirsch, M., 1966. Shallow water and channel effects on wave resistance. J Sh. Res 10, 164–181.

Kostyukov, A.A., 1968. Theory of ship waves and wave resistance.

Kountoura, K., Zacharias, I., 2014. Annual hypoxia dynamics in a semi-enclosed Mediterranean gulf. J. Mar. Syst. 139, 320–331.

Lambeck, K., Purcell, A., 2005. Sea-level change in the Mediterranean Sea since the LGM: model predictions for tectonically stable areas. Quat. Sci. Rev. 24, 1969–1988.

Lange, C.H., 2011. The battle of Actium: a reconsideration. Class. Q. 61, 608–623.

le Sophiste, E., 1972. On the characteristics of animals.

Macfarlane, G.J., Graham-Parker, K.J., 2018. Marine vessel wave wake: transient effects when accelerating or decelerating. J. Waterw. Port, Coastal, Ocean Eng. 145, 4018027.

Martin, P.M., 1995. Antoine et Cléopâtre: la fin d'un rêve. Editions Complexe.

Millward, A., 1986. Effect of shallow water on a mathematical hull at high subcritical and supercritical speeds. J. Sh. Res. 30, 85–93.

Molland, A.F., Turnock, S.R., Hudson, D.A., 2017. Ship resistance and propulsion. Cambridge university press.

Morrison, J., 2016. Greek and Roman Oared Warships 399-30BC. Oxbow Books.

Morrison, J.S., Coates, J.F., Coates, J.F., Rankov, N.B., 2000. The Athenian trireme: the history and reconstruction of an ancient Greek warship. Cambridge University Press.

Murray, W., Murray, W.M., 2012. The age of titans: the rise and fall of the great Hellenistic navies. OUP USA.

Murray, W.M., Ferreiro, L.D., Vardalas, J., Royal, J.G., 2017. Cutwaters Before Rams: an experimental investigation into the origins and development of the waterline ram. Int. J. Naut. Archaeol. 46, 72–82.

Noblesse, F., He, J., Zhu, Y., Hong, L., Zhang, C., Zhu, R., Yang, C., 2014. Why can ship wakes appear narrower than Kelvin's angle? Eur. J. Mech. 46, 164–171.

Pitassi, M., 2012. The Roman Navy: Ships, Men & Warfare 350 BC-AD 475. Seaforth Publishing.

Pitassi, M., 2011. Roman Warships. Boydell Press.

Pliny the Elder, 1857. The Natural History, Bohn's classical library. H. G. Bohn.

Plutarch, n.d. Life of Antony.

Pompée, P.-J., 2015. About modelling inland vessels resistance and propulsion and interaction vessel-waterway. Key parameters driving

restricted/shallow water effects. Proceeding Smart Rivers 2015.
Poulos, S.E., Kapsimalis, V., Tziavos, C., Paramana, T., 2008. Origin and distribution of surface sediments and human impacts on recent sedimentary processes. The case of the Amvrakikos Gulf (NE Ionian Sea). Cont. Shelf Res. 28, 2736–2745.
Rabaud, M., Moisy, F., 2013. Ship wakes: Kelvin or Mach angle? Phys. Rev. Lett. 110, 214503.
Robbins, A., Thomas, G.A., Renilson, M.R., Macfarlane, G.J., 2011. Subcritical wave wake unsteadiness. Int. J. Marit. Eng. 153, 153–161.
Rousseaux, G., Maïssa, P., Mathis, C., Coullet, P., Philbin, T.G., Leonhardt, U., 2010. Horizon effects with surface waves on moving water. New J. Phys. 12, 95018.
Russell, J.S., 1839. Experimental Researches into the Laws of Certain Hydrodynamical Phenomena that accompany the Motion of Floating Bodies, and have not previously been reduced into conformity with the known Laws of the Resistance of Fluids. Earth Environ. Sci. Trans. R. Soc. Edinburgh 14, 47–109.
Soomere, T., 2009. Long ship waves in shallow water bodies, in: Applied Wave Mathematics. Springer, pp. 193–228.
Srettensky, L.N., 1936. On the wave-making resistance of a ship moving along in a canal. London, Edinburgh, Dublin Philos. Mag. J. Sci. 22, 1005–1013.
Stigebrandt, A., 2001. Land-Sea Exchanges: Fjord circulation. Encycl. Oceanogr.
Tarn, W.W., 1931. The battle of Actium. J. Rom. Stud. 21, 173–199.
Therianos, A.D., 1974. The geographical distribution of river water supply in Greece. Bull. Geol. Soc. Greece 11, 28–58.
Variagin, M.A., 1972. Tides and tidal values of Greek harbours. Greek Hydrogr. Serv. Athens 117.

8 AUTHORS BIOGRAPHY

Johan Fourdrinoy holds the current position of PhD student at University of Poitiers - Institut Pprime, France. His thesis is about wave-current interactions. His previous experience includes engineering fluid mechanics and the study of a wave maker.

Clément Caplier holds the current position of post-doctoral researcher at the University of Poitiers - Institut Pprime, France specialized in optical measurement techniques for hydrodynamics. His previous experience includes an experimental thesis on the effects of finite water depth, lateral confinement and current on ships wakes and drag.

Yann Devaux holds the current position of teaching and research assistance at University of Poitiers - Institut Pprime, France. His thesis is about the unsteady suspension of sediment. His previous experience includes the establishment of an experimental process for studying dead-waters.

Areti Gianni is geologist – marine science researcher focusing on degraded ecosystems management and restoration. She is a technical consultant in OIKOM - Environmental Studies LTD and a postdoctoral researcher at the Patras University. Her research is focused in inland and coastal ecosystems' hydrodynamics, biogeochemistry, eutrophication and anoxia. She is specialized in hydrodynamic and ecological modelling in inland and coastal waters, and in the development of management/restoration practices and techniques.

Ierotheos Zacharias is an oceanographer focusing on marine ecosystem monitoring and restoration. He is an Associate Professor in the University of Patras, Greece. His research is focused in inland and coastal ecosystems' hydrodynamics, biogeochemistry, eutrophication and anoxia. He is specialized in hydrodynamic and ecological modeling in inland and coastal waters, and in the development of management/restoration practices and techniques.

Isabelle Jouteur holds the current position of Professor of Classics at University of Poitiers (Forellis). Her works focuses on Latin poetry of the Augustan period; she is interested in mythology and imagination with an anthropological point of view. Her previous experience includes the study of monsters and wonders in Greco-Roman culture.

Paul Martin is Professor Emeritus of the University of Montpellier-III and Honorary President of the magazine Vita Latina. Specialist in the history of royal and republican Rome, he was particularly interested in the process of return to the monarchy that led to the imperial regime. As such, he had to deal with the founding battle of the August regime: the battle of Actium, including the strange phenomenon reported by several ancient sources: the immobilization of the ships of the fleet of Antony at beginning of this battle.

Julien Dambrine holds the current position of Assistant Professor at the University of Poitiers. He is responsible for the prediction of the wave-making resistance shown in this article using actual antique galley hull shapes. His speciality is shape optimisation in the context of ship waves, which include the aforementioned predictions.

Madalina Petcu holds the current position of Associate Professor (maître de conférences, HDR) at University of Poitiers, Laboratoire de Mathématiques et ses Applications. She is member of the Partial Differential Equations team, working on the theoretical and numerical aspects of mathematical models in fluid dynamics and other models related to physics. She has also a full-time teaching duty, consisting of 192 hours of teaching for the Mathematics Department of Poitiers University.

Morgan Pierre holds the current position of associate professor at University of Poitiers (France). He is responsible of the Partial Differential Equations team at the Laboratoire de Mathématiques Appliques (Department of Applied Mathematics). His previous experience includes work on optimisation of ship hulls and wave resistance.

Germain Rousseaux is a senior research scientist at CNRS – Institut Pprime, France. He is a proponent of interdisciplinary studies like for example his recent works on analogue black holes with the measurement of Hawking radiation in the laboratory.

9 SUPPLEMENTARY INFORMATION

9.1 SUPPLEMENTARY INFORMATION ON ANCIENT HISTORY

What follows is based on a critical examination of ancient sources relating the battle of Actium between Antony's and Octavian's fleets on 2nd September 31 BC at the entrance to the gulf of Ambracia. The main sources are Plutarch's *Life of Antony,* 61- 68 and Dio Cassius's *Roman History,* 50, 14-35. Plutarch mentions one particular fact, which greatly puzzled those on Octavian's side. This happened before the battle when the two fleets were facing each other. Octavian and his admiral Agrippa were surprised to note that Antony's fleet remained at a standstill for at least three hours, until midday, instead of, as was customary in ancient times, attacking at dawn:

« Caesar (Octavian) […] was ***atonished to see the enemy lying motionless in the narrows; indeed, their ships had the appearance of riding at anchor. For a long time he was convinced that it was really the case,*** *and kept his own ships at a distance of about 8 furlongs from the enemy. But it was now* ***the sixth hour, and since a wind was rising from the sea,*** *the soldiers of Antony became* ***impatient of the delay,*** *and, relying on the height and size of their own ships as making them unassailable, they put their left wing in motion. When Caesar saw this* ***he was delighted,*** *and ordered the right wing to row backwards, wishing to draw the enemy still farther out from the gulf and the narrows, and then to surround them with his own agile vessels and come to close quarters with ships which,* ***owing to their great size and the smallness of their crews, were slow and ineffective*** (1)*. »*

In fact, it was more the crews' lack of experience which could be a real handicap and it did, indeed, hinder Antony's fleet during the battle as his ships had to move and turn in the midst of enemy vessels. On the contrary, the maneuver necessary for a forward attack using the *rostra* was well within the capability of inexperienced crews: all they had to do was to launch the ships at full speed straight ahead, towards the enemy -a good enough reason to opt for this tactic and yet Antony did not choose to do so. Plutarch suggests a possible explanation for this strange immobility: Antony would have been waiting for the wind to get up so as to take advantage of it to escape. Modern historians have religiously followed his lead in this matter and given this out as the reason for Antony's decision but the explanation doesn't hold together: at that time of the year the wind doesn't blow strongly enough to carry the ships forward before midday and Antony, who had been in the area for months, must have been aware of the fact. No doubt he intended to start waging battle in the morning and, at midday, when the wind got up, to "take off" and head for the open sea; that is why -contrary to what was customary- he had had the sails taken on board so that no enemy vessel could escape him. Thus it was not on purpose or due to either of the two adversaries that the battle only started after midday and that it lasted so long that, according to Suetonius, Octavian was unable to disembark and had to spend the night on board.

Consequently, this raises two questions. The first one, we have just asked: why did Antony wait three hours before opening hostilities? The second one is: why didn't he attempt to ram the enemy? Why didn't he resort to using the weapon of choice in such cases? The huge *rostra* on his powerful vessels would have crushed the hulls of the enemy ships, most of which were of an inferior tonnage. Instead of that, he opted for the use of projectiles and the tactic of trying to board the enemy; his ships drew slowly forward until they were within fighting distance of his adversary's fleet.

Here is what Plutarch writes: *« Though the struggle was beginning to be a close range, the ships did not ram or crush one another at all, since* ***Antony's owing to their weight, had no impetus, which chiefly gives effect to the blows of the beaks****, while Caesar's (Octavian) not only avoided dashing front to front against rough and hard bronze armour, but did not even venture to ram the enemy's ships on the side.* (2) *»* This explanation which we have already mentioned -see above- does not stand up under close scrutiny: in a frontal attack, the greater the bulk of the moving ship, the more serious the damage inflicted on the enemy . . . unless the frontal attack is handicapped not by the weight of the vessels but by the fact that they are unable to acquire enough impetus for the blows to be effective. But, when the enemy line is one and a half kilometers away, there is plenty of scope to reach the necessary speed, approximately 9 knots. Octavian's tactics are -given the lesser tonnage of his ships- as logical as Antony's are incomprehensible. Because, if we are to believe Plutarch and Dio Cassius, Antony deliberately chose to keep his vessels at a standstill and then to use projectiles and try and board the enemy. As historians in antiquity are wont to do, they fictitiously recreate Antony's and Octavian's speeches before the battle. Here is what Plutarch has the former say: *« Antony visited all his ships* ***in a row-boat,*** *exhorting the soldiers,* ***owing to the weight of their ships, to fight without changing their position, as if they were on land. He also ordered the masters of the ships to receive the attacks of the enemy as if their ships were lying quietly at anchor, and to maintain their position at the mouth of the gulf, which was narrow and difficult.*** (3) ***»***

Dio Cassius has him make a similar sort of speech: *« See* ***the length and beam*** *of our vessels, which are such that even if the enemy's were a match for them in number, yet because of these advantages on our side they could do no damage either by charging bows-on or by ramming our sides. For in the one case* ***the thickness of our timbers,*** *and in the other* ***the very height of our ships,*** *would certainly check them… »*

As for Octavian, this is what Dio Cassius has him say: *« Will they not by* ***their very height and staunchness be more difficult for their rowers to move and less obedient for their pilots?*** (4) *»*

But -let us say it once again- these are fictitious speeches and their function is none other than to cover up an incomprehensible anomaly in Antony's choice of tactics: because his ships were much bigger in size, he should

have opted for a frontal attack -charging bows- and ramming the enemy- which would have been more likely to succeed and more deadly.

Modern historians have paid little attention to this particular aspect. For the most part they have accepted the two explanations given by ancient sources for Antony's absurd tactical decision:

1. Antony's crews were not experienced enough. This is exactly why Antony shouldn't have chosen to fight at close quarters and to try and board his adversary's ships; it is the sort of tactic that requires quick and complex maneuvers in order to taunt or to avoid the enemy who, actually, turned out to be much more proficient at it.

2. Antony's ships were slow, heavy and unwieldy monsters. This statement is very likely to have been far from true although it has always been universally relayed. Florus, for instance, wrote:

« [Antony's ships] « having from 6 banks of oars to 9, and being mounted with towers and high decks, they moved along like castles and cities, while ***the sea groaned and the winds were fatigued. Yet their magnitude was their destruction.*** (5) *».*

Yet the *rostra* which have been excavated by archeologists in various parts of the Mediterranean and a study of the cavities in the *rostra* from Antony's vessels which adorn the *Tropaeum* erected by Octavian at Actium have revealed that the difference between triremes and decaremes is not mathematically proportionate. Thus, a decareme was not three times as long as a trireme but only twice as long, approximately. The difference resided mostly in the tonnage and so in the draught. Therefore, contrary to legend, Antony's largest vessels were not great monsters which were impossible to maneuver, even if they were less easy to move and turn than triremes or *liburnae.*

This legend dates back to Antiquity. How did it originate? Its roots are certainly to be found in Augustan propaganda whose aim was to stress that victory over vessels presented as monstrous sea creatures had been obtained by ships built by and for men. But the primary reason why it was so widely believed is that in Plutarch's, Florus's and Dio Cassius's day -one or two centuries after the battle- big ships like those with 6 or 10 rowers per bench- hadn't been built in a long time. In fact, they hadn't been built since Actium because the Mediterranean -*mare nostrum*- , which was now at peace only required the attention of a "maritime police" made up of much smaller vessels. For Pliny, Vitruvius and Vegetius, living under the Emperors, the quinqueremes are the biggest ships there are. Doubtless, Antony's largest vessels were, despite their size, quite effective in battle.

Out of all this, two bare facts are worth noting: 1. *Antony's ships remained motionless for a long time*. 2. *Then, they were difficult to move*. Why? Two details in a text which I have already quoted -see above- cannot fail to intrigue: 1. Why does Antony visit his ships in a row-boat in order to exhort his troops instead of cruising in front of his fleet in his command decareme? Indeed, it was contrary to common practice in ancient times for a leader to address his soldiers from below. It is as if Antony had been unable to use his flagship to move about. 2. Why does Plutarch have him tell his sailors to "*mind the difficult mouth of the gulf* "(6)? What particular dangers could have lurked in this narrow channel that ships have to go through to leave the Ambracian Gulf and reach the open sea?

The elements presented *supra* do not enable us to answer these last two questions nor those previously asked about the reason for Antony's ships being at a standstill and for his absurd tactics. Is it possible to go any further?

It is necessary here to add to the file two pieces of evidence, which have so far gone more or less unnoticed. The first is a passage by the poet Propertius, a contemporary at the time of Actium. In an elegy written in 16 BC, he recalls this battle, which became the basis on which Augustus built his regime. Before the battle, Apollo is supposed to be addressing Augustus (Octavian) thus: *« Do not fear that their ships are winged with a hundred oars:* ***their fleet rides an unwilling sea.*** (7) *»*

The language is certainly poetic with the oars being compared to wings but the main point, that which we must remember, is that the sea *is unwilling* to let Antony's fleet ride it.

The other document to be added to the file is much more telling and it is quite surprising that it isn't mentioned more often. It is a passage by Dio Cassius: *« When they (Antony's soldiers) set sail at the sound of the trumpet, and with their ships in dense array drew up their line* ***a little outside the strait and advanced no further****, Caesar (Octavian) set out as if to engage with them, if they stood their ground, or even to make them retire. But when they* ***neither came out against him on their side nor turned to retire, but remained where they were, and not only that, but also vastly increased the density of their line by their close formation, Caesar checked his course, in doubt what to do.*** *He then ordered his sailors to let their oars rest in the water, and waited for a time; after this he suddenly, at a given signal, led forward both the wings and bent his line in the form of a crescent, hoping to surround the enemy, or otherwise to breach their formation in any case. Antony, accordingly, fearing this flanking and encircling movement, advanced to meet it* ***as best he could,*** *and thus relunctantly joined battle with Caesar* (8) *»*

This account is much more detailed than Plutarch's description of the same stage of the battle. It is also slightly different, probably because the original source is not the same. What we learn from it is that hardly had Antony's vessels come out of the narrows that they stopped moving, causing a "bottleneck" behind them. This unexpected turn of events surprised Octavian. Plutarch corroborates this. Then, according to Dio Cassius, it was Octavian who was responsible for engaging; according to Plutarch, those responsible for engaging were Antony's troops because they were eager to fight. But, in any case, it was never Antony, Antony who was unwillingly compelled to do battle in conditions described as being less than favorable. In this passage,

there is no mention of a deliberate tactical choice on Antony's part to try and board the enemy; the way the battle was waged was obviously dictated by outside circumstances with Antony behaving as if he were paralyzed.

To conclude, it seems very clear, after examining ancient sources, that *something happened* which prevented Antony from launching, as was expected, his fleet against the adversary's fleet, taking advantage of the greater bulk of his ships to ram the enemy. Instead of which, he was forced, first of all, to remain *for a long time at a standstill*, to the great surprise of his adversaries, letting his vessels form a bottleneck behind his frontal line. And then, afterwards, compelled by the enemy to do battle, he advanced slowly towards them, which made ramming impossible. All that remained for him to do, then, was to get close to his opponent's vessels and try and board them, hindered though he was by the sheer size of his ships. Contrary to what our sources would have us believe, he did not *choose* these tactics, but was compelled to use them for some unknown reason. The aim of this study is, indeed, to try to find out the truth about this unknown reason.

1. Plutarch, *Life of Antony, 65*, 6-8*;* cf. Cassius Dio, *Roman History,* 50, 23, 2
2. Plutarch, *Life of* Antony*,* 66, 1
3. Plutarch, *Life of* Antony*,* 65, 4
4. Cassius Dio, *Roman History,* 50, 29, 2
5. Florus, *History of the Roman people, from Romulus to Augustus,* 2, 21, 5
6. Plutarch, *Life of* Antony*,* 65, 4
7. Propertius, *Elegies,* 2, 16, 37-38; cf. 4, 6, 47-48
8. Cassius Dio, *Roman History,* 50, 31, 3-5

9.2 SUPPLEMENTARY INFORMATION ON LINGUISTICS

For several centuries, from Ancient Greece until the 16th century, it was said, and repeatedly so, that a small fish called echeneis had the magic power of holding back ships when it latched onto their hulls. Nineteenth century naturalists, such as B. G. de Lacépède, took a rather caustic view of this ancient tale: “From the days of Aristotle until the present this animal has been the object of constant attention; its shape has been examined, its habits have been observed and its physical characteristics have been scrutinized. Not only was it considered to possess magic properties, absurd abilities and ridiculous strength, but it was viewed as a striking example of the occult qualities dispensed by nature to its offspring. It appeared as a convincing proof of nature’s qualities, secret in their origins and in essence unknowable; the fish was honored in the imagery of poets, in the analogies of orators, in travelers’ narratives and in naturalists’ descriptions. [...] How many fables and errors have been accumulated in such passages, which are also stylistic masterpieces?” (1) Nowadays, the spontaneous reaction is indeed to wonder how people could have believed in such improbable powers for so many centuries. One of the explanations is perhaps to be found in the argument put forward by the historian M. Bloch, (2) who takes the example of the remora (the Latin name of the echeneis) to demonstrate how, before the development of critical methods of checking information and witnesses in the reconstruction of history, the most intelligent minds accepted a given fact without questioning its veracity. It was based on tradition, all the more so when those “facts” were handed down by renowned minds of the past. But while this may explain the transmission of the legend, it does not solve the mystery of its origin: where did the legend begin and when? What exactly was said about the echeneis in Ancient times? When was the fish first considered to possess such extraordinary powers? **It is our intention to explore the context in which the legend was born through rigorous analysis of Ancient sources**, in order to better understand the link between beliefs and their unavoidable imaginary elements, and knowledge: the facts and discourse which they gave rise to, the level of knowledge and, perhaps, their exploitation by the elite.

Research into the occurrences of the substantive noun *echeneis* in Greek literature, and its Latin translations in the terms *mora,* and *remora*, also including the variants *remeligo*, and *remirora*, reveals the relative rarity of such texts: **only fifteen or so authors in a corpus which covers a period from the 5th century B.C. to the 7th century A.D**. The fish is mentioned in various works: naturalists’ descriptions of fish in natural history treatises or in didactic works (Aristotle, Ovid, Aelian and Oppian (3)); poetic embellishment (in Lucan’s writings, (4) for instance, where it appears as an ingredient in a magic potion); in a chapter from an encyclopaedia (Pliny the Elder (5) combines a descriptive passage of the fish with historical anecdotes and a commentary on its associated magical properties); a banquet anecdote (Plutarch 6); an allusion in the letters of a Roman statesman (Cassiodorus 7); in the writings of later commentators (grammarians or Church Fathers eager to explain the complexity of the world through etymological explanations, or through the collection of pagan knowledge which was reinterpreted in the light of the greatness of the divine: Donatius, Servius, Isadore of Seville and Ambrose 8). In addition to the noun *echeneis*, the adjective *echeneis, idos* which carries the meaning “which stops or holds back vessels”, (in Aeschylus during the 5th century B.C., Nonnos of Panopolis during the 5th century A.D. and Theaetetus Scholasticus during the 6th century A.D. 9).

This quick survey shows that the occurrences are somewhat marginal. **The most defining text is without doubt that written by Pliny the Elder a few years after the Battle of Actium,** in which he insists on the strange immobilization of Mark Antony’s fleet during that historical event, attributing the cause to the powerful action of the fish to which he gives the name *mora*, a noun which also means “a delay, or lateness” in Latin. Yet there are two striking elements: firstly, among Ancient historians who provide a detailed description of the Battle of Actium (Plutarch, Orosius Florus, Dion Cassius), none

explicitly mention the fish, not even Plutarch who refers to it in his *Table Talk* but not in his *Life of Mark Antony*; secondly, there is a concentration of occurrences in the 1st century A.D., as regards the longer descriptions (Ovid, Lucan, Pliny, Plutarch 10). **The "legend of the echeneis" would appear to be a relatively late construction**, containing several strata, the earliest of which goes back to Aristotle, with more frequent references clearly appearing from the 1st century A.D. onwards, in other words around the same time as the Battle of Actium. Aristotle does not indicate that the fish is able to hold back ships; historians writing before or at the same time as the battle between Mark Antony and Octavian do not see fit to mention it either. It is therefore tempting to postulate that the legend was born during the Roman recovery of a Greek belief (mainly transmitted through oral tradition) in the magic powers of the fish (Aristotle describes its use in making magic potions and to delay court trials and slow down justice), to which the Romans gave a new lease of life based on the events at Actium, in order to increase the marvellous powers of the fish.

One way of disentangling the skein of suppositions is to carry out an analysis of the discourses which accompany references to the fish and its exceptional powers throughout classical and late Antiquity. These discourses are clustered around five poles which need to be considered in greater detail:

magic, nature, reason, religion and politics.

9.2 (a) Magic power.

Chronologically, the first text which has been preserved is Aristotle's (11) which mentions the use of the fish to slow down court trials and in the making of potions. Lucan (12) mentions it as an ingredient for a resurrection spell in the description of witchcraft in Book 6 of the *Pharsalia*. Pliny (13) refers to the belief held by some Greeks that if worn as an amulet the fish prevents miscarriages or favours delivery at childbirth (in which case it is given the name *odinolytes*). Pliny places the fish among the list of antiaphrodisiacs, (i.e. reducing amorous passion), along with "rhinoceros skin taken from the left forehead and attached in a lamb's skin". He also repeats Aristotle's indications of its use for the making of potions (and more specifically erotic potions) and for court trials (to slow them down). We may therefore suppose that there was an idea of "mimetic" functioning despite the fact that the texts make no specific reference to this idea, and there is no indication of whether there was a *magus* involved in ordering the action through magic formulas which might use the fish symbolically to obtain this effect, or whether the power of the fish is attributed to its physical characteristics, say of a magnetic nature. Might it be the case that people believed, by analogy, that the fish also had the extraordinary power to hold back ships to the extent that it could even slow them down to a complete standstill? The only document in which the holding back of a ship is explicitly linked to magic intervention is in one of the later texts, the *Cyranides*, a compilation of works on magic written between the 1st and the 8th centuries A.D., in which it is claimed that if just a few echeneis bones are sewn into horse leather and then brought aboard a ship, hidden in clothes, then the ship will not be able to move forward (14).

We should not judge too quickly. Beyond the folklore of oral beliefs or popular traditions, magic did have a very real impact on people's attitudes. The long defensive speech from the 2nd century A.D. in which Apuleius denies the charge of having charmed his wife by the use of magic, notably through the administering of a fish-based potion, provides sufficient proof of such beliefs (15). Even Pliny, who shows himself to be sceptical as regards magic and who is keen to demystify the sham of magic at a time of firm belief, nevertheless describes some strange recipes, such as attaching a bramble-frog to the body in a piece of fresh sheep-skin, in order to put an end to love (16). Closer to our own subject, he also indicates that a boat can be held back by a no less irrational expedient: bringing the right foot of a tortoise on board (17) !

We need to return to one decisive element: the fish attaching itself to the boat. The remora certainly does attach itself to surfaces using a flat disc on its head which has cartilage blades which act as a sucker. By creating a vacuum between these blades, or by hooking the spines which cover the rear edge of the blades, the fish attaches itself to rocks, boats or to other creatures. Quite understandably, all the authors insist on the fish's ability to attach itself. Yet the curious thing is that the sole ability to attach itself seems to be used to explain the slowing down, or even the stopping of a ship. Pliny implicitly suggests there is an immediate effect on a storm when the fish attaches itself to a vessel ("It easily puts an end to force and tames the fury of the elements, effortlessly, merely by attaching itself" (18)). Is this merely a form of poetic hyperbole, which takes pleasure in developing an *adunaton*? Isidore repeats Pliny, almost word for word: "The ship seems to behave as if it were anchored to the sea and remains motionless, not because the fish is holding it back but because it has attached itself to the ship" (19). This implies that the fish does not hold the ship back as such, but rather its astonishing action is revealed only by its attaching itself. The key term which is repeated in almost all of the texts is *adhaerere*. An accurate interpretation is essential here because this is where we may understand what the authors intend by the term "adhere": of course this means first and foremost that the fish is attached and cannot be detached; yet this single element appears to explain the cause and effect relationship between the fish attaching itself to the surface and the resulting immobilization of the object, without raising any further questions.

According to L. C. Watson (20), *adhaerere* corresponds to the Greek verb *kollô* "to stick", common in Greek magical papyrus which describe love charm rituals. This "sticking" creates a physical "link", the equivalent of *katadesmos* of love charms. Indeed, the terms used by several authors (regarding the constraint, the obedience, the preventing and the link with the boat) suggest a magical connection (cf. Oppian (Hal. 1, 232-3 *ouk etelousa, pepedètai; 235-6 desma; 242-3 pedèn*); Aelian (N.A., 2, 17 *pedèsas*); Nonnos (Dion. 21, 45-8 *katasketon desmo* et 36, 367-9

desmo; Pliny H.N. 32, 2-6, *tenere uincta*). If our analysis is accurate then this signifies that it was believed that a boat could be immobilised in the same way that a man could be linked to a woman in an erotic context. Cassiodorus, who does not believe in the fish's power whatsoever, uses the verb *adligare* (21) to describe the way in which the echeneis bites the sides of the ship; yet this is the verb which is used four times by Pliny in the form of the participle *adalligatus,* (22) to designate the wearing of an object in the shape of an amulet in a magical context. He also says that the boat seems to be stuck (*infixum*(23)) to the surface of the sea.

These examples show that a specific vocabulary with a high degree of magical connotation was projected onto the fish, probably derived from the Greek beliefs in magic which are attested to by Aristotle — but this does not necessarily imply that the authors who use such terms actually believe in any magical power. This point therefore needs to be examined more closely. The notion of a magic link does at any rate explain what Pliny presents as an incongruous detail: when an echeneis was found under Caligula's ship, there was general surprise at the fact that the fish no longer had any effect when it was taken on board, as if any slowing down effect due to mechanical force or traction was out of the question. (24)

9.2 (b) One of the wonders of nature.

When Pliny mentions the astonishing characteristics of a fish able to hold back a vessel, he sees this above all as an irrefutable indication of the mysterious power of nature. The action of a small fish which is able to resist the fury of the elements leads to a consideration of the theme of nature triumphing against itself after a struggle between antagonistic forces. As we have seen above, he provides no explanation for this power, merely presenting it as a fact of nature, proven by observation which is sufficient to validate that fact. Two historical anecdotes are used to support this assertion: first of all, the Battle of Actium, and secondly the immobilization of Caligula's ship during a voyage he undertook between two Latium coastal towns. Pliny provides no further analysis on how the fish functions and concludes his description with a general formula, widening his demonstration to include a broader group than the echeneis species: "there is no doubt in our minds that these animals [in other words all the astonishing creatures produced by nature] have identical powers". To illustrate this power, he quotes a remarkable precedent to be found in the similar action of sea shells which stopped a Greek expedition during the time of Periande: these were marine gastropod molluscs called Venus shells which have a porcelain-like inner layer.

This belief in the power of nature follows a line from the paradoxography works which flourished in Greece from the Hellenistic period onwards. The authors of these works applied themselves to compiling natural wonders, attempting to astonish or amuse their readers, through exotic or sensational descriptions. Viewed from this perspective the prowess of the echeneis is no more extraordinary than that of the phoenix, the unicorn or the basilisk, and it is not unusual to read surprising stories such as that of the literate pachyderms who can read Greek (25) or that of the pilfering octopuses which climb trees to steal fruit (26). Such anecdotes correspond to the taste of their readers who were keen on such curiosities, as is revealed by the development of the notion of prodigious feats to be described below.

9.2 (c) Rational interpretations.

It might be expected that the appeal to common sense might prevail, or at least be well represented, but this is not the case. Rational interpretations are in the minority. In *Table Talk*, (27) Plutarch explains that boats slow down because of the algae which build up on the hull and the rudder, especially when the boat has been at anchor for a long period of time. The keel then becomes gorged with water and therefore accumulates a large amount of algae, the wood becoming covered with moss and losing its power of penetration in the water, while the waves which strike this sticky mass do not bounce off it effectively. Plutarch, who was aware of the phenomenon of magnetics, clearly excludes the latter explanation, which is put forward by one of his guests in an attempt to call on common sense and deconstruct the legend by reversing the relationship of cause and effect: he suggests that it is the presence of algae which attracts the fish and not the fish attached to the boat which slow it down. The idea of a whole shoal of fish having an influence on the advance of a ship might seem slightly plausible but this hypothesis is never suggested by the Ancient texts, contrary to the Renaissance emblems in which clouds of sucker fish appear attached to the keels of boats. Five centuries after Plutarch, one of Cassiodorus's letters suggests human causes: the late arrival of boats loaded with important wheat cargoes was not due to the fantastical effect of an echeneis but rather to the negligence of sailors who may have fallen asleep, or who simply did not care. The humour and cultured elegance of the statesman is combined with moral judgement: "the echeneis which slows them down is their own venality, the conch stings, it is their own unlimited passions". (28)

9.2 (d) A divine warning.

Pliny claims the echeneis is: "a fish which is worthy of counting among the omens", (29) thus superimposing the religious prism over a phenomenon which thus acquires a new dimension. Roman religion cannot be invoked without mentioning the importance of monstra, the spectacular signs which it was believed were sent by the Gods in order to warn mankind that there was a message for them. The monstrum designated both the phenomenon of the apparition which revealed divine will and, at the same time, the exceptional creatures which transmitted this sign. In our case this is a strange fish endowed with supernatural powers. The echeneis does indeed belong to the family of "monsters", and, to be more precise, it is a prodigious animal: it is thus to be distinguished from the monstrous teratological creature such as the four-legged snake; it is also to be distinguished from what we could term "prodigial" animals, that is to say ordinary animals which suddenly behave in a strange way thus announcing

a divine message, such as a bird stealing embers from a bonfire. The prodigious characteristic of the echeneis is its species' singular and intrinsic ability to hold back boats, as is repeated in Ancient etymologies. Another surprising aspect of this fish may be added: in the impressive list of prodigious animals drawn up by Julius Obsequens only two involve fish. The act of one single fish such as the echeneis is thus exceptional.

Pliny considers the echeneis to be a bad omen because it announced Caligula's death. Pliny's testimony reveals the transformation of the echeneis as a Roman prodigy during the Roman Empire: firstly, the prodigy, which was initially a sign of divine intervention in human affairs, had evolved to become much more an omen, of a divine nature. Secondly, the prodigious fish became more specific, no longer necessarily referring to a group but rather to the specific destiny of one individual. The anecdote of the role of the echeneis at Actium thus takes its place in a series of omens which announce the defeat of Mark Antony, revealing to the eyes of the world that nature and the Gods had chosen that day to side with the Octavians. A linguistic detail may corroborate this reading: the Latin term mora, and its synonym remora, which came to replace the former, present assonance with an Ancient term connected with omens, remur, which designated a bird of ill omen. It is therefore possible that the remora may have sounded as if it carried negative connotations.

In late Antiquity, Oppian (30) also describes the fish as prodigious, but in a figurative sense, implying that it was among the prodigious visions produced by dreams, with a corresponding loss of its divine quality. Yet Isidore of Seville and Ambrose reintroduce the religious interpretation by detecting a reflection of the Creator's omnipotence in the extraordinary power of the creature. "Do you think that so much power has been given to it without a gift from the Creator?", (31) writes Ambrose, who uses the example to demonstrate that a fish such as the echeneis is used to remind mankind of its limits and of its condition, by placing it in a situation in which it can only expect help and safety from the Lord when faced with the perils of life.

9.2 (e) Political exploitation.

As has just been suggested, the appearance of signs and their interpretation is always of interest for political leaders. One of our hypotheses is the following: the victors of war, Octavian and his followers, may have spread the rumour of the intervention of the echeneis for propaganda purposes, in order to prove that the Gods had decided to side with them. Such political exploitation of religious beliefs was not new. The great political events of the end of the Republic were accompanied by prodigious events which poets and historians had busily chronicled: rains of blood, rivers reversing their flow, statues of the Gods covered in sweat, a mother giving birth to a snake... During the transition between the Republic and the Empire, towards the end of the 1st century B.C., the historiographical tradition reports a number of omens regarding Octavian-Augustus and the imperial family, destined to an exceptional fate: Octavian was born of the union between Atia and Apollo-snake; (32) an eagle is said to have stolen a piece of bread from him and then returned it to him, a sign of his future sovereignty; (33) Livia is said to have warmed an egg in her hands hatching a chick with a huge crest, thus announcing prosperous offspring and the gaining of power as represented by the crown symbolism of the crest.

During the period immediately preceding the Battle of Actium, a long series of prodigies were reported, often involving animals. To take the example of one single historian, Dion Cassius describes how, in 36 B.C., a fish jumped from the sea to the feet of Sextus Pompeius, and the diviners told him that he would be master of the seas; (34) in 32 B.C., (35) a monkey interrupted a ceremony in the Temple of Ceres, a victory statue fell on the stage of a theatre, Etna erupted, a two-headed snake appeared in Etruria eventually to be struck by lightning, a statue of Mark Antony wept floods of tears, a wolf entered the Temple of Fortune, a dog was devoured by another dog during a horse race in the circus; in 31 B.C., just before Actium, Cleopatra fretted about swallows nesting on her admiral's ship, lightning knocked down the statues of Mark Antony and Cleopatra erected by the Athenians; (36) and then it rained blood, weapons appeared in the sky, drums and flutes were heard, a giant snake appeared, the statue of Apis began lowing and comets were seen….(37) In this context the attributing of the incomprehensible immobilisation of Mark Antony's vessel to the action of an echeneis and the view that this implied that the Gods had intervened in human affairs thus constituted a perfectly plausible hypothesis. The legend may have begun just after Actium, during the ten-ship dedication ceremony which was offered by the victors just after the battle. Only the Octavians could have participated in hauling the ship out of the water. The legend may have originated "from the fact that when the ship of the defeated admiral was hauled on land to be exhibited as a trophy, a remora type fish was discovered on the hull". (38) Mark Antony's boat had spent time in the waters of the Bay of Preveza and Vonitza and the hull was probably laden down by parasitic plants and animals, and it is plausible to suggest that this may have attracted fish. The witnesses to the ceremony probably associated the immobilisation of the boat to the presence of one or more fish parasites, due to the widespread belief in the Mediterranean of the immobilising power of certain sea shells or fish. (39). These beliefs may have been seized upon by the Octavians to crown their victory with divine support. (40)

This anecdote is also present in Octavian's Neptune like propaganda after Actium: he claimed to have been given mastery over the seas and that this was proof of his divine election. Used for ideological purposes, the legend of the remora suggested through its imagery that the powerful Mark Antony, his vessels like monstrous centaurs, could do nothing against the will of the Gods, who could brandish a tiny fish to put a permanent end to his advance. Conversely, a description by Propertius represents Octavian as the worthy protégé of Apollo, (41) who appeared over the stern of his boat surrounded by a triple

flame. A gloss by Servius (43) commenting on one of Virgil's lines suggests that the exegetes of late Antiquity thought that the fish had been sent by Neptune to hold back Mark Antony.

After a long period during which the echeneis was purely considered from ichthyological perspectives, critical discourse on the fish is today mostly the fruit of research by researchers in the arts and humanities. The story of the prodigious little fish and the commentaries which it gave rise to has led to four main approaches: linguistics, mythology (more specifically the mystification of history), the transmission of texts and the influence of the legend in European literature.

As regards the linguistic approach, the Ancient authors named the fish after the legend it is associated with, considering from the start that the name derived from the creature's powers. Contemporary linguists partly confirm this interpretation. They analyse the noun as a zoonym made up of two juxtaposed radicals, a verb (*echein* to hold, to hold on to) and a noun (*naus* the ship), associated in a noun which does not reveal the syntactic relationship which unites the two radicals, as is usual in this type of compound. If we look for the implicit sentence which would provide the semantic base for the creation of this noun there are two possibilities due to the fact that the verb may function either transitively or intransitively: "he holds on to the boat" or "he holds back the boat". This is where the ancient etymology (the fish was given this name because it holds back the boat) differs from contemporary linguistic reinterpretation (the compound may also signify that fish holds on to the boat). **The modern day supposition is that the animal "which attaches itself to hulls" (an intransitive construction which probably initially led to the term in Greece) was later perceived, at a time and period still to be determined, as the animal "which holds back boats" (transitive construction)**. The legend may therefore originate in an etymological shift.

A second direction concerns the spread of the legend and its relations with the field of myth. As Pastoureau has written, the collective imagination of a period allows us to understand that period as surely as the events which took place and the prevalent living conditions: "The historian must never excessively oppose imagination and reality. For the historian, as for the ethnologist, the anthropologist or the sociologist, imagination is always part of reality." (43) To take into account this imagination involves close study of a specific cultural context and reasoning within the Ancients' representation of the world. A reconstitution of the legend therefore involves the job of discriminating between what has been observed, believed, thought and imagined. Knowledge 2,000 years ago was considerably different from ours today, even in the field of an apparently accessible field such as zoology: **people were able to believe in a fish with supernatural powers in the same way that they believed in the existence of fantastic creatures such as the griffin, the phoenix, the unicorn, the manticore and the amphisbaena**, or more extraordinary still, in the metamorphosis of storks into women in the Oceanid islands. (44) The frontier between fable and reality was thus a moveable feast. Aristotle confirms the existence of a lemnian billy goat with two udders near its penis which were milked to make cheese. The same is true of **monsters, the cynocephalus, hermaphrodite foal and the hippocentaur**. The echeneis also needs to be considered alongside **imaginary marine creatures, mermaids, tritons, Nereids, Charybdis, Scylla**, whales, swordfish and all the dangers that are supposed to inhabit the troubled depths of the subaquatic world. It must lastly be viewed in relation to a whole **bestiary connected with the exercise of power** (Augustus' parrot, the salt fish caught by Mark Antony, Cleopatra's viper and dissolved pearls), their fantastic nature being heightened by the fantastic habits believed to be widespread in a mythic and sulphurous East.

If the legend was handed down through the centuries from Classical Antiquity until the Renaissance, it is without doubt due to a process which needs to be fully explored: that process is based on a **respect for tradition, which upholds the supremacy of text**. Trust in the authority of a source sometimes annihilated all critical thinking. Over a long period "any fact which was claimed in writing, was, three-quarters of the time, accepted as fact." (45) This form of unquestioning transmission is demonstrated by the filiation which may be observed between Aristotle, Pliny who translates the former, Cassiodorus and Isidore of Seville who quote the Latin encyclopaedist almost word for word, and the French texts of the 16th century which translated them in turn. From this perspective, the texts are not only to be viewed as proof of what was said and thought, but also as having generated discourse and reactions to such discourse. When the text becomes a reality in itself, the story of a text sometimes ends up replacing reality.

Lastly, the circumstances surrounding the **spread of the remora legend in European literature** need to be retraced, as well as the place of the legend in medieval bestiaries, alchemy, the marked upturn in interest for fish in the 16th century, probably due to two historic events: the Battle of Preveza and the crossing of the Cardinal of Tournon (Francisco Massari, Edward Wotton, Rabelais, Conrad Gesner, Jérôme Cardan, Rondelet, Alciat, Ambroise Paré and Montaigne), the wind of questioning in the 17th century (Kircher, Aldrovandi, Gaspar Schott, Mersènne le Père, François Bernier and Du Tertre), the refuting of its power during the Enlightenment (Diderot, J. Valmont Bomar, C. Favart d'Herbigny and Linnaeus), its metaphoric use during the 19th century (Michelet and Balzac), and its legacy in the 20th century (Rezvani and Borgès).

1. Histoire naturelle des poissons, t. 5, Ladrange and Verdière, 1831, p. 192.
2. Apologie pour l'histoire, A. Colin, 1964, 5th edition, p. 65.
3. Ar., History of Animals, 2, 14 ; Ov., Halieutica, 99 ; El., On the Characteristics of Animals, 1, 36 ; 2, 17 ; Op., Halieutica 1, 212 et seq.
4. Luc., Pharsalia, 6, 675.
5. Pl., Natural History, 9, 41 and 32, 1.

6. Plut., Moralia, 2, 7.
7. Cass., Variae, 1, 35.
8. Don., on Ter, Andria, 739 ; St Ambr., Hexameron, 5, 10, 93 ; Serv., on Aen. 8, 699 ; Isid., Origines, 12, 6, 34.
9. Esch., Agamemnon, 149 ; Non., Dionysiaca, 13, 114 ; Anthologie Palatine, 6, 27, 5.
10. Cf. above.
11. History of Animals, 2, 14.
12. Pharsalia, 6, 675.
13. Natural History, 9, 41.
14. Cyranides, 1, 12.
15. Ap., Apologia, 29-41.
16. Natural History, 32, 50.
17. Natural History, 32, 4, 41.
18. Natural History, 32, 1 , 2 : non retinendo aut alio modo quam adhaerendo.
19. Origines, 12, 6, 34 : non retinendo sed tantummodo adhaerendo.
20. The echeneis and erotic magic, Classical Quaterly 60 (02), p. 639-646.
21. Variae, 1, 35, 3.
22. Natural History, 13, 50.
23. Cass., Var., 1, 35, 3.
24. Natural History, 32, I, 5.
25. Pline, Natural History, 8, 6.
26. Elien, On the Characteristics of Animals, 9, 45.
27. Moralia, 2, 7.
28. Variae, 1, 35, 4.
29. Natural History, 32, I, 4.
30. Halieutica, 1, 236.
31. Hexameron, 5, 10, 93.
32. Dion Cass., Roman History, 45, 1, 2 ; Suet., Life of Augustus, 94, 4.
33. Suet., Life of Augustus, 94, 11.
34. Roman History, 49, 5.
35. 50, 8.
36. 50, 15.
37. 51, 17.
38. S. Barbara, Zoologie et paradoxographie en marge du bellum Actiacum, Schedae, 2009, p. 14., quoting the analysis of W.W. Tarn, The battle of Actium, JRS, 21, 2, 1931, p. 186.
39. Cf. the anecdote related by Pliny regarding the expedition of Periander's ship which was stopped by shells, an event which is commemorated in the Temple of Venus in Knidos (Natural History, 9, 25, 41).
40. This hypothesis, which suggests that the legend was invented by the victors, is more plausible than the others, notably the hypothesis which suggests that the rumour was begun by the losers in order to reduce the shame of defeat, or by Cleopatra in order to castigate the Alexandrians. Pliny's interpretation would appear to confirm the first hypothesis: the immobilisation of Mark Antony's fleet by the remora in order to highlight Octavian's naval strength. He believes the amazing small fish prevented Mark Antony from launching his attack.
41. 4, 6, 47-50 and 27-54.
42. Ad Aen. 8, 699.
43. Les animaux célèbres, Paris, Bonneton, 2001, p. 9 : "L'historien ne doit jamais opposer trop fortement l'imaginaire et la réalité. Pour lui comme du reste pour l'ethnologue, l'anthropologue ou le sociologue, l'imaginaire fait toujours partie de la réalité."
44. This is described in the works of Aelian.
45. M. Bloch, op. cit., p. 65.

9.3 SUPPLEMENTARY INFORMATION ON NAVAL ARCHETECTURAL

From historical reports (Pliny the Elder, 1857; Martin, 1995), Octave presented a fleet composed of oared galley (classes from 2 to 5, namely bireme to quinqureme). The class refers roughly speaking to the number of rowers per bench (see SI on Mathematics). Unlike Octavian fleet was light, Antonian fleet was heavy with classes from 4 to 10 (class 10 is so-called decareme). As discussed in the supplementary information on Ancient History, the flag-ship of Antony, a decareme, was delayed for several hours whereas the Octavian ships moved freely. Moreover, the contemporary reconstruction of an ancient fifth century BC Athenian trieres by John Coates, John Morrison and Boris Rankov (Morrison, 1996; Morrison et al., 2000; Rankov, 2012) during the 80's and its tests thanks to sea trials since then allowed us to have access to the naval architecture plans of an ancient galley, with the help of the Trireme Trust. In addition, we benefited from the work of William Murray and the Institute for the Visualization of History who provided us with the 3D digitization of a ram, an ancient weapon that equipped the bow of ancient galleys (Murray, 2012). We used the so-called Athlit ram for our reduced model.

Concomitantly to the end of the Hellenistic era, the construction of such big boats was stopped, what Murray calls "the big ship phenomenon". The most delicate point of our study is the following assumption: we chose to consider that the dimensions of a decareme were twice those of a trireme, a strong hypothesis that we will try to justify. Firstly, the ancient reports insist on the gigantism of the biggest boats at Actium: Florus speaks of the Antonian ships "being mounted with towers and high decks, they moved along like castles and cities, while the sea groaned and the winds were fatigued. Yet their magnitude was their destruction". Historians would certainly argue about this point but in absence of direct evidence, we can only make hypotheses (Pitassi, 2011 for a sizes comparison between a 2, 3, 4 and 5 classes). Secondly, thanks to the archaeological studies of William Murray we have indirect evidence of the massiveness of the warships at Actium. Indeed, his team was able to identify the size of the biggest boats thanks to the study of the prints of rams in the sockets of the Apollo temple in Nicopolis. Just after the battle, Octavian dedicated to Apollo a trophy with all the sizes of rams taken on the Antonian boats, from class 1 to class 10. By multiplying the dimensions of a trireme by a factor of two in order to

get a decareme, the obtained draft and beam seem to be compatible with the extrapolations of the historians. Legitimate doubts could be formulated with respect to the length since a boat of seventy meters long would maybe imply technological constraints with respect to its building, stability and resistance to flexion. Hence, by doing so, we compensate somehow with the fact that we kept the same block coefficient (the ratio of the box volume occupied by the ship, here 0.37) for the trireme and the decareme. However, as we will see, the important parameter in the context of the naval battle of Actium is not the length of the boat but the respective ships draft (1m for a trireme and 2m for a decareme, see below) versus the water depth: it is very probable that we underestimated the draft of the decareme since 2 m could be increased easily up to 3 m because of the weight of the boats as constantly described by the ancient sources. Finally, we noticed that gigantic boats built for the naumachiae of Caligula in the first century were as long as 74 meters, the so-called Nemi boat (Carlson, 2002) despite the fact that they sailed on a calm lake and not in the Mediterranean Sea.

With interpolation, from historical data on the number of rowers per class galley (Pitassi, 2011, 2012; D'Amato, 2015), we can assume the number of rowers of a decareme (Figure SI1). We find a ratio of 605/170=3.55 rowers between a decareme and a trireme, this is consistent with the resistance ratio.

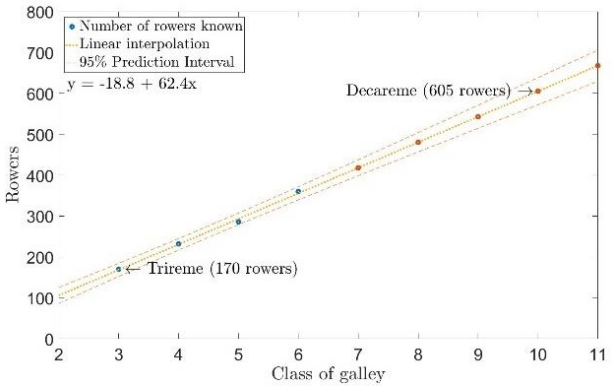

Figure SI1. Linear interpolation of number of rowers per class of galley.

9.4 SUPPLEMENTARY INFORMATION ON OCEANOGRAPHY

The Ambracian Gulf is a semi enclosed coastal system in Western Greece, with a mean depth of 26 m and a maximum depth of 63 m. The gulf is connected with the adjacent open Ionian Sea through an elongated and narrow channel, i.e. the Preveza - Actium Straits. Channel's length is about 6km while its width ranges from 0.8 to 2 km. Its eastern part, in the gulf's interior, is about 20m deep and 2.5 km wide, while the channel narrows gradually to the west, with its range reaching 0.8 km in the in the middle. At this extended shallow area, at the entrance of the Ambracian Gulf, the mean depth of which does not exceed 5 m, the battle of Actium took place. Nowadays, in the Ambracian Gulf's sill a navigational channel, of about 13.5 m deep, has been constructed (see Figures SI2 and SI3).

In the maps of Figures 1 and SI3, the reconstruction of the Ambracian Gulf's sill bathymetry, during the period of the Actium naval battle is presented. The main differences between the current and the ancient bathymetry of the area are: a) the artificial channel, which was drained in the 1970's, and b) the mean sea level, which was 75 cm, lower than today. The region where the battle took place, i.e. the gulf's entrance, was very shallow, characterized by a mean depth of about 2.5 m. The depths were progressively increased in both directions, toward the Ionian Sea and the gulf's interior.

A fjord-like water circulation, due to its oceanographic conditions and its morphology (Ferentinos et al., 2010; Kountoura and Zacharias, 2014), characterizes the Ambracian Gulf. Two large rivers, i.e Arachthos and Louros discharge large quantities of freshwater into the Ambracian Gulf (Therianos, 1974), resulting to the ecosystem's permanent water column stratification and to the reduced salinity of the surface layer. This water layer is usually well mixed, and its thickness is typically of the order of a few meters. The pycnocline layer's characteristics (intensity and extent) are spatiotemporally varied, under the influence of seasonal meteorological and hydrological changes in the area. Surface and intermediate (pycnocline layer) waters are freely connected with the open sea through the gulf's mouth. Denser water masses are trapped behind the sill, at the greater depths. Like in most fjord type basins, so in the Ambracian Gulf density variations of the open sea water are crucial for the water exchange, both above and below the sill level (Stigebrandt, 2001). At the entrance to the Ambracian Gulf semi-diurnal tide is prevailed with average range of 5cm and a maximum recorded range of 25 cm^3, while at the gulf's interior, the limited fetch of about 35 km^3 results to a low energy wave regime.

This study is focused on the gulf's sill area, which is of interest because of the interaction between the gulf's surface brackish water mass and the Ionian Sea's salty waters. This interaction, results to the development of a front, due to the presence of a horizontal salinity and density gradient, which extends from the sill's surface to its bottom. The area's water column behaves like a single layer, while its speed and direction are varied under the influence of wind and tidal phase. Hydrodynamic circulation regime, changes at the deeper parts of the region, where brackish water outflows at the surface and saline water inflows near the seabed, attaining speeds of up to 60 and 80 cm/s according to (Ferentinos et al., 2010). Summarizing, the area of the Ambracian Gulf sill is characterized of great oceanographic interest and many peculiarities, due to its morphology, its location and the interaction of currents, tides and wind.

The objective of the present study is to give a scientific explanation about the Antony's defeat in the Actium naval battle. As the truth is possibly connected with the area's oceanography, it is crucial to answer some questions about: 1) The circulation pattern in the study area today, 2) spatial distribution of the pycnocline in the study area

today, 3) The importance of morphology, tide and wind on the area's circulation pattern today and 4) The circulation and stratification pattern of the study area during the battle and their influence to the battle's outcome.

The current hydrodynamic conditions in the area of interest will help us to reproduce the prevailed water circulation during the battle. For this purpose, decisive factors will be the data and information that can be retrieved from the battle description in historical texts. Furthermore, a study of the area's: a) water column physicochemical characteristics, b) currents, c) tidal characteristics and d) meteorological parameters is essential.

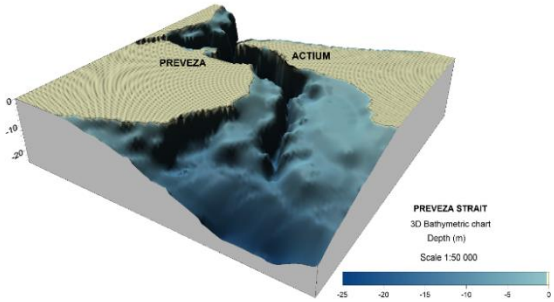

Figure SI2. Current morphological features of the Ambracian Gulf sill area. 3D block diagram.

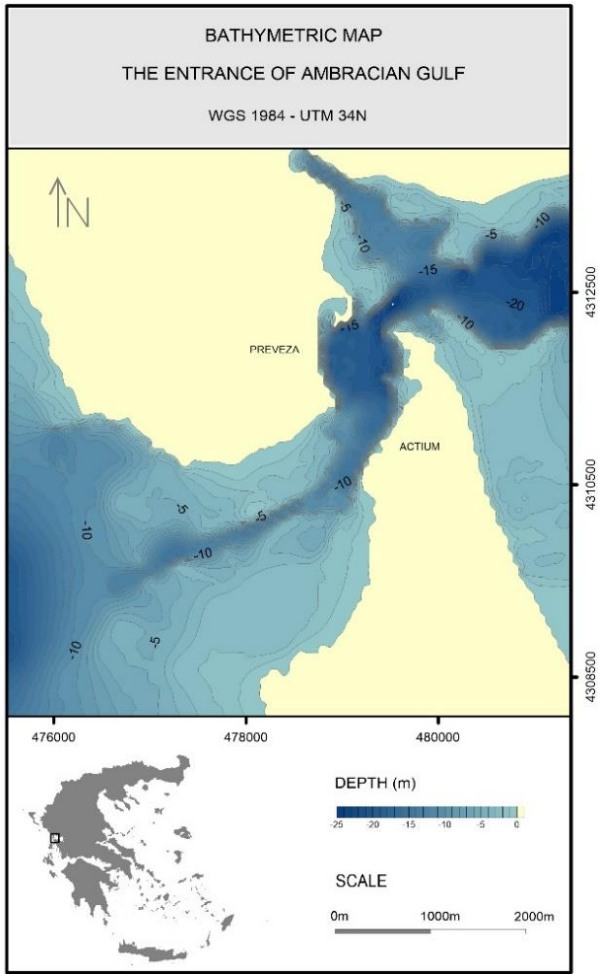

Figure SI3. The current bathymetric map of the Ambracian Gulf entrance.

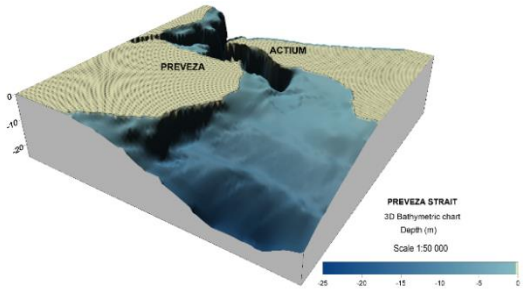

Figure SI4. Morphological features of the Ambracian Gulf sill area 2000BP. 3D block diagram.

9.5 SUPPLEMENTARY INFORMATION ON MATHEMATICS

The evaluations of the wave-making resistance for the maps is based on an analytical formula called the Sretensky formula (8). This formula is obtained by assuming the ship to be slender, and therefore the wave phenomena to be linear. Many experimental studies (see for instance (2)) have shown a good agreement between the results given by this formula and the data from experiments. This formula takes into account the water depth $\boldsymbol{h}$, the velocity of the ship $\boldsymbol{U}$, and the shape of the ship, given as an offset function f that defines the half-width of the ship for each point of the center-plane $\boldsymbol{(x,z)}$. The direction of motion of the ship is $\boldsymbol{x}$, and the depth is $\boldsymbol{z}$. The wave resistance according to Sretensky's formula hence reads:

$$R_W(U) = \frac{8\pi\rho g}{U^2}\int_{\gamma_0}^{\infty} \frac{I^2(\gamma)+J^2(\gamma)}{\left(\gamma^2 - \frac{g\gamma}{U^2}\tanh(\gamma h)\right)^{\frac{1}{2}}}\gamma d\gamma$$

Where $\boldsymbol{g} = 9.81\text{m}.s^{-2}$ and the coefficients $\boldsymbol{I}$ and $\boldsymbol{J}$ are given by

$$I(\gamma) = \lambda(\gamma)\frac{U}{2\pi}\int_{\Omega}\frac{\partial f}{\partial x}(x,z)\frac{\cosh\big(\gamma(h-z)\big)}{\cosh(\gamma h)}\sin(\lambda(\gamma)x)\,\text{dzdx}$$

$$J(\gamma) = \lambda(\gamma)\frac{U}{2\pi}\int_{\Omega}\frac{\partial f}{\partial x}(x,z)\frac{\cosh\big(\gamma(h-z)\big)}{\cosh(\gamma h)}\cos(\lambda(\gamma)x)\,\text{dzdx}$$

In which $\boldsymbol{\Omega}$ is the domain on which f is defined. The function λ is defined by

$$\lambda(\gamma) = \left(\frac{g\gamma}{U^2}\tanh(\gamma h)\right)^{\frac{1}{2}}$$

Finally, $\boldsymbol{\gamma_0}$ is computed as the positive solution of the nonlinear equation

$$\gamma_0 = \frac{g}{U^2}\tanh(\gamma_0 h)$$

whose origin is to be found in the dispersion relation for finite depth water waves (13, 14).

9.5 (a) Integration of the naval architectural data

The main advantage of using the aforementioned formula is the opportunity provided to take into account the actual data from naval architecture through the shape of the hull. Recall that the shape of the hull is given by the offset function $\boldsymbol{f}$, in our case, an approximation of it on a mesh. The geometrical data we have on the trireme is not of this

form, so our goal will be to recover if though a technique called *draping*. The data we have is in the form of a set of parametric surfaces that can be exploited with the software Rhinoceros.

The principle of the draping technique is to consider a set of points (red points, figure SI5, left) placed initially on a plane parallel to the hull's centerplane, and to project these points on the hull by considering only displacements in the $\boldsymbol{y}$ direction. The set of points we then obtain (red points, figure SI5, right) hence "drape" the object. A few points end up straight on the centerplane, their offset being zero, we trim them off the mesh to avoid unnecessary further calculations.

The draping function is already implemented in Rhinoceros. Three grid of points were used here to represent with the same level of accuracy the hull, the nose and the ram (for which some details have the typical scale of 1cm for a 30m long ship). This results in a mesh file of 413,568 points which is too large for fast and efficient calculations of the wave resistance as it is required here.

We reduce the size of the mesh by extracting a subset of points with a variable density (typically we take more points wherever small details are involved). Then a new mesh is generated with Matlab's build-in Delaunay mesh generator. The result of all these operations is a representation of the trireme's hull through a P1 finite element function on a mesh of 25,185 points (see figure SI6).

This allows us to calculate the functions $\boldsymbol{I(\gamma)}$ and $\boldsymbol{J(\gamma)}$ using a finite element method associated to this P1 representation.

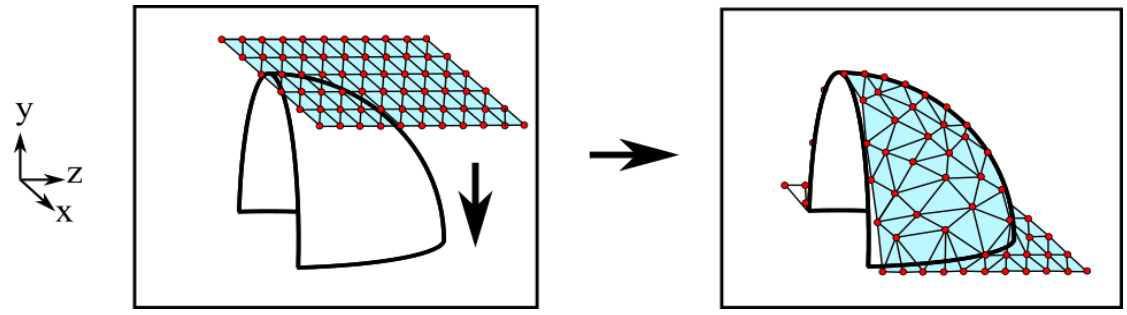

Figure SI5. Schematic representation of the draping procedure.

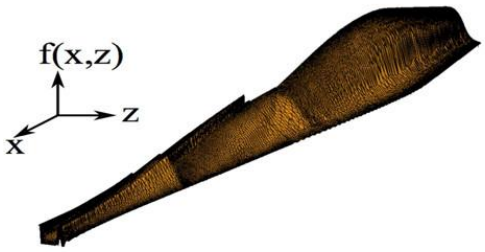

Figure SI6. Representation of the surface of the function $\boldsymbol{f}$ obtained through our reconstruction procedure.

9.5 (b) Calculation of the wave resistance integral

The first difficulty in computing the wave resistance integral (1) remains in the computation of the terms $\boldsymbol{I}$ and $\boldsymbol{J}$, which are integrals with respect to space that depend on the shape of the hull defined by $\boldsymbol{f}$. Let us focus on the computation of $\boldsymbol{I}$ (the computation of $\boldsymbol{J}$ is performed in a similar manner). If we define $\boldsymbol{\varphi}$ as

$$\varphi(\gamma, x, z) = \frac{\partial f}{\partial x}(x, z)\,\frac{\cosh(\gamma(h-z))}{\cosh(\gamma h)}\sin(\lambda(\gamma)x)$$

our goal is to integrate $\boldsymbol{\varphi}$ with respect to $(\boldsymbol{x}, \boldsymbol{z})$ for all values of $\boldsymbol{\gamma}$.

The computation of the integrals (1) - (3) is known to be delicate[3]. We detail the numerical method in two steps, first the integrals (2) and (3) with respect the space coordinates $(\boldsymbol{x}, \boldsymbol{z})$, and then the integral (1) with respect to $\boldsymbol{\gamma}$. The integrals (2) and (3) are computed using the aforementioned P1 representation f of the hull. This term is calculated in an exact manner on every triangle of the mesh by using a mapping on a reference triangle. Such an exact calculation is much preferable to the use of a quadrature formula.

Once $\boldsymbol{I(\gamma)}$ and $\boldsymbol{J(\gamma)}$ are determined, we can compute the integral (1). Two difficulties lie ahead: the singularity at $\boldsymbol{\gamma_0}$ and the infinite range of integration. The first problem is tackled using subintervals that become smaller and smaller as $\boldsymbol{\gamma}$ comes closer to the singularity. The integral at infinity is separated on subintervals that become larger and larger as $\boldsymbol{\gamma}$ grows. On each subinterval, we approach the integral with a two points Gauss integration method. Our resulting numerical wave resistance has been validated by comparison with tabulated results obtained for Wigley hulls.

9.5 (c) INTEGRATION OF THE OCEANOGRAPHIC DATA

From the methods described above, we are able to compute the wave making resistance for a given $\boldsymbol{U}$, $\boldsymbol{h}$ and $\boldsymbol{f}$. As described in methods section on Oceanography, the bathymetry is given as a 100x74 array that provides a water depth for each point of the Ambracian Gulf. Our aim here is to build an array that provides a wave resistance for each point of the Gulf, for a given velocity $\boldsymbol{U}$ and hull shape $\boldsymbol{f}$. The approach we use in order to reduce the computational costs is to compute wave resistance *vs.* depth profiles and to map these profiles into the oceanographic data by using interpolation. These profiles

will be computed with the method described earlier by selecting a limited well-chosen set of depth values ranging from the ship's draught to a depth under which the behavior of the resistance can be considered constant (deep water behavior). The result is then interpolated with splines (Figures SI7 and SI8).

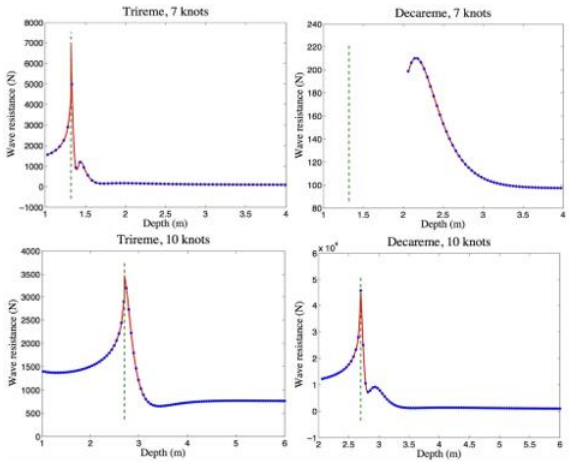

Figure SI7. Plots of the wave resistance versus depth profiles. First column: trireme. Second column: decareme. Top row, 7 knots; bottom row: 10 knots. The blue points represent the computed value of the wave making resistance and the red line is the spline interpolation. The vertical green dashed line represents the critical depth corresponding to the critical Froude number $\boldsymbol{Fr_h = \frac{V}{\sqrt{gh}} = 1}$

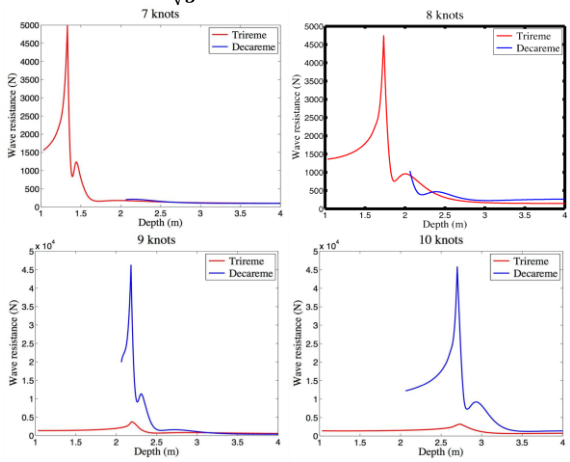

Figure SI8. Plots of the wave resistance versus depth profiles for various target velocity from 7 knots to 10 knots. Each plot shows a comparison of the wave-making resistance for each ship involved (in red the trireme, in blue the decareme). Note that the wave-making resistance for depths below the ship's draft (2 m) are not represented as they have no sense. (Gotman, 2002).

water depth for each point of the Ambracian Gulf. Our aim here is to build an array that provides a wave resistance for each point of the Gulf, for a given velocity $\boldsymbol{U}$ and hull shape $\boldsymbol{f}$.

The approach we use in order to reduce the computational costs is to compute wave resistance *vs.* depth profiles and to map these profiles into the oceanographic data by using interpolation. These profiles will be computed with the method described earlier by selecting a limited well-chosen set of depth values ranging from the ship's draught to a depth under which the behavior of the resistance can be considered constant (deep water behavior). The result is then interpolated with splines (Figures SI7 and SI8).

To the wave making resistance, we can add a viscous resistance related to the friction of the fluid on the hull. This viscous contribution can be calculated using the ITTC 57 procedure (ITTC, 1957; Molland et al., 2017):

$$R_v = C_v \frac{1}{2}\rho S V^2$$

With C_v the coefficient of friction:

$$C_F = \frac{0.075}{(\log_{10} Re\ - 2)^2}$$

Thus, we compute a total resistance, composed of a viscous resistance and a wave making resistance (Figure SI10). For small Froude numbers (equivalent to deep water regime), the wave component becomes negligible compared to the viscous component. In this configuration, the ratio of total resistance is

$R_{tD}/R_{tT} \approx 3.6 \approx R_{vD}/R_{vT}$ (Figure SI11 and SI12)

This value, close to 4, is explained by the geometry of the decareme which is twice as large as the trireme. Since the galleys have slender shapes, we can relate the ships' geometry to a board of length L and height T. The wet surface S is roughly L × T × 2 (we multiply by two to take into account both sides of the board). The length and the draft of the decareme are double that the length and the draft of the trireme. Thus, there is a factor 4 between the wet surface of decareme and the wet surface of trireme. To find the ratio 3.6, we have to start from the ITTC57 formula:

$R_{vD} = C_{FD}\frac{1}{2}\rho S_D V^2$ and $R_{vT} = C_{FT}\frac{1}{2}\rho S_T V^2$.

$$\frac{R_{vD}}{R_{vT}} = \frac{C_{FD}}{C_{FT}}\frac{S_D}{S_T}$$

$$\frac{C_{FD}}{C_{FT}} = \frac{(\log_{10} Re_T\ - 2)^2}{(\log_{10} Re_D\ - 2)^2} = \frac{(\log_{10} Re_T\ - 2)^2}{(\log_{10} Re_T + \log_{10} 2 - 2)^2}$$

$Re_T \approx 10^8$ so $\frac{C_{vD}}{C_{vT}} \approx 0.9$ and $\boldsymbol{\frac{R_{vD}}{R_{vT}} \approx 3.6}$

Without very shallow effects, a decareme has a viscous resistance 3.6 times stronger than the resistance of a trireme. To compensate this phenomenon, it is necessary to deploy a greater rowing power.

.

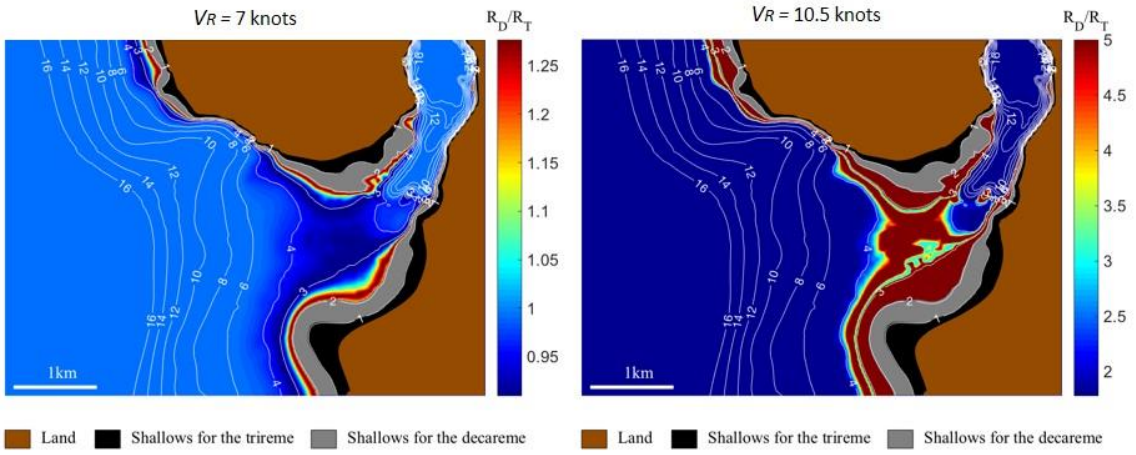

Figure SI9. Maps featuring the ancient bathymetry and theoretical predictions of wave making resistances for two different velocities: 7 knots (left) and 10.5 knots (right, which is saturated). At 7 knots, the decareme's wave resistance R_D can be lower than the trireme's wave resistance.

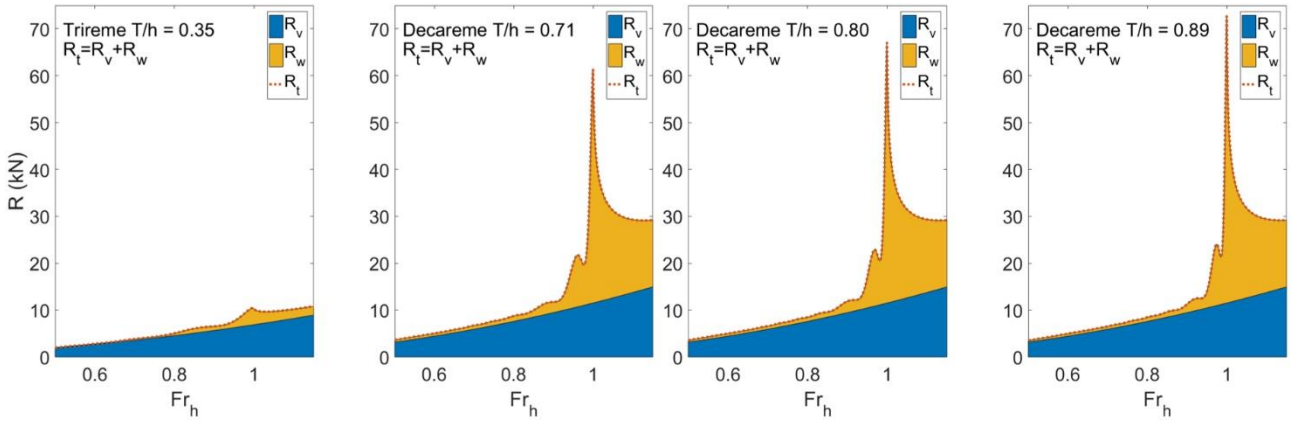

Figure SI10. Plots of total resistances broken down into viscous resistance (blue) and wave making resistance (yellow), for trireme and decareme configurations. The viscous resistance is calculated with the method (ITTC, 1957), and the wave making resistance with the Sretensky's formula.

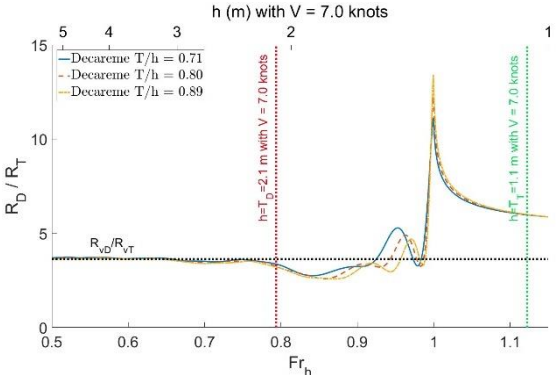

Figure SI11. Ratio between total resistances of the decareme and of the trireme, with a fixed velocity of 7.0 knots. The ratio of total resistances tends towards the ratio of viscosity resistances, equal to 3.6 for low Froude numbers (Fr_h < 0.75 and h > 2.5 m). The peak of resistance is not undergone by the decareme since it is in a zone of too shallow depth (the decareme's draft is bigger than the depth T_D>h).

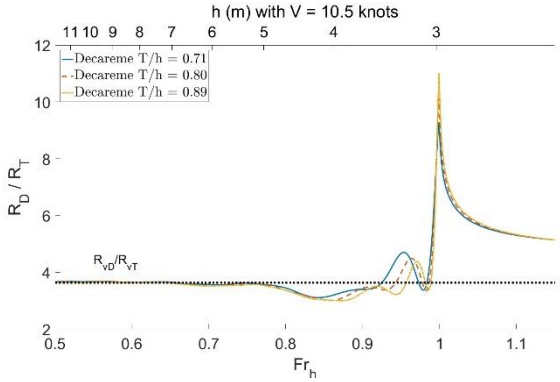

Figure SI12. Ratio between total resistances of the decareme and of the trireme, with a fixed velocity of 10.5 knots. The ratio of total resistances tends towards the ratio of viscosity resistances, equal to 3.6 for low Froude numbers (Fr_h < 0.75 and h > 5 m).

The use of the ITTC57 protocol is consistent with the experiments conducted. Indeed, if we compare this method to that used by (Coates, 1989), based on the towing tank measurements of (Grekoussis and Loukakis,

1986), we find similar results (Figure SI13). The computed viscous resistance with IITC57 is close to Coates' viscous resistance, up to 8 knots (superior to the cruising speed of 7 knots), the speed for which the wave resistance starts to play a role in deep water. According to Coates' curves (Figure SI13; Coates, 1989), from cruising speed (7-8 knots) the wave resistance starts to play a role. Thus, a greater effort must be made to increase the speed of the ship. Even in deep water, the wake clings to the ship as the echeneis-remora, and increases the difficulty in reaching the attack speed. Shallow water effects can totally prevent reaching this speed by a "wall of resistance" (Figure SI9).
In the future we may have to switch to a nonlinear Rankine-source panel method

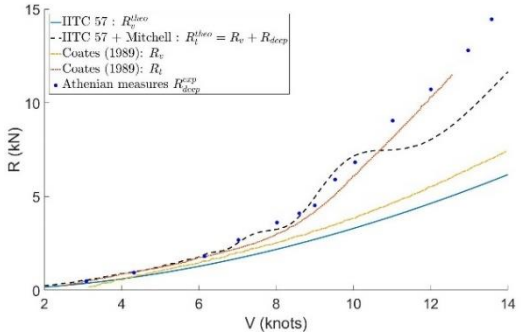

Figure SI13. Comparisons between the experimental results of (Grekoussis and Loukakis, 1986), the ITTC57 calculation with Michell's theory, and the results of (Coates, 1989). Michell's theory is the limit of Sretensky's formula for *h* infinite (Kirsh, 1966).

9.6 SUPPLEMENTARY INFORMATION ON FLUID MECHANICS

9.6 (a) Experimental Materials and method of stereovision

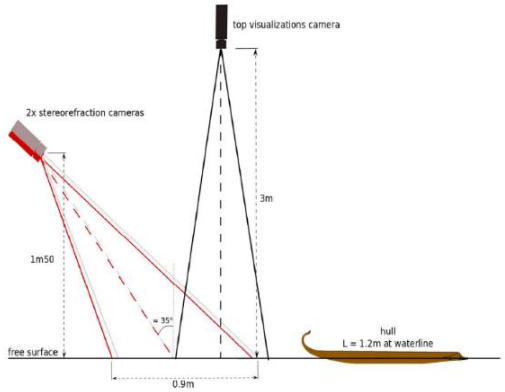

Figure SI14. Sketch of the experimental setup with the positions of the recording cameras. The stereovision method is based on the deformations of a random dots pattern glued to the bottom.

The experiments have been carried out in the towing tank of the Pprime Institute in Poitiers, France. Its geometry is a rectangular section with 1.5 m wide and a water level up to 1.2 m. The channel is 20 m long, and the measured zone, where we placed cameras, was at 10 m from the starting. The ship is towed by a trolley along the longitudinal axis x of the channel, with a speed up to 2.35 m/s. Thus, the maximum velocity of the decareme is 33 knots, and the trireme's maximum velocity is 23 knots, at real-scale. The acceleration had been fixed at 0.5 m/s², and a computer controlled the trolley's velocity. The ship was fixed (no translation or rotation), in order to test the effect of the Antonian number $A_n=T/h$ only.
As the amplitudes of the waves produced by a hull with such a length are very small, the method to measure these waves needs to be very precise and with a high resolution since the often used methods such as intrusive resistive probes cannot be applied. Such an optical method would have been difficult to apply with a bigger reduced model (such as the one of Grekoussis and Loukakis, 1985; 1986) since the extent of the visualizations windows would increase as well as the size of the data post-processing. Moreover, the limited resolution of the cameras would have been a restriction for such a large field of investigation. The wake-patterns have been measured with an original stereovision method, inspired from an earlier method developed in our team (Chatellier et al., 2013; Gomit, 2013b; Caplier, 2015) and improved for our purpose (see below). Two SpeedSense 1040 cameras from Dantec Dynamics with 28mm focal lenses have been placed above the water surface with a relative angle (Figure SI14) to capture the deformations of the random dots pattern, a roughcast of 750mm x 200mm (half the width of the water channel). The first step of the measurement is to record the image of the pattern with free surface at rest (Figure SI15). Then, the boat is launched and the two cameras capture images of the pattern deformed by the free surface undulations caused by the passage of the ship, at a frequency of 10 frames per second (fps) during 20s. The second step is to calculate the displacement of the water level in pixels on each image of the cameras, and then to calculate the displacement in millimeter for each time step. At the end we can reconstruct the whole wake behind the ship. The synchronization of the cameras and the acquisition of the images are performed with the DynamicStudio software. Each trial is recorded 3 times and then the images are processed and data are correlated with a dedicated algorithm. Then we can reconstruct the wake with a vertical precision of 0.1 mm on the water height and a horizontal spatial resolution of 10 mm (Figure SI17). The stereorefraction method has been validated with measurements of the wake produced by a 1.2 m long Wigley hull with rectangular geometry (the archetype of laboratory ships) for the deep-water configuration in the towing tank. The wake produced by this reference boat is the usual Kelvin wake in deep water (Figure SI16). Visualizations of the wake have been made from the top with a Jai CV-M2 camera with a 14mm focal lens at a frequency of 20fps.

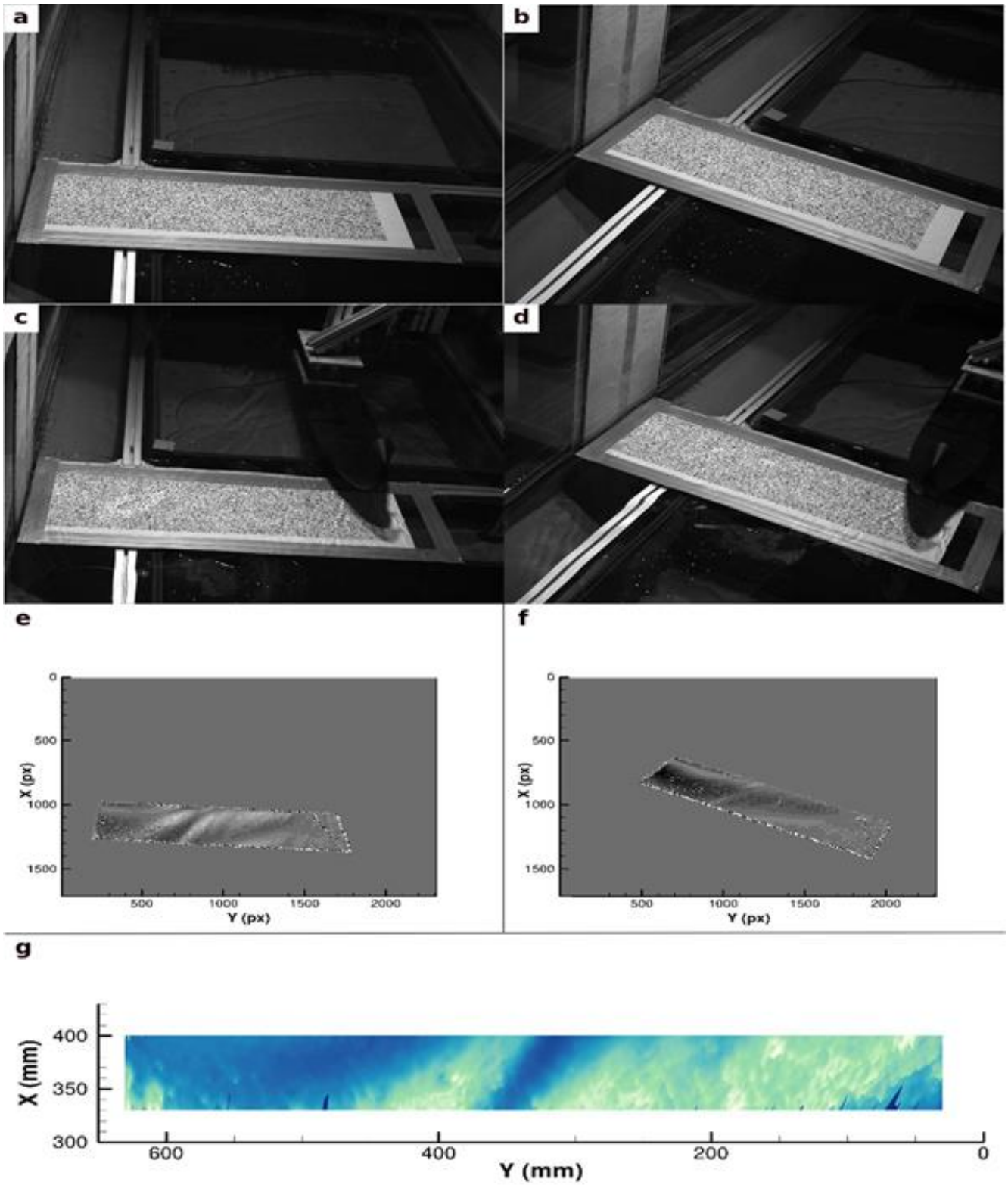

Figure SI15. The steps of the stereorefraction method from the acquisition of the reference images to the reconstruction of the surface deformation. Each column corresponds to one camera. a-b, Images of the reference pattern with the free surface at rest. c-d, Images of the pattern deformed by the free surface undulations. e-f, Free surface deformation in pixels (calculated with a correlation algorithm). g, the free surface deformation in millimeters (calculated with a reconstruction algorithm).

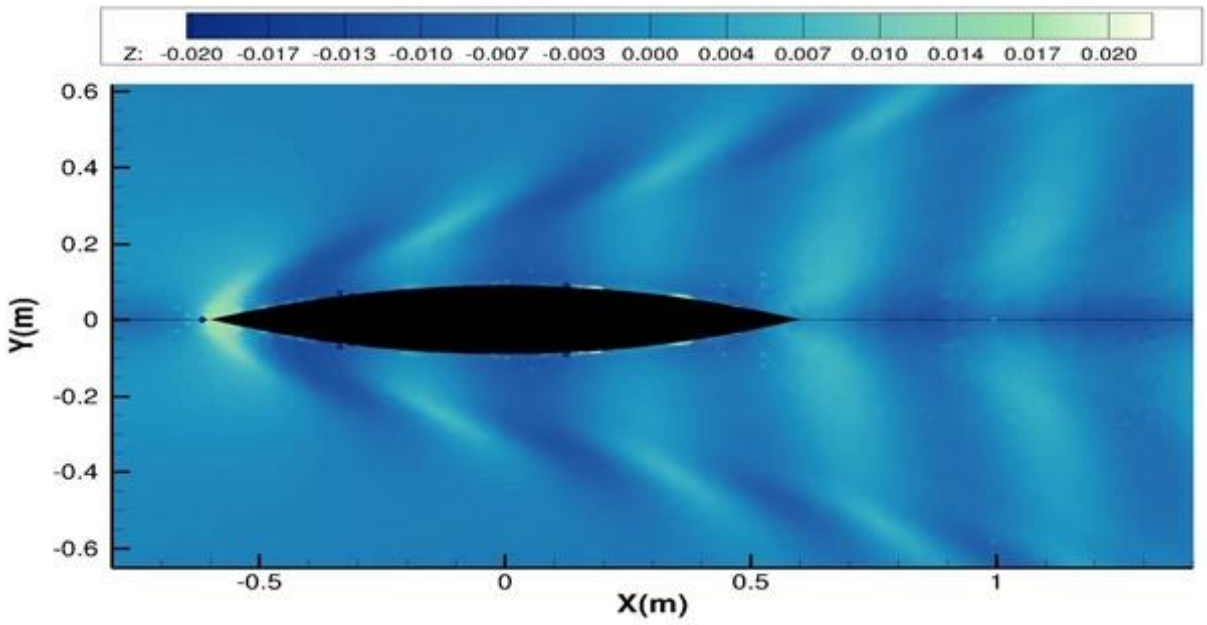

Figure SI16. The usual Kelvin deep water wake produced by a Wigley hull, measured with the stereorefraction method in the towing tank.

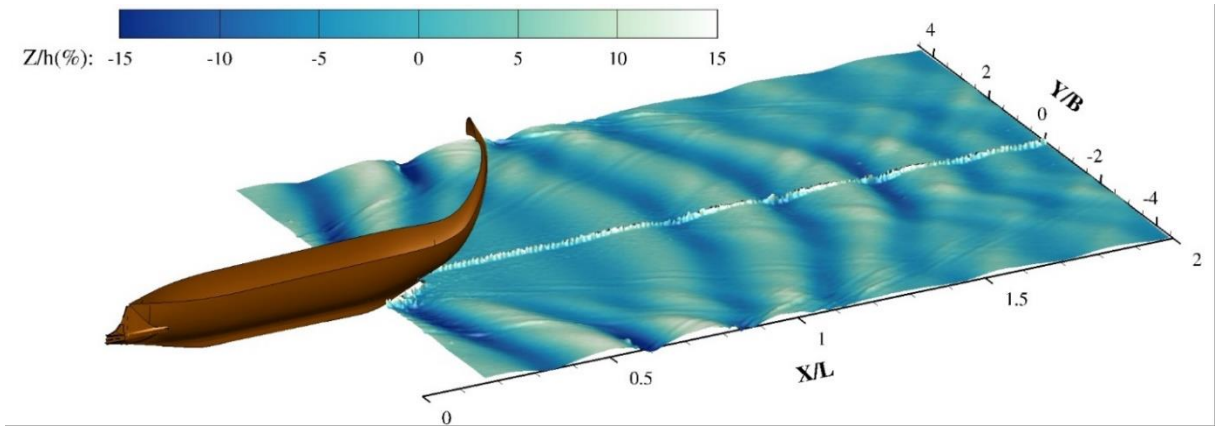

Figure SI17. The peculiar echeneidian wake behind the ship in the decareme configuration at Fr_h=0.9, measured with the stereorefraction method in the towing tank. The boat has no angle with the horizontal.

9.6 (b) Use of spectral domain

Extended views of the wake allow spectral analysis of the wake, according to the method presented (Carusotto and Rousseaux, 2013), used in deep water by (Gomit, 2014), or in confined configuration (Caplier, 2015). By selecting the stern wake, in the real space (x, y), and with a Discrete Fourier Transform, we get a representation in the Fourier space (k_x, k_y). The spectral domain brings a lot of additional information to the visualizations: the energy distribution in the wake spread over different wave numbers, or the hydraulic response around the ship. Energy is distributed along the dispersion relation:

$$0 = {V_m}^2 {k_x}^2 - \left(gk + \frac{\sigma}{\rho}k^3\right)\tanh(kh)$$

We can bring out several remarkable values: the cutoff wave number k_c, the intersection between the dispersion relation and the abscissa axis; the inflection point k_x^{infl}, where the slope is a measure of the angle of the wake: $\tan(\alpha) = \left(\frac{dk_y}{dk_x}\Big|_{infl}\right)^{-1}$. Wave numbers before and after the inflection point are respectively relative to the transverse and divergent waves. The hydrodynamic response, which depends on the speed and shape of the boat, feeds the lower part of the spectral domain with $k_x < k_c$ (Carusotto and Rousseaux, 2013; Gomit, 2013a, 2014) (Figure SI18).

The Figure SI19 shows the selection of a part of the wake, its representation in the spectral domain, and the detection of the dispersion relation. After a detection of amplitude maximums, a polynomial interpolation is carried out on the experimental measurements, in order to measure a slope and the angle of wake. Bounded harmonics are observed at high speeds hence the appearance of additional branches at high wavenumbers with a corresponding non-linear deformation of the wake in the real space.

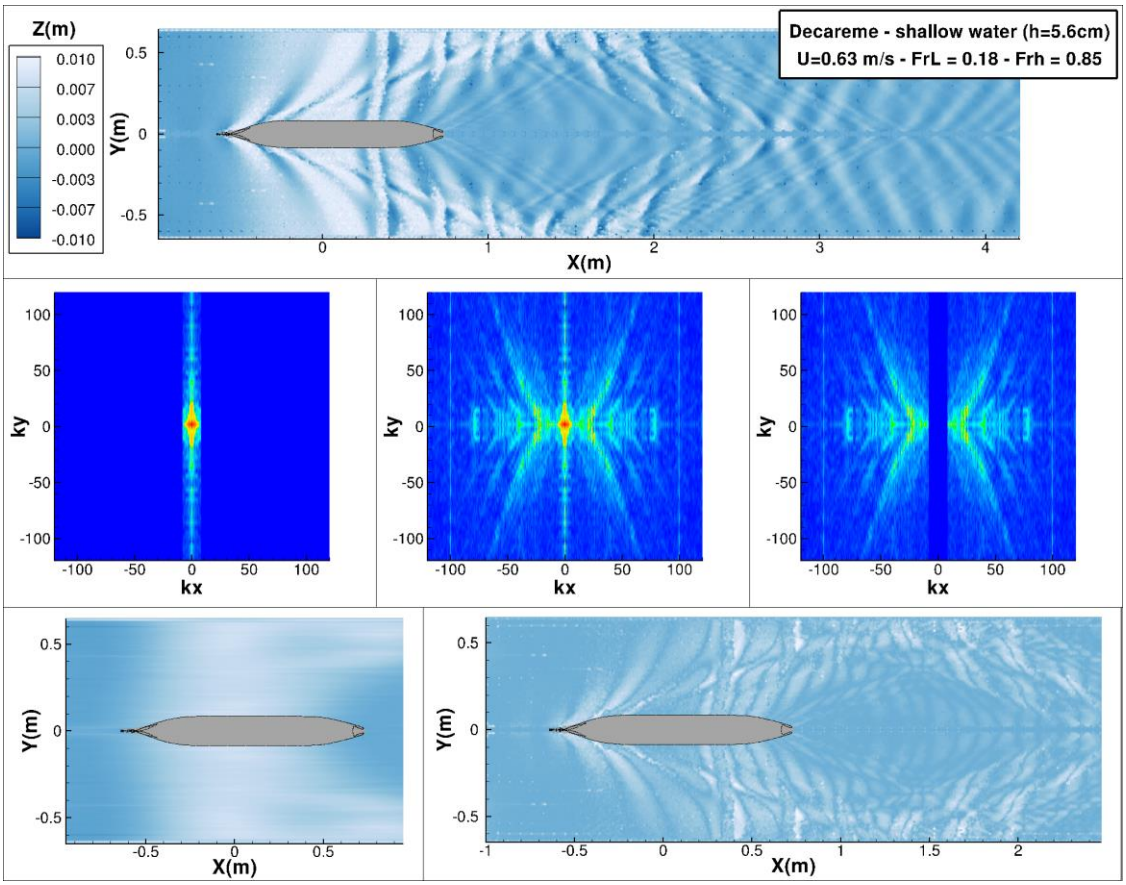

Figure SI18. Fourier space of a wake measured by stereo-refraction and effect of the filter: hydrodynamic response ($k_x < k_c$), wake ($k_x > k_c$). The keel of the boat makes an angle of 0.13 ° with the horizontal (stern sunk).

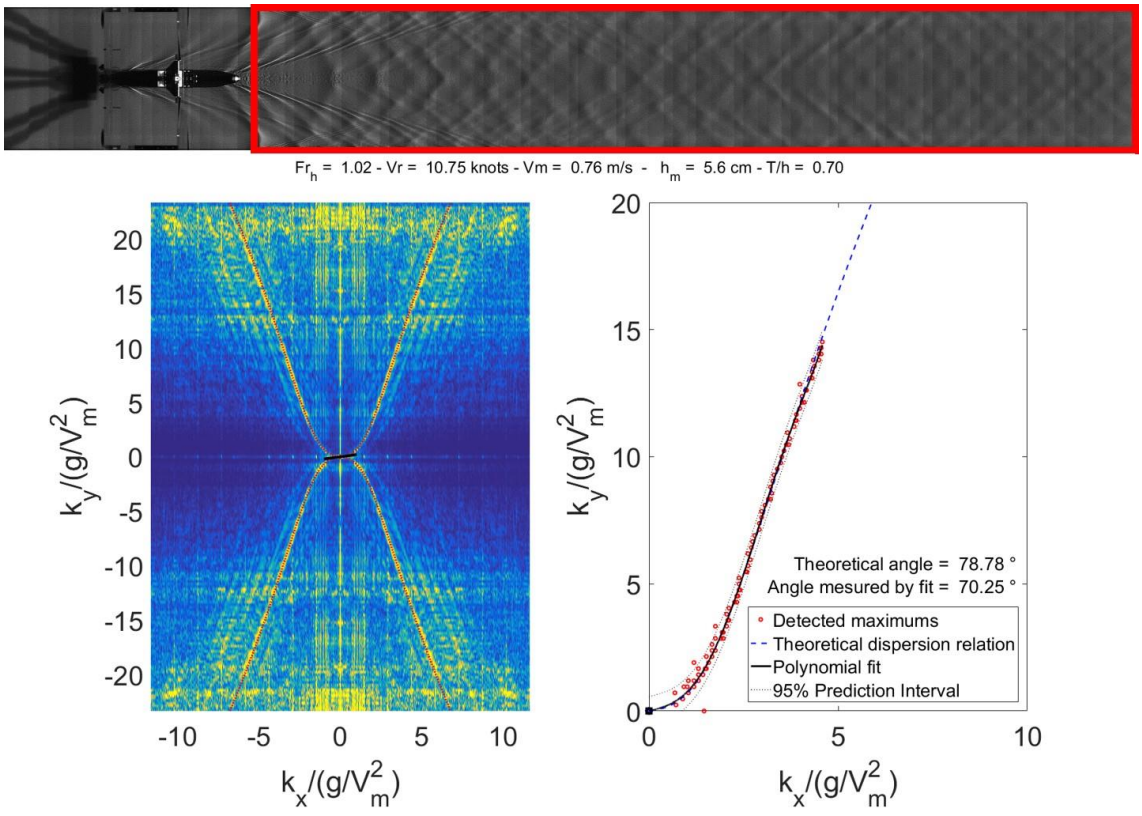

Figure SI19. Processing of a top view of the echeneidian wake by Fast Fourier Transform at Fr_h=1.02. The FFT is done on the red box with a simple visualization by a top camera.

9.6 (d) reduced model limits

On a real scale, the capillary term k^3 in the dispersion relation can be neglected, and the waves considered as purely gravity. However, by carrying out the reduced model experiments, this term can have an impact. Thus, by calculating theoretically the cut-off wavenumber for the transverse waves with (k_c) and without surface tension (k_c^σ), we may find a difference of up to more than 100% (Figure SI20). In the case of our experiments, the difference does not exceed 4%, for the lowest speeds tested in decareme configuration. Thus, the scale of our model does not involve significant additional capillary effects

$$k_y = 0 \Rightarrow k = k_x = k_c$$
$$0 = {V_m}^2 {k_c^\sigma}^2 - \left(g k_c^\sigma + \frac{\sigma}{\rho} {k_c^\sigma}^3\right) \tanh(k_c^\sigma h)$$
$$0 = {V_m}^2 {k_c}^2 - g k_c \tanh(k_c h)$$

The reduced model tests are also limited by the velocity V_m = 23 cm/s (Rousseaux et al., 2010), below which the wake is killed by capillary effects (black area on the Figure SI20).

The experiments are carried out in a towing tank, which generates additional confinements to the vertical confinement ($A_n = T/h$): a transverse confinement (W/h), and a "sectional confinement" ($m=A_b/A_c$). The first leads to reflections of the wake on the walls of the canal (reflections creating interferences). The second generates a return current and causes a water level drawdown of the ship (Pompée, 2015). According to Schijf's theory, some of tested configurations are in transcritical regime. With side visualizations, we checked that the model did not lead to a significant water level drawdown of the ship. The transcritical effect becomes important only for excessive speeds (V_R > 12 knots).

Because we have chosen a geometric scaling and a Froude scaling, hence the Reynolds scaling cannot be respected. Thus, we have a factor between the real-scale Reynolds number, and the Reynolds number model:

$$\mathrm{Re}_m = V_m L_m \frac{1}{\nu} = \frac{V_R}{\sqrt{\lambda}} \frac{L_R}{\lambda} \frac{1}{\nu} = \frac{\mathrm{Re}_R}{\lambda^{3/2}}$$

In decareme configuration, we have $\mathrm{Re}_m = \frac{\mathrm{Re}_R}{392}$, and in trireme configuration, $\mathrm{Re}_m = \frac{\mathrm{Re}_R}{138}$. Re_R is in the order of 10^8, thus, Re_m is in the order of 10^6, so we are still in a turbulent Reynolds number regime.

As the Reynolds scaling is not respected, we have to calculate the viscosity in order to take into account the effect of scales. Doutreleau et al., (2011) give a calculation of the kinematic viscosity. For the model:

$$\nu = ([0.585(t_W - 12)10^{-3} - 0.03761](t_W - 12) + 1.235)10^{-6}$$

For the real-scale:

$$\nu = ([0.659(t_W - 1)10^{-3} - 0.05076](t_W - 12) + 1.7688)10^{-6}$$

With t_W the water temperature (t_W was 15°C at Actium, and 21°C in our towing tank).

Finally, since the channel has a finite length (20 m), and our measurement zone was 10m from the starting point, unsteady effects may occur. However, apart from the high speeds tested but unrealistic at full scale (exceeding 12 knots), the wake appeared to have stabilized as the boat passed through the study area (see Robbins et al., 2011; Macfarlane and Graham-Parker, 2018).

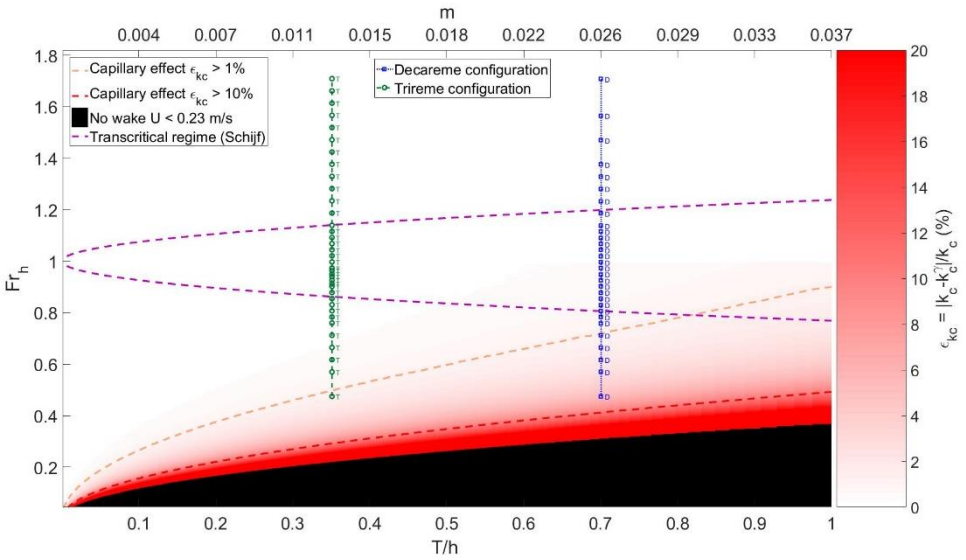

Figure SI20. Capillary effect as a function of the ratio *T/h*, and the Froude. In the black zone, the capillary effects suppress the wake. Green *T* and blue *D* are configurations made in the towing tank. Purple lines are the borders of the transcritical regime according to Schijf's theory.

INVESTIGATION OF THE NOMINAL AND EFFECTIVE PROPELLER INFLOW FOR A FAMILY OF INLAND WATERWAY VESSELS

Benjamin Friedhoff, Katja Hoyer, Sven List and **Matthias Tenzer DST,**
Development Centre for Ship Technology and Transport Systems, Duisburg, Germany

INVESTIGATION OF THE NOMINAL AND EFFECTIVE PROPELLER INFLOW FOR A FAMILY OF INLAND WATERWAY VESSELS

Benjamin Friedhoff, Katja Hoyer, Sven List and **Matthias Tenzer** DST – Development Centre for Ship Technology and Transport Systems, Duisburg, Germany

SUMMARY

Inland vessels operate in a wide range of waterway conditions and sometimes extremely shallow water, where the propeller inflow becomes critical. Knowledge of the wake field is of utmost importance for a proper and efficient design of the propulsion system. To gain a deeper understanding of the inflow conditions at different water depths, four representative inland vessels with the dimensions of a large Rhine vessel and different stern shapes were designed and built as scale models. For the detailed determination of the complex flow phenomena at the stern, a complementary approach of model tests, Stereo Particle Image Velocimetry (3C-PIV) and RANSE CFD calculations was chosen. While the measured resistance profiles differ negligibly between the designs, there are significant differences in the power demand. The integral wake fraction from the propulsion test does not adequately describe this behaviour. Finally, experimental and numerical flow fields could be compared for a deeper insight.

NOMENCLATURE

B	Ship breadth (m)
C_B	Block coefficient (-)
D	Propeller diameter (m)
h	Water depth (m)
J	Advance coefficient (-)
L	Ship length (m)
K_T	Thrust coefficient (-)
n	Propeller rotation rate (1/s)
n_{Prop}	Number of propellers (-)
T	Propeller thrust (N)
P_D	Delivered power (W)
P_E	Effective power (W)
R_{TM}	Model resistance (N)
T	Draught (m)
T_{max}	Maximum draught (m)
V	Displacement volume (m^3)
V_A	Axial inflow velocity (m/s)
V_M	Model ship velocity (m/s)
V_S	Ship velocity (m/s or km/h)
V_∞	Undisturbed inflow velocity (m/s)
v	Velocity component y-direction (m/s)
w	Velocity component z-direction (m/s)
w	Wake fraction (-)
ρ	Density of water (kg/m^3)

1 INTRODUCTION

On the European inland waterways with a total length of about 40,000 kilometres nowadays operate about 19,000 vessels. Even though inland navigation has only a small share in the total modal split, its economic interdependence is very important in certain transport chains. From a German perspective, this applies in particular to the supply of raw materials along the Rhine. Longer periods with extreme high and low water levels, such as in 2018, show this interdependence and sometimes lead to economic losses. Inland navigation is also very important from an environmental point of view, with its energy efficiency and low cost per tonne-kilometre, and is intended to relieve road traffic. Depending on their size, self-propelled inland vessels can replace 40 to 120 trucks on the roads, large pushed convoys even up to 650.

The design of inland waterway vessels has always been a major challenge, as these vessels have to operate safely and efficiently in a wide range of environmental conditions. Hekkenberg (2013) gives a good overview of the most important factors determining the economic viability of inland navigation and inland vessels. To meet these requirements various designs have been developed incorporating short aft hulls, highly loaded ducted propellers and devices like propeller tunnels and aprons to avoid ventilation at small draughts. Modern inland vessels can operate at draughts going below the propeller diameter (Zöllner, 2000). Nevertheless, the hydrodynamics of these full hullforms with large block coefficients are challenging and strongly influenced by the underkeel clearance. The resulting power demand limits the energy efficiency and may significantly affect the economic efficiency with increasing fuel costs. Due to the permanently changing sailing conditions, optimization based on operational experience with existing vessels is very limited in inland navigation. Some vessels are studied using CFD computations and model tests, which allows improving major unfavourable ship lines before the vessels are built at full scale. However, these investigations are limited to individual new-built ships and very few sailing conditions. Additionally, no data is available for older vessels which shall be equipped with updated propulsion systems. Extensive tests like PIV measurements are out of scope for most new-built projects.

To provide ship designers and propeller manufactures with generic information of these phenomena, four representative inland vessels were designed and manufactured in model scale. All designs have the overall dimensions of a large Rhine vessel and are propelled by ducted propellers mounted on conventional shafts. This family of vessels was compared extensively using

computational and experimental fluid dynamics (CFD and EFD) at three different water depths.

2 HULL GEOMETRIES

In order to cover a wide range of hull geometries of the existing fleet, four ships with the dimensions L=110 m, B=11.44 m and T_{max}=3.2 m and differing stern shapes were designed. The stern shapes resemble existing ships and all ships share the same bow shape.

All ships use ducted propellers in conventional shaft arrangement. Two designs are single screw vessels while the other two have propellers and ducts on port and starboard side. The latter is usually beneficial at low draught or very shallow water and fulfils redundancy requirements for some waterways. One design strategy follows tunnelled aft shapes (M2051, M2053), the other flat aft shapes (M2052, M2054). These four designs were built and equipped in scale 1 by 16 for model tests. The rudders were omitted for CFD and EFD. All investigations were performed at a draught of 2.8 m. The different aft shapes are shown in Figure 1.

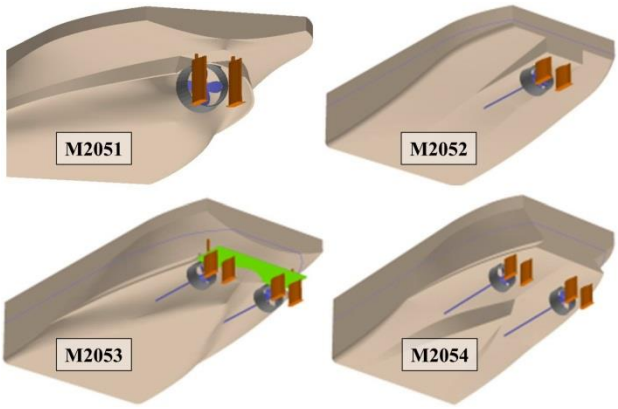

Figure 1. Stern shapes for hull geometry.

The basic shape parameters of the four vessels are shown in Table 1. Despite the different geometries, displacement and block coefficient are similar and allow extensive comparisons.

Table 1. Principle hull dimensions.

	M2051	M2052	M2053	M2054
n_{Prop}	1	1	2	2
D [m]	1.76	1.76	1.60	1.60
V [m^3]	3088	3150	3162	3129
C_B [-]	0.88	0.89	0.90	0.89

3 TOWED MODEL TESTS

Extensive model tests were done in DST's large shallow water basin. This testing facility is 200 m long, 10 m wide, has a concrete bottom and can be operated at any water depth up to 1.20 m. A unique feature of this basin is the observation tunnel with 60 mm thick acrylic windows underneath the towing track.

The resistance and self-propulsion tests were performed at three water levels corresponding to 7.5 m, 5.0 m and 3.5 m in full scale. For all ship models bare hull resistance tests were carried out at all three water depths. In preparation of the propulsion tests, propulsor open water tests were carried out for the two propeller/duct combinations used. For all four ships and three water depths, self-propulsion tests were subsequently carried out for ship velocities analogous to the resistance tests. The British method was applied with three propeller rates for each model speed. During the resistance and propulsion tests video recordings were made while passing the observation tunnel. The models were equipped with woollen threads at some exposed points to visualise the flow field at the stern of the ships.

4 PARTICLE IMAGE VELOCIMETRY

Particle Image Velocimetry (PIV) is a powerful non-invasive laser-based method for the measurements of fluid flows. Small particles in the water serve as tracer particles, which are illuminated in a thin light sheet by a pulsed laser. The reflections are captured with high speed video cameras in a stereo set-up (3C-PIV). With two images per camera taken at a defined time interval and using cross correlation, the vector field in all three spatial directions can be determined. Thus, the fluid flow in the observed area can be resolved with high precision. A detailed description of this measurement technique can be found in Raffel et al. (2007).

Optical access at small underkeel clearance and typical aft body shapes is very limited and the PIV system used at DST is not suitable for underwater use. Therefore, it is installed in the observation tunnel mentioned above. It consists of an InnoLas SpitLight PIV DPSS frequency-doubled Nd:YAG-Laser with two diode-pumped cavities. Due to the diode pumping, the beam quality is almost independent of orientation and motions. With a double pulse frequency of 100 Hz the pulse energy is about 60 mJ. Two Phantom v9.1 high speed CMOS cameras with 2 MP resolution and 6 GB internal memory each are used with 50 or 85 mm lenses mounted on Scheimpflug adapters. 14 bit colour depth allows sufficiently high contrast, even in most challenging applications. Polyamid particles with a diameter of 100 µm were used as tracer. Acquisition and post-processing were done with different subversions of the software package DaVis 8 by LaVision.

The basic PIV-setup in the view from above and from the side with first-surface mirrors mounted in the basin is shown in Figure 2. The recording of the nominal wake is basically easier, since the cameras can look at the propeller plane from behind. This path is blocked when recording the effective wake through duct and propeller. In this case, the ship's direction of travel is reversed and the cameras look from the other side at the plane in front of the propeller. Especially in shallow water this is very difficult due to the shape of the ship.

In order to minimize reflections with high intensity on the surface of the ship model, all models and appendages are coated with a fluorescent paint. The wave length of the light is shifted into the orange colour spectrum and filtered out via bandpass filters on the lenses. In this way, disturbing reflections from the surface can be significantly reduced and particles that are close to the surface can be detected.

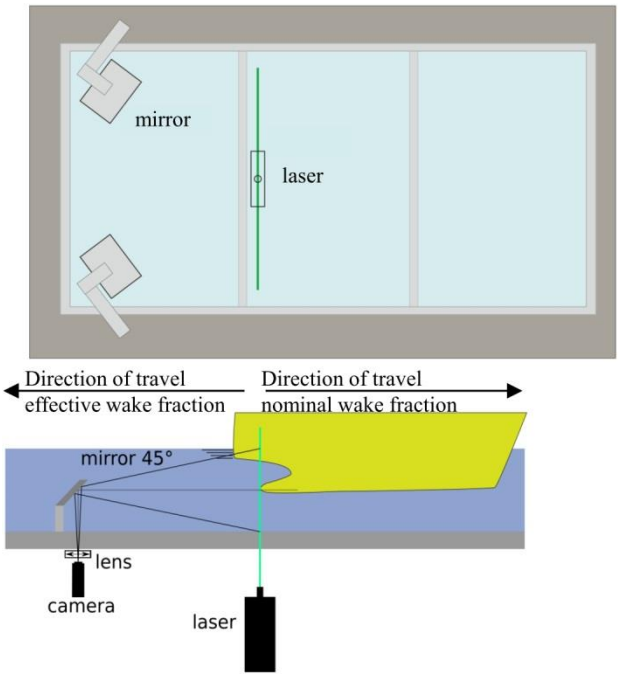

Figure 2. PIV-Setup.

The conditions in the wake of ship hulls with flow separation are highly unsteady. Coherent vortices of different length scales detach from the ship's surface and travel downstream. Thus, instantaneous vector fields from PIV are not representative and do not suffice for the validation of CFD computations. To reduce the uncertainty of PIV data and to derive adequate results for further analysis as many vector fields as possible need to be compared, filtered and averaged. This is a challenging task for applications where the stationary equipment is passed by the model. Here at least ten test runs were performed for each condition (different model and/or water depth). Each quadruple of raw images was processed independently. Afterwards, three consecutive vector fields for each run were averaged. With the sampling rate of 100 Hz this equals two periods of 0.01 s plus the interframe interval in time and a spatial averaging over e. g. ~20 mm at a towing speed corresponding to 14 km/h at full scale. The averaged data is then averaged again over all performed test runs for the same conditions.

Due to the challenges mentioned above, these measurements were only carried out with the single-screw ship M2052 and the twin-screw ship M2054 at all three water depths. In addition, depending on the water depth, only one ship speed was investigated, at which the sinkage and trims determined from the resistance and self-propulsion tests were fixed.

5 NUMERICAL COMPUTATIONS

To investigate the hydrodynamic performance and the fluid flow at the stern, all four ships were compared using RANSE computations. For this purpose the commercial software packages ANSYS fluent and ANSYS CFX were used. This software is based on the finite volume method and solves the integral equations for the conservation of mass, momentum and energy. In this technique, the volume of interest is divided into a huge number of small elements, called control volumes. Besides the k-ω-SST turbulence model from Menter (1994) the k-ε- model was also used. In addition to the calculation of pressure and velocity fields, the wave elevation was calculated using the volume of fluid method. The dynamic floating position, i.e. trim and sinkage due to forward speed, was also considered. A detailed description of the numerical calculation methodology can be found in Ferziger and Peric (2002).

In order to gather all gradients of the fluid and to resolve the free surface elevation a large number of elements was necessary. The numbers of nodes for the computational domain varied between 4 and 6 million. To reduce the number of cells, hybrid grids were used. The far field was discretised with a structured grid consisting of hexahedrons and the domain near the ship hull was discretised using tetrahedrons in combination with prism layers at the wall. A propeller model based on the experimentally determined open water characteristics was used to represent the propeller effect. All computations were carried out for the water levels 7.5 m and 3.5 m.

6 RESULTS

Propellers positioned in the viscous wake operate in a complex and inhomogeneous inflow. Shallow water effects strongly alter this wake field. With reducing underkeel clearance the flow passing between the waterway bottom and the hull is more and more blocked and the water needs to be drawn in from the sides. For the analysis of the wake conditions of the ship's hull, which is decisive for the inflow conditions to the propeller, the consideration of the wake fraction w derived with the thrust identity approach is well-established. It is calculated as follows.

$$w = 1 - \frac{V_A}{V_\infty} \tag{1}$$

Here V_A is the axial inflow velocity and V_∞ is the inflow velocity in an undisturbed environment, which usually corresponds to the ship velocity V_S. The following considerations of hydrodynamic flow conditions basically use this dimensionless ratio.

6.1 TOWED MODEL TESTS

Figure 3 initially shows the predicted ship resistance of all four ships at all three water depths. The differences between the best and worst ship design are in the range of about 20 %. At a water depth of 3.5 m, however, all designs are close together

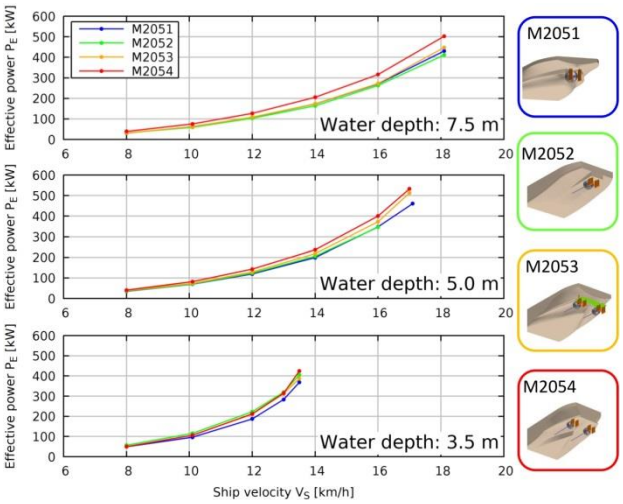

Figure 3. Full scale effective power.

One of the most relevant characteristic numbers is the power demand for a given speed. Figure 4 shows the plots of delivered power against ship speed for all models and the three tested water depths. The well-known disproportionate increase of power demand with speed becomes more pronounced while the attainable ship speed is more and more reduced with decreasing water depth. While the single-screw design M2051 performs best in all test-conditions, the results for the other three designs are not straightforward. They swap order with changing water depth. The twin-screw design M2053 is very close to the reference M2051 at high water depth, but performs worst with small underkeel clearance. The other twin-screw design M2054 is worst with sufficient water between hull and waterway bottom but doing well in shallow water conditions.

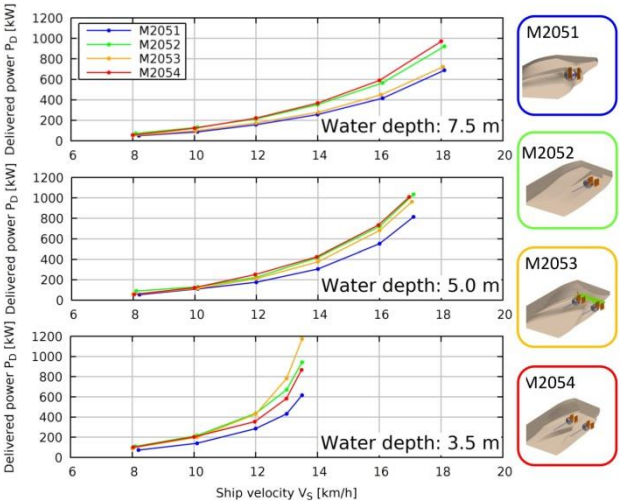

Figure 4. Full scale delivered power.

Looking at the magnitude of differences between the designs clearly demonstrates the need for proper hydrodynamic investigations for vessels operating in confined water. At 3.5 m water depth almost a factor of 2 can be found in the power demand between the best and the worst design, even though the resistance curves are relatively close. This effect must therefore result from the interaction behaviour of the ship's hull and propeller.

The thrust identity approach was used for all self-propulsion tests to compare the operating conditions with the open water tests. With the non-dimensional thrust coefficient $K_T = T/\rho n^2 D^4$ the corresponding advance coefficient $J = V_A/nD$ can be read from the propulsor open water characteristics. Using the known propeller rate n the corresponding axial inflow velocity V_A is derived and the wake fraction w calculated according to equation (1). The results are plotted in Figure 5 for the full scale ship speeds 12 km/h at 3.5 m depth, 14 km/h at 5.0 m and 16 km/h at a water depth of 7.5 m.

There is a clear tendency towards increasing wake fractions in low water depths. However, this effect is much more pronounced for the single screw vessels and especially for M2052. Considering the results of the delivered power, the integral wake fraction does not lead to a clear evaluation of the hull propeller interaction. Accordingly, a high wake fraction is not automatically synonymous with an inefficient ship design.

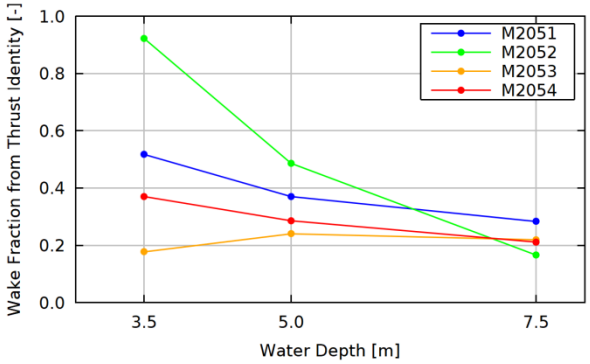

Figure 5. Wake fractions.

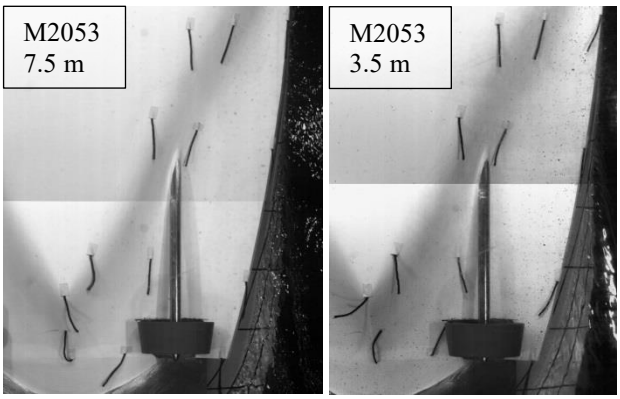

Figure 6. Underwater video recording.

As this approach does not take into account the inhomogeneous distribution in the wake field and the in-

plane velocity components *v* and *w* induced by the hull's wake, more detailed analysis is required based on detailed flow measurements and/or CFD computations. Snapshots of the underwater video recordings also allow only a limited qualitative evaluation. Figure 6 shows for the model M2053 that a tendency to fluid flow around the tunnel edge can be observed in shallow water.

6.2 DETAILED FLOW MEASUREMENTS AND NUMERICAL COMPUTATIONS

Figure 7 shows a comparison of the CFD results with the k-ω-SST turbulence model (above) and the k-ε-model (middle) with PIV measurements (below) for M2052 with ship velocity 16 km/h at 7.5 m water depth. The non-dimensional wake fraction is illustrated with colour contours while the in-plane components *v* and *w* are presented as vectors. In a similar graph, Figure 8 shows the results for M2052 with ship velocity 12 km/h at a water depth of 3.5 m.

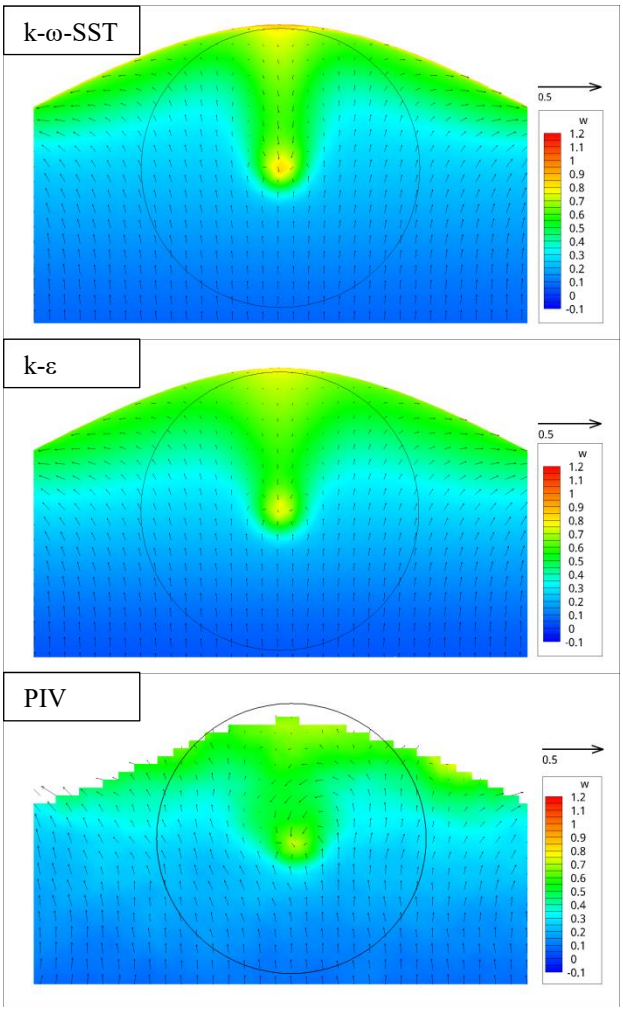

Figure 7. Nominal wake fraction in propeller plane for M2052, Vs=16 km/h, h=7.5 m.

The turbulent flow in the experiment smears out the wake shadow of the stern tube, clearly visible in the CFD results at the larger water depth. The masking of the upper edge of the propeller tunnel can be recognized in the vector fields from PIV measurements. Acceptable agreement can be seen for both cases.

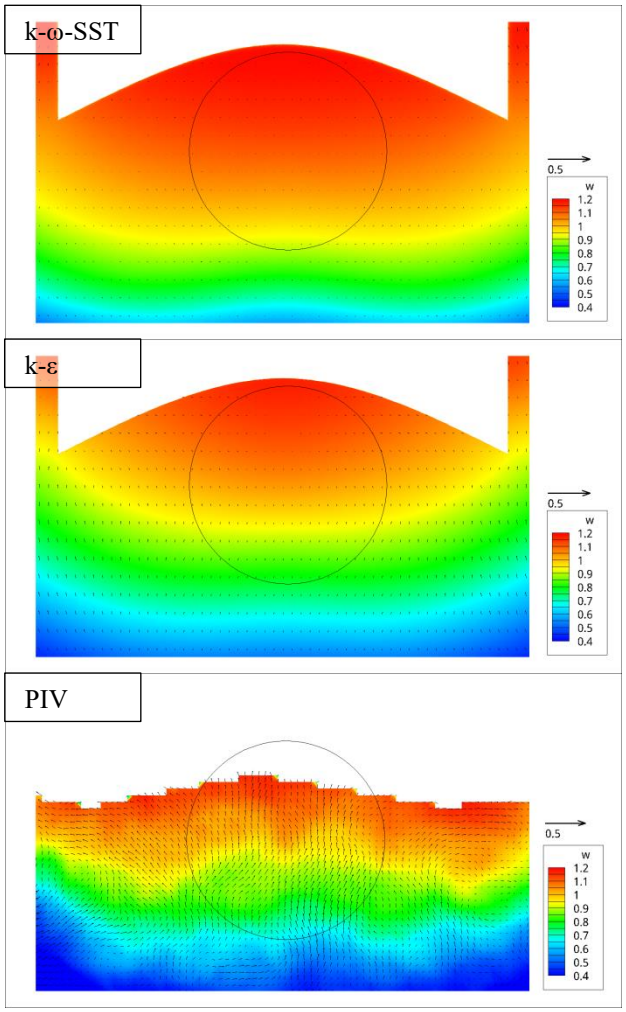

Figure 8. Nominal wake fraction in propeller plane for M2052, Vs=12 km/h, h=3.5 m.

The overall level of wake fractions matches well. However, it is noticeable that in this particular case the k-ε model shows better similarities than the widely used k-ω-SST model. The latter involves automatic switching from a k-ω model in the viscous sublayer to a k-ε model in the far field. At this point it can only be assumed that switching based on the default settings does not work sufficiently in this particular case.

Figure 9 shows the comparison of the experimentally determined model resistance compared to the numerical calculations for M2052 and two water depths. While the deviations in deeper water are around 5 %, the resistance in shallow water is systematically underestimated by the calculations. The k-ω-SST model was used in the calculations of the ship resistance. Comparisons with the k-ε model showed even worse results for the extreme shallow water case.

CFD simulations based on the Reynolds averaged Navier-Stokes equations do not resolve the complex transient flows in the detached flow behind a ship's hull. Instead,

the turbulence effects are modelled as steady state flow. The consideration of possible areas with reversed fluid flow at the stern of M2052 in Figure 10, which can give a first indication of separation zones, shows large differences for both turbulence models. The choice of the turbulence model therefore has a major influence on the numerical solution.

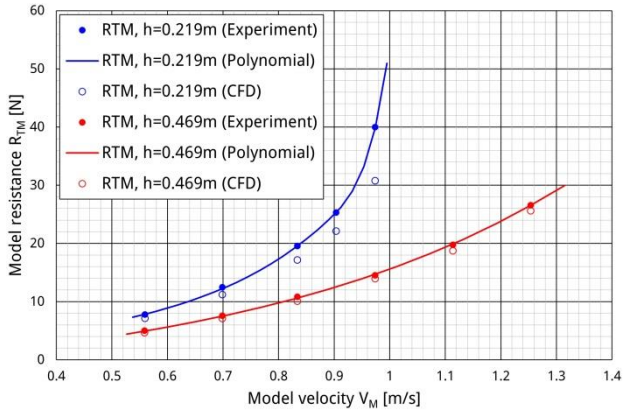

Figure 9. Comparison of model resistance for M2052.

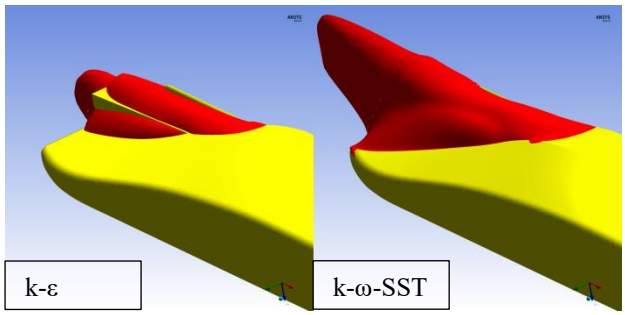

Figure 10. Area with possible reverse fluid flow for different turbulence models for M2052, V_S=12 km/h, h=3.5 m.

The deviations in the wake and resistance calculations show that for this particular case, the use of the standard turbulence models with the corresponding default settings does not automatically provide reliable data. In addition the quality of the results is highly dependent on the right choice of (local) grid resolution and calculation parameters. For the calculation of the nominal wake field, the k-ε model shows good agreement and is therefore used for further calculations.

Figures 11 and 12 show the numerical calculation of the effective wake field using the k-ε model in front of the propeller and the associated PIV measurements for the model M2052 at two water depths. The plane under consideration is half a propeller diameter in front of the propeller. The agreement between calculation and measurement is also quite good. Difficulties arise due to the partial shadowing of the measuring area by the propeller shaft and the ship's hull. In the case of shallow water in Figure 14, an over prediction of the axial inflow through the propeller model is evident.

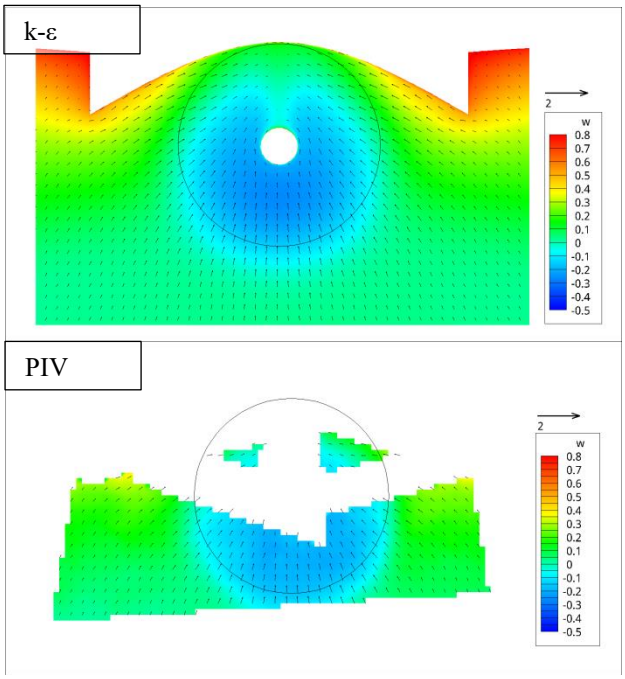

Figure 11. Effective wake fraction, 0.5 D in front of propeller, M2052, V_S=16 km/h, h=7.5 m.

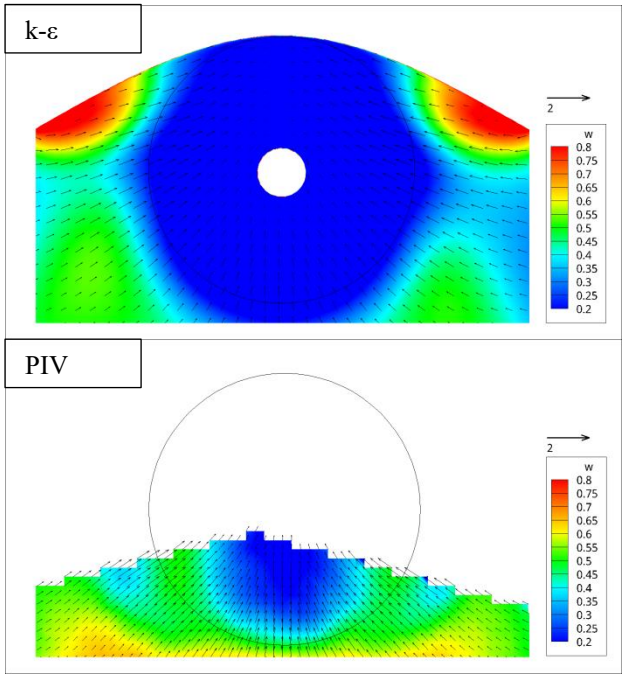

Figure 12. Effective wake fraction, 0.5 D in front of propeller, M2052, VS=12 km/h, h=3.5 m

Due to the masking in some PIV measurements, especially for the twin-screw vessels, the CFD results are used for further analysis. Figures 13 and 14 show the effective wake field of all ships in full scale for the highest and lowest considered water depth.

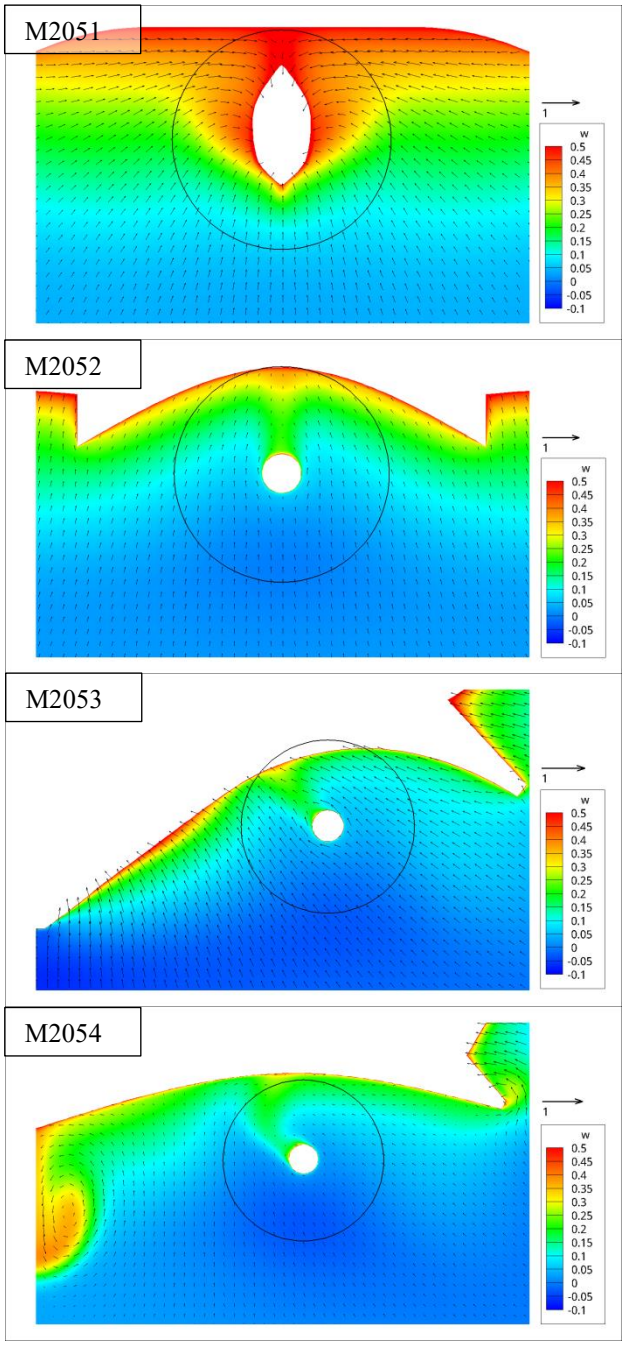

Figure 13. Effective wake fraction, 0.5 D in front of propeller, full scale, V_S=16 km/h, h=7.5 m.

For all numerically determined vector fields, it can be seen that the water depth has a significant influence on the inhomogeneity of the fluid flow at the stern. The figures also show that in case of twin screw ships the influence of the viscous wake of the ship hull is concentrated on the area between the propellers. The inflow to the propeller is therefore only slightly influenced for these ships.

Contrary to the wake fraction *w*, where only the axial component is taken into account, the calculations also provide information about the velocity components in y- and z-direction. These components have a considerable influence on the flow conditions to the propeller, especially in shallow water. The knowledge of these components is therefore of crucial importance for the design of a suitable propeller.

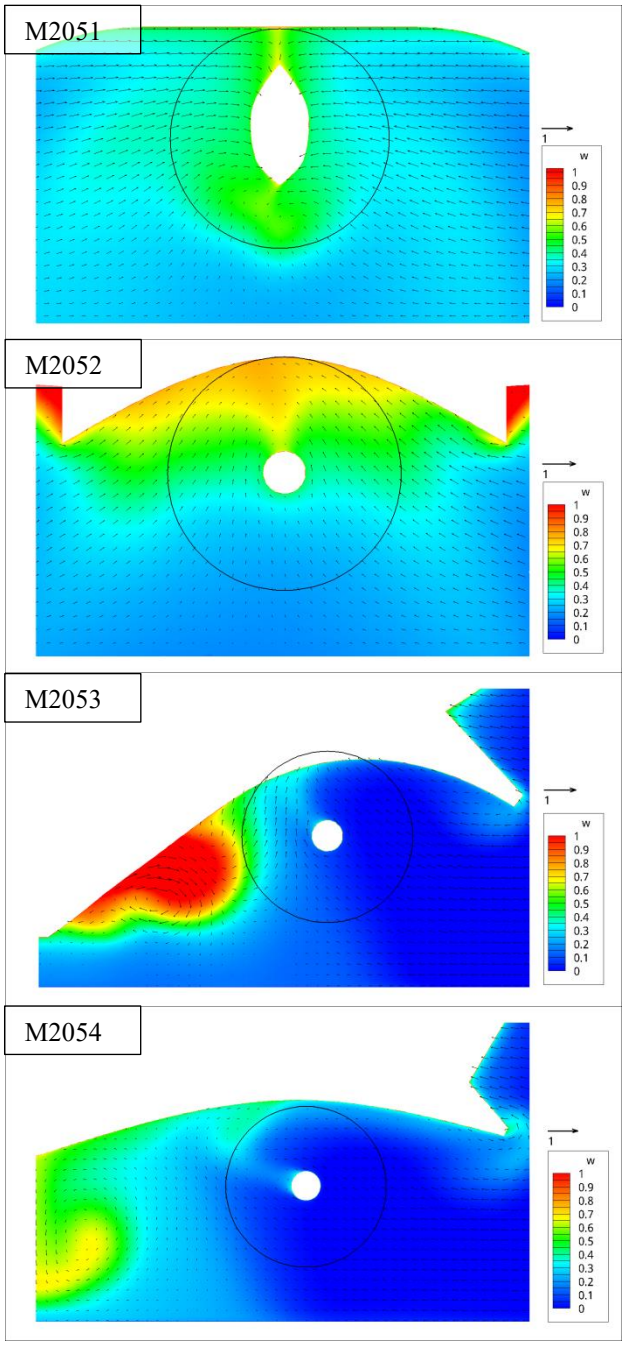

Figure 14. Effective wake fraction, 0.5 D in front of propeller, full scale, V_S=12 km/h, h=3.5 m.

7 CONCLUSIONS

The detailed investigations show that the stern shape has a significant influence on the power requirement of inland waterway vessels at variable water depths. Furthermore it

should be noted that there is no consistent trend. The design of an inland waterway vessel must therefore be carried out on an individual basis, taking into account the boundary conditions.

The classic evaluation of the interaction of ship hull and propeller with towed model tests is not straight forward, especially for shallow water. Day to day testing experience shows that for many inland ships in shallow water sometimes no advance coefficient can be identified by classic thrust or torque identity comparing with the open water characteristics. Behind the vessel sailing at a reasonable speed the propeller inflow is even worse than at zero speed in the open water test.

PIV measurements can provide detailed information for this purpose, but are very time-consuming, especially with extremely shallow water. On the basis of the PIV measurements carried out, numerical calculations could be validated under moderate conditions related to water depth and ship speed. Numerical calculations under more extreme conditions (very shallow water and high ship speeds) are strongly dependent on the modelling of turbulence properties and should be used complementary to scale model tests. In this special area, considerable research is still required to enable the comprehensive use of numerical calculations.

8 ACKNOWLEDGEMENTS

The authors would like to thank the Federal Ministry of Transport and Digital Infrastructure (BMVI) for funding the presented work within the framework of the project “Determination of the effective propeller inflow for inland navigation” (Project number 97.357/2015)

9 REFERENCES

Ferziger, J.H., Peric, M., 2002. Computational Methods for Fluid Dyanmics, Springer-Verlag, Berlin Heidelberg https://doi.org/10.1007/978-3-642-56026-2

Hekkenberg, R., 2013. Inland Ships for Efficient Transport Chains, TU Delft Library. https://doi.org/10.4233/uuid:f2ead20f-80b5-4d92-818f-7586c7b85f76

Menter, F.R., 1994. Two-equation eddy-viscosity turbulence models for engineering applications. AIAA Journal 32(8). 1598-1605 https://doi.org/10.2514/3.12149

Raffel, M., Willer, C.E., Wereley, S.T., Kompenhans, J., 2007. Particle Image Velocimetry – A Practical Guide. Springer-Verlag Berlin Heidelberg https://doi.org/10.1007/978-3-540-72308-0

Zöllner, J., 2000. Schiffbauliche Maßnahmen zur Reduzierung der Sohlbeanspruchung”, in: Mitteilungsblatt der Bundesanstalt für Wasserbau Nr. 82.

10 AUTHORS BIOGRAPHY

Benjamin Friedhoff holds a diploma degree in naval architecture and marine engineering obtained in 2005 at the University of Duisburg-Essen. Afterwards he worked for three years as a researcher at the Institute of Ship Technology and Transport Systems. In 2008 he was employed at the Development Centre for Ship Technology and Transport Systems, where he already worked as a student and graduate assistant for several years. In a wide range of research fields he did both numerical and experimental investigations on shallow water effects, ship-ship interaction, high speed craft, particle image velocimetry and marine energy converters. Since 2014 he manages the hydrodynamics department at DST.

Katja Hoyer studied physics at the Ruhr-Universität Bochum, Germany, and graduated in 2011. She continued working at the university as a research assistant and doing her doctorat in plasma physics. In 2015 she finished her doctorat and started working at the Development Centre for Ship Technology and Transport Systems. Within the hydrodynamics department she is involved in experimental investigations in a wide range of fields, including particle image velocimetry and marine energy converters.

Sven List studied Mechanical Engineering at the Wilhelm-Pieck-University of Rostock (Faculty of Ship Engineering). He is a graduate engineer for solid mechanics since 1988. Afterwards he worked for 5 years at the Ship Model Basin of Potsdam (SVA) as a development engineer and scientific assistant. Since 1995 he is working at the Development Centre for Ship Technology and Transport Systems in the field of numerical and experimental investigations.

Matthias Tenzer holds a diploma degree in naval architecture and marine engineering obtained in 2011 at the University of Duisburg-Essen. Afterwards he worked for five years as a researcher at the Institute of Ship Technology and Transport Systems. Since 2016 he is working at the Development Centre for Ship Technology and Transport Systems where he is responsible for ship manoeuvring related topics and the ship handling simulator SANDRA. His previous experience includes experimental as well as numerical investigations in the field of ship hydrodynamics.

PREDICTING MANOEUVRING CAPABILITIES OF A DTMB SHIP IN CFD WITH DYNAMICALLY CONTROLLED SURFACES

Inno Gatin, Vuko Vukčević and **Hrvoje Jasak**,
Faculty of Mechanical Engineering and Naval Architecture, University of Zagreb, Croatia

PREDICTING MANOEUVRING CAPABILITIES OF A DTMB SHIP IN CFD WITH DYNAMICALLY CONTROLLED SURFACES

Inno Gatin, Vuko Vukčević and **Hrvoje Jasak,** Faculty of Mechanical Engineering and Naval Architecture, University of Zagreb, Croatia.

SUMMARY

Numerical analysis of manoeuvring capabilities of the DTMB ship hull using Finite Volume based CFD code is presented in this work. Dynamically controlled active surfaces, namely two rudders are modelled using a novel immersed boundary approach. The moving surfaces are controlled using a PID controller in order to maintain a given course in stern quartering irregular waves. In this paper a work in progress is shown where the basic capabilities of the active surfaces and the controller to follow a designated straight path and course are tested in calm water, followed by a demo simulation of course keeping in stern quartering waves. In addition, forced oscillation pure sway and drift angle simulations are presented as a part of a larger study of the manoeuvring capabilities of the DTMB ship in the scope of the NATO AVT 253 and AVT 280 work group.

1 INTRODUCTION

Evaluating realistic behaviour of ship motion in large waves is a problem that is especially important for naval vessels considering their special exploitation conditions. In the effort within the NATO AVT, the capabilities of numerical tools to predict complex ship behaviour are being established. In the NATO AVT 280 course keeping simulations the DTMB ship is sailing in free-running conditions in irregular stern-quartering waves. The rudders are dynamically controlled using a PID controller to maintain a steady course. This paper presents the preliminary simulations that serve as a proof of concept for the methodology envisioned to tackle this problem. In addition, some of the results obtained within the AVT 253 study are also shown, where forced oscillation pure sway and drift angle simulations are conducted for the same model.

In order to have multiple surfaces in relative motion present in a CFD simulation, special numerical tools are required. Perhaps the most popular tool for this purpose is the Overset grid technology, which requires every surface to be represented by a separate, body-fitted computational grid. The difficulty with the Overset technology is that it requires significant pre-processing time to set-up the simulation, since computational grid generation is the most consuming part of the process in terms of man-hour of user interaction. In order to lower the complexity of pre-processing, a method based on the immersed boundary technique (Jasak 2018) has been developed and applied in this work. In the Immersed Boundary approach, a surface is represented by dynamically cutting the geometry of the single background computational grid, where the surface itself is represented by a STL grid, requiring no additional geometrical pre-processing. The background computational grid is body-fitted to the hull surface, enabling accurate representation of the geometry. The dynamic surfaces are controlled during the simulation using PID controllers that use yaw and sway motion as input, and controlling the deflection angle of the rudders to keep a steady course. The ship's two propellers are modelled using patch-type actuator disks as described in Jasak et al. 2018.

This paper is organised as follows. In the second section a brief description of the numerical model is given, together with basic details regarding the novel Immersed Boundary method. The third part presents a preliminary test of the Immersed Boundary method where steady resistance results are compared for a body-fitted and Immersed Boundary ONR Tumblehome hull. The fourth part shows the forced oscillation pure sway and drift angle simulations compared with experimental results. In the fifth section the self-propelled case is described comprising three different simulations: i) self-propulsion simulation in calm water conditions and passive rudders used to determine the propeller rotation rate needed to achieve the target model velocity; ii) a simulation for testing the rudder controller and rudder dynamics where the ship is initially positioned with an offset to the target straight path; iii) a simulation of a free-running model in stern-quartering irregular waves corresponding to severe weather conditions.

2 NUMERICAL MODEL

2.1 FLOW MODELLING

The numerical model is based on a collocated Finite Volume (FV) CFD software called foam-extend. A software library specialised for large-scale naval hydrodynamic problems called the Naval Hydro Pack is employed, which contains advanced free-surface modelling, multi-body handling, wave modelling, propeller modelling and other features relevant in the field. Incompressible, two-phase, viscous and turbulent flow is modelled using the momentum and continuity equations:

$$\nabla \cdot u = 0, \tag{1}$$

$$\frac{\partial u}{\partial t} + \nabla \cdot (uu) - \nabla \cdot (\nu \nabla u) = -\left(\frac{1}{\rho}\right)\nabla p_d, \tag{2}$$

where $\boldsymbol{u}$stands for the velocity field, $\nu$is the effective kinematic viscosity, comprising fluid kinematic viscosity and turbulent eddy viscosity, while $\rho$is fluid density. $p_d$stands for dynamic pressure, calculated as$p_d = p - \rho g \cdot x$, where

$p$stands for total pressure,$g$is gravitational acceleration, and$x$is the radii vector.

The free surface is captured using implicitly redistanced Level Set approach as described in Vukčević et al. 2016. Apart from surface capturing using the Level Set method, the Ghost Fluid Method (Huang et al. 2007) is employed to consistently treat the free surface boundary conditions as described in Vukčević et al. 2017, eliminating spurious air velocities.

Turbulence modelling in this work is performed using $k-\omega$model by (Menter 1994).Wall functions are used to account for near-wall phenomena.

2.2 IMMERSED BOUNDARY

Immersed Boundary method represents a family of methods where a surface geometry is introduced inside of an FV computational grid. Instead of building the computational grid to fit the surface exactly (a so called body-fitted approach), the geometry of the surface is taken into account via a special numerical treatment. The numerical discretisation is altered to accommodate to the boundary condition imposed at the immersed surface or boundary, while the finite volumes or cells that are outside of the flow domain are inactive in the solution process.

The present Immersed Boundary approach is based on a mesh cutting strategy instead of an interpolation strategy where the boundary conditions are imposed on the discretised geometry of the immersed surface, i.e. triangles. The present approach cuts the computational grid using the immersed boundary, however it does not actually alter the geometry of the grid. Instead, the faces created by cutting are used to impose realistic boundary conditions to the flow, while the cell cutting is taken into account by changing the geometric properties such as volume and cell centre position. A more detailed description of the immersed boundary technique used in this work can be found in Jasak 2018.

The main advantage of the present immersed boundary approach is that the performance of the algorithm does not depend on the relative resolution of the STL surface and computational grid. The effective resolution of the immersed boundary depends only on the FV grid resolution.

3 IMMERSED BOUNDARY TEST

In order to check the accuracy of the presented Immersed Boundary method a test is conducted where a full scale ONR Tumblehome ship ((National Maritime Reasearch Inistitute (NMRI) 2015)) steady resistance simulation is performed with a body-fitted approach and the Immersed Boundary. No turbulence modelling is used in this case since the goal is to determine the accuracy of predicting pressure forces primarily. The authors are aware that cells non-aligned with the boundary layer are going to result in poorer prediction of viscous and turbulent tangential stresses, but also that this is not the focus for appendages such as rudders.

ONR Tumblehome ship characteristics are shown in Table 1. The body fitted simulation was carried out using a computational grid comprising 3.79 million cells with four cells in the boundary layer. In the immersed boundary simulation the grid has 2.99 million cells. Figure 1 shows the comparison of hull geometry in the body-fitted and immersed boundary approach. The hull is appended with a bilge keel, which is well represented with the Immersed Boundary approach. Figure 2 shows the comparison of dynamic pressure distribution on the bow of the ship with the body-fitted and the Immersed Boundary method. The total resistance obtained with the body fitted approach is 98 kN, while the Immersed Boundary approach yielded 92 kN, which is a difference of 6%. This level of accuracy is considered sufficient for capturing forces acting on pressure-dominated dynamic appendages such as rudders and stabilisation fins.

Table 1. ONR Tumblehome ship characteristics

L_{PP}, m	154
B_{LW}, m	18.78
T, m	5.5
Δ, t	8507
C_B	0.535
V, m/s	7.72

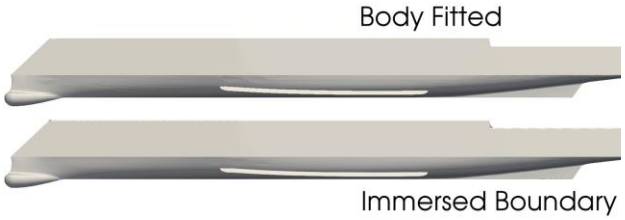

Figure 1. Comparison of ONR Tublehome geometry as represented by the body-fitted mesh and by the Immersed Boundary method.

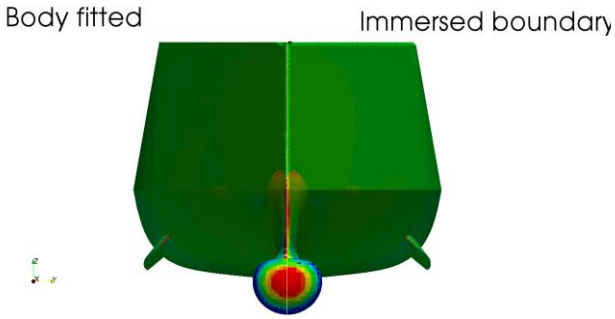

Figure 2. Comparison of dynamic pressure on the bow of the ONR Tumblehome.

4 DRIFT ANGLE SIMULATIONS AND FORCED OSCILLATION PURE SWAY

This section describes the calculation of basic manoeuvring characteristics of the DTMB 5512 model based on experimental study conducted by Yoon et al. 2014; Yoon and Stern 2017. Model particulars can be found in Table 2. Two simulations are carried out and compared: i) static drift simulations at drift angle $\beta = 10^O$; ii) pure sway simulation corresponding to drift angle of $\beta = 10^O$.

Table 2. DTMB 5512 model particulars.

Scale	1:46.6
L_{PP}, m	3.048
B_{LW}, m	0.410
T, m	0.132
Δ, kg	85.8
C_B	0.506

4.1 STATIC DRIFT SIMULATION

Static drift simulation is preformed for a towing velocity of $V = 1.531$m/s in model scale. Forces in longitudinal and transversal direction, and moment around the vertical axis are compared to experimental data in dimensionless form:

$$X = \frac{F_X}{1/2\rho V^2 L_{pp}^2}, \quad (3)$$

$$Y = \frac{F_Y}{1/2\rho V^2 L_{pp}^2}, \quad (4)$$

$$N = \frac{M_Z}{1/2\rho V^2 L_{pp}^3}, \quad (5)$$

where F_X and F_Y represent force in longitudinal and lateral direction, respectively. M_Z is the vertical moment. A grid consisting of 6.7 million cells has been used, which is comprised mostly of hexahedral (≈ 98% cells) with 4 boundary layers. y+ on most of the hull is approximately 25, while the region near the bilge keels is within 2 < y+ < 10 due to additional refinements. The grid extends $1L_{PP}$ in front of F.P, $1.5L_{PP}$ from A.P., $1L_{PP}$ towards starboard and port side, $1L_{PP}$ towards the bottom and $0.5L_{PP}$ towards the top. The simulation has been performed with a fixed maximum CFL number of 50, resulting in a time step of ΔT ≈ 0.019s and mean CFL number of 0.78. The simulation has been performed up to t = 150 s, where the oscillations in F_X, F_Y and M_Z were at most ±0.75%.

Figures 3 and 4 show the surface elevation generated by the hull in the simulation and in the experiment, respectively. In order to compare the generated wave field with experimental measurements, a wave cut at $y/L_{pp} = 0.132$ is compared in Figure 5 showing good agreement. Table 3 shows the comparison of forces and moment with experimental data, where S stands for the value and E for relative error. For surge force the error is -1.5%, while sway force and yaw moment exhibit slightly larger errors. In total, all errors are smaller than 10%, which is acceptable concerning the relatively coarse grid that is used.

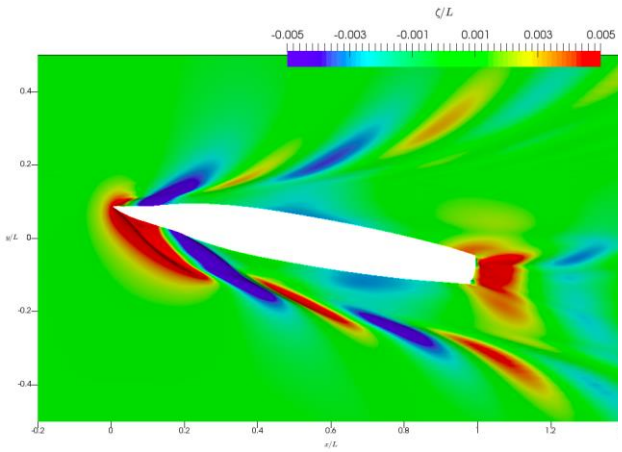

Figure 3. Surface elevation in the static drift simulation of the DTMB 5512.

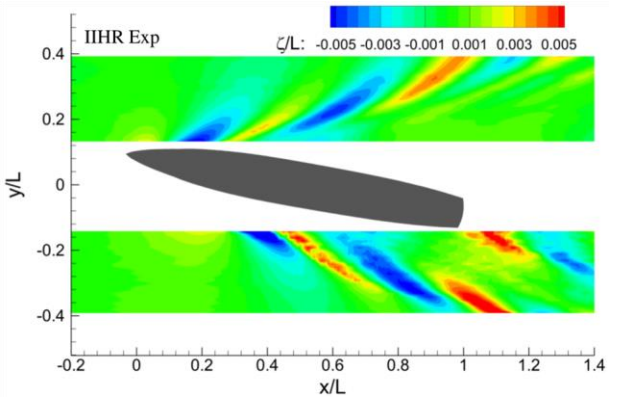

Figure 4. Surface elevation in the static drift experiment of the DTMB 5512.

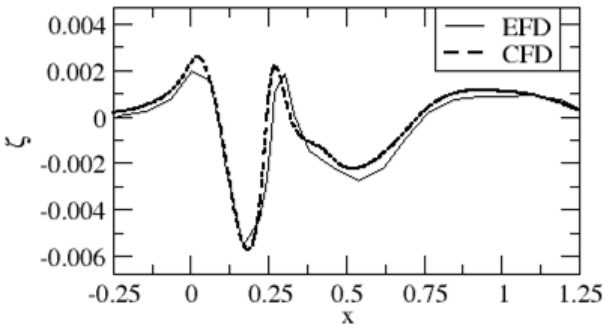

Figure 5. Wave cut comparison for the static drift simulation.

Table 3. Comparison of dimensionless forces for static drift of the DTMB 5512.

	$X \times 10^3$		$Y \times 10^3$		$N \times 10^3$	
	S	E	S	E	S	E
EFD	−19.61	N/A	58.46	N/A	28.61	N/A
CFD	−19.32	−1.5%	53.33	−8.8%	26.20	−8.4%

*$E = (S - D)/D \times 100\%$

4.2 PURE SWAY SIMULATION

Pure sway runs are performed to correspond to a drift angle of 10^{O}, where the towing velocity is the same as for the static drift. Sway motion is defined with a sinusoidal function with sway amplitude of 0.266 m and a period of 6.173 s. The simulation is carried out with a grid comprised of 7.8 million cells, while algebraic grid deformation technique is used to accommodate for the motion of the vessel, keeping the side boundaries of the domain at a fixed location, to mimic the experimental set-up.

Figure 6 shows two pictures of the simulation where the surface elevation and vortex structures are visible. The comparison is performed for the dimensionless sway force and yaw moment. Figure 7 shows the comparison of the dimensionless sway force during a single period of oscillation which is reconstructed using FFT of ten oscillation periods. Figure 8 shows the same for the dimensionless yaw moment. The agreement between the experimental and numerical data is acceptable, while the yaw moment shows slightly better agreement with experimental results. The sway force differs in amplitude as well as phase by a small amount, which is not observed for yaw moment.

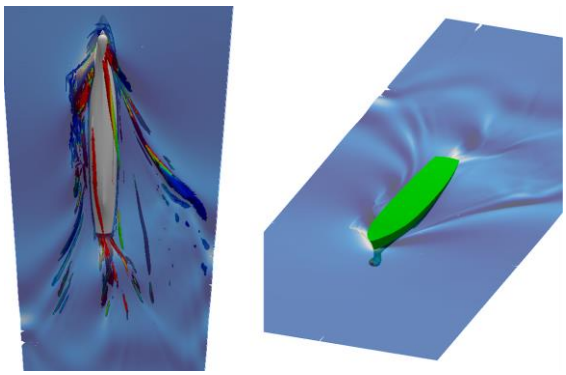

Figure 6. Pure sway simulation: (left) bottom view of the hull with the free surface and vortex structures; (right) perspective view.

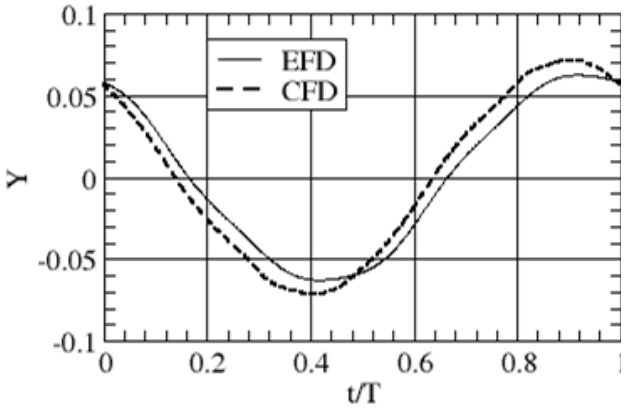

Figure 7. Comparison of dimensionless transversal force for the pure sway simulation.

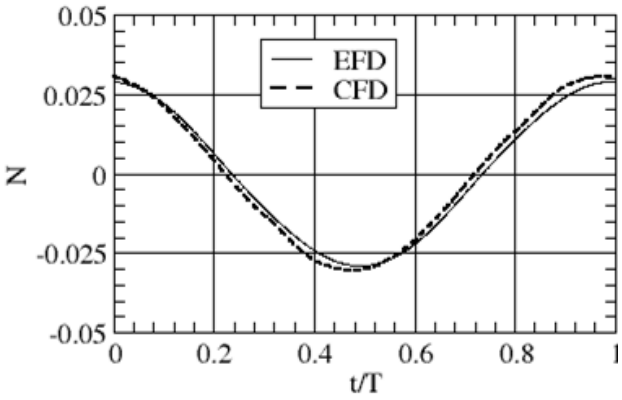

Figure 8. Comparison of dimensionless vertical moment for the pure sway simulation.

5 DTMB COURSE KEEPING SIMULATIONS

This section shows the work in progress where the goal is to perform a long-time course keeping simulation of a free-running DTMB 5415M model in irregular, stern-quartering waves. The ship characteristics are shown in Table 4 in full scale. Beside the active appendages: two rudders and propellers, the ship is appended with passive appendages, namely bilge keels, shafts and struts supporting the two propellers. Figure 9 shows the side-view of the hull with passive appendages. Three simulations are performed altogether:

i. Self-propulsion simulation in calm water condition and passive rudders used to determine the propeller rotation rate needed to achieve the target model velocity,
ii. A simulation for testing the rudder controller and rudder dynamics where the ship is initially positioned with an offset to the target straight path,
iii. A preliminary simulation of a free-running model in stern-quartering irregular waves corresponding to heavy weather conditions.

The propellers are modelled using an actuator disc approach as described in Jasak et al. 2018, while the immersed boundary method is used for the two rudders. Propeller characteristics in full scale are shown in Table 5. Rudder particulars are shown in Table 6, as well as coefficients for the rudder controller. The rudder deflection is calculated by superimposing proportional control based on three parameters: i) deviation of course angle with respect to the target course; ii) yaw rate of turn, i.e. rate of course change in time; iii) lateral distance from the centre of gravity to the target course straight path.

All simulations used the same computational grid that contains refinement regions near the rudders and near the free surface. For this preliminary set of simulations, a relatively coarse grid is used that is comprised of 3.6 million cells. Grid generation is performed automatically using software cfMesh (Juretić 2017). Figures 10 and 11 show the bottom view of discretised stern and a section of the grid, respectively. Figure 12 shows the surfaces representing the actua-

tor discs, where the pressure jump is imposed that corresponds to the propeller thrust, as well as the rudder surfaces as represented in the FV grid using the immersed boundary approach. All simulations are performed in model scale.

Table 4. DTMB 5415M full-scale particulars.

Scale	1:35.48
L_{PP}, m	142.00
B_{LW}, m	19.056
T, m	6.150
V, kt	23.6
Δ, ton	8642.6
LCB, m (from AP)	72.00
KG, m	8.453
K_{XX}, m (radius of gyration)	7.870
K_{YY}, K_{ZZ}, m	35.50

Figure 9. Side view of the appended DTMB 5415M hull.

Table 5. DTMB 5415M propeller characteristics in full-scale.

Diameter, m	6.10
Pitch ratio at 0.7R	0.865
Expanded blade area ratio	0.580
Number of propeller blades	5
Number of propellers	2

Table 6. DTMB 5415M rudder characteristics in full-scale.

Number of rudders	2
Average height, m	4.44
Average chord, m	3.49
Maximum rudder angle, ^{O}	35.0
Rudder rotation rate, ^{O}/s	16.8
Deflection angle per degree of course deviation, $^{O}/^{O}$	3.0
Deflection angle per ^{O}/s of course change, $^{O}/(^{O}/s)$	17.9
Deflection angle per meter of traverse course deviation, ^{O}/m	0.29

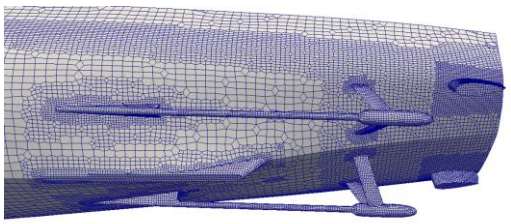

Figure 10. Bottom view of the computational grid used for DTMB 5415M.

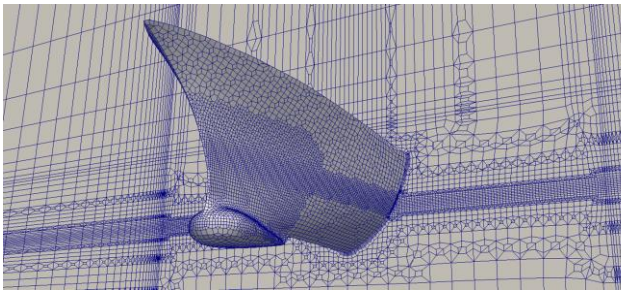

Figure 11. Section of the computational grid used for DTMB 5415M.

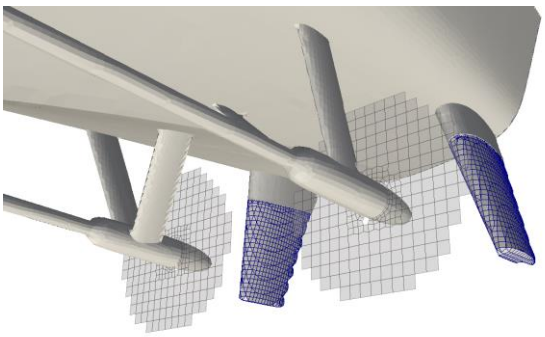

Figure 12. View of the immersed boundary surfaces representing the rudders and actuator disc surfaces.

5.1 SELF-PROPULSION SIMULATIONS

The self-propulsion simulation is carried out in order to determine the rotation rate of the propeller needed to achieve the full scale speed of 23.6 kt (2.038 m/s in model scale). Three degrees of freedom are enabled for the vessel: surge, pitch and heave. The rudders are passive, i.e. they are represented using the immersed boundary method but are not moved during the simulation. Propeller rotation rate is controlled using a PID controller that controls the rotation rate according to the difference of the current vessel speed and the target speed. The change in rotation rate causes the change in the advance coefficient *J*, which in turn causes a change in the thrust coefficient in the relation described by the open water characteristics of the propeller. Heave and pitch are enabled to account for dynamic sinkage and trim.

The simulation is initialised with the target model velocity in order to reduce the convergence time, while the propeller rotation rate was assumed to be zero initially. Figure 13

shows the converged wave field, while Figure 14 shows the dynamic pressure on actuator discs and rudders. Convergence of total surge force acting on the vessel is presented on Figure 15, showing that it converged to zero net force as expected. From Figure 16 it can be seen that the vessel achieves the target velocity with oscillations that are within 0.3% of the target speed. Rotation rate of propellers is presented in Figure 17, showing that the required rotation rate in model scale is 14.32 s^{-1} oscillating within 0.9%. This rotation rate is applied in further simulations in order to reduce the complexity of modelling.

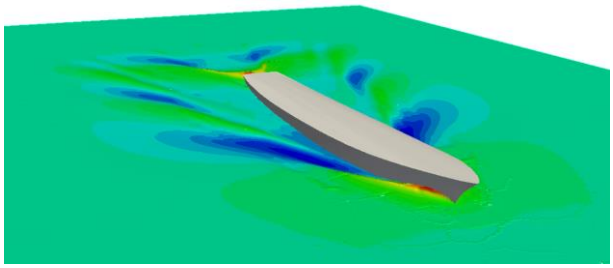

Figure 13. Perspective view of the converged wave field during the self-propulsion simulation of the DTMB 5415M.

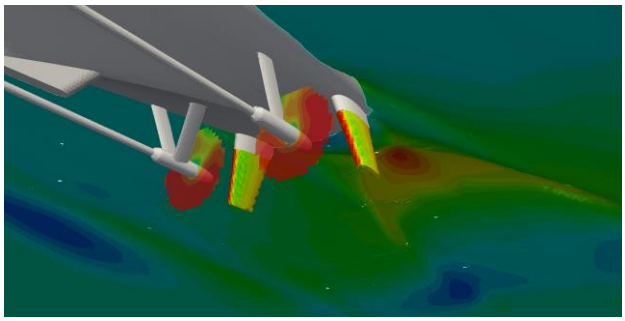

Figure 14. View of the actuator discs and rudders in the converged self-propulsion simulation of the DTMB 5415M. The colour scales represent dynamic pressure.

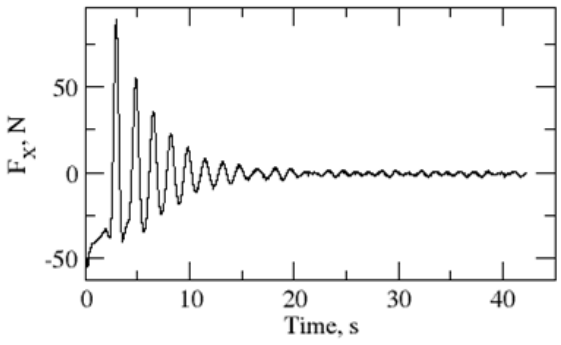

Figure 15. Convergence of total longitudinal force acting on the DTMB 5415M in the self-propulsion simulation.

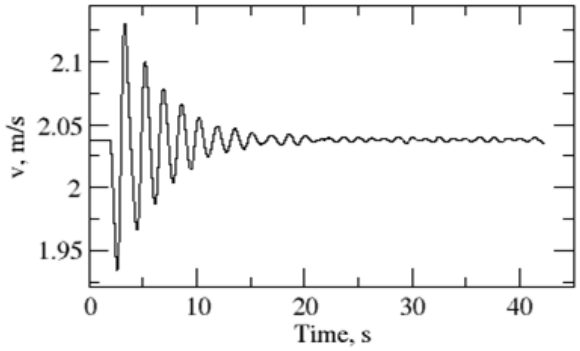

Figure 16. Speed convergence of the DTMB 5415M in the self-propulsion simulation.

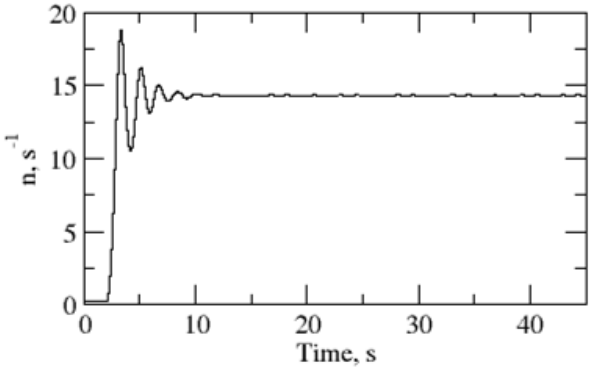

Figure 17. Convergence of propeller rotation rate of the DTMB 5415M model in the self-propulsion simulation.

5.2 RUDDER CONTROLLER TEST

In order to test the rudder controller, a simple test in calm water is performed where the ship is initially positioned 2 metres away from the target straight path in the transversal direction, as shown in Figure 18 where the top view of the converged initial condition of the simulation is shown, with the black line indicating the target straight path. After initial convergence, the rudder controllers are activated. Figures 19 and 20 show an intermediate and final position of the vessel with respect to the target path, respectively.

The time history of sway displacement is shown in Figure 21, from which the convergence of lateral position to the target path is evident. Figure 22 shows yaw displacement time history, where the initial high yaw angle can be seen which gradually reduces to zero as the vessel approaches the target path. The test simulation showed that the rudder controllers are correctly programmed, and that the rudders modelled with immersed boundary can effectively control the ship course.

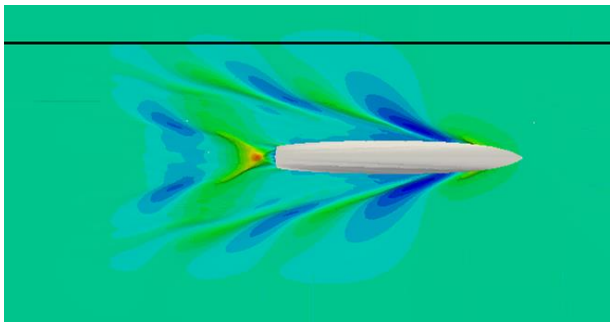

Figure 18. Initial converged condition of the rudder controller test before the activation of rudder motion. The black line indicates the target path.

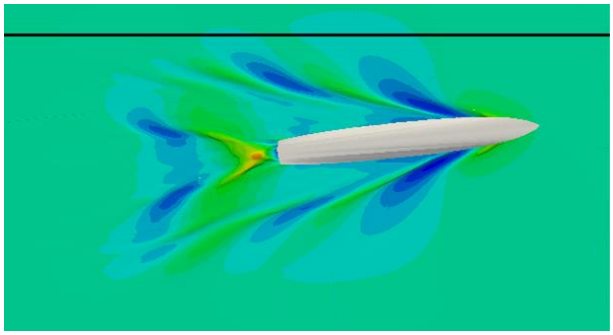

Figure 19. Intermediate position of the vessel in the rudder controller test simulation.

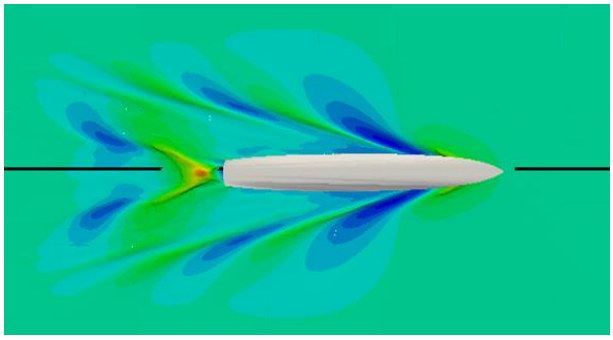

Figure 20. Final position of the DTMB 5415M in the rudder controller simulation test.

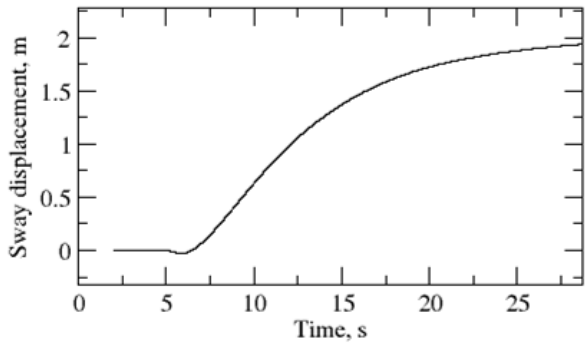

Figure 21. Time history of sway displacement in the rudder controller test simulation.

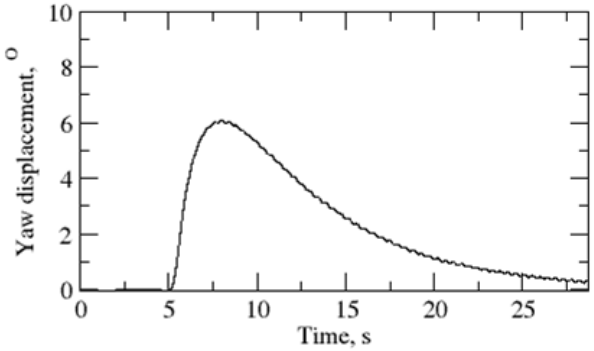

Figure 22. Time history of yaw displacement in the rudder controller test simulation.

5.3 COURSE KEEPING IN STERN-QUARTERING IRREGULAR WAVES

In this section a preliminary simulation of free-running model sailing in stern-quartering waves with active rudders is presented. The simulation depicts the work-in-progress and presents only a short portion of the final target simulation, which should encompass multiple peak periods of the sea spectrum. The irregular wave field encounters the ship at a 300^{O} angle (stern-quartering waves on the port side). The wave energy spectrum is defined with the JONSWAP theoretical spectrum model, with full scale characteristics detailed in Table 7.

Figures 23 and 24 show the top and perspective view of the simulation, where the incoming waves as well as the ship's wave system can be observed. Figures 25 and 26 show the yaw and roll displacement time history during the simulation. Large roll angles that are exhibited during the simulation create a challenging task for the numerical treatment of computational grid motion. In the current simulations, the motion of the hull is accommodated by rigidly moving the grid for translational motion, while an algebraic deformation algorithm is employed to accommodate for rotational motion. Thus, large roll angles reduce the quality of the grid, which prohibits this strategy to account for very large rotations. In the future study, an alternative solution needs to be proposed.

Table 7. Wave energy spectrum characteristics.

Significant wave height, m	7.5
Peak period, s	9.0
Heading, ^{O}	300

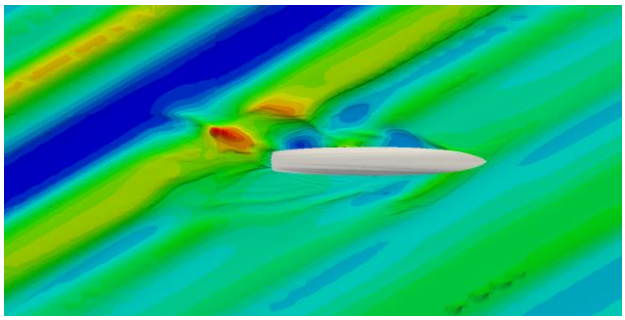

Figure 23. Top view of the stern-quartering course keeping simulation. The waves are incoming from top left corner.

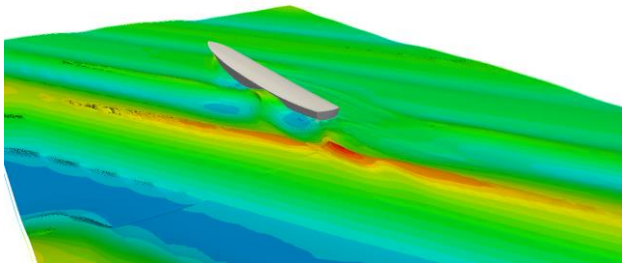

Figure 24. Perspective view of the stern quartering course keeping simulation.

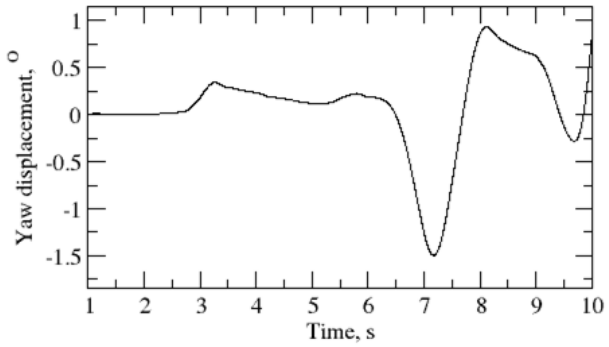

Figure 25. Yaw displacement time history in the stern-quartering course keeping simulation.

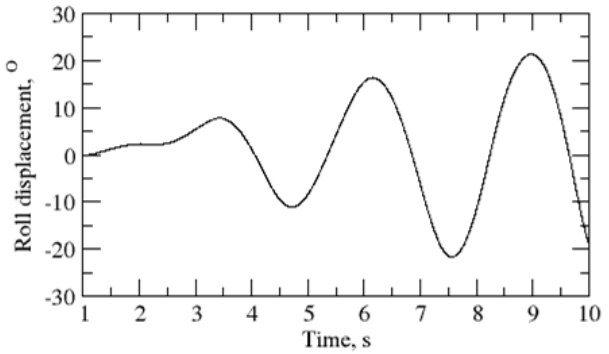

Figure 26. Roll displacement time history in the stern-quartering course keeping simulation.

6 CONCLUSION

The presented work serves as proof-of-concept for the proposed methodology for predicting ship manoeuvring capabilities where active appendages need to be considered. More specifically, the goal is to be able to perform course-keeping simulations in irregular waves. A novel immersed boundary method is applied for moving appendages during the CFD simulation. The proposed approach showed to be well suited for the task, as it enabled dynamic control of the ship during the simulation.

In order to assess the accuracy of the code for calculating manoeuvring forces a static drift and pure sway tests were first conducted as a part of the AVT 253 effort. The results are compared to experimental data and show good agreement. This gives the present numerical framework credibility needed to continue with simulations which include higher level of modelling complexity, i.e. free-running models with active appendages.

The preliminary testing of the proposed approach for simulating course-keeping in irregular waves is divided in three parts: in the first part it was necessary to estimate the rotation rate of the two propellers required to reach the target speed. In the second part the rudder controller algorithm as well as the capability of the immersed boundary representation of the rudders was tested, where they were dynamically controlled during the simulation. The test showed that the vessel is successfully navigated to the desired course. In the third part stern quartering waves are imposed and a short simulation of course keeping with six degrees of freedom is performed with moving rudders and propellers.

The work presented in this paper showed that the present numerical framework predicts basic manoeuvring forces accurately, and is capable of simulating dynamically controlled vessels. It also showed that further effort needs to be invested in order to handle large rotational motion of the vessel in terms of grid handling. Large roll motion that occur during the simulation prohibit the use of typically used techniques for handling motion of a floating body, namely rigid grid motion and grid deformation. The three specific options that will be considered in the future are:

- Immersed Boundary for representing the hull of the vessel as well as the appendages,
- Overset grid technology (Gatin et al. 2018),
- Adaptive grid refinement.

In general, the numerical framework showed acceptable accuracy for determining manoeuvring coefficients, while the course keeping simulations showed that the proposed approach can be used in order to simulate dynamic appendages.

7 REFERENCES

Gatin, I., Vukčević, V., Jasak, H., Lalović. I., 2018. Manoeuvring Simulations Using the Overset Grid Technology in

Foam-Extend, in: 32nd Symposium on Naval Hydrodynamics, Edited by Moustafa Abdel-Maksoud, Hamburg, Germany, 5-10 August 2018.

Huang, J., Carrica, P. M., Stern, F., 2007. Coupled Ghost Fluid/two--Phase Level Set Method for Curvilinear Body--Fitted Grids. Int. J. Numer. Meth. Fluids 44: 867–97. https://doi.org/10.1002/fld.1499.

Jasak, H., 2018. Immersed Boundary Surface Method in Foam-Extend, in: Proceedings of the 13th OpenFOAM Workshop, edited by D.C. Wan, J.H. Wang, W.W. Zhang, D. Deng, and Z Wang, 55–59. Shanghai, China.

Jasak, H., Vukčević, V., Gatin, I., Lalović, I. 2018. CFD Validation and Grid Sensitivity Studies of Full Scale Ship Self Propulsion. International Journal of Naval Architecture and Ocean Engineering.
https://doi.org/10.1016/j.ijnaoe.2017.12.004

Juretić, F., 2017. cfMesh: Advanced Meshing Tool.

Menter, F. R., 1994. Two-Equation Eddy-Viscosity Turbulence Models for Engineering Applications. AIAA J. 32 (8): 1598–1605.

National Maritime Reasearch Institute (NMRI), 2015. Tokyo 2015: A Workshop on CFD in Ship Hydrodynamics.

Vukčević, V., Jasak, H., Gatin, I., Uroić, T., 2017. Ship Scale Self Propulsion CFD Simulation Results Compared to Sea Trial Measurements, in: 7th International Conference on Computational Methods in Marine Engineering, MARINE 2017. Vol. 2017–May.

Vukčević, V., Jasak, H., Gatin, I., 2017. Implementation of the Ghost Fluid Method for Free Surface Flows in Polyhedral Finite Volume Framework. *Computers and Fluids* 153. Elsevier Ltd: 1–19.
https://doi.org/10.1016/j.compfluid.2017.05.003

Vukčević, V., Jasak, H., Malenica. Š., 2016. Decomposition Model for Naval Hydrodynamic Applications, Part I: Computational Method. Ocean Engineering 121:37–46.

Yoon, H., Gui, L., Bhushan, S., Stern, F., 2014. Tomographic PIV Measurements for a Surface Combatant at Straight Ahead and Static Drift Conditions, in: 30th Symposium on Naval Hydrodynamics, November: 2–7.
Yoon, H., Stern, F. 2017. Phase-Averaged Tomographic PIV Measurements for Surface Combatant 5415 in Pure Sway Maneuver : Experimental Setup , UA , and Preliminary Results, in: The 30th American Towing Tank Conference. Vol. 2.

8 AUTHORS BIOGRAPHY

Inno Gatin is a post-doctoral researcher at University of Zagreb working on several projects relating to computational fluid dynamics in the field of naval architecture and offshore engineering. He is a part of a research group responsible for development and maintenance of foam-extend and the Naval Hydro Pack.

Vuko Vukčević is a post-doctoral researcher at University of Zagreb working various projects in the field of computational fluid dynamics related to various industries. His speciality is numerical modelling in the field of naval architecture and offshore engineering. He is a part of a research group responsible for development and maintenance of foam-extend and the Naval Hydro Pack.

Hrvoje Jasak is a full time professor at University of Zagreb, leading a research group that maintains and develops the foam-extend software, as well as the Naval Hydro Pack. He is one of the principal authors of the OpenFOAM software on which the foam-extend branch is based. He leads multiple academic and industrial international projects in the field, and has a lot of experience in numerical modelling and software development.

BENCHMARKING OF DIFFRAC, FATIMA, HYDROSTAR, MOSES, NEMOH, OCTOPUS, PDSTRIP, RAPID, SEAWAY, SLENDERFLOW AND WAMIT AGAINST MEASURED VERTICAL MOTIONS OF THE DUISBURG TEST CASE CONTAINER SHIP IN SHALLOW WATER

Tim Gourlay,
Perth Hydro, Australia

Evert Lataire,
Maritime Technology Division, Ghent University, Belgium

Guillaume Delefortrie,
Flanders Hydraulics Research & Maritime Technology Division, Ghent University, Belgium

Luca Donatini and **Manasés Tello Ruiz,**
Maritime Technology Division, Ghent University, Belgium

Daniel Veen,
Bentley Systems, Australia

Tim Bunnik and **Reint Dallinga**,
Marin, The Netherlands

BENCHMARKING OF DIFFRAC, FATIMA, HYDROSTAR, MOSES, NEMOH, OCTOPUS, PDSTRIP, RAPID, SEAWAY, SLENDERFLOW AND WAMIT AGAINST MEASURED VERTICAL MOTIONS OF THE DUISBURG TEST CASE CONTAINER SHIP IN SHALLOW WATER

Tim Gourlay, Perth Hydro, Australia
Evert Lataire, Maritime Technology Division, Ghent University, Belgium
Guillaume Delefortrie, Flanders Hydraulics Research & Maritime Technology Division, Ghent University, Belgium
Luca Donatini, Maritime Technology Division, Ghent University, Belgium
Manasés Tello Ruiz, Maritime Technology Division, Ghent University, Belgium
Daniel Veen, Bentley Systems, Australia
Tim Bunnik, Marin, The Netherlands
Reint Dallinga, Marin, The Netherlands

SUMMARY

In this paper, we present a comparison of calculated and measured vertical motions of the Duisburg Test Case (DTC) container ship, in calm water or head waves, at rest or with forward speed.

At forward speed in calm water, running sinkage and trim (squat) have been compared with the potential-flow methods implemented in SlenderFlow and RAPID software. In head seas, bow and stern vertical motions have been compared with strip theory (OCTOPUS, PDStrip, SEAWAY) and panel method wave-induced motion codes (DIFFRAC, FATIMA, HydroSTAR, MOSES, NEMOH, WAMIT).

The results in this paper are intended to form a useful set of benchmarking data for assessing the suitability of each code in different conditions, for container ships in shallow water.

NOMENCLATURE

CoG	Ship centre of gravity
DTC	Duisburg Test Case container ship
RAO	Response Amplitude Operator
WG4	'Wave Gauge 4' mounted on model test carriage, 4.03 m forward of midships
s_a	Mean sinkage at aft perpendicular (m)
s_f	Mean sinkage at forward perpendicular (m)
x	Distance forward of aft perpendicular (m)
z_a	Heave amplitude at aft perpendicular (m), defined as half of peak-to-peak heave
z_f	Heave amplitude at forward perpendicular (m), defined as half of peak-to-peak heave
ε_a	Heave phase at aft perpendicular (deg), ahead of wave elevation at CoG
ε_f	Heave phase at forward perpendicular (deg), ahead of wave elevation at CoG
ζ	Wave amplitude (m), defined as half of wave height

1 INTRODUCTION

Model tests of the Duisburg Test Case (DTC) were undertaken at Flanders Hydraulics Research as part of the EU-funded SHOPERA project, and have been made available as a set of benchmarking data for the MASHCON 2019 conference (Van Zwijnsvoorde et al., 2019).

In this paper, we shall use the cases from Van Zwijnsvoorde et al. (2019) shown in Table 1.

Table 1. Test cases used for comparison

Test number	Static UKC (% draft)	Speed (full-scale)	Wave height (full-scale)	Wave period (full-scale)
C1	100%	6 knots	0.00 m	-
C2	100%	16 knots	0.00 m	-
C3	20%	6 knots	0.00 m	-
CW1	100%	0 knots	4.86 m	13.0 s
CW2	100%	6 knots	5.55 m	13.0 s
CW3	100%	16 knots	5.56 m	13.0 s
CW4	20%	0 knots	1.98 m	15.7 s
CW5	20%	6 knots	1.90 m	15.7 s

The used scale factor is 89.11. The test cases CW2 and CW5 are semi-blind, i.e. only wave data were provided.

2 MODEL TEST DATA ANALYSIS

Post-processing of the model test data described in Van Zwijnsvoorde et al. (2019) has been undertaken by Ghent University and Flanders Hydraulics Research to compare the test data with numerical predictions.

For calm water tests, the mean values are computed based on 30% to 95% of the steady state interval.

For tests in waves, a sample of the time records was selected using the time and periods recommended in

Appendix 1 of Van Zwijnsvoorde et al. (2019). Then, a Fourier analysis has been performed by fitting the data to Eq. (1) using a least square method with eight unknown parameters ($a_0, a_1, b_1, a_2, b_2, a_3, b_3, \omega_1$).

$$f = a_0 + \sum_{j=1}^{3} a_j \cos(j\omega_1 t) + b_j \sin(j\omega_1 t) \qquad (1)$$

The computed phase angles have been corrected to correspond to a case where the incident wave has a zero phase at the CoG. For this purpose the spatial phase difference ($kx_{WG4} - kx_{CoG}$) between the position of WG4 and the CoG has been used. This correction was needed to allow further comparison between experiments and numerical results. Bear in mind that only the first harmonic components for the wave and ship motions are used in this case and they are presented dimensionless. The latter has been obtained by dividing the respective magnitudes ($\sqrt{a_1^2 + b_1^2}$) by half of the wave heights reported in Table 6 in Van Zwijnsvoorde et al. (2019).

3 HULL MODELLING

The hull sections used for OCTOPUS, PDStrip, SEAWAY and SlenderFlow were developed at Perth Hydro, by reading the DTC IGES file into DELFTship and calculating offsets at 21 evenly-spaced waterlines from the keel to the design waterline. One station was placed at the aft extremity of the waterline (x = -0.7), followed by 26 evenly-spaced stations from the aft extremity of the stern bulb (x = 8.4) to the forward extremity of the bow bulb (x = 366.1).

The 4680-panel hull surface mesh used for WAMIT was developed at Perth Hydro, using the OCTOPUS 3D Mesher and the publicly-available DTC IGES file. This same mesh was converted at Ghent University to HydroSTAR format using the HydroSTAR *convert* tool, and to NEMOH format using a modified version of the open-source *meshmagick* tool. For MOSES, the mesh was refined at Bentley Systems, so that it consisted of triangles only.

The 6514-panel mesh used for DIFFRAC and FATIMA was developed at Marin from the DTC IGES file.

The section offsets and surface meshes are shown in Figure 1.

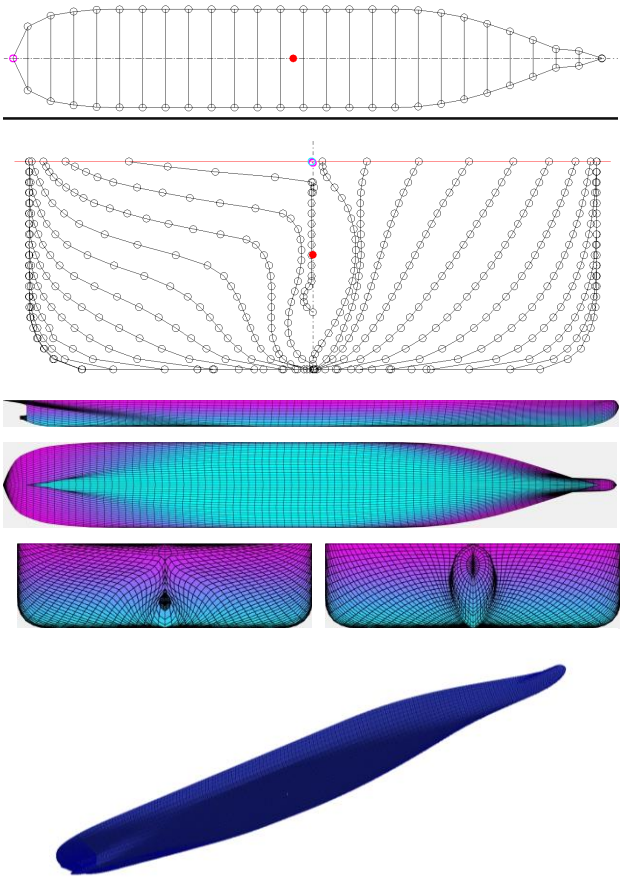

Figure 1. (top) hull sections; (middle) 4680-panel surface mesh; (bottom) 6514-panel surface mesh

4 SHIP MOTION CODES

Ship motion codes used are shown in Table 2.

Table 2. Software used for benchmarking study

Program, version	Type	Forward speed	Developer	Reference	Calculations done by
DIFFRAC	Linear 3D radiation/diffraction panel code	No	Marin	Buchner et al. (2001)	Marin
FATIMA	Linear 3D radiation/diffraction panel code using Rankine sources	Yes, using nonlinear potential flow solution (RAPID)	T.J.M. Bunnik	Bunnik (1999)	Marin
HydroSTAR v8.00	Linear 3D radiation/diffraction panel code	Yes, using encounter frequency correction	Bureau Veritas	Bureau Veritas (2011)	Ghent University
MOSES v11.0	Linear 3D radiation/diffraction panel code	Not used here	Bentley Systems	Ultramarine (2012)	Bentley Systems
NEMOH v2.03	Linear 3D radiation/diffraction panel code	No	École Centrale Nantes	Babarit and Delhommeau (2015)	Ghent University
OCTOPUS v6.4.14	Strip theory code	Yes	ABB	Amarcon (2009)	Ghent University
PDStrip v27	Rankine-source strip theory code	Yes	H. Söding	Söding (2006)	Perth Hydro
RAPID	Nonlinear Rankine-source potential flow method	Yes	H.C. Raven	Raven (1996)	Marin
SEAWAY v2017	Strip theory code	Yes	J.M.J. Journée	Journée (2001)	Ghent University
SlenderFlow	Steady slender-body shallow-water code	Yes	T.P. Gourlay	Ha and Gourlay (2018)	Perth Hydro
WAMIT v7.2	Linear 3D radiation/diffraction panel code	No	WAMIT Inc.	WAMIT (2016)	Perth Hydro

5 ADDITIONAL SOLVER SETTINGS

In NEMOH, CoG RAOs and vertical motions at specific points were calculated externally based on the wave loads and hydrodynamic coefficients returned by NEMOH.

In OCTOPUS, shallow-water hydrodynamic coefficients were calculated using the method of Keil (1974). Modified strip theory was used for all calculations. Classical wave loads were used at 100% UKC, and diffraction wave loads at 20% UKC.

In PDStrip, no flow separation was specified along the hull, with zero wave steepness (linear motions). The transom was set up as wet at zero forward speed and dry at non-zero forward speeds.

In RAPID, the open-water method was used (the effect of channel walls was neglected).

In SEAWAY, calculations were done using classical or diffraction wave loads, and ordinary or modified strip theory.

In SlenderFlow, the linear rectangular-canal method was used, based on the towing tank width.

In WAMIT, the direct solver was used, with the source method.

6 RESULTS: MEAN SINKAGE

Results for mean sinkage are shown in Table 3 and Figure 2.

Table 3. Mean sinkage results

	Sinkage at aft perpendicular s_a		
	Model test	SlenderFlow	RAPID
C1	0.049	0.050	0.029
C2	0.438	0.418	0.274
C3	0.110	0.085	0.069
CW2	blind	0.050	-
CW3	0.522	0.418	-
CW5	blind	0.085	-

	Sinkage at forward perpendicular s_f		
	Model test	SlenderFlow	RAPID
C1	0.081	0.085	0.091
C2	0.737	0.699	0.646
C3	0.132	0.144	0.131
CW2	blind	0.085	-
CW3	0.735	0.699	-
CW5	blind	0.144	-

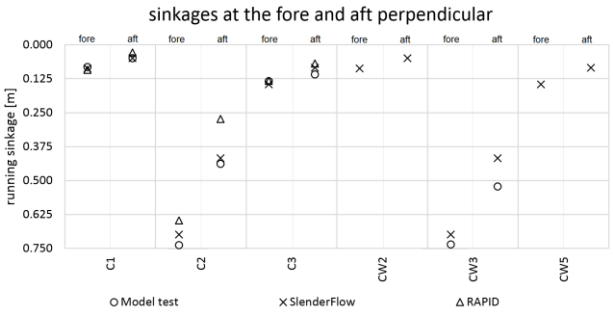

Figure 2. Sinkage results

7 RESULTS: MOTION AMPLITUDES

Motion amplitude results are shown in Table 4 to Table 8 and Figure 3 to Figure 7, for test cases CW1 to CW5.

Table 4. Results for test CW1, 100% UKC, 0 knots

	z_a/ζ	ε_a	z_f/ζ	ε_f
Model tests	0.330	52	0.502	191
DIFFRAC open water	0.262	52	0.553	176
DIFFRAC channel	0.280	25	0.615	172
HYDROSTAR	0.257	58	0.520	177
MOSES	0.272	67	0.532	178
NEMOH	0.267	57	0.526	178
OCTOPUS	0.621	105	0.188	272
PDSTRIP	0.494	90	0.419	200
SEAWAY Class. Ord.	0.674	105	0.255	256
SEAWAY Diff. Ord.	0.353	89	0.445	197
SEAWAY Class. Mod.	0.674	105	0.255	256
SEAWAY Diff. Mod.	0.353	89	0.445	197
WAMIT	0.245	59	0.513	176

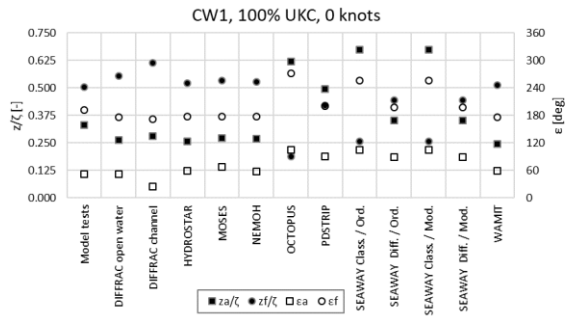

Figure 3. Results for test CW1, 100% UKC, 0 knots

Table 5. Results for test CW2, 100% UKC, 6 knots

	z_a/ζ	ε_a	z_f/ζ	ε_f
Model tests			Blind	
FATIMA	0.280	50	0.534	148
HYDROSTAR	0.420	53	0.536	161
OCTOPUS	0.635	82	0.288	237
PDSTRIP	0.585	74	0.444	179
SEAWAY Class. Ord.	0.722	86	0.394	240
SEAWAY Diff. Ord.	0.407	70	0.476	173
SEAWAY Class. Mod.	0.661	85	0.352	229
SEAWAY Diff. Mod.	0.417	68	0.498	174

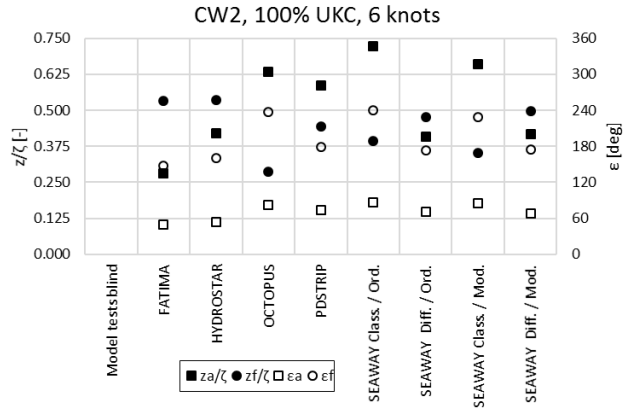

Figure 4. Results for test CW2, 100% UKC, 6 knots

Table 6. Results for test CW3, 100% UKC, 16 knots

	z_a/ζ	ε_a	z_f/ζ	ε_f
Model tests	0.282	22	0.342	133
FATIMA	0.277	355	0.427	111
HYDROSTAR	0.522	0	0.483	130
OCTOPUS	0.511	32	0.359	166
PDSTRIP	0.536	34	0.363	146
SEAWAY Class. Ord.	0.612	44	0.418	186
SEAWAY Diff. Ord.	0.432	25	0.384	142
SEAWAY Class. Mod.	0.491	39	0.342	166
SEAWAY Diff. Mod.	0.427	21	0.420	136

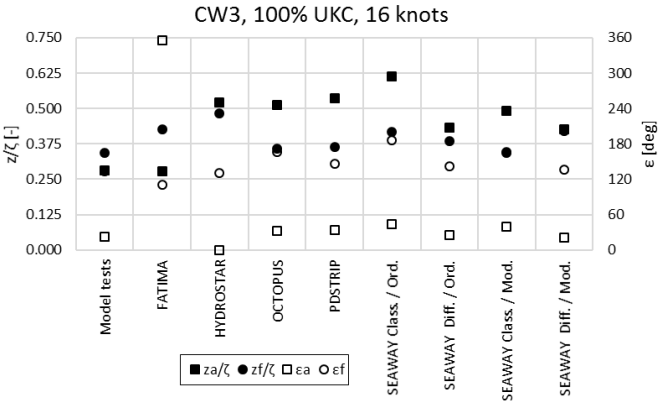

Figure 5. Results for test CW3, 100% UKC, 16 knots

Table 7. Results for test CW4, 20% UKC, 0 knots

	z_a/ζ	ε_a	z_f/ζ	ε_f
Model tests	0.275	36	0.392	180
DIFFRAC open water	0.358	57	0.465	158
DIFFRAC channel	0.353	39	0.411	176
HYDROSTAR	0.358	59	0.445	159
MOSES	0.380	64	0.452	156
NEMOH	0.368	58	0.455	161
OCTOPUS	0.538	71	0.051	273
PDSTRIP	0.563	83	0.222	187
SEAWAY Class. Ord.	0.579	59	0.175	194
SEAWAY Diff. Ord.	0.441	77	0.397	174
SEAWAY Class. Mod.	0.579	59	0.175	194
SEAWAY Diff. Mod.	0.441	77	0.397	174
WAMIT	0.349	59	0.439	158

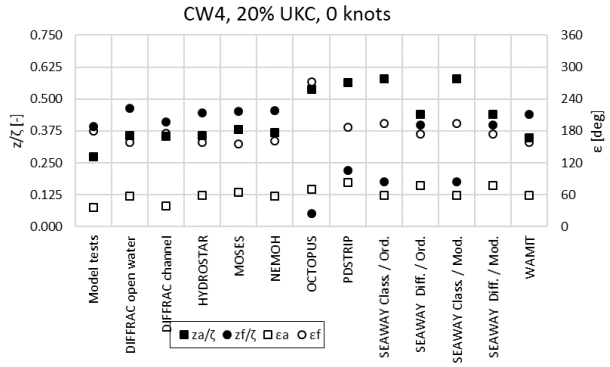

Figure 6. Results for test CW4, 20% UKC, 0 knots

Table 8. Results for test CW5, 20% UKC, 6 knots

	z_a/ζ	ε_a	z_f/ζ	ε_f
Model tests	Blind			
FATIMA	0.352	37	0.293	135
HYDROSTAR	0.474	35	0.359	154
OCTOPUS	0.501	80	0.210	258
PDSTRIP	0.586	61	0.234	204
SEAWAY Class. Ord.	0.587	49	0.247	227
SEAWAY Diff. Ord.	0.471	49	0.321	161
SEAWAY Class. Mod.	0.496	55	0.153	232
SEAWAY Diff. Mod.	0.479	47	0.352	159

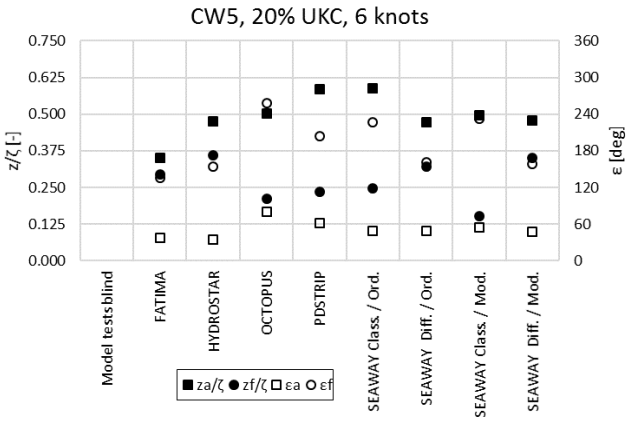

Figure 7 Results for test CW5, 20% UKC, 6 knots

8 EFFECT OF TOWING TANK WIDTH

Calculations have been done using DIFFRAC on the effect of towing tank width on wave-induced vertical motions. Results are shown in Figure 8 for 100% UKC.

We see that at certain frequencies, strong heave amplification is predicted to occur as a result of the wall effect. Strong heave amplification in towing tank model tests at particular frequencies was described in a previous benchmarking study (Gourlay et al. 2015, Figure 11).

For 20% UKC, the effect of towing tank width, as calculated using DIFFRAC, is shown in Figure 9. At the model test frequency, heave motions are predicted to be smaller in the towing tank than in open water.

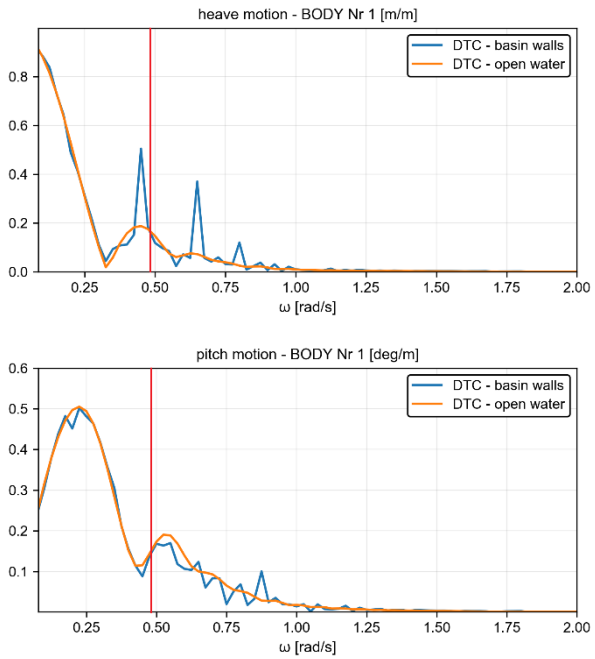

Figure 8. Heave (top) and pitch (bottom) for DTC hull at zero speed in FHR towing tank or in open water, as calculated using DIFFRAC for 100% UKC. Red line shows model test wave frequency.

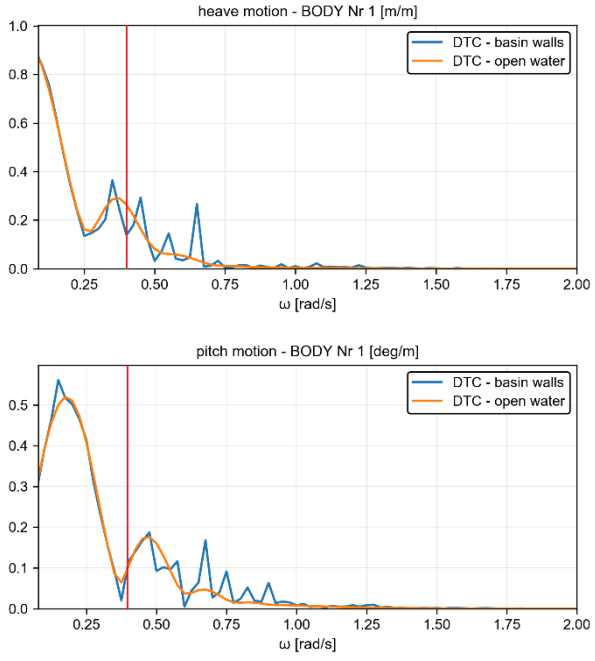

Figure 9. Heave (top) and pitch (bottom) for DTC hull at zero speed in FHR towing tank or in open water, as calculated using DIFFRAC for 20% UKC. Red line shows model test wave frequency.

9 CONCLUSIONS

Detailed conclusions on the applicability of each code may be made once the blind model test data is released. At this stage, the following preliminary conclusions may be made:

- All of the zero-speed radiation/diffraction panel codes (DIFFRAC, HydroSTAR, MOSES, NEMOH, WAMIT) give comparable results, that are much closer to the zero-speed model test results than the strip theory codes (OCTOPUS, PDStrip, SEAWAY).
- The diffraction wave load method in SEAWAY gives better results than the classical wave load method in SEAWAY, for all cases so far.
- The towing tank walls are predicted to have an important effect on vertical motions at particular frequencies.

10 REFERENCES

Amarcon 2009. Octopus-Office 6 User Manual, July 2009.

Babarit, A., Delhommeau, G. 2015. Theoretical and numerical aspects of the open source BEM solver NEMOH, in: Proceedings of the 11th European Wave and Tidal Energy Conference (EWTEC2015), Nantes, France.

Buchner, B. , van Dijk, A., de Wilde, J. 2001. Numerical multiple-body simulations of side-by-side mooring to an FPSO, in: Proceedings of the 11th International Offshore and Polar Engineering Conference (IOPEC2001), Stavanger, Norway.

Bunnik, T.H.J. 1999. Seakeeping calculations for ships, taking into account the non-linear steady waves. PhD Thesis, Delft University of Technology, The Netherlands.

Bureau Veritas 2011. HydroSTAR for Experts User Manual. Bureau Veritas, Paris.

Gourlay, T.P., von Graefe, A., Shigunov, V., Lataire, E. 2015. Comparison of AQWA, GL RANKINE, MOSES, OCTOPUS, PDSTRIP and WAMIT with model test results for cargo ship wave-induced motions in shallow water, in: Proceedings of the 34th International Conference on Ocean, Offshore and Arctic Engineering (OMAE2015). St. John's, Canada.

Ha, J.H., Gourlay, T.P. 2018. Validation of container ship squat modeling using full scale trials at the Port of Fremantle. Journal of Waterway, Port, Coastal, and Ocean Engineering, 144(1).

Journée, J. M. J. 2001. User Manual of SEAWAY, Release 4.19. Techn. Rep. 1212a, Ship Hydromechanics Laboratory, Delft University of Technology.

Keil, H. 1974. Die Hydrodynamische Kräfte bei der

periodischen Bewegung zweidimensionaler Körper an der Oberfläche flacher Gewasser, Rep. Nr. 305, Institut für Schiffbau, University Hamburg.

Raven, H.C. 1996. A solution method for the nonlinear ship wave resistance problem. PhD Thesis, MARIN / Delft University of Technology, The Netherlands.

Söding, H. 2006. Program PDSTRIP: Public Domain Strip Method. Retrieved from www.sourceforge.net.

Ultramarine Inc. 2012. Reference manual for MOSES.

Van Zwijnsvoorde, T., Tello Ruiz, M., Delefortrie, G., Lataire, E. 2019. Sailing in shallow water waves with the DTC container carrier, in: Proceedings of the 5th International Conference on Ship Manoeuvring in Shallow and Confined Water with non-exclusive focus on Manoeuvring in Waves, Wind and Current. Ostend, Belgium.

WAMIT 2016. WAMIT User Manual Version 7.2.

11 AUTHORS BIOGRAPHY

Tim Gourlay, PhD, is principal consultant at Perth Hydro. He undertakes ship hydrodynamics modelling and measurements for industry and government in Western Australia. His previous experience includes participating in a 2015 benchmarking study on model-scale ship motions in waves, as well as full-scale measurements on over 70 ships.

Evert Lataire Prof., naval architect, is currently head of the Maritime Technology Division at Ghent University. He has written a PhD on the topic of bank effects mainly based upon model tests carried out in the shallow water towing tank of FHR. His fifteen year experience includes research on ship manoeuvring in shallow and confined water such as ship-ship interaction, ship-bottom interaction and ship-bank interaction.

Guillaume Delefortrie, PhD, naval architect, is expert nautical researcher at Flanders Hydraulics Research and visiting professor at Ghent University. He is in charge of the research in the Towing Tank for Manoeuvres in Confined Water and the development of mathematical models based on model tests. He has been secretary of the 27th and 28th ITTC Manoeuvring Committee and is chairman of the 29th ITTC Manoeuvring Committee.

Luca Donatini, naval architect, is a PhD student at Ghent University. He is currently working on a project aimed at improving the modelling of hydro/meteo effects in the ship manoeuvring simulator of Flanders Hydraulic Research. His previous experiences encompass seakeeping studies to allow inland vessels on a Belgian sea trajectory and the inclusion of hydro/meteo effects in an open source mooring dynamics code. He also has an extensive experience in atmospheric and spectral wave modelling from global to regional scales.

Manasés Tello Ruiz PhD, Naval Architect and Marine Engineer, is a Research Staff at Ghent University. He has been involved in several (inter-)national projects with main focus on manoeuvring, seakeeping, and wave energy converters. Currently, he is working on ship air pollution and machine learning techniques applied to ship hydrodynamics. At present he is also a member of the ITTC Specialist Committee of Manoeuvring in Waves, at which he has been appointed as secretary.

Daniel Veen, PhD, is the Product Manager for MOSES at Bentley Systems. He is also a senior developer whose focus is the hydrodynamics solver of MOSES. His previous experience includes developing numerical techniques for modeling slam events.

Tim Bunnik, PhD, Mathematician, is senior researcher at MARIN. He is coordinating research on seakeeping, ocean engineering and offshore renewable energy. He has been involved in the development of many numerical methods for wave-structure interaction, ranging from linear diffraction codes to CFD-RANS methods.

Reint Dallinga, naval architect, is Senior Project Manager and Seakeeping Knowledge Coordinator in the Ships Department of MARIN. His interest and experience is in the impact of seakeeping hydrodynamics on the design and performance of ships at sea. Recent work covered the prediction area of added resistance by means of the FATIMA code and its application in quantifying sustained speed and understanding minimum power requirements for ships in adverse weather.

SIMULATION OF THE EFFECT OF INSTALLED POWER MINIMISATION ON SHIP MOTION

Emmanuel Irimagha, Zhiqiang Hu and **Richard Birmingham**,
Newcastle University, United Kingdom

Michael Woodward,
University of Tasmania, Australia

SIMULATION OF THE EFFECT OF INSTALLED POWER MINIMISATION ON SHIP MOTION

Emmanuel Irimagha, **Zhiqiang Hu** and **Richard Birmingham**, Newcastle University, United Kingdom
Michael Woodward, University of Tasmania, Australia

SUMMARY

Predicting the influence of adverse weather on the safety of a ship if the engine is derated for the purpose of improving the Energy Efficiency Design Index (EEDI) has been a hot topic since its recommendation. Most researches are based on predicting the power loss and speed drop. However, there is need to predict the dynamic characteristics at different levels of power in defined adverse weather conditions. Predicting this will require detailed modelling which may be very expensive and time consuming. Eshipman is a FORTRAN compiler-based program aimed at minimising the time and financial demands of carrying out these predictions with minimal but acceptable accuracy.

To test the idea, parameters of a specimen ship and its experimental results were used to simulate the motion of the ship in calm weather and the results was compared with experimental plots. The program that simulates the environmental conditions were merged with the calm water code, thereby creating in a code that simulates the motion of a ship in adverse weather condition.

The results show how the roll angle reduces with a reduction in power. Additional results show the speed drop for different sea states, under the influence of wind and waves and they are compared with published works. The heave and pitch response increases with reducing power and then starts dropping from 65% power. The prediction could guide the designer on how best to mitigate these effects.

NOMENCLATURE

L	length between perpendiculars, LBP (m)
Loa	Length overall (m)
B	Breadth moulded (m)
m	Mass of ship (kg)
D	Depth Moulded (m)
T	Mean Draught (m)
Δ	Mass Displacement of Ship (kg)
∇	Volume Displacement of ship (m^3)
FP	Forward Perpendicular
AP	Aft Perpendicular
k_{yy}	Longitudinal radius of gyration (m)
KM	Distance from Keel to Metacentre (m)
KG	Keel to Centre of Gravity (m)
$G_z(\phi)$	Righting moment as a function of roll angle (m)
I_x, I_y, I_z	Moments of inertia about the body axis system (Kg m^2)
K, N, M	Hydrodynamic moment components about body axes (Nm)
$EEOI$	Energy Efficiency Operational Indicator
$\dot{u}$	Surge acceleration (m/s^2)
$\dot{v}$	Sway acceleration (m/s^2)
$\dot{p}$	Roll acceleration (rad/s^2)
$\dot{r}$	Yaw acceleration (rad/s^2)
p, q, r	Rotational velocity components of ship relative to inertial reference system along body axes (rad/s)
X, Y, Z	Hydrodynamic force components along body axes (N)
u, v, w	Translational velocity components of ship relative to fluid along body axes (m/s)
$Y_W^{Diff}, K_W^{Diff}, N_W^{Diff}$	Diffraction components of wave loading in sway, roll and yaw.
X_{FK},Y_{FK}	Froude-Krylov forces in surge and sway respectively
F_c , F_s , K_c , K_s , N_c , N_s	Are functions that are defined in Motoki Araki (Dec 2012)
K_{FK}, N_{FK}	Froude-Krylov moments in roll and yaw respectively
V_s	Resultant velocity at mid-ship (m/s)
V	Initial velocity of ship (m/s)
ω_w	Wave frequency (rad/s)
L_w	Wave length (m)
v_{mw}	Mean velocity (m/s)
$\overline{u}$	Gust speed (m/s)

$\dot{x}$	Instantaneous velocity of the structural member (m/s)
V_c , ψ_c	Current velocity and direction $(\frac{m}{s}, rad)$
x, y, z	Distance along the principal axes (m)
x_G, y_G, z_G	Coordinates of the centre of gravity in the body axis system (m)
$xpos, ypos$	Component of the resultant position of the origin, O, of the ship along a fixed set of earth axes, x_0 and y_0 (m)
h	Time step (s)
Δ	Displacement weight of ship (kg)
ζ_w	Wave amplitude (m)
ξ_G	Longitudinal position of centre of ship gravity from a wave trough (m)
$\xi_G{}'$	ξ_G/wavelength (-)
$S(x)$	Sectional wetted area (m^2)
$S_y(x)$	Sectional added mass in sway (kg)
$S_y(x)l_n$	Section added moment of inertia in roll (kgm^2)
k	Wave number $(1/m)$
ψ	Ship's course (rad)
ρ	Mass density of sea water (kgm^3)
ϕ	Roll angle: starboard down positive (rad)
ψ	Yaw angle: bow to starboard positive (rad)
a_H	Rudder – hull interaction coefficient (-)
δ	Rudder angle (rad)
δ_E	Command rudder angle (rad).
A_R	Rudder area (m²)
K_p	Proportional action factor (-)
c_{pv}, c_{pr}	Propeller flow rectification coefficients
$c_{\delta r}, c_{\delta rrr}, c_{\delta rrv}$	Rudder wake coefficients in equation for V_R.
D_p	Propeller diameter (m)
γ	Flow rectification coefficient (-)
F_N	Normal force action on the rudder (N)
J	Advance coefficient (-)
k	Constant in the Equation for u_R
K_T	Thrust coefficient (-)
T_p	Propeller thrust (N)
T_p'	Non-dimensional propeller thrust (-)
n	Propeller shaft revolution (revs/sec)
u_p	Effective propeller inflow velocity (m/s)
u_R, v_R	Components of rudder effective inflow velocity(m/s)
V_R	Effective rudder inflow velocity (m/s)
w_p	Effective propeller wake fraction (m/s)
x_H	x – Coordinate of point on which normal force FN acts (m)
x_p	x – Coordinate of propeller position in equation for u_p (m)
x_R	x – Coordinate of point on which rudder force Y_δ acts (m)
z_R	z – Coordinate of point on which rudder force Y_δ acts (m)
Λ	Rudder aspect ratio
α_R	Effective rudder inflow angle (rad)
τ	Constant in the Equation for u_p (-)
ε	Constant in the Equation for u_R (-)
χ	heading angle from wave direction (rad)
χ_{wind}	Wind angle of attack (rad)

1. INTRODUCTION

The design and production of ships have traditionally been driven by cost, customer requirements, reliability and efficiency while ensuring that environmental regulations are considered (Irimagha et al., 2016). In its 62nd Session, the International Maritime Organisation (IMO) made mandatory the Energy Efficiency Design Index (EEDI) for new ships and Ship Energy Efficiency Management Plan (SEEMP) for all ships. IMO, (2011).

In respect of the above, there was some agreed work plan in which the Marine Environmental Protection Committee (MEPC) was tasked with amongst others, further improving:

- Interim Guidelines for determining minimum propulsion power and speed to enable safe manoeuvring in adverse weather conditions or sea states.

The option of minimum installed power on a new ship (which includes the derating of the engine of an existing ship undergoing major modification) is very useful in

reducing environmental pollution but this might end up creating other problems. For example,

- A vessel may not be able to safely manoeuvre in certain possible adverse weather conditions in service.
- Routes of vessel might change in the course of its lifetime and the vessel may operate in areas with different environmental conditions at some point in its service life.
- With age, a vessel may require more power for meeting its design speed and the engine performance generally reduces.

Motions of a ship in adverse weather conditions result in increased effects on roll, pitch and heave motions to non-negligible values that would increase the likelihood contact with seabed in shallow waters, propeller emergence, passenger discomfort, these defects may adversely affect the manoeuvrability of the vessel and certain researchers have started investigating alternative methods of improving efficiency, effects on speed and power, and there have long been proposals for methods of predicting the impact of environmental forces and moments on ship motion.

Ma et al. (2017) mentioned that considering the inclusion of waste heat recovery systems (WHRS) could improve the overall ship efficiency and as well reduce emissions simultaneously. They proposed three types of WHRS for recovering waste heat from a 10000 TEU conceptual large container ship driven by a modern low speed marine diesel engine. Two software packages were developed by them for calculating the EEDI and the EEOI (Energy Efficiency Operational Index) of the subject container ship, and their results indicated that the large container ship itself can reach the IMO requirements of EEDI at the first stage with a reduction factor of 10% under the reference line value. It was also claimed that the proposed waste heat recovery systems can improve the ship EEDI reduction factor by up to 20% under the reference line value.

In his PhD thesis, Trodden (2014) proposed a propeller selection method that is most suited to ships, which are susceptible to relatively large drift angles and/or relatively high installed power requirements. He suggested that the EEDI in its present implementation discourages design for in-service conditions. The value for the EEDI that the ship attains is verified from sea trials in calm water. A ship optimised for normal service conditions will not be optimal when run in trial conditions, and thus may even fail the EEDI requirement, however in real working conditions the design may surpass the EEDI requirement.

Lewis (1990) gave an in-depth explanation of controllability of ships and derived mathematical expressions that define the criterion for stability and the practical conditions that will affect the said criteria. Fang, et al. (2005) developed a simplified six degrees of freedom mathematical model encompassing calm water manoeuvring and traditional seakeeping theories to simulate the ship turning circle test in regular waves.

Faltinsen, et al. (1980), proposed a procedure for calculating the transverse drift force and mean yaw moment on a ship in regular waves of any wave direction. They also presented a derivation of an asymptotic formula for small wave lengths and explained the influence of wave induced motions on the wake using the direct pressure integration approach. The said procedure proposed by these authors was assumed to be valid for small Froude numbers (i.e. Fn $\leq$ 0.2), however, the deficiency of the method being limited to regular waves was made up by proposing a simplified way of applying the results from a regular wave to short waves as was further illustrated in Faltinsen (1993).

Letki and Hudson (2005) presented a summary of the principle of a unified mathematical model for the manoeuvring of a vessel travelling in a seaway. They carried out some validations of the unified mathematical model proposed earlier by Bailey (1997) using a British Bombardier tanker for defined manoeuvres and gave the results of their study of the effects of waves on the ship's manoeuvring characteristics for both following and for head seas.

Kim et al. (2017) demonstrated the capabilities of the 2-D and 3-D potential methods, and CFD with an Unsteady Reynolds-Averaged Navier-Stokes (URANS) approach to calculate the added resistance and ship motions in regular waves in various wave headings. The method is said to be capable of being used to estimate the impacts on the ship operating speed and the required sea margin in irregular seas and, they used it to estimate the ship speed loss of the S175 container ship in specific sea conditions of wind and waves. However, the speed loss estimation was driven towards assessment of how the weather conditions will affect the emissions.

This paper proposes a methodology that can be used during the design stage or before taking a decision to modify an existing ship to establish a safe lower limit for the manoeuvring performance in adverse environmental conditions that the ship might reasonably encounter in operation. The assessment of this method follows the experimental work of Son and Nomoto (1981), with which a new computer program, EShipman was used to evaluate the effects of installed power (MCR) on the roll angle when the ship is subjected to defined adverse weather conditions.

Eshipman is basically a ship manoeuvring simulation program written from start with algorithms that makes for speed with acceptable accuracy (within the scope of the available technological resources), robust and easily affordable. And it can be run a good number of times to determine performance in calm weather and in anticipated adverse weather conditions in terms of installed power, both for a new design and for the evaluation of existing

ships intending to undergo modifications towards making them meet the EEDI requirement. Thus it can be applied to substantially reduce the number of experimental or commercial computational fluid dynamic based test runs done for improved acceptability.

2. SHIP AND PROPULSION PARAMETERS, AND COORDINATE SYSTEM

Table 1 shows the characteristics of the ship that is studied and Figure 1 shows the coordinate system that is used in this study.

Table 1. Subject ship parameter

Description	Value
LBP	175m
Breadth moulded	25.4 m
Depth Moulded	11 m
Draught Ballast	8.5m
Draught Loaded	9.5 m
Displacement Volume	21222 m^3
Deadweight	2628.88
LCG aft of mid-ship	2.5 m
Longitudinal radius of gyration	0.236 L
Block coefficient	0.572
Mid-ship coefficient	0.98
KM	10.39m
KB	4.6154m
KG	10.09m
Rudder Area	33.0376
Propeller Diameter	6.533
Aspect Ratio	1.8219
Pitch ratio	1.009
Maximum Continuous Rating (MCR)	14280Kw
T'	0.000511
Engine Speed @ 100% of MCR	105 rpm

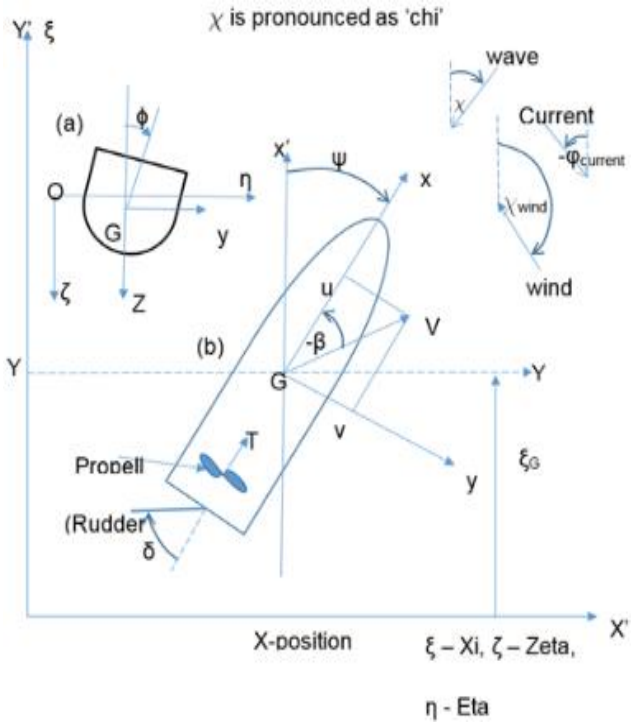

Figure 1. Earth-fixed and body-fixed coordinate system.

3. MATHEMATICAL MODEL

This section describes the major mathematical formulations utilised when developing the program, and which can be adjusted by the user to meet a particular need. In the development of this paper, a modular approach was used, which enabled the code to be written in a structured fashion with clear divisions between the forces and moments contributions in order to allow for easier maintenance and possible future modification and extensions of its capabilities, as in Ogawa and Kasai (1978) and Yasukawa and Yoshimura (2015). The forces and moments contained within each module were constructed with reference to the particular physical processes involved.

Son and Nomoto (1981), demonstrated the fact that in practice, rigid body roll motions can be observed during sharp turning in calm water because of the rudder and overall centrifugal forces and proposed a 4 degree of freedom equation which has been used in this work. The effects of these forces and moments on a moving ship are further increased by environmental wind and waves disturbances, especially leading to disturbing levels of roll, pitch and heave. EShipman was equipped with the ability to compute a coupled heave and pitch motion that are uncoupled from the other 4 degrees of freedom, however, a plot was used to demonstrate the response with different power levels and no much details will be shown here.

In a body-fixed coordinate system (Figure 1) with the origin lying in the mid-ship point assuming the ship to be symmetrical about its longitudinal centre-plane, thus $y_G = 0$, i.e. the centre of gravity has coordinates $(x_G, 0, z_G)$, and $I_{xz}\ I_{yz},\ I_{xy}$ i.e. the products of inertia about the body axis system are ignored; four of the coupled six degrees of freedom equation motion, extracted from Fossen (1994), are given by:

$$X = m[(\dot{u} - vr) - x_G(r^2) + z_G(pr)] \quad (1)$$

$$Y = m[(\dot{v} + ur) + z_G(-\dot{p}) + x_G(-\dot{r})] \quad (2)$$

$$K = I_x\dot{p} + m\{-z_G(\dot{v} + ur)\} \quad (3)$$

$$N = I_z\dot{r} + m\{x_G(\dot{v} + ur)\} \quad (4)$$

The forces and moments acting on a ship during manoeuvring in adverse weather are:

- Inertial reaction forces caused by the ship's acceleration.
- Hydrodynamic forces acting on the hull and appendages due to ship velocity, acceleration, propeller rotation and rudder deflection.
- Environmental forces due to wind, waves and currents.
- Shallow water effects.
- Seabed bank effects.
- Stabiliser forces.

The forces and moments to be discussed in this work are those that relate to the first three items.

$$X = X_H + X_P + X_R + X_E \quad (5)$$

$$Y = Y_H + Y_P + Y_R + Y_E \quad (6)$$

$$N = N_H + N_E \quad (7)$$

$$K = K_H + K_P + K_R + K_E \quad (8)$$

Subscripts $H, P, R\ and\ E$, are used to represent hydrodynamic, propeller, rudder and environmental effects.

3.1 HYDRODYNAMIC FORCES AND MOMENTS

Hydrodynamic forces are those that arise from the hull velocity through the water, which are damping forces, and those due to the acceleration of the hull through water (added mass forces).

While researching the effects of steering and roll motions of a container ship, the hydrodynamic forces and moment in non-dimensional forms, were published by Son and Nomoto (1981). The method proposed Japanese MMG for the forces and moments using hydrodynamic derivatives (in Figure 3) were applied:

$$\mathrm{X} = \mathrm{X_{uu}u^2} + (1-\mathrm{t})\mathrm{X_{vr}vr} + \mathrm{X_{vv}v^2} + \mathrm{X_{rr}r^2} + \mathrm{X_{\phi\phi}\phi^2} + \mathrm{x_p} + \mathrm{X(\delta)} \quad (9)$$

$$Y = Y_v v + Y_r r + Y_p p + Y_\phi \phi + Y_{vvv}v^3 + Y_{rrr}r^3 + Y_{vvr}v^2 r + Y_{vrr}vr^2 + Y_{vv\phi}v^2\phi + Y_{v\phi\phi}v\phi^2 + Y_{rr\phi}r^2\phi \quad (10)$$

$$K = K_v v + K_{vvv}v^3 + K_{vvr}v^2 + K_r r + K_{rrr}r^3 + K_\phi\phi + K_{\dot{\phi}}\dot{\phi} + K_{\ddot{\phi}}\ddot{\phi} + K_{vv\phi}v^2\phi + K_{v\phi\phi}v\phi^2 + K_{r\phi\phi}r\phi^2 - W(GM)\phi \quad (11)$$

$$\mathrm{N} = \mathrm{N_v v} + \mathrm{N_r r} + \mathrm{N_p p} + \mathrm{N_\phi \phi} + \mathrm{N_{vvv}v^3} + \mathrm{N_{rrr}r^3} + \mathrm{N_{vvr}v^2} + \mathrm{N_{vrr}vr^2} + \mathrm{N_{vv\phi}v^2\phi} + \mathrm{N_{v\phi\phi}v\phi^2} + \mathrm{N_{rr\phi}r^2\phi} + \mathrm{N_{r\phi\phi}r\phi^2} \quad (12)$$

$X_u, Y_v, Y_{vv}, N_v, N_{rr}$,…etc. are hydrodynamic derivatives obtained from model experiments of Son and Nomoto (1981).

To run the sets of equations, the Runge-Kutta solution of second order differential equations was applied the numerical integration using the following accelerations formulations that included the added mass and moment of inertia terms:

$$\dot{u} = X/(m + m_x) \quad (13)$$

$$\dot{v} = -\frac{(I_x+J_x)(I_z+J_z)Y+(-m_yI_y)(I_z+J_z)K+(m_y\alpha_y)(I_x+J_x)N}{(m+m_y)(I_x+J_x)(I_z+J_z)-(-m_yI_y)^2(I_z+J_z)-(m_y\alpha_y)^2(I_x+J_x)} \quad (14)$$

$$\dot{p} = -\frac{-(-m_yI_y)(I_z+J_z)Y+K(m+m_y)(I_z+J_z)-K(m_y\alpha_y)^2+(-m_yI_y)(m_y\alpha_y)N}{(m+m_y)(I_x+J_x)(I_z+J_z)-(-m_yI_y)^2(I_z+J_z)-(m_y\alpha_y)^2(I_x+J_x)} \quad (15)$$

$$\dot{r} = -\frac{-(m_y\alpha_y)(I_x+J_x)Y+K(-m_yI_y)(m_y\alpha_y)+N(m+m_y)(I_x+J_x)-N(m_yI_y)^2}{(m+m_y)(I_x+J_x)(I_z+J_z)-(-m_yI_y)^2(I_z+J_z)-(m_y\alpha_y)^2(I_x+J_x)} \quad (16)$$

This was arrived at by following the Taylor series expansion and simultaneous equation method of solution for the three degrees of freedom given in Edward Lewis (1990) was extended to create a coupled roll motions, putting equations (1 to 4) and equations (9 to 12) into perspective.

3.2 RUDDER FORCES AND MOMENTS

The rudder forces and moments are calculated as follows:

$$X_R = -(1 - t_R)F_N sin\delta \quad (17)$$

$$Y_R = -(1 + a_H)F_N cos\delta . cos\phi \quad (18)$$

$$K_R = z_R(1 + a_H)F_N cos\delta$$

$$N_R = -(x_R + a_H x_H)F_N cos\delta . cos\phi \quad (19)$$

The rudder normal force is given by

$$F_N = \left(\frac{6.13\Lambda}{\Lambda+2.25}\right)\left(\frac{A_R}{L^2}\right)V_R^2\sin(\alpha_R) \quad (20)$$

3.3 PROPELLER FORCE AND THE SHAFT SPEED

The total longitudinal force generated by the propellers is given by

$$X_p = (1-t)\sum(T_P) \quad (21)$$

$$T_p{}' = \frac{T_P}{0.5*\rho*L^2*V^2} \quad (22)$$

$$J = V_s cos\beta(1-w_p)/(n_s D_P) \quad (23)$$

$$K_T = \mathrm{T}/(\rho n_s^2 D_p^4) \quad (24)$$

$$n = C * \sqrt[3]{\frac{P_{MCR}}{D_p^5}} \quad (25)$$

Where C a constant from Diesel (2011).

For plotting the path of the ship in continuous motion, the instantaneous values of the actual trajectories relative to the fixed earth axes and the orientation of the ship are given by:

$$xpos = x_0 + h(u\cos\psi - v\sin\psi\cos\phi) \quad (26)$$

$$ypos = y_0 + h(u\sin\psi + v\cos\psi\cos\phi)) \quad (27)$$

3.4 WAVE FORCES AND MOMENTS

In the implementation of the wave force, Froude-Krylov and diffraction forces and moments are to be taken into consideration. The Froude Krylov force equations are used on the assumption that the wave shape is not altered with the presence of the ship hull. For the derivation of the wave forces one applied some formulae as in Motoki Araki (2012), for the Froude-Krylov force and the diffraction force.

Normally, near coastal waters where manoeuvring safety is a critical consideration, the waves are not normally very high, wind and current effects are more predominant. However for the purpose of this paper, wave with wind parameters based on the Beaufort scale was adopted. For this work, the wave encounter angle is computed such that it is fixed to the global coordinate and it changes relative to the ship's direction during, say, turning motions. To make the wave pattern irregular using the Bretschneider spectrum and making the frequency to be randomly selected (within a range) during the computations.

Bhattacharyya (1978) shows that the frequency of encounter is equal to:

$$\omega_e = \omega_w\left(1 - \frac{\omega_w V}{g}cos\psi\right) \quad (28)$$

Araki (2012), gave the following equations for the Froude-Krylov and the diffraction forces and moments:

$$X_{FK} = -\rho g\zeta_w k cos\psi.\sqrt{F_c^2 + F_s^2} + \sin(k\xi_G + \varepsilon_F) \quad (29)$$

$$Y_{FK} = \rho g\zeta_w k sin\psi.\sqrt{K_c^2 + K_s^2} + \sin(k\xi_G + \varepsilon_F) \quad (30)$$

$$K_{FK} = \rho g\zeta_w k sin\psi.\sqrt{F_c^2 + F_s^2} + \sin(k\xi_G + \varepsilon_F) \quad (31)$$

$$N_{FK} = \rho g\zeta_w k sin\psi.\sqrt{N_c^2 + N_s^2} + \sin(k\xi_G + \varepsilon_F) \quad (32)$$

Where:

$$\varepsilon_F = tan^{-1}\left(\frac{F_s^2}{F_c^2}\right) \quad (33)$$

$$\varepsilon_k = tan^{-1}\left(\frac{K_s^2}{F_c^2}\right). \quad (34)$$

$$\varepsilon_N = -tan^{-1}\left(\frac{N_s^2}{N_c^2}\right) \quad (35)$$

In the implementation of the diffraction force, the ship hull is assumed to be generally slender, thus the surge component was neglected and approximate formulae for estimating the diffraction forces of the other modes are applied and expressed as:

$$\mathrm{Y_W^{Diff}}(\mathrm{u},\xi_G{}',\chi) = \zeta_w\omega\omega_e\sin\chi * \left(\int_{AE}^{FE}\rho\,S_y(x)e^{\frac{-kd(x)}{2}}\sin\mathrm{k}(\xi_G{}' + x\cos\chi))\,dx - (\zeta_w\omega u\sin\psi\left[\rho S_y(x)e^{\frac{-kd(x)}{2}}\cos\mathrm{k}(\xi_G{}' + x\cos\chi)\right]_{AP}^{FP}\right) \quad (36)$$

$$K_W^{Diff}(u,\xi_G/\lambda,\chi) = -\zeta_w\omega\omega_e sin\chi(\int_{AP}^{FP}\rho\,(S_y(x)l_n)e^{\frac{-kd(x)}{2}}\sin(k(\xi_G{}' + x cos\chi))dx) - (\zeta_w\omega u sin\chi[\rho S_y(x)l_n(x)e^{\frac{-kd(x)}{2}}sin(k(\xi_G{}' + x cos\chi))]_{AP}^{FP}) \quad (37)$$

$$N_W^{Diff}(u,\xi_G/\lambda,\chi) = \zeta_w\omega\omega_e sin\chi * \int_{AE}^{FE}\rho\,S_y(x)(e^{\frac{-kd(x)}{2}})x\sin\left(\mathrm{k}(\xi_G{}' + x cos\chi)\right)dx - (\zeta_w\omega u sin\chi\left[\rho S_y(x)\left(e^{\frac{-kd(x)}{2}}\right)x\,cos(k(\xi_G{}' + x cos\chi))\right]_{AP}^{FP}\right). \quad (38)$$

Details can be seen in Araki (2012). The above equations were meant for regular waves, however, for this work, the encounter frequency was computed as a function of the instantaneous ship's velocity which varied for each time step and thereby varying the encounter frequency with time.

The exciting force for the heaving motion was determined by integrating the additional components of buoyancy due to the several waves simultaneously acting along length of the ship, and for a unit length (strip) of a ship's hull (The Strip theory assumptions applied), details are given Bhattacharyya (1978).

3.5 WIND FORCES AND MOMENTS

The forces due to the wind is assumed to be unidirectional. Additionally, for the purpose of this research. The expressions below are applied to obtain the wind force:

$$F_X = C_X \times qA_T \cos\chi_{wind} \quad (39)$$

$$F_Y = C_Y \times qA_L \sin\chi_{wind} \quad (40)$$

$$N = C_N \times qLA_L \sin\chi_{wind} \quad (41)$$

$$K = C_K \times qA_L H_L \sin\chi_{wind} \quad (42)$$

$$H_L = A_L/L$$

A_T, is Transverse projected area, A_L is longitudinal projected area.

$$V_h = v_{ref}\left(\frac{h_w}{h_{ref}}\right)^{1/n} \quad (43)$$

V_h = wind velocity at elevation h_w above the mean sea level [m/s]; v_{ref} is wind velocity at the reference height; h_{ref} is reference height (10 m or 33ft in API standard); $1/n$ is exponent of the velocity profile

According to Turk and Prpić-Oršić (2009), the instantaneous wind pressure is given by:

$$q = \frac{1}{2}\rho|v_{mw} + \overline{u} - \dot{x}|(v_{mw} + \overline{u} - \dot{x}) \quad (44)$$

Blendermann (1994), provides coefficients of lateral and longitudinal resistance, cross-force and rolling moment.

3.6 CURRENT FORCES AND MOMENTS

In restricted waters where manoeuvrability at reduced speed is a major concern (e.g. during approaching or departure ports, or in areas with reduced water depths), the magnitude of current speed is a prime consideration.

In most accident reports in coastal areas, environmental conditions such as strong wind and, sometimes strong current were mentioned, but usually no large waves are mentioned as the areas were protected Shigunov (2018).

The variation in the velocity of current is very slow, and thus current loading is being computed as a steady state phenomenon. Two dimensional (surge and sway) current model given as follows:

$$u_{current} = V_c cos(\psi - \psi_c) \quad (45)$$

$$v_{current} = V_c\, sin(\psi - \psi_c) \quad (46)$$

4. SIMULATION AND CONTROLS

A fast time simulation model code was written which incorporates the propeller thrust force and a rudder control algorithm which will tend to correct deviations and thus keep the vessel on course.

SOLAS II-1/29.3 requires that the main steering gear be capable of being turned from 35° on either side to 30° on the opposite side in not more than 28 seconds, with the ship at its deepest seagoing draught and running ahead at maximum ahead service speed and additionally, for all ships operated by power unit.

The minimum rate of turn ($\dot{\delta}$) for the rudder when using the steering gear should be 65°/28s= 2.321°/s. However, for the purpose of this study a rate of 2.5°/sec has been applied.

The algorithm for a PD controller in continuous time is given by:

$$u(t) = \left[K_p e(t) + T_d \frac{de(t)}{dt}\right] \quad (47)$$

T_d is the derivative time constant = 1 for this work.

$$T_E\dot{\delta} = \delta_E - \delta \quad (48)$$

T_E is the time constant of the steering gear.

The code is made up of a coupled four degrees of freedom motion (Surge, Sway, Yaw and Roll) computed in time domain and another two degrees of freedom motion (Heave and Pitch) in the Frequency domain (only plot was shown).

The method of simulation is summarised in the chart shown in Figure 2.

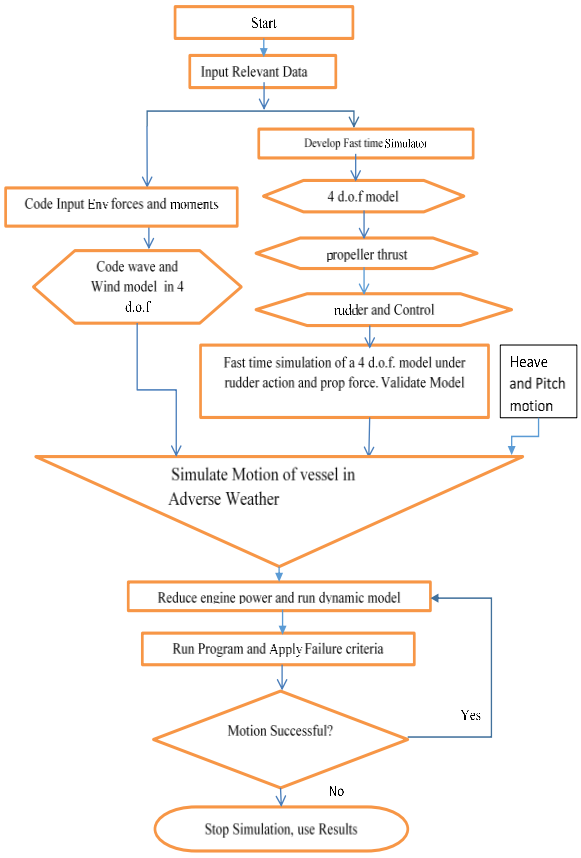

Figure 2. Method of Simulation

The program is developed such that the vessel, assumed to be a rigid body can be steered. Starting the simulation with the ship headed to the sea into both head wind and head waves, the simulation can be looped to run through a specified number of times (say a thousand times or more to create a set of motion) in order to ensure repeatable successful results. Then reducing the installed power and the above process is repeated, until a point where the simulation stops under some defined criteria, i.e. when with a reduced installed power, the vessel slows down substantially or it is not able to turn into the wave. Results can be drawn from this outcome and appropriate recommendations made.

5. DISCUSSION

Most of the simulations carried out for adverse weather conditions in this work included the influence of tidal current wind and current which are the most predominant weather conditions influencing in coastal waters. The waves in these area are not usually high however, the influence high level of waves was included to depict the need for a ship to manoeuvre in extreme conditions in the open seas.

The interim guidelines given by Shigunov (2012), require that a minimum advance speed set to 4 knots should be attainable to provide sufficient time for leaving the coastal area and some margin for ocean current. This was taken as one of the failure criterion such that if the motion being simulated causes a speed drop to 4knots, it then indicates that the vessel will not be safe when manoeuvring in the tested power level.

Figure 3 shows a zigzag motion plot the simulation of the container ship in calm water done with EShipman.

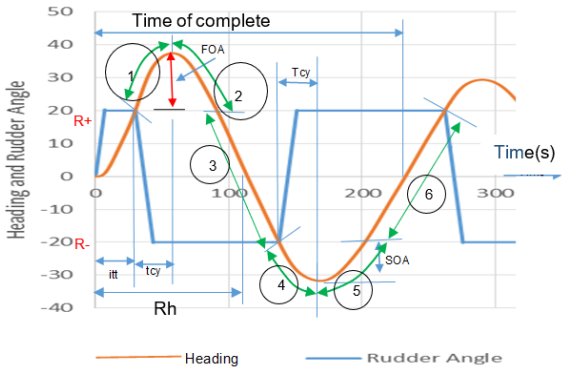

Figure 3. A Zig-Zag Manoeuvre with defined regions (plotted wth EShipman).

Table 2. is the logic table that was used to develop the zigzag program.

Table 2. Logic cases for zig-zag regions

Region	1	2	3	4	5	6
psi(i)> R+	T	T	F	F	F	F
Psi(i) > R-	T	T	T	F	F	T
Psi(i)< R-	F	F	F	T	T	F
Case True	2	2	1	1	1	1

T – Truth; F – False

The simulation of the ship performing a turning circle manoeuvre in calm water was done and compared with that experimentally performed by Son and Nomoto (1981), for the purpose of validating the functionality of the code.

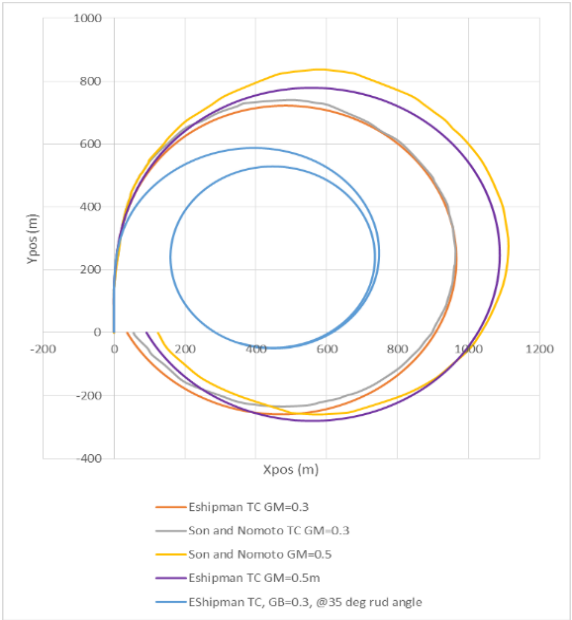

Figure 4. Calm water turning circle plot at 100% MCR (GM = 0.3m and GM=0.5). Son and Nomoto (1981) experiment vs. EShipman.

Figure 4 shows the simulation carried out and rudder command of 15 degrees given at the origin. Son and Nomoto's plots were meant to verify the yaw-sway-roll-rudder coupling due to the turning of the rudder of a high speed vessel, with the ship at its maximum speed (24.15 knots). This comparison was made for the purpose of validating the functionality of Eshipman. The plot from Eshipman is seen to have reasonable agreement with the experimental plot of Son and Nomoto. The slight difference being probably due to some empirical formulations and reasonable assumptions made in the absence of accurate data. The resultant indices of this trajectory plot obviously does not meet with the regulatory criteria because the conditions are not the same, thus EShipman was used to plot another trajectory with the command rudder angle at 35 degrees as well and the tactical diameter is 4.22 times the Ship's length. This only

shows that the ship does meet the manoeuvring criteria advised by the ITTC.

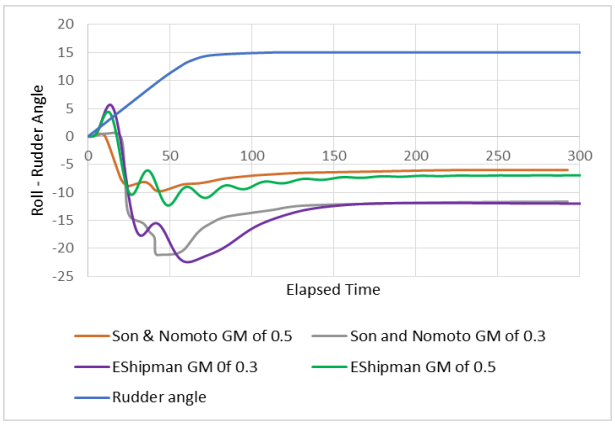

Figure 5. Roll angles from Eshipman for GM of 0.3m and GM of 0.5m rudder rate of 2.5 degrees per second.

The plots in Figure 5 compare the roll angle obtained from the experimental work of Son and Nomoto for a ship making a turning circle motion with the rudder turned to an angle of 15 degrees in calm weather.

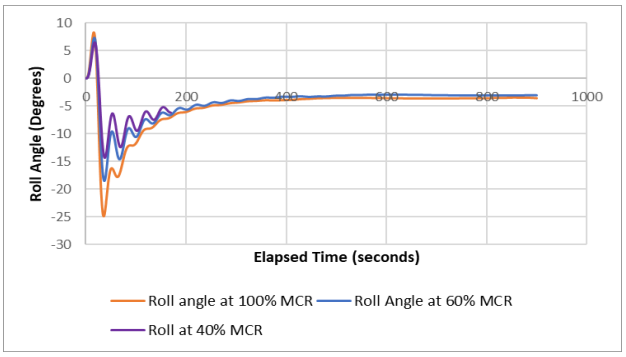

Figure 6. Roll Angle vs. Elapsed Time. GM=0.3m, $H_{\frac{1}{3}}$=3.0, wind velocity of 24knots, current of 2.0 m/s.

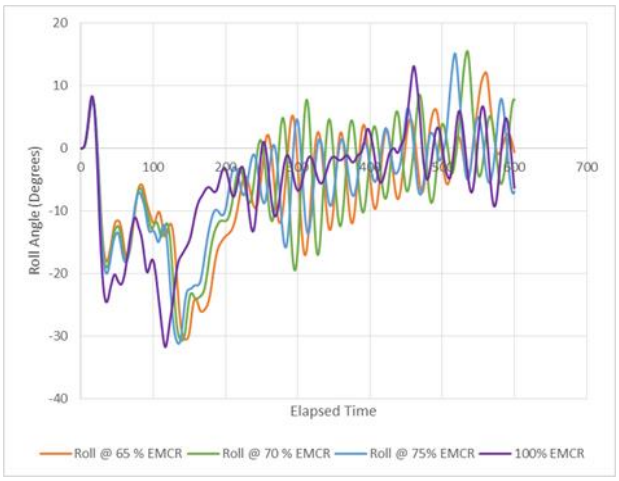

Figure 7. Roll Angle vs. Elapsed Time GM=0.3m, wave approaching at an initial angle of 20 degrees $H_{\frac{1}{3}}$=5.5m, wind velocity of 30 knot, current of 3.0 m/s.

Figure 6, gives a clearer picture of how the peak roll angle reduces with a reduction in engine power as ship makes a turning circle manoeuvre in adverse weather conditions which is a desirable property. However, the peak roll angles are dangerously high and could possibly attain an angle of loll or a capsize in the worst case scenario.

In Figure 7, higher peak roll angles occurred and in this case the vessel did roll from port to starboard and had so much fluctuations which are not desirable for passenger comfort and general vessel safety. In reality, the angle may not be as high as the slack water in the tanks may act as passive roll damping devices and will not allow for such peak angles to develop in such short period.

When simulated with the rudder command at 35 degrees for each plot (not shown here), in calm weather, the turning circle diameter at 60% MCR was being 4.35L which is still within the IMO recommended limit of 5.0L. Though the turning circle diameter is not the best indicator of the rudder performance, this plot gives an indication of how the rudder performance may reduce with reduction in speed and that the ship meets the criteria at the 60% power level.

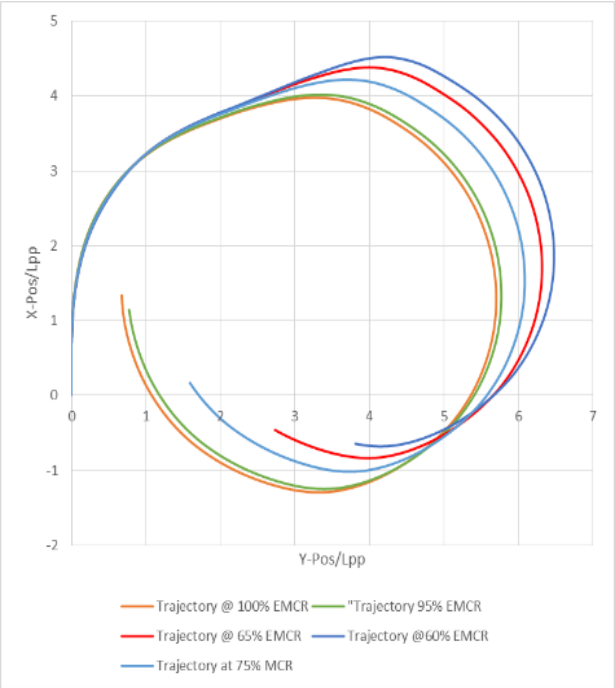

Figure 8 Vessel under the influence of wave wind and current, with wave approaching at an initial angle of 160 degrees and Engine MCR as indicated. (significant wave height of 5.5m, wind velocity of 30knots, current of 3.0 m/s).

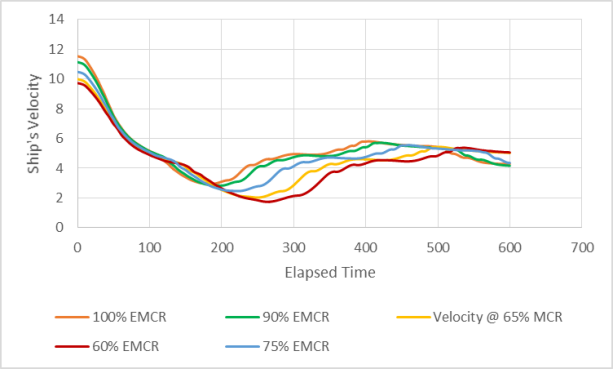

Figure 9. Velocity(m/s) vs Time(s) in Adverse Weather condition during turning circle motion in Figure 8.

Figure 8 shows the trajectory of the ship as it executes a turning motion in an adverse weather and Figure 9 shows the associated velocity in function of elapsed time. It demonstrates how the reduction in MCR of the engine to the indicated percentages, affects the turning circle manoeuvring characteristics of the ship. The influence of the tidal currents affects the shape of the curve as the ship eventually turns into a position that the current, starts adding to and increasing its speed thus the normal usual shape of the turning circle motion in calm weather is not achieved. It could be seen that, the vessel drifted further as the Engine power is reduced and the velocity reduced to less than 2m/s (3.89) which is below the test safe minimum speed of 4 knots. In practice, an alarm sounds once the ship's speed drops below five knots and the auto-pilot system changes over to manual, or is manually changed over, and the ship is manually controlled. This mostly happens during manoeuvring in restricted waters, and in extreme poor weather conditions.

As a further step towards assessing the functionality of the program, the ship was run into head wind and irregular waves (180 degrees). The speed drop during the motion in wind and waves after a set span of time is subtracted from the still water figure over the same time to obtain the figures used in Figure 10.

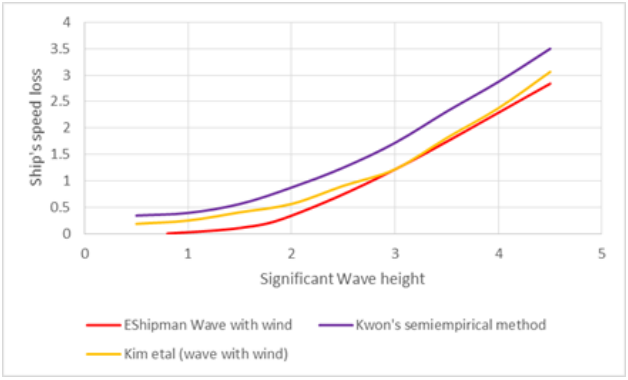

Figure 10. Speed loss under the influence of wind and waves.

This plot tends to follow the trend but shows figures lower figures than the other two authors, and presents a situation that depicts no very little or no loss of speed at significant wave height of less than 1.5meters which can be misleading, thus Eshipman needs some future improvements.

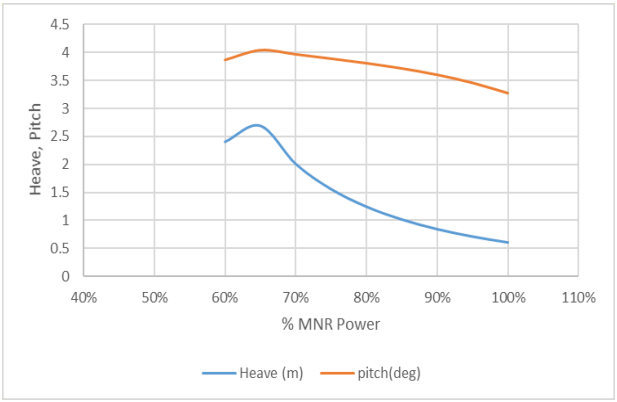

Figure 11. Heave and Pitch motions response with reduction in engine Power, Sig. Wave Height of 5.5m

Figure 11 demonstrates how the heave and pitch amplitudes increase with a reduction in installed power and then starts reducing. For this circumstance where the significant wave height is 5.5 metres, the wave period is 13s. The heave motion went as high as 2.6m at 65% power from 0.09m at full power, while the pitch angle increased from 3.2 degrees at full power to 4.04 degrees at 65% power. Though there was substantial change in motion with power reduction to 65 percent, because of the chosen wave height, these motions are still within practically safe

limits. However, with reduced power, the vessel will get susceptible to unacceptably high motions with increased wave height and at some point so that point will need to be noted so the master should not spend much time at such speed rating. The reduction in these motions with reduced power may account for why Ship masters will tend to reduce speed at very rough environmental conditions to reduce excessive motions and chance of propeller racing/emergence, etc.

The plots of turning circle motion in adverse weather condition was only meant to demonstrate one way of easily predicting the influence of ocean current in addition to wind and waves when the power is reduced thus for a new build, a program can be added to EShipman to be able to predict a suitable size of rudder that will give say, the calm water manoeuvring indices at 65% power to be as close as practically possible to that at 100% power, so that in adverse weather condition, one mode of failure has been reasonably mitigated.

6. CONCLUSION

The discussion so far attempts to point out a method that can be included in predicting the future performance of a ship in adverse weather conditions. This paper does propose a wholesome prediction of the ship motion in adverse weather condition when considering derating of a ship's engine for the purpose of improving EEDI using a fast, cheap program with reduced hardware requirement and can run on any computer, for such prediction before carrying out any detailed experiment.

This will give a clue as to what power levels the vessel will have to be reduced to so as enjoy the benefit of improved EEDI and as well have relatively safer motions in adverse weather conditions of the defined type.

The outcome, relevant equations and method of application have been explained. For this research, a ship with known experimental model test data was used but there is a need for future work especially in the area of improving the empirical formulae for manoeuvring derivatives using ship's basic dimensions.

There is room for improving the functionality of EShipman by improving the empirical prediction method for deriving hydrodynamic derivatives which will reduce the dependence on physical experimental or CFD base results. When properly improved, it can be used to conduct several tests in adverse weather conditions that will lead to some acceptable indices for assessing manoeuvrability in adverse weather condition, such that the ship will not be over powered when operating in calm weather.

7. REFERENCES

Anton, T., and Prpić-Oršić, J., 2009. Estimation of Extreme Wind Loads on Marine Objects. Brodo Gradnja Vol. 60, No. 2, pp.147 – 156.

Araki, M., 2013. Ship Maneuvering Mathematical Model Using System Identification Technique with Experimental and CFD Free Running Trials in Calm Water and Astern Waves. Osaka University Knowledge Archive : OUKA. https://ir.library.osaka-u.ac.jp/repo/ouka/all/51371/.

Bailey, P.A., 1997. A unified mathematical model describing the maneuvering of a ship travelling in a seaway. Trans RINA, 140, pp. 131-149.

Bhattacharyya, R., 1978. Dynamics of marine vehicles. Wiley, New York.

Blendermann W., 1994. Wind Loading of Ships – Collected Data from Wind Tunnel Tests in Uniform Flow. Institut fur Schiffbau der Universitat Hamburg, Bericht No 574, pp.53.

Diesel, M.A.N., 2011. Basic Principles of Ship Propulsion. MAN Diesel &Turbo, Copenhagen. www.mandieselturbo.com.

Edward L. V., 1990. Principles of Naval Architecture. The Society of Naval Architects and Marine Engineers.

Faltinsen O.M., Knut Minsaas J., Nicolas Liapis, and Svein Skjørda O., 1980. Prediction of the Resistance and Propulsion of a Ship in a Seaway. Proceedings of the 13th symposium on naval hydrodynamics, Tokyo.

Faltinsen, O., 1993. Sea loads on ships and offshore structures. Cambridge university press.

Fossen, Thor Fossen I., 1994. Guidance and control of ocean vehicles. John Wiley and sons.

Holtrop, J. and Mennen, G.G.J., 1982. An Approximate Power Prediction Method. International Shipbuilding Progress, 29(335), pp. 166–170.

IMO, 2011. Energy Efficiency Measures. http://www.imo.org/en/OurWork/Environment/PollutionPrevention/AirPollution/Pages/Technical-and-Operational-Measures.aspx.

Irimagha, E., Birmingham, R., Woodward, M. and Hu, Z., 2016. Towards Establishing Minimum Installed Power for safe Manoeuvring of Ships in Adverse Environmental condition, A Yücel Odabaşı Colloquium Series. Istanbul Technical University, 17-18 November 2016. pp.67-73. http://www.ayocol.itu.edu.tr/AYOCOL2016/files/Proceedings_of_AYOCOL_2nd_Int._Meeting_V2.pdf.

Kim, M., Hizir O. Hizir, Osman T., Sandy D., Incecik A., 2014. Estimation of Added Resistance and Ship Speed Loss in a seaway. Ocean Engineering. Vol 141, 1 Sept. 2017. pp 465-476.

Kwon, Y.J., 2008. Speed loss due to added resistance in wind and waves. Naval Architect. 2008. pp. 14-16.

Letki L., and Hudson D. A., 2005. Simulation of Ship Manoeuvring Performance in Calm Water and Waves. Ship Science Reports, 138, 106pp. University of

Southampton, Southampton UK. https://eprints.soton.ac.uk/46182/

Lewis E.V., 1989. Principles of Naval Architecture. Volume 3, Motions in Waves and Controllability. 2nd revised edition. Society of Naval Architects and Marine Engineers. Jersey City, N.J.

Ma, Z., Chen, H., and Zhang, Y., 2017. Impact of Waste Heat Recovery Systems on Energy Efficiency Improvement of a Heavy-Duty Diesel Engine. Archives of Thermodynamics, 38(3), pp. 63-75.

Ming-Chung, F.ang, et al., 2005. A Nonlinear Mathematical Model for Ships Turning Circle Simulation in Waves. Journal of Ship Research, Vol. 49, No. 2. pp. 69-79.

Ogawa, A. and Kasai, H., 1978. On the Mathematical Model Of Manoeuvring Motion Of Ships', International Shipbuilding Progress, 25(292).

Shigunov, V., 2012. Consideration of the Energy Efficiency Design Index for new ships – Minimum propulsion power to maintain the manoeuvrability in adverse conditions. SHOPERA Conference. Proc. 14th Int. Ship Stability Workshop (ISSW), Kuala Lumpur.

Shigunov, V., 2018. Manoeuvrability in adverse conditions: rational criteria and standards. Journal of Marine Science and Technology, pp. 1-19.

Son, K. H., Nomoto K., 1981. On the Coupled Motion of Steering and Rolling of a High-speed Container Ship. Proceedings of the Japan Shipbuilding Association, Volume 150, pp. 232-244.

Son, K.,young-Ho and Kensaku Nomoto, K. (1981). On the Coupled Motion of Steering and Rolling Motion of a High-speed Container Ship. J.S.N.A, Japan, Dec. 198I, Vol .150.

Trodden, D., 2014. Optimal Propeller Selection when Accounting for a Ship's Manoeuvring Response due to Environmental Loading'. PhD Thesis at Newcastle Uiversity, Newcastle Upon-Tyne.

Yasukawa, H. and Yoshimura, Y., 2015. Introduction of MMG standard method for ship maneuvering predictions. Journal of Marine Science and Technology, 20(1), pp. 37-52.

8. AUTHORS BIOGRAPHY

Emmanuel Irimagha is a PhD Research Student at Newcastle University. His previous experience includes working as an Engineer on-board Liquefied Natural Gas (LNG) Tankers.

Zhiqiang Hu holds the position of Lloyds Professor of Offshore Engineering at Newcastle University. His previous experience was at the School of Naval Architecture, Ocean & Civil Engineering in Shanghai Jiao Tong University for 15 years. He has plenty of teaching and research experiences and knowledge in naval architecture and ocean engineering related to hydrodynamics, structural dynamics and basin model test conducting technology.

Richard Birmingham is a Professor of Small Craft Design at Newcastle University and President of the Royal Institution of Naval Architects (RINA), 2018 – 2020.

Michael Woodward is the Director of the National Centre for Maritime Engineering and Hydrodynamics and he is Associate Professor of Marine Engineering. He is a Fellow of the Royal Institution of Naval Architects (RINA) and the Tasmanian section representative. He sits on the Advisory Council of the international scientific committee responsible for hydrodynamic experimentation of the International Towing Tank Conference (ITTC).

REAL-TIME ESTIMATION OF THE SHIP MANOEUVRABLE RANGE IN WIND

Toshio Iseki,
Tokyo University of Marine Science and Technology, Japan

REAL-TIME ESTIMATION OF THE SHIP MANOEUVRABLE RANGE IN WIND

Toshio Iseki, Tokyo University of Marine Science and Technology, Japan

SUMMARY

A real-time identification procedure is applied to the estimation of hydrodynamic derivatives of ship manoeuvring equations. In the procedure, not only the ship motion data but also the wind data are used for making up a CARX (Continuous Auto Regressive eXogenous) model. The main advantage of the procedure is that the coefficients of the model directly correspond to the hydrodynamic derivatives. The identification algorithm consists of the IIR (Infinite Impulse Response) digital filters and RLS (Recursive Least Square) method. To discuss the reliability of the identified coefficients, the procedure is applied to a full-scale ship's data and the results are compared to the hydrodynamic derivatives provided by the shipbuilding company. Moreover, a simple navigation support system is proposed using the identified hydrodynamic derivatives. The system can indicate the ship manoeuvrable range under wind conditions and its usefulness is shown.

1 INTRODUCTION

It is very important for mariners to be familiar with the manoeuvrability of the own ship. The ship manoeuvring performance, however, is influenced by loading conditions and water depth. Furthermore, the effect of the weather conditions should be also recognized. Therefore, it is considered necessary to develop a practical prediction method of manoeuvring performance for full-scale ships under an arbitrary condition.

From the view point of the statistical data analysis, the evaluation of the ship manoeuvring indices can be recognized as an identification procedure for a continuous system. The author applied a direct parameter estimation procedure (Sagara, et al., 1990) to the Nomoto model (Nomoto, et al., 1956) for ship manoeuvring motion (Iseki and Ohtsu, 2000; Jiang and Iseki, 2015). The results showed that the direct parameter estimation algorithm with CARX models and IIR filters was a powerful tool for real-time identification of ship manoeuvring indices.

In this paper, a real-time identification procedure is applied to the estimation of hydrodynamic derivatives of ship manoeuvring equations. In the procedure, not only the ship motion data but also the wind data are used for making up a CARX model. The main advantage of the procedure is that the coefficients of the model directly correspond to the hydrodynamic derivatives. The identification algorithm consists of the IIR digital filters and RLS method. To discuss the reliability of the identified coefficients, the procedure is applied to a full-scale ship's data and the results are compared to the hydrodynamic derivatives provided by the shipbuilding company. Moreover, a simple navigation support system is proposed using the identified hydrodynamic derivatives. The system can indicate the ship manoeuvrable range under wind condition and its usefulness is shown. This concludes that the proposed method is a powerful tool for actual ship operations.

2 REAL-TIME IDENTIFICATION PROCEDURE

In this section, the algorithm of the real-time identification method with IIR digital filter is explained, in which the coefficients of the motion equations appear explicitly and can be easily evaluated. The real-time identification procedure can be divided into three steps. In the first step, the ship manoeuvring motion equation is transformed into the integrated CARX model. The second step is the integration of the sampled data by using the IIR digital filters and the last is the RLS method.

2.1 EQUATIONS OF MOTION

In this report, the ship motions are defined in a right-handed *xyz* coordinate system with *x* to the bow, *y* to the starboard side and *z* down-words. Ignoring the motion of *x*-direction, the linearized manoeuvring equations are expressed as follows:

$$\begin{cases} (m' + m'_y)\dot{v}' = Y'_v \cdot v' + (Y'_r - m') \cdot r' + Y'_{\dot{r}} \cdot \dot{r}' + Y'_\delta \cdot \delta + Y'_W \\ (I'_{zz} + j'_{zz})\dot{r}' = N'_v \cdot v' + N'_{\dot{v}} \cdot \dot{v}' + N'_r \cdot r' + N'_\delta \cdot \delta + N'_W \end{cases} \quad (1)$$

where v' and $\dot{v}'$ denote the velocities and accelerations along the *y*-axis, r' and $\dot{r}'$ the angular velocity and the angular acceleration around the *z*-axis, $m'+m'_y$ and $I'_{zz}+j'_{zz}$ the virtual mass and the virtual moment of inertia of the ship's hull, δ the rudder angle. Y'_W and N'_W denote the wind force and moment acting on the ship's hull. The variables with prime denote the non-dimensional parameters expressed as follows (typical examples):

$$\begin{aligned} & v = U \cdot v', \quad \dot{v} = U^2 / L \cdot \dot{v}', \quad r = U / L \cdot r' \\ & Y_v = \frac{1}{2}\rho L d U \cdot Y'_v, \quad m = \frac{1}{2}\rho L^2 d \cdot m', \\ & Y_W = \frac{1}{2}\rho L d U^2 \cdot Y'_W, \quad N_W = \frac{1}{2}\rho L^2 d U^2 \cdot N'_W \end{aligned} \quad (2)$$

where ρ denotes the density of water and L, d, U are the ship's length, draft and speed, respectively.

The hydrodynamic derivatives to be identified are indicated by m'_y, Y'_v, Y'_r, $Y'_{\dot{r}}$, Y'_δ, j'_{zz}, N'_r, N'_v, $N'_{\dot{v}}$ and N'_δ.

2.2 INTEGRATED CARX MODEL

Using the differential operator *p*, Equations (1) can be rewritten as follows:

$$\begin{cases} Y'_W(t) = (m'+m'_y)pv'(t) - Y'_v \cdot v'(t) - Y'_{\dot r} \cdot p^2\psi(t) \\ \qquad -(Y'_r - m') \cdot p\psi(t) - Y'_\delta \cdot \delta(t) \\ N'_W(t) = -N'_{\dot v} \cdot pv'(t) - N'_v \cdot v'(t) + (I'_{zz} + j'_{zz})p^2\psi(t) \\ \qquad -N'_r \cdot p\psi(t) - N'_\delta \cdot \delta(t) \end{cases} \tag{3}$$

where $\psi(t)$ denotes the yaw angle of the ship and the time variables are specified to distinguish from the constants and the coefficients to be identified.
To avoid time differentiation, Equations (3) are integrated two times with respect to the time.

$$\begin{cases} Y'_{W2}(t) = (m'+m'_y) \cdot V_1'(t) - Y'_v \cdot V_2'(t) - Y'_{\dot r} \cdot \Psi_0(t) \\ \qquad -(Y'_r - m') \cdot \Psi_1(t) - Y'_\delta \cdot \Delta_2(t) \\ N'_{W2}(t) = -N'_{\dot v} \cdot V_1'(t) - N'_v \cdot V_2'(t) + (I'_{zz} + j'_{zz}) \cdot \Psi_0(t) \\ \qquad -N'_r \cdot \Psi_1(t) - N'_\delta \cdot \Delta_2(t) \end{cases} \tag{4}$$

where the variables in capital letters denote the time integrated variables and the lower suffixes indicate the number of integration.

$$\begin{aligned} &Y'_{W2} = p^{-2}Y'_W(t) = \int_0^{t'}\int_0^{\tau'} Y'_W(\tau'_1)d\tau'_1 d\tau', \\ &N'_{W2} = \int_0^{t'}\int_0^{\tau'} N'_W(\tau'_1)d\tau'_1 d\tau' \\ &V'_1 = p^{-1}v'(t) = \int_0^{t'} v'(\tau')d\tau', \\ &V'_2 = p^{-2}v'(t') = \int_0^{t'}\int_0^{\tau'} v(\tau'_1)d\tau'_1 d\tau' \\ &\Psi_0(t) \equiv \psi(t), \\ &\Psi_1(t) \equiv p^{-1}\psi(t) = \int_0^{t'} \psi(\tau')d\tau' \\ &\Delta_2 = p^{-2}\delta(t) = \int_0^{t'}\int_0^{\tau'} \delta(\tau'_1)d\tau'_1 d\tau' \end{aligned} \tag{5}$$

Equations (4) can be transformed into a CARX model as follows:

$$\phi(t) = \mathbf{\Phi}^T(t)\boldsymbol{\chi} + e(t) \tag{6}$$

where $e(t)$ denotes the white noise to be introduced to stochastic treatments and the other variable and vectors are expressed as follows:

$$\phi(t) = Y'_{W2}(t) \quad \text{or} \quad N'_{W2}(t) \tag{7}$$

$$\mathbf{\Phi}^T(t) = \left\{V'_1(t), V'_2(t), \Psi_0(t), \Psi_1(t), \Delta_2(t)\right\} \tag{8}$$

$$\begin{aligned} \boldsymbol{\chi}^T &= \left\{(m'+m'_y), -Y'_v, -Y'_{\dot r}, -(Y'_r - m'), -Y'_\delta\right\} \\ &= \left\{\chi'_{Y1}, \chi'_{Y2}, \chi'_{Y3}, \chi'_{Y4}, \chi'_{Y5}\right\} \\ &\text{or} \\ \boldsymbol{\chi}^T &= \left\{-N'_{\dot v}, -N'_v, (I'_{zz} + j'_{zz}), -N'_r, -N'_\delta\right\} \\ &= \left\{\chi'_{N1}, \chi'_{N2}, \chi'_{N3}, \chi'_{N4}, \chi'_{N5}\right\} \end{aligned} \tag{9}$$

Therefore, estimation of the hydrodynamic derivatives can be considered as a fitting problem of coefficients $\boldsymbol{\chi}$ of the CARX model Equation (6). In this study, the integration of the signals $\phi(t)$ and $\mathbf{\Phi}(t)$ are obtained by introducing IIR filters.

2.3 IIR FILTER

In actual integration of Equations (7) and (8), the accumulation of the integration error is inevitable and numerical instability is induced. Therefore, an approximated integration with the digital filter is introduced. The filter has the equivalent response to the following transfer function.

$$G(s) = \frac{1}{s+\lambda} \tag{10}$$

where λ denotes the constant that controls the damping of the signal.
It is easy to understand because the impulse response of Equation (10) corresponds to $g(t)=e^{-\lambda t}$. Consequently, the transfer function in the discrete time domain that integrates n-times (in this case, n=2) can be represented by the bilinear transformation as follows:

$$H(z) = \left.\frac{1}{(s+\lambda)^n}\right|_{s=\frac{2}{\Delta}\times\frac{1-z^{-1}}{1+z^{-1}}} = \left(\frac{2}{\Delta}\times\frac{1-z^{-1}}{1+z^{-1}} + \lambda\right)^{-n} \tag{11}$$

where z^{-1} denotes the delay operator.
If $v(k)$ is used to express the sampled values of $v(t)$ at $t=k\Delta t$ (k=0, 1, ⋯), the ith-order integration of $v(k)$ can be obtained through the digital filter $P_i(z)$.

$$V_i(k) = H(z)p^{n-i}v(k) = P_i v(k) \tag{12}$$

where Δ denotes the sampling interval and

$$\begin{aligned} &P_i(z) = \left(1 - \frac{C_2}{C_1}z^{-1}\right)C_1^{-n}\left(\frac{\Delta}{2}\right)^i (1+z^{-1})^i (1-z^{-1})^{n-i}, \\ &C_1 = 1 + \lambda\frac{\Delta}{2}, \quad C_2 = 1 - \lambda\frac{\Delta}{2} \end{aligned} \tag{13}$$

The concrete expression of $V_i(k)$ (i=0, 1, 2; k=3, 4, ⋯) are described by the following equations:

$$\begin{aligned} V_0(k) &= 3AV_0(k-1) - 3A^2V_0(k-2) + A^3V_0(k-3) \\ &\quad + B\left\{v(k) - 3v(k-1) + 3v(k-2) - v(k-3)\right\} \\ V_1(k) &= 3AV_1(k-1) - 3A^2V_1(k-2) + A^3V_1(k-3) \\ &\quad + \frac{\Delta}{2}B\left\{v(k) - v(k-1) - v(k-2) + v(k-3)\right\} \\ V_2(k) &= 3AV_2(k-1) - 3A^2V_2(k-2) + A^3V_2(k-3) \\ &\quad + \left(\frac{\Delta}{2}\right)^2 B\left\{v(k) + v(k-1) - v(k-2) - v(k-3)\right\} \end{aligned} \tag{14}$$

where

$$A = \frac{C_2}{C_1}, \quad B = \frac{1}{C_1^3} \tag{15}$$

Moreover, since $e(k)$ in Equation (6) cannot be measured, it is replaced by the estimation error $\hat{e}(k)$, which is evaluated as follows:

$$\hat{e}(k) = \phi(k) - \mathbf{\Phi}^T(k)\hat{\boldsymbol{\chi}}(k) \tag{16}$$

where $\hat{\boldsymbol{\chi}}(k)$ denotes the identified coefficient vector at time step k.
To evaluate the unknown coefficients, following cost function is introduced (k=3, 4, ⋯):

$$J(k)a = \hat{e}^2(k) + \omega\hat{e}^2(k-1) + \omega^2\hat{e}^2(k-2) + \cdots \tag{17}$$

where ω is the forgetting factor which weights the data exponentially into the past and takes on real values between $0 < \omega < 1$.

2.4 RLS METHOD

The technique, which minimizes Equation (17) with recursive method, is called RLS algorithm. The least squares solution is obtained by the following procedures (Young, 1984).

- Set the forgetting factor ω ($0 < \omega < 1$).
- Set initial values of covariance matrix $\mathbf{H}(k)$ and coefficient vector $\hat{\boldsymbol{\chi}}(k)$.
  $$\mathbf{H}(k)=c\times\mathbf{I} \tag{18}$$
  where c is a coefficient, $\mathbf{I}$ is the 5th-order identity matrix in this case.
- Make up the regressive vector $\mathbf{\Phi}(k+1)$.
- Calculate the scholar D as follows:
  $$D = 1 + \mathbf{\Phi}^T(k+1)\mathbf{H}(k)\mathbf{\Phi}(k+1)/\omega \tag{19}$$
- Calculate the time varying gain vector $\mathbf{G}(k+1)$.
  $$\mathbf{G}(k+1) = \mathbf{H}(k)\mathbf{\Psi}(k+1)/\omega D \tag{20}$$
- Estimate of the wind force or moment at the next time step.
  $$\hat{\phi}(k+1) = \mathbf{\Phi}^T(k+1)\hat{\boldsymbol{\chi}}(k) \tag{21}$$
- Sample new data of $v(k+1)$, $\psi(k+1)$ and δ(k+1).
- Estimate of the coefficient vector for the next time step.
  $$\hat{\boldsymbol{\chi}}(k+1) = \hat{\boldsymbol{\chi}}(k) + \mathbf{G}(k+1)\left\{\phi(k+1) - \hat{\phi}(k+1)\right\} \tag{22}$$
- Update the covariance matrix $\mathbf{H}(k+1)$.
  $$\mathbf{H}(k+1) = \left\{\mathbf{I} - \mathbf{G}(k+1)\mathbf{\Phi}^T(k+1)\right\}\mathbf{H}(k)/\omega \tag{23}$$
- Using the sampled data, shift the element of $\mathbf{\Phi}(k+1)$ to make up $\mathbf{\Phi}(k+2)$.
- Return to Equation (19).

2.5 ESTIMATION OF THE WIND FORCE AND THE MOMENT

The wind forces acting on the ship's hull are estimated by the following formulae:

$$\begin{aligned} Y_W &= \frac{1}{2}\rho_a A_y V_W^2 C_Y(\theta_W) \\ N_W &= \frac{1}{2}\rho_a L A_y V_W^2 C_N(\theta_W) \end{aligned} \tag{24}$$

where ρ_a, A_y, V_W, θ_W denote the density of air, lateral projected area, the wind speed and direction.
In this report, wind force coefficients are estimated by the empirical formulae (Yamano and Saito, 1997).

$$\begin{aligned} C_Y(\theta_W) &= \sum_{i=1}^{3} C_{Yi}\sin(i\theta_W) \\ C_N(\theta_W) &= \sum_{i=1}^{3} 0.1\cdot C_{Ni}\sin(i\theta_W) \end{aligned} \tag{25}$$

where the coefficients are calculated as follows:

$$\begin{cases} C_{Y1} = 0.509 + 4.904A_y/L^2 + 0.022A_y/A_x \\ C_{Y2} = 0.0208 + 0.230A_y/L^2 - 0.075x_g/L \\ C_{Y3} = -0.357 + 0.943A_y/L^2 + 0.0381L/B \end{cases} \tag{26}$$

$$\begin{cases} C_{N1} = 2.65 + 4.634A_y/L^2 - 5.876x_g/L \\ C_{N2} = 0.105 + 5.306A_y/L^2 + 0.0704A_y/A_x \\ C_{N3} = 0.616 - 1.474x_g/L + 0.0161L/B \end{cases} \tag{27}$$

where A_x ad x_g denote the transverse projected area and the distance between F.P. and the centroid of A_y.
These formulae were applied to the measured wind data considering the relative speed and direction.
On the other hand, the measured wind data includes gustiness. In the actual estimation of the wind forces, therefore, the IIR-filter has been applied to the measured wind data in order to smooth the effect of wind gustiness.

2.6 ESTIMATION OF MANOEUVRABLE RANGE IN WIND

The ship manoeuvrable range under wind conditions are evaluated as the required ship speed to maintain the current course (Nakajima, 1948; Ishibashi, 1975).
To estimate the condition in which the ship can maintain the current course by the specified rudder angle δ_s, let $\dot{v}' = \dot{r}' = r' = 0$ and $\delta(t) = \delta_s$ in Equation (3).

$$\begin{cases} Y'_W(t) = -Y'_v\cdot v'(t) - Y'_\delta\cdot\delta_s \\ N'_W(t) = -N'_v\cdot v'(t) - N'_\delta\cdot\delta_s \end{cases} \tag{28}$$

Eliminating the lateral velocity $v'(t)$ from the equations and substituting Equation (9) for Y'_v, Y'_δ, N'_v and N'_δ the equation of equilibrium is expressed as follows:

$$\left\{\frac{N'_W(t)}{\chi'_{N2}} - \frac{Y'_W(t)}{\chi'_{Y2}}\right\} = \left\{\frac{\chi'_{N5}}{\chi'_{N2}} - \frac{\chi'_{Y5}}{\chi'_{Y2}}\right\}\cdot\delta_s \tag{29}$$

If it can be assumed that the ship course is changed with constant speed U_0 and Equation (24) can be extended to the relative wind direction θ_R and the relative wind speed $V_R(\theta_R)$, the equation for real-time estimation of manoeuvrable range in wind can be obtained.

$$\frac{U}{U_0}=\sqrt{\frac{\rho_a A_y V_R^2(\theta_R)\left\{\frac{C_N(\theta_R)}{\chi'_{N2}}-\frac{C_Y(\theta_R)}{\chi'_{Y2}}\right\}}{\rho L d U_0^2\left(\frac{\chi'_{N5}}{\chi'_{N2}}-\frac{\chi'_{Y5}}{\chi'_{Y2}}\right)\cdot\delta_s}} \tag{30}$$

The equation indicates the required ship speed U when the ship must keep her course under the wind condition with the specified rudder angle δ_s.

3 FULL SCALE EXPERIMENTS

Full scale experiments were carried out using the training ship Shioji-maru (Table 1 and Figure 1) off-Tateyama Bay in Chiba Prefecture, Japan. In addition to the ship course, the rudder angle, the wind speed and direction, the ship longitudinal and lateral velocities were measured by a Doppler sonar (Atlas DOLOG23). The GPS data was not used in this report at all. The data sets were measured in the sampling interval 0.5 second. During the experiments, the observed direction and the wind speed were 170deg and 7m/s, respectively. The wind forces and moments were calculated using the formulae described in the previous section.

To observe the transient response of the real-time identification, the data includes not only the straight course but also zig-zag manoeuvres. The execution time of the zig-zag manoeuvres and the initial ship courses are shown in Table 2. The actual time histories of the rudder angle, ship course and speed are plotted in Figure 2. It can be seen that the ship speed was dropped slightly during the zig-zag manoeuvres.

Table 1. Principal particulars of T.S. Shioji-maru

Length (P.P)		46.00 (m)
Breadth (MLD.)		10.00 (m)
Depth (MLD.)		6.10 (m)
Draught (MLD.)		2.65 (m)
Displacement		659.4 (t)
Main engine	4 cycle diesel	1,030 kw × 700 rpm

Figure 1. The training ship Shioji-maru.

Table 2. Measurement conditions

Test name	Execution time	Ship course
10 Z-1	10s - 120s	180
20 Z-1	190s- 340s	180

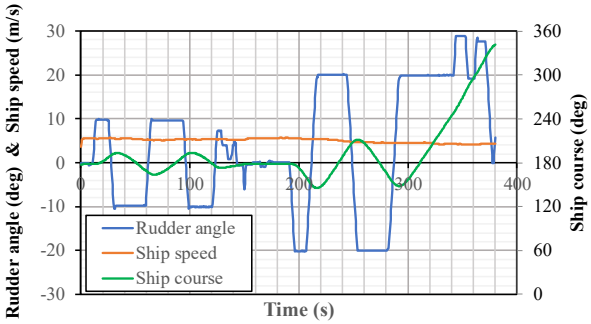

Figure 2. Measured time histories.

3.1 RESULTS OF THE REAL-TIME IDENTIFICATION

Based on the real-time identification procedure, an in-house software was developed. Figure 3 shows the graphical user interface of the program. The upper left side of the screen shows movement of the ship and her trajectory that were calculated using the Doppler sonar data. The lower left side of the screen indicates the ship manoeuvrable range calculated by Equation (29). The details are explained in the later section. On the other hand, the graphs in the middle and the right are indicating the time histories of measured data and the real-time identified hydrodynamic derivatives. Specifically, from the top, the measured δ, the identified m'_y and Y'_v, the identified $Y'_{\dot{r}}$ and Y'_r, the identified Y'_δ, the measured and the IIR-filtered v are shown in the middle column. In the right column, from the top, the measured U and the IIR-filtered V_R, the identified $N'_{\dot{v}}$ and N'_v, the identified j'_{zz} and N'_r, the identified N'_δ, the estimated and the IIR-filtered Y'_W are shown. The stability and convergence of the real-time identification can be observed by these graphs.

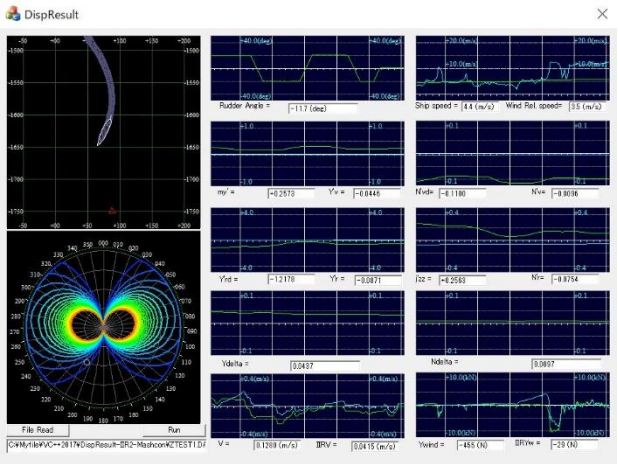

Figure 3. Screenshot of the real-time identification software.

Figure 4 shows the transition of identified added mass m'_y and added inertia moment j'_{zz}. The figure is also indicating the hydrodynamic derivatives (broken lines) provided by the shipbuilding company for reference. The identified added mass m'_y shows good agreement just after the end of the first zig-zag manoeuvre. It can be said that a certain

degree of manoeuvre is required for good identification of m'_y. On the other hand, the identified added inertia moment seems to be unstable and does not agree with the reference value.

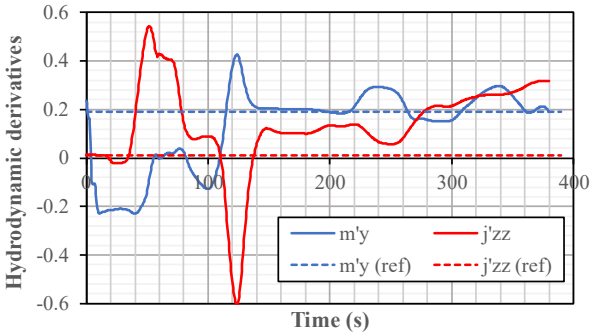

Figure 4. Comparisons of the identified added mass m'_y and added inertia moment j'_{zz}.

Figure 5 shows the transition of identified hydrodynamic derivatives Y'_v and N'_v. Looking at the figure, the results are stable, but some discrepancies can be observed. The reason of the disagreement is considered that the measured lateral velocity was too small to identify the hydrodynamic derivatives. The real-time estimation requires rather large fluctuation for both of input and output signals. This concludes that the zig-zag manoeuvre is not sufficient for precise identification of hydrodynamic derivatives concerning the ship lateral velocity. Because the lateral velocity appears in the CARX model as a double integrated valuable $V'_2(t)$ and the small fluctuations of $v'(t)$ becomes inconspicuous.

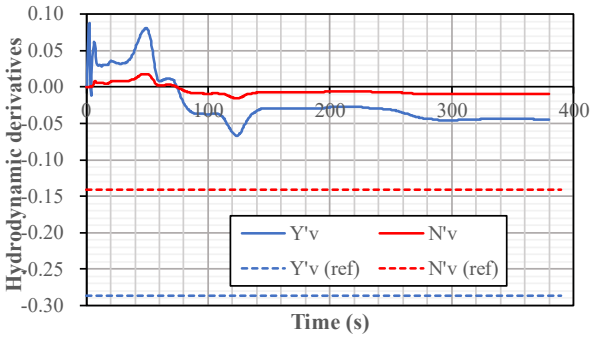

Figure 5. Comparisons of the identified hydrodynamic derivatives Y'_v and N'_v.

Figure 6 shows the transition of identified hydrodynamic derivatives Y'_r and N'_r. Looking at the figure, the identified N'_r is stable and agree well with the reference value. The reason of the agreement can be considered that the measured yaw rate (time integrated signal of ship course in the CARX model) was rather large during the zig-zag manoeuvres. On the other hand, the identified Y'_r seems to be unstable and does not agree with the reference value. It can be considered that the centrifugal force acting on the ship's hull was removed successfully in the identification process.

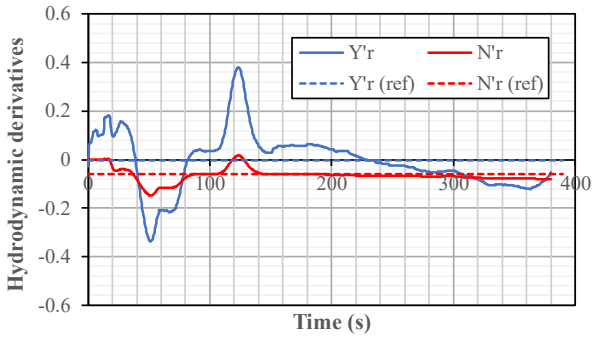

Figure 6. Comparisons of the identified hydrodynamic derivatives Y'_r and N'_r.

3.2 MANOEUVRABLE RANGE IN WIND

Figure 7 shows contour lines of the estimated manoeuvrable range under the current wind condition. The graph is almost the same as the radar chart excepting the centre point that is indicating zero ship speed. The numbers arranged in the circumferential direction denote the absolute azimuth of the bow direction of the ship. The own ship is indicated by the black circle (in the 270deg direction on the second grey circle) instead. The grey coloured concentric circles denote the non-dimensional ship speed U/U_0. The second grey circle is U/U_0=1 and the outermost grey circle is U/U_0=2. The colours of contour lines correspond to the specified rudder angle δ_s in Equation (30) that were discretized from 1deg (blue) to 35deg (red) at 1 degree intervals. Therefore, the region inside the red coloured line denotes the region in which the ship course cannot be maintained even with maximum rudder angle. The mariner can easily understand the manoeuvrable range of the own ship by looking at the indicated chart. However, the reliability of the chart should be examined carefully because the identified hydrodynamic derivatives Y'_v and N'_v appeared in Equation (30), and the identified values don't show good agreement with reference value.

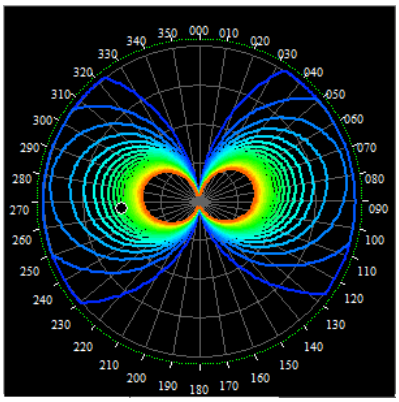

Figure 7. Indicated manoeuvrable range in wind.

4 CONCLUSIONS

In this paper, a real-time identification procedure was applied to the estimation of hydrodynamic derivatives of ship manoeuvring equations. The results are summarized below:

- Identified hydrodynamic derivatives m'_y and N'_r were stable and showed good agreement with the reference value provided by the shipbuilding company.
- Identified hydrodynamic derivatives Y'_v and N'_v were stable but some discrepancies could be observed. The fact that the lateral velocity is very small, and its fluctuation becomes inconspicuous by IIR filters can be considered as the cause.
- Identification of hydrodynamic derivatives Y'_r and j'_{zz} were unstable. The cause should be investigated in detail.
- The possibility of the simple navigation support system in winds has been shown but it is considered that the reliability of the identification procedure should be examined.

In this report, the wind force and moment were treated as the measured signals through the formulae, and the rudder force and the moment were included in the CARX model as the unknown variables. Another modelling should be examined for more accurate identification. Furthermore, the proposed real-time identification method requires conspicuous output signals responding to fluctuating input signals. Therefore, proper real-time manoeuvres should be investigated for the estimation of each hydrodynamic derivative.

5 ACKNOWLEDGEMENTS

This work is partly supported by JSPS KAKENHI Grant Number 17K06960. The authors express sincere gratitude to the above organization.

6 REFERENCES

Iseki, T., Ohtsu, K., 2000. On-Line Identification of Manoeuvring Indices by Using IIR Filter, in: MARSIM 2000 Conference Proceedings, pp. 211-218.

Ishibashi, Y., 1975. On Course Stability and Manoeuvrable Range of Wind Velocity in the Uniform Wind. J. Soc. N. A. Japan, 138, pp. 165-177.

Jiang, C., Iseki, T., 2015. Real-time Identification of Manoeuvrability Indices Using IIR Filters, in: MARSIM 2015 Conference Proceedings.

Nakajima, Y., 1948. On the Effect of Wind on the Manoeuvrability of Train Ferries. J. Soc. N. A. Japan, 84, pp. 69-79.

Nomoto, K., Taguchi, K., Honda, K. and Hirano, S., 1956. On Steering Qualities of Ships (1). J. Soc. N. A. Japan, 99, pp. 75-82.

Nomoto, K., Taguchi, K., 1957. On Steering Qualities of Ships (2), J. Soc. N. A. Japan, 101, pp. 57-66.

Sagara, S., Yang, Z. and Wada, K., 1990. Consistent Parameter Estimation for Continuous systems via IIR Digital Filters, Trans. Society of Instrument and Control Engineering, 26, No.1, 39/45, pp. 39-45.

Young, P. C., 1984. Recursive Estimation and Time-Series Analysis, Springer-Verlag, pp.42-54.

Yamano, T. and Saito, Y., 1997. An Estimation Method of Wind Forces Acting on Ships, J. Kansai Soc. N. A., Japan, 228, pp. 91-100.

7 AUTHORS BIOGRAPHY

Toshio Iseki took his doctoral degree in engineering at Kyushu University in 1989. He is a professor of Tokyo University of Marine Science and Technology. His major fields are Naval Architecture and Time Series Analysis.

SEA TRIALS FOR DETERMINATION OF MANOEUVRING CHARACTERISTICS IN SHALLOW WATER CONDITIONS

Hanne Jansch and **Carl-Uwe Böttner**,
Federal Waterways Engineering and Research Institute, Hamburg, Germany

SEA TRIALS FOR DETERMINATION OF MANOEUVRING CHARACTERISTICS IN SHALLOW WATER CONDITIONS

Hanne Jansch and **Carl-Uwe Böttner,** Federal Waterways Engineering and Research Institute, Hamburg, Germany

SUMMARY

There is a lack of recent sea trial data to validate manoeuvring performance prediction approaches. This is especially the case for shallow water conditions. As a contribution to fill this gap a comprehensive measurement campaign was set up to precisely determine the manoeuvring performance and characteristics of a mid-size multipurpose vessel. The campaign aims to provide a manoeuvring test case for numerical and physical models of manoeuvring characteristics and performance prediction.

The sea trials were performed utilizing the MV MELLUM, a pollution control vessel patrolling along the German coast, owned and operated by the Federal Waterways and Shipping Administration Germany. The sea trials were conducted in the German Bight, where the vessel is in daily operation. To determine the manoeuvring characteristics in shallow water the sea trials have been performed at different water depths. The different water depth and hence the different under keel clearances were gained from accordingly chosen tides and locations at the German Bight. The ship's responses to different under keel clearances in terms of manoeuvring behaviour could be clearly determined by the experimental set-up and the sensors in use.

1 INTRODUCTION

Obviously, sufficient manoeuvring capability is essential for a ship to be seaworthy and for safe navigation. There are two questions connected to this: first what exactly is sufficient and second how to assure that a design will lead to a ship of sufficient manoeuvring capabilities?
The first question was apparently answered by the IMO with the definition of standards for ship manoeuvrability under resolution A.751(18), but there are reasonable objections whether the criteria are sufficiently comprehensive (Oltmann, 2011; Quadvlieg, F.H.H.A. and Coevorden, P. van, 2003). Basically it is discussed if the criteria, defined and suitable for conventional propeller rudder configurations and modern ship designs, are not sufficiently considered. Additionally the manoeuvring characteristics are only valid for deep water conditions, but become very likely relevant when sailing near the coast or even in waterways and approach channels, where shallow water conditions are predominant.
The second question is even more difficult to answer and is restricted by the validity of numerical simulation models. Anyhow, it is definitely worth the effort: provided numerical predictions of manoeuvring characteristics solely based on the hull shape and propulsion data achieve a useful degree of fidelity, preciseness and correctness. Many of the objections listed before could be addressed with this approach at the same time.
The vitality of the ongoing research on numerical simulation of manoeuvres supports this statement. Promising improvements are reported and introduced at the frequent international conferences, for instance (4th MASHCON, 2016; MARSIM 2015, 2015; SIMMAN 2014, 2014).
To validate and proof numerical models and the dedicated approaches, it is a mandatory requirement to have a good to almost perfect conformity with sea trials. This was the impetus for EXXON to perform manoeuvring trials with the VLCC "ESSO OSAKA" and publish the results as a benchmark test case for the research community. This is a profound, precise and well documented test case, which includes sailing in deep waters as well as in shallow waters, that was regarded essential to enable naval architects to develop refined and precise manoeuvring models (Gray, 1978).

Table 1. Accuracy of Positioning at Sea

Method	From	Until	Accuracy
DECCA Survey	1950	1965+	8 - 100 m
LORAN-C	1957	2010	< 500 m
DECCA HiFix	1962	1983+	< 1.5 - 10 m
Syledis	1970	1995	< 2 - 10 m
GPS SA*	1976+	2000	< 100 m
GPS without SA	2000	today	5 - 10 m
DGPS	1996	today	< 0.5 - 10 m
RTK	1993	today	0.01 m

* Selective Availability

Today, the situation improved partly but there is still a lack of sea trial data of high accuracy. Many sea trial campaigns reported were performed in the last century, when accurate positioning was not yet available. In the pre-satellite positioning era hyperbolic systems such as LORAN-C or DECCA and range-range systems such as Syledis were the primary methods for navigation and positioning at sea. As listed in Table 1 they would provide a position within 1.5-500 m accuracy depending on the system and observation constellation (Lekkerkerk 2012). When the satellite based Global Position System (GPS), initialized in 1976 for the US military, was fully operational in 1993 it progressively replaced previous positioning methods (Lekkerkerk and Theijs 2017). By

today it is possible to derive horizontal positions within ± 0.01 m and vertical ± 0.02 m making use of Global Navigation Satellite Systems (GNSS) and additional real-time correction data utilizing the Real-Time Kinematic (RTK) method (Riecken and Kurtenbach 2017).

Analog to the development and improvement of positioning systems, the sensors and measurement techniques for most of the additional parameters required at sea trials like motion and heading have improved in their accuracy. Observing this development in the past decade and seeing the need for full scale measurements it was tempting to launch a manoeuvre trial campaign utilising a vessel with available ship design lines to assemble a comprehensive benchmark test case.

2 SET UP OF THE MANOEUVRE TRIALS

2.1 SELECTED SHIP FOR THE TRIALS

For the sea trials a ship was required, which was of reasonable size in terms of Length of Waterline and propelled by a conventional propeller-rudder configuration. Additionally the ship should be available on demand, whenever weather conditions are forecasted beneficial for manoeuvring tests and sea trials. Further it was regarded necessary to have the opportunity to leave the measurement set-up installed on board until the trials campaign was completed.

Figure 1. Multipurpose Vessel MELLUM (Photo: WSA Wilhelmshaven)

The multipurpose vessel MV MELLUM (Figure 1) owned by the German authorities is the ship which suited the requirements best. Her particulars were considered reasonable for physical and numerical model tests with a length of 80 m, a breadth of 15 m and draught of 5.1 m. She is a twin-screw with controllable pitch propellers in ducts and conventional rudders. An additional advantage was that regular maintenance including dry docking and painting of the underwater part of the hull was scheduled just before the trails. This ensured a clean since freshly painted underwater hull and enabled to inspect and survey the hull properly.

2.2 PREPARATION

The ship hull was scanned with a laser scanner (3D-Scanner "Z+F Imager 5010") while in dry dock (Figure 2). Based on the scans the geometry could be derived for computational fluid dynamics simulations (Figure 3).

As the aim of the project is to assemble a manoeuvring test case for computational manoeuvring models and physical model tests, all the appendages were scanned in addition to the hull with the 3D-Laser Scanner. Subsequently the data was transformed in CAD-data sets, including bow thruster tunnel, rudder profiles, head boxes, skegs, shaft brackets and profile of the ducts (Figure 3).

First use of these data was the calculation of the open water characteristics of the propellers in the duct, which is required to analyse the momentary actual thrust delivered by the propulsion system from the torque and revolution data recorded.

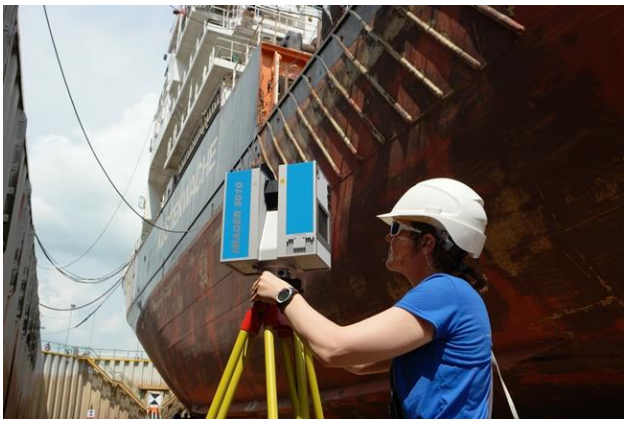

Figure 2. Multipurpose Vessel MELLUM in dry dock for regular maintenance and laser scanning (Photo: BAW)

First use of these data was the calculation of the open water characteristics of the propellers in the duct, which is required to analyse the momentary actual thrust delivered by the propulsion system from the torque and revolution data recorded.

Figure 3. 3D laser scanned data of the hull and the appendages served for CFD-Simulations (Photo/Graphic: Technical University Berlin)

During the maintenance period at the yard interfaces to the machinery automation dating back to the 80s could be adapted and installed to gain access to machinery data, like rpm, EOT etc.. There was a new sensor attached to the servo pushrod to get precise actual rudder position. The rudder commands given by the helmsman were gained together with the actual rudder position from the instrumentation on the bridge.

Table 2. Observed Parameters

Parameter	Unit	Device
Attitude		
Position (UTM)	[m]	Javad GNSS*
Heading	[°]	Octans Fibre Optic Gyro
Pitch	[°]	Octans MRU**
Roll	[°]	Octans MRU**
ROT	[°/s]	Octans MRU**
Heave	[m]	Octans MRU**
Surge	[m]	Octans MRU**
Sway	[m]	Octans MRU**
CoG	[°]	Javad GNSS*
SoG	[m/s]	Javad GNSS*
Draft	[m]	Vega Radar
Environment		
Water Current	[m/s]	ADCP***
STW	[m/s]	ADCP + Javad GNSS*
Water Depth	[m]	On Board Echosounder *2
Water Density	[kg/m³]	CTD-Sensor****
Water Level	[m]	Tide Gauge
Wind Speed	[m/s]	On Board System or DWD station
Wind Direction	[m°]	On Board System or DWD station
Wave Height *1	[m]	Wave Rider Buoy - BSH
Wave Direction	[°]	Wave Rider Buoy - BSH
Engine, Propulsion, Rudder		
RPM	[1/min]	Interface to automation
Pitch	[%]	Interface to automation
EOT-Command	[%]	Bridge instrumentation
Shaft Revolution	[1/s]	Shaft mounted sensor
Shaft Torque	[Nm]	Strain gauge ([µm/m])
Rudder Comnd	[°]	Bridge instrumentation
Rudder position	[°]	Bridge instrumentation

* RTK with SAPOS Corrections
** Motion Reference Unit
***Acoustic Doppler Current Profiler
**** Conductivity, Temperature, Depth
*1 Significant / (Helgoland only)
*2 + BSH (Federal Maritime and Hydrographic Agency of Germany) multibeam surveys from 2015

Next to rudder commands with actual position and engine data, there were torque meter and rotation counter mounted at each of the two shafts. A fibre optic gyro to gain orientation, GNSS antennas for positioning and speed, radar to determine momentary draught as well as tidal gauges, current profilers and wind sensors to detect the environmental conditions were included in the measurement set-up (Table 2).This configuration meets and partly even goes beyond the recommendations and demands presented by the SNAME (Society of Naval Architects and Marine Engineers Ships' Machinery Committee, 1990). Obtaining the vessels dynamic behaviour this precisely and in addition determining the relevant operational data, provides a thorough figure of the manoeuvring behaviour.

The installation was realized in a way that regular ship operation was not affected. The sensors and the equipment remained on board, ready for use whenever a sufficient calm weather window was forecasted.

After the dockyard period and before the MV MELLUM was brought back in service, the time at her berth was used to install the remaining sensors and subsequently the instrument offsets were precisely determined utilizing laser scanner, total station and tape measure (Figure 4). All offsets, hence the instrument positions relative to each other and respectively within the ships coordinate system, were determined with an accuracy of < 0.005 m for instruments on deck and with an accuracy of < 0.01 m for the position of the gyro. To derive best results for the vessels attitude it is necessary to mount the gyro as close as possible to the centre of gravity. Therefore its position was less accessible for offset determination, but the accuracy level is still more than sufficient for the task.

Figure 4. Determination of the sensors offsets on board (Photo: BAW)

2.3 SEA TRIALS

To determine the manoeuvring characteristics in shallow water the sea trials have been performed at three different water depths. At the German Bight being the navigation and service area of the MV MELLUM, two locations

could be defined as suitable. There the trials could be realized at different depth to draught ratios (h/T). Three depth to draft ratios 1.5, 2.0 and more than 5.0 have been defined as suitable. With a draught of 5.1 m the h/T results in the corresponding water depth of 7.5 m, 10 m and > 25 m.
The manoeuvres (Figure 5) were performed according the IMO standard manoeuvres in resolution A.751(18).

The sea trials have been conducted in winter 2016 to 2017 whenever there was calm weather. For the deep water conditions the area around the island of Helgoland was chosen, which provided some shelter from waves and weather. The shallow water conditions required an area of a level bathymetry and sandy bottom. This was found in the survey data of the BSH (Federal Maritime and Hydrographic Agency of Germany; multibeam surveys from 2015), north of Norderney island, close to its shore. Depending on the tide, both draught to depth ratios 1.5 and 2.0 could be realized there.

The MV MELLUM's manoeuvring behaviour was as expected. Being a twin-screw, the turning circles and Zig-Zag-Manoeuvres to port and starboard compared well. Additionally the turning circle in calm water without current was very close to a perfect circle shape (Figure 6), which was very helpful for the correction of the manoeuvres considering displacement by current and wind.

Unfortunately the research project is still underway and so only preliminary results and analyses are included in this paper. However theses do serve as a preview of the full scale manoeuvring trail data set and show some of the issues and problems involved.

3 ANALYSIS OF THE MANOEUVRE TRIALS

Figure 5. Zig-Zag Manoeuvre in shallow water with Multipurpose Vessel MELLUM (Photo: BAW)

3.1 CORRECTION OF CURRENT AND WIND

There were a couple of manoeuvres performed at very low or almost no tidal current. They served as the basis for the later corrections of manoeuvres in current and wind. As mentioned in 2.3 the current magnitude and direction was observed at the time of the trials using ADCP at a position in the vicinity of the trials, so the magnitude and direction are known. The determination of the tidal current directly at the vessels position was not possible especially in shallow water, as the manoeuvres induce too high turbulences in the water for a precise ADCP measurement.

Figure 6 shows the relative position of the course over ground (blue) overlaid with the position shifted for tidal current to get the actual track through water. In that case, the detected mean value for current speed was 0.12 m/s. Based on the almost perfect circle observed at low current speeds, the correction for higher currents was calculated according the criteria of the lowest eccentricity after occurrence of constant rate of turn. When manoeuvring in higher currents, the turning circle manoeuvres' positions over ground get deformed to ellipses with their principal axis perpendicular to the current direction. The course through water remains a circle, which radius is one of the characteristic manoeuvring behaviour criteria.

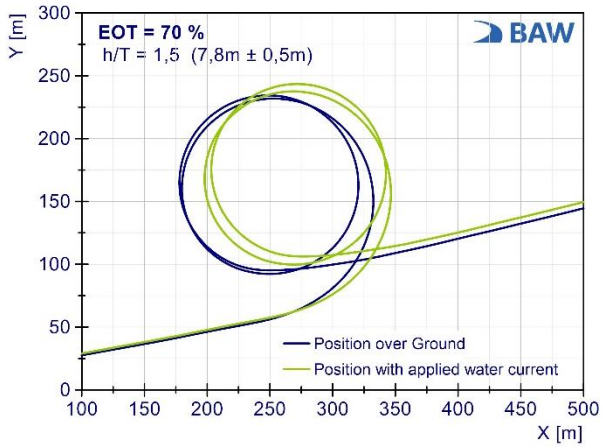

Figure 6. Relative Position of Turning Circle Manoeuvre in shallow water at very low current speed (mean value 0.12 m/s) and 70% EOT, with and without applied tidal current

3.2 EFFECT OF SHALLOW WATER

As depicted in 2.3 there were three ratios of draught to depth (h/T) chosen: 1.5, 2.0 and more than 5.0, respective 7.5 m, 10 m and > 25 m water depth. Shallow water conditions correspond to h/T = 1.5.The 2.0 case is part of the transition regime from deep to shallow water.

There is a clear correlation of the rate of turn and the under keel clearance as one of the shallow water effects. After initial turning, the ship gets into a constant movement characterized by a constant rate of turn and the course

through water prescribing a circle with characteristic radius. Figure 7 illustrates the finding of direct impact of remaining under keel clearance when getting in the regime h/T < 2.0. The rate of turn (blue) shows small but significant variation in correlation with small changings in the water depth (red) and accordingly the remaining under keel clearance.

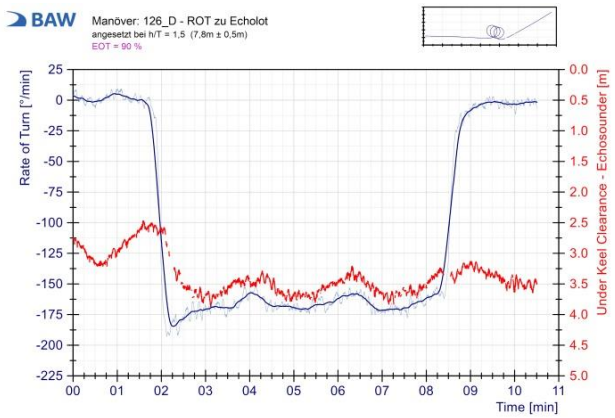

Figure 7. Turning Circle Manoeuvre in shallow water at 90% EOT, blue: Rate of Turn, red: Under Keel Clearance.

Generally it is observed, that the radius increases with decreasing water depth. The analyzed turning circle radii of this campaign given in Table 3 follow and support this empiric rule. The mean radius is larger by 1% for h/T = 2 and 14% h/T = 1.5 compared to deep water conditions of h/T = 5. While the tactical diameter shows a similar behavior as the radius, with an increase of 4% (h/T = 2) and 14% (h/T =1.5), the decrease in advance in shallow waters is less obvious with 5% (h/T = 2) and 6-7% (h/T =1.5) compared to deep water condition.

3.3 INFLUENCE OF PROPULSIVE POWER

All standard manoeuvres have been performed at least 4 times to check repeatability and for average determination. The variance of the initial conditions was next to the water depth the initial speed. For comparability and ease of numerical modelling, not the actual speed was prescribed, but the proportion of engine power delivered. In shallow water the speed reduces compared to deep water at the same power delivered. Since in the campaign the delivered power and thrust were determined, it was regarded beneficial to follow this approach.

Table 3 offers a comparison of the characteristics of the turning circle manoeuvre in terms of shallow water effect as well as of propulsive power delivered over the entire manoeuvre. It can be observed that the initial speed varies with the power delivered by an average of 15% between EOT 70% and EOT 90%. However the mean speed in the uniform phase of the turning shows smaller speed drop at less propulsive power. There is an average decrease of 47% for 70% EOT and 52% for 90% EOT. Hence the speed decrease between deep water and shallow water for the uniform phase coincides for both the propulsion powers, with having the same speed for h/T = 5 and h/T = 2 and a 10% higher speed for h/T = 1.5 compared to the deep water uniform phase. This is in good agreement with the turning radius' determined, which are of comparable sizes.

Table 3. Turning circle characteristics

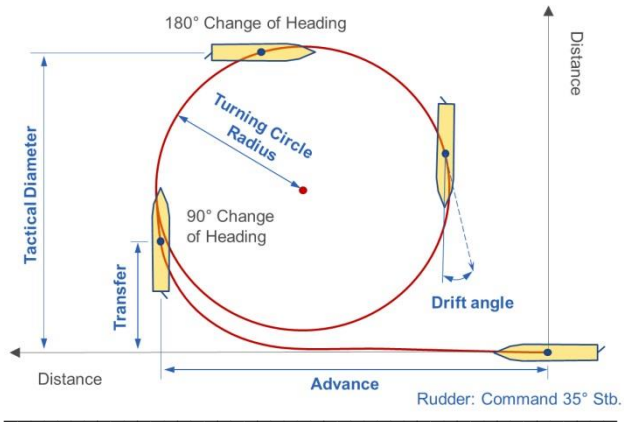

h/T	Propulsion Power EOT 70% advance / tactical diam. / radius [m]	EOT 90% advance / tactical diam. / radius [m]
>5.0	161.3 / 151.3 / 65.0	168.5 / 156.7 / 65.5
2.0	153.2 / 157.3 / 65.7	159.7 / 163.5 / 66.1
1.5	151.7 / 172.9 / 74.3	156.1 / 179.5 / 74.5
	Mean speed through water: initial / manoeuvre [kn]	
>5.0	12.2 / 6.1	14.0 / 6.4
2.0	11.8 / 6.1	13.9 / 6.4
1.5	11.5 / 6.7	13.0 / 7.0
	Mean UKC: initial / manoeuvre [m]	
>5.0	46.2 / 45.1	43.6 / 43.9
2.0*	5.0 / 5.8	5.1 / 6.3
1.5*	2.5 / 3.4	2.8 / 3.8

* Seafloor is slightly sloped and manoeuvres were generally performed towards deeper water.

4 CONCLUSIONS

An elaborate sea trails campaign was successfully finished providing the full set of data for tuning and validation of manoeuvring models, numerical as well as scaled physical model tests. The data set consists of the planned hull shape, the actual hull shape in the moment of the sea trails, the shape of the appendages and the profiles of all lifting surfaces, the ducts and the propeller blades, the thrust delivered, the environmental conditions like water depth and current speed and all of them linked with attitude determination of very high precision.

In the first step, the turning circle manoeuvre characteristics were analysed and evaluated as presented here. The other manoeuvres still to be analysed will complete the figure. After finishing the analysis, the full

set of manoeuvring data shall serve as a public test case and will be published as a thorough benchmark test.

5 ACKNOWLEDGEMENTS

The authors wish to express their warm thanks to the entire Crew of MV MELLUM for their kind assistance and hospitality. Many thanks also to the WSA Wilhelmshaven for their spontaneous willingness to agree in this campaign and their generous and constant support in terms of man-power and equipment during the entire period of the campaign.

6 REFERENCES

4th MASHCON (ed), 2016. Proceedings of the 4th International Conference on Ship Manoeuvring in Shallow and Confined Water with Special Focus on Ship Bottom Interaction. https://izw.baw.de/e-medien/4th-mashcon/PDF/4th%20MASHCON.pdf.

Gray, WO., 1978. ESSO OSAKA Maneuvering Trials: Shallow Draft Maneuvering of VLCC's. In: Proceedings of the 1978 Tanker Conference, Innisbrook, Tarpon Springs, Florida. Washington, DC: Inst, WOG D10/A2 - WOG D10/A19.

Lekkerkerk, H.-J., 2017. GNSS - The System, in: GNSS survey & engineering, Handbook for surveyors and survey engineers. pp. 11-32.

Lekkerkerk, H.-J.; Theijs, M.-J., 2012. Positioning, in: Handbook of offshore surveying, Positioning & Tides. pp. 59-79.

MARSIM 2015, (ed) 2015. Proceedings of the International Conference on Ship Manoeuvrability and Maritime Simulation. http://www.imsf.org/documents/marsim2015-conferenceproceedings.pdf.

Oltmann, P., 2011. Zigzag is not enough: The valuation of the manoeuvring behaviour of ships. Hansa international maritime journal 148(10): pp. 35–39.

Quadvlieg, F.H.H.A., van Coevorden, P., 2003. Manoeuvring criteria: more than IMO A751 requirements alone! In: International Conference on Marine Simulation and Ship Manoeuvrability 2003 (MARSIM'03): pp. 291–298.

Riecken J.; Kurtenbach E., 2017. Der Satellitenpositionierungsdienst der deutschen Landesvermessung - SAPOS. zvf 142 (5/2017), pp. 293–300. https://doi.org/10.12902/zfv-0180-2017

SIMMAN 2014, 2014. Proceedings of the Workshop on simulation of manoeuvring. Benchmark the capabilities of different ship manoeuvring simulation methods.

Society of Naval Architects and Marine Engineers Ships' Machinery Committee, 1990. Guide for sea trials 1989.

7 AUTHORS BIOGRAPHY

Hanne Jansch holds a Diploma in surveying and is responsible for field measurements at the Federal Waterways Engineering and Research Institute (BAW) in Hamburg.

Carl-Uwe Böttner currently works as a Research Engineer with the Federal Waterways Engineering and Research Institute (BAW) in Hamburg on the fields of hydrodynamics, ship dynamics and ship handling simulation. He is responsible for consulting the authorities in terms of ship handling simulation.

APPLICATION OF NOVEL SYSTEM IDENTIFICATION METHODOLOGY FOR FINDING ROLL DAMPING AND RESTORING PARAMETERS BY USING THE MEASURED RESPONSE AT SEA

Mohammadreza Javanmardi, Chris Hens, Jack Bucher and **Gregory Hibbert**,
OMC International, Australia

APPLICATION OF NOVEL SYSTEM IDENTIFICATION METHODOLOGY FOR FINDING ROLL DAMPING AND RESTORING PARAMETERS BY USING THE MEASURED RESPONSE AT SEA

Mohammadreza Javanmardi, Chris Hens, Jack Bucher and **Gregory Hibbert,** OMC International, Australia

SUMMARY

This paper introduces a technique for identifying the parameters in the equation describing the rolling motion of a ship using only its measured response at sea. The parameters being identified are the linear and nonlinear damping and restoring coefficients. These are identified using a reinforcement learning technique. The proposed method would be particularly useful in identifying the nonlinear damping and restoring parameters for a ship rolling under the action of unknown excitations caused by a realistic sea state. The rolling motion of a 1.5 m model and the recorded data for two ships' rolling motion in random seas are used to test the accuracy and the validity of the method. It was shown that the method is reliable in the identification of the parameters of the equation of the rolling motion using only the measured response at sea.

1 INTRODUCTION

The accurate prediction of rolling motions is very critical for estimating the change in vessel draught due to ship motions when considering under keel clearance (UKC). A mistake in roll prediction in shallow water can cause irreversible disaster. Aside from considerations of UKC, ship stability in realistic sea conditions is mostly dependent on its rolling motion, which is the most critical factor in defining ship survivability. In fact, most available approaches for the assessment of ships' survivability in a seaway are based on the study of rolling motion (Mahfouz, 1998).

Two approaches are used in the assessment of survivability: static (quasi-static) and dynamic approaches. The static approach is based on the minimum value that the metacentric height (GM) should have and the shape of the static stability curve (GZ curve). This approach is still very useful for ship's stability criterion assessment. The dynamic approach is based on an analysis of the stability of the roll equation of motion. This involves constructing a model for a ship rolling in a realistic sea state.

Predicting ship response to incident waves has been a topic of discussion since 1960s. Several methods have been developed to predict the vessel response to the incident waves. To investigate and predict hydrodynamic performance of ships and offshore structures, Computational Fluid Dynamics or seakeeping computer codes based on potential theory play an increasingly important role. However, the linearization of the problem in most potential flow codes neglects several important effects: Firstly, pressure integration is performed over the time-average wetted surface, neglecting changes of the wetted surface due to waves and ship motions (geometric non-linearity). Secondly, the influence of the changing wetted surface on the flow and hydrodynamic forces is not considered (hydrodynamic non-linearity). Recently, work on modelling the non-linear aspects of seakeeping using time-domain methods has become more common.

For a considerable time, model tests have been (and arguably still are) the most reliable method for determining ship reactions in waves. However, the effect of scaling should not be ignored. There is a growing tendency to include uncertainty evaluations when presenting experimental results of seakeeping tests as recommended by the ITTC (2011), although it is clearly a difficult task. Different groups of uncertainties should be identified and analysed such as: uncertainty of instruments, uncertainty of model mass properties, model geometry uncertainty, uncertainty of the test setup, calibration uncertainty, measurement uncertainty, and data reduction uncertainty.

System identification (SI) is a methodology for building mathematical models that provide relationships between the input and output variables of dynamic systems. SI methodology has been shown to provide a good fit to system behaviour in several use cases Haddara and Wu, 1993 ; Haddara and Xu, 1998 ; Haddara and Hinchey, 1995). Using this methodology to identify hydrodynamic coefficients could be very useful in the study of ship roll motions. This technique requires no simplifications or assumptions and has been claimed to be more accurate than linear and weakly nonlinear methods (Somayajula and Falzarano, 2017). It has been suggested by Haddara and Hinchey (1995) that artificial neural network (ANN) methodology has the potential to be a very useful tool for identifying the unknown parameters in the equation of motion for roll. Xing (2009) used a neural network to identify the roll parameters of two ship models. He used

the roll angle and roll velocity as the roll response to estimate the parameters in an equivalent roll equation of motion. Somayajula and Falzarano (2017) have applied SI techniques to extract the frequency dependent roll damping from a series of model tests run in random waves.

Using supervised learning techniques such as ANN to find the parameters in the equation of roll motion may not be the best method. To train an ANN, a set of labelled output is required. In addition, to use back propagation techniques, it is usually necessary to calculate the error gradients of outputs and propagate them backward through the network to correct the weights and biases. In this case, the only available data to evaluate the network is the difference between the predicted roll and the measured roll; however, the number of the ANN outputs is equal the number of unknown parameters in the roll equation of motion. Therefore, finding the error of each output or allocating each ANN output share to the error is not straightforward.

Since the only data available for evaluating the coefficients is roll error, the difference between the measured roll angle and the predicted roll angle, the network lacks the required set of labelled data for correcting its targets (the hydrodynamic coefficients). For this study, it was decided that reinforcement learning techniques are more suitable than supervised methods. This study is conducted to investigate the ability of SI techniques to predict a vessel's linear and nonlinear damping and restoring coefficients by employing reinforcement learning techniques. For this purpose, the vessel roll motion in random seas is the only required data.

2 ROLL EQUATION OF MOTION

The rolling motion of a ship at sea can be mathematically modelled by the following second-order ordinary, nonlinear differential equation of motion (Mahfouz, 2004):

$$I\ddot{\varphi} + N(\dot{\varphi}, \varphi) + K(\varphi) = M(t) \quad (1)$$

Where φ is the roll angle of the vessel, I is the total roll moment of inertia (including added moment of inertia), $N(\dot{\varphi})$ is the nonlinear damping moment which is a function of roll angle and roll speed, $K(\varphi)$ is the nonlinear restoring moment which is a function of roll angle, and $M(t)$ is the roll exciting moment. A dot over the variable φ indicates differentiation with respect to time.

The equation (1) can be re written as:

$$\ddot{\varphi} + B(\dot{\varphi}, \varphi) + C(\varphi) = F(t) \quad (2)$$

Where *B=N/I, C=K/I* and *F=M/I.*

The damping moment can be expressed as the sum of two terms: linear and nonlinear. It was shown that the linear plus cubic model is quantitatively and qualitatively equivalent to the linear plus quadratic model (Haddara and Wu, 1993):

$$B(\dot{\varphi}, \varphi) = b_1\dot{\varphi} + b_3\dot{\varphi}^3 \quad (3)$$

Where b_1 and b_3 are the linear and nonlinear damping coefficients respectively. It was shown that exclusively using the linear damping moment results in a maximum roll amplitude that is 50% higher at the resonant frequency than the corresponding value when the nonlinear damping moment is also used (Taylan, 1996). The restoring moment is a function of the form of the underwater part of the ship hull. It is usually expressed as an odd series in the roll angle. Thus, $C(\varphi)$ can be expressed as:

$$C(\varphi) = c_1\varphi + c_3\varphi^3 + c_5\varphi^5 \quad (4)$$

Where c_1, c_3 and c_5 are stiffness coefficients.

The exciting moment per unit virtual moment of inertia of the ship is assumed in the following form:

$$F(t) = f\sin(\omega_e t + \emptyset_0) + f_0 \quad (5)$$

Where ω_e is encounter frequency of the exciting moment, $\emptyset_0$ is phase angle and f_0 is a constant moment due to some mean bias (wind, loading, etc).

Equation 1 to 5 are combined to form:

$$\ddot{\varphi} + b_1\dot{\varphi} + b_3\dot{\varphi}^3 + c_1\varphi + c_3\varphi^3 + c_5\varphi^5 = f\sin(\omega_e t + \emptyset_0) + f_0 \quad (6)$$

The linear restoring parameters can be obtained from ship hydrostatics; however, the damping parameters cannot. To calculate roll by solving equation (6), all coefficients and exciting moment parameters should be known. Some of these are very difficult to calculate/predict. The main objective of this study is to find if reinforcement learning techniques are a reliable and robust method of identifying the parameters involved in this equation using only the measured roll motions of a ship in random seas.

3 REINFORCEMENT LEARNING TECHNIQUES

Machine learning algorithms can be divided into 3 broad categories—supervised learning, unsupervised learning, and reinforcement learning. Supervised learning is useful in cases where a property (*label*) is available for a certain dataset (*training set*) but is missing and needs to be predicted for other instances. Unsupervised learning is useful in cases where the challenge is to discover implicit relationships in a given *unlabelled* dataset (items are not pre-assigned). Reinforcement learning falls between these

two extremes—there is some form of feedback available for each predictive step or action, but no precise label (Sutton and Barto, 2018).

Reinforcement learning techniques compute the utility of the actions without a model for the environment. It takes the help of expected reward from the current action. During this process the agent learns to move around the environment and understand the current state. The optimal policy is taking the action with the highest reward. In this case, the state is the required coefficients in equation (6) and reward is the inverse absolute error. This means that the goal is the state for which the error is equal to zero (reward is infinity).

To Identify the coefficients using reinforcement learning, all coefficients $(C_1, C_2, \dots, C_n)$ are initialized randomly at the beginning (current state). According to the roll equation (equation 6), these coefficients are the damping coefficients (b_1, b_3), restoring coefficients (c_1, c_3, c_5) and the parameters related to the excitation moment $(f, \omega_e, \emptyset_0, f_0)$.

The error (E), which is the difference between the measured roll data $(\underline{\varphi})$ and the predicted roll $(\underline{\hat{\varphi}})$ can be calculated for the current state. To find the next state, a step is considered (ΔC). The possible coefficients could be $C_{inew} = C_i \pm \Delta C_i \;\; i = 1,2, \dots, n$. Therefore, the next possible states could be any combination of C_{inew}. The error caused by all possible combinations will be calculated. Since the optimal policy is taking the action with the highest reward, the combination which generates the minimum error (maximum reward) will be selected as the next state. Then those coefficients are chosen as the current coefficients and this state is considered as the current state. This process continues until reaching an acceptable error value (the goal state). The coefficients that generate the acceptable error are selected as the result of SI. There are some parameters which have effect on the convergence and the cost (CPU time). General speaking, having a rough idea of the coefficients values makes the search domain smaller. Choosing an appropriate step size (ΔC) can also decrease the simulation time.

A MATLAB program was developed based on the algorithm above to find the unknown parameters of the roll equation. The inputs of the program are the roll angle, roll speed and roll acceleration for a series of individual oscillations. The roll velocity and acceleration for each oscillation were calculated from the measured roll data. The program uses these data to find the coefficients that satisfy equation 6. It should be mentioned that environmental conditions and wave parameters can change for each oscillation in the roll motion time series. Therefore, it is expected that values for the coefficients related to the roll exciting moment will not be constant. Additionally, damping values are susceptible to roll and speed variations (frequency-dependent) (Pesman et al., 2007), therefore, each oscillation is considered separately.

4 VERIFICATION OF THE PROPOSED ALGORITHM

Two cases of the rolling motion of a 1.5 m model presented by Haddara and Wu (1993) and two series of real measured data are used to verify the algorithm proposed in section 3. The model data was generated by the numerical integration of the free roll equation and the real data was recorded aboard two separate bulk carriers in random seas using an “iHeave”; an inertial motion device developed by OMC International to accurately measure heave, roll and pitch (Hibbert and Lesser, 2013). Table 1 shows the damping and restoring coefficients of two cases used as benchmarks (Haddara and Wu, 1993).

The damping and restoring coefficients predicted for Case 1 and 2 by the proposed method are presented in Table 2. Note that the values in Table 1 and Table 2 are slightly different. Despite this, the roll angle calculated using the SI predicted coefficients is very similar to free decay curve generated by the numerical integration. The results for Case 1 are shown in Figure 1. The results for Case 2 were very much similar. To further investigate the performance of the SI prediction, the calculated damping and restoring moments are compared with the free decay damping and restoring moments of the benchmark data (Figure 2 and Figure 3). Despite the predicted linear and nonlinear coefficients being slightly different from the benchmark values, the roll angle, damping and restoring moments are very similar to that generated by the numerical integration, which is the most important metric for the performance of this technique.

Table 3 presents some information about the bulk carriers and the recorded roll motions for two vessels are presented in Figure 4 and Figure 5. As mentioned, sea conditions can change for each oscillation in the roll motion time series and damping values are also dependent on roll and speed variations. To account for this, the recorded data was split into single oscillations prior to calculating the coefficients with SI. The roll velocity and acceleration for each oscillation were calculated from the measured roll data.

Table 1. The damping and restoring coefficients used in the simulation (Haddara and Wu, 1993)

Case	b_1	b_3	c_1	c_3	c_5
1	0.080	0.256	11.88	1.758	-18.624
2	0.077	0.407	7.661	2.496	-18.832

Table 2. The predicted damping and restoring coefficients by reinforcement learning

Case	b_1	b_3	c_1	c_3	c_5
1	0.085	0.241	11.95	1.27	-52.37
2	0.009	0.611	7.352	9.095	-16.734

Table 3. Bulk carriers' parameters

	Vessel A	Vessel B
Vessel Class	Bulk Carrier	Bulk Carrier
LBP (m)	278	318
Beam (m)	45	55
Draught (m)	9.95	18
GM_f (m)	9.64	9.5

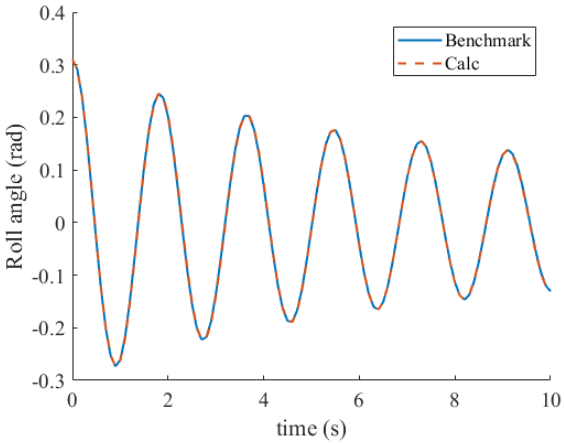

Figure 1. Comparison of free roll decay curve for Case 1

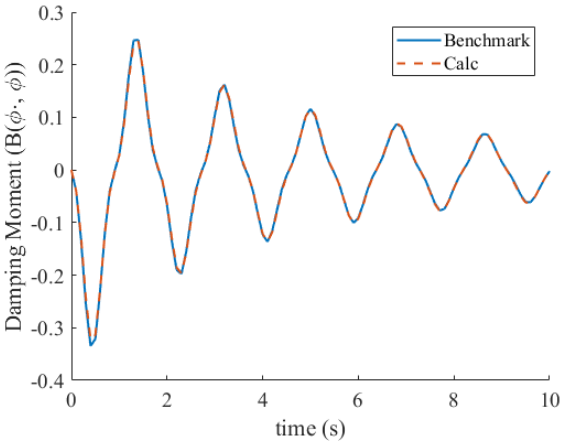

Figure 2. Comparison of damping moments for Case 1

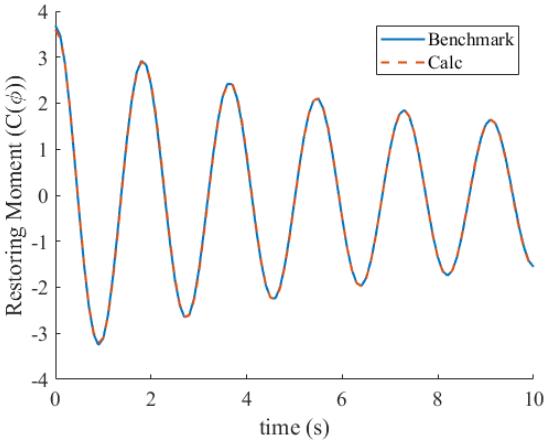

Figure 3. Comparison of restoring moments for Case 1

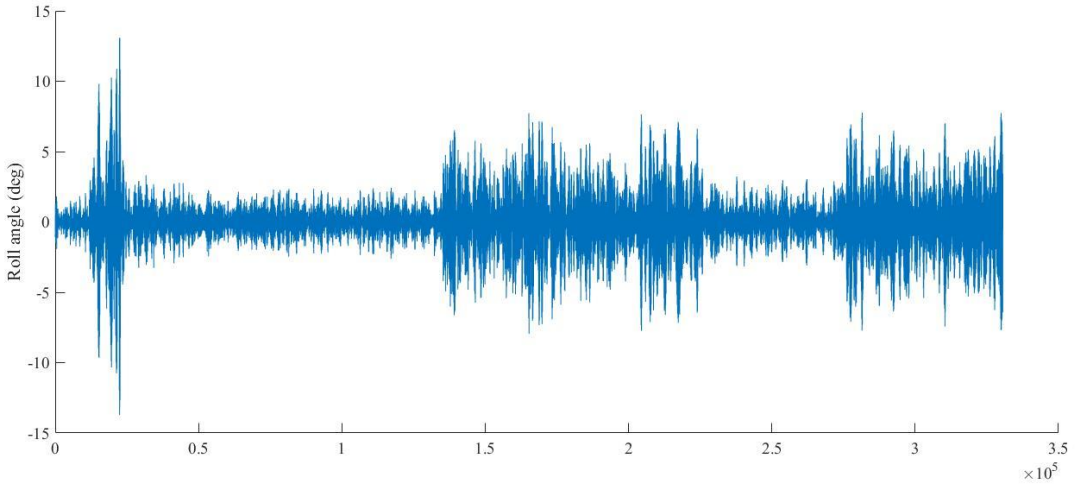

Figure 4. Recorded roll data for vessel A

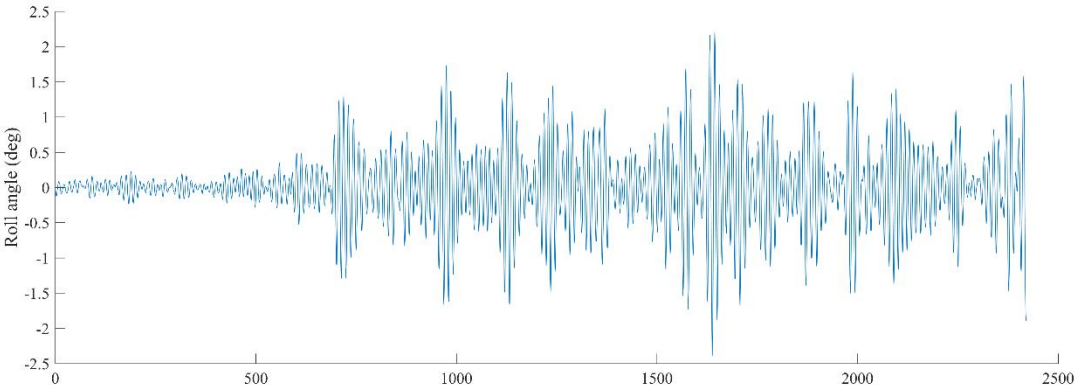

Figure 5. Recorded roll data for vessel B

More than 900 roll oscillations from the recorded roll data of Vessel A and 158 oscillations from Vessel B were used for this study. The amplitude of this measured roll data ranged from 0.02 to 13 degrees for vessel A. For vessel B, roll was less than 2.5 degrees throughout the transit. Figure 6 presents a comparison of a measured roll oscillation to roll calculated using the coefficients predicted by the proposed SI method. The average error for the 900+ oscillations of vessel A was 0.4 percent and for vessel B was almost zero. The maximum error for vessel A was 51% and occurred when the amplitude of the roll angle was 3.6 degrees. For some oscillations more than one excitation frequencies are involved. Therefore, the results can be improved with adding more frequency terms in right side of equation (6). The error at the maximum roll angle (13 degrees) was about one percent. It should be mentioned that slight differences between the roll speed and acceleration can be observed in some roll oscillations, despite there being no errors in the predicted roll magnitude (Figure 9). This could be due to numerical errors occurring when calculating the roll derivatives from the measured roll. Additionally, there is a potential for algorithm to find a local rather than the global minimum error. Adjustments to the algorithm could help to avoid local minimum.

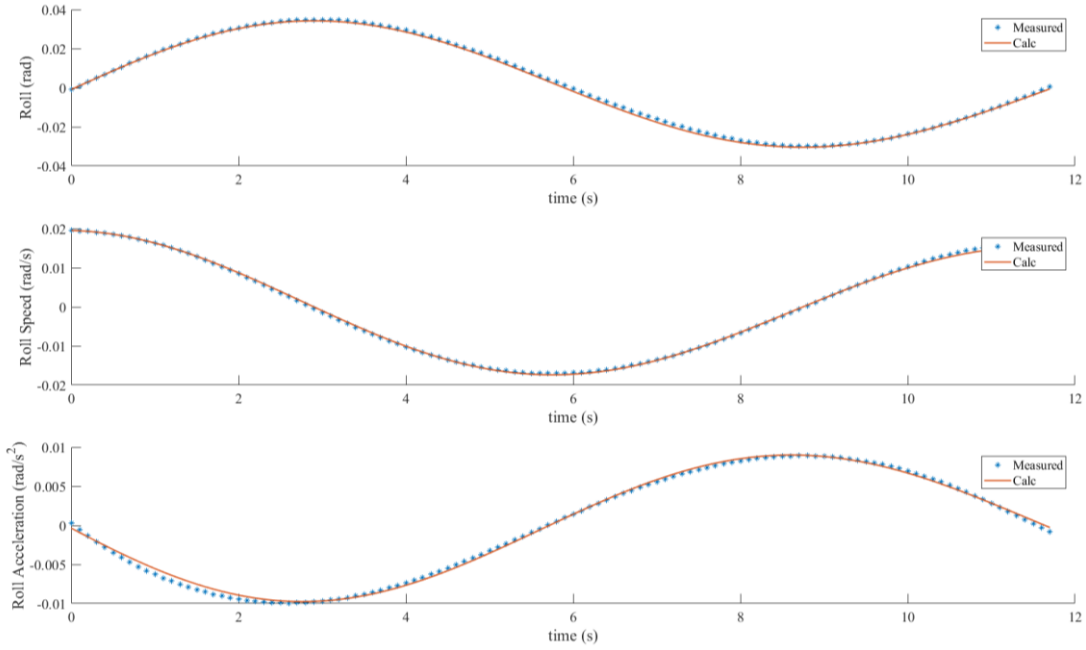

Figure 6. A comparison of measured roll and calculated using the coefficients predicted by the proposed SI method for vessel A

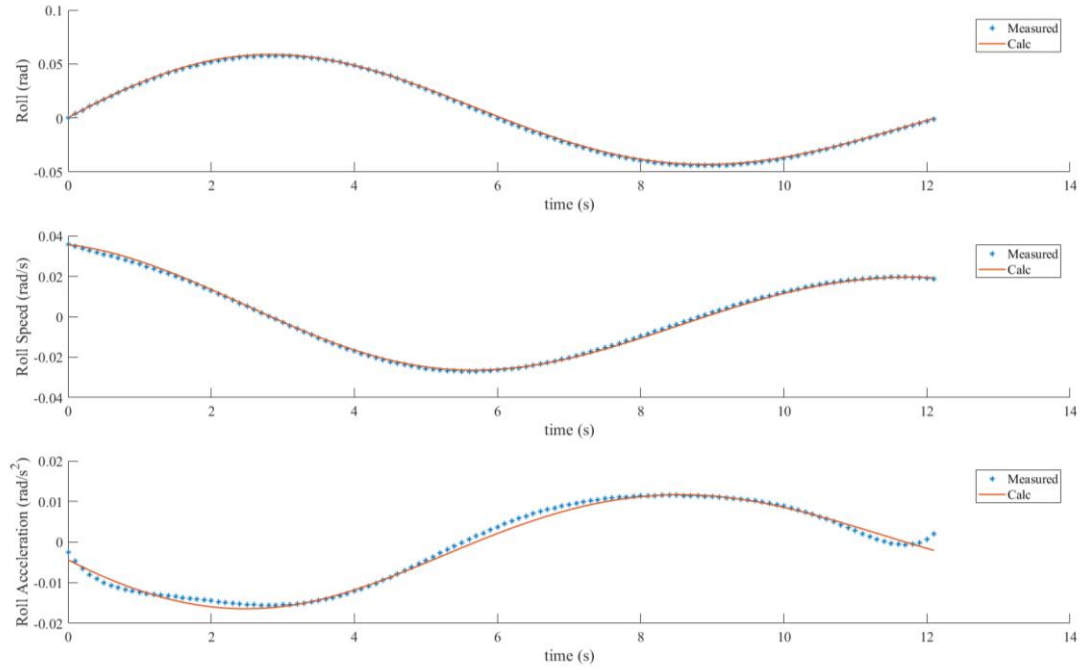

Figure 7. A comparison of measured roll and calculated using the coefficients predicted by the proposed SI method for vessel A

Since the damping and restoring coefficients are frequency dependent (Perez et al., 2004), and vessel speed and roll frequency (as shown in Figure 8) are not constant at sea, the predicted damping and restoring coefficients cannot be expected to be constant for all oscillations. To produce a single set of accurate, reliable coefficients, the average of the coefficients that produced the most accurate oscillations were taken. In the case of "Vessel B" the 50 oscillations that produced the lowest error were used ($\overline{C_i} = \frac{1}{50}\sum_1^{50} C_i\,,\ \ i = 1,2,\ldots,5$).

The damping and restoring coefficients were then set to the predicted averages ($\bar{C}_i, i = 1,2,..,5$) and the program ran again to correct the roll exciting moment parameters and calculate the roll amplitudes. The results of this study are presented in Figure 9. The average error for 158 oscillations of vessel B was about 2.3% and the maximum error was 22% where the roll amplitude was 0.35 degree. It was concluded that these average coefficients can satisfy the roll equation to an acceptable degree.

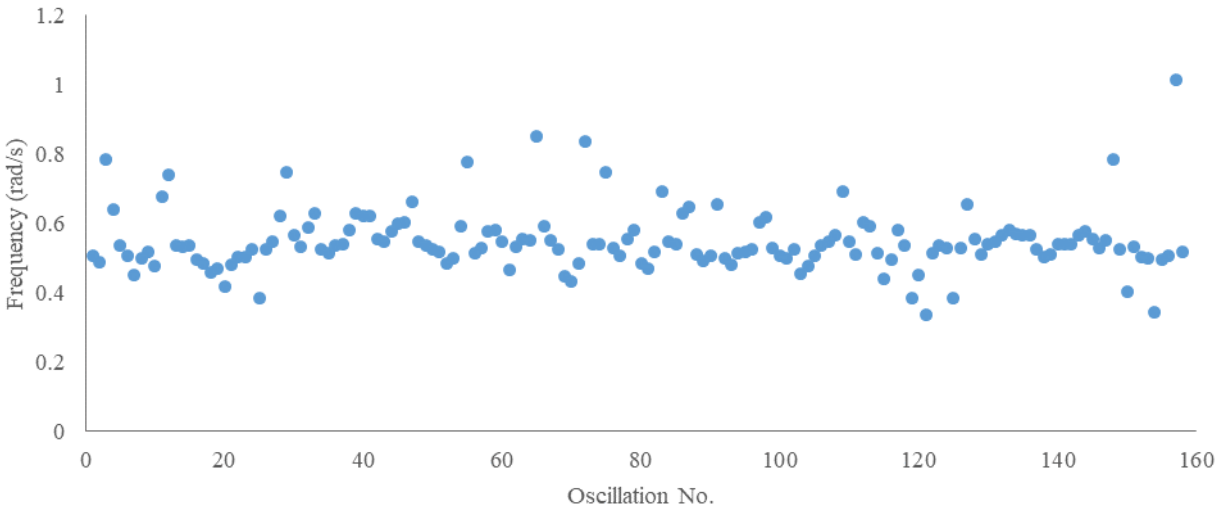

Figure 8. Roll frequencies of recorded data for vessel B

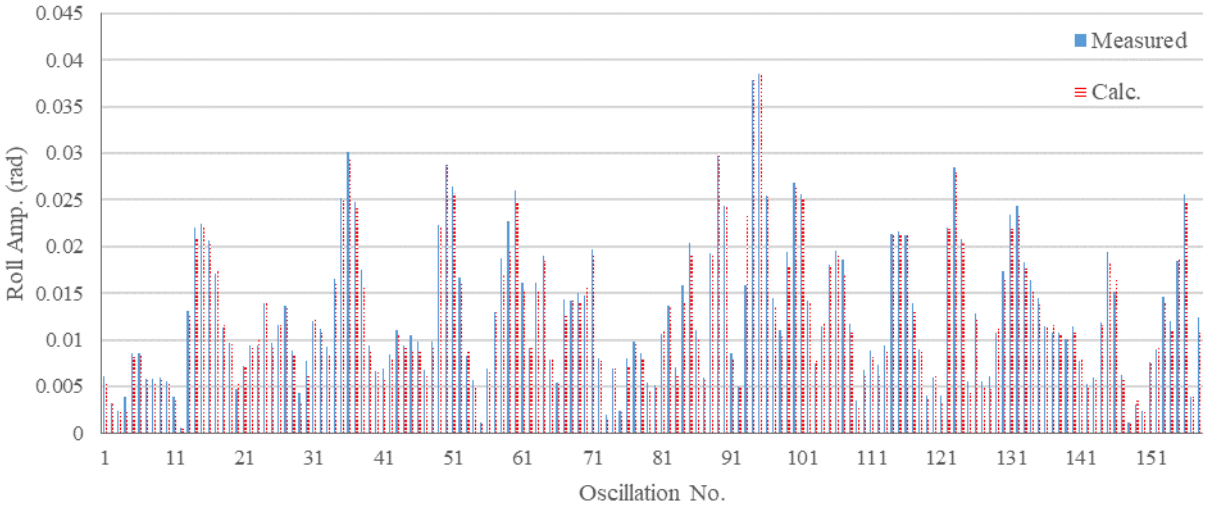

Figure 9. Comparison of the measured roll amplitude and calculated roll amplitude by solving roll equation of motion and using average of predicted coefficients by SI method for 158 roll oscillations of vessel B

5 CONCLUSION

This study was conducted to investigate the applicability of system identification techniques using the reinforcement learning method to predict the coefficients of the equation of roll motion. The reinforcement algorithm was programmed in MATLAB to estimate the linear and nonlinear coefficients of the damping, restoring and excitation moment parameters of the roll equation of motion. To verify the proposed method, the roll motion of modelled and real measured roll data of two different vessels were used as benchmarks. Comparing the predicted roll angle with the simulation and measured roll data proved that predicted coefficients with SI are accurate and that the reinforcement technique is an appropriate method for this purpose.

6 REFERENCES

Haddara, M., Wu, X., 1993. Parameter Identification of Nonlinear Rolling Motion in Random Seas, Int. Shipbuild. Progr., vol. 40, pp. 247-260.

Haddara, M., Hinchey, M., 1995. On the Use of Neural Network Techniques in the Analysis of Free Roll Decay Curves, Int. Shipbuild. Progr., vol. 42, pp. 166-178.

Haddara M., Xu, J., 1998. On the identification of ship coupled heave pitch motions using neural networks, Ocean Engineering, vol. 26, pp. 381-400.

Hibbert, G., Lesser, G., 2013. Measuring Vessel Motions using a Rapid-Deployment Device on Ships of Opportunity, in: 21st Australasian Coastal and Ocean Engineering Conference and the 14th Australasian Port and Harbour Conference (Coasts & Ports 2013), Sydney.

ITTC, 2011, ITTC- Recommended procedures and Guidlines; Global Loads Seakeeping Procedure.

Mahfouz, A. B., 2004. Identification of the nonlinear ship rolling motion equation using the measured response at sea, Ocean Engineering, vol. 31, 2004.

Perez, T., Fossen, T. I., Sørensen, A., 2004. A Discussion About Seakeeping and Manoeuvring Models For Surface Vessels, Technical Report (MSS-TR-001), Centre for Ships and Ocean Structures (CESOS) Norwegian University of Science and Technology NTNU, Trondheim.

Pesman, E., Bayraktar, D., Taylan, M., 2007. Influence of Damping on the Roll Motion of Ships, in: 2nd International Conferenc on Marine Research and Transportation (ICMRT'07), Ischia Naples.

Somayajula, A., Falzarano, J., 2017. Application of advanced system identification technique to extract rolldamping from model tests in order to accurately predict roll motions, Applied Ocean Research, Vol. 67, pp. 125-135.

Sutton, R. S., Barto, A. G., 2018. Reinforcement Learning: an introduction, London: The MIT Press.

Taylan, M., 1996. Nonlinear roll motion of ships in beam waves, Bulletin of the Technical University of Istanbul, Vol. 49, pp. 459-479.

Xing, Z., 2009, Parameter Identification for Two Nonlinear Models of Ship Rolling Using Neural Networks, in: 10th International Conference on Stability of Ships and Ocean Vehicles, St Petersburg.

7 AUTHORS BIOGRAPHY

Mohammadreza Javanmardi holds the current position of Senior Engineer at OMC International. He is responsible for the research and development of algorithms for integrating live ship motion measurement into ship motion predictions. Mohammadreza received his BSc (2005) in Naval Architecture and Maritime Engineering from Amir-Kabir University of Technology, MSc (2008) in Mechanical Engineering from Sharif University of Technology and his Ph.D. (2014) in Hydrodynamics from University of Tasmania, and then served as Lecturer (2015-2016) at AMC and a Postdoctoral associate (2016-2017) at Sharif University of Technology.

Chris Hens holds current position of General Manager Product Design and Development at OMC International. In his role as GM he is responsible for overseeing product research, development and bringing new products to market. He has extensive experience in software Product Management and Project Management as well as DUKC® System implementations, ship motion analysis and vessel passing studies.

Jack Bucher holds the current position of Research Engineer (Ship Motions Team) at OMC International. He is responsible for the research and development of methods for predicting/managing vessel motions and the creation of new products and technologies within that space. He holds a degree in Naval Architecture and has worked on a number of projects related to the measurement, analysis, and prediction of ship motions and under keel clearance.

Gregory Hibbert is a Senior Engineer and the Manager of OMC International's Research & Development section. His responsibilities include developing environmental

prediction models, full-scale vessel motion measurements and analysis techniques. Greg took a lead role in the development of the OMC iHeave® device which subsequently won the 2013 IBJ award for Innovation.

ESTIMATION OF MATHEMATICAL MODEL FOR SHIP MANEUVERING IN WAVES BASED ON ESTIMATION-BEFORE-MODELING TECHNIQUE

MyungJun Jeon and **Hyeon Kyu Yoon**,
Changwon National University, Rep. of Korea

Dong Jin Kim,
Korea Research Institute of Ships and Ocean engineering, Rep. of Korea

ESTIMATION OF MATHEMATICAL MODEL FOR SHIP MANEUVERING IN WAVES BASED ON ESTIMATION-BEFORE-MODELING TECHNIQUE

MyungJun Jeon and **Hyeon Kyu Yoon,** Changwon National University, Rep. of Korea
Dong Jin Kim, Korea Research Institute of Ships and Ocean engineering, Rep. of Korea

SUMMARY

This paper introduces the application of Estimation-Before-Modeling Technique (EBMT), one of the System Identification methods, to estimate mathematical model for ship maneuverability targeting KVLCC2(KRISO Very Large Crude oil Carrier). The accuracy of the wave force acting on a ship is the most important force component for prediction of maneuverability of a ship. EBMT is divided into two steps in this study. First, the motion variables and forces are estimated by Extended Kalman Filter and Modified Bryson-Frazier smoother. Second, the wave forces are determined by removing the hydrodynamic forces acting on a ship during motion. Also, the database consisting of wave length and incident wave angles is constructed during the second step of EBMT. All estimated variables are based on data obtained by free running model tests in regular waves. Finally, the estimated wave force is interpolated and added to the hydrodynamic force component of the 3-DOF equations of motion and then the turning simulation of the ship in waves is performed. The results are compared with the results of free running model tests to confirm that the established model is valid.

NOMENCLATURE

SI	System Identification
KVLCC2	KRISO Very Large Crude oil Carrier 2
EBMT	Estimation-Before-Modeling Technique
FRMTs	Free Running Model Tests
EKF	Extended Kalman Filter
MBFS	Modified Bryson-Frazier Smoother
DOF	Degree of Freedom
MMG	Maneuvering Modeling Group
RPS	Revolutions Per Second

1 INTRODUCTION

The role of System Identification(SI) in ship dynamics has been studied to identify the hydrodynamic coefficients in the hydrodynamic force model. Abkowitz (1980) and Hwang (1980) applied the SI method for the first time to estimate the hydrodynamic coefficients of a ship. The SI method was used for the estimation of coefficients using EKF. In this case, the hydrodynamic coefficients were augmented in the state variables and were simultaneously estimated with other state variables together. However, the magnitude of the covariance matrix was large and the assumption of the initial values affected the convergence.
Estimation-Before-Modeling Technique (EBMT), one of the SI methods, has been mainly used to estimate aircraft parameters (Hoff and Cook, 1996). Yoon and Rhee (2003) first applied EBMT to resolve the problems detected in the study of Abkowitz (1980). Yoon et al. (2007) applied EBMT to develop a roll hydrodynamic moment model. The main purpose of the studies Abkowitz (1980), Hwang (1980), Yoon and Rhee (2003) and Yoon et al. (2007) is similar in terms of estimating hydrodynamic coefficients. However, EBMT is divided into two steps. First, it estimates state variables including motion variables and hydrodynamic force and moments. Second, it estimates the hydrodynamic coefficients using correlation and regression analysis.
The purpose of this study is to estimate the wave force and to construct a database instead of estimating the coefficients. The EBMT, which uses Extended Kalman Filter(EKF) and Modified Bryson-Frazier Smoother(MBFS) as dynamic state estimators without considering the coefficients as state variables, is employed as the SI method.
As the mathematical models included wave forces for the prediction of ship maneuvering in waves, Yasukawa (2006a) developed a practical simulation method which takes only wave drift forces into account in the maneuvering simulation model and mentioned its feasibility to predict maneuverability in waves. Yasukawa (2006b) introduced a practical method for simulations of both ship maneuvering and wave-induced motions. The equations of motions were separated into a high frequency wave induced-motion problem and a low frequency maneuvering problem. In 2013, the minimum power guidelines to maintain the stability and the maneuverability of a ship in adverse condition has been raised by the MEPC (IMO MEPC, 2013; Seo et al., 2018). For this reason, there is a growing interest in predicting ship maneuverability in waves recently. Seo et al. (2018) calculated wave drift forces based on potential theory and validated the calculations by performing maneuvering simulations and comparing them with experimental results.
This study represents fundamental research into the estimation of the wave force including wave drift force using the SI method and the development of a mathematical model. Kim et al.(2019) carried out FRMTs of KVLCC2 in regular waves with various wave lengths. All measured values used in this study were derived from the FRMTs. Mathematical models regarding ship maneuvering in waves are introduced in Chapter 2. Chapter 3 discusses the concepts of EBMT, and the 1st and 2nd steps of EBMT. The results of the estimation are summarized in Chapter 4. Finally, the maneuvering simulation of a ship in waves is performed using the estimated wave force, and the results are compared with one of the FRMTs. These results are described in Chapter 5 with the results of comparison for trajectory drift index.

2 MATHEMATICAL MODELS

2.1 COORDINATE SYSTEMS

There are two kinds of coordinate systems, which describe the ship's horizontal motion. The first is the earth-fixed coordinate system $O - x_o y_o$ to express a ship's trajectory. The other system is a ship-fixed coordinate system $o - xy$ defining the equations of motion and expressing external force acting on a ship. Both use right-handed orthogonal coordinate system as shown in Figure 1. Although the absolute wave direction is constant in the earth-fixed coordinate system, the wave incident angle is always altered in the ship-centered coordinate system when the ship turns. χ_0 shown in Figure 1 means the absolute wave direction with respect to the earth-fixed coordinate system.

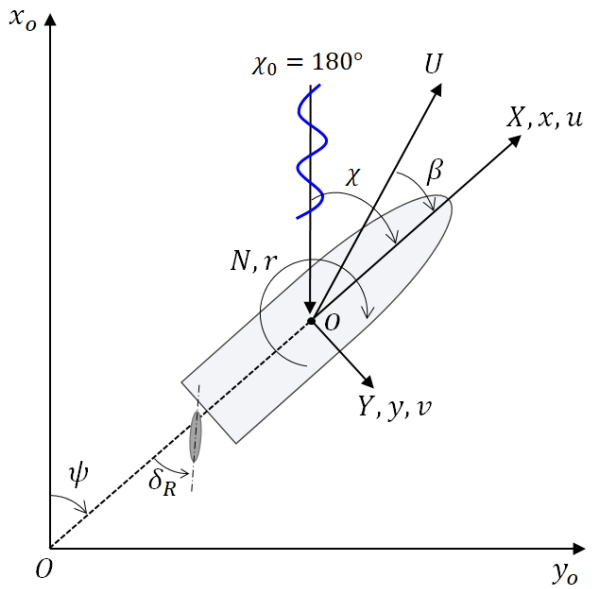

Figure 1. Coordinate systems and definition of wave incident angle

2.2 EQUATIONS OF MOTION

The three DOF equations of motion based on Newton's 2nd law are expressed in Eq.(1). The right side of the equations describes external force on a ship maneuvered by steering in waves.

$$\begin{aligned} m(\dot{u} - vr - x_G r^2) &= X_{man} + X_{wave} \\ m(\dot{v} + ur + x_G \dot{r}) &= Y_{man} + Y_{wave} \\ I_{zz}\dot{r} + mx_G(\dot{v} + ur) &= N_{man} + N_{wave} \end{aligned} \quad (1)$$

The subscripts 'man' and 'wave' represent the force due to maneuvering motion and wave, respectively. It can be divided into specific components as shown in Eq.(2). The following models are based on MMG model including hydrodynamic force, thrust and rudder force (Yasukawa and Yoshimura, 2015).

$$\begin{aligned} X_{man} &= X_{\dot{u}}\dot{u} + X_{vv}v^2 + X_{vvvv}v^4 + X_{vr}vr + X_{rr} - R_0 \\ &\quad +(1 - t_P)\rho n^2 D^4 K_T - (1 - t_R)F_N sin\delta_R \end{aligned}$$

$$\begin{aligned} Y_{man} &= Y_{\dot{v}}\dot{v} + Y_{\dot{r}}\dot{r} + Y_v v + Y_r r + Y_{vvv}v^3 + Y_{vvr}v^2 r \\ &\quad +Y_{vrr}vr^2 + Y_{rrr}r^3 - (1 + a_H)F_N cos\delta_R \end{aligned}$$

$$\begin{aligned} N_{man} &= N_{\dot{v}}\dot{v} + N_{\dot{r}}\dot{r} + N_v v + N_r r + N_{vvv}v^3 + N_{vvr}v^2 r \\ &\quad + N_{vrr}vr^2 + N_{rrr}r^3 - (x_R + a_H x_H)F_N cos\delta_R \end{aligned} \quad (2)$$

It is assumed that the total external force and moment acting on a maneuvering ship in waves can be divided into two components like in Eq.(1). Therefore, it is necessary to predict the force and moment in calm water accurately. It is assumed that the mathematical model parameters regarding external forces in still water are accurate and known values. All parameters including hydrodynamic coefficients, interaction coefficients among hull, propeller and rudder written in Yasukawa and Yoshimura (2015) were used in this study. The non-dimensional expressions of force and moment are defined as Eq.(3) and Eq.(4), respectively (Yasukawa and Yoshimura, 2015; Yasukawa, 2006a).

$$F'_{man} = \frac{F_{man}}{\frac{1}{2}\rho L d U^2}, \quad M'_{man} = \frac{M_{man}}{\frac{1}{2}\rho L d U^2} \quad (3)$$

$$F'_{wave} = \frac{F_{wave}}{\rho g \xi_a^2 B^2 / L}, \quad M'_{wave} = \frac{M_{wave}}{\rho g \xi_a^2 B^2} \quad (4)$$

where L, B, d, U, and ξ_a are ship length between perpendicular, breadth, mean draft, speed and wave amplitude, respectively.

3 EBMT APPLICATION

3.1 THE CONCEPTS OF EBMT

The estimation of the hydrodynamic coefficients of a ship in still water was adequately explained by Yoon and Rhee (2003) and Yoon et al. (2007). EBMT is divided into two steps as shown in Figure 2. The first step is to construct state equations and estimate state variables including motion variables and external force. EKF and MBFS are used as the dynamic state estimators. The first step in this study is similar to that of the pervious study. The second step is to determine the wave force based on the external force estimated in the first step by removing the force and moment in calm water expressed in Eq.(2).

3.2 1ST STEP OF EBMT

3.2 (a) State space model

In order to estimate motion variables and external force and moment, the state space model incorporate state and measurement equations. The components of state vector represent the final estimated variables in this step and are defined as in Eq.(5).

$$\underline{x} = [\underline{x_1} \quad \underline{x_2} \quad \underline{x_3}]^T \quad (5)$$

where,

$$\underline{x_1} = [u \quad v \quad r]^T$$
$$\underline{x_2} = [x_o \quad y_o \quad \psi]^T$$

$$\underline{x_3} = \begin{bmatrix} X_{man} + X_{wave} \\ \dot{X}_{man} + \dot{X}_{wave} \\ \ddot{X}_{man} + \ddot{X}_{wave} \\ Y_{man} + Y_{wave} \\ \dot{Y}_{man} + \dot{Y}_{wave} \\ \ddot{Y}_{man} + \ddot{Y}_{wave} \\ N_{man} + N_{wave} \\ \dot{N}_{man} + \dot{N}_{wave} \\ \ddot{N}_{man} + \ddot{N}_{wave} \end{bmatrix}$$

The vector $\underline{x_1}$ and $\underline{x_2}$ represent motion variables including velocity and displacement, respectively, and $\underline{x_3}$ is the external force and moment. Since the external force and moment are assumed as the third-order Gauss-Markov processes, state variable vector includes those first and second order time derivatives (Yoon and Rhee, 2003; Yoon et al., 2007). In order to estimate state variable vector, the state equation which is the dynamic model of state variable vector is necessary as follows,

$$\dot{\underline{x}} = M_T^{-1} \underline{f(x)} + \underline{w}(t) \tag{6}$$

where $\underline{w}(t)$ denotes white Gaussian noise expressing the errors caused by modeling error. The dimensions of matrix M_T and vector $\underline{f(x)}$ include 15 x 15 and 15 x 1, respectively and are defined as follows.

$$M_T = \begin{bmatrix} M & 0_{3\times12} \\ 0_{12\times3} & I_{12\times12} \end{bmatrix}$$

$$M = \begin{bmatrix} m - X_{\dot{u}} & 0 & 0 \\ 0 & m - Y_{\dot{v}} & mx_G - Y_{\dot{r}} \\ 0 & mx_G - N_{\dot{v}} & I_{zz} - N_{\dot{r}} \end{bmatrix}$$

$$\underline{f(x)} = \begin{bmatrix} m(vr + x_G r^2) + X_{man} + X_{wave} \\ -mur + Y_{man} + Y_{wave} \\ ucos\psi - vsin\psi \\ usin\psi + vcos\psi \\ r \\ \dot{X}_{man} + \dot{X}_{wave} \\ \ddot{X}_{man} + \ddot{X}_{wave} \\ 0 \\ \dot{Y}_{man} + \dot{Y}_{wave} \\ \ddot{Y}_{man} + \ddot{Y}_{wave} \\ 0 \\ \dot{N}_{man} + \dot{N}_{wave} \\ \ddot{N}_{man} + \ddot{N}_{wave} \\ 0 \end{bmatrix}$$

The vector $\underline{f(x)}$ includes Coriolis and centrifugal force terms, which are known values before solving Eq. (6).

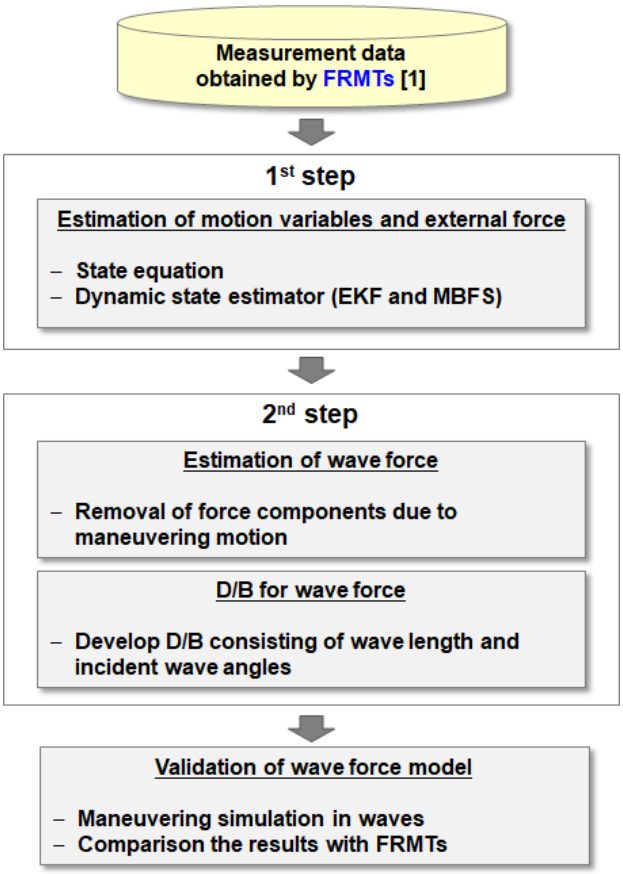

Figure 2. Procedure for EBMT

Also, since it is assumed that the added mass coefficients are known in advance, those values are included in the inertia matrix M. Because the acceleration is not a state variable vector element, it is convenient to subtract the force associated with acceleration when estimating force.
Another equation that is part of the state space model is the measurement equation. Kim et al.(2019) performed the FRMTs of KVLCC2 and its details are described in reference. In this study, all measurement data were obtained from FRMTs. The type of measured data includes trajectory, yaw angle, speed, yaw rate, propeller RPS, and rudder angle. Propeller RPS and rudder angle are only necessary at the second step of EBMT. Therefore, the measurement equation is defined as in Eq.(7).

$$\underline{z} = \underline{h}(\underline{x}, t) = [x_o \quad y_o \quad \psi \quad U \quad r]^T \tag{7}$$

3.2 (b) State estimator

The motion variables and external force and moment are estimated by state estimator. There are three kinds of estimators: predictor, filter and smoother. In this study, EKF and MBFS were used as the estimators. Both EKF and MBFS can be used to estimate state variables. However, MBFS estimates state variables using all the data including past, present and future. Therefore, MBFS is more accurate and it is used as the final state estimator (Yoon and Rhee, 2003).

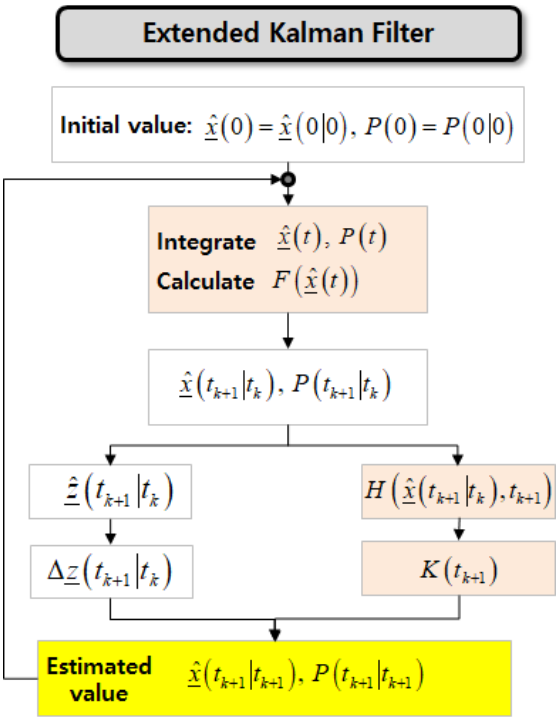

Figure 3. EKF procedure

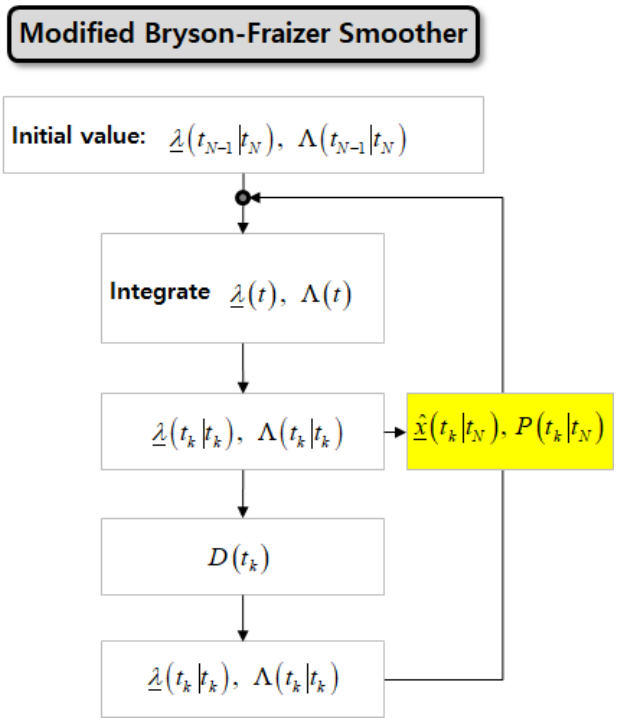

Figure 4. MBFS procedure

Although MBFS is the final state estimator, it needs filtered state variables, Kalman gain matrix, and error covariance matrix calculated by EKF. Therefore, both EKF and MBFS are considered state estimators in the first step of EBMT. The procedures of EKF and MBFS are shown in Figure 3 and Figure 4. EKF is presented in Figure 3.

Yoon and Rhee (2003) introduced the procedure for estimating the state variables through EKF and MBFS in detail, and a brief introduction is given in this paper.

First of all, EKF is divided into two steps: state prediction and measurement update. State prediction step is to predict the present value using the previous estimated value. The predicted state variables and error covariance matrix are defined as Eq.(8) and Eq.(9).

$$\hat{\underline{x}}(k|k-1)=\hat{\underline{x}}(k-1|k-1)+\int_{t_{k-1}}^{t_k}\dot{\hat{\underline{x}}}(t)dt \tag{8}$$

$$P(k|k-1)=P(k-1|k-1)+\int_{t_{k-1}}^{t_k}\dot{P}(t)dt \tag{9}$$

where,

$\hat{\underline{x}}(k|k-1)$: predicted state variables (15 x 1)

$P(k|k-1)$: predicted error covariance matrix (15 x 15)

$$\dot{P}(t)=F\left(\hat{\underline{x}}(t)\right)P(t)+P(t)F^T\left(\hat{\underline{x}}(t)\right)+Q(t)$$

$$F\left(\hat{\underline{x}}(t)\right)=\left.\frac{\partial\underline{f}\left(\underline{x}(t)\right)}{\partial\underline{x}(t)}\right|_{\underline{x}(t)=\hat{\underline{x}}(t)}$$

$\dot{\hat{\underline{x}}}(t)$ can be obtained by solving Eq.(6). Matrix Riccati differential equation to get $\dot{P}(t)$ includes jacobian matrix $F\left(\hat{\underline{x}}(t)\right)$ and process noise $Q(t)$ of state equation.

When it comes to measurement update step, it requires predicted state variables, error covariance matrix, measured data, jacobian matrix of Eq.(7) and Kalman gain matrix to get estimated state variables. Eq.(10) and Eq.(11) are estimated state variables and error covariance matrix and these values are reused in Eq.(8) and Eq. (9) to obtain the predicted value at next step.

$$\hat{\underline{x}}(k|k)=\hat{\underline{x}}(k|k-1)+K(k)\Delta\underline{z}(k|k-1) \tag{10}$$

$$P(k|k)=[I-K(k)H(k)]P(k|k-1)[I-K(k)H(k)]^T+K(k)R(k)K^T(k) \tag{11}$$

where,

$\Delta\underline{z}(k|k-1)=\underline{z}(k)-\hat{\underline{z}}(k|k-1)$

$\hat{\underline{z}}(k|k-1)=\underline{h}\left(\hat{\underline{x}}(k|k-1),t_k\right)$

$K(k)=P(k|k-1)H^T(k)[H(k)P(k|k-1)H^T(k)+R(k)]^{-1}$

$$H(k)=\left.\frac{\partial\underline{h}\left(\underline{x}(t_k),t_k\right)}{\partial\underline{x}(t_k)}\right|_{\underline{x}(t_k)=\hat{\underline{x}}(k|k-1)}$$

The residual $\Delta\underline{z}$, so called innovation process, is the difference between measured and predicted values. When estimating the state variables $\hat{\underline{x}}(k|k)$, Kalman gain $K(k)$ compensates for this difference. $R(k)$ is the measurement noise matrix, which is determined by the noise characteristics of measurement sensors. $H(k)$ is the Jacobian matrix of measurement equation Eq.(7). The state variable error covariance matrix are obtained through EKF. However, all variables obtained from EKF are stored only for MBFS as a more accurate estimator. The variables to be stored in order to estimate the final state variables and error covariance through MBFS are as follows.

$\underline{\hat{x}}(k|k), K(k), P(k|k-1), P(k|k), \Delta\underline{z}(k|k-1),$
$F\left(\underline{\hat{x}}(t)\right), H(k)$

MBFS estimates the values at $t = t_{k-1}$ with the state variables estimated by EKF at $t = t_k$ as the initial values. The initial conditions for the adjoining variable vector and matrix are expressed by

$$\underline{\lambda}(N-1|N) = -H^T(N)D^{-1}(N)\Delta\underline{z}(N|N-1) \quad (12)$$

$$\Lambda(N-1|N) = H^T(N)D^{-1}(N)H(N) \quad (13)$$

where,
$D(N) = H(N)P(N|N-1)H^T(N) + R(N)$
t_k : Final measurement time

The time propagation equations of adjoining vector variables and matrix can be expressed as follows using the Jacobian matrix of state equations.

$$\dot{\underline{\lambda}}(t) = -F^T\left(\underline{\hat{x}}(t)\right)\lambda(t) \quad (14)$$

$$\dot{\Lambda}(t) = -F^T\left(\underline{\hat{x}}(t)\right)\Lambda(t) - \Lambda^T(t)F\left(\underline{\hat{x}}(t)\right) \quad (15)$$

The above differential equations should be solved backward direction of time. The solutions obtained by solving Eq.(14) and Eq.(15) are $\underline{\lambda}(k|k)$ and $\Lambda(k|k)$ which are used as variables to solve Eq.(16) and Eq.(17) used for iterative calculations.

$$\underline{\lambda}(k-1|k) = \underline{\lambda}(k|k) - H^T(k)D^{-1}(k) \left[\Delta\underline{z}(k|k-1) + D(k)K^T(k)\underline{\lambda}(k|k)\right] \quad (16)$$

$$\Lambda(N-1|N) = [I - K(k)H(k)]^T\Lambda(k|k)[I - K(k)H(k)] + H^T(k)D^{-1}(k)H(k) \quad (17)$$

where,
$D(k) = H(k)P(k|k-1)H^T(k) + R(k),$
$k = N-1,..,1$

The final estimated state variables and error covariance matrix using all measurement data can be obtained using Eq.(18) and Eq.(19).

$$\underline{\hat{x}}(k|N) = \underline{\hat{x}}(k|k) - P(k|k)\underline{\lambda}(k-1|k) \quad (18)$$

$$P(k|N) = P(k|k) - P(k|k)\Lambda(k|k)P(k|k) \quad (19)$$

3.3 SECOND STEP OF EBMT

The second step of EBMT involves estimation of wave force and database construction for wave force. Figure 5 shows the time series for each force component. The total external force ($F_{man} + F_{wave}$) is included in the components of state variable vectors written in Eq.(5). It can be obtained by MBFS in the first step of EBMT. The force due to maneuvering (F_{man}) is obtained using Eq.(2). When using Eq.(2) to calculate F_{man}, the estimated motion variables written in Eq.(5) should be substituted into Eq.(2) at every time step. Finally, the wave force is obtained by subtracting the force due to maneuvering from the total external force.

When the wave force is obtained using the above calculation procedure, it is represented as a function of encountering wave direction and wave length. Database construction for wave force entails tabulation of the results of the force and moment with respect to encountering wave direction and wave length. The details are provided Section 4.

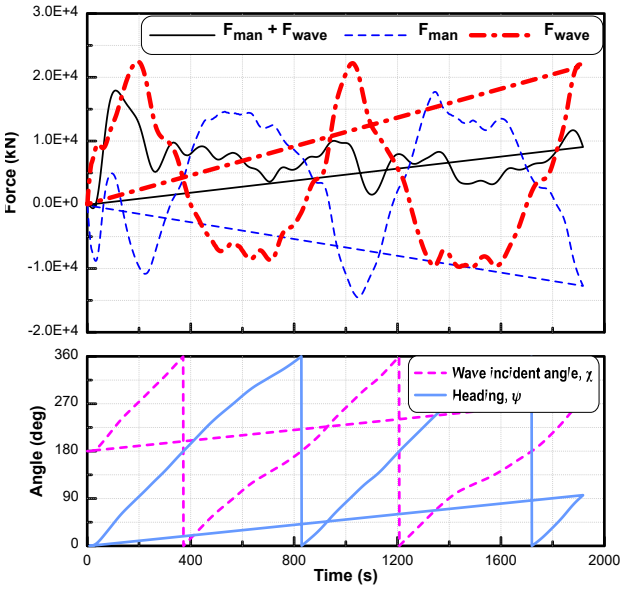

Figure 5. Sample time series of force components and encountering wave direction of a turning ship in regular wave

4 ESTIMATION RESULTS

4.1 ESTIMATION OF STATE VARIABLES

In this Section, all motion variables, force and moment are expressed in full-scale dimensions. The state variables are estimated based on the first step of EBMT. First, the estimated motion variables and external forces using the data measured by FRMTs in still water condition are shown in Figures 6 and 7, respectively. Since the speed and yaw rate were measured by FRMT, they were compared with the estimated values. Figure 6 shows that the estimated values agree adequately with the measured values . Except for the sway velocity, the force and moment exclusively exist as estimated values. Figure 7 represents the time series of the forces estimated and calculated using Eq.(2). The differences between the results of simulation and estimation should be small to accurately identify the wave force. Therefore, the parameters constituting Eq.(2) were slightly adjusted using FRMT in this study.

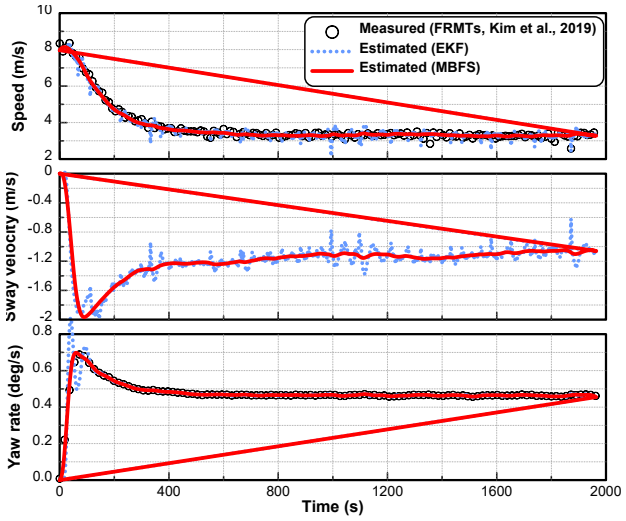

Figure 6. Time series of motion variables of a turning ship turns in calm water

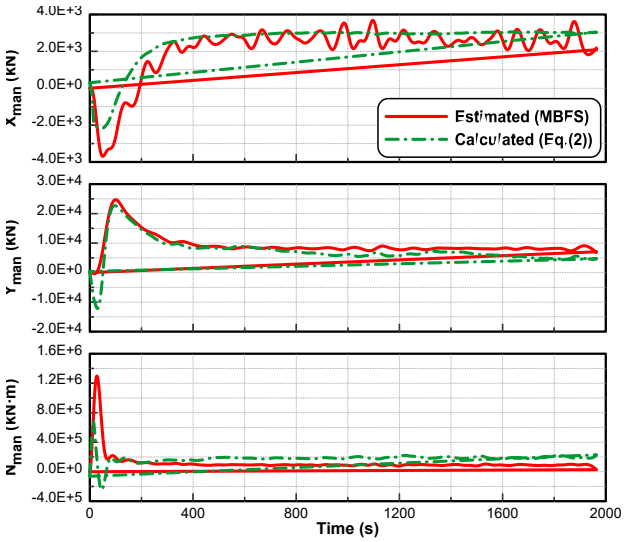

Figure 7. Time seriesof force and moment acting on a turning ship in calm water

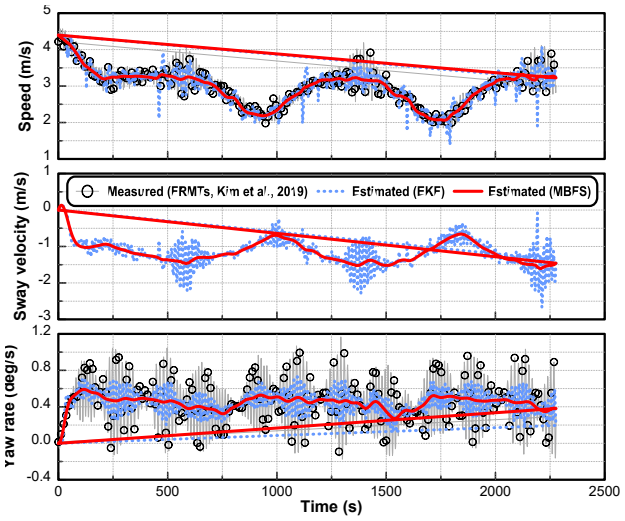

Figure 8. Time series of motion variables of a turning ship in regular wave (λ/L = 1.0)

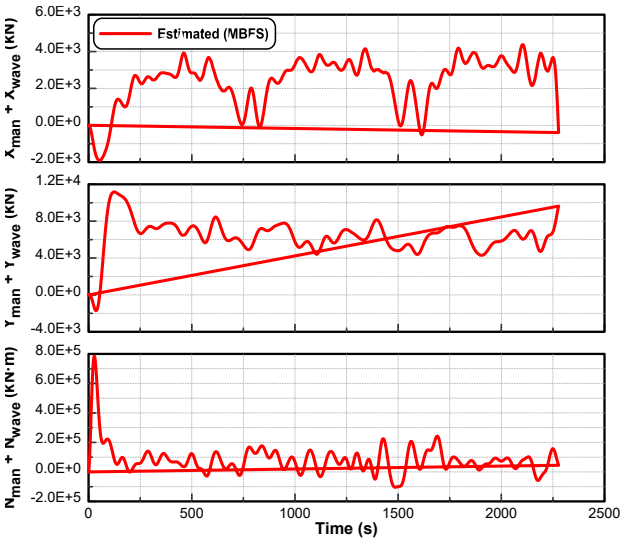

Figure 9. Time series of force and moment acting on a turning ship in regular wave (λ/L = 1.0)

Figure 7 highlights the difference between the calculated values using Eq.(2) and the estimated force is not large.
Figures 8 and 9 show the estimated state variables in waves when the wave length to ship length ratio is equal to 1.0. As in the case of calm water, the estimated and measured motion variables coincide well and the total external and wave forces are also consistent. The conditions of regular waves were applied to the FRMTs. In this paper, we introduce that the estimated state variables in calm water and in wave length to ship length ratio 1.0 and absolute wave direction 180° case only as an example. The estimated motion variables are used for validation of wave force model and the estimated force and moment are used for validation and estimation of wave force.

4.2 WAVE FORCE

Figure 10 shows the non-dimensional wave force and moment with respect to incident wave angle during the turning of the ship, and the wave length to ship length ratio. These forces and moments are obtained by the procedure described in the second step of EBMT, which triggers drifting trajectory. These results are validated by performing simulation and comparing with FRMTs.
The distributions of non-dimensional wave force and moment shown in Figure 11 constitute the database as the components of external force in the mathematical models in Eq.(1). When performing maneuvering simulation in waves, the force and moment are interpolated at every time interval.

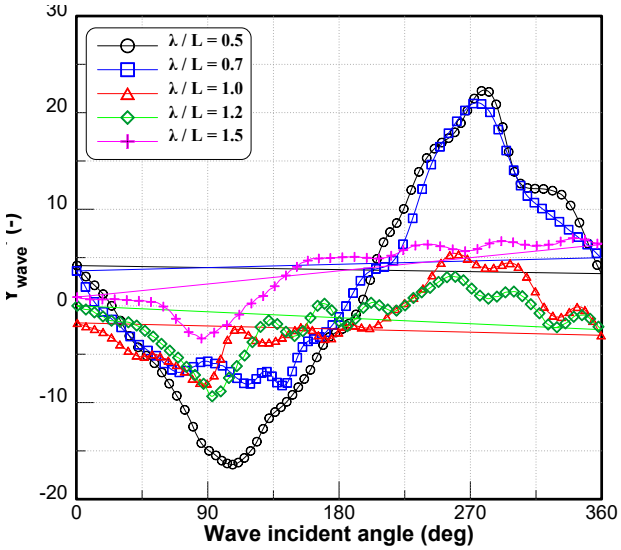

(a) Lateral wave force

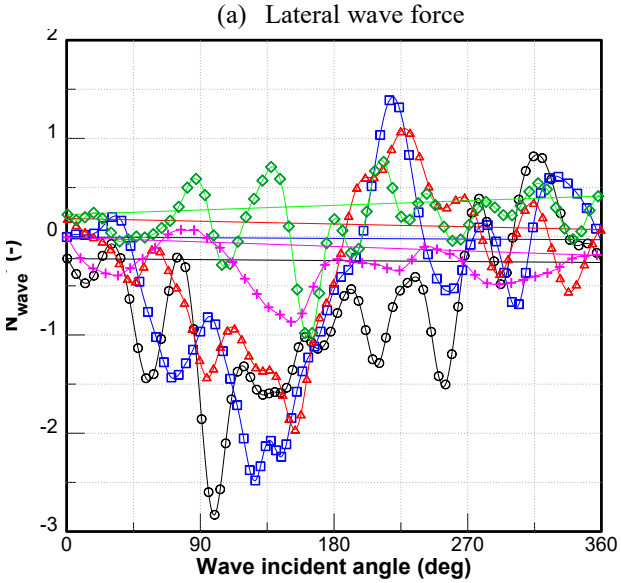

(b) Yawing wave moment

Figure 10. Non-dimensional wave force and moment acting on a turning ship under various wave length ratios.

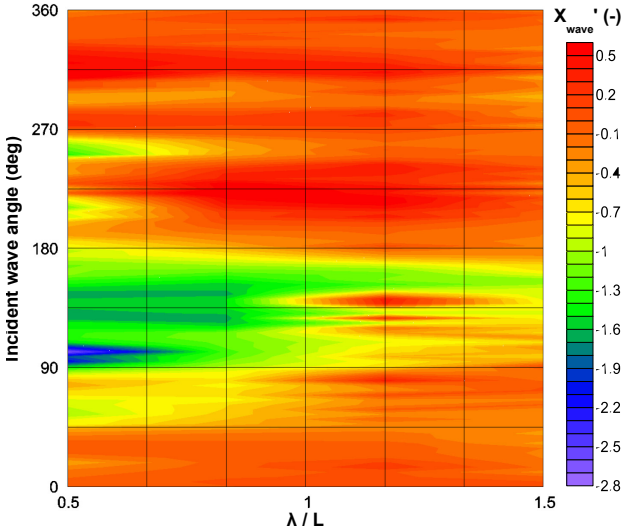

(a) Axial wave force

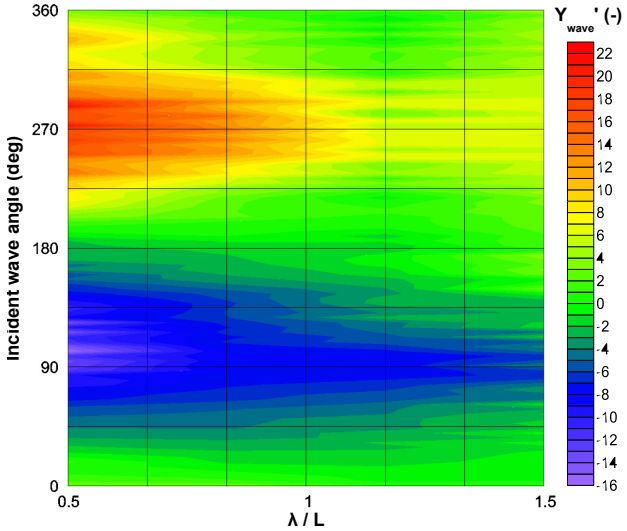

(b) Lateral wave force

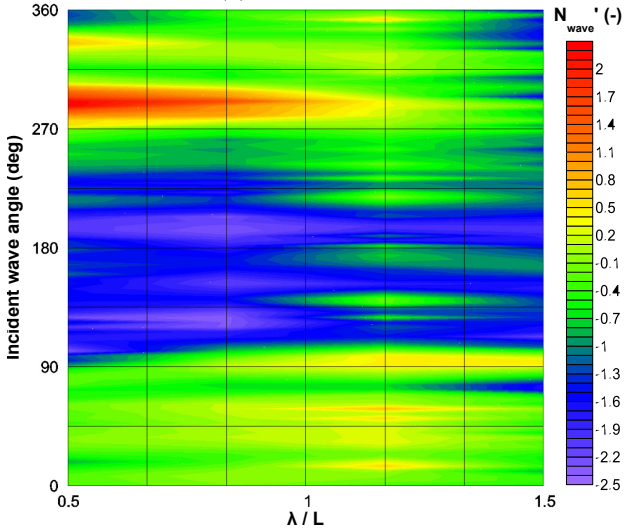

(c) Yawing wave moment

Figure 11. Distributions of non-dimensional wave force and moment acting on a turning ship under various wave angles and wave-length ratios.

5 SIMULATION AND VALIDATION

5.1 35 STARBOARD TURNING SIMULATIONS IN REGULAR WAVES

All types of simulation results shown in Figures 12 through 17 are compared with the results of FRMTs and estimated ones by MBFs. As noted before, the accuracy of the maneuvering mathematical model in calm water is required because it significantly affects the estimation process. Figure 12 shows the simulation results in calm water without considering wave force. It is in good agreement with FRMTs results, except for the initial turning trajectory. However, it seems that the error in the initial turning in calm water has some overall effects to the error in initial turning trajectory in waves shown in Figure 13 through 17. Therefore, it is necessary to further improve the accuracy of mathematical model in terms of the initial trajectory written in Eq.(2).

In case of a trajectory, the speed and yaw rate are considered as actual values to be compared. Otherwise, the estimated values are considered. The conditions of regular waves include various wave-length ratios of 0.5, 0.7, 1.0, 1.2 and 1.5. The wave height and initial wave-incident angles are $0.02L$ and 180°, respectively. Most of the results exhibit similar trends between FRMTs and simulation. However, the trajectory shifts due to the initial errors involving motion variables and forces in case of λ/L = 0.5, 0.7, and 1.5. These are the reason why the differences between the force estimated by MBFS and calculated by Eq.(2) in transient time. The transient time refers to the time during steering rudder. The force obtained during these intervals represents the wave forces near 180° incident wave angle in Figure 10. Improvement in the force during transient time enhances the accuracy of the motion variables. Especially, the error of surge velocity is relatively large because straight motion without lateral and yawing motion is rare when the ship turns. Therefore, it is recommended to perform straightforward tests in various wave-length conditions due to acquisition of accurate axial wave force X_{wave}.

5.2 INDICES FOR TURNING TRAJECTORY DRIFT IN WAVES

Kim et al. (2019) summarized the drifting distance and angle at different turning maneuvers in waves. It is appropriate that the trajectory drift and angles are defined as the magnitude and direction of a vector between two positions with the heading 360° and 720° expressed as $Ddr_{360-720}$ and $Adr_{360-720}$ respectively. Table 1 lists the main indices $Ddr_{360-720}$ and $Adr_{360-720}$ between FRMTs and present simulation. In case of the drifting angle $Adr_{360-720}$, the error is within 10 % and which is similar with the one of FRMTs. On the other hand, the drifting distance $Ddr_{360-720}$ is somewhat different from the one of FRMTs especially $\lambda/L = 1.5$. The reason having those large errors is the difference of surge velocity when steering the rudder. So, the improvement of accurate axial wave force should be needed.

6 CONCLUSIONS

This study focuses on validation of wave force identified using EBMT, which is one of the SI methods. In order to validate the identification method using EBMT, a two-step estimation procedure was carried out and all the estimated variables were verified for each step by comparing with the value obtained from FRMTs. The conclusions of this study can be summarized as follows.

- The motion variables estimated by MBFS are almost identical to those of FRMTs. So, there is no matter to estimate motion variables despite of the conditions in waves.
- It is confirmed that the estimated external force is also the force causing the real motion. Therefore, the first step of EBMT is valid because the motion variables estimated by MBFs are consistent with FRMTs.
- However, based on the results of simulation, it is necessary to improve the accuracy of estimation when steering the rudder during the initial turning.

In addition, the expected effects of this study can be summarized as follows.

- If it is possible to improve the second step of EBMT, this method may be used to develop a wave force model instead of performing a number of captive model tests. Thus, the time to develop mathematical models for ship maneuver in waves could be reduced since many cases of captive model tests are needed, especially in waves.
- In the future, this study can be used as a basic research foundation to develop a dynamic model using the operational data obtained from a ship sailing on rough seas in real time.

For further development of the approach, The 4-DOF equations of motion including roll motions are applied to identify the wave force.

Table 1. Comparison of drifting distance and angles in case of 35 starboard turn
($\chi_0 = 180°$, $\xi_a/L = 0.01$)

Wave length	$Ddr_{360-720}$ (L)		$\lvert Error \rvert$ (%)
	FRMTs	Sim.	
$\boldsymbol{\lambda/L = 0.5}$	2.28	2.27	0.4
$\boldsymbol{\lambda/L = 0.7}$	2.46	2.33	5.3
$\boldsymbol{\lambda/L = 1.0}$	1.16	1.07	7.8
$\boldsymbol{\lambda/L = 1.2}$	0.47	0.38	19.1
$\boldsymbol{\lambda/L = 1.5}$	0.13	0.33	153.8
Wave length	$Adr_{360-720}$ (deg)		$\lvert Error \rvert$ (%)
	FRMTs	Sim.	
$\boldsymbol{\lambda/L = 0.5}$	171	172	0.6
$\boldsymbol{\lambda/L = 0.7}$	143	156	9.3
$\boldsymbol{\lambda/L = 1.0}$	129	126	2.3
$\boldsymbol{\lambda/L = 1.2}$	163	152	6.7
$\boldsymbol{\lambda/L = 1.5}$	173	187	8.1

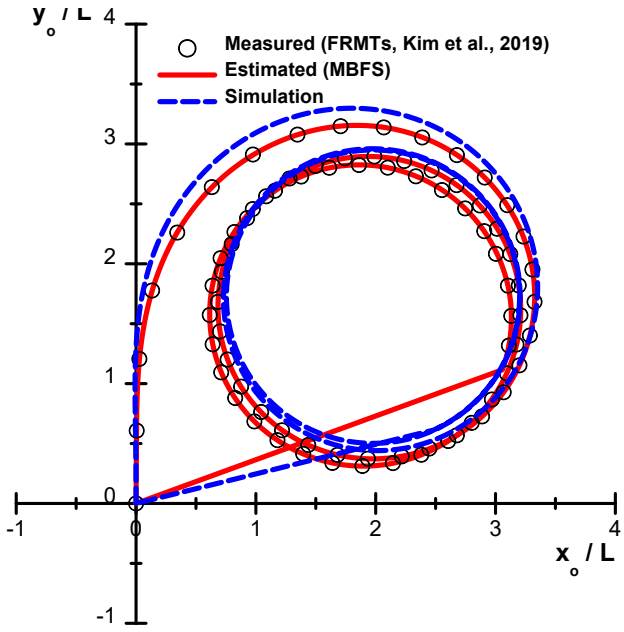

(a) Trajectory

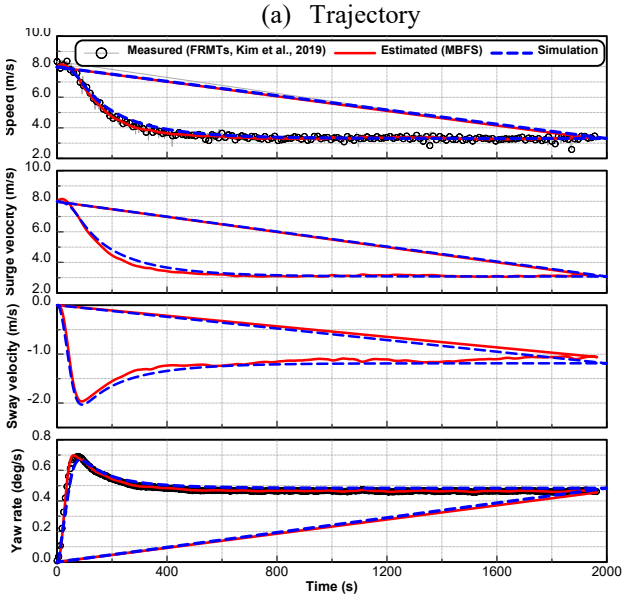

(b) Motion variables

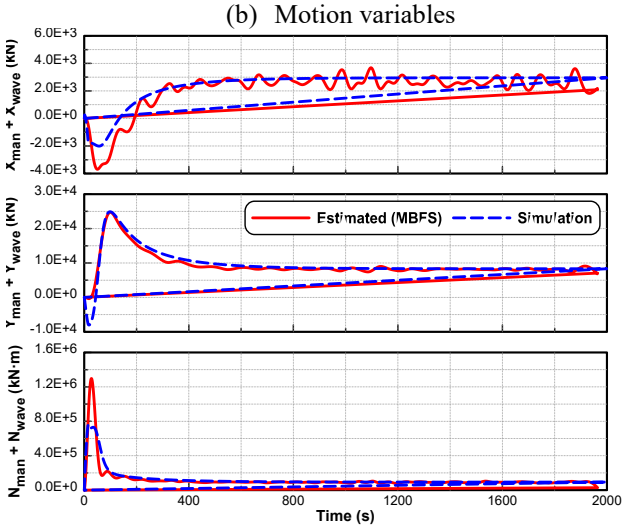

(c) External force and moment

Figure 12. Results of comparison among FRMTs, MBFS and Simulation (in calm water)

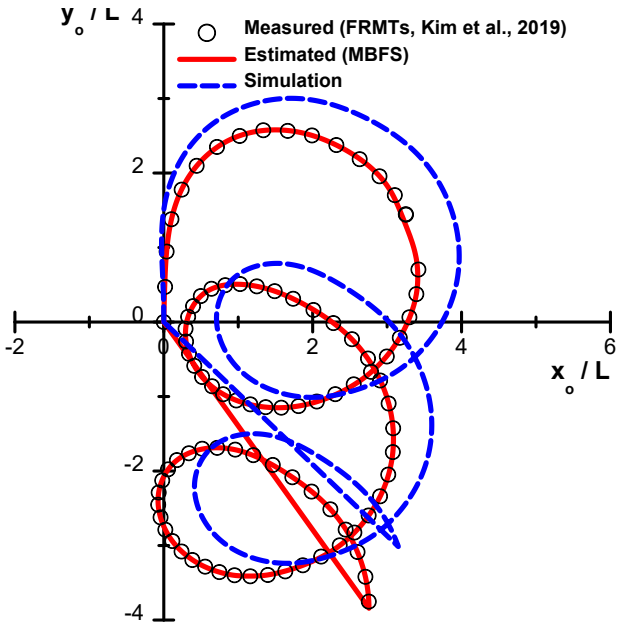

(a) Trajectory

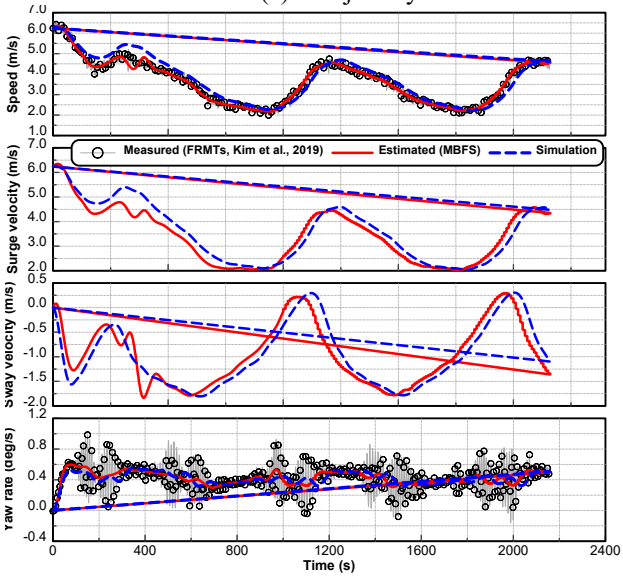

(b) Motion variables

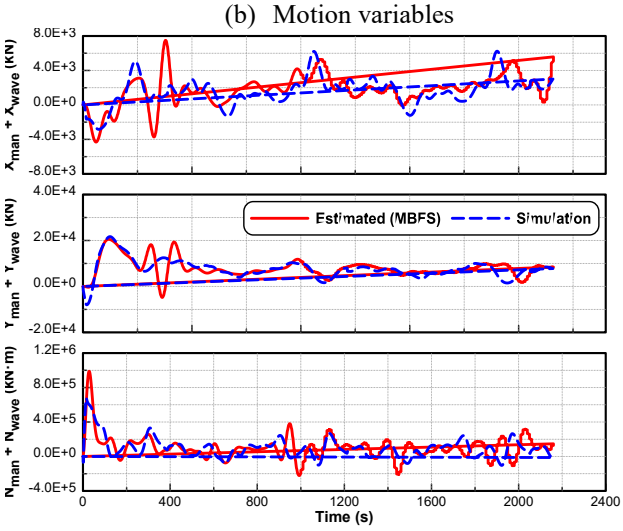

(c) External force and moment

Figure 13. Results of comparison among FRMTs, MBFS and Simulation ($\lambda/L = 0.5$)

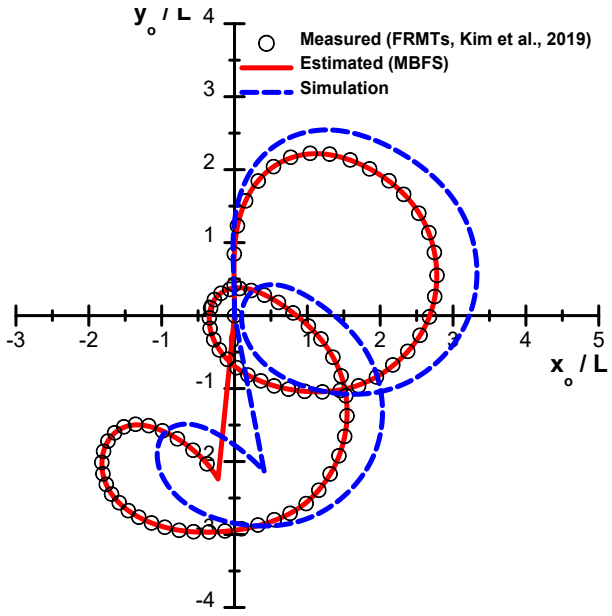

(a) Trajectory

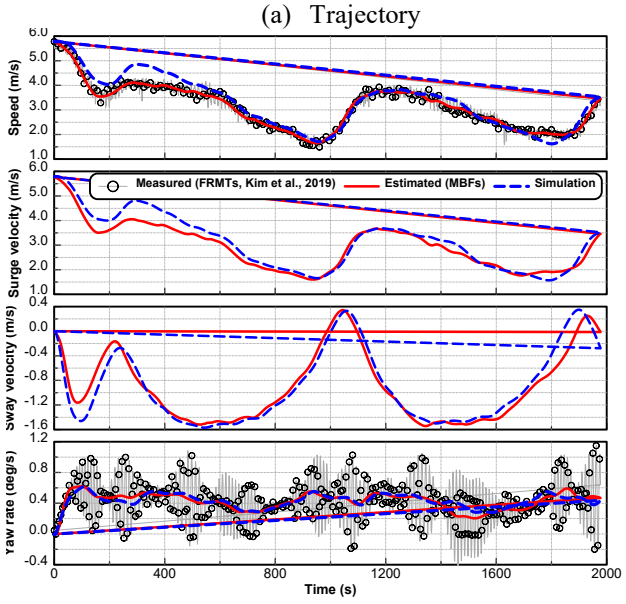

(b) Motion variables

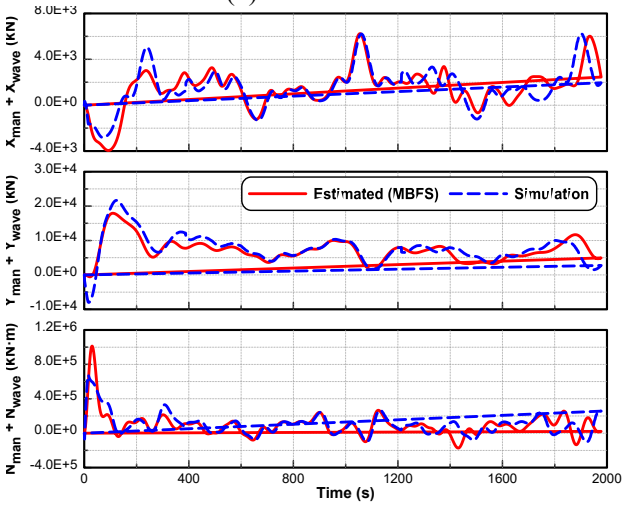

(c) External force and moment

Figure 14. Results of comparison among FRMTs, MBFS and Simulation ($\lambda/L = 0.7$)

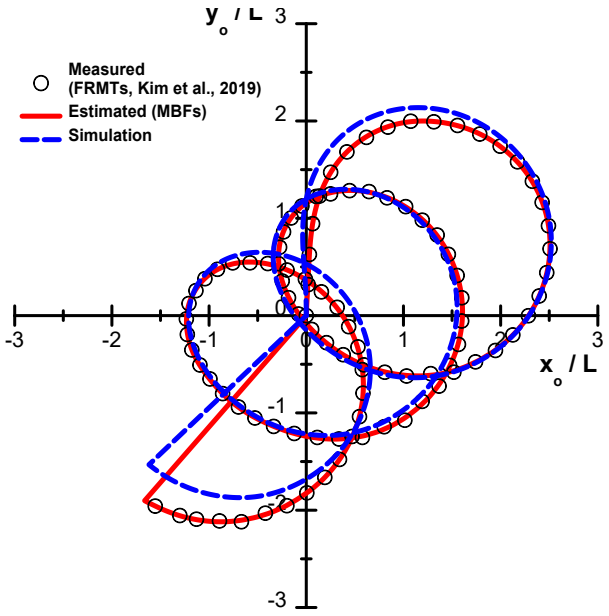

(a) Trajectory

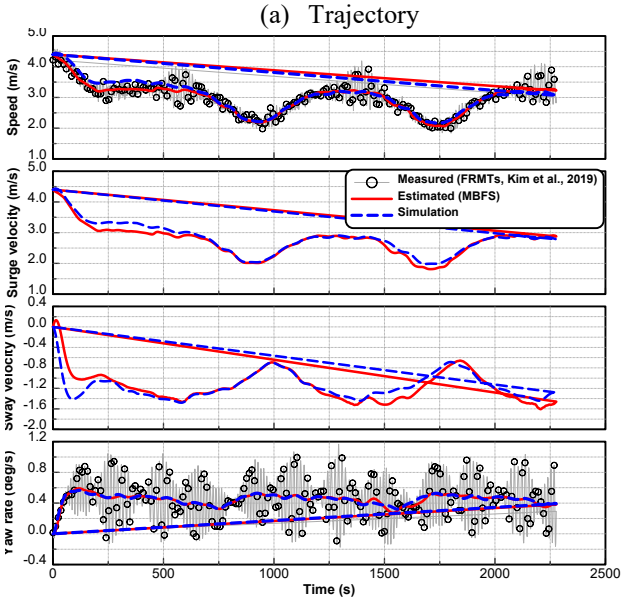

(b) Motion variables

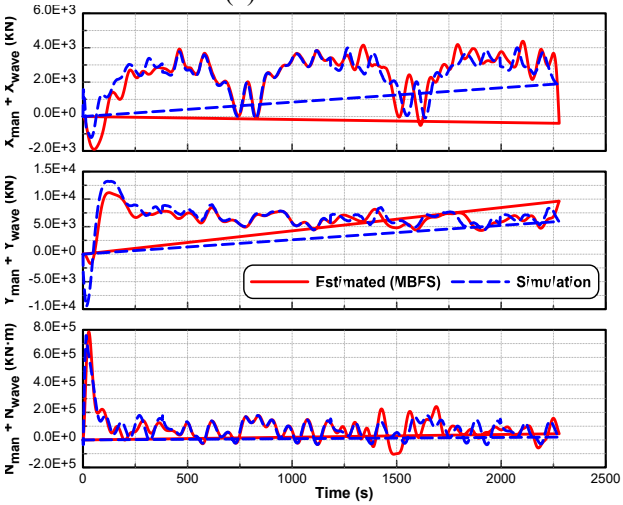

(c) External force and moment

Figure 15. Results of comparison among FRMTs, MBFS and Simulation ($\lambda/L = 1.0$)

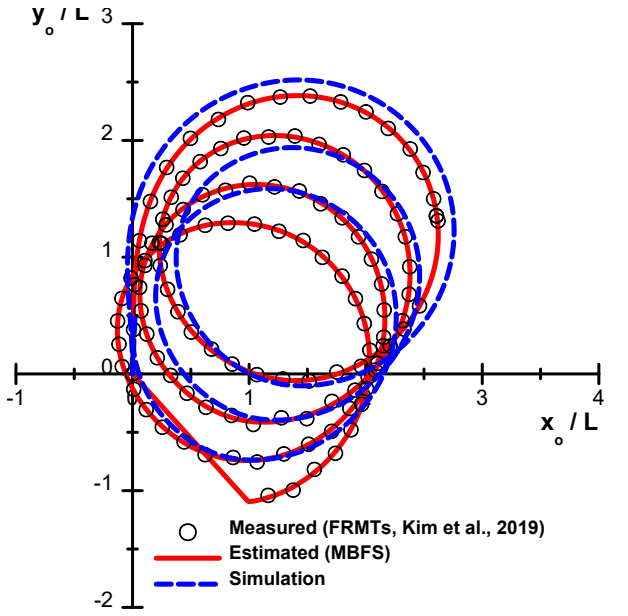

(a) Trajectory

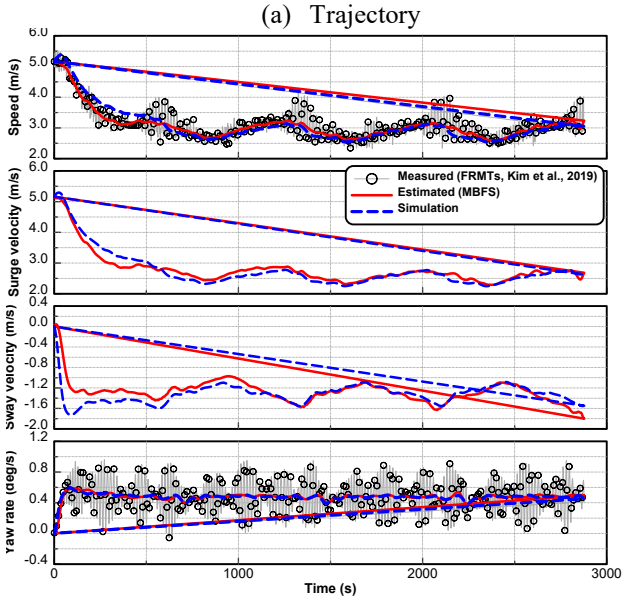

(b) Motion variables

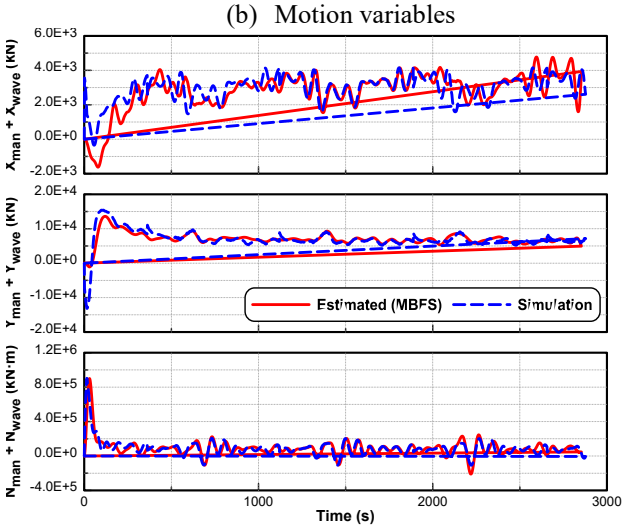

(c) External force and moment

Figure 16. Results of comparison among FRMTs, MBFS and Simulation ($\lambda/L = 1.2$)

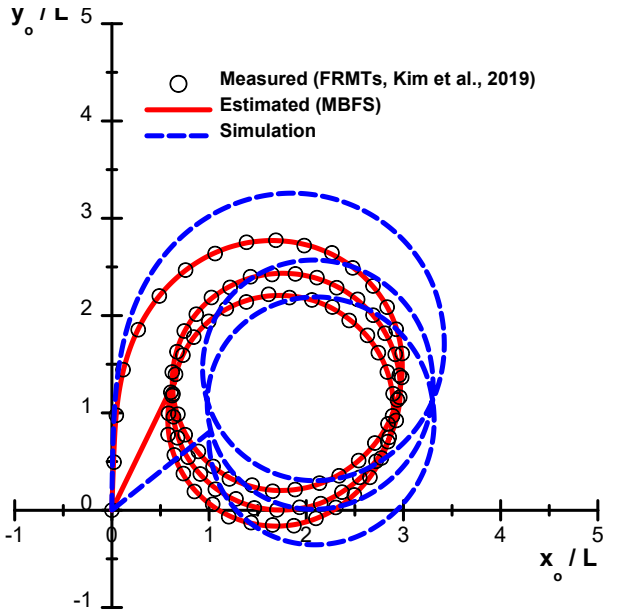

(a) Trajectory

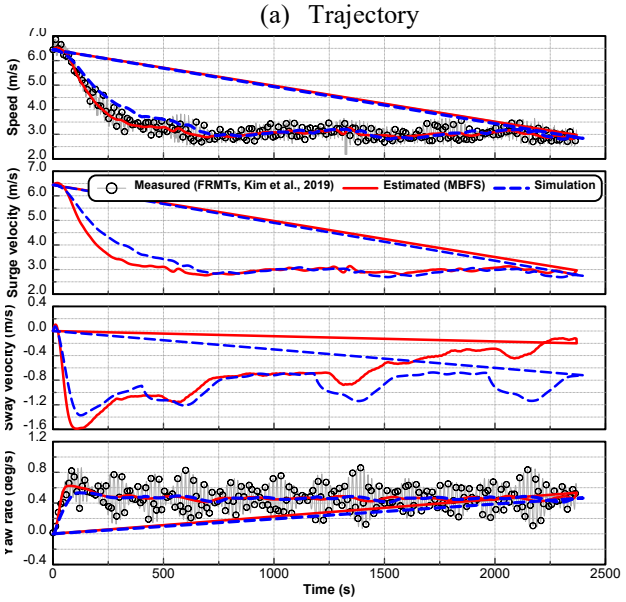

(b) Motion variables

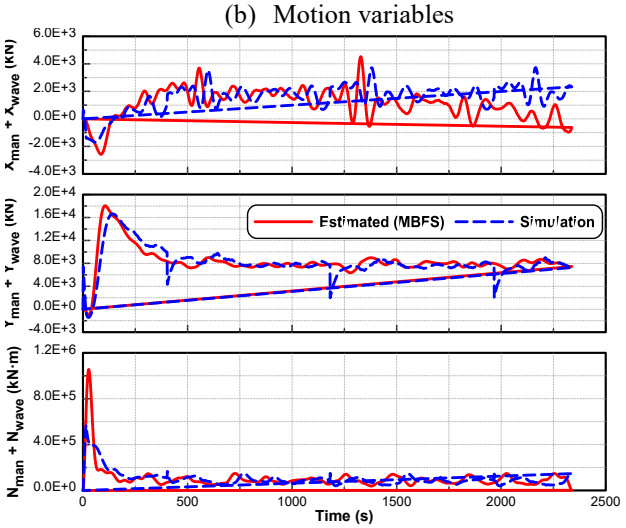

(c) External force and moment

Figure 17. Results of comparison among FRMTs, MBFS and Simulation ($\lambda/L = 1.5$)

7 REFERENCES

Abkowitz, M.A., 1980. Measurement of Hydrodynamic Characteristics from Ship Maneuvering Trial by System Identification. SNAME Trans Vol.88

Hoff, J.C., Cook, M.V., 1996. Aircraft parameter identification using an estimation-before-modelling technique. Aeronautical Journal.

Hwang, W., 1980. Application of System Identification to Ship Maneuvering. Ph.D Thesis. Massachusetts Institute of Technology.

IMO MEPC., 2013. INTERIM GUIDELINES FOR DETERMINING MINIMUM PROPULSION PWER TO MAINTAIN THE MANEOEUVRABILITY OF SHIPS IN ADVERSE CONDITIONS. RESULUTION MEPC. 232(65).

Kim, D.J., Yun, K., Park, J.Y., Yeo, D.J., Kim, Y.G., 2019. Experiment investigation on turning characteristics of KVLCC2 tanker in regular waves. Ocean Engineering Vol 175: pp. 197-206.

Seo, M.G., Nam, B.W., Kim, Y., 2018. Numerical Analysis of Turning Performance in Waves by Considering Wave Drift Forces. Journal of the Society of Naval Architects of Korea Vol. 55: pp. 103-115.

Yasukawa, H., 2006a. Simulations of Ship Maneuvering in Waves (1st report: turning motion). Journal of the Japan Society of Naval Architects and Ocean Engineers Vol. 4: pp. 127-136.

Yasukawa, H., 2006b. Simulations of wave-induced motions of a turning ship. Journal of the Japan Society of Naval Architects and Ocean Engineers Vol. 4: pp. 117-126.

Yasukawa, H., Yoshimura, Y., 2015. Introduction of MMG Standard Method for Ship Maneuvering. Journal of Marine Science and Technology Vol. 20: pp. 37-52.

Yoon, H.K., Rhee, K.P., 2003. Identification of hydrodynamic coefficients in ship maneuvering equations of motion by Estimation-Before-Modeling technique. Ocean Engineering Vol 30: pp. 2379-2404.

Yoon, H.K., Son, N.S., Lee, G.J., 2007. Estimation of the Roll Hydrodynamic Moment Model of a Ship by Using the System Identification Method and the Free Running Model Test. IEEE Journal of Oceanic Engineering Vol 32: pp. 798-806.

8 AUTHORS BIOGRAPHY

MyungJun Jeon is a Ph.D. candidate student in the department of Naval Architecture and Marine Engineering in Changwon National University, Korea. He got bachelor and master degrees in the department of Naval Architecture and Marine Engineering in Changwon National Univer, Korea in 2015 and 2017. His main interests are modeling and simulation of marine vehicles such as a ship and underwater vehicles.

Hyeon Kyu Yoon is a professor in the department of Naval Architecture and Marine Engineering in Changwon National University, Korea. He got bachelor, master and Ph.D degrees in the department of Naval Architecture and Ocean Engineering in Seoul National University, Korea, in 1989, 1991, and 2003. He worked for Agency for Defence Development from 1991 to 1996, and worked for Maritime Ocean Engineering and Research Institute from 2003 to 2009. His main interests are the simulation of marine vehicles such as a ship and underwater vehicles, and the model test in the water tank.

Dong Jin Kim is a senior engineer at Korea Research Institute of Ships and Ocean Engineering. He received a bachelor, master and Ph.D. degrees of Engineering in a department of Naval Architecture and Ocean Engineering at Seoul National University. His major fields are manoeuvring and seakeeping analysis of high speed vessels as well as other surface vehicles.

NUMERICAL MODELLING OF THE MUDDY LAYER EFFECT ON SHIP SQUAT AND RESISTANCE

Sami Kaidi,
CEREMA-DtecEMF, France, and Sorbonne universités, Université de technologie de Compiègne, laboratoire Roberval, France ;

Mohamed Ali Sorbonne universités,
Université de technologie de Compiègne, laboratoire Roberval, France ;

Emmanuel Lefrançois,
Sorbonne universités, Université de technologie de Compiègne, laboratoire Roberval, France ;

Hassan Smaoui,
CEREMA-DtecEMF, France, and Sorbonne universités, Université de technologie de Compiègne, laboratoire Roberval, France

NUMERICAL MODELLING OF THE MUDDY LAYER EFFECT ON SHIP SQUAT AND RESISTANCE

Sami Kaidi, CEREMA-DtecEMF, France, and Sorbonne universités, Université de technologie de Compiègne, laboratoire Roberval, France ;
Mohamed Ali Sorbonne universités, Université de technologie de Compiègne, laboratoire Roberval, France ;
Emmanuel Lefrançois, Sorbonne universités, Université de technologie de Compiègne, laboratoire Roberval, France ;
Hassan Smaoui, CEREMA-DtecEMF, France, and Sorbonne universités, Université de technologie de Compiègne, laboratoire Roberval, France ;

SUMMARY

The increasing use of maritime transport leads to an increase in ship size in order to minimize the transport costs. On the other hand the dimension of channels and harbors cannot follow the expansion rate of the vessels. Large ships will experience shallow water effects more severely such as the bottom effect which plays an important role on the maneuverability and the stability of vessels, especially when the bottom is mainly formed by a muddy layer (see Figure 1). To enlarge the navigation restriction, the Word Association for Waterborne Transport Infrastructure (PIANC) established a concept which is the Nautical Bottom. Using this concept, vessels can navigate under small and negative Under Keel Clearance (UKC) relative to the water-mud interface. The presence of the mud at the bottom leads to new problems and open questions that should be answered such as : (i) how the vessel will feel the mud layer and (ii) what is the effect of the mud on forces exerted on the ship and consequently the ship sinkage. Hence, the aim of this work, is to conducted a numerical investigation to give answers to the questions asked. For this, a 3D Computational fluid dynamics (CFD) model was used for several setups to reproduce the muddy layer and to simulate its effect.

Figure 1. Ship sailing in the Gironde estuary.

1 INTRODUCTION

The ship navigating through confined and shallow waters is strongly affected by hydrodynamic effects, as opposed to open seas. One major impact of the limited navigating width and water depth (h) is the squat effect and ship resistance increase. The water in front of the bow is pushed away, and flows down to the sides and under the keel of the ship with an increased velocity (See Figure 2) due to the reduced section. According to the Bernoulli's law, the velocity increasing under hull indicates a vertical pressure drop, and consequently a sinking of ship. In addition, the ship generally trims forward or aft, as the bow or stern may experience more or less pressure drop depending on the ship type. The effects of sinkage and trim are called the ship squat. It has a great influence on the ship resistance and can leads to serious safety issues such as grounding, loss of steering or collision.

In the Gironde estuary the squat is an essential parameter for vessels traffic management. In fact, the water level at the estuary depends on the tide. From where, to accommodate ships of large size it is necessary to wait until the tide is high. Vessels have to sail at the same speed as the propagation of the tide wave which is of the order of 10 knots.

However, this is not always the case, because in some situations ships can no longer keep up with the speed of the tidal wave for various reasons mainly related to the significant increase in ship resistance caused by the ship squat in the mud which slows down ship speed considerably. In other situations, Ships are equipped with a power limiter that stops the operation of the propulsive system if the ship meets a strong resistance. In that situation, ships will be moored and wait for the next tide. In order to better manage the estuarine network as well as to ensure a safety navigation, it is then essential to study

the phenomena of the ship resistance, their origins as well as their consequence on navigation.
To predict the ship squat several empirical formulas were proposed in the past. Barrass and Derrett (1999) concluded some important factors to the squat effect:

- The main factor is the ship speed relative to the water, and the squat is approximately proportional to the square of this velocity;
- The decrease of water depth will increase the ship squat;
- The block coefficient of ship, that is a ratio of the ship underwater volume to the volume of box surrounding it, is proportional to the squat;
- Similarly the blockage factor, a ratio of ship immersed cross section to that of canal, has a direct impact on the squat.

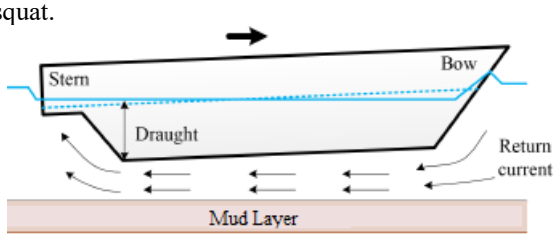

Figure 2. Flow around a ship in shallow water.

Numerical efforts have been devoted to estimation of ship resistance and squat over the years. The slender-body method assumes that the ship beam, free surface wave amplitude and water depth are small compared to the ship length. This allows the simplification of the flow simulation in two dimensions using the slender-body theory (Gourlay, 2008; Tuck, 1964). To take into account the dynamic coupling of ship motions with flow, the potential flow theory can be applied, which only assumes the flow to be irrotational. It has been widely used to the squat prediction and very good results have been obtained (Debaillon, 2010; Ma et al., 2016; Sergent et al., 2015). Whereas it is difficult to apply the potential flow model to the resistance prediction, since it neglects the viscous stresses, which however is crucial for evaluating the ship resistance.

Modern CFD techniques based on solving the fully viscous Navier-Stokes equations have been extensively applied to ship hydrodynamics with fruitful results, as they consider the important features of the actual flow, such as the viscous effects and the turbulence. Hence, they are more reliable for predicting ship resistance and motions. (Stern, 2013) summarized the achievements towards the ship hydrodynamics using CFD in the last decade. There are recent progresses of modern computational ship hydrodynamics with respect to shallow and confined water. (Eloot et al., 2015) performed a turning circle and a zigzag test on KVLCC2 hull model to determine the maneuvering performance in shallow water zone. To study the scale effect, (Tezdogan et al., 2016) performed unsteady RANS simulation at full-scale for the squat in shallow water with the commercial software STAR-CCM+. They compared the results to the 3D potential flow theory and the experimental data of (Mucha et al., 2014). They reported an underestimation of the ship squat and pointed out that the ship resistance is sensitive to the ship sinkage. (Linde et al., 2016) validated this observation with FLUENT by simulating the ship resistance with and without the consideration of ship sinkage. The predicted value of resistance with sinkage was closer to the experimental data. (Kaidi et al., 2017) further studied the ship maneuvering with FLUENT under the effect of bank-propeller hull interaction in shallow water.

In ports, flow stratification may occur as the non-saline, light river water flows into the colder and heavier saline sea water, leading to large horizontal or vertical fluid density variations. Highly density-stratified waters are known to pose particular challenges to navigating ships. When a ship keel (bottom) is traveling just above the interface of the water layers, the vessel experiences large wave resistance. This resistance occurs particularly if the ship is traveling close to the speed of the fastest internal waves due to the generation of large internal waves. This phenomenon, known as `dead water', impacts the ability of ships to move through stratified water. Accurately assessing the impacts of stratified flow on ship navigation requires a detailed knowledge of the flow field including turbulent mixing and in particular the generation of internal waves on the interface between the two layers of water.

(Crapper, 1967; Hudimac, 1961) presented analytical approaches to study the internal wave modes caused by a moving body in a two-layered ocean. It follows from their work that, just as for surface waves, at ship speeds sufficiently larger than the internal wave speed only divergent waves travel downstream of the ship, while both divergent and transverse waves are present for slower vessels. (Tulin et al., 2000) suggested a nonlinear theory to capture internal wave behavior at high Fn in weakly stratified flow that compared satisfactorily with available experimental results for a semi-submerged spheroid. (Delefortrie et al., 2004; Delefortrie and Vantorre, 2005) carried out a large number of experiments on towing tank. They studied the mud layer effect on the ship maneuvering by considering several parameters. They also developed a mathematical model to take into account the mud effect. (Chang et al., 2006) presented one of the few available examples of CFD computation for a vessel in a stratified medium. (Esmaeilpour et al., 2016) studied the evolution of the stratified flow in the near-field of a surface ship in details. They showed that the generation of internal waves requires energy which results in an increase in resistance.

In this paper we present an overview of a numerical study of the mud layer effect on the ship resistance and sinkage by using a multi-phases CFD method. Three parameters were tested : the mud properties, the mud thickness and the ship speed. As assumption the mud was considered as a Newtonian fluid (constant viscosity) because after the critical shear stress the mud viscosity is constant. The UKC level was referenced to the water-mud interface, hence, it can takes a positive and negative values.

2 NUMERICAL METHOD AND SIMULATIONS

2.1 MATHEMATICAL FORMULATION

The fluid flow is governed by the incompressible viscous Navier-Stokes equations with the continuity equation.

$$\nabla . u = 0 \quad (1)$$

$$\frac{\partial u}{\partial t} + \nabla . (u \otimes u) = -\frac{1}{\rho}\nabla p + \nu \nabla^2 u \quad (2)$$

where u, p represent the velocity vector and pressure respectively. ρ and ν are the fluid properties of density and kinematic viscosity.

For modeling turbulence effect, the Reynolds averaging was computed on the flow variable in time, which gives rise to

$$\nabla . U = 0 \quad (3)$$

$$\frac{\partial u}{\partial t} + \nabla . (U \otimes U) = -\frac{1}{\rho}\nabla p + \nu \nabla^2 U - \nabla . (u' \otimes u') \quad (4)$$

Where $u = U + u'$ and $p = P + p'$ The last term in the RANS momentum equation is the Reynolds stress which is often approximated by turbulence models. In this research we employ the *SST k-ω* turbulence model, which is actually a combination of *k-ω* model and *k-ε* model while a shifting function is used to switch one from another. The VOF method was used to simulate three phases interactions (interface air/water and water/mud). Using this approach the both interfaces can be captured in a fixed grid by solving the continuity equation of the volume fraction (Eq. 3).

$$\frac{\partial \alpha_p}{\partial t} + u \nabla \alpha_p = 0 \qquad (p = 1, 2) \quad (5)$$

α_p denotes the volume fraction of the p^{th} fluid, and:

$$\sum_{p=1}^{n} \alpha_p = 1 \qquad (n = 2) \quad (6)$$

Equations given previously (Eq. 1-6) are solved using the commercial code "Ansys-Fluent 13.0" based on the finite volume method. The pressure-velocity coupling, was assured by using a steady Pressure-Based Coupled Algorithm and the interpolation method selected to compute the cell-face pressure is PREssure STaggering Option (PRESTO). The second order was set for the VoF's special discretization.

3 VERFICATION

The verification and validation of the CFD software was studied and performed in several previous works (Kaidi et al., 2018; Razgallah et al., 2018). The procedure of verification and validation was carried out in accordance with the ITTC recommendations.

In these works, we applied the CFD method for three-dimensional applications and compare the numerical results to the experiments performed at the University of Liège and the Ecole Centrale de Nantes. These experiments were performed without considering the mud layer. The container carrier at a model scale of 1/80 respectively were tested for a range of ship speed and UKC respectively.

4 STUDIED SHIP AND CHANNEL CONFIGURATION AND BOUNDARY CONDITIONS

To carry out this investigation, we used a container cargo ship form (see Figure 3). This kind of ships was selected because it is one of ships sailing the most in the Gironde estuary. Table 1 gives the main characteristics of the hull.

Where, L_{PP} is the length between perpendicular, L_{OA} is the length over all, B is the ship beam, T is the ship draft and C_B is the block coefficient.

Figure 3. Container carrier hull form.

Table 1. Ship dimensions and scales

Ship	Container cargo	
Scale	1/1	1/80
L_{PP} (m)	230.0	2.875
L_{OA} (m)	232.5	2.906
B (m)	32.2	0.402
T (m)	10.0	0.125
C_B	0.681	0.681

In the present study we will consider only the confinement effect through the use of the UKC. To prevent large body motions, the reference frame is fixed on the ship and hence the fluid and other parts move relatively to the hull. The computational domain is chosen with a rectangular section and large enough such that there are little influence of the position of inlet and outlet :1-2L_{pp} for the inlet and 3-5L_{pp} for the outlet are recommended by ITTC (ITTC, 2011). Half of the computational domain is used to reduce computational time.

As for the boundary conditions, at inlet the flow velocity is imposed; at outlet the out flow condition is used; symmetric boundary conditions are applied at mid-plane and at the bank; At atmosphere total pressure is applied; at bottom moving wall condition is employed to take into account of the relative motion; at hull surface no-slip wall condition is used.

5 RESULTS AND DISCUSSION

5.1 MUD PROPRETIES INFLUENCE ON THE SEABED UNDULATION AND FREE SURFACE ATTENUATION

Four combinations of mud properties were selected to conduct this investigation. These properties represent the average values measured at different zones in the Gironde estuary and some ports. Table 2 shows the combination of the density and the viscosity of the mud.

Table 2. Physical properties of tested mud

Mud type	density (kg/m^3)	viscosity (Pa.s)
Mud A	1085	0.025
Mud B	1160	0.068
Mud C	1210	0.128
Mud D	1230	0.260

Here, the mud layer thickness (hm) was set to 2m in full scale (0.025m in the scaled model). The ship draft (T) and speed were set to 10m (0.125m scaled model) and 10 knots (0.575 m/s) respectively. The effective UKC's value chosen is +10%*T which corresponds to the nautical bottom value defined by the PIANC.

Figure 4 illustrates the profile of the mud layer deformation caused by the ship passage. As it can be seen, the deformation is composed by a principal undulation and a secondary undulations. The principal undulation is similar to the free surface deformation with a small shift. Where, a stern divergent wave is observed (Figure 5). The divergence angle, the wave height and the wavelength of this wave depends on the mud properties as is shown in Figure 6. In this study we focus only on the principal undulation which has an impact on the ship maneuvering, principally on the ship squat and the ship resistance. This undulation is characterized by a maximum trough and crest. Where, generally the trough is located at the mid hull, while, the crest is located in the hull's stern. For all tested mud properties the mud layer trough starts from the same position which is the ship bow. However, compared to the initial mud setup the trough level and its length increase by decreasing the mud viscosity. We note that the origin of this trough is principally the pressure variation along the ship hull caused by the return flow which is influenced by the mud properties. From the same figure it can be seen that the relative increase of the mud trough has a linear variation for viscosities varying between 0.025 and 0.12 Pa.s.

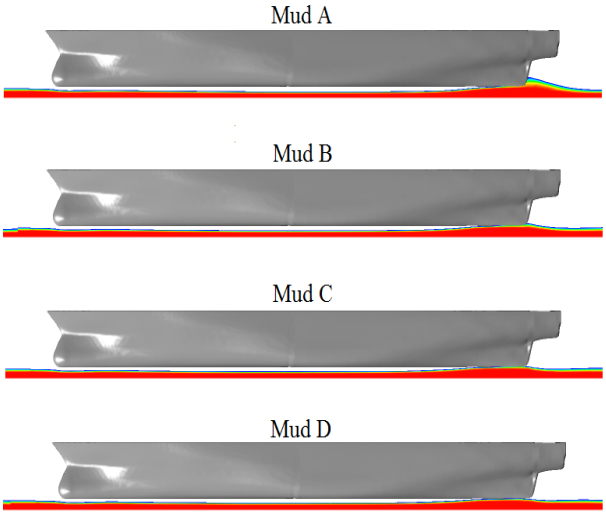

Figure 4. Profile of the mud layer undulation at the ship symmetry plane.

It can also be observed that the physical properties of the mud play an important role on the mud crest, the location of this crest and in some situation the hull/mud contact area. When the density and viscosity of the mud are smaller, the mud is considered more fluid, hence the later behaves as a denser fluid and follows the water flow. While, when the viscosity of the mud is larger, the mud layer is more solid and its behavior is more rigid. From where, we note a maximum uprising value for the mud D ~20 % smaller than the mud B while an insignificant variation is noted between the mud B and A.

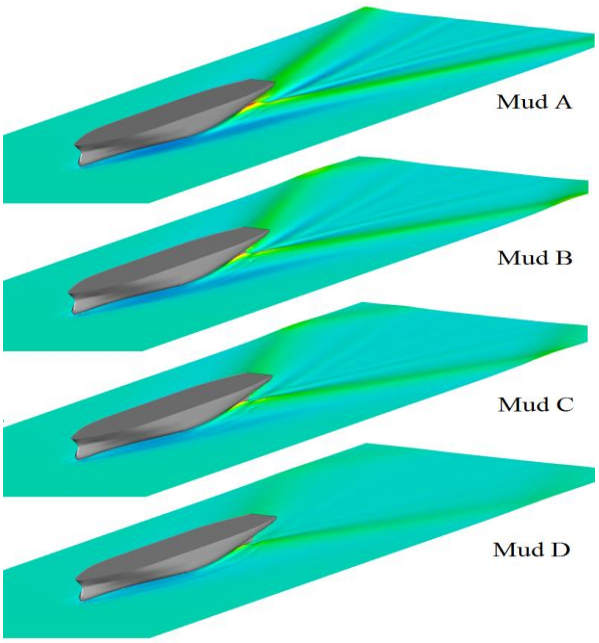

Figure 5. Iso-surface of the mud undulation as a function of mud properties.

For all tested properties the mud uprising position varies as the mud properties variation. From simulated cases, it was noted that, the lower the viscosity, the more the mud uprising moves backwards. The same observations were also noted by (Delefortrie and Vantorre, 2005). A contact between the hull and the mud was also observed for mud A and B and the contact area is slightly larger in the case of the mud A.

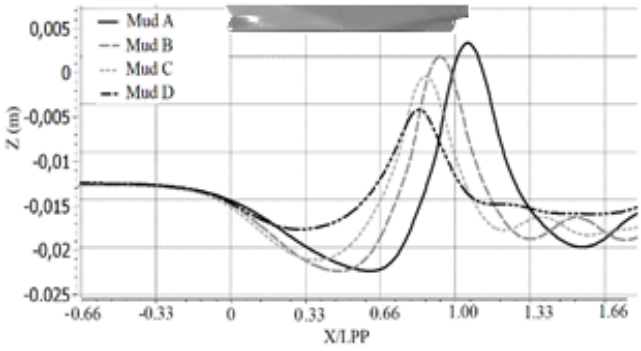

Figure 6. Mud layer undulation along the channel as a function of mud properties . X is the longitudinal position.

Figure 7 shows the free surface attenuation caused by the mud layer. For this, we compared the free surface deformation of a channel with muddy layer to the free surface deformation of a channel without muddy layer (rigid bottom). The same total depth was kept for both tests. Knowing that, the total depth of the channel is the sum of the ship draft, the UKC and the mud thickness. As it can be seen, we observe that the allure of the free surface is similar to the mud layer undulation. We also observe that the trough and crest of the free surface is approximately similar between the rigid seabed and the mud A, B and C. However, for the mud D we note a lowering of the free surface. This lowering is essentially caused by shallow water effect. As mentioned above, the higher the viscosity, the mud is more solid hence, it can be considered as solid seabed. The shear stress due to the high viscosity of the mud slowdown the flow velocity on the interface mud/water under the ship hull inducing an acceleration of the water flow and consequently a pressure drop.

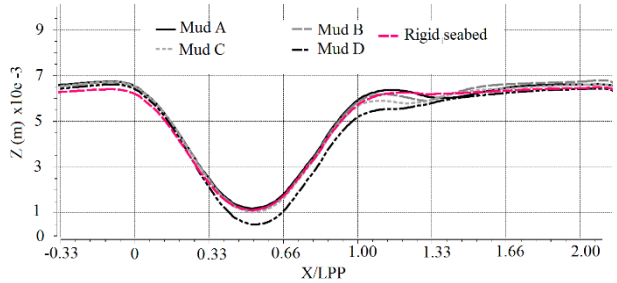

Figure 7. Comparison between the free surface elevation of rigid seabed and muddy seabed.

5.2 SHIP RESISTANCE VARIATION DUE TO MUD PROPRITIES

It is known that the ship resistance is very impacted by the channel configuration (confinement, restriction,..). In shallow water the ship resistance increases significantly due to the accelerated water around the hull as explained above. The presence of the mud layer affects in turn the flow under the ship hull inducing a variation on the ship resistance. The effect of the latter can be considerably amplified if the effective UKC is negative.
In this section the impact of the mud layer was studied firstly by testing the mud properties effect. Hence, the forth mud properties were tested for an effective UKC of +10%*T. No squat was considered in these simulations.

Figure 8 shows the ship resistance variation caused by the mud properties variation. From this figure we remark that the ship resistance increases with mud viscosity although there was no contact between the hull and the mud with mud C and D. This leads us to conclude that this increase concerns only the frictional component of the resistance. The flow velocity is larger when the seabed is solid because the mud undulation is smaller consequently the section of the water flow.

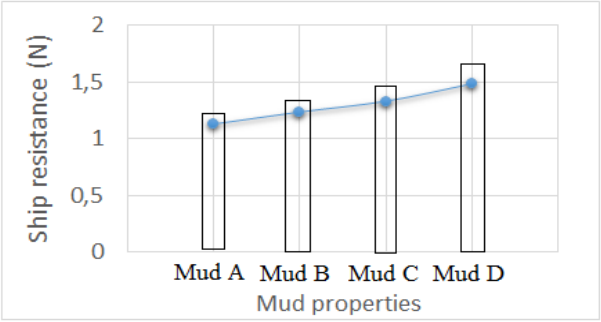

Figure 8. Ship resistance (half of ship) as a function of mud properties.

In the second part of this section, the ship resistance was studied as a function of the effective UKC. The mud C was used for six values of UKC +10%, +5%, 0, -5 %, -10% and -15% of the ship draft. The ship draft here is 10m and the ship speed used is 10knots.

From Figure 9, we observe increase of the total resistance with the decrease of the effective UKC. The pressure resistance dominates for UKC varying between +10 and -5%*T. Less than that, the frictional force dominates considerably. We observe also, that ship resistance increase is very slight for UKC values between +5% and -5% and upper to -10%. The ship resistance increase is significant only between +10% and 5%, and between -5% and -10%. By analyzing Figure 10 plotting the area of contact hull/mud, we note that for UKC range [+10% ; 5%] the contact area is almost the same and the total resistance increase is principally due to the shallow water effect. For the UKC range [-5% ; -10%] the resistance increase is principally due to the hull/mud contact. As is shown in Figure 9, the frictional resistance dominates

while the pressure resistance increases slightly.

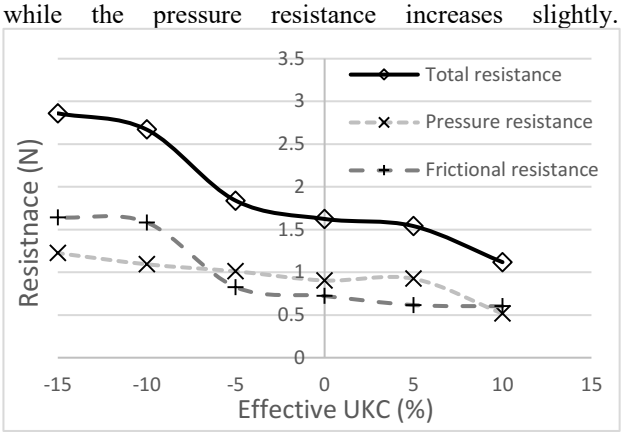

Figure 9. Mud layer undulation as a function of effective UCK (%)

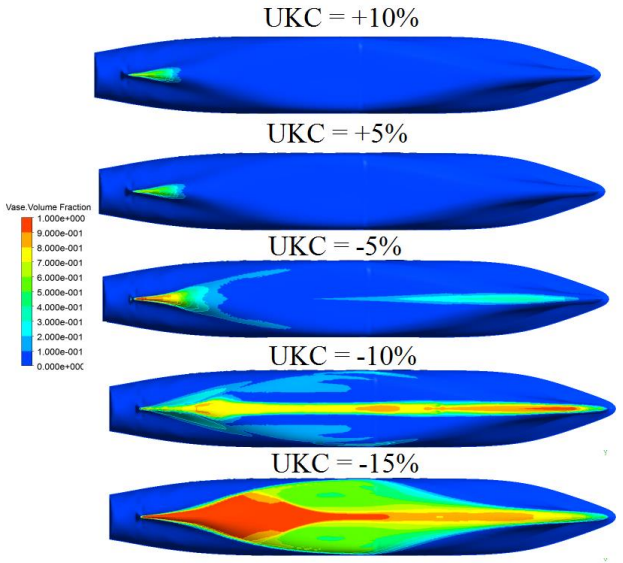

Figure 10. Hull/Mud contact area as a function of effective UKC.

5.3 EFFECT OF THE MUDDY SEABED ON THE SHIP SQUAT

One of the aim of this work is the numerical study of the influence of the muddy layer on the ship squat (sinkage and trim). The Fluid-Structure Interaction is treated by a modified Newton algorithm coupled to a steady RANS (Linde et al., 2016). The standard dynamic Newton algorithm wasn't used because several numerical complications encountered. The origin of these complications is essentially the bad estimation of the added mass due to the high blockage coefficient which affect considerably the stability and convergence of the numerical solution.

Because of the large computation time only one mud layer thickness was considered (2 m) for an effective UKC of +10%*T. The effect of the mud properties on the squat was simulated for the four types of the mud and for three ship speeds 6, 8 and 10 knots which corresponds to a Froude depth number of 0.297, 0.396 and 0.495.

The ship sinkage as a function of the mud type was plotted in Figure 11 and compared to the experimental and numerical sinkage for a rigid bottom.

Concerning the ship sinkage, a similar observations given by (Delefortrie, 2016) were noted. We observe firstly that the sinkage obtained numerically for a rigid seabed is in accordance with measurements. We observe also that the sinkage increases by increasing the ship speed in all configurations with or without the mud layer. However, the sinkage values decreases slightly with the mud properties change. Where, for a larger viscosities (Mud C and D) we observe an insignificant decrease, while, a moderate decrease is observed for Mud A and B. This decrease augment in turn with the ship speed increases. In fact, this increase is due to the add buoyancy generated by the contact hull/mud. This contact as mentioned above is located at the ship stern when the undulation crest is larger in cases of the Mud A and B.

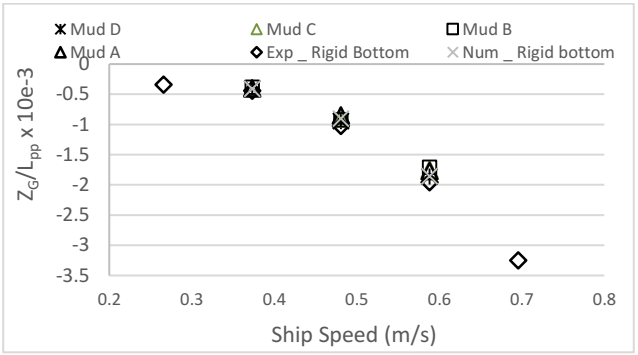

Figure 11. Ship sinkage as a function of the mud properties for an effective UKC of +10%. Z_G is the sinkage at the midship

The ship trim was plotted in Figure 12. For the selected UKC, the trim has a positive values which corresponds to a trim by aft. The plotted results show that the numerical results are in the same range as measurements without mud. It can also be seen, that the mud has an insignificant effect on the trim at low ship speed (6 knots) in the case of Mud B, C and D. Except in the case of the Mud A a significant deviation compared to the rigid bottom case was observed. While, for a ship speed of 10 knots, this deviation decreases due to the mud-hull contact located at the stern of the ship which creates an asymmetry on the ship buoyancy. However, the trim behaves differently in the case of the Mud D where, the trim deviation compared to the rigid bottom case increases with ship speed. this increase can be explained by the confinement that this type of mud generate.

Note that, some of these observations are not in agreement with observations made by (Delefortrie, 2016) basing on measurements carried out in the towing tank of Ghent University.

Figure 12. Ship trim as a function of the mud properties for an effective UKC of +10%.

6 CONCLUSIONS

In the present paper an overview of a numerical investigation on the impact of the mud on the ship squat and resistance was presented. A multi-phases CFD model was used to estimate the ship resistance and ship squat on different configurations. The CFD Model was verified and validated with several configurations.
Basing on observations noted in the present work, we conclude:

- The obtained numerical results are in agreement with physical models results;
- The ship squat and resistance depends on the mud undulation which in turn depends on several parameters : mud properties, effective UKC and the Ship speed;
- The effect of the mud layer on the ship sinkage is significant only when the effective UKC is negative;
- The effect of the mud on the ship resistance can be felt even when the UKC is positive and it depends to the mud properties.

The ability of the CFD method to simulate the different interactions between fluids and also between the fluid and the structure was demonstrated. Some difficulties were met in the squat simulations. An improvement can be made in future works.

7 ACKNOWLEDGEMENTS

The work presented in this paper was performed within the project “Gironde-XL” funded by “Le Grand Port Maritime de Bordeaux” and the European commission.

8 REFERENCES

Chang, Y., Zhao, F., Zhang, J., Hong, F.-W., Li, P., Yun, J., 2006. Numerical simulation of internal waves excited by a submarine moving in the two-layer stratified fluid. J. Hydrodyn. Ser. B 18, 330–336.

Crapper, G.D., 1967. Ship waves in a stratified ocean. J. Fluid Mech. 29, 667–672.

Debaillon, P., 2010. Numerical investigation to predict ship squat. J. Sh. Res. 54, 133–140.

Delefortrie, G., 2016. Ship Manoeuvring Behaviour in Muddy Navigation Areas, in: Proceedings of 4th MASSHCON. pp. 26–36. https://doi.org/10.18451/978-3-939230-38-0

Delefortrie, G., Vantorre, M., 2005. Modelling navigation in muddy areas, Hydronav’05 - Manoeuvring ’05: Joint 16th International Conference on Hydrodynamics in Ship Design and 3rd International Symposium on Ship Manoeuvring, Ostróda, Poland, September 2005.

Delefortrie, G., Vantorre, M., Eloot, K., 2004. Linear manoeuvring derivatives in muddy navigation areas. Trans. R. Inst. Nav. Archit. Int. J. Marit. Eng. 146, 1–13.

Eloot, K., Delefortrie, G., Vantorre, M., Quadvlieg, F., 2015. Validation of ship manoeuvring in shallow water through free-running tests, in: Proceedings of the ASME 2015 34th International Conference on Ocean, Offshore and Arctic Engineering.

Esmaeilpour, M., Martin, J.E., Carrica, P.M., 2016. Near-field flow of submarines and ships advancing in a stable stratified fluid. Ocean Eng. 123, 75–95.

Gourlay, T., 2008. Slender-body methods for predicting ship squat. Ocean Eng. 35, 191–200.

Hudimac, A.A., 1961. Ship waves in a stratified ocean. J. Fluid Mech. 11, 229–243.

ITTC, 2011. ITTC – Recommended Procedures and Guidelines - Verification and validation of linear and weakly nonlinear seakeeping computer codes. 7.5-02-07-02.5 (Revision 01) 17.

Kaidi, S., Smaoui, H., Sergent, P., 2018. CFD Investigation of Mutual Interaction between Hull , Propellers , and Rudders for an Inland Container Ship in Deep , Very Deep , Shallow , and Very Shallow Waters. J. Waterw. Port, Coastal, Ocean Eng. 144. https://doi.org/10.1061/(ASCE)WW.1943-5460.0000458.

Kaidi, S., Smaoui, H., Sergent, P., 2017. Numerical estimation of bank-propeller-hull interaction effect on ship manoeuvring using CFD method. J. Hydrodyn. 29. https://doi.org/10.1016/S1001-6058(16)60727-8

Linde, F., Ouahsine, A., Huybrechts, N., Sergent, P., 2016. Three-dimensional numerical simulation of ship resistance in restricted waterways: Effect of ship sinkage and channel restriction. J. Waterw. Port, Coastal, Ocean Eng. 6016003.

Ma, C., Zhang, C., Chen, X., Jiang, Y., Noblesse, F., 2016. Practical estimation of sinkage and trim for common generic monohull ships. Ocean Eng. 126, 203–216.

Mucha, P., el Moctar, O., Böttner, C.-U., 2014. Technical Note: PreSquat – Workshop on Numerical Prediction of Ship Squat in Restricted Waters. Sh. Technol. Res. 61, 162–165.

Razgallah, I., Kaidi, S., Smaoui, H., Sergent, P., 2018. The impact of free surface modelling on hydrodynamic forces for ship navigating in inland waterways: water depth, drift angle, and ship speed effect. J. Mar. Sci. Technol. https://doi.org/10.1007/s00773-018-0566-y

Sergent, P., Lefrançois, E., Mohamad, N., 2015. Virtual bottom for ships sailing in restricted waterways (unsteady squat). Ocean Eng. 110, 205–214.

Stern, F., 2013. Computational ship hydrodynamics: nowadays and way forward. Int. Sh. Build Prog. 60, 3–105.

Tezdogan, T., Incecik, A., Turan, O., 2016. Full-scale unsteady RANS simulations of vertical ship motions in shallow water. Ocean Eng. 123, 131–145.

Tuck, E.O., 1964. A systematic asymptotic expansion procedure for slender ships. J. Sh. Res. 8, 15–23.

Tulin, M.P., Yao, Y., Wang, P., 2000. The generation and propagation of ship internal waves in a generally stratified ocean at high densimetric Froude numbers, including nonlinear effects. J. Sh. Res. 44, 197–227.

9 AUTHORS BIOGRAPHY

Sami Kaidi holds the current position of researcher at Centre for Studies and Expertise on Risks, Environment, Mobility, and Urban and Country Planning. Hi is responsible for Ship Hydrodynamic and Maneuvering researches. His previous experience includes : CFD method; Fluid-structure interaction, numerical methods,

Mohamed Ali holds the current position of researcher at University of Technology of Compiegne. His previous experience includes : Finite element method, numerical methods.

Emmanuel Lefrançois holds the current position of Professor at University of Technology of Compiegne. Hi is responsible for Fluid-structure interaction researches. His previous experience includes : the fluid-structure interaction methods and the development of innovative numerical methods for engineering problems.

Hassan Smaoui holds the current position of research director at Centre for Studies and Expertise on Risks, Environment, Mobility, and Urban and Country Planning. He is responsible for laboratory of numerical hydraulic. His previous experience includes : the sedimentary transport, the bank erosion and finite element method.

INITIAL AND STEADY TURNING CHARACTERISTICS OF KRISO CONTAINER SHIP (KCS) IN REGULAR WAVES

Dong Jin Kim, Kunhang Yun, Dong Jin Yeo and **Yeon Gyu Kim**,
Korea Research Institute of Ships and Ocean Engineering, Rep. of Korea

INITIAL AND STEADY TURNING CHARACTERISTICS OF KRISO CONTAINER SHIP (KCS) IN REGULAR WAVES

Dong Jin Kim, Kunhang Yun, Dong Jin Yeo, Yeon Gyu Kim, Korea Research Institute of Ships and Ocean Engineering, Rep. of Korea

SUMMARY

In general, calm water manoeuvring tests or simulations are performed to evaluate ship's manoeuvrabilities. But a ship encounters external wave loads in actual sea, so it is necessary to analyze the ship's manoeuvring performance in waves at early design stage for the safe operation. In this study, turning characteristics of KRISO container ship (KCS) were investigated by free-running model tests in waves. 35 degree turning circle tests in regular waves were carried out in KRISO Ocean Engineering Basin with the variations of regular wave conditions such as wave heights, lengths, and directions. Wave heights were varied from 0.01 to 0.02 L, lengths were 0.5 to 1.2 L, and directions were 150 to 270 degrees. In all the tests propeller revolution rate (RPS) was fixed as the constant values corresponding to the full-scale speed of 16 knots in calm water, rudder was deflected at the moment when the wave crests pass the model midship. For some test cases propeller revolution rate was changed and the effects of the approach speeds on the turning performance were confirmed. Ship's turning behaviours in waves can be divided into two stages such as initial transient motions and steady turns. Initial turn abilities for emergent collision avoidance, and trajectory drifts in steady turns were obtained from the present model tests, and the effect of wave conditions on the turning characteristics were investigated. New index which represents hard-over initial turning ability for collision avoidance in waves is proposed by using advance and transfer. The relations between initial turning characteristics and steady turn drifting angles are discussed.

1 INTRODUCTION

In actual rough sea, ship speed is generally lower than calm sea operation, and the external wave loads are acted on the ship. The ship should have at least not only the course keeping ability to reach desired destination, but also the course changing ability in order to avoid the collision in spite of wave loads. It is necessary to investigate the manoeuvrabilities of a ship with consideration of wave loads at the design stage for its safe operation in seaway.

There are some previous researches about the model tests for the analyses of the ship manoeuvrability in waves. Ueno et al. (2003) carried out manoeuvring model tests, and suggested the index of turning trajectory drifts. Yasukawa and Nakayama (2009) conducted free-running model tests and simulations of S175 container ship. Yasukawa et al. (2015) performed turning and zig-zag tests of KVLCC2 tanker in irregular waves. Kim et al. (2019) carried out turning circle tests of KVLCC2 tanker in regular waves, and proposed the indices to represent the drifting distance and angles of steady turning circles.

In this study turning circle tests of KRISO container ship (KCS) are performed in regular waves, and its initial and steady turning characteristics are analysed. New index is proposed to represent hard over turning ability for collision avoidance at the beginning of turns by using advance and transfer in waves. Effects of wave conditions such as wave lengths, heights, and directions on the initial turning abilities are analysed. Next the characteristics of trajectory drifts during steady turns are analysed according to the wave conditions. Indices proposed by Kim et al. (2019) are used to describe the drifting distances and angles. The relation between initial turning characteristics and trajectory drifting angles are discussed.

2 MODEL TEST

2.1 MODEL SHIP

1/65.833 scaled KCS model ship was constructed for free running model tests. The length of model ship is 3.5 meters approximately. Principal particulars of full-scale and model ships are described in Table 1, and the constructed model ship is shown in Figure 1.

Table 1. Principal particulars of KCS full-scale and model ship

Particulars	Full-scale	Model (1/65.833)
Ship		
Lpp [m]	230.0	3.497
Breadth [m]	32.2	0.489
Draft [m]	10.8	0.164
Displacement [m^3]	52030	0.182
LCB, fwd + [% of Lpp]	-1.48	-1.48
Metacentric height(GM) [m]	0.6	0.009
Roll radius of gyration [B]	0.40	0.404
Yaw radius of gyration [L]	0.25	0.258
Rudder (Semi-balanced horn type)		
Lateral area [m^2]	54.45	0.0126
Turn rate [degree/sec]	2.32	18.82
Propeller (Fixed pitch, 5 blades)		
Diameter [m]	7.9	0.120

Figure 1. KCS model ship

Self-propulsion and steering systems are installed on the model ship. Data measuring devices such as gyro, inclinometer, onboard PC, batteries, and wireless modem are mounted as well.

2.2 TEST SETUP

Figure 2 shows a schematic view of the setup in KRISO Ocean Engineering Basin (56m (L) x 30m (B) x 4.5m (D)) for free-running model tests. Regular waves are generated by short and long end wave makers. All synchronized signals of the model ship are transmitted to the ground control PC wirelessly, no carriage is used. Two total stations are used to measure positions and headings of the model ship, which is referred by Matsuda et al. (2016). And ultrasonic type relative wave probes are mounted along the deck side in order to estimate the incident wave profiles. Device configuration and the basin setup are similar to the previous study by Kim et al. (2019).

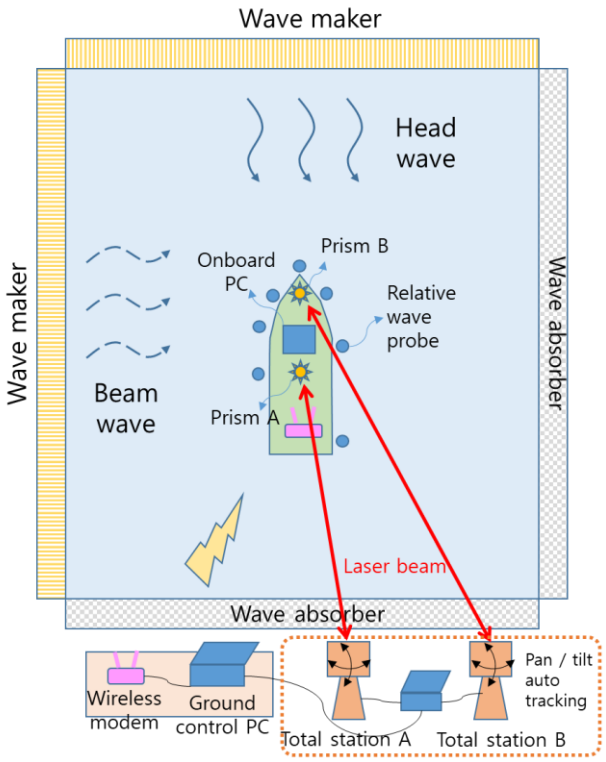

Figure 2. Test setup in KRISO Ocean Engineering Basin

Coordinate system in the horizontal plane is described in Figure 3. It consists of earth-fixed (O-XY) and body fixed (o-xy) coordinates. Wave directions of 180° and 270° mean head and port beam waves, respectively.

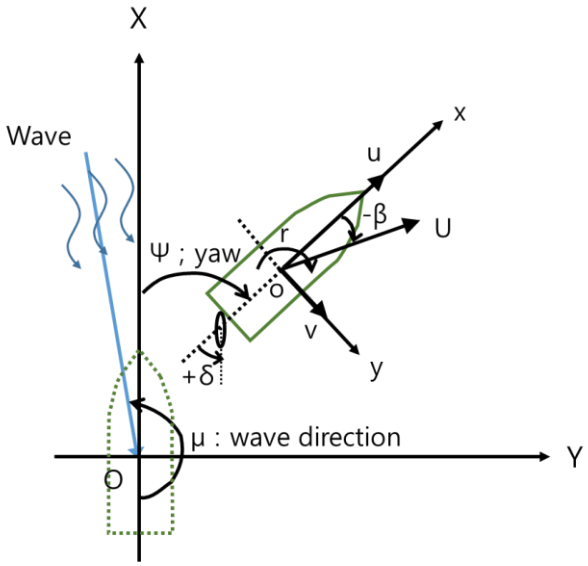

Figure 3. Coordinates system

2.3 TEST SCENARIO

35° turning circle test conditions are shown in Table 2. Wave directions are varied 150° to 270°, heights are 0.01 L to 0.02 L, and wave lengths are 0.5 L to 1.2 L. Propeller revolution rate (RPS) are mostly fixed as 10.7 which corresponds to the full-scale speed of 16 knots in calm water. RPS is varied as 8.2 and 15.0 for one port turn case.

Table 2. Turning circle test conditions

Rudder angle, δ	Wave direction, μ	Wave height, H_w	Wave length, λ_w	Propeller revolution rate, n
[degree]	[degree]	[L]	[L]	[RPS]
+35, -35	No waves (calm water)			10.7
+35, -35	180, 270	0.01, 0.015, 0.02	0.5, 0.7, 1.0, 1.2	10.7
+35	150, 240	0.015	1.0	10.7
-35	180	0.02	1.0	8.2, 10.7, 15.0

For all the tests, rudder angles are deflected when the wave crests pass the model midship. Detailed procedures of estimation of incident waves are described in the

previous research by Kim et al. (2019). Figure 4 shows one example of present model tests.

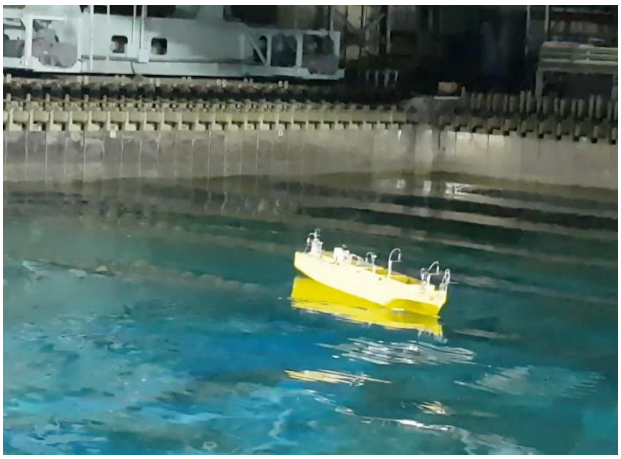

Figure 4. Free-running model tests in waves

RPS is fixed as 10.7, the approach speeds of the model ship are changed depending on the wave conditions due to the added resistance. In particular, the approach speed in head waves is around 65% of calm water speed in case that the wave height is 0.02 L and the wave length is 1.0 L.

3 INITIAL TURN IN WAVES

3.1 INDEX OF INITIAL TURNING ABILITY IN WAVES

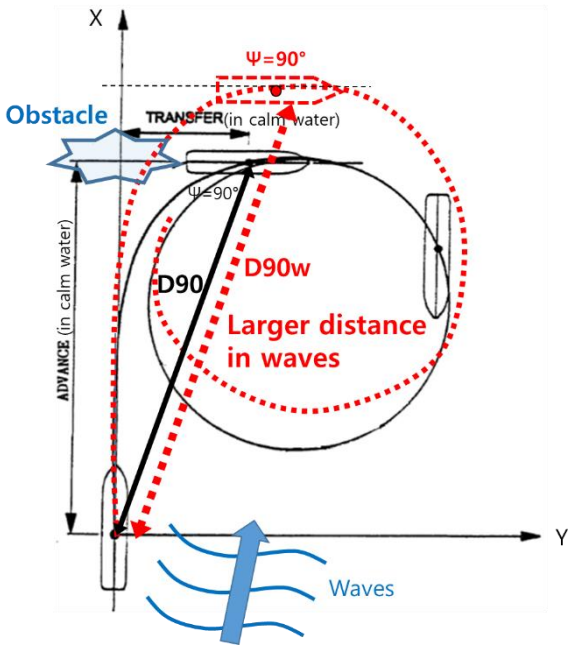

Figure 5. Dangerous situation with front obstacle in waves – (1) large distance

Ship's manoeuvrabilities in calm water are classified into course keeping, course changing, yaw checking, turning, and stopping abilities (International Maritime Organization, 2002). When the ship is operated in actual rough sea, the ship speed is mostly low and the strong wave forces are acted on the ship. Therefore course keeping ability and emergent turning ability are very important for the safe operations in waves.

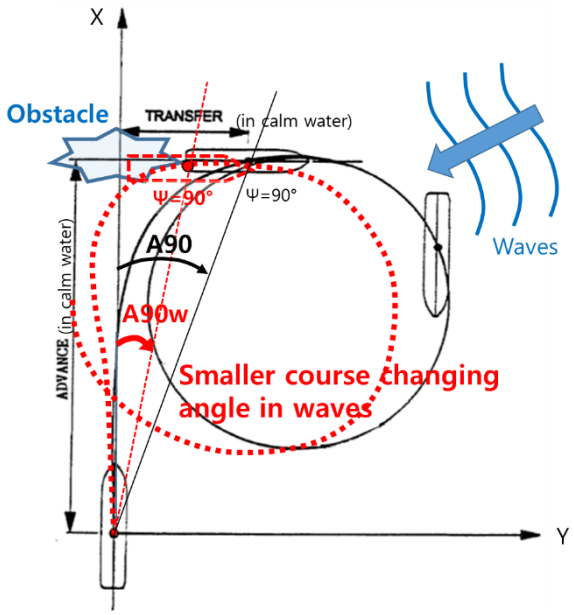

Figure 6. Dangerous situation with front obstacle in waves – (2) small course changing angle

This study focuses on the emergent turning ability in waves. On the assumption that the fixed obstacle exists in front of the ship closely, it is necessary to avoid the collision by hard-over turns as soon as possible. In waves, initial turning abilities remarkably change depending on the wave conditions. Two kinds of dangerous situations are described in Figure 5 and 6. When the forward distance in waves is larger than calm water distance, the collision risk is increased. And the collision risk increases with smaller course changing angle as well. Distance and course changing angle up to headings of 90° can be defined as Eq. (1) and (2). Subscript 'w' on D90w, A90w means the value in waves.

$$\mathrm{D90} = \sqrt{\mathrm{Advance}^2 + \mathrm{Transfer}^2} \tag{1}$$

$$\mathrm{A90} = \tan^{-1}(\mathrm{Transfer}/\mathrm{Advance}) \tag{2}$$

New index is proposed as Figure 7, which represents the safety in hard-over turns with front obstacle in waves. The ratio of advances in calm water and in waves as well as that of transfers are used to formulate new index, 'STw' as shown in Eq. (1). STw is zero in calm water. Positive value means safe situation and negative value indicates dangerous situation, compared with calm water operation.

$$STw = \frac{A90w}{A90} \Big/ \frac{D90w}{D90} - 1 \tag{3}$$

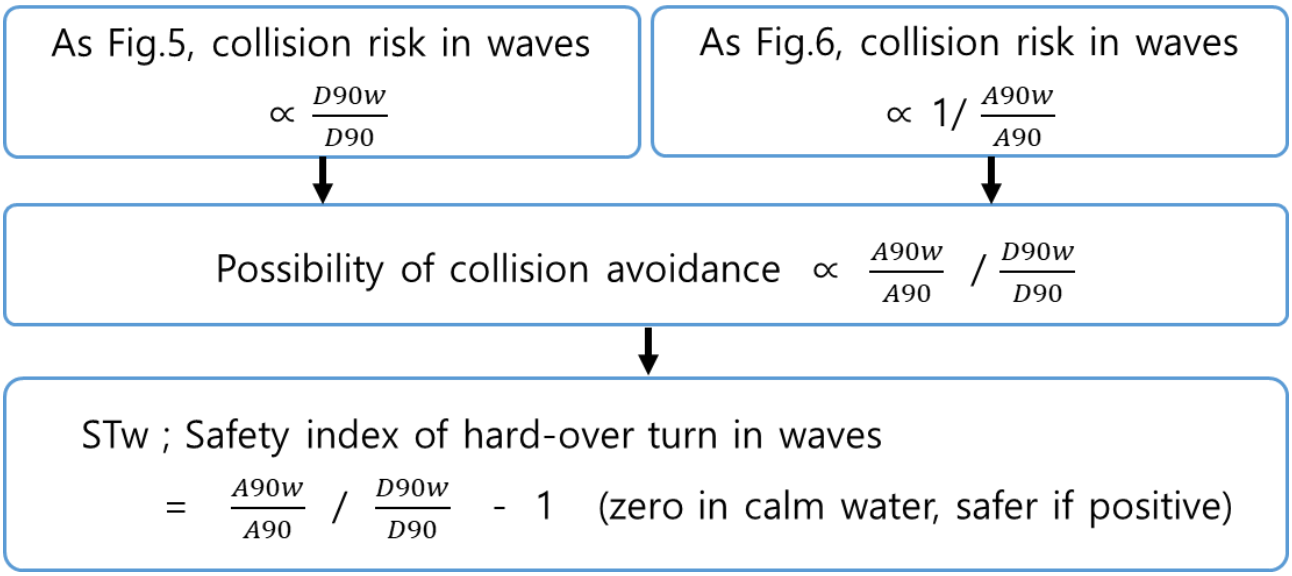

Figure 7. Safety index of hard-over turn for avoiding front obstacle in waves

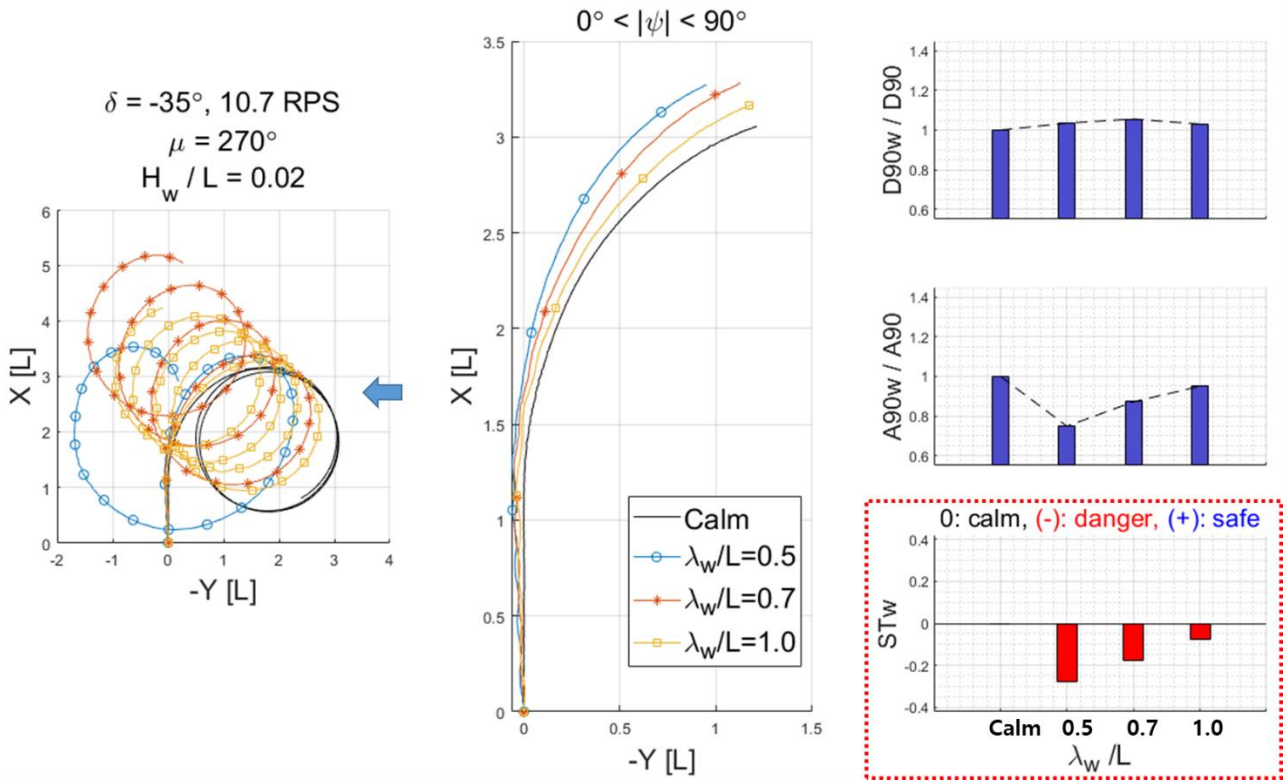

Figure 8. 35° initial turns depending on 'wave lengths' – (1) PORT turns in port beam waves

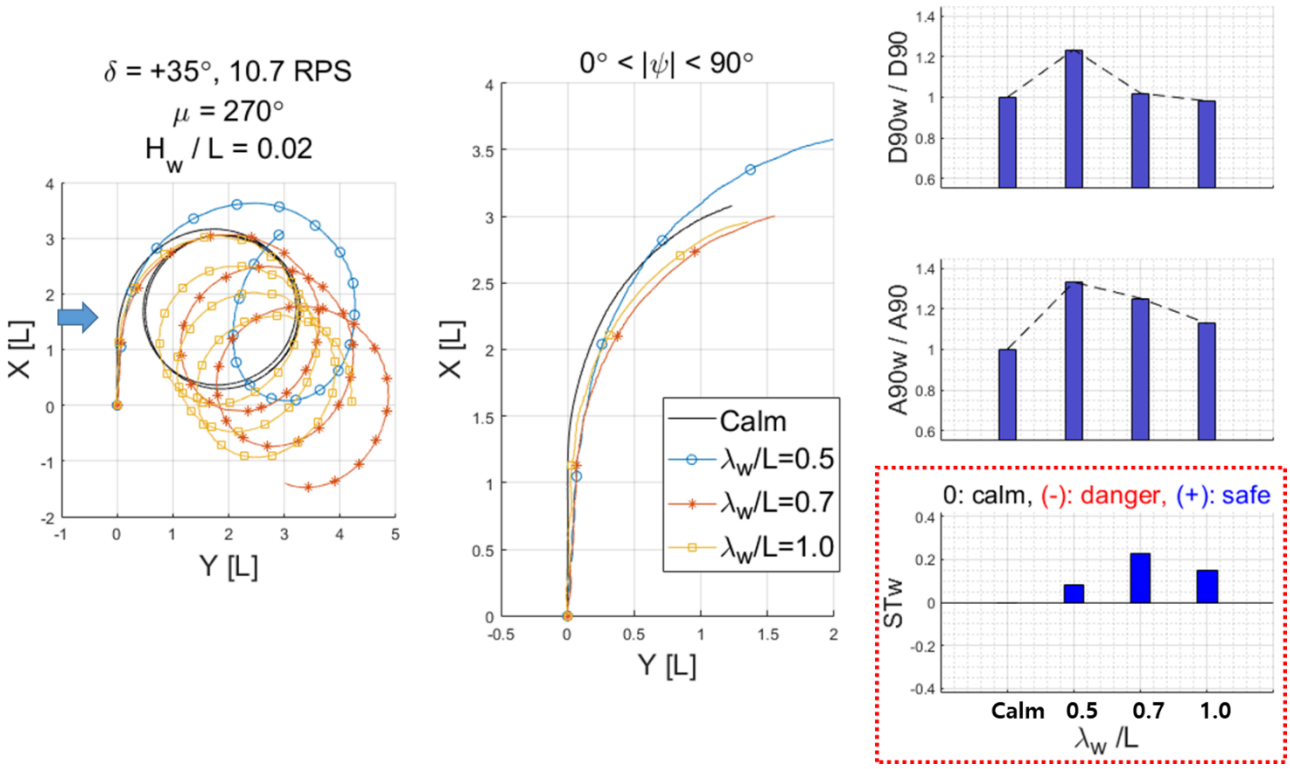

Figure 9. 35° initial turns depending on 'wave lengths' – (2) STBD turns in port beam waves

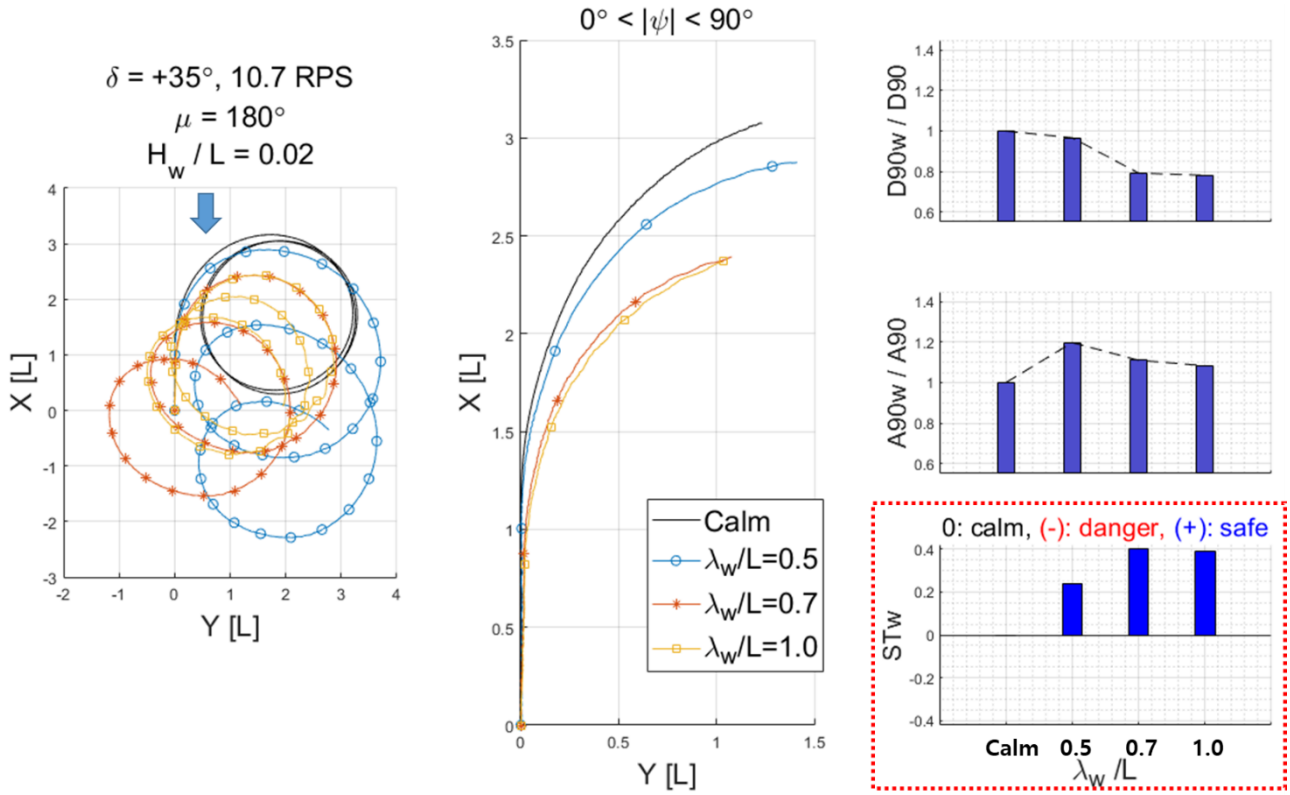

Figure 10. 35° initial turns depending on 'wave lengths' – (3) STBD turns in head waves

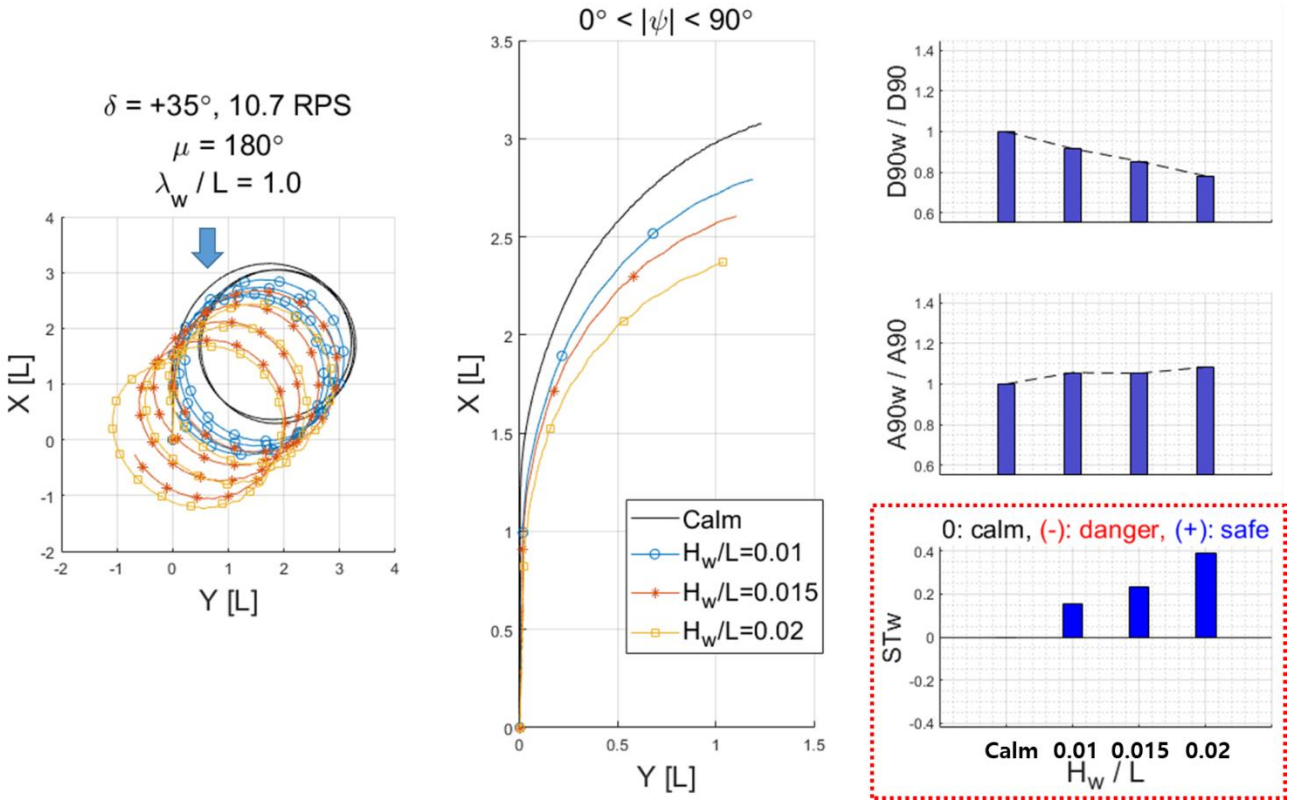

Figure 11. 35° initial turns depending on 'wave heights'

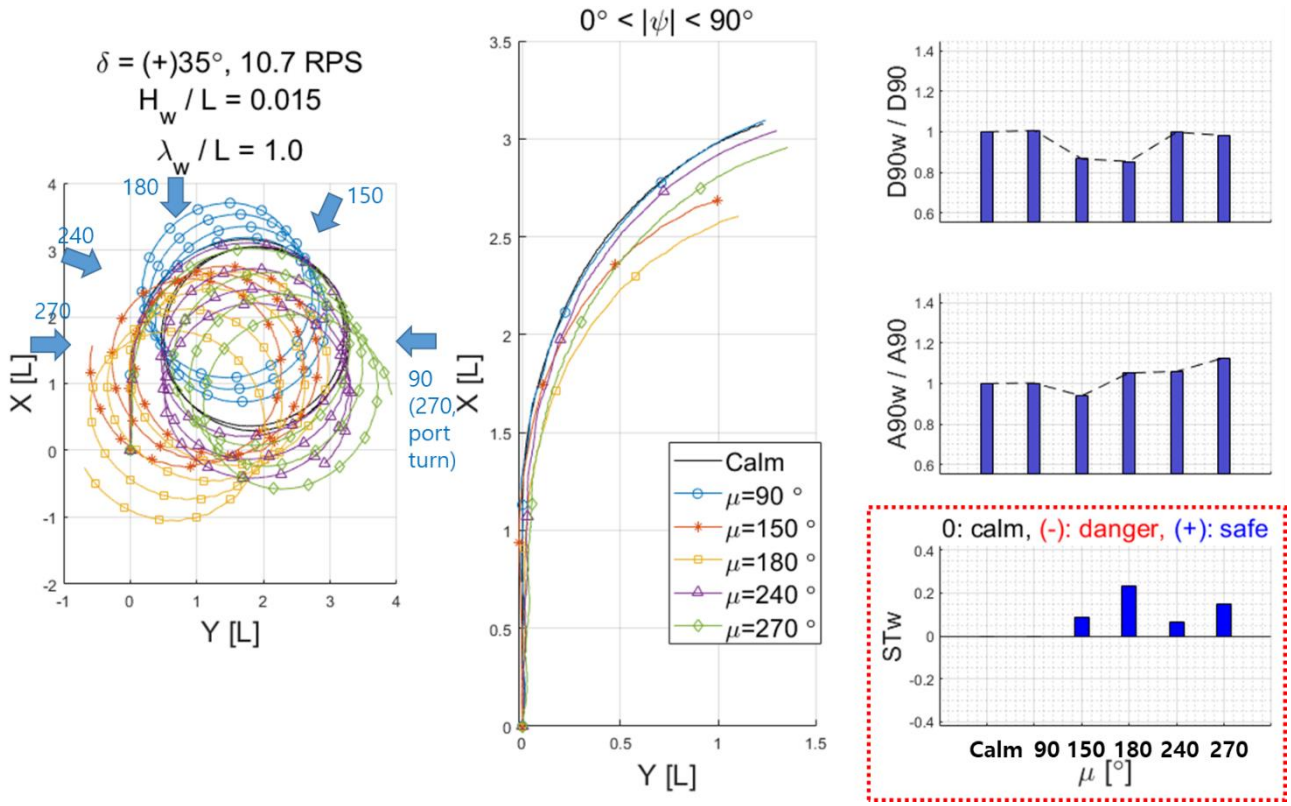

Figure 12. 35° initial turns depending on 'wave directions'

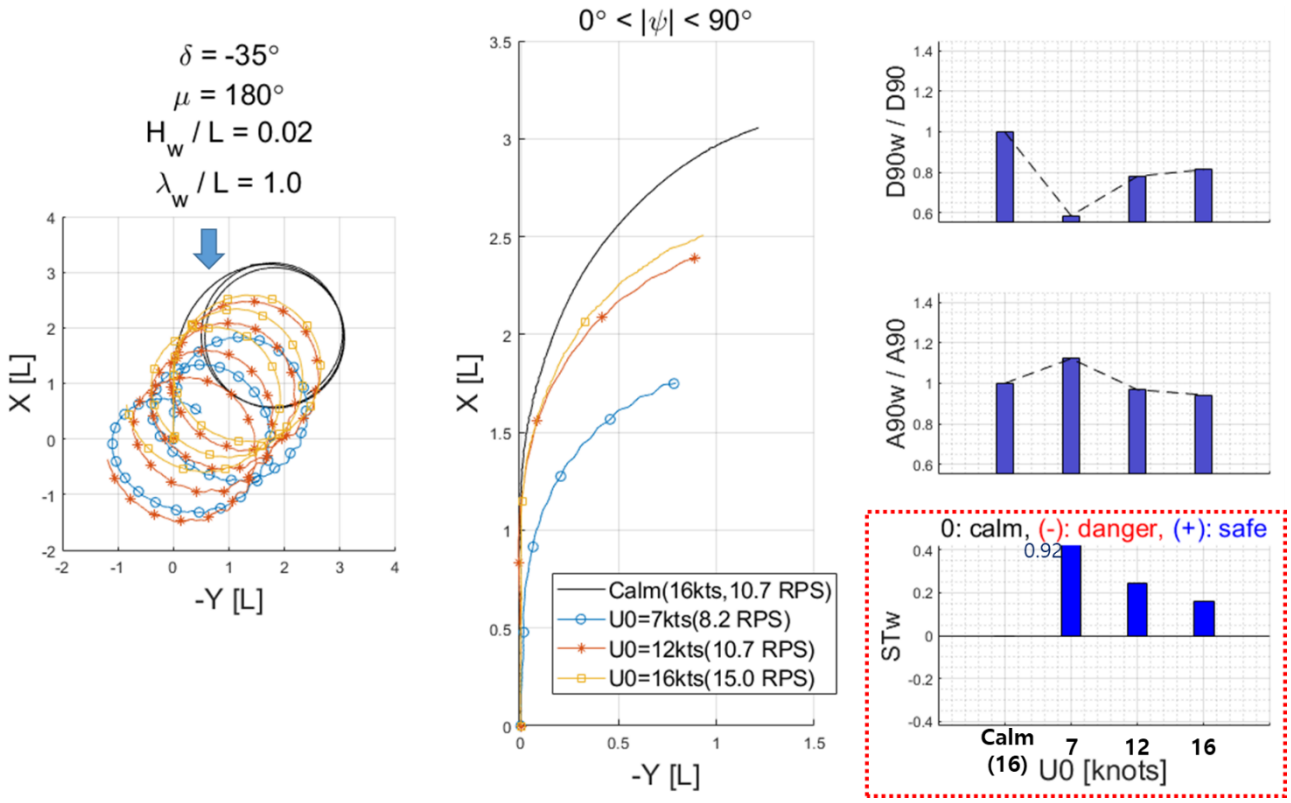

Figure 13. 35° initial turns depending on 'approach speed'

3.2 EFFECTS OF REGULAR WAVE CONDITIONS ON INITIAL TURNING ABILITY

Figure 8 shows -35 turns in port beam waves, and Figure 9 and 10 show +35° turns in starboard beam waves and in head waves with variations of wave lengths. Port and starboard turning abilities of the present model ship are very similar to each other, so -35° turns in port beam(270°) waves are plotted as +35° turns in starboard beam(90°) waves as Figure 8.

In Figure 8, 'STw' is negative. That is, for starboard turns in starboard beam waves the collision risk increases, in particular, when the wave length is smaller than the ship length.

In Figure 9 and 10, 'STw' is positive. For starboard turns in port beam and head waves the collision risk decreases. Under the same wave height and length conditions, the collision risk in head waves is lower than that in port beam waves due to small initial distances in head waves. Even if in port beam waves, when the wave length is half of the ship length the distance D90w is especially larger than other wave lengths. It can be estimated that the wave drifting yaw moments in short wave lengths are large, that prevents the model ship from turning to starboard.

Figure 11 describes +35° turns in head waves with variations of wave heights. As the wave height is higher, there is not much change in course changing angle A90w, but the initial distance D90w is significantly reduced. So the collision risk is decreased with increasing wave heights in head wave conditions.

Figure 12 represents +35° turns with variations of wave directions. Wave height is fixed as 0.015 L, and wave length is 1.0 L. The ship becomes a little danger in starboard beam(90°) waves than calm water, and is safer in other wave directions. For starboard turns the ship is safe in head waves due to small initial distance D90w, and is also safe in port beam waves due to large course changing angle A90w.

In Figure 13, the approach speeds are varied from 7 to 16 knots for -35° turns in waves. The distance D90w is significantly small with low approach speed, the ship becomes safer than the calm water run. From a point of view of collision avoidance, the ship is safe at initial turns with low approach speeds so long as it can turn.

4 RELATION BETWEEN INITIAL AND STEADY TURNS

4.1 INDEX FOR TURNING TRAJECTORY DRIFT IN WAVES

Indices of drifting distance and angle of steady turning trajectory were proposed in the previous research by Kim et al. (2019). Drifting distance and angle are defined by using a vector between two ship positions with headings of 360° and 720° as shown in Figure 14.

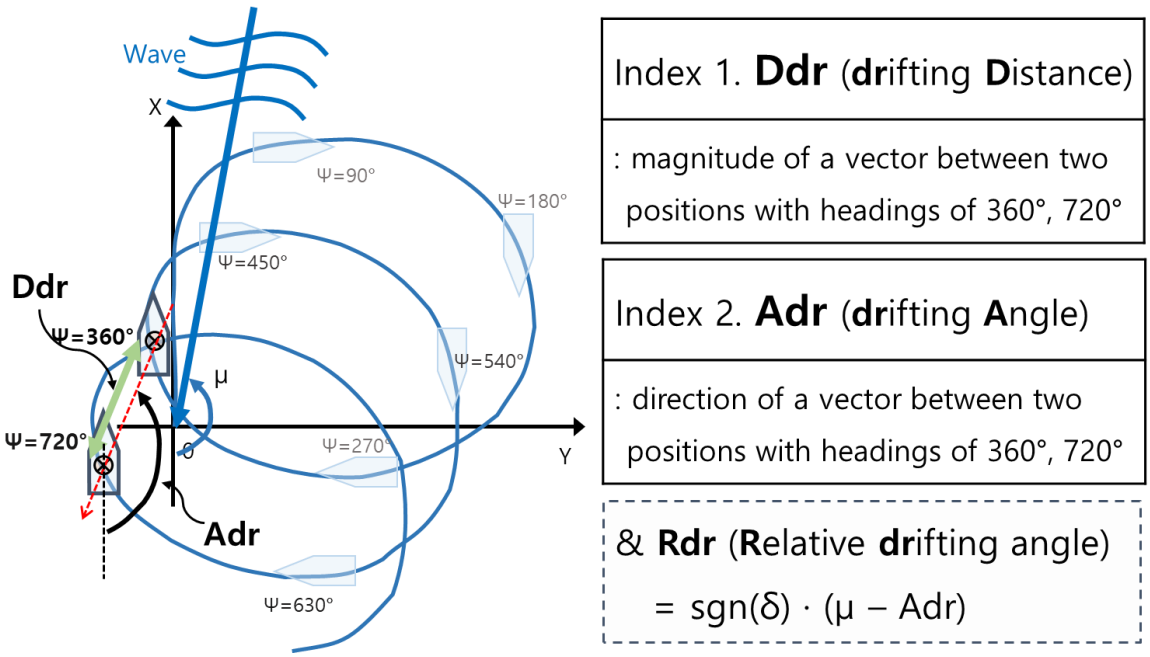

Figure 14. Indices for turning trajectory drifts in waves (Kim et al., 2019)

Table 3. +35° initial and steady turning characteristics

μ [°]	H_w/L	λ_w/L	Initial turn			Steady turn	
			D90w/D90	A90w/A90	STw	Ddr [L]	Adr [°]
90 (-35° turns @ χ=270°)	0.010	0.5	0.98	0.91	-0.07	0.63	80
		0.7	1.02	0.90	-0.12	0.35	60
		1.0	1.02	1.00	-0.02	0.15	49
	0.015	0.5	1.00	0.88	-0.12	1.13	79
		0.7	1.03	0.96	-0.07	0.61	49
		1.0	1.01	1.01	0.00	0.20	28
	0.020	0.5	1.04	0.75	-0.28	1.98	85
		0.7	1.06	0.87	-0.17	0.87	42
		1.0	1.03	0.95	-0.08	0.46	46
150	0.015	1.0	0.87	0.94	0.08	0.32	98
180	0.010	0.5	0.99	1.13	0.14	0.44	181
		0.7	0.93	1.04	0.12	0.21	133
		1.0	0.92	1.06	0.15	0.15	134
	0.015	0.5	0.97	1.16	0.19	0.96	170
		0.7	0.88	1.10	0.25	0.55	143
		1.0	0.85	1.05	0.23	0.42	129
	0.020	0.5	0.97	1.20	0.24	1.39	183
		0.7	0.79	1.11	0.40	1.08	137
		1.0	0.78	1.08	0.39	0.53	128
240	0.015	1.0	1.00	1.06	0.06	0.32	185
270	0.010	0.5	1.05	1.17	0.11	0.64	272
		0.7	1.00	1.07	0.07	0.24	226
		1.0	0.99	1.04	0.05	0.13	200
	0.015	0.5	1.12	1.23	0.10	1.03	262
		0.7	1.01	1.16	0.15	0.57	234
		1.0	0.98	1.13	0.15	0.39	218
	0.020	0.7	1.02	1.25	0.23	0.93	223
		1.0	0.98	1.13	0.15	0.60	212

4.2 INITIAL AND STEADY TURNING CHARACTERISTICS

Indices of initial and steady turns with +35° rudders are summarized in Table 4. Propeller revolution rate is fixed as 10.7. As mentioned in chapter 3.2, -35° turns with wave direction of 270° are regarded as +35° turns with wave direction of 90° for the convenience of comparison.

As previous research by Kim et al. (2019), the initial wave directions have little influences on the drifting distances in steady turns. As shown in Figure 15, Drifting distances (Ddr) increase with increasing wave heights. Drifting distances are, in particular, large when the wave length is 0.5 L.

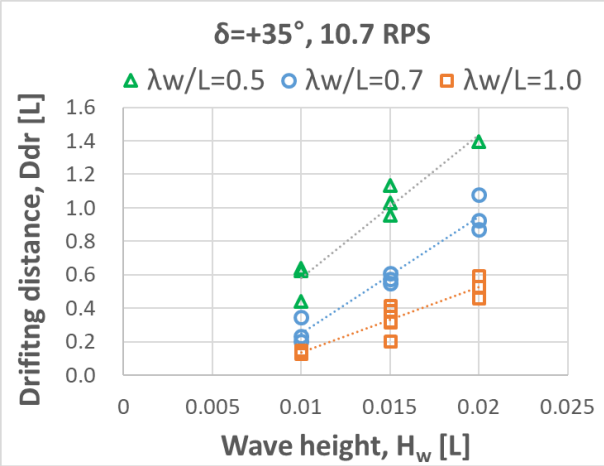

Figure 15. Relation between drifting distances and wave heights according to wave lengths

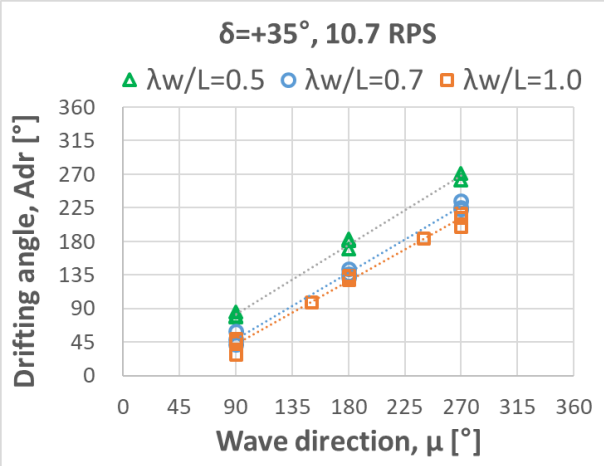

Figure 16. Relation between drifting angles and wave directions according to wave lengths

In Figure 16, drifting angles (Adr) are mainly affected by the wave lengths and directions. When the wave length is 0.5 L, the drifting angles are almost the same as the wave directions. It means that the steady turn trajectories are drifted in the wave directions at that condition. The differences between the wave directions and the drifting angles, in other words, relative drifting angles (Rdr) are around 45° in the case that the wave lengths are 0.7 L and 1.0 L. Wave heights have little influence on the drifting angles.

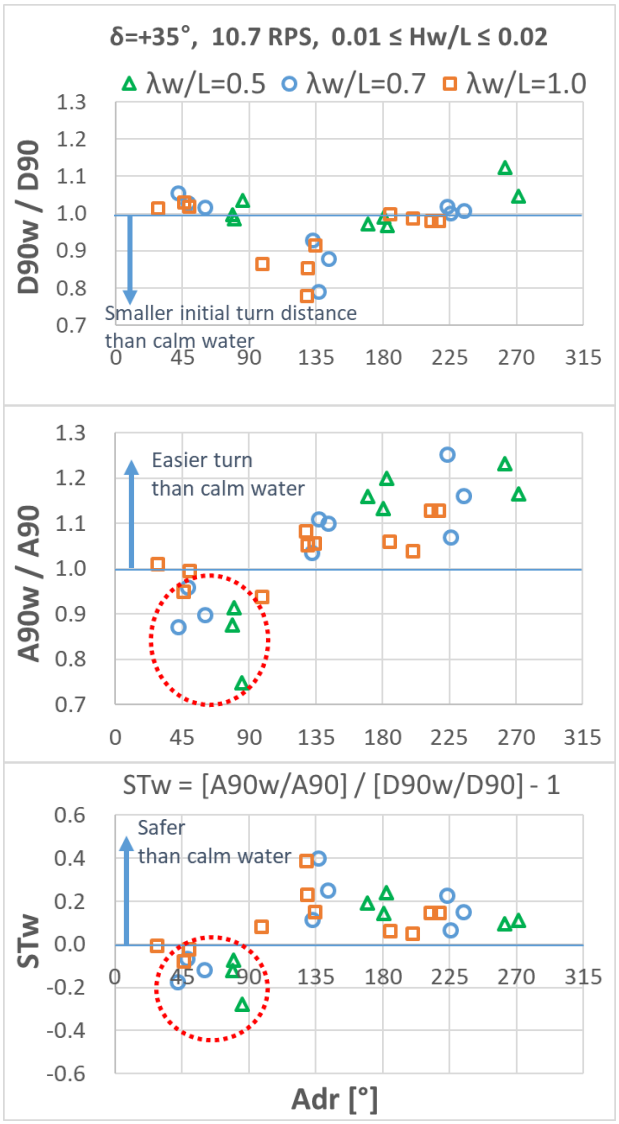

Figure 17. Initial turn characteristics with steady turn drifting angle

Figure 17 describes the indices of initial turns such as D90w, A90w, and STw with respect to steady turn drifting angles (Adr). D90w and A90w are normalized with D90 and A90 in calm water. D90w/D90 which is less than 1.0 means that the initial turn distance in waves is smaller than calm water. If A90w/A90 is more than 1.0, it is easier to turn in waves than calm water. So the positive 'STw' means the safer turns with front obstacle than calm water from a point of view of collision avoidance. As marked by dotted circle in Figure 17, 'STw's are negative when the steady turn drifting angles are below 90°, mostly due to the small A90w. When the ship turns to starboard, turning

behaviours are prevented by wave forces in starboard beam or bow quartering waves. In particular, it is hard to turn in short wave lengths below the ship length as shown in Figure 8 and 17.

5 CONCLUSIONS

In this research, turning circle tests of a KCS model ship are performed in regular waves. The effects of wave conditions and approach speeds on the initial and steady turning characteristics of the model ship are investigated. Main conclusions are as followings.

- New index, 'STw' is proposed to represent the hard over initial turn abilities for collision avoidance by using advance and transfer in waves.
- For starboard turns, STw is negative (worse initial turn ability than calm water) in starboard beam waves mostly due to smaller course changing angles than calm water, and positive (better initial turn ability than calm water) in head or port beam waves.
- The model ship shows better initial turn abilities in head waves as the wave heights are larger and the approach speeds are lower.
- In steady turns, drifting distances increase with increasing wave heights, they are particularly large when the wave length is 0.5 L. Relative drifting angles between trajectory drifting angles and wave directions are zero with the wave length of 0.5 L, and about 45° when the wave lengths are 0.7 L and 1.0 L.
- For 35° starboard turns, STw is negative (worse initial turn ability than calm water) when the steady turn drifting angles are smaller than 90° mostly due to the smaller course changing angles than calm water.

6 ACKNOWLEDGEMENTS

This research was supported by a grant from Endowment Project of "Development of the Analysis Technology of Ship's Integrated Ability of Maneuvering and Seakeeping (3/3)" funded by Korea Research Institute of Ships and Ocean Engineering (PES3010).

7 REFERENCES

Kim, D.J., Yun, K., Park, J.Y., Yeo, D.J., Kim, Y.G., 2019. Experimental investigation on turning characteristics of KVLCC2 tanker in regular waves. Ocean Engineering. 197–206.

International Maritime Organization (IMO), 2002. Explanatory Notes to the Standards for Ship Manoeuvrability. MSC/Circ 1053.

Matsuda, A., Hashimoto, H., Terada, D., Taniguchi, Y., 2016. Validation of free running model experiments in heavy seas, in: Proceedings of the 3rd International Conference on Violent Flows. Osaka, Japan.

Ueno, M., Nimura, T., Miyazaki, H., 2003. Experimental study on manoeuvring motion of a ship in waves, in: Proceedings of International Conference on Marine Simulation and Ship Manoeuvrability (MARSIM). Kanazawa, Japan.

Yasukawa, H., Nakayama, Y., 2009. 6-DOF simulations of a turning ship in regular waves, in: Proceedings of International Conference on Marine Simulation and Ship Manoeuvrability (MARSIM). Panama City, Panama.

Yasukawa, H., Hirata, N., Yonemasu, I., Terada, D., Matsuda, A., 2015. Maneuvering simulation of a KVLCC2 tanker in irregular waves, in: Proceedings of International Conference on Marine Simulation and Ship Manoeuvrability (MARSIM). Newcastle upon Tyne, UK.

8 AUTHORS BIOGRAPHY

Dong Jin Kim is a senior engineer at Korea Research Institute of Ships and Ocean Engineering. He received a bachelor, master, and Ph.D. degrees of Engineering in a department of Naval Architecture and Ocean Engineering at Seoul National University. His major fields are manoeuvring and seakeeping analyses of high speed vessels as well as other surface vehicles.

Kunhang Yun holds the current position of senior researcher at Korea Research Institute of Ships and Ocean Engineering. He is responsible for manoeuvring simulation of maritime vehicles and maritime simulator.

Dong Jin Yeo holds the current position of principal researcher at Korea Research Institute of Ships and Ocean Engineering. He is responsible for identification, performance prediction, and control of ocean vehicles' dynamics. His previous experience includes design of optimal inputs for the identification of ocean vehicles' dynamics, modeling of ocean vehicles' dynamics, etc.

Yeon Gyu Kim holds the current position of principal researcher at Korea Research Institute of Ships and Ocean Engineering. He is responsible for prediction of manoeuvrability of ships and submersible bodies.

STUDY ON THE MANEUVERING SIMULATION OF A SHIP WITH WAVE EFFECT IN REGULAR WAVES

Yeon-Gyu Kim, Dong Jin Yeo , Dong-Jin Kim, Kunhang Yun, Gyeong-Joong Lee, Bo-Woo Nam and **Min-Guk Seo**,
Korea Research Institute of Ships and Ocean Engineering, Rep. of Korea

STUDY ON THE MANEUVERING SIMULATION OF A SHIP WITH WAVE EFFECT IN REGULAR WAVES

Yeon-Gyu Kim, Dong Jin Yeo , Dong-Jin Kim, Kunhang Yun, Gyeong-Joong Lee, Bo-Woo Nam and **Min-Guk Seo,**
Korea Research Institute of Ships and Ocean Engineering, Rep. of Korea

SUMMARY

The interest on the prediction of a ship's maneuverability in waves becomes larger, because the regulation of EEDI and the guideline of minimum propulsion power of IMO become stronger. Generally to predict the maneuverability of a ship in waves the model tests and simulation method are used. However the simulation method is more reasonable than model tests in time and cost. In this research the maneuvering simulations of S-175 container ship in regular waves are conducted. To simulate, the wave drift forces and moments are calculated, and the 4 degree of freedom maneuvering mathematical equations are used in the consideration of wave effect. The target ship of this research is S-175 container ship. The simulation results are compared with the free running model tests in regular waves by Yasukawa & Nakayama(2009). To improve the accuracy of simulation results the wave drift forces and moments are obtained with the drift angle considering during turning test. The wave effect at the approach speed, rudder force and thrust force are checked at the simulation. The discussion is also presented in this paper.

1 INTRODUCTION

The interest about a ship's maneuvering in waves becomes larger, because the regulation of EEDI and the guideline of minimum propulsion power of IMO become stronger (Kim et al., 2015). To predict the maneuverability of a ship in waves the free running model test and simulation method should be carried out. The free running model test gives better accuracy than simulation method. However the simulation method is more reasonable and practical than free running model test in time and cost.

There are two types of simulation method. The one is Two Time Scale Model, and the other is Hybrid Approach Model(Tello et al., 2012). Two Time Scale Model is the simulation method which is separated into fast varied motion of ship by waves and relatively slow varied motion of maneuvering(Skejic & Faltinsen, 2008, Seo & Kim 2011, Seo et al., 2018). Hybrid Approach Model is the simulation method which is direct calculation of six degree of freedom equations with integrated maneuvering and seakeeping motion(Lee et al., 2006, Sung et al., 2012). Two Time Scale Model is practical and easy to analyze the physical phenomena by separating the maneuvering and sea keeping characteristics. Hybrid Approach Model is used for the analysis of flow around the ship in maneuvering motion with wave effect. The simulation method in this paper is maneuvering part of Two Time Scale Model.

In the previous research a maneuvering simulation of a ship in waves at the real ship and model ship scale were carried out(Kim et al., 2017, Kim et al., 2018). The target ship is S-175 container ship, and the simulation results were compared with the free running model test in waves of Yasukawa & Nakayama(2009). To improve the simulation results the drift angle during turning test was considered at the calculation of wave drift forces and moments. The simulation results at λ/L=0.5, 0.7 showed good agreement with the model tests. But the drifting effects at the simulations of λ/L=1.0, 1.2 were weaker than model tests.

In this study the wave drift forces and moments are obtained with the drift angle considering during turning test. And to improve the accuracy of simulation results the wave effect at the approach speed is simulated. The drifting effect by wave at λ/L=1.0 is checked by variation of rudder and thrust forces at the simulation.

2 MATHEMATICAL MODEL AND TARGET SHIP

The mathematical equations with the wave drift forces and moments are used for the simulation of maneuvering motion in waves. The mathematical models of maneuvering motion are based on MMG model(Kim et al., 2003). The wave drift forces and moments are obtained by SWAN1 program. SWAN1 is developed by MIT(Massachusetts Institute of Technology), which is based on Rankine panel method and double body approximation at the frequency domain. SWAN1 consider the ship speed and is modified to consider the drift angle on the body boundary condition during turning test by KRISO(Seo et al., 2018).

2.1 MATHEMATICAL MODEL

With the body-fixed coordinates system shown in Figure 1, the equations of maneuvering motion with four degrees of freedom are composed as follows.

$$\begin{aligned} m(\dot{u} - vr - x_G r^2 + z_G pr) &= X_H + X_P + X_R + X_w \\ m(\dot{v} + ur - z_G \dot{p} + x_G \dot{r}) &= Y_H + Y_P + Y_R + Y_W \\ I_x \dot{p} - mz_G(\dot{v} + ur) &= K_H + K_P + K_R + K_W \\ I_z \dot{r} + mx_G(\dot{v} + ur) &= N_H + N_P + N_R + N_W \end{aligned} \quad (1)$$

where the terms with subscripts H, P, R and W represent the hull, propeller, rudder and wave drift forces and moments, respectively. x_G and z_G represent the x-

coordinate and z-coordinate of the center of gravity of the ship. And the dots on u, v, r and p represent the time derivatives of each variable. The details of mathematical model was shown in the reference Kim et al.(2017).

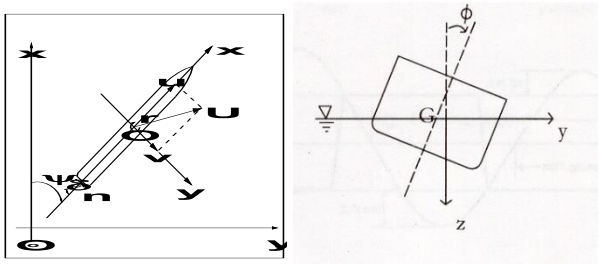

Figure 1. Coordinates system and sign conventions

2.2 TARGET SHIP

The target ship of this study is S-175 container ship. Yasukawa(2006a, 2006b) carried out free running model tests in regular and irregular waves. Free running mode test results in waves of S-175 have been used for the comparison of simulation results in many papers(Seo & Kim 2011, Seo et al., 2018, Sung et al., 2012, Kim et al., 2017, Seo et al., 2017). The principal dimensions of S-175 container ship are presented in Table 1.

Table 1. Principle dimensions of S-175 container ship

Item	Ship
Scale ratio	50.0
Length (m)	175.0
Breadth (m)	25.4
Draft (m)	9.5
Trim by stern (m)	0.0
Displacement (m^3)	24,154
Transverse gyration (kxx/B)	0.338
Longitudinal gyration (kyy/L, kzz/L)	0.269
Propeller diameter (m)	6.507
Rudder area (m^2)	32.46
Aspect ratio	1.83

3 COMPARISON RESULTS OF SIMULATION

The speed of free running model test is corresponding to 12 knots of real ship in clam water. The wave lengths(λ) over ship length(L) are 0.5~1.5, and straight running tests and turning tests are carried out.

3.1 COMPARISON RESULTS OF PREVIOUS STUDY(KIM ET AL., 2018)

In the previous study the simulation in waves was carried out by considering the drift angle during turning motion in model scale ship. The wave drift forces and moments considering the drift angle were used at the simulation in regular waves.

To simulate the maneuvering motion in calm water the maneuvering coefficients of mathematical model are obtained from empirical formula of KRISO. The propeller revolution by empirical formula is 8.66 rps. The propeller revolution of free running model test was 10.05 rps. To fit the turning trajectory the rudder coefficient f_α is corrected in the consideration of horn type rudder. And the turning trajectory of model scale simulations are compared with the free running test results in Figure 2. The simulation results in calm water have a good agreement with the free running model test results.

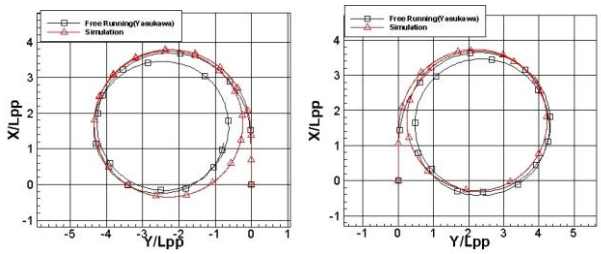

Figure 2. Turning tests with rudder angle of 35°(Kim et al., 2018)

Simulations of maneuvering motion in waves including the drift angle consideration are carried out by using mathematical model with four degree of freedom. The ratio of wave height to ship length is 0.02. The simulation results of turning test in head sea with(red lines) and without(green lines) drift angle considering are compared with the free running model tests(blue dotted lines). In Figure 3 the result of λ/L=0.5, 0.7, 1.0 and 1.2 are shown. At λ/L=0.5 and 0.7 the simulation results with drift angle considering show a very good agreement with the model test results. However the simulation results of λ/L=1.0 and 1.2 show a worse agreement than simulation results without drift angle effect. So it is necessary to study about the simulation method and model test at the large wave length region.

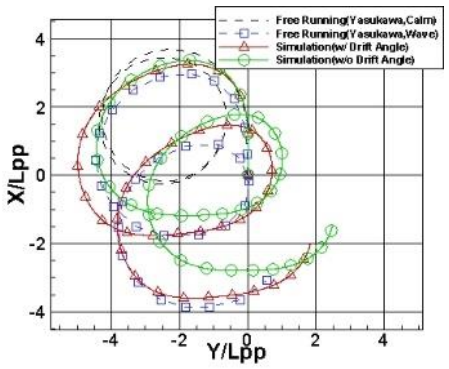

(a) λ/L=0.5

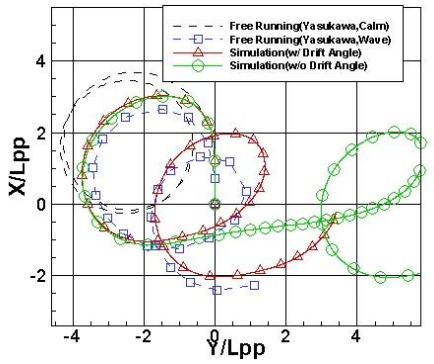

(b) λ/L=0.7

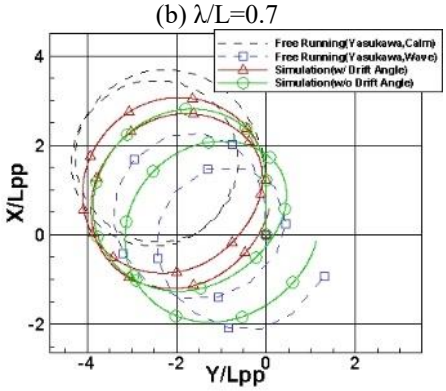

(c) λ/L=1.0

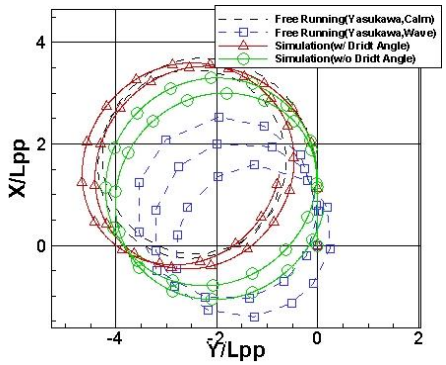

(d) λ/L=1.2

Figure 3. Comparison results of turning test with rudder angle of 35º in regular waves (head sea) (Kim et al., 2018)

3.2 SIMULATION BY CONSIDERING SPEED LOSS IN WAVES

The approach speeds of simulations in waves were 12.0 knots of real ship in calm water. However the approach speeds of free running model tests in waves are different with the wave conditions. To consider the speed loss by waves the straight motion simulation is carried out before the rudder executes. In Figure 4 the simulation result of speed loss, and the approach speeds of simulations are compared with those of free running model tests in Figure 4. The model speed corresponding to 12.0 knots in real ship is 0.873m/s. The simulated approach speeds show good agreements with model tests.

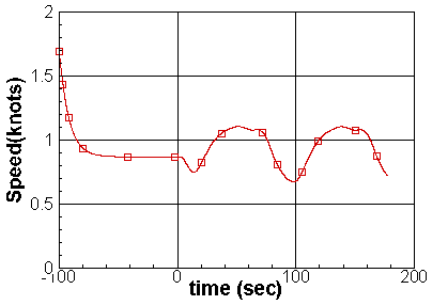

(a) Simulation result of speed loss(λ/L=1.0)

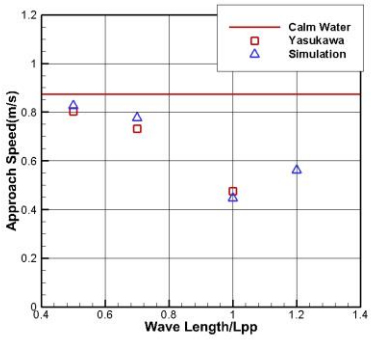

(b) Comparison results

Figure 4. The simulation result of speed loss and comparison result of approach speeds in regular waves (head sea)

The trajectories with speed loss considering(red lines) are compared with free running model tests(blue dotted lines) and simulations without speed loss considering(green lines). The differences between with and without speed loss considering aren't big.

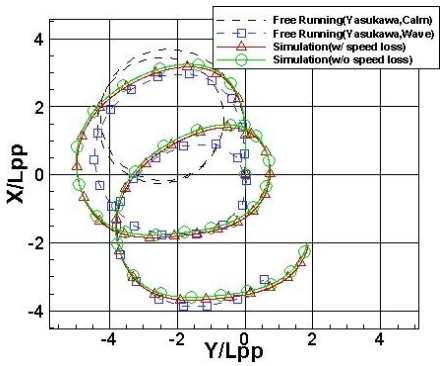

(a) λ/L=0.5

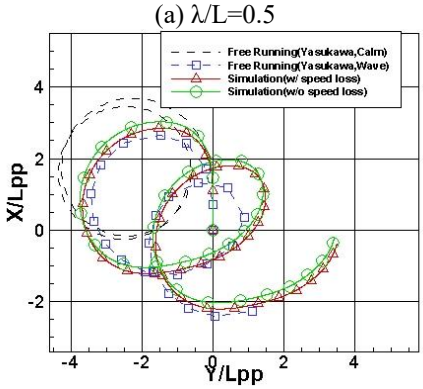

(b) λ/L=0.7

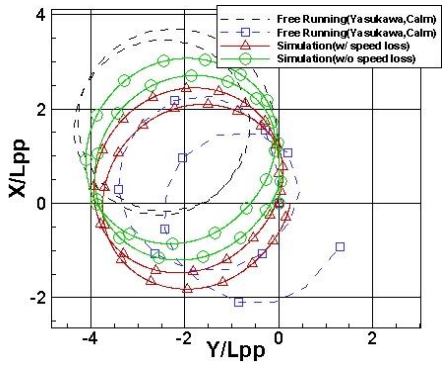

(c) λ/L=1.0

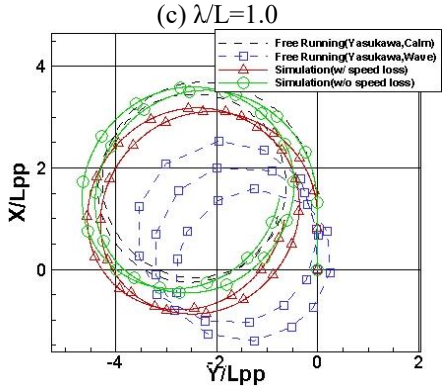

(d) λ/L=1.2

Figure 5. Comparison results of turning test with speed loss considering in regular waves (head sea)

3.3 SIMULATION BY RUDDER AND THRUST FORCES VARIATION IN REGULAR WAVES

From the above results the simulation results with speed loss considering agree better at λ/L=1.0 and 1.2, but the accuracy is not enough. To improve the simulation at λ/L=1.0 some factors are multiplied to rudder and thruster forces respectively. The influence on the hull by waves is included at the wave drift forces and moments.

New Rudder & Thruster Forces =

Factor ×Rudder & Thruster Forces (2)

The range of factors are 0.7 ~ 1.3. Factor 0.7 means -30% variation, and factor 1.3 means +30% variation. The simulation results with rudder force variations are shown in Figure 6. And the simulation results with thrust force variations are shown in Figure 7. From Figure 6 the turning diameters of weaker rudder forces become larger, and the turning diameters of stronger rudder forces become smaller. However the drifting motion by waves wasn't changed. From Figure 7 the differences of turning diameters with thrust force variation weren't shown. The drifting motion by waves become larger as thrust forces become weaker. But the change of drifting distance is very small by comparing with model test result.

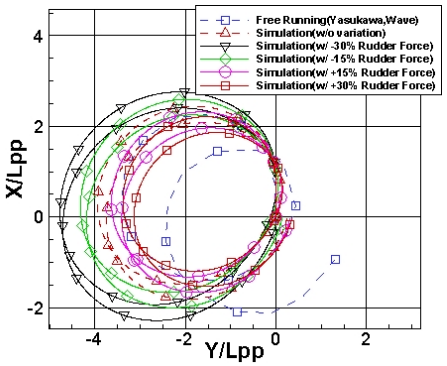

Figure 6. Comparison result of turning test with rudder force variation in regular waves (λ/L=1.0, head sea)

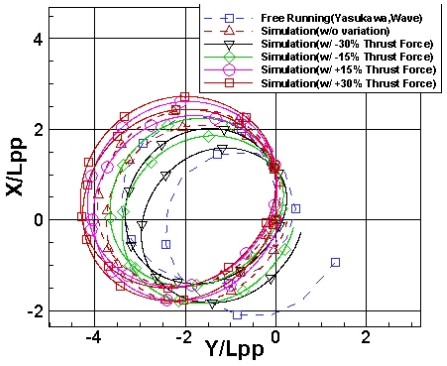

Figure 7. Comparison result of turning test with thrust force variation in regular waves (λ/L=1.0, head sea)

The rudder and thrust forces would be changed with the wave angles. In the initial stage of modelling the forces can be modelled by cosine sinusoidal fluctuation as follows.

New Rudder & Thruster Forces =

S_factor ×Rudder & Thruster Forces (3)

S_{factor} = 1.0+(1.0-Factor) ×cos(2.0χ)

χ : wave angle (180° : head sea, 0 ° : following sea)

In Figure 8 S_{factor} is calculated for Factor 0.7. Factor 0.7 means that the rudder or thrust forces are changed in the range of -30% ~ +30% from the original values by considering the wave angle. At the head and following seas it is thought that the rudder and thrust forces would be stronger than calm water.

Simulation results with cosine sinusoidal rudder and thrust forces variation are compared with simulation without variation and free running model tests in Figure 9. The turning diameter of simulation with rudder force variation is larger than that without variation because of the weaker rudder force at beam sea. The drifting effect of simulation with thrust force variation isn't improved because of stronger thrust force at head and following seas.

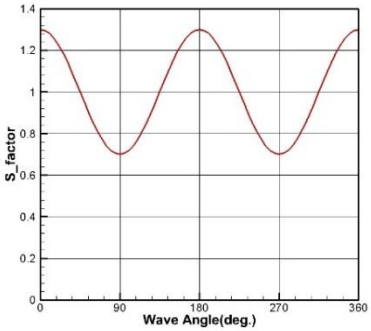

Figure 8. Calculated cosine S_{factor} for Factor 0.7 with the wave angle variation

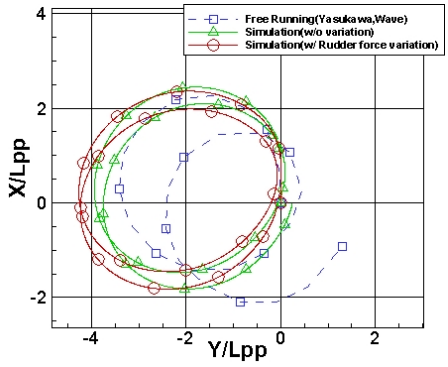

(a) Rudder force variation

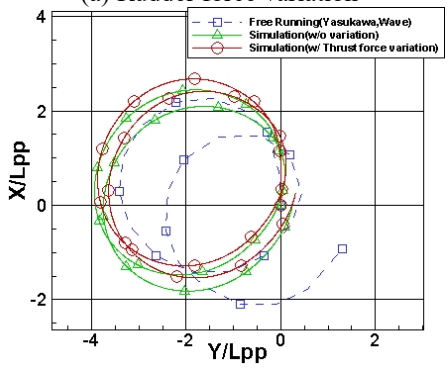

(b) Thrust force variation

Figure 9. Comparison results of turning test with cosine rudder and thrust forces variation in regular waves (λ/L=1.0, head sea)

To improve the drifting motion by waves the sine variation of rudder and thrust forces with wave angles is considered using following equation and Figure 10. The rudder and thruster forces are treated weaker than calm water at head and following seas.

$$S_{factor} = 1.0+(1.0\text{-Factor}) \times \sin(2.0(\chi\text{-}45^{o})) \quad (4)$$

χ : wave angle (180° : head sea, 0 ° : following sea)

The comparison results of simulation are shown in Figure 11. The drifting motion by wave is larger than above simulation. However it's not enough, so more research about modelling of rudder and thruster forces in waves should be necessary.

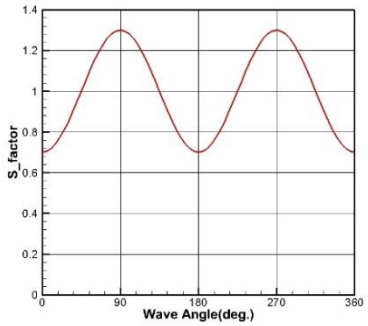

Figure 10. Calculated sine S_{factor} for Factor 0.7 with the wave angle variation

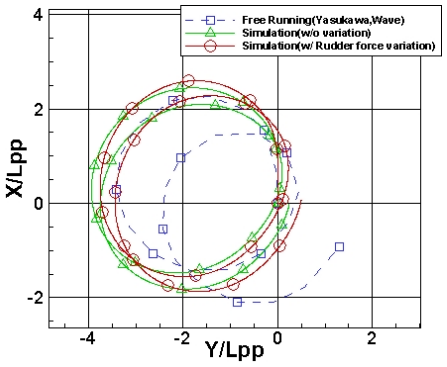

(a) Rudder force variation

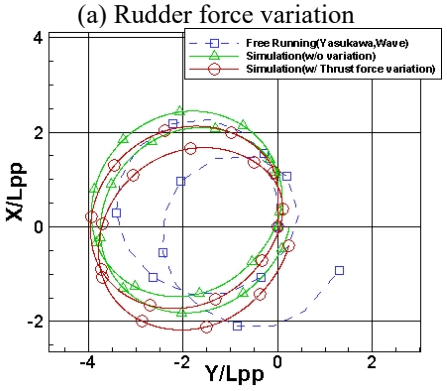

(b) Thrust force variation

Figure 11. Comparison results of turning test with sine rudder and thrust forces variation in regular waves (λ/L=1.0, head sea)

3.4 ANALYSIS OF DRIFTING DISTANCE AND DRIFTING ANGLE AT TURNING TEST IN WAVES

At turning tests in calm water the indexes like as advance, transfer and tactical diameter are good values for comparison and measure of accuracy. However, at the turning tests in waves it is difficult to compare the research results except the turning trajectory. Ueno et al.(2003) explained the drifting distance and drifting angle by waves. In Figure 12 the definition of drifting distance and drifting angle is shown. It would be one of the good index at turning tests in waves.

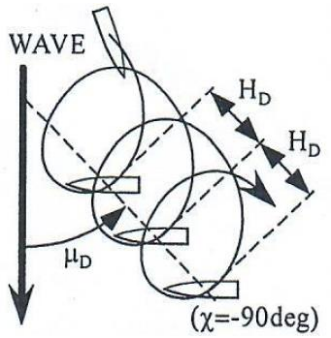

Figure 12. Definition of drifting distance and drifting angle(Ueno et al., 2003)

Kim et al.(2018) described that the first 90° heading angle value is not suitable for wave effect index because its state is not stable in turning motion. So the drifting effect is stable after 180° heading angle, the results of 360° heading angle and 720° heading angle are proposed for the best calculation of drifting distance and drifting angle. But the free running model tests by Yasukawa were finished before 720° heading angle, so the results of 270° heading angle and 630° heading angle are used for the analysis in this paper. The comparison results of drifting distance and drifting angle are shown in Figure 13. There are some differences between simulations and model tests. At λ/L=1.0 the drifting motion of simulation is very weaker than model tests, so the calculated results of drifting motion are not reasonable.

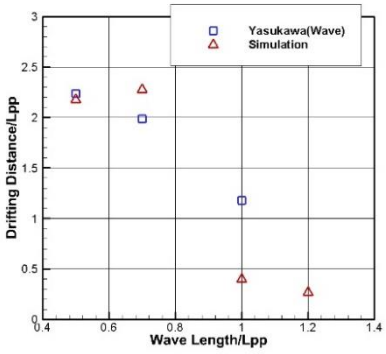

(a) Drifting distance

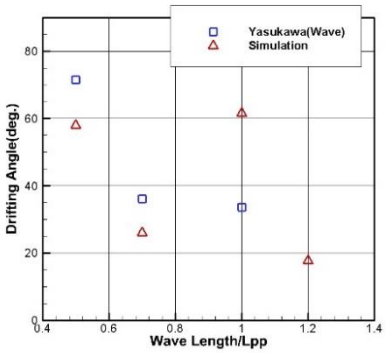

(b) Drifting angle

Figure 13. Comparison results of drifting distance and drifting angle

The analysis of simulations with thruster force variation of section 3.3 is carried out. The calculated results are shown in Figure 14. The tendencies of drifting distance and drifting angle are shown in the figure. The drifting motion by wave at factor 0.7 is largest, and that of factor 1.3 is smallest. The drifting distance and drifting angle are good indexes of wave effect at the turning maneuver in waves.

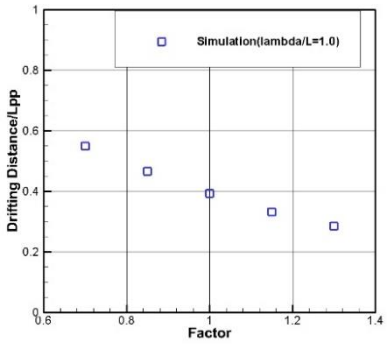

(a) Drifting distance

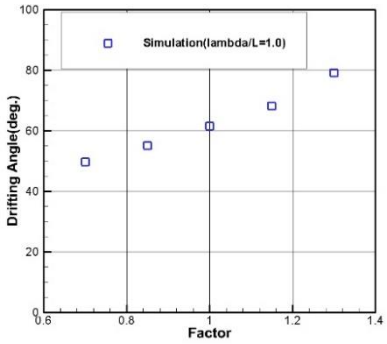

(b) Drifting angle

Figure 14. Drifting distance and drifting angle with thrust force factor variation(λ/L=1.0, head sea)

4 CONCLUSIONS

In this study the simulations of a ship's maneuvering in waves are conducted. Some simulations are carried out to improve the simulation method in waves at a model scale with the wave drift forces and moments by considering drift angles during turning test. The target ship is S-175 container ship. To improve the drifting motion by waves at λ/L=1.0 and 1.2 speed loss by wave is considered in the simulation. And some variations of rudder and thrust forces are studied in the simulations. The simulation results are compared with free running model test.

- The effect of speed loss in waves has improved the drifting motion by waves. But the effect is not enough as comparing with model tests.
- The stronger variation of rudder and thrust force hasn't improved the simulation. The weaker rudder force has also not improved the simulation. But the weaker thrust force has improved the drifting motion in the simulation. But the drifting motion isn't enough. The cosine and sine

variations of rudder and thruster forces are carried out, but the results aren't meaningful.
- Drifting distance and drifting angle are checked as an index for the turning test in waves. They show a meaningful index.

In the future some simulations with wave drift forces and moments by considering drift and heel angles during turning test will be conducted. The mathematical modelling of rudder and thrust forces will be studied.

5 ACKNOWLEDGEMENTS

This research was carried out under a project titled "Development of the analysis technology of ship's integrated ability of maneuvering and seakeeping[PES3010]" funded by Korea Research Institute of Ships and Ocean Engineering(KRISO).

6 REFERENCES

Kim, D.J., Yun, K., Park, J.Y., Yeo, D.J., Kim, Y.G., 2018. Turning characteristics of KVLCC2 in regular head and beam waves", Proceedings of International Conference on Marine Simulation and Ship Manoeuvrability(MARSIM'18).

Kim, S.Y., Kim, Y.G., Son, N.S., Lee, S.W., Park, K.D., 2003. Maneuvering characteristics of a large container ship. Proceedings of International Conference on Marine Simulation and Ship Maneuverability(MARSIM'03).

Kim, Y.G., Yeo, D.J., Shin, M.S., Yun, K.H., Lee, G.J., 2015. IMO's movements about the minimum propulsion power in the adverse weather conditions. Journal of Ships & Ocean Engineering, Vol. 56, pp. 51-60.

Kim, Y.G. Kim, D.J., Lee, G.J., Nam, B.W., Seo, M.K., Yeo, D.J., Yun, K., 2017. Study on the simulation of a ship's maneuvering in waves. Proceedings of the 17th Asian Conference on Maritime System and Safety Research, pp.119-124.

Kim, Y.G. Lee, G.J., Nam, B.W., Seo, M.K., Kim, D.J., Yeo, D.J., Yun, K., 2018. Simplified maneuvering simulation of a ship in waves. Proceedings of the 18th Asian Conference on Maritime System and Safety Research, pp.29-36.

Lee, G.J., Yoon, H.K., Kim, Y.G., Kim, S.Y., 2006. Wave force modelling in time-domain ship motion. Proceedings of the 9th International Conference on Stability of Ships and Ocean Vehicles.

Seo, M.G., Kim, Y., 2011. Numerical analysis on ship maneuvering coupled with ship motion in waves. Ocean Engineering, 38, pp. 1934-1945.

Seo, M.K., Nam, B.W., Kim, Y.G., 2017. Study of effects of wave drift force on maneuvering performance in waves. Proceedings of Spring Conference of The Society of Naval Architects of Korea, pp.79-89.

Seo, M.G., Nam, B.W., Kim, Y.G., 2018. Numerical analysis of turning performance in waves by considering wave drift forces. Journal of the Society of Naval Architects of Korea, Vol. 55, No. 2, pp. 103-115.

Skejic, R., Faltinsen, O.M., 2008. A unified seakeeping and maneuvering analysis of ships in regular waves. Journal of Marine Science and Technology, Vol. 13, No. 4, pp. 371-394.

Sung, Y.J., Lee, H.H., Lee, T.I., Kim, S., 2012. Captive model test and numerical simulation on the manoeuvring forces in waves. Proceedings of the 11th International Conference on the Stability of Ships and Ocean Vehicles.

Tello Ruiz, M., Candries. M., Vantorre, M., Delefortrie, G., Peeters, D., Mostaert, F., 2012. Ship manoeuvring in waves (a literature review). Flanders Hydraulics Research & Ghent University.

Yasukawa, H., 2006a. Simulation of wave-induced motions of a turning ship. Journal of the Japan Society of Naval Architects and Ocean Engineers, pp. 117-126.

Yasukawa, H., 2006b. Simulation of ship maneuvering in waves (1st report: turning motion). Journal of the Japan Society of Naval Architects and Ocean Engineers, No. 4, pp. 127-136.

Yasukawa, H., Nakayama, Y., 2009. 6-DOF motion simulations of a turning ship in regular waves. Proceedings of International Conference on Marine Simulation and Ship Manoeuvrability(MARSIM'09). pp. M-13-M-22.

Ueno, M., Nimura, T., Miyazaki, H., 2003. An experimental study on manoeuvring motion of a ship in waves. Proceedings of International Conference on Marine Simulation and Ship Maneuverability (MARSIM'03), pp. RC-13-1 -RC-13-7.

7 AUTHORS BIOGRAPHY

Yeon-Gyu Kim holds the current position of principal researcher of Korea Research Institute of Ships & Ocean Engineering (KRISO). He received his Ph.D. degree in naval architecture and ocean engineering from Chungnam National University in 2005. He received his B.S. and M.S. degrees of engineering in naval architecture and ocean engineering from Seoul National University. He has interests in the prediction of maneuverability of ships and submergible bodies.

Dong Jin Yeo holds the current position of a principal researcher of KRISO. He graduated with Dr. of engineering degree in naval architecture and ocean engineering from Seoul National University in 2005. He also received his B.S. and M.S. degrees of engineering in

naval architecture and ocean engineering from the same university. His research interests include identification, performance prediction, and control of ocean vehicles' dynamics.

Dong-Jin Kim holds the current position of a senior researcher of KRISO. He graduated with Dr. of engineering degree in naval architecture and ocean engineering from Seoul National University in 2012. He also received his B.S. and M.S. degrees of engineering in naval architecture and ocean engineering from the same university. His research interests in the prediction of maneuverability of ships and submergible bodies, and ocean vehicles' dynamics.

Kunhang Yun holds the current position of a senior researcher of KRISO. He received his B.S. and M.S. degrees of engineering in naval architecture and ocean engineering from Seoul National University. His research interests include maneuverability of ships and underwater vehicles.

Gyeong-Joong Lee holds the current position of a principal researcher of KRISO. He graduated with Dr. of engineering degree in naval architecture and ocean engineering from Seoul National University in 1990. He also received his B.S. and M.S. degrees of engineering in naval architecture and ocean engineering from the same university. His research interests include performance prediction, and control of ocean vehicles' dynamics.

Bo-Woo Nam holds the current position of a senior researcher of KRISO. He graduated with Dr. of engineering degree in naval architecture and ocean engineering from Seoul National University in 2015. He also received his B.S. and M.S. degrees of engineering in naval architecture and ocean engineering from the same university. His research interests include seakeeping performance prediction of ships and offshore plant.

Min-Guk Seo holds the current position of a researcher of KRISO. He graduated with Dr. of engineering degree in naval architecture and ocean engineering from Seoul National University in 2016. He also received his B.S. and M.S. degrees of engineering in naval architecture and ocean engineering from the same university. His research interests include seakeeping performance prediction of ships and offshore plant.

A MODULAR MATHEMATICAL APPROACH TO PREDICT THE MANEUVERING ABILITY OF DUISBURG TEST CASE IN REGULAR WAVES

Omer Kemal Kinaci, Omer Faruk Sukas and **Sakir Bal**,
Faculty of Naval Architecture and Ocean Engineering, Istanbul Technical University, Turkey

A MODULAR MATHEMATICAL APPROACH TO PREDICT THE MANEUVERING ABILITY OF DUISBURG TEST CASE IN REGULAR WAVES

Omer Kemal Kinaci, Omer Faruk Sukas and **Sakir Bal,** Faculty of Naval Architecture and Ocean Engineering, Istanbul Technical University, Turkey

SUMMARY

As the current trend in the maritime industry is moving toward controlling the ships (either remotely or autonomously); today, the main focus is shifted to the effects of the external disturbances rather than motions in an ideal environment. However, a fundamental part of maneuvering tests is still made in calm water although external disturbances play a vital role in ship motions during maneuvering. One of the biggest contributors of external disturbances, which also determines the severity of seas, are waves. In this study; the maneuvering motion of a benchmark ship, the Duisburg Test Case (DTC in short), was numerically solved both in calm water and in regular waves. First, maneuvering coefficients were obtained by numerical PMM tests and then, control surface parameters (for rudder and propeller) were calculated. These coefficients and parameters were then utilized into the MMG mathematical model to estimate the turning circle ability of the ships in calm water condition. Then, the effects of waves were added to the mathematical model in terms of forces and moments using Ankudinov's (1985) empirical relations. The turning circle trajectory in waves was obtained using the same mathematical model. Comparisons with experiments show that this modular approach is satisfactory in determining the ship maneuvering abilities in waves.

1 INTRODUCTION

Prediction of maneuvering motion of a ship in waves is quite important for safe ship navigation and it requires a knowledge beyond the prediction of maneuverability in calm water. Although prediction of maneuvering in calm water provides an information at the initial design stage, it is essential that wave-induced forces and moments acting on the hull are included in the maneuvering problem to be able to simulate the environment more realistically.

Several experimental and numerical studies about maneuvering in waves have been presented in recent years. In the framework of SHOPERA (Energy Efficient Safe Ship Operation) project, experimental tests were conducted for three different ship forms (DTC container vessel, KVLCC2 tanker, RoPax Ferry) to investigate ships' maneuverability in adverse weather conditions (Sprenger et al., 2017; el Moctar et al., 2016). Thus, available experimental data were provided for validation of numerical studies to be done. In literature, numerical approaches can be classified as direct CFD method, two-time scale method and hybrid method. The direct CFD approach in waves (Sadat-Hosseini et al., 2015; Shen and Korpus, 2015) generally provides an adequate accuracy to understand the physics during maneuvering, but it requires considerable computational effort which makes its application impractical. Two-time scale and hybrid methods, which are based on potential flow theory, are also used to simulate maneuvering motion in waves (Chillcce, el Moctar; 2018). In two-time scale method, the equations of motion are solved in parallel by seakeeping and maneuvering solvers. The second order wave forces are calculated in seakeeping solver, while the kinematical parameters are calculated in maneuvering solver. The estimated parameters are transferred to each other at every time step during simulation. Several studies which use two-time scale (unified) model can be found in the literature, for instance, Skejic and Faltinsen (2008) investigated the behavior of a ship in regular waves during maneuvering using two-time scale model. The mean second-order wave forces were estimated by three different approaches based on potential flow theory and they have been incorporated into maneuvering model. Their feasibilities were investigated in different wave environments. Seo and Kim (2011) performed 4-DOF numerical maneuvering simulation coupled with ship motion in the presence of incident waves. They estimated second-order mean drift forces by using a direct pressure integration method, while the ship maneuvering problem was solved by using a MMG model. A state-of-art study about two-time scale method which was used to predict turning trajectory of a ship in regular waves can be found in Zhang and Zou (2017). Different from two-time scale methods, hybrid methods are also widely used in many studies (Fang et al., 2005; Fournarakis et al., 2016; Cura-Hochbaum and Uharek, 2016). Basically, this approach combines the maneuvering and seakeeping motions in a set of motion equations and can be adopted to mathematical models in different ways. A wider literature about maneuvering in waves can be found in (Sukas et al., 2017a; 2017b).

In this study, the maneuvering motion of DTC container vessel is numerically simulated in regular waves. The mathematical model for maneuvering simulation is based on MMG model, while the wave forces are calculated by an empirical expression proposed by Ankudinov(1985). Hydrodynamic derivatives were determined by CFD in calm water. Propeller parameters were calculated from self-propulsion estimations and rudder parameters were taken from the empirical relations suggested by (Yoshimura and Masumoto, 2012). Turning circle trajectories were predicted both in calm water and in waves for different wave headings. The predicted turning trajectories were compared with the model tests, which were conducted at MARINTEK in the framework of the SHOPERA project.

2 HYDROSTATIC PROPERTIES OF THE SHIP

The ship considered in this study is the benchmark Duisburg Test Case (DTC) Post-Panamax Container Ship. It is a 14000TEU container ship developed solely for benchmarking and validation purposes by the Institute of Ship Technology, Ocean Engineering and Transport Systems (ISMT). The ship only exists as a virtual CAD model. It is a single-screw vessel which has a bulbous bow.

A 1/100 model scale was taken into consideration in this study. There are results for different model scales in the literature but no tests were carried out for this model scale. Model scale was intentionally chosen to carry out experiments in Ata Nutku Towing Tank Laboratory of Istanbul Technical University in the future. The hydrostatic and geometric properties of the ship are given in Table 1 for both full and 1/100 model scales.

Water density was taken as $\rho = 997.561 kg/m^3$. The moment of inertia of the ship was calculated by;

$$I = \Delta * k^2$$

The vertical center of the full scale ship was over the free surface; $VCG = 19.851m$ measured from the baseline. Due to double body flow simulation which only takes into account the underwater hull form, vertical center of gravity of the ship in this study was taken as $VCG = 0$. The value given for longitudinal center of gravity, LCG, in the table is the distance from the aft perpendicular.

Table 1. Hydrostatic and geometric properties of Duisburg Test Case (DTC).

	Units	Full Scale 1:1	Model Scale 1:100
L_{pp}	m	355	3.55
B_{wl}	m	51	0.51
T_m	m	14.5	0.145
∇	m^3	173467	0.1735
C_B	-	0.661	0.661
S	m^2	22032	2.2032
Δ	kg	$1.73*10^8$	173.0439
LCG	m	174.059	1.7406
U	kn	6	0.6
k_{xx}	m	20.25	0.2025
k_{yy}	m	88.19	0.8819
k_{zz}	m	88.49	0.8849

Table 2. Test matrix of numerical simulations.

TESTS	$U\ (m/s)$	$\beta\ (deg)$	$\psi\ (deg)$	y_{max}/L	$r_{max} * L/U$	$\omega L/U$
Static Drift (SD)	0.3086	12	0	0	0	0
	0.3086	9	0	0	0	0
	0.3086	6	0	0	0	0
	0.3086	3	0	0	0	0
SD and PY	0.3086	0	0	0	0	0
Pure Yaw (PY)	0.3086	0	-5.71 / 5.71	0.040	0.25	2.5
	0.3086	0	-6.84 / 6.84	0.048	0.30	2.5
	0.3086	0	-7.97 / 7.97	0.056	0.35	2.5
PY and YD	0.3086	0	-4.57 / 4.57	0.032	0.20	2.5
Yaw and Drift (YD)	0.3086	2	-2.57 / 6.57	0.032	0.20	2.5
	0.3086	4	-0.57 / 8.57	0.032	0.20	2.5
	0.3086	6	1.43 / 10.57	0.032	0.20	2.5
	0.3086	8	3.43 / 12.57	0.032	0.20	2.5
	0.3086	12	7.43 / 16.57	0.032	0.20	2.5

3 DETERMINATION OF HYDRODYNAMIC DERIVATIVES

The maneuvering ability of DTC was determined by numerically simulating the captive model tests. The advantage of this system based maneuvering simulation is the practicality in simulation of any desired ship trajectory. Hydrodynamic derivatives are computed and used in the motion equations in this method. Compared to the direct CFD based maneuvering simulation methods (where no hydrodynamic derivative is calculated), this approach reduces time and cost of numerical simulations.

The hydrodynamic derivatives were calculated by curve-fitting force and moment data obtained from PMM tests. Curve-fitting was applied directly in static drift tests but for dynamic tests (pure yaw and yaw and drift cases) the multiple-run method (MR) was used.

3.1 MULTIPLE-RUN (MR) METHOD

Hydrodynamic derivatives from pure yaw and yaw and drift simulations can be determined by the Multiple-run method. Force and moment data from dynamic tests were used to calculate both the low-order and high-order harmonics at different yaw rates and drift angles. These harmonics were then used for curve-fitting and calculating the hydrodynamic derivatives. Harmonics were calculated by the equations given below:

$$f_0 = \frac{1}{T}\int_0^T f(t)dt$$
$$f_{C_n} = \frac{2}{T}\int_0^T f(t)\cos(n\omega t)\,dt \qquad (1)$$
$$f_{S_n} = \frac{2}{T}\int_0^T f(t)\sin(n\omega t)\,dt$$

In these equations $f = X, Y, N$ and $n = 1,2,3$. Period was calculated by $T = 2\pi/\omega$. Derivatives were determined by PMM tests over a range of parameters such as r_{max} or v (or β). Polynomial functions, which can be denoted by $f(x)$, were fitted with respect to these parameters. In this case $x = r_{max}$ or v.

3.2 PMM TEST CONDITIONS

The PMM test conditions used in numerical simulations are given in Table 2. Conditions about the selection of test cases are given below:

- Drift angle β for the static drift case was limited between $0° \leq \beta \leq 12°$ to avoid stall.
- Range of the lateral amplitude y'_{max} was selected to be lower than $y'_{max} < 0.06$ for all dynamic PMM tests in this study.
- ITTC recommends non-dimensional circular frequency $\omega_1 = \omega L/U$ to be between $2 < \omega_1 < 3$ for yaw tests (ITTC 7.5-02-06-02; 2014).
- Range of yaw rates r'_{max} in PMM tests usually lie between $0.2 \leq r'_{max} \leq 0.75$ according to (ITTC 7.5-02-06-02; 2014).
- Heading angle ψ was limited between $-20° < \psi < 20°$.
- Maximum tangent of model trajectory was limited to $\varepsilon < 0.15$ to prevent violation of steady advance speed condition (Yoon, 2009).
- Combining two recommendations of the ITTC given above and avoiding risks of stall and steady advance speed violation; ranges of r'_{max} and ω_1 got bounded. Therefore; for pure yaw and yaw and drift simulations in this study, the non-dimensional frequency was set fixed to $\omega_1 = 2.5$ and the maximum yaw rate range was $0.2 \leq r'_{max} \leq 0.35$.

Some numerical simulations were used in multiple tests. $\beta = 0°$ case of static drift tests can also be regarded as $r'_{max} = 0$ of pure yaw. Therefore, zero-drift angle case $\beta = 0°$ was used both in static drift and pure yaw. The other zero-drift angle case where $r'_{max} = 0.20$ can also be regarded as $\beta = 0°$ case of yaw and drift tests. This case ($\beta = 0°$ and $r'_{max} = 0.20$) was both used in pure yaw and yaw and drift.

4 NUMERICAL IMPLEMENTATION

Numerical PMM tests were carried out at a low speed of 6 knots ($Fr = 0.0523$). Due to the relatively low Froude number in maneuvering, no free surface effects were included in the computations. Only the underwater part of the hull was modeled and symmetry condition was imposed at the upper boundary to simulate the PMM tests as a double body. Star CCM+ version 10.02.010 was used for simulations.

The size of the fluid domain (16m x 10m x 3m) was in correspondence with the recommendations of the ITTC (7.5-03 04-01, 2011). The inlet and outlet boundary conditions were selected as velocity inlet and pressure outlet respectively. Velocity inlet boundary condition was imposed on side and bottom walls and symmetry condition on the upper wall (due to double body flow simulation), where free water surface normally exists. Figure 1 shows the fluid domain and its properties.

Small differences in the number of elements in the fluid domain might apply depending on the drift angle of the ship. For $\beta = 0°$ case number of elements were around 1.026M, while it was 1.041M for $\beta = 12$. Base sizes of 0.01m on the hull and 0.16m on side walls, bottom wall, inlet and outlet were selected. 0.16m was also the maximum cell size in the whole fluid domain. Element sizes linearly increased within the distance between the hull and the outer boundaries. For resolving the boundary layer; 8 prism layers were implemented on the hull, the closest having 0.000625m height. Refinements on the hull were made to places where high pressure gradients are likely to occur. A coarse mesh view on the hull and intersecting planes are given in Figure 2.

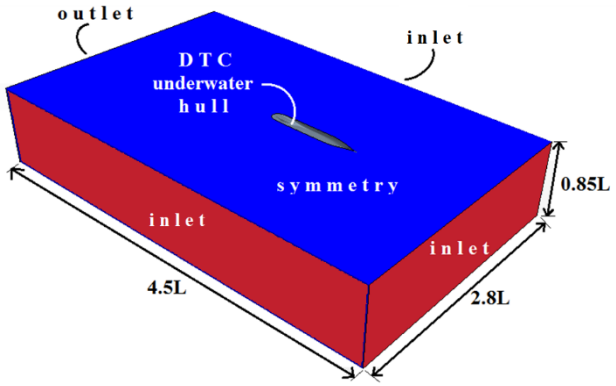

Figure 1. A view of the fluid domain.

Due to slender form of the hull ($L/B \approx 7$) $k-\epsilon$ turbulence model was selected to solve for the turbulent flow around the ship (Duman and Bal, 2017). The steady solver was used for static drift tests and the implicit unsteady solver was selected for pure yaw and yaw and drift due to the nature of dynamic tests. Time step was taken as $\Delta t = 0.04s$ in dynamic tests which corresponds to $\Delta t \approx T/750$.

There were 5 inner iterations at each time step. For dynamic tests, at least two periods of motion were solved before extracting the force and moment data from the simulations.

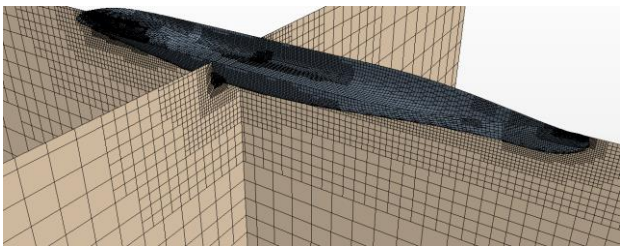

Figure 2. Coarse mesh structure on the hull.

5 UNCERTAINTY OF NUMERICAL SIMULATIONS

Uncertainty of numerical simulations were calculated based on the verification and validation procedure proposed by (Stern et al., 2001). Calculations were made for static drift test at $\beta = 0$. Surge force X was taken as the integral variable. Static drift tests were steady; therefore, time step uncertainty U_T was not applicable. In this case the total numerical uncertainty U_N would be,

$$U_N = \sqrt{{U_I}^2 + {U_G}^2} \qquad (2)$$

where U_I is the iterative uncertainty and U_G is the grid uncertainty. The upper and lower bounds (S_U and S_L respectively) of the surge force are given in Table 3, with the iterative uncertainties for each grid system.

Table 3. Upper and lower bounds of the integral variable in different grids.

	Grid 3	Grid 2	Grid 1
No. of elements	390k	1026k	2697k
S_U	0.5292	0.5607	0.5648
S_L	0.5291	0.5605	0.5641
S_G	0.5292	0.5606	0.5645
U_I	5E-05	1E-04	3.5E-04
$100 * U_I/S_G$	0.01	0.02	0.06

Ratio of the iterative uncertainty U_I is very small as compared to the integral variable S_G at each grid (i.e. 0.02% at grid 2). Therefore, it was considered as a fair assumption to take $U_I \approx 0$. In this case, the total uncertainty becomes equal to the grid uncertainty. Grid convergence parameters are given in Table 4. It can be observed from this table that the grid uncertainty is $U_G = 11\%S_G$ for grid 2.

Table 4. Parameters for grid convergence.

ε_{21}	ε_{32}	R_{G_2}	r_G	p_G	δ_{RE}	C_G	U_G
-0.004	-0.032	0.122	1.38	6.518	-0.004	7.922	0.065

For the verification part; experimental results for this model scale is not present in the literature. Therefore, surge force for the underwater part of the hull was calculated by $R_T = R_V = (1 + k)R_F$ (in this case $R_T = R_V$ due to double body model). ITTC-1957 frictional correlation line for the frictional resistance was used to calculate C_F to find R_F. The form factor was taken from the experiments of (el Moctar et al., 2012) and it is given as $k = 0.094$ in the reference study. Please refer to the end of the section entitled "static drift tests" in the next section for details.

The surge force was calculated by the method described above and taken as *data* in validation study. In this case, the error becomes $|E| = 0.0336$ which is 6.38% of S_G. Therefore, $|E| < U_G$ and the simulation results are validated.

6 PMM TEST RESULTS

Numerical PMM tests in this study include static drift tests, pure yaw tests and yaw and drift tests. Pure sway tests were not carried out due to the structure of the MMG modular mathematical model. Hydrodynamic derivatives that are related to added mass terms in MMG model were not obtained by pure sway tests; but instead, estimations of these terms were made using Motora's empirical charts (Motora, 1959; Motora, 1960a; Motora; 1960b) as advised by (Yasukawa and Yoshimura, 2015). Rudder tests to obtain parameters related to rudder were also numerically simulated but it is explained in Section 7.2.

Table 5. Static drift results of DTC from Papanikolaou et al. (2016). The model scale is 1/63.65.

$\beta\ (deg)$	v'	EFD			CFD		
		${X'}_H$	${Y'}_H$	${N'}_H$	${X'}_H$	${Y'}_H$	${N'}_H$
0	0	-0.01714	0	0	-0.01621	0	0
5	-0.087	-0.01836	0.015179	0.008569	-0.01702	0.013172	0.008667
10	-0.174	-0.01959	0.030359	0.017113	-0.01763	0.036724	0.016624
15	-0.259	-0.02079	0.045538	0.025707	-0.01856	0.052638	0.026197
20	-0.342	-0.02306	0.108948	0.032807	-0.01993	0.09989	0.032562

6.1 STATIC DRIFT TESTS

Static drift tests were carried out numerically and three surge derivatives (R'_0, X'_{vv} and X'_{vvvv}) and four sway derivatives (Y'_v, Y'_{vvv}, N'_v and N'_{vvv}) were obtained and compared with the results given in (Papanikolaou et al., 2016). The reference study has both experimental and numerical results for a model scale of $\alpha = 1/63.65$ while the model scale in the present study was $\alpha = 1/100$.

Non-dimensionalization in (Papanikolaou et al., 2016) was made by dividing the hydrodynamic forces by $^1/_2\,\rho U^2 L^2$ and hydrodynamic moment by $^1/_2\,\rho U^2 L^3$. However; due to the mathematical model, non-dimensionalization in this study was made by;

$$X'_H = \frac{X_H}{^1/_2\rho U^2 LT} \quad Y'_H = \frac{Y_H}{^1/_2\rho U^2 LT} \quad N'_H = \frac{N_H}{^1/_2\rho U^2 L^2 T} \qquad (3)$$

Therefore, results presented in the reference study was multiplied by L/T to be able to make a proper comparison between results. Experimental and numerical static drift results in (Papanikolaou et al., 2016) are given in Table 5 for a drift angle range of $0° < \beta < 20°$.

Numerical study was carried out using a steady solver in this study. Therefore, range of β was constrained to prevent stall that might occur at high drift angles. Static drift test results obtained in this study for a model scale of $\alpha = 1/100$ is given in Table 6 for $0° < \beta < 12°$. Results presented in these tables are graphically compared in Figure 3. There was a good agreement between results except the surge forces. Non-dimensional sway velocity v' was obtained by using the equation;

$$v' = -\sin\beta \qquad (4)$$

Table 6. Static drift results of DTC of this study. The model scale is 1/100.

$\beta\ (deg)$	v'	X'_H	Y'_H	N'_H
0	0	-0.0229	0	0
3	-0.0523	-0.0226	0.0062	0.0057
6	-0.1045	-0.0221	0.0154	0.0112
9	-0.1564	-0.0218	0.0283	0.0166
12	-0.2079	-0.0205	0.0446	0.0230

Hydrodynamic derivatives from the static drift tests were obtained from the data taken over the range of drift angle β. Using the polynomial functions;

$$\begin{aligned} X'_H &= -R'_0 + X'_{vv}v'^2 + X'_{vvvv}v'^4 \\ Y'_H &= Y'_v v' + Y'_{vvv}v'^3 \\ N'_H &= N'_v v' + N'_{vvv}v'^3 \end{aligned} \qquad (5)$$

per the implemented mathematical model, a curve was fitted and hydrodynamic derivatives were derived. Results are presented in Table 7.

Table 7. Hydrodynamic derivatives obtained from static drift tests.

	EFD	Papanikolaou et al. (2016)	Present study
R'_0	0.0176	0.0165	0.0228
X'_{vv}	-0.0617	-0.0383	0.0428
X'_{vvvv}	0.1304	0.0762	0.2080
Y'_v	-0.0903	-0.1445	-0.1253
Y'_{vvv}	-1.86	-1.214	-2.0960
N'_v	-0.1005	-0.1006	-0.1043
N'_{vvv}	0.0359	0.0392	-0.1397

There is a satisfactory agreement for the linear terms Y'_v and N'_v but the difference is larger for the nonlinear terms. It can be said that both numerical studies were unable to retain the experimental results for the higher order terms. On the other hand, the difference in R'_0 values in this study is accounted to the smaller model scale. The hydrodynamic derivative R'_0 is actually a form of the frictional resistance coefficient C_F (only the non-dimensionalization is different) and it is known that frictional resistance coefficient increases as the model scale decreases. It might be useful here to remember the ITTC-1957 frictional correlation line, given as;

$$C_F = \frac{0.075}{(\log Re - 2)^2} \qquad (6)$$

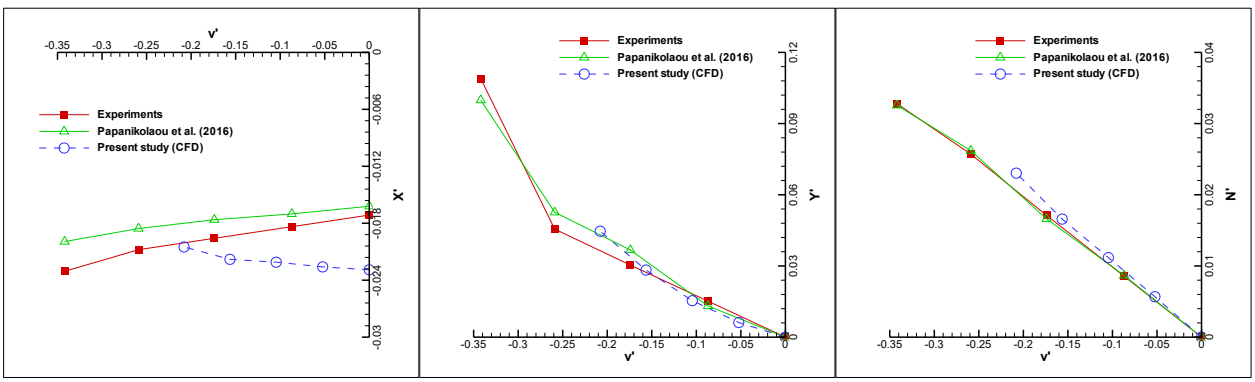

Figure 3. Non-dimensional hydrodynamic forces (X', Y') and (N') from static drift tests compared with other results in literature. The difference in model scales between the present study and other studies should be noted.

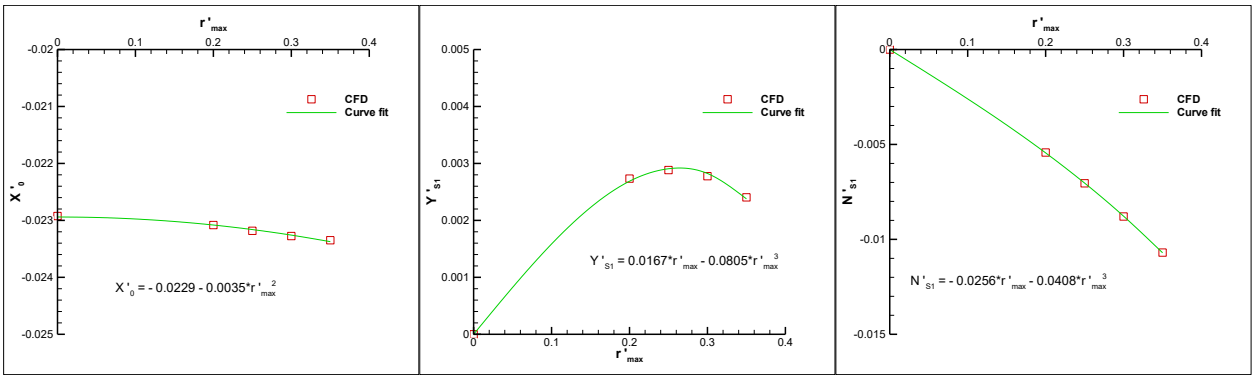

Figure 4. Non-dimensional low-order harmonics from pure yaw tests obtained by multiple run method. Fitted polynomial functions are also provided in graphs.

Since numerical results were obtained for a double body solution ignoring free surface effects, R'_0 can be calculated using the ITTC-1957 frictional correlation line and the form factor provided in (el Moctar et al., 2012) which is $1+k=1.094$. In this case, the total resistance R_T (and the surge force X_H) for the double body DTC would be $X_H = R_T = R_V$ (Kinaci et al., 2016). Comparison between empirically obtained R'_0 versus the numerically obtained one is given in Table 8.

Table 8. Empirical calculation of R'_0 and comparison with numerical results.

α	C_F (-)	R_F (N)	R_V (N)	R'_0 (emp)	R'_0 (CFD)
1/63.65	0.003997	1.623	1.775	0.0187	0.0165*
1/100	0.004601	0.482	0.527	0.0215	0.0228**

* Numerical result of Papanikolaou et al. (2016).
** Numerical result of this study.

6.2 PURE YAW TESTS

Numerical pure yaw tests were carried out to derive yaw related derivatives (X'_{rr}, Y'_r, Y'_{rrr}, N'_r and N'_{rrr}). The dynamic tests were numerically simulated for four yaw rates of $r'_{max}=0.2$, $r'_{max}=0.25$, $r'_{max}=0.30$ and $r'_{max}=0.35$. These yaw rates correspond to a non-dimensional circular frequency of $\omega_1=2.5$ and are in accordance with the recommendations of the ITTC (7.5-02-06-02, 2014). An additional case was taken into calculations from the static drift tests where $\beta=0$. This static drift case of $\beta=0$ can also be regarded as a pure yaw test where $r'_{max}=0$. Due to the nature of dynamic PMM tests, the implicit unsteady solver of the software was used. Results are provided in Figure 4. Hydrodynamic forces and moments in this figure were obtained using a low-order multiple run method, MR_L (Yoon, 2009). Then; using the sets of the harmonic data from the PMM tests, a polynomial function was fitted which helps in determining the hydrodynamic derivatives from pure yaw tests. The polynomial functions are also provided in Figure 4.

The mathematical model simplified for pure yaw test can be given as follows:

$$\begin{aligned} X'_H &= -R'_0 + (X'_{rr} + x'_G m')r'^2 \\ Y'_H &= (Y'_r - m - m'_x)r' + Y'_{rrr}r'^3 \\ N'_H &= (N'_r - x'_G m')r' + N'_{rrr}r'^3 \end{aligned} \tag{7}$$

Equations of polynomial functions in Figure 4 were used with the equation set provided above to derive the maneuvering coefficients that can be determined from pure yaw tests. It should be noted that the sway equation (Y'_H and N'_H) contains the inertial terms (m' and m'_x) due to the effects of centrifugal force and added mass. Obtained results were compared with the empirical relations provided by (Yoshimura and Masumoto, 2012) and provided in Table 9. A fair agreement was found between numerical and empirical results.

Table 9. Numerical pure yaw test results of DTC in comparison with the empirical relations provided by Yoshimura and Masumoto (2012).

	Yoshimura and Masumoto (2012)	Present study
X'_{rr}	0.0016	-0.0071
Y'_r	0.0566	0.2161
Y'_{rrr}	-0.0510	-0.1074
N'_r	-0.0374	-0.0256
N'_{rrr}	-0.0323	-0.0544

6.3 YAW AND DRIFT TESTS

Yaw and drift tests were numerically simulated to obtain coupled derivatives (X'_{vr}, Y'_{vvr}, Y'_{vrr}, N'_{vvr} and N'_{vrr}). The dynamic tests were carried out at a yaw rate of $r'_{max}=0.20$ and drift angles $\beta=2°, 4°, 6°, 8°$ and $12°$. Using the results from pure yaw test ($r'_{max}=0.20$ and $\beta=0°$), derivatives were obtained using six numerical simulations. The mathematical model simplified for yaw and drift can be given as follows:

$$\begin{aligned} X'_H &= -R'_0 + X'_{vv}v'^2 + \left(X'_{vr} + m + m'_y\right)v'r' \\ &\quad + X'_{rr}r'^2 + X'_{vvvv}v'^4 \\ Y'_H &= Y'_v v' + (Y'_r - m - m'_x)r' + Y'_{vvv}v'^3 \\ &\quad + Y'_{vvr}v'^2 r' + Y'_{vrr}v'r'^2 + Y'_{rrr}r'^3 \\ N'_H &= N'_v v' + (N'_r - x'_G m')r' + N'_{vvv}v'^3 \\ &\quad + N'_{vvr}v'^2 r' + N'_{vrr}v'r'^2 + N'_{rrr}r'^3 \end{aligned} \tag{8}$$

Similar to pure yaw case; the inertial terms, due to the effects of centrifugal force and added mass, are included in these equations. A low-order multiple run method, MR_L, was used to calculate the low-order harmonics (X'_{S1}, Y'_0, Y'_{S1}, N'_0 and N'_{S1}) and the high-order multiple run method, MR_H, to calculate the high-order harmonics (Y'_{C2}, N'_{C2}). Polynomial functions were fitted to the harmonic data obtained from yaw and drift tests. Polynomial function equations for each harmonic are given below:

$$\begin{aligned} X'_{S1} &= r'_{max}\left(X'_{vr} + m + m'_y\right)v' \\ Y'_0 &= \left(\frac{Y'_{vrr}r'^2_{max}}{2} + Y'_v\right)v' + Av'^3 \quad \text{or} \\ Y'_{C2} &= -\frac{Y'_{vrr}r'^2_{max}}{2}v' \\ Y'_{S1} &= B + Y'_{vvr}r'_{max}v'^2 \\ N'_0 &= \left(\frac{N'_{vrr}r'^2_{max}}{2} + N'_v\right)v' + Cv'^3 \quad \text{or} \\ N'_{C2} &= -\frac{N'_{vrr}r'^2_{max}}{2}v' \\ N'_{S1} &= D + N'_{vvr}r'_{max}v'^2 \end{aligned} \tag{9}$$

A, B, C and D are constants in these equations and their values are trivial. After graphing the results from yaw and drift tests with respect to non-dimensional sway velocity v', coupled derivatives were obtained using polynomial function equations. Sway force and moment derivatives in polynomial function equations can be taken from static drift test results but it was not needed in this study because Y'_{C2} and N'_{C2} were used to obtain Y'_{vrr} and N'_{vrr}. Hydrodynamic derivatives obtained from yaw and drift tests are given in Table 10. Results can be compared from the same table with the empirical formulations given by (Yoshimura and Masumoto, 2012).

Table 10. Hydrodynamic derivatives of DTC obtained from numerical simulations of yaw and drift tests.

	Yoshimura and Masumoto (2012)	Present study
X'_{vr}	0.0641	-0.2156
Y'_{vvr}	-0.75	-1.099
Y'_{vrr}	-0.7251	-0.6655
N'_{vvr}	-0.6132	-0.768
N'_{vrr}	0.2754	-0.18

7 CONTROL SURFACE PARAMETERS AT SELF-PROPULSION

MMG mathematical model allows superposition of forces and moment from the hull and its control surfaces. Hydrodynamic derivatives of hull were presented in the previous section. In this section, propeller and rudder parameters at self-propulsion point of the ship was presented. Propeller parameters were obtained combining the experimental results with basic engineering knowledge while rudder parameters were obtained by numerical simulations.

7.1 PROPELLER PARAMETERS

Propeller parameters in MMG mathematical model were obtained by traditional engineering approach as explained in (Kinaci et al., 2018). In this approach; when the total bare hull resistance R_T, wake fraction w, thrust deduction factor t and open-water propeller performance curve are known apriori, the self-propulsion parameters can be calculated by hand. Bare hull resistance at $U = 0.3086m/s$ (corresponding to 6knots in full scale ship) was found to be $R_T = 0.56N$. The other required parameters were taken from (Kinaci et al., 2018) and given in Table 11.

Table 11. Self-propulsion parameters for DTC. w and t were taken from (Kinaci et al., 2018).

R_0 (N)	w_{P0} (-)	t_P (-)
0.56	0.268	0.188

According to (Kinaci et al.; 2018), self-propulsion is achieved when,

$$R_0 - SFC = T(1 - t_P) \tag{10}$$

Thrust T is calculated by,

$$T = K_T \rho n^2 D^4 \tag{11}$$

Water density was taken as $\rho = 997.561kg/m^3$ and the propeller dimension for a $1/100$ scaled DTC would be $D = 0.089m$. K_T is taken from open-water propeller performance curves. So for each rotation rate n, thrust T could be calculated. The skin friction correction according to (ITTC 7.5-02-03-01.4, 2011) for $1/100$ scaled DTC was $SFC = 0.33N$. In this case, self-propulsion equation becomes;

$$0.56N - 0.33N = T(1 - 0.169)$$

Using the open-water propeller performance diagram of DTC, which is available in (el Moctar, Shigunov and Zorn; 2012), the rotation rate that satisfies self-propulsion equation was found to be $n = 4.42rps$. Propeller parameters used in maneuvering mathematical model are given in Table 12.

Table 12. Propeller parameters used as inputs for the MMG mathematical model.

D (m)	n (rps)	t_P (-)	x_P (-)
0.089	4.42	0.188	-0.48

w_{P0} (-)	k_0 (-)	k_1 (-)	k_2 (-)
0.268	0.513	-0.419	-0.098

7.2 RUDDER PARAMETERS

The hydrodynamic forces and moment due to steering of the rudder were estimated based on the rudder normal force (F_N) as follows (Yasukawa and Yoshimura, 2015):

$$\begin{aligned} X_R &= -(1-t_R)F_N sin\delta \\ Y_R &= -(1+a_H)F_N cos\delta \\ N_R &= -(x_R + a_H x_H)F_N cos\delta \end{aligned} \quad (12)$$

where t_R, a_H and x_H are called as hull-rudder interaction parameters. x_R is the longitudinal distance of rudder from midship and δ is rudder angle. It should be noted that tangential component of the rudder force was neglected in rudder force and moment equations. Hull-rudder interaction coefficients are calculated from the empirical relations given by (Yoshimura and Masumoto, 2012). These relations are as follows:

$$\begin{aligned} 1-t_R &= 0.32\tau' + 0.61 \\ a_H &= 3.6C_B * B/L \\ {x_H}' &= -0.4 \end{aligned} \quad (13)$$

Our calculations are made for a fixed ship; therefore, trim of the ship in this study is neglected in formulations ($\tau' = 0$). Rudder normal force (F_N) is expressed as (Yasukawa and Yoshimura, 2015):

$$F_N = 0.5\rho A_R[{u_R}^2 + {v_R}^2]\frac{6.13\Lambda}{\Lambda + 2.25}\sin\alpha_R \quad (14)$$

where ρ is the water density, A_R is profile area of the moveable part of the rudder and Λ is the rudder aspect ratio. The effective rudder angle in maneuvering motion is defined as the following equation.

$$\alpha_R = \delta - \tan^{-1}\left(\frac{v_R}{u_R}\right) \quad (15)$$

The longitudinal and lateral rudder inflow velocities in rudder normal force equation are determined by the following expressions:

$$\begin{aligned} u_R &= \varepsilon u(1 - w_P)\sqrt{\eta\left\{1+\kappa\left(\sqrt{1+\frac{8K_T}{\pi(J_p)^2}}-1\right)\right\}^2 + (1-\eta)} \\ v_R &= U\gamma_R(\beta - l'_R r') \end{aligned} \quad (16)$$

w_P is the effective wake fraction in maneuvering motion. η denotes the ratio of propeller diameter to rudder span, $\eta = 0.6923$. Necessary coefficients ε and κ to calculate u_R for merchant vessels are given as (Yoshimura and Masumoto, 2012):

$$\begin{aligned} \varepsilon &= 2.26 - 1.82(1-w) \\ \kappa &= 0.55/\varepsilon \end{aligned} \quad (17)$$

The flow straightening coefficient of rudder (γ_R) and the flow straightening factor due to yaw rate ($l'_R = l_R/L$) were assumed as symmetrical for port and starboard turnings and estimated by the formulas proposed by Yoshimura and Masumoto (2012) as follows:

$$\begin{aligned} l'_R &= -0.9 \\ \gamma_R &= \frac{2.06C_B B}{L} + 0.14 \end{aligned} \quad (18)$$

All parameters related to rudder force and moment are given in Table 13.

Table 13. Parameters obtained by CFD and empirical formulas related to rudder.

Parameters	Source	Value
x'_R	Ship Geometry	-0.5
A'_R	Rudder Geometry	0.0095
Λ	Rudder Geometry	1.756
η	Prop. & Rudder Geom.	0.6923
a_H	Yoshimura and Masumoto (2012)	0.34
t_R		0.39
x'_H		-0.40
ε		0.93
κ		0.59
γ_R		0.33
l'_R		-0.9

8 TURNING CIRCLE MANEUVERING RESULTS

Using the hydrodynamic derivatives presented in the preceding sections, maneuvering aspects in calm water and in-waves were investigated in this section. The derivatives are utilized with the MMG mathematical model and the turning circle results are compared with the experiments conducted by MARINTEK (Sprenger et al.; 2017). Equation of motion is solved by an in-house code called MANSIM which exhibits a modular structure to include external disturbances in maneuvering.

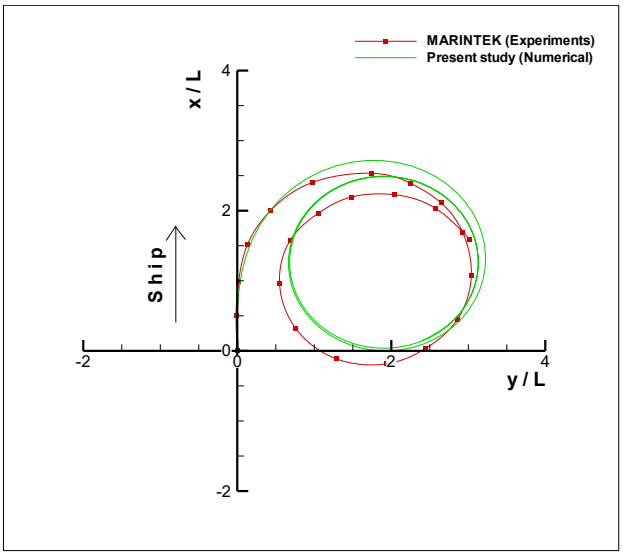

Figure 5. Experimental and numerical turning circle maneuver of DTC.

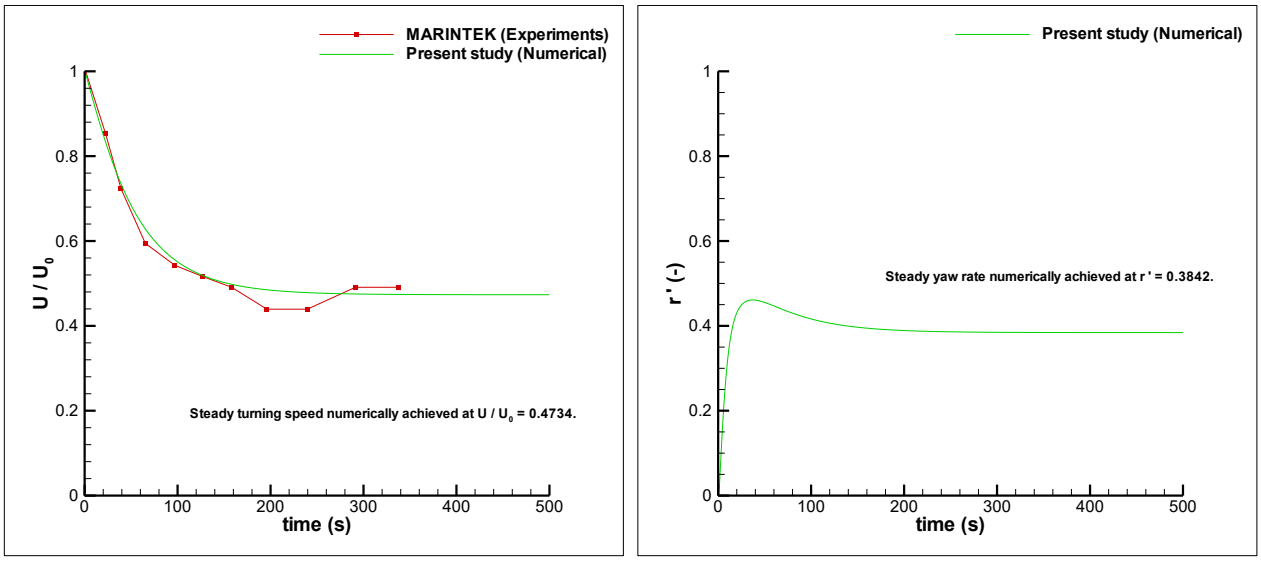

Figure 6. Speed loss (left) and yaw rate (right) of DTC in calm water.

8.1 MANEUVERING IN CALM WATER

Control surface parameters at self-propulsion are used with the hull hydrodynamic derivatives obtained by numerical PMM tests and the turning ability of DTC in calm water was calculated. Comparison with experiments is given in Figure 5.

Parameters associated with the turning circle definitive maneuver obtained numerically is compared with the empirical formulations suggested by (Lyster and Knights; 1979) and given in Table 14. There was a noticeable discrepancy in results. All computational results were lower compared to empirical formulations; having the highest difference in the transfer distance of the ship. The speed and yaw rate during the turning in time domain is given in Figure 6.

8.2 MANEUVERING IN WAVES

Numerical maneuvering derivatives, self-propulsion estimates and empirical rudder parameters in calm water were used along with Ankudinov's (1985) empirical relations to calculate the turning circle trajectory of DTC in waves. Forces and moment, which are obtained by empirical approach given in equation (19), were added to the right hand side of the MMG mathematical model as an external disturbance. Ankudinov's equation set was modified for infinite wave period and water depth. Due to the modular structure of the model, maneuvering and wave forces do not interact with each other. Hydrodynamic forces and propulsion properties were estimated in calm water conditions. Rudder was set to starboard with an angle of $\delta = 35°$.

$$
\begin{aligned}
X_W &= \left[0.0388\rho g B C_B {H_{1/3}}^2 + 0.311\rho g B^2 \frac{{H_{1/3}}^{2.5}}{L^{1.5}}\right]\cos\theta_w \\
Y_W &= \left[0.0388\rho g L {H_{1/3}}^2\right]\sin\theta_w \\
N_W &= \left[-0.125\rho g L T {H_{1/3}}^2\right]\cos\theta_w \sin\theta_w - 0.03 Y_W L
\end{aligned}
\tag{19}
$$

It should be noted here that in equation set (19), water density is given in terms of $tonnes/m^3$. Trajectories of DTC in turning circle test are given in Figure 7 for a time period of $t = 500s$. Numerical results obtained in this study are compared with the experimental results presented in (Sprenger et al.; 2017) except $\theta_w = 270°$ case, which is not provided in the reference article. The wave periods for all cases in this section are infinite, $T = \infty$. Overall, maneuvering results in waves obtained numerically have a higher drift when compared with experiments. There are two distinct reasons for this difference. The first is due to the higher steady turning diameter in calm water numerical results. The second reason is the deviation between the target and the measured wave heights in experiments. It is mentioned in the reference article that the target wave height was $H = 0.02m$ but the measured value was $H \approx 0.018m$. The drift in experiments would have been higher had the targeted wave height been achieved. On the other hand, the direction of the drift is generally in accordance with experiments.

Table 14. Comparison of numerical and empirical turning indices in calm water (Lyster and Knights; 1979).

	Advance	Transfer	Tactical Diameter	Steady Turning Diameter	Steady Yaw Rate	Steady Turning Speed
Present study	2.6890	1.5633	3.2286	2.5792	0.3842	0.4734
Lyster and Knights (1979)	3.3970	1.9144	3.9827	3.5529	-	0.4437

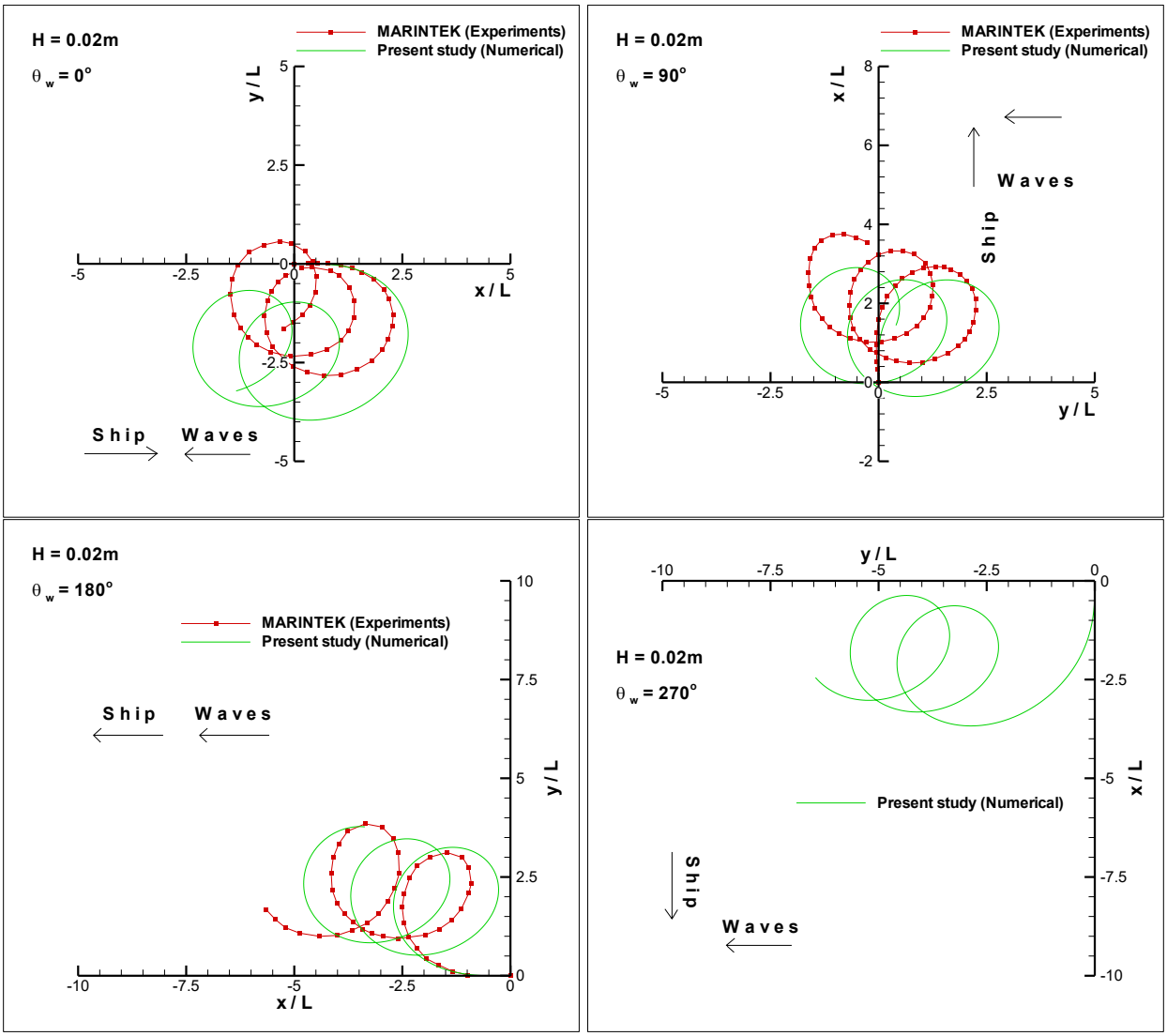

Figure 7. DTC turning circle in waves. Significant wave height is $H_{1/3} = 0.02m$. Wave heading angles $\theta_w = 0°$ (top left), $\theta_w = 90°$ (top right), $\theta_w = 180°$ (bottom left) and $\theta_w = 270°$ (bottom right). Experimental results are taken from (Sprenger et al.; 2017).

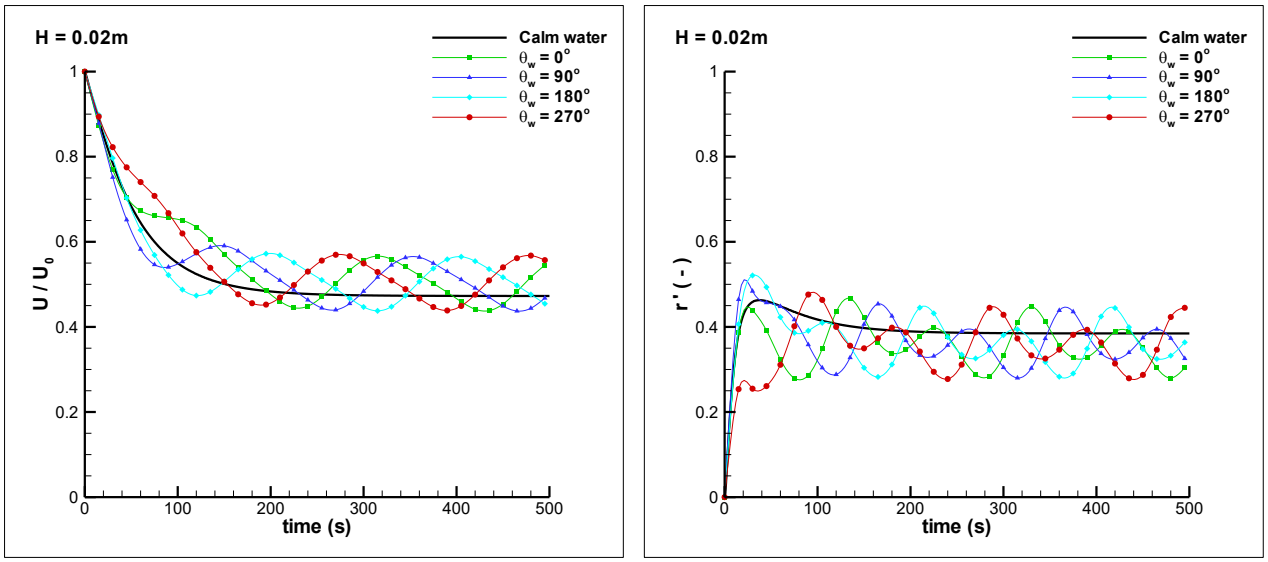

Figure 8. Speed losses (left) and yaw rates (right) of DTC at different wave headings in comparison with calm water case.

Speed losses and yaw rates in waves as compared to the calm water case are given in Figure 8. The speed U/U_0 and the yaw rate r' reach a stable value after some time during the turning circle in calm water. However, they have oscillatory behavior in waves. The drift of the ship during maneuvering in waves change the speed and the yaw rate in time as well as the ship's course. Still, they are periodic and oscillate around the stable value of the calm water case. Another thing to note in this figure is that there is only a phase difference in speed and yaw rate when the ship is subjected to different wave headings.

9 CONCLUSIONS

In this study; the turning ability of the benchmark ship, Duisburg Test Case, was obtained both in calm water and in waves at a relatively low speed. Hydrodynamic derivatives from calm water PMM tests and control surface parameters at self-propulsion were used to calculate forces and moments that the modular mathematical model requires. A good agreement with experiments was found for calm water case. Effect of waves was introduced in the mathematical model in terms of forces and moments using Ankudinov's (1985) empirical relations. The turning circle trajectory in waves was then extracted and compared with experiments. Both the turning diameter and the drift of the ship in waves were in good accordance.

Although there are several experimental results showing the turning circle and zigzag trajectories of DTC in the literature, there is no study (at least to the authors' knowledge) presenting the experimentally obtained hydrodynamic derivatives. PMM experiments of DTC are planned in the future to calculate the hydrodynamic derivatives experimentally. It is expected that the numerical derivatives presented in this study will then be fully validated.

10 ACKNOWLEDGEMENTS

The first author was supported by Research Fund of the Istanbul Technical University. Project Number: 41103. The authors would like to express their thanks to Prof. Kadir Sarioz for his valuable guidance throughout the study.

11 REFERENCES

Ankudinov V., 1985. Ship Maneuvering Simulation Model Including Regimes of Slow Speeds and Large Drift Angles. MARSIM 85, Munich, Germany.

Chillcce, G., el Moctar, O., 2018. A numerical method for manoeuvring simulation in regular waves. Ocean Eng. 170, 434–444. https://doi.org/10.1016/j.oceaneng.2018.09.047

Cura-Hochbaum, A., Uharek, S., 2016. Prediction of Ship Manoeuvrability in Waves Based on RANS Simulations. 31st Symp. Nav. Hydrodyn. 11–16.

Duman, S., Bal, S., 2017. Prediction of the turning and zig-zag maneuvering performance of a surface combatant with URANS. Ocean Systems Engineering-An International Journal, 7 (4), 435–460. https://doi.org/10.12989/ose.2017.7.4.435

el Moctar, O., Shigunov, V., Zorn, T., 2012. Duisburg test case: post-panamax container ship for benchmarking. Ship Technol. Res. 59 (3), 50–64. https://doi.org/10.1179/str.2012.59.3.004

el Moctar, O., Sprenger, F., Schellin, T., Papanikolaou, A., 2016. Numerical and experimental investigations of ship maneuvers in waves. In: International Conference on Offshore Mechanics and Arctic Engineering, vol. 2 CFD and VIV, ASME.

Fang, M., Luo, J., Lee, M., 2005. A Nonlinear Mathematical Model for Ship Turning Circle Simulation in Waves. J. Sh. Res. 49, 69–79. https://doi.org/10.1038/srep02412

Fournarakis, N., Papanikolaou, A., Chroni, D., Liu, S., Plessas, T., 2016. Estimation of the maneuvering characteristics of the DTC containership using URANS based simulations. Marit. Technol. Eng. III 259–268. https://doi.org/10.1201/b21890-37

ITTC – Recommended Procedures and Guidelines. 7.5-02 03-01 rev. 03, 1978 ITTC Performance Prediction Method (2014).

ITTC – Recommended Procedures and Guidelines. 7.5-02-06-02 rev. 04, Captive Model Test Procedure (2014).

ITTC – Recommended Procedures and Guidelines. 7.5-03-04-01 rev. 00, Guideline on Use of RANS Tools for Maneuvering Prediction (2011).

Kinaci, O. K., Gokce, M. K., Alkan, A. D., Kukner, A., 2018. On Self-Propulsion Assessment of Marine Vehicles. Brodogradnja, 69, 4, 29-51. https://doi.org/10.21278/brod69403

Kinaci, O.K., Sukas, O.F., Bal, S., 2016. Prediction of wave resistance by a Reynolds-averaged Navier-Stokes equation-based computational fluid dynamics approach. Proc. Inst. Mech. Eng. Part M J. Eng. Marit. Environ. 230. https://doi.org/10.1177/1475090215599180

Lyster, C. A., Knights, H. L., 1979. Prediction Equations for Ships' Turning Circles. Trans. NECIES, 95, 217-232.
Motora, S., 1959. On the measurement of added mass and added moments of inertia for ship motions (in Japanese). J. Soc. Nav. Archit. Jpn. 105, 83–89.

Motora, S., 1960a. On the measurement of added mass and added moments of inertia for ship motions, Part 2: added mass for the longitudinal motions (in Japanese). J. Soc. Nav. Archit. Jpn. 106, 59–62.

Motora, S., 1960b. On the measurement of added mass and added moments of inertia for ship motions, Part 3: added mass for the transverse motions (in Japanese). J. Soc. Nav. Archit. Jpn. 106, 63–68.

Papanikolaou, A., Fournarakis, N., Chroni, D., Liu, S., 2016. Simulation of the Maneuvering Behavior of Ships in Adverse Weather Conditions. 31st International Symposium on Naval Hydrodynamics, Monterey CA, 212, 11–16.

Sadat-Hosseini, H., Sanada, Y. and Stern, F., 2015. Experiments and CFD for ONRT Course Keeping and Turning Circle Maneuvering in Regular Waves. WMTC 15, Providence, Rhode Island, USA, 17 pp.

Seo, M.G., Kim, Y., 2011. Numerical analysis on ship maneuvering coupled with ship motion in waves. Ocean Eng. 38, 1934–1945.
https://doi.org/10.1016/j.oceaneng.2011.09.023

Shen, Z. and Korpus, R., 2015. Numerical Simulations of Ship Self-Propulsion and Maneuvering Using Dynamic Overset Grids in OpenFOAM. A Workshop on CFD in Ship Hydrodynamics, Tokyo, Japan, Vol. 3.

Skejic, R., Faltinsen, O.M., 2008. A unified seakeeping and maneuvering analysis of ships in regular waves. J. Mar. Sci. Technol. 13, 371–394.
https://doi.org/10.1007/s00773-008-0025-2

Sprenger, F., Maron, A., Delefortrie, G., van Zwijnsvoorde, T., Cura-Hochbaum, A., Lengwinat, A., Papanikolaou, A., 2017. Experimental Studies on Seakeeping and Maneuverability of Ships in Adverse Weather Conditions. J. Sh. Res. 61, 131–152.
https://doi.org/10.5957/JOSR.170002

Stern, F., Wilson, R. V., Coleman, H. V., Paterson, E. G., 2001. Comprehensive approach to verification and validation of CFD simulations—part 1: methodology and procedures. Journal of Fluids Engineering, 12, 4, 793-802.
https://doi.org/10.1115/1.1412235

Sukas, O.F., Kinaci, O.K. Bal, S., 2017. A review on prediction of ship manoeuvring performance, part 1. GMO Journal of Ship and Marine Technology, 210, 37–75 (In Turkish).

Sukas, O.F., Kinaci, O.K. Bal, S., 2017. A review on prediction of ship manoeuvring performance, part 2. GMO Journal of Ship and Marine Technology, 210, 76–105 (In Turkish).

Yasukawa, H., Yoshimura, Y., 2015. Introduction of MMG standard method for ship maneuvering predictions. J. Mar. Sci. Technol. 20, 37–52.
https://doi.org/10.1007/s00773-014-0293-y

Yoon, H., 2009. Phase-averaged stereo-PIV flow field and force / moment / motion measurements for surface combatant in PMM maneuvers, PhD Thesis, The Univ. of Iowa.

Yoshimura, Y., Masumoto, Y., 2012. Hydrodynamic database and maneuvering prediction method with medium high-speed merchant ships and fishing vessels. In: International Conference on Marine Simulation and Ship Maneuverability (MARSIM'12). Singapore. Apr.

Zhang, W., Zou, Z.J., Deng, D.H., 2017. A study on prediction of ship maneuvering in regular waves. Ocean Eng. 137, 367–381.
https://doi.org/10.1016/j.oceaneng.2017.03.046

12 AUTHORS' BIOGRAPHY

Omer Kemal Kinaci started his academic career in Yildiz Technical University where he became a research assistant in 2010. He obtained his PhD. from Istanbul Technical University in 2013. The subject of his thesis was ship-propeller-rudder interactions. He worked with Prof. Michael Bernitsas on vortex-induced vibrations of circular cylinders as a post-doc at the University of Michigan. After working two years as an assistant professor in Yildiz Technical University, he started working in Istanbul Technical University as an associate professor in 2017. His research interests include ship hydrodynamics, underwater acoustics and flow-induced motions.

Omer Faruk Sukas is a PhD candidate at Istanbul Technical University, Department of Naval Architecture and Ocean Engineering. His major research interests are ship maneuverability and application of numerical methods in ship hydrodynamics.

Prof. Sakir Bal is currently working on Ship Motions and Maneuvering, Ship Propulsion and Propeller Acoustics in the Department of Naval Architecture and Marine Engineering of Istanbul Technical University. Prof. Bal teaches "Fluid Mechanics", "Ship Motions and Maneuvering", and "Ship Propulsion", courses at undergraduate level and "Boundary Element Methods in Ship Hydrodynamics" and "Hydrodynamics of Marine Propellers" courses at graduate level. He did research in Helsinki University of Technology (1995-1996), the University of Texas at Austin (1998-1999 and 2005) and University of Newcastle upon Tyne (2005) and also taught in University of Liege. He published more than 50 refereed international journal papers and 45 papers appeared in conference proceedings. He also published many research reports. He is a full member of SNAME (Society of Naval Architects and Marine Engineers), a fellow of RINA (Royal Institution of

Naval Architects) and was a member of Technical Programme Committee of ISOPE (International Society of Offshore and Polar Engineers) between 2006 and 2011. In addition, he supervised and prepared some research projects.

TRANSIENT RESPONSE OF A MOORED VESSEL INDUCED BY A PASSING SHIP

Liang Li and Zhi-Ming Yuan,
Department of Naval Architecture, Ocean and Marine Engineering, Glasgow, UK

TRANSIENT RESPONSE OF A MOORED VESSEL INDUCED BY A PASSING SHIP

Liang Li and **Zhi-Ming Yuan,** Department of Naval Architecture, Ocean and Marine Engineering, Glasgow, UK

SUMMARY

A passing ship sets up the wash waves, which are able to propagate a long distance with limited dissipation. The wash waves will induce transient loads on a moored vessel. In the present research, a hybrid model is developed to estimate the transient response of a moored vessel induced by another passing ship far away. The hybrid method is based on the combination of the 3-D Rankine source method and the impulse response theory. The wash waves and the impact loads acting on the moored vessels are addressed using the 3-D Rankine source method. The transient response of the vessel is simulated with the impulse response theory. The transient response is found to increase with the passing ship's speed. In addition, the propagation distance of the wash waves has a limited influence on the transient response due to the dissipation feature of the divergent wash waves.

1 INTRODUCTION

A ship moored in a port is subjected to complicated external loads, which may induce strong motions of the moored ship. When the motions become very large, marine operations must be terminated and the downtime will be consequently increased. For the safety of operation, the motions of a moored ship in a port should be investigated carefully. Apart from the incident sea waves, a passing ship also causes the moored ship to move. Vantorre et al. (2002) carried out model tests to investigate the hydrodynamic interaction between a moored ship and a passing ship during overtaking operation. Li et al. (2018b) investigated the hydrodynamic interactions between two passing ships during the encountering. Both works proved that the moored ship is subject to considerable hydrodynamic loads due to the passing effect induced by the other ship.

Until now, most studies on the passing ship effect focus on the suction effects induced by the 'double-body' flow around the passing vessel. It inherently implies that the free-surface disturbance and the surface wave propagation are not considered. It is probably because the forward speed of the passing ship is not high in most cases. However, nowadays have seen an increasing number of high-speed vessels, in both open sea and restricted waterways. In this circumstance, the wash waves must be considered. Janson et al. (2003) calculated the wash waves using a combine Rankine/Kelvin source method. Jiang et al. (2002) extended the Boussinesq's equation to capture the far-field wash waves. As well-known (van der Molen and Wenneker, 2008), the wash waves produced by an advancing ship with high speed can travel a long distance with little dissipation so that the moored ship will be subjected to substantial wash wave force even if the passing ship is far away as long as the forward speed is high enough. Pinkster (2009) proposed a computation method to examine the suction, the seiche and the wash effects induced by a passing ship. Pinkster and Naaijen (2003) investigated the passing ship effect accounting for the free-surface disturbance. Li et al. (2018a) simulated the transient motions of a moored ship under the joint action of wash waves and sea waves.

In this work, a hybrid numerical model is developed to investigate the transient response of a ship moored in a port when a ship is passing by with high forward speed. The wash waves and their impact loads on the moored ship are simulated with the 3-D boundary element method based on the Rankine Green function. Subsequently, a hydro-mooring coupled analysis is performed in time-domain to investigate the transient response of the ship.

2 HYBRID NUMERICAL MODEL

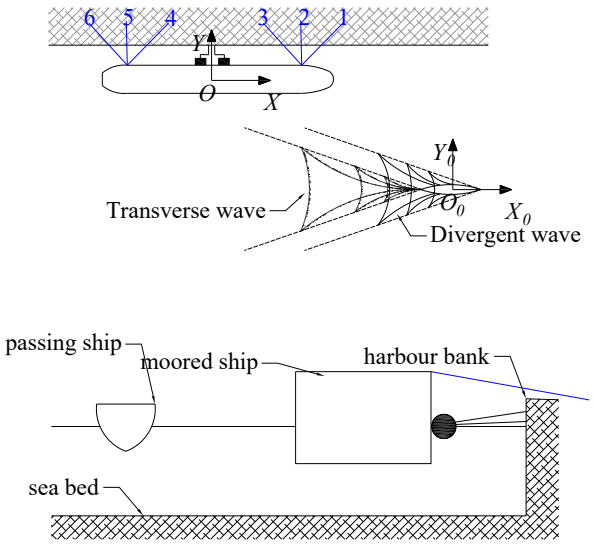

Figure 1. Sketch of a ship passing a ship moored at a port.

The present study is to investigate the transient response of a moored ship in a port subject to the wash waves produced by another passing ship (see Figure 1). The passing ship is a Wigley vessel with the main dimensions listed in Table 1. It is enforced to travel along positive X direction with a constant forward speed V. The Froude number Fr of the passing ship is 0.8 ($Fr = V / \sqrt{gL_1}$, g is the gravity

acceleration). No oscillating motions of the passing ship are allowed. The lateral distance B_S between the two ships is 40 m. The water depth is set to 10 m.

Table 1. Main dimensions of the passing ship.

Parameter	Value
Length (L_1)	30 m
Breath (B_1)	6 m
Draft (D_1)	1.875 m

The ship is moored in the port through the hawser-fender system. The gap width between the moored ship and the port bank is 13 m. The main dimensions of the moored ship are listed in Table 2.

Table 2. Main dimensions of the moored ship.

Parameter	Value
Length (L_2)	120 m
Breath (B_2)	14 m
Draft (D_2)	4.5 m
Centre of gravity	(0 m, 0 m, -0.5 m)
Displacement (V_D)	7,773 m^3
Roll inertia moment (I_{xx})	2.35×10^8 kg·m^2
Pitch inertia moment (I_{yy})	1.04×10^{10} kg·m^2
Yaw inertia moment (I_{zz})	1.17×10^{10} kg·m^2

The properties of the hawsers are summarized in Table 3 and the mooring configuration is shown in Table 4.

Table 3. Properties of the hawser lines

	Diameter	Density	EA	Length
Hawser1	0.052 m	10.3 kg/m	3120 kN	28.8 m
Hawser2				16.8 m
Hawser3				28.8 m
Hawser4				28.8 m
Hawser5				16.8 m
Hawser6				28.8 m

Table 4. Configuration of the hawser system

	Fairlead	Anchor
Hawser1	(50 m, 7 m 2 m)	(74 m, 24 m 1 m)
Hawser2	(50 m, 7 m 2 m)	(50 m, 24 m 1 m)
Hawser3	(50 m, 7 m 2 m)	(26 m, 24 m 1 m)
Hawser4	(-50 m, 7 m 2 m)	(-26 m, 24 m 1 m)
Hawser5	(-50 m, 7 m 2 m)	(-50 m, 24 m 1 m)
Hawser6	(-50 m, 7 m 2 m)	(-74 m, 24 m 1 m)

The hybrid numerical model used in the present simulation is based on the combination of the 3-D Rankine source method (Yuan et al., 2014) and the impulse response theory (Cummins, 1962). The 3-D Rankine source method is used to address the wash waves and the corresponding impact loads. Subsequently, the time-domain transient response of the moored ship subject to the wash waves is captured using the impulse response theory.

2.1 3-D RANKINE SOURCE METHOD

Assuming that the fluid is ideal, the velocity potential is used to describe the flow at any point within the fluid domain. It is well-known that the velocity potential satisfies the Laplace equation in the fluid domain, and therefore the calculation of the velocity potential is handled as the boundary value problem.

The potential φ_S of the wash wave is dealt with in the body-fixed coordinate system O_0-$X_0Y_0Z_0$ that moves together with the passing ship.

$$\begin{aligned}
&\nabla^2\varphi_s = 0, \text{in the fluid domain}\\
&\frac{\partial\varphi_s}{\partial \boldsymbol{n}} = Vn_1, \text{ on the passing ship}\\
&\frac{\partial\varphi_s}{\partial \boldsymbol{n}} = 0, \text{ on the moored ship}\\
&V^2\frac{\partial^2\varphi_s}{\partial x^2} + g\frac{\partial\varphi_s}{\partial z} = 0, \text{ on } z_0 = 0\\
&\frac{\partial\varphi_s}{\partial \boldsymbol{n}} = 0, \text{ on the harbour bank}
\end{aligned} \tag{1}$$

where $\boldsymbol{n} = (n_1, n_2, n_3)$ is the unit normal vector inward on the ship body surface. Once the wash wave potential φ_S is obtained, the wash wave impact loads acting on the moored ship are given by

$$\begin{aligned}
&F_i = \iint_S pn_i dS\\
&p = -\rho\left(\frac{\partial\varphi_s}{\partial t} - V\frac{\partial\varphi_s}{\partial x}\right)
\end{aligned}, \; i = 1, 2, \ldots, 6 \tag{2}$$

in which ρ is the water density and S is the wetted surface of the moored ship. The generalized normal vector n_i is defined as

$$n_i = \begin{cases} \boldsymbol{n}, i = 1,2,3 \\ \boldsymbol{r}\times\boldsymbol{n}, i = 4,5,6 \end{cases} \tag{3}$$

where $\boldsymbol{r} = (x, y, z)$ is the position vector.

In principle, it is required that the Rankine source should be distributed exactly on the undisturbed free surface. Nevertheless, a desingularized method is commonly used which raises the elements on the free water surface a short distance upwards (see Figure 2) (Zhang et al., 2010b). Meanwhile, the collocation points, where the boundary condition is satisfied, still stay exactly on the calm free surface. A raised distance $\nabla z = \sqrt{S}$ suggested by Zhang et al. (2010a) is selected, where S is the local element area.

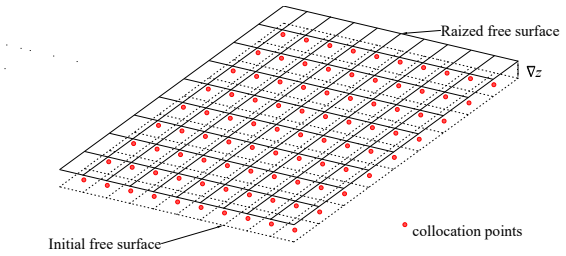

Figure 2. Raise of the free surface.

According to the description, the boundary of the fluid domain keeps varying during the passing process, requiring an update of the free surface truncation at each time step and the boundary value problem should be solved alongside with the update of the mesh distribution on the free surface. A re-meshing algorithm based on the concepts of the local mesh and the global mesh is developed. The local mesh is body-fixed and moves with the ship throughout the passing process. Comparatively, the global mesh can be understood as a kind of background mesh, which is fixed to the selected coordinate system. The essential idea of the re-meshing algorithm is to use the local mesh to overlap the global mesh and the complicated re-meshing problem will be converted in this way to a simple connection operation.

2.2 IMPULSE RESPONSE THEORY

According to the impulse response theory (Cummins, 1962), the time-domain motion equation of a floating body is given by

$$\sum_{j=1}^{6}\left[\left(M_{ij}+\mu_{ij}(\infty)\right)\ddot{x}_j(t)+\int_0^t h_{ij}(t-\tau)\dot{x}_j(t)d\tau+C_{ij}x_j(t)\right]=f_i(t)$$
$$i=1,2,...,6 \tag{4}$$

where M is the mass matrix, $\mu(\infty)$ is the added mass matrix at infinite frequency, $x(t)$, $\dot{x}(t)$ and $\ddot{x}(t)$ are the motion, the velocity and the acceleration, C is the static restoring stiffness matrix, $h_{ij}(t)$ is known as the retardation function, which can be represented by either the added mass or the radiation damping. $f_i(t)$ are the resultant external forces, including the wash wave impact loads and the hawser-fender tension forces. The wash wave impact loads are addressed with the 3-D Rankine source method (Eq. (2)).

The fender is simulated numerically with a linear-spring model, which is assumed to possess restoring stiffness on sway and roll modes merely. The restoring stiffness matrix of the fender is given by

$$K=\begin{bmatrix}0&0&0&0&0&0\\0&k&0&0&0&0\\0&0&0&0&0&0\\0&0&0&-k\cdot L&0&0\\0&0&0&0&0&0\\0&0&0&0&0&0\end{bmatrix} \tag{5}$$

where k = 3800 kN is the stiffness of the fender. L is the lever arm. Considering that the fender is 0.5 m above the centre of gravity of the moored ship, L = 0.5 m is used in the present research.

The hawser is simulated with the lumped-mass approach. As shown in Figure 3, the hawser is divided into a series of evenly-sized segments, which are represented by connected nodes and spring and damper systems. Please refer to (Hall and Goupee, 2015) for more details of the model.

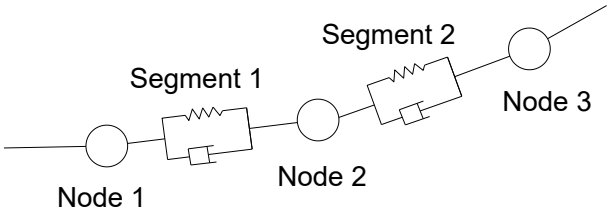

Figure 3. Lumped-mass model of the hawser.

3 VALIDATION

The simulation results given by Janson et al. (2003) are used here to check whether the present simulation tool is able to capture the wash wave pattern. A combined Rankine/Kelvin source method was developed by Janson et al. (2003), where the near-field and far-field wash waves were computed by the higher-order Rankine source and the Kelvin source, respectively. Figure 4 shows the far-field wash wave elevation η produced by a sailing Wigley ship in open calm water with forward speed Fr = 0.316. Considering that the far-field wash wave was calculated with the Kelvin source in (Janson et al., 2003) whereas the present model uses the linear Rankine source, the agreement is acceptable.

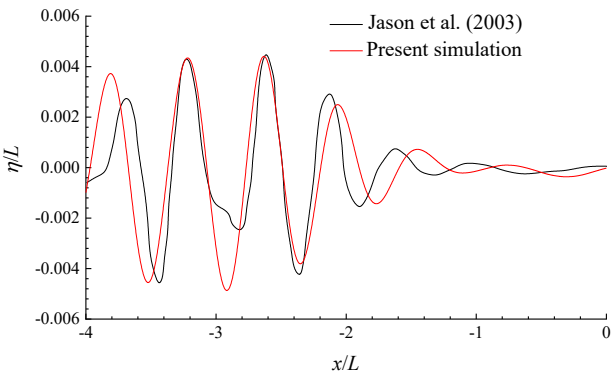

Figure 4. Validation of wash wave cut at y = 0.75L, Fr = 0.316.

4 SIMULATION RESULTS

4.1 TRANSIENT RESPONSES

Figure 5 displays the wash wave pattern throughout the passing process in calm water. The Froude number *Fr* is 0.8. The lateral separation between the two ships is 40 m. When the wash waves reach the port bank, they are reflected and propagate back to the transverse wave region. On the contrary, the wash waves on the other side are free to propagate outward. Three stages are identified during the passing process. In the first stage, the Kelvin wave has not arrived the moored ship yet, so that the near-field water surface around the moored ship is still. As the passing ship continues advancing ahead, the moored ship enters the divergent wave region. It can be seen that the divergent wash waves are reflected at the starboard of the moored ship, implying that the moored ship is subject to the wash wave impact load. Finally, the divergent wave region passes by the ship in which stage the ship is surrounded by the transverse waves and the reflected divergent waves.

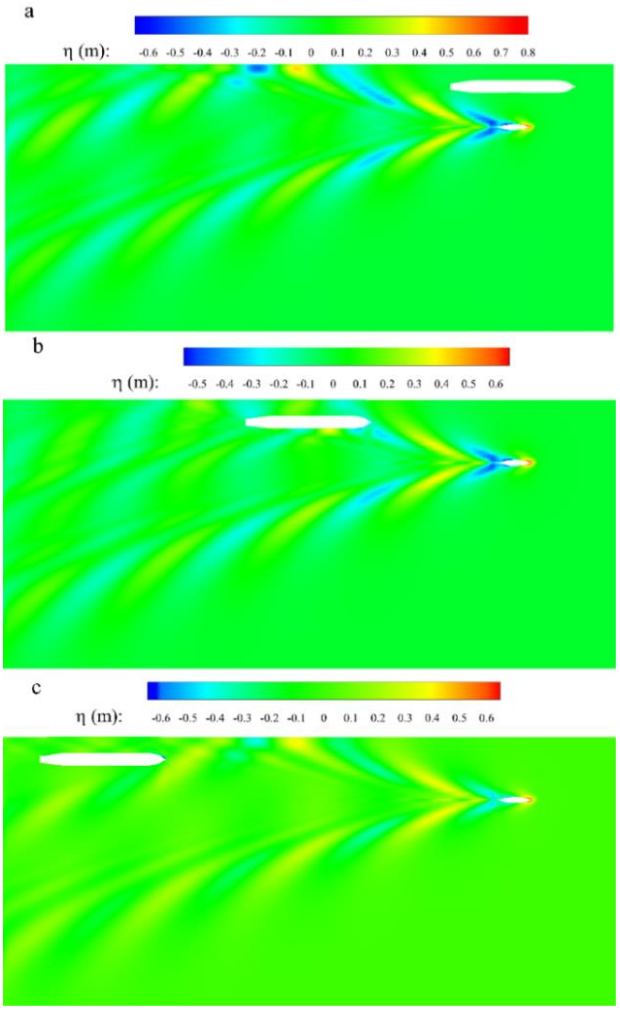

Figure 5. Wash wave patterns (displayed in the body-fixed coordinate system), *Fr* = 0.8, *BS* = 40 m. (a) Stage 1; (b) Stage 2; (c) Stage 3.

Figure 6 plots the transient motions of the moored ship induced by the wash waves alone. When the wash waves reach, the moored ship is subject to the impact load immediately and strong response is induced in a short time. Afterward, the ship decays gradually since the wash wave region has overtaken the moored ship. Therefore, decay-type responses are observed during the process. Due to the pre-tension of the hawsers, the mean positions of sway and roll are non-zero.

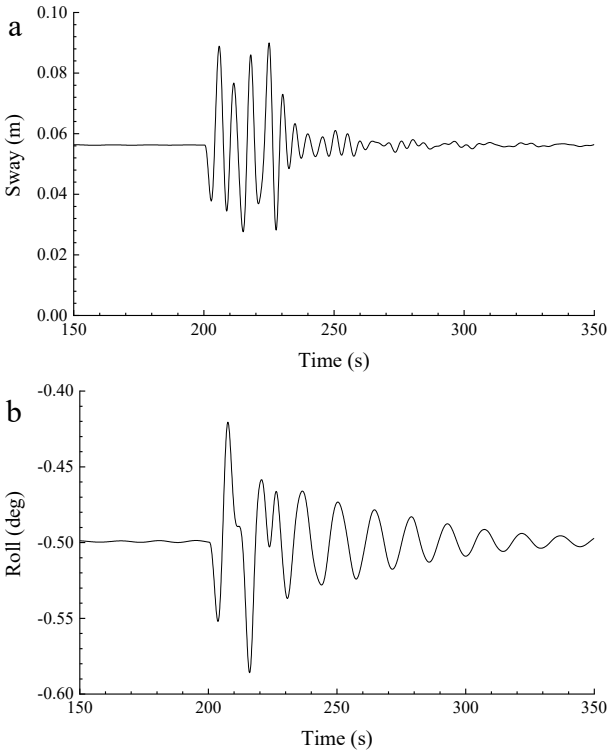

Figure 6. Time series of ship motions, *Fr* = 0.8, *BS* = 40 m. (a) sway motion; (b) roll motion.

The transient effect is also observed in the fender compression force. As shown in Figure 7, the compression force is initially stable at 215 kN to resist the pre-tension of the hawsers. During the transient stage, the fender also experiences a decay-type response and returns to the initial state finally. A similar phenomenon is also observed in the hawser force as displayed in Figure 8.

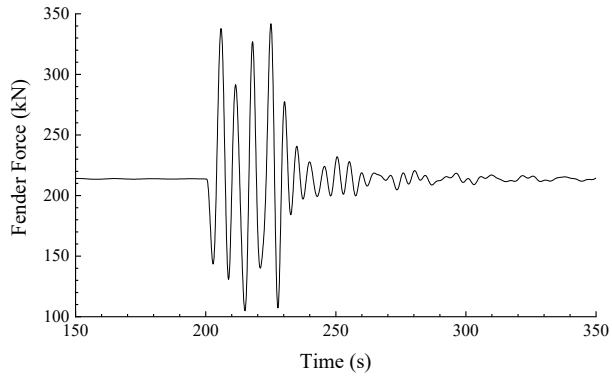

Figure 7. Time series of fender compression, *Fr* = 0.8, *BS* = 40 m.

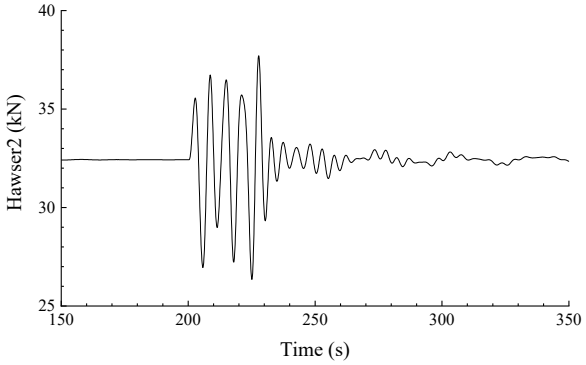

Figure 8. Time series of hawser force (hawser 2), *Fr* = 0.8, B_S = 40 m.

4.2 EFFECT OF FORWARD SPEED

The ship motions with different passing ship's forward speeds are compared in Figure 9 (The lateral distance is fixed at 40 m). As the forward speed of the passing ship drops, the transient ship motions reduce accordingly. The maximum amplitude of heave motion is 0.048 m when *Fr* = 0.8. This value drops to as low as 0.01 m if *Fr* reduces to 0.5. It is straightforward to understand such a variation trend as the wash wave elevation drops if the forward speed becomes smaller. The divergent wash waves are very limited for low Froude number condition, in which case the energy is mainly carried by the transverse waves.

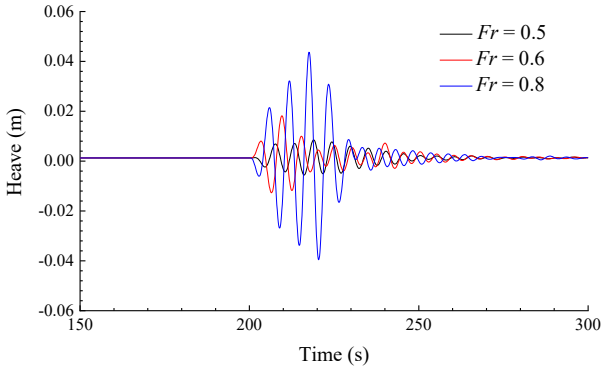

Figure 9. Times series of ship heave motion at different forward speeds, B_S = 40 m.

A similar variation trend is seen in the fender force and the hawser force, which is displayed in Figure 10 and Figure 11, respectively.

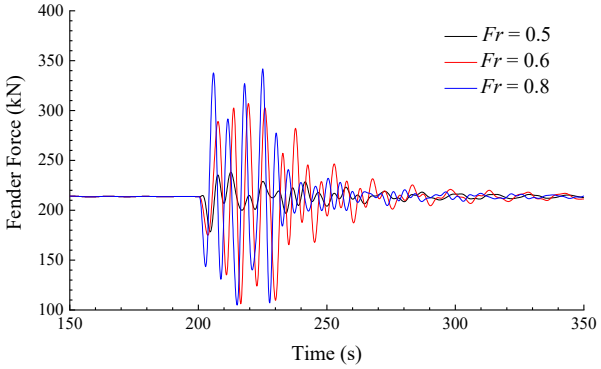

Figure 10. Time series of fender compression at different forward speeds, B_S = 40 m.

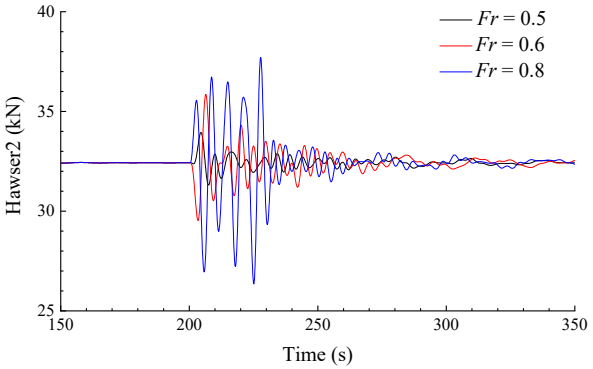

Figure 11. Time series of hawser force (hawser 2) at different forward speeds, B_S = 40 m.

4.3 EFFECT OF DISTANCE

The influence of the wash waves propagation distance on the transient response is investigated by increasing the lateral distance from 40 m to 60 m so that the wash waves will travel another 20 m to reach the moored ship (The Froude number is fixed at 0.8). Figure 12 displays the transient ship motions with different propagation distances. The fender forces are shown in Figure 13. As shown, the characteristics of the two curves are very similar. It seems that the propagation of the wash waves has a tiny influence on the ship transient motions.

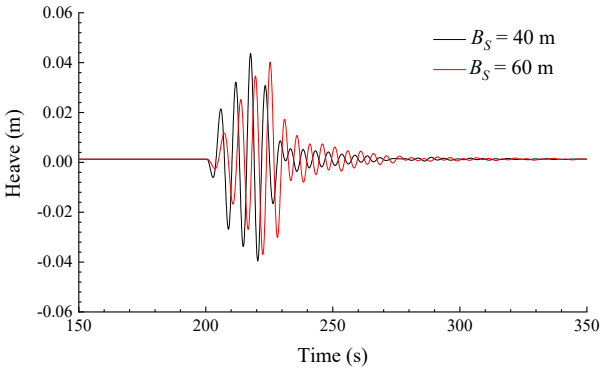

Figure 12. Time series of ship motions with various lateral distances, B_S = 0.8.

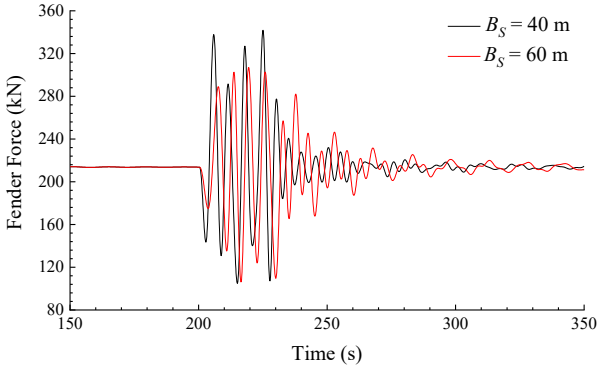

Figure 13. Time series of fender force with various lateral distances, B_S = 0.8.

The propagation distance effect on the transient response is tiny, since the divergent wash waves dissipate little during the propagation process. Figure 14 compares the wash wave patterns and Figure 15 shows the near-field wave elevation at the starboard of the moored ship (along the black line in Figure 14), when the divergent waves just arrive the bow of the moored ship. It is shown that the wave patterns are similar and the divergent waves dissipate hardly even if they travel a longer distance. Therefore, the transient responses in the two cases are similar to each other.

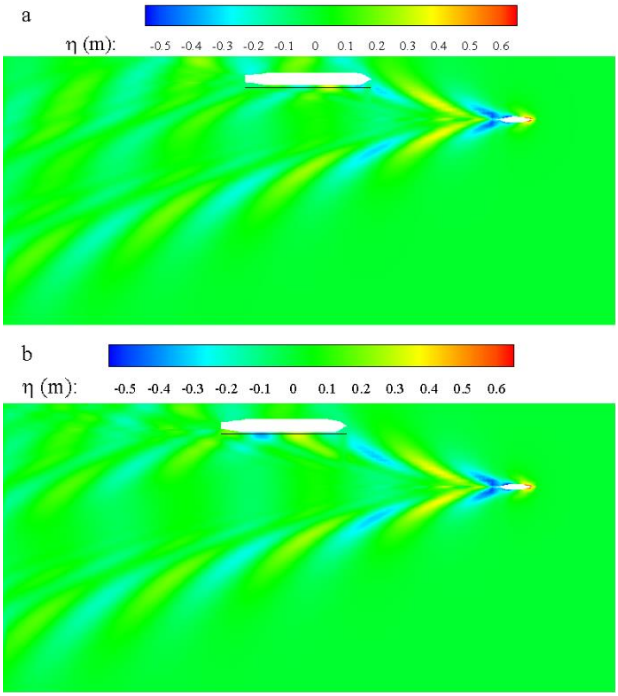

Figure 14. Wash wave pattern with different propagation distances (displayed in the body-fixed coordinate system), Fr = 0.8. (a) B_S = 40 m; (b) B_S = 60 m.

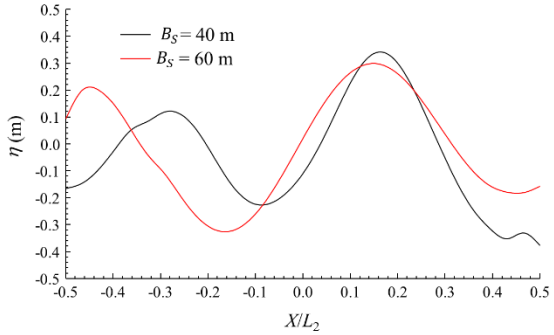

Figure 15. Near-field wave elevation at the starboard of the moored ship, Fr = 0.8.

5 CONCLUSIONS

A hybrid numerical model based on the 3-D Rankine source method and the impulse response theory is developed to address the transient response of a moored ship under the wash waves produced a passing ship. The wave-structure interaction is firstly simulated with the 3-D Rankine source method. Afterwards, a time-domain analysis is performed to simulate the transient response of the moored ship.

The moored ship is subjected to significant wash wave impact loads even if the passing ship is travelling far away. The transient effect is observed in the ship motions and the mooring line tensions. A decay-type response is observed during the transient duration.

The propagation distance of the wash waves seems to have little influence on the transient response. The transient response is sensitive to the ship speed. A fast passing ship induces strong transient response of the moored ship.

6 REFERENCES

Cummins, W., 1962. The impulse response function and ship motions. David Taylor Model Basin, Washington DC, pp. 101-109.

Hall, M., Goupee, A., 2015. Validation of a lumped-mass mooring line model with DeepCwind semisubmersible model test data. Ocean Engineering 104, 590-603. https://doi.org/10.1016/j.oceaneng.2015.05.035

Janson, C.E., Leer-Andersen, M., Larsson, L., 2003. Calculation of deep-water wash waves using a combined Rankine/Kelvin source method. Journal of Ship Research 47 (4), 313-326.

Jiang, T., Henn, R., Sharma, S.D., 2002. Wash waves generated by ships moving on fairways of varying topography, in: Proceedings of the 24th Symposium on Naval Hydrodynamics, Fukuoka, Japan, pp. 441-457.

Li, L., Yuan, Z.-M., Ji, C., Li, M.-X., Gao, Y., 2018a. Investigation on the unsteady hydrodynamic loads of ship passing by bridge piers by a 3-D boundary element

method. Engineering Analysis with Boundary Elements 94 (C), 122-133.
https://doi.org/10.1016/j.enganabound.2018.06.010

Li, L., Yuan, Z.M., Gao, Y., 2018b. Wash wave effects on ships moored in ports. Applied Ocean Research 77, 89-105.
https://doi.org/10.1016/j.apor.2018.06.001

Pinkster, J., Naaijen, P., 2003. Predicting the effect of passing ships, in: Proceedings of the 18th Int. Workshop on Water Waves and Floating Bodies. Le Croisic, France.

Pinkster, J.A., 2009. Suction, Seiche and Wash Effects of Passing Ships in Ports, in: Proceedings of the Annual Meeting of the Society of Naval Architects and Marine Engineers (SNAME), Providence.

van der Molen, W., Wenneker, I., 2008. Time-domain calculation of moored ship motions in nonlinear waves. Coastal Engineering 55 (5), 409-422.
https://doi.org/10.1016/j.coastaleng.2008.01.001

Vantorre, M., Verzhbitskaya, E., Laforce, E., 2002. Model test based formulations of ship-ship interaction forces. Ship Technology Research 49, 124-141.

Yuan, Z.M., Incecik, A., Alexander, D., 2014. Verification of a new radiation condition for two ships advancing in waves. Applied Ocean Research 48, 186-201.
https://doi.org/10.1016/j.apor.2014.08.007

Zhang, X.S., Bandyk, P., Beck, R.F., 2010a. Seakeeping computations using double-body basis flows. Applied Ocean Research 32 (4), 471-482.
https://doi.org/10.1016/j.apor.2010.10.003

Zhang, X.S., Bandyk, P., Beck, R.F., 2010b. Time-Domain Simulations of Radiation and Diffraction Forces. Journal of Ship Research 54 (2), 79-94.

7 AUTHORS BIOGRAPHY

Liang Li holds the current position of Research Associate at University of Strathclyde. His previous experience includes ship hydrodynamics, offshore renewable energy and energy control.

Zhi-Ming Yuan holds the current position of Lecturer at University of Strathclyde. His previous experience includes ship hydrodynamics, multi-body hydrodynamic interactions.

NUMERICAL ASSESSMENT OF ADDED RESISTANCE IN WAVES OF THE DTC CONTAINER SHIP IN FINITE WATER DEPTHS

Ivana Martić,
Faculty of Mechanical Engineering and Naval Architecture, University of Zagreb, Croatia Guillermo Chillcce Institute of Ship Technology, Ocean Engineering and Transport Systems (ISMT), the University of Duisburg-Essen, Germany

Manases Tello Ruiz,
Maritime Technology Division, Ghent University, Belgium

Jorge Ramirez,
Knud e Hansen A/S, Denmark

Nastia Degiuli,
Faculty of Mechanical Engineering and Naval Architecture, University of Zagreb, Croatia

Bettar Ould el Moctar,
Institute of Ship Technology, Ocean Engineering and Transport Systems, the University of Duisburg-Essen, Germany

NUMERICAL ASSESSMENT OF ADDED RESISTANCE IN WAVES OF THE DTC CONTAINER SHIP IN FINITE WATER DEPTHS

Ivana Martić, Faculty of Mechanical Engineering and Naval Architecture, University of Zagreb, Croatia
Guillermo Chillcce Institute of Ship Technology, Ocean Engineering and Transport Systems (ISMT), the University of Duisburg-Essen, Germany
Manases Tello Ruiz, Maritime Technology Division, Ghent University, Belgium
Jorge Ramirez, Knud e Hansen A/S, Denmark
Nastia Degiuli, Faculty of Mechanical Engineering and Naval Architecture, University of Zagreb, Croatia
Bettar Ould el Moctar, Institute of Ship Technology, Ocean Engineering and Transport Systems, the University of Duisburg-Essen, Germany

SUMMARY

In this study, added resistance in waves of DTC container ship at full draft is investigated by means of Reynolds Averaged Navier-Stokes (RANS) solver in finite water depths. Validation is conducted against the experimental results of tests carried out with a scale model of DTC in the Towing Tank for Manoeuvres in Confined Water at Flanders Hydraulic Research (in co-operation with Ghent University and in the framework of the SHOPERA project). Following the numerical study of the ship resistance in calm water, the increase in resistance introduced by incoming waves for different advancing speeds is computed. This study shows the capabilities and reliability of RANS based methods to calculate the added resistance in finite water depth waves.

NOMENCLATURE

a_i	Face area vector (-)
a_0	Zeroth harmonic amplitude (-)
A_1	First harmonic amplitude (-)
A_2	Second harmonic amplitude (-)
B	Ship breadth (m)
C_{AW}	Added resistance coefficient (-)
C_ε	Turbulence model coefficient (-)
C_μ	Turbulence model coefficient (-)
f	Frequency (1/s)
f_c	Curvature correction factor (-)
Fr	Froude number (-)
$\overline{F}_x$	Average longitudinal force (N)
g	Gravitational acceleration constant (m^2/s)
G_k	Turbulent production term (kg/ms^3)
G_b	Production term due to buoyancy (kg/ms^3)
h	Water depth (m)
H_{max}	Fourier series maximum value (-)
H_W	Wave height (m)
k	Turbulent kinetic energy (m^2/s^2)
L_{PP}	Ship length between perpendicular (m)
P	Pressure (N/m^2)
$\overline{p}$	Mean pressure (N/m^2)
R_{AW}	Added resistance in waves (N)
R_F	Frictional resistance (N)
R_P	Pressure resistance (N)
R_T	Calm water resistance (N)
S_ε	User specified source term (kg/ms^4)
S_k	User specified source term (kg/ms^3)
T_e	Encounter period (s)
T_W	Wave period (s)
u_i	Velocity vector (m/s)
$\overline{u}_i$	Average components of the velocity vector (m/s)
u_{gi}	Grid velocity vector (m/s)
v	Velocity (m/s)
V	Cell volume (m^3)
$y+$	Non-dimensional wall distance (-)
α	Volume fraction of fluid (-)
ε	Turbulent dissipation rate (m^2/s^3)
ε_0	Ambient turbulence value (m^2/s^3)
ζ_A	Wave amplitude (m)
λ	Wave length (m)
μ	Dynamic viscosity (Pas)
μ_t	Eddy viscosity (kg/ms)
ν	Kinematic viscosity (m^2/s)
ρ	Density of water (kg/m^3)
σ_k	Turbulent Schmidt number (-)
σ_ε	Turbulent Schmidt number (-)
$\overline{\tau}_{ij}$	Mean viscous stress tensor (N/m^2)
Υ_M	Dilatation dissipation (m^2/s^3)

1 INTRODUCTION

The prediction of the ship added resistance in waves has increased in importance since the emission of harmful gases has been subjected to more stringent regulations via the Energy Efficiency Design Index (EEDI) (IMO MEPC.203(62), 2011). Added resistance in waves is understood as an increase in the required power to attain in waves a ship speed equal to the one in calm water, which in turn means more fuel consumption and therefore an increase in the amount of air pollutants emission.

An accurate prediction of attainable ship speeds when sailing in waves is then essential to assess the ship's performance in operating conditions and to determine the ship's impact on the environment. In literature, one can find that most studies have been conducted in open seas, see e.g. Sigmund and el Moctar (2018), Kim et al., (2017), Riesner and el Moctar (2018), Yasukawa and Adnan, (2006) and Chen et al. (2018). The study of the added resistance in waves in finite water depths should also be carried out. This is relevant when ship sails in finite water depths in close proximity of densely populated areas, when approaching or leaving a port, where restrictions on pollutants emissions are even more stringent.

The influence of waves on the sailing ship in finite depths has been investigated by few authors, for instance in Vantorre and Journée (2003), Tello Ruiz et al. (2015) and Tello Ruiz et al. (2016 and 2019). In Vantorre and Journée (2003) the analysis is focused on the ship motions of a container ship, a tanker and a bulk carrier. Experimental results were compared against numerical results obtained with 2D strip theory (Octopus Seaway). The comparison showed a fair agreement for wave lengths close to the ship length. For shorter waves, the discrepancy between the results was observed to be larger but still remained a good approximation. In Tello Ruiz et al. (2015) KVLCC2 at model scale has been investigated in regular waves, at different under keel clearances (UKCs), and different ship speeds. The test results for ship motions and wave forces (including the mean second order wave forces) were compared with numerical results obtained with three different potential codes (WAMIT for the zero speed case, HydroStar and Octopus Seaway). The numerical results obtained with all three potential codes showed a fair agreement with the experimental values for the ship motions, but none of them predicted the wave forces with a sufficient accuraccy. In Tello Ruiz et al. (2016 and 2019) similar results were obtained for ship motions and wave induced forces when the results of model tests, conducted with an ultra large container ship (ULCS), were compared against the numerical results obtained with HydroStar.

Potential methods, especially at forward speed, do not accurately deal with the interaction of the steady and unsteady oscillatory wave system. Such interaction will be even stronger in shallow water, thus the suitability of potential methods for the shallow water problems is questionable. As pointed out in Chen et al., (2018) the proximity of the bottom will increase the relevance of viscous effects and their influence on the ship motions and ship behaviour in general.

Reynolds-Averaged Navier Stokes (RANS) methods are a very good alternative to potential methods as they account for viscous effects in the numerical calculations. In that way, they can provide a better insight into the fluid phenomena for the shallow water problems. In literature, one can find a fair amount of studies where Computational Fluid Dynamics (CFD), based on the viscous flow theory, has been used in finite water depths, but most of them are either conducted in calm water (e.g. Toxopeus et al., 2013; Liu et al., 2017; Van Hoydonck et al., 2018) or at zero forward speed (e.g. Tezdogan et al., 2016). Only in Tello Ruiz et al. (2017), an ULCS sailing in waves at shallow water conditions has been studied with main focus on the interaction effects between the ship and the tank sidewalls, but no specific attention was drawn to the motions or forces, nor were the results validated.

In order to calculate ship added resistance in waves accurately, the prediction of ship motions is of great importance. In Tezdogan et al. (2015) an overset mesh was used to accommodate ship motions and the verification study showed small numerical uncertainties. This technique can accommodate large and arbitrary ship motions using overlapping technique. Besides its application for deep water cases (Carrica et al., 2007, Tezdogan et al., 2015), overset mesh has also been successfully used in confined water cases (Tezdogan et al., 2016) to calculate ship motions, and forces and moments acting on the ship hull. An alternative method to accommodate ship motions is the use of morphing mesh, which deforms locally around the ship hull as the ship moves. In Sigmund and el Moctar (2018) it has been successfully used for the calculations of ship motions and resistance in waves for both full and slender hull forms in deep water, and in Toxopeus et al. (2013) and Van Hoydonck et al. (2018) for the manoeuvring analysis in shallow water.

Even though it is generally assumed that the added resistance in waves is pressure driven and viscous effects are negligible, the viscous effects in short waves can increase in deep water, as shown in Sigmund and el Moctar (2018), and these effects should be investigated in finite water depths as well. When waves in shallow water start to be affected by proximity of the bottom, the orbital motion of fluid particles is disrupted, and water particles near the bottom flatten their orbit. As the water depth decreases, waves become steeper which will also have a noticeable influence on the added resistance (Chen et al., 2018).

To the authors' best knowledge, there are no specific studies dealing with the estimation of the added resistance due to waves in shallow and very shallow water. In this paper, this is numerically investigated for DTC container ship and validated against the experimental data. The experimental data are obtained from scale model tests conducted

in the Towing Tank for Manoeuvres in Confined Water at Flanders Hydraulic Research, within the framework of the European SHOPERA project (Van Zwijnsvoorde et al., 2019). The numerical calculations are performed with bare hull at 100% and 20% UKC, for two different speeds, with and without waves, Table 1.

2 SHIP GEOMETRY AND CONDITIONS

DTC (Duisburg Test Case) container ship was developed at the Institute of Ship Technology, Ocean Engineering and Transport Systems in Duisburg-Essen, Germany for benchmark purposes (see el Moctar et al., 2012). Captive and free running tests have been performed in the Towing Tank for Manoeuvres in Confined Water at Flanders Hydraulic Research (in co-operation with Ghent University) with a scaled model (1:89.11). A perspective view of the 3D model of DTC container ship is shown in Figure 1. Hull parameters and mass characteristics of the ship model can be found in Van Zwijnsvoorde et al., (2019). In this research, numerical simulations of captive model tests with the bare hull are performed in calm water and in regular waves, Table 1.

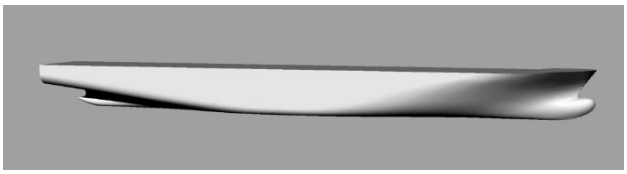

Figure 1. 3D model of DTC container ship.

Table 1. Test cases for numerical simulations

Test ID	Velocity, m/s	UKC, %	λ/L_{PP}	Wave height, mm	Wave period, s
C1	0.327	100	/	/	/
CW2	0.327	100	0.55	62.31	1.38
C3	0.327	20	/	/	/
CW5	0.327	20	0.55	21.26	1.66
C2	0.872	100	/	/	/
CW3	0.872	100	0.55	62.35	1.38

A post-processing analysis of the experimental data has been carried out for further comparison with the numerical estimations. The analysis was performed following the recommendations in Van Zwijnsvoorde et al., (2019) with respect to the selection of the time windows and adopting the approach described in Tello Ruiz et al. (2016) for harmonic signals. In this method, the signal is filtered with a band pass filter and further fitted with a least square method up to a third order Fourier expansion with eight unknown parameters, see equation (1).

$$f(t) = a_0 + \sum_{i=1}^{3} a_i \sin(i\omega t) + b_i \cos(i\omega t) \quad (1)$$

In Eq. (1) a_0 and ω are the mean and the frequency of harmonic signal, respectively; the remaining terms a_i, and b_i are the harmonic components related to the first, second and third order Fourier series. For the cases in calm water the analysis has been conducted over the same regions defined in the analysis selected for waves.

3 GOVERNING EQUATIONS

Numerical simulations of incompressible viscous flow around the ship hull are performed using the commercial software package STAR-CCM+. Navier Stokes equations and continuity equation are used for the description of the fluid motion. RANS equations and averaged continuity equation obtained by time averaging of Navier-Stokes equations and continuity equation are given as follows (Ferziger and Perić, 2012):

$$\frac{\partial(\rho\bar{u}_i)}{\partial t} + \frac{\partial}{\partial x_j}\left(\rho\bar{u}_i\bar{u}_j + \rho\overline{u_i'u_j'}\right) = -\frac{\partial\bar{p}}{\partial x_i} + \frac{\partial\bar{\tau}_{ij}}{\partial x_j} \quad (2)$$

$$\frac{\partial(\rho\bar{u}_i)}{\partial x_i} = 0 \quad (3)$$

where ρ is the fluid density, $\bar{u}_i$ is the averaged Cartesian components of the velocity vector, $\rho\overline{u_i'u_j'}$ is the Reynolds stress tensor, $\bar{p}$ is the mean pressure and $\bar{\tau}_{ij}$ is the mean viscous stress tensor defined as follows:

$$\bar{\tau}_{ij} = \mu\left(\frac{\partial\bar{u}_i}{\partial x_j} + \frac{\partial\bar{u}_j}{\partial x_i}\right) \quad (4)$$

where μ is the dynamic viscosity.

To close the system of equations (2) and (3), Realizable $k-\varepsilon$ (RKE) turbulence model is used as isotropic eddy-viscosity model based on the assumption that turbulence effects can be described as increased viscosity:

$$-\rho\overline{u_i'u_j'} = \mu_t\left(\frac{\partial\bar{u}_i}{\partial x_j} + \frac{\partial\bar{u}_j}{\partial x_i}\right) - \frac{2}{3}\rho\delta_{ij}k \quad (5)$$

where k is the turbulent kinetic energy defined as follows:

$$k = \frac{1}{2}\overline{u_i'u_j'} \quad (6)$$

The $k-\varepsilon$ turbulence model is commonly used in engineering applications providing good agreement with the experimental results while keeping the reasonable CPU time required to perform numerical simulations (Quérard et al., 2008).

Within $k-\varepsilon$ turbulence models, one equation is solved for turbulent kinetic energy k and one for turbulent dissipation rate ε, while eddy viscosity is described as follows:

$$\mu_t = \rho C_\mu \frac{k^2}{\varepsilon} \quad (7)$$

The transport equations for RKE are given as (CD-adapco, 2018):

$$\frac{\mathrm{d}}{\mathrm{d}t}\int_V \rho k \mathrm{d}V + \int_A \rho k(u_i - u_{gi})\cdot \mathrm{d}a_i = \int_A \left(\mu + \frac{\mu_t}{\sigma_k}\right)\frac{\partial k}{\partial x_i}\cdot \mathrm{d}a_i + \int_V \left[f_c G_k + G_b - \rho\left((\varepsilon - \varepsilon_0) + \Upsilon_M\right) + S_k\right]\mathrm{d}V \quad (8)$$

$$\frac{\mathrm{d}}{\mathrm{d}t}\int_V \rho \varepsilon \mathrm{d}V + \int_A \rho \varepsilon(u_i - u_{gi})\cdot \mathrm{d}a_i = \int_A \left(\mu + \frac{\mu_t}{\sigma_\varepsilon}\right)\frac{\partial \varepsilon}{\partial x_i}\cdot \mathrm{d}a_i + \int_V \left[f_c C_{\varepsilon 1} S\varepsilon + \frac{\varepsilon}{k}(C_{\varepsilon 1} C_{\varepsilon 3} G_b) - \frac{\varepsilon}{k+\sqrt{\nu\varepsilon}} C_{\varepsilon 2}\rho(\varepsilon - \varepsilon_0) + S_\varepsilon\right]\mathrm{d}V \quad (9)$$

where V is the cell volume, u_i is the velocity vector, u_{gi} is the grid velocity vector, a_i is the face area vector, σ_k and σ_ε are turbulent Schmidt numbers, f_c is the curvature correction factor, G_k is the turbulent production term, G_b is the production term due to the buoyancy, ε_0 is the ambient turbulence value in the source terms that counteracts turbulence decay, Υ_M is the dilatation dissipation, S_k and S_ε are user specified source terms, $C_{\varepsilon 1}$, $C_{\varepsilon 2}$ and $C_{\varepsilon 3}$ are model coefficients, S is the modulus of the mean strain rate tensor and ν is the kinematic viscosity.
The Volume of Fluid (VOF) method is used to capture the free surface between two phases in both calm water simulations and in waves, introducing the additional transport equation solved for the volume fraction:

$$\frac{\partial}{\partial t}\alpha + \nabla\cdot(\alpha u_i) = 0 \quad (10)$$

where the volume fraction of the phase in a computational cell α is 0 for air and 1 for water, and the value of 0.5 indicates the free surface. It enables modelling of two fluids as a single fluid whose physical characteristics calculated in each computational cell depend on the volume fraction of the phase in that particular cell, while the same governing equations as for a single-phase problem are being solved. The second order convection scheme is used to capture the interface between two phases. Segregated flow model is used to solve the flow equations in an uncoupled manner and SIMPLE algorithm is used for implicit coupling between the pressure and the velocity. Convection terms in RANS equations are discretized by second-order upwind scheme. RANS solver calculates forces acting on the ship hull based on the Dynamic Fluid Body Interaction (DFBI) model, which enables motions of the rigid body and re-positioning at each time step. It should be noted that only two degrees of freedom are activated for the ship, i.e. heave and pitch motion.

4 COMPUTATIONAL DOMAIN AND BOUNDARY CONDITIONS

Boundaries of the computational domain are all placed 1.2 L_{PP} away from the ship except for the bottom boundary. It should be noted that for the sake of reducing the computational time, only half of the domain is simulated and the symmetry condition is applied. Before running the simulation, initial and boundary conditions have to be defined, depending on the problem that is being solved. Velocity inlet is applied on the inlet and top boundary. For simulations in calm water, the velocity is equal to the ship velocity but in opposite direction and for simulations in waves the initial velocity is set to the corresponding velocity of the incoming waves. Side and bottom boundaries are set as non-slip wall condition, moving with velocity equal to ship velocity but in the opposite direction. The hull surface is also set as non-slip wall condition. The outlet boundary is set as the pressure outlet condition to fix static pressure at the outlet of the computational domain. As already mentioned, the symmetry condition is applied to the symmetry plane.

The problem is solved in an inertial coordinate system that travels along with the ship. In that way, the ship has zero forward speed and the fluid has a velocity equal to the ship speed but in opposite direction. In the case of simulations in waves, besides the characteristics of the incoming waves, at the inlet boundary the additional velocity is set to simulate the ship advancing in waves and to achieve the correct wave encounter frequency.

A mesh morphing algorithm is used to deform the numerical grid and accommodate ship motions in the computational domain. An unstructured grid is generated using hexahedral control volumes. Local grid refinements are used near the bow, stern and between the ship and the bottom boundary to properly capture the features of complex flow around the ship hull. A refinement where the free surface is expected is made to capture the ship's wake. The finest free surface refinement has a minimum of 100 cells per wave length and 20 cells per wave height. Mesh section for the 100% UKC case can be seen in Figure 2. To model the inner region of the boundary layer, all *y*+ wall treatment is used which consists of a hybrid treatment that emulates the low and high *y*+ treatment depending on the size of the cell near the wall (CD-adapco, 2018).

Six prism layers are used to resolve the boundary layer flow near the hull. The initial aim was to achieve *y*+ less than one, but this gave a numerical ventilation problem due to very thin cells near the wall. Therefore, all *y*+ value treatment was adopted. The numerical domain for the calm water simulations has about 7.1 million cells for C1 and C2, and 7 million cells for case C3. In the case of waves, CW2 and CW3 have up to 7.6 million cells while CW5 has 8.9 million cells. It should be noted that the same mesh could have been used for both simulations in calm water and in waves at certain ship speed. However, with the respect to the required computational time, the mesh for test cases in waves has been additionally refined near the free surface in the vertical direction in order to better capture the free surface elevation.

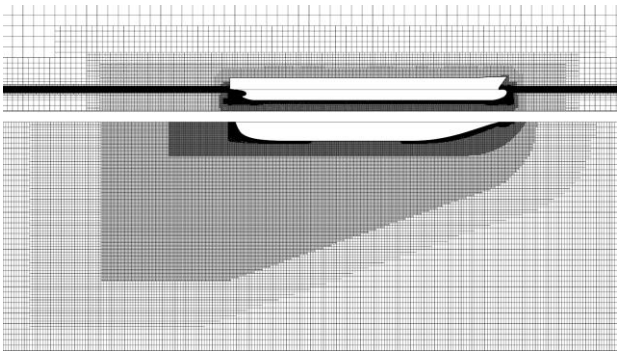

Figure 2. Mesh section for 100% UKC case.

To prevent wave reflection from the boundaries, for simulations in calm water, VOF wave damping is used at inlet, outlet and side boundaries. The damping length is set as a function of physical time, to speed up the convergence at the beginning of the simulation, reducing the size of the damping zone to 0.6 L_{PP} as the simulation advances. For simulations in waves, a forcing method is applied to prevent wave reflections from the boundaries. In this way, a significant reduction in the size of the computational domain is possible compared to the size of the domain that would have to be used if a wave damping method would be applied. Forcing is applied at inlet, outlet and side boundary as well, up to a distance of 2.4 m and it ensures that in that region the wave amplitude is equal to the amplitude of the incoming wave. Both damping and forcing methods use additional source terms in the momentum equations.

5 COMPUTATIONAL PROCEDURE

In order to generate regular incoming head waves a fifth-order Stokes wave was used. To monitor the elevation of the generated waves, a wave probe is placed in front of the ship. Note that the amplitude of the first harmonic obtained from the Fourier series fitting applied to the wave amplitude has been further used for the normalization of added resistance in waves.

In the unsteady simulations in waves, the time step is chosen such that the Courant number is lower than 0.4 and following the ITTC's recommendation to use at least 100 time steps per wave period (ITTC, 2014). In this research, the time step equal to 0.002 s is used for the CW2 and CW5 cases, and 0.0015 s for the CW3 case.
To analyse the unsteady time series of forces acting on the ship hull their Fourier series is used as well.

Added resistance in waves is thus calculated by subtracting the calm water resistance R_T from the zeroth-order harmonic amplitude of the Fourier series, i.e. the average longitudinal force $\overline{F}_x$. The added resistance coefficient is obtained as follows:

$$C_{AW} = \frac{\overline{F_x} - R_T}{\rho g \zeta_a^2 B^2 / L} \tag{11}$$

where ζ_A is the wave amplitude.

6 RESULTS

6.1 CALM WATER RESISTANCE

All numerical simulations in calm water are performed as unsteady simulations with time step equal to 0.02 s. Initially a larger time step, based on the time required for the flow to pass one ship length, is reduced for cases C1 and C3 due to the appearance of numerical ventilation. This occurs when air particles get into the boundary layer below the free surface, and it affects the calculation of the frictional part of the total resistance. In other words, shear stress calculated using the air characteristics instead of water characteristics decreases.

The comparison between the numerically and experimentally obtained results can be seen in Table 2. The numerical results are taken as the average values of the last 10 s of the time series. From the comparison it can be seen that the smallest relative deviation (RD of 6.84%) is obtained for the C1 case. A significant increase in pressure resistance is noticed between test cases C1 and C3. In the case of C3 (shallower water) the pressure resistance contribution is over 30% of the total resistance, which is approximately twice larger than in the case of C1. It appears that pressure resistance increases faster than frictional resistance and is more affected by the proximity of the bottom.

For case C2, large relative deviation in the total resistance is possibly obtained due to numerical ventilation that could be observed in the large part of the ship hull, which could have consequently led to an underestimation of the frictional resistance. It occurred despite the small values of Courant number and even though a second-order upwind scheme was used. It should be noted that the trim and sinkage are underestimated as well.

Table 2. Comparison of total resistance values obtained numerically and experimentally

Test ID	EXP, (N)	CFD, (N)	RD, (%)	R_F, (N)	R_P, (N)
C1	0.81	0.75	6.84	0.62	0.13
C3	1.11	0.99	10.33	0.67	0.32
C2	5.5	4.77	13.25	3.76	1.01

6.2 WAVE ELEVATION

Wave elevation has also been measured at the position of the wave probe WG4 during the experiment. It is located at 4.03 m in the positive *x* direction and 0.65 m in portside direction with respect to amidships. Time series of the wave elevation measured during the numerical simulation and the comparison with the experimental values for the CW5 can be seen in Figure 3. The 1st harmonic wave amplitude, obtained from Fourier series fitting based on the last 10 s of the time series, is equal to 10.71 mm which

overestimates the experimental value by approximately 12%, Table 3. The differences encountered indicate that the wave amplitude does not remain constant as waves propagate along the tank, considering that the amplitude of wave generated at the inlet boundary was based on WG2, located upwards the model during the experiment. This has also been observed in Tello Ruiz (2018), where a region along the tank has been defined at which waves remain approximately (within 5%) constant. These variations indicate that when testing numerical methods in shallow water a larger domain would be required to model such phenomenon, however, this was not possible at this stage considering the large computational power required. Note that theoretical ratio between the wave length and ship length is equal to 0.55 which classifies the generated waves as medium waves relative to the ship length, and they correspond to the intermediate water depth waves in the case of both water depths investigated.

Table 3. Harmonic decomposition of the computed and measured time series for wave elevation

CW5		H_{max}, (mm)	f, (1/s)	a0, (mm)	A1, (mm)	A2 (mm)
ζ_A	EXP	19.51	4.72	1.48	9.56	1.52
	CFD	21.78	4.72	0.82	10.71	1.54

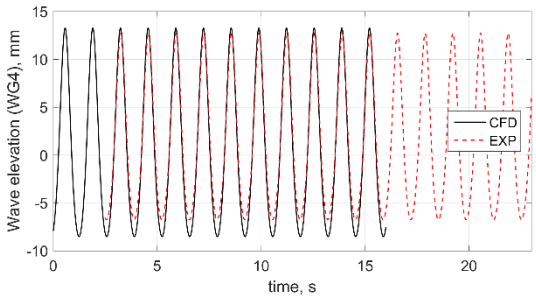

Figure 3. Time series of wave elevation at the position of wave probe WG4 for case CW5.

6.3 VALIDATION OF NUMERICAL SIMULATIONS IN WAVES

Validation of the numerical results for the simulations in waves is performed for the CW3 case, which corresponds to 100% UKC and model speed equal to 0.872 m/s. Numerical values obtained for the last eight encounter periods are taken to perform a Fourier fitting analysis. The computed longitudinal force in waves and its post-processed time series (obtained by applying the Fourier series up to the 3rd order) can be seen in Figure 4. The comparison with the post-processed experimental values is shown in Figure 5. The corresponding parameters obtained from the harmonic decomposition of the time series (the zeroth, the first and the second order harmonics) can be seen in Table 4. From Table 4 it can be observed that the mean value (the zeroth-order term) for the longitudinal force is equal to 7.71 N, which overestimates the experimental value by about 4.6%. In spite of the satisfactory agreement obtained, a numerical verification of the results is desired to exclude the grid and time step dependency of the numerical results.

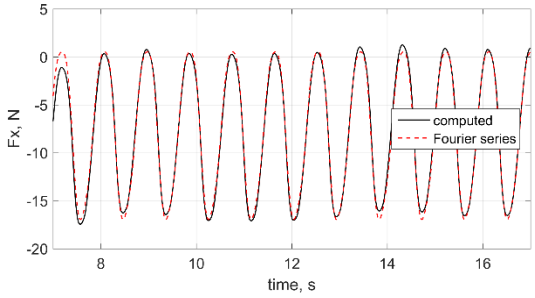

Figure 4. Fourier series approximation of the time series of longitudinal force for the CW3 case.

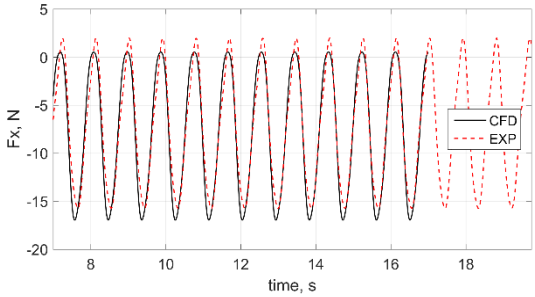

Figure 5. Comparison between numerical and experimental results obtained for the longitudinal force for the CW3 case.

Table 4. Harmonic decomposition of the computed and measured time series for the longitudinal force in waves

Test ID		H_{max}, (N)	f, (1/s)	a0, (N)	A1, (N)	A2 (N)
CW2	EXP	/	/	/	/	/
	CFD	17.00	5.48	-2.15	8.33	1.13
CW5	EXP	/	/	/	/	/
	CFD	6.94	4.71	-1.32	3.48	0.17
CW3	EXP	17.40	7.05	-7.37	8.55	0.90
	CFD	17.55	7.03	-7.72	9.08	0.74

6.4 RESULTS FOR 100% UKC

Time series of the longitudinal force for the CW2 case is shown in Figure 6. Again, the last eight encounter periods of the computed time series are used for the Fourier analysis. The magnitude of the zeroth-order harmonic of the Fourier series is equal to 2.15 N, which is a significant increase in in waves compared to the calm water resistance (0.75 N, see Table2). The orbital velocity of wave particles have a tendency to increase the shear stress and thus increase the frictional resistance in waves compared to the calm water case. For the CW2 case, the comparison shows that the frictional resistance has increased by about 20%, while for the CW3 case this increase is approximately 8%. From the results, it can be observed that there is a significant increase in the pressure resistance in waves for both cases. For the CW2 case, the mean value for pressure resistance accounts for 60 % of the total resistance in waves, which also leads to a significant increase in added resistance in waves. It is important to mention that in the

CW2 case numerical ventilation was also observed for a large portion of the hull wetted surface, especially in the fore part, see Figure 7. This was observed in the CW3 case as well, mostly in the front part of the hull. The transition between the air and water occurred over a large number of cells, resulting in a large number of cells having approximately the same volume fraction of air and water. This did not have a significant influence on the results for the test case CW3 unlike in the test case CW2 where large number of cells in the bow area have a volume fraction of water lower than 1 but higher than 0.5. The stronger numerical ventilation observed for the CW2 case causes an overestimation of the friction velocity, which is further used for the calculation of shear stress. Also, due to the high wave elevation at the bow part of hull, parts of the wave crests are captured by the coarser free surface refinement rather than the finest one.

The wave pattern around the DTC hull, at the end of the simulation, can be seen in Figures 8 and 9 for cases CW2 and CW3 respectively. The Kelvin wake is formed for both 100% UKC cases and is more emphasized for the test case conducted at the higher speed.

Table 5. Numerical and experimental values of the total resistance in waves

Test ID	EXP, (N)	CFD, (N)	$\overline{R_F}$, (N)	$\overline{R_P}$, (N)
CW2	/	2.15	0.75	1.40
CW5	/	1.32	0.75	0.57
CW3	7.37	7.71	4.06	3.65

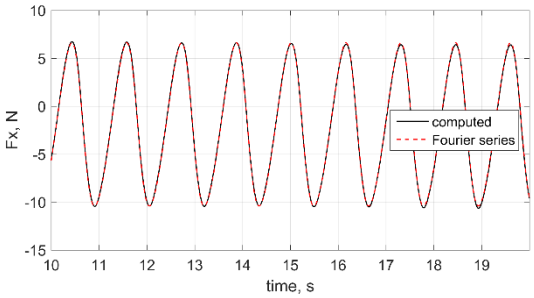

Figure 6. Time series of the computed longitudinal wave force for CW2.

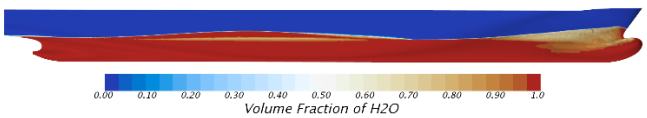

Figure 7. Free surface representation on the model hull for CW2.

In deep water where waves propagate freely, the group velocity is considered twice as small as the actual wave velocity. In shallow water, at large wave lengths, the group velocity and wave velocity are equal. If the ship velocity is smaller than the wave velocity, a Kelvin wake should be formed. However, in the case CW2 the system of divergent and transverse waves has not been fully developed.

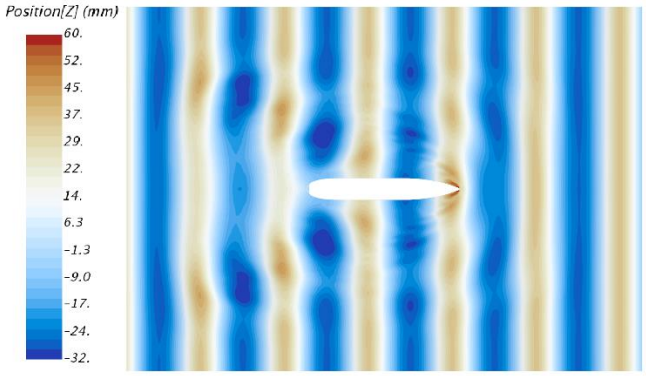

Figure 8. Free surface elevation for the test case CW2.

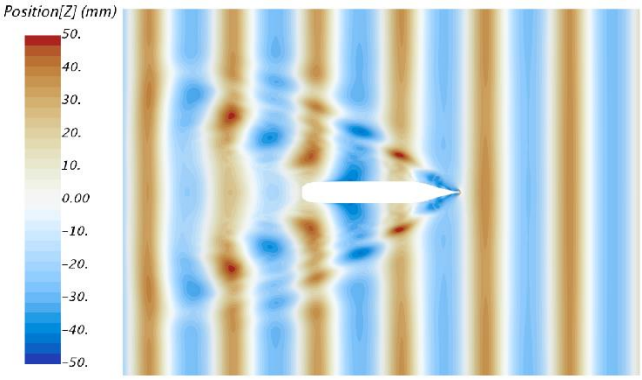

Figure 9. Free surface elevation for the test case CW3.

6.5 RESULTS FOR 20% UKC

In the test case CW5, which corresponds to 20% UKC at model speed equal to 0.327 m/s, the total resistance in waves is about 30% larger than the calm water resistance, Table 5. The frictional part has increased by about 11% compared to the calm water case. However, the frictional part of added resistance is about 24% of the total value. This is also common for relative short waves in deep water (Sigmund and el Moctar, 2018), where viscous effects are important and the corresponding increase in the frictional component of the added resistance in waves is larger than 20%.

Comparing the results with the similar test conditions with respect to waves and ship speed but different water depth (test case CW2 for 100% UKC) it can be observed that the mean value of frictional resistance remained almost the same, while pressure resistance increased by about 60%. However, taking into account the shortcomings that were observed in the numerical results for CW2, the numerical setup of that particular case should be improved in order to properly compare the results and draw valid conclusions.

For the CW2 and the CW5 cases a comparison of wall shear stress can be seen in Figure 10, and a comparison of the hydrodynamic pressure in Figure 11. Both hydrodynamic pressure and longitudinal shear stress in waves are presented at a time step corresponding to encounter period T_e.

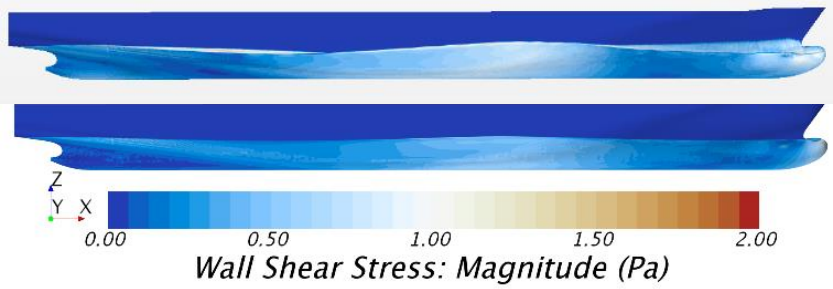

Figure 10. Wall shear stress for the CW2 case (top) and the CW5 case (bottom).

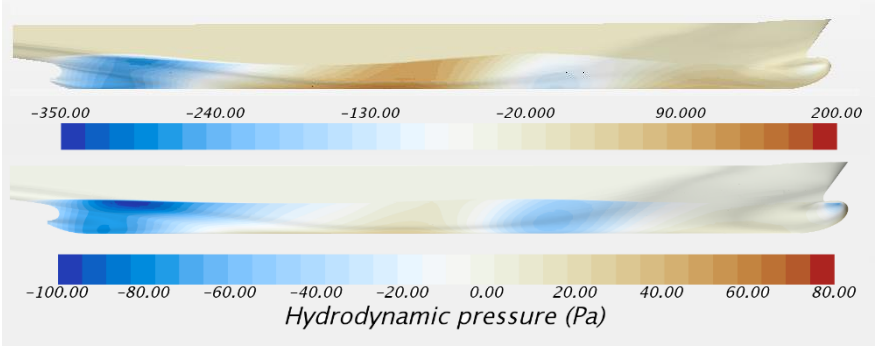

Figure 11. Hydrodynamic pressure on hull for the CW2 case (top) and the CW5 case (bottom).

The shear stress is larger for the CW2 case in the bow region due to the diffraction of the incident waves.

When it comes to hydrodynamic pressure, large differences can be observed. Pressure resistance consists of wave resistance and viscous pressure resistance, where the latter is in numerical sense very responsive to the numerical setup and different numerical disturbances, such as small pressure level changes during the simulation with larger numerical uncertainty compared to the frictional resistance (Raven et al., 2008). In the case of the CW5 results, it appears that very short waves are being reflected from the forcing zone at the side boundary, Figure 12. Parameters in the source term functions used to prevent wave reflections are dependent on wave characteristics and should be adjusted to the particular wave that is being forced. The same forcing coefficient is used for both CW2 and CW5, which possibly led to waves of approximately three times smaller elevation, in the case CW5, being reflected, Figure 12.

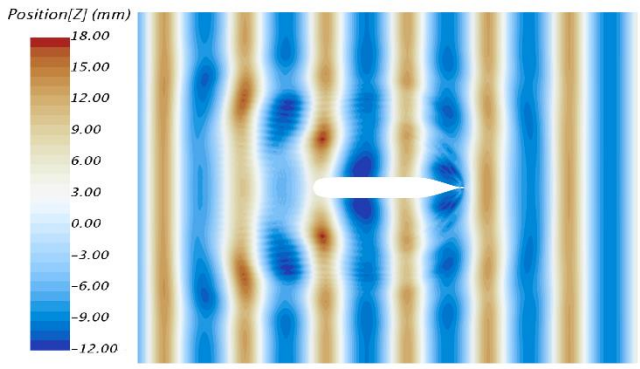

Figure 12. Free surface elevation for the CW5 case

In Table 6, the added resistance in waves for all tested cases can be seen along with the added resistance coefficient normalized using equation (11). As can be seen in the table, the largest added resistance coefficient is obtained for CW5 test case. Since added resistance in waves is very dependent on the ship speed, for the two comparable cases with the same wave characteristics, a larger added resistance coefficient is obtained for CW3 as expected. CW5 has the smallest added resistance, about 24% of the total resistance in waves, but also has the smallest wave amplitude. By comparing the results, it could be concluded that for waves of medium length in shallow water, added resistance in waves is not proportional to the square value of the wave amplitude, but that exponent becomes notably smaller.

Table 6. Added resistance in waves for all test cases

Test ID	R_{AW} , N	C_{AW}
CW2	1.39	1.35
CW3	2.94	2.85
CW5	0.32	3.50

7 CONCLUSIONS

A numerical investigation of added resistance in waves for DTC containership at model scale was carried out for two different speeds and water depths. The numerical results were validated against the experimental data and satisfactory agreement was obtained for cases with lower model speed at both 100% and 20% UKC considering that very small values were measured during the experiment. A somewhat larger relative deviation was obtained for test case with higher speed due to the numerical ventilation

that was observed on a large portion of the wetted surface area. The validation of test case CW3, which corresponds to higher model speed at 100% UKC, shows satisfactory agreement with the experimentally obtained force in the longitudinal direction. Even though numerical ventilation can be observed on a small part of the model hull in CW3 as well, it did not affect the results significantly, unlike in the case CW2 where a notable increase not only in pressure resistance but in frictional resistance as well was observed. It caused a large added resistance that is not only pressure driven, but viscous driven as well. Based on the obtained results it could be concluded that added resistance in medium waves of intermediate water depths is mostly pressure driven as in deep water as well.

8 FUTURE WORK

Plans for future work will include a verification of the numerical results by performing the analysis of grid and time step dependency. Additional steps with the respect to avoiding the occurrence of numerical ventilation will be taken in order to improve the numerical results.

9 ACKNOWLEDGEMENTS

This research was partially carried out within the framework of the Innoship project (project number 03SX416B). The authors acknowledge the financial support by the Federal Ministry for Economic Affairs and Energy (Bundesministerium für Wirtschaft und Energie) of Germany. Furthermore, the authors would like to thank the Faculty of Mechanical Engineering and Naval Architecture, University of Zagreb, for funding the licence of the software package STAR-CCM+.

10 REFERENCES

Carrica, P.M., Wilson, R. V., Noack, R.W., Stern, F., 2007. Ship motions using single-phase level set with dynamic overset grids. Comput. Fluids 36, 1415–1433. https://doi.org/10.1016/j.compfluid.2007.01.007

CD-adapco, 2018. STAR-CCM+ User Guide.

Chen, S., Hino, T., Ma, N., Gu, X., 2018. RANS investigation of influence of wave steepness on ship motions and added resistance in regular waves. J. Mar. Sci. Technol. 23, 1–13. https://doi.org/10.1007/s00773-018-0527-5

el Moctar, O., Shigunov, V., Zorn, T., 2012. Duisburg Test Case : Post-Panamax Container Ship for Benchmarking. Sh. Technol. Res. J. 59, 50–64.

Ferziger, J.H., Perić, M., 2012. Computational Methods for Fluid Dynamics. Springer Science & Business Media, Berlin.

IMO MEPC 203(62) (2011). Amendments to the annex of the protocol of 1997 to amend the international convention of pollution from ships, 1973, as modified by the protocol of 1978 relating thereto.

ITTC – Recommended Procedures and Guidelines, 2014. Practical Guidelines for Ship CFD Applications, No. 7.5–03–02–03

Kim, M., Hizir, O., Turan, O., Incecik, A., 2017. Numerical studies on added resistance and motions of KVLCC2 in head seas for various ship speeds. Ocean Eng. 140, 466–476. https://doi.org/10.1016/j.oceaneng.2017.06.019

Liu, Y., Zou, L., Zou, Z.J., Lu, T.C., Liu, J.X., 2017. Numerical Predictions of Hydrodynamic Forces and Squat of Ships in Confined Waters. Proc. 8th ICCM 1095–1110.

Quérard, A., Temarel, P., Turnock, S.R., 2008. Influence of Viscous Effects on the Hydrodynamics of Ship-Like Sections Undergoing Symmetric and Anti-Symmetric Motions, Using RANS, in: Proceedings of the ASME 27th International Conference on Offshore Mechanics and Arctic Engineering OMAE2008, June 15-20, 2008, Estoril, Portugal. pp. 683–692.

Raven, H., Van Der Ploeg, A., Starke, B., Eça, L., 2008. Towards a CFD-based prediction of ship performance.

Riesner, M., el Moctar, O., 2018. A time domain boundary element method for wave added resistance of ships taking into account viscous effects. Ocean Engineering, 162, 290-303.

Sigmund, S., el Moctar, O., 2018. Numerical and experimental investigation of added resistance of different ship types in short and long waves. Ocean Eng. 147, 51–67. https://doi.org/10.1016/j.oceaneng.2017.10.010

Tello Ruiz, M., 2018. Manoeuvring model of a container vessel in coastal waves. PhD Thesis. Ghent University.

Tello Ruiz, M., De Caluwé, S., Van Zwijnsvoorde, T., Delefortrie, G., Vantorre, M., 2015. Wave effects in 6DOF on a ship in shallow water, in: Marsim 2015. Newcastle, UK, pp. 1–15.

Tello Ruiz, M., Mansuy, M., Delefortrie, G., Vantorre, M., 2019. Modelling the manoeuvring behaviour of an ULCS in coastal waves. Ocean Eng. 172, 213–233. https://doi.org/10.1016/j.oceaneng.2018.11.046

Tello Ruiz, M., Van Hoydonck, W., Delefortrie, G., Vantorre, M., 2017. Side wall effects of ship model tests in shallow water, in: LLoys, T., van der Ploeg, A. (Eds.), 20th Numerical Towing Tank Symposium. Wageningen, The Netherlands, pp. 193–198.

Tello Ruiz, M., Vantorre, M., Delefortrie, G., 2016. Induced wave forces on a ship manoeuvring in coastal

waves. Ocean Eng. 121, 472–491.

Tezdogan, T., Demirel, Y.K., Kellett, P., Khorasanchi, M., Incecik, A., Turan, O., 2015. Full-scale unsteady RANS CFD simulations of ship behaviour and performance in head seas due to slow steaming. Ocean Eng. 97, 186–206. https://doi.org/10.1016/j.oceaneng.2015.01.011

Tezdogan, T., Incecik, A., Turan, O., 2016. Full-scale unsteady RANS simulations of vertical ship motions in shallow water. Ocean Eng. 123, 131–145. https://doi.org/10.1016/j.oceaneng.2016.06.047

Toxopeus, S.L., Simonsen, C.D., Guilmineau, E., Visonneau, M., Xing, T., Stern, F., 2013. Investigation of water depth and basin wall effects on KVLCC2 in manoeuvring motion using viscous-flow calculations. J. Mar. Sci. Technol. 18, 471–496. https://doi.org/10.1007/s00773-013-0221-6

Van Hoydonck, W., Toxopeus, S., Eloot, K., Bhawsinka, K., Queutey, P., Visonneau, M., 2018. Bank effects for KVLCC2. J. Mar. Sci. Technol. 0, 1–26. https://doi.org/10.1007/s00773-018-0545-3

Van Zwijnsvoorde, T., Tello Ruiz, M., Delefortrie, G., Lataire, E. 2019. Sailing in shallow water waves with the DTC container carrier, in: Proceedings of the 5th International Conference on Ship Manoeuvring in Shallow and Confined Water with non-exclusive focus on Manoeuvring in Waves, Wind and Current. Ostend, Belgium.

Vantorre, M., Journée, J., 2003. Validation of the strip theory code SEAWAY by model tests in very shallow water. Flanders Hydraul. Res. Numer. Model. Colloquium.

Yasukawa, H., Adnan, F.A., 2006. Experimental study on wave-induced motions and steady drift forces of an obliquely moving ship. J. Japan Soc. Nav. Archit. Ocean Eng. 3, 133–138.

11 AUTHORS BIOGRAPHY

Ivana Martić is a doctoral student of Naval Architecture and teaching/research assistant at the Faculty of Mechanical Engineering and Naval Architecture, University of Zagreb. Her area of research includes ship hydrodynamics.

Guillermo Chillcce holds the current position of research assistant at the Institute of Ship Technology, Ocean Engineering and Transport Systems (University of Duisburg-Essen). His area of expertise is seakeeping and manoeuvring analysis by means of boundary element methods and field methods.

Manases Tello Ruiz PhD, Naval Architect and Marine Engineer, is a Research Staff at Ghent University. He has been involved in several (inter)national projects with main focus on manoeuvring, seakeeping, and wave energy converters. Currently, he is working on ship air pollution and machine learning techniques applied to ship hydrodynamics. At present he is also a member of the ITTC Specialist Committee of Manoeuvring in Waves, at which he has been appointed as secretary.

Jorge Ramirez holds the current position of naval architect at Knud e Hansen in Denmark. He is responsible for performing different analyses to assist in the design process of a vessel, such as trim optimization, resistance analysis, wind loads and ship propulsion. His previous experience includes research for wave loadings on offshore wind turbines experimental and numerical analysis, wave energy converters.

Nastia Degiuli is a full professor at the Faculty of Mechanical Engineering and Naval Architecture, University of Zagreb and head of the Chair of Ship Hydrodynamics. Her area of expertise involves experimental and numerical ship hydrodynamics.

Ould el Moctar, Prof. Dr.-Ing. is full Professor in Ship Technology and Ocean Engineering at the University of Duisburg-Essen. His publications cover various aspects of hydrodynam-ics and Fluid-Structure-Interaction. The focus of his research is seakeeping, hydroelasticity, slamming and sloshing, cavitation, manoeuvring and propulsion in waves. He is editor and co-editor of many international journals.

NUMERICAL AND EXPERIMENTAL STUDY ON THE WAVE–BODY INTERACTION PROBLEM WITH THE EFFECT OF FORWARD SPEED AND FINITE WATER DEPTH IN REGULAR WAVES

Tianlong Mei,
School of Naval Architecture, Ocean and Civil Engineering, Shanghai Jiao Tong University, China; Maritime Technology Division, Ghent University, Belgium

Guillaume Delefortrie,
Flanders Hydraulics Research and Maritime Technology Division, Ghent University, Belgium

Manasés Tello Ruiz, Changyuan Chen, Evert Lataire and **Marc Vantorre**,
Maritime Technology Division, Ghent University, Belgium

Zaojian Zou,
State Key Laboratory of Ocean Engineering, Shanghai Jiao Tong University, China; School of Naval Architecture, Ocean and Civil Engineering, Shanghai Jiao Tong University, China

NUMERICAL AND EXPERIMENTAL STUDY ON THE WAVE–BODY INTERACTION PROBLEM WITH THE EFFECT OF FORWARD SPEED AND FINITE WATER DEPTH IN REGULAR WAVES

Tianlong Mei, School of Naval Architecture, Ocean and Civil Engineering, Shanghai Jiao Tong University, China; Maritime Technology Division, Ghent University, Belgium
Guillaume Delefortrie, Flanders Hydraulics Research and Maritime Technology Division, Ghent University, Belgium
Manasés Tello Ruiz, **Changyuan Chen, Evert Lataire** and **Marc Vantorre**, Maritime Technology Division, Ghent University, Belgium
Zaojian Zou, State Key Laboratory of Ocean Engineering, Shanghai Jiao Tong University, China; School of Naval Architecture, Ocean and Civil Engineering, Shanghai Jiao Tong University, China

SUMMARY

In this study, a time domain higher-order Rankine panel method is developed and applied to solve the wave–body interaction problem in regular waves. The hydrodynamic effects of forward speed and finite water depth are accounted for. In order to verify the proposed numerical method, the Duisburg Test Case (DTC) containership is chosen as a case study. The numerical results for the wave induced ship's motions and the added resistance will be validated against model tests, which were carried out in the Towing Tank for Manoeuvres in Confined Water at Flanders Hydraulics Research (FHR) in cooperation with Ghent University (UGent) as part of the SHOPERA project.

1 INTRODUCTION

With more and more deep drafted ships navigating or manoeuvring near shore or in coastal areas, it is desired to have a better insight in the effects of shallow water. Shallow water would lead to a more complicated hydrodynamic behaviours compared to the open sea. What is more, these areas are often subjected to wave conditions. In fact, under the presence of waves in shallow water areas, not only the safety related issues of the manoeuvring ship should arouse concern, but also the seakeeping behaviour, such as wave-induce motions and added resistance, needs to be taken into account to avoid grounding and to quantify speed reduction. Hence, it is essential to investigate the wave-induced motions and second order forces in finite water depth.

For this reason, many researchers have focused on the corresponding numerical scheme of wave body interaction problems in finite water depths. In an early stage, the 2D strip method was used for its practicability and high efficiency in the initial design, see e.g. (Kim, 1968; Hwang and Lee, 1975; Takaki, 1977; Takaki et al. 1978; Andersen, 1979; Perunovic and Jensen, 2003; Kim, 1999; Kim and Kim, 2012; Vantorre and Journée, 2003). The mentioned method, however, is only suitable for relatively high frequencies and a slender body ship hull. Because of this limitation, researchers turned their attention to the matched asymptotic expansion method (MAEM), which performed matching of solutions on the interface boundary by using different numerical techniques on the divided field zones, e.g. (Tuck, 1970; Vorobyov and Stasenko, 2010). The main problem with this method is that because of the long wave assumption large deviations found when the wave length is close to the ship length.

More advance techniques, available nowadays, such as the Green function based 3D panel method and the Rankine source based 3D panel method. The free surface Green function based 3D panel method has been initially applied by researchers, e.g. (Oortmerssen, 1976; Chan, 1990; Li, 2001). Though the accuracy seems to be better than the 2D method or MAEM, the form and evaluation of Green function is relatively complex and difficult. Furthermore, the Neumann-Kelvin linearization of the method cannot consider the interaction between steady and unsteady flow. In comparison, the Rankine source based 3D panel method has been widely used for its flexible treatment of the free surface as well as the simpler kernel form (Söding et al., 2014; Riesner et al., 2016; Riesner and Moctar, 2018). Gao et al., 2008and Yao et al., 2017, among others, applied the Rankine panel method for shallow water conditions, in the frequency domain. In their method, however, the coupling effect with the nonlinear external force cannot be considered (Kim and Kim, 2012). The time domain Rankine panel method is applied for the wave induced motion problems in shallow water, e.g. (Kim and Kim, 2012; Kim and Kim, 2013; Feng et al., 2016; Wang et al., 2016), but their studies only focus on the zero forward speed cases.

In the present study, a time domain higher-order Rankine panel method is developed to investigate the motion responses and added resistance of a moving ship in various water depths in regular waves. The image method is used to satisfy the bottom boundary condition. A good agreement is achieved when comparing the numerical results with the model tests which were executed in the Towing Tank for Manoeuvres in Confined Water at Flanders Hydraulics Research in cooperation with Ghent University as part of the SHOPERA project.

2 MATHEMATICAL FORMULATION

2.1 BOUNDARY VALUE PROBLEM OF RANKINE PANEL METHOD

In the frame of potential theory, a coordinate system $o-xyz$ fixed to a ship with the forward speed U_0 is introduced as shown in Figure 1. Then the total velocity potential $\Psi(\vec{x},\mathrm{t})$ can be written as,

$$\Psi(\vec{x},\mathrm{t}) = \phi_s(\vec{x}) + \varphi_I(\vec{x},\mathrm{t}) + \varphi_d(\vec{x},\mathrm{t}) \quad (1)$$

where ϕ_s, φ_I and φ_d are the basic velocity potential, the regular incoming wave potential and the disturbance velocity potential respectively.

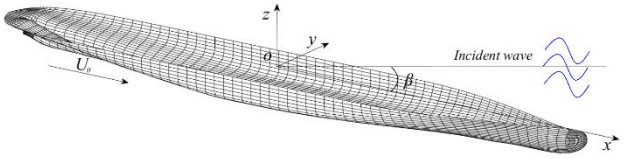

Figure 1. Coordinate system.

Similarly, the wave elevation $\zeta(\vec{x},\mathrm{t})$ can be written as,

$$\zeta(\vec{x},\mathrm{t}) = \zeta_I(\vec{x},\mathrm{t}) + \zeta_d(\vec{x},\mathrm{t}) \quad (2)$$

Naturally, the regular incoming wave potential $\varphi_I(\vec{x},\mathrm{t})$ is given as follows,

$$\varphi_I(\vec{x},t) = \frac{\zeta_A g}{\omega}\frac{\cosh[k(z+h)]}{\cosh kh} sin[k(xcos\beta + ysin\beta) - \omega_e t] \quad (3)$$

where ζ_A is the wave amplitude, ω the wave natural frequency, β the wave angle and k the wave number. The dispersion relation in finite water depth (Figure 2) is:

$$\omega^2 = kgtanh(kh) \quad (4)$$

ω_e is the encounter frequency defined as:

$$\omega_e = \omega - kU_0 cos\beta \quad (5)$$

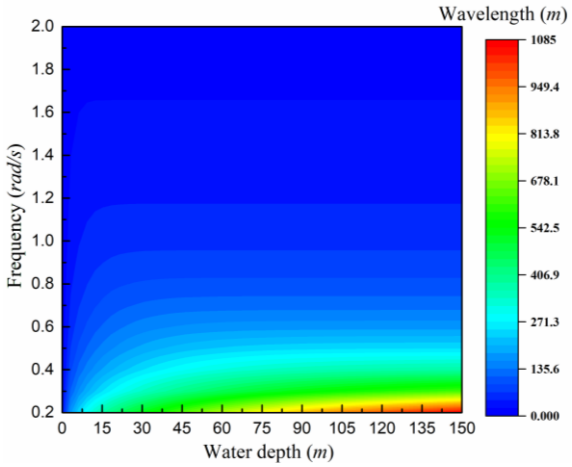

Figure 2. The dispersion relation in finite water depth.

The velocity $\Psi(\vec{x},\mathrm{t})$ satisfies the following boundary value problem (BVP),

$$\nabla^2\Psi = 0, \text{ in the fluid domain} \quad (6)$$

The kinematic and dynamic free surface conditions on the free surface $\mathrm{z} = \zeta(x,y,t)$:

$$\left[\frac{\partial}{\partial \mathrm{t}} - \left(\vec{U} - \nabla\Psi\right)\cdot\nabla\right]\left(\mathrm{z} - \zeta(x,y,t)\right) = 0 \quad (7)$$

$$\left[\frac{\partial}{\partial \mathrm{t}} - \left(\vec{U} - \nabla\Psi\right)\cdot\nabla\right]\Psi = -g\zeta + \frac{1}{2}\nabla\Psi\cdot\nabla\Psi \quad (8)$$

$$\frac{\partial\Psi}{\partial n} = U_0 n_1 + \frac{\partial\vec{\delta}}{\partial t}\cdot\vec{n}, \text{ on body surface } S_b \quad (9)$$

$$\frac{\partial\Psi}{\partial n} = 0, \text{ on the seabed } z = -h \quad (10)$$

where $\vec{\delta}$ is wave induced motion vector and can be written as $\vec{\delta} = \vec{\xi}_T + \vec{\xi}_R \times \vec{r}$, translation vector $\vec{\xi}_T = (\xi_1,\xi_2,\xi_3)$, rotation vector $\vec{\xi}_R = (\xi_4,\xi_5,\xi_6)$.

In present study, the double body linearization is used. By submitting Eq. (1) in Eq. (6) - Eq. (10), the linearized BVP of $\varphi_d(\vec{x},\mathrm{t})$ can be derived as follows,

$\nabla^2\varphi_d = 0$, in the fluid domain;

The kinematic and dynamic free surface conditions on the free surface $\mathrm{z} = 0$

$$\left[\frac{\partial}{\partial \mathrm{t}} - \left(\vec{U} - \nabla\phi_s\right)\cdot\nabla\right]\zeta_d = \frac{\partial\varphi_d}{\partial \mathrm{z}} + \frac{\partial^2\varphi_d}{\partial \mathrm{z}^2}\zeta - \nabla\phi_s\cdot\nabla\zeta_I \quad (11)$$

$$\left[\frac{\partial}{\partial \mathrm{t}} - \left(\vec{U} - \nabla\phi_s\right)\cdot\nabla\right]\varphi_d = -g\zeta_d - \nabla\phi_s\cdot\nabla\zeta_I + \vec{U}\cdot\nabla\phi_s - \frac{1}{2}\nabla\phi_s\cdot\nabla\phi_s \quad (12)$$

$$\frac{\partial\varphi_d}{\partial n} = \sum_{j=1}^{6}(\dot{\xi}_j n_j + \xi_j m_j) - \frac{\partial\varphi_I}{\partial n}, \text{ on mean body surface } \vec{S}_b \quad (13)$$

$$\frac{\partial\varphi_d}{\partial n} = 0, \text{ on the seabed } z = -h \quad (14)$$

$$\varphi_d = 0, \partial\varphi_d/\partial t = 0 \text{ at } t = 0 \quad (15)$$

where $m_j, j = 1\sim6$ represents the interaction between steady and unsteady flows, defined as:

$$\begin{aligned}(m_1,m_2,m_3) &= (\vec{n}\cdot\nabla)\left(\vec{U} - \nabla\phi_s\right)\\ (m_4,m_5,m_6) &= (\vec{n}\cdot\nabla)[\vec{x}\times\left(\vec{U} - \nabla\phi_s\right)]\end{aligned} \quad (16)$$

The detailed evaluation of the m_j term can be found in Mei et al..

2.2 EQUATIONS OF SHIP MOTIONS AND FORCES

The 6-DOF ship motion equations can be obtained based on Newton's Second Law,

$$M_{ij}\ddot{\xi}_j(t) + C_{ij}\xi_j(t) = F_i\left(\dot{\xi}_j, \xi_j, t\right), \quad i,j = 1\sim6 \tag{17}$$

where M_{ij} and C_{ij} represent mass and restoring coefficients matrix, respectively.

The hydrodynamic forces and moments $F_i\left(\dot{\xi}_j, \xi_j, t\right)$ can be evaluated by,

$$F_i = -\iint_{\vec{S}_b} \rho[\frac{\partial}{\partial t} - \left(\vec{U} - \nabla\phi_s\right)\cdot\nabla]\,\varphi_{I,d} n_i ds, i = 1\sim6 \tag{18}$$

For a harmonic forced ship, the radiation force F_{ij} can be expressed as:

$$\begin{aligned} F_{ij} &= -\left[A_{ij}(\omega_e)\ddot{\bar{\xi}}_j(t) + B_{ij}(\omega_e)\dot{\bar{\xi}}_j(t)\right] \\ &= \left[\omega_e^2 A_{ij}(\omega_e) - i\omega_e B_{ij}(\omega_e)\right]\bar{\xi}_j e^{i\omega_e t} \end{aligned} \tag{19}$$

where ω_e and $\bar{\xi}_j$ are the harmonic forced motion frequency and amplitude, respectively.

Then the added mass and damping coefficient can further be obtained by:

$$\begin{aligned} A_{ij} &= \frac{Re(F_{ij})}{\omega_e^2 \bar{\xi}_j} \\ B_{ij} &= \frac{Im(F_{ij})}{\omega_e \bar{\xi}_j} \end{aligned} \tag{20}$$

In this study, the added wave resistance is evaluated by applying the pressure integration method (also known as near field method) proposed by Joncquez (2009),

$$\begin{aligned} &\vec{F}^{(2)} = -\rho\iint_{\vec{S}_b} \nabla\left(\frac{\partial}{\partial t} - \left(\vec{U} - \nabla\phi_s\right)\cdot\nabla\varphi\right)\cdot\vec{\delta}\,\vec{n}_0 ds \\ &-\rho\iint_{\vec{S}_b} \vec{H}\vec{x}\cdot\nabla\left(\vec{U}\cdot\nabla\phi_s + \frac{1}{2}\nabla\phi_s\cdot\nabla\phi_s + gz\right)\vec{n}_0 ds \\ &-\rho\iint_{\vec{S}_b} \frac{1}{2}\nabla\varphi\cdot\nabla\varphi\,\vec{n}_0 ds \\ &-\rho\iint_{\vec{S}_b} \left[\frac{\partial\varphi}{\partial t} - \vec{U}\cdot\nabla\varphi + \nabla\phi_s\cdot\nabla\varphi + g(\xi_3 + \xi_4 y - \right. \\ &\left.\xi_5 x)\right]\cdot\vec{n}_1 ds \\ &-\rho\iint_{\vec{S}_b} \left[\nabla\left(-\vec{U}\cdot\nabla\phi_s + \frac{1}{2}\nabla\phi_s\cdot\nabla\phi_s\right)\right]\vec{\delta}\vec{n}_1 ds \\ &-\rho\iint_{\vec{S}_b} \left(-\vec{U}\cdot\nabla\phi_s + \frac{1}{2}\nabla\phi_s\cdot\nabla\phi_s + gz\right)\vec{H}\,\vec{n}_2 ds \\ &+\frac{1}{2}\rho g\int_{wl}[\zeta - (\xi_3 + \xi_4 y - \xi_5 x)]^2\frac{\vec{n}_0}{sin\alpha}dl \\ &-\rho\int_{wl}\left[-\vec{U}\cdot\nabla\phi_s + \frac{1}{2}\nabla\phi_s\cdot\nabla\phi_s\right][\zeta - (\xi_3 + \xi_4 y - \\ &\xi_5 x)]\frac{\vec{n}_1}{sin\alpha}dl \end{aligned} \tag{21}$$

where $\varphi = \varphi_I(\vec{x}, t) + \varphi_d(\vec{x}, t)$, the wave induced motion vector is $\vec{\delta} = \vec{\xi}_T + \vec{\xi}_R \times \vec{x}$, and the vectors $\vec{n}_0$, $\vec{n}_1$ and $\vec{n}_2$ mean the zero, first and second-order components of the normal vector on the hull surface, $\vec{H}$ is second-order transformation matrix. α represents the angle of the hull flare at free surface.

$$\vec{n}_0 = \begin{Bmatrix} \vec{n} \\ \vec{x}\times\vec{n} \end{Bmatrix};\ \vec{n}_1 = \begin{Bmatrix} \vec{\xi}_R\times\vec{n} \\ \vec{\xi}_T\times\vec{n} + \vec{\xi}_R\times(\vec{x}\times\vec{n}) \end{Bmatrix};$$

$$\vec{n}_2 = \begin{Bmatrix} \vec{H}\vec{n} \\ \vec{H}(\vec{x}\times\vec{n}) + \vec{\xi}_T\times(\vec{\xi}_R\times\vec{n}) \end{Bmatrix};$$

$$\vec{H} = \frac{1}{2}\begin{bmatrix} -(\xi_5^2 + \xi_6^2) & 0 & 0 \\ 2\xi_4\xi_5 & -(\xi_4^2 + \xi_6^2) & 0 \\ 2\xi_4\xi_6 & 2\xi_5\xi_6 & -(\xi_4^2 + \xi_5^2) \end{bmatrix}.$$

2.3 NUMERICAL IMPLEMENTATION

According to the Green's second theorem, the boundary integral equation (BIE) can be derived as,

$$\begin{aligned} &2\pi\varphi_d(\vec{x}, t) = \iint_{\vec{S}_f + \vec{S}_b} \frac{\partial\varphi_d(\vec{x}', t)}{\partial n} G(\vec{x}, \vec{x}')ds - \\ &\iint_{\vec{S}_f + \vec{S}_b} \varphi_d(\vec{x}', t)\frac{\partial G(\vec{x}, \vec{x}')}{\partial n}ds \end{aligned} \tag{22}$$

where $\vec{x} = (x, y, z)$ and $\vec{x}' = (x', y', z')$ are field point and source point, respectively; $\vec{S}_f$ and $\vec{S}_b$ are mean free surface and mean wetted hull. By using the image method, the Green function $G(\vec{x}, \vec{x}')$ can be expressed as,

$$G(\vec{x}, \vec{x}') = \frac{1}{r} + \frac{1}{r'} \tag{23}$$

where,

$$\begin{cases} r = \sqrt{(x - x')^2 + (y - y')^2 + (z - z')^2} \\ r' = \sqrt{(x - x')^2 + (y - y')^2 + (z + z' + 2h)^2} \end{cases} \tag{24}$$

In order to avoid numerical errors due to a direct difference method, the related physical variables are approximately described by quadratic B-spline function,

$$\begin{cases} \varphi_d(\vec{x}, t) \approx \sum_{j=1}^{9}(\varphi_d)_j(t)B_j(\vec{x}) \\ \zeta_d(\vec{x}, t) \approx \sum_{j=1}^{9}(\zeta_d)_j(t)B_j(\vec{x}) \\ \frac{\partial\varphi_d}{\partial z}(\vec{x}, t) \approx \sum_{j=1}^{9}(\partial\varphi_d/\partial z)_j(t)\,B_j(\vec{x}) \end{cases} \tag{25}$$

By submitting Eq. (23) in Eq. (20), a set of linear equations can be obtained according to the distribution of source points on $\vec{S}_b$ and $\vec{S}_f$,

$$\begin{aligned} &2\pi(\varphi_d)_i + \sum_{j=1}^{N_b} Q_{i,j}(\varphi_d)_j - \sum_{j=N_b+1}^{N_b+N_f} P_{i,j}\left(\frac{\partial\varphi_d}{\partial n}\right)_j \\ &= \sum_{j=1}^{N_b} P_{i,j}\left(\frac{\partial\varphi_d}{\partial n}\right)_j - \sum_{j=N_b+1}^{N_b+N_f} Q_{i,j}(\varphi_d)_j \\ &, i = 1\sim N_b \end{aligned} \tag{26}$$

$$\sum_{j=1}^{N_b} Q_{i,j}\,(\varphi_d)_j - \sum_{j=N_b+1}^{N_b+N_f} P_{i,j}\left(\frac{\partial\varphi_d}{\partial n}\right)_j = \sum_{j=1}^{N_b} P_{i,j}\left(\frac{\partial\varphi_d}{\partial n}\right)_j - \sum_{j=N_b+1}^{N_b+N_f} Q_{i,j}\,(\varphi_d)_j - 2\pi(\varphi_d)_i \quad ,i = N_b+1 \sim N_b+N_f \quad (27)$$

where N_b and N_f are the numbers of discretized panels on $\vec{S}_b$ and $\vec{S}_f$ respectively. The detailed evaluation method for the influence coefficients $P_{i,j}$ and $Q_{i,j}$ can be found in Mei et al...

In addition, an artificial damping beach is installed in the kinematic free surface condition to satisfy the radiation condition which can be found in Huang (1997). Also, an artificial spring model by Kim and Kim (2011) should be installed for evaluation of surge motion and added resistance to avoid numerical divergence.

3 EXPERIMENTAL BENCHMARK TESTS

The tests in shallow water were executed using a 1:89.11 scale model of the DTC in the Towing Tank for Manoevres in Confined Water (cooperation FHR and UGent). Eight captive model tests and two tests in free running mode are selected. The details of the experimental setup can be found in Van Zwijnsvoorde et al., (2019), here only the selected benchmark test conditions are listed in Table 1 and Table 2.

For the experimental setup of the DTC container ship in deep water, tests in regular waves have been conducted by MARINTEK (Now SINTEF Ocean), see el Moctar et al. (2015). The presented model test results for deep water in this paper are from Lyu and el Moctar, (2017). Here, the selected test conditions are given in Table 3.

Table 1. Benchmark tests: Captive tests with the bare hull in waves.

Test ID	Velocity		Environment	
	Model scale (m/s)	Full scale (kts)	UKC	λ/L
CW1;CW2;CW3	0;0.327; 0.872	0;6; 16	100%	0.55
CW4;CW5	0;0.327	0;6	20%	0.55

Table 2. Benchmark tests: Free running wave tests.

Test ID	Velocity		Environment	
	Model scale (m/s)	Full scale (kts)	UKC	λ/L
FW1	0.327	6	100%	0.55
FW2	0.872	16	100%	0.40

Table 3. Model tests of the DTC container ship in deep water.

Run	*Fr*	H(*m*)	T(*s*)	$\beta(°)$
CE4000	0.139	11.3236	15.7628	180
CE4010	0.139	12.5025	15.0429	180
CE4090	0.139	9.463	15.0119	180
CE4100	0.139	6.2325	14.9913	180
CE4241	0.139	9.0174	14.3478	180
CE4251	0.139	6.1649	14.312	180
CE4260	0.139	7.6006	14.2829	180
CE4020	0.139	13.0552	9.9868	180
CE4030	0.139	9.9967	9.0284	180
CE4040	0.139	7.2495	8.0136	180
CE4050	0.139	4.448	7.0066	180
CE4060	0.139	1.5009	5.008	180
CE4070	0.139	0.9966	5.0049	180
CE4080	0.139	0.65	5.0033	180

4 RESULTS AND DISCUSSIONS

The main particulars the Duisburg Test Case (DTC) container ship are listed in Table 4. Due to the symmetry of the numerical field, only half of the computational domain is used. Figure 3 shows the discretized panels on boundaries, where the truncated free surface computational domain is 1.5L upstream, 2L downstream and 0.8L half width. The total number of discretized panels are 4950, where 1200 on half-ship hull and 3750 on half-free surface.

Table 4. Main particulars of DTC

Length (L) (m)	355.0
Breadth (B) (m)	51.0
Draft (T) (m)	14.5
Longitudinal centre of gravity (m)	-2.941
Vertical centre of gravity (m)	19.851
Displacement (m^3)	173467
Block coefficient (C_B)	0.661
Froude number (F_r)	0.139

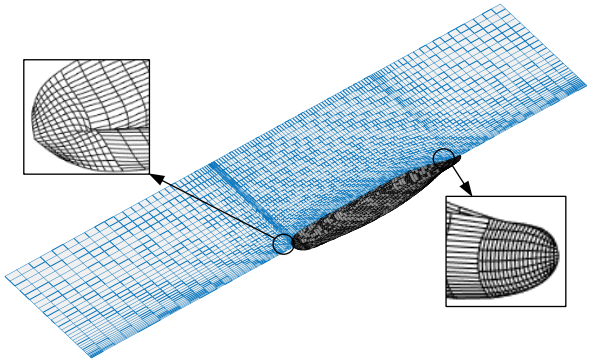

Figure 3. Discretized panels on body and free surface.

4.1 WAVE EXCITING FORCE

Figure 4 shows the time histories of wave exciting force and moment at four water depths, i.e. infinite water depth, 100% UKC, 50% UKC and 20% UKC. As can be seen, all

of the curves are smooth, which demonstrates the good numerical stability of the present program. It's worth noting that, even for the same wave frequency of the incident wave ($\omega_0\sqrt{L/g} = 3.0$), the time history curves at four water depths show different encounter wave frequencies due to the dispersion relation in finite water depth (see Figure 2).

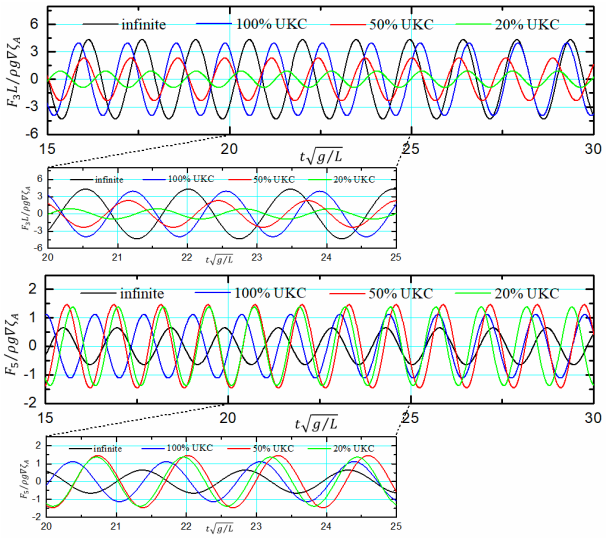

Figure 4. Time histories of wave exciting force and moment at four water depths. Heave force (top), Pitch moment (bottom), $\omega_0\sqrt{L/g} = 3.0$, $F_r = 0.139$.

The non-dimensional wave exciting heave force and pitch moment with respect to frequencies at different water depths are plotted in Figure 5. The amplitudes of frequency results are obtained by using Fourier series expansion from the time history results corresponding to the same frequency. From Figure 5, it can be observed that the obvious difference mainly occurs at low frequencies for four water depths, whereas the values at high frequencies don't show obvious differences except for phase shift persistence. In low frequency areas, the most distinct feature is that the peak values of wave excitation force and moment RAO move toward lower frequencies with decreasing water depth, the same conclusion can also be found in Kim and Kim (2012) for the zero forward speed case by Rankine panel method and in Perunovic and Jensen (2003) for the nonzero forward speed case by strip method. The reason is because the peak value is closely related to the ratio of wave length to the projected length of the ship on the direction of incident wave (i.e. $\lambda/L\cos\beta$).

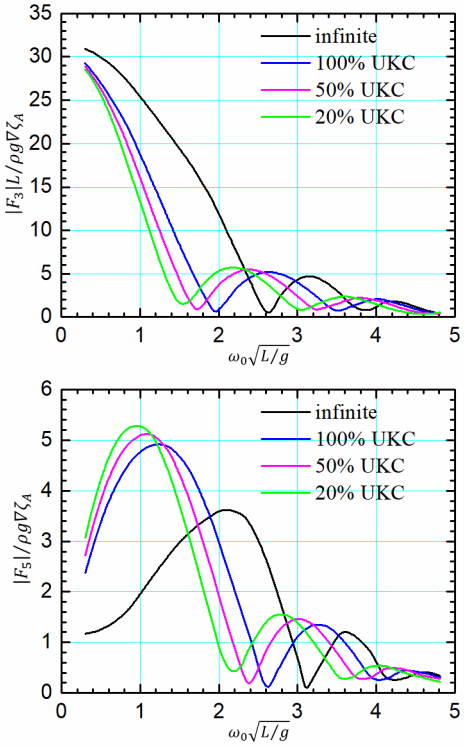

Figure 5. RAO of wave exciting force and moment. Heave force (top), Pitch moment (bottom), $F_r = 0.139$.

4.2 HYDRODYNAMIC COEFFICIENTS

Figure 6 presents the added mass and damping coefficients due to forced heave and pitch motion for different water depths. From the figures in (a) and (c), it can be observed that the added mass decline sharply in low frequencies, while almost tend to flatten with increasing of the frequency; as for the damping coefficients in (b) and (d), the results increased in the dimensionless frequency areas lower than 1.0 and then decreased with the increased frequency. Generally speaking, a shallow water induces larger hydrodynamic coefficients; low frequency incident wave makes enormous contributions to the hydrodynamic coefficients in both deep and shallow water, especially for the added mass, while the results almost converge to the deep-water case with increasing wave frequency. The reason is that the wave length does not change dramatically at high wave frequency areas according to the dispersion relation (see Figure 2). However, the shallow water effect is much more significant. This is because the incident waves are limited by the sea bottom for such low frequency and therefore more energy is needed to accelerate the fluid movement around the ship in the low frequency range in shallow water.

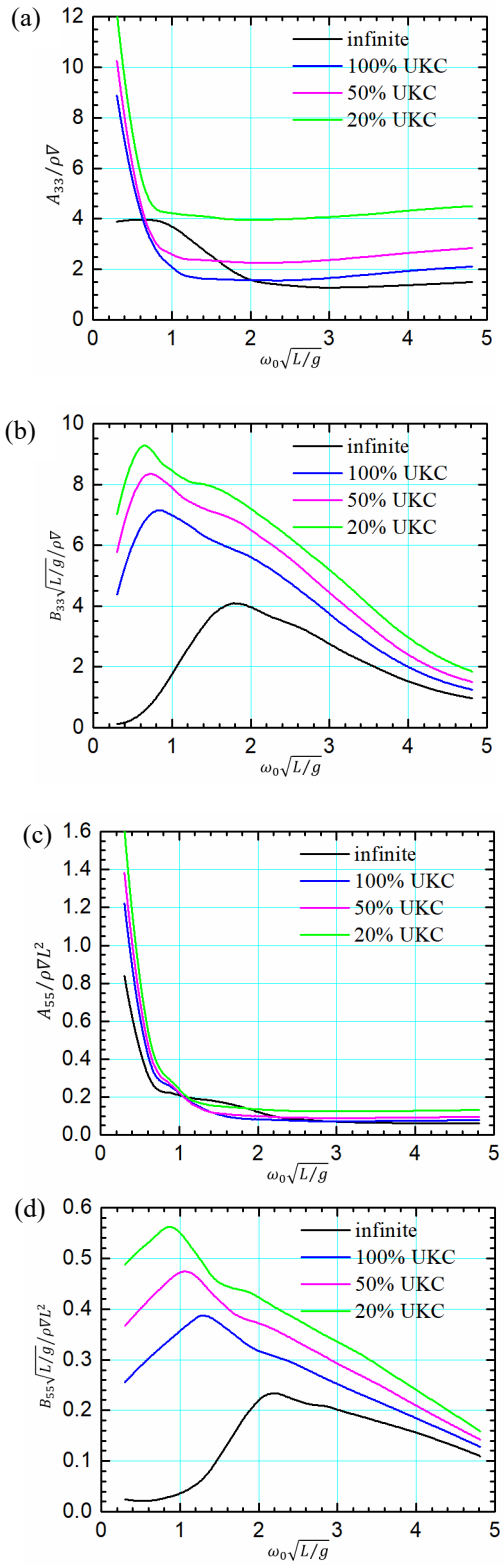

Figure 6. Added mass and damping coefficients. (a), (b) are added mass and damping coefficients due to heave motion; (c), (d) are added mass and damping coefficients due to pitch motion. $F_r = 0.139$.

4.3 MOTIONS IN REGULAR WAVES

Figure 7 shows the time series of heave and pitch motion under four water depths at $\omega_0\sqrt{L/g} = 3.0$, $F_r = 0.139$. Similar to the time histories of wave exciting force in Figure 3, the curves in Figure 7 also show good smoothness and stability. Bear in mind that the wave induced motions show different encounter wave periods even for the same incident wave frequency. The reason is the orbit of a wave fluid particle is strongly dependent on water depth, so in the shallow water, the flow is obstructed by the keel clearance which is different from those of in deep water.

The top figures in Figure 8 (a) and (b) present the comparison of numerical and experimental time history results for heave and pitch motion at $\lambda/L = 0.55$ ($\omega_0\sqrt{L/g} \approx 2.89$) in 100% UKC condition, where the experimental amplitude and numerical amplitude are 0.031m and 1.0m, respectively. As can be seen from experimental time signals, during the experimental process, the acceleration and transition zones exist before the ship reaches a stable state (between two dotted lines), after then, the intended regular wave pattern is disturbed because of reflections by the beach and the wave maker. In addition, due to the significant squat behaviour in shallow water, the mean values of experimental heave and pitch motion time signals (red line) are not zero anymore, which are different from the values calculated by the linear potential method (blue line). However, when the mean values of the experimental time histories in steady state (between two dotted lines) are transformed to zero (see the bottom figures in Figure 8 (a) and (b)), though some phase angle deviations exist due to measurement, a good consistency can be found by comparing with numerical results.

Figure 9 depicts the present numerical results of heave and pitch motion RAO at different water depths, obtained from time series of corresponding wave frequency by Fourier series expansion in comparison with the experimental data. Here, the experimental results in shallow water come from the Towing Tank for Manoeuvres in Confined Water (cooperation FHR and UGent) and the deep water test data and CFD results are obtained from Lyu and el Moctar (2017). As can be seen, generally the numerical results are consistent with experimental data, however some deviations can still be found, especially for heave motion, even for the case in deep water. Similar discrepancies are reported in Lyu and el Moctar (2017) . One reason, as explained in Lyu and el Moctar (2017), might be the pitch resonance which has an influence on heave motions; another reason may be the linear potential method, which does not consider nonlinearities, such as transient wetted surface, being used in this study. Therefore, it is likely that the linear-based Rankine panel method should be extended to a nonlinear one when considering the forward speed seakeeping problem in shallow water.

Figure 10 shows the wave contours around DTC containership at different water depths in regular wave at normalized wave frequency $\omega_0\sqrt{L/g} = 1.98$. It can be seen that the shallower the water depth, the shorter the wavelength at the same wave frequency. This can also be verified in Figure 2.

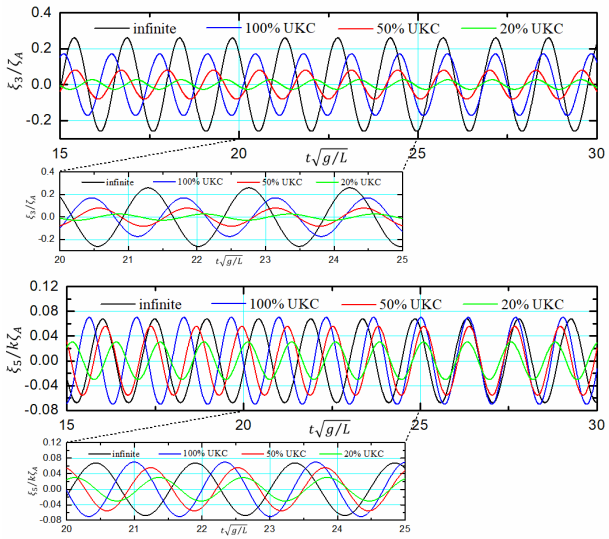

Figure 7. Time histories of heave and pitch motion at four water depths. Heave motion (top), Pitch motion (bottom), $\omega_0\sqrt{L/g} = 3.0$, $F_r = 0.139$.

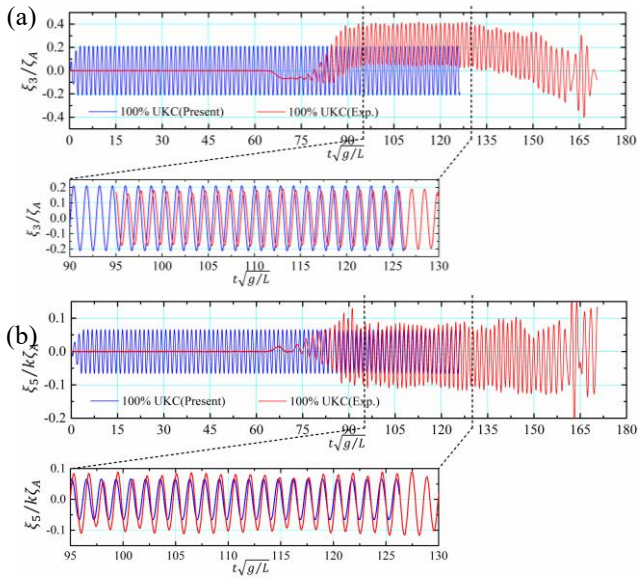

Figure 8. Comparison of numerical and experimental time history results. (a) Heave motion; (b) Pitch motion. $\lambda/L = 0.55$, $F_r = 0.139$.

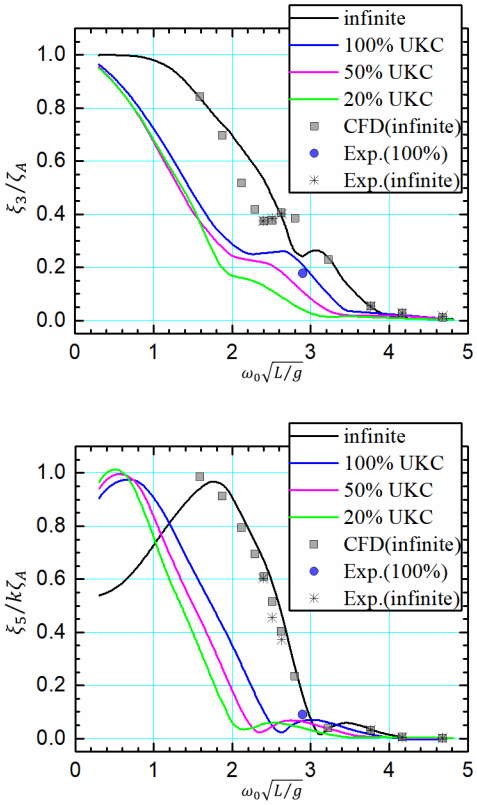

Figure 9. Heave and pitch motion RAO at four water depths. Heave motion RAO (top), Pitch motion RAO (bottom). $F_r = 0.139$.

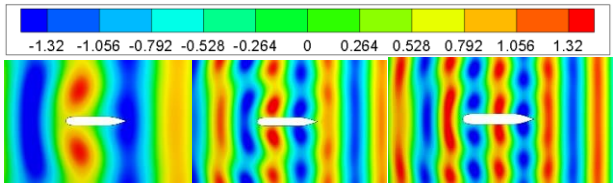

Figure 10. Wave contours around DTC containership at different water depths. Infinite water (left), 100%UKC (middle) and 20%UKC (right). $F_r = 0.139$. $\omega_0\sqrt{L/g} = 1.98$

4.4 ADDED RESISTANCE

Figure 11 presents the time series of the first and second order surge force at three water depths (i.e. infinite water, 100%UKC and 20%UKC), where the second order surge force is obtained by the pressure integration method, as presented in Eq. (21). From the figures, the oscillation period of the second order surge force is almost twice as large as the first order surge force. In addition, the convergence speed of the second order force is slower than the first order, which implies that longer simulation time are needed.

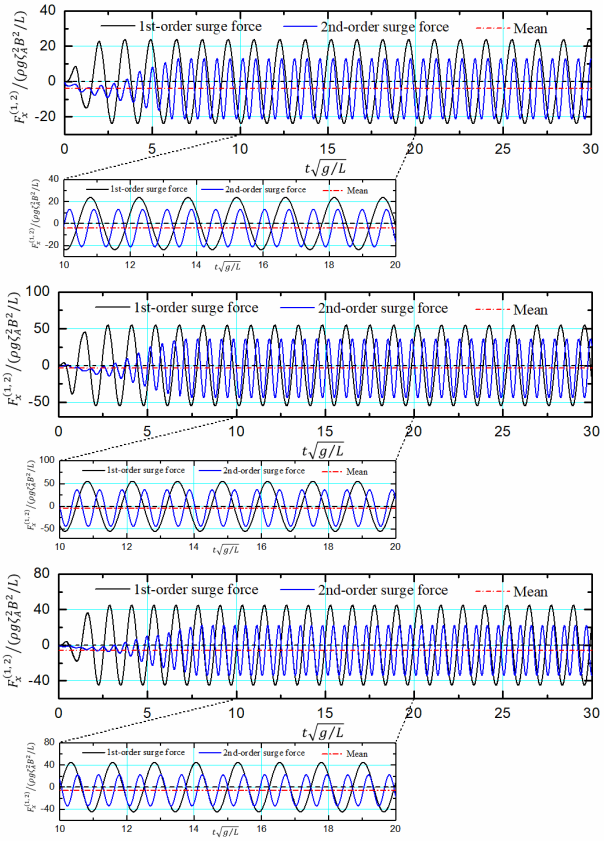

Figure 11. Time histories of added resistance at three water depths. Infinite water (top), 100% UKC (medial) and 20% UKC (bottom), $\omega_0\sqrt{L/g} = 3.0, F_r = 0.139$.

Figure 12 shows the comparisons of added wave resistance at infinite and 100%UKC water depths with experiment data. As can be seen, the normalized added resistance RAO values in infinite water show fair agreement with experimental results, but the values are overestimated in the low wavelength areas. Though some deviations exist, the order of magnitudes between numerical and experimental results for 100%UKC are acceptable. In general, the peak values of numerical added resistance RAO shift toward to lower wave lengths with the decrease of water depth.

In addition, though the numerical values for 100% UKC (Figure 12) and 20% UKC (Figure 13) have a similar trend with the infinite water case, it is not clear to find a consistent trend compared with experiment results, especially for the case in 20% UKC, which is significantly higher than other conditions. The reasons can be explained as follows: on one hand, in fact, the 20% UKC is no more a static condition but a dynamic one for the measurement from the experimental runs; what's more, an issue worth noting in experiment processing is that the incident wave amplitudes should be very small in order to avoid the bottom contact problem in such low under keel clearances, while it is accompanied by measurements and accuracies problems in such an extreme test condition; the detailed explanation can be found in Sprenger et al. (2017). On the other hand, due to the fact that a linear potential method is applied, without considering the obvious squat and viscous effect in shallow water, the numerical accuracy can be questioned as well. Therefore, the effect of water depths on added resistance needs to be further investigated for both numerical and experimental in a future study. Anyway, to an extent, the results can still be used as a qualitative analysis at the initial stages of design.

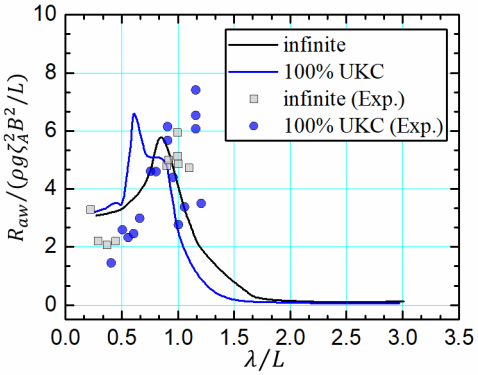

Figure 12. Comparisons of added wave resistance at infinite and 100%UKC water depths. $F_r = 0.139$.

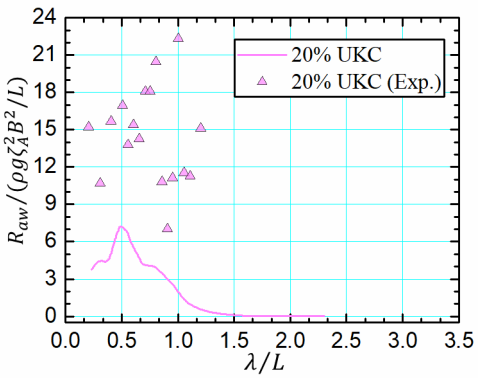

Figure 13. Comparisons of added wave resistance at 20%UKC water depths. $F_r = 0.139$.

5 CONCLUSIONS

In the present study, the wave-body interaction problems, including hydrodynamic forces, motion response and added resistance, is investigated in finite water by using a time domain Rankine panel method. Experimental tests are also carried out to validate the present program. From the results and discussions, the following conclusions can be obtained:

1) Generally, in shallow water larger hydrodynamic coefficients are obtained. Regarding the added mass, lower frequency waves induce larger hydrodynamic coefficients compared to high frequency waves in both deep and shallow water, while the results will converge to the deep-water case with the increasing of wave frequency;

2) The shallower the depth, the larger the peak value of the wave induced force and moment is. Peak values of excitation RAO shift toward to lower frequencies with regard to the decreased water depth; similar results can also be

found for the peak values of heave and pitch motion responses. Through the comparison of numerical results with experimental data for motion responses in different water depths, it can be concluded that the present linear approach is applicable for the prediction of wave body interaction problems related to motion dynamics in shallow water, which also had been proven in Kim and Kim, 2013.

3) As for the added wave resistance, the peak values of added resistance RAO shift toward to lower wave lengths with the decrease of water depth. Though the numerical results in deep water can agree well with test data, it is not clear to find a consistent trend for finite water depths, especially for the extreme test condition (20% UKC). In order to estimate the second order force in shallow water as accurately as possible, it is necessary to extend the present potential method to consider squat and viscous effects.

6 ACKNOWLEDGEMENTS

This work was supported by the Lloyd's Register Foundation (LRF) and China Scholarships Council (CSC). LRF and CSC help to protect life and property by supporting engineering-related education, public engagement and the application of research. The authors acknowledge the contributions of MARINTEK and the Towing Tank for Manoeuvres in Confined Water (cooperation FHR and UGent) with respect to the experimental data for the Duisburg Test Case (DTC) Containership. The authors would also like to thank the SHOPERA (Energy Efficient Safe SHip OPERAtion) consortium and the 5th MASHCON international conference for making available the model test.

7 REFERENCES

Chan, H. S., 1990. A three-dimensional technique for predicting first and second order hydrodynamic forces on a marine vehicle advancing in waves. University of Glasgow, Glasgow, UK.

el Moctar, Sigmund S., Schellin T., 2015. Numerical and experimental analysis of added resistance of ship in waves. In: Proceedings of the ASME 2015 34th International Conference on Ocean, Offshore and Arctic Engineering OMAE 2015, St. John's, NL, Canada.

Feng, A. C., Bai, W., You, Y. X., Chen, Z. M., Price, W. G., 2016. A Rankine source method solution of a finite depth, wave–body interaction problem. Journal of Fluids and Structures, 62: pp. 14-32.

Gao, Z. L., Zou, Z. J., Wang H. M., 2008. Numerical solution of the ship wave-making problem in shallow water by using a high order panel method. Journal of Ship Mechanics, 12 (6): pp. 858-869.

Huang, Y., 1997. Nonlinear ship motions by a Rankine panel method. Massachusetts Institute of Technology, Cambridge, USA, (Ph.D. Thesis).

Hwang, J. H. Lee, S. J., 1975. The effect of forebody forms on the ship motion in water of finite depth. Bulletin of the Society of Naval Architects of Korea, 2(12): pp. 59-66.

Joncquez, S. A. G., 2009. Second-order forces and moments acting on ships in waves. DTU Mechanical Engineering, Denmark. (Ph.D. Thesis).

Kim, C. H., 1968. The influence of water depth on the heaving and pitching motions of a ship moving in longitudinal regular head waves. Schiffstechnik, 15 (79): pp. 127-132.

Kim, Y. H., 1999. Computation of higher-order hydrodynamic forces on ships and offshore structures in waves. Institute of Technology, Massachusetts, USA, (Ph.D. Thesis).

Kim, K. H., Kim, Y., 2011. Numerical study on added resistance of ships by using a time-domain Rankine panel method. Ocean Engineering, 38(13): pp. 1357-1367.

Kim, T. Y., Kim, Y. H., 2012. Numerical study on floating-body motions in finite depth. International Journal of Ocean System Engineering 2(3): pp. 176-184.

Kim, T. Y., Kim, Y. H., 2013. Numerical analysis on floating-body motion responses in arbitrary bathymetry. Ocean Engineering, 62 (4): pp. 123-139.

Li, L., 2001. Numerical seakeeping predictions of shallow water effect on two ship interactions in waves. Dalhousie University, Nova Scotia, Canada. (Ph.D. Thesis).

Lyu, W., el Moctar O., 2017. Numerical and experimental investigations of wave-induced second order hydrodynamic loads. Ocean Engineering, 131: pp. 197-212.

Mei, T. L., Zhang, T., Candries, M., Lataire, E., Zou, Z. J. (2019). Comparative study on ship motions in waves based on two time domain panel methods. Under review.

Perunovic, J. V., Jensen, J. J., 2003. Wave loads on ships sailing in restricted water depth. Marine Structures, 16: pp. 469-485.

Riesner, M., von Graefe, A., Shigunov, V., el Moctar, O., 2016. Prediction of non-linear ship responses in waves considering forward speed effects. Ship Technology Research, 63(3): pp. 135-145.

Riesner, M., el Moctar, O., 2018. A time domain boundary element method for wave added resistance of ships taking into account viscous effects. Ocean Engineering, 162: pp. 290-303.

Söding, H., Shigunov, V., Schellin, T. E., el Moctar, O., 2014. A Rankine panel method for added resistance of ships in waves. Journal of Offshore Mechanics and Arctic Engineering, 136(3).

Sprenger, F., Maron, A., Delefortrie, G., Van Zwijnsvoorde, T., Cura-Hochbaum, A., Lengwinat, A., Papanikolaou, A., 2017. Experimental studies on seakeeping and maneuverability of ships in adverse weather conditions. Journal of Ship Research 61(3): pp. 131-152.

Takaki, M., 1977. On the ship motions in shallow water (Part 3): Comparison of the experimental results with the calculated results of ship motions in waves. Transactions of the West Japan Society of Naval Architects, 54: pp. 103-114.

Takaki, T., Takaki, M., Ohkusu, M., 1978. Ship motions in restricted waters. Transactions of the West Japan Society of Naval Architects, 56: pp. 33-45.
Andersen, P., 1979. Ship motions and sea loads in restricted water depth. Ocean Engineering, 6(6): pp. 557-569.

van Oortmerssen, G., 1976. The motions of a ship on shallow water. Ocean Eng. 3: pp. 221-255.

Vantorre, M., Journée, J., 2003. Validation of the strip theory code SEAWAY by model tests in very shallow water. In Colloquium on Numerical Modelling: pp. 23-24.
Tuck, E. O., 1970. Ship motions in shallow water, J. Ship Res. 14 (4): pp. 317-328.

Van Zwijnsvoorde, T., Tello Ruiz, M., Delefortrie G., Lataire E., 2019. Sailing in shallow water waves with the DTC container carrier: open model test data for validation purposes. In: Proceedings of 5th MASHCON International Conference on Ship Manoeuvring in Shallow and Confined Water, Ostend, Belgium.

Vorobyov, Y. L., Stasenko M. S., 2010. Asymptotic theory of ship motions in regular waves under shallow water conditions. Transnav the International Journal on Marine Navigation and Safety of Sea Transportation, 4(4): pp. 415-420.

Wang, L. X., Tang, H., Wu, Y. H., 2016. Wave interaction with a surface-piercing body in water of finite depth: a parametric study. Engineering Applications of Computational Fluid Mechanics, 10(1): pp. 514-530.

Yao, C. B., Sun, X. S., Wang W., Ye Q., 2017. Numerical and experimental study on seakeeping performance of ship in finite water depth. Applied Ocean Research, 67: pp. 59-77.

8 AUTHORS BIOGRAPHY

Tianlong Mei, PhD student at School of Naval Architecture, Ocean and Civil Engineering, Shanghai Jiao Tong University and the division of Maritime Technology at Ghent University. His experience includes numerical studies on wave structure interaction and ship manoeuvring in waves.

Guillaume Delefortrie, PhD, naval architect, is expert nautical researcher at Flanders Hydraulics Research and visiting professor at Ghent University. He is in charge of the research in the Towing Tank for Manoeuvres in Confined Water and the development of mathematical models based on model tests. He has been secretary of the 27th and 28th ITTC Manoeuvring Committee and is chairman of the 29th ITTC Manoeuvring Committee.

Manasés Tello Ruiz, PhD, naval architect and marine engineer, is a researchs at Ghent University. He has been involved in several (inter)national projects with main focus on manoeuvring, seakeeping, and wave energy converters. Currently, he is working on ship air pollution and machine learning techniques applied to ship hydrodynamics. At present he is also a member of the ITTC Specialist Committee of Manoeuvring in Waves, at which he has been appointed as secretary..

Changyuan Chen, a PhD candidate at the Maritime Technology Division, which belongs to the Faculty of Engineering and Architecture of Ghent University. His experience includes research on trajectory controller, intelligent control strategies, machine learning techniques applied to ship hydrodynamics, etc.

Evert Lataire, PhD, naval architect, is currently post-doctoral assistant at the division of Maritime Technology at Ghent University. He has written a PhD on the topic of bank effects mainly based upon model tests carried out in the shallow water towing tank of FHR. His fifteen year experience includes research on ship manoeuvring in shallow and confined water such as ship-ship interaction, ship-bottom interaction and ship-bank interaction.

Marc Vantorre, naval architect, is full senior professor of marine hydrodynamics and head of the Maritime Technology Division at Ghent University, Belgium. His research focuses on ship behaviour in shallow and confined waters, mainly in close co-operation with Flanders Hydraulics Research in Antwerp. He is member of PIANC Working Groups and former member of the ITTC Manoeuvring Committee. The investigation of manoeuvring behaviour in muddy areas has been a topic throughout his career.

Zaojian Zou, holds the current position of full professor at School of Naval Architecture, Ocean and Civil Engineering, Shanghai Jiao Tong University. He is responsible for teaching and research on marine hydrodynamics. His previous experience includes PI of some projects on manoeuvring and control of ships and other marine vehicles. He was a member of the 22nd, 23rd, 25th and 26th ITTC MC.

FULL SCALE MEASUREMENT OF SHIP MOTIONS TO VALIDATE STRIP THEORY

Butteur Mulumba Ntamba Ntamba,
Cape Peninsula University of Technology, South Africa

Bernhard Schwarz-Röhr,
Jade Hochschule, Elsfleth, Germany and Ghent University, Belgium

Chen Zhang,
Jade Hochschule, Elsfleth, Germany and Universität Oldenburg, Oldenburg, Germany

Alexander Härting,
Jade Hochschule, Elsfleth, Germany

FULL SCALE MEASUREMENT OF SHIP MOTIONS TO VALIDATE STRIP THEORY

Butteur Mulumba Ntamba Ntamba, Cape Peninsula University of Technology, South Africa
Bernhard Schwarz-Röhr, Jade Hochschule, Elsfleth, Germany and Ghent University, Belgium
Chen Zhang, Jade Hochschule, Elsfleth, Germany and Universität Oldenburg, Oldenburg, Germany
Alexander Härting, Jade Hochschule, Elsfleth, Germany

SUMMARY

Ship motion measurements were conducted on the SA Agulhas II (L = 121.3 m) on a regular voyage in the Southern Ocean. Two gyro- and accelerometer-based sensors were used at different locations in the ship, with one close to the centre of gravity. Thus linear accelerations could be obtained that were unmasked by rotational influences. RAOs were computed numerically for roll, pitch, heave and surge. These were used with accessible wave data to compute motion spectra that could be compared with the measurements.

Initially, only wave data recorded on board from visual estimation were available. These were used with a spread in frequency to compute motion spectra. Allowing for errors in the visual observations it was still not possible to get a reasonable agreement with the measured spectra for all degrees-of-freedom. Later, when directional wave spectra from a re-analysis of remote sensing data became available, a much better agreement could be achieved.

1 INTRODUCTION

The work presented in this paper is part of a larger project, whose purpose is to estimate the directional wave spectrum from the observable ship motions in deep as well as shallow water (Nielsen 2005, Nielsen et al. 2013, Schwarz-Röhr et al. 2016). The transition between deep and shallow water for waves depends on the ratio between water depth and wave length, whereas for ship motions it depends on the ratio between under-keel-clearance and the ship's size. It seems advisable at first to establish a benchmark case in deep water, where conditions are simpler.

Oscillating ship motions can be divided into high frequency structural vibrations and lower frequency oscillations, in which the ship can be regarded as a rigid body, and these are the ones considered in this paper. The three rotational and three translational degrees of freedom are described in a co-ordinate system which coincides with the ship's body-fixed frame when it is travelling with constant speed at its equilibrium attitude. The motions are governed by forces and moments induced by waves. Water waves are a stochastic phenomenon and realistic seaway is described by a directional spectrum.

The reaction of a ship to a particular harmonic wave can be calculated numerically depending on speed and angle of incidence in the form of Response Amplitude Operators (RAO). Within the limitations of linear theory, the calculations can be extended to non-harmonic excitations. Although the ship motions are recorded as a time series, analyses can only be done in the frequency domain. The approach followed here consists of using the available wave data and the theoretical response characteristics, compute the expected motion spectra for several degrees of freedom and compare to actual observations. It is so intended to validate the process of comparing measured ship motions to predicted ones in a realistic full scale environment. As opposed to model tank experiments there is no need to correct for scale effects. However, uncertainties are introduced by the input sea state and the actual vessel characteristics (mass distribution, damping) on which the RAOs are based.

Trials were carried out on the 123m research vessel "Agulhas II" in the Southern Ocean, where sea conditions were quite stable. Initially, only visual observations of the sea state were available. Later, directional wave spectra modelled by ECMWF from remote sensing data were added into the analyses.

2 SEA TRIALS

The S.A Agulhas II is a South African Polar Supply and Research vessel (PSRV). Designed to carry cargo, personnel (50 crew and 100 scientists), bunker oil, helicopter fuel and also equipped with laboratories, the PSVR S.A Agulhas II was built by STX Finland at the Rauma Shipyard. Figure 1 shows a photograph of the ship.

Figure 1. Photograph of the SA Agulhas II. (Bekker, A. et al 2018)

Table 1. S.A Agulhas II specifications

Lpp	121.8 m
Beam	21.7 m
Draught, design	7.65 m

Measurements were performed during her voyage Cape Town – Antarctica – Cape Town from 28th June 2017 to 12th July 2017. Ship motions were recorded using autonomous sensor boxes with low cost gyros and accelerometers. Sensor boxes were placed at two locations on the vessel. The first sensor was located in the engine control room within a few metres of the centre of mass of the vessel, this sensor measured accelerations in three dimensions and the roll and pitch rate. The second sensor box was located on the observation deck above the navigation bridge giving full 3d-information on both accelerations and angular rates. This sensor had GPS-reception to provide accurate time and position tags. Using correlation between the angular rates from both sensors it was possible to synchronise the sensors and to demonstrate a nearly perfect agreement of the angular data.

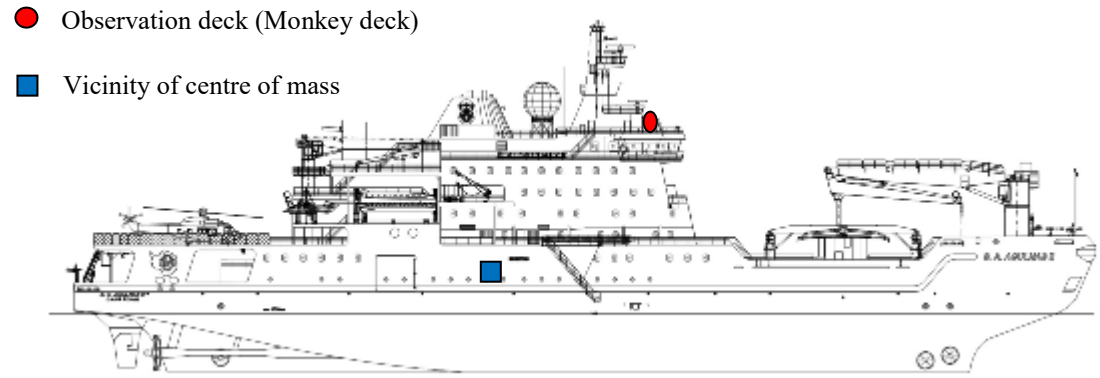

Figure 2. Location of the sensor boxes on the SA Agulhas II (Bekker and Omer, 2018)

3 FUNDAMENTAL RELATIONS

The sea state is generally described by the directional wave spectrum $S(\omega,\alpha)$, which gives power density for a certain wave direction α and sea state frequency ω, the latter is measured at a fixed point in space. The abovementioned RAOs $h_n(\omega,\alpha)$ are defined as the ratio of the complex ship motion amplitude $A_n(\omega)$ to complex wave amplitude $A(\omega,\alpha)$

$$A_n(\omega) = h_n(\omega,\alpha)\, A(\omega,\alpha) \tag{1}$$

for a single wave excitation. Here $A_n(\omega)$ is the complex amplitude of ship motion in the n-th degree of freedom, n=1...3 denotes the linear motions in x-, y- and z-directions, n=4…6 the rotations about the corresponding axes. Taking the magnitude squared of the previous equation leads to a relationship of the corresponding power spectra $S_n(\omega)$

$$S_n(\omega,\alpha) = |h_n(\omega,\alpha)|^2\, S(\omega,\alpha) \tag{2}$$

For a general directional wave spectrum, the contributions for waves of different angles are added by integrating over the wave direction

$$S_n(\omega) = \int |h_n(\omega,\alpha)|^2 S(\omega,\alpha) d\alpha \tag{3}$$

So the power spectra of ship motions can be predicted from knowledge of the RAOs and the directional wave spectrum.

The spectra $S_n(\omega)$ and $S(\omega)$ in equation (3) are given in terms of the sea state frequency. In order to compare these to measurements obtained on a moving vessel they have to be transformed to encounter spectra. For the experiments the deep water assumption is valid. In this case the encounter frequency ω_e as observed on a moving vessel is related to the sea state frequency by

$$\omega_e = \omega\left(1 - \frac{v}{g}\omega\right) \tag{4}$$

Here

$$v = v_0 \cos\alpha \tag{5}$$

denotes the component of the vessel's velocity vector in the direction of the waves, v_0 is the ship speed and α the angle between the wave vector and the ship velocity. An angle α of zero degrees means waves from aft. The constant g is the gravitational acceleration. The sea state spectra are transformed to encounter spectra by (Price, 1974)

$$S_n^e(\omega_e) = \frac{S_n(\omega)}{\left|\frac{d\omega_e}{d\omega}\right|} \tag{6}$$

4 RAO COMPUTATIONS

Oscillating ship motions appear in six degrees of freedom: three modes of translation (surge, sway and heave) and three modes of rotation (roll, pitch and yaw). For a particular ship speed and incident wave angle, the RAOs give amplitude and phase for each mode of the ship motion in relation to wave height and wave frequency.

RAOs may be obtained from model experiments or computed using specialised software. In strip theory (Bertram et al, 2006, Journee and Adegeest, 2003) the forces and moments on a three-dimensional floating body can be determined using results from two–dimensional hydrodynamics coefficients and exciting wave loads. The ship is considered as being made up of a finite number of transverse two dimensional strips or cross sections that are rigidly connected to each other. Each strip is treated hydro-dynamically as if it were a segment of an infinitely long floating cylinder. In the experimental test cases the amplitudes of pitch and roll remained moderate with less than 5°, so that linear theory should still be applicable. Two alternative software packages were used to determine the RAOs of the vessel: a commercial program SEAWAY (Octopus Office) and an open source program PDstrip. Both require a hull form description as well as hydromechanics input data. For the SA Agulhas II a 3D-laser scan was performed while the ship was in dry dock.

The required mass and stability parameters were provided by the loading computer. The radius of inertia for roll k_{xx} was chosen such that the resonance peak in the RAOs matches the resonance peak in the roll motion spectra. This technique is not applicable for pitch because the resonance is not very pronounced here. Therefore the radius of inertia was approximated by means of (Journee and Adegeest 2003)

$$k_{yy} \approx 0.22 \cdot L \ \ to \ 0.28 \cdot L$$

with the ship length L, the proportionality factor was tuned to 0.24. Viscous damping was modelled by the Ikeda method with the parameters given in table **2.**

Table 2. Input data for RAO computations.

Stability and Mass data		
Draft	D	6.67 m
Metacentric height (corr.)	GM	1.41 m
Radius of Inertia Roll	k_{xx}	6.45 m
Radius of Inertia Pitch	k_{yy}	30.31 m
Damping		
Amplitude for Linearisation		5 m
Damping: Bilge Keel		
Height	HBK	0.39 m
Dist. APP to aft of BK	XBKA	42.44 m
Dist. APP to fwd end of BK	XBKF	78.81 m

As a comparison between the two software packages, figure 3 shows the RAO-pitch amplitudes for the SA Agulhas II for a speed of 8.25 knots and two different angles of wave incidence. For the other degrees of freedom there is a similarly good agreement except for roll, where viscous damping seems to be insufficiently modelled in PDstrip. Therefore, it was decided to use the RAOs as computed by SEAWAY.

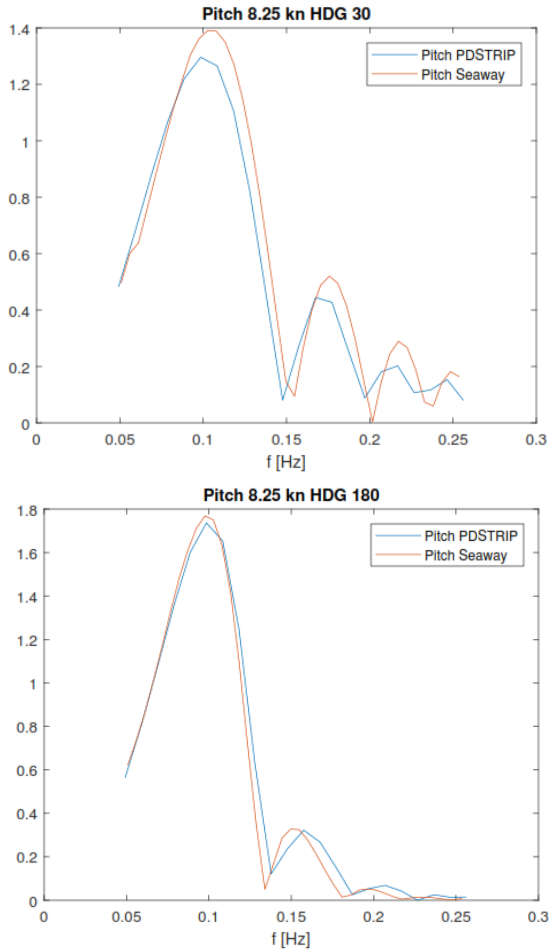

Figure 3. Comparison of RAOs calculated by two different strip theory programs.

5 EXPERIMENTAL DATA

For the data processing a coordinate system with the origin in the center of gravity was chosen. The x-axis is oriented midships pointing to the bow, the y-axis points to portside, the z-axis upright. Roll, pitch and yaw are defined as right handed rotations around the corresponding axes as demonstrated in figure 4. The sensors provide time series of the sensor accelerations and the angular rates in the local frame of the sensors which rotated with respect to the horizontal frame due to roll, pitch and yaw motions. In principle the vector components have to be rotated into the horizontal frame. Since amplitudes of roll and pitch turned out to be less than 5° and 4° respectively, the rotational rates needed no transform within the accuracy of the measurements.

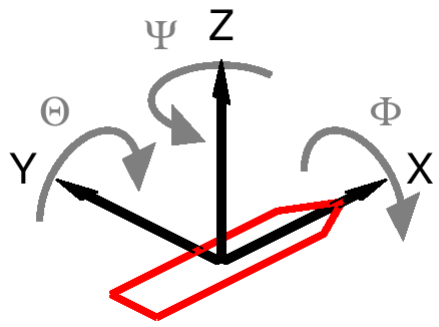

Figure 4. The coordinate system used in this paper. The angles for roll Ψ, pitch Θ and yaw Ψ are counted positive in the direction of the arrows.

In contrast the acceleration vector has to be transformed into the earth frame in order to remove the gravitational acceleration. This requires knowledge of the roll, pitch and yaw angles which are denoted by ϕ,θ,ψ respectively. These angles were calculated from the angular rates. As a first step offset and drift were removed from the angular rates by means of a high-pass filter.

The filtered signals were integrated in time domain, a second high-pass filter step was necessary to remove the long term sensor drift. The rotation from the sensor to the horizontal frame is accomplished by the transform matrix R which is composed of three rotation matrices for the individual axes:

$$R = R_\psi \cdot R_\theta \cdot R_\phi \tag{7}$$

with

$$R_\phi = \begin{pmatrix} 1 & 0 & 0 \\ 0 & cos\phi & -sin\phi \\ 0 & sin\phi & cos\phi \end{pmatrix}, R_\theta = \begin{pmatrix} cos\theta & 0 & sin\theta \\ 0 & 1 & 0 \\ -sin\theta & 0 & cos\theta \end{pmatrix},$$

$$R_\psi = \begin{pmatrix} cos\psi & -sin\psi & 0 \\ sin\psi & cos\psi & 0 \\ 0 & 0 & 1 \end{pmatrix} \tag{8}$$

The results shown in the following sections are obtained from the sensor located at the center of gravity. This sensor provides rotational rates and linear accelerations for all degrees of freedom at a sample rate of 8 Hz. Segments of the data stream where wave conditions as well as course and speed were nearly constant were selected for processing, the duration of one segment ranges from 2 hours to 4 hours. Power spectra of motion were calculated using the Welsh method with N=512 points per FFT and 75% overlap, this leads to more than 400 averages in the Welsh algorithm. The power spectra were found stable against variations of the FFT-length, this indicates that the duration of the time series is sufficient for estimating the power spectra. Power spectra for angular motion were obtained by integrating in Fourier space, namely dividing by ω_e^2.

Regarding the rotational degrees of freedom only pitch and roll were examined. During all of the measurement runs the ship was steered by autopilot, which creates rudder moments to counteract any yaw motion. Therefore, the measured yaw spectrum is not the direct ship response to the waves as described in the corresponding RAO and was not considered in the present analysis.
Wave data were obtained by visual observations recorded by the South African weather service meteorologists on board. These observations were recorded on a 3-hourly basis and consist of estimations of characteristic height, peak period and peak direction for both, swell and wind sea. At a later stage directional wave spectra could be incorporated. These became available after a re-analysis of remote sensing data by ECMWF.

6 RESULTS

6.1 BASED ON VISUAL OBSERVATIONS

Wave data consist of estimations of significant height $H_{1/3}$, peak period (Tp) and peak direction for both, swell and wind sea. For our analyses we used only data sets, where the ship was on a steady heading with constant speed for several hours and the estimated wind sea was negligible. As for the available information, the exciting wave "spectrum" was thus reduced to a single point.

To calculate motion spectra from the visually estimated peak period a frequency spread was introduced with the sole purpose of avoiding a singularity. For simplicity, a Bretschneider Spectrum

$$S(\omega) = \frac{A}{\omega^5} e^{-\frac{B}{\omega^4}} \tag{9}$$

was used, where the parameters A and B are related to significant wave height and peak frequency. For a narrow banded spectrum (ocean swell) (Bjornsson, 2013),

$$B = \frac{5}{4}\omega_p^4 \quad \text{with} \quad \omega_p = \frac{2\pi}{T_p} \quad \text{and} \quad A = \frac{1}{4}H_{1/3}^2 B \tag{10}$$

Then, computation of the motion spectra is done via equation (3) with the angle index of the RAOs selected according to the ship's heading and the recorded wave direction. The result is transformed to encounter frequency to compare with the measurements.

As an example a data set recorded on July 5th, 2017 was selected where the ship's speed was 7.5 kn. The entries in the meteorologists' log are given in the first column of table 3:

Table 3. Visual observation data recorded

	recorded observations	modified values
Significant height [m]	7	6
Peak period [s]	11	13
Peak direction [° port bow]	15	35

Entering these values, the computed spectra (green) are shown in figure 5 in relation to the measured spectra (blue). Apart from pitch the computed spectra come out far too small and, apart from roll, they appear at too high frequencies. Given some uncertainties in the visual estimates, it seems justified to modify these values to a certain extent. Using the parameters in the right hand column of the table we get the spectra plotted in red. Now, the computed roll spectrum is too narrow, but agrees in total power with the measured one. The comparisons for pitch, heave and surge improve somewhat, but are still far from satisfactory.

The measured spectrum of surge seems to be corrupted at low frequencies. To calculate the motion spectra for heave, surge and sway, as outlined in chapter 5, the observed angles must be used to transform the linear accelerations from the sensor system to the horizontal system. This is challenging where small errors in the angles can cause a spurious coupling of the gravitational acceleration into the linear degrees of freedom. The low frequency artifact in surge can be attributed to this source. As the roll amplitudes are generally larger than pitch, the uncertainty in sway will be considerably higher, whence it was decided to exclude sway from the present analysis.

Modification of the wave incidence angle from 15° to 35° port was necessary to fit the total power in roll. The roll RAO exhibits a strong resonance. The measured spectrum, on the other hand, is considerably wider. This could indicate the presence of an angular spread in the exciting wave spectrum. Ten more data sets have been investigated, all leading to similar qualitative statements. No attempt has been made here to do a variational calculation to fit the parameters to the measured data or to include an angular spread. The results with the Agulhas II show however that, even for ocean swell, three wave parameters (height, period and direction) are not enough to account for the observable ship motions.

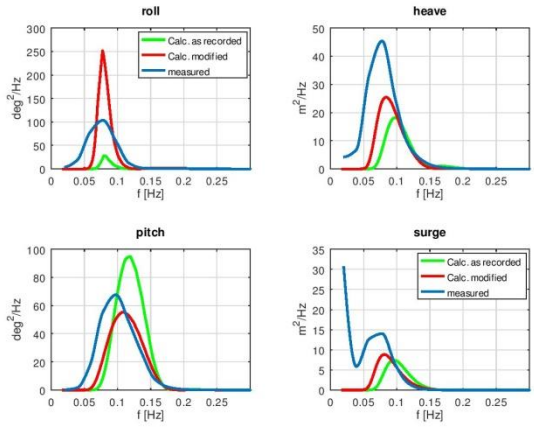

Figure 5.Power spectra of ship motions, measured (blue) and computed with two parameter sets (green and red)

6.2 BASED ON DIRECTIONAL WAVE SPECTRA

For analyses of past measurements ECMWF provides directional wave spectra modelled from remote sensing data on a narrow grid of positions and time. The closest grid point was taken without interpolation to compare with the Agulhas data set of July 5th 2017. The wave spectrum is given with a frequency spacing of about 0.01Hz and an angular resolution of 15°. The peak of the wave spectrum was found at 20° on the port bow with a period of 13.5s and the significant height was 6.9m, in fair agreement with the visual recordings.

Calculated motion spectra were generated by applying equation (2) to all of the wave grid points and integrating over angles after a power conserving transformation to encounter frequency. The result is shown in figure 6. The measured spectra for pitch and heave are now reproduced very well and, apart from the low frequency limit, surge also matches closely. The wave spectrum exhibits a spread of about 0.04Hz in frequency and 40° in angle and this, obviously, is substantial to make the computed spectra agree with the measured ones in position and width.

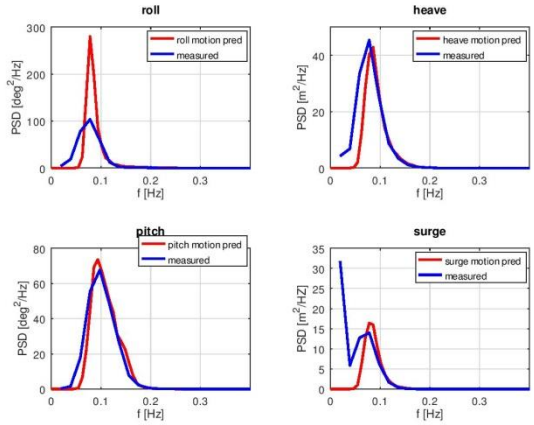

Figure 6. Power spectra of ship motions, measured (blue) and computed from the full 2D-wave spectrum supplied by ECMWF (red)

There remains a question about the shape of the peak in the computed roll spectrum. It should be noted that the power spectra depend on the square of the RAOs. To correctly represent roll damping in the RAO a delicate adjustment is required. Possibly, in a natural environment, a roll moment from rudder action, if by the autopilot, could manifest itself as additional damping.

7 CONCLUSIONS

Oscillating ship motions were measured on a large research vessel in the open ocean. These were compared in the frequency domain with predictions obtained from available sea state data and RAOs computed by strip theory. A good agreement would be desirable for practical purposes of seakeeping. It was found that a sea state reduced to peak values of direction, period and height is not sufficient to account for the observed motions, even when a long-crested ocean swell is dominant. A full directional wave spectrum improves the agreement between prediction and measurement considerably. The reason for a general tendency to overestimate the roll response remains to be investigated.

8 ACKNOWLEDGEMENTS

- NRF South African National Antarctic Programme (SANAP) (grant no. No. 93070)
- South African Department of Environmental Affairs for the Agulhas, Crew Agulhas
- Sound and Vibration Research Group, Stellenbosch University
- South African Weather Services
- Jean Dublot from European Centre for Medium-Range Weather Forecast (ECMWF)

9 REFERENCES

Bekker, A., Omer, H., 2018. Human responses to wave slamming vibration on a polar supply and research vessel. Applied Ergonomics 67. 71-82
https://doi.org/10.1016/j.apergo.2017.09.008

Bekker, A., Suominem, M., Kujala, P., Oscar De Wall, R.J., Soal, I.K., 2018. From data to insight for a polar supply and research vessel. Ship Technology Research (Schiffstechnik).
https://doi.org/10.1080/09377255.2018.1464241

Bjornsson, L., 2013. Comparison of idealised 1D and forecast 2D wave spectra in ship response predictions. Thesis. KTH Engineering Science.
https://www.diva-portal.org/smash/get/diva2:706783/FULLTEXT01.pdf

European centre for medium-range weather forecast.
https://confluence.ecmwf.int/display/CKB/About+ERA+wave+spectra

Journee, J. M. J., Adegeest, L. J. M, 2003. Theoretical Manual of Strip Theory Program "Seaway for Windows", Report 1370, TU Delft.

Kuik, A. J., Van Vledder G. Ph., Holthuusen, L. H., 1988. A Method for the Routine Analysis of Picth-and-Roll Buoy Wave Data.J. of Physical Oceanography, 18. 1020-1034
https://doi.org/10.1175/1520-0485(1988)018<1020:AMFTRA>2.0.CO;2

Nielsen, U., 2005. Estimation of directional wave spectra from measured ship responses. PhD-Thesis, DTU Lyngby
http://orbit.dtu.dk/files/5442536/Dam.pdf

Nielsen, U., Andersen I. M. V., Koning J., 2013. Comparison of Means for Estimating Sea States from an Advancing Large Container Ship, in: Proceedings of the 12th International Symposium on Practical Design of Ships and Other Floating Structures. Changwon City, South Korea. pp. 1–9
http://orbit.dtu.dk/files/58988707/Comparisons_of_Means_for_Estimating.pdf

Price, W. G., Bishop R. E. D., 1974. Probabilistic theory of ship dynamics, Chapman and Hall, London

Schwarz-Röhr, B., Ntamba Ntamba, B., Härting, A., 2016. Estimating seaway from ship motions, in: Proceedings of the 13th International Symposium on Practical Design of Ships and Other Floating Structures. Copenhagen, Denmark.
http://hdl.handle.net/1854/LU-8516168

10 AUTHORS BIOGRAPHY

Butteur Mulumba Ntamba Ntamba holds the current position of lecturer and research coordinator at the Cape Peninsula University of Technology in the department of Maritime Studies. His research work is on ship response in waves.

Bernhard Schwarz-Röhr holds his diploma degree of physics, and now he is a PhD candidate in Faculty of Engineering and Architecture, Ghent University, Belgium. He is responsible for wave estimation, sea state analysis, and measurement of ship movements.

Chen Zhang received her bachelor and master degree from Northwestern Polytechnical University, China in 2010 and 2013 respectively. Now she is a PhD candidate in the Department of Computer Science, Carl von Ossi-etzky University of Oldenburg, Germany. Her research interests contain measurement and analysis of ship movements at sea states, also including motion control.

Alexander Härting is a professor in the Department of Maritime Studies, Jade University of Applied Science, Germany. His research interests include measurement and analysis of dynamic ship movements in seaway, integration of different navigation sensors, and measurement of the squat of seagoing vessels in narrow fairways.

DETAILED ASSESSMENT OF NAVIGABLE AREAS FOR ENCOUNTER MANOEUVRES USING NUMERICAL MODELS

Lourdes Pecharroman, Raul Atienza, Carlos Cal, Raul Redondo and **Miguel de Ros**,
Siport21, Spain

DETAILED ASSESSMENT OF NAVIGABLE AREAS FOR ENCOUNTER MANOEUVRES USING NUMERICAL MODELS

Lourdes Pecharroman, Raul Atienza, Carlos Cal, Raul Redondo and **Miguel de Ros,** Siport21, Spain

SUMMARY

A detailed methodology is presented to assess and define navigable areas for ship encounter manoeuvres by means of numerical models and real time manoeuvring simulations. The results are compared with those obtained from concept design based on national and international guidelines and recommendations.

Encounter manoeuvres generate high hydrodynamic interaction forces between vessels involved, which depend on several factors (vessels characteristics and speed, passing distance, water depth and channel blockage). These forces can reach very high values and should be carefully considered when assessing this type of manoeuvres.

The interaction forces are calculated in detail using the numerical model ROPES for a combination of different encounter speeds, distances and water depths. Then, these forces are included in the manoeuvring model in order to consider them in the real time manoeuvre simulations.

As a result, the encounter area requirements (dimensions) are determined after a detailed analysis of manoeuvres performed in real time simulator. This usually leads to an improvement on safety in an optimized design.

NOMENCLATURE

B	Beam (m)
T	Draft (m)
Loa, L	Length overall (m)
Lpp	Length between perpendiculars (m)
T	Draft (m)
W	Total width of manoeuvring lanes (m)
W_{BM}	Width of basic manoeuvring lane as a multiple of the design ship's beam (m) depending on the type of vessel
$\sum W_i i$	Additional widths to allow for the effects of wind, current, etc. (m)
W_{BR}, W_{BG}	Bank clearance on the 'red' and 'green' sides of the channel (m)
$\sum W_P$	Passing distance, comprising the sum of a separation distance between both manoeuvring lanes W_M and an additional distance for traffic density (m)
Dp	Stopping distance (m)
V	Speed (m/s)
t_r	Response time (s)
ρ	Density of water (kg/m^3)
u	Vessel speed (m/s)
Cx, Cy and *Cn*	Passing force coefficients (-)
h	Depth (m)
δ	Rudder angle (º)

1 INTRODUCTION

Encounter manoeuvres in a channel require a two-way channel stretch. The main parameters of this area are the horizontal dimensions (width and length) and water depth. This paper presents the methodology and a practical case for a detailed design of an encounter area.

The encounter area is set up in a straight leg. The width of a meeting area will allow to minimize the interaction effects between the two vessels during the encounter. The length will allow both vessels to have a stable course from just before crossing until the crossing ends.

The interaction effect between vessels depends on the passing distance and therefore on the channel width. There are other critical factors such as the characteristics of the vessels, the vessels' speeds at the time of the encounter, the slope of the channel, blockage, and the depth.

A sensitivity analysis is presented to assess the influence of each parameter on the interaction forces. In addition, the dimensions of the crossing area will depend on the local conditions of the area (wind, waves or current) which also affects the vessel response.

In the first phase of design, the dimensions of the encounter area can be estimated applying concept design (deterministic). This method provides adequate navigational safety. For a detailed design, the use of numerical models and numerical tools gives more accurate results and assessment of the dimensions of the encounter area. The detailed analysis includes the assessment of the interaction effects between vessels during the crossing and allows to quantify them.

In addition, manoeuvres in a real time simulator, including the effects mentioned before, and the local conditions of the area (wind, waves and/or currents), will make it possible to assess the dimensions of the crossing area more precisely and to decide if it is adequate or, on the contrary, if it is recommended to take some action (widening / narrowing the width of the crossing section).

2 METHODOLOGY

The methodology to assess the navigable areas for encounter manoeuvres is presented. Firstly, an estimation of the dimensions of the encounter area with deterministic method is done in order to have a preliminary definition for the crossing area.

In a second stage, hydrodynamic interaction forces and moments are assessed taking into account different factors such as: characteristics of encounter vessels, vessels speed, depth, bank slopes and separation distance between vessels during the encounter. The forces and moments obtained are included in the manoeuvring model in order to run manoeuvres using real time simulator including detailed passing ships effects. This step needs to obtain the passing ship coefficients derived from the forces and moments obtained from ROPES and then translate them into the simulator formulation.

Manoeuvres are developed by an experienced captain familiar with the use of the simulator for port and waterway design. Local pilots, from the studied area, also participate in the work. The manoeuvres are developed under characteristic local conditions (wind, waves and current). Real-time simulations also allow assessing the proposed Aids tl Navigation (AtoN) elements in the area.

The advantage of the proposed methodology is that it is possible to analyze in detail and assess a possible optimization of the dimensions of the proposed encounter area from a safety point of view. Moreover, this methodology permits to determine the required rudder angle to compensate the passing forces and moments and to maintain the heading. Furthermore, it allows the participation of local pilots in the process, as future users of the area.

2.1 CONCEPT DESIGN

Concept Design proposed by National and International guidelines is considered in the initial stage of the process. Report 121-2014 of PIANC "Harbour Approach Channels Design Guidelines" and Part VIII of ROM 3.1-99 (Spanish recommendations) propose a simple formulation to estimate the width of a two-way channel (PIANC, 2014 ; Puertos del Estado, 2003).

The overall bottom width (W) of a two-way channel with straight section given by PIANC is (Figure 1):

$$W = 2 \cdot W_{BM} + 2 \cdot \sum W_i + W_{BR} + W_{BG} + \sum W_P = 2 \cdot W_M + W_{BR} + W_{BM} + \sum W_P \quad (1)$$

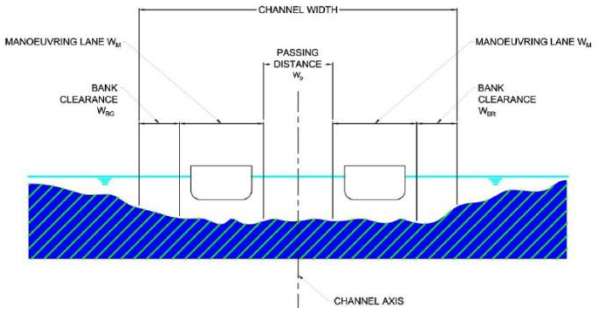

Figure 1. Two-way channel section (PIANC 121)

The length of the two-way stretch is given by the next formula and shown in Figure 2:

$$\geq 2(Dp + L + 0.4 \cdot V \cdot t_r) \quad (2)$$

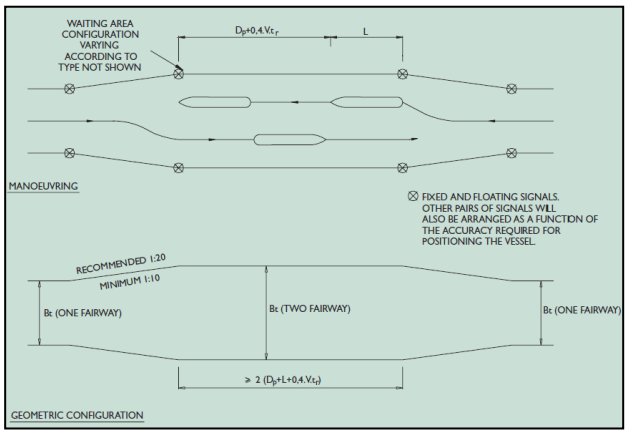

Figure 2. Two-way channel configurations for encounter manoeuvres (Puertos del Estado, 2003)

This definition considers the possibility that the vessels reach the beginning of the stretch either at the same time or with a certain lag. It also considers either of the two vessels accessing the passing area with a reduced speed (40% of the absolute maximum admissible in the fairway), and stop at least in a waiting area (quay, mooring area, anchorage, etc.) located at the beginning or end of the double width area. The longitudinal development of the stretch will include space for the stopping distance plus the area covered during a reaction time of 60 sec plus the design vessel's length overall. Then, the length is at least twice as long as the theoretically necessary. Recommended width transitions consider ground plan variations not greater than 1:10 (preferably 1:20) on each end.

2.2 PASSING FORCE COEFFICIENTS

Specific numerical models allow to evaluate the hydrodynamic interaction (forces and moments in six degrees of freedom) between passing vessels during the encounter manoeuvre on a specific meeting area, especially in narrow and constrained depth areas.

Therefore, the forces and moments produced over the navigating vessel due to the constrains caused by the bathymetry restrictions, banks and hull interactions can be obtained.

In order to assess the interaction forces and moments produced over a vessel under different speeds, at different passing distances and at different drift angles, the numerical model ROPES, developed by PMH BV (Pinkster Marine Hydrodynamics, 2013), is considered. An example screenshot of ROPES is shown in Figure 3.

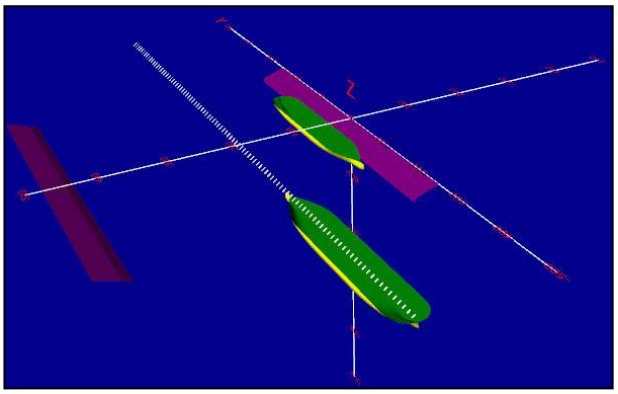

Figure 3. Image of ROPES software of a sailing vessel

The model takes into account the specific hull forms of each vessel, on an established load condition, considering the effects of bathymetry changes and lateral restrictions (navigation channels, vertical structures, slopes, ...), and allows the calculations of passing forces and moments for a wide range of sailing speeds and passing distances, even when this passing distance is small (i.e. less than one beam).

The system calculates the forces on the vessels in all 6 degrees of freedom (surge, sway, heave, roll, pitch and yaw) in the time domain, as shown in Figure 4 as an example. The computations are based on 3-dimensional flow calculations for real hull forms. These flow calculations are based on the double-body flow method.

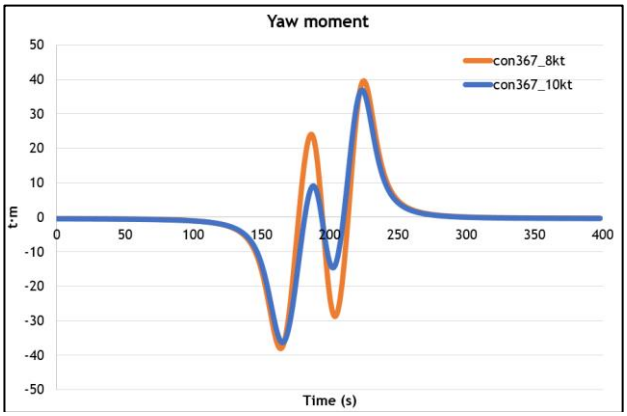

Figure 4. Example of yaw moment time series output of the numerical model ROPES

The predictions of ship-to ship interaction during encounter manoeuvres using potential flow models, such as ROPES, are considered with good level of reliability (Yuan, 2018) as the cross-flow effects are less important compared with hydrodynamic interaction.

Once all bank and interaction forces and moments are obtained from the numerical model ROPES, the passing ship coefficients for surge force (Fx), sway force (Fy) and yaw moment (Fn) can be estimated in order to introduce them into the real time manoeuvring simulator.

The passing ships effects are calculated for the passing vessels in the proposed two-way stretch. The objective is to quantify the passing effects and then introduce the results in the simulator so as to develop the most realistic manoeuvres possible.

From the formulation of passing ship forces and moments in the real time manoeuvring simulator it is possible to obtain the related passing ship coefficients from the ROPES results, and then introduce them in the simulator system.

The governing equations of the passing ship forces in the case assessed within this paper are the following:

$$F_x = 0.5 \cdot \rho \cdot u^2 \cdot C_x \cdot B \cdot T \quad (3)$$

$$F_y = 0.5 \cdot \rho \cdot u^2 \cdot C_y \cdot L_{pp} \cdot T \quad (4)$$

$$F_n = 0.5 \cdot \rho \cdot u^2 \cdot C_n \cdot L_{pp}^2 \cdot T \quad (5)$$

It is also necessary to consider correction factors in the simulator system for h/(h-T) factor and the vessels' speed.

Passing ship coefficients depend on:

- Vessels hull forms and dimensions
- Vessels load condition (draught)
- Passing distance between vessels
- Mean depth
- Vessels speed
- Channel blockage

Performing a series of different runs for the same vessels and different depth, speed and passing distance allow to both assess the effect of the speed, passing distance and depth in the passing ship forces, and to estimate the passing ship coefficients by minimizing the averaged mean quadratic error of the series of forces derived in ROPES and the estimated forces obtained through successive estimations of the passing ship coefficients.

Then, the passing ship coefficients are obtained based on the results of different runs which combine different passing distance and encounter speed. A set of coefficients are defined for each combination of vessel, h/T ratio and a range of passing speeds and passing distances.

These coefficients are introduced in the simulator system according to the simulator formulation in order to include the passing effects during simulations (MARIN, 1997). So

that the interaction effects (passing forces and moments) during the encounter manoeuvres performed in the real time manoeuvring simulator will be quite close to those obtained in the numerical model ROPES, thus increasing the complexity and the accuracy of the simulated scenario.

2.3 RESULTS AND SENSITIVITY ANALYSIS

Figure 5 to 7 show the variation of the passing ship forces (average) for two New Panamax container vessels (14.5 m draft) as a function of the passing distance for different vessel speed and h/T.
The results of the cases of ROPES are summarize in these graphs which include the maximum value of force and moment included in the time series for each case analyzed.

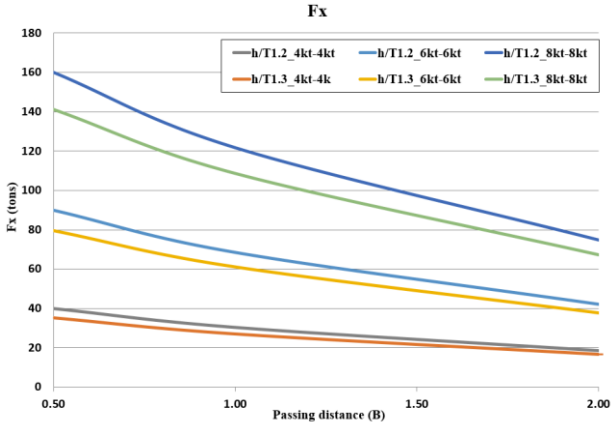

Figure 5. Fx (surge force) as a function of passing distance

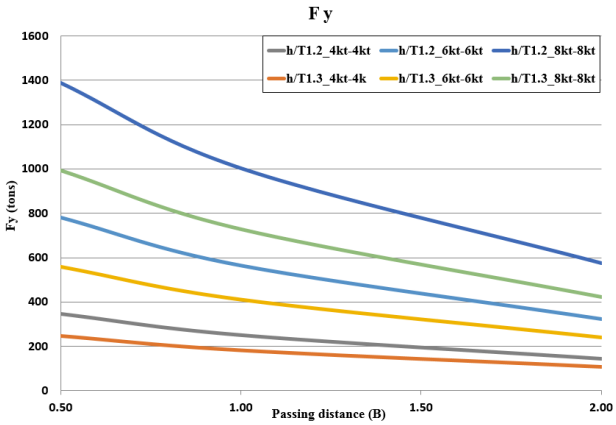

Figure 6. Fy (sway force) as a function of passing distance

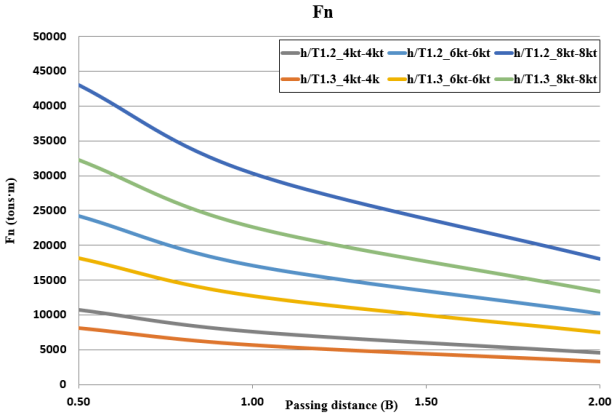

Figure 7. Fn (yaw moment) as a function of passing distance

The results for sway forces (Fy) increase about 35%-40% when h/T decreases 9% (from 1.3 to 1.2). This range considers a passing ship variation from 0.5·B and 2.0·B and a range speed from 4.0 to 8.0 knots. For a constant passing speed, sway force increases 142% from that obtained for a passing distance of 2.0·B, when the distance decreases to 0.5·B. The force increases about 75% when the passing distance decreases 50% (to 1.0·B). In case of constant passing distance, when the speed increases up to 6 knots the force increases 125% from that obtained for 4 knots. When the speed increases up to 8 knots the sway force increases 300%. Regarding yaw moment (Fn), the percentages are similar to those obtained for Fy.

The main conclusion is that the passing speed is the factor which most affects the results, causing the biggest differences.

Even though force increase due to h/T is lower, it becomes more important if certain speed has to be maintained and passing distance cannot be increased. Therefore, assessing both vertical and horizontal dimensions is required.

2.4 RUDDER REQUIREMENTS TO COMPENSATE PASSING EFFECTS

The rudder requirements (time and angle used) to compensate the forces and moments due to encounter manoeuvres is also assessed. The consequences of passing ship effects over the vessels are a more or less continuous use of the rudder and engine, required to counteract those external forces. Furthermore, the usage of a certain percentage of the vessel own manoeuvrability capacity to overcome encounter effects is directly translated in a reduced reserve of manoeuvrability to overcome the different met-ocean conditions. Therefore, a limit on the rudder angle to compensate the passing force should be considered in order to overcome the response of the vessel due to other external factors (wind, waves or current).

To assess the rudder requirements to compensate the passing effects, ship's manoeuvring characteristics are

considered based on the hydrodynamic coefficients and also the results obtained from ROPES.

Rudder force in combination with the engine at certain speed is assessed for different rudder angles, in a scenario with h/T=1.2. Then, the area of the curve (Fy and Fn) obtained with ROPES along the time is calculated. This step is made only for the region with the maximum value, as it is the maximum force that may be compensated by the vessel. The units of the resulting area are kN · s, which is an impulse (integral of the force over the time interval),.Afterwards, the rudder force obtained is considered to estimate the time (for each rudder angle) to compensate the area of the curve.

The required rudder angle for a New Panamax container vessel with 14.5 m draft, as a function of the time required using that angle to counteract the passing ships effects (sway force (Fy) and yaw moment (Fn)) is shown in Figure 8 for h/T=1.2, 1.0·B passing distance and 8 knots passing speed (both vessels).

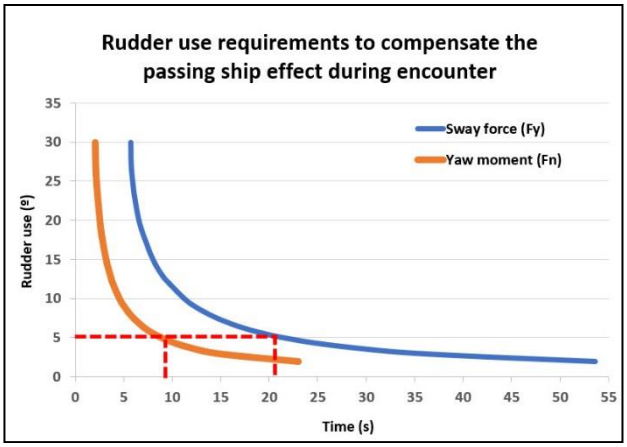

Figure 8. Rudder use requirements to compensate passing effects

As shown, in order to compensate the yaw moment with 5º rudder angle, 8 seconds use is required. However, this time is not enough to compensate the sway force, which requires about 21 seconds. On the other hand, the combination 5º and 21 seconds will cause too much course change.

As a result, during the encounter manoeuvre, the pilot maintains the course, applying rudder angle to compensate the yaw moment, but the sway force will not be fully compensated. Therefore, a minimum passing distance is required that also compensates the drift due to the sway force.

2.5 MANOEUVRES (REAL TIME SIMULATOR)

Using the passing ship coefficients (estimated for the selected vessels and h/T ratio, and taking into account the passing distance and encounter speed) included in the simulator the following step is to validate the effect of the encounter manoeuvres in the simulator.

Some tests are performed with the vessels for different values of passing speed and passing distance. It is checked that the passing forces and moments during the simulations are similar to those obtained from ROPES.

The required rudder use (angle and time with that angle) to compensate the passing effects (force and moment) is also verified. These values, rudder actions, are verified by the local pilots considering the common practice in the area for encounter manoeuvres. Their opinion and comments are very important and part of the process to verify that the results are accurate enough and similar to reality.
After the calibration and validation of the ship response during the encounter in the simulator, the simulation matrix can be performed with the two vessels under local conditions (wind, waves, currents and real depths).

For the simulated manoeuvres a preliminary configuration for the crossing area is considered. The dimensions and the layout are defined by taking into account the results of concept design in combination with the forces and moments obtained from ROPES and the assessment of rudder use.

Figure 9 shows the trackplot of an encounter manoeuvre of two container vessels in the proposed crossing area.

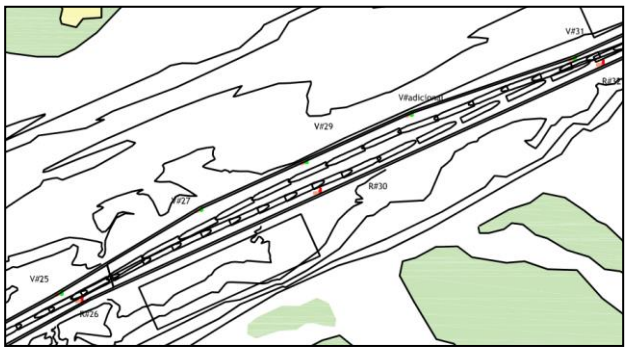

Figure 9. Trackplot of an encounter manoeuvre performed in the real time simulator

In order to define a safety area for encounter manoeuvres, it is proposed to develop a detailed analysis of horizontal navigable areas. The manoeuvres developed under the same conditions and strategy are used to obtain a statistical spread of the swept paths of the vessels (the envelope of the vessel extreme horizontal positions). At various sections of the channel the spreading of the extreme positions of the ship during the passages are computed, from which a standard deviation of the vessels' swept path can be calculated. A Normal probability distribution with a certain probability of exceedance (risk level) is considered for this stage of the analysis.

3 PRACTICE CASE

3.1 VESSELS

Two New Panamax container vessels (13 100 TEUS) with 366 m Loa, 49 m beam and 14.5 m draft (Figure 10) were considered for the assessment as design vessel for the encounter area.

Figure 10. New Panamax container vessel

3.2 CONCEPT DESIGN

The dimensions of the two-way stretch following PIANC guidelines and ROM 3.1-99 recommendations were the following:

- Length of the two-way channel: 7000 m (19.1·Loa). [Inputs: stopping distance=3000 m (for 10 kt) / $V_{encounter}$ =8 kt / t_r =60 s]
- Width of the two-way channel: 343 m (7.0·B) [Inputs: W_{BM}=1.5·B / slow speed during encounter (8 kt) (W_a) / moderate wind (15-33 kt) (W_b)/ no cross-current (W_c) / moderate longitudinal current (<3 kt) (W_d) / wave (Hs<1 m) (W_e)/ good AtoN (W_f) / bottom surface <1.5·T rought and hard (W_g) / h/T =1.2 inner channel (W_h) / gentle slope 1:10 (W_{BR} ,W_{BG})/ additional width for heavy traffic=0.15·B (W_p)]
- Depth: 17.5 m (1.2·T) [Inputs: inner channel / sand bottom / 1º roll angle]

3.3 DETAILED DESIGN USING ROPES AND REAL TIME SIMULATOR

Hydrodynamic interaction (forces and moments in six degrees of freedom) between the two passing vessels during the encounter were calculated with ROPES for a range of encounter speeds (6, 8, 10 and 12 knots) and passing distances (0.5·B, 1.0·B and 2.0·B). Value for h/T is constant.

The matrix (Figure 11) takes into account a range of speeds and passing distances derived from the information provided by the local pilots.

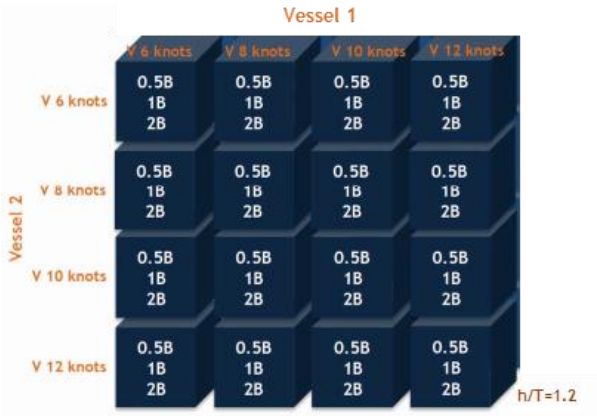

Figure 11. Matrix of ROPES simulation cases

The results obtained from ROPES were used as input in the simulator. So that the simulated manoeuvres using a real time simulator included the local conditions (wind, waves, current, proposed two-way channel layout and depths) and the passing ship effects during the encounter.

Taking into account that the concept design gives conservative results, a reduction in the initial dimensions of the encounter area was initially considered for manoeuvres. The dimensions of the two-way channel were the following:

- Length of the two-way channel: 3000 m (8.2·Loa)
- Width of the two-way channel: 318.5 m (6.5·B)
- Depth: 17.5 m (1.2·T)

The manoeuvres were performed with the assistance of local pilots in order to verify the validity of the model, regarding the local conditions (wind, waves, current and water level) and the coordination of the encounter manoeuvres (similar to reality). The participation of the pilots was essential for the success of the study.

The manoeuvres were performed with 20 knots wind speed aligned with the channel axis and 2.0 knots current speed also aligned with the channel. At the moment of the encounter, the speed of both vessels was 10 kt, and the minimum passing distance was of 74 m (1.5·B). With this combination the rudder angles were between 15º-25º.

Figure 12. Encounter manoeuvre in the real-time simulator

The encounter took place in the middle of the crossing area and required a perfect coordination between both vessels to control their relative position.

The assessment of the dimensions of the proposed encounter area was developed applying a probabilistic analysis of the repeated encounter manoeuvres (8 runs) of the two vessels (Figure 13). The manoeuvres were repeated under the same meteorological conditions and strategy. This methodology for the definition of manoeuvring areas is supported by PIANC.

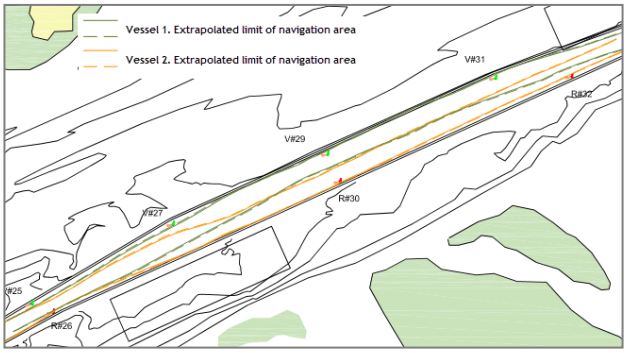

Figure 13. Extrapolated manoeuvring space obtained for encounter manoeuvres of two New Panamax vessels

3.4 RESULTS

After the detailed analysis of the encounter manoeuvres of the two New Panamax container vessels the following dimensions were proposed for the encounter area (Figure 14 and Figure 15):

- Length of the two-way channel: 2000 m (5.5·Loa) with a transition zone slope 1V:10H

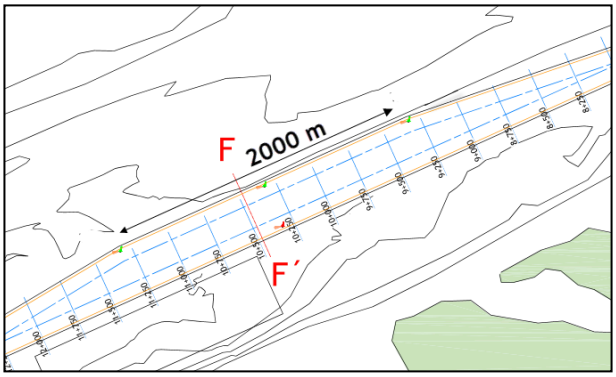

Figure 14. Layout configuration of the final encounter area

- Width of the two-way channel: 308.5 m (6.3·B)
- Depth: 17.5 m (1.2·T)

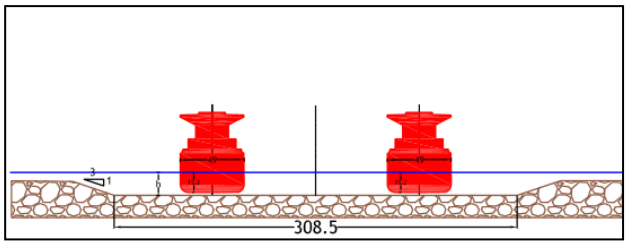

Figure 15. Section F-F of the final encounter area

These results were also validated by the local pilots and meant a significant optimization on the preliminary estimation of the dimensions based on concept design.

The final length of the encounter areas was reduced 71% and the width reduction was 11.2% from the concept design proposal. The final dimensions were reduced from the initial dimensions considered in the simulator 60% for the length of the encounter areas and 3.2% for the width. The dredging requirement was significantly reduced from the initial proposal and the cost of dredging was optimized. The results also guarantee an adequate safety level for the manoeuvres in the area.

4 CONCLUSIONS

The use of numerical modeling tools allows to perform a detailed assessment and definition of encounter areas. The combination of the results from the numerical model ROPES, and the use of real time simulations including the interaction effects derived from ROPES allow to optimize the dimensions proposed based on concept design.

The validation and calibration of the passing effects in the simulator by experts in this type of manoeuvres is an important part of the design process. The aim is to obtain an accurate model to simulate in a realistic area. The result is an optimization in the preliminary proposed encounter area, involving significant cost reduction but at the same time keeping adequate safety levels.

5 REFERENCES

MARIN, 1997. System User Manual for the Siport XXI simulator.

PIANC, 2014. Report nº121-2014. Harbour Approach Channel Design Guidelines

Pinkster Marine Hydrodynamics, 2013. User Manual for Ropes 1.1.

Puertos del Estado, 2003. ROM 3.1-99. Designing the maritime configuration of ports, approach channels and flotation areas.

Talstra, H. and Bliek, A. J., 2014. Loads on moored ships due to passing ships in a straight harbour channel. PIANC World Congress. San Francisco, USA.

Yuan, Z., 2018. Ship hydrodynamics in confined waters. Journal of Ship Research, Paper no. JSR-04-17-0020.

6 AUTHORS BIOGRAPHY

Lourdes Pecharroman holds the current position of Project Manager at Siport21. She is responsible for manoeuvring studies carried out with numerical tools (fast-time simulation and real-time simulations). She is specialized on numerical models of vessels.

Raul Atienza holds the current position of Technical Director at Siport21 and Head of Manoeuvring and Nautical Studies Department. He coordinates and checks the technical projects. He specializes in ship manoeuvrability in port areas, both using numerical models and real-time simulation. He has previously worked as Project Manager at Siport21 and as a teacher in the Technical University of Madrid (Naval Architecture College).

Carlos Cal holds the current position of Head of Nautical Advisory Division and Training at Siport21. He is an expert Captain in the use of simulator for port design and manoeuvring studies using numerical tools. He also coordinates the training programmes in the simulator for Pilots and Captains.

Raul Redondo holds the current position of Project Manager at Siport21. He coordinates and checks the technical projects. He specializes on moored ship dynamics and ship manoeuvrability in port areas, both using numerical models and real-time simulation.

Miguel de Ros holds the current position of Senior Project Engineer at Siport21. He performs the technical projects. He specializes on ship manoeuvrability in port areas, both using numerical models and real-time simulation.

MANOEUVRING SIMULATION MODELS FOR INLAND SHIPS

Frans Quadvlieg, Chris Willemsen, Wytze de Boer and **Guido Oud**,
Maritime Research Institute Netherlands (MARIN), the Netherlands

MANOEUVRING SIMULATION MODELS FOR INLAND SHIPS

Frans Quadvlieg, Chris Willemsen, Wytze de Boer and **Guido Oud,** Maritime Research Institute Netherlands (MARIN), the Netherlands

SUMMARY

The paper presents a set of model results available for a typical inland ship. We describe the mathematical model used to describe the manoeuvrability. In addition, there are ideas and initiatives to deepen the knowledge on mathematical simulation models. For this, benchmark data can be made available. During MASHCON 2019, MARIN wants to explore which parties are interested in sharing data for the development and validation of inland ship manoeuvring models (inland ships, ships+barges and pushboat convoys), in order to stimulate (academic) development, validation and application of manoeuvring simulation in shallow waters, focussed on inland ships. By this initiative, we are aiming for bundling expertise and sharing data to boost model development for inland ship manoeuvring.

NOMENCLATURE

B	Breadth (m)
C_B	Block coefficient (-)
D_P	Propeller diameter (m)
h	Water depth (m)
L_{PP}	Length between perpendiculars (m)
N'_β	Overall non-dimensional linear yaw coefficient for pure drift
r'	Non-dimensional rate of turn (-)
T_A	Draught at aft perpendicular (m)
T_F	Draught at fore perpendicular (m)
T_x	Draught of section x (m)
V_x	Local transverse velocity at section x (m)
Y'_β	Overall non-dimensional linear sway coefficient for pure drift
Y''_β	Sectional linear sway coefficient for pure drift
Δ	Displacement (t)
β	Drift angle of the ship (deg)
ρ	Density of water (kg/m^3)

1 INTRODUCTION

Inland waterway transport plays an important role in the transport of cargo in Western Europe. In 2016 inland ships transported about 365 million tons of cargo on the Dutch inland waterways. Transport of containers is growing rapidly: in 2007 over 3.8 million TEU were transported, in 2016 over 5.3 million TEU (source CBS: www.cbs.nl). The prediction of manoeuvring behaviour is an important aspect in assessing the capacity of existing waterways given increased traffic density and larger ship sizes. The types and sizes of inland ships are changing. The designs have been more or less constant in the periods up to 1990, but since then we observe that many innovations are taking place in ship design (different ratios of main particulars, different rudders, different propulsion arrangements). Because of climate changes the duration of periods of shallow water seem to increase, and continuity of the transport is to be maintained.

Knowing that the manoeuvrability dictates amongst others the capacity of the waterways, it is essential to raise the quality of manoeuvring predictions for inland ships. To increase the quality of manoeuvring predictions, benchmark studies are essential. Many international benchmark studies are focusing on sea-going ships. Considering the foregoing, there are the important reasons to also take inland ship manoeuvrability in scope.

It is very obvious that especially the behaviour in shallow water is important. To this extent, MARIN has different sets of information available, developed over five years:

- Results of captive model tests of an 110m inland ship, in which in particular the rudder forces are measured (see Quadvlieg (2013)), in shallow water.
- CFD calculations to quantify hull forces on inland ships and some pushboat convoys. New techniques are investigated, not just to quantify linear coefficients, but especially focussing at the forces at large drift angles and rates of turn, and at small under keel clearances.

Using these two insights, mathematical models are being composed. However, an end-to-end validation of these mathematical models is still needed, which is why free sailing tests are needed.

2 SIMULATION MODELS

2.1 OVERVIEW OF METHODS TO OBTAIN SIMULATION MODELS

The objective of simulation models is to be able to perform fast time and real time simulations. Using these simulation models, the limiting conditions for safe and swift transport over inland waterways can be explored.

There are two aspects to the simulation model: the structure of the mathematical model and the obtaining of adequate coefficients for these mathematical models.

On the structure of mathematical models, several papers have been written. Gronarz (1997), Yasukawa et al (2007), Tabaczek, and Kulczyk (2016) have published papers with mathematical models for inland ships. The structure of

most of these methods was similar: these were models in which the coefficients are determined by a regression of the data measured during captive model tests or CFD for a particular ship..

The challenge is to obtain coefficients. Model tests are the conventional way to obtain coefficients with a high degree of accuracy. Gronarz (1997) has been using PMM type model tests to derive coefficients. Yasukawa et al (2007) have been using CMT type of model tests to obtain coefficients. Both are captive model tests, but the difference is that the PMM tests are using sinusoidal tests to obtain the rotation terms, while in CMT tests, stationary rotations are used to obtain the rotation coefficients.
Captive model tests are still a very efficient and accurate way of obtaining coefficients. For use in the early design stage, it is however a method that is time-consuming.

Quadvlieg (2013) and Liu et al (2017) investigated methods to predict the manoeuvring coefficients of inland ships based on as little as possible data. Empirical methods are investigated. These empirical methods are employed to estimate the manoeuvring coefficients based on main parameters such as length, draught, breadth and block coefficient, and in particular the water depth.

Tabaczek and Kulczyk (2016) have calculated the coefficients for the hull using CFD. In these CFD simulations, captive conditions are imposed, and the forces and moments are calculated by integration of the friction and pressure forces over the hull. By performing these simulations for a suitable range of drift angles and rotation rates, and also combined drift and rotation, enough material can be obtained to derive manoeuvring coefficients for a mathematical model.

The advantage of CFD is that this can be used in the early design stage. The disadvantage is that the modelling of the CFD is a typical expert job. The modelling of rudders, appendages, and the typical propulsion arrangement such as tunnels is a significant effort. It is easy to obtain an answer, but not easy to obtain a reliable answer.

2.2 CHOICE OF MATHEMATICAL MODEL

The mathematical model selected for the simulations will depend on the use of the mathematical model. There are two applications foreseen: 1) a mathematical model suitable for sailing on a canal, with relatively small speed variations, moderate rudder angles and relatively small rates of turn. 2) a mathematical model that is suitable for more elaborate (harsher) manoeuvre such as turning from a river into a harbour, on the spot turning, astern sailing.

A type 1 mathematical model is less elaborate that a type 2 mathematical model. The present paper discusses only the type 1 mathematical model. The type 2 mathematical model is worth a separate paper. Both mathematical models use a different approach to describe the hull forces on one hand and the propulsor / rudder forces on the other hand.

2.2 (a) Mathematical model for the hull forces

The type 1 (limited) model is for a validity range of drift angles up to +- 20° and non-dimensional rate of turn of r'=0.6. For a mathematical model with this restricted validity range, the mathematical model of the hull for the X-force, Y-force and N-moment is composed as follows:

$$X' = X'_0 + X'_{\beta\beta} \cdot sin^2\beta + X'_r \cdot r^2 + X'_{\beta r} \cdot sin\beta \cdot r \quad (1)$$

$$Y' = Y_\beta \cdot \beta + Y_\beta \cdot \beta \cdot |\beta| + Y_r \cdot r + Y_r \cdot r^3 + Y_{\beta\beta r} \cdot \beta^2 \cdot r + Y_{\beta rr} \cdot \beta \cdot r^2 \quad (2)$$

$$N' = N_\beta \cdot \beta + N_\beta \cdot \beta \cdot |\beta| + N_r \cdot r + N_{r|r|} \cdot r \cdot |r| + N_{\beta\beta r} \cdot \beta^2 \cdot r + N_{\beta rr} \cdot \beta \cdot r^2 \quad (3)$$

It is noted that the equations and the coefficients are non-dimensional. The following formulas are used to make the non-dimensional:

$$X' = \frac{X}{\frac{1}{2}\rho V_S^2 \cdot L \cdot T}$$

$$Y' = \frac{Y}{\frac{1}{2}\rho V_S^2 \cdot L \cdot T}$$

$$N' = \frac{N}{\frac{1}{2}\rho V_S^2 \cdot L^2 \cdot T}$$

N is the moment around the z-axis, measured around O (which is located halfway between F_{PP} and A_{PP}). For the sign of the coefficients, it is of importance to realise that the MARIN sign convention for the drift angle is β =atan(v/u), while the ITTC sign convention is β=atan(-v/u).

2.2 (b) Mathematical model for the propeller and rudder forces

Rudder arrangements on inland ships are quite different from the rudder arrangements on seagoing ships. Rudders are typically twin rudders, often of special designs, selected to generate high lift forces, especially at large rudder angles. Rudders are often constructed such that high rudder angles are possible, often up to near 90° of rudder angle. In this high rudder angle, the inner and outer rudder may not have the same angle.

A second aspect are the shapes of the hull. Compared to seagoing ships, European inland ships are having high L/B ratios, high B/T ratios and high block coefficients. Furthermore the tunnels are playing a role. The aft ships are designed such that also when sailing in shallow water, the water flows towards the propeller.

The propellers are usually equipped with nozzles, and the propellers have large diameters compared to the sometimes low draughts of the ships. Tunnels are used to guide the water towards the propeller – nozzle arrangement.

It is obvious that to obtain hydrodynamic coefficients for a simulation model for inland ships, these aspects need to be quantified. For hull forces (alone), CFD is an economical attractive alternative to model tests, even given the fact that CFD neglects several hydrodynamic aspects. For the forces on rudders and propellers, systematic model tests are carried out.

3 SYSTEMATIC MODEL TESTS TO STUDY PROPELLER AND RUDDER FORCES BEHIND INLAND SHIPS

A representative, but not existing, inland ship is designed, and a model is made. The fact that this is a non-existing ship allows that the lines plan can be shared with interested parties around the world, and it can be used to simulate knowledge on inlands ships. Using this model, model tests have been carried out in 2013.

3.1 SHIP HULL

3.1 (a) Hull main particulars

The most common ship in the west European inland river estuary would be the ship with main dimensions of L×B×T of 110×11.4×3.5 meter. Most ships are equipped as a single screw ship. The rudder arrangements are varying amongst the fleet of inland ships. The most common is a twin rudder arrangement behind the single propeller.

Table 1. Main particulars for the inland ship

Characteristic	full & model value		unit
L	110.0	6.111	m
B	11.4	0.633	m
T_F	3.5	0.194	m
T_A	3.5	0.194	m
Δ	3832	0.657	t
C_B	0.88	0.88	-
D_P	1.8	0.100	m

A model was made to scale 18, resulting in a model scale propeller diameter of 10 cm, which was deemed the absolute minimum.

3.1 (b) Propulsion arrangements

Usually the inland ships of this size are equipped with a single, ducted propeller and a pair of rudders (see Figure 1). However, with the increasing breadth of the inland ships, it is noted that more ships are equipped with twin propellers and consequently also with more rudders, hence 4 rudders instead of 2 rudders.
Because it is desired that systematic information is present on the most common rudder designs, the model tests are carried out with two arrangements: the same foreship with two aft ship arrangements. The single screw arrangement is shown in Figure 1 and Figure 2. The twin screw aft ship arrangement is shown in Figure 3 and Figure 4.

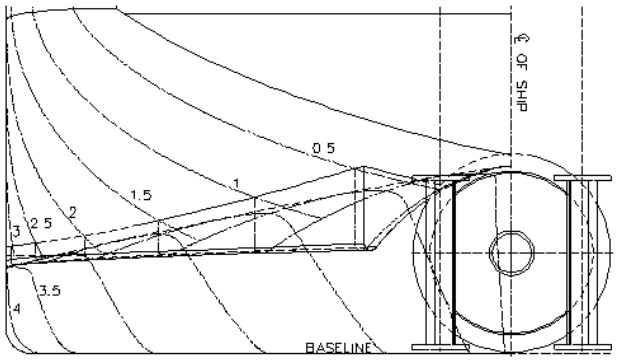

Figure 1. Propeller and rudder arrangement for the single screw variant: lines plan

Figure 2. Propeller and rudder arrangement for the single screw variant: ship model

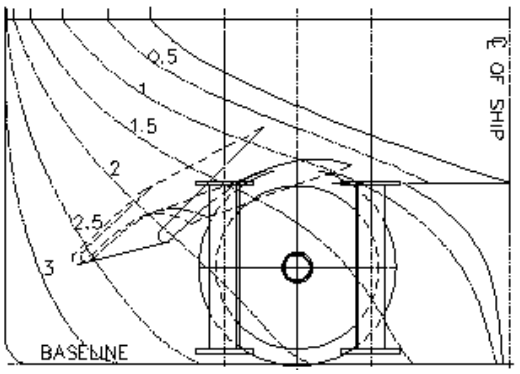

Figure 3. Propeller and rudder arrangement for the twin screw variant: lines plan

Figure 4. Propeller and rudder arrangement for the twin screw variant: ship model

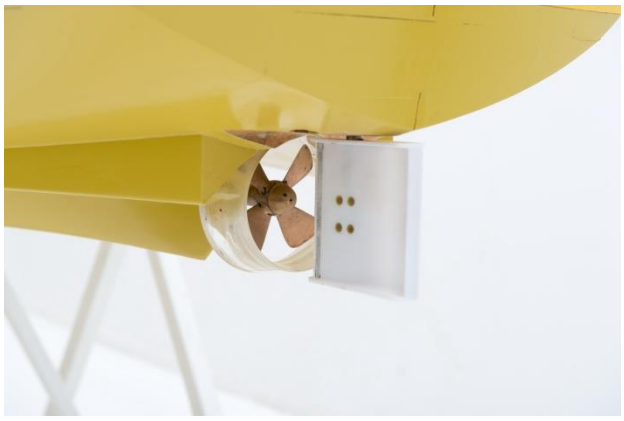

Figure 5. Propeller rudder arrangement for the single screw arrangement with a single fishtail rudder: ship model

Figure 6. Propeller rudder arrangement for the single screw arrangement with a twin NACA rudder: ship model

3.2 MODEL SETUP

The model is connected to the main carriage in MARIN's shallow water basin. This basin measures 220×15.8 meter in length and width. The water level in the basin can be adjusted to any depth between 0 and 1.10 meter. The suitability of the basin, including an assessment on the flatness of the bottom of the basin is given by Tonelli and Quadvlieg (2015).

The model is connected to the main carriage by a yoke, allowing the model to freely sink and trim. The motions in surge, sway, yaw and roll are fixed. Especially the free-to-sink-and-pitch is important for shallow water tests. A photograph of the test set-up is given in Figure 7.
A turn-table is mounted between the carriage and the measurement frame. This turn-table can be rotated to give a drift angle to the model with respect to the sailing direction. Figure 8 shows the model with -40° drift angle.

During the tests, the following signals are measured:

- Longitudinal and transverse force
- Turning moment, measured around midship (=ordinate 10)
- Propeller RPM, thrust and torque
- Longitudinal and transverse force on the nozzle
- Longitudinal and transverse forces and the rudder stock torque on each of the rudders;
- Trim and sinkage
- Carriage coordinates, of which the carriage speed and hence the speed of the model is derived.

3.3 MODEL TESTS AND TEST MATRIX

The test matrix to determine rudder and propeller forces is given in the Table 2.

Table 2. Test matrix

	Rudder	h/T	Bollard pull with rudder angles	Rudder angles variations sailing at speed, zero drift	Rudder angles variations sailing at speed, drift 20° and 40°
Twin screw	Twin fish tail per propeller	1.4	X	X	X
Twin screw	Twin fish tail per propeller	2.0	X	X	X
Single screw	Twin fish tail	1.4	X	X	X
Single screw	Single fish tail	1.4	X	X	
Single screw	Twin NACA	1.4	X	X	

The rudder angles have been varied every 5°. The tests were captive tests, and the model was given a fixed speed through fixing the carriage speed. The propeller RPM is adjusted to several RPM's with n_0 = the RPM corresponding to the self propulsion point when sailing straight ahead.

Figure 7. Set-up of model test

Figure 8. Set-up of model test with -40° drift angle (bow to portside)

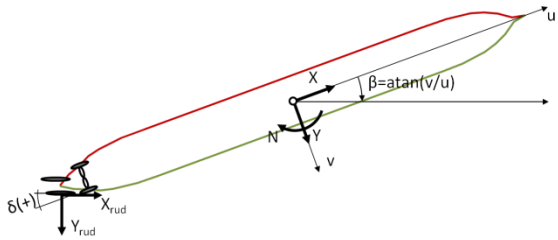

Figure 9. Coordinate system for forces, moments, velocities and drift and rudder angles

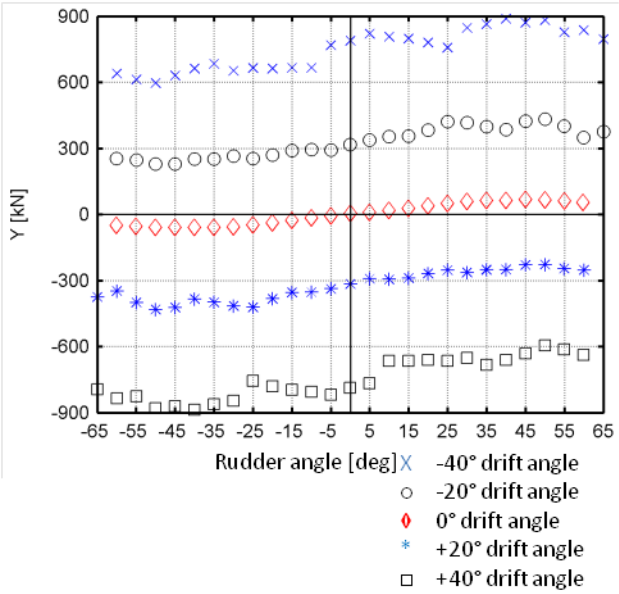

Figure 10. Sample of the results: total forces on the ship, plotted against the rudder angle for drift angles -40°, -20°, 0°, 20° and 40° (for the single screw, twin rudder arrangement),

3.4 RESULTS

The analysis of these tests gives insight in the forces on the rudders of these typical inland ships. A sample of the results is given in Figure 6 and Figure 7. This shows the Y-force on the complete ship (in full scale) for a speed of 6 km/h. Different lines are given for drift angles of 0°, -20° and -40°. In addition to the forces on the complete ship, we give the results for the starboard rudder and the portside rudder separately. The presented rudder side force is given in a rudder coordinate system. The presented ship side forces are given in the ship coordinate system. The sign convention of the total forces, the rudder forces is given in Figure 9. Note that the drift angle is defined as +v/u and that the rudder angle is defined positive with the trailing edge to portside. The rudder side force is a magnitude that has the same angle as the rudder angle. The global (ship-fixed) force is measured in the coordinate system of the ship.

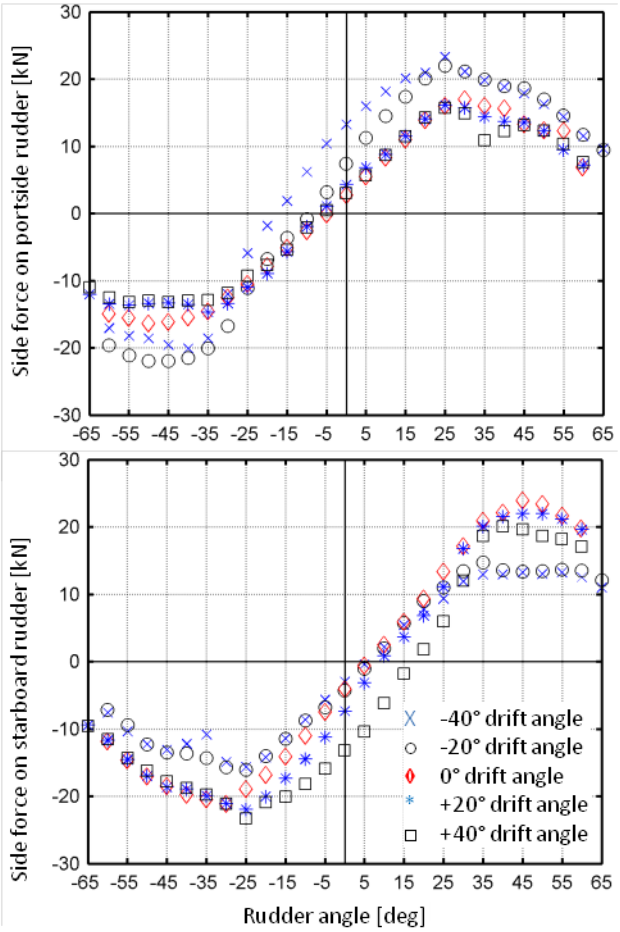

Figure 11. Sample of the results: Rudder forces on the starboard and portside rudder (for the single screw, twin rudder arrangement), plotted against the rudder angle. Different lines for drift angles -40°, -20°, 0°, 20° and 40°

The sample of results shows only the forces for one speed, for the water depth draught ratio of 1.4. The speed for these tests was 6 km/h, with an RPM of 182, which is an overloaded propeller of 1.5 times the RPM for a self-propulsion point.

In these results, it is shown that the rudder which is on the leeward side of the ship, experiences hardly any effect of the drift angle. The rudder that is on the weather side, experiences quite some effect. Apperently the flow aligns on the weather side from 40° towards some 20°, while on the leeward side, it aligns from 40° towards 0°.

4 DETERMINATION OF THE HULL FORCES

To determine the hull forces on inland ships, so-called virtual captive model tests are carried out. MARIN performs these virtual captive tests on a routine basis. The objective is to determine the manoeuvring coefficients for the bare hull conditions, sailing in various water depths.

4.1 CALCULATION MATRIX FOR VIRTUAL CAPTIVE TESTS

Based on experiences, MARIN has defined a matrix of conditions that we typically carry out to determine the manoeuvring coefficients. There are some options in this, in the case that astern sailing also needs to be present.

The default calculation matrix consists of the series given in Table 3.

Table 3. Default calculation matrix for virtual captive tests to determine hull forces

Series #	*type*	*range*
Series 1	Pure drift, small angles	0:2:20
Series 2	Pure drift, large angles	20:10:90
Series 2b	Pure drift, astern angles	90:10:180
Series 3	Pure yaw	r'=0.1:0.1:0.6
Series 4	Yaw and drift	r'=0.1:0.1:0.6, β=-10°
Series 5	Yaw and drift	r'=0.1:0.1:0.6, β=-20°

Depending on the objective of the mathematical model, and the expected behaviour of the ship, the r' range is extended towards 1.0 instead of 0.6.

The reasoning behind this set of coefficients is that for small drift angles, a dense grid (being drift angles from 0° to 20° with a step of 2°) is needed, especially to be able to determine the linear coefficients with sufficient resolution. The same holds for the rate of turn. A rate of turn of r'=0.2 yields small values, but it is important to determine the linear coefficients.

It is furthermore important that CFD calculations for the rates of turn and in particular the combinations of drift and yaw are determined correctly in CFD. The results are quite sensitive for the way in which the domain is shaped.

4.2 CFD SETTINGS

For the CFD calculations, the ReFRESCO code is used. ReFRESCO computes the steady incompressible viscous flow around a ship. It solves the RANS equations, using a finite-volume method. The code is a community based open-usage and open-source CFD code for the Maritime World. It is coordinated by MARIN. A unstructured grid was generated using Hexpress for a rectangular computational domain, with a length of 7 L_{PP}, a width of 4 L_{PP} and a height of 2 L_{PP}. Both sides of the domain have to be modelled. This domain size is based on good practice guidelines following MARIN's grid sensitivity studies for comparable ships and is chosen sufficiently large in order to ensure a negligible influence of the boundary conditions on the solution.
For this objective, the calculations are carried out with wall functions, so the y+ values are in the order of magnitude of 100. The amount of grid cells is in the order of 15

million. The calculations are carried out for full scale Reynolds number.
The k-ω SST model from 2003 is used. This turbulence model has proven its strength for typical flows during manoeuvring of ships, especially for flow with large amounts of separated vortices. This ensures a better solution for forces and moments including the effect of vortices of lifting surfaces and blunt bodies.
The calculations are performed for a double body-setup, meaning that the deformation of the free surface is not taken into account. The simulations are performed until convergence criteria are met, which means that the convergence criteria are below 10^{-4}.

Figure 12 gives an impression of the results that can be obtained, in this case for a 6-barge push system.
Validations are taking place as well. For pure drift, such a validation is demonstrated in Figure 13. Figure 13 shows in red the side force and yawing moments obtained through CFD simulations for an inland ship in shallow water. In blue, the measured force and moment are given. Around the blue dots, an uncertainty is indicated. This validation shows that CFD is not predicting the forces entirely correct, however there are some differences between the CFD simulations and the model tests. The basin width is namely not taken into account in the CFD simulations. Furthermore the CFD simulations are carried out double-body, while the model tests, the ship model was experiencing trim and sinkage. We expect that especially the first one is a major influencer for the determination of the forces and moments.
For now, it is concluded that CFD is not a perfect predictor, but a cost efficient predictor with a reasonable error margin.

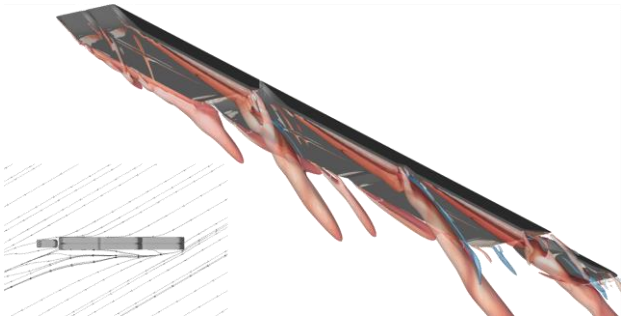

Figure 12. Example: 6-barge push convoy at a drift angle of 30°, deep water

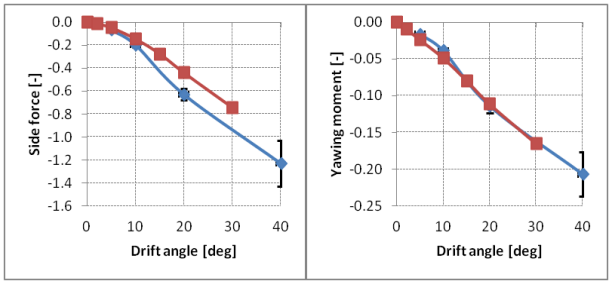

Figure 13. Comparison of the non-dimsniaional side force and the non-dimensional yawing moment between CFD calculations and drift force measurements for an inland ship in h/T = 1.4

4.3 DATA REDUCTION

The forces and moment on the hull are obtained by integration of the pressures on the hull.

In addition to the forces and moments on the complete ship, a so-called segmented analysis is carried out. In the segmented analysis, we divide the ship in 100 longitudinal strips. The pressure over this strip is integrated to obtain the forces per strip. Analysis of these forces per strip leads to interesting fundamental insights.

4.4 RESULTING GLOBAL COEFFICIENTS

A selection of the results is presented here. Figure 14 and Figure 15 are giving the side force and yawing moment on the hull of a 110×11.4×3.5 sized inland ship, single screw version (see Table 1). Other graphs can be made, showing the forces from 0° up to 90° drift angle, etcetera, but they are left out of this paper at this moment. Also the longitudinal hull forces are left out of the paper at this moment. This paper restricts itself to the hull forces up to 20° drift angle.

The resulting coefficients as presented here can be fitted and a “coefficient-based” mathematical model can now be obtained.

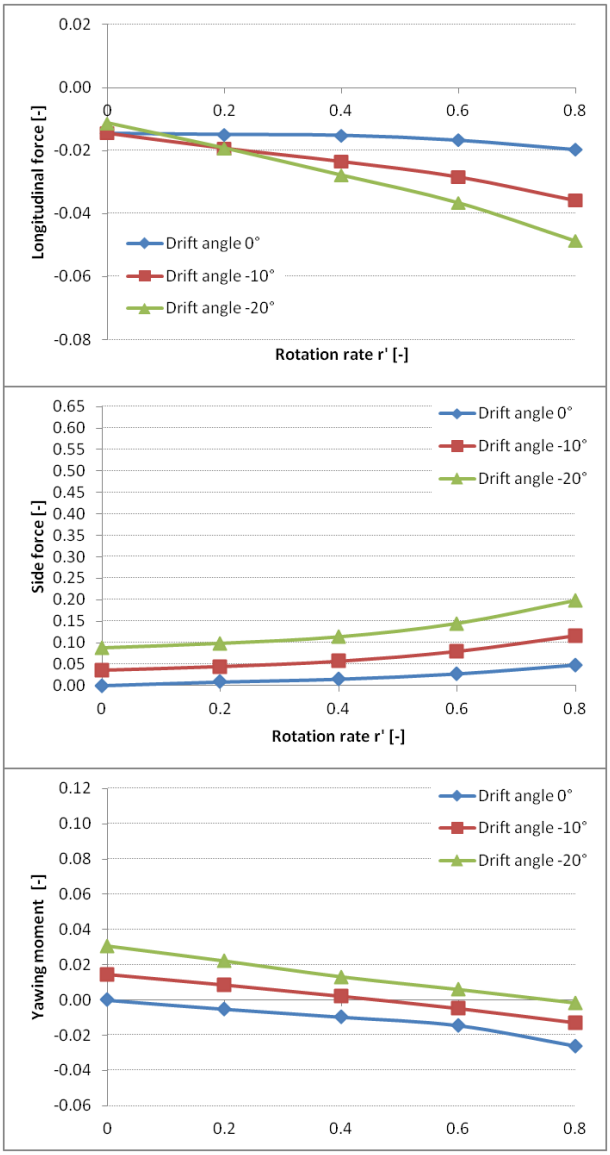

Figure 13. Resulting manoeuvring force and moment for a combination of rotation rates and drift angles, in deep at a speed of 3.5 m/s

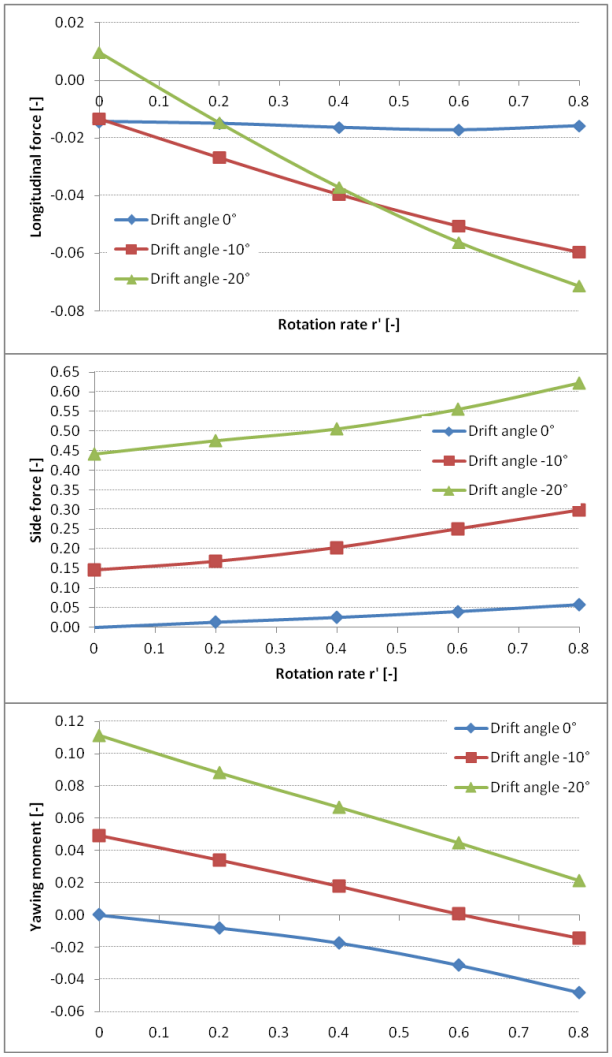

Figure 14. Resulting manoeuvring force and moment for a combination of rotation rates and drift angles, in waterdepth to draught h/T=1.4

The resulting non-dimensional coefficients for drift, rotation and combined yaw and rotation are given in Table 4.

Table 4. Derived non-dimensional coefficients in deep and shallow water for the hull

Coefficient	Deep water	Shallow water
Y'_{β}	-0.156	-0.578
$Y'_{\beta\|\beta\|}$	-0.293	-1.87
Y'_{r}	0.0318	0.0624
Y'_{rrr}	0.0441	-0.0161
$Y'_{\beta\beta r}$	-0.108	0.656
$Y'_{\beta rr}$	-0.319	-0.457
N_{β}	-0.0775	-0.279
$N'_{\beta\|\beta\|}$	-0.0375	-0.107
N'_{r}	-0.0145	-0.0289
$N'_{r\|r\|}$	-0.0213	-0.0392
$N'_{\beta\beta r}$	-0.199	-0.364
$N'_{\beta rr}$	0.0208	0.0519

This classical way of describing the coefficients has however its limitations. This mathematical model and its coefficients are not valid outside the range of -20° < β +20° and -0.8 < r' < 0.8.

These coefficients are a "best fit" of all data points. This means that it may be dangerous to use the coefficients outside the box of applicability. The order of fitting is to first fit the pure drift, then the pure yaw, and fixing these coefficients to determine the combined yaw and drift coefficients.
A second point of consideration is that during many simulations, it is needed to extend the range of applicability towards low speed manoeuvres, harbour entry simulations, tight turns, harbour access simulations. For these type of manoeuvres, a different mathematical model form is needed.

5 INSIGHT IN THE MANOEUVRING FORCES

Detailed information extracted from the CFD results allows a better understanding of the forces on the hull. In particular, insight in the longitudinal distribution of the lateral forces as function of drift angle and rotation rates. A similar technique was used by Hooft and Quadvlieg (1996), at that time applied on segmented model tests. This technique is now applied on the results generated by CFD.

5.1 DERIVATION OF LINEAR COEFFICIENTS

To increase the insight in the manoeuvring forces acting on the ship, the linear coefficients are derived per section. These linear coefficients can be fitted well because the results from the virtual captive tests are available for a range of small drift angles. The derivation of the linear coefficient is done by asymptotically looking at the derivative of the force.
For every drift angle β, formula (3) is calculated.

$$Y_\beta"(x,\beta) = \frac{Y(x,\beta)}{\frac{1}{2}\cdot\rho\cdot {V_S}^2\cdot cos\beta\cdot sin\beta\cdot T_x\cdot dx} \quad (3)$$

The interception between the range of $Y_\beta(x,\beta)$ and $Y_\beta(x,0)$ is the linear coefficient per section. Further explanation about the derivation of linear coefficient and cross flow drag coefficients is given by Hooft and Quadvlieg (1996). For an inland ship (not the same as the above ship!), this is calculated and derived. The results are given in Figure 15, for a deep water case and a shallow water (h/T=1.4) case.

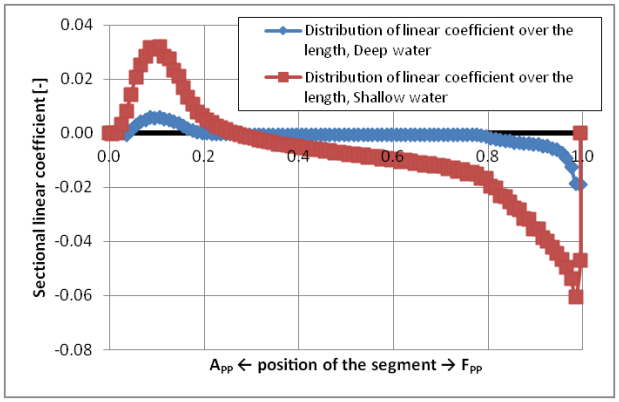

Figure 15. Distribution of the linear coefficients over the length of the ship

The following aspects are noteworthy:

- The total linear coefficient for sway as function of drift in deep water is around -0.1, while in shallow water, this is -0.8. The fact that this Y_β is much larger in shallow water than in deep water is known, and it is quite important.
- Both in shallow and in deep water, one can recognise the typical longitudinal distribution of forces which results in the Munk moment in airship theory.
- In deep water, the lift coefficient in the parallel midship area is zero. This is in agreement with the slender body theory. In shallow water, this is not the case. the flow in shallow water is fundamentally different. The shape of the blue and the red curve in Figure 10 is completely different. This suggests that the slender body theory as used in Quadvlieg (2013) is indeed valid for inland ships in deep water. But in shallow water, this needs to be revised.

5.2 CROSS FLOW DRAG COEFFICIENTS FOR PURE DRIFT

For the 90° drift angle, the sectional forces over the length of the vessel can be taken. Based on this, the cross flow drag coefficient of every section can be obtained. Formula (4) explains how CD_{90} is obtained. The local draught per section is used for that.

$$CD_{90}(x) = \frac{Y(x)}{\frac{1}{2}\cdot\rho\cdot V_x\cdot|V_x|\cdot T_x\cdot dx} \quad (4)$$

When this distribution of $CD_{90}(x)$ is plotted against the length of the ship, Figure 16 is obtained.

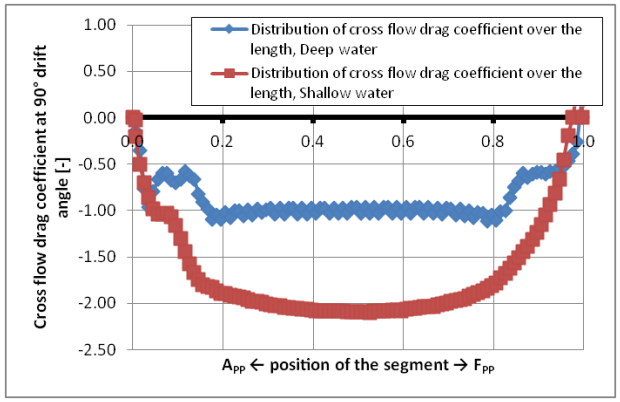

Figure 16. Distribution of the cross flow drag coefficients over the length of the ship

The following aspects are noteworthy:

- Apparently the cross flow drag at midship is around 1 in deep water, while this is around 2 in shallow water of h/T=1.4.
- In deep water, there are hardly any 3D effects in the parallel midship. In the bow area (0.8<x<1.0) and in the stern area (0<x<0.18), there are 3D effects.
- In shallow water (at least in h/T=1.4), 3D effects are taking place over the complete length of the ship.

5.3 FUTURE STEPS IN THE ANALYSIS OF HULL FORCES

Using this method, so far 6 different inland ships have been systematically investigated, to obtain the segmented information in deep and in shallow water. The intention is to compare trends in the linear and non-linear coefficients. CFD simulations for the following ships have been performed:

- 6 barge push convoy (3×2 arrangement)
- 6 barge push convoy (2×3 arrangement)
- 4 barge push convoy (2×2 arrangement)
- 2 barge push convoy (2×1 arrangement)
- 3 different 110×11.4 motorships
- 135 ×14.2 motorship

Analysis is underway to determine the distributions of coefficients over the length of the ship.

It is the intention that based on the insights derived from the analysis of the longitudinal distribution to upgrade the insights of slender body and cross flow drag theories in shallow water. The reason to upgrade slender body and cross flow drag theory is that with these upgraded theories, simulations can be performed much quicker than when CFD would be calculated every time step in a full mission simulator.

6 BENCHMARKING AND COOPERATION

As indicated by Liu et al (2016), there is no international public benchmark data available for inland ships. For seagoing ships, benchmark data is becoming available and increasing in quality. The benchmark ships for manoeuvring are KVLCC2, KCS and 5415M. Recently, ONR-T and DTC (see Shigunov et al, 2018) is added to the benchmarks. For KVLCC2 and KCS, also shallow water cases are created as benchmark. The past SIMMAN workshops have led to good investigations and the manoeuvring community has been progressing because many parties performed research on these ships. Stern et al (2011) and Quadvlieg et al (2015) have reported on these international benchmark studies. In 2020, the next SIMMAN workshop is held in South Korea to further investigate the predictive qualities of manoeuvring prediction methods. The workshop will treat KVLCC2 and KCS in deep and shallow water, and ONRT in deep water. KCS and ONRT will also cover manoeuvring in waves.

Knowing the impulse that these workshops gave, it is the intention to make data for inlands ships available to a group of researchers that would be devoted to use the data and compare the results of manoeuvres carried out with the simulation program. In addition, it will at some point be necessary to have access to free running manoeuvring tests on inland ships.

7 CONCLUSIONS

The following conclusions are justified:

- It is possible to use CFD to generate hull forces on ships under a variety of drift angles and rotation rates. With the resulting forces and moments, a mathematical simulation model can be made. The cost are very affordable.
- The aft ship of inland ships and the propeller rudder arrangement is very specific. Insight in this has been obtained using model tests with systematic variation of many parameters.
- There is no benchmark data found to make a worldwide comparison of manoeuvring predictions for inland ships. But the inland ship under consideration can be made available. Organisation of a workshop specifically for inland ship manoeuvring predictions would give an impulse to this research.
- From the observation of the longitudinal distribution of the linear coefficients and the cross flow drag coefficients (for inland ships), we observe that the flow in shallow water is much more 3Dimensional than in deep water. The often used approach in literature to multiply every coefficient in a mathematical model with a factor depending on h/T seems nice, but lacks any correlation with physics.

8 ACKNOWLEDGEMENTS

The support of the Dutch Ministry of Infrastructure and Water Management is acknowledged. The model tests on the 110×11.4 motorship are sponsored by this ministry as

part of the IDVV project, including the follow up with respect to first validations and additional CFD simulations on inland ships.

9 REFERENCES

Gronarz, A., 1997, Rechnerische Simulation der Schiffsbewegung beim Manövrieren unter besonderer Berücksichtigung der Abhängigkeit von der Wassertiefe. PhD Dissertation.

Liu, J., Hekkenberg, R., Quadvlieg, F., Hopman, H. Zhao, B., 2017. An integrated empirical manoeuvring model for inland vessels. Ocean Engineering, Vol. 137, pp. 287-308

Liu, J., Hekkenberg, R., Rotteveel, E., Hopman, H., 2015. Literature review on evaluation and prediction methods of inland vessel manoeuvrability. Ocean Engineering, Vol. 106, pp. 458-471.
https://doi.org/10.1016/j.oceaneng.2015.07.021

Hooft, J.P., Quadvlieg, F.H.H.A., 1996, Non-linear hydrodynamic hull forces derived from segmented model tests. In: MARSIM International Conference on marine simulation and ship manoeuvrability, Copenhagen, 1996

Quadvlieg, F.H.H.A., Simonsen, C., Otzen, J., Stern, F., 2015. Review of the SIMMAN2014 Workshop on the State of the Art of Prediction Techniques for Ship Manoeuvrability International Conference on Ship Manoeuvrability and Maritime Simulation (MARSIM), Newcastle, UK, 2015

Quadvlieg, F.H.H.A., 2013, Mathematical models for the prediction of manoeuvring of inland ships; does the ship fit in the river? Smart Rivers 2013 Paper 187.

Stern, F., Agdrup, K., Kim, S.Y., Cura Hochbaum, A., Rhee, K.P., Quadvlieg, F.H.H.A., Perdon, P., Hino, T., Broglia, R. and Gorski, J., 2011, Experience from SIMMAN 2008-The First Workshop on Verification and Validation of Ship Maneuvering Simulation Methods. Journal of Ship Research 55(2):135-147.

Shigunov, V, El Moctar, O, Papanikolaou, A., Potthoff, R. and Liu, S., 2018, International Benchmark Study on Numerical Simulation Methods for Prediction of Manoeuvrability of Ships in Waves. Ocean Engineering 165. DOI: 10.1016/j.oceaneng.2018.07.031

Tabaczek, T.,Kulczyk, J., 2016, Heeling moment acting on a river cruiser in manoeuvring motion. Polish maritime research 1(89) 2016 Vol. 23; pp. 45-51 10.1515/pomr-2016-0007

Tonelli, R., Quadvlieg, F.H.H.A., 2015, New Benchmark Data for Manoeuvring in Shallow Water Based on Free Running Manoeuvring Tests Including Uncertainty of the Results. OMAE ASME 34th International Conference on Ocean, Offshore and Arctic Engineering, St. John's, Newfoundland, Canada, 2015

Yasukawa, H., Hirata, N. , Koh, K.K., Punayangkool, K., Kose. K., 2007. Hydrodynamic force characteristics on maneuvering of pusher-barge systems, Journal of Japan Society of Naval Architecture and Ocean Engineering, No. 5, 2007 (in Japanese)

10 AUTHORS BIOGRAPHY

Frans Quadvlieg holds the position of Senior Project Manager. He is responsible for manoeuvring projects and complicated and very cool projects. He has more than 25 years of experience in manoeuvring related research at MARIN, in commercial projects, joint industry projects and fundamental research. He was for 9 years member of the ITTC manoeuvring committee and active in the SIMMAN workshops.

Chris Willemsen holds the position of Project Manager Ships CFD. He is responsible for carrying out CFD simulations for manoeuvring of ships and submarines. He has experience in performing virtual captive manoeuvring tests and the derivation of manoeuvring simulation models. In addition, he performs time domain free running CFD simulations, especially for the manoeuvrability of ships.

Wytze de Boer holds the position of Senior Project Manager Ships – transport and shipping. He is responsible for projects with inland ships, including the definition, planning and realisation of the research projects realised in cooperation with the Dutch Ministry of Infrastructure and Water Management.

Guido Oud holds the position of Researcher. He investigates applications for manoeuvring using CFD. At present he is involved in carrying out CFD simulations for manoeuvring of ships, especially in performing virtual captive manoeuvring tests.

FREE RUNNING MANEUVERING TESTS OF THE DTC HULL IN CALM WATER AND REGULAR WAVES WITH FOCUS ON UNCERTAINTY ANALYSIS BASED ON REPETITION TESTS

Øyvind Rabliås and **Trygve Kristiansen**,
Dept. of Marine Technology, Norwegian University of Science and Technology, Norway

FREE RUNNING MANEUVERING TESTS OF THE DTC HULL IN CALM WATER AND REGULAR WAVES WITH FOCUS ON UNCERTAINTY ANALYSIS BASED ON REPETITION TESTS

Øyvind Rabliås and **Trygve Kristiansen,** Dept. of Marine Technology, Norwegian University of Science and Technology, Norway

SUMMARY

Free running maneuvering tests were performed with the DTC hull in the Ocean basin at SINTEF Ocean in Trondheim, Norway. Course keeping tests, turning circles, and Zig-Zag tests were performed in calm water conditions and in regular waves, with emphasis on tests in waves. Seven wavelengths, in the range $\lambda/L_{pp} = 0.280 - 1.120$, were tested. The maneuvers were tested for different approach wave headings. Emphasis was made on repetition tests and uncertainty analysis. The analysis revealed that global responses repeated well in general. The relative uncertainty was typically below 5%, for a set of selected responses.

NOMENCLATURE

B	Moulded beam of ship (m)
C_B	Block Coefficient (-)
D_t	Tactical diameter (m)
Fn	Froude number
GM	Metacentric height (m)
H	Wave height (m)
I_{xx}	Roll moment of inertia (kgm^2)
I_{yy}	Pitch moment of inertia (kgm^2)
I_{zz}	Yaw moment of inertia (kgm^2)
k	Wave number
KG	Height of the ship's center of gravity above keel (m)
L_{bk}	Length of bilge keel segment (m)
L_{pp}	Length between perpendiculars (m)
N	Number of observations
q	Random quantity
RPS	Rotations per second
s_q	Experimental standard deviation of q
T	Moulded Draught (m)
t_α	Inverse student-t distribution
U	Expanded uncertainty
XCOG	Longitudal center of gravity (m)
YCOG	Lateral center of gravity (m)
Δ	Ship displacement (kg)
η_i	Rigid-body motion in degree of freedom i
μ	Wave encounter angle (deg)
λ	Wavelength (m)
ζ_a	Incident wave amplitude (m)

DTC	Duisburg Test Case
TEU	Twenty-Foot Equivalent Unit
VLCC	Very Large Crude Carriers

1 INTRODUCTION

Numerical simulations of maneuvering in waves has received increasing attention in recent years, in particular for real-time simulation for training. Accurate benchmark data is necessary to validate the numerical methods. To increase our understanding of the dominant mechanisms of ship maneuvering in waves, and to obtain valuable benchmark data for validation, ITTC has called for more experimental research (ITTC, 2011). To ensure that a numerical model is capable of simulation of various scenarios, the model must be validated for a range of maneuvers and environmental conditions. This leads to the need of extensive benchmark data. There are different type of tests relevant for ship maneuvering. Captive tests, propulsion tests, and seakeeping test are examples of such tests. However, all numerical models should be validated against free running maneuvering experiments. Since there is a limited number of facilities capable of performing such experiments, and the fact that maneuvering is investigated in calm water traditionally, there are only a few available benchmark tests for free running maneuvering in waves.

Ueno et al. (2003) performed free running turning circle tests, Zig-Zag 20/20, and stopping tests with a VLCC model in regular waves. Three wavelengths between $\lambda/L_{pp} = 0.4$ and $\lambda/L_{pp} = 1.0$ were tested, with wave amplitude of 0.02 m for all wavelengths.
The Zig-Zag tests indicated that the overshoot angles were slightly higher in following waves than in head waves. The turning circle tests indicated, for the three wavelengths tested, that the drifting distance was decreasing with increasing wavelength, and the drifting direction was typically at an angle relative to the wave propagation.
Yasukawa and Nakayama (2009) performed free running tests with a model of the S-175 ship. They tested four wavelengths, with constant wave height. The same trends as in Ueno et al. (2003) were observed.
During the SHOPERA project, a model of the Duisburg Test Case (DTC) was extensively tested (Sprenger et al., 2017). Turning circles and Zig-Zag tests in calm water

and regular waves, were included in the test program. Wavelengths $\lambda/L_{pp} = 0.494$ and $\lambda/L_{pp} = 0.855$ with wave steepness $H/\lambda = 0.011$ and $H/\lambda = 0.006$ respectively, were used for the maneuvering tests. Here λ refers to the wavelength, L_{pp} refers to the length between perpendiculars, and H refers to the wave height. They observed similar trends as previous maneuvering experiments. For the Zig-Zag tests, they compared results where the maneuvers were initiated at a wave crest with maneuvers where the maneuver was initiated at wave a trough. The results indicated that the phasing of the rudder execution had a negligible influence on the overshoot angles (Sprenger and Fathi, 2015).

In November 2018, we performed free running maneuvering tests with the same model of the DTC hull in the Ocean basin at SINTEF Ocean in Trondheim, Norway. Turning circles, Zig-Zag maneuvers, and course keeping were tested in calm water and regular waves. The tests were performed with a constant number of rotations per second (RPS) for the propeller, corresponding to Froude number 0.14 in calm water. Different rudder angles and headings were tested. Seven different wave periods, two different wave heights, and four different approach headings were included in the test program. These tests were phase 2 of the test program. Phase 1 was completed in August 2018. The objective of phase 1 was to document the waves in the Ocean basin. This means that the waves intended for phase 2 were documented. Wave probes were placed with 2 m spacing covering most of the basin. 14 regular waves and two irregular waves were documented this way. According to Araki et al. (2011), Lee et al. (2009), and Skejic (2008), the second order mean loads is the dominating contribution from regular waves in the maneuvering equations. Therefore, the ship trajectory will be sensitive to variations in the wave field. In order to quantify the uncertainty of model experiments, it is therefore favorable to document the waves in the entire testing area compared to document the waves in a few locations only.
Phase 3 is planned to take place during fall 2019. The focus in this phase will be standard maneuvers in irregular waves.

The following maneuvers were included in the test program: Course keeping, Zig-Zag 10/2, Zig-Zag 10/10, Zig-Zag 20/20, and turning circles with 25° and 35° rudder angle.
Repetition tests of selected maneuvers were performed with up to five repetitions. An uncertainty study based on the repetition tests will be presented in the present paper. Next, selected results from turning circles with 35° rudder angle and Zig-Zag 20/20 in regular waves will be presented.

2 EXPERIMENTAL TEST SET-UP

A 1:63.65 scale model of the Duisburg Test Case (DTC) was tested in the Ocean basin at SINTEF Ocean in Trondheim. Experienced staff from SINTEF Ocean was involved in preparing the model and the execution of the tests.

2.1 SHIP MODEL

The DTC hull is a 14000 TEU Container ship developed at the Institute of Ship Technology, Ocean Engineering and Transport Systems at the University of Duisburg-Essen. A model with scale 1:63.65 was made at SINTEF Ocean in conjunction with the SHOPERA project (Sprenger and Fathi, 2015). The same model was used for the present experiments. The model was equipped with a 5-bladed fixed pitch propeller, and a twisted rudder. Segmented bilge keels were mounted to the model, and a wire was mounted at the bow for turbulence stimulation.
The main particulars of the model can be found in Table 1. For detailed information of model, rudder and propeller see ship specification in el Moctar et al. (2012).

Table 1. Ship Particulars

Particulars		Ship	Model
L_{pp}	[m]	355	5,577
B	[m]	51	0,801
T	[m]	14,500	0,228
Δ	[kg]	173468000	672,6*
C_B	[-]	0,661	0,661
XCOG**	[m]	174,059	2,721*
YCOG	[m]	0,000	0,000*
KG	[m]	19,851	0,314*
GM	[m]	5,100	0,078*
I_{xx}	[kgm^2]	7,148E+10	68,400
I_{yy}	[kgm^2]	1,322E+12	1266,330*
I_{zz}	[kgm^2]	1,325E+12	1268,4
L_{bk}	[m]	14,85	0,23*

* Measured values.
** Relative to aft perpendicular.

6-dof motions of the model were measured with the optoelectronic measuring system OQUS. Five accelerometers measured the accelerations of the model for quality control of the motion measurements. Propeller thrust and torque were measured with a dynamometer. Rudder angle and propeller RPS were logged during the tests.
No external force was applied, to correct for the difference in boundary layer flow in model scale and full scale.

2.2 TEST FACILITY

The tests were carried out in the Ocean basin at SINTEF Ocean in Trondheim. The basin has a length, from wavemaker to the intersection between beach and water surface, of 80 m. The breadth of the basin is 50 m. The total depth of the basin is 10 m, with an adjustable floor. A water depth of 4.8 m was used for the tests.

2.3 DESCRIPTION OF SET-UP

The free running ship model was controlled by SINTEF Ocean's autopilot software. An umbilical was connected to the model from a manually driven gondola.
All tests were carried out with constant propeller RPS. However, to reduce the acceleration time, a "boost" was applied to the RPS until the test speed was achieved. The autopilot kept the model at the correct course until the maneuver was initiated.
Realistic rudder rate of $25\,\mathrm{deg/s}$ model scale was applied for all tests.

All maneuvers were initiated at a random time instant after a steady velocity was achieved. This means that it was not attempted to initiate the maneuvers at a wave crest or wave trough. Results from SHOPERA indicated that the phasing of the rudder execution had a negligible effect on global responses (Sprenger and Fathi, 2015). Moreover, it was considered that it would be challenging to initiate the maneuver at the exact time instant where a wave crest or wave trough passed the midship.

2.4 COORDINATE SYSTEMS

A right-handed coordinate system with the x-axis pointing towards the bow and z-axis pointing downwards is applied.
0° wave heading refers to head sea, 180° wave heading refers to following sea, and 90° wave heading refers to beam sea from starboard.

A positive rudder angle refers to a rudder execution towards port side.

2.5 MODEL TEST PROGRAM

A summary of the test program in phase 2 is presented in Table 2.

The maneuvers were tested with an RPS of the propeller of 11.5, which corresponds to Froude number 0.14 and a velocity of 16 knots in calm water, full scale.

The initial conditions of all maneuvers should be identical, with correct heading, zero yaw and yaw rate, zero rudder angle, and constant velocity. However, due to the wave climate and the space restrictions in the basin, the initial conditions can deviate slightly from the target values. This will be further discussed in section 3.1.

The maneuvers that were tested were: Course keeping tests, Zig-Zag 10/2, Zig-Zag 10/10, Zig-Zag 20/20, and turning circles with rudder angle $25°$ and $35°$.
These maneuvers were systematically tested for different wave headings and wavelengths. Reference tests in calm water were performed for all maneuvers.
All Zig-Zag maneuvers and turning circles in waves were initiated with rudder angle towards starboard. However, calm water turning circles were tested both towards starboard and port side.
Repetition tests were carried out for chosen maneuvers. The number of repetition tests is provided in Table 2. An uncertainty analysis based on the repetition tests is presented in section 3.1.

The course keeping tests were tested for four different wave headings, $\mu = 0°, 45°, 90°$ and $180°$.
Five wave periods with wavelength $\lambda/L_{pp} = 0.280$, 0.438, 0.630, 0.858, and 1.120, at wave steepness $H/\lambda = 1/40$ were tested.
These regular wave conditions were documented during phase 1, in July/August 2018.

The wave steepness (H/λ) referred to above, is the target wave steepness. The results from the wave documentation in phase 1 revealed that the actual wave steepness in general deviates from the target value, as expected. The wave amplitude varies slightly throughout the basin. Preliminary results indicate that, in a region of 20x24 m in the center of the basin, the deviation of the wave amplitude was below 5.5% relative to the wave amplitude in the center of the basin. Outside this region, the deviation was up to 10% relative to the wave amplitude in the center of the basin.
There will also be a deterioration of the wave climate over time. A regular wave will be steady for a limited time-window only, before reflection from the beach will influence the wave amplitude throughout the basin. To minimize the uncertainty from the wave climate, it was attempted to conduct the tests in the steadiest regions, both in time and space.
Due to space limitation, the wave documentation tests (phase 1) will not be reported in more detail. They will be described more thoroughly in future work related to the development of our theoretical maneuvering model.

All Zig-Zag maneuvers were tested for the same five waves as the course keeping tests, with approach wave headings $\mu = 0°$, 90°, and 180°.
The Zig-Zag 20/20 maneuver was tested for two additional wavelengths $\lambda/L_{pp} = 0.530$ and 0.740, one additional wave steepness $H/\lambda = 1/60$, and one additional wave heading $\mu = 45°$.

Turning circles with 25° rudder angle were tested in initial head waves with $H/\lambda = 1/40$, and $\lambda/L_{pp} =$ 0.280, 0.438, 0.630, 0.858, and 1.120.
Turning circles with 35° rudder angle were tested for the same five wave conditions, in head waves and following waves. In addition, the 35° turning circle was tested in head waves for one additional wavelength $\lambda/L_{pp} =$ 0.530.

Most tests were performed with wave steepness $H/\lambda = 1/40$. The choice of using constant steepness, lead to relatively high waves for the longest wavelengths. The wave height of the longest wave was 9.93 m in full scale. One could argue that this wave condition is out of range of operational limits relevant for maneuvering. However, for validation, it is necessary to identify limitation of model. Therefore, it can be valuable to have experimental results outside the typical range of operations.

Table 2. Summary of Test Program. All tests were performed with constant propeller RPS, corresponding to $Fn = 0.14$.

Maneuver	# Calm water runs	Wavelengths $[\lambda/L_{pp}]$	Approach wave headings	Wave steepness $[H/\lambda]$	# Repetition tests
Course keeping	2	0.280, 0.438, 0.630, 0.858 and 1.120	0°, 45°, 90° and 180°	1/40	1
Zig-Zag 10/2	2	0.280, 0.438, 0.630, 0.858 and 1.120	0°, 90° and 180°	1/40	4
Zig-Zag 10/10	5	0.280, 0.438, 0.630, 0.858 and 1.120	0°, 90° and 180°	1/40	12
Zig-Zag 20/20	4	0.280, 0.438, 0.530, 0.630, 0.740, 0.858 and 1.120	0°, 45°, 90° and 180°	1/40 and 1/60	28
Turning Circle 25°	5	0.280, 0.438, 0.630, 0.858 and 1.120	0°	1/40	7
Turning Circle 35°	3	0.280, 0.438, 0.530, 0.630, 0.858 and 1.120	0° and 180°	1/40	11

3 UNCERTAINTY ANALYSIS

ITTC lists three different approaches to quantify the uncertainty from free running model tests (ITTC, 2014):

- **Measurement uncertainty analysis**
- **Repeatability analysis**
- **Uncertainty propagation analysis**

Measurement uncertainty analysis estimates the uncertainty range of the measuring equipment.
Repeatability analysis reveals the stochastic uncertainty, which will be reduced by a high number of repetitions.
Uncertainty propagation analysis estimates how the uncertainty in the results is affected by uncertainties in input variables.

3.1 REPEATABILITY ANALYSIS

A repeatability analysis, following the recommendations in ITTC (2014) is presented next.

Results from the repeatability analysis of Zig-Zag 20/20 in head sea with wavelength $\lambda/L_{pp} = 0.438$ and wave steepness $H/\lambda = 1/40$, are summarized in Table 3. The table presents an uncertainty analysis for the first and second overshoot angles, and the time to reach these angles.

N is the number of repetitions, $\bar{q}$ is the mean of the measured quantity, s_q is the standard deviation of the quantity, $s_{\bar{q}}$ is the standard deviation of the mean $\bar{q}$, $t_{\frac{\alpha}{2}}(\nu)$ is the inverse student distribution, with $\nu = (N-1)$ degrees of freedom. An alpha value of 0.05 is

used in the analysis, which corresponds to a 95% confidence interval [$\bar{q}$-U, $\bar{q}$+U].
The uncertainty U is presented in percentage relative to the mean value $\bar{q}$.
The relative uncertainty for all quantities in Table 3 is below 4.2%. The highest uncertainty occurs for the second overshoot angle.

Table 3. Example result of uncertainty analysis, for one selected wave condition, based on repetition tests. Zig-Zag 20/20 maneuver in initial head waves, $\lambda/L_{pp} = 0.438$, $H/\lambda = 1/40$. Full scale values.

	1st Overshoot angle		2nd Overshoot angle	
	angle [deg]	t [s]	angle [deg]	t [s]
N	5	5	5	5
$\bar{q}$	9,8	103,7	11,3	278,7
s_q	0,3	1,4	0,4	2,3
$s_{\bar{q}}$	0,1	0,6	0,2	1
$U=t_{\frac{\alpha}{2}}s_{\bar{q}}$	0,4	1,7	0,5	2,9
$U/\bar{q}$	3,8%	1,6%	4,2%	1,0%

The described standard repeatability analysis was performed for Zig-Zag 20/20 in calm water and in regular waves with seven different waves and/or headings. Table 3 summarizes only the results for one wave condition. However, the rest of the wave conditions show a similar degree of repeatability. Based on this, the maneuvers repeat quite well in general, to our understanding. However, two exceptions were observed. For wavelength $\lambda/L_{pp} = 0.630$ in head waves, and wavelength $\lambda/L_{pp} = 0.438$ in following waves, both with wave steepness $H/\lambda = 1/40$, the relative uncertainty for the first overshoot angle was 12.0% and 7.2% respectively. For the rest of the responses for these two conditions, and all responses for the rest of the conditions, the relative uncertainty was below 5%.
The responses "Reach", "Initial length", and time to complete the maneuver, have a relative uncertainty below 4.1% for all conditions, and typically below 2%.
The first overshoot angle for Zig-Zag 20/20 is presented in Figure 1. 95% confidence intervals, based on the repetition tests, where available, are indicated with error bars in the figure. A significant higher uncertainty can be recognized for wavelength $\lambda/L_{pp} = 0.630$ with initial head sea. The variations with respect to wave heading and wave length were in general higher than the variability due to repetition uncertainty.

Possible sources of stochastic uncertainty in the maneuvering experiments are

- Uncertainty in the initial conditions
- Transients in motions and wave field
- Nonlinear phenomena

Due to space restrictions in the basin, some maneuvers were initiated before fully steady motions were obtained. Transients in the wave field could also be present, especially for turning circles where reflections from the beach could affect the wave field. However, it was attempted to execute the maneuvers in the most steady time-window. Furthermore, the repetition tests were initiated at approximately the same time instant relative to the wave field. Therefore, we believe that these effects mainly contribute to bias. Experimental bias is not investigated in detail in this paper. The contribution from initial conditions and nonlinear phenomena will be discussed next.

To quantify the contribution from the uncertainty in the initial conditions to the stochastic uncertainty, a thorough uncertainty propagation analysis would be needed. Without such analysis, the best we can do is to investigate the variation of the initial conditions, with the stochastic uncertainty in mind. Initial velocity, initial rudder angle, initial yaw, and initial yaw rate, are relevant quantities. These initial conditions, for Zig-Zag 20/20 maneuvers in initial head waves with wavelength $\lambda/L_{pp} = 0.438$, 0.630 and 0.858, are discussed briefly. Five repetition tests were available for these three conditions.

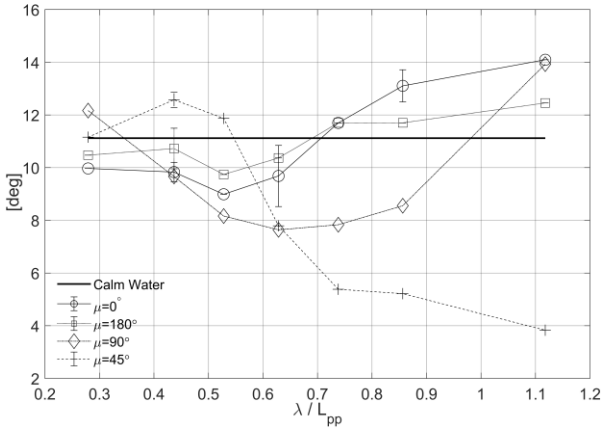

Figure 1. Overshoot angle 1 in Zig-Zag 20/20 tests with four approach headings, $H/\lambda = 1/40$. 95% confidence interval, based on five repetitions, indicated with error bars

The standard deviation of the initial velocity normalized by the average nominal velocity U_0, was $s_{U_0}/U_0 = 0.004$, 0.019, and 0.021 respectively, where the average nominal full scale velocity U_0 was 8.47 m/s, 8.21 m/s, and 7.82 m/s respectively. The average initial rudder angle was below 1° for the three wavelengths, with corresponding standard deviation 0.88°, 1.55°, and 1.09°. The average initial yaw rate deviate less than 0.006 deg/s from the target, while the standard deviation was 0.0041 deg/s, 0.0176 deg/s and 0.0145 deg/s respectively. Considering the initial yaw, for the same three wavelengths, the average initial yaw was below 0.12°. The standard deviation was 0.11°, 0.15° and 0.08°.

In summary, for Zig-Zag 20/20 in head waves, the standard deviation of the initial conditions was largest for $\lambda/L_{pp} = 0.630$. From Figure 1 we see that the stochastic uncertainty of the first overshoot angle is largest for the same wavelength, which is qualitatively consistent. We emphasize, an uncertainty propagation analysis would be needed to quantify the contribution of the stochastic variation due to initial conditions. However, other effects would probably also have a significant contribution to the stochastic uncertainty.

Increased motions, which caused strongly nonlinear phenomena, were observed for the longest waves. Pronounced heave, pitch, and roll motion lead to effects as slamming in bow and stern, propeller ventilation and rudder out of water. For wave steepness $H/\lambda = 1/40$, ventilation of the propeller was observed for wavelength $\lambda/L_{pp} = 0.630$ and above. Slamming and rudder out of water were observed for wavelength $\lambda/L_{pp} = 0.740$ and above. The behavior of these phenomena became more violent for increasing wavelength, and this could probably contribute to the stochastic uncertainty.

It is challenging to separate physical effects directly from free running tests. ITTC (2014) recommend using simulation tools to estimate uncertainty propagation coefficients. Faltinsen (2011) investigated the sensitivity of cross-flow drag coefficient *Cd*, thrust deduction factor *t*, wake factor *w*, and flow rectification factors γ_v and γ_r, with the modular maneuvering model of Skejic (2008) for a turning circle in calm water. The variation of the cross-flow drag coefficient had the largest influence. The yaw moment due to cross-flow drag will be sensitive to flow separation at the ship ends due to the long distance to the center of gravity. This may therefore be important for maneuvering in waves, in particular for wavelength close to heave and pitch resonance, where the wetted area of the bulb and stern will vary due to ship motions. This will lead to a variation of the yaw moment due to cross-flow drag.

Following a perturbation analysis based on potential flow theory assumption, the mean second order yaw moment due to regular waves is only dependent on the first order velocity potential for linear motions. However, when you have significant ship motions where the bulb and stern moves in and out of water, the mean forces and moments will be influenced by fully nonlinear effects.
The variation of forces and yaw moment from cross-flow drag and regular waves, due to ship motions, will probably not repeat perfectly. This is a possible contribution to the stochastic uncertainty.

We emphasize that the maneuvers were initiated at a random time instant relative to the incoming wave, such that possible uncertainties due to initiating the maneuver on wave crest or wave trough, is included in the repeatability analysis.

The presented repeatability analysis is sensitive to the number of repetitions N. The Zig-Zag 20/20 in calm water was repeated four times, while the chosen Zig-Zag 20/20 maneuvers in regular waves were repeated five times. For turning circles in initial head waves with wavelength $\lambda/L_{pp} = 0.438$ and 0.858, the number of repetitions were five and three respectively.
The tactical diameter, from regular wave tests is presented in Figure 2. Where repetition tests were available, 95% confidence intervals are indicated with error bars. The relative uncertainty for tactical diameter, advance, and transfer, was below 2.6% for the tested conditions. The presented tactical diameters were calculated from the first circle. In calm water, the turning circle test was repeated once to starboard. Two tests are not sufficient to apply the student-t approach.
The tactical diameter varies rapidly with λ/L_{pp} in the range 0.438 – 0.858. This is the same trend as for Zig-Zag 20/20 in Figure 1, where the first overshoot angle varies rapidly in the same range of wavelengths. This is related to significant heave and pitch motion.

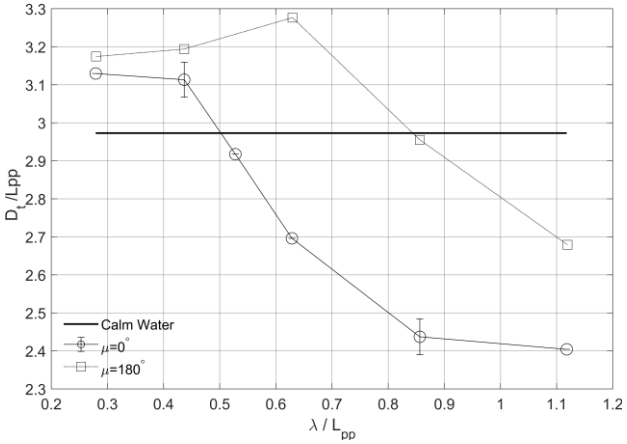

Figure 2. Tactical diameter of turning circles with 35° rudder angle toward starboard with two approach headings, $H/\lambda = 1/40$. 95% confidence interval indicated with error bars.

Trajectories and time series from four repetitions of 35° turning circles and Zig-Zag 20/20, both in head waves with wavelength $\lambda/L_{pp} = 0.438$ and wave steepness $H/\lambda = 1/40$, are presented in Figure 3. For the turning circle, the trajectories are presented only, while the heading and rudder angle are presented for the Zig/Zag maneuver.

The focus in the presented uncertainty analysis is on the stochastic uncertainty. Experimental bias is another source of uncertainty, which needs further investigation. For instance by means of theoretical and numerical investigations. However, the uncertainty propagation method proposed by ITTC (2014) should be applied with care for free running tests in regular waves, since the propagation is only as good as the numerical model applied. An alternative is to perform experiments where the initial conditions are slightly changed, and then study the effect on the outcome.

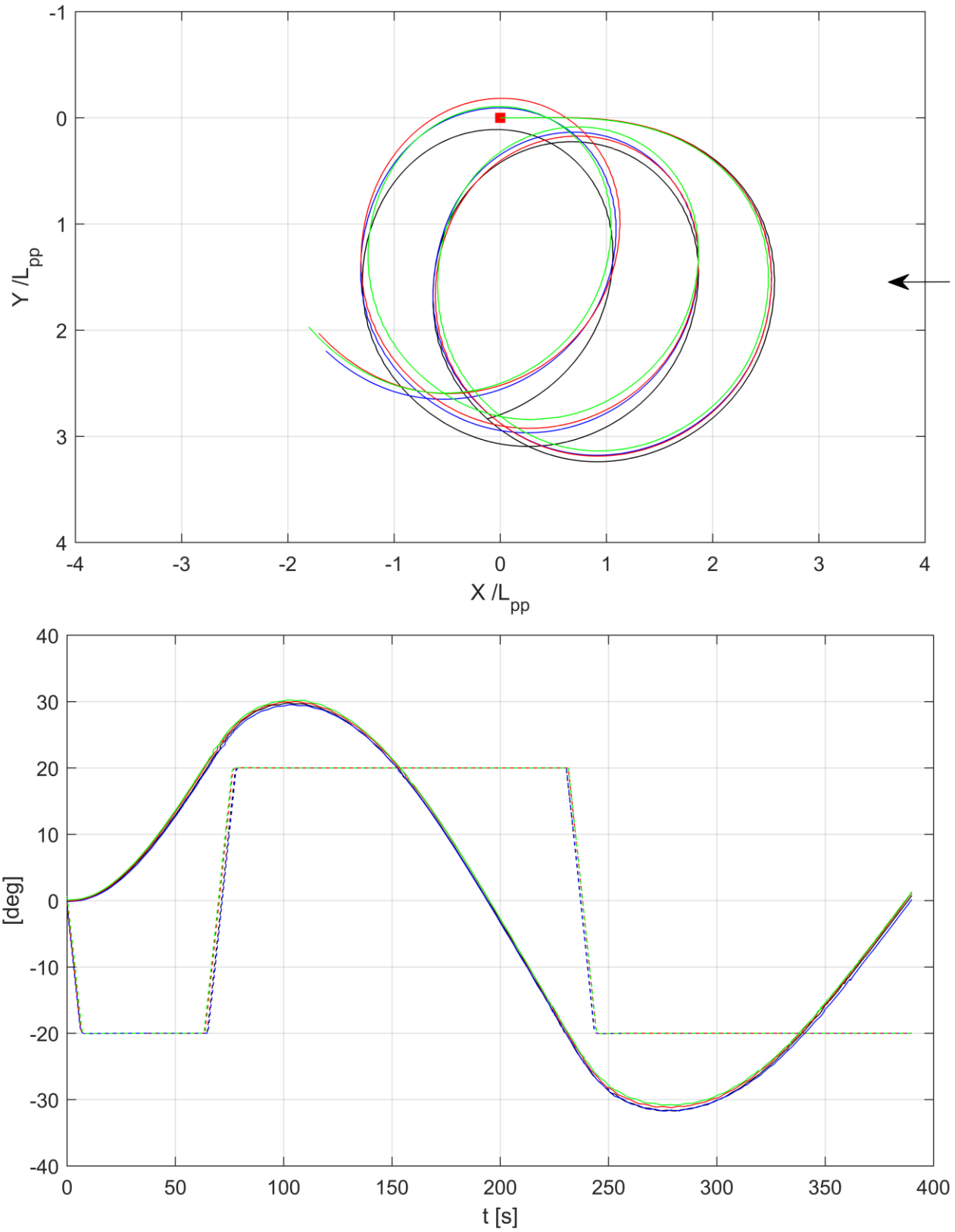

Figure 3. Top: Trajectories for 35° turning circles in head sea. Four repetitions. Bottom: Ship heading and rudder angle for Zig-Zag 20/20. Four repetitions. Both maneuvers were initiated in head waves with wavelength $\lambda/L_{pp} = 0.438$ and wave steepness $H/\lambda = 1/40$.

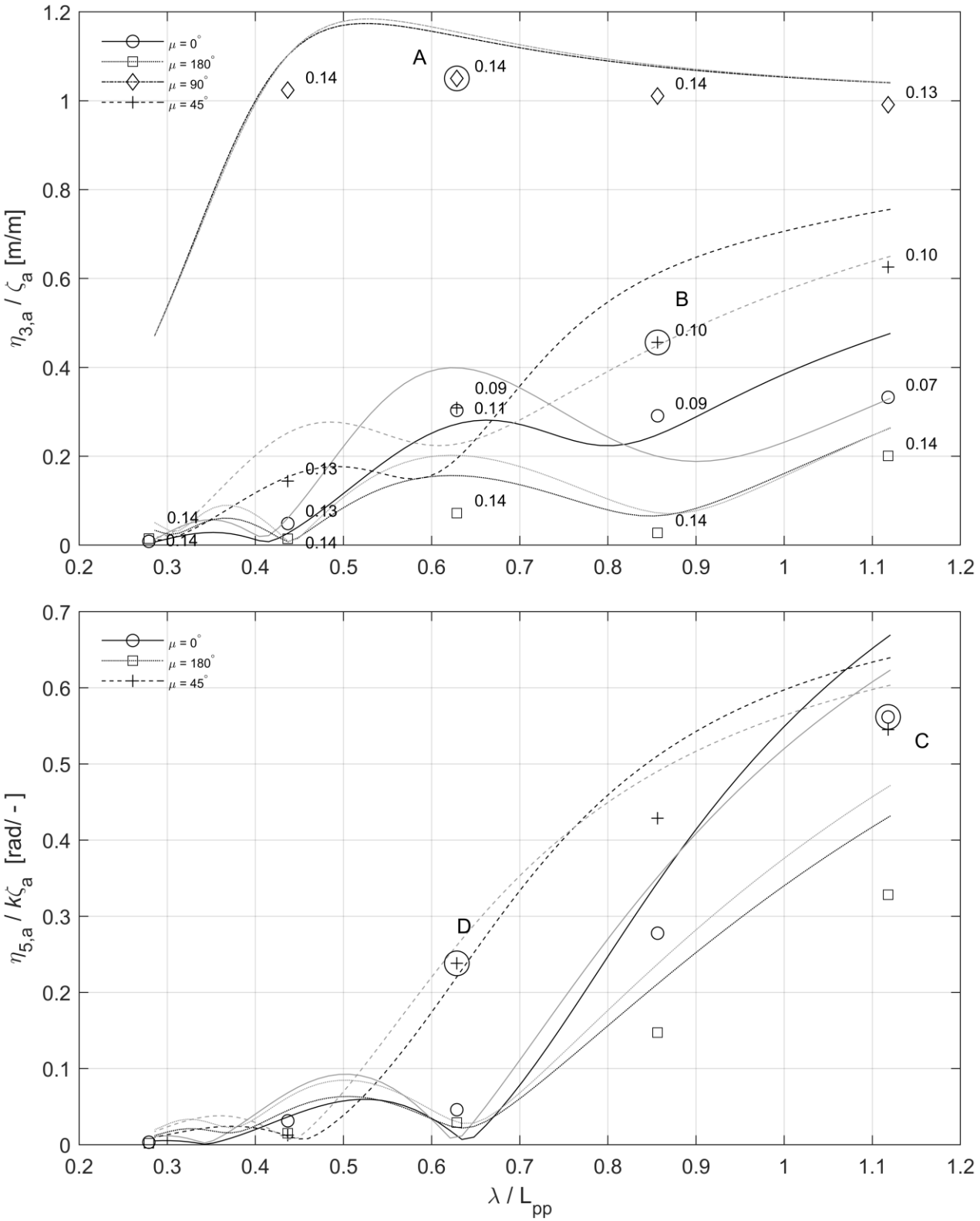

Figure 4. RAO in Heave and Pitch. Experimental RAOs are represented by markers, strip-theory calculations by Veres are presented with lines. Black lines for Froude number of 0.14, grey lines for Froude number of 0.07. Steady Froude number for experiments are given next to the markers. Letters indicate time series in Figure 5. $\eta_{3,a}$ and $\eta_{5,a}$ are the heave and pitch amplitude respectively. ζ_a is the incident wave amplitude and k is the wave number.

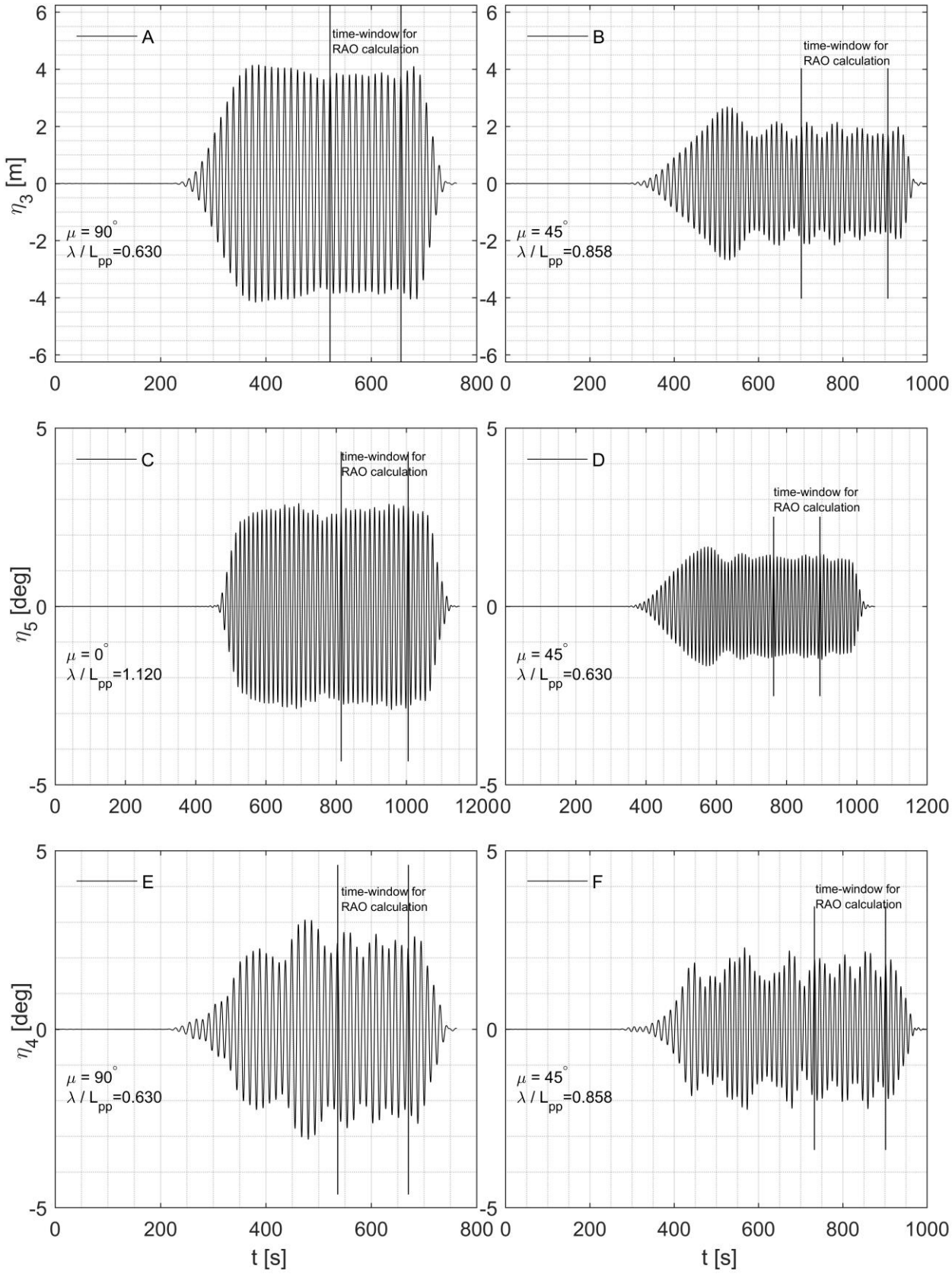

Figure 5. Band-pass filtered time series (full scale) used for RAO calculations. η_3, η_4, η_5 are motion in heave, roll, and pitch respectively. Legend A-D indicate which point in the RAO, for heave and pitch, the time series represent, as presented in Figure 4. E and F are time series of roll motion for direction μ = 90° and 45°, with wavelength $\lambda/L_{pp} = 0.630$ and 0.858 respectively.

4 SELECTED RESULTS

RAOs and time series from the course keeping tests are presented next. Then, results from turning circles with 35° rudder execution, will be presented.

4.1 RAOS AND TIME SERIES

Since the second order mean loads are sensitive to waves generated by the ship, and hence ship motions, RAOs are an important part of the discussion. Experimental and numerical calculated RAOs in heave and pitch, for the first harmonic motions, are presented in Figure 4. The numerical RAOs are represented with lines, while the experimental RAOs are represented with markers.

The experimental RAOs were constructed from the course keeping tests. The RAOs are taken as first harmonic of the body motion relative to the first harmonic of the incident wave. The incident wave amplitude is the mean wave amplitude in the basin, as measured during phase 1. The amplitudes of the first harmonics were obtained by applying a band-pass filter to the time series. The unfiltered time series were smoothed at the ends, to avoid end effects from the band-pass filter. The cut-off frequency was set 10% below and 10% above the encounter frequency. Then a steady region was manually chosen, from the filtered time series, to calculate the RAOs. Examples of band-pass filtered time series of the motions are provided in Figure 5.

The magnitude of the second harmonic is relatively small. For heave, the magnitude is negligible for the shortest wavelengths, while it increases from 0.9% to 4.4%, relative to the first harmonic, from wavelength $\lambda/L_{pp} = 0.630$ to $\lambda/L_{pp} = 1.120$. The magnitude of the second harmonic in pitch is below 2.1%, relative to the first harmonic, for all wavelengths.

The numerical RAOs in Figure 4 were calculated with Veres. Veres is a commercial software to calculate vessel motions and global loads, based on linear potential flow theory and the classical STF strip-theory (Salvesen et al., 1970). The STF theory neglects the steady part of the disturbance potential, and assume that the wavelength λ is approximately in the same order as the ship beam. This is the same strip-theory which is implemented in the two-time scale modular maneuvering model developed by Skejic (2008), for simulation of maneuvering in regular waves.
It is important to emphasize that the numerical RAOs were calculated with constant forward speed, corresponding to $Fn = 0.07$ and 0.14, while the experimental results were tested with constant RPS. The graphs should be interpreted with this in mind. The actual near steady Froude number is indicated by numbers next to the experimental markers. The agreement between experimental and numerical RAO is in general reasonable.

Heave resonance can be recognized close to wavelength $\lambda/L_{pp} = 0.630$. The numerical results indicate pitch resonance for head and following waves close to wavelength $\lambda/L_{pp} = 0.5$.

The speed loss in waves can be significant for the tested wave conditions. The speed loss was negligible for the shortest waves, but increase with wavelength. The most extreme case was for wavelength $\lambda/L_{pp} = 1.120$ in head waves, where the mean steady velocity was 8.1 knots, full scale. This corresponds to $Fn = 0.07$, compared to $Fn = 0.14$ in calm water. For following waves, the change of speed due to waves was relatively small. In fact, for some wavelengths, there was an increase in forward speed due to following waves.

In Figure 5, representative time series are presented. The RAOs were constructed from the near steady part of the time series. However, because of space restrictions in the basin, some maneuvers were initiated before this fully "steady" region. This is relevant for roll in particular, since the roll damping is relatively low compared to heave and pitch. This is a possible error source for the experiments, and needs further investigation.

4.2 TURNING CIRCLE WITH 35° RUDDER ANGLE

We last present selected results from turning circles with 35° rudder angle. All turning circles in waves were performed toward starboard. Reference tests in calm water were performed both towards starboard and port side. This revealed a significant asymmetry in the turning behavior. The tactical diameter was 17.6% shorter and the advance was 8.8% shorter in the turning circle towards port side compared to starboard. This is illustrated in the trajectory in Figure 6.
One repetition is included for the turning circle toward starboard.

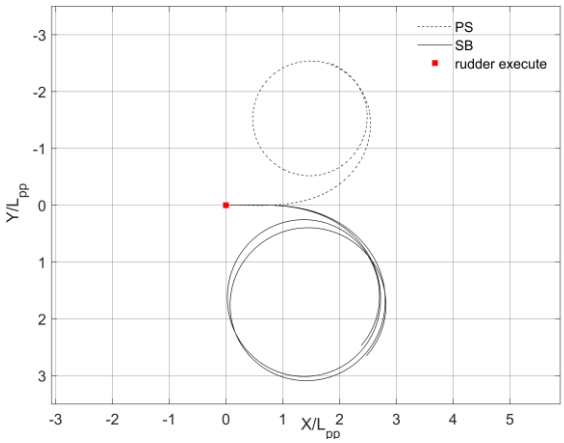

Figure 6. Trajectory of calm water turning circles. One repetition was performed for the turning circle toward starboard.

The propulsion set-up with a right-hand single screw propeller and a twisted rudder, are two possible candidates for this asymmetry. It is well known that a right-hand single screw propeller will induce a lateral propeller force toward starboard, at least at very low Froude numbers. A twisted rudder can have asymmetric lifting characteristics. This was investigated numerically and experimentally by Collazo and Fernández (2010) and Shin et al. (2018).
When the same model was tested during the SHOPERA project, a similar asymmetry was observed (Sprenger and Fathi, 2015).

The characteristic oblique drifting pattern of the trajectory of turning circles in regular waves is illustrated in Figure 7. In head waves, the drift angle was towards the point of rudder execute, while in following waves the drift angle was in the opposite direction. This is consistent with other experiments (Sprenger et al. (2017); Ueno et al. (2003); Yasukawa and Nakayama (2009)).

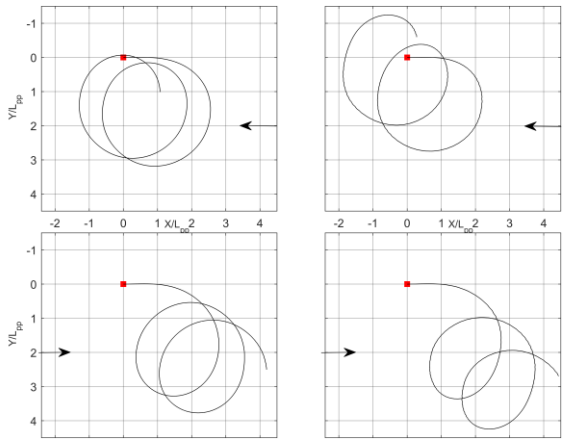

Figure 7. Trajectory of turning circles in regular waves with two different wavelengths. Left column $\lambda/L_{pp} = 0.438$. Right column $\lambda/L_{pp} = 0.630$. $H/\lambda = 1/40$. Wave direction is indicated with an arrow. The point of rudder execute is indicated with a red square.

5 CONCLUSION

Free running maneuvering experiments with the DTC hull were performed in the ocean basin at SINTEF Ocean. Course keeping tests, turning circles with 25° and 35° rudder angle, Zig-Zag 10/2, Zig-Zag 10/10 and Zig-Zag 20/20 were included in the test program. Regular waves with wavelengths in the range $\lambda/L_{pp} = 0.280 - 1.120$ were tested with different approach wave headings. High quality experimental results for validation of numerical maneuvering models was the objective of the test program. The focus in the present paper is on the results from course keeping tests, Zig-Zag 20/20, and turning circles with 35° rudder angle.

Repetition tests were given a high priority in the test program. For Zig-Zag maneuvers, the stochastic uncertainty of the first and second overshoot angle was investigated. For turning circles, the uncertainty analysis was performed for the tactical diameter. The uncertainty analysis revealed that the scatter in the global responses was low in general. For the majority of the tests, the relative uncertainty for all the investigated responses was below 5%. The highest stochastic uncertainty was found for Zig-Zag 20/20 in head waves with wavelength $\lambda/L_{pp} = 0.630$, close to heave resonance. The relative stochastic uncertainty for this condition was 12%. The initial velocity, initial rudder angle, initial yaw, and initial yaw rate were investigated for Zig-Zag 20/20 in head waves. The average initial velocity, rudder angle, yaw and yaw rate, deviated less than 2 %, 1°, 0.12° and 0.006 deg/s from the target respectively. The largest standard deviation of initial rudder angle, initial yaw and yaw rate were found for wavelength $\lambda/L_{pp} = 0.630$, which also has the highest stochastic uncertainty. The standard deviations for this wavelength were 1.55°, 0.15° and 0.0176 deg/s respectively.
We conclude that the variability of the initial conditions contributes to the stochastic uncertainty, but other effects would probably have a significant contribution.
Nonlinear phenomena as slamming and propeller ventilation are possible candidates.

We conclude that, in general, global responses for turning circles and Zig-Zag repeated well in regular waves. The variation with respect to wave heading and wavelength was significantly higher than the stochastic variability. Due to space restrictions in the basin, the ship motions did not fully reach steady-state at the initiation of the maneuver in some conditions. This is a possible source of bias. Only the stochastic uncertainty was investigated in the present paper.

6 REFERENCES

Araki, M., Umeda, N., Hashimoto, H., Matsuda, A., 2011. An improvement of broaching prediction with a nonlinear 6 degrees of freedom model. Journal of the Japan Society of Naval Architects and Ocean Engineers 14, 85-96. https://doi.org/10.2534/jjasnaoe.14.85.

Collazo, A.C., Fernández, A.S., 2010. Flow adapted rudder geometry for energy efficiency improvement on fishing vessels, Proceedings of the First International Symposium on Fishing Vessel Energy Efficiency. E-Fishing, Vigo, Spain.

el Moctar, O., Shigunov, V., Zorn, T., 2012. Duisburg Test Case: Post-Panamax Container Ship for Benchmarking. Ship Technology Research 59 (3), 50-64. https://doi.org/10.1179/str.2012.59.3.004.

Faltinsen, O.M., 2011. Modelling of manoeuvring with attention to ship-ship interaction and wind waves, 2nd International Conference on Ship Manoeuvring in Shallow and Confined Water: Ship to Ship Interaction, pp. 1-11.

ITTC, 2011. The Manoeuvring Commitee - Final report and reccommendations to the 26th ITTC, ITTC, Rio de Janeiro.

ITTC, 2014. Uncertainty Analysis for Free Running Model Tests. ITTC, ITTC - Recommended Procedures and Guidelines.

Lee, S.-K., Hwang, S.-H., Yun, S.-W., Rhee, K.-P., Seong, W.-J., 2009. An experimental study of a ship manoeuvrability in regular waves, International Conference on Marine Simulation and Ship Maneuverability, Panama, pp. 17-23.

Salvesen, N., Tuck, E.O., Faltinsen, O.M., 1970. Ship motions and sea loads. Trans. SNAME 78 (8), 250-287.

Shin, Y.J., Kim, M.C., Lee, J.-H., Song, M.S., 2018. A numerical and experimental study on the performance of a twisted rudder with wavy configuration. International Journal of Naval Architecture and Ocean Engineering https://doi.org/10.1016/j.ijnaoe.2018.02.014.

Skejic, R., 2008. Maneuvering and Seakeeping of a Single Ship and of Two Ships in Interaction, Department of Marine Technology. Faculty of Engineering and technology, NTNU.

Sprenger, F., Fathi, D., 2015. D3.3 Report on Model Tests at MARINTEK, SHOPERA.

Sprenger, F., Maron, A., Delefortrie, G., van Zwijnsvoorde, T., Cura-Hochbaum, A., Lengwinat, A., Papanikolaou, A., 2017. Experimental Studies on Seakeeping and Maneuverability of Ships in Adverse Weather Conditions. Journal of Ship Research 61 (3), 131-152. https://doi.org/10.5957/JOSR.170002.

Ueno, M., Nimura, T., Miyazaki, H., 2003. Experimental study on manoeuvring motion of a ship in waves, International Conference on Marine Simulation and Ship Maneuverability, MARSIM'03, Kanazawa.

Yasukawa, H., Nakayama, Y., 2009. 6-DOF motion simulations of a turning ship in regular waves, Proceedings of the International Conference on Marine Simulation and Ship Manoeuvrability.

7 AUTHORS BIOGRAPHY

Øyvind Rabliås is a phd candidate at the department of Marine Technology at the Norwegian University of Science and Technology. He develops a rational simulation model for maneuvering in waves.

Trygve Kristiansen hold the current position of Professor at the department of Marine Technology at the Norwegian University of Science and Technology.

SHALLOW-WATER EFFECTS IN SHIP MODEL TESTING AND AT FULL SCALE

Hoyte C. Raven,
Maritime Research Institute Netherlands (MARIN), Netherlands

SHALLOW-WATER EFFECTS IN SHIP MODEL TESTING AND AT FULL SCALE

Hoyte C. Raven, Maritime Research Institute Netherlands (MARIN), Netherlands

SUMMARY

This paper addresses shallow-water ship model testing, and the determination of water depth effects on ship resistance. It is shown how effects of water depth, towing tank width, and the scaling of viscous resistance interact, and are of large importance for ship performance prediction. A new method to correct model tests for tank width effects is briefly described. For a set of shallow-water model-test data, it is shown how tank width effects apparently double the water depth influence. Also the model-to-ship extrapolation strongly affects the predicted water depth effect for the ship, easily leading to an overestimation. The procedure to be used, with a depth-dependent form factor, is proposed. A new procedure to correct ship speed trials for water-depth effects is introduced, and validations are shown with full-scale trial data, with the same set of model-test data and with the full-scale predictions based on these.

NOMENCLATURE

A_M	midship sectional area of ship (m^2)
b	width of model basin or channel (m)
C_T	total resistance coefficient
C_W	wave resistance coefficient
C_V	viscous resistance coefficient
C_{F0}	flat-plate friction coefficient
Fr_h	depth Froude number
h	water depth (m)
Re	Reynolds number
R_T	ship total resistance (N)
T	ship draft (m)
u	longitudinal flow velocity (m/s)
V_M	model speed (m/s)
z_s	dynamic sinkage (m)
$1+k$	form factor
β	blockage, A_M/bh
γ	overspeed ratio
Δ	ship displacement (m^3)
$\Delta\gamma$	additional overspeed ratio in channel
η_D	propulsive efficiency
ν	Kinematic viscosity (m^2/s)
ρ	Density of water (kg/m^3)

1 INTRODUCTION

Shallow water normally increases a ship's resistance, required power, and squat. For estimating the performance of a ship in shallow water, model tests are frequently done. But also, available empirical estimation methods for shallow water effects are largely based on model-test data. Examples of such methods are Schlichting (1934), Lackenby (1963), Jiang (2001).

However, shallow-water model tests are affected by the limited width of the model basin; far more than deep-water model tests. In the present paper it is demonstrated to what extent the model basin width can affect the apparent water depth influence, and how it can easily lead to wrong conclusions. A new approximate method to correct model test data for this tank width effect was recently published (Raven, 2018) and is outlined and demonstrated below.

It is pointed out that it is essential to distinguish 3 different physical effects, often occurring simultaneously:

1. Effect of limited depth on viscous resistance;
2. Effect of limited depth on wave resistance and squat
3. Effect of limited width on resistance and squat.

As, for a given model basin width, effect 3 increases with decreasing water depth, ignoring it yields wrong results for 1 and 2.

Separate computational studies have been done on effects 1 and 2 (Raven, 2012, 2016). These respond to different water depth parameters, therefore it is important to deal with them separately. For model and ship there is a different relative importance of viscous and wave resistance, and thereby also a different dependence of the total resistance on water depth. It is shown that the model-to-ship extrapolation method used has a large influence on the assumed water depth effect for the ship at full scale; which is another aspect apparently neglected so far. A naïve application of usual methods yields a much stronger shallow-water effect on resistance for the ship than for the model.

The paper is set up as follows. In Section 2 the effect of model basin or channel width is discussed, and the correction method is described. In Section 3 it is applied to model-test data for a ferry in shallow water, demonstrating the large effect on the apparent water depth influence. Section 4 addresses the model-to-ship extrapolation of the measured data. A computational study on the scaling of the viscous resistance and its shallow-water effect is discussed in Section 5, and the required model-to-ship extrapolation approach is indicated.

In Section 6, the related development of a correction procedure for small shallow-water effects in ship speed trials is considered, and some validations with full-scale and model-scale data are shown.

Thus, the paper summarises, synthesises and illustrates some of the research on shallow-water hydrodynamics done in recent years at MARIN.

2 FINITE-WIDTH EFFECTS ON SHIP RESISTANCE AND FLOW

2.1 GENERAL

In ship model testing, usually the measurements should lead to a prediction for infinite waterway width. The finite width of the model basin then is a disturbing factor, in particular in shallow water. The magnitude of this disturbance is considered.

A ship model in a towing tank of width b and depth h is considered. The flow is described in a coordinate system moving with the model, so there is an incoming flow with velocity V_M from ahead. The flow speed next to the model must be larger than V_M to let all water pass. The larger the blockage β (ratio of model cross section to tank cross section), the larger this overspeed (also called return flow). But the increased flow speed causes a drop of the water level next to the model, which also results in an increased dynamic sinkage of the ship. Both lead to a further reduction of the tank cross section and a resulting further increase of the flow speed. Kreitner (1934) proposed a simple estimation for these effects, by assuming that the flow speed is uniformly distributed over the channel cross section; which is a good approximation for a ship with a long parallel midbody in a narrow channel. Consistently, he assumed the sinkage of the ship to be equal to the drop of the water level, which in turn follows from the Bernoulli equation. The resulting expression for the overspeed ratio $\gamma = \mathrm{u} / V_M$, with u the longitudinal component of the flow velocity next to the ship, is:

$$\gamma\left[1-\beta+\frac{1}{2}Fr_h^2(1-\gamma^2)\right]=1 \qquad (1)$$

where the depth Froude number $Fr_h = \sqrt{V/gh}$. In practical applications, for ships with a not so long parallel midbody, the overspeed is not uniformly distributed; but Kreitner's formula still provides a useful estimate of the mean overspeed over the channel section at the midship position.

However, this is not what is needed for estimating finite-width effects. The objective is to compare the overspeed in a model basin of restricted width, and that in infinitely-wide water of equal depth. But for the latter, there is zero blockage and Kreitner's formula yields zero overspeed, just as for an infinite-depth case. Essentially, Kreitner yields the difference with a case of infinite width and infinite depth, not equal depth. The use of a 'virtual tank width' has sometimes been proposed in order to get an overspeed value for infinite width; but as that virtual width should depend on blockage and depth Froude number again, this is an unpromising approach. Useful other methods to deal with just the finite-width effect (tank wall effect) seemed not to be available.

2.2 A CORRECTION METHOD FOR TANK WALL EFFECTS

In (Raven, 2018) a new method to correct resistance and squat measurements for the effect of the finite tank width has been proposed. The first step is to estimate the difference in overspeed along the hull, between the situations of finite and infinite width, at equal water depth. To study this, flow computations have been made for ships in various water depths and channel widths.

The free-surface potential-flow code RAPID (Raven, 1996) has been used for this. It computes the inviscid flow along a ship hull, in restricted or unrestricted water, using a panel method. Source panels are distributed over the ship hull surface and a surrounding part of the water surface. An iterative solution is required as the free-surface boundary conditions are nonlinear and the dynamic trim and sinkage need to be incorporated. This method is in continuous use for ship design, at MARIN and elsewhere, since 1994. Some of the required adjustments for application to ships in narrow channels are described in (Raven, 2018).

Fig. 1 shows the computed distribution of the longitudinal flow velocity at the water surface next to the midship section of a given model. The ship hull is at the left of the figure, y = 0 is the centreplane and the lines start at the ship's waterline. The lower line is for deep water of infinite width. There is just a little overspeed next to the model, plus a disturbance where a diverging bow wave passes, also seen in all other lines. The line just above it is for shallow water (h/T = 1.54) of infinite width. The overspeed is a lot larger here, and extends to much larger distances as a result of the more two-dimensional situation. The other 3 lines are for the same ship at the same speed, in the same water depth but in channels of different widths. The channel walls further increase the overspeed; and the *mean* overspeed is fairly well indicated by Kreitner's formula. However, the pure tank wall effect is just the difference between the overspeed in a shallow channel, and that in shallow water of infinite width; and that is a much smaller quantity. E.g. for the channel with b/L = 1.31, Kreitner predicts 11.3% overspeed, but the actual channel wall contribution is just some 5%.

Remarkably this additional overspeed caused by the tank walls, is quite constantly distributed over the channel section: the line for shallow water seems just shifted upward by a small amount. As discussed in (Raven, 2018) this can be understood from the similar streamline curvature in the different cases. The new estimation method now is built on this assumption of a uniformly distributed additional overspeed. Note that this is a different assumption than Kreitner's, who assumed the entire overspeed to be constant over the channel cross section; which clearly is not the case here.

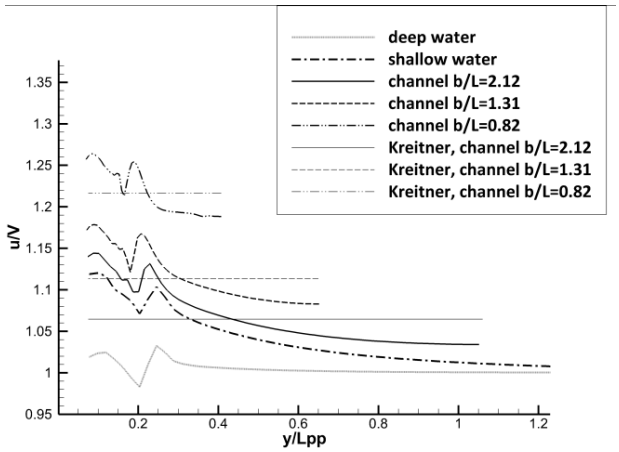

Figure 1. Crosswise distribution of overspeed next to the midship section, at the water surface; in deep water, in shallow water (*h/T*=1.54, Fr_h=0.559), and in channels of same depth and various widths. Series 60 C_B =0.60 ship at *Fr* = 0.160. y=0 at ship's centreplane.

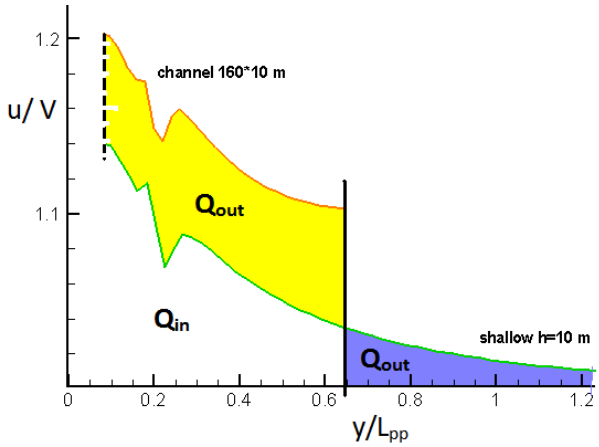

Figure 2. Schematic representation of volume fluxes

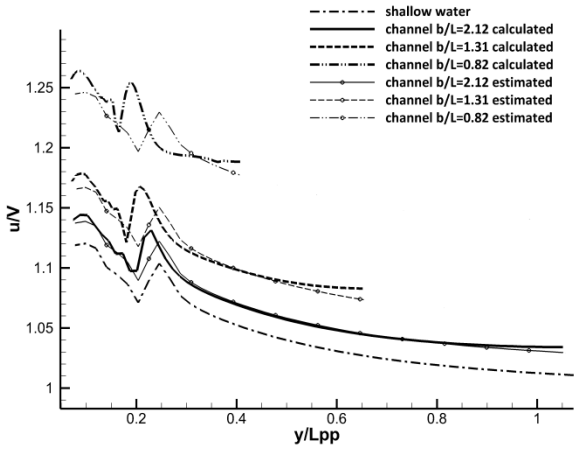

Figure 3. Overspeed distribution, as in Fig. 1; as computed, and as estimated from eq. (2).

As derived in (Raven, 2018), the additional overspeed as a fraction of ship speed, $\Delta\gamma = (u_{channel} - u_{shallow})/V$, can be solved from the following equation:

$$\Delta\gamma\left(1-\beta+\frac{1}{2}Fr_h^2(1-3\bar{\gamma}^2-3\bar{\gamma}\Delta\gamma-\Delta\gamma^2)\right)=\frac{Q_{out}}{VA_C} \quad (2)$$

in which $\bar{\gamma}$ is the overspeed ratio in shallow water of infinite width, averaged over the width of the channel. The equation is clearly similar to Kreitner's, but provides the *additional* overspeed, the upward shift of the lines for the channels in Fig. 1. Like Kreitner's formula, it predicts a quick increase of the additional overspeed when the speed approaches the critical channel speed.

The term at the right hand side is explained in Fig. 2, a sketch with the same setup as Fig. 1. If a comparison is made between the overspeed for the ship in a shallow channel and in shallow water of infinite width, in the latter case there is still an overspeed occurring outside the location of the channel wall (indicated by the blue area). This overspeed carries an 'excess volume flux' Q_{out}. But in the channel case, that excess flux has to be accommodated inside the channel walls. It is this additional volume flux Q_{out} that determines the increase of the overspeed due to the channel walls, as indicated by the yellow area. (While the flux is equal, the areas in this graph are not since due to the additional drop of the water level, the overspeed increase is relatively large.)

To actually calculate the overspeed increase for a given ship in a shallow channel, it is necessary to make a single free-surface potential flow computation for the same case in water of unlimited width and equal depth. From this, the nondimensional flux $Q_{out}/V\,A_C$, the mean overspeed ratio over a part of the water surface $\bar{\gamma}$, and the mean overspeed ratio along the ship's waterline in shallow water of infinite width, $\gamma_{WL} = u_{WL}/V$, are deduced. It is noted that the integration for Q_{out} would need to be extended to 'infinity', but a way to evaluate it from the finite-domain potential-flow computation is described in Raven (2018). To good approximation these quantities can subsequently be used for a range of speeds and channel widths. After substitution in eq. (2), the overspeed increase is obtained immediately. An increase of the dynamic sinkage z_s caused by the tank walls is also obtained, as:

$$(z_s)_{channel} - (z_s)_{shallow} = \frac{1}{2}Fr_h^2 h(2\gamma_{WL}\Delta\gamma + \Delta\gamma^2) \quad (3)$$

As shown in the reference, this method provides a good estimation of the overspeed increase $\Delta\gamma$ caused by the limited channel width. For the same case as in Fig. 1, Fig. 3 illustrates this. The 'estimated' lines are found by adding $\Delta\gamma$ from eq. (2) to the computed overspeed distribution in shallow water of unlimited width. The agreement with the lines directly computed is quite good.

Now that the overspeed increase can be estimated, an assumption is still needed to estimate its effect on the ship's resistance'. One can resort to a simplification made in most earlier 'blockage correctors', that the effect on resistance corresponds with that of a model speed increase, equal to the relative increase of the flow speed along the hull caused by the additional overspeed:

$$V_{M\,shallow} = V_{M\,tank}(1 + \Delta\gamma / \gamma_{WL})$$
$$R_{T\,shallow}(V_{M\,shallow}) = R_{T\,tank}(V_{M\,tank}) \quad (4)$$

This amounts to a shift of the points of the resistance curve measured in the towing tank, to a slightly higher speed. This correction is made prior to the further processing of the model test data. Besides, the measured dynamic sinkage values are corrected using eq. (3).

While the procedure may seem complicated, in practice it is straightforward. From the result of the potential flow computation, a postprocessor evaluates the required coefficients and solves eq. (2) for all input model speeds. The corrected model speeds and sinkage corrections are output immediately. The method is used for all shallow-water resistance tests at MARIN since several years.

Validations (Raven, 2018) have shown that the additional overspeed is estimated quite well. The resulting estimate of the effect on resistance appears to be valid as long as the correction is not too large, e.g. a speed correction up to 5%. Therefore, use of the method is limited to cases not too close to critical channel speed. The sinkage correction was found to be accurate for not too large corrections, but tends to overestimate for stronger effects.

In passing, an alternative use of the correction can be mentioned, for predicting the speed loss of a ship in channels of various widths, from the known speed in shallow water of infinite width.

3 EFFECT OF WATER DEPTH ON RESISTANCE OF A FERRY MODEL

As an illustration, a set of older model test data for a ferry of 150 m length, 28 m beam and 6 m draft is considered. Model scale was 20.5. The basin width was 2.16 times the model length, almost 12 times the model beam. Five water depths were tested, from 13.1 to 22.5 m.

The dashed lines in Fig.4 are the measured model resistance curves for 3 water depths. With decreasing water depth the resistance increases significantly, and the steep part of the curve shifts to lower speeds. For the smallest water depth, the critical shallow-water speed, Fr_h = 1, corresponds with 22 kn, beyond the range of the measurements; but the blockage β = 0.0386, so the highest speed of 17 kn (ship scale) is near critical channel speed. So, serious effects of the towing tank width are present.

If this tank width correction is applied, one gets the corresponding curves shown as solid lines. The smaller the water depth and the higher the speed, the larger is the correction. Towards the higher speeds, the lines become significantly less steep, and the difference between the curves for different water depths is reduced. For the highest speeds in the two smaller water depths though, one cannot precisely trust the correction as it is larger than what the simple assumptions permit.

To determine the effect of water *depth* on model resistance, an intersection is made of the lines in Fig.4 at constant speeds of 15 and 16.5 kn, thus obtaining Fig.5. There is a large difference of the apparent water depth effect between the uncorrected and corrected model measurements. The uncorrected data suggest a depth influence on resistance twice as large as the corrected data. Much of this actually is a towing tank width effect; one is largely looking at the wrong physics.

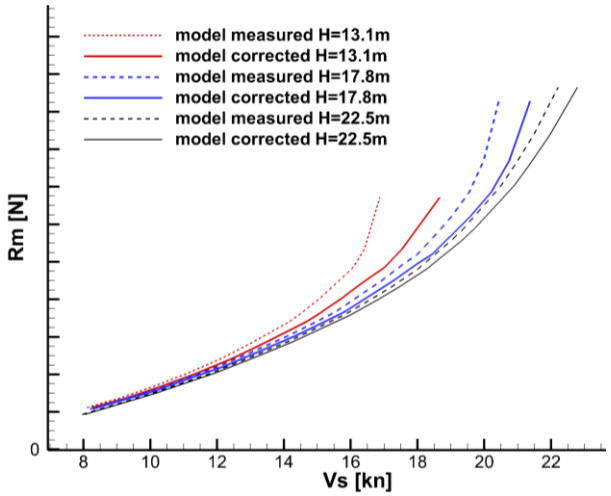

Figure 4. Model resistance in various water depths. Dashed lines: measured; solid lines: corrected for tank width effect.

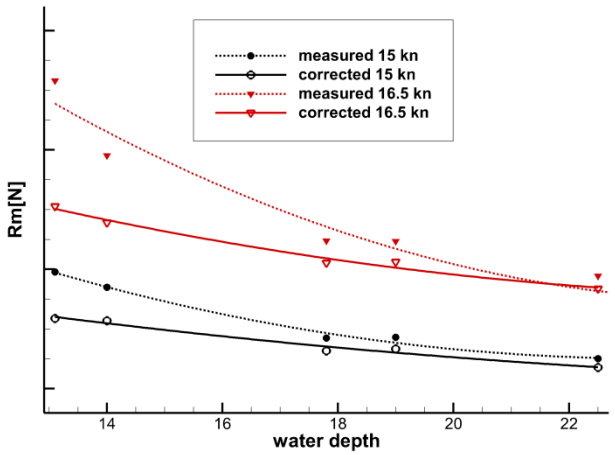

Figure 5. Effect of water depth on model resistance, for ship speed 15 and 16.5 kn; without and with tank width correction.

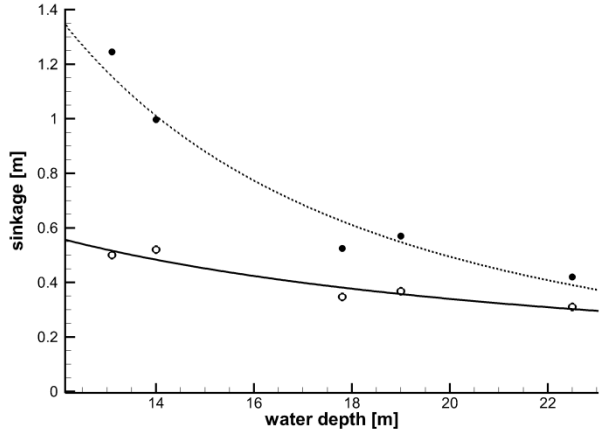

Figure 6. Effect of water depth on measured model dynamic sinkage, for ship speed 16.5 kn. without and with tank width correction.

Fig.6 shows the increase of the dynamic sinkage (squat) for decreasing water depth, at 16.5 kn speed. Here the tank width correction is even more important, and is still significant for the largest water depth. This sinkage correction is not always as accurate, but at least can be considered as indicative.

It can be concluded that in model testing in shallow water, it is essential to apply a correction for the finite width of the model basin; otherwise misleading results may be obtained, with a far too strong apparent water depth effect. It seems likely that similar errors have affected data underlying empirical estimation methods for the water depth effect, both for resistance and for squat, unless tank width or blockage has been taken into account explicitly. The different tank widths used possibly explain the large mutual discrepancy of empirical squat formulas.

4 SCALING OF SHALLOW-WATER MODEL TEST DATA

4.1 MODEL-TO-SHIP EXTRAPOLATION

So far, model-test results corrected for the effect of the finite width of the model basin have been derived. To predict the resistance of the ship at full scale from these, one can apply 'model-to-ship extrapolation' techniques, see e.g. (Larsson & Raven, 2010, Ch. 8). Model resistance tests are done at equal length Froude number as the ship, and according to Froude's hypothesis, a part of the resistance, essentially associated with wave making, can then be directly scaled up by multiplication with model scale to the third power. The other part, related with the viscous flow, depends on the Reynolds number *Re* which differs much between model and ship. Therefore this part needs to be scaled up differently. The simplification is:

$$C_T(Fr,Re) = C_W(Fr) + C_V(\mathrm{Re}) \qquad (5)$$

such that

$$C_{Ts}(Fr,Re_s) = C_{Tm}(Fr,Re_m) - C_V(\mathrm{Re}_m) + C_V(\mathrm{Re}_s) \qquad (6)$$

Here the resistance coefficients are defined as $C_T = R_T / (\frac{1}{2}\rho V^2 S)$ where S is the wetted surface.

Different assumptions can be made for this difference of the viscous resistance coefficients at ship and model Reynolds number.

- In the classical Froude extrapolation method, the viscous resistance coefficient is simply taken equal to the frictional resistance coefficient of a flat plate at equal Reynolds number, $C_{F0}(Re)$. The remaining part, consisting of wave resistance and some viscous components, is called 'residuary resistance'. Instead of flat-plate friction coefficients, often a somewhat adjusted expression is used, the so-called ITTC `57 model-ship correlation line.
- Alternatively, the viscous resistance coefficient of the ship, as a function of the Reynolds number, is supposed to be *proportional* to the flat-plate friction coefficient (or ITTC `57 coefficient):

  $$C_V(Re) = (1+k)C_{F0}(Re)$$

  The proportionality constant $(1+k)$ is called the form factor. It depends on the hull form, increasing with the fullness of the hull; normal values lying between 1.1 and 1.4. Its value can either be found from low-speed resistance tests, or from empirical relations, expressed in geometric properties of the hull form.

While in essence these methods lead to different full-scale resistance predictions, much of the difference is compensated by empirical 'correlation allowances' that are ultimately added, deduced from experimental full-scale trial data. These allowances are specific for each extrapolation method, and on average bring all of them to the level measured in full-scale trials.

4.2 APPLICATION TO SHALLOW-WATER MODEL TESTS

Applying different model-to-ship extrapolation methods to shallow-water tests however, may cause very large differences. Consider the same ferry model data, for speed 16.5 kn.

- Without correcting for the tank width effect, the increase of the resistance for decreasing water depth is exaggerated, as seen: in water depth 13.1 m, the measured model resistance is 41.5 % higher than for depth 22.5 m. If the Froude model-to-ship extrapolation is now applied, flat-plate friction remains flat-plate friction and all this resistance increase is absorbed in the remainder, the residuary resistance coefficient, which is supposed equal for model and ship. But the frictional resistance coefficient of the ship at full scale is roughly half of that of the model. The residuary resistance, and thereby the shallow-water resistance increase, thus counts more strongly for the ship: in the prediction for the ship, the resistance in 13.1 m water depth now comes out as 56% higher than that for 22.5 m water depth!

- If, as advocated, first the model data are corrected for the tank width effect, the shallow-water resistance increase at model scale becomes 18%, that at full scale 24% --- still an appreciable difference.
- For this vessel, the form factor (in deep water) has been found as $1+k = 1.22$. Using that form factor in the extrapolation, the shallow-water resistance increase is still absorbed in the 'wave resistance' part and supposed equal for the ship; which yields again a 24% difference between both water depths.

Thus it is seen that both model-to-ship extrapolation methods, as naively applied here, lead to the conclusion that the shallow-water effect on resistance is significantly larger for the ship than for the model. But this critically depends on how the viscous resistance is affected by shallow water. This is considered in the next section.

5 EFFECT OF WATER DEPTH ON SHIP VISCOUS RESISTANCE

5.1 A COMPUTATIONAL STUDY

The effect of water depth on the flow around the hull is a lot more specific than that of the tank width. While tank walls are always fairly remote and were shown to cause a rather constant overspeed increase, the bottom can be quite close and can lead to a more horizontal flow past the hull, larger streamline curvature, larger pressure gradients, earlier flow separation. It is likely that the viscous resistance increases by this.

A study has been done on this effect (Raven, 2012), using viscous flow computations by a RANS code. To obtain a pure viscous resistance, 'double-body flow' computations have been made, i.e. computations in which wave making is omitted and the still water surface is modelled as a symmetry plane. The ratio of the resulting viscous resistance coefficient to the ITTC `57 friction coefficient is the form factor 1+k; which then normally is assumed to be independent of the Reynolds number. However, computations have been made for model and ship Reynolds numbers, to verify the equality of the form factor in shallow water.

One particular issue in such computations is again, to avoid channel effects. In many RANS codes, at the side boundaries of the domain either a free-slip boundary condition can be imposed, or some sort of constant-pressure condition. Both are inadequate for shallow-water cases and would act more or less as a channel flow, introducing the same false water-depth effects as were discussed before. In the study done, computations have been made using the PARNASSOS code (Hoekstra, 1999), which has a particular treatment of the boundary conditions on the lateral boundaries of the domain, adequately simulating an infinite domain width.

In (Raven, 2012), 4 ships of very different type are considered; each in several water depths. The overall conclusion was that the viscous resistance increases strongly with decreasing water depth (Fig.8). Moreover, the relative increase of the viscous resistance was found to be very similar for model and full scale, at least for not too shallow situations ($T/h < 0.5$). This was confirmed later for other cases.

For the model-to-ship extrapolation this means the following:

- The relative increase of the viscous resistance in shallow water, by a factor $C_V/C_{V\text{deep}}$, is supposed equal for model and ship; as was found in the study.
- The assumption for the viscous resistance thus becomes: $C_V(Re,h) = [\frac{C_V}{C_{V\,deep}}(\frac{T}{h})].(1+k)C_{F0}(Re)$
- The 'shallow-water form factor' $1+k^* = [\frac{C_V}{C_{V\,deep}}(\frac{T}{h})].(1+k)$ can be found from low-speed tests in the water depth considered, or alternatively, $C_V/C_{V\text{deep}}$ can be estimated from a general relation.
- Thus, a large part of the resistance increase in shallow water is correctly interpreted as viscous resistance, not as an increase of the wave or residuary resistance. This part decreases from model to ship, consequently the resulting full-scale resistance prediction in shallow water comes out as lower.

5.2 APPLICATION TO FERRY MODEL

The ferry model is reconsidered. From the measurements, form factors in shallow water could be estimated. For water depth 22.5 m, 1+k* = 1.27. For water depth 13.1 m, 1+k* = 1.39 so the viscous resistance has increased by 14% compared with the deep water value 1+k = 1.22. For 16.5 kn, half of the resistance increase from depth 22.5 m to depth 13.1 m is a viscous resistance increase.

Then extrapolating to full scale, a total resistance difference between both water depths of 19% is found --- actually very close to the percentage resistance increase at model scale. It may be noted that 56% and 24% were obtained before.

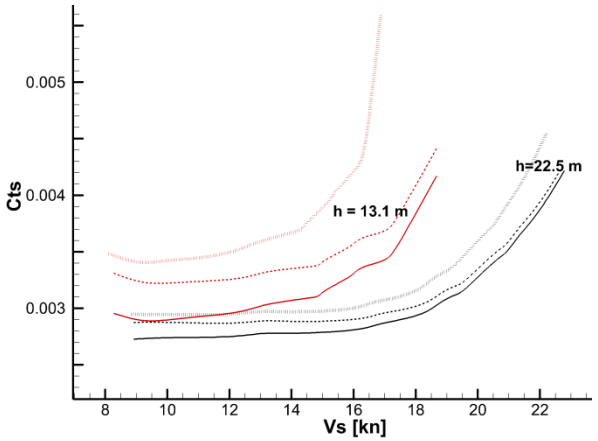

Figure 7. Predicted resistance coefficients for the ship. Dotted: no tank wall correction, Froude extrapolation. Dashed: Tank wall correction, Froude extrapolation.

Solid: tank wall correction, and depth-dependent form factor used.

Fig. 7 shows the complete ship resistance coefficient curves against speed, obtained with different extrapolation methods. The Froude extrapolation of the model data uncorrected for tank wall effect (dotted lines) suggests a very large shallow-water effect and high level of the resistance. The dashed lines were found by Froude extrapolation of the data corrected for tank wall effects. The solid lines are found by using a depth-dependent form factor in the extrapolation of the data corrected for tank wall effects, our recommended method. The effect of the tank width corrections is dominant for the higher speeds, the model-to-ship extrapolation method has more influence at lower speeds. The joint effect on the full-scale prediction is very large.

Therefore, also the model-to-ship extrapolation method used is of critical importance for predicting ship performance in shallow water.

6 A SHALLOW-WATER CORRECTION FOR SHIP SPEED TRIALS

6.1 LACKENBY'S CORRECTION

A related development, but distinct from model testing, concerned a new correction method for ship speed trials (Raven, 2016). Usually, in the delivery of a new ship from yard to owner, speed trials are performed to check compliance with the building contract. In most cases the required speed is prescribed for deep water. However, for practical reasons frequently trials are done in a slightly limited water depth, resulting in incipient shallow-water effects that reduce the speed achieved. A speed correction may then be made, supposing a deep-water speed slightly higher than what was actually measured.

Until recently, the single recommended correction method was Lackenby's formula (Lackenby, 1963), which gives a speed correction by:

$$\partial V / V = 0.1242\left(\frac{A_M}{h^2} - 0.05\right) + 1 - \sqrt{\tanh\left(\frac{gh}{V^2}\right)} \qquad (7)$$

Several objections to this formula have been discussed in (Raven 2012, 2016). Based on what was discussed in the previous sections, the following remarks are made:

- Shallow-water effects on viscous and wave resistance depend on different parameters. Lackenby proposes a formula that contains both parameters but is applied to the total resistance curve.
- The relative magnitude of viscous and wave resistance differs for different vessels, and for model and full scale. Any shallow-water correction meant to cover a variety of cases should correct separately for these two resistance components.
- Lackenby's formula is based on the method of Schlichting (1934), recast in a different form. Schlichting postulated a depth effect on the wave resistance, and derived an additional correction for frictional resistance from the remaining effect in his model data. Those data were just for 3 very slender ships at high speed. The frictional resistance correction thus lacks a sound physical basis but happens to be the dominant part in most practical applications.

In practice, it has been frequently found that the Lackenby correction led to too large corrections, and improvement was desired.

6.2 A NEW CORRECTION PROCEDURE

A new correction procedure has been developed, partly based on the study discussed in Section 5.1. This procedure has actually been accepted, under the name 'Raven shallow-water correction', by the International Towing Tank Conference (ITTC, 2017a) as an alternative next to the classical Lackenby method, in order to have other institutes validate it.

It is noted that in this application there are just incipient shallow-water effects, which simplifies the problem. From the study on water-depth effects on viscous resistance, it is found that the relative increase for model and ship was very similar, for not too shallow cases. Also, for a substantial collection of ships and models, the increase of the form factor for decreasing water depth was well approximated by the mean line (Fig.8):

$$C_V / C_{V\,deep} = 1 + 0.57\left(\frac{T}{h}\right)^{1.79} \qquad (8)$$

valid for T/h < 0.5; beyond that value, specifics of the ship become more important and disturb the uniform trend. As this relation essentially applies to the form factor, the increase of the dynamic sinkage in shallow water is not yet incorporated here.

For wave resistance, a computational study has been done for various ships, water depths and speeds, leading to Fig.9. Here again, computations were done for fixed sinkage and trim, as this was found to give a clearer, more uniform water depth dependence than with free trim and sinkage. From the figure, it is noted that the determining parameter is the depth Froude number; that (unless for large T/h) little uniform trend is visible until Fr_h = 0.7 – 0.75, with sometimes a little increase or decrease; and that wave resistance increases very quickly at higher Fr_h. For the present purpose, no change of wave resistance is assumed as long as $Fr_h < 0.7$.

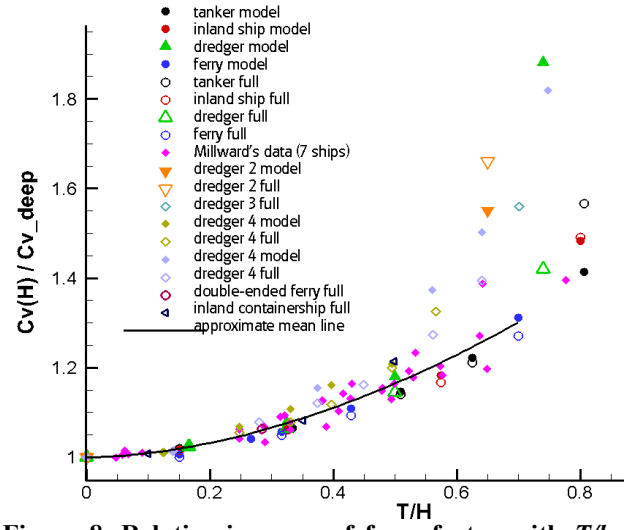

Figure 8. Relative increase of form factor with *T/h*, from computations (and some experiments)

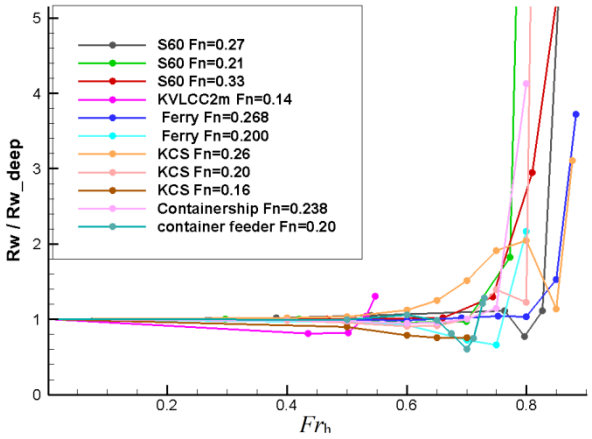

Figure 9. Computed variation of wave resistance for constant speed, variable water depth.

For both resistance components corrections have thus been derived for the effect of shallow water, but the increase of the dynamic sinkage has still been disregarded. This is equivalent to the hypothetical case of a ship in shallow water that is too light, such that it has unchanged sinkage. An additional contribution is therefore needed, the effect of the increase of displacement to its true value. For this one can resort to an accepted approximation, already used in speed trial analysis, for the effect of a draft change on resistance. It supposes that the total resistance is proportional to $\Delta^{2/3}$, in which Δ is the ship's displacement. To estimate the change of Δ, a relation has been derived for the increase of the dynamic sinkage caused by shallow water, based on a relation from Tuck (1966). Details are given in (Raven, 2016).

Thus both resistance components are addressed separately. However, it requires that the magnitude of the viscous and wave resistance contributions in deep water is known, such that corrections to each can be applied. While in the reference this relative magnitude was an input quantity, to be derived from available model tests or just estimated, this was considered undesired for a standard procedure for speed trial analysis. The procedure has now been adapted to be self-contained and is described in (ITTC, 2017b). The following steps are made, starting from a trial measurement of speed and shaft power:

- Estimate additional sinkage in shallow water, calculate corresponding displacement increase, and reduce measured power by assuming proportionality with $\Delta^{2/3}$.
- Estimate viscous resistance in deep water, R_{Vdeep}:
  - Calculate C_{f0} from ITTC `57 line
  - Estimate form factor 1+k from empirical relation by Gross and Watanabe
  - Increase viscous resistance coefficient by a roughness allowance from Townsin's formula
- Apply correction for water depth effect on viscous resistance, using the mean line (8). This yields a resistance deduction $\Delta R_V = R_{Vdeep} * 0.57\ (T/h)^{1.79}$
- Reduce power by $\Delta R_V . V / \eta_D$, where η_D is the estimated propulsive efficiency.

Subject to the limitations $Fn_h < 0.70$, $T/h < 0.5$ and displacement change due to sinkage < 5%, the procedure adjusts the measured power at the trial speed measured.

6.3 VALIDATION

6.3 (a) Experimental validation at full scale

The easiest way to validate the procedure would be by model tests, and this will be shown in Section 6.3(b). However, proper corrections for the limited tank width, and a correct model-to-ship extrapolation, are essential for determining the shallow-water influence for the ship. While for both adequate methods have been proposed (Sections 2.2 and 5.1), for an indisputable validation of the trial corrections we have resorted to full-scale testing; even while the less well-controlled conditions will cause larger errors and scatter.

Dedicated trials in various water depths have been done for three different ships: an inland tanker, a dredger and a naval academy vessel. The measurements and validations for the first two are discussed in (Raven, 2016). Here just the final graphs are shown (Fig. 10), comparing the speed

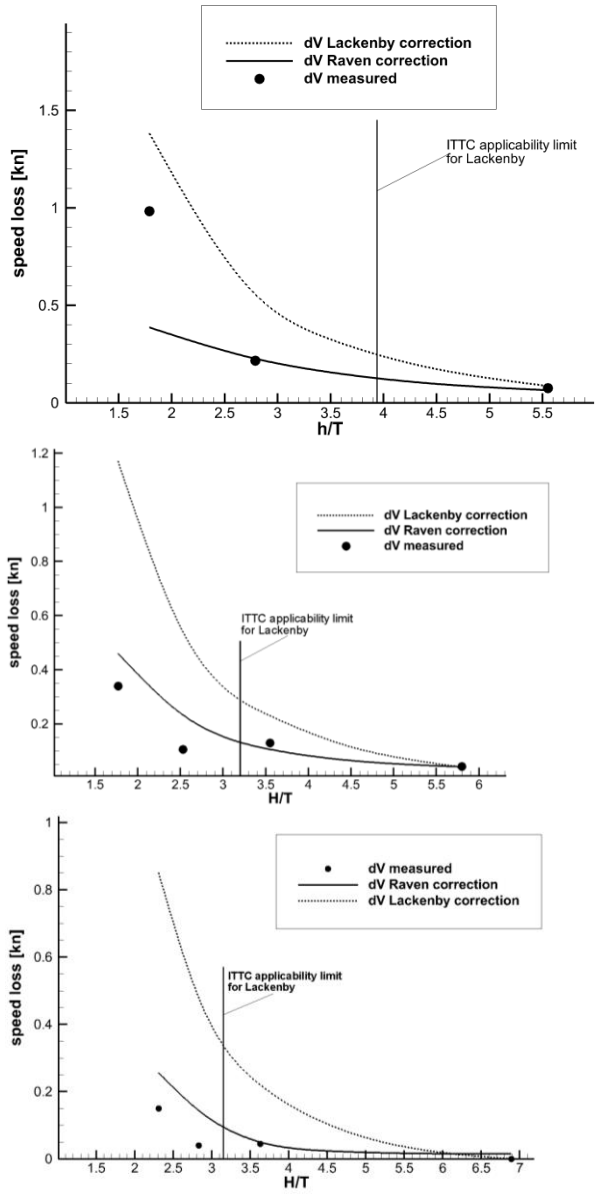

Figure 10. Speed loss in shallow water. Markers: measured. Solid line: method of Section 6.2; dashed line: Lackenby's formula. Top to bottom: inland tanker, dredger, naval academy vessel.

loss in shallow water actually measured, and the predicted speed loss. The picture is consistent for these ships: Lackenby's correction overestimates the speed loss, the new method is much closer, in particular for the not too small water depths. In most cases its trend seems correct, although some deviations still occur: It does remain an approximate procedure based on just very little input of the ship. Validation for a fourth vessel, an LNG carrier, is shown in (ITTC, 2017a), with largely similar outcome.

6.3 (b) Application to model-test data

Let us now apply this shallow-water correction to the model-test data for the ferry considered before. Computations for this ship were included in Figs 8 and 9, so, while now just experimental data are used, it may not be a completely independent test, but an interesting illustration all the same. A range of water depths had been tested, but no deep-water resistance values are available. When the shallow-water correction procedure is now applied to the measurements for each depth, does one get every time the same deep-water curve?

An important point needs to be made first. In speed trials, the speed and shaft power are measured, not the resistance. The present shallow-water correction procedure predicts a correction for the resistance at equal speed; and the correction for the power follows from the assumption of an unchanged propulsive efficiency, so it is the same percentage. In Lackenby's method however, the correction is a speed shift; and as power is proportional to resistance * speed, there is an essential difference between applying the Lackenby correction to the resistance curve, or to the power curve. For the purpose of ship trial analysis, the intended way is application to the power curve; but as Lackenby's formula was derived from Schlichting's method, which corrected resistance curves, one wonders whether Lackenby noticed this difference. For a proper comparison, the curves for effective power $Pe = Rt.V$ are compared, again assuming that η_D is not affected.

The model-test data corrected for tank width effect are used and the shallow-water correction is applied to obtain a deep water power curve. Actually some of the points lie outside the prescribed range of application of the shallow-water corrections, in particular for the sinkage increase. Still, Fig.11 shows that the deep-water power curves, deduced from the measured data in 3 water depths, coincide perfectly, until near Fr_h = 0.75 (16.5 kn for h=13.1 m, 19.3 kn for h=17.8 m) the wave resistance starts changing and also the sinkage change exceeds the bounds. Therefore, up to that speed the shallow-water correction completely represents the substantial shallow-water effects present in these model tests. Instead, Lackenby's correction is again too large, and the lowest deep-water curve is obtained from the measurements in the smallest water depth.

As a final step, the model-test data are extrapolated to full scale in the recommended way, i.e. using a water-depth dependent form factor (obtaining the solid lines in Fig. 7). Next the shallow-water correction is applied to the full-scale *Pe*-curves so found. Fig. 12 shows that again, the deep-water curves corrected from the predictions for the largest and smallest water depth coincide well, for the shallow-water correction proposed; but not for Lackenby's method. Therefore, there is complete consistency between the assumptions in the model-to-ship extrapolation and the new shallow-water correction, such that the latter represents the water depth effect both at model and at full scale.

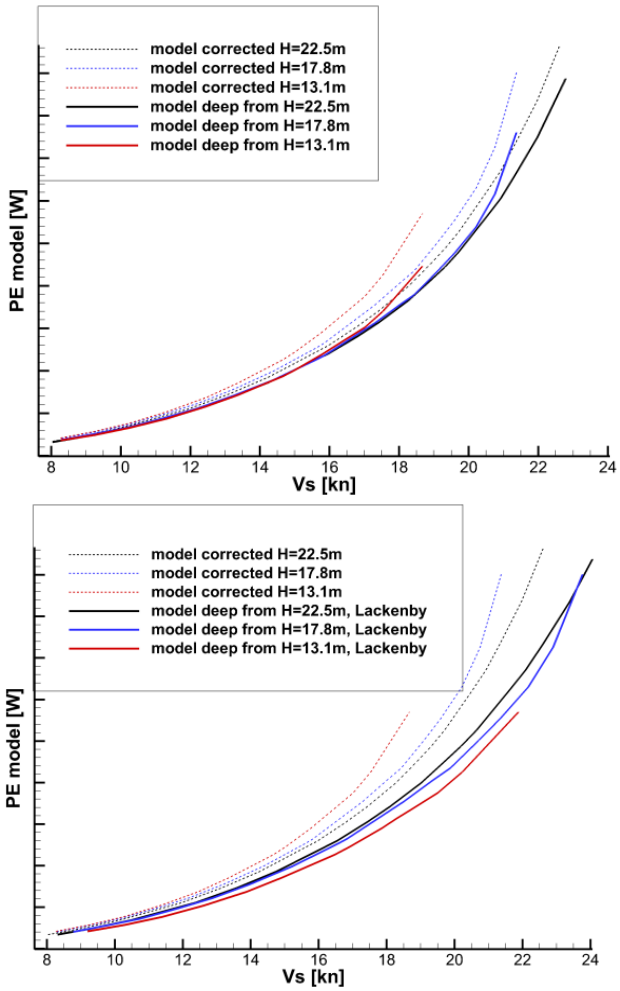

Figure 11. Effective power curves for the model, as measured (dashed lines), and as corrected to deep water, using shallow-water correction proposed (top) or Lackenby (bottom).

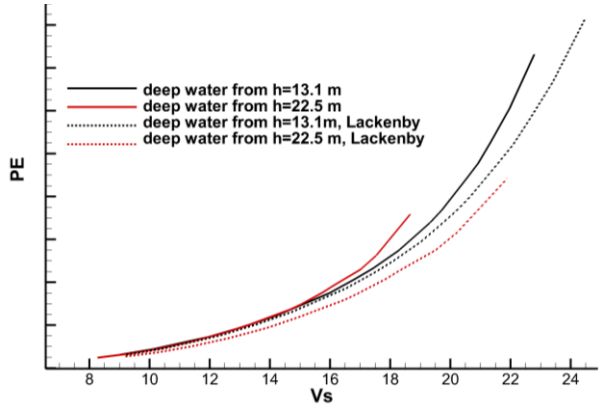

Figure 12. Effective power curves for the ship, extrapolated from model test, and corrected to deep water. Solid: method proposed. Dashed: Lackenby.

These results suggest that now it is understood precisely what is going on in these model tests, with tank wall effects, change of the viscous resistance, increased dynamic sinkage effects, and ultimately an increase of the wave resistance. An understanding that was missing 30 years ago when these measurements were done. Together with the insights gained on the scaling, a more solid basis has been given to model testing in shallow water.

7 CONCLUSIONS

The main conclusions can be summarised as follows:

- The limited width of a model basin significantly influences the resistance and squat of a model in shallow water. It may easily double the apparent water-depth effect on the resistance. Similar effects can occur in RANS computations due to limited domain width.
- An approximate method to correct for tank width effects has been proposed. It predicts the additional overspeed very well, the increase of the resistance and sinkage well as long as these are not too strong.
- The model-to-ship extrapolation of the measurements needs to take into account the increase of the viscous resistance in shallow water and its scaling; otherwise the water depth effect on the resistance of the ship is overestimated.
- A form-factor extrapolation method with a form factor determined for the actual water depth has been found to be an adequate method.
- A simple model for incipient effects of shallow water on the resistance has been derived, and has been accepted as a possible correction procedure for ship speed trials by the ITTC.
- This shallow-water correction procedure agrees very well with the water-depth influence in the model-test data; and equally well with the water-depth influence in the full-scale predictions derived from the model-test data by the extrapolation method advocated.

It is thought that the steps made in this research have given a more solid basis to model-testing in shallow water and to the prediction of ship performance based on it.

8 ACKNOWLEDGEMENT

This research has been largely funded by the Dutch Ministry of Economic Affairs. The full-scale validation in Section 6 has been supported by the Ship Trial Analysis (STA) Joint Industry Project and by Nederland Maritiem Land in the 'SHOALS Power' project, grant IC_MIIP230913-216. This support is gratefully acknowledged.

9 REFERENCES

Hoekstra, M., 1999. Numerical simulation of ship stern flows with a space-marching Navier Stokes method, Thesis, Delft Univ. Techn., October 1999.

ITTC, 2017a. Report of Specialist Committee on Performance of Ships in Service; in: Proceedings of 28th ITTC, Wuxi, China

ITTC, 2017b. Preparation, conduct and analysis of speed/power trials. ITTC Recommended procedures and guidelines, 7.5-04-01-01.1.

Jiang, T., 2001. A new method for resistance and propulsion prediction of the ship performance in shallow water, Proceedings 8th PRADS Symposium, Shanghai, 2001.

Kreitner, J., 1934. Über den Schiffswiderstand auf beschränktem Wasser. Werft, Reederei, Hafen, 15-7, pp. 77–82.

Lackenby, H., 1963. The effect of shallow water on ship speed. Shipbuilder Marine Engine Builder, pp. 446-450.

Larsson, L., and Raven, H.C., 2010. Ship Resistance and Flow. Principles of Naval Architecture Series, SNAME, Jersey City, USA.

Raven H.C., 1996. A solution method for the nonlinear ship wave resistance problem. Thesis, Delft Univ. Techn.

Raven, H.C., 2012. A computational study of shallow-water effects on ship viscous resistance,. In: Proc. 29th Symp. Naval Hydrodynamics, Gothenburg, Sweden.

Raven, H.C., 2016. A new correction procedure for shallow-water effects in ship speed trials, in: Proc. PRADS 2016 Symposium, Kopenhagen, Denmark.

Raven, H.C., 2018. A method to correct shallow-water model tests for tank wall effects. Jnl Marine Science Techn., in press. https://doi.org/10.1007/s00773-018-0563-1 or https://rdcu.be/TCwx

Schlichting, O.,1934. Schiffswiderstand auf beschränkter Wassertiefe --- Widerstand von Seeschiffen auf flachem Wasser. STG Jahrbuch Vol. 35.

Tuck, E.O., 1966. Shallow-water flow past slender bodies, J Fluid Mech Vol. 26 – 1, pp 81-95.

10 AUTHORS BIOGRAPHY

Hoyte Raven is a Senior Researcher at the Maritime Research Institute Netherlands (MARIN). His main interests are the development of computational methods for ship hydrodynamics, and their application in practical ship design and hull form optimisation. Shallow-water ship hydrodynamics is another topic of his interest.

THE INFLUENCE OF WAVE DRIFT FORCES COEFFICIENTS IN THE ASSESSMENT OF NAVIGABLE AREAS OF PORTS AND HARBOURS EXPOSED TO HIGH WAVES. EFFECT OF VESSEL SPEED AND WAVE SPECTRUM CONSIDERED

Raul Redondo, Juan Carlos Carmona and **Raul Atienza**,
Siport21, Spain

THE INFLUENCE OF WAVE DRIFT FORCES COEFFICIENTS IN THE ASSESSMENT OF NAVIGABLE AREAS OF PORTS AND HARBOURS EXPOSED TO HIGH WAVES. EFFECT OF VESSEL SPEED AND WAVE SPECTRUM CONSIDERED

Raul Redondo, Juan Carlos Carmona and **Raul Atienza,** Siport21, Spain

SUMMARY

This paper presents a further assessment of the paper presented in MARSIM 2018 entitled "The influence of Wave Drift Forces Coefficients in the Assessment of navigable areas of Ports and Harbours exposed to high waves" and dealing with the influence of wave drift forces for the design of navigable areas in ports or harbours subject to high swell waves in terms of resources required for the manoeuvres (speed, rudder angle, engine rpm, …) as well as in the area occupied by the vessels during the transit in approach channels.

Nowadays, Operators and Terminals want to increase operational limits and for that reason wave limits are increasing to significant wave heights over 3 and 4 meters in exposed approach channels, which increases the difficulty of the manoeuvres and therefore the design requirements of the navigable areas both in vertical and horizontal dimensions.

This assessment evaluates the modification of wave forces not only due to water depth, but considering also vessel speed, and the displacement of the peak force at wave directions. Different wave spectra used to transform transfer functions into mean drift wave forces would be considered in order to understand the differences in forces that different theoretical spectra might produce, as well as compare with some real, non-directional, spectra.

The numerical model AQWA is used to assess and obtain the wave drift forces of the KVLCC2 model at different vessel speeds and water depths. Results at speed cannot be compared with physical results, but this assessment will allow to understand the influence of all combined effects on wave forces (wave period, wave direction, wave spectrum, water depth and vessel speed) and the effects over the manoeuvrability of a vessel and the design of port and navigable areas.

1 INTRODUCTION

The influence of wave drift forces in the assessment of navigable areas is of critical importance in zones prone to high swell waves over 3/4 meters height, leading to overestimations or underestimations depending of the determination method of wave coefficients.

Figure 1. Vessel on waves at an approach channel

If the wave coefficients considered in the studies are not adequate, results could lead either to optimistic results, which could mean safety faults and risks in the operation, or to conservative results, affecting the operability of the port.

Last year a detailed assessment on wave drift forces influence over the manoeuvrability of the vessels and the design of navigable areas was started.

At that time the influence of mean wave drift forces for channel design focused on the influence of the following parameters.

- Water depth
- Wave peak period

This paper continues with the assessment and future works recommended in the first paper, and therefore, identifies the importance of the wave forces based on the following parameters:

- Vessel speed
- Spectra peak enhancement factor
- Theoretical spectra vs Real spectra
- Directional spectra vs Scalar spectra

2 WAVE DRIFT FORCES DETERMINATION

The determination of the wave drift forces produced over a vessel can be assessed both from numerical models and physical models. These wave drift forces, obtained as transfer functions, allow to derive the mean wave drift forces coefficients required as input for manoeuvring models. Numerical models have the advantage of the timing and the cost compared to physical modelling.

The numerical model AQWA from ANSYS has been used to assess and obtain the wave drift forces of the vessels (ANSYS 2017a-c). The Near Field Solution has been considered in this assessment as allows a more detailed description, without requiring the complete QTF matrix, therefore, reducing the limitation of the Far Field Solution. The model allows for accounting mean wave forces at speed with Froud number up to 0.3, for the KVLCC2 case, 8.6 knots.

Considering the regular wave elevation as

$$\zeta_{jm}\left(\vec{X},t\right) = a_{jm}e^{i(-\omega_{jm}t+k_{jm}X\cos\chi_m+k_{jm}Y\sin\chi_m+\alpha_{jm})} \quad (1)$$

where a_{jm} is the wave amplitude, ω_{jm} is the frequency, k_{jm} is the wave number, χ_m is the direction, and α_{jm} is the phase, the mean drift force and moment are expressed as the triple summation:

$$\vec{F} = \sum_{m=1}^{N_d}\sum_{n=1}^{N_d}\sum_{j=1}^{N_w} a_{jm}a_{jn}\left\{\overrightarrow{P_{jjmn}}\cos\left(\alpha_{jm}-\alpha_{kn}\right) - \overrightarrow{Q_{jjmn}}\sin(\alpha_{jm}-\alpha_{kn})\right\} \quad (2)$$

Where the numbers of wave components of every individual wave directions are the same ($N_m = N_n = N_w$). For a long-crested wave case ($N_d = 1$), the mean drift force can be further simplified as:

$$\vec{F} = \sum_{j=1}^{N_w} a_{j1}{}^2\overrightarrow{P_{jj11}} \quad (3)$$

in which the out of phase item Q_{jjmn} where $m = n = 1$ in the first equation is no longer included. The above expressions are known as the near field solution, and valid for both a single and multiple floating structure system with or without hydrodynamic interaction effects.

For an irregular wave spectrum $S(\omega)$, based on equation (3), the mean wave drift force can be obtained as:

$$\overline{F_{Irr}} = 2\cdot\int_0^\infty S(\omega)\cdot P(\omega)\cdot d\omega \quad (4)$$

Validation of this calculation was given by Redondo et al. (2018).

For the purpose of the paper the KVLCC2 model has been used in loaded condition at different speeds and water depths. Table 1 summarizes the main particulars of the vessel considered.

Table. 1 KVLCC2 main characteristics

Description	Load Condition
Lbp (m)	320.0
B (m)	58.0
T (m)	20.8
Displacement (ton)	320438
KM (m)	24.3
GM (m)	5.7
KG (m)	18.6
XG (m)	171.1
Rxx (%B)	40
Ryy (%Lbp)	25

In order to evaluate the influence of wave drift coefficients on the manoeuvrability of vessels and on the design of navigable areas and ports, several vessel speed and wave spectra (theoretical, real, scalar and directional) have been considered. Therefore, it is possible to evaluate the importance of these parameters, allowing to select the most appropriate wave coefficients for manoeuvring models.

Figure 2 shows the KVLCC2 model in ANSYS AQWA.

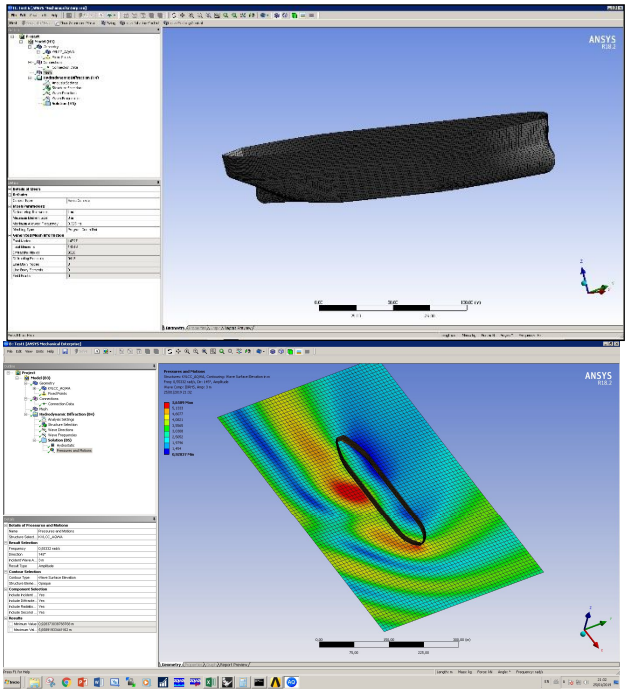

Figure 2. KVLCC2 model in ANSYS AQWA

The results obtained with ANSYS AQWA are the transfer functions of the mean wave drift forces and moments.

3 EVALUATION OF MEAN WAVE DRIFT FORCES

Prior to assessing the effects of different wave drift forces coefficients in manoeuvring models, an assessment based only on the mean wave forces curves is done. This

assessment is done by comparing wave forces and moments under different conditions.
This paper identifies the importance of the wave forces based on the following parameters:

- Vessel speed
- Spectra peak enhancement factor
- Theoretical spectra vs Real spectra
- Directional spectra vs Scalar spectra

The following subsections assess these parameters in detail.

3.1 VARIATION WITH VESSEL SPEED

Figure 3 shows the variation of transverse wave drift force for different vessel speeds for the same water depth, in this case 1.5 times the vessels draught, and for a wave condition with a peak period of 12s.

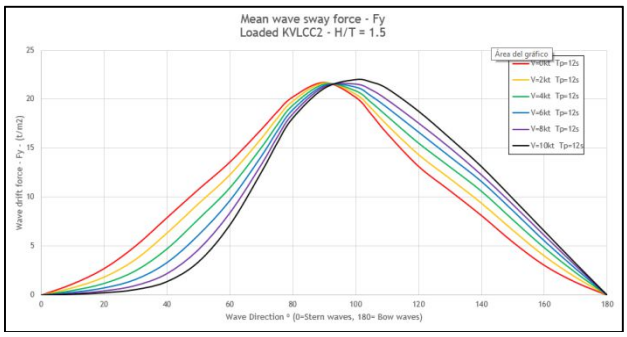

Figure 3. Comparison of transverse mean wave force for different vessel speeds

As it can be seen from the above image, wave drift forces vary significantly with vessel speed. This is due to the variation in the encounter frequency and encounter direction that appears when encountering waves at speed.

In this sense, it can be seen how stern quarter sway wave forces (20º-60º) reduce as vessel speed increases, which is a typical condition for port approaches, and increase for bow quarter waves (120º-160º), which is a typical condition for port departures. This effect of vessel speed is the same for different wave periods, only modifying the amplification/reduction factor.

Figure 4 shows the variation of wave yaw moment, both for wave peak periods of 12s and 17s.

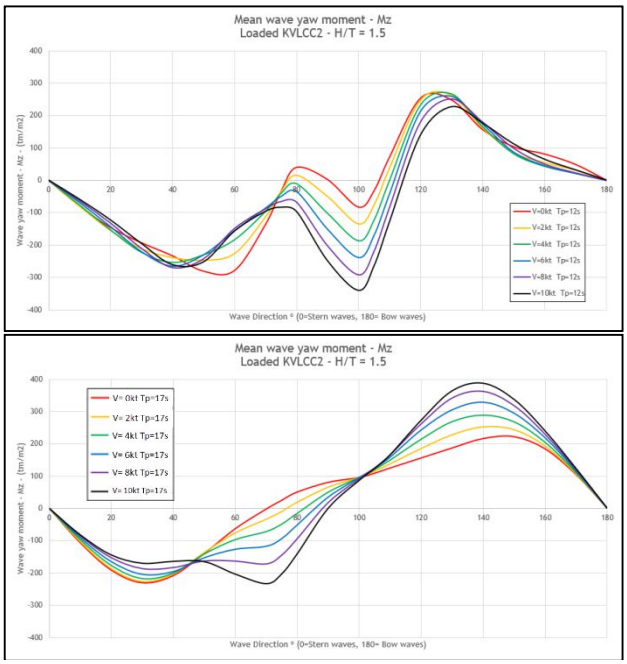

Figure 4 Comparison of mean wave yaw moment for a wave peak period of 12s (top) and 17 s (bottom)

Concerning yaw moments, they are modified as well. In this case the effects of speed are more dependent on wave peak period, increasing or decreasing for different wave directions. Moreover, and as it can be seen from above images, implications over yaw moment are higher than over sway forces, as the direction of the moment can even change (to port or starboard). Therefore, speed variations are not only linked with a smaller or bigger reaction, but with a different one.

The sway force is directly linked with lateral drifting in terms of vessel manoeuvrability, producing an offset of vessel position which is difficult to control using own resources. The ship must then sail with some drift angle to compensate. On the other hand, yaw moment is directly linked with the course keeping ability. Therefore, external yaw moment forces tend to change vessel course, which can be “easily” overcome by means of the rudder, as rudder mainly corrects the course.

Nevertheless, changes in the wave yaw moment direction might be of extreme importance when considering other external factors such as wind or currents, as all external factors can act together in the same direction or in opposite directions, counteracting their effects. Therefore, having the right yaw moment directions is required, so accuracy in deriving these forces (yaw moment and sway force) is of very high importance when assessing navigable areas exposed to high swell waves.

All this assessment leads to the fact that, when dealing with port and fairway design in areas exposed to high swell waves, causing large forces, elaborating adequate coefficients or forces, based on actual vessel speed, is of very high importance.

3.2 VARIATION WITH SPECTRUM PEAK ENHANCEMENT FACTOR

As already known, and as can be seen from Figure 5, different peak enhancement factors modify the energy distribution of the waves significantly.

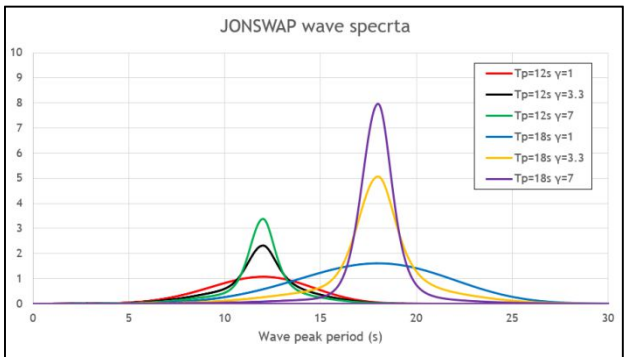

Figure 5. Wave spectra with different peak periods and peak enhancement factors

The difference in the energy distribution allows to vary and redistribute the energy of the wave along the vessel transfer functions, and therefore modifies the total force and moment upon the vessel.

Figure 6 shows the variation of transverse wave drift force for different peak enhancement factors for both 12s and 17s peak period and different vessel speed (0 knots and 10 knots) (h/T=1.5 in all cases).

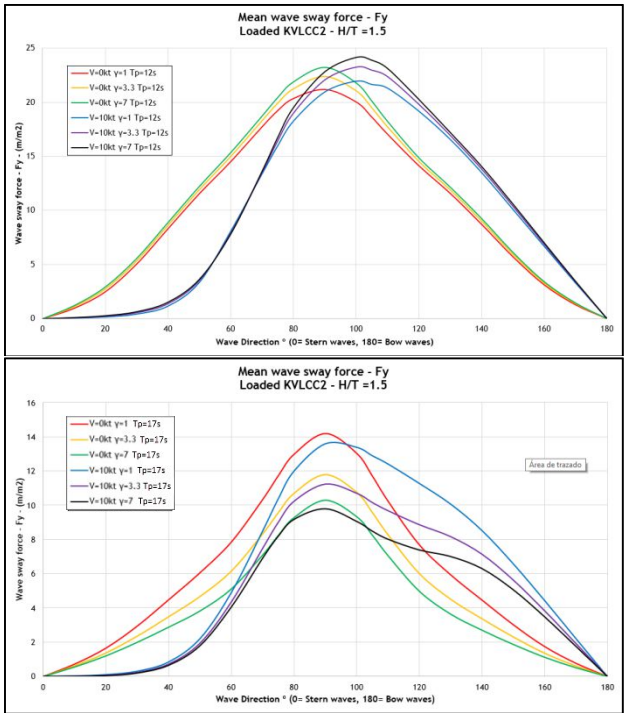

Figure 6. Comparison of transverse mean wave force for different wave periods and γ values

As can be seen from Figure 6, the wave drift forces and moments change with peak enhancement factor. In this case, the variation is dependent on the wave peak period and vessel transfer functions.

In this sense, it can be seen how for a 12s peak period, the variations are not very relevant (below 10%), mainly because at the relevant frequencies the vessel transfer function is almost constant. On the other hand, and for this particular vessel, different peak enhancement factors for wave periods of 17s are much more relevant, as wave forces for beam waves increase approximately 20% when gamma values vary from 7 to 3.3 and 40% when gamma values vary from 7 to 1, as wave transfer functions have a higher variability in the frequencies for 17s peak period waves.

Figure 7 shows the variation in wave yaw moment, both for wave peak periods of 12s and 17s.

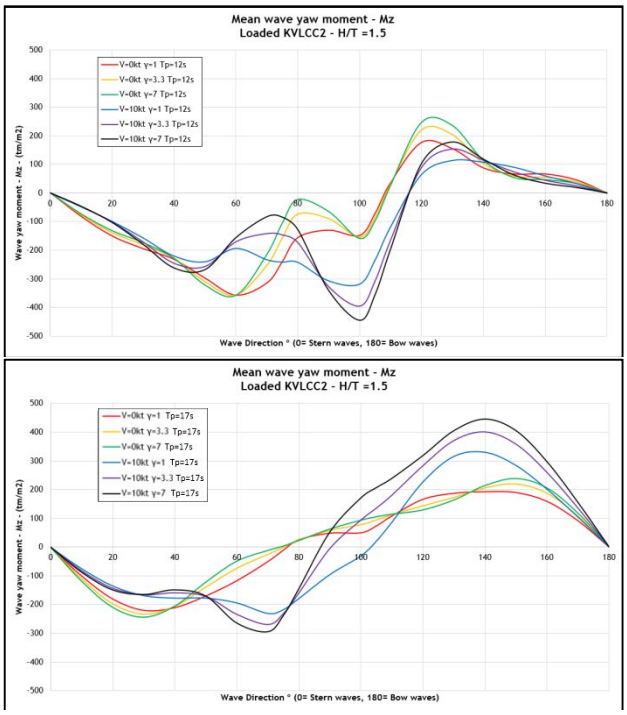

Figure 7. Comparison of mean wave yaw moment for different wave periods

As it can be seen, yaw moment can vary significantly with peak enhancement factor, as for sway force, but even with higher implications. The direction of the moment can even change, as happened with vessel speed. There is not just a smaller or bigger reaction, but a different one (port or starboard tendency).

This assessment indicates that having an adequate knowledge of the wave spectrum in the area of the study is of importance. Therefore, when assessing navigable areas and fairway it is required to have available detailed met ocean studies (mainly waves in this case).

Usually, wave forces are computed using wave coefficients which were determined for a specific wave

spectrum. This should be in accordance with local data and the proper input to perform the manoeuvre simulations.

3.3 THEORETICAL SPECTRA VS REAL SPECTRA

In order to assess wave forces for theoretical spectra or real spectra, several RAW spectrums, obtained from measurements on South American Pacific coast, for different wave peak periods, have been analysed.

Figure 8 shows the RAW spectra for three wave peak periods (12s, 17s, 21s).

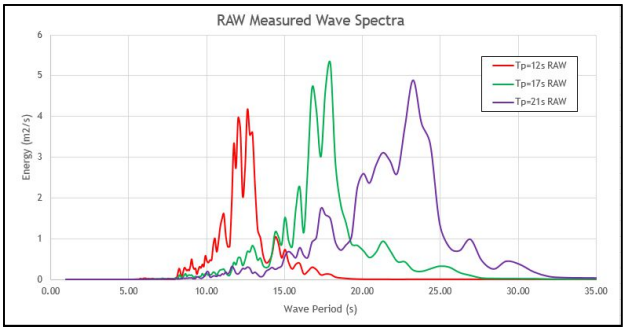

Figure 8. RAW Measured spectra

Before comparing these spectra with theoretical Jonswap spectra, the measured spectra have been smoothed by the Welch method.

Figure 9 shows the smoothed spectra compared with RAW spectra.

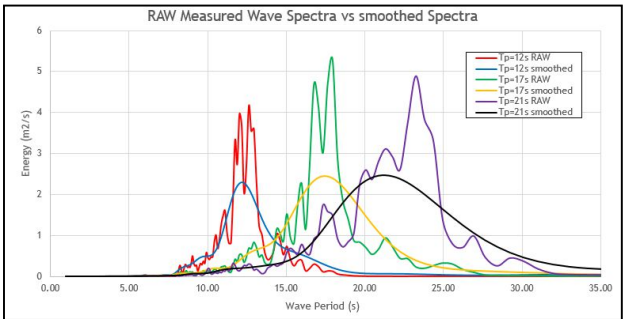

Figure 9. RAW Measured spectra and smoothed spectra

These new smoothed spectra are similar to theoretical wave spectra representations, and therefore, it is possible to compare theoretical vs real spectra. Figure 10 shows this comparison (frequency based).

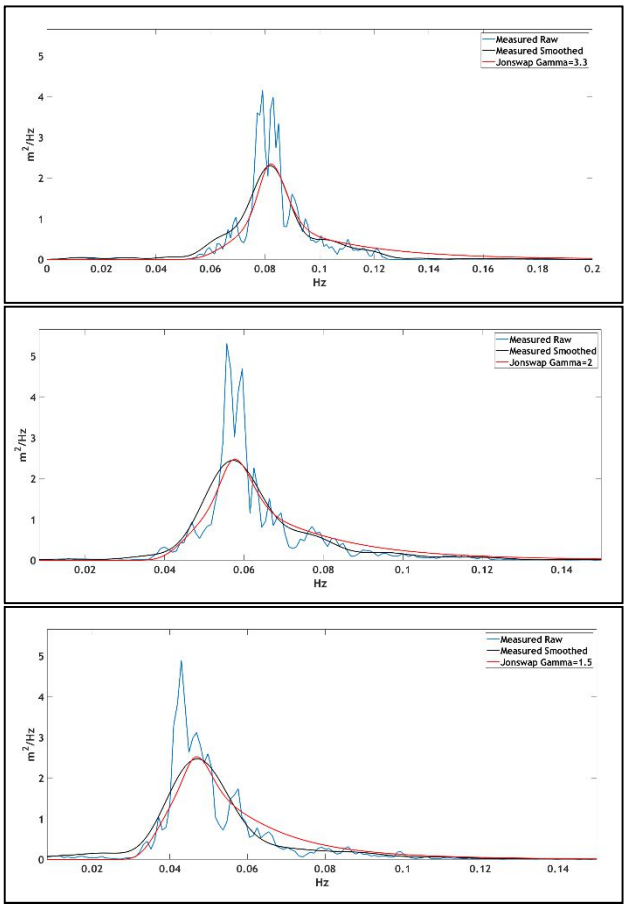

Figure 10. Smoothed spectra vs Jonswap spectra

As can be seen, there are differences when comparing the smoothed measured spectra with Jonswap spectra for all peak periods. Moreover, a verification of the most adequate peak enhancement factor for each of the measured spectra has been done, leading to a 3.3 factor for Tp=12s, 2.0 factor for Tp=17s and 1.5 factor for Tp=21s.

In the previous section, an assessment on the impact on wave forces, when considering variations on the peak enhancement factor, was performed. In this subsection it has just been verified that there are as well differences between real and theoretical scalar spectra. Moreover, and as already known, spectra on the same locations vary depending on waves peak period and direction.

Each one of these spectra analysed (RAW, smoothed and adjusted JONSWAP) will lead to different wave forces and moments. Therefore, having available actual measured data is very relevant when assessing manoeuvring and navigable areas, especially when swell waves are relevant (over 3 meters).

3.4 SCALAR SPECTRA VS DIRECTIONAL SPECTRA

Several factors have been assessed in order to verify how wave coefficients change, and therefore, the relative importance of each of the variables on the results.

Nevertheless, one of the main parameters (which is almost never considered) that might seriously affect wave forces is to consider either a scalar or a directional spectrum.

In this section an assessment of RAW measured spectra, scalar, sectorized or fully directional is performed.

Two different spectra are used, corresponding to 12s peak period and 21s peak period.

3.4 (a) Scalar spectra

Scalar spectra obtained from directional spectra are represented in previous figures (Figures 8 and 9). Those spectra correspond to the sum in each frequency of the energy in all wave directions.

3.4 (b) Directional spectra

The complete and detailed wave representation obtained from the measurement is the following, showing the complete directional spectra for both peak periods 12s and 21s.

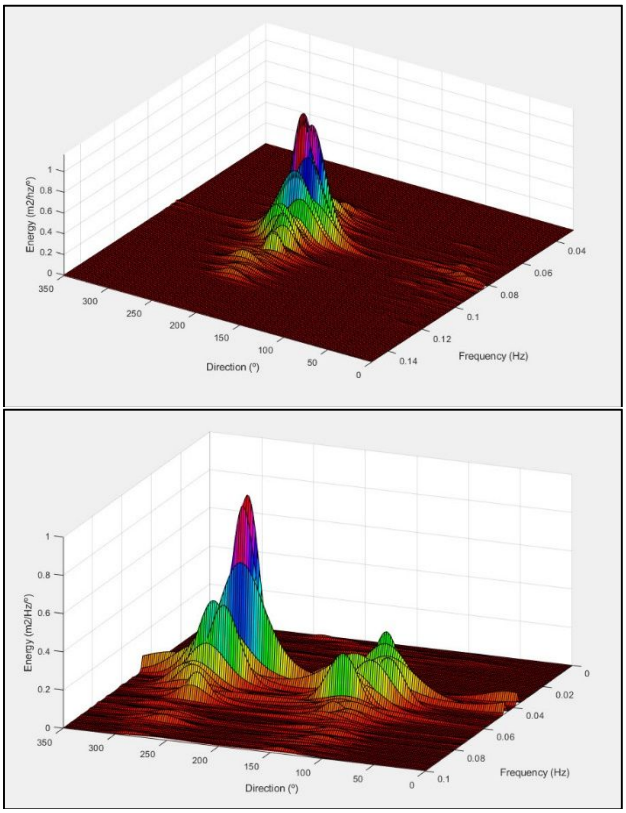

Figure 11. Directional spectra for Tp=12s (top) and Tp=21s (bottom)

As can be seen clearly from Figure 11, the 12s swell is quite concentrated in a sector of 60º to 80º width, meanwhile the 21s swell is clearly bidirectional, with two main wave directions of approximately 130º and 260º. This second wave spectrum is considered very relevant for the purpose of this paper.

3.4 (c) Sectorized spectra

It is common for assessment of navigable areas that a representative wave direction is considered (highest frequency or highest intensity), based usually in sectors of 22.5º or 45º. In this sense, it seems logic to consider, as well, a scalar spectrum based in the corresponding wave directions for wave forces determination. Figure 12 shows the directionality of both spectra and typical sectors (22.5º (30º) and 45º (50º)).

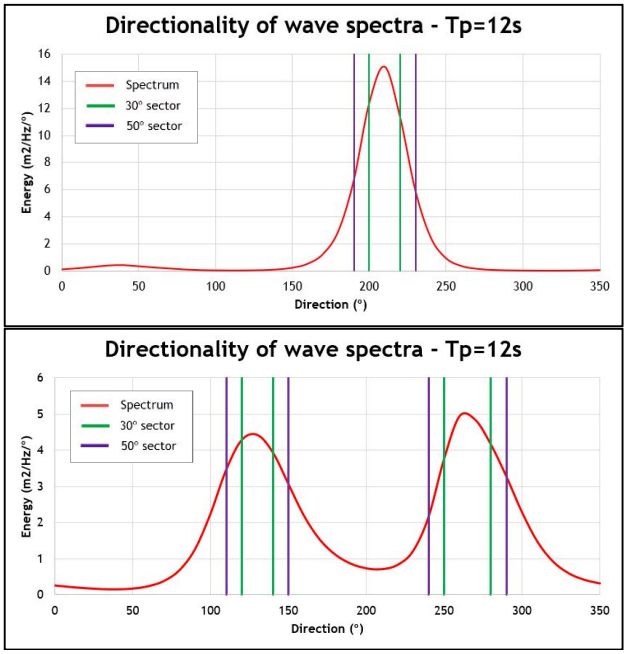

Figure 12. Directional spectra sectors for Tp=12s (top) and Tp=21s (bottom)

3.4 (d) Comparison of wave forces

In order to determine the influence of the different spectra over wave forces, all different combinations have been considered. Therefore, wave forces have been obtained multiplying the transfer function by:

- Complete scalar spectrums
- Sectorized scalar spectrums (30º and 50º)
- Directional spectrums

The results obtained are compared with each other in terms of vessel course, as, due to the usage of directional spectrum, results cannot be described by the incident direction of waves, but in terms of wave course. In this case, zero vessel speed and h/T=1.3 is considered.

Figure 13 shows sway wave force and yaw moments in terms of vessel course for the 12s peak period spectra.

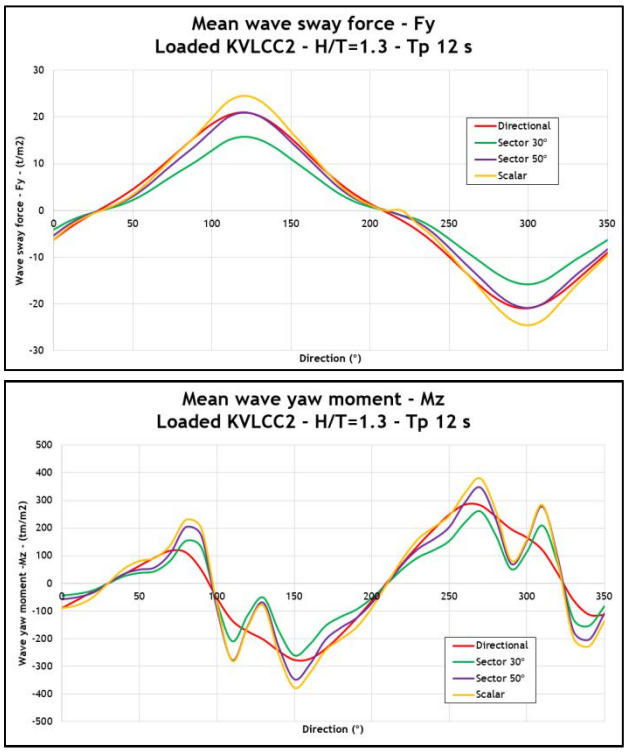

Figure 13. Wave sway force and yaw moment as a function of vessel course (wave spectra Tp=12s)

As can be seen from Figure 13, there is a significant difference in wave forces depending on the type of spectrum considered. Considering that the adequate wave forces are those derived from the directional spectra (most detailed information, red line), using the pure scalar spectrum produces a force increase up to 20% (yellow). Meanwhile forces decrease approximately 30% if the sectorized 30º spectrum is considered (green). For the sectorized 50º spectrum (purple), results are very similar to those of the full directional spectrum. Therefore, the adequate scalar spectra to be used if no directionality can be implemented, is 50º for this particular case if "correct" sway forces are wanted.

Concerning the yaw moment, the results are similar: pure scalar spectrum gives, in general, higher values; in this case both sectorized spectra show better agreement, nevertheless not as good as for sway. It can be also seen that when using the directional spectrum curves are smooth. Scalar spectra show variable peaks in direction making it more difficult to compare.

Figure 14 shows wave sway force and yaw moment relative to vessel course for the Tp=21s spectra. In this case, a very different spectrum is considered due to bidirectionality (130º and 260º). For this case one single sector has been considered as relevant. As it is common in assessment of navigable areas to consider single acting wave directions and not simultaneous.

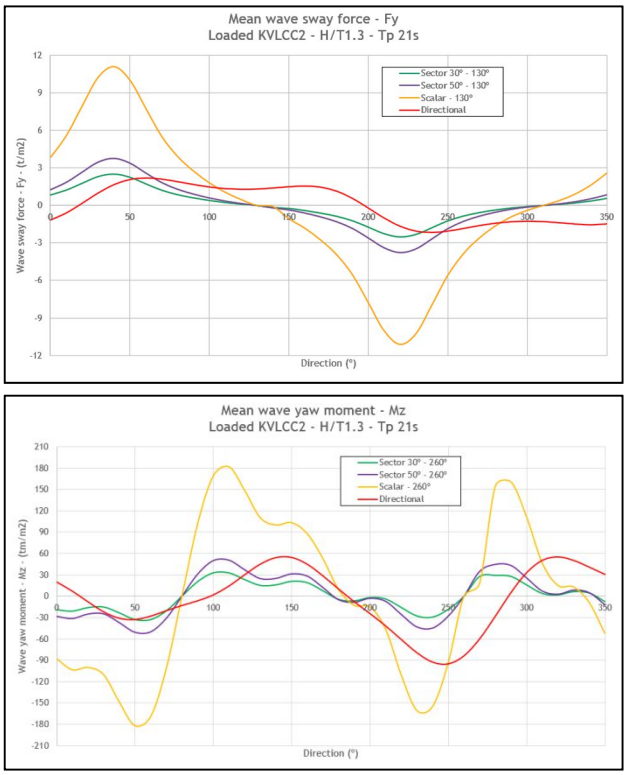

Figure 14. Wave sway force (top) and yaw moment (bottom) as a function of vessel course (wave spectra Tp=21s) when a directional spectrum or a sectorized spectrum is considered

Figures 13 and 14 show clear differences when the directional spectrum (red line) or a scalar spectrum for only one main direction is considered. Sway force considers 130º spectra and yaw moment considers 260º spectra. Not only the force or moment values are different, but the general behaviour is also different, with forces acting in different directions depending on the schematization of spectra considered.

Therefore, this method considering only one main direction results in very misleading determination of wave forces.

Figure 15 show wave sway force and yaw moment relative to vessel course for the Tp=21s spectra, but now considering both sectors acting simultaneously.

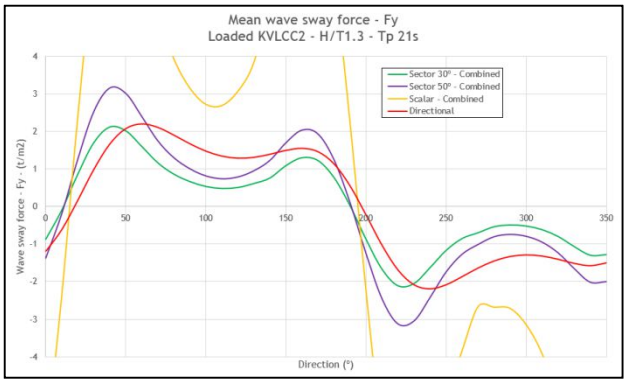

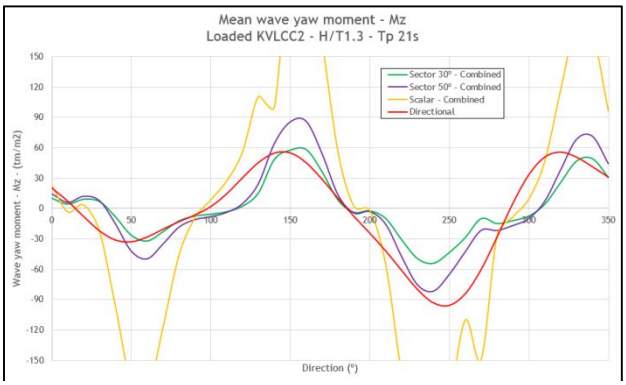

Figure 15. Wave sway force and yaw moment as a function of vessel course (wave spectra Tp=21s) – both sectors spectra considered

In this case, combining scalar spectra with two main directions of both sectorized spectra simultaneously provides a much more realistic behaviour (compared to full directional spectrum). In this case, forces and moments always go in the same direction, even if absolute values differ.

The figures are out of scale so it can be easily understood that pure scalar spectra used in both directions simultaneously gives extreme forces. Nevertheless, when considering the addition of sectorized spectra, for both 30º and 50º sectors, values are much more reasonable and can be easily compared.

Considering the sectorized results, for some vessel courses forces and moments are higher, and others are lower, with differences that can reach 50% to 100%. This indicates that a certain part of the directional spectrum, which has not been included, has relevant effects, so a very careful description is needed.

In this case, results in terms of force are not very high as this bidirectional spectrum has a peak period in which the KVLCC2 reference ship does not respond, but this bidirectionality together with a peak period of 12s, would be critical for this vessel.

Compiling all the information obtained from the assessment of the directional spectra the following ideas can be extracted in order to obtain accurate wave drift forces:

- If a spectrum shows bidirectionality, it is necessary to consider the whole directional spectra.
- If a spectrum has a clear main direction, with a certain spreading, it is required: either to assess the whole directional spectrum, or to assess in detail the required sectorized scalar spectrum width (30º, 50º, 70º …) to obtain realistic values.
- It has to be noted that when considering a bidirectional spectrum, symmetry of forces and moments over the vessel is lost and, therefore, forces and moments should be expressed in terms of vessel course and not incident wave direction.
- If the spectrum has a main direction with a narrow spreading angle, forces and moments still keep an adequate symmetry. Nevertheless, vessel course becomes relevant and not wave direction.

4 CONCLUSIONS

The results presented in this paper show how numerical model AQWA can be used to obtain the wave drift forces that can later be used in manoeuvring models. In a previous paper it was verified that the numerical results in deep water at zero speed are in good agreement with the results of physical models.

Wave drift forces in shallow water and at certain vessel speed have not yet been compared and verified, as physical model results were not available at the moment. This item is still pending to be assessed and verified to confirm the complete applicability of AQWA to derive wave forces, both at deep and shallow water and at different ship speeds.

In this paper different scenarios have been investigated further in detail, like the influence of vessel speed and different wave spectra shape (theoretical with different peak enhancement factors and real spectra (scalar spectra, sectorized scalar spectra and directional spectra)).

Vessel speed has been proven to be a relevant factor when assessing navigable areas in high swell conditions, as it modifies not only the intensity of sway force exerted by waves, but even the direction of the moment. Therefore, taking into account adequate force and moment coefficients, based on actual vessel speed, is of very high importance.

Moreover, as vessel speed usually varies when at an approach/departure of a port or harbour area, considering its effect is of relevance. This leads to think about creating matrix models of wave coefficients for manoeuvring models, so that not only wave period and wave direction, but also UKC (Redondo et al. 2018) and vessel speed are considered altogether in determining wave forces and moments.

Nowadays, part of this issue is solved, as developers are already taking into account wave forces based on real time calculation by computing excitation and radiation forces (Donatini et al. 2019). Therefore, this approach might be already considering UKC and vessel speed as well. However, verifications should be made whether the simplified methodology and vessel models required nowadays to allow real time calculation are capable of providing accurate forces reliable for navigable areas design. It seems they give an adequate feeling while manoeuvring, useful for training purposes, but more precise results seem to be necessary.

Regarding wave spectra, it is basic to understand the importance of having accurate and reliable local wave information before performing a nautical assessment of navigable areas. This paper has enhanced the significant differences in wave forces obtained by using different spectral descriptions, and that has a serious effect in ship controllability.

Scalar theoretical spectrum formulations, widely used, have proven to give an approximation. Nevertheless, differences in certain spectral parameters, such as peak enhancement factor, provide different forces and moments. Therefore, using local measured spectra is recommended in high swell scenarios (if available).

If measured spectra show a main wave direction with a narrow spreading angle, it is possible to determine the sectorized scalar spectra that best fit to derive wave forces and moments without considering full directional spectra. Nevertheless, case by case analysis of required wave sector width (30º, 50º, 70º) is required before determining specific wave forces in the area.

If wave spectra show significant bidirectionality, accurate results will only be provided by directional spectrum formulation. Even if two different sectorized scalar spectra are used simultaneously, those would require to very big, and results will not be accurate. Therefore, the best option is to consider directionality with the full spectrum.

Wave forces coefficients are obtained as a function of wave period and wave direction, but this paper suggests to expand to a matrix structure including variable water depth and ship speed for the sake of accurate results. Based on the results of wave forces transfer functions, computed using numerical models such as ANSYS AQWA, and deriving mean wave drift forces through local spectra, it is possible to obtain quite accurate forces and moments, specific for each particular case and spectrum, varying input data and considering vessel course instead of incident wave direction.

Port design is continuously demanding more and more accurate and reliable models, limits are expanding and numerical models are requested to improve every day. This paper focuses on one important parameter for port design, such as wave drift forces over vessels in exposed navigable areas, even more important in high swell conditions and increasing wave operational limits.

Not only matrix models to include wave direction and period, UKC and vessel speed are important to consider (alternatively, accurate real-time calculation of excitation and radiation forces), but spectral schematization of waves is also relevant, mainly directional spreading.

It is considered important to assess the feasibility of ship access including measured directional wave spectra in real-time simulation, and not only theoretical scalar spectra, even if several wave trains from different directions can be included.

As stated in Reference 1, if the wave coefficients considered in the studies are not adequate, results could lead either to optimistic results, which could mean safety faults and risks in the operation, or to conservative results, affecting the operability of the port. Therefore, elaborating port design studies using accurate wave forces coefficients is required.

5 REFERENCES

ANSYS, 2017a. AQWA Reference Manual Release 18.2

ANSYS, 2017b. AQWA Theory Manual Release 18.2

ANSYS, 2017c. AQWA User Manual Release 18.2

Donatini, L., Vantorre, M., Verwilligen, J., Delefortrie, G., 2019. Description of hydro/meteo data in ship manoeuvring simulators: a survey on the state of the art. MASHCON 2019. Ostende, Belgium

Redondo, R., Atienza, R., Carmona, J.C., 2018. The influence of wave drift forces coefficients in the assessment of navigable areas of ports and harbours exposed to high waves. MARSIM 2018. Halifax, Canada

6 AUTHORS BIOGRAPHY

Raul Redondo holds the current position of Project Manager at Siport21. He coordinates and performs technical projects. He specializes on moored ship dynamics and ship manoeuvrability in port areas, both using numerical models and real-time simulation. Development of numerical models for the resolution of hydrodynamics problems and ship dynamics.

Juan Carlos Carmona holds the current position of Project Engineer at Siport21. He performs technical projects. He specializes on moored ship dynamics and ship manoeuvrability in port areas, both using numerical models and real-time simulation. Development of numerical models for the resolution of hydrodynamics problems and ship dynamics.

Raul Atienza holds the current position of Technical Director at Siport21. He coordinates and checks the technical projects. He specializes on moored ship dynamics and ship manoeuvrability in port areas, both using numerical models and real-time simulation. Development of numerical models for the resolution of hydrodynamics problems and ship dynamics. He has previously worked as a teacher in the Technical University of Madrid.

SHALLOW WATER POWER CORRECTION FOR HIGH-SPEED VESSELS

Jan Richter, Lars-Uve Schrader and Oliver Reinholz,
Hamburg Ship Model Basin, Germany

SHALLOW WATER POWER CORRECTION FOR HIGH-SPEED VESSELS

Jan Richter, Lars-Uve Schrader and **Oliver Reinholz,** Hamburg Ship Model Basin, Germany

SUMMARY

The power demand required to attain a certain ship speed is higher in restricted than in unconstrained waterways. For the conversion of speed trials that have been carried out in shallow water to a contractual deep water condition - or vice versa - ITTC recommends correction procedures as formulated by Lackenby or, more recently according to Raven. Both are intended for conventional displacement vessels and Froude numbers.
For a recent speed trial with a fast displacement to semi-planning vessel, these methods proved inappropriate. For this reason the speed trial campaign has been extended to include speed power recordings at different ship speeds as well as different water depths. The findings have been condensed into an empirical correction method for this specific vessel. A promising speed to water depth relation has been identified which is worth a more thorough investigation by means of an extensive systematic study.

NOMENCLATURE

A	Channel cross sectional area (m^2)
A_M	Midship area submerged (m^2)
A_{WP}	Waterplane area (m^2)
b	Channel width (m)
B_{WL}	Beam at the height of the waterline (m)
C_B	Block coefficient (-)
c_P	Non-dimensional pressure (-)
c_T	Total resistance coefficient (-)
Fr	Froude number (-)
Fr_h	Depth Froude number (-)
Fr_{HD}	Depth Froude number in deep water (-)
g	Gravitational acceleration (m/s^2)
h	Water depth (m)
K_1	Scott's factor (-)
K_2	Scott's factor (-)
L_{PP}	Length between perpendiculars (m)
m	Blockage (-)
R	Resistance (N)
R_T	Total resistance (N)
R_V	Viscous resistance (N)
T_m	Midship draught (m)
v	Ship speed (kn, m/s)
z_{sink}	Dynamic sinkage (m)
ϕ_{trim}	Trim (°)
∇	Displacement volume (m^3)

1 INTRODUCTION

For a recent speed trial with a fast displacement to semi-planning vessel, the contract condition is defined as a shallow water condition. Although the under keel clearance is, with a draught to depth ratio of 0.07, unspectacular, the high depth Froude number of about 0.79 is notable. During speed trial depth Froude numbers of up to 0.96 are reached due to the restricted water depth and high speeds. The problem addressed by this publication therefore is dominated by wave resistance effects.

For the conversion of speed trials that have been carried out in shallow water to a contractual deep water condition - or vice versa - ITTC recommends correction procedures as formulated by Lackenby or, more recently according to Raven. Both are intended for a specific range of displacement vessels at conventional Froude numbers. The problem at hand is not covered by these methods.

For this reason the speed trial campaign has been extended to not only include speed power recordings at different ship speeds but also at different water depths. The findings have been condensed into an empirical correction method for this specific vessel. The procedure has been successfully applied to the vessel at hand as well as geometrically similar vessels of the same shipyard. A promising speed to water depth relation has been identified which is worth a more thorough investigation by means of an extensive systematic study. The campaign aims at giving more insights into the power demand and squat behaviour of high speed displacement and semi-planning vessels in restricted waterways (i.e. at high depth Froude numbers). A corresponding research project is presently under development with several industrial and research partners involved.

This paper gives an overview of established shallow water correction methods and presents the findings of the trial recordings which resulted in an empirical procedure for the specific ship. The present state of the research project that aims at generalising the findings is described and aspects for future investigations are outlined.

2 REFERENCE TRIAL

2.1 REFERENCE VESSEL

The reference vessel is a search and rescue (SAR) cruiser for which the contract speed is defined in shallow water ($h = 25.0$ m). Relevant main particulars of the vessel are summarised by table 1.

Table 1. Main dimensions of the benchmark vessel

Parameter	Unit	Value
L_{PP}	[m]	24.70
B_{WL}	[m]	5.99
T_M	[m]	1.75
C_B	[-]	0.43

2.2 TRIAL AREA AND PROCEDURE

The sea trial has taken place on the 12th of May 2015 South-South-Westerly of Helgoland. The water temperature was about 9.2 °C. The true wind speed of 11 knots originated from 265° with waves of a height of 0.3 m from approximately the same direction.

The preparation and conduct of the speed trial followed the recommended procedures (ITTC 2017b) and consisted of double-runs, one of which with and the other against the primary wind direction. In addition to the conventional speed trial, recordings at two engine settings have been made during transition from deep (water depth of some 40 m) to shallow water (about 19 m).

The speed and water depth information has been read off manually from the on-board system while dynamic sinkage could not be monitored. The collected data is therefore less accurate than averages of recorded time series would be. Consequently the empirical findings are less robust than would ideally be desired.

3 SHALLOW WATER CORRECTION

3.1 ESTABLISHED CORRECTION METHODS

3.1 (a) Lackenby

One of the most commonly used shallow water correction methods has been formulated by Lackenby (1963) and is based on a test series that has been carried out by Schlichting (1934):

$$\frac{\Delta v}{v} = 0.1242\left(\frac{A_M}{h^2} - 0.05\right) + 1 - \left(\tanh\frac{g\cdot h}{v^2}\right)^{0.5} \quad (1)$$

The underlying data is a limited and very specialised set. The limiting factor is given as:

$$\frac{A_M}{h^2} \geq 0.05 \quad (2)$$

For the present case this ratio is much lower (about 0.02) and according to theory no correction needs to be applied. Consequently, when using the approach, a significant over-correction of the speed is observed.

3.1 (b) Raven

The latest ITTC procedures for speed/power trial analyses (ITTC 2017b) recommend using the procedures outlined by Raven (2016). In contrast to the Lackenby approach, the procedure describes a correction of the resistance instead of the ship speed.

The added resistance without consideration of sinkage effect is defined as:

$$\Delta R_V = R_{V.deep} \cdot 0.57 \cdot \left(\frac{T_M}{h}\right)^{1.79} \quad (3)$$

The additional power demand due to sinkage is based on the Admiral formula and an empirical determination of the sinkage:

$$\Delta P_{D.z} = P_{D.deep} \cdot \left[1.46 \cdot \frac{A_{WP}}{L_{PP}^2}\left[\frac{Fr_h^2}{\sqrt{1-Fr_h^2}} - \frac{Fr_{HD}^2}{\sqrt{1-Fr_{HD}^2}}\right]\right]^{2/3} \quad (4)$$

$$Fr_{HD} = \frac{v_S}{\sqrt{0.3\cdot g\cdot L_{PP}}} \qquad Fr_h = \frac{v_s}{\sqrt{g\cdot h}} \quad (5)$$

The limiting factors are given as:

$$\frac{T_M}{H} < 0.50 \qquad Fr_h < 0.65 \quad (6)$$

The procedure therefore does not cover the range of interest for the present case. If applied anyway, the correction in resistance is negligible and no correction due to sinkage is expected.

3.1 (c) Kreitner

Originally developed to remove the effect of tank dimensions from model test results Kreitner's method (Kreitner 1934) iteratively solves the following condition:

$$\frac{\Delta v+v}{v} + 1\left[1 - m - \frac{1}{2}\cdot Fr_h^2 \cdot \left(\left(\frac{\Delta v+v}{v}\right)^2 - 1\right)\right] = 1 \quad (7)$$

For calculating the waterways cross section which is required for determining the blockage *m*, the width of influence is calculated using the formulation of Barras (2004):

$$b = \left(\frac{7.04}{C_B^{0.85}}\right)\cdot B_{WL} \quad (8)$$

$$m = \frac{A_M}{b\cdot h} \quad (9)$$

Kreitner's assumption that the dynamic sinkage is equal to the drop of water in constrained waterways is sufficiently accurate for bulky vessels (i.e. long parallel midship sections) but may be an inappropriate simplification for the present vessel.

Overall the corrections seem to be too conservative for the present low-blockage vessel with the exception of very high depth Froude numbers for which the output of Kreitner's method increases drastically and tends to infinity.

3.1 (d) ITTC blockage and finite depth corrections

The definitions of Schuster, Scott and Tamura included in ITTC 2017a are intended for blockage correction during model testing.

The approach of Schuster (1956) shown in equation (10) uses the term Fr_h^{10} which approximates the finite depth wave velocity well up to depth Froude numbers of 0.7 and is therefore unsuitable for the high values occurring during the trial. This manifests itself as significant over-corrections of the ship speed.

$$\frac{\Delta v}{v} = \frac{m}{1-m-Fr_h^2} + \left(1 - \frac{R_V}{R_T}\right) \cdot \frac{2}{3} \cdot Fr_h^{10} \qquad (10)$$

In equation (11) formulated by Scott (1970), K_1 is defined in the range of typical Reynolds numbers occurring in model scale and K_2 is only defined for Froude numbers up to 0.38. The method therefore cannot be simply applied to a full scale analysis in a Froude number range of about 0.6 to 0.8.

$$\frac{\Delta v}{v} = K_1 \cdot \nabla \cdot A^{-\frac{3}{2}} + B \cdot L_{PP}^2 \cdot K_2 \cdot A^{-3/2} \qquad (11)$$

Tamura's (1972) approach yields insufficient speed corrections for the present case due to the linear influence of the blockage in the equation.

$$\frac{\Delta v}{v} = 0.67 \cdot m \cdot \left(\frac{L_{PP}}{b}\right)^{\frac{3}{4}} \cdot \frac{1}{1-Fr_h^2} \qquad (12)$$

3.2 DIMENSIONAL CORRECTION PROCEDURE

For the immediate analysis of the sea trial, the speed reduction at a water depth of approximately 19 m has been correlated with the corresponding ship speed in deep water. Under consideration of the amount and quality of the available data, a linear relationship between speed loss and ship speed has been assumed. For the reference vessel and a ship speed between 19 kn and 24 kn, equation (13) sufficiently reflects the speed reduction due to shallow water of about 19 m that has been observed. For intermediate water depths between the defined shallow and deep water conditions, a linear interpolation to Δv = 0 kn at a water depth of h = 40 m is carried out. The procedure has been successfully applied to the reference ship as well as geometrically similar vessels of the same shipyard.

$$\Delta v = 0.0235 \cdot v_{deep} - 0.1541 \quad \text{[kn]} \qquad (13)$$

3.3 NUMERICAL SUBSTANTIATION

3.3 (a) Test case

For substantiation of the empirical findings a numerical test case has been set up. The SAR vessel's hull form as built is considered in the simulations. The shaft lines, rudders and appendages are omitted (bare hull, cf. figure 1) while the integrated trim wedge is included. This simplification is deemed justified as the hull appendages do not have any significant shallow water effect. The flow field around the reference vessel is calculated in full scale using the in-house numerical code FresCo$^+$ (Rung et al. 2009). This is a finite-volume based flow solver optimised for unstructured hexahedral CFD meshes. The governing equations for mass and momentum conservation are solved using a segregated iterative method based on the SIMPLE algorithm. The turbulent boundary layer forming on the hull is treated by a k-ω shear-stress transport model in conjunction with wall functions. A volume-of-fluid method combined with a HRIC scheme is used to capture the free-surface elevation created by the hull. The CFD mesh is massively refined around the free surface so as to capture potential wave breaking of the bow and stern waves.

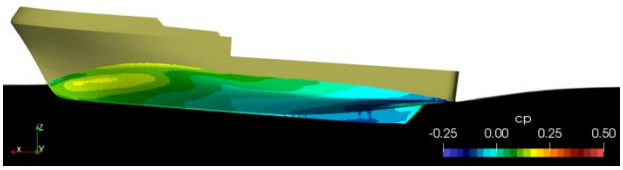

Figure 1. Bare hull of the reference SAR vessel

In the first phase, only resistance computations are carried out, i.e. the propulsion influence is omitted. Although this simplification will have a certain effect on the dynamic flotation (squat) of the ship, it is assumed that the results nonetheless sufficiently reflect the empirical findings because the shallow water effects for the present case are mostly due to wave making rather than blockage (i.e. a large depth Froude number in conjunction with a slender hull) which are well described by resistance computations. The purpose of the simulations is a check of the trend described by equation (13) rather than a strict validation.

The CFD test matrix consists of nine simulations covering three speeds at three different water depths. These depths represent typical values encountered in the course of the sea trials. The corresponding depth Froude numbers are compiled in table 2.

Table 2. Depth Froude number Fr_h vs. speed and water depth

	v = 19 kn Fr = 0.63	v = 22 kn Fr = 0.73	v = 24 kn Fr = 0.79
h = 19.5 m	**0.71**	**0.82**	**0.89**
h = 26.8 m	**0.60**	**0.70**	**0.76**
h = 42.0 m	**0.48**	**0.56**	**0.61**

3.3 (b) Findings of the CFD study

The CFD simulations reveal a strong dependence of the dynamic sinkage on both the ship speed and the water depth (figure 2a). In shallow water, the hull is significantly

lifted out of the water ($z_{sink} < 0$) for increasing speed, yielding a nearly linear relation with negative slope. The opposite holds in deep water, where a much weaker variation of sinkage versus speed is observed. The trim angle is in general less sensitive to the speed and the water depth than the sinkage (figure 2b). The largest sternward trim is observed at the lowest speed which is consistent with deep-water model tests of the SAR vessel conducted at HSVA.

Figure 3 shows a comparison of the pressure distribution on the hull in shallow and deep water for the intermediate ship speed (22 kn) exemplarily. The hull pressure does not differ very much, confirming that flow acceleration below the hull owing to blockage does indeed not play a significant role. In contrast, the ship-created wave field exhibits somewhat greater differences between shallow and deep water (figure 4). Most remarkably, the transverse waves downstream of the vessel become longer for decreasing water depth, which is a known shallow-water effect in the subcritical Fn_h regime. For a water depth of 19.5 m, the maximum and minimum wave elevations are 1.42 m and -1.16 m, respectively, while the corresponding values for 42.0 m water depth are 1.35 m and -1.13 m. This may be interpreted as a first indicator of the increased wave resistance in shallow water, although the differences are small and possibly within the numerical accuracy of the volume-of-fluid method.

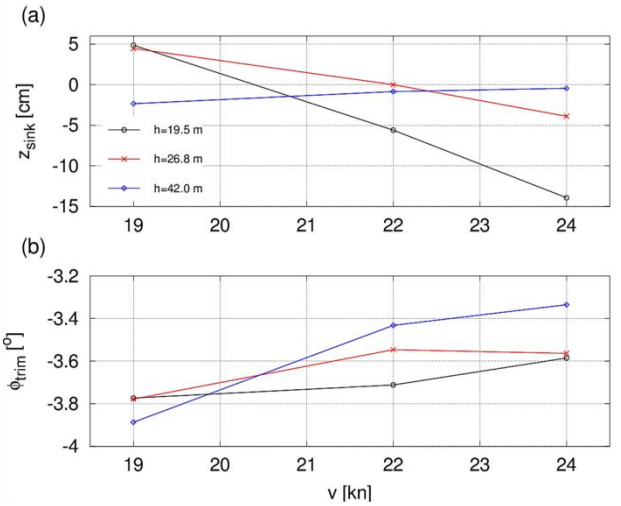

Figure 2. (a) Sinkage at $L_{pp}/2$ and (b) trim angle (< 0: sternward) vs. speed for three water depths

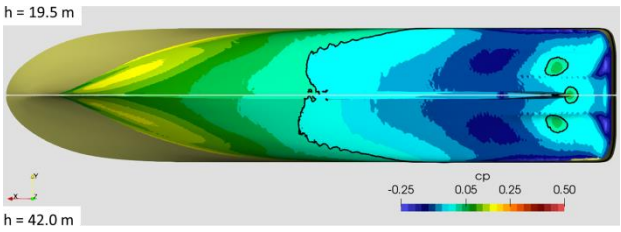

Figure 3. Hull pressure in shallow (top) and deep water (bottom) for v = 22 kn

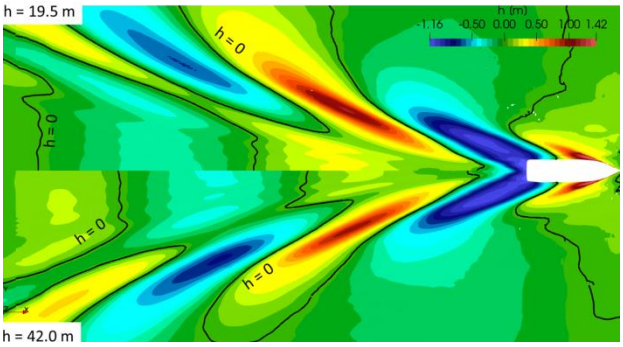

Figure 4. Wave pattern in shallow (top) and deep water (bottom) for v = 22 kn

At the lowest tested speed of 19 kn, the total resistance of the two shallower water conditions is remarkably higher compared to the deep water condition (figure 5a and table 3). This is partly attributed to the observed larger sinkage of the vessel. It is also seen that the resistance difference between shallow and deep water is larger at 24 kn than at the two lower speeds. This becomes even more manifest when considering the total resistance coefficient (figure 5b and table 4): while $c_{T,bare}$ is nearly constant at 19 kn there is a larger difference at 22 and 24 kn. This finding is in line with the trend given by equation (13) in that the speed loss (i.e. added resistance) due to shallow water grows for increasing ship speed. The resistance coefficients reported in table 4 are in good agreement with those obtained in the tank tests of the SAR vessel conducted at HSVA.

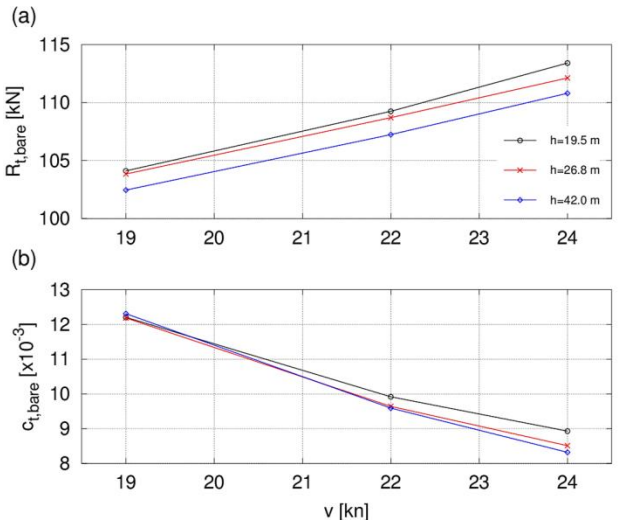

Figure 5. (a) Bare-hull resistance and (b) resistance coefficient vs. speed for three water depths

Table 3. Bare-hull resistance $R_{T,bare}$ [kN] vs. ship speed and water depth

	v = 19 kn	v = 22 kn	v = 24 kn
h = 19.5 m	**104.1**	**109.3**	**113.4**
h = 26.8 m	**103.8**	**108.7**	**112.1**
h = 42.0 m	**102.5**	**107.2**	**110.8**

Table 4. Resistance coefficient $c_{T,bare}$ [$\times 10^{-3}$] based on the actual wetted surface vs. ship speed and water depth

	v = 19 kn	v = 22 kn	v = 24 kn
h = 19.5 m	**12.20**	**9.92**	**8.93**
h = 26.8 m	**12.18**	**9.64**	**8.51**
h = 42.0 m	**12.30**	**9.59**	**8.32**

3.4 COMPARISON OF CFD AND EFD RESULTS

The relative change in resistance that has been found by means of CFD computations for each speed is used to convert the model test predictions to shallow water conditions. The intermediate speeds that were not part of the numerical test matrix are interpolated using an Akima (1970) spline. From the relation of the deep and the shallow water resistance curves, the corresponding speed losses are determined.

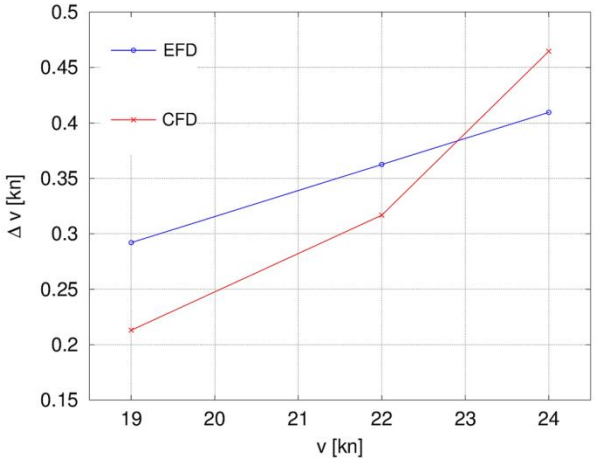

Figure 6. Speed loss as a function of ship speed for h = 19.5 m according to empricial findings (EFD) and numerical simulations (CFD)

In line with the observations made during the speed trial, the relative speed loss at 19 kn is about 0.2-0.3 kn and increases with increasing ship speed (figure 6). It is noted that the slope of the Δv-v curve of the numerical analysis is predicted steeper than the experimentally determined curve, resulting in a somewhat higher speed correction at 24 kn and lower corrections at the low speeds when compared to the empirical equation (13).

4 CONCLUSIONS

The promising speed to water depth relation that has been identified for the specific field case has been substantiated by means of a basic numerical study. From comparing EFD with CFD it is found that the empirical correction, which has been developed and used for the analysis of the speed trials, may be considered a representative approach for determining the speed loss due to shallow water of ships comparable to the present SAR vessel.

The purpose of the CFD study was to confirm the general trend of speed loss – or added resistance – observed during the sea trials while it cannot be seen as a strict validation owing to the different physical quantities considered (speed vs. resistance). It is also pointed out that full-scale CFD simulations of semi-planning ships at high Froude numbers are still challenging, and therefore the present numerical results have limited accuracy (about ±5%). The shallow-water speed correction found by CFD is in the range of 0.2-0.5 kn for the present vessel, and the corresponding corrections obtained by equation (13) fall within this range.

It is concluded that this newly developed empirical correction formula is superior to the established correction methods (cf. section 3.1) for the present type of displacement to semi-planning hull form.

5 FURTHER INVESTIGATIONS

It seems worthwhile to further the investigation by means of an extensive systematic study that covers a wider range of speeds and water depths as well as different ship shapes and sizes. The first gives a means for improving the present empirical equation while the latter provides information on the feasibility of generalising the findings for other field cases.

Besides of numerical analyses (resistance as well as propulsion), physical model tests should be conducted for further validation and as base for a more sophisticated empirical formulation of the speed loss due to shallow water for high speed vessels. Additional CFD calculations should be carried out at a constant resistance/power level for each water depth to determine the actual speed loss instead of analysing the resistance/power increase at one speed. If the opportunity arises, additional speed trial recordings at different water depths should be conducted, in which the speed and locations are taken from a GPS or the on-board system to extract even more reliable averaged data from the time series.

6 ACKNOWLEDGEMENTS

The authors would like to thank the participating shipyard and the owner of the reference vessel for extending the speed trial test scope and sharing the valuable data.

7 REFERENCES

Akima, H., 1970, A new method of interpolation and smooth curve fitting based on local procedures, Journal of the ACM, vol. 17, no. 4

Barras, C. B., 2004, Thirty-two years of research into ship squat, 2nd Squat Workshop

ITTC, 2017a, Resistance Test, Recommended procedures and guidelines 7.5-02-02-01, rev. 04

ITTC, 2017b, Preparation, conduct and analysis of speed/power trials, Recommended procedures and guidelines 7.5-04-01-01.1, rev. 07

Kreitner, J., 1934, Über den Schiffswiderstand auf beschränktem Wasser, Werft, Reederei, Hafen, 15-7 (in German)

Lackenby, H., 1963, The effect of shallow water on ship speed, Shipbuilder No. 672

Raven, H. C., 2016, A new correction procedure for shallow-water effects in ship speed trials, in Proc. PRADS2016

Raven, H. C., 2018, A method to correct shallow-water model tests for tank wall effects, Journal of Marine Science and Technology Issue 2

Rung, T., Wöckner, K., Manzke, M., Brunswig, J., Stück, A., Ulric,h C., 2009, Challenges and Perspectives for Maritime CFD Applications, Jahrbuch der Schiffbau-technischen Gesellschaft 103

Schlichting, O., 1934, Schiffswiderstand auf beschränkter Wassertiefe – Widerstand von Seeschiffen auf flachem Wasser, Jahrbuch der Schiffbau-technischen Gesellschaft 35 (in German)

Schuster, S., 1955/56, Beitrag zur Frage der Kanalkorrektur bei Modellversuchen, Schiffstechnik Bd, 3 (in German)

Scott, J. R., 1970, A comparison of two ship resistance estimators, RINA Transactions Vol 112

Tamura, K., 1972, Study of the blockage correction, Journal of the Society of Naval Architects of Japan Vol 131

8 AUTHORS BIOGRAPHY

Jan Richter holds the current position of software engineer and project manager at HSVA. He is responsible for in-house software development, calm water model tests and full scale trials. His previous experience includes model testing and simulations of manoeuvrability in shallow and confined waters.

Lars-Uve Schrader holds the current position of researcher and project manager at HSVA. He is responsible for the development and application of CFD methods in the marine field. His previous experience includes the simulation of hydro- and aerodynamics in the maritime and aeronautical context.

Oliver Reinholz holds the current position of deputy head of HSVA's resistance and propulsion department. He is responsible for calm water model tests and full scale trials. His previous experience includes model testing and sea trial participations in shallow and confined water.

SIMULATION STUDY OF APPROACH MANOEUVRE IN LIGHTERING AND REVERSE LIGHTERING OPERATIONS

Masaaki Sano and Hironori Yasukawa,
Hiroshima University, Japan

SIMULATION STUDY OF APPROACH MANOEUVRE IN LIGHTERING AND REVERSE LIGHTERING OPERATIONS

Masaaki Sano and **Hironori Yasukawa,** Hiroshima University, Japan

SUMMARY

Generally, there exists a case wherein a laden service ship approaches a partially loaded very large crude carrier (VLCC) for cargo transfer. This process is called 'reverse lightering operation'. The manoeuvrability of these nearly fully loaded ships, taking the interaction loads, should be understood for the operation safety. This study first establishes a practical method to simulate the approach manoeuvre, considering the interaction loads estimated by a 3D panel method, and other loads based on experiments. A standard approach manoeuvre of an Aframax tanker to a VLCC is simulated, and the difference in the behaviour of conventional lightering operation and reverse lightering operation is discussed. As a result, the service ship was found to be more difficult in keeping the heading angle in parallel with the VLCC, at the final phase of the approach manoeuvre in the reverse lightering operation. This is because of the increase of the interaction loads.

NOMENCLATURE

F_r	Froude number
F_{Ai}	Force and moment due to time derivative of velocity potential (N, N m)
F_{Di}	Force and moment due to square of velocity potential (N, N m)
F_{VEi}	Force and moment due to manoeuvre, propeller and rudder (N, N m)
G-$x_s y_s z_s$	Ship-fixed coordinate system (m)
I_z	Yaw moment of inertia of ship (kg m^2)
k	Ship's number
L_{PP}	Ship's length of perpendiculars (m)
m	Ship's mass (kg)
m_{ji}	Added mass with respect to j^{th} force induced by motion of i^{th} mode (kg, kg m^2)
N_H	Yaw moment acting on bare hull due to manoeuvre (N m)
O-xyz	Earth-fixed coordinate system (m)
P, D, G_y	Feedback control gains of steering (-)
r	Yaw velocity (s^{-1})
t	time (s)
u	Surge velocity (m s^{-1})
U_i	Unified notation representing motions of two ships (m s^{-1}, s^{-1})
v	Sway velocity (m s^{-1})
(x_a, y_a)	Coordinate value based on relative positional relationship of two ships (m)
Y_H	Sway force acting on bare hull due to manoeuvre (N)
β	Drift angle
δ	Rudder angle
ψ	Heading angle
Δx	Contact location from midship (m)

1 INTRODUCTION

When a large fully loaded ship faces difficulty in accessing a port due to insufficient water depth, a lightering operation is commonly performed. In this operation, cargoes such as crude oil and petroleum products are transferred from a large ship, typically a very large crude carrier (VLCC), to a small service ship, like an Aframax tanker. Conduction of this operation is anticipated to grow, as the size of ships continues to increase to take advantage of the huge economies of scale. The ship-to-ship (STS) transfer guidebook published by ICS/OCIMF (2005) describes a common procedure of the operation, and contains recommendations on safety. It has been widely used and will be important for the years to come.

On the other hand, there exists a case where a laden service ship approaches a larger and partially loaded ship, and the cargoes are transferred from the service ship to the larger ship. This is called as reverse lightering operation. Because the nearly fully loaded ships have to move in close proximity, a high potential collision risk is of concern. Therefore, the manoeuvrability of these ships, along with the interaction loads between them, should be understood well for the operation safety. Although the information paper (2009) published by OCIMF provides the guidelines and considerations applicable to a reverse lightering operation, it would be more preferable to discuss the behaviours of these ships during the approach manoeuvre, in association with the interaction loads.

Because the STS transfer and the interaction between two ships in close proximity have always been some interesting topics, many experimental studies (e.g., Vantorre et al., 2002; Lataire et al., 2012), theoretical studies (e.g., Yasukawa, 2003; Xiang et al., 2011) and computational fluid dynamics (CFD) works (e.g., Mousaviraad et al., 2011; Zou and Larsson, 2013) have been performed. In this study, we first establish an original practical method to simulate the approach manoeuvre in both lightering and reverse lightering operations. The added masses and the non-lifting hydrodynamic interaction loads acting on the two ships in close proximity are calculated by a three-dimensional boundary element method which was suggested by one of the authors, Yasukawa (2003). When solving the motion equations, they are updated in each time step, according to the relative positional relationship. This kind of method based on potential theory has a weak point that it could not consider the viscous effect on interaction loads between hulls. However, because of the quick

calculation, it would facilitate simulations and could be regarded as one of practical methods applicable to a simulator. Other terms, i.e. resistance, hydrodynamic manoeuvring loads (damping terms due to viscosity), and propeller thrust and rudder force, are assumed not to interact with each other, and are estimated by a towing tank experiment for each ship. The mathematical modelling of these terms follows the MMG model (Yasukawa and Yoshimura, 2015).

A standard approach manoeuvre of an Aframax tanker to a VLCC is simulated. Especially, the difference in the behaviour of these ships in conventional lightering operation and reverse lightering operation is discussed in association with the difference of the interaction loads. The outcome of such a discussion would be useful to understand points to notice for the safe manoeuvring technique.

2 MANOEUVRING MOTION EQUATIONS

The coordinate systems are shown in Figure 1. The right hand and space-fixed coordinate system with the *xy* plane referring to the water surface is defined as *O-xyz*. The heading angle of each ship is defined from this *x* axis. $G^{(k)}$-$x_s^{(k)}y_s^{(k)}z_s^{(k)}$ is the right-hand and ship *k*-fixed coordinate system in which the origin is defined at the centre of gravity of the ship *k*. $x_s^{(k)}$ and $y_s^{(k)}$ are each ship's forward and lateral directions.

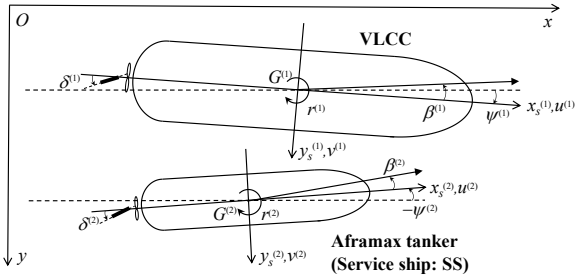

Figure 1. Space and ship-fixed coordinate systems for two ships manoeuvring in proximity

The manoeuvring motion equations of two ships in close proximity were presented Yasukawa (2003). They were derived within the potential theory simply assuming a rigid wall free surface. It might be accepted because the speed of both vessels is sufficiently small during operations. Eq. (1) shows the three-dimensional motion equations for surge, sway, and yaw respectively. The interaction loads acting on these hulls explicitly appear in the right hand side of each equation, i.e., F_{Ai} and F_{Di}.

$$\left.\begin{aligned} m^{(k)}\left(\dot{u}^{(k)} - v^{(k)}r^{(k)}\right) &= F_{A1}^{(k)} + F_{D1}^{(k)} + F_{VE1}^{(k)} \\ m^{(k)}\left(\dot{v}^{(k)} + u^{(k)}r^{(k)}\right) &= F_{A2}^{(k)} + F_{D2}^{(k)} + F_{VE2}^{(k)} \\ I_z^{(k)}\dot{r}^{(k)} &= F_{A3}^{(k)} + F_{D3}^{(k)} + F_{VE3}^{(k)} \end{aligned}\right\} \quad (1)$$

where differential function of time is distinguished by putting a dot above the character. $F_{Ai}^{(k)}$ denotes the load term of Ship *k* in the i^{th} (1:surge, 2:sway, 3:yaw) direction due to the time derivative of the velocity potential, and $F_{Di}^{(k)}$ indicates the load term due to the quasi-steady pressure with respect to the square of the velocity potential. They are considered as interaction loads, and calculated by a 3D panel method as a function of the ship position in every time step. The complete expression of each term can be referred in Yasukawa (2003) and is omitted here because of their complexity. As an example, $F_{A2}^{(1)}$ is eventually expressed as follows:

$$F_{A2}^{(1)} = -\sum_{i=1}^{6}\left[\dot{U}_i m_{2i} + U_i \dot{m}_{2i} + U_i U_3 m_{1i}\right] \quad (2)$$

where *i* takes the value from 1 to 6, *i*<=3 and *i*>4 corresponding to the surge, sway, and yaw motions of Ship 1 and Ship 2, respectively. U_i has the following relation with each velocity component:

$$U_{i=1,2,3,4,5,6} = u^{(1)}, v^{(1)}, r^{(1)}, u^{(2)}, v^{(2)}, r^{(2)} \quad (3)$$

m_{ji} in Eq. (2) indicates the added mass and added moment of inertia with respect to the j^{th} force induced by motion of the i^{th} mode. For example, m_{25} indicates the added mass in sway of Ship1 due to the sway motion of Ship 2. Meanwhile, m_{53} indicates the equivalent term of Ship 2 due to the yaw motion of Ship 1. Therefore, they can be considered as the interaction between two ships, and we see the interaction can be represented by these terms in the manoeuvring simulation. For the validation of this method, we have applied essentially the same method to the case of a ship-bank interaction and ship-ship interaction, and compared to experimental results (Yasukawa et al., 2009). Although the quantitative accuracy was not necessarily sufficient, the qualitative tendency of the interaction loads could be captured by this method.

$F_{VEi}^{(k)}$, represents the damping forces in manoeuvres due to viscous fluid, propeller thrust, and rudder force. It is formulated based on the MMG model. A series of coefficients required to express each hydrodynamic load needs to be identified by towing tank experiments for each ship. They are described in the following chapter.

3 TOWING TANK EXPERIMENT

3.1 SUBJECT SHIPS

Since the combined use of a VLCC and an Aframax tanker is standard for ships engaged in STS transfers, KVLCC2 (SIMMAN workshop, 2008) was selected as the VLCC, and an Aframax tanker which was designed with reference to Lataire et al. (2009), was used as the service ship (SS). The principal dimensions of each ship including the two loading conditions are listed in Table 1. The fully-loaded VLCC and the SS in ballast condition combination was considered for lightering operation, whereas the partially loaded VLCC and the fully laden SS combination was assumed for reverse lightering operation. Hereinafter, the VLCC is labeled as "*k*=1", and the SS as "*k*=2". Figure 2 shows the illustration of each operation.

Table 1. Principal dimensions of the VLCC and SS

Ship type	VLCC		SS	
Loading condition	Full	Partial	Ballast	Full
Length (m)	320	320	230.4	230.4
Breadth (m)	58	58	42	42
Draft at F.P. (m)	20.8	15.12	7.5	15
Draft at midship (m)	20.8	15.12	8.3	15
Draft at A.P. (m)	20.8	15.12	9.1	15
Displacement (m^3)	312622	219625	58207	112694
WSA (m^2)	27194	22985	10257	13785
Block coefficient	0.810	0.783	0.725	0.776
LCB (m)	11.33	14.56	6.77	7.50

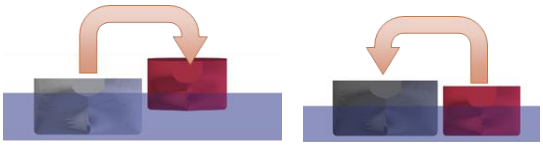

Figure 2. Illustration of lightering operation (left) and reverse lightering operation (right)

Captive model tests with 1/110 scale ship models were conducted to identify the term $F_{VEi}^{(k)}$ for the conditions of the full-load SS, ballast-load SS, and partially-loaded VLCC. In the case of full-load VLCC, most experimental coefficients were available for this study from Sano and Yasukawa (2008). The experimental ship's speed was set at $F_r = 0.055$, corresponding to 6 knots in real scale. Figure 3 shows photos of the VLCC and SS models.

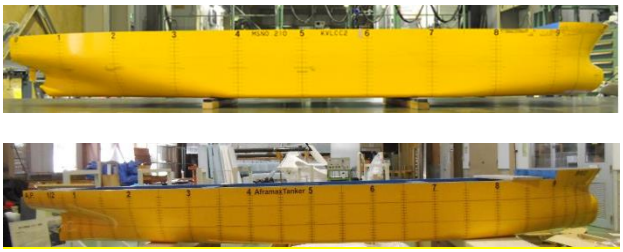

Figure 3. Photos of the 1/110-scale VLCC model (upper) and Aframax tanker model (lower)

3.2 MEASURED HYDRODYNAMIC LOADS

Figure 4 shows the sway force and yaw moment around the midship for the bare hull of the SS in manoeuvring, nondimensionalized by using the length and draft of each loading condition of the SS, i.e., $Y_H^{(2)\prime}$ and $N_H^{(2)\prime}$. The superscript $'$ means it is the nondimensional value. They were measured in the circular motion test (CMT) with multiple combinations of yaw velocity and drift angle. Because the component of the rudder force was subtracted from the measured value, they show symmetry about the origin. Meanwhile, they still include the inertia term so that the symbol, "*", is added to be distinguished from the excluded one. It can be seen that the hydrodynamic load in manoeuvring is influenced by the loading condition of the SS. Especially, the nondimensional yaw moment on the bare hull under the full-load condition seems significantly different from the ballast condition.

4 MANOEUVRING SIMULATION OF THE SS

Since the loading condition of the SS is different between the lightering and reverse lightering operations, the basic manoeuvrability of the SS should be investigated first. The turning and zigzag simulations were executed, simply based on the model scale, assuming the interaction terms of $F_{Ai}^{(k)}$ and $F_{Di}^{(k)}$ to be zero.

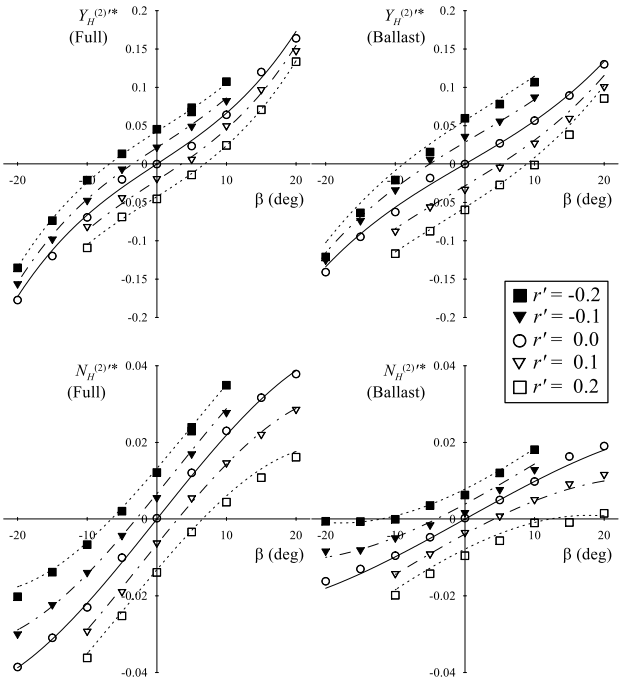

Figure 4. Hydrodynamic loads acting on the bare hull of the SS under the full-load and ballast-load conditions measured in CMT

Figure 5 shows the 5° turning trajectories, and Figure 6 shows the time-series of heading and rudder angles in 5°/5° zigzag manoeuvres. Such a small steering angle was used for the simulations because a sufficiently small and slow manoeuvre by the small steering of the SS was anticipated during the operation. The values of x, y and t were nondimensionalized by using the length of the SS and its initial velocity.

The turning circle diameter of the full-load SS is smaller than that of the ballast condition. Although it indicates a better turning ability, the deterioration of the course keeping performance should be considered. Further, the longer advance for turning signifies the late response to the steering. Indeed, we see the steering response of the full-load SS significantly worsens than the ballast condition during zigzag manoeuvres. This would concern us about the difficulty in approach manoeuvres of the SS during the reverse lightering operation.

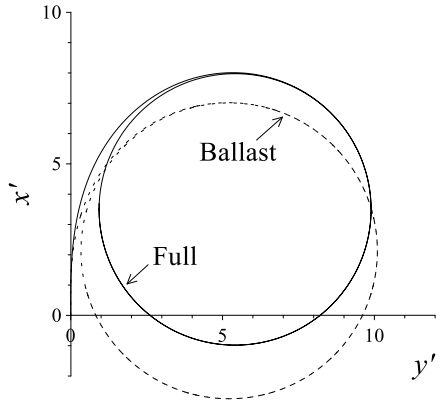

Figure 5. Simulated trajectories of 5° turning manoeuvre of the full-load and ballast-load SS

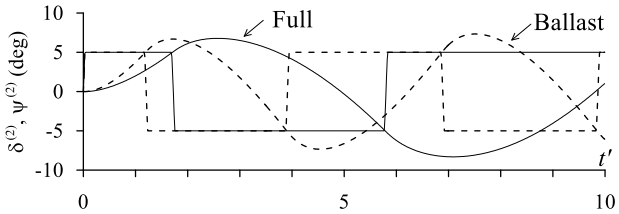

Figure 6. Simulated time-series of heading and rudder angles in 5/5 zigzag manoeuvre of the SS

5 HYDRODYNAMIC INTERACTION LOADS BETWEEN TWO HULLS

The magnitude of interaction loads, which changes according to the positional relationship of the two ships and each loading condition, is evaluated by the three-dimensional panel method based on potential theory. Figure 7 shows the panel arrangement of the bare hull of the full-load VLCC and the full-load SS where each hull surface was divided by 720 panels. This number of panels were adopted, because the added masses in surge and sway, and added moment of inertia in yaw of the same VLCC calculated by the same panel method agreed with the result based on 1320 panels, and it also agreed with the result based on Motora's empirical charts (Sano and Yasukawa, 2019).

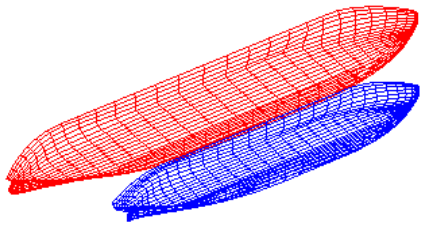

Figure 7. Panel arrangement of the partially loaded VLCC and the full-load SS in the reverse lightering

We define the relative position of the midship of the SS from the midship of the VLCC as (x_a, y_a). Assuming the VLCC and the SS head in the same direction, the contours of nondimensional sway force and yaw moment acting on the SS due to the interaction, i.e., $F_{A2}^{(2)\prime} + F_{D2}^{(2)\prime}$ and $F_{A3}^{(2)\prime} + F_{D3}^{(2)\prime}$, are shown in Figure 8 and Figure 9 respectively. They were nondimensionalized by the length and the full-load draft of the VLCC. The relative positions nondimensionalized by the length of the VLCC are taken as the vertical and horizontal axes in these figures. The range of the vertical axis is from $x_a'(= x_a/L_{PP}^{(1)})$ = -0.5 to 0.5, and the left end of the horizontal axis is taken as y_a'=0.167, corresponding to the diameter of the fender which was assumed as 3.3 m. The interpretation of the contour maps is as follows. The contour colour represents the magnitude of interaction sway force (Figure 8) and yaw moment (Figure 9) experienced by the SS. When the SS is located at the relative position from the VLCC indicated by the circle in the left side illustration, it is supposed to take the interaction load corresponding to the contour colour at the same position in the contour maps.

From Figure 8, the comparison of the contour maps of these operations show that a significant interaction sway force acts on the SS during the reverse lightering operation. The negative sign denotes that the SS takes the attraction force to the VLCC. Because the counter colour is the darkest near the relative position (x_a', y_a') = (0, 0.167) which is the final stage of the approach manoeuvre, the SS takes the largest attraction force when the two ships are parallel and run close.

Furthermore, in the case of interaction yaw moment in Figure 9, the bow-out moment which turns the bow outside acts on the SS, when its midship is located ahead of the midship of the VLCC. Meanwhile, the bow-in moment acts on the SS when it is behind the VLCC. It can be clearly seen that the direction of the interaction yaw moment depends on the relative positional relationship. In the reverse lightering operation, it becomes more significant, and the SS would be influenced in the wider area around the VLCC. This result indicates that it would be preferable for two ships to run while arranging each midship side by side and come close, because the SS could easily maintain the heading angle during the approach manoeuvre due to the small interaction yaw moment.

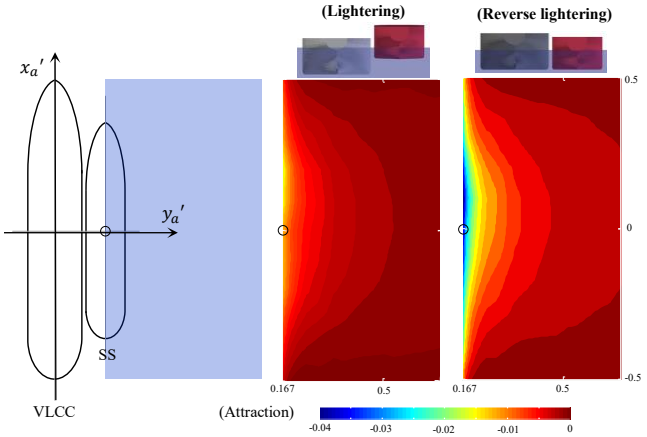

Figure 8. Contours of the interaction sway force: $F_{A2}^{(2)\prime} + F_{D2}^{(2)\prime}$ acting on the SS with respect to the relative position from the VLCC

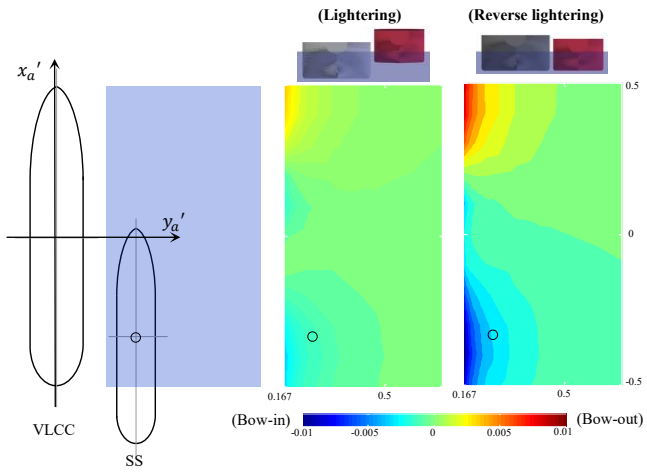

Figure 9. Contours of the interaction yaw moment: $F_{A3}^{(2)\prime} + F_{D3}^{(2)\prime}$ acting on the SS with respect to the relative position from the VLCC

6 APPROACH MANOEUVRE SIMULATION

6.1 MATHEMATICAL MODEL

Manoeuvring motion equations described in Chapter 2 were solved to simulate the lightering and reverse lightering operations. The term $F_{VEi}^{(k)}$ including the damping force due to the manoeuvre, propeller thrust, and rudder force was identified by the towing tank experiments (Chapter 3), and the term $F_{Ai}^{(k)} + F_{Di}^{(k)}$ as the interaction loads was estimated by the 3D panel method (Chapter 5). They were simply scaled up to the real scale and used for the following simulation. Because the fender was not modelled, the approach manoeuvre was suspended when the SS contacted the VLCC.

Hereinafter, the length, the full-load draft and the initial velocity of the VLCC were consistently used for the non-dimensionalization.

6.2 RESULT AND DISCUSSION

6.2 (a) Scenario

The STS transfer guidebook (2005) provides the guidelines for manoeuvring, alongside two ships under power. It recommends that the port side of the SS approaches and berths to the starboard side of the VLCC, and the two ships should preferably travel parallel and at the same speed. In this study, the scenario where the SS tries to contact the constant heading VLCC which runs parallel to the SS at 6 knots along the straight line of y=0 was considered. The initial position was set at y=140 m or $y'(=y/L_{PP}^{(1)})$=0.438, far from the VLCC in the lateral direction.

The PD control was adopted for steering during the approach manoeuvre, based on which the deviation of the heading angle and yaw velocity from the target value, i.e., zero, was adjusted. In addition, the deviation of the lateral distance from the line of y'=0 was feedback controlled to make the VLCC keep the course and make the SS close to the VLCC. The rudder angle of these ships during the approach manoeuvre is given by the following equation:

$$\delta^{(k)} = P^{(k)}\psi^{(k)} + D^{(k)}r'^{(k)} + G_y^{(k)}y'^{(k)} \quad (4)$$

Where the gains of P and D were fixed at 6. According to Eda (1971) who discussed the directional stability and control of ships in restricted channels, these gains are called 'control with high sensitivity' derived from the pattern of rudder activity. The gain of the deviation of the lateral distance, G_y, was set at 6 for the steering of the VLCC to enable maintaining the straight course. Meanwhile, it was set as 1 for the SS to enable reducing the excessive change of the SS's heading direction during the approach manoeuvre. The propeller revolution of these ships was also adjusted by feedback control to compensate the deviation of the speed from the target speed due to manoeuvres and the deviation of the longitudinal position from the target contact point.

6.2 (b) Trajectory

The simulated ship trajectories are shown in Figure 10. When the ships engaged in the reverse lightering operation are controlled by the same steering technique as the lightering operation, a longer distance would be required to complete the approach manoeuvre until the contact. This is because a larger displacement (the inertia force), added mass, and damping sway force act on the full-load SS, and the sway motion does not occur earlier. Therefore, it is seen that a large sea area would be recommended for the reverse lightering operation.

The paths of the center of gravity (CoG) of the VLCC are drawn in Figure 11. The VLCC, which is supposed to maintain a constant course during the operation, deviates from the path slightly towards the SS in the reverse lightering operation. This is caused by the strong interaction sway force, which acts on the VLCC as the attraction force attracting its hull towards the SS, and the small sway damping force due to the small draft of the partially loaded VLCC.

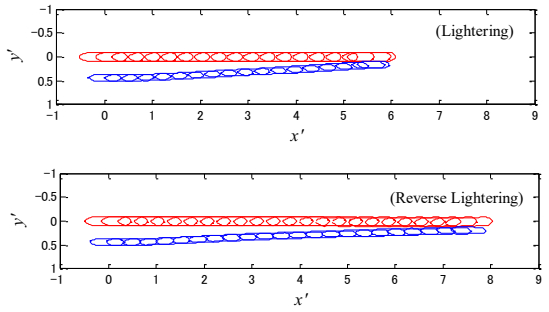

Figure 10. Simulated trajectories of two ships during approach manoeuvre

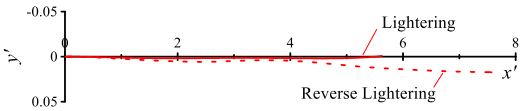

Figure 11. Deviation of the path of the CoG of the VLCC during approach manoeuvre

6.2 (c) Heading angle and rudder angle

The time-series graphs of the heading angle and rudder angle during the approach manoeuvre are shown in Figure 12 (Lightering) and Figure 13 (Reverse lightering). The non-dimensional time is taken as the horizontal axis.

The heading direction of the SS shifts towards the VLCC, i.e. $\psi^{(2)} < 0$, at the initial stage to start moving closer to the VLCC. Although these ships come nearly parallel, i.e., $\psi^{(2)} \approx \psi^{(1)}$, they eventually turn the bow outside each other at the end of the approach, i.e., $\psi^{(1)} < 0$ and $\psi^{(2)} > 0$. This is caused by the interaction bow out moment. The resultant deviation of the heading angle, i.e. the difference in the heading angle between the SS (blue line) and the VLCC (red line), seems more significant in the reverse lightering operation. This indicates that the parallel contact, which is commonly recommended, would be more difficult under this operation.

Further, the time-series of the rudder angle signifies the difficulty in the reverse lightering operation, because a large amount of steering would be required during the operation. Such a large steering in close proximity might impose heavy stresses on the ship operators, who are responsible for the safe operation.

6.2 (d) Sway velocity and added mass

In order to select proper fenders, the kinetic energy at the contact is important. Because the sway velocity and the amount of added mass, as well as the mass are key factors, Figures 12 and 13 show the time series of the sway velocity and nondimensional added mass in sway during each operation.

From the slope of the line of the sway velocity, the sway acceleration of the SS in the reverse lightering operation is smaller than that in the lightering operation, and it eventually contacts the VLCC at a slower sway speed. Meanwhile, because the VLCC in the reverse lightering operation is attracted due to the large interaction sway force and moves towards the SS, the resultant relative sway velocity of the SS at contact does not seem significantly different between these operations. From the same figure, it is seen that the added mass in sway of the SS and the VLCC, i.e., m_{22}' and m_{55}' respectively, increases as the SS closely approaches the VLCC in both operations. This is the same phenomenon as a bank effect on the added mass for a ship sailing near a bank (Sano et al., 2014). The added mass in sway of the SS at the contact in the reverse lightering operation reaches about three times larger than that in the lightering operation.

Due to the increase of the mass and added mass in sway of the SS, the kinetic energy significantly increases in the reverse lightering operation. This kind of simulation would be helpful in evaluating the approach manoeuvre, and for proper fender selection according to the operation type.

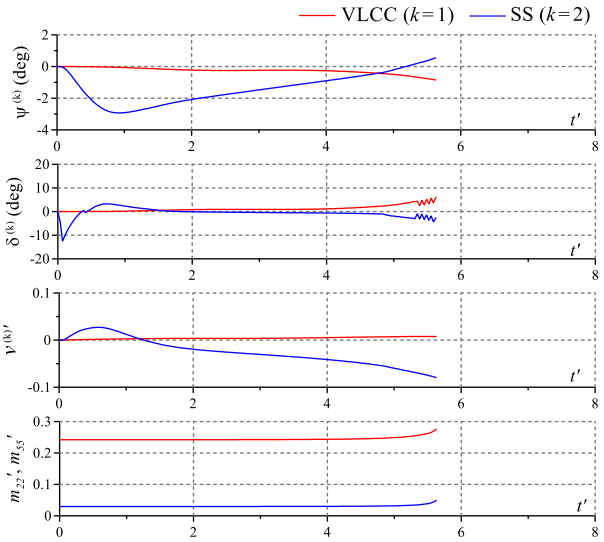

Figure 12. Time-series of heading angle, rudder angle, sway velocity and added mass in sway during the lightering operation

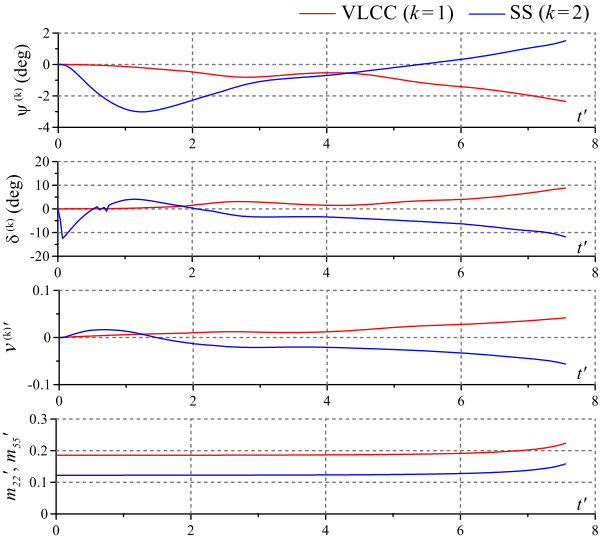

Figure 13. Time-series of heading angle, rudder angle, sway velocity and added mass in sway during the reverse lightering operation

6.2 (e) Influence of contact location

A scenario when the SS contacts the VLCC with a small deviation from the midship is simulated. The contact location of the SS is assumed at the front and back of the midship of the VLCC as $\Delta x = \pm 0.1 L_{PP}^{(1)}$. The time-series graphs of the heading and rudder angles are shown in Figures 14 (Lightering) and Figure 15(Reverse lightering).

It can be seen that the heading direction is influenced by the contact location, especially in the case of the VLCC in the reverse lightering operation, i.e., red lines in Figure 15. In this case, the required rudder angle for course keeping of the VLCC increases beyond $\delta^{(1)}$=+10 ° steering to the starboard side, when they are contacted at $\Delta x'$= -0.1. However, the steering to the port side, i.e., $\delta^{(1)}$<0, is required in the case of +0.1. This fact indicates that a sensitive steering of the VLCC would be required for course keeping, corresponding to a slight deviation of the contact location. A similar difference in steering between different contact locations is seen in the lightering operation, too (Figure. 14).

The SS, i.e., blue lines, meanwhile, has a small difference in steering between them in both operations. It is because the SS needs to keep steering to the port, i.e., $\delta^{(2)}$<0, to move closer to the VLCC, and the difference does not seem noticeable.

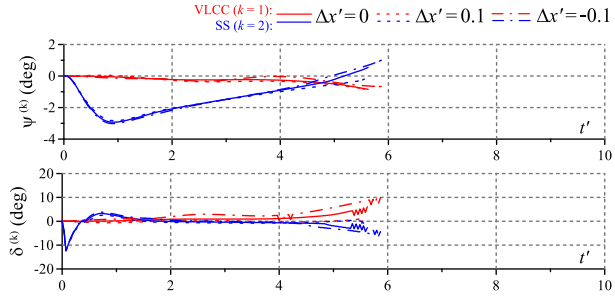

Figure 14. Influence of multiple contact locations on the heading angle and rudder angle during the lightering operation

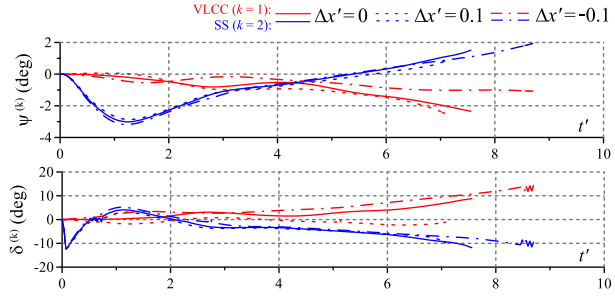

Figure 15. Influence of multiple contact locations on the heading angle and rudder angle during the reverse lightering operation

7 CONCLUSION

One of mathematical models to simulate the approach manoeuvre in the lightering and reverse lightering operations was presented. As two ships move in close proximity, the pattern of streamlines between their hulls changes, indicating the flow velocity, pressure distribution there and lateral force acting on two ships changes. In the presented method, this phenomenon is represented through the change of added mass due to the time-dependent velocity potential. It is regarded as one of main components of the interaction loads. Although the viscous effect on the interaction loads or the influence of the growth of boundary layer on each side hull surface when the gap is too small cannot be considered, this potential theory-based method would be preferable for a simulator because of its quick calculation.

To evaluate the damping loads on the bare hull due to the manoeuvres, propeller thrust, and rudder force, we conducted towing tank experiments and identified experimental coefficients, which were used in the mathematical model.

The magnitude of interaction loads acting on the SS in both lightering and reverse lightering operations was investigated. Because it was presented by the contour map depending on the relative position of the SS from the VLCC, it would be helpful to understand the area where the manoeuvre of the SS is influenced by the interaction. These maps are also available to grasp the area where the VLCC takes the strong interaction as the reaction.

The differences in the approach manoeuvres of the SS and the VLCC according to the operation type were discussed based on the simulation in which manoeuvring loads based on the experiments were simply scaled up to the actual scale. In particular, in the case of the reverse lightering operation, the following findings were found to be of concern for safe operation:

a) The VLCC was attracted towards the SS due to a strong interaction sway force, and resulted in a difficulty in maintaining the constant course.

b) The bows of the SS and the VLCC turned the heading directions outside of each other due to a strong interaction bow out moment. This might result in the sterns of the SS and the VLCC to be contacted first, making a parallel contact difficult.

c) The heading direction and steering pattern of the VLCC during the course keeping are sensitively influenced by the contact location of the SS.

8 ACKNOWLEDGEMENTS

The authors would like to express their gratitude to Mr. Kitagawa who was a master course student in Hiroshima University, and contributed to the experiment and simulation in this study. This study was supported by Grant-in-Aid for Young Scientists (B) of JSPS KAKENHI Grant Number 24760676. The authors would like to express their gratitude to the grant-in-aid.

9 REFERENCES

Eda, H. 1971. Directional stability and control of ships in restricted channels. Transactions of the Society of Naval Architects and Marine Engineers (SNAME) 79, 71–116.

FORCE Technology and Iowa Institute of Hydraulic Research, 2008. Part B: Benchmark test cases, KVLCC2 description, in: Proceedings of the Workshop on Verification and Validation of Ship Manoeuvering Simulation Methods (SIMMAN 2008), Copenhagen. pp. B6–B9.

ICS/OCIMF, 2005. Ship to ship transfer guide (Petroleum), 4th edition.

Lataire, E., Vantorre, M., Delefortrie, G., 2009. Captive model testing for ship-to-ship operations, in: Proceedings of the International Conference on Marine Simulation and Ship Manoeuvrability (MARSIM'09), Panama City. pp. M106–M115.

Lataire, E., Vantorre, M., Vandenbroucke, J., Eloot, K., 2011. Ship to ship interaction forces during lightering operations, in: Proceedings of the 2nd International Conference on Ship Manoeuvring in Shallow and Confined Water: Ship to Ship Interaction, Trondheim. pp. 211–221.

Lataire, E., Vantorre, M., Delefortrie, G., Candries, M., 2012. Mathematical modelling of forces acting on ships during lightering operations. Ocean Engineering 55, 101-115.

Mousaviraad, S., Sadat-Hosseini, S., Carrica, P., Stern, F., 2011. Urans studies of ship-ship interactions in calm water and waves for replenishment and overtaking conditions, in: Proceedings of the 2nd International Conference on Ship Manoeuvring in Shallow and Confined Water: Ship to Ship Interaction, Trondheim. pp. 253–264.

OCIMF, 2009. Ship to Ship Transfers considerations applicable to reverse lightering operations, 1st edition.

Sano, M., Yasukawa, H., 2008. Maneuvering motions of KVLCC1 and KVLCC2 using MMG model, in: Proceedings of Workshop on Verification and Validation of Ship Manoeuvering Simulation Methods (SIMMAN2008), Copenhagen. pp. E51–E55.

Sano, M., Yasukawa, H., Hata, H., 2014. Directional stability of a ship in close proximity to channel wall. Journal of Marine Science and Technology 19 4, 376-393.

Sano, M., Yasukawa, H., 2019. Maneuverability of a combined two-ship unit engaged in underway transfer. Ocean Engineering 173, 774-793.

Vantorre, M., Verzhbitskaya, E., Laforce, E., 2002. Model test based formulations of ship-ship interaction forces. Ship Technology Research 49, 124–141.

Xiang, X., Skejic, R., Faltinsen, M. O., Berg, E.T., 2011. Hydrodynamic interaction loads between two ships during lightering operation in calm water, in: Proceedings of the 2nd International Conference on Ship Manoeuvring in Shallow and Confined Water: Ship to Ship Interaction, Trondheim. pp. 383–392.

Yasukawa, H., 2003. Simulation of ship collision caused by hydrodynamic interaction between ships, in: Proceedings of the International Conference on Marine Simulation and Ship Maneuverability (MARSIM'03), Kanazawa. pp. 841–850.

Yasukawa, H., Kawamura, S., Tanaka, S., Sano, M., 2009. Evaluation of ship-bank and ship-ship interaction forces using a 3D panel method, in: Proceedings of the International Conference on Ship Manoeuvring in Shallow and Confined Water: Bank Effects, Antwerp, pp.127-133.

Yasukawa, H., Yoshimura, Y., 2015. Introduction of MMG standard method for ship maneuvering predictions. Journal of Marine Science and Technology 20, 37–52.

Zou, L., Larsson, L., 2013. Numerical predictions of ship-to-ship interaction in shallow water. Ocean Engineering 72, 386–402.

10 AUTHORS BIOGRAPHY

Masaaki SANO holds the current position of assistance professor at the Department of Transportation and Environmental Systems, Hiroshima University. He is responsible for research on ship manoeuvrability based on experiment, simulation technique, and CFD calculation.

Hironori YASUKAWA holds the current position of professor at the Department of Transportation and Environmental Systems, Hiroshima University. He is responsible for research on ship dynamics and hydrodynamics.

VERIFICATION OF RAOS IN SEA TRIALS

Bernhard Schwarz-Röhr,
Jade Hochschule Elsfleth, Germany and Maritime Technology Division, Ghent University, Belgium

Alexander Härting,
Jade Hochschule Elsfleth, Germany

Marc Mansuy and Marc Vantorre,
Maritime Technology Division, Ghent University, Ghent, Belgium

Jeroen Verwilligen,
Flanders Hydraulics Research, Antwerp, Belgium

Butteur Ntamba Ntamba,
Cape Peninsula University of Technology, Cape Town, South Africa

Chen Zhang,
Jade Hochschule Elsfleth and University of Oldenburg, Germany

VERIFICATION OF RAOS IN SEA TRIALS

Bernhard Schwarz-Röhr, Jade Hochschule Elsfleth, Germany and Maritime Technology Division, Ghent University, Belgium
Alexander Härting, Jade Hochschule Elsfleth, Germany
Marc Mansuy and **Marc Vantorre,** Maritime Technology Division, Ghent University, Ghent, Belgium
Jeroen Verwilligen, Flanders Hydraulics Research, Antwerp, Belgium
Butteur Ntamba Ntamba, Cape Peninsula University of Technology, Cape Town, South Africa
Chen Zhang, Jade Hochschule Elsfleth and University of Oldenburg, Germany

SUMMARY

A method to estimate the directional wave spectrum from measured ship motions is currently under development. The algorithm relies on response amplitude operators (RAOs) to link ship motions to the sea state. In order to verify numerically obtained RAOs in realistic sea states, two campaigns of extensive sea trials were performed on the RV Simon Stevin in the North Sea close to Ostend. Ship motions were recorded in six degrees of freedom, in this paper analysis was restricted to roll and pitch. Data from several directional wave buoys in the vicinity of the trial runs were available. RAOs were calculated using *OCTOPUS* and *HYDROSTAR*. Spatial and temporal fluctuations were found in the wave buoy data, so there is some uncertainty in the wave spectrum seen by the vessel. Considering these uncertainties, *HYDROSTAR* gave reasonable agreement for pitch, larger discrepancies were found for roll especially close to the resonance frequency.

1 INTRODUCTION

This work is part of a project that aims at developing a novel algorithm for estimating the directional wave spectrum from motions of a vessel underway. Knowledge of the sea state is one important factor for achieving safe operations at sea. In many areas wave rider buoys are routinely operated providing the directional wave spectrum with high reliability. However, with few exceptions, the measurement sites are restricted to coastal areas. Larger areas are covered by hydrodynamic models which utilize several data sources including wave buoys and satellites for sea climate estimates and forecasts, one example is given in (EMWF, 2018). Despite these tools, visual wave observations are routinely performed onboard and entered into the ship's log. In these observations the directional wave spectrum is reduced to a few parameters for each detected wave system, namely significant wave height and period and the wave direction. This simplified model of the sea state may not be sufficient for safe operations, estimating the full directional spectrum onboard is hence desirable.

There are different approaches in the literature for estimating the sea state parameters from ship motions. While a complete review is beyond the scope of this paper, it can be stated that most publications fall into two categories, the Bayesian modelling (Iseki, Ohtsu, 2000; Nielsen, 2005) and parametric methods (Hinostroza, Soarez 2016). A more detailed and comprehensive overview on literature is given in (Pascoal et al, 2017). In the latter group the wave spectrum is approximated by a spectral function with several parameters such as JONSWAP. The parameters are then determined from the motion spectra. In the current project a different approach is chosen, the wave spectrum is expanded into angular distribution functions at each frequency point, the expansion coefficients are determined from the measured motion spectra. The method is described in more detail in (Schwarz-Röhr et al., 2016), first results of sea trials are reported in (Schwarz-Röhr et al., 2015).

For all methods the quality of the sea state estimates depends on the accuracy of the model that relates ship motions to the exciting wave fields. In the spectral domain ship responses are modelled by the response amplitude operators (RAOs). Several methods for the calculation of RAOs using different approximations and therefore with different limitations are known. In this paper data of sea trials are used to study whether RAOs calculated by two software packages, Octopus and Hydrostar, are suitable for sea state estimates.

The trials took place in two dedicated campaigns (1-3 Aug 2017, 6-8 Nov 2017) in the North Sea close to Ostend. In this area directional spectra of several wave buoys are available. By means of the calculated RAOs predicted motion spectra were calculated from the wave data and compared against ship motion measurements.

Details on the vessel (RV Simon Stevin), the instrumentation and the track layout are presented in the next chapter. The subsequent chapter discusses the calculation of the RAOs. The evaluation of wave buoy data and the calculation of the predicted motion spectra is explained in chapter 4, followed by the presentation of experimental results.

2 EXPERIMENTAL SETUP

Trials runs were performed in two campaigns (1-3 Aug 2017, 6-8 Nov 2017) on the RV Simon Stevin operated by the VLIZ (Flanders Marine Institute), the ship particulars are given in table 1. Trials took place in Belgian waters close to Ostend (figure 1). The water depth in the operational area was generally greater than 20 m with the exception of a few sandbanks where the water depth could be as low as 12 m.

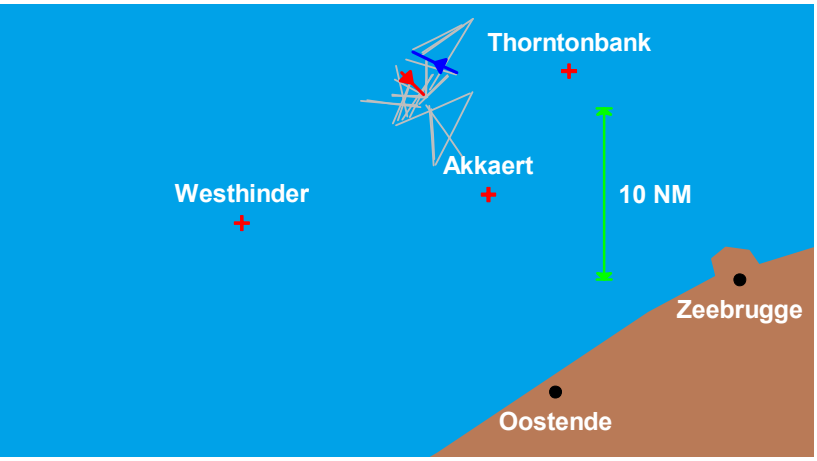

Figure 1. Tracks of sea trials for November 7th together with the closest directional wave buoys. The two trials discussed in the text are marked red (trial #11) and blue (trial #3).

Table 1: Ship particulars of the RV Simon Stevin

Length	36 m
Beam	9.4 m
Draught	3.6 m

The motions were measured in all six degrees of freedom by two independent devices, namely an Octans IMU which is installed permanently on the Simon Stevin and a GPS/IMU based system developed by Flanders Hydraulics Research (FHR). Motion data from both devices agree very well. The speed through water is logged onboard and included in the Octans data. Heading and speed over ground is obtained from the FHR measuring system based on GPS data.

In total 43 trial runs were conducted, a duration of 30 minutes per trial run was considered sufficient to obtain proper averaging of the motion spectra. The speed was kept constant during each trial run. Courses were set in steps of 45°, the speed was varied from 3 knots to 12 knots. Due to weather and traffic conditions not all combinations are available.

3 RAO CALCULATIONS

Two software packages, the strip theory code *Octopus* 6.4.14 and *Hydrostar* V8.00 were used to calculate the RAOs. As shown in the following section a huge angular spread was found in the wave buoy data necessitating RAOs for almost all directions of wave incidence. As a compromise between accuracy and computational time, RAOs were calculated in steps of 5° and interpolated to 1° for data evaluation.

The required hull models were created from the lines plan provided by Damen Shipyards. The hull file for Octopus is composed of 27 stations placed more densely at bow and aft compared to the midship section. The Hydrostar model is composed of 1083 quadrilateral panels.

The stability data gave no indication of the current metacentric height $\overline{GM}$ and the radii of gyration, the latter were estimated from the empirical rules given in (Journee, Adegeest, 2003) to k_{xx} = 3.2 m, k_{yy}= 8.0 m and k_{zz}= 8.03 m. $\overline{GM}$ was adjusted iteratively such that the roll resonance in the RAOs matches the clearly visible peak in the motion spectra, a metacentric height of 0.7 m was found.

The strip theory approach used in Octopus is described in detail in (Journee, Adegeest, 2003), basically the hull is divided into sections along the longitudinal axis. In each section two dimensional potential theory is applied to calculate hydrodynamic and wave loads as if the section were infinitely long. Within this approximation all diffracted and radiated waves propagate perpendicular to the longitudinal ship axis which is observed experimentally in the midship sections only. Thus this approach is well suited for long and slender ships, according to (Journee, Adegeest, 2003) the ratio of length to breadth should be greater than three “at least from the practical point of view”.

Potential theory does not handle viscous damping. The semi-empirical Ikeda method offered by Octopus was applied in the RAO-calculations, the parameters are given in table 2. Setting the WAVAMP parameter asks Octopus to determine the roll amplitude at which the nonlinear damping terms are linearized. This parameter was set to 1 m. In the initial calculations a very low roll damping was found in the RAOs, thus additional damping was introduced by adding a fictitious bilge keel with parameters given in table 2.

Hydrostar solves the hydrodynamical problems in three dimensions and is therefore not limited to slender ships (Chen, 2004). This software offers different methods for introducing additional damping. Following the recommendations in the manual (Bureau Veritas, 2018), linear damping was introduced in the damping matrix by means of the parameter LINVISCOUSDAMPING. The damping was set to 4.5% of the critical damping.

Table 2. Damping and bilge keel parameter used in *Octopus*

Type	Name	Value
WAVE AMPLITUDE FOR LINEARISATION	WAVAMP	1 m
HEIGHT OF BILGE KEEL	HBK	0.16 m
DISTANCE OF A.P.P. TO AFT END B.K.	XBKA	11.24 m
DISTANCE OF A.P.P. TO FORWARD END B.K.	XBKF	20.88 m

4 WAVE DATA

Directional wave buoys in the vicinity (figure 1) of the operational area provided wave spectra. The wave buoy data contain data sets for each half hour of the day, a sample is shown in figure 2. There are three data records with the mean wave direction $\theta_m(f)$, the wave power $S_B(f)$ and the wave spread $\sigma(f)$ for each frequency point. Here f denotes the sea state frequency as measured at a fixed point in space. The complete directional wave spectrum spectrum $S(f,\theta)$ is given by

$$S(f,\theta) = D(\theta,\theta_m)\, S_B(f) \tag{1}$$

The angular distribution function $D(\theta,\theta_m)$ is not clearly defined in the wave buoy documentation. In this paper the distribution function

$$D(\theta,\theta_m) = \cos^{2s}(\theta-\theta_m) \tag{2}$$

was adopted. The spread values σ in the data sets are read as standard deviation which are related to the parameter s by (Kuik et al., 1988)

$$\sigma = \sqrt{\frac{2}{s+1}} \tag{3}$$

A sample of a resulting directional wave spectrum is shown in figure 4.

In order to calculate the motion spectrum an intermediate variable

$$S_n(f,\theta) = |h_n(f,\theta)|^2\, S(f,\theta) \tag{4}$$

is introduced, where n denotes the degree of freedom and $h_n(f,\theta)$ the corresponding RAO in terms of the sea state frequency. $S_n(f,\theta)$ can be read as the directional motion spectrum in terms of the sea state frequency.

On a moving vessel wave power at a sea state frequency f is observed in the motion spectrum at the encounter frequency f_E

$$f_E = f\left(1 - \frac{v_0\cos(\mu)}{\frac{g}{2\pi}\tanh\left(\frac{2\pi h}{\lambda_W}\right)} f\right) \tag{5}$$

Here g is the gravitational acceleration, v_0 denotes the ship speed through water and μ the angle between the wave vector and the ship velocity. An angle μ of zero corresponds to waves from aft. The hyperbolic tangent depends on the ratio of water depth h to wavelength λ_W, this term equals one in the deep water approximation. Considering the water depth of 20 m and a lower frequency limit of 0.15 Hz as indicated by the buoy spectra (e. g. figure 2) results in an upper limit for the wavelength of roughly 65 m. The hyperbolic tangent deviates from unity by less than 5% under these conditions, the deep water approximation is used for data processing.

The motion spectrum $S_n^e(f_E)$ at a certain encounter frequency f_E is obtained by summing all contributions of $S_n(f,\theta)$ for which equation (5) holds such that the total power is preserved.

5 SAMPLE RESULTS

As the experiments were performed in real seaway, several uncertainties limit the precision of the estimated motion spectra. In some cases several independent wave systems were observed visually which cannot be represented properly by the single angular distribution function in the wave buoy data. The wave spectra obtained from the different wave buoys showed both temporal and spatial fluctuations even for the duration of one 30 minutes trial run. Temporal fluctuations are illustrated by two consecutive datasets for the wave buoy closest to the operational area (Thorntonbank) in figure 2. The spatial variations are apparent in figure 3, here the power spectra of the neighbouring buoys (Akkaert, Westhinder) for one point in time are shown.

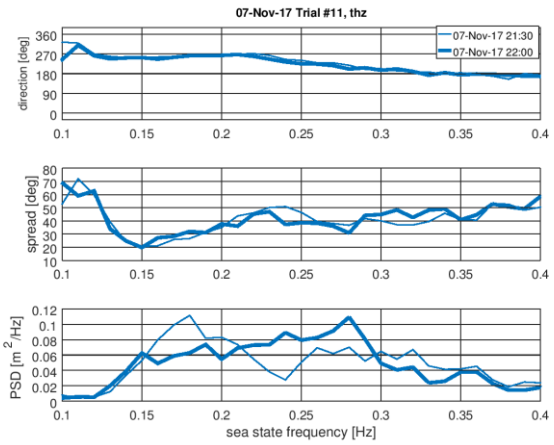

Figure 2. Two consecutive data records of the wave buoy at Thornton Bank with panels for mean wave direction, spread and power as a function of frequency.

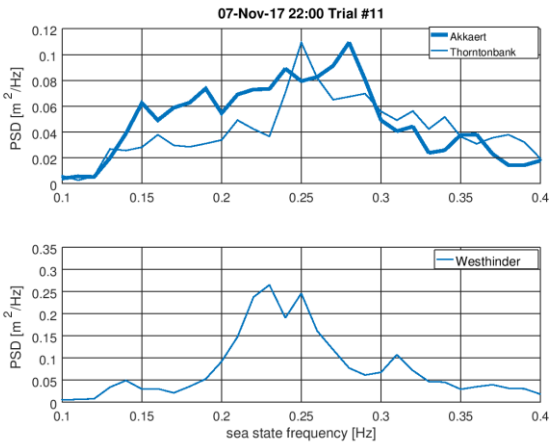

Figure 3. Comparison of power spectra measured by the three wave buoys close to the operational area indicating the spatial variation of the wave field. The mean wave direction and the wave spread are not shown here as they do not differ much among the data sets.

During the experiments different sea states in wave height, period and direction were observed, the wave spread in the important frequency range was between 30° and 40° in all trials.

Results of two trial runs are discussed in detail in the following paragraphs. The first case (trial #11) is marked red in figure 1, there are almost beam sea conditions with an angle between mean wave direction and heading of 73° from aft, the speed through water is 4.7 knots. The water depth is between 27 m and 28 m. The wave buoy data is shown in figure 2, the dataset for 22:00 hours is used in the calculations. The spread leads to a rather wide angular distribution in the directional wave spectrum as shown in figure 4.

The resulting motion spectra using the RAOs of *Octopus* and *Hydrostar* are compared against the measured data in figure 5. The RMS values obtained by taking the square root of the area under the power spectra are given in the legend. In addition the wave encounter spectrum is plotted in the upper panel, the legend contains the significant wave height.

The curves indicate that roll damping close to the resonance is not modelled very well by both programs, the peaks in the predicted roll power are approximately five times higher than the measured one. It should be noted that the corresponding roll amplitudes differ by a factor of $\sqrt{5} \approx 2.25$ in this case. Since the roll damping plays a dominant role close to the resonance only, measured and predicted RMS values are in much better agreement.

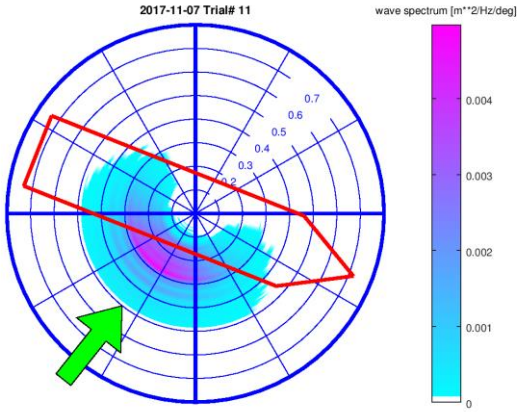

Figure 4. Directional wave spectrum calculated from the data in Figure 2 (22:00) by means of the angular distribution function. As a rough measure of the main wave direction, the green arrow indicates the average of the buoy's directional data close to the maximum of power (0.23 Hz - 0.3 Hz).

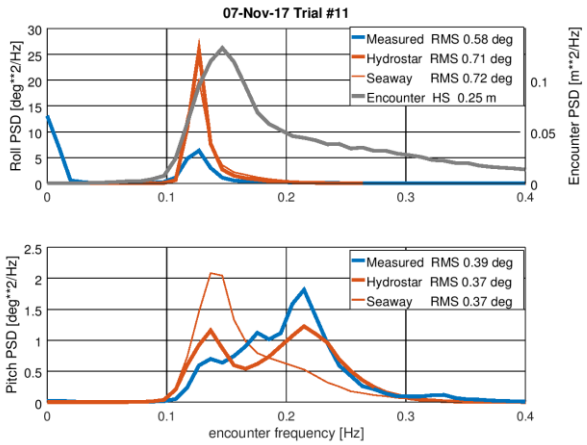

Figure 5. Comparison of measured and calculated motion spectra for the trial of Fig. 2 and Fig. 3. The wave encounter spectrum is plotted in the upper panel on a separate y-axis.

Regarding the pitch reasonable agreement between measured motion and the Hydrostar prediction is found, while the Seaway calculation does not reflect the shape of the measured motion spectrum. This result was found in the majority of cases.

In order to understand the reason for the discrepancies in the motion predictions, it would be desirable to relate these to the RAOs and the underlying terms in the equation of motion. However, this turned out to be unfeasible, because the motion prediction contains contributions for the whole angular distribution of the wave spectrum and the RAOs change remarkably with the wave angle. This is illustrated in figure 6, where three pitch RAOs from the main lobe of the wave spectrum are shown.

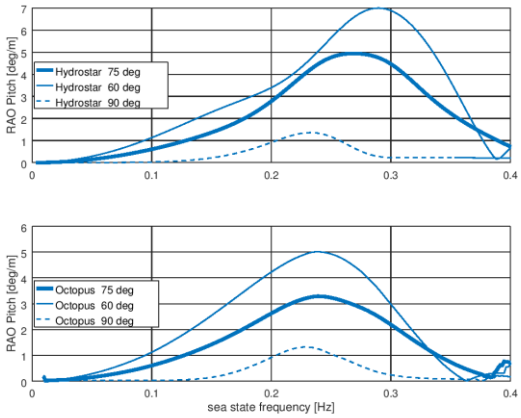

Figure 6. Amplitude of pitch-RAOs for 5 knots. The thick line corresponds to the mean wave direction, the other curves are 15° closer to bow and aft respectively.

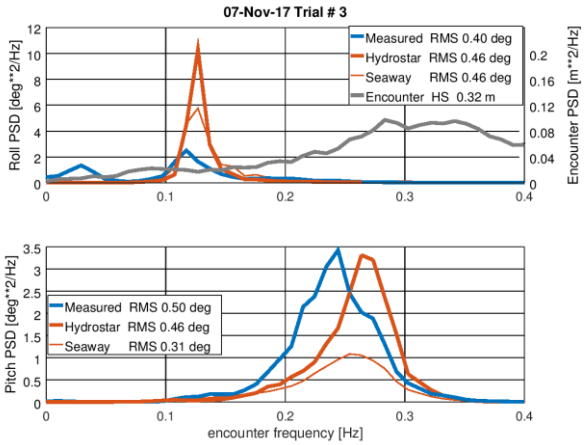

Figure 7. Comparison of measured and calculated motion spectra. Calculations are based on the RAOs from Hydrostar and Seaway. The wave encounter spectrum is plotted in the upper panel on a separate y-axis.

A similar results is obtained in the almost head sea example (trial #3) marked in blue in figure 1, here the mean wave angle is 163° from aft, the speed through water 6.9 knots. The initial and final water depth is 25 m, during 20% of the track a sandbank with a minimum water depth of 12 m was passed. The motion spectra are shown in figure 7. Again the measured roll is smaller than the calculated one. For pitch calculated and measured motions have a very similar shape but appear at different encounter frequencies. This might be caused by inaccurate parameters in the calculation of the encounter spectrum, candidates are wave direction, heading and speed through water.

The two trial runs discussed here are typical in several aspects: both RAOs exhibit too low damping at the roll resonance, pitch is modelled more accurately by Hydrostar, probably because the length to breadth ratio is too low for strip theory.

6 CONCLUSIONS

Extensive sea trials were performed in order to verify RAOs calculated by Hydrostar and Seaway. Measurements took place in the North Sea close to Ostend. The required directional wave spectra were derived from wave buoy data. Motion measurements were done in six degrees of freedom, in this paper roll and pitch are analysed.

The sea climate during the trial runs poses some challenges for the data interpretation: in the coastal area spatial and temporal fluctuations are quite common, the wave spectrum seen by the vessel during one track is therefore not very well defined.

Considering these uncertainties, reasonable agreement was found for pitch using *Hydrostar*, larger deviations were found in the *Octopus* calculations, probably because the strip theory is no strictly applicable to this vessel. The roll damping was poorly modelled by both software packages in the default settings. Obviously the RAOs as tested here cannot directly be used for the sea state estimating algorithm. Adjusting the damping parameters based on empirical data will be required. Since wind sea was dominating, a rather large directional wave spread was observed. This means that RAOs of many different angles contribute to the motion spectrum, thus optimizing RAO parameters is not straightforward and left for future work.

7 ACKNOWLEDGEMENTS

The authors are grateful for the opportunity to conduct experiments with the RV Simon Stevin offered by Flanders Marine Institute (VLIZ). They are indebted to Damen Shipyards for providing the lines plan of the RV Simon Stevin, Bureau Veritas for the use of Hydrostar, and Flanders Hydraulics Research for providing the ship motions measuring system. Special thanks are due to the crew of the RV Simon Stevin for the cordial and efficient support.

8 REFERENCES

Bureau Veritas, 2018. Hydrostar for experts, user manual, the manual is part of the software download https://www.veristar.com/portal/veristarinfo/detail/downloads/Calculation Software/hydrostar

Chen, X.B., 2004. Hydrodynamics in Offshore and Naval Applications, in: Proceedings of the 6th International Conference on Hydrodynamics. Perth, Australia

ECMWF, 2018. https://www.ecmwf.int

Hinostroza, M. A., Guedes Soares C., 2016. Parametric estimation of the directional wave spectrum from ship motions, Intl. J. Maritime Engineering, pp. A121-A130

Iseki, T., Ohtsu, K., 2000. Bayesian estimation of directional wave spectra based on Ship motions. Control Engineering Practice (8), pp. 215-219

Journée, J. M. J., Adegeest, L. J. M., 2003. Theoretical Manual of Strip Theory Program "SEAWAY for Windows"., Rep. Nr. 1370, Ship Hydromechanics Laboratory, Delft University of Technology

Kuik, A. J., van Vledder G. Ph., Holthuijsen, L. H., 1988. A method for the routine analysis of pitch-and-roll buoy wave data, J. Phys. Oceanogr. (18), pp. 1020-1034

Nielsen, U. D., 2006. Estimation of on-site directional wave spectra from measured ship responses. Marine Structures (19), pp. 33-69

Pascoal, R., Perera, L. P., Soares C. G., 2017. Estimation of directional sea spectra from ship motions in sea trials. Ocean Engineering (132), pp. 126-137

Schwarz-Röhr, B., Ntamba Ntamba, B., Härting, A., 2015. Extending sea state measurements from wave buoys to vessels underway, in: Proceedings of the Hydro2015, Cape Town, South Africa, pp. 11-20.

Schwarz-Röhr, B., Ntamba Ntamba, B., Härting, A., 2016. Estimating seaway from ship motions, in: Proceedings of the 13th International Symposium on Practical Design of Ships and Other Floating Structures (PRADS' 2016)

9 AUTHORS BIOGRAPHY

Bernhard Schwarz-Röhr holds his diploma degree of physics, and now he is a PhD candidate in Faculty of Engineering and Architecture, Ghent University, Belgium. He is responsible for wave estimation, sea state analysis, and measurement of ship movements.

Alexander Härting is a professor in Department of Maritime Studies, Jade University of Applied Science, Germany. His research interests include measurement and analysis of dynamic ship movements in seaway, integration of different navigation sensors, and measurement of the squat of seagoing vessels in narrow fairways.

Marc Mansuy holds the current position of research staff at Gent University. He has been working on different projects related to maneuvering in shallow and confined water at Flanders Hydraulic Research and Ghent University.
He has some expertise in waterway accessibility, ship maneuverability on real time and fast time simulators and full scale measurements.

Marc Vantorre, naval architect, is full senior professor of marine hydrodynamics and head of the Maritime Technology Division at Ghent University, Belgium. His research focuses on ship behaviour in shallow and confined waters, mainly in close co-operation with Flanders
Hydraulics Research in Antwerp. He is former member of PIANC Working Groups and of the ITTC Manoeuvring Committee.

Butteur Ntamba Ntamba hold a bachelor degree in mechanical engineering from University of Lubumbashi, Democratic Republic of Congo and a master degree from Cape Peninsula University of Technology (CPUT), South Africa. He is now a lecturer in the Faculty of Engineering and a PhD candidate with CPUT. His research work is on ship response in waves.

Jeroen Verwilligen holds the current position of senior expert in nautical research at Flanders Hydraulics Research. He is experienced with simulation studies, nautical accessibility studies and full-scale measurements. He is member of the PIANC MarCom WG 171 on Ship Handling Simulation Dedicated to Channel and Harbour Design.

Chen Zhang received her bachelor and master degree from Northwestern Polytechnical University, China in 2010 and 2013 respectively. Now she is a PhD candidate in the Department of Computer Science, Carl von Ossietzky University of Oldenburg, Germany. Her research interests contain measurement and analysis of ship movements at sea states, also including motion control.

NUMERICAL INVESTIGATION OF SCALE EFFECTS ON SQUAT IN SHALLOW WATER

Ivan Shevchuk,
Technical University Hamburg, Germany

Carl-Uwe Böttner,
Federal Waterways Engineering and Research Institute, Germany

Nikolai Kornev,
University of Rostock, Germany

NUMERICAL INVESTIGATION OF SCALE EFFECTS ON SQUAT IN SHALLOW WATER

Ivan Shevchuk, Technical University Hamburg, Germany
Carl-Uwe Böttner, Federal Waterways Engineering and Research Institute, Germany
Nikolai Kornev, University of Rostock, Germany

SUMMARY

This paper is aimed at clarifying, to what extent the scale factor influences the squat phenomenon. In order to do that, a series of squat computations for three containerships (one Panamax and two Post-Panamax) were conducted in three scales: 1:1, 1:6, 1:40, and a range of depth to draft (*h/T*) ratios from 2.0 to 1.15. Also, a range of hull roughness values was considered by different diameters of Nikuradses equivalent sand roughness k_s.
It was found out that for the two of the three considered ships, the scaling error for squat grows as the *h/T* ratio is reduced. At the same time, the increase of the sand roughness leads to a better agreement between the full scale and the model scale results. For most of the considered cases the maximum scaling error was estimated to be 15cm (in full scale) or 10%, which is quite moderate and does not necessary require a correction. The dependence of scale effects on the Froude number, the *h/T* ratio and the roughness height is not the same among the considered ships. Therefore, one of the conclusions is that a development of a generally valid correction would be a challenging task.

NOMENCLATURE

h	Fairway depth (m)
T	Ship draft (m)
λ	Scale factor (-)
k_s	Nikuradse's sand roughness (m)
k_s^+	Dimensionless sand roughness (-)
θ	Trim angle (deg)
$\delta\theta$	Trim angle scaling error (deg)
S_M	Sinkage at midship (m)
S_B	Sinkage at the bow (m)
S_H	Kinematic viscosity (m)
$\delta S_{M,B,H}$	Scaling error for sinkage at midship, at the bow and at the stern respectively (m)
U	Uncertainty of the computed quantity
$\|E\|\%D$	Discrepancy between the experimental and the computed values
U_V	Validation uncertainty

1 INTRODUCTION

Nowadays, the results of the model tests for squat are converted to full scale by direct multiplication with the scale factor. By doing so one assumes, that the difference of Reynolds number between the model and the ship cannot considerably influence the squat phenomenon. However, in extremely shallow water even a small change of the effective gap between the ship and the fairway bottom may have noticeable consequences for ship behavior. Therefore, the difference between the relative boundary layer thickness in the model and the full scale caused by the difference in Reynolds number may indeed play a significant role in this case. In order to clarify the role of the scale effects on squat, a research project, named ReSquat was conducted at the University of Rostock in collaboration with the Federal Waterways Engineering and Research Institute (BAW). The aim of the project was to estimate the order of magnitude of the direct scaling error for the squat between the model and the ship using CFD.
Prediction of squat effect has nowadays become a routine task for CFD, at least in model scale and for moderate h/T ratios. Multiple papers describe the successful application of CFD codes for this purpose. (Jachowski, 2008) conducted squat simulations using commercial CFD code for a range of Froude numbers and h/T ratios and obtained good agreement with the average result of empirical methods. Drastic intensification of squat was observed for the smallest h/T. (Linde et al., 2015) developed a quasi-steady simulation procedure to speed up the squat computations and obtained fair agreement with experimental data. (Tezdogan et al., 2016) conducted a thorough CFD investigation of squat and resistance for a DTC hull moving in a canal. The discrepancy with experimental results was found to be smaller than the uncertainty of the experimental data.
In the context of the present paper, the work of (von Graefe et al., 2011) is especially important to mention. Authors compared the performance of a commercial CFD solver with potential methods for prediction of squat in restricted waterways. The CFD computations showed best agreement with the full scale measurements. Comparing the results between the computations at full scale and the model scale authors concluded that squat in full scale is larger than in model scale. However, no systematic information on this effect was presented. Moreover, the information on the hull roughness used in full scale computations was not present in the paper.
Even though the studies on scale effects for ship resistance, viscous wake and wave making are presented in literature, see e.g. (Raven, 2008), to the authors' best knowledge systematic studies of scale effects on squat have not been published yet. The present paper is an attempt to fill this gap.

2 CONSIDERED HULL FORMS

Three hull forms were considered in the present study: two Post-Panamax-container ships (PPM52, PPM55) and one Panamax-container ship (PM32). The hull forms of the mentioned ships are shown in Figures 1 and 2, whereas the main ship dimensions are given in Table 1. The hull forms were specifically selected in such a way, that PM32 has a C_B lying between the C_B values of PPM52 and PPM55. This way, the dependence of the studied phenomena on the block coefficient could be analyzed.

3 CONSIDERED CONDITIONS

Following parameters were varied in the framework of the study for each of the hull forms: the scale factor λ, the depth-to-draft ratio h/T, the Froude number Fr and the equivalent sand roughness k_s. Three scale factors were considered: full scale ($\lambda = 1$), model scale ($\lambda = 40$) and the intermediate scale ($\lambda = 6$). The depth-to-draft ratio was varied in the range $h/T = 2.0, 1.5, 1.4, 1.25, 1.15$ whereas the range of the Froude numbers was $Fr = 0.07, 0.09, 0.11, 0.13$. The Reynolds numbers for the model scale vary in the range from $6 \cdot 10^6$ to $\cdot 10^7$, whereas for the full scale from $1.4 \cdot 10^9$ -to $2.7 \cdot 10^9$, which is at least two orders of magnitude larger, than for the model. Next important parameter is the hull surface roughness. Four roughness diameters were considered k_s = 0.15mm (ITTC recommended, (ITTC, 2017)), 0.5mm, 1mm, 2mm. In total 720 computations were conducted (3 ships x 4 roughness heights x 5 depths x 3 scale factors x 4 Froude numbers). The conduction of a large number of RANS computations in a relatively short period of time was possible due to the development of a quasi-steady-state free-surface flow solver, which is briefly described in the next section.

Table 1. Main dimensions of the considered hull forms

	PPM52	PPM55	PM32
L_{pp}	347	355.8	281.6
B	52	55	32.3
T	16	16	11.8
C_B	0.668	0.689	0.679

4 NUMERICAL METHOD

The simulations in the present study were conducted using a quasi-steady-state volume-of-fluid solver, developed by the authors in collaboration with the research group of the University of Zagreb. This solver uses the ghost-fluid method (also known as embedded free-surface) to account for the presence of the air/water interface in the computational domain (Vukcevic, 2016). The momentum equations are solved in a steady-state manner, whereas the transport equations for the volume fraction are solved in an unsteady formulation with high Courant numbers. This way the convergence of the wave pattern and the forces acting on the ship can be attained already after a few thousand iterations, analogous to the single-phase steady-state solvers. The discretisation of the governing equations was done using the finite volume method with the schemes of nominally second order accuracy for all terms. The Menter's $k - \omega$ SST model was used for the turbulence modelling.

In order to account for the influence of the propeller on the flow in the stern and by these means increase the accuracy of trim and sinkage prediction an actuator disc (AD) model proposed in (Hoekstra, 2006) was used. This model was extended with the ability to predict the propeller rps, based on the propeller K_T and K_Q curves, provided by the user. The values of V_A and J are estimated based on local flow quantities. The adaptation of rps was done in an iterative manner.

The effect of the roughness on the flow was accounted for by the application of the wall functions. In order to properly apply the wall functions, the y^+ value of the first wall-adjacent computational node had to be larger than k_s^+, which in some cases led to the y^+ values of up to 700. In order to avoid the influence of the switch between different wall functions, the same roughness-based wall functions were used for all scales, but the sand roughness was scaled accordingly.

It is known, that the application of wall functions for flows with separations/strong pressure gradients (which is the case for the considered task) can be problematic. However, the wall-resolved simulations could not be used for two reasons. First, the use of wall resolved meshes for full scale would drastically increase the computational costs. Second, even if the wall-resolved meshes were used, this would require the modification of k and omega equations, introducing the influence of roughness into the turbulence model. Such models to authors' knowledge are neither widely used, nor well established and would definitely lead to some influence on separation behavior too.

The experimental observations as well as computational results (Shevchuk et al., 2016) indicate, that the flow at the ship stern in very shallow water is considerably unsteady, which raises a concern, to what extent RANS models are applicable for such cases. However, application of RANS/LES for this task resulted in just 5% change of the mean sinkage at the stern compared to RANS results. Therefore, authors believe, that application of RANS would not pose a significant problem for the accuracy of the results even for the smallest h/T considered.

5 VERIFICATION AND VALIDATION OF THE TRIM AND SINKAGE PREDICTION

The verification and validation (V&V) of the computational method, described in the previous section, was only possible for the model scale, since the experimental values for trim and sinkage for other scales were not available. The determination of the numerical uncertainty was on the other hand conducted for all scales. Three meshes for each scale were generated using snappyHexMesh generator: from 0.9M to 3.1M of cells for a half of ship hull. Due to the symmetry about the middle line plane only the left half of the flow was

simulated. The special step-by-step meshing procedure allowed for the 99.6% coverage of the ship surface with prism layers. Examples of the mesh structure (slice at the stern) are shown in Figure 3.

Table 2. V&V study for the PPM52 hull at model scale, Fr=0.12. Res – result. CONV-convergence, DIV-divergence. Val. –was the validation achieved?

Mesh	θ [˚]	ε	S_M [m]	ε
C	0.063	-	-0.028	-
M	0.066	2.59E-03	-0.028	4.30E-05
F	0.067	1.17E-03	-0.028	9.94E-05
Res	CONV		DIV	
U [%]	4.37		1.53	
|E| % D	10.88		7.31	
U_v *%*	15.48		7.63	
Val. ?	Yes		Yes	

Table 3. Uncertainty estimation for PPM52, h/T=1.25, scale 1:1

Mesh	θ [˚]	ε	S_M [m]	ε
C	0.053		-1.194	-
M	0.055	1.74E-03	-1.168	2.61E-02
F	0.054	-4.57E-04	-1.162	5.45E-03
Res	OCONV	-	CONV	-
U[%]	1.991	-	0.370	-

Table 4: Uncertainty estimation for PPM52, h/T=1.25, scale 1:6

Mesh	θ [˚]	ε	S_M [m]	ε
C	0.055		-0.198	-
M	0.067	1.22E-02	-0.201	-2.71E-03
F	0.067	-9.27E-05	-0.199	1.87E-03
Res	OCONV	-	CONV	-
U[%]	1.991	-	0.370	-

Only one hull form (PPM52) was considered in V&V studies, since the other hull forms are considered similar from the point of view of the numerical method. Only the results for the depth-by-draft ratio of 1.25 and the Froude number of 0.12 are shown in the present paper for the sake of brevity. The V&V procedure as recommended by the ITTC was used (ITTC, 2008).

In Table 2 one can see the results of the V&V study for the model scale. The values of the experimental uncertainties were chosen based on the results presented by the ITTC in 2011 on the facility biases for the trim and sinkage measurements (ITTC, 2011). One can notice, that the values of the trim angle show monotone grid convergence (CONV), whereas the values of squat at the midship formally show grid divergence (DIV), which strictly speaking means that no uncertainty estimation can be done. However, the difference in the results between the coarsest and the finest grid are obviously negligibly small and therefore it seems reasonable to assume that the solution is converged. The uncertainty estimation in this case was done using the formula $U = (\Phi_{max} - \Phi_{min}) \cdot F_s$, where Φ_{max}, Φ_{min} are the maximum and minimum values of the quantity and $F_s = 3$ - safety factor. Using this formula validation both for trim and sinkage could be attained.

Tables 3 and 4 contain information on the uncertainty estimation for the scales 1:1 and 1:6 respectively. In most cases either the monotone or the oscillatory convergence were observed. The estimated values of the uncertainty are quite small: for the sinkage it lies below 0.8%, whereas for the trim angle the value is much higher - up to 11%.

Table 5. Comparison of the rps obtained from the actuator disc model with the experimental data, PPM52, model scale, h/T=1.25

Fr	rps, CFD	rps, Exp	Discr. [%]
0.07	3.93	4.05	0.03
0.09	4.99	5.07	0.02
0.11	6.13	6.18	0.01
0.13	7.42	7.36	-0.01

All the previously described verification and validation results were obtained using an actuator disc model. However, the version of AD model, without the determination of the rps was used. In order to make sure, that the values of the rps are predicted accurately, the flow computations for the model of PPM52 at depth-by-draft ratio (1.25) were conducted for a range of Froude numbers. The values of the rps were compared to the self-propulsion tests, conducted by SVA-P (Anschau, 2016). Results of the comparison can be seen in Table 5 and were considered satisfactory. No grid convergence study was conducted for this quantity.

6 ANALYSIS OF THE SCALING ERROR FOR THE SQUAT EFFECT

In order to analyze the scaling error for squat, one can compare two pairs of quantities between the model and the ship scale: either the sinkage at midship and the trim angle (S_M, θ) or the sinkage at the bow and at the stern (S_B, S_H). The former two quantities seem to be more suitable for the explanation of the physical phenomena, because sinkage depends just on the vertical force, whereas the trim angle on the trimming moment. At the same time S_B, S_H are more practically important, because they allow for evaluation of the effective differences in the under-keel clearance between the model and the full scale. In our opinion, both the practical and the physical aspects of the studied phenomena are important, therefore the analysis for both sets of variables (S_M, θ and S_B, S_H) will be presented.

In the following only the results for $\lambda = 40$ and $\lambda = 1$ are going to be compared. The results for $\lambda = 6$ almost in all cases showed oscillatory dependence of the scaling error on the scale factor. For example, in some cases the scaling errors between $\lambda = 1$ and $\lambda = 6$ surprisingly turned out to be higher, than between $\lambda = 1$ and $\lambda = 40$. Because of this

behavior of the numerical model it was decided to neglect the results for $\lambda = 6$, until the reasons are clarified.

6.1 SCALING ERROR FOR S_M AND θ

In Figures 4, 5 and 6 one can see the scaling error for sinkage at midship (δS_M). The value of δS_M was calculated according to the following formula:

$$\delta S_M = S_M^{ship} - S_M^{model}\lambda, \quad (1)$$

where S_M^{ship}, S_M^{model} are the sinkages calculated at the full scale and model scale and λ - scale factor. S_M is the change of the vertical coordinate of the ship's center of gravity, which is negative for squat. This means, that if δS_M is negative, then the center of gravity of the ship is lower, than for the model and vice versa.

The analysis of the mentioned plots allows to notice the following trends. First of all, one can see, that the most plots for $h/T = 1.15$ do not correspond very well to the ones for higher h/T. Only for PPM52 the curve $h/T = 1.15$ follows the overall trends and seems reasonable, whereas for PPM55 and PM32 the results for h/T=1.15 do not agree at all with other depths. Therefore, one can conclude, that the numerical solution at h/T=1.15 obviously has a higher numerical uncertainty, than that for h/T=1.25. Because of this, the results for h/T could not be considered reliable. However, the behavior of the solution for PPM52 points to the fact, that the absolute value of the scaling error increases, when the depth-by-draft ratio diminishes and at $h/T = 1.15$ there is rapid growth compared to $h/T = 1.25$ (see Fig. 5). Second of all, in most cases the scaling error for S_M is negative. This means, that the ship vertical position is lower than that of the model ($S_M^{ship} < S_M^{model}\lambda$). This agrees well with the observations made in (von Graefe, 2011). However, in all considered cases the absolute value of the error is smaller than 15 cm (the evaluation in percent will be shown for δS_B, δS_H in the next subsection (see Figs. 10, 11 and 12). Third of all, the increase of the roughness height obviously results in the reduction of δS_M and in some cases not only the absolute value, but also the sign of the scaling error changes (see e.g. Fig. 4).

Unfortunately, it does not seem possible, to determine general trends in the behavior of δS_M: for each ship the dependence of the scaling error on h/T, Fr and k_s looks differently, e.g. for PPM52 one can see a monotone trend, for PPM55 the data contains a jump between $Fr = 0.11$ and 0.13, whereas for PM32 the scaling error turned out to be almost independent of the mentioned parameters.

Therefore, one can draw a conclusion, that the derivation of a generally valid correction for the scaling error cannot be undertaken, at least with the available database.

The scaling error for the trim angle was calculated according to the following formula:

$$\delta\theta = \theta^{ship} - \theta^{model}, \quad (1)$$

where θ^{ship}, θ^{model} are the values computed for the ship and the model respectively. If $\delta\theta$ is positive, the ship is trimmed more to the bow, than the model, and vice versa. The curves for $\delta\theta$ can be seen in Figures 7, 8 and 9. Exactly as it was noticed for S_M, the plots for $h/T = 1.15$ do not agree well with the plot for other h/T, even though in case of $\delta\theta$ the situation is a bit better. The scaling error of θ obviously strongly depends on the roughness height, used for the full scale simulations, which is an expected result, since the roughness affects the viscous forces under the hull and the pressure drop. However, the trends vary between the ships. For PPM55 the dependence is oscillatory, whereas for PPM52 and PM32 the error is positive at small k_s ($\theta^{ship} > \theta^{model}$), but starting from k_s = 1mm it changes the sign. In computations of (von Graefe, 2011) the error in trim angle was positive as well, i.e. the ship trimmed more to the bow. However, the values of the roughness used in the computations were not reported in that work.

The $\delta\theta$ increases, when h/T is reduced and when Fr grows. Generally, the values of $\delta\theta$ are quite small ($< 0.02^{\circ}$), but significantly different for all hull forms.

6.2 SCALING ERROR FOR THE MAXIMUM SINKAGE

As it has already been mentioned, analysis the differences in maximum sinkage between the model scale and the full scale can be undertaken using the plots for δS_B and δS_H. Whether the sinkage at the bow or at the stern is larger, depends on the sign of the trim angle. If the sign is positive, then the sinkage at the bow is larger, than at the stern and vice versa. The containerships PPM55 and PM32 are trimmed to the stern, but PPM52 - to the bow. Therefore, in this section the quantity S_H is analyzed for PPM55 and PM32, whereas for PPM52 - δS_B. Formulae for δS_B and δS_H are similar to the one used for δS_M.From the plots shown in Figures 10, 11, 12, 13, 14 and 15 one can draw the following conclusions. In most cases (h/T = 1.25 - 2.0), the scaling error of maximum sinkage is under 10%. The only exception is the case h/T =1.15, where the relative deviation can reach 12-15%. However, one has to keep in mind that the results for h/T = 1.15 have higher uncertainty. The maximum absolute discrepancy in the maximum sinkage between the model and the ship is 19cm (PPM52, h/T=1.15, k_s=0.15mm). The values of δS_B, δS_H are obviously very sensitive to the roughness height. The larger the value of k_s is, the better is the agreement between the ship and the model squat estimations. For example, the scaling error of S_B has maximum value of 15% for PPM52 at k_s = 0.15mm, but at k_s=2mm its value diminishes to 5%. In the majority of the considered cases the scaling error is negative (squat effect is more pronounced for the ship, that for the model), which has to be taken into account in practice.

Similarly to the previously analyzed quantities, the trends for the scaling error of maximum sinkage vary strongly among the ships and therefore a generally valid correction seems hard to derive. One has to mention the interesting results observed for PM32, where the scaling error is in general much smaller than for other two ships and is almost independent of the sand roughness or the Froude number.

7 CONCLUSION

The conducted numerical analysis of the scale effects on squat for the range of depth-by-draft ratio h/T = 1.25 - 2.0 has shown, that the conversion of the data from the model to the full scale using linear scaling leads to an error of about 10% (15cm) percent of the maximum sinkage. Under very shallow water conditions (h/T =1.15) this error can reach up to 15% (19cm). The squat effect in model scale is normally less intense, than at full scale. This means, that for a ship the values of the sinkage can be from $7-10\%$ (at $h/T \geq 1.25$) to 15% (h/T = 1.15) larger, than that observed in model tests. Other authors drew similar conclusions on this matter (von Graefe, 2011). As the h/T is reduced, the conversion error grows, because of the increasing importance of the viscous effects. The reliability of the results for the lowest h/T considered in the present work (1.15) unfortunately remains an open question. Since at smaller values of h/T the physics of the flow becomes more complex and the numerical solution of the task is more challenging, additional study is needed, to determine the source of the errors. The authors consider this to be an important task, since at h/T = 1.15 a dramatic increase of the scaling error was observed and one has to make sure, that this phenomenon is accurately captured.

The parameters of the ship hull roughness have a significant influence on the studied phenomenon due to the influence on the boundary layer thickness. Up to some particular point the increase of k_s leads to a reduction of the scaling error, but at high values of k_s the error changes its sign and its absolute values start growing again.

The initial idea of the conducted research was to derive scaling laws, which would help to decrease the error of linear scaling for the values of sinkage from model scale to full scale. However, as it was shown the δS_M, $\delta\theta$, δS_B, δS_H as the functions for h/T, k_s, Fr behave themselves completely differently for each ship, even though the considered ships have similar hull forms and block coefficients and thus it is hard to propose a generally valid correction even for one class of ships. The derivation of the correction for one ship would lead to increase of the error for the other hull forms. But keeping in mind, that the overall maximum scaling error observed in numerical analysis was 8% of the UKC (19cm in full scale), the necessity of a correction is questionable.

8 ACKNOWLEDGEMENTS

The authors gratefully acknowledge the help of the research group of the Faculty of Mechanical Engineering and Naval Architecture of the University of Zagreb (H. Jasak, V. Vukcevic, I. Gatin) with the development of the computational method, used in the present study. The computational resources were provided by the Deutsche Forschungsgemeinschaft (German Research Foundation) under the grant INST 264/113-1 FUGG.

9 REFERENCES

Anschau, P., 2016. LDV-Messungen an einem Containerschiffsmodell im Flachwasser. Report 349/4447 of Potsdam model basin (SVATech), Schiffbau-Versuchsanstalt, 2016.

Hoekstra, M., 2006. A RANS-based analysis tool for ducted propeller systems in open water condition. International Shipbuilding Progress, 53(3)
Jachowski, J. Assessment of ship squat in shallow water using CFD, Archives of Civil and Mechanical Engineering, Volume 8, Issue 1, 2008

ITTC, 2008. Recommended Procedures and Guidelines , Uncertainty Analysis in CFD Verification and Validation Methodology and Procedures, 7.5-0.3-01-01. http://ittc.info/media/4184/75-03-01-01.pdf.

ITTC, The ITTC Resistance Committee, 2011. Final report and recommendation to the 26th ITTC, volume I of Proceedings of 26th ITTC.

ITTC, 2017. Recommended Procedures and Guidelines, 1978 ITTC Performance Prediction Method,7.5–02-03–01.4

Linde, F., Ouashine, A., Huybrechts, N., Sergent, P., 2015. Numerical prediction of ship resistance and squat in confined waters. Proceedings of VI International Conference on Computational Methods for Coupled Problems in Science and Engineering.

Raven, H.C., Ploeg, A., Starke, A. R., 2008. Towards a CFD-based prediction of ship performance - Progress in predicting full-scale resistance and scale effects. RINA - International Conference - Marine CFD 2008 - Papers.

Shevchuk, I., Böttner C.-U., Kornev, N., 2016. Numerical analysis of the flow in the gap between the ship hull and the fairway bottom in extremely shallow water, Proceedings of the 4th MASHCON.

von Graefe A., el Moctar O., Shigunov V., Söding H., Zorn T., 2011. Squat Computations for Containerships in Restricted Waterways, Proceedings of the 2nd MASHCON

Vukcevic, V., 2016. Numerical Modelling of Coupled Potential and Viscous Flow for Marine Applications. PhD thesis, University of Zagreb, 2016.

10 AUTHORS' BIOGRAPHY

Ivan Shevchuk works at Hamburg University of Technology as a research engineer on the field of hydrodynamics and computational fluid dynamics. He holds a diploma and a PhD degree in Naval Architecture

Carl-Uwe Böttner currently works as a research engineer with the Federal Waterways Engineering and Research Institute (BAW) in Hamburg on the fields of ship dynamics and ship handling simulation. He is responsible for consulting the authorities in terms of ship handling simulation.

Nikolai Kornev is the head of the chair of modelling and simulation at the University of Rostock.

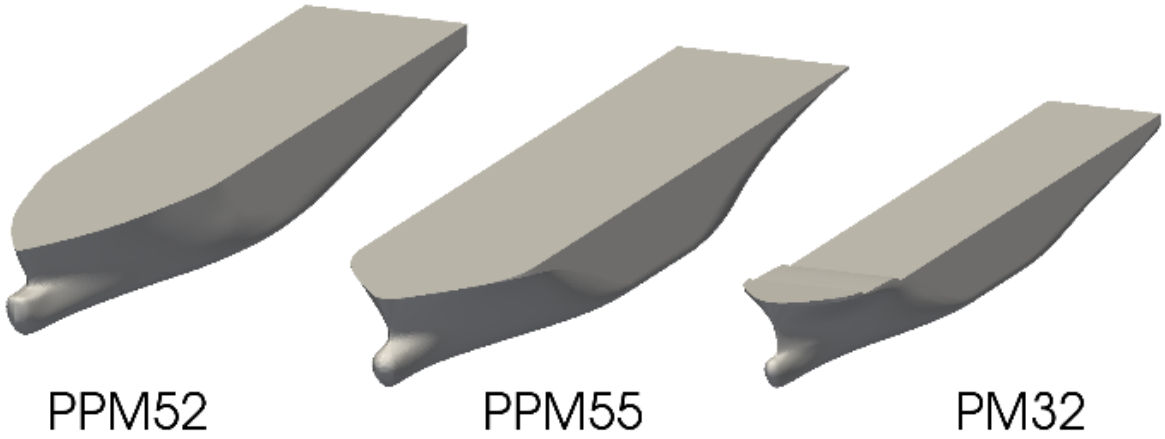

Figure 1. Considered hull forms, I

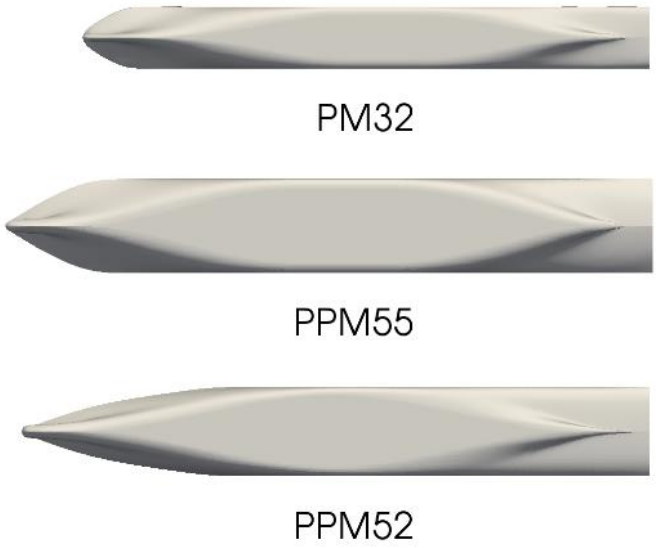

Figure 2. Considered hull forms, II

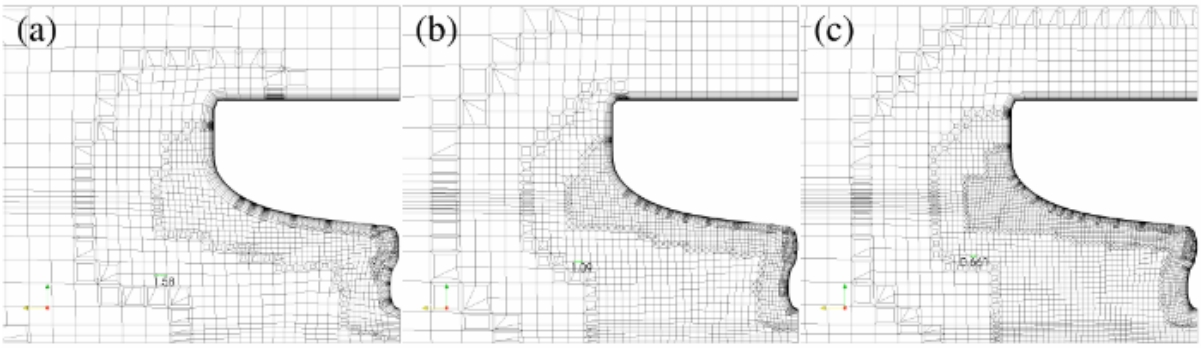

Figure 3. Slices of the computational mesh at the ship stern (a) –coarse, (b) –medium, (c) - fine

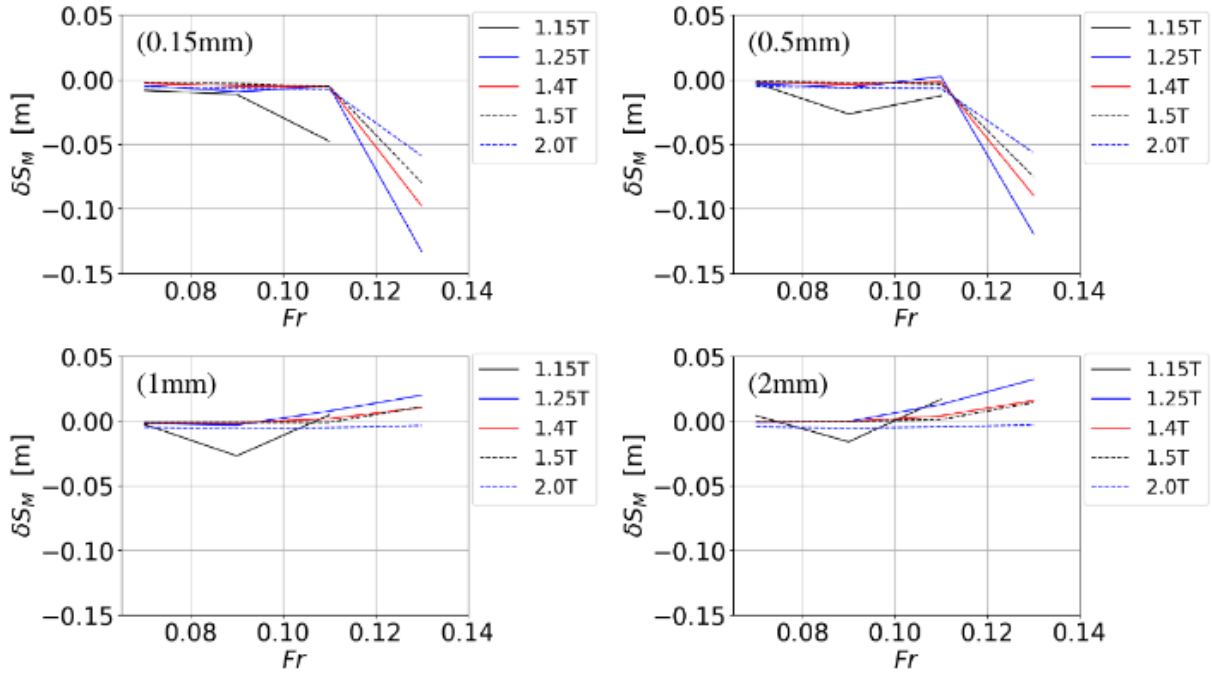

Figure 4. δS_M for different sand roughnesses, PPM55

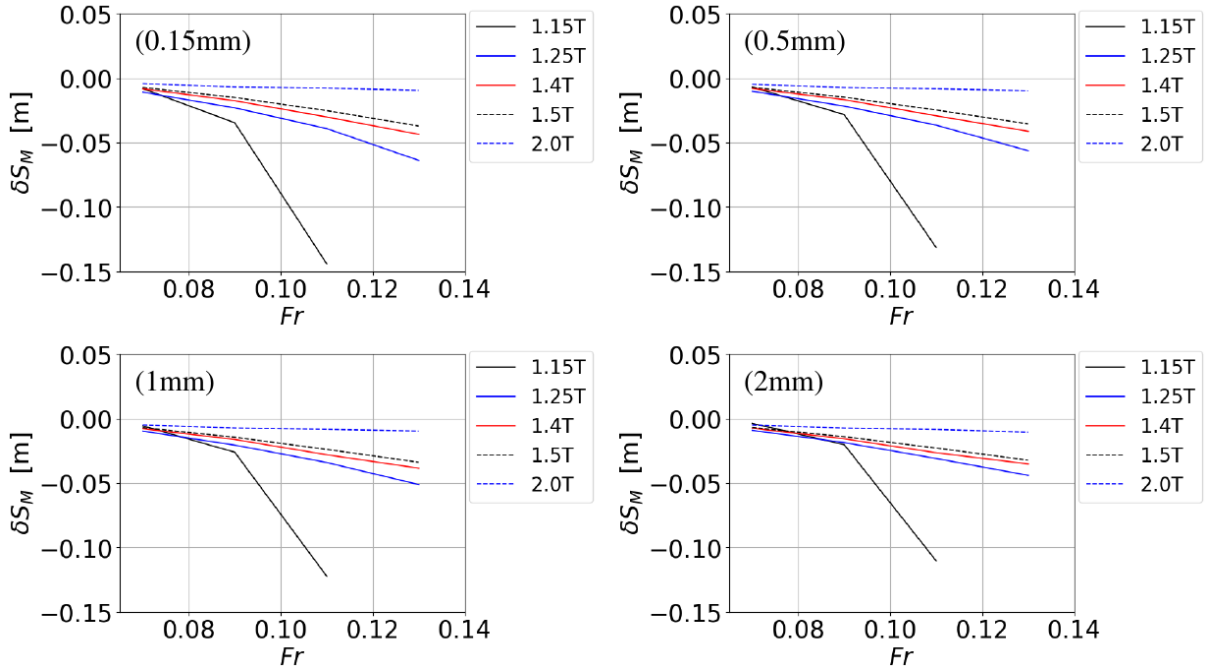

Figure 5. δS_M for different sand roughnesses, PPM52

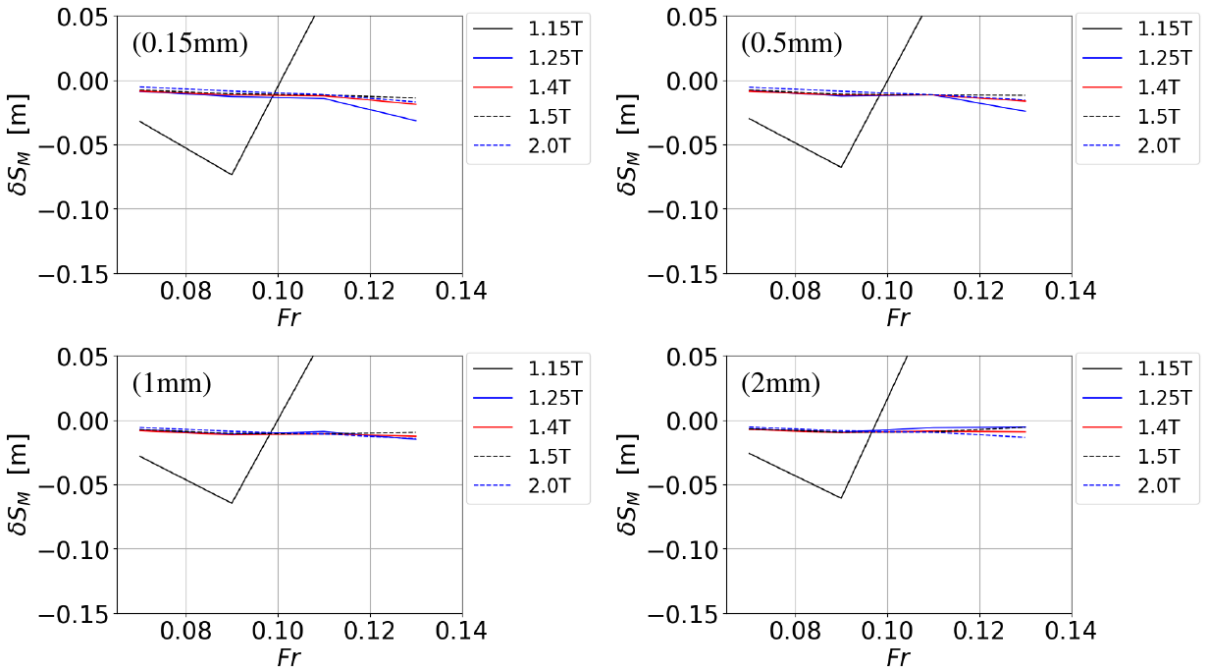

Figure 6. δS_M for different sand roughnesses, PM32

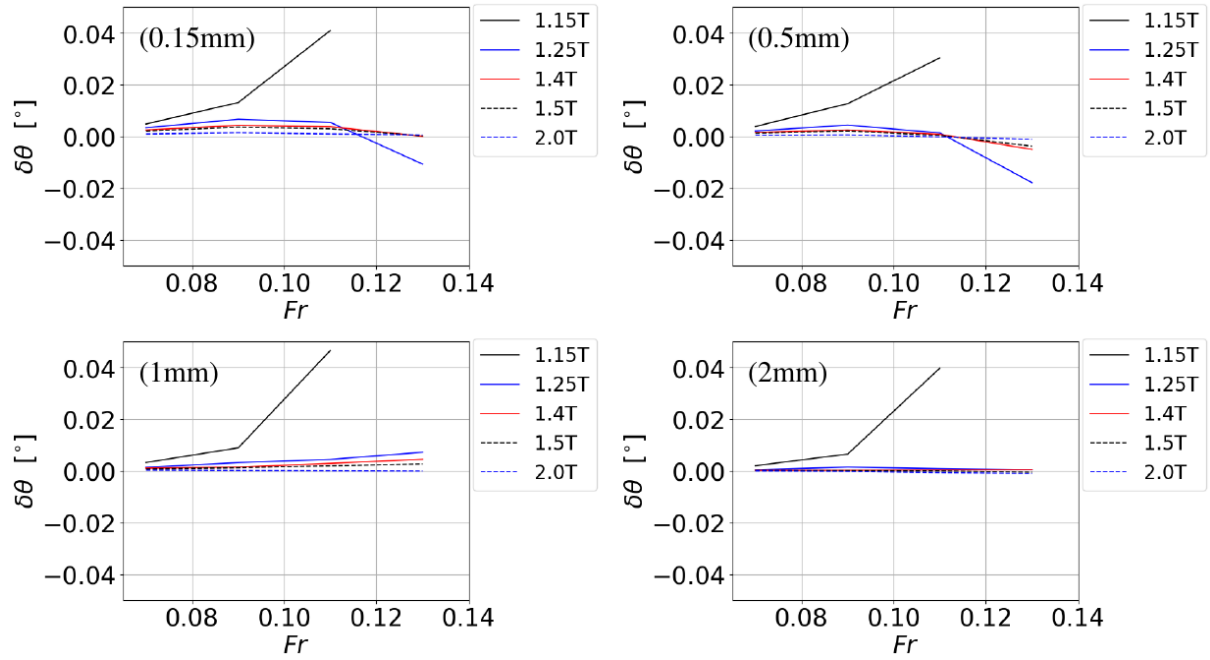

Figure 7. $\delta\theta$ for different sand roughnesses, PPM55

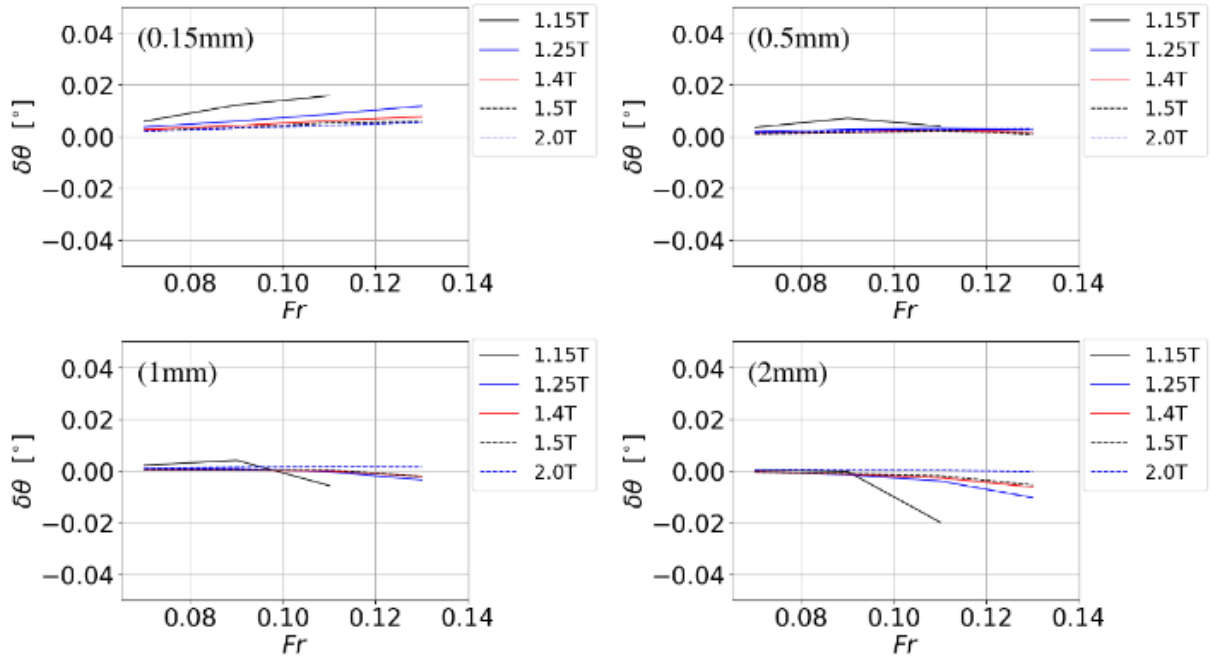

Figure 8. $\delta\theta$ for different sand roughnesses, PPM52

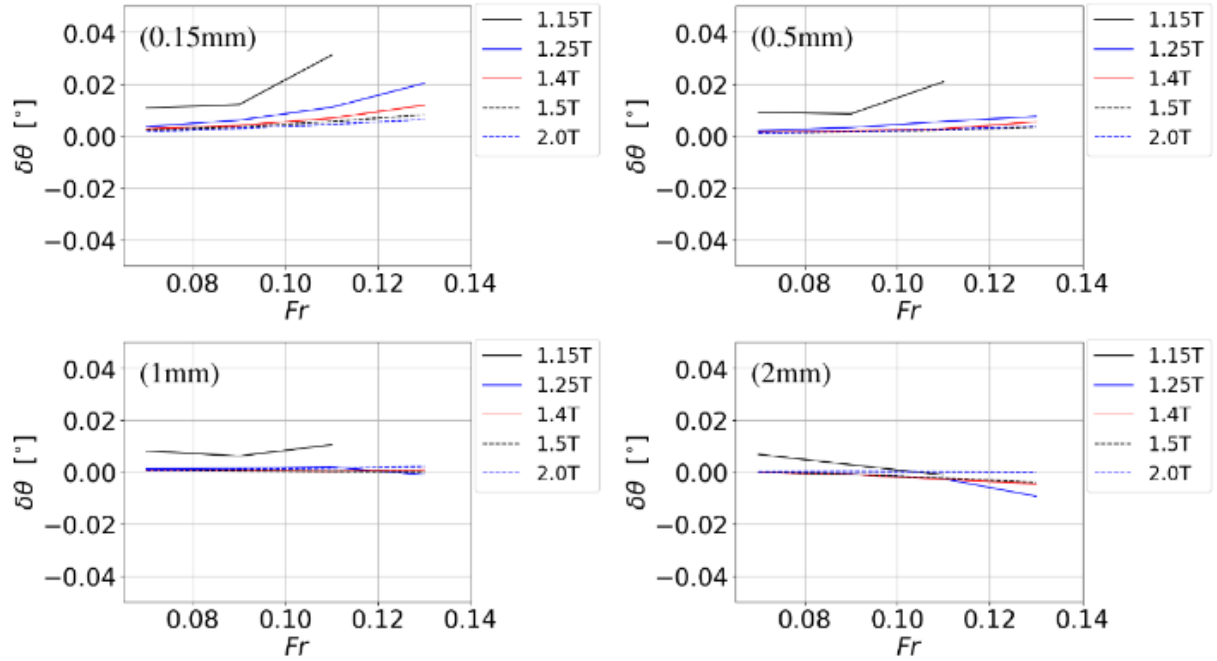

Figure 9. $\delta\theta$ for different sand roughnesses, PM32

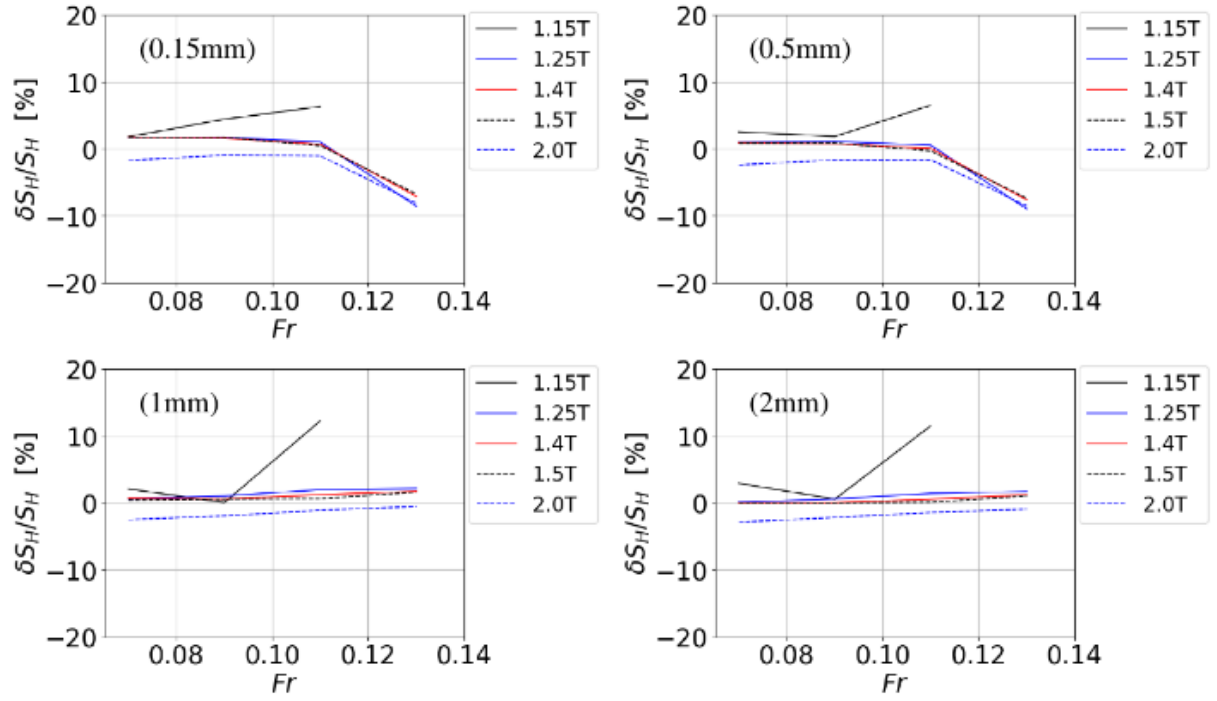

Figure 10. δS_H(in % of S_H^{ship}) for different sand roughnesses, PPM55

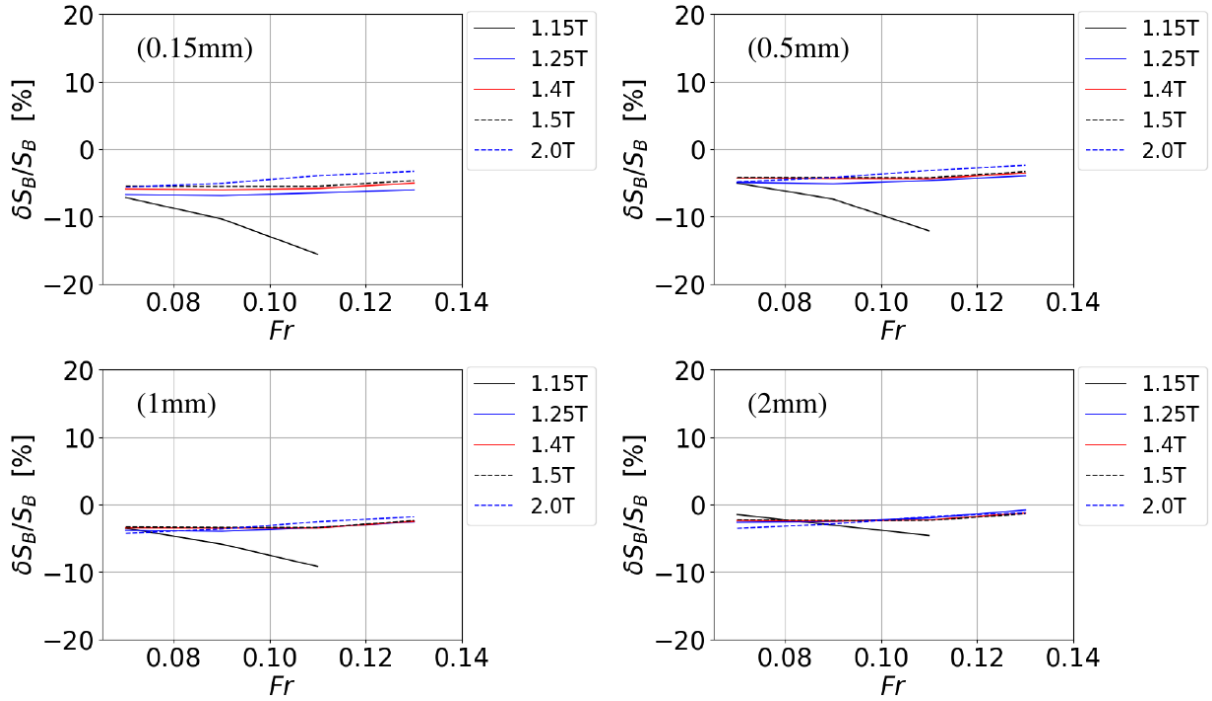

Figure 11. δS_B(in % of S_B^{ship}) for different sand roughnesses, PPM52

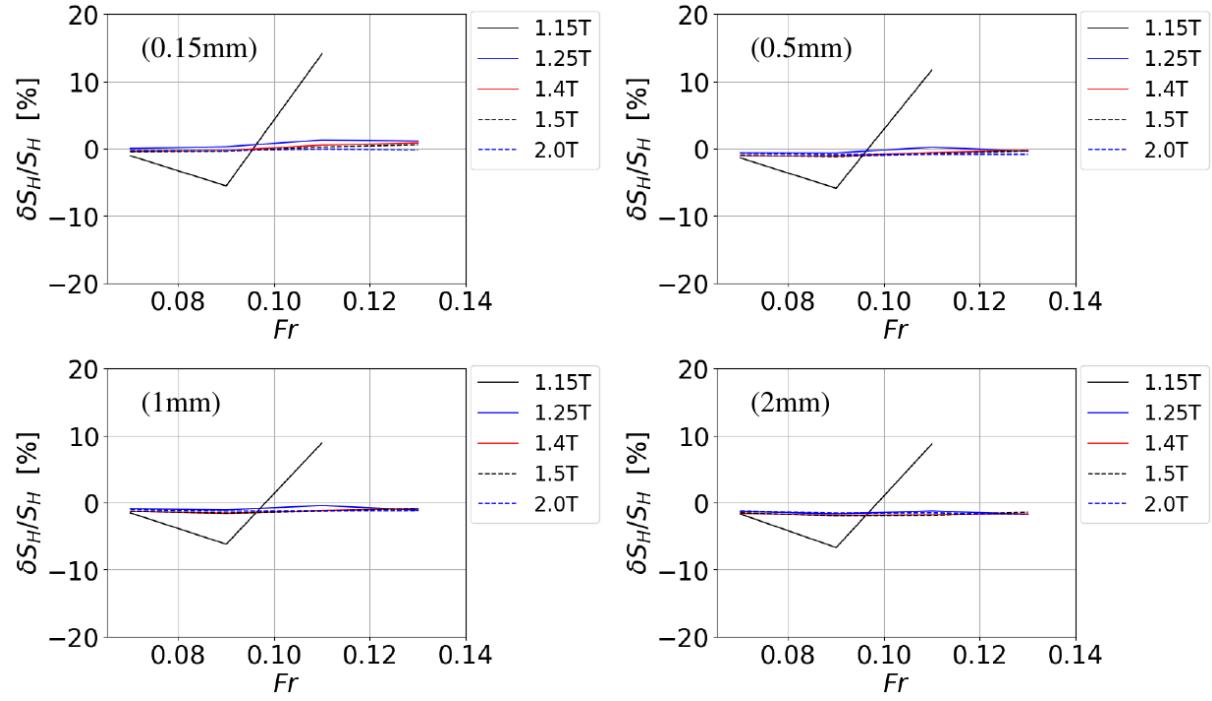

Figure 12. δS_H(in % of S_H^{ship}) for different sand roughnesses, PM32

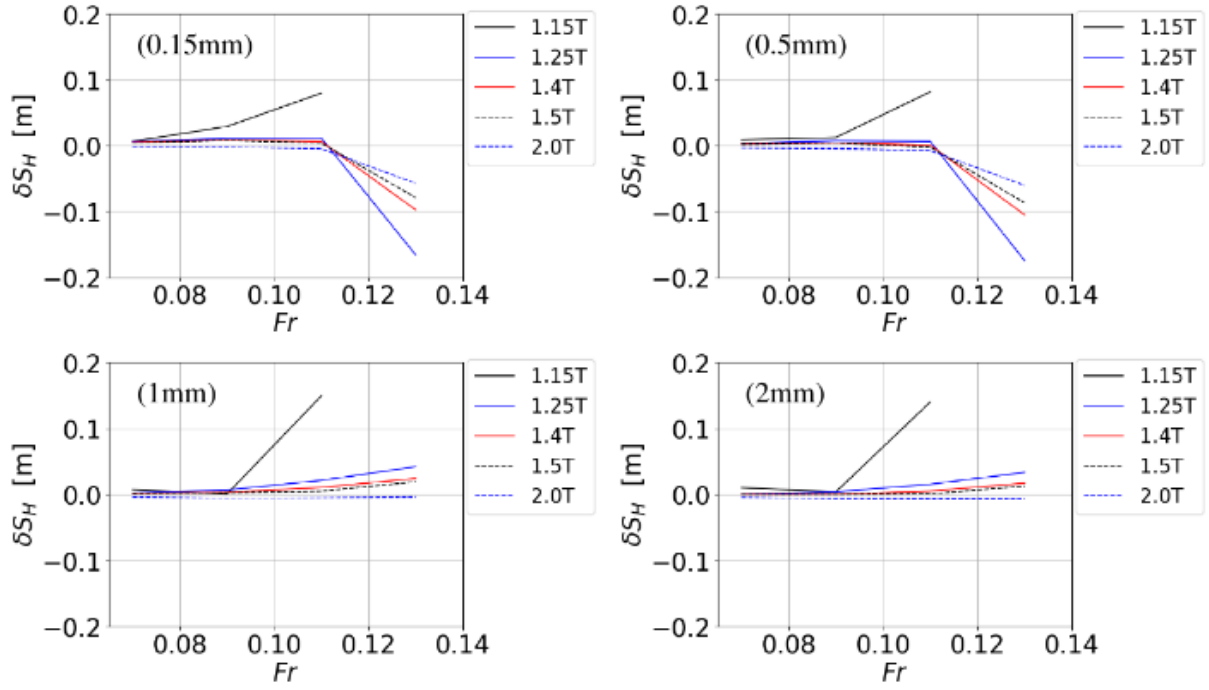

Figure 13. δS_H(in m) for different sand roughnesses, PPM55

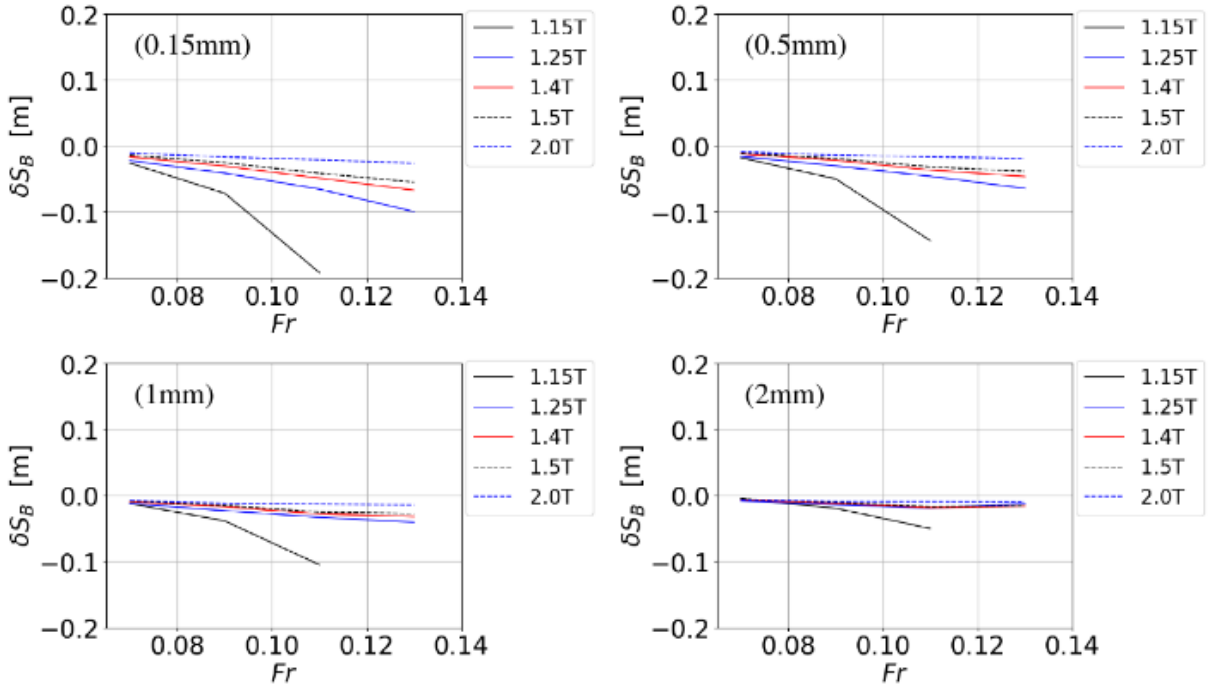

Figure 14. δS_B(in m) for different sand roughnesses, PPM52

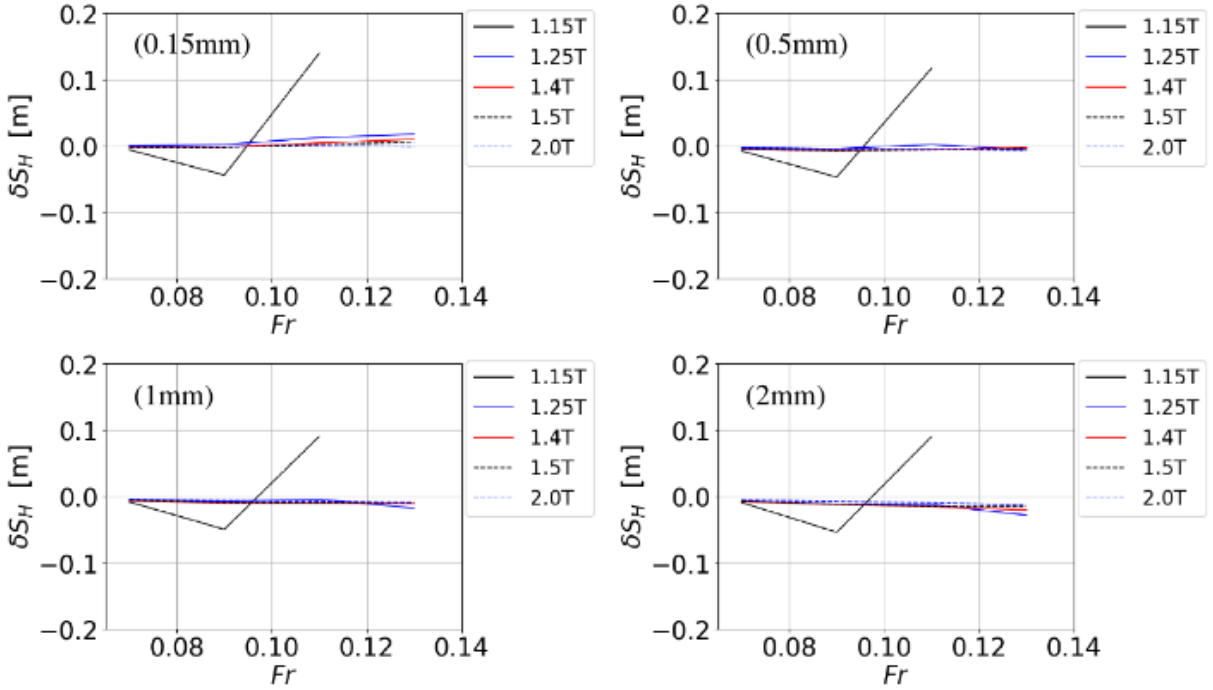

Figure 15. δS_H(in m) for different sand roughnesses, PM32

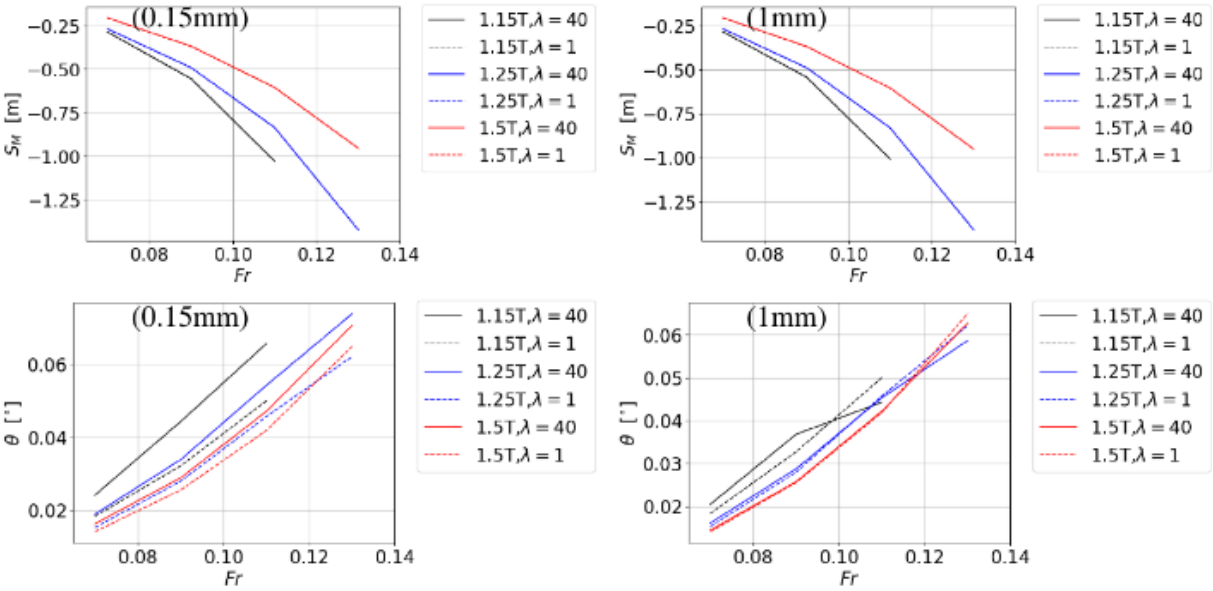

Figure 16. Comparison of the sinkage at midship and trim angle between the model scale and the full scale for two values of the sand roughness, PPM52

ON THE ASSESSMENT OF SHIP SQUAT AND VERTICAL WAVE MOTIONS FOR DTC CONTAINER CARRIER IN SHALLOW WATER IN A REAL TIME MANEUVERING SIMULATOR

Eduardo A. Tannuri,
Universidade de São Paulo, São Paulo, Brazil

ON THE ASSESSMENT OF SHIP SQUAT AND VERTICAL WAVE MOTIONS FOR DTC CONTAINER CARRIER IN SHALLOW WATER IN A REAL TIME MANEUVERING SIMULATOR

Eduardo A. Tannuri, Universidade de São Paulo, São Paulo, Brazil

SUMMARY

The accurate prediction of ship squat and vertical wave motions is important to assess ship underkeel clearance in shallow water and to define the maximum draft (or the minimum depth) for a safe navigation. Although the real-time ship maneuvering simulators are not the most adequate tool to the vertical design of the nautical access, they are used to check the vertical maneuvering margin and to execute tests with the aid of pilots and captains to verify the proposed nautical layout. Therefore, the simulators must have reasonable and realistic models of vertical movements, considering the limitations imposed by the real-time calculation. This paper presents the mathematical models for vertical motions (squat and wave motions) adopted in the Brazilian simulator SMH, and a comparison with benchmark data from (Van Zwijnsvoorde et al., 2019), comprising model tests conducted with the DTC container carrier.

NOMENCLATURE

B	Vessel's beam (m)
C_B	Vessel's block coefficient
C_S	Coefficient of ICORELS regression
F_S	Equivalent squat force (N)
F_{nh}	Froude number $(adim.)$
g	Gravitational acceleration (m/s^2)
h	Water depth (m)
k	wave number $(1/m)$
K_{ij}	Hydrostatic restoring matrix
L_{pp}	Vessel's length between perpendiculars (m)
$S_{s,b}$	Stern / Bow squat (m)
x_3	Vessel's vertical displacement (m)
x_5	Vessel's pitch angle (rad)
Z VA	Running sinkage at aft perpendicular (mm)
Z VF	Running sinkage at fore perpendicular (mm)
∇	vessel's displacement (ton)
λ	wavelength (m)
ω	wave frequency (rad/s)
ω_e	wave encounter frequency (rad/s)
CONAPRA	Brazilian Maritime Pilots Association
DTC	Duisburg Test Case (container carrier)
RAO	Response Amplitude Operator
SMH	USP Maritime and Waterways Simulator
TPN	Numerical Offshore Tank Laboratory
USP	University of São Paulo

1 INTRODUCTION

The accurate prediction of ship squat and wave motions is important to assess ship underkeel clearance in shallow water. The dimensions of the new large containerships operating in ports are beyond the design ship of these locations, which require advanced analysis and simulations to improve the navigation safety and efficiency. The limiting environmental conditions (due to waves and tide) for safe navigation are obtained from accurate mathematical models of vertical forces and motions. These models are based on potential flow and on the discretization of the fluid domain, requiring high computer processing capacity. A very large number of tides, drafts and waves are simulated offline to define the operational window and/or safe draft for navigation. Another approach that is becoming more usual today is the dynamic underkeel clearance systems, that execute the mathematical model on demand, based on the present ship and measured environmental conditions.

The real-time ship maneuvering simulators are a complementary tool to the vertical design of the nautical access. They are used to test the vessel's maneuverability in restricted areas and to check the maneuvering margin (minimum vertical margin required to guarantee the maneuverability of the vessel). However, they are not adequate tools for a comprehensive verification of the underkeel clearance and safety margins in relation to vertical movements, because the tests are performed in real time and few maneuvers can be done, do not covering all the variability of directions, periods and wave heights that may occur at the study site. Furthermore, the mathematical models must be executed in real time, imposing barriers to the level of sophistication and computational requirements. However, the simulators must have reasonable models of vertical movements, because of the dependence that the underkeel clearance exerts on the maneuverability of the vessel.

This paper presents the mathematical models for vertical motions (squat and wave motions) adopted in the Brazilian simulator SMH (Portuguese acronym for Maritime and Waterways Simulator). The results from the simulator are compared to the benchmark data from (Zwijnsvoorde et al., 2019), comprising model tests conducted with the DTC container carrier. The comparison is used to discuss the validity of the adopted models.

The SMH has been developed by the Numerical Offshore Tank Laboratory of the University of São Paulo (TPN-

USP), Petrobras (Brazilian oil state company), with a technical partnership with the Brazilian Maritime Pilots Association (CONAPRA). The SMH is the core simulation software adopted in the TPN-USP Maneuvering Simulation Center, composed by 6 simulators, being 3 of them classified as full-mission (immersive system with more than 270º angle of projection). All simulators can run together in the same run (multiplayer simulation). Some simulators are shown in Figure 1.

Figure 1. TPN-USP Maneuvering Simulation Center

The SMH has been used for a large number of port analysis in Brazil, as shown in (Tannuri and Martins, 2018). The complete mathematical formulation and physical fundaments of the SMH models are presented in (Queiroz Filho et al., 2014; Tannuri et al., 2014).

2 WAVE FORCES AND MOTIONS

The calculation of the wave forces considers the second order drift components (mean and slow varying drift forces) and the first order high frequency (HF) components separately. The second-order drift coefficients and first-order Hasking Forces are obtained by the potential theory, with the hypothesis of zero advance speed. This approximation is valid for low-speed maneuvering, and its utilization for vessels with advance speed is associated with errors that will be estimated in this paper. The simulator is able to import the hydrodynamic coefficients from different commercial codes, such as Wamit. In the case of shallow waters, the domain of the Wamit model must contains the sea bottom, normally assumed as flat.

The HF motion comes from the application of the wave first order forces to the 6 DOF equations of motions (Pinkster, 1980) (Faltinsen, 1993). The exciting forces are computed by sub-dividing the sea spectrum in hundreds of components with random uneven frequency ranges and random phases. Combining (summing up) these components, we define the irregular incident wave. These components combined with the exciting force RAO in each degree of freedom will define the exciting wave forces. These exciting forces are computed only as a function of the incident wave, so they do not double count with other non-potential effects.

The added mass and damping effects are taken into consideration through the convolution of the IRF (impulse response functions) obtained from the frequency domain hydrodynamic coefficients (added mass or potential damping) and the past motions of the ship. These IRF functions are computed under the assumption of an impulsive velocity applied to the floating bodies. The IRF functions are convolved with the past velocities of the body. Only oscillatory motions will give rise to added mass and damping forces, corresponding to an energy balance between the body motions and the waves radiated due to these ship oscillations. They are function only of the past motions of the ship, and properly include the effect of the waves radiated due to these past oscillations (Oortmerssen, 1976).

The (Aranha and Fernandes, 1995) approximation to the quadratic transfer functions is applied to the calculation of the slow drift wave forces. Wave-drift damping effects (current-wave interaction) are also considered, following the formulation presented by (Aranha, 1994).

The effect of the advance speed is partially considered in the model adopted in the SMH simulator. The relative velocity between the ship and the wave cause a modification in the wave encounter frequency (ω_e). Therefore, a correction in the incident wave spectrum must be done, in which the wave frequency is replaced by the encounter frequency, while still maintaining the wave total energy.

For the specific case of this paper of a regular wave with frequency ω (rad/s), bow incidence and ship advance U (m/s), the encounter frequency is given by:

$$\omega_e = \omega + k.U \tag{1}$$

Where $k = 2\pi/\lambda$ is the wave number, λ is the wavelength (m) in shallow water obtained from the dispersion relation:

$$\lambda = \frac{2\pi g}{\omega^2}\tanh\left(\frac{2\pi h}{\lambda}\right) \tag{2}$$

being g the gravitational acceleration (m/s^2) and h the depth (m).

3 SQUAT FORCE

The SMH adopts a squat vertical force model based on the ICORELS regression, outlined in the PIANC Working Group 30 Report. Although it is developed only for open or unrestricted channel, we assume as a simplified formulation for all cases. The bow squat S_b (m) is given by:

$$S_b = C_S \frac{\nabla}{L_{pp}^2} \frac{F_{nh}^2}{\sqrt{1-F_{nh}^2}} \tag{3}$$

Being L_{pp} the vessel´s length between perpendiculars (m), ∇ the displacement (ton), the dimensionless $F_{nh} = U/\sqrt{gh}$ and:

$$C_S = \begin{cases} 1.7 & C_B < 0.7 \\ 2.0 & 0.7 \leq C_B < 0.8 \\ 2.4 & C_B \geq 0.8 \end{cases} \quad (4)$$

We have to obtain an equivalent vertical force (F_s) applied on the vessel that will result in a bow squat S_b (m) as given in (3). We assume the hypothesis that the force is applied in the center of gravity of the vessel. Being x_3 the vertical displacement at the center of gravity (positive upwards), x_5 the pitch angle (positive when the bow enters the water) and K_{ij} the terms of the hydrostatic restoring matrix, and disregarding coupling with other displacements, we can write:

$$\begin{pmatrix} F_s \\ 0 \end{pmatrix} = \begin{pmatrix} K_{33} & K_{35} \\ K_{35} & K_{55} \end{pmatrix} \begin{pmatrix} x_3 \\ x_5 \end{pmatrix} \rightarrow$$
$$\begin{pmatrix} x_3 \\ x_5 \end{pmatrix} = \begin{pmatrix} K_{33} & K_{35} \\ K_{35} & K_{55} \end{pmatrix}^{-1} \begin{pmatrix} F_s \\ 0 \end{pmatrix} \quad (5)$$

The bow (b) and stern (s) squat is given by

$$S_b = -x_3 + \frac{L_{pp}}{2} x_5$$
$$S_s = -x_3 - \frac{L_{pp}}{2} x_5 \quad (6)$$

With (5) and (6) we can obtain the equivalent vertical force (F_s) that results, after a transient, into the desired bow squat given by (3).

4 COMPARISONS WITH EXPERIMENTAL TESTS

In this section, the results obtained with the SMH simulator are compared to experimental data from towing tank tests in calm water and in waves presented in (Zwijnsvoorde et al., 2019) . The objective is to verify the reliability of the prediction and the expected deviations.

The tests were executed using a 1:89.11 scale model of the 14,000TEU containership DTC (Table 1), in the Towing Tank for Manoeuvres in Shallow Water (cooperation FHR and UGent).

Table 1. Ship particulars

Particular	Full Scale	Model Scale (1:89.11)
L_{pp} (m)	355	3.984
B (m)	51	0.572
Draft (m)	14.5	0.163
C_B	0.661	0.661
∇	171,800ton	242.8kg

Two sets of captive tests are reproduced in the SMH simulator and compared with the experimental results, including calm water tests (C1, C2, and C3) and tests in waves (CW1 to CW5). During captive tests the ship is fixed in the horizontal plane (surge, sway and yaw), allowing roll, pitch and heave. The hull forces are measured using load cells and the ship's heave, trim and roll are measured by using potentiometers.

All numerical simulations were executed in the free-running mode, because the SMH does not provide the possibility of doing a numerical captive test. In the simulations, a longitudinal external force is applied at the midship and adjusted to deliver the final speed equal to the experimental captive test. After speed stabilizations, the squat, wave motions and resistance forces were compared.

4.1 CALM-WATER TESTS

The results of the tests C1, C2 and C3 in calm water are presented in Table 2. The maximum difference for the bow squat (Z VF) is -6%, what is quite acceptable. However, due to the simplifications of the squat model adopted in the simulator, the stern squat (Z VA) differences are larger (up to 38%). We must remember that the ICORELS regression only provides the value of the bow squat, and the stern squat results from the hypotheses adopted in the model of the simulator. The resistance force is well represented in the simulator, with differences smaller than 4%.

Table 2. Tests in calm water – comparison between experimental and simulation results

C1 V=6kn (0.327m/s model scale), UKC 100%			
	Exper.	Simul.	Dif. (%)
Z VF mm	0.88	0.91	3%
Z VA mm	0.58	0.44	-24%
Z MidShip mm	0.73	0.67	-8%
Resistance N	0.80	0.82	2%

C2 V=16kn (0.872m/s model scale), UKC 100%			
	Exper.	Simul.	Dif. (%)
Z VF mm	8.34	7.81	-6%
Z VA mm	5.01	3.64	-27%
Z MidShip mm	6.68	5.72	-14%
Resistance N	5.82	6.08	4%

C3 V=6kn (0.327m/s model scale), UKC 20%			
	Exper.	Simul.	Dif. (%)
Z VF mm	1.56	1.58	1%
Z VA mm	1.26	0.78	-38%
Z Midship mm	1.41	1.18	-16%
Resistance N	1.09	1.09	0%

4.2 TESTS IN WAVES

4.2 (a) 100% UKC

The Case CW1 represents a stationkeeping test, with no advance speed and 100% UKC. The Table 3 shows that the vertical motion amplitude is slightly overestimated by the simulator model, mainly for the aft point. The comparisons are based on the period in which the captive model test could be considered in a stationary oscillation (from 50s to 100s). Since the average ZVF and ZVA is close to zero, the difference in terms of percentage would be a

meaningless high value, which is not calculated. Figure 2 shows the time series of the vertical motion.

The longitudinal force due to wave action (generically refereed as Resistance) is also well estimated by the simulator, as indicated in Table 3 and in Figure 3.

Table 3 .Test CW1 (in waves, no advance speed) – comparison between experimental and simulation results

CW1 UKC 100%, model scale: V=0m/s, Wave H=54.49mm 1.38s full scale: V=0kn, Wave H=4.85m 13.03s			
	Exper.	Simul.	Dif (%)
ZVF amp. mm	20.91	22.27	6.5%
ZVF aver. mm	0.20	-0.07	-
ZVA amp. mm	10.77	13.34	23.9%
ZVA aver. mm	-0.05	0.04	-
Resistance X amp. N	23.46	21.56	-8.1%
Resistance X aver. N	-0.77	-0.81	4.7%

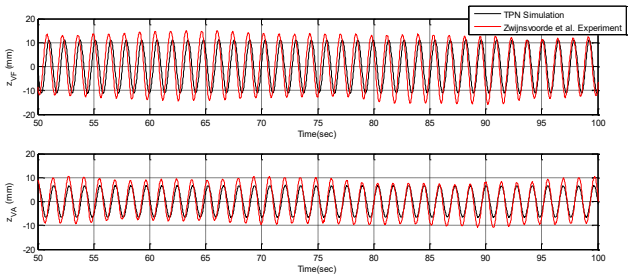

Figure 2. Vertical motion at the forward and aft points – CW1 test

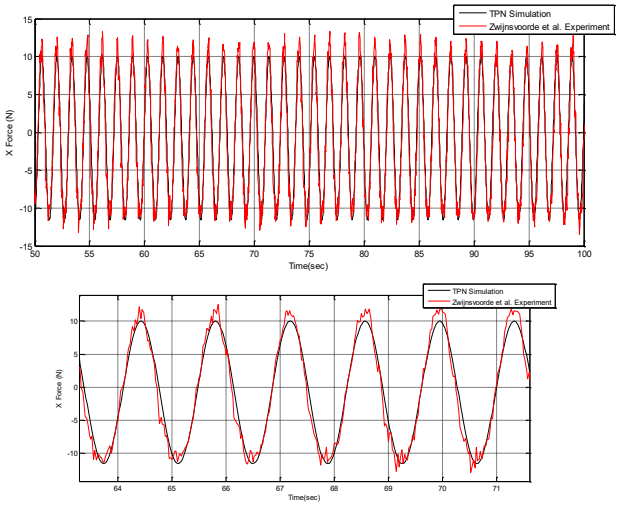

Figure 3. Longitudinal force – CW1 test (up): complete time series – 50s ; (down) detail – 8s

In the case CW3, the carriage is moving with 0,872m/s (16 knots in real scale) and the vessel is subjected to a bow incident wave with the same period of the previous test, and a height slightly larger. The results are presented in the Table 4.

The amplitude of the motions is smaller than that of the no advance speed test (CW1), what can be partially explained by the higher encounter frequency (apparent period in model scale 0.89s, real scale 8.4s). The average sinkage is also in agreement with the results from C2 test (same speed, no waves), since the squat effect is the main responsible for it. Figure 4 shows the time series of the vertical motion. The resistance force is reasonably well estimated by the simulator, as can be verified in Figure 5.

Table 4. Test CW3 (in waves, advance speed) – comparison between experimental and simulation results

CW3 UKC 100% model scale: V=0.872m/s, Wave H=62.35mm 1.38s full scale: V=16kn, Wave H=5.56m 13.03s			
	Exper.	Simul.	Dif (%)
ZVF amp. mm	20.94	22.32	7%
ZVF aver. mm	8.10	7.99	-1%
ZVA amp. mm	17.33	17.93	3%
ZVA aver. mm	5.40	3.92	-27%
Resistance X amp. N	-18.60	-20.00	8%
Resistance X aver. N	-7.31	-7.43	2%

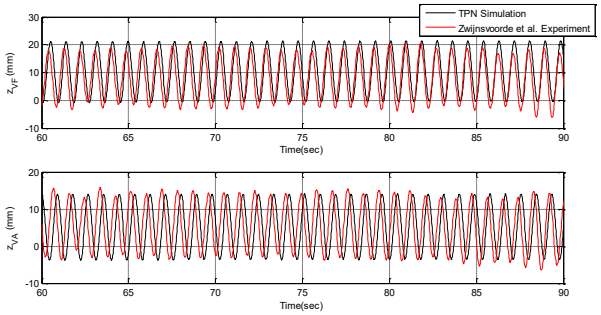

Figure 4. Vertical motion at the forward and aft points – CW3 test

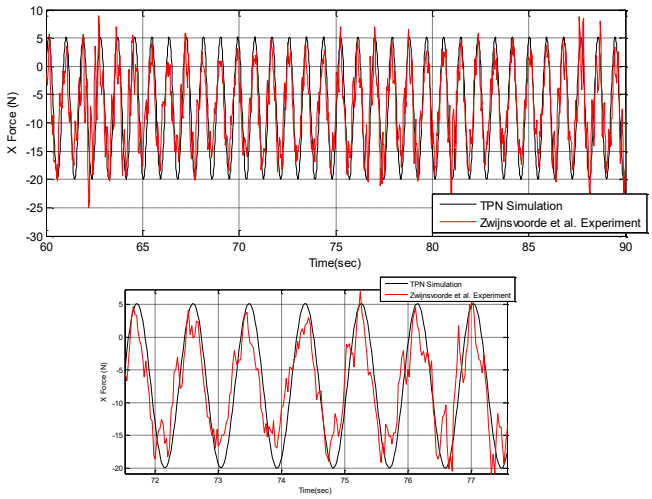

Figure 5. Longitudinal force – CW3 test (up): complete time series – 30s ; (down) detail – 6s

The case CW2 is a blind test, with no experimental ship motions presented by Van Zwijnsvoorde et at. (2019). The results obtained by the simulator model are presented in

Table 5, Figure 6 (vertical motion) and Figure 7 (resistance force).

Table 5. Test CW2 (in waves, advance speed) –simulation results

CW2 UKC 100% model scale: V=0.327m/s, Wave H=62.31mm 1.38s full scale: V=6kn, Wave H=5.55m 13.02s	
	Simul.
ZVF amp. mm	28.76
ZVF aver. mm	1.35
ZVA amp. mm	23.61
ZVA aver. mm	0.62
Resistance X amp. N	26.10
Resistance X aver. N	-1.73
Apparent Period s	10.79s (real scale) 1.14s (mode scale)

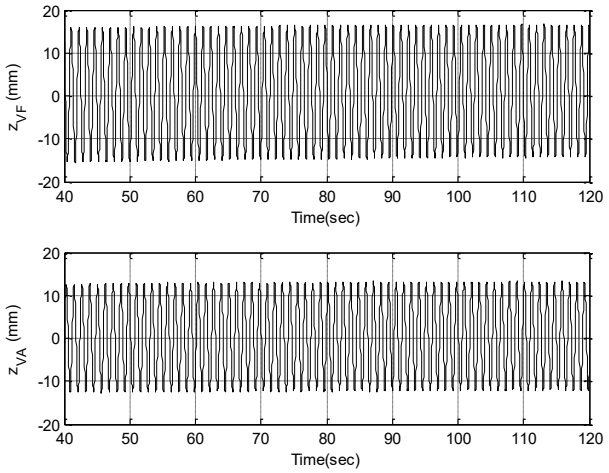

Figure 6. Vertical motion at the forward and aft points – CW2 test

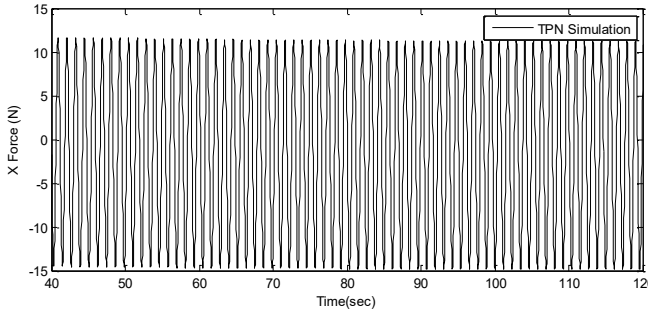

Figure 7. Longitudinal force – CW2 test

4.2 (b) 20% UKC

The Case CW4 represents a stationkeeping test, with no advance speed and 20% UKC. Table 6 shows the comparison between experimental and numerical results. Figure 8 shows the time series of the vertical motion. The longitudinal force due to wave action is shown in Table 6 and in Figure 9. In this case, the simulator underestimated the bow amplitude by 18%.

Table 6. Test CW4 (in waves, no advance speed) – comparison between experimental and simulation results

CW4 UKC 20%, model scale: V=0m/s, Wave H=54.49mm 1.38s full scale: V=0kn, Wave H=4.85m 13.03s			
CW4 V=0kn, UKC 20%	Exper.	Simul.	Dif (%)
ZVF amp. mm	9.19	7.53	-18%
ZVF aver. mm	0.04	-0.01	-
ZVA amp. mm	6.55	8.11	24%
ZVA aver. mm	-0.06	0.01	-
Resistance X amp. N	10.17	10.57	4%
Resistance X aver. N	-0.07	-0.18	-

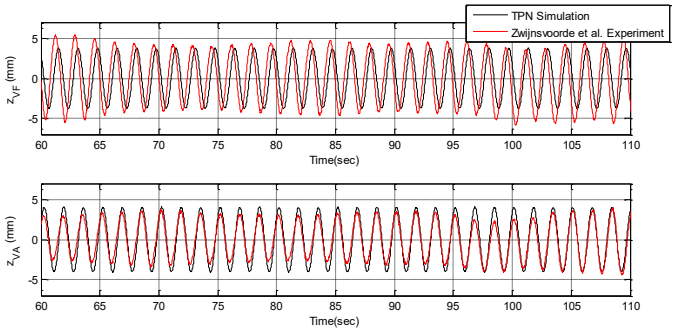

Figure 8. Vertical motion at the forward and aft points – CW4 test

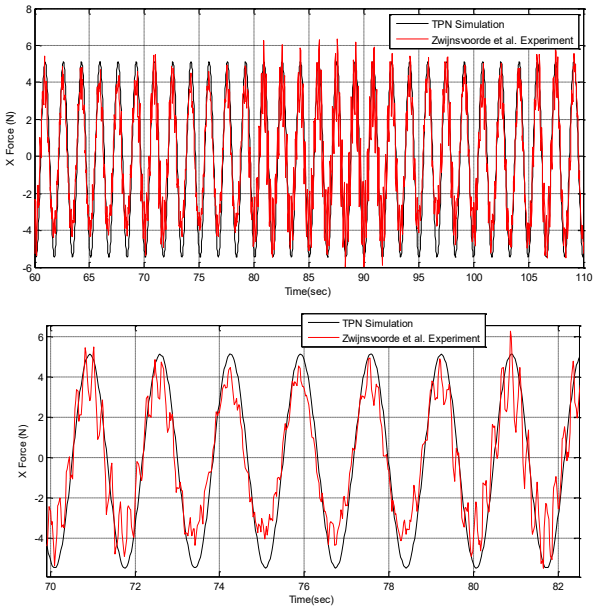

Figure 9. Longitudinal force – CW4 test (up): complete time series – 50s ; (down) detail – 6s

The case CW5 is a blind test. The results obtained by the simulator model are presented in Table 7, Figure 10 (vertical motion) and Figure 11 (resistance force).

Table 7. Test CW2 (in waves, advance speed) –simulation results

CW2 UKC 20% model scale: V=0.327m/s, Wave H=21.36mm 1.66s full scale: V=6kn, Wave H=1.90m 15.67s	
	Simul.
ZVF amp. mm	9.01
ZVF aver. mm	1.55
ZVA amp. mm	10.48
ZVA aver. mm	0.66
Resistance X amp. N	11.04
Resistance X aver. N	-1.12
Apparent Period s	12.55s (real scale) 1.33s (mode scale)

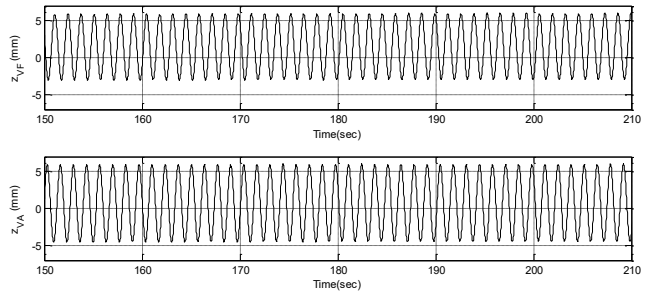

Figure 10. Vertical motion at the forward and aft points – CW5 test

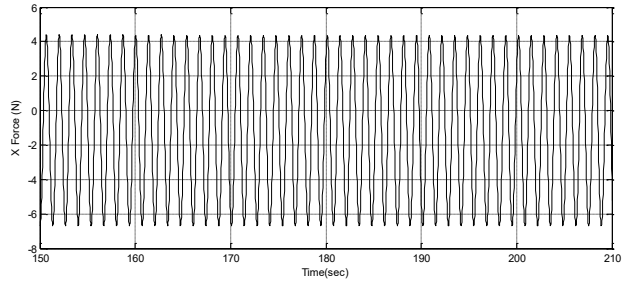

Figure 11. Longitudinal force – CW5 test

5 CONCLUSIONS

The paper carried out the comparison between experimental results and numerical results from the SMH real time maneuvering simulator, regarding the vertical movements of a container vessel. We evaluated cases with or without advance speed (6 and 16 knots) in shallow waters (20% and 100% UKC), subjected to bow waves or in calm waters.

The results showed that the models adopted in the maneuvering simulator are adequate to represent the maximum bow sinkage of the vessel due the squat, with maximum differences of 6%. For the cases with waves, there is an acceptable adhesion among the results, in spite of the simplifications used in the mathematical model implemented in the simulator. The differences between the amplitude of motion in the bow (which shows greater movement) reach 18%.

The stern squat predicted by the model is less accurate, with a difference up to 38% (calm water tests) and 24% (amplitude in wave tests). The squat model adopted in the simulator is based on a vertical force applied in the center of gravity of the ship. The force is adjusted so that the bow squat is equal to the ICORELS regression (base model). The model must be improved to better predict the stern squat. A possible solution, still keeping the necessary simplicity for a real time simulator, is a better definition of point of application of the vertical force. Another approach is the utilization of a more comprehensive base model that predicts both the bow squat and trim, such as the Ankudinov model (Briggs et al., 2013). In this case, a vertical force and pitch moment must be applied in the ship to induce the squat and trim of the Ankudinov model.

6 ACKNOWLEDGEMENTS

The author thanks the Brazilian Research Council (CNPq process 308645/2013-8) for the research grant. He also acknowledges Petrobras for the sponsoring and the technical cooperation in the simulator´s development. Dr. Felipe Ruggeri, from Argonáutica Engineering and Research, also collaborated in the hydrodynamic modelling.

7 REFERENCES

Aranha, J.A.P., 1994. A formula for‘wave damping’ in the drift of a floating body. J. Fluid Mech. 275, 147–155. https://doi.org/10.1017/S0022112094002314

Aranha, J.A.P., Fernandes, A.C., 1995. On the second-order slow drift force spectrum. Appl. Ocean Res. 17, 311–313. https://doi.org/10.1016/0141-1187(95)00013-5

Briggs, M.J., Kopp, P.J., Ankudinov, V.K., Silver, A.L., 2013. Comparison of Measured Ship Squat with Numerical and Empirical Methods. J. Sh. Res. 57, 73–85. https://doi.org/10.5957/josr.57.1.120007

Faltinsen, O., 1993. Sea loads on ships and offshore structures. Cambridge university press.

Pinkster, J., 1980. Low frequency second order wave exciting forces on floating structures. PhD Thesis. TU Delft.

Queiroz Filho, A.N., Zimbres, M., Tannuri, E.A., 2014. Development and Validation of a Customizable DP System for a Full Bridge Real Time Simulator, in: Volume 1A: Offshore Technology. ASME, p. V01AT01A047. https://doi.org/10.1115/OMAE2014-23623

Tannuri, E.A., Martins, G.H.A., 2018. Application of a Maneuvering Simulation Center and Pilots Expertise to the Design of New Ports and Infrastructure Optimization in Brazil, in: Proceedings of 34th PIANC World Congress 2018. Panama City, pp. 1–18.

Tannuri, E.A., Rateiro, F., Fucatu, C.H., Ferreira, M.D., Masetti, I.Q., Nishimoto, K., 2014. Modular Mathematical Model for a Low-Speed Maneuvering Simulator, in:

Volume 1B: Offshore Technology. ASME, p. V01BT01A036. https://doi.org/10.1115/OMAE2014-24414

van Oortmerssen, I.G., 1976. The motions of a moored ship in waves. PhD Thesis. Delft University of Technology.

Van Zwijnsvoorde, T., Tello Ruiz, M., Lataire, E., 2019. Sailing in Shallow Water Waves With the Dtc Container Carrier: Open Model Test Data for Validation Purposes, in: 5th MASHCON International Conference on Ship Manoeuvring in Shallow and Confined Water. pp. 1–20.

8 AUTHOR BIOGRAPHY

Eduardo Aoun Tannuri holds the current position of Full Professor at the Department of Mechatronics Engineering, University of São Paulo (USP), and coordinator of the Maneuvering Simulation Center of the Numerical Offshore Tank (TPN). Member of ITTC Maneuvering Committee (2012-2020). Works on Dynamic Positioning (DP) Systems applied to offshore vessels and platforms, Maneuvering and Sea-keeping time-domain simulators development with applications to ports, vessels and floating structures design. He was graduated in Mechatronics Engineering, in 1998, and completed his doctorate degree in 2002, both at USP. He already coordinated more than 120 maneuvering simulation studies in different Brazilian Ports and offshore operations.

SAILING IN SHALLOW WATER WAVES WITH THE DTC CONTAINER CARRIER: OPEN MODEL TEST DATA FOR VALIDATION PURPOSES

Thibault Van Zwijnsvoorde and **Manases Tello Ruiz**,
Maritime Technology Division, Ghent University, Belgium

Guillaume Delefortrie,
Flanders Hydraulics Research, Belgium & Maritime Technology Division, Ghent University, Belgium

Evert Lataire,
Maritime Technology Division, Ghent University, Belgium

SAILING IN SHALLOW WATER WAVES WITH THE DTC CONTAINER CARRIER: OPEN MODEL TEST DATA FOR VALIDATION PURPOSES

Thibault Van Zwijnsvoorde and **Manases Tello Ruiz,** Maritime Technology Division, Ghent University, Belgium
Guillaume Delefortrie, Flanders Hydraulics Research, Belgium & Maritime Technology Division, Ghent University, Belgium
Evert Lataire, Maritime Technology Division, Ghent University, Belgium

SUMMARY

After successful conferences on bank effects, ship-ship interaction, ship behaviour in locks and ship-bottom interaction, the Fifth International Conference on Ship Manoeuvring in Shallow and Confined Water (MASHCON) has a non-exclusive focus on wind, waves and current action on manoeuvring ships. A clear understanding of the ship's manoeuvring characteristics in waves, wind and currents is essential in both everyday operations and ship safety in so-called adverse conditions. To open a joined research effort on the validation and verification of the different research methods, the Knowledge Centre Manoeuvring in Shallow and Confined Water has selected model test data which were obtained during the execution of seakeeping tests with the DTC container carrier in the framework of the European SHOPERA project. The benchmark data are both captive and free running model tests with the DTC at full draft in calm water and in waves.

NOMENCLATURE

a_0	[mm]	Mean Fourier series
a_i	[mm]	ith order cosine terms Fourier series
B	[m]	Breadth of the ship
b_i	[mm]	ith order sine terms Fourier series
C_B	[-]	Block coefficient
$\overline{GM}$	[m]	Transverse metacentric height
H	[mm]	Measured wave height
I_{xx}	[kg m²]	Mass moment of inertia about Ox-axis
I_{yy}	[kg m²]	Mass moment of inertia about Oy-axis
I_{zz}	[kg m²]	Mass moment of inertia about Oz-axis
L_{PP}	[m]	Length between perpendiculars
m	[kg]	Mass
n	[rps]	Propeller rate
n_{max}	[rps]	Maximum propeller rate
N_z	[-]	Population Z
O	[-]	Origin of the ship-bound axis system
O_0	[-]	Origin of the earth-bound axis system
$O_{0x0y0z0}$	[-]	Earth bound axis system
O_{xyz}	[-]	Ship bound axis system
T	[s]	Measured wave period
T_{design}	[m]	Design draft
$t_{acc,end}$	[s]	End time captive acceleration
$t_{acc,start}$	[s]	Start time captive acceleration
t_{dec}	[s]	Start time deceleration
$t_{reg,end}$	[s]	End time regime condition
$t_{reg,start}$	[s]	Start time regime condition
t_{wave}	[s]	Meeting between ship and waves
u	[m/s]	Longitudinal component of ship speed
v	[m/s]	Lateral component of ship speed
V	[m/s]	Ship speed
$x_{0acc,end}$	[m]	End position captive acceleration
$x_{0acc,start}$	[m]	Start position captive acceleration
x_{0dec}	[m]	Start position deceleration
x_G	[m]	Centre of gravity (longitudinal)
$x_{0reg,end}$	[m]	End position regime condition
$x_{0reg,start}$	[m]	Start position regime condition
x_{0wave}	[m]	Meeting between ship and waves
X	[N]	Longitudinal force
Y	[N]	Transversal force
Z	[-]	Random variable
z_G	[m]	Centre of gravity (vertical)
z_{VF}	[mm]	Running sinkage at fore perpendicular
z_{VA}	[mm]	Running sinkage at aft perpendicular
β	[°]	Hull drift angle
δ_R	[°]	Rudder angle
$\dot{\delta}_R$	[°/s]	Rudder rate
Δx_{0WM}	[mm]	Wave maker position
ζ	[mm]	Position of the free surface
ζ_i	[mm]	ith harmonic amplitude (Fourier)
η	[°]	Wave angle
λ_{theo}	[m]	Theoretical wave length
μ	[°]	Wave encounter angle
μ_z	[-]	Average value Z
σ_z	[-]	Standard deviation Z
ψ	[°]	Ship's heading
ω	[rad/s]	Wave frequency

C1-3	Captive calm water model tests 1-3
G	Centre of Gravity
CM	Clamping mechanism
CW1-5	Captive wave model tests 1-5
P1-4	Potentiometers 1-4
DTC	Duisburg Test Case
EEDI	Energy Efficiency Design Index
FHR	Flanders Hydraulics Research
FW1-2	Free running wave model tests 1-2
LC1-2	Load cells 1-2
PID	Proportional integral derivative
R1-4	Reflector plates 1-4
H1-2	Height meters 1-2
MASHCON	Manoeuvring in shallow and confined water
S1-4	Lasers 1-4
SHOPERA	Energy Efficient Safe Ship operation
UKC	Under keel clearance
VLIZ	Flanders Marine Institute
WG1-4	Wave gauges 1-4

1 INTRODUCTION

The Fifth International Conference on Ship Manoeuvring in Shallow and Confined Water (MASHCON) is held at the seaside city of Ostend, Belgium, from May 20th until May 22nd 2019 and is organised by Flanders Hydraulics Research (FHR), Ghent University (UGent) and Flanders Marine Institute (VLIZ). The venue of Ostend not only offers the opportunity to organise a morning walk/run along the picturesque coastline, it also provides the opportunity of visiting the shallow water towing tank (currently under construction) at the Flanders Maritime Laboratory. The main, non-exclusive, topic of the conference is manoeuvring in wind, waves and current, three important factors when sailing in shallow and confined waters. This conference is the successor to previous editions with non-exclusive focus on bank effects (Vantorre and Eloot, 2009) (Antwerp, May 2009), ship-ship interaction (Pettersen et al., 2011) (Trondheim, May 2011), ship behaviour in locks (Vantorre et al., 2013) (Ghent, May 2013) and ship-bottom interaction (Uliczka et al., 2016) (Hamburg, May 2016). These topics fit within the scope of the Knowledge Centre Manoeuvring in Shallow and Confined water, which aims to consolidate, extend and disseminate knowledge on the behaviour of ships in navigation areas with major vertical and horizontal restrictions.

A clear understanding of the ship's manoeuvring characteristics in waves, wind and currents is essential in both everyday operations and ship safety in so-called adverse conditions. Sailing in confined waterways adds to the complexity of the problems, forcing the ship to have non-favourable headings towards the main wind and current directions. The restriction of engine power (EEDI regulations) to reduce emissions emphasises the importance of a good understanding of the behaviour of ships in adverse conditions, which could limit the possible power reduction from the viewpoint of the ship's safety. These concerns have led to the establishment of the EU funded project 'Energy efficient safe SHip OPERAtion' (SHOPERA) (Papanikolaou et al., 2015). In the framework of this project, a substantial amount of model tests have been performed by four leading European institutes (SINTEF Ocean, FHR, TU Berlin and CEHIPAR). The Knowledge Centre has made a selection of the tests performed with the DTC (Duisburg Test Case container ship) in shallow water, in order to stimulate validation and verification of different research methods.

2 MODEL TEST SET-UP

The tests were executed using a scale model of the DTC in the Towing Tank for Manoeuvres in Shallow Water (cooperation FHR and UGent). The dimensions and layout of the tank define the range of wave climates which can be generated.

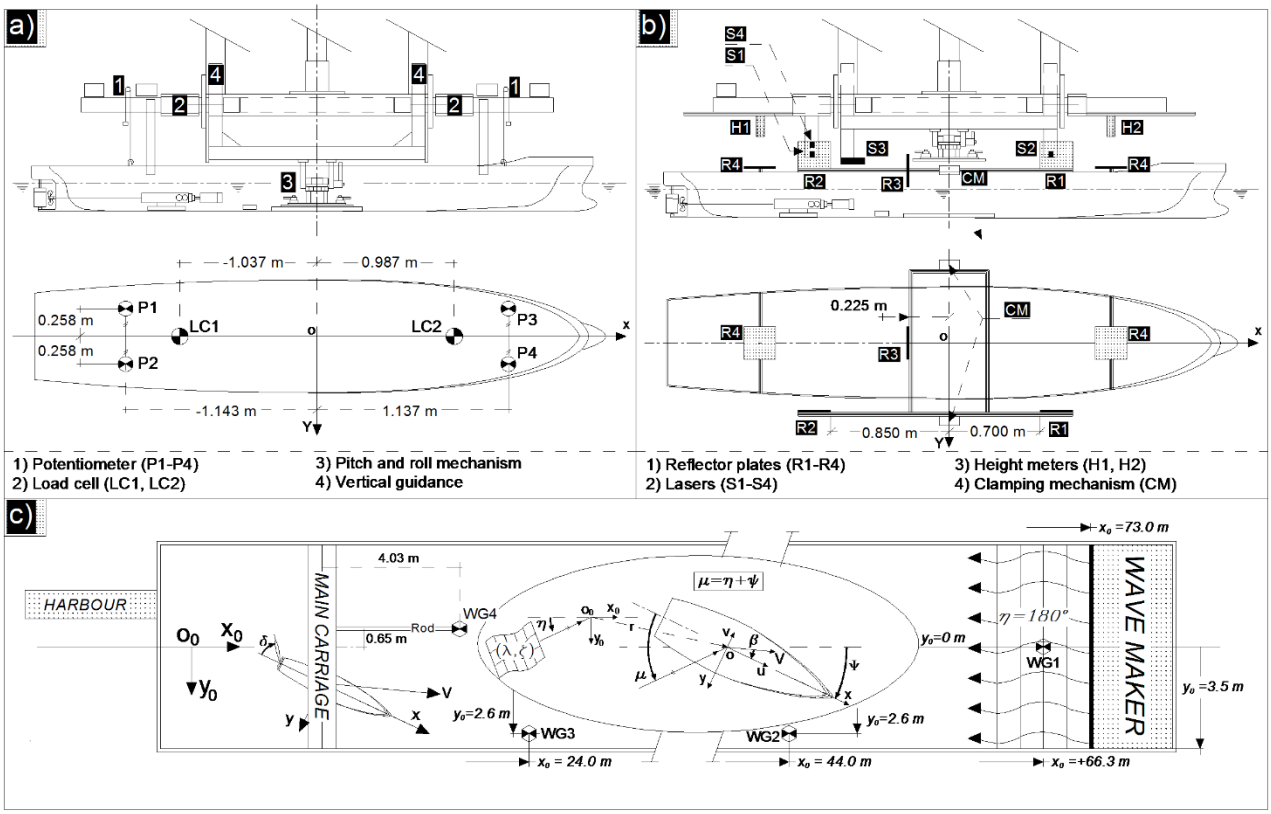

Figure 1. Towing tank at FHR, (a) set-up for captive test, (b) set-up for free running test, and (c) general configuration in the towing tank. ±1 mm uncertainty of dimensions.

2.1 TOWING TANK

The towing tank at FHR has a total length of 87.5 m, a width of 7.0 m and a maximum water depth of 0.5 m. Because of the presence of the harbour and the wave maker, the useful towing tank length is limited to 68.0 m. The towing tank mechanism consists of a main carriage and a lateral carriage, combined with a yawing table, allowing all possible movements in the horizontal plane. The carriage mechanism allows the execution of both captive and free running tests by using two different set-ups (Delefortrie et al., 2016). The towing tank's general configuration, the captive and free running setups are shown in Figure 1.

During captive tests the ship is fixed in the horizontal plane (surge, sway and yaw), allowing roll, pitch and heave (during the calm water tests, roll is fixed and then the moment is measured). The hull forces are measured using load cells LC1 (separate measurement of X and Y force) and LC2. The ship's heave, trim and roll are measured by using four potentiometers P1 to P4 (see Figure 1a). In the case of free running tests, the vessel uses its own propeller and rudder to sail through the towing tank, while the carriage mechanism follows the ship minutely, recording its trajectory through the tank. The ship's relative position with respect to the carriage is measured in six degrees of freedom by a combination of four lasers S1 to S4 (see Figure 1b).

To define the ship's position and orientation along the tank two coordinate systems are used, $O_{0x0y0z0}$ is the earth-bound axis system, and O_{xyz} is the ship fixed axis system, with its origin amidships on the water plane. Both systems have the $z_{(0)}$ axis defined positive downwards. The ship's position/orientation during tests is defined by the wave encounter angle (μ), hull drift angle (β) and ship's heading (ψ), as shown in Figure 1c.

The wave profile along the tank was measured by using four wave gauges WG1 to WG4. Three of them, WG1 to WG3, were at a fixed position in the towing tank while the fourth wave gauge WG4 was attached to the carriage (see Figure 1c). In the $O_{0x0y0z0}$ axis system, its lateral position is constant (y_{WG4} = -0.65). It moves along the x0-axis along with the carriage, being located 4.03 m in front of midship ($x_{WG4} = x_0 + 4.03$)

2.2 DTC.

The DTC is a hull design of a 14,000 TEU container ship, developed at the Institute of Ship Technology, Ocean Engineering and Transport Systems (Duisburg-Essen, Germany), for benchmarking and validation of numerical methods (el Moctar et al., 2012). The DTC is a single screw vessel with a bulbous bow and a large bow flare. The captive tests are performed bare hull (absence of movable part of the rudder and propeller). For the appended free running tests the model is equipped with a fixed-pitch five-bladed propeller with right rotation and a twisted rudder with a Costa bulb. The first set of parameters is hull form specific (Table 1), the second set is a function of the loading condition of the ship (Table 2).

Table 1. Ship particulars: general.

Particular	Full scale	Model scale
Scale [-]	1	1:89.11
L_{PP} [m]	355.0	3.984 ± 0.001
B [m]	51.0	0.572 ± 0.001
T_{design} [m]	14.5	0.163 ± 0.001
C_B [-]	0.661	0.661

Table 2. Ship particulars: loading specific parameters.

Particular	Captive	Free-running
m [kg]	242.8 ± 0.2	243.5 ± 0.2
x_G [m]	-0.052 ± 0.002	-0.049 ± 0.002
z_G [m]	-0.059 ± 0.003	-0.059 ± 0.003
I_{xx} [kgm^2]	12 ± 1	16 ± 1
I_{yy} [kgm^2]	221 ± 1	273 ± 2
I_{zz} [kgm^2]	230 ± 1	356 ± 2
$\overline{GM}$ [m]	0.058 ± 0.003	0.055 ± 0.003

3 BENCHMARK TESTS

Ten model tests have been selected: eight captive model tests and two tests in free running mode. The captive model tests, which were all performed with the bare hull only, can be subdivided into three calm water tests and five tests in waves. The three captive model tests in calm water are presented in Table 3. Appendix 1 presents the time series of all measured variables during these captive tests.

Table 3. Benchmark tests: captive tests with the bare hull in calm water.

	Velocity		
Test ID	Model scale [m/s]	Full scale [kts]	UKC [%]
C1; C2	0.327 ; 0.872	6 ; 16	100
C3	0.327	6	20

A description of the captive tests in waves is given in Table 4. The free running tests in waves are given in Table 5. The variables logged during the free running tests are given in Appendix 2. The wave height and wave period are function of time and position in the towing tank. This is discussed in Section 4.

Table 4. Benchmark tests: Captive tests with the bare hull in waves.

	Velocity		Environment	
Test ID	Model scale [m/s]	Full scale [kts]	UKC [%]	λ_{theo}/L_{PP} [-]
CW1; CW2 ; CW3	0 ; 0.327 0.872	0; 6; 16	100	0.55
CW4; CW5	0 ; 0.327	0; 6	20	0.55

Table 5. Benchmark tests: Free running wave tests.

	Velocity		Environment	
Test ID	Model scale [m/s]	Full scale [kts]	UKC [%]	λ_{theo}/L_{PP} [-]
FW1	0.327	6	100	0.55
FW2	0.872	16	100	0.40

4 WAVE PROPAGATION IN THE TANK.

Performing model tests in waves requires a thorough investigation of the wave propagation through the tank. The steadiness of the wave pattern as a function of position and time is deemed important.

4.1 WAVE CLIMATE AS A FUNCTION OF POSITION

To verify the main wave characteristics along the tank, the wave profiles obtained at WG1 and WG2 have been further investigated by fitting a Fourier series up to the third order with the eight parameters a_0, a_1, a_2, a_3, b_1, b_2, b_3, and ω.

$$\zeta = a_0 + \sum_{j=1}^{3}\left[a_j \cos(j\omega t) + b_j \sin(j\omega t)\right] \quad (1)$$

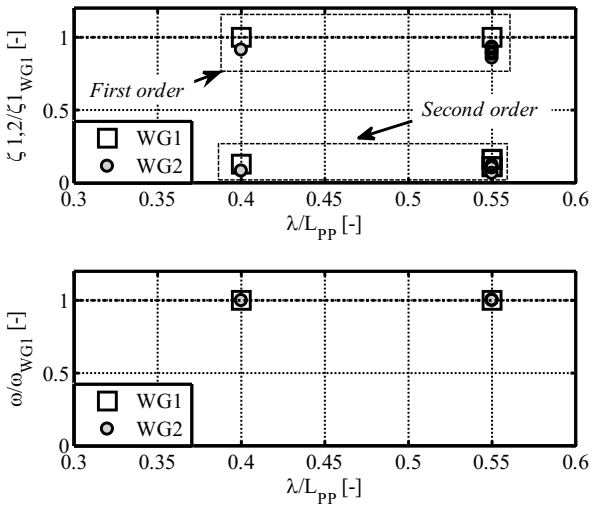

Figure 2. Regular waves at WG1 and WG2. Non-dimensional first and second order harmonics (top) and wave frequency (bottom).

The results shown in Figure 2 are presented dimensionless. For the wave amplitudes, the first and second order amplitudes (ζ_1 and ζ_2) are divided by the first order amplitude at WG1. The wave frequency (ω) is divided by the wave frequency measured at WG1. Third order magnitudes (ζ_3) have been excluded because they are relatively small. It is worth mentioning that from the regression analysis, a relative high R^2 has been found for all tests, with a lowest value of $R^2 = 0.98$ obtained at WG2 for the CW5 test.

From the results presented in Figure 2, it can be observed that the wave amplitudes for both the first and the second order harmonics present slightly different magnitudes at WG1 and WG2 (see Figure 2 top), while the wave frequencies (see Figure 2 bottom) show a better agreement and remain approximately the same along the tank. Thus, the limited discrepancies observed in the wave parameters at WG1 and WG2 guarantee that the wave along the tank can be considered as steady and regular.

4.2 WAVE CLIMATE AS A FUNCTION OF TIME

The variability in wave heights measured at one gauge is investigated using the readings at WG2, as they are the most representative for the wave climate which the ship encounters during the regime condition (see Section 5). For all the wave tests, the wave height, calculated based on maximum and minimum surface elevations, and zero up-crossing period, are determined. The mean and standard deviation are calculated based on 15 wave cycles, using equation 2.

$$\mu_z = \sum_{i}^{N} Z_i \quad ; \quad \sigma_z = \sqrt{\sum_{i}^{N} \frac{(Z_i - \mu_z)^2}{N_z - 1}} \quad (2)$$

Table 6 shows that the deviation of the wave height as a function of time is limited. The period of the measured wave can be seen as invariant. The wave climate for CW4 and CW5 is moderate, as larger waves cause bottom touch at 20% UKC.

Table 6. Measured wave height (*H*) and wave period (*T*) at gauge 2, based on 15 cycles.

ID	$\mu_H \pm \sigma_H$ [mm]	$\mu_T \pm \sigma_T$ [s]
CW1	54.49 ± 1.96	1.38 ± 0.01
CW2	62.31 ± 0.95	1.38 ± 0.01
CW3	62.35 ± 0.64	1.38 ± 0.01
CW4	22.21 ± 0.33	1.66 ± 0.02
CW5	21.26 ± 0.31	1.66 ± 0.03
FW1	56.92 ± 0.51	1.39 ± 0.01
FW2	60.72 ± 1.12	1.09 ± 0.01

5 CAPTIVE WAVE MODEL TESTS (CW)

5.1 MEASURED TIME SERIES.

The logged data, at 40 Hz, is available on request for all captive tests, except for the semi-blind captive wave tests at 6 knots (i.e. CW2 and CW5), for which only the carriage position, wave gauge readings and the wave maker position as a function of time are given. Appendix 1 gives an overview of the time series which are delivered. Appendix 3 shows the time series, averaged over 0.25 s for visualization purposes.

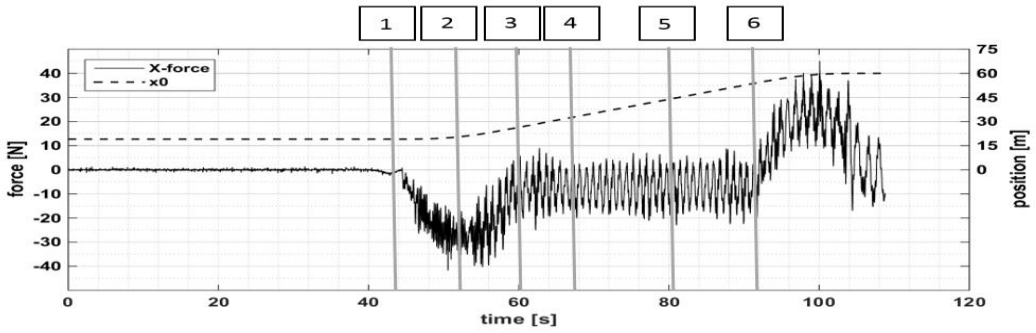

Figure 3. Time series X-force (sum two load cells LC1 and LC2) and longitudinal ship position as a function of time [test CW3, see Table 3].

Testing the ship in waves complicates the post-processing of the times series. Figure 3 shows the logged X-force and longitudinal ship position in the tank, as a function of time, during the execution of a captive wave test. Six vertical lines denote key moments during the execution of the test. For these six transitions, the longitudinal tank position (x_0) and the corresponding time (t) are also included in Appendix 1.

Vertical line 1 indicates the start of the acceleration phase, at position $x_{0acc,start}$ and time $t_{acc,start}$. The meeting between ship and the initial waves is indicated by line 2 (x_{0wave}, t_{wave}). The end of the acceleration phase is denoted by line 3 ($x_{0acc,end}$, $t_{acc,end}$). The meeting with the first waves can be during the acceleration phase (as in Figure 3) or after sailing in calm water for a certain time (Figure 4). This depends on the optimal parameter selection in order to obtain the longest steady interval for sailing in waves (Section 5.3). When the ship meets the waves, a transition zone exists before the ship shows a steady behaviour ($x_{0reg,start}$, $t_{reg,start}$) (line 4). Due to the presence of the beach and the wave maker, the intended regular wave pattern is disturbed because of reflections ($x_{0reg,end}$, $t_{reg,end}$) (line 5). Line 6 shows the start of the deceleration phase of the vessel (x_{0dec}, t_{dec}).

5.2 UNCERTAINTY IN THE TIME SERIES.

The uncertainty of the measured time series has to be known to achieve a good interpretation of the model tests. Forces and motions are registered during the execution of captive model tests, using eight measuring devices (see Figure 1). Four loads cells measure the forces in the horizontal plane (X and Y at two positions) and four potentiometers (Figure 1a) measure the vertical motion of the vessel.

The contribution to the uncertainty due to the precision of the load cells and potentiometers is determined based on the output of 26 model tests, performed with the DTC corresponding to 6 knots full scale at 100% and 20% UKC. Although the ship model encounters waves during these tests, there is a sufficiently long time window present during which the ship sails at a steady state in calm water before encountering any waves. The selection of this time window is shown in Figure 4. The average of the load cell readings is calculated within the calm water condition for each of the 26 model tests. Equation 2 is used to calculate the mean μ and standard deviation σ of the sample.

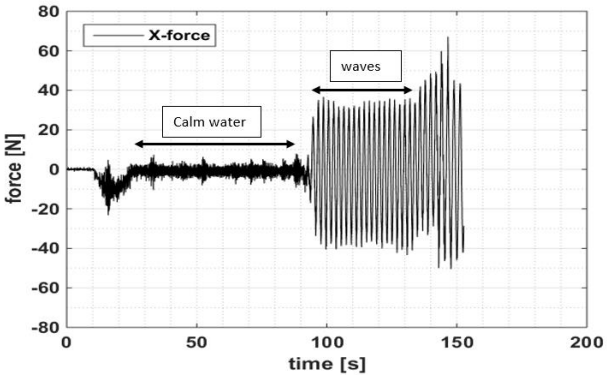

Figure 4. X-force (sum two load cells LC1 and LC2) during captive, bare hull wave test with the DTC at 6 knots, 100% UKC (λ/L_{PP} = 1.00).

Both X-force load cells are mounted on the same beam which connects the ship model with the carriage. This means that both X-force load cells influence each other (due to a hyperstatic configuration). Not only does it cause noise in the signal, it also means that the individual cell readings have no physical meaning. Only the mean and standard deviation of the sum of both readings are thus relevant. As the tests are performed in head waves, the lateral forces are primarily caused by waves reflecting off the tank's side walls (see also Section 5.3). These forces are not discussed here. Table 7 gives the results for the two series of model tests.

Table 7. Mean load cell and potentiometer readings with associated standard deviation, based on model tests performed with the DTC at 6 knots, 26 tests at 100% UKC and 26 tests at 20% UKC.

	100% UKC		20% UKC	
Variable	$\mu_z \pm \sigma_z$	σ_z/μ_z	$\mu_z \pm \sigma_z$	σ_z/μ_z
X	-0.86 ± 0.02 N	0.02	-1.05 ± 0.05 N	0.05
P1	0.79 ± 0.04 mm	0.05	1.53 ± 0.08 mm	0.05
P2	0.75 ± 0.03 mm	0.04	1.48 ± 0.08 mm	0.05
P3	0.69 ± 0.03 mm	0.04	1.45 ± 0.06 mm	0.04
P4	0.69 ± 0.03 mm	0.04	1.41 ± 0.06 mm	0.04

Table 8. Mean value and standard deviation for motions, derived from the individual potentiometer readings P1 to P4, based on model tests performed with the DTC at 6 knots, 26 tests at 100% UKC and 26 tests at 20% UKC.

	100% UKC		20% UKC	
	$\mu_f \pm \sigma_f$	σ_f/μ_f	$\mu_f \pm \sigma_f$	σ_f/μ_f
heave	0.73 ± 0.02 mm	0.03	1.47 ± 0.03 mm	0.02
trim	-0.04 ± 0.01 mm/m	0.25	-0.03 ± 0.03 mm/m	1.00
roll	-2.43E-03 ± 5.93E-05°	0.02	-4.34E-03 ± 1.19E-05°	0.00
z_{VF}	0.80 ± 0.04 mm	0.05	1.53 ± 0.08 mm	0.05
z_{VA}	0.66 ± 0.03 mm	0.05	1.40 ± 0.06 mm	0.04

The uncertainty on the mean of the X-force reading is important to evaluate the added wave resistance. For tests at 100% UKC, the average measured calm water resistance is 0.86 N. In waves, for a ratio λ_{theo}/L_{PP} equal to 0.90 (not included as benchmark), the total average resistance measured during the steady state condition (region between line 4 and 5 in Figure 3) is 2.06 N. Thus, the added resistance due to wave action is 1.20 N ± 0.03 N, assuming the deviation is constant. The obtained value of added resistance can thus be seen as significant with regard to the standard deviation on the load cell readings.

The tests at 20% UKC, however, have been performed with smaller wave heights, which leads to smaller magnitudes for the added wave resistance. The calm water resistance is 1.05 N ± 0.05 N, whereas the added resistance in waves is 0.15 N ± 0.07 N (λ_{theo}/L_{PP} = 0.75). The obtained value for the added resistance is only twice the standard deviation.

Based on the potentiometers (P1 to P4), the uncertainty on the derived heave, trim, roll and the running sinkages at fore and aft perpendicular (z_{VF} and z_{VA}) (see delivered time series), can be calculated. The trim is defined in equation 3 (positive bow up)

$$\text{trim} = \frac{z_{VA} - z_{VF}}{L_{PP}} \left[\frac{\text{mm}}{\text{m}}\right] \tag{3}$$

Because of uncertainty in the position of the potentiometers and length of the vessel (see Table 1), the standard deviation is calculated with the uncertainty propagation method, using equation 4. Cross correlation between the variables is neglected. The lateral as well as the longitudinal position of the potentiometers comes with an uncertainty of ± 1 mm, as does the length of the vessel. The results are given in Table 8.

$$\begin{aligned} f &= f(x_1, \dots, x_i, \dots, x_n) \\ \mu_f &= f(\mu_1, \dots, \mu_i, \dots, \mu_n) \\ \sigma_f &= \sqrt{\sum_{i=1}^{n} \left(\frac{\partial f}{\partial x_i}\right)^2 \cdot {\sigma_{xi}}^2} \end{aligned} \tag{4}$$

5.3 SELECTION OF THE STEADY STATE TIME WINDOW.

ITTC (2014) recommends performing model tests with a ship model in waves in absence of wave reflection and tank side wall interaction. It is advised to reach a minimum of 10 oscillation cycles at steady condition, where the amplitude and period of oscillations are constant. Transition zones in the time records should be avoided.
The above general recommendations are mostly suited for deep water tanks, where solutions to the problem of tank side wall interaction in wave tests can be simply achieved by choosing realistic ship forward speeds higher than a critical one defined in the ITTC recommendations (ITTC, 2014). In contrast with deep water, tests in shallow water are additionally restrained by problems such as bow wave generation, and squat effects which increase significantly the bottom touch probability.

Testing the ship in a restrained scenario is then a challenging task to achieve. At FHR, studies have been conducted to limit these problems (Tello Ruiz et al., 2015; Tello Ruiz et al., 2016). The ship tests in waves have been designed to obtain a time window characterised by:

- steady forward speed of the ship;
- absence of reflections from the beach;
- steady wave climate;
- minimised tank side wall reflection.

From all the complications mentioned above, the tank side wall interaction is the most challenging. Waves radiated by the ship are reflected by the tank side wall back to the ship, hence, altering the desired wave exciting condition. By selecting wave frequencies that lie outside the heave/roll/pitch resonance frequencies, together with choosing wave amplitudes of moderate magnitudes, tank side wall interaction can be further restricted. A more recent study (Tello Ruiz et al., 2017) on tank side wall interaction reveals that such magnitudes are rather small and can be neglected for moderate wave amplitudes. When comparing the model test results to calculation methods it is highly recommended to include the tank side walls.

6 FREE RUNNING MODEL TESTS (FW)

In self-propelled free running model tests, the vessel uses its own propeller and rudder to sail through the towing tank, whilst the carriage mechanism follows the ship and records the position of the ship as well as propeller and rudder readings. For the present benchmark data, two free running tests are selected (see Table 5). With respect to the safety of the vessel in harsh weather conditions, it is valuable to know the speed loss when sailing in head seas. In order to determine this speed loss, the calm water

velocity as a function of the propeller rate (revolutions per second) is determined. Free running tests in waves are performed at a rotational speed by which the velocities corresponding to 6 knots and 16 knots full scale are achieved. The straight course in waves is guaranteed using a PID controller, which controls the rudder based on a feedback system.

6.1 MEASURED TIME SERIES.

All logged time series for the test corresponding to 16 knots at full scale (test FW2, see Table 5) are given in ASCII format. For the test corresponding to 6 knots at full scale (FW1), only the wave gauge readings, wave maker position and the position and velocity of the vessel, are given. The variables which are given in the time series, with their respective units, are presented in Appendix 2. The time series averaged over 0.25 s, are given in Appendix 3. During the free running test, the ship is decoupled from the towing carriage (see Figure 1 b). The latter follows the ship model throughout the test, with a precision of ± 1.4 mm.

As the tests are self-propelled, propeller (rpm, thrust and torque) and rudder (deflection, X-force rudder, Y-force rudder and torque) are recorded (at 40 Hz) during the entire test.

As for the captive tests in waves, the time series can be split in various zones, using six vertical line indicators, which correspond again with a time and towing tank position (see Figure 5). Line 1 indicates the start of the acceleration of the ship model, which is done in captive mode ($x_{0acc,start}$, $t_{acc,start}$). The captive acceleration ends and the ship is released at line 2, the position $x_{0acc,end}$ and time $t_{acc,end}$. The target regime velocity of the free running test FW2 corresponds to 16 knots full scale, or 0.872 m/s model scale. The velocity after captive acceleration is 0.800 m/s. Line 3 indicates the meeting between ship and waves (x_{0wave}, t_{wave}). In between line 3 and 4, there is a transition zone for motions and forces. At line 4 ($x_{0reg,start}$, $t_{reg,start}$), the speed slightly increases to end up with a steady velocity of about 0.872 m/s. The wave maker and the beach both cause reflective waves which travel back to the ship. Line 5 indicates the position and time when the wave pattern is no longer free of reflections ($x_{0reg,end}$, $t_{reg,end}$). The end of the free running phase is indicated by the sixth vertical line (x_{0dec}, t_{dec}).

6.2 CALM WATER SELF-PROPULSION TESTS.

The speed loss in waves can only be estimated, if the corresponding calm water velocity of the vessel at the given propeller rate is known. In order to obtain this reference, six self-propelled calm water tests have been performed. The tests are listed in Table 9. In this table, the attained forward speed in steady condition is given together with the measured propeller rate. The ratio of the vessel's forward speed and the angular velocity of the propeller is constant for all self-propelled tests. Calculating velocities at intermediate rotational speeds can thus be performed using linear interpolation.

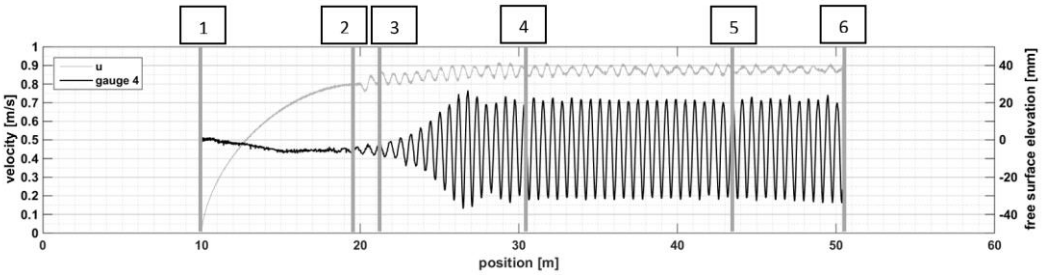

Figure 5. Longitudinal component velocity and WG4 readings as a function of longitudinal position in the towing tank [test FW2, see Table 5]

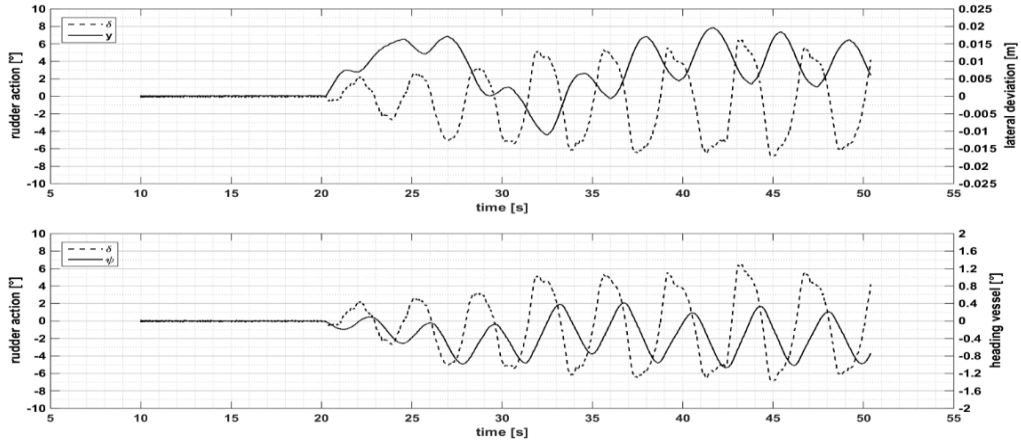

Figure 6. Performance autopilot for self-propelled test in waves [test FW2, see Table 5].

Table 9. Self-propelled calm water tests performed with the DTC at 100% UKC.

n_{theo}/n_{max} [%]	n [rps]	u [m/s]	u/n [m/(s.rps)]
30	4.93	0.315	1.07E-03
40	6.56	0.439	1.12E-03
50	8.19	0.562	1.14E-03
65	10.63	0.741	1.16E-03
75	12.27	0.849	1.15E-03
85	13.90	0.973	1.17E-03

6.3 PERFORMANCE OF THE PID CONTROLLER

A PID controller is used to steer the rudder to follow an intended course. The PID system is tested to its limits in high and/or long waves, as there are drift forces (direct wave action / reflections form side wall) which cause the vessel to deviate from its desired path. An extensive testing phase was needed to tune the PID coefficients to react appropriately to the feedback information provided by the towing carriage. The main objectives were ensuring that the deviation (lateral position of the CoG and yaw motion) is limited and the rudder deflection (δ_R) and its time derivative ($\dot{\delta_R}$) are within the limits of normal operations on full scale vessels. An example of the PID-controlled course as a function of the vessel's longitudinal tank position is given in Figure 6.

7 CONCLUSIONS

The Knowledge Centre Manoeuvring in Shallow and Confined Water has selected model test data which were obtained during the execution of seakeeping tests with the DTC container carrier in the framework of the European SHOPERA project, to open a joint research effort on the validation and verification of different research methods. The paper discusses eight captive (bare hull) and two free running benchmark tests, carried out in the Towing Tank for Manoeuvres in Shallow Water (cooperation Flanders Hydraulics Research – Ghent University), at two under keel clearances: 100% and 20% of the ship's draft.

As seven of the ten tests were performed in waves, the propagation of the waves through the tank is discussed. The influence of position and time on the measured wave pattern is presented based on Fourier analysis and an uncertainty analysis of the wave height and period. The tests at 20% UKC are performed with limited wave heights to avoid bottom touch.

The measured time series for captive and free running model tests are given in Appendix 1 and 2, respectively. For the tests performed at 0.327 m/s (6 knots full scale - CW2, CW5 and FW1), only the wave gauge readings, the wave maker position and the vessel's position and velocity components are disclosed. For the other tests, the entire time series are made available upon request, including acceleration and deceleration phase of the vessel. For both captive and free running tests, the typical time series is discussed, indicating six key moments in the series.

Captive tests are further elaborated on by investigating the uncertainty in the load cell and potentiometer readings and summarising the available knowledge concerning the selection of the steady state time window in waves.

The free running tests are performed to map the speed loss when sailing in waves. In order to do this, six self-propelled tests in calm water were performed with increasing propeller rate, to obtain the calm water velocity as a function of the propeller angular velocity. A PID controller is used to correct deviations from the desired (straight) course. The followed course and rudder angles are given for test FW2.

The benchmark data are digitally available upon request at info@shallowwater.be.

8 ACKNOWLEDGEMENTS

The work presented in this paper is supported by the Collaborative Project SHOPERA (Energy Efficient Safe SHip OPERAtion), Grant Agreement number 605221, http://www.shopera.org, co-funded by the Research DG of the European Commission within the RTD activities of the FP7 Thematic Priority Transport, FP7-SST-2013-RTD-1, Activity 7.2.4 Improving Safety and Security, SST.2013.4-1: Ships in Operation. The authors would like to thank the SHOPERA consortium for the permission to publish the data and dr. Zhiming Yuan (University of Strathclyde) for reviewing the present article.

9 REFERENCES

Delefortrie, G., Geerts, S., Vantorre, M., 2016. The Towing Tank for Manoeuvres in Shallow Water, *4th MASHCON International Conference on Ship Manoeuvring in Shallow and Confined Water with Special Focus on Ship Bottom Interaction*, Hamburg, Germany. BAW: pp. 226-235. DOI: 10.18451/978-3-939230-38-0_27.

El Moctar, O., Shigunov, V., Zorn, T., 2012. Duisburg Test Case : Post-Panamax Container Ship for Benchmarking. J*ournal of Ship Technology Research* 59: pp. 50–64.

ITTC, 2014. ITTC – Recommended Procedures and Guidelines - Seakeeping Experiments. *7.5-02-07-02.1 (Revision 04)*. ITTC: pp. 1-22.

Papanikolaou, A., Zaraphonitis, G., Bitner-Gregersen, E., Shigunov, V., el Moctar, O., Guedes Soares, C., Reddy, D.N., Sprenger, F., 2015. Energy Efficient Safe Ship Operation, *Influence of EEDI on Ship Design*, London, UK. R.I.N.A.: pp. 1-14.

Pettersen, B., Berg, T., Eloot, K., Vantorre, M. (Eds.), 2011. *2nd International Conference on Ship Manoeuvring in Shallow and Confined Water: Ship to Ship Interaction*, Trondheim, Norway. R.I.N.A.: 441 pages.

Tello Ruiz, M., De Caluwé, S., Van Zwijnsvoorde, T., Delefortrie, G., Vantorre, M., 2015. Wave effects in 6DOF on a ship in shallow water, *MARSIM 2015*. Newcastle upon Tyne, UK. Newcastle University: Paper 2.2.2, pp. 1–15.

Tello Ruiz, M., Vantorre, M., Van Zwijnsvoorde, T., Delefortrie, G., 2016. Challenges with ship model tets in shallow water, *Proceedings of The 12th International Conference on Hydrodynamics*, *ICHD2016*, Egmond aan Zee, The Netherlands. TU Delft, Paper 59: pp. 1-10.

Tello Ruiz, M., Van Hoydonck, W., Delefortrie, G., Vantorre, M., 2017. On the limitations of ship model tests in waves in a shallow water and narrow towing tank. Submitted to the *20th Numerical Towing Tank Symposium (NuTTS 2017)*, Wageningen, The Netherlands.

Uliczka, K., Böttner, C.-U., Kastens, M., Eloot, K., Delefortrie, G., Vantorre, M., Candries, M., Lataire, E. (Eds.), 2016. *4th MASHCON International Conference on Ship Manoeuvring in Shallow and Confined Water with Special Focus on Ship Bottom Interaction*, Hamburg, Germany. BAW: 334 pages. DOI: 10.18451/978-3-939230-38-0_27.

Vantorre, M., Eloot, K., 2009. *International Conference on Ship Manoeuvring in Shallow and Confined Water: Bank Effects*, Antwerp, Belgium. R.I.N.A: 167 pages.

Vantorre, M., Eloot, K., Delefortrie, G., Lataire, E., Candries, M. (Eds.), 2013. *3rd International Conference on Ship Manoeuvring in Shallow and Confined Water: with non-exclusive focus on Ship Behaviour in Locks*, Ghent, Belgium. R.I.N.A: 376 pages.

10 AUTHORS BIOGRAPHY

Thibaut Van Zwijnsvoorde, civil engineer, research staff member at the division of Maritime Technology at Ghent University. He has carried out the model tests in waves in the scope of the SHOPERA project. His experience includes research on probabilistic calculations of ship responses in waves and studies of moored vessels in Flemish ports.

Manasés Tello Ruiz, naval architect and marine engineer, research staff member funded by FHR. He has been involved in several research projects such as, wave structure interaction, wave energy devices, seakeeping, risk analysis of fishing vessels and most recently manoeuvring in waves in shallow water.

Guillaume Delefortrie, PhD, naval architect, is expert nautical researcher at Flanders Hydraulics Research and visiting professor at Ghent University. He is in charge of the research in the Towing Tank for Manoeuvres in Confined Water and the development of mathematical models based on model tests. He has been secretary of the 27th and 28th ITTC Manoeuvring Committee and is chairman of the 29th ITTC Manoeuvring Committee.

Evert Lataire, PhD, Professor and head of the Maritime Technology Division at Ghent University. He has written a PhD on the topic of bank effects mainly based upon model tests carried out in the shallow water towing tank of FHR. His fifteen year experience includes research on ship manoeuvring in shallow and confined water such as ship-ship interaction, ship-bottom interaction and ship-bank interaction.

APPENDIX 1 : CAPTIVE MODEL TESTS.

Table 10. Time series given in ASCII output files captive model tests in waves.

variable	unit	Description
time	s	
x_0	m	Long. position ship model
y_0	m	Trans. position ship model
psi	°	Course angle vessel
u	m/s	Long. velocity component
heave	mm	Mean sinkage of the ship
trim	mm/m	Trim motion
roll*	°	Roll motion
	Nm	Roll moment
z_{VF}	mm	Sinkage fore pp, centreline
z_{VA}	mm	Sinkage aft pp, centreline
X	N	Surge force
Y	N	Sway force
N	Nm	Yaw moment
WG1	mm	Free surface elevation WG1
WG2	mm	Free surface elevation WG2
WG3	mm	Free surface elevation WG3
WG4	mm	Free surface elevation WG4
Δx_{0WM}	mm	Position wave maker

* During calm water captive tests, the roll moment is measured, in Nm. During the wave tests, the roll motion is obtained.

Table 11. Longitudinal position and time indication captive model tests in waves with 100% UKC.

	Test CW1		Test CW2		Test CW3	
Zone	**x_0 [m]**	**t [s]**	**x_0 [m]**	**t [s]**	**x_0 [m]**	**t [s]**
acc,start	/	/	4.0	10.1	19.0	44.1
acc,end	/	/	6.5	25.1	25.5	59.1
wave	36.0	36.8	28.6	92.8	19.1	47.0
reg,start	36.0	51.0	33.2	106.9	29.4	63.5
reg,end	36.0	72.6	40.6	129.6	43.1	79.2
dec	/	/	43.6	138.6	53.7	91.4

Table 12. Longitudinal position and time indication captive model tests in waves with 20% UKC.

	Test CW4		Test CW5	
Zone	**x_0 [m]**	**t [s]**	**x_0 [m]**	**t [s]**
acc,start	/	/	4.0	10.1
acc,end	/	/	6.5	25.1
wave	35.0	40.8	26.8	87.3
reg,start	35.0	58.4	31.8	102.5
reg,end	35.0	86.9	38.5	123.0
dec	/	/	44.6	141.6

APPENDIX 2 : FREE RUNNING MODEL TESTS.

Table 13. Time series given in ASCII output files free running model tests in waves.

variable	unit	Description
time	s	
x_0	m	Long. position ship model
y_0	m	Trans. position ship model
psi	°	Course angle vessel
u	m/s	Long. velocity component
v	m/s	Trans. velocity component
heave	mm	Mean sinkage of the ship
trim	mm/m	Trim motion
roll	°	Roll motion
z_{VF}	mm	Sinkage fore pp, centreline
z_{VA}	mm	Sinkage aft pp, centreline
n	rps	Propeller rate
T_p	N	Propeller thrust
Q_p	Nmm	Propeller shaft torque
d_{rud}	°	Rudder angle
X_{rud}	N	X-comp. rudder force
Y_{rud}	N	Y-comp. rudder force
Q_{rud}	Nmm	Rudder torque
WG1	mm	Free surface elevation WG1
WG2	mm	Free surface elevation WG2
WG3	mm	Free surface elevation WG3
WG4	mm	Free surface elevation WG4
Δx_{0WM}	mm	Position wave maker

Table 14. Longitudinal position and time indications free running model tests at 100% UKC.

	Test FW1		Test FW2	
Zone	**x_0 [m]**	**t [s]**	**x_0 [m]**	**t [s]**
acc,start	15.0	10.1	10.0	25.1
acc,end	22.6	60.1	20.0	50.1
wave	23.8	64.3	20.9	51.1
reg,start	29.8	81.8	30.4	62.3
reg,end	40.5	114.6	48.9	83.5
dec	42.4	120.5	50.4	85.2

FULL-SCALE MEASUREMENTS OF VERTICAL MOTIONS ON ULTRA LARGE CONTAINER VESSELS IN SCHELDT ESTUARY

Jeroen Verwilligen and Katrien Eloot,
Flanders Hydraulics Research, Belgium

Marc Mansuy and Marc Vantorre,
Maritime Technology Division, Ghent University, Belgium

FULL-SCALE MEASUREMENTS OF VERTICAL MOTIONS ON ULTRA LARGE CONTAINER VESSELS IN SCHELDT ESTUARY

Jeroen Verwilligen and **Katrien Eloot,** Flanders Hydraulics Research, Belgium
Marc Mansuy and **Marc Vantorre,** Maritime Technology Division, Ghent University, Belgium

SUMMARY

From September 2017 to July 2018 the Flemish Pilotage executed nine ship measurements on container ships to and from Antwerp. The measurement results were processed by Flanders Hydraulics Research and Ghent University providing 6 DoF motions of the vessels. Furthermore environmental data regarding tide, currents, waves, bathymetry and AIS were processed in order to assess the influence of environmental conditions on the vertical motions of container ships.
The paper presents the vertical ship motions separately for steady and unsteady sinkages in different DoF. As such the relation with ship squat, hydrostatics, sea keeping, turning, steering and ship-to-ship interaction could be assessed and related to the driving parameters such as ship speed, rate of turn, under keel clearance, water density, waves, rudder action and ship meetings.

NOMENCLATURE

B	Beam (m)
C_B	Block Coefficient (-)
GG'	Free Surface Correction (m)
GM	Metacentric Height (m)
L_{OA}	Length over All (m)
L_{PP}	Length between Perpendiculars (m)
s	Running Distance (km)
SOG	Speed over Ground (kn)
T_A	Draft at Aft Perpendicular (m)
T_F	Draft at Fore Perpendicular (m)
UKC	Under Keel Clearance (% of draft)

1 INTRODUCTION

1.1 ACCESSIBILITY PORT OF ANTWERP

The port of Antwerp is the largest port in the Scheldt estuary. The port is connected to the deep water channels in the North Sea by restricted access channels in coastal waters (sea trajectory of 55 km or 30 nm, routes 1, 2, 3, 4, 6 and 7 in Figure 1) and on the river Scheldt (river trajectory of 70 km or 38 nm, route 8 and 9 in Figure 1).

The restricted depth of the access channels on the sea- and river trajectory, combined with an important tidal range of 4 to 6 m, results in tidal restrictions for the accessibility for deep-drafted vessels. The Common Nautical Authority (CNA) provides the tidal windows during which vessels are allowed to sail inbound or outbound.
At present the CNA evaluates the accessibility of the port of Antwerp based on a deterministic method considering a minimum value for the gross under keel clearance (vertical distance between the water depth and the static draft), expressed either in metre or as a percentage of the ship's draft. This accepted keel clearance criterion depends on the channel and the ship type, taking account of the local wave climate and the ships' speed range. For ships in arrival to or departure from the port of Antwerp, the following limitations are currently applied in the approach channels (see Figure 1):

- 15.0% of draft at the sea trajectory (routes 1, 2, 3, 4, 6, 7);
- 12.5% of draft for the Western Scheldt (route 8);
- 10.0% of draft for the Lower Sea Scheldt (route 9).

Figure 1. Access channels and harbours in the Scheldt estuary. 1: VG1, 2: A1, 3: West Rond, 4: Scheur West, 5: Pas van het Zand, 6: Scheur East, 7: Wielingen, 8: Western Scheldt, 9: Lower Sea Scheldt. A: Antwerp/Antwerpen (B), T: Terneuzen (NL), V: Flushing/Vlissingen (NL), Z: Zeebrugge (B), Wa: Wandelaar, Sb: Steenbank.

In order to optimize the accessibility for deep-drafted vessels, the CNA is evaluating the application of a probabilistic access policy based on criteria related to bottom touch and manoeuvring margin. In a probabilistic approach a prediction tool for vertical ship motions is the basis for defining minimal under keel clearances (Vantorre et al., 2014).

1.2 FULL-SCALE MEASUREMENTS

Since 2014, the CNA is initiating projects to collect actual data regarding the vertical ship motions in the access channels to the ports along the river Scheldt. In 2015 the CNA ordered a measurement campaign on cape size bulk carriers with a draft of 16.5 m, sailing inbound to the port of Flushing/Vlissingen (NL), part of North Sea Port (Verwilligen et al., 2018a and Verwilligen et al., 2018b). In 2017 a similar project was initiated for deep drafted container vessels sailing to or from the port of Antwerp. In both cases the measurements were performed by the pilotage (Dutch and Flemish Pilotage, respectively) while processing and analysis were performed by Flanders Hydraulics Research (FHR) and Ghent University, Maritime Technology Division (UGent).
This paper will present the vertical ship motions for nine container vessels sailing outbound (8) from or inbound (1) to the port of Antwerp.

1.3 VERTICAL SHIP MOTIONS

In order to relate the vertical motions to different causes, the motions are split into steady (low frequency) and unsteady (high frequency) motions. Steady motions can be related to slowly varying parameters such as ship speed; rate of turn; under keel clearance and blockage; tidal level and currents; salinity of water; overtaking manoeuvres; constant rudder angles and wind. Unsteady motions on the other hand can be the result of phenomena like: ship response to waves (seakeeping); ship meetings (encounters); rudder deviations and wind gusts.

2 SHIP MEASUREMENTS

2.1 SHIPS AND VOYAGES

From September 2017 to July 2018 the Flemish Pilotage executed nine full-scale measurements on container ships, designated as ULCS 1 – 9, to and from Antwerp. Figure 2 and Table 1 present the shipping trajectories and the main particulars of the ships and voyages, respectively.
It can be observed that the first eight measurements corresponded to outbound trajectories. The focus on outbound measurements is resulting from different reasons, such as the shorter tidal windows (and most likely occurrence of small UKCs), the (in general) larger drafts and the favourable conditions to set up the measurement equipment when the vessel was moored. For the eight outbound container vessels, seven were sailing to the Western pilot station Wandelaar, while the vessel ULCS 5 was sailing to the Northern pilot station Steenbank. The Northern trajectory included an important turning manoeuvre at sea. For the vessel sailing to the Wandelaar, only ULCS 6 applied the fairway via A1, while the others applied the fairway via VG1 (see Figure 1). The last measurement concerned an inbound voyage. ULCS 9 was also coming from the Northern pilot station Steenbank.
Based on the horizontal dimensions the vessels can be divided into two groups. Six out of nine vessels had a length close to 366 m and a beam close to 51.2 m. The mean draft of those vessels (all outbound) varied between 11.3 m and 14.8 m. The three other container vessels all had a length superior to 397 m and a beam larger than 56 m. The mean draft of the three largest container vessels varied between 10.1 m for the inbound vessel and 15.1 m for one of the outbound vessels.
For the first seven voyages the crew performed a water density measurement when the vessel was at the quay.
 presents these densities with the corresponding hydrostatic position of the ship. For the last two voyages no density measurements were provided. For these vessels the drafts are presented for fresh water conditions (1000 kg/m³).

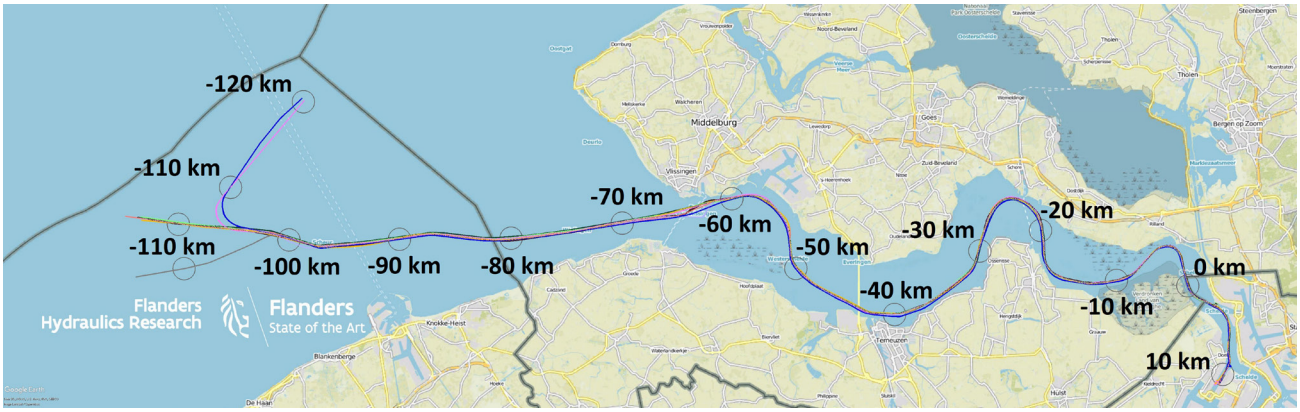

Figure 2. Trajectories for nine container vessels with running distances (colour code see Table 1)

Table 1. Main particulars of nine container vessels measured

Identification Ship and Voyage											
Date voyage	[-]	14/09/2017	28/09/2017	10/11/2017	15/12/2017	16/01/2018	5/02/2018	24/04/2018	20/06/2018	23/07/2018
Ship	[-]	ULCS 1	ULCS 2	ULCS 3	ULCS 4	ULCS 5	ULCS 6	ULCS 7	ULCS 8	ULCS 9
Colour	[-]									
Start position	[-]	Antwerp	Antwerp	Antwerp	Antwerp	Antwerp	Antwerp	Antwerp	Antwerp	Steenbank
End position	[-]	Wandelaar	Wandelaar	Wandelaar	Wandelaar	Steenbank	Wandelaar	Wandelaar	Wandelaar	Antwerp
Main Particulars										
L_{OA}	[m]	364	368	369	369	399	366	398	366	400
L_{PP}	[m]	349	352	352	358	379	350	376	350	386
B	[m]	50.6	51.1	51.1	51.1	58.6	51.2	56.4	51.2	58.6
Loading condition										
		At Berth (1005 kg/m³)	At Berth (1014 kg/m³)	At Berth (1013 kg/m³)	At Berth (1006 kg/m³)	At Berth (1006 kg/m³)	At Berth (1010 kg/m³)	At Berth (1007 kg/m³)	Fresh water (1000 kg/m³)	Fresh water (1000 kg/m³)
T_F	[m]	14.15	14.05	14.7	13.1	13.25	11.1	15.1	14.09	9.28
T_A	[m]	14.15	14.04	14.85	13.2	13.45	11.52	15.05	14.16	10.87
Displacement	[tons]	153423	154530	176590	151515	195845	132394	191407	173018	146288
C_B	[-]	0.61	0.62	0.66	0.64	0.67	0.66	0.60	0.68	0.64
Stability										
GM	[m]	3.37	4.28	3.62	4.84	8.18	7.91	5.51	3.25	11.62
Free Surface Correction (GG')	[m]	0.52	0.36	0.45	0.69	1.74	1.23	0.55	0.39	1.92
Rolling period	[s]	16.5	15.4	16.9	15.4		12.7	21.0	18.5	12.6
Upper structure										
Air Draft	[m]	54.2	54.3	54.4	54.4	68.1	56.3	63.1	56.1	65.5

2.2 MEASUREMENT EQUIPMENT

During the full-scale measurements to and from the port of Antwerp, dedicated measurement equipment was installed to monitor:

- ship positioning in 6 DoF;
- the application of rudder and propeller.

An important requirement for the measurement system was related to the installation and set up on board: two pilots should spend no more than 45 minutes to set up the measuring equipment and to start the measurements.

2.2 (a) Positioning equipment

Full SNMS (ADX)

Similar to the measurements performed on the cape-size bulk carriers to Flushing/Vlissingen (Verwilligen et al., 2018a), the measurement equipment used on container vessels was based on the Full SNMS positioning system (van Buuren, 2005). The Full SNMS positioning system provides both Dutch and Flemish Pilotage with accurate positioning of marginal ships referred to an electronic chart with highly accurate and recent information on bathymetry, aids to navigation and nautical infrastructure. In the SNMS-application, the position of the ship's contour is based on a horizontal position and a heading defined for a reference point. In case of a Full SNMS the horizontal positioning is based on the positioning information from two RTK-GPS antennas that come with the SNMS equipment. The positioning system related to the Full SNMS is also referred to as the AD Navigation ADX-Series (short: ADX). The Full SNMS pilot will install the ADX-antennas on a suitable ship position (e.g. the bridge wings) and relates the position of the antennas to the ship contour by measuring the longitudinal (to bow) and lateral (to starboard side) distance for each antenna. The ADX provides periodic updates of the ship's positioning (5 Hz) with high accuracy (2 cm). However, the quality of the ADX positioning depends on the online availability of RTK-corrections. This external input is provided through a dual sim GPRS-modem, so that accurate positioning is only available in case of a stable data connection to the RTK-server. This results in missing positioning data (gaps) during the measurements.
The Full SNMS application is developed to assist ship manoeuvring and focusses on the representation of the horizontal positioning. As such the software is optimized to provide accurate information on the longitude, latitude and heading of the vessel, corresponding to the three horizontal degrees of freedom: surge, sway and yaw. Furthermore, when the RTK-GPS antennas are installed laterally then the altitude (height) measurement of the antennas can be applied to provide the heave motion and the roll motion of the vessel as well. As a result the standard application of the ADX provides measurements for five out of six degrees of freedom. In order to perform ship position measurements in six degrees of freedom, additional measurement equipment is required to provide pitch information of the vessel.
For measurements on cape-size bulk carriers the pitch motion was obtained by installing a third RTK-GPS antenna on the bow of the ship (Verwilligen et al., 2018a). Unfortunately for container vessels no convenient positions are available to install a third RTK-GPS at bow or stern so that another measurement device was required to measure the pitch motion of container ships.

Octans 4

In order to allow accurate measurements of the pitch motion of the container vessels, the Dutch ministry of infrastructure and water management (Rijkswaterstaat), provided the Octans 4 measurement device. The Octans combines a gyrocompass (three axis) and motion sensor. According to the manufacturer a standalone application of the Octans 4 provides orientations (roll, pitch and heading) at a RMS-accuracy of 0.01 degree. This accuracy is agreed to be acceptable for the pitch measurement on container ships. The Octans 4 provides motion measurements at 25 Hz frequency.

2.2 (b) Installation and setup

For the application of ADX antennas and Octans on board of container vessels the following configuration was applied (see Figure 3):

- ADX antennas POS and HDG1 installed laterally at a wide distance (e.g. at both bridge wings);
- Octans 4 installed midships on the ship bridge and orientated (exactly) towards the bow.

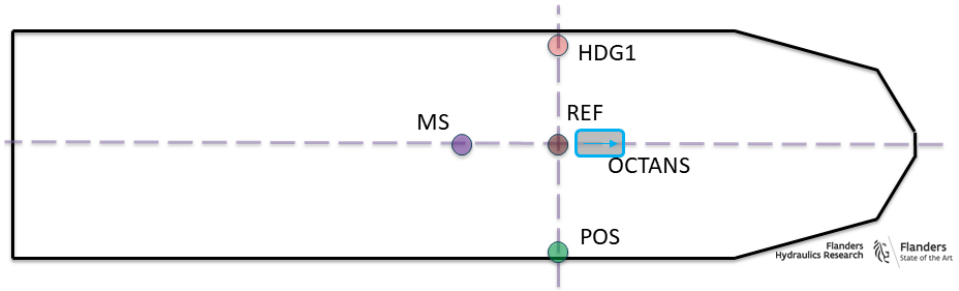

Figure 3. Positions of measuring setup applied on container vessels

2.2 (c) Camera monitoring

In order to monitor the evolution of indicators on the ship bridge, FHR developed a portable camera setup (Geerts et al., 2016). The camera setup consists of three independent camera units that allow to log images at a predefined frequency. The camera units have a magnetic housing, allowing to install them fast and easy on the ceiling of the ship bridge (see Figure 4). For all measurements performed on container vessels, the cameras were installed by the Flemish Pilotage to monitor the rudder indicator, the propeller indicator and the wind indicator at a frequency of 1Hz.

Figure 4. Application of one camera unit on board of an ULCS

3 DATA PROCESSING

3.1 POSITIONING IN 6 DOF

From the raw measuring data provided by the pilotage, the ship's positions in 6 DoF were processed.
At first, the absolute position of the reference point (REF) is calculated from the ADX-positioning. The reference point is defined as a point in the centreplane of the vessel at the same longitudinal position as the ADX-antennas (see Figure 3). The heading of the vessel is also calculated based on the positions of the ADX-antennas. The roll and pitch angles at the reference point are provided by the Octans 4 measurement. As such the absolute positions of the reference point are defined in six degrees of freedom. By applying the corresponding lever arms, the motions of the vessel's midship (MS) could be calculated.

3.2 REFERENCE TRAJECTORY

In order to allow a geographical analysis on the data, the horizontal ship positions (MS) were related to the running distance (km) with respect to a reference trajectory. As a basis for the reference trajectory a mid-fairway curve was applied.
The origin of the reference trajectory was defined at passage point CP (Coordination Point) closely corresponding to the Dutch-Belgian Border. Positive running distances correspond to positions upstream CP and negative running distances correspond to positions downstream CP. Figure 2 presents the running distances for the different trajectories applied.
The following areas can be distinguished:

- Port trajectory (0 km < s): vessels are sailing at relatively low speed and waves are absent
- Scheldt trajectory (-65 km < s < 0 km): vessels are sailing at moderate speed and waves are absent
- Sea trajectory (s < -65 km): vessels are sailing at relatively high speed and important sea states may occur.

3.3 FALL-BACK FUNCTIONALITY

The weakest point in the ship monitoring corresponds to dependency of the ADX to RTK-corrections provided through a GPRS-modem. Drop outs of the RTK-corrections results in (sometimes long) unavailability of ADX-measurements. When ADX measurements are absent, no information on ship positioning is available, so that no geographical processing (on bathymetry and hydro-meteo data) can be performed. Also information on ship speed is missing in case ADX is not working properly.
In case both ADX and Octans were not measuring (e.g. in case of a crash or reboot of the equipment) then also information on heading and rate of turn was missing.
For abovementioned reasons the positioning data coming from AIS were used in case that the measuring devices were not working properly. AIS-information was obtained from the Scheldt Radar Chain (SRK). It was observed that on condition that the antenna-offsets in the AIS-data were correctly defined, the AIS data were a good alternative for the horizontal ADX positioning. For six out of nine vessels the antenna-offsets were correctly defined in the AIS-data, resulting in a (mean) deviation to the ADX-measurement smaller than 2 m. For the three other vessels the lateral offset in the AIS-data presented larger deviations to the ADX-measurement (up to 28 m). For these vessels a manual update of the AIS information was performed.
The AIS-data (combined with the optimized antenna offsets based on ADX) were processed into the following parameters allowing to be applied as a fall-back for the corresponding motion measurements obtained with ADX and Octans:

- latitude MS;
- longitude MS;
- heading;
- ship speed over ground;
- rate of turn.

3.4 RELATIVE VERTICAL POSITIONS TO THE WATER LEVEL

In the project it is the objective to study the evolution of the vertical ship motions for a sailing vessel. This means the vertical motions should be related to the hydrostatic vertical position for the vessel at the quay (in Antwerp):

- rolling and pitching angle are referred to their static and undisturbed value;
- heave motions are related to the water level and referred to a static condition.

3.4 (a) Static trim and heel

For each measurement a timeslot of approximately 5 minutes was selected (when possible) for which the vessel was operating in static and free conditions. This static measurement was performed in proximity of the quay because on this location the ship speed was negligible. The following conditions need to be satisfied when defining the static measurement:

- negligible ship speed or rate of turn;
- high quality of ADX positioning;
- the vessel is sailing free and undisturbed (no mooring lines attached, no contact with quay fendering, limited tug action).

The mean roll and pitch angles during the static measurement are defined as the static roll and static pitch and were subtracted from the raw roll and pitch angles measured along the full trajectory.
For some measurements the static conditions defined above could not be met. In that case some uncertainty remains on the absolute value of the roll angle during the measurement.
Throughout this document *roll* and *pitch* are defined as the motions corrected with a static offset as described above.

3.4 (b) Heave referred to water level

The measurements provides ship positioning with respect to an earth bound coordinate system. In order to assess the sinkage of a vessel, the ship positions should be referred to the instantaneous water plane (see Figure 5).
To achieve this the altitude measurements with respect to the GRS80 ellipsoid were converted to a geodetic reference level (NAP). Then the hydrostatic vertical distance between the antennas and the water surface (ΔZ_{Static}) was deduced from a static measurement (at negligible ship speed). Once the hydrostatic position of the antennas is known, the sinkage of the antenna can be obtained by subtracting the vertical distance between the antenna and the actual waterline ($Z_{Tide} - Z_{Antenna}$) from the static vertical distance (ΔZ_{Static}).

In a tidal environment, the accuracy of the sinkage measurement depends on (Verwilligen et al., 2018a):

- the accuracy of the altitude measurement by the RTK-antennas (0.03 m);
- the accuracy of the conversion method to a geodetic reference level (0.02 m);
- the accuracy of the pitch measurement (0.01 deg);
- the longitudinal distance of the antennas with respect to bow and stern of the vessel;
- the accuracy by which the water level along the trajectory could be reproduced (0.05 m on the river trajectory).

As such, when assuming the vessel to be a rigid body the accuracy of the squat was between 0.12 m and 0.14 m at the bow and between 0.13 m and 0.15 m at the stern.

The vessel is referred to its hydrostatic position so that hydrostatic hogging or sagging of the vessels was taken into account. Nevertheless the measurements do not account for the effect of dynamic hogging and sagging during the voyage (e.g. longitudinal bending due to sea keeping).

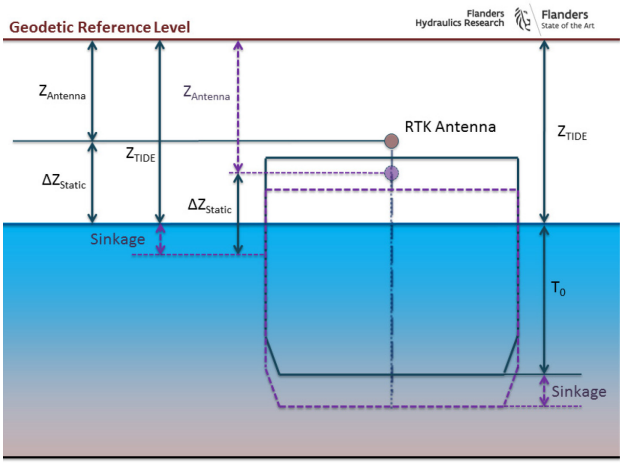

Figure 5. Calculating sinkage in case of constant draft. Full line: static condition; dashed line: sailing condition (Verwilligen et al., 2018a).

3.5 STEADY AND UNSTEADY MOTIONS

In order to perform a first analysis on the cause of vertical ship motions, the motions are separated in a steady part and an unsteady part. The steady motions were defined as the 60 seconds running average ([t-30 s; t+30 s]) of the full motion. The unsteady motions were obtained by subtracting the steady motions of the full motion. As a result the sum of the steady and unsteady motions equals the full motion of the vessel.

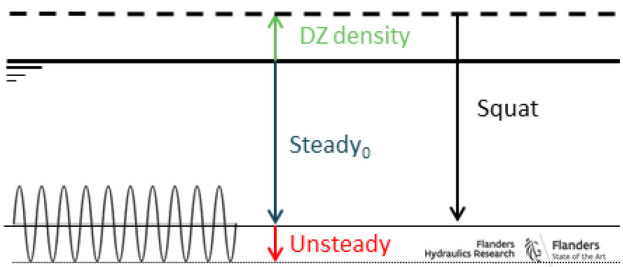

Figure 6. Heave motion components corresponding to unsteady (red), steady (blue) and static (green) motion

3.5 (a) Heave and pitch

Figure 6 visualizes the determining phenomena that cause the heave motion of the vessel. From the measurements, the steady and unsteady heave motions are retrieved. The unsteady part of the heave motion corresponds to the response of the vessel to waves or other dynamic external forces. The steady part of the heave motion corresponds to a hydrostatic effect due to density changes and a downwards motion due to squat. In order to investigate ship's squat the steady sinkages provided from the processing in §3.4 (b) should be corrected to the varying hydrostatics (draft fore and aft) corresponding to density changes. For vessels sailing outbound, the density effect will have an upward effect on the ship's vertical position (negative sinkage). In case of low ship speeds (and consequently small squat) at a downstream position, this may result in a negative value of the steady sinkage (see § 5.1).
In this respect, the pitch motion of the vessel is similar to the heave motion with unsteady motions related to waves and dynamic phenomena and steady motions related to squat and density variations.

3.5 (b) Roll

For roll motions the distinction between steady and unsteady motions is less straightforward. The reason is that many parameters can influence the roll motion of the vessels, such as the following parameters that can be considered steady:

- ship speed and rate of turn influencing heeling in bends;
- ship encounters (overtaking);
- constant rudder angles;
- steady wind components.

and the following phenomena related to unsteady motions:

- ship response to waves (seakeeping);
- ship encounters (meetings);
- rudder deviations;
- wind gusts.

Furthermore the unsteady roll motion is strongly influenced by the dynamic rolling behaviour of the vessel, depending on the stability (GM), the rotational inertia and the roll damping of the vessel.

4 CONDITIONS

In this chapter the operational and environmental conditions during the nine voyages are presented. Chapter 7 provides a graphical presentation of the measurement results. In those figures the results are referred to the running distance (see §3.2) presented on the horizontal axis. The running distances are presented with decreasing values so that for outbound voyages, time is increasing from left to right. For the inbound voyage of ULCS 9, the start of the measurement corresponds to the right side of the figure.

4.1 TIDE AND CURRENT

In order to reproduce the tide along the trajectory with good accuracy, the results of hindcast simulations performed with the numerical model ZUNOv4 (Dutch ministry of infrastructure and water management, Rijkswaterstaat) were combined with tide measurements available at several stations along the trajectory (see Figure 7). The numerical model provides both tidal levels and 2D current vectors for the full study area with an update period of 30 minutes. From the tide measurements at specific positions, an additional geographically and time varying correction factor for the ZUNOv4 grids was deduced.
Due to lack of measurement data, no optimisation could be performed on the current vectors derived from the ZUNOv4 output. The ZUNOv4 is a two-dimensional model, so that the provided current vectors can be assumed to be depth averaged.
Figure 8 presents the evolution of the **water level** for the nine container vessels measured. Vessels with a tide dependent draft are presented in a full line and tide independent vessels are presented in a dotted line
It can be observed that despite the small draft of the (only) inbound vessel (ULCS 9), the vessel was following the flood current, leading to rather high water levels along the trajectory.
For the outbound vessels it can be observed that four out of eight outbound vessels (ULCS 2, ULCS 3, ULCS 7 and ULCS 8) did optimise their voyage around high tide. Those vessels depart from the port of Antwerp in flood conditions and reach high tide at a position between -40 km (Terneuzen) and -50 km (Pas van Borssele). These trajectories are typical for tide dependent vessels. The four vessels mentioned all had a draft of more than 14.0 m which is more than the tide independent draft on the Scheldt (13.1 m).

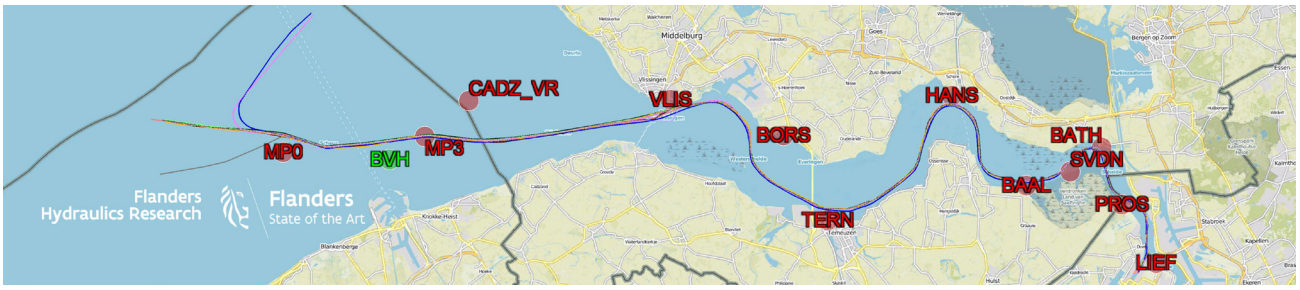

Figure 7. Location of tide (red) and wave (green) measurement stations applied

Three of the other outbound vessels (ULCS 4, ULCS 5 and ULCS 6) were, at some point of the trajectory, sailing at low tide. Those vessels however did have a significantly lower draft, so that on most of the days these vessels will be tide independent. Finally, the vessel ULCS 1 did have a draft of 14.15 m making the vessel tide dependent (especially on the Western Scheldt).
It can be observed that this vessel was sailing at the end of its tidal window resulting in relatively low tides at the sea trajectory.
The **current** conditions highly depend on the tidal conditions. In Figure 9 the magnitude of the current vector is presented for the nine measurements. On the sea trajectory (s < -65 km) the current is changing gradually while on the Western Scheldt more geographical variations in current speed can be observed. These variations are related to the varying topology of the fairway (e.g. in bends and straight sections). It can be observed that for two vessels (ULCS 6 and ULCS 8) rather large flood currents, with a magnitude of more than 3 kn, were experienced.
It should be noticed that the current speeds retrieved from the ZUNO v4 model are depth averaged, while the vessel is only present in the top layers of the water. In general the tide the current is stronger in the top layers of the water then over the complete water column. Some uncertainty remains on the actual current speed (and as a consequence also on the speed through water) experienced by the vessel.

4.2 BATHYMETRY

The bottom profile present during the measurements was retrieved from the most recent survey data available at the time of the measurement. For this purpose historical soundings from the Scheldt ECS database (Flemish Hydrography and Rijkswaterstaat) were applied. The survey data were projected on the trajectory followed by the midship (MS), fore perpendicular (FP) and aft perpendicular (AP) of the vessel. The water depth is obtained by summing the tide to the bottom depth.

In Figure 10 the **water depth** experienced by the nine vessels is presented. It can be observed that especially on the river Scheldt (s > - 65 km), there is an important geographical variation in depth conditions related to the morphology of the river. For example the river bends correspond to deeper water than the straight stretches. Also the influence of tidal conditions can be observed. For example at running distance -10 km (Baalhoek) relatively small water depths were experienced by the vessels ULCS 4 and ULCS 6. Because of their small drafts, these vessels were tide independent and could pass Baalhoek at low tide conditions.
Figure 11 shows the gross under keel clearance experienced by the vessels. The gross under keel clearance is presented as a percentage of the hydrostatic draft of the vessel at the berth or in fresh water (see Table 1)
) and corresponds to the deterministic definition of the under keel clearance. This figure shows that the smallest under keel clearances occurred in the port trajectory (s > 0 km), i.e. at upstream locations close to the port of Antwerp (at the entrance of the Deurganckdok (s=9 km) and at the shallow patch of Frederik (s=7 km)). For all measurements the under keel clearances at Scheldt and sea trajectory were larger than 20%.
It should be noticed that the minimum under keel clearance available during the measurements is significantly larger than the minimum keel clearance that is prescribed in the actual deterministic calculation (12.5% on the river trajectory and 15% at sea). Actually, the required under keel clearance percentages will eventually be overruled when a probabilistic approach policy will be implemented. The gross under keel clearance should be sufficient to reduce the probability of bottom touch to an acceptably low value, but also the remaining manoeuvring margin, i.e. the average vertical distance between the ship's keel and the bottom during the transit (Pianc - Maritime navigation commission, 2014), should allow the ship to perform the required manoeuvres. While Pianc - Maritime navigation commission (2014) rather arbitrarily suggests a manoeuvring margin of 5% of draft (with a minimum of 0.60 m), it will be investigated whether this recommended value is sufficient for guaranteeing the controllability and manoeuvrability of ULCS over the complete trajectory. Possibly, the required manoeuvring margin will be variable along the trajectory; in straight stretches the manoeuvring margin could be less compared to bends. With respect to the latter, reference is made to (Eloot et al., 2007), where it was concluded that in confined river bends with steep banks, additional keel clearance is required to compensate for bank effects.

4.3 WAVE CONDITIONS

In order to relate the unsteady ship motions at sea to the acting **wave climate**, the significant wave height and the swell height (≤ 0.1 Hz) were derived from spectra measured at the directional wave buoy *Bol van Heist* (BVH, see Figure 7).

Table 2. Wave parameters at Bol van Heist

Ship	Significant Wave Height	Significant Swell Height
	[m]	[m]
ULCS 1	1.16	0.18
ULCS 2	0.30	0.02
ULCS 3	0.95	0.06
ULCS 4	0.89	0.07
ULCS 5	0.29	0.04
ULCS 6	1.20	0.06
ULCS 7	1.04	0.05
ULCS 8	0.57	0.04
ULCS 9	0.46	0.02

Table 2 presents the wave parameters for the nine voyages, revealing important wave and swell heights for the vessel ULCS 1 and a large significant wave height for ULCS 6.

4.4 SHIP ENCOUNTERS

Encounters with other **shipping traffic** revealed to have an important effect on vertical motion of the vessel. The presence of other shipping traffic was processed from AIS-information provided by the Scheldt Radar Chain (SRC). By means of a dedicated AIS-processing tool developed by FHR, the AIS data of the vessels that operated in the proximity of a reference vessel were identified and a table with (significant) ship meetings was generated. When presenting the squat motions of the vessels (see §5.2), some examples of ship encounters will be presented.

4.5 SHIP SPEED

In Figure 12 the **speed over ground** for the nine voyages is presented. An important variation in ship speed can be observed for different vessels. Also at some locations an important decrease of the ship speed can be noticed. The most striking example is the passage at Vlissingen (s = -65 km), where the speed is reduced in order to facilitate the pilots to (dis)embark. Also at position -17 km a drop in ship speed can be observed for all vessels. This location corresponds to the port of Walsoorden. The speed reduction at Walsoorden is applied in order to minimize the ship waves hindering the inland vessels moored in the port and the operations in a small drydock for ship repair. On the river Scheldt, for ULCS, it is required frequently to reduce speed to mitigate the interaction effects on inland barges.
From a hydrodynamic point of view, the **speed through water** is determining (see Figure 13). The speed through water is the relative speed between the vessel and the current. For most outbound voyages the river trajectory corresponded to flood currents. In this situation the sailing direction of the vessel is opposite to the current, leading to a higher speed through water than speed over ground. One can note that on the river trajectory the large speed over ground of the vessel ULCS 5 was strongly related to the ebb current this vessel was operating in. Looking to the speed through water the differences between the different vessels on the Western Scheldt are smaller than when the speed over ground was compared.
On the sea trajectory the largest ship speeds (up to 18 kn) were applied by the vessel ULCS 8.

4.6 RATE OF TURN

In Figure 14 the **rate of turn** of the nine vessels is presented. Note that the one vessel following an inbound trajectory (ULCS 9) shows opposite values (s < -5 km).
On the sea trajectory, in general, smaller yawing rates can be observed, except for the vessels using the Northern pilot station Steenbank (ULCS 5 and ULCS 9). Especially for the outbound ULCS 5 the bending manoeuvre at *West Rond* (s= -107km) did correspond to a high rate of turn (30 deg/min).
On the Western Scheldt the rate of turn reaches several peaks corresponding to the bends of the river. The most important rate of turn can be observed at s=-4 km (Bath) and s=-24km (Hansweert) and were applied by the vessels ULCS 4 and ULCS 8 (approximately 28 deg/min).
When comparing the rate of turn of the vessels (Figure 14) with the speeds of the vessels (Figure 13) a close relation between ship speed and rate of turn can be observed as the drifting and yawing motion of a vessel results in a decrease of the speed.

5 VERTICAL SHIP MOTIONS

In this chapter a first observation of the vertical motions will be presented. In order to separate the motions from different sources, the motions will be presented for the longitudinal (heave and pitch) and lateral (roll) sinkage and for the steady and unsteady motions separately.

5.1 STEADY LONGITUDINAL SINKAGE

The steady longitudinal sinkage is defined as the maximum sinkage at bow or stern resulting from the combined effect of the steady heave and steady pitch motions. The processing of this parameter depends on the ADX-measurement, the Octans-measurement and the tide reproduction. The results are only available in case both ADX and Octans were operational and provided accurate measuring results. The results of the steady longitudinal motions are presented in Figure 16.
The steady longitudinal sinkage can be considered to be mainly related to the squat of the vessel and the effect of the varying water density. For ship **squat** the main influencing parameters are the ship‘s speed (see Figure 13) and the under keel clearance (see Figure 11). Focussing on the motions on the sea trajectory, the relation between the steady longitudinal sinkage and the ship’s speed is indeed noticeable. For example the vessel with the lowest ship speed (ULCS 9) did experience the smallest sinkages

while the vessel applying the highest ship speeds (ULCS 8) did experience the largest sinkages reaching more than 1.6 m. On the other hand the squat at the midship's position of vessel ULCS 6 was very limited, despites the important speed of more than 16 kn. The moderate squat motion for ULCS 6 is probably related to the small draft of this vessel and the corresponding large under keel clearances. Also when studying the longitudinal sinkage of a vessel on the Scheldt trajectory, the influence of under keel clearance on ship squat is clearly demonstrated.

The longitudinal sinkage is resulting from both heave and pitch motions. Full ship types, as studied in (Verwilligen et al., 2018b), will experience a bow down trim resulting in maximum squat occurring at the bow at all time. The present measurements of steady pitch on ULCS (see Figure 15) reveal that for the more slender container vessels the **trim due to squat** is less straight forward. For example focussing on the sea trajectory it can be observed that different ships experience an opposite trim. For most of the container vessels a bow down motion can be observed. However, for two of the vessels (ULCS 5 and ULCS 6), the trim resulting from squat was opposite (bow up) and for two of the vessels (ULCS 1 and ULCS 7) the trim on the sea trajectory was negligible. On the river trajectory (s > -65 km) for most of the vessels the trim was changing between bow down and bow up. Comparing the results of the trim to the UKC (see Figure 11) reveals that the squat trim of the individual vessels tended to the bow in deep water and to the stern in more shallow water. This observations correspond to the results of squat measurements on scaled ULCS performed in the Towing Tank for Confined Water (Eloot et al., 2008). In the same reference, the trim motion is related to the draft of the vessel, stating that deep-drafted ULCS will squat more to the bow than the ballasted ULCS. From the full-scale measurements on the sea trajectory (s < -65 km), this statement is confirmed for (most of the) the vessels with L_{OA} 366 m, showing bow up trim for the vessels with a draft of 11.3 m (ULCS 6) and bow down trim for most 366m vessels with draft more than 13.0 m (ULCS 2, ULCS 3, ULCS 4 and ULCS 8). The bow up trim of ULCS 6 may also be related to the static trim of the vessel. ULCS 6 was trimmed by the stern with 0.4 m. On the other hand ULCS 1, drafted 14.15 m presents negligible trim on the sea trajectory. Of course the draft of the vessel and the tidal conditions also influence the keel clearance. In §4.2 it was noticed that vessel ULCS 1 was sailing at the end of its tidal window corresponding to relatively low under keel clearances on the sea trajectory (see Figure 11). The small under keel clearances for vessel ULCS 1 may explain the trim to be less bow down than expected based on the draft of the vessel.

For the longer ULCS (L_{OA}>397 m) the relation between the ship's draft and the trim at the sea trajectory motions is less consistent, showing negligible trim for ULCS 7 with draft 15.1 m and (mainly) bow down trim for ULCS 9 with draft 10.1 m.

From the steady longitudinal sinkage, also the **density effect** on the ship's draft is observed. The vessel's speed is reduced at Vlissingen (s = -65 km) in order to facilitate the pilot change (see Figure 13). At this low speed the sinkage of the vessel due to squat becomes very small so that for outbound vessels, the main effect on the steady heave motion corresponds to the decrease of the ship's draft and change in trim due to the increase in water density (see Table 1).

The negative sinkages (upwards) at low speeds for outbound vessels (see Figure 16) correspond to the hydrostatic effect of the water density on the ship's draft.

5.2 UNSTEADY LONGITUDINAL SINKAGE

In Figure 17 the unsteady longitudinal sinkage is presented. On the sea trajectory only two vessels (ULCS 1 and ULCS 6) experienced a significant motion due to waves. This relation between **sea state** and unsteady motions is illustrated by comparing the motions of the vessel to the significant wave height and the swell component in the coastal wave spectra (see §4.3).

Furthermore, also for other vessels isolated unsteady longitudinal motions could be observed both on river and sea trajectory. When comparing these motions to the results of the AIS-processing (see §4.4) these motions could be related to **ship encounters**. In this paper two examples are presented for which the conditions and added sinkages are summarized in Table 3.

A first example concerns the meeting of the vessel ULCS 4 with a 319 m container vessel in the Wielingen (sea trajectory). The vessels were meeting at a relatively large lateral distance but at rather important ship speed's over ground of 14.6 and 21.0 kn respectively. Taking into account the current, the meeting vessel was sailing at a speed through water of approximately 19.5 kn leading to an added sinkage of 0.4 m. A second example concerns the vessel ULCS 5 being overtaken by a 205 m ConRo vessel, leading to an increased sinkage of 0.3 m on the ULCS. In this case, the overtaking vessel applied a speed through water of approximately 18.5 kn which was 6.2 kn more than the vessel ULCS 5.

Table 3. Conditions of two important ship encounters based on AIS-analysis

Date	[-]	15/12/2017	27/01/2018
Time UTC	[-]	9:07:35	1:45:05
Own ship name	[-]	ULCS 4	ULCS 5
Own ship SOG	[kn]	14.6	13.8
Own ship UKC	[%]	45%	28%
Meeting ship type	[-]	Container vessel	ConRo vessel
Meeting ship Length	[m]	319	205
Meeting ship Beam	[m]	40	26
Meeting ship Draft	[m]	11.1	8.3
Meeting ship SOG	[kn]	21.0	20.0
Minimal Distance	[m]	227	165
Relative speed between ships	[kn]	35.5	-6.2
Extra sinkage	[m]	0.4	0.3

5.3 STEADY LATERAL SINKAGE

In Figure 18 the steady lateral sinkage is presented as the vertical downward motion of the ship bilges related to the steady roll motion of the vessels. Large steady roll motions can be observed in the **bends** at Bath (-4 km), Hansweert (-24 km) and Borssele (-55 km). The most important steady roll motions are observed on the vessels ULCS 8 and ULCS 3 and to a lesser extent on ULCS 1. Those vessels were also those with the smallest metacentric height (GM' < 3.2 m). Compared to the other vessels the stability of these vessels could be considered low.
A strong relation between rate of turn (see Figure 14), ship speed (see Figure 13) and steady roll motion can be observed. Furthermore also at straight trajectories a small steady roll angle remains that could not be related to the yawing motion of the vessel. Further analysis will investigate the effect of wind and other parameters (current, banks) on the rolling motion of the vessel.

5.4 UNSTEADY LATERAL SINKAGE

Figure 19 presents the sinkage related to the unsteady roll motion of the vessels. Although wave action is absent on the river trajectory, the unsteady roll motions seem to be significantly larger on the river than at sea, so that the main reason for unsteady roll motion is not related to the ship responses to waves but to another disturbance of the vessel. From the results of the camera monitoring (see §2.2 (c)), it could be analysed that the unsteady roll motion was strongly correlated to deviations in **rudder angle**. The rolling moment induced by the lifting force on the rudder seems to have an important impact on the roll motions of the vessels on the river Scheldt. Also on the sea trajectory some important roll motions, probably related to rudder action, can be observed.
From the measurement results it can be deduced that the main effects influencing the roll motions are the roll moments induced by the centrifugal force and by rudder forces . In a steady bend, the centrifugal forces are acting in the centre of gravity of the vessel to a direction outwards of the bend. As also the rudder induced force is acting outwards, a hydrodynamic reaction force is required so as to obtain a force equilibrium. For container vessels the centre of gravity is at a relatively high position (at least higher than the vertical position of the application point of the hydrodynamic reaction force which is approximately at half draft) so that the centrifugal force makes the vessel heel to the outer bend. However, in case of a rudder command (i.e. a sudden change of the rudder angle), initially the rudder force and the lateral inertia force will generate a heeling moment which has an opposite sign compared to the eventual steady state. This effect is particularly important when the rate of turn of the vessel needs to be reduced, and counter rudder is given. At that moment the roll moment induced by the rudder action acts in the same direction as the roll moment induced by the centrifugal force. As a consequence the largest roll motions occur when the rate of turn of a vessel is reduced drastically due to a large counter rudder. However, also large unsteady motions occur on straight stretches when consecutive (short) applications of large rudder angles are applied and resonate with the roll dynamics of the vessel. An example of this effect corresponds to the significant unsteady roll motion of ULCS 2 at s = -101 km.
In §5.3 it was noticed that the steady roll motion showed some relation with the stability of the vessel. Also for the unsteady roll motions the vessels ULCS 8 and ULCS 3 with low metacentric height did experience large unsteady motions, but the largest unsteady roll motions occurred on the vessel ULCS 4 (GM = 4.84 m). It can be concluded that the stability of the vessel is not the only parameter influencing the unsteady rolling motion. Other parameters involved are most likely related to the rudder and propeller equipment and the application of rudder angles by the helmsman.
The impact of waves of the (unsteady) roll motion could not be deduced from the measurement results.

6 CONCLUSIONS

From September 2017 to July 2018 the Flemish Pilotage executed nine ship measurements on container ships to and from Antwerp. The measurement results were processed by Flanders Hydraulics Research and Ghent University providing 6 DoF motions of the vessels.

Furthermore environmental data regarding tide, currents, waves, bathymetry and AIS were processed in order to assess the influence of environmental conditions on the vertical ship motions.
The vertical ship motions are presented separately for the longitudinal and lateral sinkages and for steady and unsteady motions.
The longitudinal steady sinkages correspond mainly to squat, and to a lesser extent to varying water density along the trajectory. The influence of ship speed and under keel clearance on ship squat is demonstrated. Also the relation of the ship's loading condition and keel clearance on the trim direction is discussed and compared to previous observations based on towing tank results.
The unsteady longitudinal sinkages are related to sea keeping and to added squat due to ship encounters.
The major phenomena driving the roll motions on the river trajectory concern heeling in bends (steady) and the dynamic response on the rolling moment due to rudder actions (unsteady). Especially the steady roll motions show a strong relation with the initial stability of the vessels. For the unsteady roll motions also other parameters (e.g. rudder design) seem to be important.
The paper presents the first results of an extensive data processing. The data opens opportunities for an in depth analysis for the ship behaviour in shallow and confined water, not only related to vertical ship motions but also to the manoeuvring behaviour of the vessel. At present future work is planned in the field of squat modelling and on the roll behaviour of ULCS. In a next step Flanders Hydraulics Research and Ghent University like to apply the measurement results to validate the mathematical manoeuvring models derived from the towing tank.

7 ACKNOWLEDGEMENTS

The work presented in this paper is the result of a fruitful collaboration between several partners involved. The authors want to acknowledge in particular the Common Nautical Authority and the Flemish Pilotage DAB Loodswezen.
For reproducing the environmental conditions a lot of data from different sources and databases were provided by:
the Flemish Hydrography, Dutch ministry of infrastructure and water management (Rijkswaterstaat) and the Scheldt Radar Chain.
This research could not be executed without the financial support of the Common Nautical Authority in which the Flemish Shipping Assistance Division (BE) and the Dutch ministry of infrastructure and water management, Rijkswaterstaat (NL) are represented.

8 REFERENCES

Eloot, K., Verwilligen, J., Vantorre, M., 2008. An Overview of Squat Measurements for Container Ships in Restricted Water, in: International Conference on Safety and Operations in Canals and Waterways SOCW 2008, 15-16 September. Glasgow, UK, pp. 106−116.

Eloot, K., Verwilligen, J., Vantorre, M., 2007. A methodology for evaluating the controllability of a ship navigating in a restricted channel, in: Archives of Civil and Mechanical Engineering: Quarterly. Oficyna Wydawnicza Politechniki Wroclawskiej, pp. 91−104. https://doi.org/10.1016/S1644-9665(12)60016-8

Geerts, S., Verwilligen, J., Eloot, K., Mostaert, F., 2016. Ontwikkeling meetapparatuur aan boord van schepen: Deelrapport 6 − Gebruikershandleiding camerasysteem MIM_FHR_v2. Antwerp.

Pianc - Maritime navigation commission, 2014. Harbour approach channels design guidelines - Report n° 121 - 2014. Brussels, Belgium.

van Buuren, W., 2005. Beschrijving van de NMS type ADX. November 2005.

Vantorre, M., Candries, M., Verwilligen, J., 2014. Optimisation of Tidal Windows for Deep-Drafted Vessels by Means of a Probabilistic Approach Policy, in: PIANC World Congress. San Francisco, USA.

Verwilligen, J., Mansuy, M., Vantorre, M., Eloot, K., 2018a. Full-scale measurements to assess squat and vertical motions in exposed shallow water, in: Proceedings of the 34th PIANC World Congress 2018 in Panama City, Panama. PIANC.

Verwilligen, J., Mansuy, M., Vantorre, M., Eloot, K., 2018b. Squat formula for cape-size bulk carriers based on towing tank results and full-scale measurements, in: MARSIM 2018, Halifax, Canada, 12 - 16 August 2018. IMSF.

9 AUTHORS BIOGRAPHY

Jeroen Verwilligen holds the current position of senior expert in nautical research at Flanders Hydraulics Research. He is experienced with simulation studies, nautical accessibility studies and full scale measurements. He is member of the PIANC MarCom WG 171 on Ship Handling Simulation Dedicated to Channel and Harbour Design.

Katrien Eloot holds the current position of senior expert in nautical research at Flanders Hydraulics Research. Through her PhD on selection, experimental determination and evaluation of mathematical manoeuvring models she is active in the field of math model development for ship behaviour in shallow and confined water and the execution of simulation studies for clients coping with issues on shallow water manoeuvring. She is member of PIANC InCom WG 141 on Design Guidelines for Inland Waterway Dimensions which will disseminate the report results through 2019.

Marc Mansuy holds the current position of research staff at Gent University. He has been working on different

projects related to maneuvering in shallow and confined water at Flanders Hydraulic Research and Ghent University.
He has some expertise in waterway accessibility, ship maneuverability on real time and fast time simulators and full scale measurements.

Marc Vantorre, naval architect, is emeritus professor of marine hydrodynamics and former head of the Maritime Technology Division at Ghent University, Belgium. His research focuses on ship behaviour in shallow and confined waters, mainly in close co-operation with Flanders Hydraulics Research in Antwerp. He is former member of PIANC Working Groups and of the ITTC Manoeuvring Committee.

10 APPENDIX: GRAPICAL PRESENTATION OF MEASUREMENT RESULTS

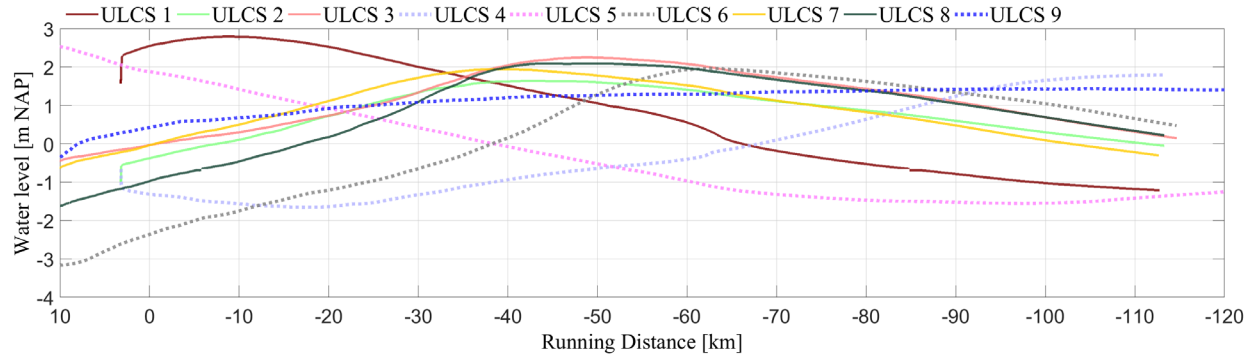

Figure 8. Tide evolution during nine voyages

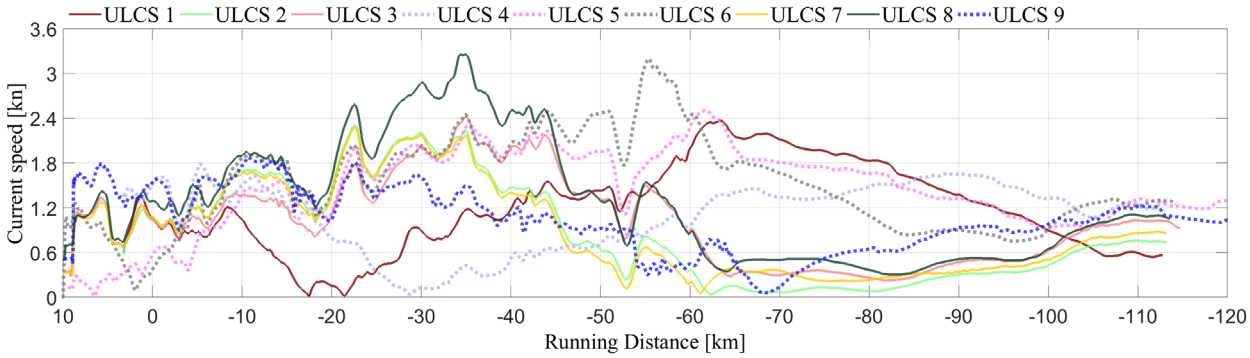

Figure 9. Current magnitude during nine voyages

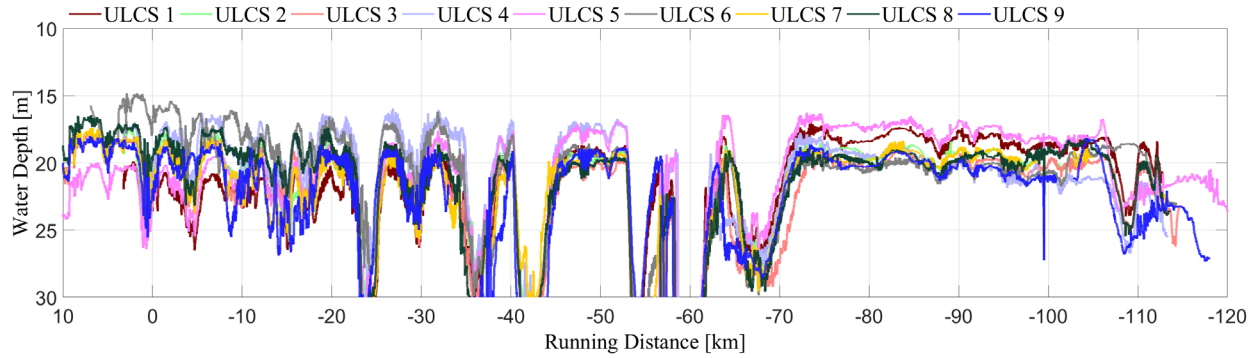

Figure 10. Water depth during nine voyages

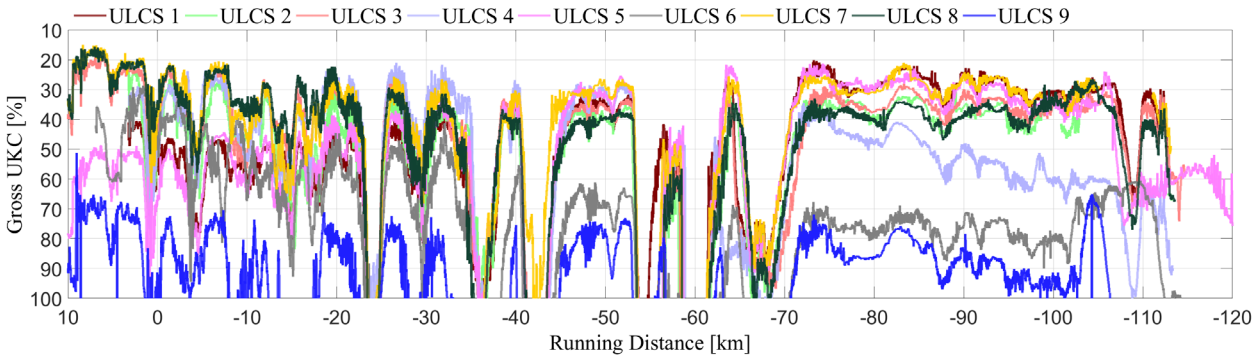

Figure 11. Gross UKC during nine voyages

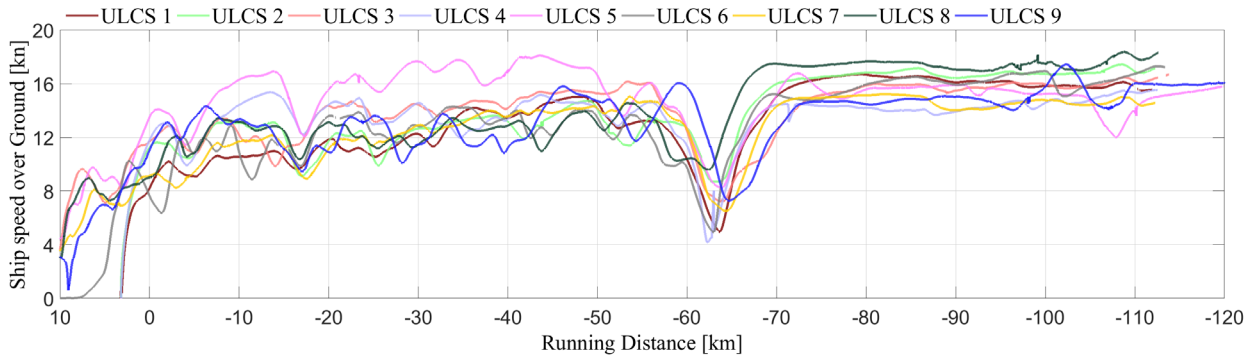

Figure 12. Ship speed over ground during nine voyages

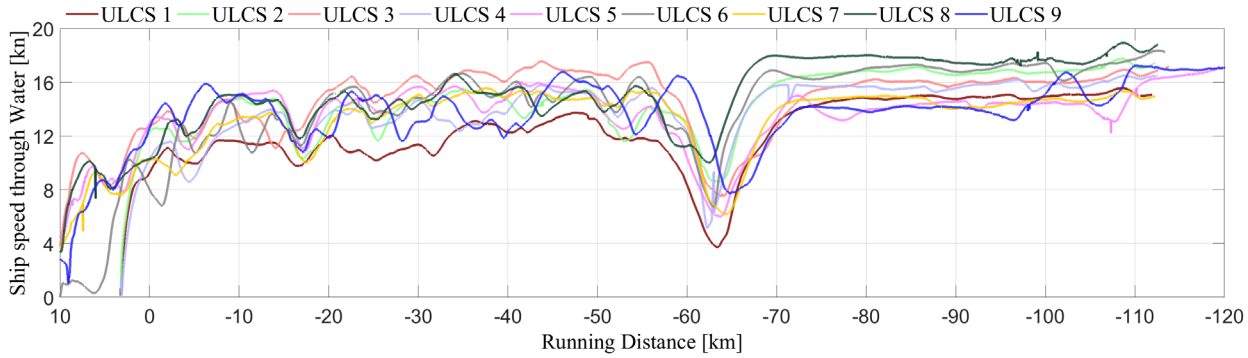

Figure 13. Ship speed through water during nine voyages

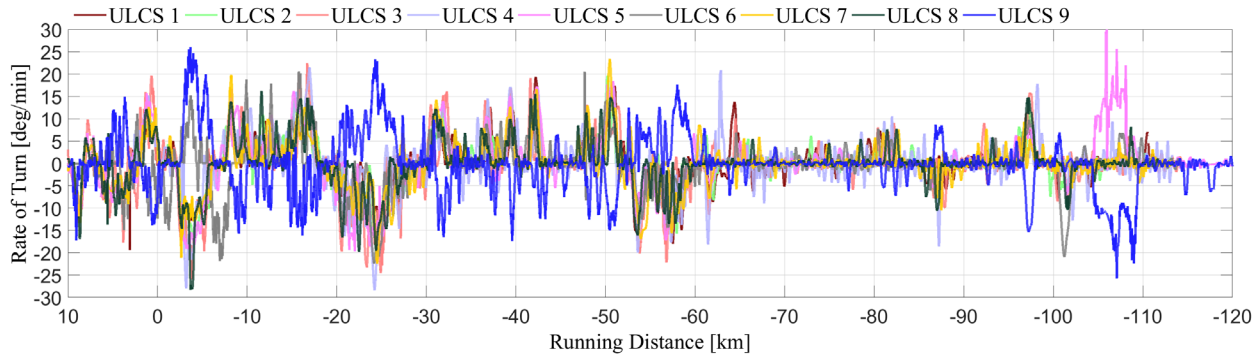

Figure 14. Rate of Turn during nine voyages

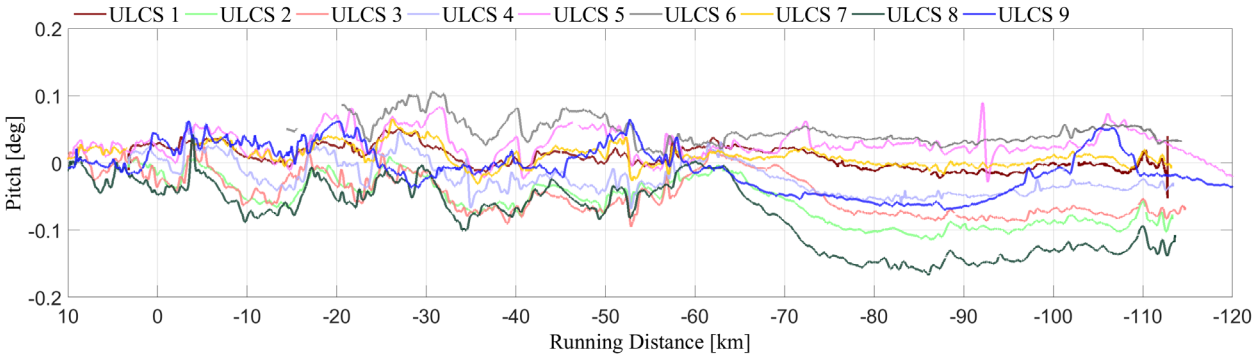

Figure 15. Steady pitch motion (trim) during nine voyages

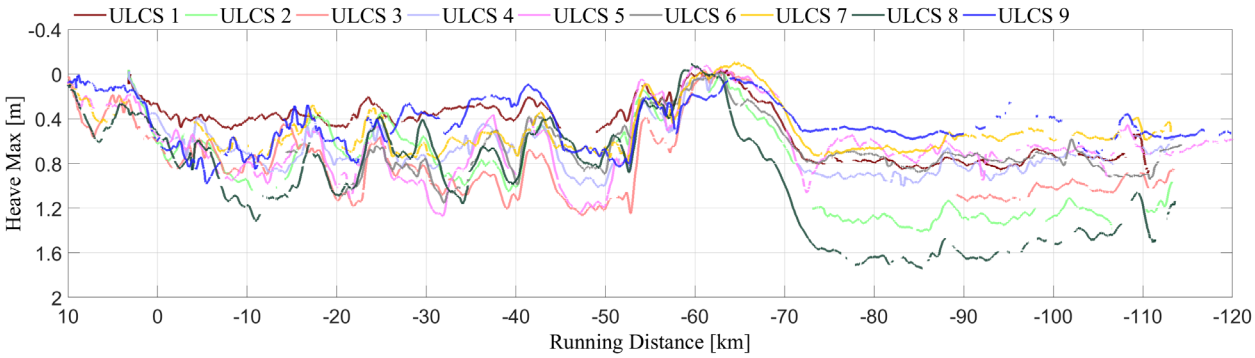

Figure 16. Steady longitudinal sinkage during nine voyages

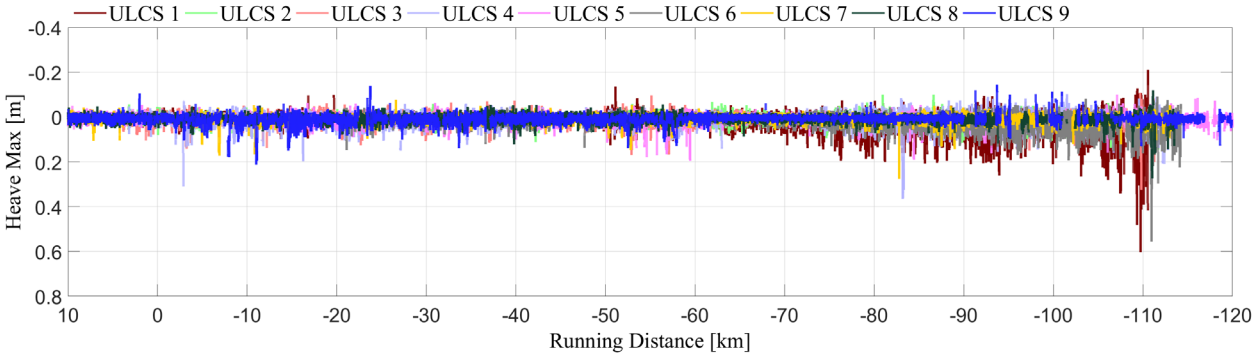

Figure 17. Unsteady longitudinal sinkage during nine voyages

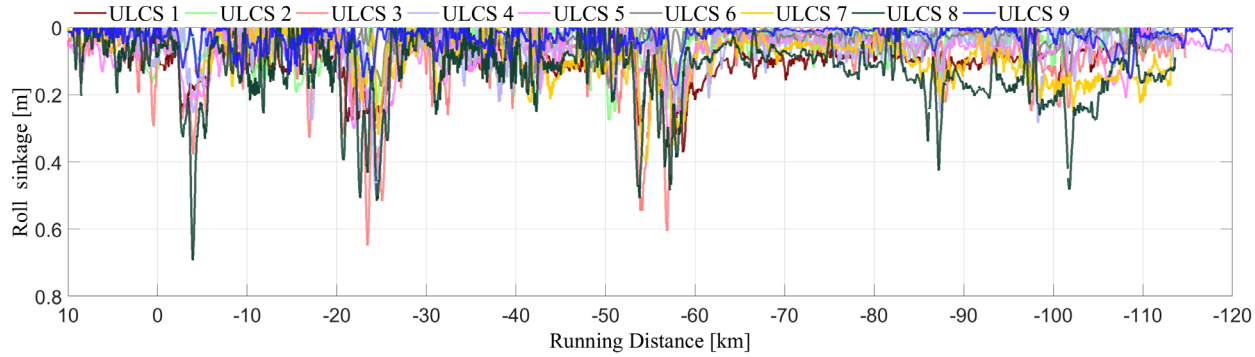

Figure 18. Steady lateral sinkage (heel) during nine voyages

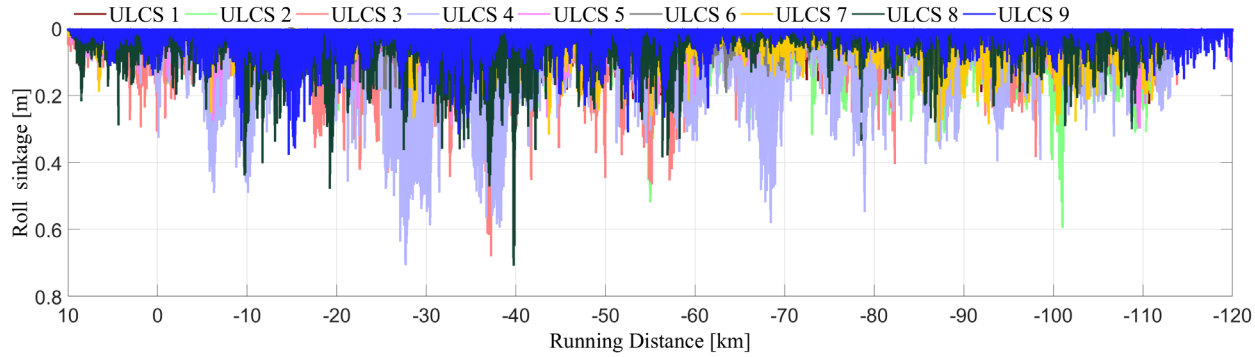

Figure 19. Unsteady lateral sinkage during nine voyages

AN ECONOMICAL ALGORITHM FOR COMPUTATION OF SHIP TO SHIP INTERACTION FORCES IN REAL TIME

Grigory Vilenskiy,
SimTech Ltd, Russia.

AN ECONOMICAL ALGORITHM FOR COMPUTATION OF SHIP TO SHIP INTERACTION FORCES IN REAL TIME

Grigory Vilenskiy, SimTech Ltd, Russia.

SUMMARY

A theoretical method for computation of hydrodynamic forces and moments resulting on a ship's hull due to the presence of one or more other ships moving in its vicinity is presented. The three projections of forces and moments on the vessel's coordinate axes are calculated as functions of ships' instantaneous positions, angular orientations, linear and angular velocities. The algorithm builds upon an integral equation representation of the related potential flow boundary-value problem formulation for N bodies. The second Green's identity is used for this purpose. The problem is then solved by means of a perturbation technique based on the Liouville-Neumann series representation and a slender body theory formalism. As a result, analytical expressions for the forces and moments are recovered up to the second order in the slenderness parameter. These are presented in the form of two- and three-dimensional integrals over the length of the ship, respectively.

NOMENCLATURE

H_i	*i*-th moving body (ship)
$(O, \xi_1', \xi_2', \xi_3')$	Earth-fixed (absolute) coordinate system (without primes, if non-dimensional)
$\left(o^i, x_1^{i\prime}, x_2^{i\prime}, x_3^{i\prime}\right)$	Coordinate system fixed with the body H_i (without primes, if non-dimensional)
$\left\{\vec{I}_j\right\}_{j=1}^3$	Unit vectors of earth fixed coordinate axes
$\left\{\vec{i}_j^{\,i}\right\}_{j=1}^3$	Unit vectors of *i*-th body coordinate vectors
α_{jk}^i	Transformation matrix from *i*-th body frame to the absolute frame.
L_i, B_i, T_i	Length, breadth and trim of *i* - th body
t	Time
$\vec{U}_\infty^i = (U_{\infty 1}^i, U_{\infty 2}^i, U_{\infty 3}^i)$	Velocity of *i* - th body
$\vec{\omega}^i = (\omega_1^i, \omega_2^i, \omega_3^i)$	Angular velocity of *i* - th body
$\left(\beta_1^i, \beta_2^i, \beta_3^i\right)$	Position of the center of *i*-th body frame
p	Fluid pressure
Φ	Flow potential
Φ_o	Approximation of the source term of the flow potential
Φ_1	Approximation of the dipole term of the flow potential
Fn	Typical Froude number
$\varepsilon_3(\vec{x}, \vec{y})$	Minus Green's function of the fluid domain without ships
$\varepsilon^i = \frac{B_i}{L_i}$	Slenderness parameter of *i*-th body
l^i	Non-dimensional length of *i*-th body
a^i	B_i/T_i
∂_x	$\partial/\partial x$
$\vec{n}^i$	Unit normal to *i*-th body (directed out of the fluid)
(u, v)	Parameterization variables of *i*-th body surface used in computation of flow potential $\Phi_o(\vec{x})$
$(\tilde{u}, \tilde{v})$	Parameterization variables of *j*-th body surface used in computation of flow potential $\Phi_1(\vec{x})$
$(\bar{u}, \bar{v})$, (u', v')	Wetted surface parameterization variables used in computation of forces and moments
$2f^j(x, 0)$	Scaled width of the water line of *j*-th body ($x = u, \tilde{u}, \bar{u}$ or u')
S^i	Cross-sectional area of *i*-th body

1 INTRODUCTION

The aim of the present study is twofold. On the one hand, this work was motivated by the demand for a fast computational method of ship interaction forces in real time maneuvering simulators. Although a considerable

body of work currently exists in the technical literature on the subject of ship-to-ship interaction (Pettersen *et al* 2011), construction of an appropriate real time computational algorithm still remains a challenging task.

On the other hand, the author's recent work in the field of automated route control, modelling of tugging operations, *etc*. has brought out the significance of the knowledge of the orders of magnitude of the involved forces and moments and, ideally, their analytical structure for arbitrary relative vessel positions. This was the second motivation for the study presented in what follows.

Owing to the complexity of the involved physical phenomena, a trade-off is required between computational robustness and hydrodynamic effects to be included into the mathematical model. In consequence of these limitations, in this study we choose to discard viscous effects, including all types of flow separation and dynamic stall induced by the interacting hulls. Waves are also neglected. Although these are, no doubt, important physical features of ship interaction, we confine ourselves to a slender body, small Froude number, non-lifting three-dimensional potential flow problem. The reason for this is that such formulation allows for considerable analytical advance in calculation of flow potential and interaction forces and moments on the basis of an appropriate perturbation theory technique. This saves the trouble of a time consuming direct numerical solution of the potential flow problem in three dimensions. Although the resulting formulas look rather cumbersome, they are mainly algebraic in nature and reduce the need for evaluation of complicated surface integrations over wetted hulls to a minimal number of linear integrals over the hulls' lengths.

The effect of finite depth or canal width are known to play an important role in the problem of ship interaction. They can be readily accounted for within the proposed analysis through introduction of an appropriate Green's function (which is equal to $-\varepsilon_3(\vec{x},\vec{y})$ in this paper's notation) into the obtained solution. Since such Green's functions have been well studied in the literature, their expressions are not provided in the paper.

We hasten to note that a very similar problem was theoretically studied in the paper by Tuck & Newman (1974) in the special case of planar motion of two slender ships moving along parallel paths with constant speeds. The proposed study extends the results of Tuck & Newman (1974) to a fully three-dimensional case.

As of now, the potential flow problem considered in this work can be effectively solved numerically by panel methods, see *e.g.*, Pinkster & Bhawsinka (2013), Sutulo *et al* (2012). Recently, Pinkster (2013) extended the panel method to a GPU based computational approach. A wealth of literature on various aspects of the subject of ship interactions, including review articles, can be further found in the Proceedings of the Second International Conference on Ship Maneuvering in Shallow and Confined Water, see Pettersen *et al* (2011).

It is hoped that this analytical study will serve as a useful analytical supplement to the above mentioned numerical works.

2 PROBLEM FORMULATION

2.1 DEFINITION OF COORDINATE SYSTEMS

Consider N rigid bodies $\{H_i\}_{i=0}^{N-1}$ moving on the surface of a heavy incompressible inviscid fluid. Let g be the acceleration due to gravity, ρ – the fluid density.

Introduce an earth-fixed (*i.e.,* absolute) right-handed coordinate system (O,ξ_1',ξ_2',ξ_3'), with the axis $O\xi_3'$ oriented downward, (O,ξ_1',ξ_2') being the plane of the unperturbed free surface, and $\{\vec{I}_j\}_{j=1}^{3}$ - the unit vectors of the related coordinate axes.

Let $(o^i,x_1^{i\prime},x_2^{i\prime},x_3^{i\prime})$ be the coordinate system fixed with the body H_i. Its axis $o^ix_1^{i\prime}$ is directed forward along the ship's plane of symmetry $x_2^{i\prime}=0$, axis $o^ix_2^{i\prime}$ is directed starboard, axis $(o^ix_3^{i\prime})$ - downward. Origin o^i lies in the intersection of the plane of symmetry, the water plane and the middle cross-section of the vessel; $\{\vec{i}_j^{\,i}\}_{j=1}^{3}$ are the unit vectors of the related axes of the i - th body frame.

The equation of the wetted surface of each body H_i (in the unperturbed position) is given in either of the following two alternative forms:

$$\left|x_2^{i\prime}\right| = B_i f^i\left(\frac{x_1^{i\prime}}{L_i},\frac{x_3^{i\prime}}{B_i}\right), \qquad (1.1)$$

or

$$x_3^{i\prime} = B_i h^i\left(\frac{x_1^{i\prime}}{L_i},\frac{x_2^{i\prime}}{B_i}\right). \qquad (1.2)$$

Here $-0.5L_i \le x_1^{i\prime} \le 0.5L_i$, $-0.5B_i \le x_2^{i\prime} \le 0.5B_i$, $0 \le x_3^{i\prime} \le T_i$, L_i, B_i and T_i are the length, the breadth and the trim of the i - th body.

2.2 NONDIMENSIONALIZATION PROCEDURE

Let $\vec{U}_\infty^{i\prime}(t')$ be the velocity vector of the origin o^i , $\vec{\Omega}^i$ – the angular velocity of the body H_i , (u_1',u_2',u_3') - the projections of the fluid velocity vector on the absolute axes (ξ_1',ξ_2',ξ_3'), respectively, t' - the time variable, p' - the fluid pressure, p_a' - the atmospheric pressure. The following nondimensional variables are introduced:

$$t=\frac{t'U_\infty'}{L'},\ \xi_l=\frac{\xi_l'}{L'},\ x_l^i=\frac{x_l^{i\prime}}{L'},\ u_l=\frac{u_l'}{U_\infty'},\ l=1,2,3;$$

$$\vec{U}_\infty^i = \frac{\vec{U}_\infty^{i\prime}}{U_\infty'}, p = \frac{p'-p_a'}{\rho(U_\infty')^2}, \vec{\omega}^i = \frac{\vec{\Omega}^i L'}{U_\infty'}, Fn^{-2} = \frac{gL'}{(U_\infty')^2},$$

Here $i = 0,1,2,3,\cdots,N-1$; L' and U_∞' are some typical nonzero length and velocity, *e.g.*, $L' = L_o$, $U_\infty' = |\vec{U}_\infty^{o\prime}|$. On the introduction of the scaling parameters

$$\varepsilon^i = \frac{B_i}{L_i}, \; l^i = \frac{L_i}{L'}, \; a^i = \frac{B_i}{T_i}, \qquad (2.1)$$

equations (1.1) and (1.2) can be rewritten as

$$|x_2^i| = \varepsilon^i l^i f^i\left(\frac{x_1^i}{l^i}, \frac{x_3^i}{\varepsilon^i l^i}\right), \qquad (2.2)$$

$$x_3^i = \varepsilon^i \, l^i h^i\left(\frac{x_1^i}{l^i}, \frac{x_2^i}{\varepsilon^i l^i}\right). \qquad (2.3)$$

Here $-0.5\, l^i \le x_1^i \le 0.5\, l^i$, $-0.5\varepsilon^i \, l^i \le x_2^i \le 0.5\varepsilon^i \, l^i$, $0 \le x_3^{i'} \le \varepsilon^i \, l^i/a^i$. It is assumed in what follows that all H_i are slender bodies, that is,

$$\varepsilon^i \ll 1, \; l^i = O(1), a^i = O(1), \; i = 0,1,2,3,\cdots,N-1.$$

3 GOVERNING EQUATIONS

Introduce the velocity potential Φ:

$$\partial_{\xi_1}\Phi = u_1, \partial_{\xi_2}\Phi = u_2, \partial_{\xi_3}\Phi = u_3.$$

It satisfies the Laplace equation and the condition of no perturbations at infinity, since the fluid is at rest there:

$$\nabla^2\Phi = 0, \qquad (3.1)$$

$$|\nabla\Phi| \to 0 \text{ as } \sum_{l=1}^3 \xi_l^2 \to \infty. \qquad (3.2)$$

Its normal derivative is equal to the normal velocity of the body on the wetted surface

$$\partial_{n_i}\Phi(A) = v_n(A). \qquad (3.3)$$

Here A is a point on the i - th wetted surface, $\vec{n}^i$ is the unit normal at A , assumed to be directed out of the fluid.

On the free surface $\xi_3 = \zeta(t,\xi_1,\xi_2)$ the dynamic and the kinematic boundary condition are satisfied:

$$p = 0, \;\; \partial_t\zeta + \partial_{\xi_1}\Phi\partial_{\xi_1}\zeta + \partial_{\xi_2}\Phi\partial_{\xi_2}\zeta - \partial_{\xi_3}\Phi = 0.$$

On the vertical walls $\xi_2 = \eta_r$, $\xi_2 = \eta_l$ and on the flat bottom $\xi_3 = h$ (if present) the normal velocity is zero:

$$\partial_{\xi_2}\Phi(\xi_2 = \eta_r, \eta_l) = \partial_{\xi_3}\Phi(\xi_3 = h) = 0. \qquad (3.4)$$

The pressure is given by the Lagrange – Cauchy integral

$$p + \partial_t\Phi + 0.5(\nabla\Phi)^2 - Fn^{-2}\xi_3 = const(t).$$

The fluid is at rest at $t = 0$, that is, $\nabla\Phi = \zeta = 0$.

3.1 LINEARIZED PROBLEM

In addition to slenderness, we postulate that, with the exception of certain singular regions such as vicinities of bows and sterns, perturbations of pressure, fluid velocities and the free surface are small. Their products can then be discarded in the free surface boundary conditions, and these are reduced to one equation

$$\partial_{tt}\Phi - Fn^{-2}\partial_{\xi_3}\Phi = 0,$$

The pressure and the free surface elevation are given by the following well known formulas:

$$p = Fn^{-2}\xi_3 - \partial_t\Phi, \zeta = Fn^2\partial_t\Phi.$$

3.2 SMALL FROUDE NUMBER LIMIT

The finally, assume that the Froude number is small ($Fn \to 0$). In this case the free surface condition further reduced to that of a flat rigid wall:

$$\partial_{\xi_3}\Phi(\xi_3 = 0) = 0, \qquad (3.5)$$

with (3.1)-(3.5) being the resulting governing system of equations.

3.3 THE MAIN SINGULAR SOLUTION

Consider now the fluid domain of the problem (3.1)-(3.5) in the absence of floating bodies H_i. Following Vladimirov (1984), define the main singular solution for the resulting domain as a function $\varepsilon_3(\vec{x},\vec{y})$ which satisfies homogeneous boundary conditions on the remaining boundaries of the domain and the equation

$$\nabla^2\varepsilon_3(\vec{x},\vec{y}) = \delta(\vec{x}-\vec{y})$$

inside it. Here differentiation is carried out with respect to the coordinates of the point $\vec{y} = (\eta_1,\eta_2,\eta_3)$, with the point $\vec{x} = (\xi_1,\xi_2,\xi_3)$ being a parameter; δ is Dirac's delta function. It can be inferred from the above definition that $\varepsilon_3(\vec{x},\vec{y})$ is equal to minus Green's function for the described fluid domain (with no floating bodies inside). For instance, for an infinite depth open sea $\varepsilon_3(\vec{x},\vec{y}) = -(R^{-1} + \bar{R}^{-1})/(4\pi)$, where $R = |\vec{x}-\vec{y}|$, $\bar{R} = |\vec{x}-\vec{y}^*|, \vec{y}^* = (\eta_1,\eta_2,-\eta_3)$. Because methods of its construction are well documented in the literature, see *e.g.* Vladimirov (1984), function $\varepsilon_3(\vec{x},\vec{y})$ is assumed known in what follows. The subscript 3 in this function has been introduced as a reminder that the spatial, rather than planar problem, is to be considered here.

3.4 THE SECOND GREEN'S IDENTITY

The second Green's identity for the functions Φ and $\varepsilon_3(\vec{x},\vec{y})$ has the following form:

$$\Phi(\vec{x}) = \sum_{i=0}^{N-1} \iint_{H_i} \left\{ \Phi(\vec{y}) \partial_{n_y} \varepsilon_3(\vec{x},\vec{y}) - \varepsilon_3(\vec{x},\vec{y}) \partial_{n_y} \Phi(\vec{y}) \right\} dS_y \quad (3.6)$$

The subscript y here is used to signify the fact that the normal derivatives and surface integrations are performed with respect to the variable $\vec{y}$.

The solution to the problem (3.1)-(3.5) can be built in a form of a perturbation series expansion in the slenderness parameters ε^i. One way to generate this expansion is to construct the Neumann series for equation (3.6), starting by some initial approximation $\Phi = \Phi_o(\vec{x})$ and to develop the successive terms iteratively:

$$\Phi_{n+1}(\vec{x}) = \sum_{i=0}^{N-1} \iint_{H_i} \left\{ \Phi_n(\vec{y}) \partial_{n_y} \varepsilon_3(\vec{x},\vec{y}) - \varepsilon_3(\vec{x},\vec{y}) \partial_{n_y} \Phi_n(\vec{y}) \right\} dS_y, \quad n = 0,1,2,3, \ldots$$

Since by virtue of (3.3) $\partial_{n_i}\Phi$ is a known function, we define $\Phi_o(\vec{x})$ as follows:

$$\Phi_o(\vec{x}) = -\sum_{i=0}^{N-1} \iint_{H_i} \varepsilon_3(\vec{x},\vec{y}) v_n(\vec{y}) dS_y. \quad (3.7)$$

Then

$$\Phi_1(\vec{x}) = \sum_{i=0}^{N-1} \iint_{H_i} \left\{ \Phi_o(\vec{y}) \partial_{n_y} \varepsilon_3(\vec{x},\vec{y}) - \varepsilon_3(\vec{x},\vec{y}) \partial_{n_y} \Phi_o(\vec{y}) \right\} dS_y, \quad (3.8)$$

etc. In what follows, we restrict ourselves to the asymptotic expansion up to the second order in ε^i, assuming that all ε^i are of the same order of magnitude. The terms, whose order is higher than $(\varepsilon^i)^2$ are discarded.

4 COORDINATE TRANSFORMATIONS

It is noteworthy that the integration surfaces in (3.6) are functions of time, since the vessels H_i are assumed to be moving through the fluid. Thus, evaluation of integrals (3.7) & (3.8) requires the knowledge of transformation formulas between absolute and body coordinates.

4.1 BODY KINEMATICS

Let $\vec{r}_A(t) = (\xi_1^i, \xi_2^i, \xi_3^i)$ be the absolute coordinates of a point A of the surface H_i, $\vec{r}_o^i(t) = (\xi_1^{oi}, \xi_2^{oi}, \xi_3^{oi})$ be the absolute coordinates of the origin of the i – th body frame, and $\vec{r}^i = (x_1^i, x_2^i, x_3^i)$ – the coordinates of A relative to the frame of reference of the i – th body. Obviously,

$$\vec{r}_A = \vec{r}_o^i + \vec{r}^i, \qquad \frac{d\vec{r}_o^i}{dt} = \vec{U}_\infty^i, \qquad \frac{d\vec{r}_A}{dt} = \vec{U}_\infty^i + \vec{\omega}^i \times \vec{r}^i,$$

where $\vec{U}_\infty^i = (U_{\infty 1}^i, U_{\infty 2}^i, U_{\infty 3}^i)$. After some algebra these equations yield the relationship

$$\begin{pmatrix} \xi_1^i \\ \xi_2^i \\ \xi_3^i \end{pmatrix} = \begin{pmatrix} \beta_1^i \\ \beta_2^i \\ \beta_3^i \end{pmatrix} + \begin{pmatrix} \alpha_{11}^i & \alpha_{12}^i & \alpha_{13}^i \\ \alpha_{21}^i & \alpha_{22}^i & \alpha_{23}^i \\ \alpha_{31}^i & \alpha_{32}^i & \alpha_{33}^i \end{pmatrix} \begin{pmatrix} x_1^i \\ x_2^i \\ x_3^i \end{pmatrix}, \quad (4.1)$$

here

$$\beta_j^i = \xi_j^i(0) + \int_0^t U_{\infty j}^i \, dt,$$

$$\alpha_{jk}^i = \vec{I}_j \cdot \vec{\imath}_k^i = \cos\left(\widehat{\vec{I}_j \vec{\imath}_k^i}\right), \; j,k = 1,2,3$$

is the transformation matrix from the body fixed to the absolute frame: $\vec{I}_j = \sum_{k=1}^3 \alpha_{jk}^i \vec{\imath}_k^i$. Its transpose defines the inverse transformation: $\vec{\imath}_j^i = \sum_{k=1}^3 \alpha_{kj}^i \vec{I}_k^i$. Its rows (columns) are orthogonal vectors. We note in passing, that the following well known formulas hold for the derivatives of the unit vectors $\{\vec{\imath}_j^i\}_{j=1}^3$:

$$\frac{d\vec{\imath}_1^i}{dt} = \omega_3^i \vec{\imath}_2^i - \omega_2^i \vec{\imath}_3^i,$$
$$\frac{d\vec{\imath}_2^i}{dt} = \omega_1^i \vec{\imath}_3^i - \omega_3^i \vec{\imath}_1^i,$$
$$\frac{d\vec{\imath}_3^i}{dt} = \omega_2^i \vec{\imath}_1^i - \omega_1^i \vec{\imath}_2^i.$$

4.2 DIFFERENTIAL GEOMETRY OF THE HULL

In agreement with formulas (3.7) & (3.8), we need to be able to evaluate surface integrals of the following type:

$$I^i = \iint_{H_i} \varphi(\vec{y}) (\vec{n}^i \cdot \vec{\psi}) dS_y,$$

where φ and $\vec{\psi} = (\psi_1, \psi_2, \psi_3)$ are some known functions.

Let $\vec{y} = (\xi_1^i, \xi_2^i, \xi_3^i)$ denote a point of the surface H_i, and assume that H_i is given in a parametric form $\vec{y} = \vec{y}(u,v)$. Then, as is known (Korn & Korn 1973),

$$\vec{n}^i = -\frac{\vec{a}^i}{|\vec{a}^i|}, \qquad dS = |\vec{a}^i| \, du dv, \qquad \vec{a}^i = \sum_{l=1}^3 a_l^i \vec{I}_l,$$

$$a_1^i = \begin{vmatrix} \xi_{2u}^i & \xi_{2v}^i \\ \xi_{3u}^i & \xi_{3v}^i \end{vmatrix}, a_2^i = \begin{vmatrix} \xi_{3u}^i & \xi_{3v}^i \\ \xi_{1u}^i & \xi_{1v}^i \end{vmatrix}, a_3^i = \begin{vmatrix} \xi_{1u}^i & \xi_{1v}^i \\ \xi_{2u}^i & \xi_{2v}^i \end{vmatrix}.$$

Here and in what follows subscripts u and v stand for the derivatives with respect to the corresponding parametric variables, whose order must be chosen so that the correct direction of $\vec{n}^i$ is insured. Integral I^i then takes the form:

$$I^i = -\iint\limits_{D^i} \varphi(\vec{y})\left(\sum_{n=1}^{3} a_n^i \psi_n\right) du dv\,. \qquad (4.2)$$

D^i is the domain in the plane of parametric variables (u, v) used to define the surface H_i. In case of (2.3) this parametric representation is

$$x_1^i = l^i u,\ x_2^i = \varepsilon^i\, l^i v,\ x_3^i = \varepsilon^i\, l^i h^i(u, v\,), \qquad (4.3)$$

where $|u| \le 0.5,\ |v| \le 0.5, 0 \le x_3^i \le \varepsilon^i\, l^i/a^i$.

According to (4.1),

$$\tilde{\xi}_l^i = \beta_l^i + \alpha_{l1}^i\, l^i u + \varepsilon^i\, l^i\{\alpha_{l2}^i v + \alpha_{l3}^i h^i(u, v\,)\}, l = 1,2,3.$$

This results in the following explicit formulas for a_l^i :

$$a_l^i(u, v) = \varepsilon^i(\, l^i)^2\{w_{l1}^i + w_{l2}^i h_v^i + \varepsilon^i w_{l3}^i h_u^i\}\,, l = 1,2,3.$$

$$w_{11}^i = \begin{vmatrix} \alpha_{21}^i & \alpha_{22}^i \\ \alpha_{31}^i & \alpha_{32}^i \end{vmatrix}, w_{12}^i = \begin{vmatrix} \alpha_{21}^i & \alpha_{31}^i \\ \alpha_{32}^i & \alpha_{33}^i \end{vmatrix},$$

$$w_{13}^i = \begin{vmatrix} \alpha_{23}^i & \alpha_{33}^i \\ \alpha_{22}^i & \alpha_{32}^i \end{vmatrix},$$

$$w_{21}^i = -\begin{vmatrix} \alpha_{11}^i & \alpha_{12}^i \\ \alpha_{31}^i & \alpha_{32}^i \end{vmatrix}, w_{22}^i = -\begin{vmatrix} \alpha_{11}^i & \alpha_{13}^i \\ \alpha_{31}^i & \alpha_{33}^i \end{vmatrix},$$

$$w_{23}^i = -\begin{vmatrix} \alpha_{13}^i & \alpha_{33}^i \\ \alpha_{12}^i & \alpha_{32}^i \end{vmatrix},$$

$$w_{31}^i = \begin{vmatrix} \alpha_{11}^i & \alpha_{12}^i \\ \alpha_{21}^i & \alpha_{22}^i \end{vmatrix}, w_{32}^i = \begin{vmatrix} \alpha_{11}^i & \alpha_{13}^i \\ \alpha_{21}^i & \alpha_{23}^i \end{vmatrix},$$

$$w_{33}^i = \begin{vmatrix} \alpha_{13}^i & \alpha_{23}^i \\ \alpha_{12}^i & \alpha_{22}^i \end{vmatrix}\,.$$

Finally, equation (4.2) can be rewritten as follows

$$I^i = -\int_{-0.5}^{0.5} du \int_{-f^i(u,0)}^{f^i(u,0)} \varphi(\vec{y})\left(\sum_{n=1}^{3} a_n^i \psi_n\right) dv. \quad (4.4)$$

Here $f^i(u, 0) = f^i(u, v = 0)$ is the water line equation of the i – th body; note, that $0 \le f^i(u, 0) \le 0.5$.

5 ASYMPTOTICS OF VELOCITY POTENTIAL

5.1 SOURCE TERM, INTEGRAL (3.7)

In this case $\Phi_o(\vec{x}) = -\sum_{i=0}^{N-1} I_s^i$, where

$$I_s^i = \sum_{i=0}^{N-1} \iint\limits_{H_i} \varepsilon_3(\vec{x}, \vec{y}) v_n(\vec{y}) dS_y$$

We set $\varphi = \varepsilon_3(\vec{x}, \vec{y})$, $\vec{\psi} = \vec{U}_\infty^i + \vec{\omega}^i \times \vec{r}^i$ in (4.4), and, thus, need to calculate the expansions of the scalar product $\overrightarrow{\psi \cdot} \vec{a}^i$ and $\varepsilon_3(\vec{x}, \vec{y})$ up to the second order in ε^i. After simple, but considerable algebra we get the required slender body expansion of the source part of the velocity potential

$$I_s^i(\vec{x}, t) = -\varepsilon^i(\, l^i)^2 \int_{-0.5}^{0.5} \varepsilon_3\left(\vec{x}, \vec{y}_o^i(t)\right) \gamma^i(u, t) + \varepsilon^i\, l^i \sum_{m=1}^{3} \left(\nabla_y\, \varepsilon_3\left(\vec{x}, \vec{y}_o^i(t)\right)\right)_m \kappa_m^i(u, t)\, du. \quad (5.1)$$

$$\gamma^i(u, t) = \sum_{l=1}^{3}\left[\psi_l^o w_{l1}^i 2 f^i(u, 0) + \varepsilon^i\left(\psi_l^o w_{l3}^i \frac{dS^i}{du} + l^i S^i\left\{\left(\omega_2^i \alpha_{l1}^i - \omega_1^i \alpha_{l2}^i\right) w_{l1}^i - \left(\omega_1^i \alpha_{l3}^i - \omega_3^i \alpha_{l1}^i\right) w_{l2}^i\right\}\right)\right],$$

$$\kappa_m^i(u, t) = \sum_{l=1}^{3} \psi_l^o S^i\left(w_{l1}^i \alpha_{m3}^i - w_{l2}^i \alpha_{m2}^i\right).$$

Here

$$S^i = \int_{-f^i(u,0)}^{f^i(u,0)} h^i(u, v\,)\, dv$$

is the scaled cross-sectional area,

$$\psi_l^o \equiv \psi_l^o(u, t) = U_{\infty l}^i + \left(\omega_3^i \alpha_{l2}^i - \omega_2^i \alpha_{l3}^i\right) l^i u;$$

$$\vec{y}_o^i(t) \equiv \vec{y}(\varepsilon^i = 0, t),$$
$$y_l^i(\varepsilon^i = 0, t) = \beta_l^i(t) + \alpha_{l1}^i(t)\, l^i u, l = 1,2,3;$$

$$\left(\nabla_y\, \varepsilon_3\left(\vec{x}, \vec{y}_o^i(t)\right)\right)_l = \frac{\partial \varepsilon_3(\vec{x}, \vec{y})}{\partial \tilde{\xi}_l^i} \text{ at } \vec{y} = \vec{y}_o^i(t).$$

The major advantage of formula (5.1) over the original expression (3.7) is that it replaces the problem of surface integration over H_i with that of the calculation of a single one-dimensional integral over the longitudinal axis.

5.2 DIPOLE TERM IN INTEGRAL (3.8)

Consider the expression $\Delta\Phi_1(\vec{x}) = \Phi_1(\vec{x}) - \Phi_o(\vec{x})$, or,

$$\Delta\Phi_1(\vec{x}) = \sum_{j=0}^{N-1} I_d^j,\ I_d^j = \iint\limits_{H_j} \Phi_o(\vec{y}) \partial_{n_y} \varepsilon_3(\vec{x}, \vec{y}) dS_y.$$

Here I_d^j is the sum of all dipoles distributed over the hull H_j.

To calculate I_d^j , we substitute the superscript i with j and let $\varphi = \Phi_o(\vec{y})$, $\vec{\psi} = \nabla\varepsilon_3(\vec{x}, \vec{y})$ in formula (4.4). After some algebra, this yields the leading order solution

$$I_d^j = \sum_{i=0}^{N-1} I_d^{ji}(\vec{x}, t),$$

where

$$I_d^{ji}(\vec{x}, t) = \varepsilon^j (\, l^j)^2 \varepsilon^i (\, l^i)^2 \sum_{m=1}^{3} w_{m1}^j \sum_{l=1}^{3} w_{l1}^i \int_{-0.5}^{0.5} d\tilde{u}\; 2 f^j(\tilde{u}, 0) \cdot \frac{\partial \varepsilon_3\left(\vec{x}, \vec{z}_o^i(t)\right)}{\partial \tilde{\zeta}_m^j} \int_{-0.5}^{0.5} du\; 2\, f^i(u, 0)\, \psi_l^o\, \varepsilon_3\left(\vec{z}_o^i(t), \vec{y}_o^i(t)\right), \tag{5.2}$$

Here $\vec{z}_o^i(\tilde{u}, t) = \left(\tilde{\zeta}_1^j, \tilde{\zeta}_2^j, \tilde{\zeta}_3^j\right)$, $\tilde{\zeta}_m^j = \beta_m^j + \alpha_{m1}^j\, l^j \tilde{u},\ m = 1,2,3;$ $\vec{y}_o^i(u, t) = \left(\tilde{\eta}_1^i, \tilde{\eta}_2^i, \tilde{\eta}_3^i\right),$ $\tilde{\eta}_l^i = \beta_l^i + \alpha_{l1}^i\, l^i u,\ l = 1,2,3;$

Note, that when calculating interaction forces acting on the k –th body, the 'self-induced' potential I_d^k which results from the distribution of dipoles over its own hull H_k must be excluded from the operation of summation in j in the formula for $\Delta\Phi_1(\vec{x})$.

6 INTERACTION FORCES AND MOMENTS

In principle, all interaction forces and moments can be computed numerically on the basis of formulas (5.1) & (5.2). The advantage of this approach is in that the squares of the velocities in the Lagrange – Cauchy integral can be systematically taken into account, which is a difficult analytical exercise. Yet, in real time computations it is often desirable to have explicit analytical approximations for the forces and moments, in order to further expedite the computational procedure. In what follows we derive such formulas, although at the cost of neglecting the squares of the fluid velocities and retaining only the unsteady term in the formula for the pressure. This reduces the accuracy of the obtained approximations to the leading order only. However, in what follows we choose to retain the second order terms in expansions (5.1) and (5.2) as we hope to recover the input from the inertia terms due to the squares of the fluid velocity $0.5(\nabla\Phi)^2$ in the future work. Besides, the expressions for forces and moments obtained under this simplifying assumption, give an important estimate of the role of the unsteadiness effect caused by the term $-\partial_t\Phi$ of the Lagrange – Cauchy integral in the ship interaction phenomenon.

6.1 INPUT OF THE SOURCE TERM (3.7)

Consider the leading order part of the pressure due to the source term $\Phi_o(\vec{x})$

$p = -\partial_t\Phi_o = \sum_{i=0}^{N-1} p_s^i$, where $p_s^i = -\partial_t I_s^i(\vec{x}, t)$.

The corresponding total force and moment acting on the j – th hull owing to the source term Φ_o are as follows:

$$\vec{R}_{\text{total}}^j = \iint_{H_j} p\vec{n}^j dS_x\ ,\ \vec{L}_{\text{total}}^j = \iint_{H_j} p(\vec{r}^j \times \vec{n}^j) dS_x.$$

Since the unit normal $\vec{n}$ is directed out of the fluid, the sign before these integrals is positive; $\vec{r}^j = \vec{x} - \vec{r}_o^j$ is the position vector of an integration point $\vec{x}$ on the hull's surface in the body frame; $\vec{x}$ and $\vec{r}_o^j$ are the absolute coordinates of the integration point and the origin of the body system. Thus, the moment $\vec{L}^j$ is calculated relative to the point $\vec{r}_o^j$. The interaction part of force and moment is

$$\begin{pmatrix} \vec{R}^j \\ \vec{L}^j \end{pmatrix} = -\sum_{\substack{i=0,\\ i\neq j}}^{N-1} \iint_{H_j} \partial_t I_s^i(\vec{x}, t) \begin{pmatrix} \vec{n}^j \\ (\vec{r}^j \times \vec{n}^j) \end{pmatrix} dS_x\,.$$

Although here $\vec{x}$ is a function of t, $\vec{x} = \vec{x}(t)$, the operator ∂_t does not operate on $\vec{x}(t)$. To stress this fact, write

$$\begin{pmatrix} \vec{F}_{ji}(t, \tau) \\ \vec{M}_{ji}(t, \tau) \end{pmatrix} = -\iint_{H_j} I_s^i(\vec{x}, \tau) \begin{pmatrix} \vec{n}^j \\ (\vec{r}^j \times \vec{n}^j) \end{pmatrix} dS_x, \tag{6.1}$$

so that

$$\begin{pmatrix} \vec{R}^j \\ \vec{L}^j \end{pmatrix} = \sum_{\substack{i=0,\\ i\neq j}}^{N-1} \begin{pmatrix} \partial_\tau \vec{F}_{ji}(t, \tau) \\ \partial_\tau \vec{M}_{ji}(t, \tau) \end{pmatrix}, \text{ when } \tau = t. \tag{6.2}$$

In view of (5.1), evaluation of functions $\vec{F}_{ji}(t, \tau)$ and $\vec{M}_{ji}(t, \tau)$ requires the knowledge of the quantities $(i \neq j)$:

$$\begin{pmatrix} I_{ji}^{\uparrow} \\ I_{ji}^{\downarrow} \end{pmatrix} = -\iint_{H_j} \varepsilon_3\left(\vec{x}, \vec{y}_o^i(\tau)\right) \begin{pmatrix} \vec{n}^j \\ \vec{r}^j \times \vec{n}^j \end{pmatrix} dS_x,$$

$$\begin{pmatrix} I_{jim}^{\uparrow} \\ I_{jim}^{\downarrow} \end{pmatrix} = -\iint_{H_j} \left(\nabla_y\, \varepsilon_3\left(\vec{x}, \vec{y}_o^i(\tau)\right) \right)_m \begin{pmatrix} \vec{n}^j \\ \vec{r}^j \times \vec{n}^j \end{pmatrix} dS_x.$$

Calculation of these integrals can be performed along the same lines as those of the source term (3.7), *i.e.*, through the employment of parameterization (4.3) of section (4.2), which we now designate as $(\bar{u}, \bar{v})$, and subsequently taking the limit in the slenderness parameters ε^i. Owing to shortage of available space and formidable algebraic complexity of this procedure, the derivation details are omitted here and only the final result is presented:

$$\begin{pmatrix} \vec{F}_{ji}(t, \tau) \\ \vec{M}_{ji}(t, \tau) \end{pmatrix} = -\varepsilon^j \varepsilon^i (\, l^j\, l^i)^2 \int_{-0.5}^{0.5} \gamma^i(u, \tau) \int_{-0.5}^{0.5} \varepsilon_3\left(\vec{x}_o^j(t), \vec{y}_o^i(\tau)\right) \vec{A}_j^{\uparrow\downarrow}$$

$$+\varepsilon^j\, l^j \sum_{\nu=1}^{3} \frac{\partial \varepsilon_3\left(\vec{x}_o^{\,j}(t), \vec{y}_o^{\,i}(\tau)\right)}{\partial \tilde{\eta}_\nu^j}\, \vec{B}_{j\nu}^{\uparrow\downarrow}$$

$$+\varepsilon^i\, l^i \sum_{m=1}^{3} \kappa_m^i(u,t)\left(\nabla_y\, \varepsilon_3\left(\vec{x}_o^{\,j}(t), \vec{y}_o^{\,i}(\tau)\right)\right)_m \vec{A}_{jm}^{\uparrow\downarrow} d\bar{u}du. \quad (6.3)$$

Here $\vec{x}_o^{\,j}(t) = \left(\tilde{\eta}_1^j, \tilde{\eta}_2^j, \tilde{\eta}_3^j\right),\ \tilde{\eta}_\nu^j = \beta_\nu^j + \alpha_{\nu 1}^j\, l^j \bar{u}, \nu = 1,2,3;$

$\vec{A}_j^{\uparrow}(\bar{u},\tau) = \sum_{k=1}^{3} \vec{I}_k \left\{2f^j(\bar{u},0) w_{k1}^j + \varepsilon^j w_{k3}^j \frac{dS^j}{d\bar{u}}\right\},$
$\vec{B}_{j\nu}^{\uparrow}(\bar{u},\tau) = \sum_{k=1}^{3} \vec{I}_k S^j(\bar{u}) \left(\alpha_{\nu 3}^j w_{k1}^j - \alpha_{\nu 2}^j w_{k2}^j\right),$

$\vec{A}_j^{\downarrow}(\bar{u},\tau) = l^j \sum_{k=1}^{3} \vec{I}_k \{\left(\alpha_{k_+1}^j w_{k_-1}^j - \alpha_{k_-1}^j w_{k_+1}^j\right) 2\bar{u} f^j(\bar{u},0) + \varepsilon^j \left[\left(\alpha_{k_+1}^j w_{k_-3}^j - \alpha_{k_-1}^j w_{k_+3}^j\right)\bar{u}\frac{dS^j}{d\bar{u}} - \left(\alpha_{k_+2}^j w_{k_-2}^j - \alpha_{k_-2}^j w_{k_+2}^j\right) S^j(\bar{u}) + \left(\alpha_{k_+3}^j w_{k_-1}^j - \alpha_{k_-3}^j w_{k_+1}^j\right) S^j(\bar{u})\right]\},$

$\vec{B}_{j\nu}^{\downarrow}(\bar{u},\tau) = l^j \sum_{k=1}^{3} \vec{I}_k \bar{u} S^j(\bar{u}) \{-\alpha_{\nu 2}^j \left(\alpha_{k_+1}^j w_{k_-2}^j - \alpha_{k_-1}^j w_{k_+2}^j\right) + \alpha_{\nu 3}^j \left(\alpha_{k_+1}^j w_{k_-1}^j - \alpha_{k_-1}^j w_{k_+1}^j\right)\},$

$\vec{A}_{jm}^{\uparrow}(\bar{u},\tau) = \sum_{k=1}^{3} \vec{I}_k 2f^j(\bar{u},0) w_{k1}^j,$

$\vec{A}_{jm}^{\downarrow}(\bar{u},\tau) = l^j \sum_{k=1}^{3} \vec{I}_k \left(\alpha_{k_+1}^j w_{k_-1}^j - \alpha_{k_-1}^j w_{k_+1}^j\right) 2\bar{u} f^j(\bar{u},0),$

$k_+ = (k+1) - 3\Delta_3^k,\ k_- = (k-1) + 3\Delta_1^k,$
$\Delta_l^k = \begin{cases} 1, k = l \\ 0, k \neq l \end{cases}, k, l = 1,2,3.$

In the above formulas, the upward arrow ↑ corresponds to vector $\vec{F}_{ji}$, whereas the downward arrow ↓ corresponds to $\overrightarrow{M}_{ji}$. Formulas (6.2), (6.3) give the required interaction forces due to the flow induced by the source term (3.7). Their major computational advantage is in that only one integral over a unit square needs to be numerically evaluated in place of a four dimensional integral over a Cartesian product of surfaces $H_i \times H_j$.

6.2 INPUT OF THE DIPOLE TERM (3.8)

Consider now the pressure term Δp_1 due to the dipole potential $\Delta\Phi_1(\vec{x})$. To leading order,

$$\Delta p_1 = -\partial_t \Delta\Phi_1 = -\sum_{j=0}^{N-1} \partial_t I_d^j = -\sum_{j=0}^{N-1}\sum_{i=0}^{N-1} \partial_t I_d^{ji}(\vec{x},t).$$

The corresponding increment of the total force and moment acting on the k – th hull are

$$\Delta\vec{R}_{\text{total}}^k = \iint_{H_k} p\vec{n}^k dS_x\ ,\ \Delta\vec{L}_{\text{total}}^k = \iint_{H_k} p(\vec{r}^{\,k} \times \vec{n}^k) dS_x.$$

The related ship interaction part of these expressions is

$$\begin{pmatrix}\Delta\vec{R}^k \\ \Delta\vec{L}^k\end{pmatrix} = -\sum_{\substack{j=0 \\ j\neq k}}^{N-1}\sum_{i=0}^{N-1} \iint_{H_k} \partial_t I_d^{ji}(\vec{x},t) \begin{pmatrix}\vec{n}^k \\ (\vec{r}^{\,k} \times \vec{n}^k)\end{pmatrix} dS_x\ .$$

Thus, we need to calculate the integrals

$$\begin{pmatrix}\Delta I_{kji}^{\uparrow} \\ \Delta I_{kji}^{\downarrow}\end{pmatrix} = \iint_{H_k} I_d^{ji}(\vec{x},\tau) \begin{pmatrix}\vec{n}^k(t) \\ (\vec{r}^{\,k} \times \vec{n}^k)(t)\end{pmatrix} dS_x,$$

since

$$\begin{pmatrix}\Delta\vec{R}^k \\ \Delta\vec{L}^k\end{pmatrix} = -\sum_{\substack{j=0 \\ j\neq k}}^{N-1}\sum_{i=0}^{N-1} \partial_\tau \begin{pmatrix}\Delta I_{kji}^{\uparrow} \\ \Delta I_{kji}^{\downarrow}\end{pmatrix}, \text{when } \tau = t. \quad (6.4)$$

By analogy with the previous parameterizations (u, v) and $(\bar{u}, \bar{v})$, introduce one more parameterization (4.3) which is now denoted by (u', v'). It is to be used to calculate the integrals $\Delta I_{kji}^{\uparrow\downarrow}$:

$$\Delta I_{kji}^{\uparrow\downarrow} = \varepsilon^k (l^k)^2 \sum_{\nu=1}^{3} \vec{I}_\nu \int_{-0.5}^{0.5} I_d^{ji}(\vec{x}_o^{\,k}(t),\tau) \cdot 2f^k(u',0) \times \begin{Bmatrix} w_{\nu 1}^k \\ \left(\alpha_{\nu_+1}^k w_{\nu_-1}^k - \alpha_{\nu_-1}^k w_{\nu_+1}^k\right) u' l^k \end{Bmatrix} du',$$

$\vec{x}_o^{\,k}(u',t) = (\tilde{\chi}_1^k, \tilde{\chi}_2^k, \tilde{\chi}_3^k),\ \tilde{\chi}_\nu^k = \beta_\nu^k + \alpha_{\nu 1}^k\, l^k u', \nu = 1,2,3;$

$\nu_+ = (\nu+1) - 3\Delta_3^\nu,\ \nu_- = (\nu-1) + 3\Delta_1^\nu\ , \Delta_\mu^\nu = 1,$
if $\nu = \mu$ and zero, if otherwise, $\mu = 1,2,3.$

Substitution of (5.2) into the above formula for $\Delta I_{kji}^{\uparrow\downarrow}$ yields the sought expression:

$$\Delta I_{kji}^{\uparrow\downarrow} = \varepsilon^k (l^k)^2 \varepsilon^j (l^j)^2 \varepsilon^i (l^i)^2 \sum_{\nu=1}^{3} \vec{I}_\nu \times \begin{Bmatrix} w_{\nu 1}^k(t) \\ \left(\alpha_{\nu_+1}^k(t) w_{\nu_-1}^k(t) - \alpha_{\nu_-1}^k(t) w_{\nu_+1}^k(t)\right) l^k \end{Bmatrix}$$

$$\times \sum_{m=1}^{3} w_{m1}^j(\tau) \sum_{l=1}^{3} w_{l1}^i(\tau) \int_{-0.5}^{0.5} du' \int_{-0.5}^{0.5} d\bar{u} \int_{-0.5}^{0.5} du$$

$$\times \begin{Bmatrix} 1 \\ u' \end{Bmatrix} \cdot 2f^k(u',0) \cdot 2f^j(\bar{u},0) \cdot 2\, f^i(u,0) \psi_l^o(u,\tau)$$

$$\times \frac{\partial \varepsilon_3\left(\vec{x}_o^{\,k}(u',t), \vec{z}_o^{\,j}(\bar{u},\tau)\right)}{\partial \tilde{\zeta}_m^j} \varepsilon_3\left(\vec{z}_o^{\,j}(\bar{u},\tau), \vec{y}_o^{\,i}(u,\tau)\right). \quad (6.5)$$

Formulas (6.4), (6.5) give the sought explicit expressions for the interaction forces and moments due to the dipole distribution over the surfaces of the hulls. They require numerical integration over a unit cube and, thus, are more complicated than their source term counterparts (6.3). Yet, they still save the need for numerical solution of a high order system of linear algebraic equations for the flow

potential with the subsequent pressure integration over the wetted surface, as would be the case with a finite difference or integral equations approach.

7 CONCLUSIONS

Theoretical solution of the ship–to–ship interaction problem based on the potential flow formulation has been obtained in the limit of slender body approximation and small Froude numbers. It is given by formulas (5.1), (5.2) for the source and dipole parts of the flow potential and formulas (6.2) – (6.5) for the related forces and moments.

If considered from the stand point of the method of marched asymptotic expansions (MMAE), formulas (5.1), (5.2) could be hypothesized to be an outer expansion of the flow potential, whose range of validity in the immediate vicinity of the body H_i remains unknown. In the method of matched asymptotic expansions it must be established via the analysis of the related inner problem.

Indeed, it could be observed that, although formulas (5.1), (5.2) are, certainly, applicable at distances that are much larger than the slenderness parameter ε^i, the analysis of the previous sections does not seem to give an insight into the structure of the solution in the immediate vicinity of the body.

However, the true situation is more subtle than it might appear at first glance, and the construction of the inner solution, in fact, is not required in the present method.

To shed some light on the nature of the relationship between the obtained 'outer' solution and its inner counterpart, consider, for simplicity, one ship only. In this case the inner solution in the vicinity of the body of size ε^i which corresponds to our solution (5.1) can be shown to be contained in formula (5.1), at least to leading order. We omit the derivation procedure of this inner solution, since it, almost word for word, reproduces the related conventional slender body theory solution, whose in depth description can be found, *e.g.*, in the monograph by Cole (1972).

The major difference between the present approach based on the second Green's identity and the conventional methodology based on hieratical solution of inner, intermediate and outer problems used in MMAE (Cole 1972), in order to derive boundary conditions for these problems by means of their asymptotic matching is that the latter procedure is not required, when the second Green's identity is used, since it already contains the information about boundary conditions.

Secondly, it must be emphasized that, when calculating the pressure, the second order term $0.5(\nabla\Phi)^2$ was discarded due to the associated analytic complexity of the related expressions for the forces and moments. Unfortunately, the author is unaware of an appropriate generalization of the Lagally theorem, whose application might simplify this analysis. If required, this term can be taken into account numerically with the help of formula (5.1). Its analytic evaluation is planned for the future.

Finally, it is worth mentioning that the presented analysis is not restricted to two-dimensional motion in horizontal plane, but is of an essentially three-dimensional nature. Apart from horizontal forces and vertical moment, it contains the expressions for the vertical force component, roll and trim moments as well as the dependencies on all three components of ships' velocities, angular velocities and three angular displacements (via α^i_{jk}).

8 REFERENCES

Cole, J.D., 1972. Perturbation Methods in Applied Mathematics. MIR Publishers. Russian Edition. Section 4.5 Singular boundary value problems. PP. 193 – 206.

Korn, G.A., Korn, T.M., 1973. Mathematical Handbook for Scientists and Engineers. Definitions, Theorems and Formulas. Russian Edition. P. 525.

Pettersen, B., Berg, T.E., Eloot, K., Vantorre, M., (Editors). 2011. Second International Conference on Ship Maneuvring in Shallow and Confined Water: Ship to Ship Interaction. Trondheim. Norway. Conference Proceedings.

Pinkster J.A., Bhawsinka K., 2013 A Real-time simulation technique for ship-ship and ship-port interactions. 28th Int. Workshop Water Waves Floating Bodies, L'Isle sur la Aorgue, France, 2013.

Pinkster, J.A., 2013. GPU as means to realize real-time ship-ship and ship-shore interaction effect on ship bridge simulators. Talk at GPGPU-day 2013. http://www.platformparallel.com/nl/applied-gpgpu-days-2013/speakers/jo-pinkster-pmh/

Sutulo S., C. Guedes Soares, J. Otzen, 2012. Validation of Potential-Flow Estimation of Interaction Forces. Journal of Ship Research, Vol. 56, No.3, pp. 129–145.

Tuck, E.O. and Newman, J.N. 1974. Hydrodynamic interactions between ships. Proc. 10th Symp. On Naval Hyd. Cambridge. Mass. USA. PP. 35-70.

Vladimirov, V.S., 1984. Equations of mathematical Physics. MIR Publishers. Moscow.

9 AUTHORS BIOGRAPHY

Grigory Vilenskiy holds the current position of a Leading Researcher, Head of Eng. Dept. at SimTech Ltd. He is responsible for algorithmic work in fluid dynamics, analytical mechanics, automated control and numerical

methods. His previous job experience includes Dept. Mathematics University College London, Group of Applied Analysis TU/e, School of Mathematics at The University of Manchester, Dept. Mech. Eng. University College London, Kongsberg Maritime Ltd. He holds a PhD in applied mathematics. His doctoral theses was dedicated to high-Reynolds-Number asymptotic analysis of 3D separated flows.

COUPLING DYNAMIC MOORING ANALYSIS WITH SAILING VESSEL EFFECTS FOR THE ESTIMATION OF MOORING LOADS. A CASE STUDY

Damián Villaverde Vega, Bart Verheyen and **Francisco Aracil**,
International Marine and Dredging Consultants, Antwerp, Belgium

COUPLING DYNAMIC MOORING ANALYSIS WITH SAILING VESSEL EFFECTS FOR THE ESTIMATION OF MOORING LOADS. A CASE STUDY.

Damián Villaverde Vega, Bart Verheyen and **Francisco Aracil,** International Marine and Dredging Consultants, Antwerp, Belgium

SUMMARY

Nowadays the passing vessel effects on moored vessels have to be considered in the mooring design. The risk of mooring failures increases when passing vessels are sailing too close or too fast. Local pilots and authorities demand a better understanding of the passing vessel effects as a part of the development or upgrade of new or existing berthing facilities. An integrated design approach has been applied by coupling the effect of the environmental conditions at the project site and the effect of the induced waves and currents generated by the nearby passing vessels. This paper discusses how a simplified modelling approach can be applied, in order to account for this in early stages of the design.

1 INTRODUCTION

The Oil Companies International Marine Forum (OCIMF) suggests that the number of terminal operators being severely or fatally injured, when mooring lines fail under tension, is a widespread problem which has been intensively discussed within the industry and at the International Maritime Organization (IMO) in the latest years. Customers, users, owners and authorities of oil and gas facilities have to have reassurance about the performance of a mooring system and have a clear view on the operational risks associated with it.

To gain more insight, an integrated design approach has been applied by coupling the effect of the environmental conditions at the project site and the effect of the induced waves and currents generated by the nearby passing vessels in a dynamic mooring model. A case study in the Ringvaart canal around Ghent (Belgium) is presented.

2 METHODOLOGY

The environmental conditions considered for the mooring analysis are wind, currents and water levels. Currents and water levels are directly related to each other since at the Ringvaart canal the currents are induced by the discharges of the locks located upstream.

The used wind data is obtained from the monthly bulletins published by the Belgium Royal Meteorological Institute. Those bulletins include average wind speed, maximum gust speed and wind direction. A 10-year omnidirectional return period is determined as design value. This value is then compared with the recommendations of OCIMF, where a value of 60 knots is suggested for mooring design. The omnidirectional wind velocity for a 10-year return period is approximately 110 km/h.

Water levels are mainly affected by the discharge of the lock located at Evergem. Using results from a 1D model that was calibrated with real data from the water level in the canal Ringvaart Noord, the water levels for different return periods have been determined. The water level with a return period of 10 years corresponds to approximately 5 m TAW ('TAW' being the reference level in Belgium). It has to be noticed that for return periods above 10 years, the water level variation is quite small. Variations of 10 cm are linked with very high return periods (in the order of 1000 years). This is due to the fact that the water level in the canal is controlled as much as possible to accommodate navigation.

The design vessel selected for mooring calculations is defined as the bigger inland tanker vessel foreseen to call the facility (L = 135 m, B = 11.5 m, T = 3.5 m, Displacement = 4200 tons, which belongs to CEMT class Va). The design vessel used to simulate the passing vessel effect has been selected with the same dimensions and properties as the design vessel for mooring analysis. The navigation velocity of the passing vessel has been determined based on the analysis of AIS data. Approximately 35500 AIS records are found in the project area. The sailing direction can be indirectly obtained based on the difference in between the time of the recorded items and the position. A passing navigation velocity of 10 km/h is considered.

The methodology, in short, can be described as follows. A full 3D model, based on a real inland navigation tanker vessel of 135 m length, has been generated with the software Rhinoceros. The passing vessel effect calculation is performed in the software XBeach, and the dynamic mooring analysis is performed in the software ANSYS-Aqwa.

The OCIMF guideline is used to determine the wind and current forces acting on the moored vessel. These values are given as input directly in ANSYS-Aqwa together with the passing vessel effects.

A berthing analysis has been performed based on the methodology described in PIANC guidelines for design of fenders (PIANC, 2002). Berthing analysis is performed to determine the berthing energy of the vessel, necessary for the selection of the fenders.

The worst environmental scenarios are combined for different ballast conditions.

3 XBEACH MODEL

3.1 SOFTWARE

XBeach is an open-source numerical model which originally was developed to simulate hydrodynamic and morphodynamic processes and impacts on sandy coasts with a

domain size of kilometers and on the time scale of storms (Deltares, 2015).
Since then, the model has been applied to other types of coasts and purposes. The Xbeach software in non-hydrostatic mode is capable to calculate the waves (mainly the long primary wave, in less extent the secondary waves) caused by passing ships (Deltares, 2015). In addition Xbeach has the advantage over other common softwares to calculate ship-induced waves that it can take into account the interaction of the impact of bathymetrical variations on the waves (e.g. shallow arrows causing wave shoaling) and can represent more complex geometries (such as port layouts) and shorelines (De Jong et al., 2013).
The vessel geometry is included via a sub-grid in the model and is, as such, a simplification of the shape. In the direct vicinity of the vessel all complex (3D) flow patterns are therefore not fully captured, but in the broader area (such as a distance in the order of magnitude as that to moored vessels) the model behaves well to represent the primary wave that is of importance to study the impact on a moored ship (De Jong et al., 2013).
Xbeach has been used before to study the impact of passing ships on the flow fields around moored vessels such as in Zhou et al. (2014). For this study, a validation exercise has been performed with the experimental setup described in (Zhou et al., 2014), demonstrating that the Xbeach model is adequate to study the passing ship effect.

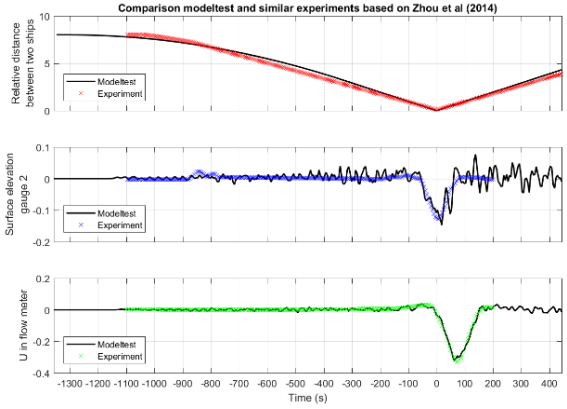

Figure 1. Comparison of the water level and velocity variations between Xbeach modeltest and experiments according to (Zhou et al., 2014). From top to bottom: 1) Relative distance from the passing vessel to the moored vessel expressed in m; 2) Surface elevation in m; 3) Current induced by the passing vessel in m/s

3.2 MODEL SETUP

A non-hydrostatic Xbeach model has been set up to study the hydrodynamic impact of the passing vessel. The model domain is a representation of the local bathymetry of the Ringvaart canal near the jetty extrapolated to a straight canal section as visualized in Figure 2. The computational domain consists of 625 × 5050 cells with a mesh resolution of 4 m × 2 m. Observation points to record water level and current variations are included along the transect at chainage 5298 m.

An inland navigation vessel of CEMT class Va has been considered as passing vessel. The geometry (based on the vessel model) is included in the Xbeach model via a sub-grid mesh. The design water level has been applied. No wind or ambient currents have been applied in order to allow calculation of the impact of the ship on the hydrodynamics.
Based on the AIS data analysis it was found that there is limited space for ship manoeuvring. It was therefore decided to simulate the track of the passing vessel through the center of the canal, as is the main path followed by the vessels. As ships sail faster, higher waves are generated. Therefore maximum sailing velocities are applied, which, according to the AIS data analysis, correspond to about 10 km/h or approximately 5 knots. In order to reduce spurious motions at the start of the simulation by the sailing vessel, the vessel is accelerating in the model from 0 to 5 knots.

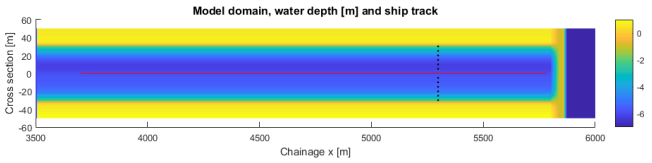

Figure 2. Overview of the Xbeach model domain showing the extent, the water depth based on the bathymetry of chainage section 5298 m and the design water level, the observation points and the ship track.

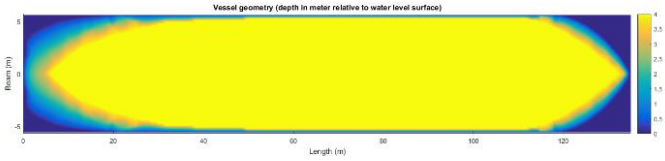

Figure 3. Interpolated geometry of the passing vessel on sub mesh level (depth in meter relative to the water level surface in a scale from 0 to – 4 m TAW).

4 ANSYS-AQWA MODEL

4.1 INTRODUCTION

Vessel movements and loads at the mooring lines can be evaluated by means of a static or dynamic analysis. Static analysis is more suitable when the environmental forcing does not lead to a dynamic response of the mooring system. This happens in rather sheltered environments or in places where no rapid changes of forces occur. However in most of the cases this is not common, and a more detailed assessment with a dynamic analysis is necessary.
In general, there is not a set of design criteria to establish whether a system should be assessed using a static or dynamic approach. The approach has to be decided depending on site specific conditions, project specifications and requirements, and experience. However, some guidance can be found in literature (GL Noble Denton, 2015, and OCIMF, 2018).
In the studied case, the jetty is located in a sheltered area (i.e. inland canal). In this context, the moored ship may

experience dynamic motions as a consequence of the water induced movements originated by the passing vessels. Therefore, in order to understand whether the vessel is prone to develop dynamic behaviour for the given environmental loads, a model with ANSYS® Aqwa™ is developed.

4.2 SOFTWARE DESCRIPTION

ANSYS® Aqwa™ (or Aqwa in short) provides a toolset for investigating the effects of environmental forcing on floating structures.
The software simulates hydrodynamic fluid wave loading on floating and fixed bodies using 3D radiation and diffraction theory, and can as well be used to estimate the equilibrium characteristics and static and dynamic stability of mooring systems under steady environmental loads. Real-time simulations of bodies operating in regular or irregular waves can be simulated under first and second order wave excitations, wind and currents.

4.3 METHODOLOGY

The mooring analysis is carried out in ANSYS® Aqwa™ v 18.2 by a four step approach:

a) 3D Hydrodynamic radiation and diffraction analysis
b) Static equilibrium
c) Environmental static equilibrium
d) Time domain analysis

Each step is further detailed below.

4.3 (a) 3D Hydrodynamic Radiation and Diffraction Analysis

Assuming that the flow is ideal (viscosity is neglected), irrotational and incompressible, the flow field around a floating body can be expressed as a velocity potential.
In Aqwa the source distribution method is applied to solve the fluid potential (Ansys, 2017). In order to do that, the structure of the vessel is represented by a series of diffraction panels in which the wave force is determined. The basic idea behind this method is that at each of these elements a source term is placed, the strength of these sources is determined so that the net flow caused by the incoming wave through this virtual hull is null, resulting in the reflected and diffracted wave velocity potentials. Because the vessel is moving, the source strengths have to compensate as well the motions of the vessel in all degrees of freedom, resulting in the radiated wave velocity potentials. In addition, the potential function has to satisfy a number of boundary conditions. This is explained more in detail in Newman (1978).
When velocity potentials are known, the forces at the hull of the structure can be calculated. Fluid forces can be split in active and reactive forces. The active forces consist of the Froude-Krylov force and the diffraction force. The reactive force is the one caused by the radiated waves originated by the vessel movements.
If we assume a linear relation between the wave amplitude and the ship response, then the relation between the ship motion and the incoming wave can be expressed, for one direction (X), in the frequency (ω) domain as follows:

$$[-\omega^2(M_s + M_a(\omega)) - i\omega B(\omega) + C)]\mathrm{X}(\omega) = \mathrm{F}(\omega) \quad (1)$$

Where:
M_s is the structural mass
M_a is the added mass
B is the damping
C is hydrostatic stiffness
F is the wave force (incident and diffracting)

The linear response amplitude operators (RAOs) and resistance coefficients (added mass and damping coefficients) are calculated by Aqwa for a range of incoming wave frequencies and directions at each structure. Hydrodynamic interaction between structures is taking into account during the calculations. As it can be seen from expression (1), the RAOs are not an inherent property of a structure because it depends on the radiation and diffraction forces resulting from the potential flow field.
In total, 3 structures have been included in the model, namely: (1) Vessel, (2) River Bank, and (3) Jetty. Structures 2 and 3 are introduced as fixed, and therefore they do not radiate waves, although they can diffract and therefore interact with the whole system.
The added mass, the wave damping and the hydrodynamic wave forces and moments constitutes the hydrodynamic database of each structure. The result of this analysis is used in the static and dynamic mooring analysis since it involves response of structures as function of different frequencies and directions.

4.3 (b) Static Equilibrium

Prior to any mooring analysis, calculation of the static equilibrium of the vessel, connected to the appropriate lines and in still water, is performed. The hydrodynamic response has been computed in the previous step, in this part we deal with the equilibrium related to the vessel when moored at the jetty, which implies that the hull is in contact with the fender system as a consequence of the line pretension. This equilibrium configuration is used as a starting point for subsequent static or dynamic analysis.
The pretension of the lines is defined at this stage in an iterative process which depends on the initial length of the cable (input) and the still water line tension (output). This last term is used to describe the tension of the lines after the system achieves the hydrostatic equilibrium for the target pre-tensions.

4.3 (c) Environmental Static Equilibrium

The starting position of the structures for this analysis is calculated in the previous step, i.e. the static equilibrium. In this step the external forces are introduced to compute the new environmental equilibrium in which the fenders and the mooring lines interact with the external environmental forcing. Following forces are present during the static analysis:

- Current forces calculated analytically at the vessel;
- Wind forces calculated analytically at the vessel.

4.3 (d) Time Domain Analysis

The steady state determined in the previous section is used as the starting position for the time domain analysis.
The position and velocity of the vessel are determined at each time step by integrating the accelerations due to the external forces in the time domain. The position of the system at the end of one time step is used as a starting position in the next time step. This way, a time series of the motion (position, velocity, and acceleration) of the tanker connected to the mooring lines, is simulated.
The mooring lines and fenders interact with the whole system. All the forces calculated in the previous steps are included in the time domain calculation. The solver Aqwa Nautical is used to simulate the real-time motion of the tanker in a "regular wave". This analysis involves meshing the total surface of a structure to create a hydrodynamic and hydrostatic model at each time step of the simulation.

4.4 MODEL SETUP

4.4 (a) Mass properties

The centre of gravity (COG) is determined based on the list of all the weights of the reference vessel, for ballast and loaded conditions.
Inertia is estimated using individual weight and distances to the COG of each element for the reference vessels, and are compared with the general recommendations given in the ITTC recommendation (2011).

4.4 (b) Geometry and Mesh

The mooring system is formed by the tanker, the river bank and the pier. The geometry of the tanker is imported in ANSYS DesignModeler directly from the CAD model made in Rhinoceros (v6.0).

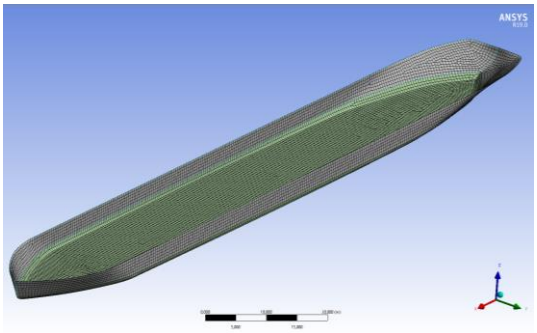

Figure 4. Vessel geometry imported in ANSYS Design Modeler

The pier is made up by four dolphins equipped with fenders. The dolphins are used to connect the spring and breast lines with the tanker.
The crest of the dolphins is set to +6 m TAW. In addition, two bollards, located at the river banks, allow for the connectivity with the head and stern lines. These bollards are set in the model to a level of +7 m TAW. All the fairleads of the vessel are assumed to be at the deck level of the vessel, which is +3.1 m TAW and +0.4 m TAW for ballast and loaded condition respectively. The mesh size for the inland tanker is around 1 m. This resolution is required to take into account the complex hull geometry. To give some numbers: there are 12139 elements from which 8362 elements are diffracting panels for the tanker in unloaded condition.
The pier and the river banks are meshed with an element size between 2 m and 0.5 m respectively. This resolution is sufficient to capture the geometry of both the pier and the river bank.

4.4 (c) Mooring Lines

The principal design parameters of the mooring lines are related to the stiffness of the lines, the mooring system layout and the line pretension. The mooring layout consists of 6 lines connected and named as shown in Figure 5.

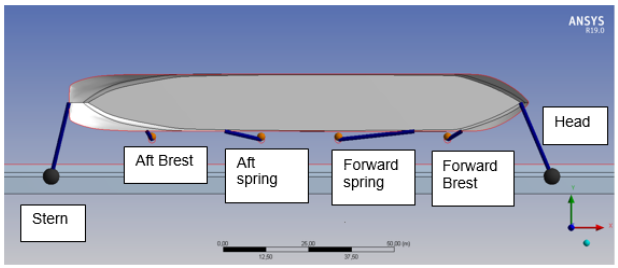

Figure 5. Mooring system layout

The mooring line make-up is the same for all the lines. The properties of each line section are calculated taking into account average commercial specifications. For fibre rope an estimation of appropriate values based on catalogue data is used. Line properties are shown in Table 1.

Table 1. Polyester fibre used for mooring lines

Diameter (mm)	60
Area (mm²)	1286
MBL (kN)	680
Stiffness (kN)	3924

On this basis, different axial stiffness values are obtained depending on the mooring length. As a first iteration, some pretension is applied at the spring lines to reduce movements and more evenly distribute the tension. As the lines are attached and tensioned in sequence, the tension of the already-attached lines changes. Achieving the line pretensioning (still-water tension) is an iterative process between the initial length of the line and the tension of the lines after equilibrium is achieved.
Line pretension is a very important parameter in the mooring layout. Pretension of the lines will reduce the vessel motions and decrease the mooring loads compared with a non-pretensioned moored configuration.

It has been decided to pretension the lines up to around 1% of the MBL, in the assumption that a manual mooring procedure is normally used aboard inland navigation vessels. Only spring lines are tensioned to cope with the front wave

of the passing vessel, so surge movements are more restricted.

4.4 (d) Fender system

A fender system at the jetty area is proposed. In order to do so, a berthing energy calculation is performed. This area is categorised by assuming conditions of an easy berthing, and a sheltered, approaching berthing velocity of 0.2 m/s. Safety factors have been applied and the procedure to define the abnormal berthing energy of the fenders, established in PIANC (2002), followed.
Once the abnormal energy is determined, a fender system is chosen. A polynomial function is fitted to the deflection curve provided by a commercial manufacturer and introduced in Aqwa. This way nonlinearities in the deflection-reaction curve can be taken into account.

4.4 (e) Environmental forcing

OCIMF (2008) has published a methodology to estimate the current and wind loads acting on tankers. This method is used to compute the wind and current loads.
The wind force prediction is based on the use of curves that relate the angle of attack of the wind with non-dimensional drag coefficients for surge, sway and yaw.
For current forces, the approach takes into account the influence of water depth-to-draught ratio and the use of different bow shapes to estimate the drag coefficients.
Regarding the wave loads, a linear regular wave is introduced in Aqwa to model the bow wave of the passing vessel. The first-order wave loading is calculated by Aqwa using three-dimensional linear radiation and diffraction.

4.4 (f) Scenarios

The environmental forcing defined in the previous sections has been combined to define the design cases for the mooring calculation. Here it can be mentioned that the cases are defined to calculate the design load at the mooring lines and not at the fenders.
To determine the design cases, it is first necessary to analyse the wind condition. This wind condition will act together with the passing vessel which can sail upstream and downstream. The passing vessel effect is defined by a primary wave and a return current. Secondary waves caused by the passing vessel are not included in this analysis since they are smaller and with periods of one order of magnitude lower than the front wave.
The above results in the definition of the following scenarios:

- Only Wind (static analysis): 60 knots of wind coming from any of the 8 principal directions.
- Passing Vessel (time domain): Sailing either upstream or downstream. The effect of the passing vessel is a disturbance of the water level of approximately 20 cm during a period of around 55 seconds and a return current of 0.5 m/s.
- Worst Case Scenario (time domain): Worst Wind + Passing Vessel Scenario.

During extreme discharge events, sailing is not allowed in the canal. So the combination of a maximum current and passing vessel effect was not considered.

5 RESULTS

5.1 PASSING VESSEL

Using the XBeach model the hydrodynamic behaviour due to a passing vessel is examined. The XBeach model calculates the variations of water level and currents over time. Figure 6 presents the water level at a moment in time when the passing vessel reaches chainage 5298. At the bow and stern of the ship small water level increases can be observed. The primary wave consisting of a water level drop of about 15-20 cm is clearly visible around the ship. Since the Ringvaart canal is relatively narrow compared to the vessels cross section, the primary wave is connected to the banks. Return currents between the vessel and the bank of about 0.5 m/s are calculated. In the wake of the vessel secondary, smaller waves are generated.

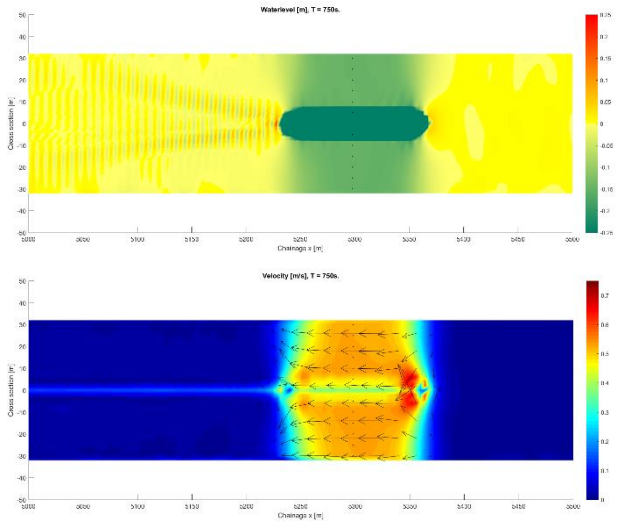

Figure 6. Map of calculated water level variation (top) and velocities (bottom) in the canal at $t = 750$ s.

More detail can be found in the time series of the observation points in the Xbeach model. For an observation point near the bank of the canal at chainage 5298, Figure 7 presents the variations in time of: the distance of passing ship to the observation point, the water level, and the currents. Based on these time series it can be derived that the primary wave of the water level drop has a period of about 55 s.

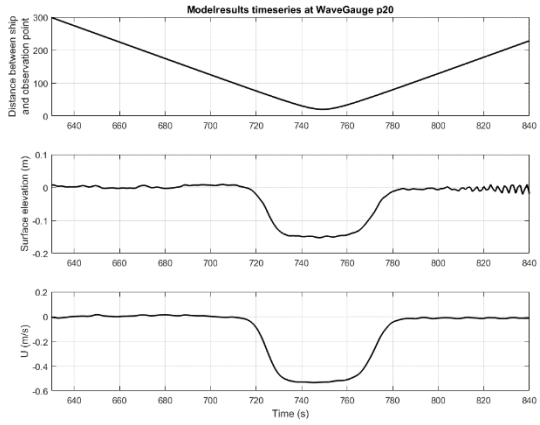

Figure 7. Modelresults showing the variation in time at an observation point near the bank at chainage 5298 of: the distance to the passing vessel (top), the water level (middle) and return current (bottom).

5.2 DIFFRACTION/RADIATION ANALYSIS

The hydrodynamic diffraction and radiation analysis is carried out with the vessel free (no mooring lines) and gives an indication of the behaviour of the inland tanker under wave conditions. The analysis is carried out for eight wave directions, and frequencies ranging from 2.5 seconds to 65 seconds (with 24 intermediate frequency values) plus another range of frequencies going from 70 seconds to 150 seconds (20 intermediate frequencies). Using parallel computation in 4 cores, the model takes approximately 8 hours to complete the calculation.

From Figure 8 to Figure 10, the diffracted, radiated and resulting wave field are shown for an incident wave with an amplitude of 1 m and a period of 65 seconds. The phase of the wave corresponds in the images when the crest is at the COG of the vessel.

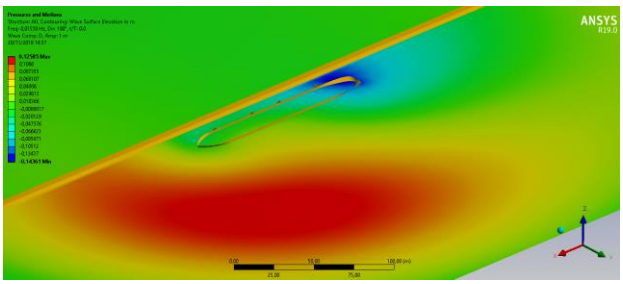

Figure 8. Diffracted wave field

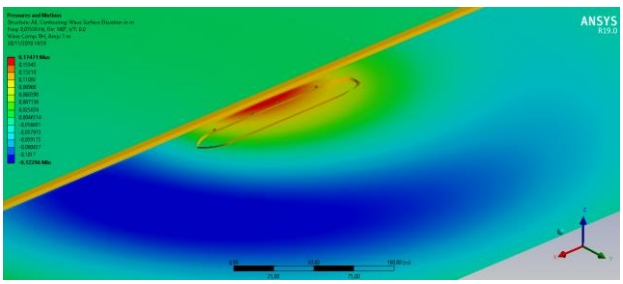

Figure 9. Radiated wave field

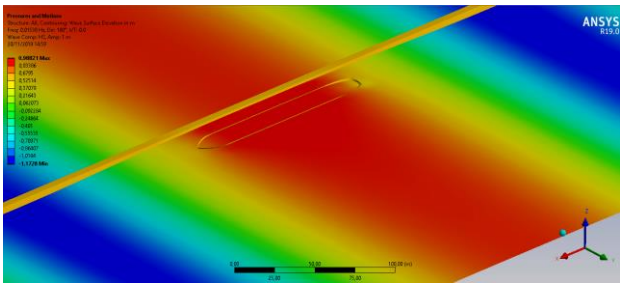

Figure 10. Resulting wave field

5.3 RAOS

As was expected, the most critical vessel response is in surge direction. For waves longer than 20 seconds, the response in surge starts being important. Since the period of the induced front wave is related directly to the speed of the passing vessel, and wave periods for the front wave are higher than 20 seconds, it can be already anticipated that motions in surge will be dominant.

The pitch response shows a typical behaviour of a vessel in head seas, with two marked peaks, one corresponding to the natural frequency of the vessel, and another one dominated by the wave excitation that occurs when the ship length is equal to the wave length. For low frequencies the ship follows the slope of the wave.

Differences between loaded and unloaded condition in the RAOs can be seen in sway, roll and yaw.

5.4 STATIC ANALYSIS

A static analysis is performed to determine the most unfavourable wind direction for ballast conditions. In order to do so eight wind directions are screened. The worst condition is obtained when the vessel is in ballast mainly because the windage area is greater.

Results for mooring loads are given in Figure 11. Aft spring lines work the most for port and starboard bow winds, reaching a maximum of 112 kN for bow winds. Forward spring lines work the most for stern winds peaking up to 32 kN. Brest lines work the most for the starboard beam winds with maxima of 149 and 175 kN for aft and brest lines respectively.

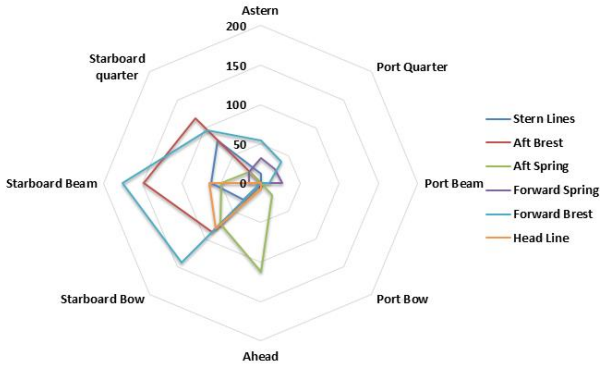

Figure 11. Mooring Loads for Ballast Condition

5.5 TIME DOMAIN ANALYSIS

The starboard wind (W) causes the highest tensions in the brest lines, which are working closer to 25% of the MBL, therefore this case seems appropriate for further investigation. Although the chance of having an extreme wind with a passing vessel event is rather limited, it has been decided to include it in the simulations for further discussion. The results for translations and rotations are expressed as the difference between the minimum and maximum value achieved during the simulation. These values should be understood as indicative for the amplitude of the movement.

Maximum mooring loads are shown in Figure 12 and Figure 13. The results are given for the vessel sailing downstream (SD) or upstream (SU) in combination with and without a starboard wind (W). Two load conditions are tested, namely ballast and load condition.

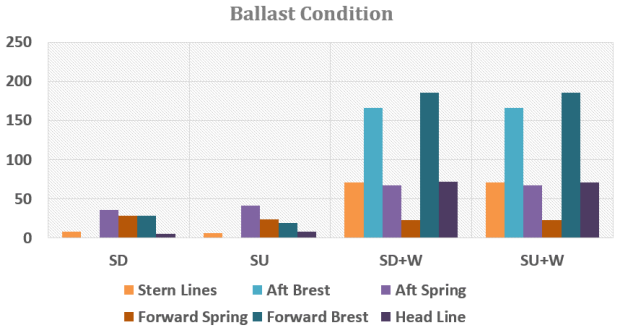

Figure 12. Maximum Mooring Load (kN) for Ballast Condition

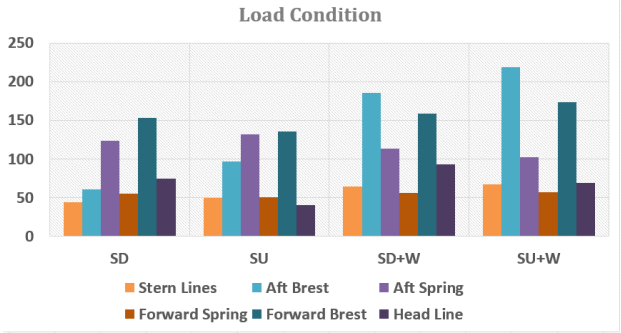

Figure 13. Maximum Mooring Load (kN) for Load Condition

For ballast condition the maximum mooring loads occur in the forward and aft brest lines during the passing vessel event and the starboard beam wind. The maximum mooring loads are equal to 166 and 185 kN for brest lines. There is not significant difference between the passing vessels sailing upstream or downstream because the environmental forcing is quite similar. In ballast condition the wind is the critical load.

For load condition the vessel reacts more dynamically than in ballast condition. This is mainly because the first order wave excitation is higher in load condition. In addition, radiation forces in surge direction are low for ballast condition whereas for load condition they are not.

As consequence, the mooring for load conditions is deemed to be the most critical, with maximum loads up to 219 kN for brest lines and 132 kN for spring lines.

Critical vessel movements during the offloading cycle are determined by thresholds imposed by the unloading arm and set to 2 m in surge direction and 1 m in sway. Maximum surge and sway movement is around 63 cm and 65 cm respectively. This is within the limits of operability.

6 CONCLUSIONS

An integrated design approach has been presented by coupling the effect of the environmental conditions at the project site and the effect of the induced waves and currents generated by nearby passing vessels.

The passing vessel effect is considered as a combination of return currents and primary waves generated by the sailing vessel. These effects are assessed using a specific non-hydrostatic model which is capable of resolving the low frequency wave and the flow at the moored tanker. The primary wave consisting of a water level drop of about 15-20 cm is clearly visible around the ship. Since the Ringvaart canal is relatively narrow compared to the vessel's cross section, the primary wave is connected to the banks. Return currents between the vessel and the bank of about 0.5 m/s are calculated.

A dynamic mooring model was set up to investigate the response of the moored vessel due to a passing vessel. The wave calculated with the non-hydrostatic model is introduced in Aqwa as a regular wave with identical amplitude and period. This model couples the response of the vessel and the mooring lines in the time domain and aims for a realistic representation of the vessel, the mooring stiffness, and the response of the system to the surge wave of the passing vessel.

Maximum mooring load achieved during the static analysis is 175 kN, whereas for the dynamic analysis it is 153 kN for the passing vessel scenario, and 219 kN for the passing vessel scenario in wind conditions. Maximum mooring loads occur at the brest lines for all scenarios. Mooring loads are not distributed evenly in the mooring system because the mooring layout is not symmetrical, and because the axial stiffness of the lines is different, since stiffness of the lines depends on length where shorter lines tend to absorb more loads.

In surge direction, the diffracted and the incident wave forces are higher in load than in ballast condition, and hence, so are the maximum mooring loads and expected movements. In sway direction, the incident wave forces are very small because the direction of the incident passing vessel wave is either head or sternwards. However diffracted and more specifically the radiated wave forces cause movements in sway which translates into additional loads in the brest lines.

The results show that despite the magnitude of the primary wave being rather small, its period is large enough to produce low frequency motions, which in turn affects the design loads in the spring and brest mooring lines.

7 REFERENCES

ANSYS, 2017. Aqwa Theory Manual v 18.2, pp. 33-38.

Deltares, 2015. Xbeach Technical Reference Kingsday Release. Model description and reference guide to functionalities.

GL Noble Denton, 2015. Guidelines for Moorings, pp 22.

ITTC, 2011. 'Seakeeping experiments', Recommended Procedures and Guidelines - International Towing Tank Conference.

de Jong, M.P.C., Roelvink, D., Reijmerink, S.P., Breederveld, C., 2013. Numerical modelling of passing-ship effects in complex geometries and on shallow water. SMART RIVERS 2013, Liege (BE), Maastricht (NL).

Newman, J.N., 1978. The theory of ship motions, Advances in Applied Mechanics, Vol. 18, pp 221-283.

OCIMF, 2008. Mooring Equipment Guidelines3rd Edition. Witherby Seamanship International, London.

PIANC, 2002. Guidelines for the Design of Fenders Systems 2002. PIANC MarCom WG33 2002.

OCIMF, 2018. Mooring Equipment Guidelines (MEG4), pp. 56–57.

Zhou, M., Roelvink, D., Zou, Z., van Wijhe, H.J., 2014. Effects of passing ship with a drift angle on a moored ship. Proceedings of the ASME 2014 33rd International Conference on Ocean, Offshore and Arctic Engineering OMAE2014. June 8-13, 2014, San Francisco, California, USA.

8 AUTHORS BIOGRAPHY

Damián Villaverde is civil and coastal engineer and has more than 8 years of experience in marine and river engineering. He currently holds the position of Engineer Advisor at IMDC. His previous experiences are related to the design of marine and river infrastructure, environmental modelling, and the study of hydrodynamics of floating structures.

Bart Verheyen currently holds the position of Engineer-Advisor at IMDC. He has 10 years of experience as a civil engineer. His previous experiences include the use of a wide range of numerical models in coastal, marine and estuarine studies. As such he was responsible for the study of the ship wave.

Francisco Aracil is naval architect with 12 years of experience in naval construction and navigation. He currently holds the position of Engineer-Advisor at IMDC. His previous experiences include naval inspections, design of navigation channels and navigation aids, and port layouts.

UNCERTAINTY QUANTIFICATION OF HYDRODYNAMIC FORCES ON THE DTC MODEL IN SHALLOW WATER WAVES USING CFD AND NON-INTRUSIVE POLYNOMIAL CHAOS METHOD

Li Xia, Shuai Yuan, Zao-Jian Zou and **Lu Zou**,
School of Naval Architecture, Ocean and Civil Engineering, Shanghai Jiao Tong University, Shanghai, China

Zao-Jian Zou,
State Key Laboratory of Ocean Engineering, Shanghai Jiao Tong University, Shanghai, China

UNCERTAINTY QUANTIFICATION OF HYDRODYNAMIC FORCES ON THE DTC MODEL IN SHALLOW WATER WAVES USING CFD AND NON-INTRUSIVE POLYNOMIAL CHAOS METHOD

Li Xia, Shuai Yuan, Zao-Jian Zou and **Lu Zou,** School of Naval Architecture, Ocean and Civil Engineering, Shanghai Jiao Tong University, Shanghai, China
Zao-Jian Zou, State Key Laboratory of Ocean Engineering, Shanghai Jiao Tong University, Shanghai, China

SUMMARY

In this paper, verification and validation (V&V) and uncertainty quantification (UQ) in uncertainty analysis for CFD simulation are compared. A state-of-the-art method for uncertainty quantification problems, the non-intrusive polynomial chaos (NIPC) method is introduced and validated to be effective by studying a stochastic function, together with the Monte-Carlo (MC) method. NIPC method is applied to quantify the uncertainty of the resistance, heave motion and pitch motion of the DTC model in shallow water waves. The uncertainty induced by waves treated as stochastic variables with Gaussian distribution is studied. Computations are performed with the CFD software STAR-CCM+. UQ results obtained by MC method and NIPC method are compared with the benchmark data. The results obtained by NIPC method show better agreement with the benchmark data than by MC method.

NOMENCLATURE

A	Wave amplitude (m)
B	Breadth of the ship (m)
c	Coefficients of polynomial chaos
C_b	Block coefficient
d	Dimension of stochastic variables
GM	Metacentric height (m)
I_{xx}	Moment of inertia about Ox-axis (kgm^2)
I_{yy}	Moment of inertia about Oy-axis (kgm^2)
I_{zz}	Moment of inertia about Oz-axis (kgm^2)
K	Wave number (m^{-1})
L_{pp}	Length between perpendiculars (m)
m	Mass (kg)
N_{runs}	Number of CFD runs
N_c	Number of coefficients in PCE
p	Order of polynomial chaos expansion
T_{design}	Design draft (m)
T_e	Encounter period (s)
U	Uniform distribution
x_G	Longitudinal canter of gravity (m)
X	Longitudinal force on the hull (N)
y^+	Dimensionless wall distance
z	Heave motion (m)
z_G	Vertical center of gravity (m)
δ_{nm}	Kroenecker-delta function
θ	Pitch motion (rad)
λ	Wave length (m)
μ	Expected value
ξ	Stochastic variable
σ	Standard deviation
CDF	Cumulative distribution function
CFD	Computational Fluid Dynamics
DFBI	Dynamic fluid body interaction
DTC	Duisburg Test Case
EV	Expected value
IPC	Intrusive polynomial chaos
LHS	Latin Hypercube Sampling
MC	Monte Carlo
NIPC	Non-intrusive polynomial chaos
PC	Polynomial chaos
PCE	Polynomial chaos expansion
PDF	Probability density function
RANS	Reynolds Averaged Navier-Stokes
RAO	Response Amplitude Operator
SA	Sensitivity analysis
SD	Standard deviation
UKC	Underkeel clearance
UQ	Uncertainty quantification
V&V	Verification and Validation
VOF	Volume of fluid

1 INTRODUCTION

Along with the rapid development of computer science and technology, Computational Fluid Dynamics (CFD) technology has been widely and successfully applied in industrial production and scientific research. However, the quality and credibility of CFD is always a concern. Verification and Validation (V&V) is a useful method for CFD uncertainty analysis. Verification is to analyze the numerical error in order to ensure the accuracy of numerical methodology; Validation is mainly to find the modelling errors by comparing the simulated results with experimental ones. In the procedure of V&V, all results are estimated in conditions of deterministic factors. Actually, there is a great deal of nondeterministic factors in the real physical problems, such as fluid properties, boundaries, variation of geometry. The cumulative effect of these uncertain factors may have a huge impact on the results obtained by CFD calculation. For the above reasons, it is necessary to measure the uncertainty of the system response.

The main work of uncertainty quantification (UQ) is to characterize the impact of stochastic input parameters on the model quantitatively. In other words, UQ focuses on the statistical characters of the response variables, such as expected value (EV), standard deviation (SD), skewness, kurtosis, cumulative distribution function (CDF) and probability density function (PDF), as a consequence of a set of uncertain input variables with known distribution (Diez et al., 2014).

Normally, there are two components in uncertainty quantification problems. The first one is to determine the distribution of random input parameters from the reliable data. The second one strives to quantify the propagation of uncertainty. This paper focuses on the second aspect.

Traditional methods for studying UQ problems can be divided into two types. One is non-statistic methods, such as sensitivity analysis (SA), moment methods and perturbation method, which are suitable to solve the linear UQ problems. The other is statistic methods, the most famous of which is Monte Carlo (MC) method. MC method is technically feasible to solve UQ problems with large degrees of uncertainty, but not economically.

In recent years, the state-of-the-art method, polynomial chaos expansion (PCE), is employed in UQ problems, which is derived from homogeneous chaos method proposed by Wiener (1938) and developed by Ghanem and Spanos (1991) in solid mechanics field. Recently, several research groups applied this method to CFD field, such as Xiu et al. (2002); Xiu and Karniadakis (2002a, 2002b, 2003); Loeven (2010); Loeven et al. (2007); Mathelin and Hussaini (2003); Mathelin et al. (2005); Lacor and Smirnov (2007, 2008); Lacor et al. (2013); Hosder et al. (2006, 2007); Hosder and Walters (2010); Salehi et al. (2017a, 2017b); Wang and Kang (2010); Wang et al. (2013); Schmelter et al. (2015, 2016,); Ahlfeld and Montomoli (2017); Ahlfeld et al. (2017, 2018). As for ship hydrodynamics, some scholars have done some research in this field, such as He et al. (2013), Stern et al. (2017).

PC method can be divided into the intrusive and the non-intrusive method according to whether it is necessary to modify the solver. Intrusive polynomial chaos (IPC) method requires significant modifications to the solver, hence it was only applied to one/two dimensional stochastic problems. To overcome the difficulties and complexities of IPC method, non-intrusive polynomial chaos (NIPC) method has been proposed and developed. The solver is treated as a black box in NIPC method. The output variables of interest are expanded in polynomial chaos with unknown polynomial coefficients, which can be obtained by projection method or regression method. The former is based on a numerical integration; the latter performs a regression analysis based on a selected set of points.

In this paper, the regression-based NIPC method is applied to stochastic problems related to ship's hydrodynamic performances in restricted waters. The hydrodynamic performance of the ship will change dramatically when entering restricted waters due to the hydrodynamic interaction between the hull and the seabed. It is of great significance to investigate the behaviour of ship in shallow and confined navigation areas, such as rivers, harbors, dredged channels and other coastal areas.

Nowadays, CFD technique has been applied to a large number of numerical simulations of ship's manoeuvring performances in restricted waters.

Jachowski (2008) investigated the restricted water effects on ship motion using commercial CFD software FLUENT. Senthil and Chandra (2013) estimated the resistance of a river-sea ship in shallow water based on CFD method, and the numerical results were compared with the measurement data. Carrica et al. (2016) studied the performance of KCS container ship in a zigzag test under shallow water condition both experimentally and numerically. Deng et al. (2016) simulated 4 different pure sway/yaw tests in shallow water using their in-house numerical solver ISIS-CFD code, and the predicted results were compared with the benchmark data. Liu et al. (2016) simulated the viscous flow around the DTC model manoeuvring in shallow water. Simulations of static drift and pure sway tests at 20% UKC were carried out. Tezdogan et al. (2016a) analyzed the DTC model's hydrodynamic performance under different ship drafts with different speeds using the CFD software STAR-CCM+, and the squat results were compared with experimental data. Tezdogan et al. (2016b) conducted a series of simulations of shallow water waves to investigate a full-scale large tanker's characteristics and studied the ship's heave/pitch motion in head waves at zero speed and various water depths, and found that the shallow water effect is an important cause of the vertical movement of the hull. Terziev et al. (2018) investigated the behaviour of DTC model when advancing through restricted shallow waters using three methods, CFD, slender-body theory and empirical methods. The results showed that there were significant differences in the computed parameters for the ship entering confined waters. Although the above work is important and excellent, the uncertainty induced by stochastic parameters is ignored. The present paper focuses on UQ for the numerical predictions on resistance and motion of the DTC) model in shallow water waves.

2 MATHEMATICAL MODELS OF UQ

2.1 DEFINITION OF UQ PROBLEMS

Equation (1) shows a problem in space $\boldsymbol{x}$ and time t, where $\boldsymbol{\xi} = [\xi_1, \xi_2, \cdots, \xi_d]^T$ is a vector of uncertain input parameters with known joint probability density function $p(\boldsymbol{\xi})$. UQ problem is defined as a problem to quantify the uncertainty of response Y.

$$Y = f\left(\boldsymbol{x}, t, \boldsymbol{\xi}\right) \tag{1}$$

According to homogeneous chaos theory, if the stochastic input variables ξ_j $(j = 1, 2, \cdots)$ are independent, the response Y can be divided into a stochastic part and a deterministic part:

$$Y = c_0\Phi_0 + \sum_{i_1=1}^{d} c_{i_1}\Phi_1\left(\xi_{i_1}\right) + \sum_{i_1=1}^{d}\sum_{i_2=1}^{i_1} c_{i_1 i_2}\Phi_2\left(\xi_{i_1}, \xi_{i_2}\right) + \cdots \tag{2}$$

where $c(\boldsymbol{x}, t)$ are coefficients and $\Phi(\boldsymbol{\xi})$ are multivariate polynomials. The compact form of Equation (2) can be expressed as:

$$Y = \sum_{i=0}^{\infty} c_i\Phi_i\left(\boldsymbol{\xi}\right) \tag{3}$$

In order to solve the UQ problem, the polynomials are truncated by both order p and dimension d:

$$\begin{aligned}\hat{Y} = {} & c_0\Phi_0 + \sum_{i_1=1}^{d} c_{i_1}\Phi_1\left(\xi_{i_1}\right) + \sum_{i_1=1}^{d}\sum_{i_2=1}^{i_1} c_{i_1 i_2}\Phi_2\left(\xi_{i_1}, \xi_{i_2}\right) + \\ & \cdots + \sum_{i_1=1}^{d}\cdots\sum_{i_d=1}^{i_{d-1}} c_{i_1\cdots i_d}\Phi_p\left(\xi_{i_1}, \cdots, \xi_{i_d}\right)\end{aligned} \tag{4}$$

Polynomial chaos expansion (PCE) is defined as a polynomial approximation as in Equation (4), where $\Phi(\xi)$ satisfies orthogonality to the weight functions:

$$\left\langle \Phi_n\left(\boldsymbol{\xi}\right), \Phi_m\left(\boldsymbol{\xi}\right)\right\rangle = \left\langle {\Phi_n}^2\left(\boldsymbol{\xi}\right)\right\rangle \delta_{nm} \tag{5}$$

where δ_{nm} is the Kroenecker-delta function. The inner product $<\cdot,\cdot>$ can be defined as:

$$\left\langle \Phi_n\left(\boldsymbol{\xi}\right), \Phi_m\left(\boldsymbol{\xi}\right)\right\rangle = \int \Phi_n\left(\boldsymbol{\xi}\right)\Phi_m\left(\boldsymbol{\xi}\right) p\left(\boldsymbol{\xi}\right) d\boldsymbol{\xi} \tag{6}$$

where $p(\boldsymbol{\xi})$ is the joint probability density function. Under the assumption of independent stochastic input variables $\boldsymbol{\xi}$, $p(\boldsymbol{\xi})$ can be expressed as:

$$p\left(\boldsymbol{\xi}\right) = \prod_{i=1}^{d} p_i\left(\xi_i\right) \tag{7}$$

where $p_i(\xi_i)$ is the probability density function of ξ_i.

It can be seen from Equation (4), there are N_c coefficients to be solved in PCE, given in Equation (8).

$$\begin{aligned}N_c = {} & 1 + \frac{p!}{(p-1)!} + \frac{(p+1)!}{(p-1)!2!} + \\ & \cdots + \frac{(p-1+d)!}{(p-1)!d!} = \frac{(p+d)!}{p!d!}\end{aligned} \tag{8}$$

2.2 ORTHOGONAL POLYNOMIALS

PCE was originally developed for the Hermite polynomials and the Gaussian distribution. The convergence rate of Hermite polynomial chaos is optimum for the Gaussian processes (Salehi et al., 2017a). As shown in Equation (6), orthogonal polynomials have to be reconstructed for each distribution. Xiu and Karniadakis (2002a) developed the Wiener-Askey polynomial chaos to deal with more kinds of stochastic variables, as shown in Table 1.

For example, the multidimensional Legendre polynomials with respect to a second order PCE and two random variables ($\boldsymbol{\xi} = \left[\xi_1, \xi_2\right]^T \sim U(-1,1)$) are:

$$\left\{\boldsymbol{\Phi}_n\right\} = \left\{1, \xi_1, \xi_2, \frac{1}{2}(3{\xi_1}^2 - 1), \xi_1\xi_2, \frac{1}{2}(3{\xi_2}^2 - 1)\right\} \tag{9}$$

Table 1. Corresponding orthogonal polynomials with respect to different distributions

Distribution	Polynomial	Support
Gaussian	Hermite	(-∞, ∞)
Gamma	Laguerre	[0, ∞]
Beta	Jacobi	[a, b]
Uniform	Legendre	[a, b]

2.3 PROJECTION-BASED NIPC METHOD

The main idea of projection-based NIPC method is to use Galerkin projection to solve the coefficients.

$$\left\langle \hat{Y}, \Phi_k\left(\boldsymbol{\xi}\right)\right\rangle = \left\langle \sum_{i=0}^{p} \boldsymbol{c}_i\Phi_i\left(\boldsymbol{\xi}\right), \Phi_k\left(\boldsymbol{\xi}\right)\right\rangle \tag{10}$$

Equation (10) can be transformed as follows because of the orthogonality.

$$\left\langle \hat{Y}, \Phi_k\left(\boldsymbol{\xi}\right)\right\rangle = c_k\left\langle {\Phi_k}^2\left(\boldsymbol{\xi}\right)\right\rangle \tag{11}$$

Hence, the polynomial coefficients can be expressed as:

$$c_k = \frac{1}{\left\langle {\Phi_k}^2\left(\boldsymbol{\xi}\right)\right\rangle}\int \hat{Y}\Phi_k\left(\boldsymbol{\xi}\right) p\left(\boldsymbol{\xi}\right) d\boldsymbol{\xi} \tag{12}$$

The expression involves high-dimensional integrals, which requires efficient numerical integration technique.

$$c_k = \frac{1}{\left\langle {\Phi_k}^2\left(\boldsymbol{\xi}\right)\right\rangle}\sum w_j\, p\left(\boldsymbol{\xi}_j\right)\hat{f}\left(\mathbf{x}, t, \boldsymbol{\xi}_j\right)\Phi_k\left(\boldsymbol{\xi}_j\right) \tag{13}$$

where w_j are weights and $\boldsymbol{\xi}_j$ are abscissas in a quadrature scheme. For different numerical integration technique, different weights and abscissas are needed, such as Gauss-Hermite quadrature, Clenshaw-Curtis quadrature, Leja quadrature. However, such numerical integration techniques suffer from the curse of dimensionality and cost a lot, though sparse grid quadrature rules can be used. Projection-based NIPC method is efficient for problems with limited input variables, while regression-based NIPC is viable for problems with a large number of input variables.

2.4 REGRESSION-BASED NIPC METHOD

Regression-based NIPC method requires a certain number of sampling points where the responses are computed. The number of sampling points M should be more than the number of unknown coefficients N+1. The over-determined system can be expressed as follows:

$$\begin{bmatrix} \Phi_0\left(\boldsymbol{\xi}^{(1)}\right) & \cdots & \Phi_N\left(\boldsymbol{\xi}^{(1)}\right) \\ \vdots & & \vdots \\ \Phi_0\left(\boldsymbol{\xi}^{(M)}\right) & \cdots & \Phi_N\left(\boldsymbol{\xi}^{(M)}\right) \end{bmatrix}\begin{bmatrix} c_0 \\ \vdots \\ c_N \end{bmatrix} = \begin{bmatrix} \hat{f}\left(\boldsymbol{x}, t, \boldsymbol{\xi}^{(1)}\right) \\ \vdots \\ \hat{f}\left(\boldsymbol{x}, t, \boldsymbol{\xi}^{(M)}\right) \end{bmatrix} \tag{14}$$

or in a compact form:

$$\boldsymbol{\Phi c} = \boldsymbol{y} \tag{15}$$

The vector of unknown coefficients $\boldsymbol{c}$ can be determined using the least-square approach.

$$\boldsymbol{c} = \left(\boldsymbol{\Phi}^T \boldsymbol{\Phi}\right)^{-1} \boldsymbol{\Phi}^T \boldsymbol{y} \tag{16}$$

Compared to projection-based NIPC method, this one requires well-placed random sampling points instead of quadrature abscissas. The influence of the number of sampling points can be analyzed by oversampling ratio n_p, defined as:

$$n_p = \frac{\text{number of points}}{N_c} \tag{17}$$

The oversampling ratio of 2 gives a better approximation at each polynomial degree (Hosder et al., 2007).

2.5 WORKFLOW OF NIPC METHOD

The workflow of UQ for CFD problems using NIPC method is summarized in Figure 1.

Step 1: Determine the distribution of random input variables and then compute the orthogonal polynomials. It is very difficult to obtain the distribution of all random variables accurately. It is necessary to assume that the random variables are independent and the distribution is known. If the distribution is classical, the orthogonal polynomials can be chosen from Table 1; otherwise, three-term recursion should be executed.

Step 2: Compute the points where the responses will be calculated using CFD method. In projection-based NIPC method, quadrature points and quadrature weights have to be solved, while in regression-based NIPC method, random sampling points should be well placed by effective sampling methods.

Step 3: Calculate the responses of interest for each points by CFD. This one is the most time-consuming. For one thing, many points are needed in the case with high order of PCE and multidimensional random variables. For another, the calculation costs a lot and there may be a lot of output parameters of interest for each point.

Step 4: Evaluate the coefficients and then compute the statistical characteristics of output parameters, such as EV and SD. After solving the coefficients via projection-based or regression-based NIPC method, the EV and SD of output variables of interest can be evaluated based on Equations 18 and 19. Other statistical characteristics, such as CDF and PDF can be reconstructed by using MC method.

$$\mu\left(\mathbf{x},t\right) = c_0\left(\mathbf{x},t\right) \tag{18}$$

$$\sigma^2\left(\mathbf{x},t\right) = \sum_{i=1}^{p} c_i^2\left(\mathbf{x},t\right)\left\langle \Phi_i^2\left(\boldsymbol{\xi}\right)\right\rangle \tag{19}$$

2.6 COMPARISON OF MC METHOD AND NIPC METHOD

MC method is a famous computational algorithm that uses random numbers to solve computational problems. It is considered to be a very effective method, especially when it is difficult or impossible to use other methods. MC method is widely used in optimization, numerical integration, and probability problems.

As for CFD UQ problems, the main steps of MC method are:
1) Determine the distribution of random variables;
2) Generating sampling points using MC method;
3) Perform CFD calculations at these sampling points;
4) Statistical properties such as EV and SD are obtained by statistical analysis of CFD results.

The EV and SD obtained by MC method are expressed as:

$$\mu\left(\boldsymbol{x},t\right) = \frac{\sum f\left(\boldsymbol{x},t,\boldsymbol{\xi}\right)}{N_{\text{runs}}} \tag{20}$$

$$\sigma^2\left(\boldsymbol{x},t\right) = \frac{\sum\left(f\left(\boldsymbol{x},t,\boldsymbol{\xi}\right)\text{-}\mu\left(\boldsymbol{x},t\right)\right)^2}{N_{\text{runs}}} \tag{21}$$

where N_{runs} is the number of CFD runs.

As mentioned above, the first three steps using MC method are necessary in applying regression-based NIPC method to UQ problems. As for post-processing, instead of statistical analysis of CFD results, regression-based NIPC solves a linear system based on these selected sampling points using least square method.

As two solutions for UQ problems, MC method and NIPC method have the following characteristics:

Both MC method and NIPC method do not need to change the solver, while IPC method requires much modifications of the codes.

MC method is straightforward and simple. It has a wide range of applications in science and is easy to implement. However, it requires a lot of computing resources and is usually not feasible for many practical engineering problems. Therefore, MC method is often regarded as a final resort to solving engineering problems.

Recently, NIPC method has drawn attention of a lot of researchers because of its high accuracy and low computational cost. It is more feasible from the engineering point of view.

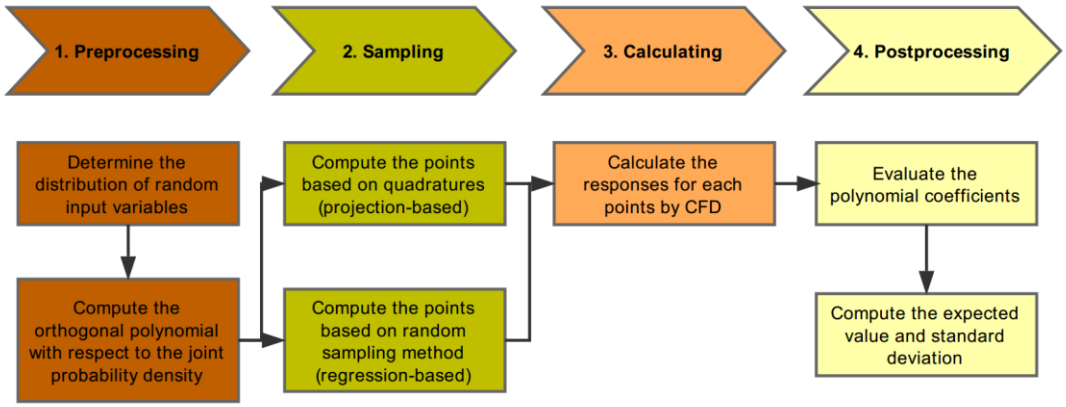

Figure 1. Workflow of NIPC methods

3 SAMPLING METHODS

In this paper, Latin hypercube sampling (LHS) is used to generate sampling points.

LHS is a stratified sampling method for generating sampling points from a multidimensional distribution. In statistical sampling, the Latin square array refers to a square matrix with only one sample per row and column. The Latin hypercube is a generalization of the Latin square in a multidimensional way. Each hyperplane perpendicular to the axis contains at most one sample. Assuming that there are N variables, each variable can be divided into M intervals with the same probability, then M sample points satisfying the Latin hypercube condition can be selected. It should be noted that LHS requires the same number of partitions for each variable as M. However, this method does not require that the number of samples M increases as the variable increases.

4 CASES FOR STUDY

4.1 GEOMETRY AND MAIN PARTICULARS

DTC is a 14,000 TEU container ship with a single propeller, a bulbous bow, large bow flare, and a transom stern (el Moctar et al, 2012). Hull lines and profile view of DTC are shown in Figure 2. In this paper, the bare hull of DTC model with a scale ratio 1:88.11 is selected for the simulation. Main particulars of the DTC model are listed in Table 2.

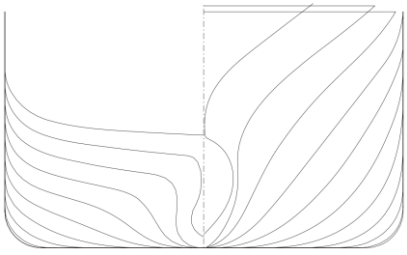

Figure 2. Body plans of DTC

Table 2. Main Particulars of DTC

Particular	Model
L_{pp} [m]	3.984
B [m]	0.572
T_{design} [m]	0.163
C_b [-]	0.661
m [kg]	242.8
x_G [m]	-0.052
z_G [m]	-0.059
I_{xx} [kg m^2]	12
I_{yy} [kg m^2]	221
I_{zz} [kg m^2]	230
GM [m]	0.058

4.2 CONDITIONS OF SIMULATIONS

The conditions of simulations in Table 3 are determined by the benchmark test case of the 5th MASHCON conference (Van Zwijnsvoorde et al., 2019). In this paper, the height and period of head waves are treated as stochastic variables with Gaussian distribution. The specific values of the wave height and wave period are obtained by the LHS method. If the polynomial chaos is expanded to 1st order, 6 sampling points are required with respect to two random variables, as shown in Table 4.

Table 3. Conditions of simulations

Particular	Value
Wave direction	Head waves
UKC (%)	100
Ship speed [m/s]	0.872
λ/L_{pp}	0.55
Wave height [mm]	62.35±0.64
Wave period [s]	1.38±0.01

Table 4. Sampling points using LHS

	Wave height [mm]	Wave period [s]
Case1	61.305	1.377
Case2	62.204	1.374
Case3	63.584	1.389
Case4	62.380	1.395
Case5	62.880	1.369
Case6	61.752	1.380

5 CFD METHOD

In this paper, CFD computations are performed with the general software STAR-CCM+.

5.1 GOVERNING EQUATIONS AND PHYSICS MODELLING

The flow in the captive tests are treated as a three-dimensional incompressible viscous flow. The governing equations are the continuity equation and Reynolds Averaged Navier-Stokes (RANS) equations.

Finite volume method is used in the employed solver. The continuity and momentum equations are linked by using a predictor–corrector approach in the RANS solver. The SST k-ω turbulent model is used to close the governing equations. The equations of the segregated flow are solved using uncoupled method in the RANS solver. Second-order upwind scheme is applied to discretize convection terms. The overall solution is implemented by SIMPLE algorithm.

The Volume of Fluid (VOF) method is adopted to model the free surface of a regular wave. In this paper, 1st-order wave is adopted. Dynamic Fluid Body Interaction (DFBI) module is used to simulate the motion of ship. The DFBI module enables the solver to calculate the hydrodynamic forces on the DTC model and solve the governing equations of rigid body motion. The DFBI morphing module is adopted in this paper.

5.2 COMPUTATIONAL DOMAIN AND BOUNDARY CONDITIONS

To solve a physical problem by CFD methods, it is necessary to define the initial and boundary conditions depending on the mechanisms in the problem in order to obtain accurate results. The computational domain and boundary conditions with the DTC model is shown in Figure 3. A velocity inlet boundary condition is set on the inflow plane in the positive x-direction, where head waves are generated. The outflow plane is modelled as a pressure outlet, which can prevent backflow and keep static pressure accurate. The inlet boundary and outlet boundary are positioned $1.5L_{pp}$ and $3L_{pp}$ ahead and behind the hull respectively. The top boundary is also modelled as a velocity inlet for purpose of numerical efficiency and convergence. The bottom and side boundaries are set as a moving no-slip wall in order to study the shallow-water and bank effects. The ship hull is set as the no-slip wall. Since only the condition of the ship in forward motion is considered, the flow field on both sides of the ship is symmetrical. It is reasonable to consider only half of the ship. Correspondingly, the plane that coincides with the longitudinal center plane of the hull is modelled as a symmetry boundary. The VOF wave damping module is applied in order to prevent wave reflection. The damping length is approximately $1.5L_{pp}$ (5.976 m).

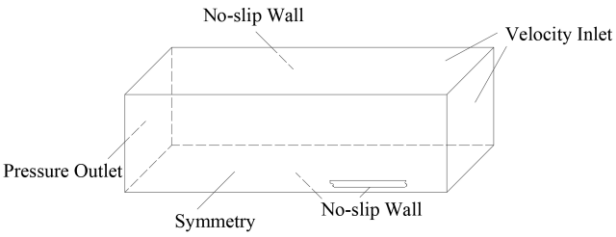

Figure 3. Computational domain and its boundaries

5.3 MESH GENERATION

The trimmed cell mesher in STAR-CCM+ is used to generate mesh, which is a useful tool for producing a high-quality unstructured hexahedral grid. The mesh in the area around the hull and the expected free surface is refined progressively in order to capture the complex flow features appropriately. Prism layer mesher is used to generate boundary layer grids adjacent to the surface of the hull, seabed and bank. The y^+ value of the hull surface is less than 1, while the y^+ value of the seabed/bank is larger than 30.

Figure 4 provides a cross-sectional look at the mesh inside the computational domain. Figure 5 depicts an entire view of the mesh around the free surface, and the free surface mesh has refinements in the areas where the Kelvin waves are expected. Figure 6 displays the surface mesh on the bow and stern of the hull. The mesh density on the surface of the bare hull is refined, to capture the near wall flow accurately.

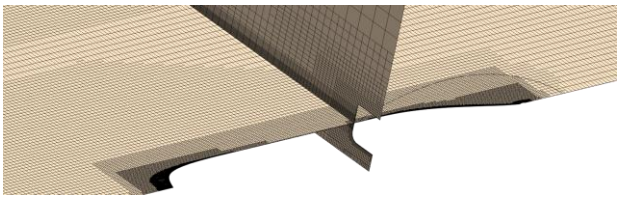

Figure 4. The volume mesh inside the domain

Figure 5. The volume mesh around the free surface

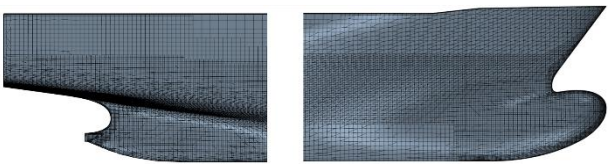

Figure 6. Surface mesh on the bow and stern of the bare hull

6 VALIDATION OF NIPC METHOD

Due to the time-consuming CFD calculations in reality, it is difficult to conduct large-scale random experiments and solve the UQ problems. In order to demonstrate the validity of the NIPC method, this section introduces an exponential function as a test case for UQ (Feinberg and Langtangen, 2015). The results obtained by regression-based NIPC method are compared with ones obtained by MC method.

6.1 TEST FUNCTION

A model function is defined as follows:

$$f(x) = ae^{-bx}, \quad x \in [0,10] \tag{22}$$

$f(x)$ can be assumed as a wrapper for some larger numerical solver. The parameters a and b in Equation (22) are unknown, but their probability distributions are given.

$$\begin{cases} a \sim U(1,2) \\ b \sim U(0.1,0.2) \end{cases} \tag{23}$$

The goal is to describe the behavior of uncertainty propagation via $f(x)$ function. The EV and SD of the function value are investigated.

6.2 RESULTS OF TESTCASE

In this case, the order of polynomial chaos is expanded to 2nd order. Sampling points, the values of stochastic variables a and b, are generated by LHS method.

The results obtained by MC and NIPC methods are shown in Figures 7-10. The numbers of sampling points are 6, 72 400, 1000 respectively. The sub-figures of relative error show that the relative differences of two UQ methods, MC and NIPC, are gradually decreasing with the increase of sampling points. It can be seen from Figure 11 that the convergence of MC method is much slower than the regression-based NIPC method. When the sampling points exceed 100, the results obtained by regression-based NIPC method are basically stable.

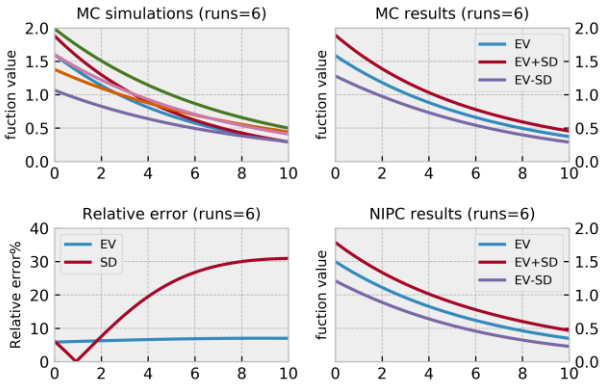

Figure 7. Results based on 6 sets of (a, b)

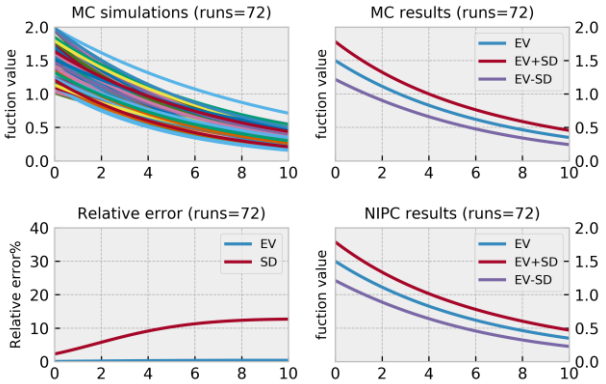

Figure 8. Results based on 72 sets of (a, b)

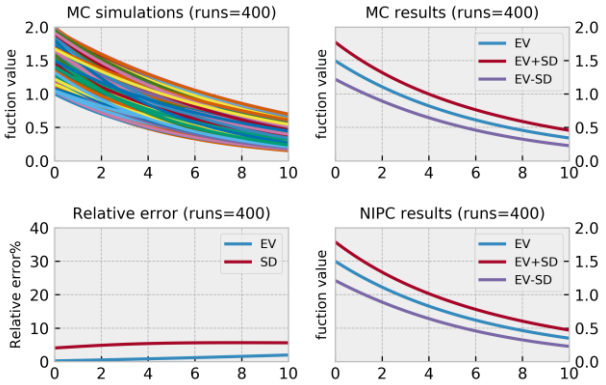

Figure 9. Results based on 400 sets of (a, b)

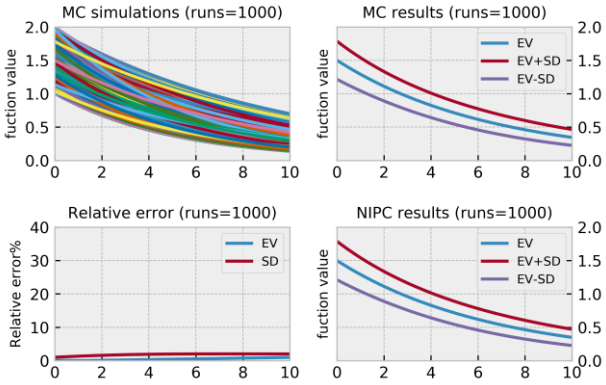

Figure 10. Results based on 1000 sets of (a, b)

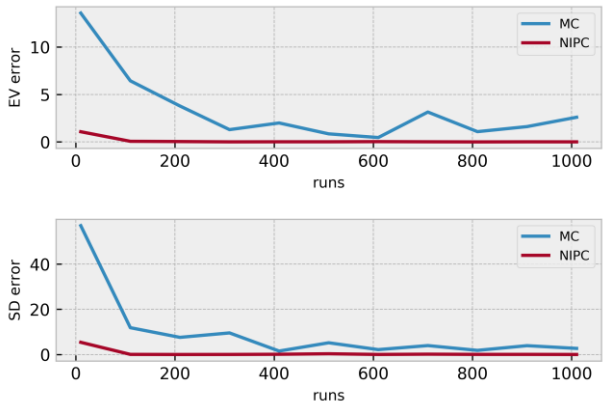

Figure 11. Comparison of convergence

7 RESULTS AND DISCUSSIONS

In this section, regression-based NIPC method is used to quantify the resistance, the RAO of heave and pitch motion of DTC model in shallow water waves. The polynomial chaos with two random parameters is expanded to 1st order. According to Equation (8), there are three unknown coefficients. As demonstrated (Hosder et al., 2007), six sampling points are generated, on which CFD simulations are carried out. The flow field details are shown in Section 7.1, taking one of six cases as an example. The results of UQ are displayed and discussed in Section 7.2.

7.1 DETAILS OF FLOW FIELD

Figure 12 shows that the y^+ of the surface of DTC model is small (less than 1), which means cells around the hull can be resolved directly without wall treatment.

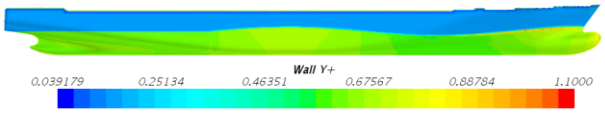

Figure 12. Wall y^+ on hull surface

Figure 13 illustrates the wave patterns around the DTC model at depth Froude number 0.488 and λ/L_{pp}=0.55 in one encounter period, where the model is free to heave and pitch. This figure is obtained based on symmetry (half ship mirrored). As can be seen, the waves generated by the hull with forward speed in shallow water waves are clearly visible while the waves reflected from the side wall of the tank are not obvious. This shows that the bank effect is not significant in this case.

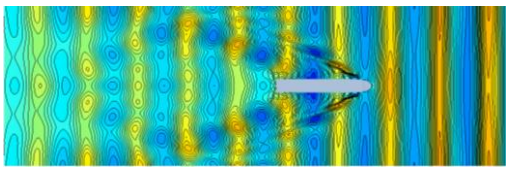

(a) $t/T_e = 0$

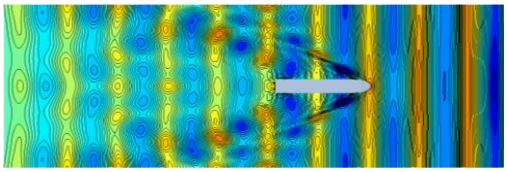

(b) $t/T_e = 0.25$

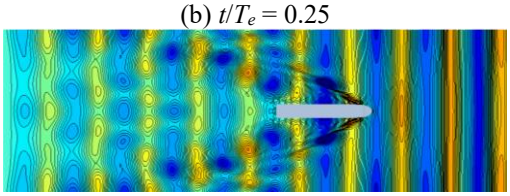

(c) $t/T_e = 0.5$

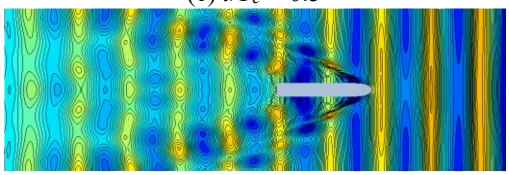

(d) $t/T_e = 0.75$

Figure 13. Wave patterns in one encounter period

Figure 14 shows the free surface elevation around the DTC model and the pressure distribution on the surface of the hull in one encounter period. The periodic pressure difference between the bow and stern of the hull will cause the pitch motion.

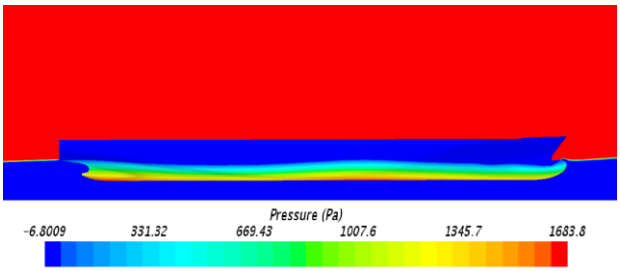

(a) $t/T_e = 0$

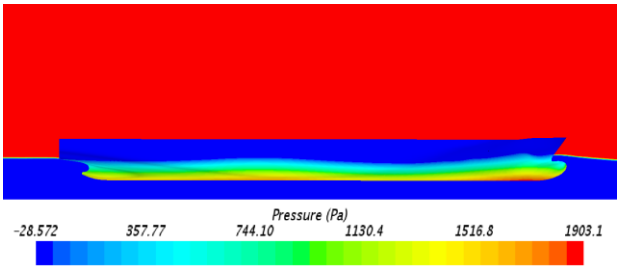

(b) $t/T_e = 0.25$

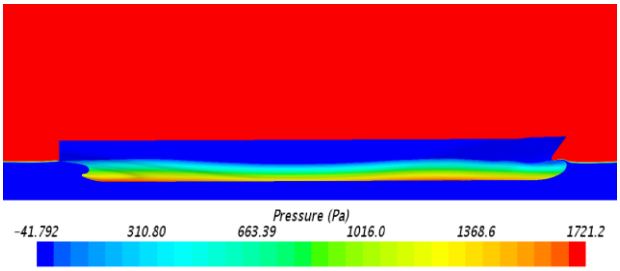

(c) $t/T_e = 0.5$

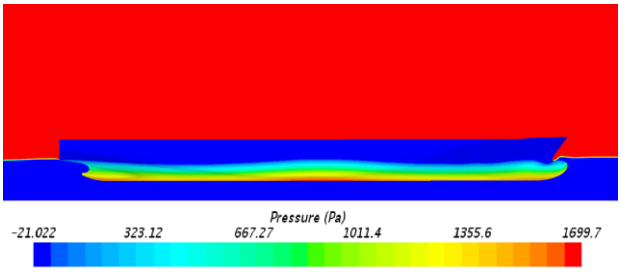

(d) $t/T_e = 0.75$

Figure 14. The free surface elevation and pressure distributions on the hull in one encounter period

7.2 UQ RESULTS

In this subsection, the EFD and CFD results of heave motion, pitch motion and total resistance are post-processed. The least-square method is used to fit the data series of heave/pitch motion. The total resistance refers to the average longitudinal force on the hull. The statistical properties of these variables are obtained by MC method and regression-based NIPC method according to the CFD results. Finally, the UQ results obtained from the EFD and CFD data are compared.

Figures 15 and 16 show the EFD/CFD data and the fitted sine curves, respectively. After obtaining the fitted sinusoid, the RAO of heave and pitch motion can be calculated by the amplitude of sine curve:

$$\mathrm{RAO}_{\mathrm{heave}} = \frac{z_1}{A}, \quad \mathrm{RAO}_{\mathrm{pitch}} = \frac{\theta_1}{AK} \tag{24}$$

where z_1 is the amplitude of heave motion (m), θ_1 is the amplitude of pitch motion (rad), A is the wave amplitude (m) and K is wave number (m^{-1}).

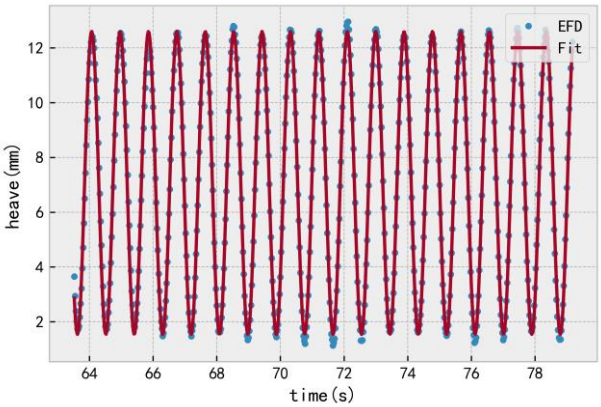

(a) Heave motion

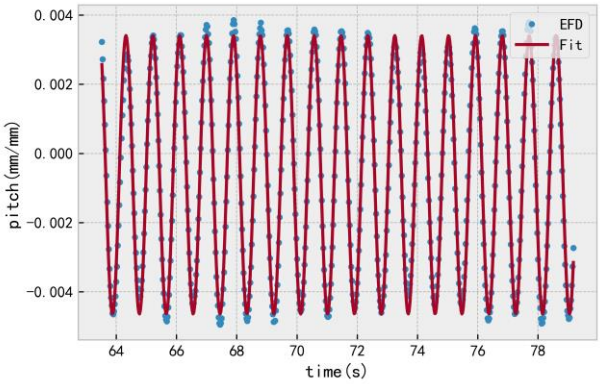

(b) Pitch motion

Figure 15. Time series of EFD data

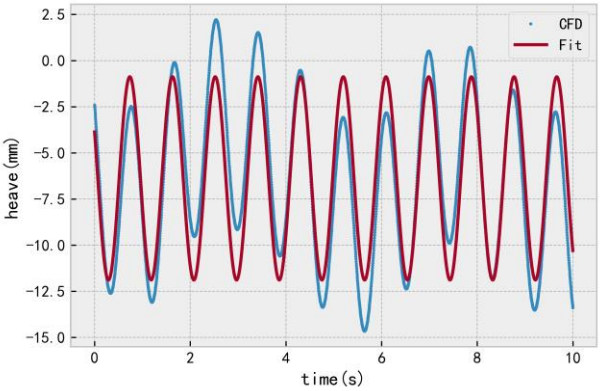

(a) Heave motion

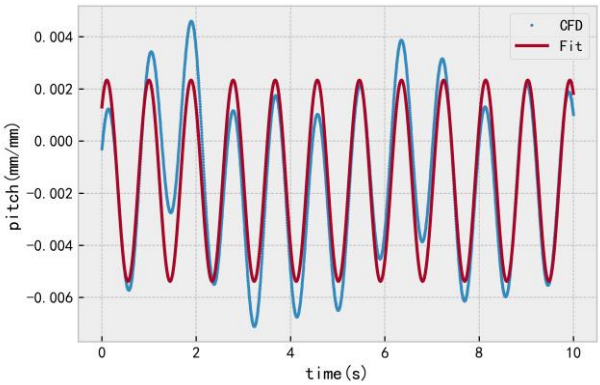

(b) Pitch motion

Figure 16. Time series of CFD data in Case1

Table 5 lists the results of CFD simulations on sampling points. The comparison error and the statistical characteristics obtained by MC method and NIPC method are shown in Tables 6-8, where the comparison error $E\%D$ is defined as follow:

$$E\%D = \frac{D - S}{D} \times 100 \tag{25}$$

where D is the EFD value; S is the value obtained by MC/NIPC method.

Table 5. EFD data and CFD results

	RAO_{heave} [-]	RAO_{pitch} [-]	X [N]
EFD	0.1775	0.0450	-7.2670
Case1	0.1765	0.0432	-6.8951
Case2	0.1761	0.0438	-7.0056
Case3	0.1907	0.0422	-6.8918
Case4	0.1898	0.0400	-6.8447
Case5	0.1729	0.0445	-7.1009
Case6	0.1799	0.0427	-6.8869

Table 6. RAO_{heave} results obtained by MC and NIPC

	EV	SD	E%D
EFD	0.1775	-	-
MC	0.1810	0.0069	1.995
NIPC	0.1804	0.0072	1.664

Table 7. RAO_{pitch} results obtained by MC and NIPC

	EV	SD	E%D
EFD	0.0450	-	-
MC	0.0427	0.0014	5.127
NIPC	0.0429	0.0017	5.826

Table 8. X results obtained by MC and NIPC

	EV	SD	$E\%D$
EFD	-7.2670	-	-
MC	-6.9375	0.0879	4.534
NIPC	-6.9453	0.1012	4.427

In order to demonstrate the results more visually, the data in Tables 6-8 are displayed in Figure 17. It can be seen that the EV of RAO_{heave}, RAO_{pitch} and X obtained by NIPC method is closer to experimental value than MC method. It should be noted that the error bar shown in the figure does not refer to the uncertainty from the numerical calculation, but indicates the randomness from the input variables, including wave height and wave period. Unfortunately, the SD of CFD results cannot be compared with those of EFD data because the experiment did not consider the uncertainty of the parameters.

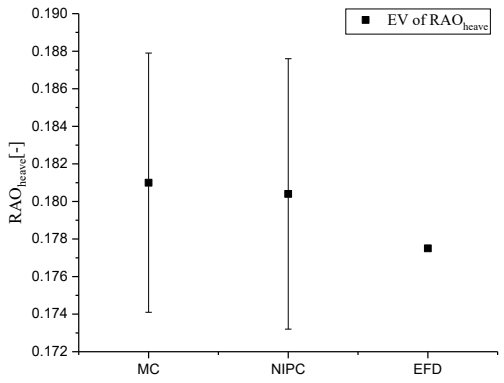

(a) Statistical properties of RAO_{heave}

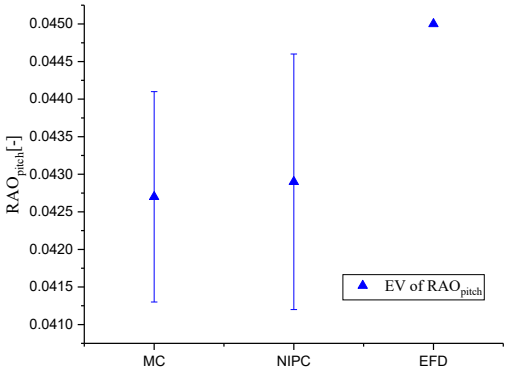

(b) Statistical properties of RAO_{pitch}

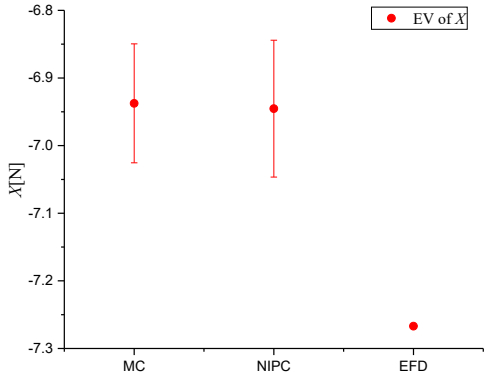

(c) Statistical properties of X

Figure 17. Statistical properties of output variables

8 CONCLUSIONS

In this paper, V&V and UQ for CFD uncertainty problems are investigated. A state-of-the-art method for uncertainty quantification problems, non-intrusive polynomial chaos (NIPC) method, is introduced in detail. In order to prove the validity of NIPC method, a UQ problem for an exponential function with two random parameters is studied using NIPC method and MC method. The results show that NIPC method is much better than MC method.

As for CFD UQ problems, stochastic RANS-based simulations for the DTC model advancing at 100% UKC in shallow water waves are carried out, considering its dynamic heave and pitch motion. The uncertainty induced

by waves treated as stochastic variables with Gaussian distribution is studied. The results of RAO_{heave}, RAO_{pitch} and X obtained by NIPC method show better agreement with the benchmark data than those by MC method.

However, the benchmark data were obtained from experiment which was carried out deterministically, so that the SD (namely error bar) cannot be compared with the benchmark data.

On-going and future work includes studying the effect of order of polynomial chaos expansion on the propagation of uncertainty, comparing projection-based NIPC method and regression-based NIPC method, extending the present case to a more realistic problem, considering more stochastic input variables, such as main particulars of the hull and boundary conditions.

9 ACKNOWLEDGEMENTS

This work is supported by the National Natural Science Foundation of China (Grant No: 51779140).

10 REFERENCES

Ahlfeld, R., Carnevale, M., Salvadori, S., Montomoli, F., 2017. An autonomous uncertainty quantification method for the digital age: transonic flow simulations using multivariate Pade approximations, in: Proceedings of ASME Turbo Expo 2017: Turbomachinery Technical Conference and Exposition. Charlotte, NC, USA, V02CT47A023-V02CT47A023.
https://doi.org/10.1115/gt2017-64968

Ahlfeld, R., Montomoli, F., 2017. A single formulation for uncertainty propagation in turbomachinery: SAMBA PC. J Turbomach. 139(11): 111007.
https://doi.org/Artn 11100710.1115/1.4037362

Ahlfeld, R., Montomoli, F., Carnevale, M., Salvadori, S., 2018. Autonomous uncertainty quantification for discontinuous models using multivariate Pade approximations. J Turbomach. 140(4): 041004.
https://doi.org/Artn 04100410.1115/1.4038826

Carrica, P.M., Mofidi, A., Eloot, K., Delefortrie, G., 2016. Direct simulation and experimental study of zigzag maneuver of KCS in shallow water. Ocean Eng. 112, 117–133.
https://doi.org/10.1016/j.oceaneng.2015.12.008

Deng, G., Leroyer, A., Guilmineau, E., Queutey, P., Visonneau, M., Wackers, J., 2016. CFD simulation of PMM motion in shallow water for the DTC container ship, in: Proceedings of 4th International Conference on Ship Manoeuvring in Shallow and Confined Water with Special Focus on Ship Bottom Interaction. Hamburg, Germany, pp. 93–98.
https://doi.org/10.18451/978-3-939230-38-0

Diez, M., He, W., Campana, E.F., Stern, F., 2014. Uncertainty quantification of Delft catamaran resistance, sinkage and trim for variable Froude number and geometry using metamodels, quadrature and Karhunen–Loève expansion. J. Mar. Sci. Technol. 19, 143–169.
https://doi.org/10.1007/s00773-013-0235-0

El Moctar, O., Shigunov, V., Zorn T., 2012. Duisburg Test Case: Post-Panamax container ship for benchmarking. Ship Technol. Res. 59(3), 50-64.
https://doi.org/10.1179/str.2012.59.3.004

Feinberg, J., Langtangen, H.P., 2015. Chaospy: An open source tool for designing methods of uncertainty quantification. J. Comput. Sci. 11, 46–57.
https://doi.org/10.1016/j.jocs.2015.08.008

Ghanem, R.G., Spanos, P.D., 1991. Stochastic Finite Elements: A Spectral Approach. Springer Berlin 224.
https://doi.org/10.1007/978-1-4612-3094-6

He, W., Diez, M., Campana, E.F., Stern, F., Zou, Z.J., 2013. A one-dimensional polynomial chaos method in CFD-based uncertainty quantification for ship hydrodynamic performance. J. Hydrodyn. 25, 655–662.
https://doi.org/10.1016/S1001-6058(13)60410-2

Hosder, S., Walters, R., Perez, R., 2006. A non-intrusive polynomial chaos method for uncertainty propagation in CFD simulations, in: Proceedings of 44th AIAA Aerospace Sciences Meeting and Exhibit. Reno, Nevada, USA, pp. 891.
https://doi.org/10.2514/6.2006-891

Hosder, S., Walters, R., Balch, M., 2007. Efficient sampling for non-intrusive polynomial chaos applications with multiple uncertain input variables, in: Proceedings 48th AIAA/ASME/ASCE/AHS/ASC Structures, Structural Dynamics, and Materials Conference. Honolulu, Hawaii, USA, pp. 1939.
https://doi.org/10.2514/6.2007-1939

Hosder, S., Walters, R., 2010. Non-intrusive polynomial chaos methods for uncertainty quantification in fluid dynamics, in: Proceedings of 48th AIAA Aerospace Sciences Meeting Including the New Horizons Forum and Aerospace Exposition. Orlando, Florida, USA, pp. 129.
https://doi.org/10.2514/6.2010-129

Jachowski, J., 2008. Assessment of ship squat in shallow water using CFD. Arch. Civ. Mech. Eng. 8, 27–36.
https://doi.org/10.1016/s1644-9665(12)60264-7

Lacor, C., Dinescu, C., Hirsch, C., Smirnov, S., 2013. Implementation of intrusive polynomial chaos in CFD codes and application to 3D Navier-Stokes, in: Uncertainty Quantification in Computational Fluid Dynamics. pp. 193–223.
https://doi.org/10.1007/978-3-319-00885-1_5

Lacor, C., Smirnov, S., 2007. Uncertainty propagation in the solution of compressible Navier-Stokes equations using polynomial chaos decomposition, in: Proceedings of NATO AVT Symposium. Athens, Greece, pp. 13.

Lacor, C., Smirnov, S., 2008. Non-deterministic compressible Navier-Stokes simulations using polynomial chaos, in: Proceedings of 5th European Congress on Computational Methods in Applied Sciences and Engineering. Lido Island, Venezia, Italy.

Liu, Y., Zou, Z.J., Zou, L., 2016. RANS-based numerical simulation of captive model tests in shallow water for the DTC container carrier, in: Proceedings of 4th International Conference on Ship Manoeuvring in Shallow and Confined Water with Special Focus on Ship Bottom Interaction. Hamburg, Germany, pp. 73–82. https://doi.org/10.18451/978-3-939230-38-0

Loeven, G.J.A., Witteveen, J.A.S., Bijl, H., 2007. Probabilistic collocation: An efficient non-intrusive approach for arbitrarily distributed parametric uncertainties, in: Proceedings of 45th AIAA Aerospace Sciences Meeting and Exhibit. Reno, Nevada, USA, pp. 317. https://doi.org/10.2514/6.2007-317

Loeven, G.J.A., 2010. Efficient uncertainty quantification in computational fluid dynamics. TU Delft.

Mathelin, L., Hussaini, M.Y., 2003. Uncertainty quantification in CFD simulations: A stochastic spectral approach. J. Comput. Fluid Dyn. 2002 65–70. https://doi.org/10.1007/978-3-642-59334-5_5

Mathelin, L., Hussaini, M.Y., Zang, T.A., 2005. Stochastic approaches to uncertainty quantification in CFD simulations. Numer. Algorithms 38, 209–236. https://doi.org/DOI 10.1007/s11075-004-2866-z

Salehi, S., Raisee, M., Cervantes, M.J., Nourbakhsh, A., 2017a. Efficient uncertainty quantification of stochastic CFD problems using sparse polynomial chaos and compressed sensing. Comput. Fluids 154, 296–321. https://doi.org/10.1016/j.compfluid.2017.06.016

Salehi, S., Raisee, M., Cervantes, M.J., Nourbakhsh, A., 2017b. The effects of inflow uncertainties on the characteristics of developing turbulent flow in rectangular pipe and asymmetric diffuser. J. Fluids Eng. ASME 139. https://doi.org/Artn 04140210.1115/1.4035302

Schmelter, S., Fiebach, A., Model, R., Bar, M., 2015. Numerical prediction of the influence of uncertain inflow conditions in pipes by polynomial chaos. Int. J. Comut. Fluid Dyn. 29, 411–422. https://doi.org/10.1080/10618562.2015.1112899

Schmelter, S., Fiebach, A., Weissenbrunner, A., 2016. Polynomial chaos for uncertainty quantification in flow simulations for metrological applications. Tech. Messen. 83, 71–76.

Senthil, P.N., Chandra, B., 2013. Numerical estimation of shallow water resistance of a river-sea ship using CFD. Int. J. Comput. Appl. 71, 33–40. https://doi.org/10.5120/12357-8670

Stern, F., Volpi, S., Gaul, N.J., Choi, K.K., Diez, M., Broglia, R., Durante, D., Campana, E., Iemma, U., 2017. Development and assessment of uncertainty quantification methods for ship hydrodynamics, in: Proceedings of 55th AIAA Aerospace Sciences Meeting. Grapevine, Texas, USA, pp. 1654. https://doi.org/10.2514/6.2017-1654

Terziev, M., Tezdogan, T., Oguz, E., Gourlay, T., Demirel, Y.K., Incecik, A., 2018. Numerical investigation of the behaviour and performance of ships advancing through restricted shallow waters. J. Fluids Struct. 76, 185–215. https://doi.org/10.1016/j.jfluidstructs.2017.10.003

Tezdogan, T., Incecik, A., Turan, O., 2016a. A numerical investigation of the squat and resistance of ships advancing through a canal using CFD. J. Mar. Sci. Technol. 21(1), 86–101. https://doi.org/10.1007/s00773-015-0334-1

Tezdogan, T., Incecik, A., Turan, O., 2016b. Full-scale unsteady RANS simulations of vertical ship motions in shallow water. Ocean Eng. 123, 131–145. https://doi.org/10.1016/j.oceaneng.2016.06.047

Van Zwijnsvoorde, T., Tello Ruiz, M., Delefortrie, G., Lataire, E. 2019. Sailing in shallow water waves with the DTC container carrier, in: Proceedings of the 5th International Conference on Ship Manoeuvring in Shallow and Confined Water with non-exclusive focus on Manoeuvring in Waves, Wind and Current. Ostend, Belgium.

Wang, X.D., Hirsch, C., Liu, Z.Y., Kang, S., Lacor, C., 2013. Uncertainty-based robust aerodynamic optimization of rotor blades. Int. J. Numer. Methods Eng. 94, 111–127. https://doi.org/10.1002/nme.4438

Wang, X.D., Kang, S., 2010. Application of polynomial chaos on numerical simulation of stochastic cavity flow. Sci. China-Technological Sci. 53, 2853–2861. https://doi.org/10.1007/s11431-010-4097-y

Wiener, N., 1938. The homogeneous chaos. Am. J. Math. 60(4), 897–936.

Xiu, D., Karniadakis, G.E., 2002a. The Wiener--Askey polynomial chaos for stochastic differential equations. Siam J. Sci. Comput. pp. 619–644. https://doi.org/10.21236/ada460654

Xiu, D., Karniadakis, G.E., 2002b. Modeling uncertainty in steady state diffusion problems via generalized polynomial chaos. Comput. Methods Appl. Mech. Eng. 191(43), 4927–4948.
https://doi.org/10.21236/ada460658

Xiu, D., Karniadakis, G.E., 2003. Modeling uncertainty in flow simulations via generalized polynomial chaos. J. Comput. Phys. 187, 137–167.
https://doi.org/10.21236/ada461813

Xiu, D., Lucor, D., Su, C.H., Karniadakis, G.E., 2002. Stochastic modeling of flow-structure interactions using generalized polynomial chaos. J. Fluids Eng. Trans. ASME. 124(1), 51–59.
https://doi.org/10.21236/ada461832

11 AUTHORS BIOGRAPHY

Li Xia holds the current position of PhD student at School of Naval Architecture, Ocean and Civil Engineering, Shanghai Jiao Tong University. His previous experience includes numerical studies on the ship manoeuvring in restricted waters, uncertainty quantification, etc.

Shuai Yuan holds the current position of master student at School of Naval Architecture, Ocean and Civil Engineering, Shanghai Jiao Tong University. His previous experience includes numerical studies on the ship manoeuvring in restricted waters, seakeeping, etc.

Zaojian Zou holds the current position of full professor at School of Naval Architecture, Ocean and Civil Engineering, Shanghai Jiao Tong University. He is responsible for teaching and studying ship hydrodynamics and ship's steering and control. His previous experience includes PI of some projects on manoeuvring and control of ships and other marine vehicles. He was a member of the 22nd, 23rd, 25th and 26th ITTC MC.

Lu Zou is a lecturer at School of Naval Architecture, Ocean and Civil Engineering, Shanghai Jiao Tong University. Her major research interest is in the ship manoeuvring in confined waters, as well as Verification and Validation in CFD simulations.

Paper - 43

MANEUVERING HYDRODYNAMIC DERIVATIVES AND COURSE STABILITY OF A SHIP CLOSE TO A BANK

Hironori Yasukawa,
Department of Transportation and Environmental Systems, Hiroshima University, Japan

MANEUVERING HYDRODYNAMIC DERIVATIVES AND COURSE STABILITY OF A SHIP CLOSE TO A BANK

Hironori Yasukawa, Department of Transportation and Environmental Systems, Hiroshima University, Japan

SUMMARY

Captive model tests are conducted for a pure car carrier in the proximity of a bank with variations in water depth, distance between ship hull and bank, hull drift angle and heel angle. Using the hydrodynamic derivatives obtained, the check helm and hull drift angle required at equilibrium conditions are estimated. Course stability of the ship sailing in the proximity of the bank is also studied based on a simplified analysis method. In h/d =1.2 where h/d means ratio of water depth h to ship draft d, the check helm of the ship reaches 35° near η_0/L =0.27 where η_0 is the distance between the ship center line and the bank. Although this ship is course unstable in case of no rudder control, the ship becomes course stable in any water depths by employing the autopilot with appropriate control gains. The present analysis method is useful for conventionally assessing the course stability of a ship in the proximity of a bank.

1 INTRODUCTION

The recent enlargement of the ships forces ships sometimes to sail close to banks in ports and channels. For checking the navigational safety of a ship sailing in such restricted water area, on the assumption that the ship moves in parallel to the bank, the following investigation is conducted:

1. Calculating the equilibrium condition of the ship (check helm, hull drift angle, etc.) required for course keeping of the ship sailing close to a bank.
2. Confirming the dynamic yaw stability (course stability) of the ship at the equilibrium condition.

Fujino (1968)(1970) measured the hydrodynamic forces acting on a ship moving in a channel with changing parameters such as water depth, distance from the ship to the centerline of the channel, hull drift angle, rudder angle, etc. in tank tests. Based on the measured results, check helm and hull drift angle required for overcoming the bank suction force were calculated, and the course stability of a ship moving in the centerline of the channel was theoretically investigated. Eda (1971) carried out a similar study, and discussed a guideline to indicate acceptable ship size relative to waterway dimensions. Sano et al. (2012)(2014) derived a course stability criterion for a ship off-centerline in a channel, and investigated the course stability for an inland container ship based on the measured hydrodynamic force derivatives of the ship moving in a channel with variation of the parameters mentioned above. There seems to be still few comprehensive studies about the navigation safety of the ship with inclusion of detailed hydrodynamic force data, discussions about the equilibrium conditions and course stability analysis, although there are many studies about the force prediction of ships in restricted water (Norrbin, 1974), (Li, et al., 2003), (Vantorre et al., 2003), (Lataire and Vantorre, 2008), (Yasukawa et al., 2009), (Zou et al., 2011).

In this paper, an analysis of the course stability is presented for a pure car carrier (PCC) in proximity of a bank. The analysis is based on the method proposed by Sano et al. (2014), however, a modification is made to the method to treat the problem conventionally. For the analysis, the hydrodynamic derivatives are required. To capture those, captive model tests are performed in deep and shallow water. Oblique towing test (OTT) and circular motion test (CMT) are conducted. To know the heel effect on the derivatives in shallow water, OTT and CMT are also conducted with variation of the heel angle of the ship model. Heel-related derivatives in shallow water were not published so far, although the heel-related derivatives have been indicated in deep water by, for instance, Yasukawa and Yoshimura (2014). Further, OTT is conducted for capturing bank effect on the derivatives. Using the derivatives obtained, the course stability is analyzed for the PCC close to the bank. The present analysis method is useful for conventionally capturing the course stability of the ship in the proximity of a bank.

2 HULL FORCE MODEL OF A SHIP IN CLOSE PROXIMITY TO A BANK

2.1 COORDINATE SYSTEMS

Fig. 1 shows the coordinate systems and notation used in this paper. Consider a ship moving close to a bank. The ship moves in a straight line along the bank wall. It is supposed that the bank's horizontal shape is uniform, and the bank is starboard of the ship. The bank wall inclines 45° as shown in Fig.1 (left). The water depth h is assumed to be constant.

Consider the space fixed coordinate system $o_0 - x_0 y_0 z_0$ where the $x_0 - y_0$ plane coincides with the still water surface and the z_0-axis is taken vertically downwards. The x_0-axis is taken in parallel to the bank wall with a distance W from the bank toe at the sea bottom as shown in Fig.1. s is the distance from the bank toe to the ship side. The y_0-axis is taken laterally as being the right-handed system. The ship is assumed to sail only in the region of $y_0 \geq 0$. If sailing in the region of $y_0 < 0$, the bank effect vanishes.

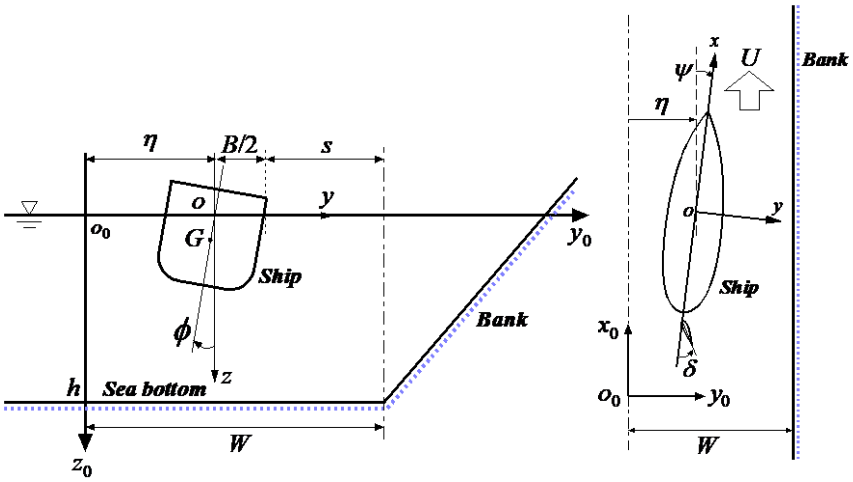

Figure 1. Coordinate systems and notations (left: vertical ship section view, right: horizontal plane view)

In addition, consider the horizontal body-fixed coordinate system (Hamamoto and Kim, 1993) $o-xyz$. The x-axis is taken toward ship's bow direction, the y-axis is taken laterally and the z-axis vertically downwards. The $x-y$ plane also coincides with the still water surface. Therefore, the origin o is located at the midship position on the still water surface. The heading angle ψ is defined as the direction between x_0-axis and x-axis, and the roll angle is denoted by ϕ. Clockwise rotation is positive for roll when looking from ship's stern to the fore direction. u and v denote the velocity components of x -axis and y -axis directions respectively, and r the yaw rate around z -axis. δ denotes the rudder angle. The center of gravity G is approximately located at the position $(x_G, 0, z_G)$. Then, the lateral velocity component at midship position v_m is expressed as:

$$v_m = v - x_G r + z_G \dot{\phi} \tag{1}$$

Total velocity U is defined as $U = \sqrt{u^2 + v_m^2}$, and the hull drift angle at midship position β is evaluated by $\beta = \tan^{-1}(-v_m/u)$. Note that ψ coincides with β when the ship moves to the direction of x_0-axis as shown in Fig.1. Lateral deviation of the ship centerline at midship position from x_0-axis is denoted by η. Between η and the velocity components, u and v_m, the following relation is hold as

$$\dot{\eta} = u \sin\psi + v_m \cos\psi \tag{2}$$

Here, the dot notation is used to represent the ordinary differential with respect to time *t*.

2.2 HULL HYDRODYNAMIC FORCE MODEL

Hydrodynamic forces acting on ship hull (X_H, Y_H, N_H) are:

$$X_H = (1/2)\rho L d U^2 X'_H(v'_m, r', \phi, \eta')$$
$$Y_H = (1/2)\rho L d U^2 Y'_H(v'_m, r', \phi, \eta')$$
$$N_H = (1/2)\rho L^2 d U^2 N'_H(v'_m, r', \phi, \eta') \tag{3}$$

where ρ, L and d are water density, ship length and ship draft, respectively. v'_m is defined by v_m/U. r' is defined by rL/U and η' is defined by η/L. Here, X'_H, Y'_H, and N'_H are expressed as:

$$\begin{aligned} X'_H(v'_m, r', \phi, \eta') &= -R'_0 + X'_{vv} v'^2_m + X'_{vr} v'_m r' \\ &+ X'_{vvvv} v'^4_m + X'_{v\phi} v'_m \phi + X'_{r\phi} r' \phi + X'_{\phi\phi} \phi^2 + X'_{\eta\eta} \eta'^2 \\ &+ X'_{v\eta} v'_m \eta' \end{aligned} \tag{4}$$

$$\begin{aligned} Y'_H(v'_m, r', \phi, \eta') &= Y'_v v'_m + Y'_r r' + Y'_{vvv} v'^3_m + Y'_{vvr} v'^2_m r' \\ &+ Y'_\phi \phi + Y'_{vv\phi} v'^2_m \phi + Y'_{v\phi\phi} v'_m \phi^2 + Y'_{rr\phi} r'^2 \phi \\ &+ Y'_{r\phi\phi} r' \phi^2 + Y'_\eta \eta' + Y'_{\eta\eta\eta} \eta'^3 + Y'_{vv\eta} v'^2_m \eta' \\ &+ Y'_{v\eta\eta} v'_m \eta'^2 \end{aligned} \tag{5}$$

$$\begin{aligned} N'_H(v'_m, r', \phi, \eta') &= N'_v v'_m + N'_r r' + N'_{vvv} v'^3_m \\ &+ N'_{vvr} v'^2_m r' + N'_\phi \phi + N'_{vv\phi} v'^2_m \phi + N'_{v\phi\phi} v'_m \phi^2 \\ &+ N'_{rr\phi} r'^2 \phi + N'_{r\phi\phi} r' \phi^2 + N'_\eta \eta' + N'_{\eta\eta\eta} \eta'^3 \\ &+ N'_{vv\eta} v'^2_m \eta' + N'_{v\eta\eta} v'_m \eta'^2 \end{aligned} \tag{6}$$

R'_0 is the resistance coefficient in straight moving, and X'_{vv}, Y'_v, N'_v etc. are called hydrodynamic derivatives on maneuvering.

Roll moment except roll restoring moment K_H is expressed as (Hirano and Takashina, 1980):

$$K_H = -Y_H z_H \tag{7}$$

K_H is expressed by multiplying the lateral force Y_H to the vertical acting points z_H.

3 STUDIED SHIP

A pure car carrier (PCC) was selected as studied ship in this paper. Table 1 shows the principal particulars of the PCC. The load condition is full load, even keel. B denotes the breadth, ∇ the displacement volume, C_b the block coefficient, $\overline{GM}$ the metacentric height, $\overline{KM}$ the metacenter height above baseline, $A_R/(Ld)$ the rudder area ratio, and H_R the rudder span length. Fig. 2 shows the side view of the PCC model used in the tank tests.

Table 1. Principal particulars of a PCC

	Full-scale	Model
L (m)	180.00	2.000
B (m)	32.20	0.358
d (m)	8.20	0.091
∇(m^3)	26000	0.036
x_G (m)	-2.53	-0.028
C_b	0.547	0.547
$\overline{GM}$ (m)	1.25	0.014
$\overline{KM}$ (m)	15.60	0.173
$A_R/(Ld)$	1/39.5	1/39.5
H_R (m)	7.200	0.080

Figure 2. Side view of a PCC model

4 CAPTIVE MODEL TESTS

4.1 TESTS WITH VARIATION OF HEEL ANGLE IN SHALLOW WATER

To capture the heel effect on the hydrodynamic force characteristic in deep and shallow water, oblique towing test (OTT) and circular motion test (CMT) with variation of the heel angle were carried out in the Hiroshima University Towing Tank (length: 100 m, width: 8 m, water depth: 3.5 m). OTT and CMT are the tests to measure the hydrodynamic forces acting on the ship model in oblique moving and/or steady turning. The water depths were changed by a vertically moving bottom equipped to the tank as 38.5, 1.5 and 1.2 in h/d. The case of h/d =38.5 is called ``deep".

4.1 (a) Outline

The tests were carried out using a PCC model shown in Fig. 2 in the condition with rudder and without propeller. In the tests, surge force (X_H), lateral force (Y_H), yaw moment around midship (N_H) and roll moment (K_H) were measured for a fixed model in the motions using a four-component dynamometer. The roll moment was measured only in case of ϕ =0°. Ship speed U in the deep water was 0.651 m/s (equivalent to 12.0 kn for full-scale ship, F_n =0.147), and the speed in h/d =1.5 and 1.2 was 0.325-m/s (equivalent to 6.0 kn for full-scale ship, F_n =0.074). The measurements were made for the hull drift angle β from −20° to 20° every 5°, non-dimensional yaw rate r' from −0.3 to 0.3 with the step 0.1, and heel angle ϕ of 0°, 5° and 10°.

The four-component dynamometer was arranged above the still water surface since internal space of the ship model was limited. Then, the moment component due to centrifugal force (inertia force component) is induced in the measured roll moment, which was deducted from the measured roll moment using other measured force components. By converting the resulting roll moment, the roll moment around x-axis located on the still water surface was obtained. Static restoring roll moment was deducted from the results.

4.1 (b) Test results

Figs.3 ~ 5 show the surge force, the lateral force and yaw moment coefficients (X'_H, Y'_H and N'_H) of ϕ =0° and 10° in three different water depths. In the figures, dotted lines represent the fitting results using Eqs.(4) to (6). Table 2 shows the hydrodynamic derivatives obtained. Absolute values of Y'_v, N'_v and N'_r increase with decrease of water depth. This is a typical shallow-water effect in the hydrodynamic derivatives. In addition, absolute values of Y'_ϕ and N'_ϕ also increase with decrease of water depth.

Next, we consider the vertical acting point of the hull lateral force. Fig.6 shows the roll moment coefficient K'_H versus the lateral force coefficient Y'_H with ϕ =0° in three different water depths. Inclination of K'_H to Y'_H means the vertical acting point of the lateral force z'_H. In the figure, the results are classified to three categories such as OTT results (``Pure Sway" in the graph), CMT results without $\beta$ (``Pure Yaw") and CMT results with β (``Sway+Yaw"). Mean lines of $K'_H$ versus $Y'_H$ are drawn for each in the figure. Table 3 shows the non-dimensional vertical acting point $z'_H(\equiv z_H/L)$ for each. Each value is quite different. In deep water, $z'_H$ is positive for ``Pure Sway". On the other hand, z'_H is negative for ``Pure Yaw", and this means the vertical acting point is located above the free-surface. In ``Sway+Yaw", z'_H is positive, but the value is about 60% of the value in ``Pure Sway". Thus, the vertical acting point of the hull lateral force takes different values according to the maneuvering mode such as oblique moving and turning. Similar results in deep water were indicated by Fukui et al. (2016). In shallow water, z'_H changes to negative direction as a whole. It is considered that this comes from the effect of not only the lateral force component acting on the hull but also the vertical force component which was neglected in this analysis. However, the detailed mechanism is not clear at present.

Table 3. Comparison of vertical acting points of lateral force z_H' in three different water depths

h/d	deep	1.5	1.2
z_H' in Pure Sway	0.022	0.000	-0.008
z_H' in Pure Yaw	-0.070	-0.108	-0.107
z_H' in Sway + Yaw	0.013	-0.007	-0.013

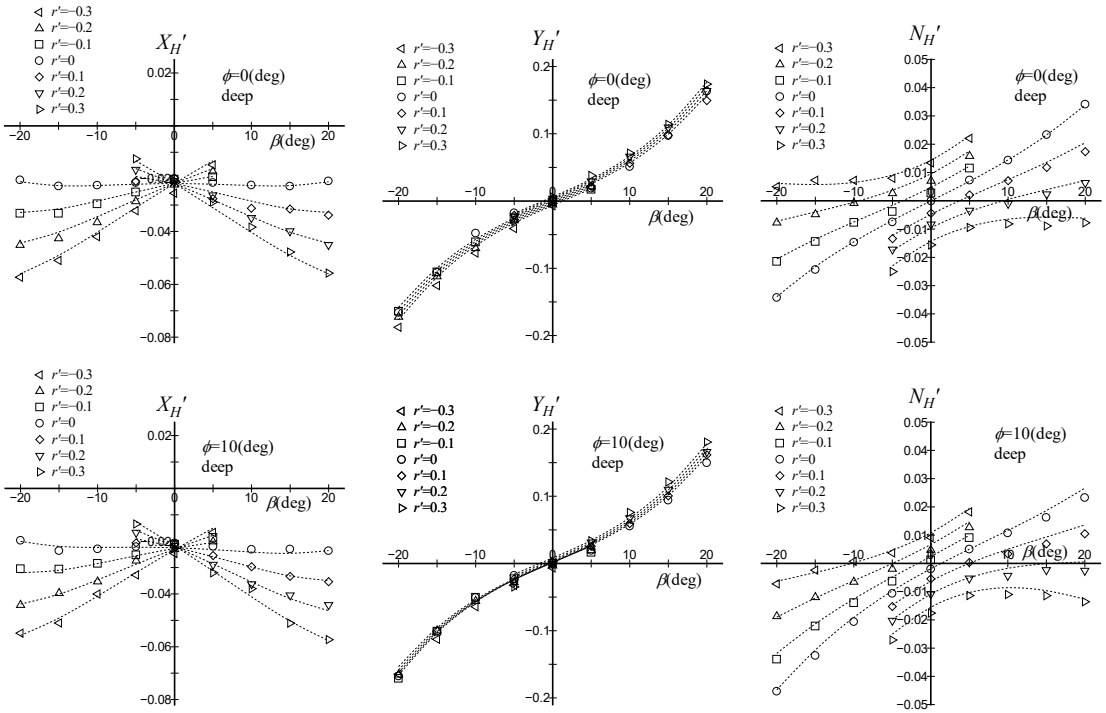

Figure 3. Surge force coefficient (X_H'), lateral force coefficient (Y_H') and yaw moment coefficient (N_H') versus hull drift angle (β) of ϕ=0° and 10° in deep water

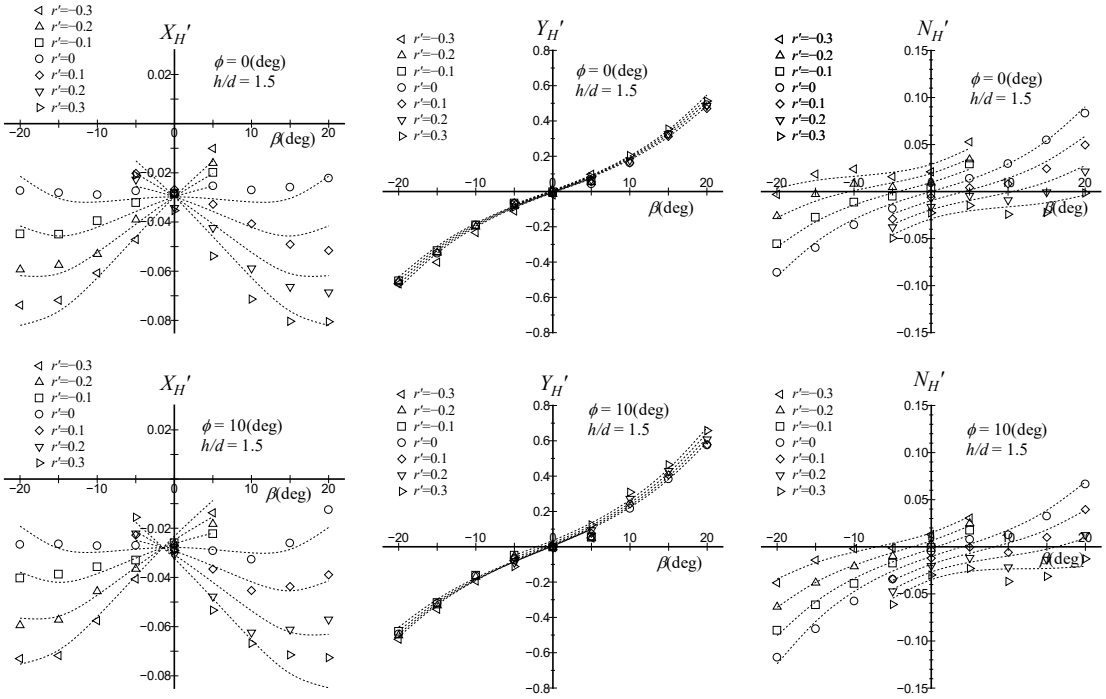

Figure 4. Surge force coefficient (X_H'), lateral force coefficient (Y_H') and yaw moment coefficient (N_H') versus hull drift angle (β) of ϕ=0° and 10° in h/d=1.5

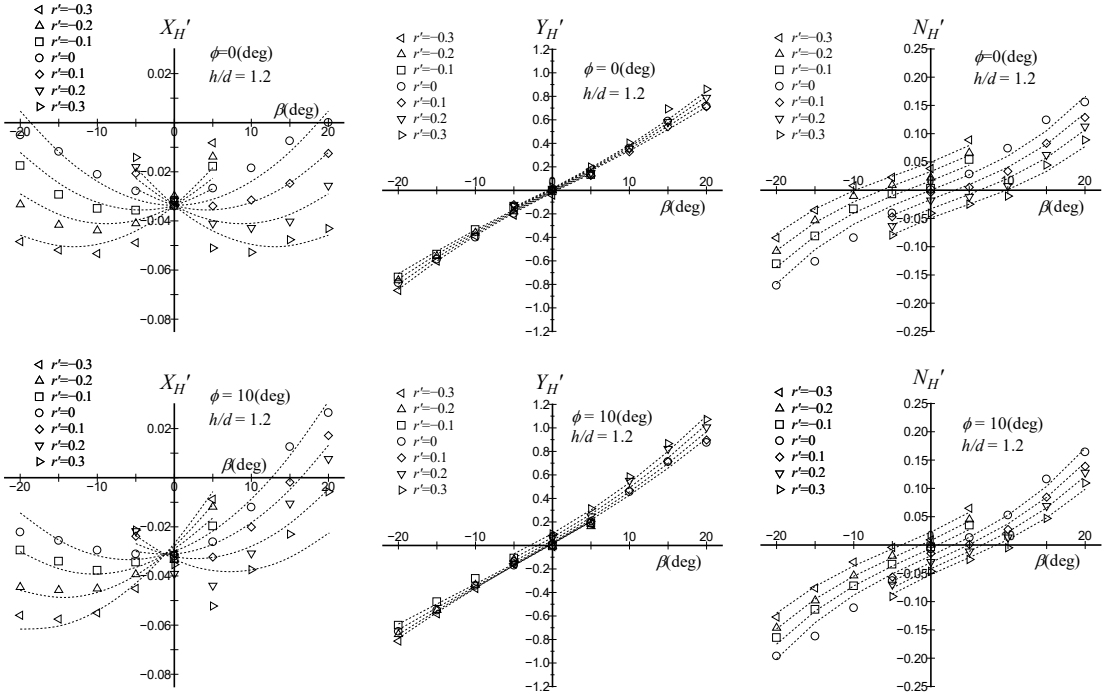

Figure 5. Surge force coefficient (X_H'), lateral force coefficient (Y_H') and yaw moment coefficient (N_H') versus hull drift angle (β) of ϕ=0° and 10° in h/d=1.2

Table 2. Hydrodynamic derivatives

h/d	deep	1.5	1.2	h/d	deep	1.5	1.2
R_0'	0.0223	0.0297	0.0333	$X_{v\phi}$'	0.029	0.005	-0.380
X_{vv}'	-0.034	-0.135	0.322	$X_{r\phi}$'	0.014	-0.086	-0.061
X_{vr}'+m_y'	0.215	0.365	0.155	$X_{\phi\phi}$'	-0.021	0.065	0.121
X_{vvvv}'	0.359	1.770	0.054	Y_{ϕ}'	0.013	0.044	0.144
Y_v'	-0.287	-0.912	-1.888	$Y_{vv\phi}$'	0.043	2.966	4.699
Y_r'-m_x'	0.021	0.017	0.080	$Y_{v\phi\phi}$'	0.132	-3.749	-7.715
Y_{vvv}'	-1.66	-4.14	-1.05	$Y_{r\phi\phi}$'	-0.348	0.739	2.533
Y_{vvr}'	0.223	1.89	3.61	$Y_{rr\phi}$'	0.188	0.897	2.264
N_v'	-0.080	-0.136	-0.300	N_{ϕ}'	-0.011	-0.059	-0.108
N_r'	-0.049	-0.097	-0.160	$N_{vv\phi}$'	-0.350	-0.850	0.183
N_{vvv}'	-0.182	-1.093	-1.565	$N_{v\phi\phi}$'	-0.173	-0.604	-1.947
N_{vvr}'	-0.743	-1.835	-1.167	$N_{r\phi\phi}$'	0.128	0.444	1.315
				$N_{rr\phi}$'	-0.029	0.019	0.267

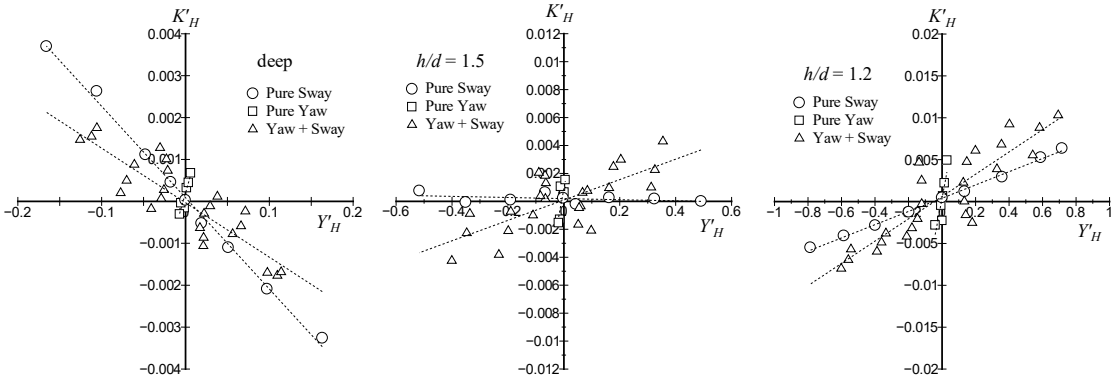

Figure 6. Roll moment coefficient (K_H') versus lateral force coefficient (Y_H') in three different water depths

4.2 TESTS FOR CAPTURING BANK EFFECT ON HYDRODYNAMIC FORCES

To capture the bank effect on the hydrodynamic force characteristics in shallow water, OTT tests with variation of distance between ship centerline and bank wall were carried out.

4.2 (a) Outline

The tests were carried out using the same PCC model. In the tests, surge force, lateral force, yaw moment around midship were measured for fixed model in the motions using a three-component dynamometer. Ship speed U in h/d =1.5 and 1.2 was 0.325 m/s (equivalent to 6.0 kn for full-scale ship, F_n =0.074).

Fig.7 shows a ship model moving in the proximity of the bank model. In the tank tests, W was set to be $0.45L$ (900mm in the model), and η/L was changed as 0.09, 0.18 and 0.27, and for each, we changed β as $-10° \sim 10°$ with interval 5°. We also added the tests in the conditions of η/L =0.31 and 0.36 for only $\beta = 0°$. Table 4 shows the values of s/L for $\beta = 0°$ when changing η/L from 0.09 to 0.36. For η/L =0.36, s/L becomes zero, and this means that the ship side position coincides with the bank toe position at the sea bottom.

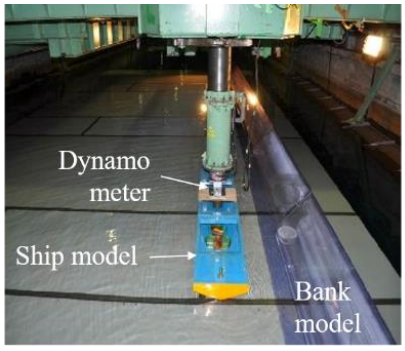

Figure 7. A picture of the ship model moving in the proximity of the bank model

Table 4. Lateral deviation of ship centerline η, and distance from the bank toe to ship side s in the model tests

η (mm)	(η/L)	s (mm)	(s/L)
180	0.09	540	0.27
360	0.18	360	0.18
540	0.27	180	0.09
620	0.31	100	0.05
720	0.36	0	0.00

4.2 (b) Test results

Fig.8 shows test results of surge force coefficient (X'_H), lateral force coefficient (Y'_H) and yaw moment coefficient (N'_H) with three different η/L in h/d =1.5 and 1.2. The horizontal axis is non-dimensionalized lateral velocity (v') which is defined as $-\sin\beta$. In the figure, dotted lines represent the fitting results using Eqs.(4) to (6). A vertical shift is observed in X'_H and N'_H with changing η/L, although Y'_H does not change very much. Then, the hydrodynamic derivatives related to η are shown in Table 5.

Table 5. Hydrodynamic derivatives related to η'

h/d	1.5	1.2
$X_{\eta\eta}$'	-0.040	-0.066
$X_{v\eta}$'	-0.036	-0.087
Y_{η}'	0.063	0.093
$Y_{\eta\eta\eta}$'	0.047	0.233
$Y_{vv\eta}$'	-0.585	0.721
$Y_{v\eta\eta}$'	-0.718	-0.293
N_{η}'	-0.012	-0.039
$N_{\eta\eta\eta}$'	-0.154	-1.923
$N_{vv\eta}$'	-1.307	0.031
$N_{v\eta\eta}$'	-0.056	-0.344

Fig.9 shows hydrodynamic force coefficients acting on the ship hull with $\beta = 0°$ when moving parallel to the bank. X'_H is negative, i.e. the resistance acting on the hull. With increase of η/L, the absolute value of X'_H increases slightly. Y'_H, i.e. the bank suction force, increases with increase of η/L. N'_H is negative, i.e. the bow-out moment from the bank acts on the ship hull. The shallow water effect on N'_H is more significant.

5 COURSE STABILITY ANALYSIS OF THE SHIP CLOSE TO A BANK

We discuss the course stability of the ship sailing close to a bank using the hydrodynamic derivatives obtained.

5.1 MOTION EQUATIONS

It is assumed that ship speed U is given and the surge-coupling effect is negligible. The roll-coupling effect is also neglected since the ship speed is slow and the heel/roll angle is small. Then, the motion equations with respect to sway and yaw are expressed as

$$(m' + m'_y)\dot{v'_m} + (m' + m'_x)r' + m'x'_G\dot{r'} = Y'_H + Y'_\delta\delta \quad (8)$$

$$(I'_z + J'_z + m'x'^2_G)\dot{r'} + m'x'_G(\dot{v'_m} + r') = N'_H + N'_\delta\delta \quad (9)$$

In the equations, Eq.(8) is non-dimensionalized by division of $(1/2)\rho LdU^2$, and Eq.(9) is non-dimensionalized by division of $(1/2)\rho L^2dU^2$. Here, m is ship's mass, and I_z is moment of inertia for yaw. m_x, m_y, and J_z denote added mass for surge, added mass for sway, and added moment of inertia for yaw, respectively. Y'_δ and N'_δ are steering-induced lateral force (rudder force) coefficient and steering-induced yaw moment coefficient, respectively.

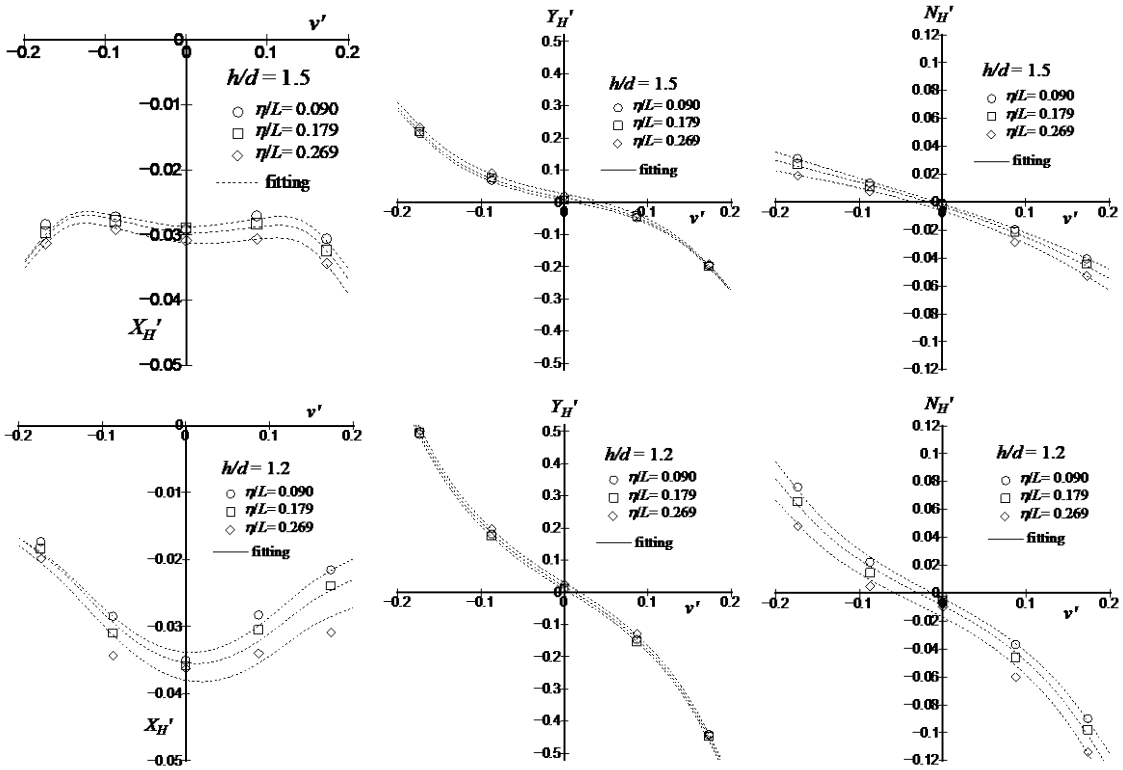

Figure 8. Surge force coefficient (X_H'), lateral force coefficient (Y_H') and yaw moment coefficient (N_H') with changing distance between ship centerline and bank wall (η) in h/d=1.5 and 1.2

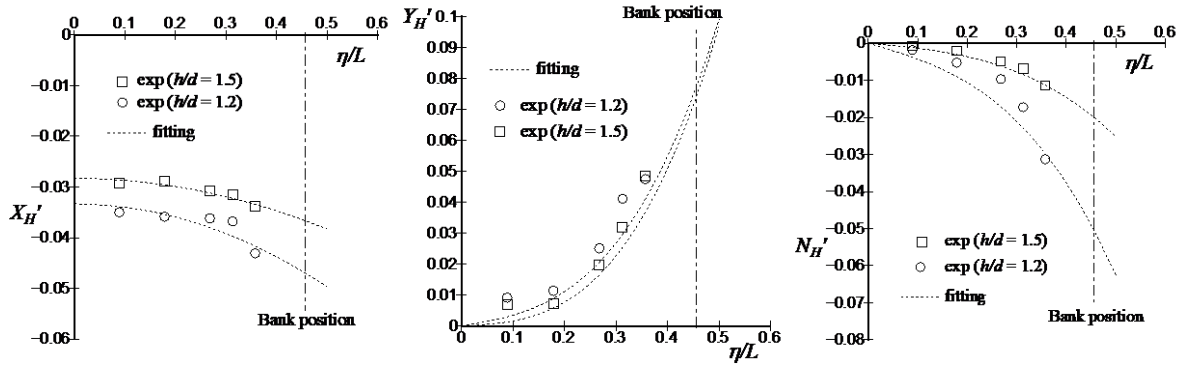

Figure 9. Surge force coefficient (X_H'), lateral force coefficient (Y_H') and yaw moment coefficient (N_H') when ship model moves straight in parallel to the bank

Here, v_m', ψ, δ, and η' are expressed as

$$\begin{aligned} v_m' &= v_0' + \Delta v' \\ \psi &= \psi_0 + \Delta\psi \\ \delta &= \delta_0 + \Delta\delta \\ \eta' &= \eta_0' + \Delta\eta' \end{aligned} \tag{10}$$

In Eq.(10), subscript 0 means the steady term, and putting Δ means the unsteady term. All the terms except η_0' are assumed to be $O(\varepsilon)$ where ε is small quantity. It is assumed that η_0' is given. From Eq.(2), v_m' is expressed as

$$v_m' = -\psi + \dot{\eta}' + O(\varepsilon^2) \tag{11}$$

Therefore, $v_0' = -\psi_0$ and $\Delta v' = -\Delta\psi + \Delta\dot{\eta}'$. From Eqs.(8) and (9), the steady terms are obtained as follows:

$$Y_\delta'\delta_0 + Y_v^{*\prime} v_0' + Y_\eta^{*\prime}\eta_0' = 0 \tag{12}$$

$$N_\delta'\delta_0 + N_v^{*\prime} v_0' + N_\eta^{*\prime}\eta_0' = 0 \tag{13}$$

where

$$\begin{aligned} Y_v^{*\prime} &= Y_v' + Y_{v\eta\eta}'\eta_0'^2 \\ N_v^{*\prime} &= N_v' + N_{v\eta\eta}'\eta_0'^2 \\ Y_\eta^{*\prime} &= Y_\eta' + 3Y_{\eta\eta\eta}'\eta_0'^2 \\ N_\eta^{*\prime} &= N_\eta' + 3N_{\eta\eta\eta}'\eta_0'^2 \end{aligned} \tag{14}$$

From Eqs.(12) and (13), check helm (δ_0) and non-dimensionalized lateral velocity (v_0') can be calculated by the following formulae:

$$\delta_0 = \eta_0' \frac{Y_\eta^{*\prime} N_v^{*\prime} - N_\eta^{*\prime} Y_v^{*\prime}}{Y_v^{*\prime} N_\delta' - N_v^{*\prime} Y_\delta'} = \eta_0' C_\eta Y_v^{*\prime} \left(\frac{N_v^{*\prime}}{Y_v^{*\prime}} - \frac{N_\eta^{*\prime}}{Y_\eta^{*\prime}} \right) \quad (15)$$

$$v_0' = -\eta_0' \frac{Y_\eta^{*\prime} N_\delta' - N_\eta^{*\prime} Y_\delta'}{Y_v^{*\prime} N_\delta' - N_v^{*\prime} Y_\delta'} = -\eta_0' C_\eta Y_\delta' \left(\frac{N_\delta'}{Y_\delta'} - \frac{N_\eta^{*\prime}}{Y_\eta^{*\prime}} \right) \quad (16)$$

where $C_\eta \equiv Y_v^{*\prime}/(Y_v^{*\prime} N_\delta' - N_v^{*\prime} Y_\delta')$. δ_0 is proportional to the difference between the longitudinal acting point of the hull lateral force in oblique motion ($N_v^{*\prime}/Y_v^{*\prime}$) and the longitudinal acting point of the bank suction force ($N_\eta^{*\prime}/Y_\eta^{*\prime}$). v_0' is proportional to the difference between the longitudinal acting point of the rudder force (N_δ'/Y_δ') and the longitudinal acting point of the bank suction force ($N_\eta^{*\prime}/Y_\eta^{*\prime}$).

Next, from Eqs.(8) and (9), the unsteady terms are obtained as follows:

$$\begin{aligned} &(m' + m_y')\Delta\ddot{\eta}' + m' x_G' \Delta\ddot{\psi}' = \Delta\dot{\eta}' Y_v^{*\prime} + \Delta\eta' Y_\eta^{*\prime} \\ &\quad + \Delta\dot{\psi}'(Y_r' - m_x' + m_y') - \Delta\psi Y_v^{*\prime} + \Delta\delta Y_\delta' \end{aligned} \quad (17)$$

$$\begin{aligned} &m' x_G' \Delta\ddot{\eta}' + (I_z' + J_z' + m' x_G'^2)\Delta\ddot{\psi}' = \Delta\dot{\eta}' N_v^{*\prime} + \Delta\eta' N_\eta^{*\prime} \\ &\quad + \Delta\dot{\psi}'(N_r' - m' x_G') - \Delta\psi N_v^{*\prime} + \Delta\delta N_\delta' \end{aligned} \quad (18)$$

Eqs.(17) and (18) are coupled-linear differential equations with unknown variables $\Delta\psi$ and $\Delta\eta'$ which are the base equations for discussing course stability.

For modeling the autopilot, the rudder angle $\Delta\delta$ is assumed to be expressed as follows:

$$\Delta\delta = -G_1 \Delta\psi - G_2 \Delta\dot{\psi}' \quad (19)$$

where G_1 and G_2 are control gains.

Then, the characteristic equation of Eqs.(17) and (18), where λ denotes the solution, is expressed as follows:

$$D_4\lambda^4 + D_3\lambda^3 + D_2\lambda^2 + D_1\lambda + D_0 = 0 \quad (20)$$

where

$$D_4 = (m' + m_y')(I_z' + J_z' + m' x_G'^2) - x_G'^2 m'^2 \quad (21)$$

$$\begin{aligned} D_3 = &-(m' + m_y')(N_r' - m' x_G' - N_\delta' G_2) \\ &-(I_z' + J_z' + m' x_G'^2) Y_v^{*\prime} \\ &+ x_G' m' (N_v^{*\prime} + Y_r' - m_x' + m_y' - Y_\delta' G_2) \end{aligned} \quad (22)$$

$$\begin{aligned} D_2 = &Y_v^{*\prime}(N_r' - m' x_G' - N_\delta' G_2) \\ &-(Y_r' - m' - m_y' - Y_\delta' G_2) N_v^{*\prime} \\ &-Y_\eta^{*\prime}(I_z' + J_z' + m' x_G'^2) + N_\delta' G_1 (m' + m_y') \\ &+ x_G' m' (N_\eta^{*\prime} - Y_v^{*\prime} - Y_\delta' G_1) \end{aligned} \quad (23)$$

$$\begin{aligned} D_1 = &Y_\eta^{*\prime}(N_r' - m' x_G' - N_\delta' G_2) \\ &-(Y_r' - m_x' + m_y' - Y_\delta' G_2) N_\eta^{*\prime} \\ &-G_1(Y_v^{*\prime} N_\delta' - N_v^{*\prime} Y_\delta') \end{aligned} \quad (24)$$

$$D_0 = (Y_v^{*\prime} + Y_\delta' G_1) N_\eta^{*\prime} - Y_\eta^{*\prime}(N_v^{*\prime} + N_\delta' G_1) \quad (25)$$

Motion stability can be examined by Routh-Hurwitz stability criterion, according to which, necessary conditions for the course stability are written as

$$D_0, D_1, D_2, D_3, D_4 > 0 \quad (26)$$

$$D_5 \equiv D_3 D_2 D_1 - D_3^2 D_0 - D_4 D_1^2 > 0 \quad (27)$$

If these conditions are satisfied, the course instability theoretically never occurs. D_4 , D_3 , and D_0 becomes hydrodynamically positive for usual ships, so that we have to check the plus-minus signs of D_1, D_2, and D_5.

5.2 ANALYSIS RESULT

The course stability analysis of the PCC sailing close to a bank is carried out using the formulae mentioned above. As the hydrodynamic derivatives, the measured data obtained in the captive model test mentioned in previous section are used. Table 6 shows the rudder force and virtual mass coefficients used in the analysis. Virtual mass coefficients such as $m' + m_x'$, $m' + m_y'$, and $I_z' + J_z'$ were determined according to Yoshimura (1984), and were assumed to be constant in variation of η_0/L. Y_δ' and N_δ' in the table were determined based on the tank test data by Sano et al. (2014).

Table 6. Rudder force and virtual mass coefficients

h/d	1.5	1.2
Y_δ'	-0.050	-0.050
N_δ'	0.025	0.025
$m' + m_x'$	0.232	0.301
$m' + m_y'$	0.413	0.544
$I_z' + J_z'$	0.0262	0.0293

Fig10 shows the calculation results of $Y_v^{*\prime}$, $N_v^{*\prime}$, $N_v^{*\prime}/Y_v^{*\prime}$, $Y_\eta^{*\prime}$, $N_\eta^{*\prime}$ and $N_\eta^{*\prime}/Y_\eta^{*\prime}$ versus η_0/L, which are calculated using Eq.(14). $N_v^{*\prime}/Y_v^{*\prime}$ means the longitudinal acting point of lateral force in oblique towing condition, and $N_\eta^{*\prime}/Y_\eta^{*\prime}$ means the longitudinal acting point of the bank suction force. In both h/d =1.5 and 1.2, absolute values of $Y_v^{*\prime}$, $Y_\eta^{*\prime}$, and $N_\eta^{*\prime}$ increase with increase of η_0/L. As a result, $N_\eta^{*\prime}/Y_\eta^{*\prime}$ also increases. Change of $N_\eta^{*\prime}/Y_\eta^{*\prime}$ to positive direction means that the longitudinal acting point shifts forewards. Compared with those, change of $N_v^{*\prime}/Y_v^{*\prime}$ with increase of η_0/L is small, and this value is always positive.

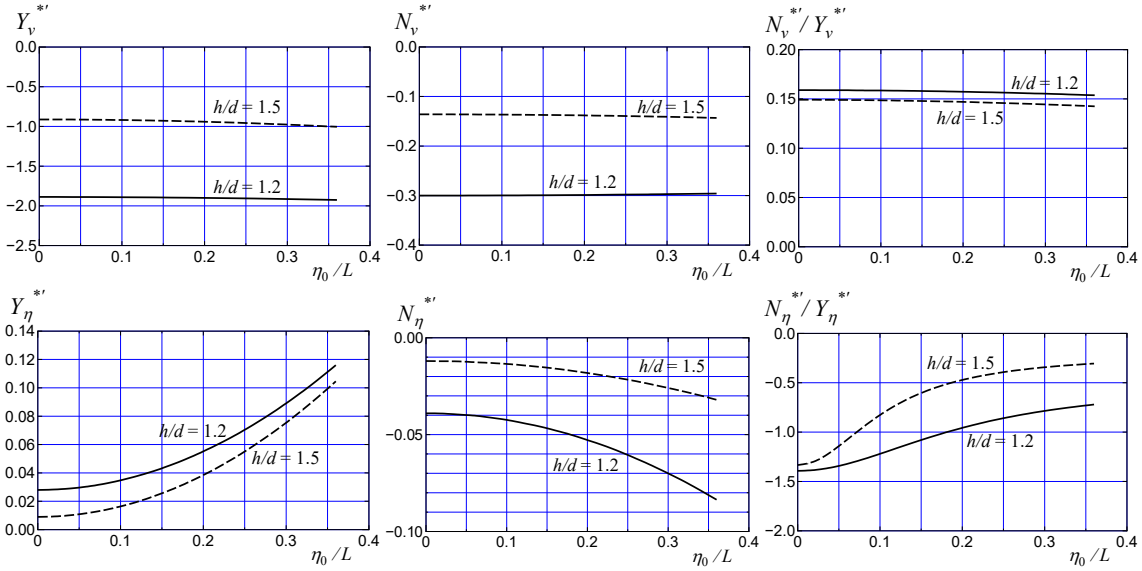

Figure 10. $Y_v^{*\prime}$, $N_v^{*\prime}$, $N_v^{*\prime}/Y_v^{*\prime}$, $Y_\eta^{*\prime}$, $N_\eta^{*\prime}$ and $N_\eta^{*\prime}/Y_\eta^{*\prime}$ versus η_0/L

Fig.11 shows calculation results of check helm δ_0 and heading angle $\psi_0(\equiv -v_0')$ versus η_0/L. With increase of η_0/L, δ_0 increases, and this tendency is more significant in $h/d = 1.2$. δ_0 reaches 35° near $\eta_0/L = 0.27$ in $h/d = 1.2$. If the ship sails any closer to the bank wall, there is a collision risk with the bank due to insufficient rudder force. On the other hand, ψ_0 is quite small. The reason why δ_0 increases significantly with increase of η_0/L is that $N_\eta^{*\prime}/Y_\eta^{*\prime}$ changes significantly with η_0/L, and $N_v^{*\prime}/Y_v^{*\prime}$ is positive and almost constant (see Fig.10). Additionally, the reason why ψ_0 is smaller than δ_0 by one order of magnitude is that the absolute value of Y_δ' is smaller than that of $Y_v^{*\prime}$ by one order of magnitude mainly. Where the water depth changes from $h/d = 1.5$ to $h/d = 1.2$, check helm δ_0 becomes significantly large. The helmsman must pay attention to the change for safe navigation.

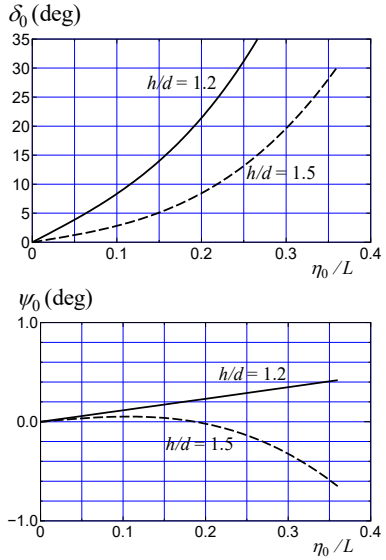

Figure 11. Check helm (δ_0) and heading angle (ψ_0) versus η_0/L

Fig.12 shows calculation results of D_1, D_2, and $100D_5$ in both $h/d = 1.5$ and $h/d = 1.2$, for $G_1 = G_2 = 0$. In $h/d = 1.5$, D_2 is always positive, D_1 is partially negative and D_5 is fully negative. In $h/d = 1.2$, D_1 and D_2 are always positive, and only D_5 becomes negative. When discussing the course stability of ships in proximity of a bank, D_5 is the most important. This is the same as the analysis result by Sano et al. (2014) for an inland container ship. In case of no rudder control ($G_1 = G_2 = 0$), this ship is course unstable.

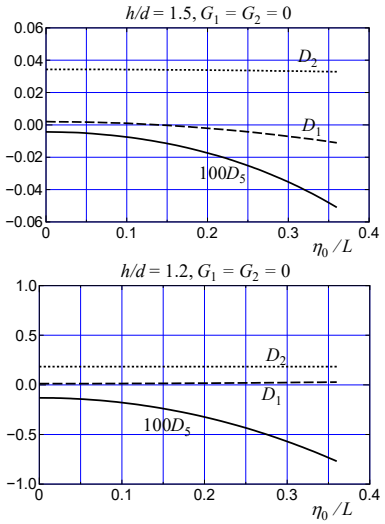

Figure 12. D_1, D_2, and $100D_5$ versus η_0/L (G_1=G_2=0)

To improve the course stability, rudder control gains for autopilot change as follows:

1. $G_1 = G_2 = 0$ (No Control)
2. $G_1 = G_2 = 4$ (Control with mild sensitivity)
3. $G_1 = G_2 = 6$ (Control with high sensitivity)

According to Eda (1971), the control of $G_1 = G_2 = 4$ is called as ``Control with mild sensitivity" and that of $G_1 = G_2 = 6$ as ``Control with high sensitivity". Fig.13 shows calculation result of $100\,D_5$ in both $h/d = 1.5$ and h/d =1.2. For $G_1 = G_2 = 0$, $100D_5$ is fully negative and this ship is course unstable. Changing the gains to $G_1 = G_2 = 4$ and $G_1 = G_2 = 6$, the line of $100\,D_5$ shifts vertically upward and the value of $100\,D_5$ becomes positive. For $G_1 = G_2 = 4$ in h/d =1.2, $100D_5$ becomes fully positive and the ship is course stable. Although D_1 was partially negative without rudder control in h/d =1.5 as shown in Fig.12, D_1 becomes positive by employing the autopilot with small gains.

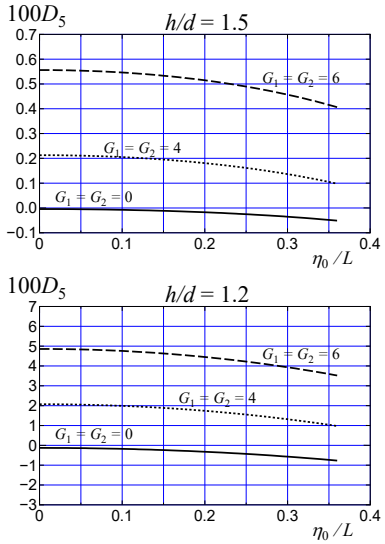

Figure 13. $100D_5$ in three different control gains

6 CONCLUSIONS

In this paper, an analysis of the course stability was presented for a pure car carrier (PCC) in proximity to a bank. The analysis is based on the method proposed by Sano et al. (2014); however, a modification is made to the method to treat the problem conventionally. For the analysis, the hydrodynamic derivatives are required. To capture those, captive model tests were performed in deep and shallow water. Oblique towing test (OTT) and circular motion test (CMT) were conducted with variation of the heel angle of the ship model to know the heel effect of the derivatives. Further, OTT was conducted for capturing bank effect on the derivatives. Using the derivatives obtained, the course stability was analyzed for the PCC in bank proximity.

In h/d =1.2, the check helm reaches 35° near η_0/L =0.27 where η_0 is the distance between the ship center line and the bank. The helmsman must pay attention to the steering for safe navigation in this situation. Additionally, this ship is course unstable in case of no rudder control in any water depths, however, the ship becomes course stable by employing the autopilot with gains $G_1 = G_2 = 4$ which is called as ``Control with mild sensitivity" (Eda, 1971). The present analysis method is useful for conventionally assessing course stability of a ship in the proximity of a bank.

7 ACKNOWLEDGEMENTS

This study was supported by JSPS KAKENHI Grant Number JP26249135. The author expresses his sincere gratitude to Mr. R. Sakuno for his assistance with the tank tests in deep and shallow water.

8 REFERENCES

Eda, H., 1971. Directional Stability and Control of Ships in Restricted Channels, Trans. SNAME, Vol.79, 71-116.

Fujino, M., 1968. Experimental Studies on Ship Manoeuvrablity in Restricted Waters -- Part I, International Shipbuilding Progress, Vol.15, No.168, 279-301.

Fujino, M., 1970. Experimental Studies on Ship Manoeuvrablity in Restricted Waters -- Part II, International Shipbuilding Progress, Vol.17, No.186, 45-65.

Fukui, Y., Yokota, H., Yano, H., Kondo, M., Nakano, T. and Yoshimura, Y., 2016. 4-DOF Mathematical Model for Manoeuvring Simulation Including Roll Motion, J. Japan Society of Naval Architects and Ocean Engineers, Vol.24, 167-179 (in Japanese).

Hamamoto, M. and Kim, Y., 1993. A New Coordinate System and the Equations Describing Manoeuvring Motion of a Ship in Waves, J. Society of Naval Architects of Japan, Vol.173, 209-220 (in Japanese).

Hirano, M. and Takashina, J., 1980. A Calculation of Ship Turning Motion Taking Coupling Effect due to Heel into Consideration, Trans. West-Japan Society of Naval Architects, No.59, 71-81.

Lataire, E., and Vantorre, M., 2008. Ship-Bank Interaction Induced by Irregular Bank Geometries, Proc. 27th Symposium on Naval Hydrodynamics, vol.2, Seoul, 511-524.

Li, D. Q., Ottoson, P, and Tragardh, P., 2003. Prediction of Bank Effects by Model Tests and Mathematical Model, Proc. International Conference on Marine Simulation and Ship Maneuverability (MARSIM'03), Vol.3, Kanazawa, 803-814.

Norrbin, N. H., 1974. Bank Effects on a Ship Moving Through a Short Dredged Channel, Proc. 10th Symposium on Naval Hydrodynamics, Cambridge, 71-88.

Sano, M., Yasukawa, H. and Hata, H., 2012. Experimental Study on Ship Operation in Close Proximity to Bank Channel, Proc. International Conference on Marine

Simulation and Ship Maneuverability (MARSIM'12), Singapore.

Sano, M., Yasukawa, H. and Hata, H., 2014. Directional Stability of a Ship in Close Proximity to Channel Wall, J. Marine Science and Technology, Vol.19, No.4, 376-393.

Vantorre, M., Delefortrie, G., Eloot, K. and Laforce, E., 2003. Experimental Investigation of Ship-Bank Interaction Forces, Proc. International Conference on Marine Simulation and Ship Maneuverability (MARSIM'03), Vol.3, Kanazawa, 815-823.

Yasukawa, H, Kawamura, S, Tanaka, S and Sano, M., 2009. Evaluation of Ship-Bank and Ship-Ship Interaction Forces Using a 3D Panel Method, Proc. International Conference on Ship Manoeuvring in Shallow and Confined Water: Bank Effects, Antwerp, 127-133.

Yasukawa, H. and Yoshimura, Y., 2014. Roll-Coupling Effect on Ship Maneuverability, Ship Technology Research, Vol.61, No.1, 16-32.

Yoshimura, Y., 1984. Mathematical Model for the Manoeuvring Ship Motion in Shallow Water, J. Kansai Society of Naval Architects, Japan, No.200, 41-51 (in Japanese).

Zou, L., Larsson, L., Delefortrie, G. and Lataire, E., 2011. CFD Prediction and Validation of Ship-Bank Interaction in a Canal, Proc. 2nd International Conference on Ship Manoeuvring in Shallow and Confined Water: Ship to Ship Interaction, Trondheim, 413-422.

9 AUTHORS BIOGRAPHY

Hironori Yasukawa holds currently the position of professor at Hiroshima University, Japan. He is responsible for research on ship dynamics and hydrodynamics. Currently, he is also the chairman of the ITTC Specialist Committee on Manoeuvring in Waves.

CFD-BASED NUMERICAL PREDICTION OF VERTICAL MOTIONS AND RESISTANCE FOR DTC CONTAINER CARRIER IN SHALLOW WATER WAVES

Shuai Yuan and Li Xia,
School of Naval Architecture, Ocean and Civil Engineering, Shanghai Jiao Tong University, Shanghai, China

Zao-Jian Zou,
School of Naval Architecture, Ocean and Civil Engineering, Shanghai Jiao Tong University, Shanghai, China & State Key Laboratory of Ocean Engineering, Shanghai Jiao Tong University, Shanghai, China

Lu Zou,
School of Naval Architecture, Ocean and Civil Engineering, Shanghai Jiao Tong University, Shanghai, China

CFD-BASED NUMERICAL PREDICTION OF VERTICAL MOTIONS AND RESISTANCE FOR DTC CONTAINER CARRIER IN SHALLOW WATER WAVES

Shuai Yuan and **Li Xia,** School of Naval Architecture, Ocean and Civil Engineering, Shanghai Jiao Tong University, Shanghai, China
Zao-Jian Zou, School of Naval Architecture, Ocean and Civil Engineering, Shanghai Jiao Tong University, Shanghai, China & State Key Laboratory of Ocean Engineering, Shanghai Jiao Tong University, Shanghai, China
Lu Zou, School of Naval Architecture, Ocean and Civil Engineering, Shanghai Jiao Tong University, Shanghai, China

SUMMARY

In shallow water waves, the risk of ship grounding due to ship's periodic oscillatory motion and the resistance are larger than those in calm and deep water. In this paper, numerical simulations of a DTC model advancing in calm water and in head waves with various wavelengths in shallow water are carried out by using CFD-based RANS method to predict ship motions and resistance. The numerical uncertainties are analyzed, which are found small for heave motion and resistance, but relatively large for pitch motion. The comparison between the CFD results and the model test data in head waves shows a favorable agreement. Using the verified CFD setting, the effects of waves and bank on the ship's vertical motion and resistance are investigated.

NOMENCLATURE

a	Cosine coefficient of FS Expansion (-)
A	Wave amplitude (m)
b	Sine coefficient of FS Expansion (-)
B_{wl}	Waterline Breadth (m)
C_{aw}	Added resistance coefficient in waves (-)
C_{t}	Total resistance coefficient in calm water (-)
E%D	Relative error (-)
e_{a}^{21}	Approximate relative error (-)
e_{ext}^{21}	Extrapolated relative error (-)
f	Body force (N/m^3)
f_{β}	Vortex-stretching modification factor (-)
f_{β^*}	Free-shear modification factor (-)
f_{e}	Encounter frequency of wave (s^{-1})
$\boldsymbol{F}$	Resultant force vector (N)
g	Gravitational acceleration (m/s^2)
GCI_{fine}^{21}	Fine-grid convergence index (-)
h	Depth of water (m)
k	Turbulent kinetic energy (m^2/s^2)
K	Wave number (m^{-1})
$\mathbf{K}$	Wave vector (m^{-1})
L_{pp}	Length between perpendiculars (m)
L_{d}	Length of wave damping zone (m)
m	Mass of ship (kg)
$\boldsymbol{M}$	Tensor of the moments of inertia (kg·m^2)
$\boldsymbol{N}$	Resultant moment vector (N·m)
P	Order of accuracy (-)
$\bar{P}$	Mean pressure (Pa)
P_{k}	Production term of turbulent kinematic energy (kg/(m·s^3))
P_{ω}	Production term of turbulent specific dissipation rate (kg/(m^3·s^2))
r	Refinement ratio (-)
R	Convergence ratio (-)
R_{c}	Mean resistance in calm water (N)
R_{w0}	Mean resistance in waves (N)
s_{ext}^{21}	Extrapolated value (-)
S_{w}	Wetted surface (m^2)
T	Wave period (s)
T_{e}	Wave encounter period (s)
U	Ship forward speed (m/s)
$\bar{\boldsymbol{u}}$	Mean velocity vector (m/s)
$\boldsymbol{u}'$	Turbulent velocity fluctuation (m/s)
$\boldsymbol{v}$	Velocity of ship's center of gravity (m/s)
v_{h}	Horizontal velocity of wave (m/s)
v_{v}	Vertical velocity of wave (m/s)
w	Wave frequency (rad/s)
W_{tank}	Tank width (m)
$X(t)$	Time series of parameter X
X_{n}	n$^{\mathrm{th}}$ harmonic amplitude of parameter X
y^+	Dimensionless wall distance (-)
z	Heave motion (m)
Z	Vertical distance from the mean water level (m)
γ	Phase of response (rad)
γ_0	Initial wave phase at ship's center of gravity (rad)
γ'	Adjusted phase of response (rad)
η	Free surface elevation (m)
λ	Wavelength (m)
μ	Dynamic viscosity (Pa·s)
μ_{t}	Turbulent viscosity (Pa·s)
ω	Turbulent specific dissipation rate (s^{-1})
$\boldsymbol{\omega}$	Angular velocity vector of ship (rad/s)
ρ	Density of water (kg/m^3)
σ_{k}	Model coefficient in equation of turbulent kinematic energy (-)
σ_{ω}	Model coefficient in equation of turbulent specific dissipation rate (-)
θ	Pitch motion (rad)
CFD	Computational Fluid Dynamics
DFBI	Dynamic Fluid Body Interaction
DOF	Degree of Freedom
FS	Fourier Series
GCI	Grid Convergence Index

HRIC	High-Resolution Interface Capturing
RANS	Reynolds-averaged Navier-Stokes
RAO	Response Amplitude Operator
UKC	Underkeel Clearance
VOF	Volume of Fluid

1 INTRODUCTION

During the last decade, a rapid increase in the ship size has been seen globally, especially for the container ships and tankers that sails frequently in restricted areas such as channels, harbors and other coastal areas. As the effect of water depth on ship hydrodynamic performances becomes non-negligible when the ratio of water depth to ship draft is getting smaller, the waters are considered to be shallow for these larger ships. Ship squat (namely sinkage and trim) due to the shallow water effect has always been a primary concern for coastal engineering and ship navigation safety. Moreover, wave-induced ship's vertical motion will exacerbate squat phenomenon, and further increase the risk of grounding for large ships sailing in vertically and horizontally restricted water areas.

With the rapid development of computer technique, Computational Fluid Dynamics (CFD) method has been successfully applied to numerical simulations of ship sailing in shallow water and in waves during the last decade. Jachowski (2008) investigated the ship squat under various underkeel clearance (UKC) by using CFD software Fluent, and compared the squat values calculated using the empirical methods and the CFD method. Moctar et al. (2012) described available data from model tests for a model-scale DTC, including resistance and propulsion tests and roll decay tests. They also presented CFD results by using RANS method for comparison with measurements. Senthil and Chandra (2013) carried out the numerical prediction of the shallow water resistance of a river-sea ship at subcritical, critical and supercritical speeds, and obtained the corresponding wave patterns. Tezdogan et al. (2015) performed fully nonlinear unsteady RANS simulations to predict the ship squat and resistance of a model-scale DTC container carrier advancing in an asymmetric canal at three different ship drafts and various speeds, the trajectories of the waves generated by the vessel and reflected from the canal side walls were obtained. Carrica et al. (2016) carried out the direct simulation of zigzag maneuver in very shallow water for the KCS model. Deng et al. (2016) carried out the CFD simulations of four different pure yaw and pure sway test cases at 20% UKC in shallow water with the ISIS-CFD flow solver. Liu et al. (2016) carried out the RANS-based simulations of static drift and pure sway test of a bare hull of the DTC container carrier maneuvering in shallow water at 20% UKC, and the effects of ship speeds, dynamic squat and tank wall effect were investigated. Terziev et al. (2018) extended their former researches (Tezdogan et al., 2015) to different canal geometry to investigate the effect of the presence of steps in the channel.

However, few studies of wave effects on ships sailing in shallow and confined waters have been reported so far. Tezdogan et al. (2016) investigated the characteristics of shallow water waves and predicted the heave and pitch responses of a full-scale large tanker to head waves at zero speed at various water depths by using CFD software STAR CCM+, and found that the vertical motions were significantly influenced by shallow water.

To investigate the effect of shallow water waves, RANS-based simulations of ship squat and resistance in calm water together with ship motions and added resistance in shallow water waves are carried out for a model-scale DTC container carrier by using the CFD software STAR CCM+. Parts of the numerical results are compared with the benchmark test data provided by Flanders Hydraulics Research (FHR) and Ghent University for the 5th International Conference on Ship Manoeuvring in Shallow and Confined Water (MASHCON2019).

2 NUMERICAL MODELLING

2.1 COORDINATE SYSTEMS

To establish the numerical wave tank, two sets of Cartesian coordinate systems are used: the earth-fixed coordinate system (O_0-$X_0Y_0Z_0$) and the ship-fixed coordinate system (O-XYZ). The ship-fixed coordinate system has the origin fixed at the center of gravity of the ship, and the O-XZ plane located in the longitudinal center plane of the ship with the O-X axis defined positive upstream and the O-Z axis positive upwards. At the initial moment when the ship is at rest, the two sets of coordinate system coincide with each other.

2.2 GOVERNING EQUATIONS

The time-averaged continuity and momentum equations based on the RANS method for the incompressible viscous flow are written as follows:

$$\begin{cases} \dfrac{\partial \overline{u}_i}{\partial x_i} = 0 \\ \rho\left[\dfrac{\partial}{\partial t}\left(\overline{u}_i\right) + \dfrac{\partial}{\partial x_j}\left(\overline{u}_i\overline{u}_j\right)\right] = \rho f_i - \dfrac{\partial \overline{P}}{\partial x_i} \\ \qquad + \dfrac{\partial}{\partial x_j}\left(\mu\dfrac{\partial \overline{u}_i}{\partial x_j} - \rho\overline{u_i'u_j'}\right) \quad (i=1,2,3) \end{cases} \tag{1}$$

The SST k-ω turbulent model is used to close the governing equations. The equation of the turbulent kinetic energy k and the equation of the specific dissipation rate ω are written as follows (CD-Adapco, 2017):

$$\begin{cases} \rho\left[\dfrac{\partial k}{\partial t} + \nabla\cdot\left(k\overline{\boldsymbol{u}}\right)\right] = \nabla\cdot\left[\left(\mu+\sigma_k\mu_t\right)\nabla k\right] \\ \qquad + P_k - \rho\beta^* f_{\beta^*}\left(\omega k - \omega_0 k_0\right) \\ \rho\left[\dfrac{\partial}{\partial t}\left(\omega\right) + \nabla\cdot\left(\omega\overline{\boldsymbol{u}}\right)\right] = \nabla\cdot\left[\left(\mu+\sigma_\omega\mu_t\right)\nabla\omega\right] \\ \qquad + P_\omega - \rho\beta f_\beta\left(\omega^2 - \omega_0^2\right) \end{cases} \tag{2}$$

where k_0 and ω_0 are the ambient turbulence values that counteract turbulent decay.

The finite volume method is applied for the discretization of governing equations above, and a segregated solver is used to solve the pressure-velocity coupling equations. The convection terms in the RANS equations are discretized by applying a 2nd-order upwind difference scheme, and the diffusion terms are discretized by a central difference scheme. The transient terms in the RANS equations are discretized by a first-order Euler implicit temporal scheme for calm water cases but a second-order backward-differencing temporal scheme for head wave cases. The VOF Multiphase model is used to capture the free surface with flat waves for calm water cases and regular waves for head wave cases. The spatial distribution of the two phases (namely water and air) at each given time is defined in terms of a variable called the volume fraction (CD-Adapco, 2017). The free surface can be visualized by setting this variable as 0.5. In order to obtain a sharp interface, the 2nd-order discretization scheme is used for the convection terms, and the angle factor in the HRIC scheme is adjusted to 0.15.

2.3 WAVE GENERATION AND DAMPING

A flat wave is used to represent the calm plane of water for the calm water cases, and a 1st-order wave based on a 1st-order approximation to the Stokes theory of waves is used to simulate the regular periodic sinusoidal profile on the free surface for the head wave cases. For the 1st-order wave, the equation for the horizontal velocity, vertical velocity and the surface elevation can be written as follows respectively:

$$v_h = Aw\cos(\mathbf{K}\cdot\mathbf{x} - wt)e^{KZ} \tag{3}$$

$$v_v = Aw\sin(\mathbf{K}\cdot\mathbf{x} - wt)e^{KZ} \tag{4}$$

$$\eta = A\cos(\mathbf{K}\cdot\mathbf{x} - wt) \tag{5}$$

The wave period T and the wavelength λ are as follows:

$$T = \frac{2\pi}{w} \tag{6}$$

$$\lambda = \frac{2\pi}{K} \tag{7}$$

The dispersion relation for 1st-order waves in finite water depth is:

$$T = \left[\frac{g}{2\pi\lambda}\tanh\left(\frac{2\pi h}{\lambda}\right)\right]^{-1/2} \tag{8}$$

The wave damping is introduced to the vicinity of the boundaries of the computational domain to reduce wave oscillation. In STAR-CCM+ the damping of waves is done by adding a resistance term to the vertical motion equation.

2.4 SHIP MOTIONS AND DFBI MORPHING

The DFBI module is used to simulate the rigid motion of the ship. The general workflow is: 1) the 6-DOF solver computes fluid forces, moments, and gravitational forces acted on the ship, and pressure and shear forces are integrated over the surfaces of the ship; 2) The forces and moments are used to compute the translational motion of the center of gravity of the ship and the angular motion of the orientation of the ship by solving the governing equations of ship motions to find the new position of the ship; 3) The 6-DOF motion solver moves the vertices of the grid according to the ship motion calculated by the 6-DOF solver; 4) Repeat the above steps. The governing equations of free motion of the ship are as follows:

$$\begin{cases} m\dfrac{d\boldsymbol{v}}{dt} = \boldsymbol{F} \\ \boldsymbol{M}\dfrac{d\boldsymbol{\omega}}{dt} + \boldsymbol{\omega}\times\boldsymbol{M}\boldsymbol{\omega} = \boldsymbol{N} \end{cases} \tag{9}$$

The DFBI morphing motion is activated to account for the ship rigid motions at each time step by moving the grid nodes according to the calculated ship motions, thus morphing the grids on the basis of the selected morphing conditions on the corresponding boundaries. For the ship motions in waves, all boundaries of the computational domain are set as fixed except that the morphing condition on the ship surfaces are set as the 6-DOF body.

3 NUMERICAL SIMULATION

3.1 STUDY OBJECT AND CASES

The DTC container carrier with the scale ratio 1:89.11 is taken as the study object. The length of the model is 3.984m. The detailed main particulars and loading parameters of the model can be found in Van Zwijnsvoorde (2019). The numerical cases carried out are summarized in Table 1.

Table 1. Numerical simulation cases

Particular	Calm water	Head waves
UKC (%)	100	
Ship speed (full scale)	16kn	
λ/L_{pp}	-	0.55; 0.7; 0.85; 1.0
A	-	62.35mm
Tank width	7m; $2\times(1L_{pp}+1L_d)$	

3.2 COMPUTATIONAL DOMAIN AND BOUNDARY CONDITIONS

The boundary conditions are selected according to Tezdogan et al. (2016) and the recommendations of CD-Adapco for numerical simulations of calm water and seakeeping problems. Figure 1 depicts a general view of the computational domain and the selected boundary conditions. A velocity inlet boundary condition is set to the upstream inlet boundary, where flat waves and 1st-order Stokes waves are generated for calm water cases and head wave cases, respectively. A pressure outlet boundary condition is applied to the downstream outlet boundary, where the hydrostatic pressure is assumed constant. The top boundary of the computational domain is also modelled by a velocity inlet boundary condition as it

facilitates the numerical efficiency and convergence in STAR-CCM+. The bottom boundary of the domain is modelled by a moving no-slip wall boundary with the wall tangential speed equal to the negative ship speed to account for the presence of the tank floor as in the model tests. In order to study the bank effect in shallow water as the bank distance is less than $1L_{pp}$, the side boundary of the domain is first modelled by a moving no-slip wall boundary with the same setting as the bottom boundary, and a comparison simulation is then made by altering the boundary condition on the side boundary to a velocity inlet boundary condition. The ship hull surface is set as the no-slip wall. Besides, a symmetry boundary condition is set on the boundary plane of the domain that coincides with the longitudinal center plane of the ship as only half ship is considered in the numerical simulation of the symmetrical flow fields.

The positions of all boundaries are determined based on the principle that the flow is fully developed downstream and the distance between the hull and the inlet or outlet boundary is larger than the wave damping length. Thus, the inlet boundary and outlet boundary are positioned $1.5L_{pp}$ and $3L_{pp}$ away from the hull, respectively. The top boundary is positioned $1L_{pp}$ away from the calm water plane. The side boundary is positioned either 3.5m or 6m ($\approx 1.5L_{pp}$) away from the hull longitudinal center plane for bank effect study. The bottom boundary is positioned according to the water depth. The wave damping is applied to the inlet and outlet boundaries for calm water cases, and only to the outlet boundary for head wave cases. The wave damping length is set as $1.25L_{pp}$ for calm water cases and $1.5L_{pp}$ for head wave cases.

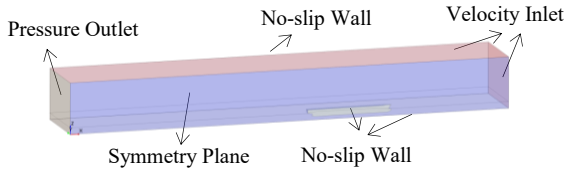

Figure 1. Computational domain and boundary conditions.

3.3 MESH GENERATION

The trimmed cell mesher is used to generate the unstructured hexahedral cells with polyhedral trimmed cells adjacent to the surface. The mesh around the hull, the expected free surface and in the wake produced by the moving ship are progressively refined by using customized volumetric refinements to capture the complex flow features, as shown in Figure 2.

In order to study the effect of wall reflections, the mesh adjacent to the tank side boundary is also progressively refined as shown in Figure 2. The size of the first grid layer adjacent to the hull makes sure $y^+ < 1$, and 20 layers with a stretching ratio equal to 1.15 are generated by using the prism layer mesher to deal with the computation within the viscous sublayer of the boundary layer by solving the transport equations all the way to the wall cell. Three layers of grids adjacent to the tank bottom boundary with a stretching ratio equal to 1.1 are also generated, and the size of the first layer makes sure $y^+ > 30$ when the wall function works.

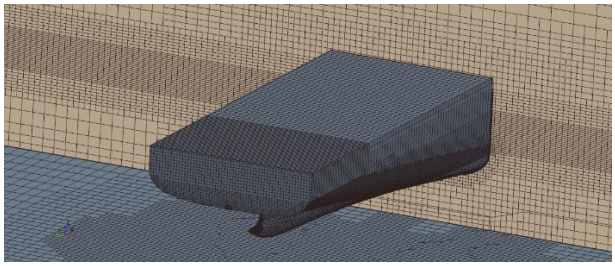

(a) Ship hull mesh (stern)

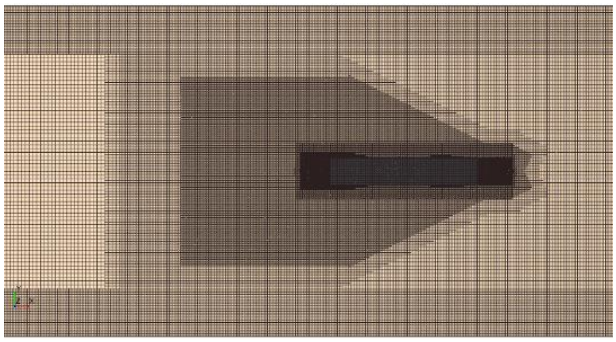

(b) Free surface mesh (top view)

Figure 2. Computational mesh.

3.4 POST-PROCESSING

For calm water cases, the mean value of the resistance is extracted from the data series as the calm water resistance. For head wave cases, the data series of heave motion, pitch motion, heave force, pitch moment, wave elevation and resistance are processed by means of the Fourier Series (FS) expansion. The FS is expanded to the 3rd-order as follows:

$$\begin{cases} X(t) = \sum_{n=0}^{3}\left[a_n \cos\left(2\pi f_e n t\right) + b_n \sin\left(2\pi f_e n t\right)\right] \\ \qquad = X_0 + \sum_{n=1}^{3} X_n \cos\left(2\pi f_e n t + \gamma'_n\right) \\ \cos\gamma_n = \dfrac{a_n}{\sqrt{a_n^{\,2} + b_n^{\,2}}}, \quad \sin\gamma_n = \dfrac{-b_n}{\sqrt{a_n^{\,2} + b_n^{\,2}}} \\ X_n = \sqrt{a_n^{\,2} + b_n^{\,2}} \\ \gamma'_n = \gamma_n - \gamma_0 \end{cases} \tag{10}$$

The mean value (namely the 0th harmonic amplitude), 1st harmonic amplitude and phase of the corresponding parameters together with the calm water resistance are used to calculate the total resistance coefficient in calm water, added resistance coefficient in waves, and the RAOs of heave and pitch motions.

$$\begin{cases} C_t = \dfrac{R_c}{\frac{1}{2}\rho S_w U^2}, \quad C_{aw} = \dfrac{R_{w0} - R_c}{\rho g A^2 B_{wl}^2 / L_{pp}} \\ \mathrm{RAO}_{heave} = \dfrac{z_1}{A}, \quad \mathrm{RAO}_{pitch} = \dfrac{\theta_1}{AK} \end{cases} \tag{11}$$

4 RESULTS AND ANALYSIS

4.1 VERIFICATION STUDY

The numerical uncertainties due to the grid resolution and time step are analyzed respectively. Other numerical uncertainties due to ship free motions or mesh deforming are not discussed here. Verification studies are first carried out for the calm water case and the head wave case (λ/L_{pp}=0.55). The Richardson extrapolation (RE) method is used as the basis for discretization error estimation. Based on the RE method (Stern et al. 2006, Celik et al. 2008), the Grid Convergence Index (GCI) method is used to estimate the numerical uncertainties. Following the recommended procedure for estimation of discretization error, the convergence study is carried out with triple solutions using systematically refined grid spacing or time step respectively. To be specific, for the grid convergence study, the grid base size is systematically refined with a constant refinement ratio (r) equal to $\sqrt{2}$ by multiplying or dividing the grid base size by $\sqrt{2}$ while all other input parameters are kept constant. The same setting is established for the time-step convergence study. The grid convergence study is performed with the smallest time step, while the time-step convergence study is conducted with the medium grid spacing, which is the suitable grid size based on the grid convergence study in terms of numerical accuracy and computational consumption. It should be noted that although performing the grid convergence study with the smallest time step instead of a constant Courant number may result in a dependency between the temporal and the spatial uncertainty, as long as a small time step is used and the numerical stability is guaranteed for the chosen temporal discretization scheme, the dependency may be considered small.

In the convergence study, the convergence ratio (R), order of accuracy (P), extrapolated value (s_{ext}^{21}), approximate relative error (e_{a}^{21}), extrapolated relative error (e_{ext}^{21}), and the fine-grid convergence index (GCI_{fine}^{21}) are defined as:

$$R=\frac{\varepsilon_{21}}{\varepsilon_{32}}=\frac{S_2-S_1}{S_3-S_2} \qquad P=\frac{\left|\ln\left|\varepsilon_{32}/\varepsilon_{21}\right|\right|}{\ln(r)}$$
$$s_{\text{ext}}^{21}=\frac{r^P S_1-S_2}{r^P-1} \qquad e_{\text{a}}^{21}=\frac{\left|S_1-S_2\right|}{\left|S_1\right|} \tag{12}$$
$$e_{\text{ext}}^{21}=\frac{\left|s_{\text{ext}}^{21}-S_1\right|}{\left|s_{\text{ext}}^{21}\right|} \qquad GCI_{\text{fine}}^{21}=\frac{1.25e_{\text{a}}^{21}}{r^P-1}$$

where S is the simulation results by CFD; S_1, S_2 and S_3 are the simulation results by fine-grid, medium-grid and coarse-grid respectively, or the simulation results by smallest, medium and largest time step respectively.

For different convergence ratios, the convergence conditions can be divided into four types: a) Monotonic convergence ($0<R<1$); b) Oscillatory convergence ($-1<R<0$); c) Monotonic divergence ($R>1$); d) Oscillatory divergence ($R<-1$). Only the monotonic convergence and the oscillatory convergence conditions are analyzed.

The verification parameters of sinkage and coefficient of total resistance for grid and time-step convergence studies for the calm water case are listed in Table 2 and Table 3, respectively. It can be seen that the numerical uncertainties due to grid resolution and time step for ship sinkage and total resistance in calm water are all small, especially for sinkage. The numerical uncertainty due to either grid or time-step discretization error for total resistance is relatively larger than that for ship sinkage, but the largest uncertainty quantified by *GCI* equals to 3.95% for total resistance due to the time-step discretization error. Thus, the calm water case is later studied by the medium grid size and smallest time step. It should be noted that the verification of trim is not carried out as the predicted trim angle is very small and the differences between three solutions are close to zero so that the verification procedure above does not work. This may be an indication of oscillatory convergence or that the "exact" solution has been obtained (Celik et al. 2008).

Table 2. Grid convergence study for calm water case

	$z_0/L_{\text{pp}}\times10^2$	$C_{\text{t}}\times10^3$
S_1	-0.1179	4.5545
S_2	-0.1183	4.5339
S_3	-0.1202	4.5592
R	0.2161	-0.8125
P	4.4211	0.5990
s_{ext}^{21}	-0.1178	4.6437
e_{a}^{21}	0.34%	0.45%
e_{ext}^{21}	0.09%	1.92%
GCI_{fine}^{21}	0.12%	2.45%
Convergence	monotonic	oscillatory

Table 3. Time-step convergence study for calm water case

	$z_0/L_{\text{pp}}\times10^2$	$C_{\text{t}}\times10^3$
S_1	-0.11834	4.5339
S_2	-0.11819	4.5134
S_3	-0.11841	4.5368
R	-0.6752	-0.8751
P	1.1334	0.3849
s_{ext}^{21}	-0.1186	4.6771
e_{a}^{21}	0.13%	0.45%
e_{ext}^{21}	0.26%	3.06%
GCI_{fine}^{21}	0.33%	3.95%
Convergence	oscillatory	oscillatory

The verification parameters of the 1st harmonic amplitude of heave and pitch motions, generated waves and the coefficient of added resistance for grid and time-step convergence studies for the head wave case are listed in

Table 4 and Table 5 respectively. It can be seen that the numerical uncertainties for heave motion, wave elevation and added resistance in waves are all small, while the numerical uncertainty for pitch motion is relatively large, approximately 17% and 10% of the results obtained with the finest grid and the smallest time step respectively. This may be due to the small value of ship pitch angles and the contribution from the numerical uncertainty of mesh deforming due to the pitch motion. Based on the verification results, the head wave cases are later studied by the medium grid size and the smallest time step.

Table 4. Grid convergence study for head wave case (λ/L_{pp}=0.55)

	z_1/A	θ_1/AK	A_1/A	C_{aw}
S_1	0.1927	0.0451	0.9256	2.4278
S_2	0.1938	0.0460	0.9350	2.4002
S_3	0.1919	0.0450	0.9469	2.2720
R	-0.587	-0.872	0.790	0.215
P	1.536	0.394	0.682	4.438
s_{ext}^{21}	0.1911	0.0390	0.8903	2.4353
e_a^{21}	0.57%	2.00%	1.02%	1.13%
e_{ext}^{21}	0.81%	15.83%	3.96%	0.31%
GCI_{fine}^{21}	1.01%	17.08%	4.76%	0.39%
Converge nce	oscillat ory	oscillat ory	monoto nic	monoto nic

Table 5. Time-step convergence study for head wave case (λ/L_{pp}=0.55)

	z_1/A	θ_1/AK	A_1/A	C_{aw}
S_1	0.1938	0.0460	0.9350	2.4002
S_2	0.1905	0.0472	0.9226	2.3291
S_3	0.1815	0.0486	0.9011	2.0792
R	0.3720	0.7677	0.5794	0.2844
P	2.8529	0.7629	1.5749	3.6280
s_{ext}^{21}	0.1958	0.0423	0.9521	2.4285
e_a^{21}	1.71%	2.44%	1.33%	2.96%
e_{ext}^{21}	1.01%	8.78%	1.80%	1.16%
GCI_{fine}^{21}	1.27%	10.09%	2.29%	1.47%
Converge nce	monoto nic	monoto nic	monoto nic	monoto nic

4.2 CALM WATER CASE

Ship straight-ahead motions at 16 knots (full-scale) under 100% UKC in calm water are numerically simulated to obtain the resistance. The tank wall effect is investigated. The dimensionless sinkage, trim and coefficients of total resistance together with the comparison errors are listed in Table 6, where the comparison error E%D is defined as follow:

$$\text{E\%D} = \frac{D-S}{D} \times 100 \quad (13)$$

where D is the processed model test data.

It can be seen that when the bank wall effect is considered as in the model test, the relative errors between CFD results and model test data are relatively large for ship squat, while the relative error of the coefficient of total resistance is smaller, equal to 13% approximately. Actually, for sinkage and trim, the large discrepancies may be due to the small values of these parameters, especially for trim angle (which is approximately 0.06°). To further improve the prediction accuracy of the coefficient of total resistance by CFD method, a finer grid resolution may be needed, especially grids near and after the hull, near the free surface and the side wall of the tank. Moreover, it should be noted that in the present simulation study only the SST *k-ω* model is adopted, the limitation of its applicability in this shallow water problem may also lead to the inaccuracy in the prediction results by CFD method.

It can also be seen from Table 6 that the bank wall effect on the ship sinkage is large, while it is small on the trim and the coefficient of total resistance. Overall, in the two cases considered, the bank wall has a non-negligible effect on ship squat, while the bank wall effect on the total resistance is negligible.

Table 6. Numerical results of calm water case

	$z_0/L_{pp} \times 10^2$	Trim (mm/m)	$C_t \times 10^3$
Narrow tank	-0.1183	-1.0497	4.5339
E%D	29.181	-25.642	13.14
Wide tank	-0.0960	-1.0582	4.4268

The wave patterns generated around the ship advancing in the narrow tank and in the wide tank are shown in Figure 3. As can be seen in the figure, for the narrow tank, the waves generated by the ship are reflected by the tank wall, and the reflected waves dissipate as they further propagate downstream. However, for the wide tank, the reflection no longer exists.

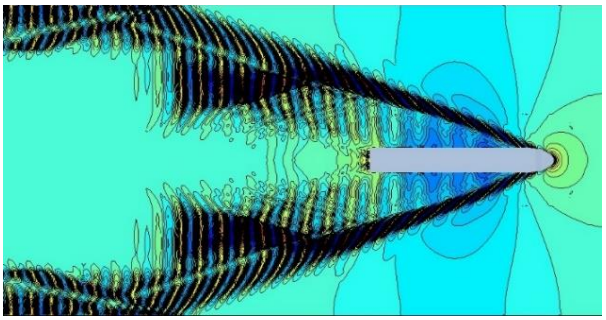

(a) Narrow tank (W_{tank}/L_{pp}=1.757)

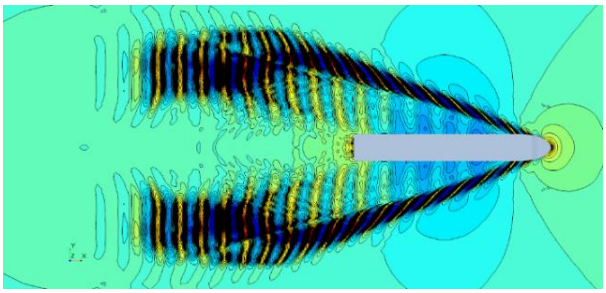

(b) Wide tank (W_{tank}/L_{pp}=4.5)

Figure 3. Wave patterns generated around ship.

4.3 HEAD WAVE CASE

Ship sailing in head waves (λ/L_{pp}=0.55) at 16 knots (full-scale) under 100% UKC are numerically simulated. Ship heave motion, pitch motion, heave force, pitch moment and added resistance are obtained and processed according to the method described in Section 3.4. The available raw experimental data and the raw CFD time series data together with the processed CFD time series data by FS expansion for λ/L_{pp}=0.55 are compared as shown in Figure 4. The CFD results together with the comparison errors are listed in Table 7.

Table 7. Numerical results of head wave case (λ/L_{pp}=0.55)

	z_1/A	$z_0/L_{pp} \times 10^2$	θ_1/AK	C_{aw}	A_1/A
Narrow tank	0.194	-0.184	0.046	2.400	0.935
E%D	-8.99	-3.84	-1.69	-0.61	2.47
Wide tank	0.195	-0.122	0.048	2.659	0.950

As shown in Figure 4, the fitted curves reconstructed by FS expansion of ship motions, total resistance in waves and wave elevation agree favorably with the model test data. As can be seen in Table 7, the generated shallow water waves show very small decay near the ship's center of gravity in both tanks (narrow tank and wide tank), indicating a stable and regular numerical wave environment, which is similar to the model test results (Van Zwijnsvoorde, 2019). When the bank wall effect is considered, the largest errors between the CFD results and the model test data exist in ship heave motion, where the RAO and the mean value are over-predicted by 8.99% and 3.84% respectively, which means that the current CFD results give a more conservative estimation of ship UKC in shallow water waves. The error between the RAO of pitch motion predicted by CFD and the model test data is small, equal to -1.69%, but the mean value of pitch motion is not compared to the model test data as the values obtained by CFD and model test are both very small, which may lead to large uncertainty. On the other hand, the CFD method predicts the added resistance in waves quite well with an error of -0.61%.

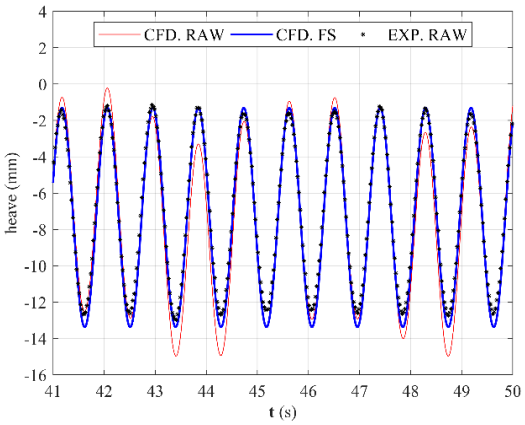

(a) Heave motion

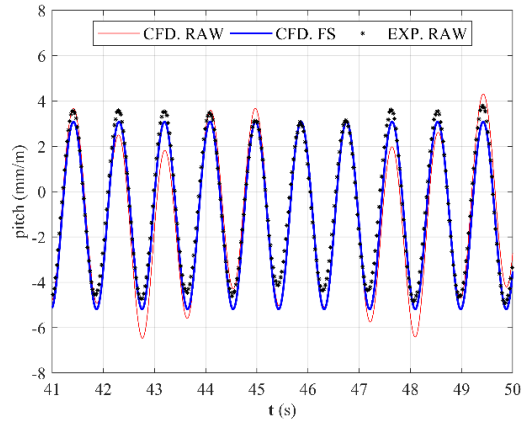

(b) Pitch motion

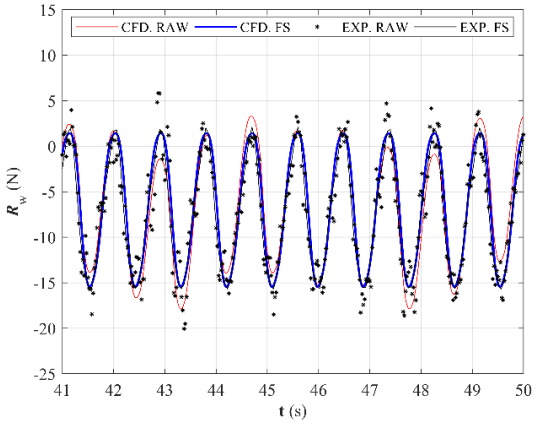

(c) Total resistance in waves

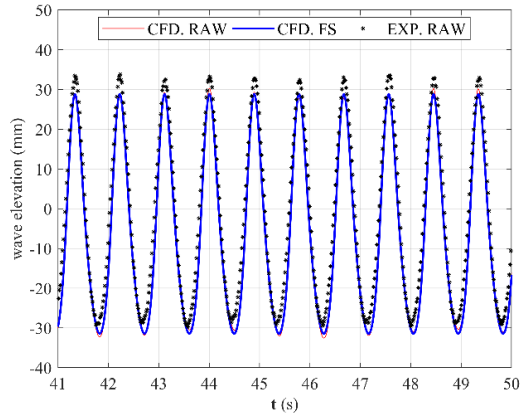

(d) Wave elevation

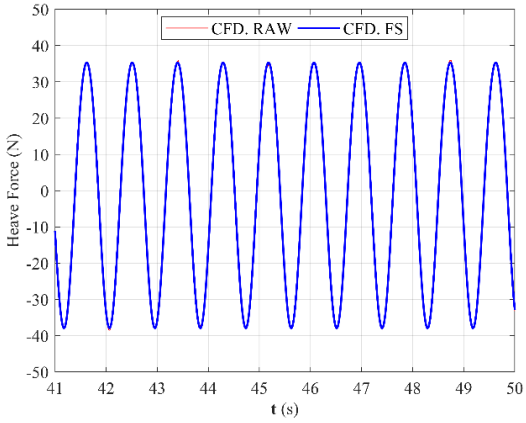

(e) Heave force

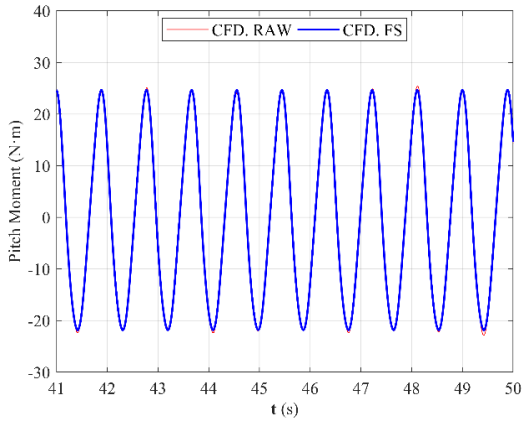

(f) Pitch moment

Figure 4. Comparison of Time series data, λ/L_{pp}=0.55

Similar to the calm water case, the discrepancies may be attributed to the discretization error due to grid resolution and time step, especially the resolution of grids underneath the ship hull, near the free surface and the side wall of the tank, and to the capability of SST k-ω turbulence model applied in the shallow water wave problems. Besides, the numerical uncertainties due to geometry modelling and mesh deforming as well as the experimental uncertainties may also lead to the discrepancies between the CFD results and model test data.

Comparing the results of the two tanks, it can be seen that the bank wall effect is significant for the mean value of heave motion; in the narrow tank, the sinkage is larger than that in the wide tank, indicating that ships sailing in shallow water areas with restricted width have greater risks in grounding. Besides, it can be seen that the bank wall effect on the added resistance is not negligible.

The pressure distributions on the hull are illustrated in Figures 5 and 6. Figure 7 depicts the wave pattern on the free surface. The correlation between ship motions and wave forces in two encounter periods is shown in Figure 8. The velocity field near the hull is shown in Figures 9, 10 and 11. The change of turbulent viscosity ratio below the free surface due to ship motions is shown in Figure 12. The boundary layer represented by axial velocity is illustrated in Figures 13.

As can be seen in Figure 8, ship heave motion is in the opposite phase with heave force acting on the ship hull, and the same for pitch motion and pitch moment. According to the pressure distributions shown in Figure 5 and 6, wave patterns in Figure 7, the correlations between ship motions and wave forces are analyzed in the following.

At $t/T_e = 0$, when a wave crest is located at the ship's center of gravity, the phase of heave motion is approximately 45° ahead of the wave, and the phase of pitch motion is approximately 45° behind the wave. At this moment, there exists a high-pressure area near the midship, and the ship hull is sinking and trimming by bow. During the first half of encounter period, the pitch moment acting on the ship hull first makes the hull continue to trim to bow until it approaches the maximum trim angle by bow when the pitch moment also reaches its maximum value. Then, the hull begins to trim to stern with an increasing angular velocity and a decreasing pitch moment. For heave motion, the heave force first makes the hull continue to sink until it approaches the lowest position when the heave force also reaches its maximum value. Then, the hull begins to uplift with an increasing upward translational velocity and a decreasing upward heave force. Meanwhile, the high-pressure area shifts to the back half of ship hull as the wave crest propagates towards the stern. During the second half of encounter period, the correlations between ship motions and wave forces are the same as those during the first half, but the variation trends are reversed.

As shown in Figure 9, the propagation of velocity field underneath the hull follows the wave propagation, and the water depth has an obvious restrictive influence on the velocity. The velocity vectors in Figure 10 and 11 depict the complicated change of velocity field close to the bow and stern under the effect of shallow water waves. This complexity in velocity field indicates that special attentions should be paid to the bow and stern regions in spatial discretization for further improving the numerical results.

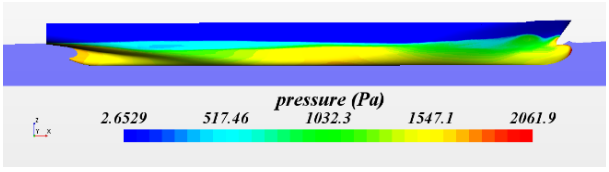

(a) $t/T_e = 0$

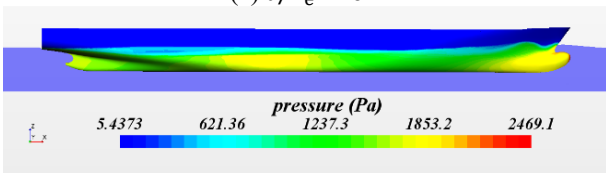

(b) $t/T_e = 0.25$

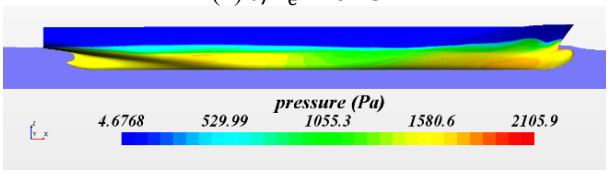

(c) $t/T_e = 0.5$

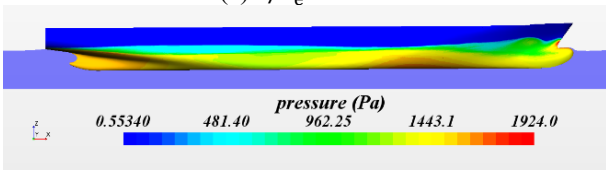

(d) $t/T_e = 0.75$

Figure 5. Pressure distribution on the hull (side view) in one encounter period for λ/L_{pp}=0.55

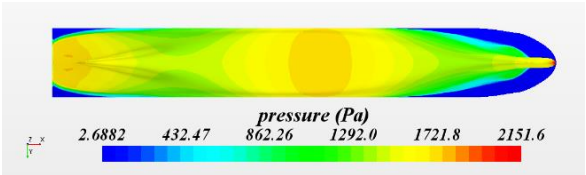

(a) $t/T_e = 0$

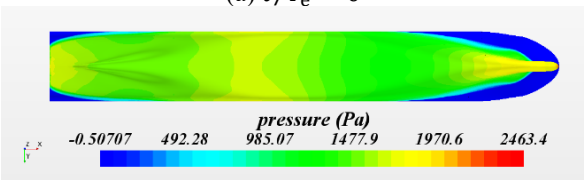

(b) $t/T_e = 0.25$

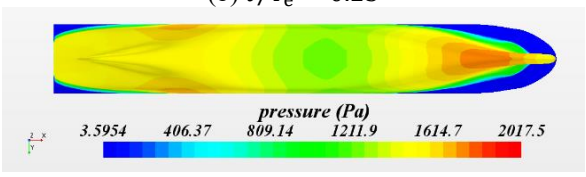

(c) $t/T_e = 0.5$

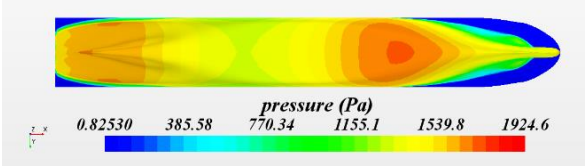

(d) $t/T_e = 0.75$

Figure 6. Pressure distribution on the hull (bottom view) in one encounter period for λ/L_{pp}=0.55

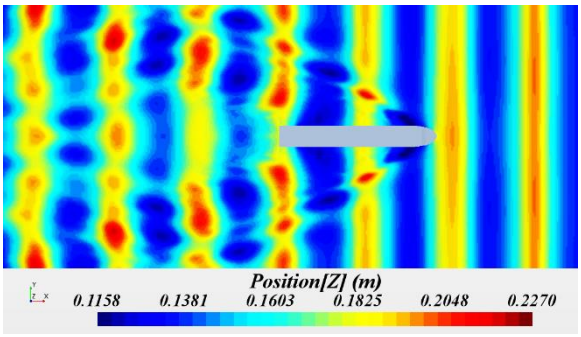

(a) $t/T_e = 0$

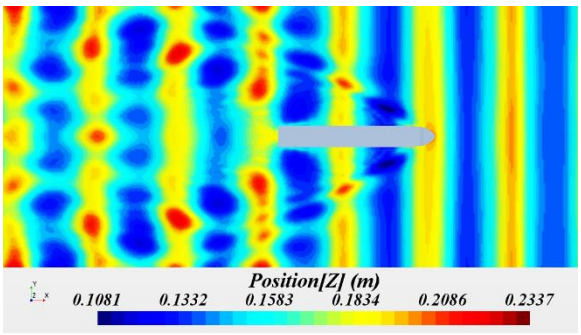

(b) $t/T_e = 0.25$

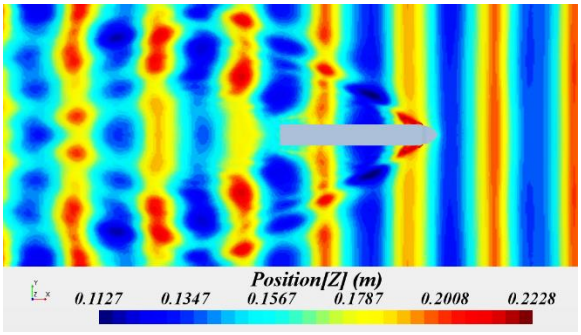

(c) $t/T_e = 0.5$

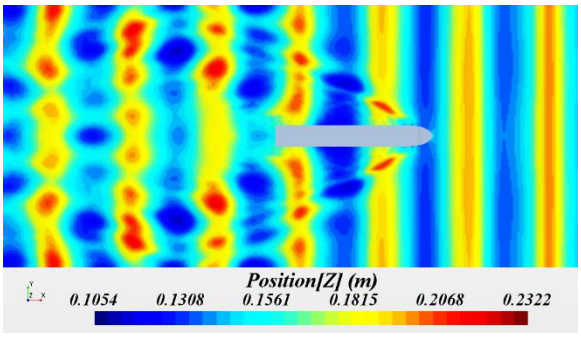

(d) $t/T_e = 0.75$

Figure 7. Wave patterns on the free surface in one encounter period for λ/L_{pp}=0.55

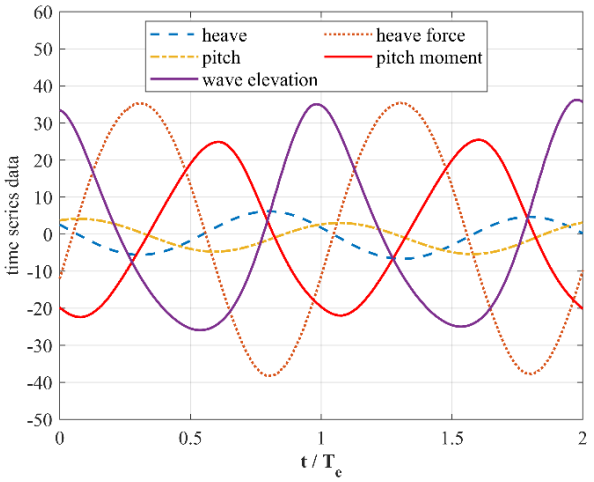

Figure 8. Wave elevation, ship motions and wave forces in two encounter periods for λ/L_{pp}=0.55

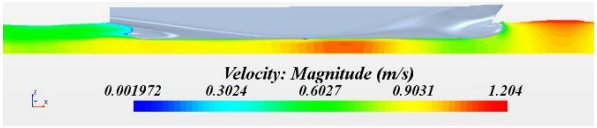

(a) $t/T_e = 0$

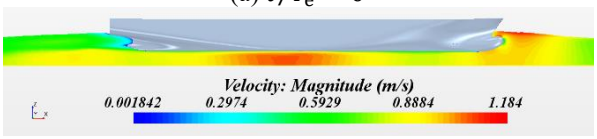

(b) $t/T_e = 0.25$

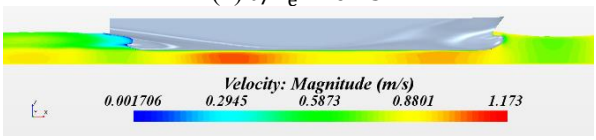

(c) $t/T_e = 0.5$

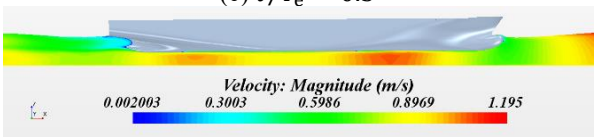

(d) $t/T_e = 0.75$

Figure 9. Velocity scalar fields near the hull in one encounter period for λ/L_{pp}=0.55

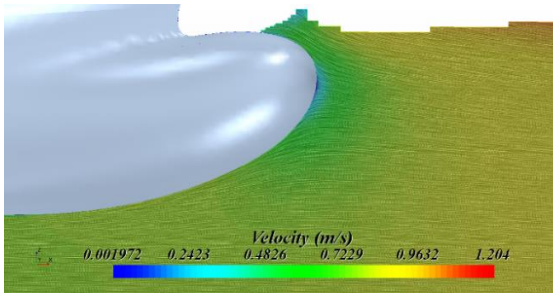

(a) $t/T_e = 0$

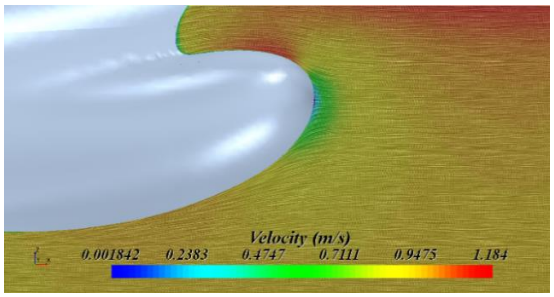

(b) $t/T_e = 0.25$

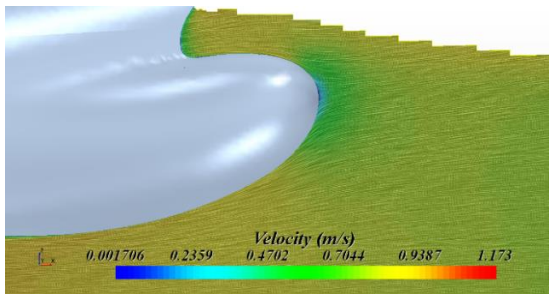

(c) $t/T_e = 0.5$

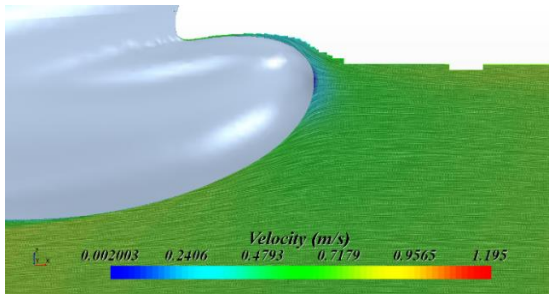

(d) $t/T_e = 0.75$

Figure 10. Velocity vectors near the bow in one encounter period for λ/L_{pp}=0.55

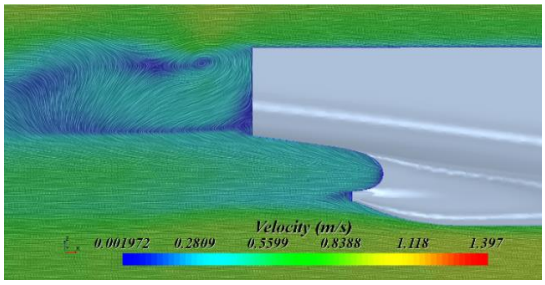

(a) $t/T_e = 0$

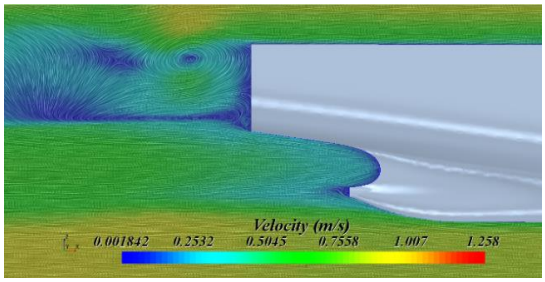

(b) $t/T_e = 0.25$

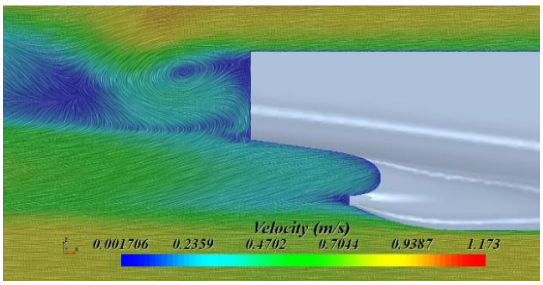

(c) $t/T_e = 0.5$

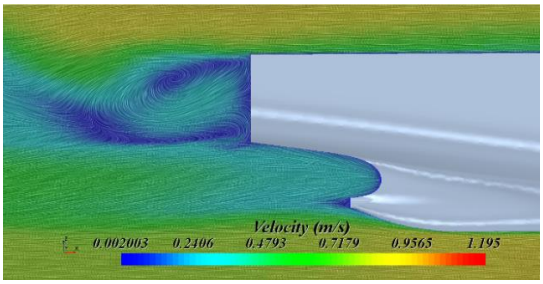

(d) $t/T_e = 0.75$

Figure 11. Velocity vectors near the stern in one encounter period for λ/L_{pp}=0.55

The turbulent viscosity ratio in Figure 12 shows that the turbulent dispersion is nearly homogeneous underneath the hull, similar to the findings for a zero-speed tanker ship by Tezdogan et al. (2016). As the turbulent viscosity ratio is in proportion to the Reynold number, the distribution of turbulent viscosity ratio after the ship is similar to the velocity field after the ship as shown in Figure 9. The turbulent viscosity ratio in the boundary layer is gradually increased. Besides, a very low magnitude of the turbulent viscosity ratio is found in front of the bow in the present paper while Tezdogan et al. (2016) found a peak in turbulent viscosity ratio in front of the bow region. The reason may be that a zero-speed together with long shallow water wave case was considered in their work, while in the present study, the wavelength is only about half the ship length and a forward speed case is simulated.

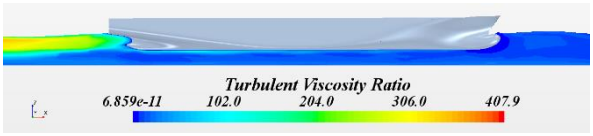

(a) $t/T_e = 0$

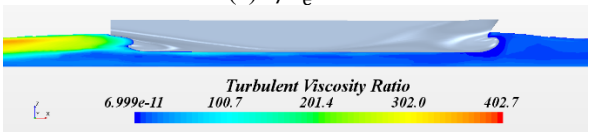

(b) $t/T_e = 0.25$

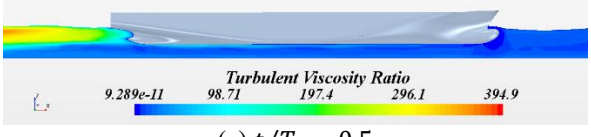

(c) $t/T_e = 0.5$

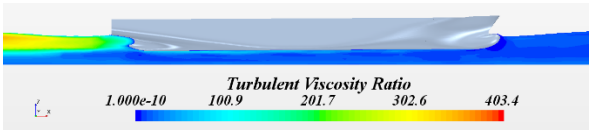

(d) $t/T_e = 0.75$

Figure 12. Turbulent viscosity ratio below the free surface in one encounter period for λ/L_{pp}=0.55

According to Figures 8 and 13, the change of boundary layer can be analyzed as follows. In the first quarter of encounter period, ship is below the mean position of heave motion and has a trim by bow, and continues to sink and trim to bow, so the vortices underneath the hull are transported downstream, the thickness of the boundary layer at the aft half of the hull increases. In the second quarter of encounter period, ship lifts up and starts to trim towards stern from the maximum trim by bow, so the thickness of boundary layer at the aft half of the hull continues to increase until the instant when the ship sinks and has a trim by stern. From that moment on, the thickness of boundary layer at the front half of the hull shows a trend of increase. During the second half of the encounter period, the change of boundary layer reverses.

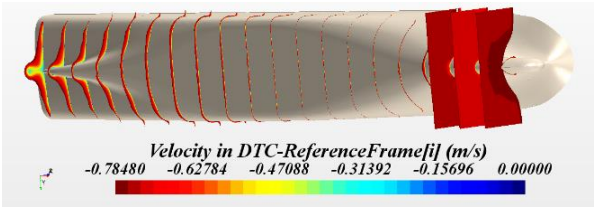

(a) $t/T_e = 0$

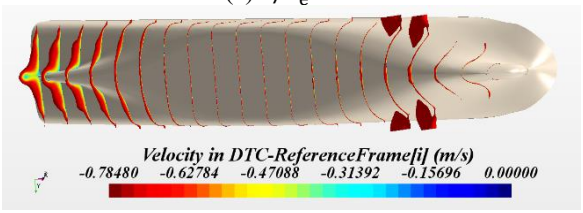

(b) $t/T_e = 0.25$

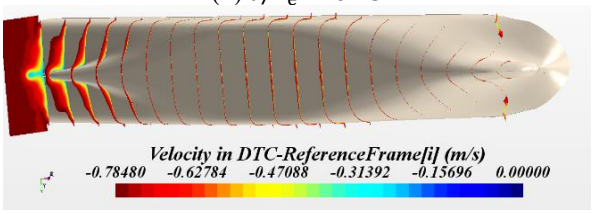

(c) $t/T_e = 0.5$

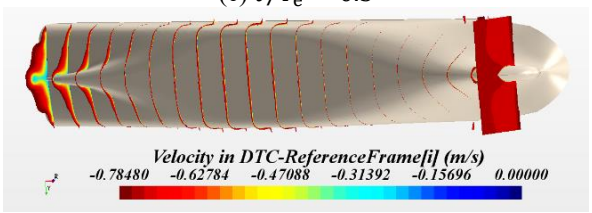

(d) $t/T_e = 0.75$

Figure 13. Boundary layers in one encounter period for λ/L_{pp}=0.55

The RAO of heave and pitch motions, wave elevation and the coefficient of added resistance at four wavelengths are listed in Table 8, and the results fitted by spline interpolation method are shown in Figure 14. The minimum clearance between the tank bottom and the two most critical positions on the ship hull (i.e., the lowest points on the fore and aft half of ship hull) are calculated and plotted in Figure 15.

As shown in Table 8 and Figure 14, for shallow water waves with wavelength ranging from $0.55L_{pp}$ to $1L_{pp}$, all four considered wavelengths can be successfully generated with sufficient stability and accuracy based on a first-order Stokes wave theory. As the wavelength increases, the RAO of heave motion and the coefficient of added resistance in waves firstly increase and then decrease; the mean value of heave motion decreases monotonically; and the RAO of pitch motion increases monotonically.

Table 8. Numerical results of head wave cases

λ/L_{pp}	z_1/A	$z_0/L_{pp} \times 10^2$	θ_1/AK	C_{aw}	A_1/A
0.55	0.194	-0.184	0.046	2.400	0.935
0.70	0.302	-0.158	0.134	3.855	1.083
0.85	0.285	-0.138	0.299	4.811	0.977
1.00	0.268	-0.096	0.459	2.495	0.981

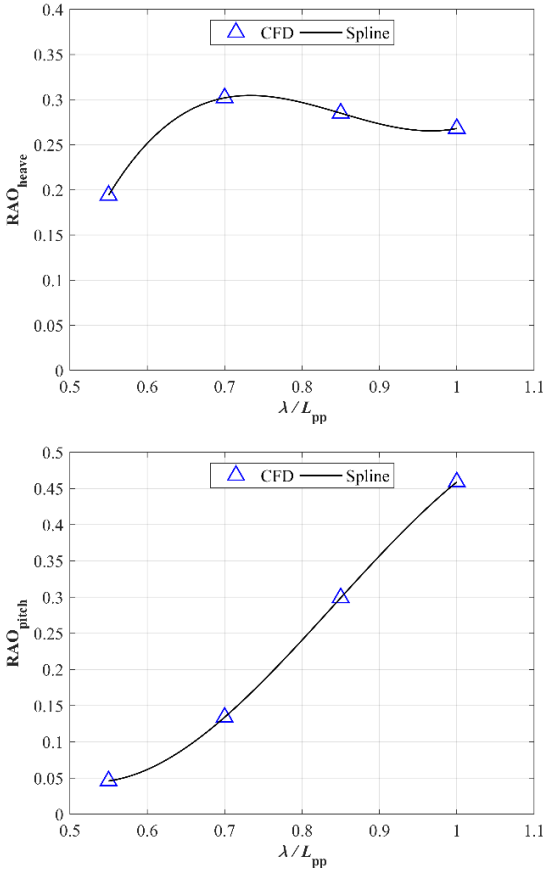

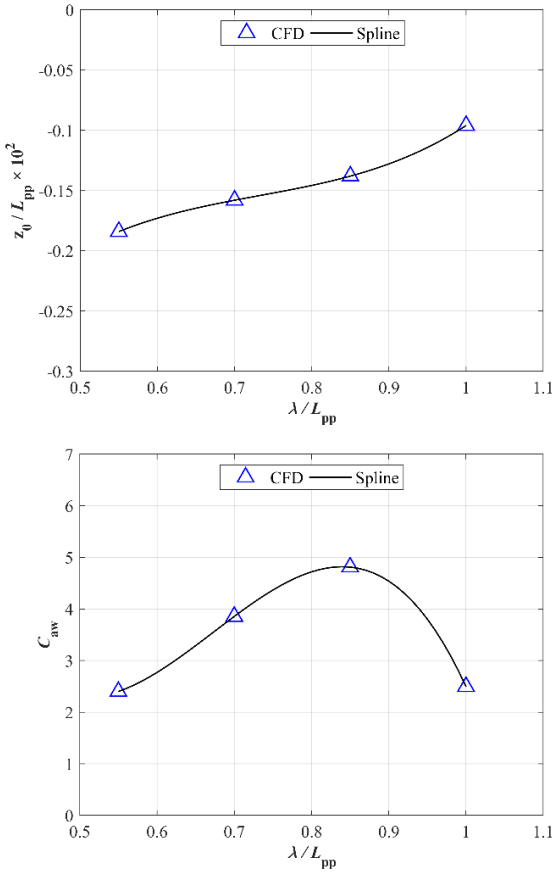

Figure 14. Numerical results at different wavelengths

As can be seen in Figure 15, the minimum clearance between the ship hull and the tank bottom decreases monotonically as the wavelength increases, and it approaches a value of 58% for the longest wave when the initial UKC is 100%, indicating that it is much more dangerous for ship sailing in long shallow water waves.

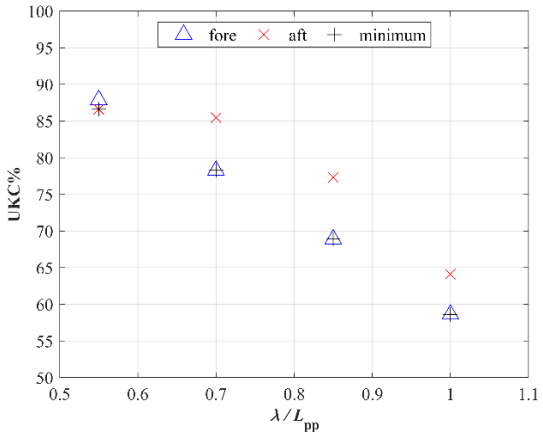

Figure 15. Minimum clearance between the ship hull and the tank bottom for head wave cases

5 CONCLUSIONS

In this paper, CFD software STAR-CCM+ is used to carry out the RANS-based numerical simulations of a DTC model sailing straight-forward in calm water and in head waves in shallow water with 100% UKC. The ship squat and total resistance are predicted for a calm water case, and ship heave and pitch motions, wave forces, added resistance in waves are predicted for head wave cases.

The verification study of the numerical method is carried out by applying GCI method to analyze the discretization error due to grid resolution and time step. The verification results show small numerical uncertainties for the sinkage and the total resistance in calm water and heave motion, wave amplitude, and added resistance in waves, but a relatively large numerical uncertainty for pitch motion in waves.

Systematic simulations are carried out at λ/L_{pp}=0.55 as in the model tests, and the flow properties including the wave patterns on the free surface, the pressure distribution on the ship hull, the velocity field near the hull, turbulent viscosity ratio underneath the free surface and the boundary layer on the hull are obtained. The correlations between ship motions and wave forces acting on the hull are further investigated based on the flow properties. The bank wall effect is also investigated for the calm water case and the head wave case. Moreover, the minimum clearance between the ship hull and the tank bottom is predicted for four wavelengths based on the time series data obtained by CFD computation.

The comparison between the CFD results and model test data shows that the error of ship squat in calm water is relatively large, but the error of total resistance in calm water is smaller; the error of ship heave motions in waves is relatively large, but the error of added resistance is small. The heave motion in waves is a little over-predicted, which gives a more conservative estimation of ship UKC. The bank wall effect is found to be significant for the mean value of heave motion and is not negligible for the added resistance. Moreover, by investigating the lowest position at the fore and aft parts of ship hull, it is found that ship tends to have smaller clearance underneath the bottom of the hull in longer shallow water waves.

It should be noted that in the present study, the numerical simulations are only carried out for one water depth and one ship speed; only the numerical simulations at λ/L_{pp}=0.55 are compared with the model test data; only the SST k-ω turbulence model is used, and the numerical uncertainties of trim angle in calm water as well as the mean value of pitch motion in waves are not discussed. In the future study, numerical studies of ship motions and resistance in shallow water waves with various ship speeds and water depths need to be carried out. Numerical simulations for wavelengths other than λ/L_{pp}=0.55 need to be validated when the corresponding model test data are available. The influences of different turbulence models on the CFD predictions need to be analyzed, and the numerical uncertainties of more parameters need to be investigated.

6 ACKNOWLEDGEMENTS

This work is supported by the National Natural Science Foundation of China (Grant No: 51779140).

7 REFERENCES

Carrica, P. M., Mofidi. A., Eloot, K., Delefortrie, G., 2016. Direct simulation and experimental study of zigzag maneuver of KCS in shallow water. *Ocean Engineering*, 112: pp. 117-133. DOI: 10.1016/j.oceaneng.2015.12.008.

CD-Adapco, 2017. User guide STAR-CCM+ Version 12.02

Celik, I., Ghia, U., Roache, P.J., Freitas, C., Coloman, H., Raad, P.E., 2008. Procedure of estimation and reporting of uncertainty due to discretization in CFD applications. *Journal of Fluids Engineering*, 130(7): 078001. DOI: 10.1115/1.2960953.

Deng, G., Leroyer, A., Guilmineau, E., Queutey, P., Visonneau, M., Wackers, J. 2016. CFD simulation of PMM motion in shallow water for the DTC container ship, *4th MASHCON International Conference on Ship Manoeuvring in Shallow and Confine Water with Special Focus on Ship Bottom Interaction*, Hamburg, Germany, pp. 93-98. DOI: 10.18451/978-3-939230-38-0_12.

Jachowski, J., 2008. Assessment of ship squat in shallow water using CFD. *Archives of Civil & Mechanical Engineering*, 8(1): pp. 27-36.

Liu, Y., Zou, Z. J., Zou, L., 2016. RANS-based numerical simulation of captive model tests in shallow water for the DTC container carrier, *4th MASHCON International Conference on Ship Manoeuvring in Shallow and Confine Water with Special Focus on Ship Bottom Interaction*, Hamburg, Germany, pp. 73-82. DOI: 10.18451/978-3-939230-38-0_10.

Moctar, O. E., Shigunov, V., Zorn, T., 2012. Duisburg test case: post-panamax container ship for benchmarking. *Ship Technology Research*, *59*(3), 50-64.

Senthil, P. N., Chandra, B., 2013. Numerical estimation of shallow water resistance of a river-sea ship using CFD. *International Journal of Computer Applications*, 71(5): pp. 33-40.

Stern, F., Wilson, R., Shao, J., 2006. Quantitative V&V of CFD simulations and certification of CFD codes. *International Journal for Numerical Methods in Fluids*, 50(11): pp. 1335-1355. DOI: 10.1002/fld.1090.

Tezdogan, T., Incecik, A., Turan, O., 2015. A numerical

investigation of the squat and resistance of ships advancing through a canal using CFD. *Journal of Marine Science & Technology*, 21(1): pp. 1-16. DOI: 10.1007/s00773-015-0334-1.

Tezdogan, T., Incecik, A., Turan, O. 2016. Full-scale unsteady RANS simulations of vertical ship motions in shallow water. *Ocean Engineering*, 123: pp. 131-145. DOI: 10.1016/j.oceaneng.2016.06.047

Terziev, M., Tezdogan, T., Oguz, E., Gourlay, T., Demirel, Y. K., Incecik, A. 2018. Numerical investigation of the behaviour and performance of ships advancing through restricted shallow waters. *Journal of Fluids & Structures*, 76: pp. 185-215. DOI: 10.1016/j.jfluidstructs.2017.10.003.

Van Zwijnsvoorde, T., Tello Ruiz, M., Delefortrie, G., Lataire, E. 2019. Sailing in shallow water waves with the DTC container carrier, in: Proceedings of the 5th International Conference on Ship Manoeuvring in Shallow and Confined Water with non-exclusive focus on Manoeuvring in Waves, Wind and Current. Ostend, Belgium.

8 AUTHORS BIOGRAPHY

Shuai Yuan holds the current position of master student at School of Naval Architecture, Ocean and Civil Engineering, Shanghai Jiao Tong University. His previous experience includes numerical studies on the ship manoeuvring in restricted waters, seakeeping, etc.

Li Xia holds the current position of PhD student at School of Naval Architecture, Ocean and Civil Engineering, Shanghai Jiao Tong University. His previous experience includes numerical studies on the ship manoeuvring in restricted waters, uncertainty quantification, etc.

Zaojian Zou holds the current position of full professor at School of Naval Architecture, Ocean and Civil Engineering, Shanghai Jiao Tong University. He is responsible for teaching and studying ship hydrodynamics and ship's steering and control. His previous experience includes PI of some projects on manoeuvring and control of ships and other marine vehicles. He was a member of the 22nd, 23rd, 25th and 26th ITTC MC.

Lu Zou is a lecturer at School of Naval Architecture, Ocean and Civil Engineering, Shanghai Jiao Tong University. Her major research interest is in the ship manoeuvring in confined waters, as well as Verification and Validation of CFD simulations.

PREDICTION OF SHIP-LOCK INTERACTION BY USING A MODIFIED POTENTIAL FLOW SOLVER

Zhi-Ming Yuan,
Department of Naval Architecture, Ocean and Marine Engineering, University of Strathclyde, UK

PREDICTION OF SHIP-LOCK INTERACTION BY USING A MODIFIED POTENTIAL FLOW SOLVER

Zhi-Ming Yuan, Department of Naval Architecture, Ocean and Marine Engineering, University of Strathclyde, UK

SUMMARY

Ship-lock interactions are very difficult to predict. The hydrodynamics of ships entering (or leaving) a lock is always accompanied with shallow water and bank effects. When a ship enters or leaves a lock with a closed end, a so-called piston effect will be provoked due to the translation waves trapped in the gap between the ship and the lock door. Meanwhile, as the water is accumulating or evacuating in a lock with closed end, a return flow will be generated. The nature of the complex hydrodynamics involved in ship-lock interactions have not been fully understood so far and it is very challenging to develop a mathematical model to predict ship hydrodynamics in a lock. In the 4th MASHCON, the author presented his original simulation results of the hydrodynamic forces on a ship when it entered a lock based on a potential flow solver MHydro. A very large discrepancy was found between the numerical results and experimental measurements. It was concluded that the potential flow theory failed to predict the hydrodynamic forces on a ship when it entered a lock. Over the past two years, the author has continuously worked on ship-to-lock problem and proposed a modified potential flow method by adding a proper return flow velocity to the boundary value problem. The results showed the modified method could predict the resistance and lateral forces very well. However, it failed to predict the yaw moment due to the flow separation at the lock entrance.

1 NOMENCLATURE

Φ	Velocity potential
A_s	Cross sectional area of a ship (m^2)
C_B	Block coefficient of the ship
d	Water depth (m)
F_1	Longitudinal force (N)
F_2	Transverse force (N)
F_6	Yaw moment (N·m)
F_r	Froude number
g	Gravitational acceleration (m/s^2)
L	Length of the ship (m)
l	Length of the lock (m)
p	Pressure (Pa)
t	Time (s)
T	Draft of the ship (m)
t_c	The time when the ship is completely in the lock (s)
t_e	The time when the ship bow reaches the lock entrance (s)
U	Forward speed of the ship (m/s)
v	Velocity of the return flow (m/s)
X_G	Longitudinal centre of gravity (m)
Z_G	Vertical centre of gravity (m)
δ	Block coefficient of the lock
ζ	Free-surface wave elevation (m)
κ	Acceleration coefficient
λ	Wave length (m)
ρ	Density of the fluid (kg/m^3)
φ_s	Steady velocity potential
φ_u	Unsteady velocity potential
Ω	Computational fluid domain
Δy	Eccentricity (m)

2 INTRODUCTION

Prediction of the hydrodynamic forces of a ship while entering or leaving a lock is very challenging. The main challenges include:

1) The hydrodynamics of ships entering (or leaving) a lock are always accompanied with shallow water and bank effects. By comparing with the hydrodynamic problems in restricted channels, the gaps between ship and bank, and the under-keel clearance are even smaller in the locks. As a result, a very strong ship-bank and ship-bottom interaction occurs, which makes the hydrodynamic behaviour be totally different from that in unrestricted waterways.
2) The manoeuvring of ships in confined inland waterways, e.g. in shallow and narrow channels, is usually treated as a steady problem. The width and depth of the channel are assumed to be unchanged. However, the ship-lock interaction is typically an unsteady problem. During the entering (or leaving) process, the width of the waterways is changing with the time. If we establish a body-fixed coordinate system in the mathematical model, the boundaries of the computational domain are time-dependent. An unsteady analysis in time-domain must be performed to deal with this unsteady lock entering problem, which requires a higher spatial and temporal resolution.
3) In the lock area, the waterways are restricted not only by the bank and bottom, but also by the lock door. As a result, when a ship is entering a lock, the fluid in front of the ship is blocked, accumulating in the gap between the ship and door. Two consequences are accompanied: a return flow and unsteady waves in the lock with closed end. To model these waves/return flow, a sophisticated

nonlinear free surface condition must be proposed. The complicated wave systems in the gap between the ship and the door are not yet fully understood.

To address the above mentioned issues, the 3rd International Conference on Ship Manoeuvring in Shallow and Confined Water (3rd MASHCON) focused on ship behaviour in locks non-exclusively (Vantorre et al., 2012). The benchmark model test data obtained at Flanders Hydraulics Research were made publicly accessible, which enables validations for different numerical methods and tools. Henn (2013) used the benchmark data to validate his numerical method, which could be potentially implemented into ship handling simulators for lock manoeuvres. Lindberg et al. (2013) proposed a numerical model based on potential flow theory that uses a linear or non-linear free surface boundary condition and high-order accurate numerical approximations. The benchmark tests were used to evaluate the free surface elevation. They found the pressure distribution model could not represent the body surface boundary condition.

The benchmark data have also been widely used to validate the numerical results obtained by CFD (computational fluid dynamics) tools. De Loor et al. (2013) used the benchmark data to validate the lateral and longitudinal forces on a vessel by using OpenFOAM. It was concluded the application of CFD was not yet able to predict absolute design values with sufficient accuracy. Wang and Zou (2014) performed numerical simulations to solve the unsteady RANS equations with a RNG k - ε turbulence model by using ANSYS FLUENT. Dynamic mesh method and sliding interface technique were used to deal with the relative motion between the passing ship and the lock. By comparing with the benchmark test data, it was found the lateral force and yaw moment were well predicted, while the longitudinal force was underestimated, due to the neglect of the free surface elevation. Similar numerical simulations studies were also conducted by Toxopeus and Bhawsinka (Toxopeus and Bhawsinka, 2016). They used a viscous-flow solver ReFRESCO to predict the ship-lock interaction effects. The results of the hydrodynamic forces were validated against the benchmark data. Very good agreement was achieved in Case G. But in Case H, the predictions showed a large discrepancy. They also included the results obtained by using potential flow solver ROPES in the comparison and concluded that the ship-lock interaction could not be captured by potential flow solver, in which the viscous effects were not accounted. It coincides with Yuan and Incecik's (2016) conclusion that the potential flow solver failed to predict the ship-lock interaction problem.

None of the above mentioned studies address the unsteady wave problems associated with ship-lock interaction. In most of the CFD simulations (De Loor et al., 2013; Toxopeus and Bhawsinka, 2016; Wang and Zou, 2014), the free surface was replaced by a rigid wall condition. As a result, the water elevation in the lock area cannot be captured. Toxopeus and Bhawsinka (Toxopeus and Bhawsinka, 2016) concluded that the interaction forces experienced in the lock were not primarily determined by the translation waves travelling in the lock. However, the wave phenomenon was physically measured in the benchmark tests, especially in lock exit tests (Test C, D and E) (Vantorre et al., 2012). As shown in **Figure 1**, when the ship model enters the lock, a harmonic wave with period of 25s was measured at the door. To the author' knowledge, such piston-like free surface elevation are not yet fully understood. No published numerical works are able to capture these waves, including those CFD works that take the free surface condition into account (Meng and Wan, 2016). Although some primary works proposed some mathematical model to represent the waves in the lock, the estimations were not validated against the benchmark data (Vergote et al., 2013; Vrijburcht, 1988). Therefore, more sophisticated mathematical models are required to help us to understand the fundamental aspect of the waves in the lock.

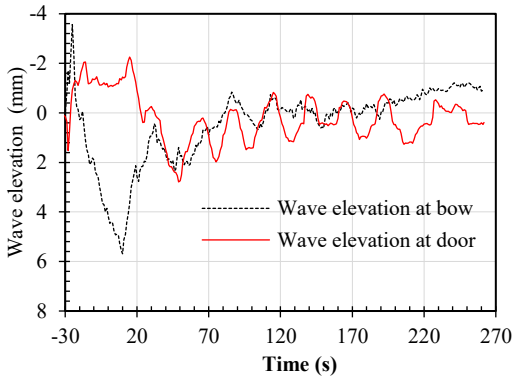

Figure 1. Measurement of wave elevation of Test D (Vantorre et al., 2012).

The limitation of potential flow method on ship-lock interaction problem is fully recognized by the author when he presented his original prediction in the 4th MASHCON. However, the high efficiency of potential flow solver is highly demanded in manoeuvring simulator. Since then, the author has been continuously working on proposing on a modified potential flow solver that could provide reasonable prediction of ship-lock interaction. The only published results based on a potential flow solver (Toxopeus and Bhawsinka, 2016) are shown in Figure 2. The potential flow method only captures the initial interaction effects before the bow reaches lock entrance (X = 20.5 m) and it completely fails to predict the full physics of the flow when the ship is partly or fully in the lock. The authors attribute the discrepancies to the viscosity, which dominates the interaction effects inside the lock. However, it cannot explain the discrepancies in lateral forces which are not dominated by viscosity, as shown in Figure 2 (b). Therefore, the discrepancies between the measured and calculated forces may be mostly due to the boundary value problem, more specifically, the body surface boundary condition.

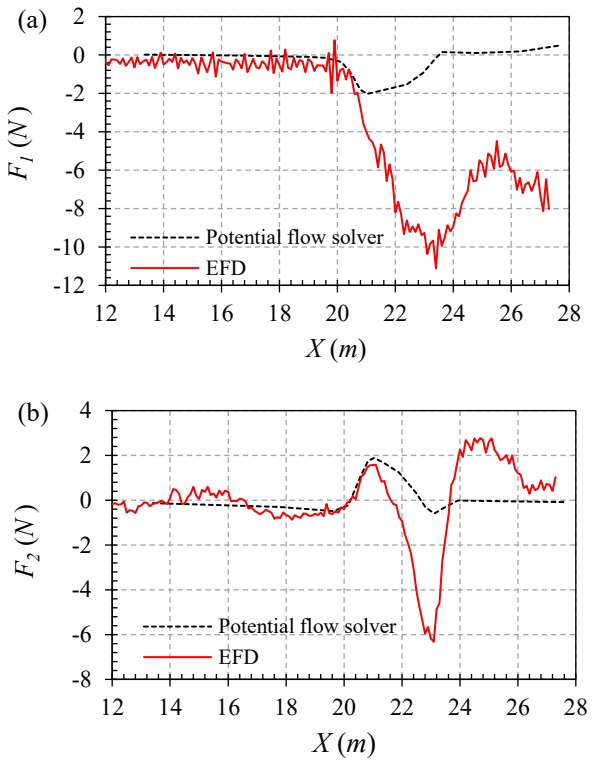

Figure 2. Resistance of a ship entering a lock. The potential flow results are provided by Toxopeus and Bhawsinka (2016) by using their in-house potential flow solver ROPES. EFD results are provided by Vantorre et al. (2012).

In the present study, a modified potential flow method will be proposed to deal with the ship-lock interaction problem. No attempts will be made to address the unsteady waves in the lock. The present work will mainly focus on proposing a body boundary condition, which could reasonably account for the return flow effects.

3 MATHEMATICAL FORMULATION

3.1 THE ORIGINAL BOUNDARY VALUE PROBLEM

A right-handed Cartesian coordinate system $\mathbf{x} = (x, y, z)$ is fixed to a ship with its positive x-direction pointing towards the bow, positive z-direction pointing upwards and $z = 0$ on the undisturbed free-surface. The ship is translating at forward speed $U(t)$ with respect to the space-fixed coordinate system. The fluid is assumed to be incompressible and inviscid with irrotational motion. The water wave motion is described by the velocity potential $\Phi(x, y, z, t)$ and the free-surface wave elevation $\zeta(x, y, t)$.

In the body-fixed reference frame, the velocity potential $\Phi(x, y, z, t)$ can be decomposed as

$$\Phi(x,y,z,t) = \varphi_s(x,y,z) + \varphi_u(x,y,z,t) \tag{1}$$

in which $\varphi_s(x, y, z)$ is the time-independent part and $\varphi_u(x, y, z, t)$ is the unsteady part representing the flow motion induced by the external disturbance such as the presence of other vessels or changes in the waterway topography. In the present study, considering the speed in the confined waterways is always restricted, the uniform-flow approximation is applied as the basic steady flow. This assumption leads to a relatively easy free-surface condition. Thus, EQ. (1) can be written as

$$\Phi(x,y,z,t) = -Ux + \varphi_u(x,y,z,t) \tag{2}$$

The velocity potential $\varphi_u(x, y, z, t)$ satisfies the Laplace equation

$$\frac{\partial^2\varphi_u}{\partial x^2} + \frac{\partial^2\varphi_u}{\partial y^2} + \frac{\partial^2\varphi_u}{\partial z^2} = 0 \tag{3}$$

The dynamic and kinetic free-surface conditions are

$$\frac{\partial\varphi_u}{\partial t} - U\frac{\partial\varphi_u}{\partial x} + g\zeta + \frac{1}{2}\nabla\varphi_u\cdot\nabla\varphi_u + \frac{p}{\rho} = 0 \text{ , at } z = \zeta \tag{4}$$

$$\frac{\partial\zeta}{\partial t} - U\frac{\partial\zeta}{\partial x} + \frac{\partial\varphi_u}{\partial x}\frac{\partial\zeta}{\partial x} + \frac{\partial\varphi_u}{\partial y}\frac{\partial\zeta}{\partial y} - \frac{\partial\varphi_u}{\partial z} = 0 \text{ , at } z = \zeta \tag{5}$$

where g is the gravitational acceleration, ρ is the fluid density and p is the forcing pressure on the free-surface. By applying Taylor series expanded about $z = 0$ and only keeping the linear terms, the dynamic and kinetic free-surface conditions can be linearized as

$$\frac{\partial\varphi_u}{\partial t} - U\frac{\partial\varphi_u}{\partial x} + g\zeta = 0 \text{ , at } z = 0 \tag{6}$$

$$\frac{\partial\zeta}{\partial t} - U\frac{\partial\zeta}{\partial x} - \frac{\partial\varphi_u}{\partial z} = 0 \text{ , at } z = 0 \tag{7}$$

By performing the operation $\partial/\partial t - U\partial/\partial x$ on EQ. (6) and then substituting it into EQ. (7), the combined linearized free-surface condition is then

$$\frac{\partial^2\varphi_u}{\partial t^2} - 2U\frac{\partial^2\varphi_u}{\partial x\partial t} + U^2\frac{\partial^2\varphi_u}{\partial x^2} + g\frac{\partial\varphi_u}{\partial z} = 0 \tag{8}$$

Theoretically, the boundary value problem should be solved at each time step by applying nonlinear dynamic and kinetic free-surface boundary conditions in EQ. (4) and (5). Only in this way the complex translation waves trapped in the narrow gap can be captured. In the present study, no attempt will be made to model the wave phenomenon in the lock and its associated piston effect. Our main objective is to propose an effective methodology based on simplified empirical methods. Therefore, the time dependent term in EQ. (8) is neglected and a linearized steady free-surface condition can then be obtained

$$U^2\frac{\partial^2\varphi_u}{\partial x^2} + g\frac{\partial\varphi_u}{\partial z} = 0 \tag{9}$$

The body surface boundary condition follows from the requirement that there be no flow through the hull surface. This means

$$\frac{\partial\varphi_u}{\partial n} = Un_1 \tag{10}$$

Where $\partial/\partial n$ is the derivative along the normal vector $\mathbf{n} = (n_1, n_2, n_3)$ to the hull surface. The normal vector is defined to be positive into the fluid domain. The boundary condition on the sea bottom and side walls can be expressed as

$$\frac{\partial \varphi_u}{\partial n} = 0 \tag{11}$$

A radiation condition is imposed on the control surface to ensure that waves vanish at upstream infinity

$$\varphi_u \to 0, \quad \zeta \to 0 \ \ as \ \sqrt{x^2 + y^2} \to \infty \tag{12}$$

A Rankine source panel method is used to solve the boundary value problem in EQ. (3), (9), (10), (11) and (12). The details of the numerical implementation are demonstrated by Yuan et al. (2014). The same in-house developed programme MHydro is utilized in the present study as the framework to investigate ship hydrodynamics in restricted waterways. Special care should be taken to implement a suitable open boundary condition to satisfy EQ. (12). In numerical calculations, the computational domain is always truncated at a distance away from the ship hull. In general, waves will be reflected from the truncated boundaries and contaminate the flow in the computational domain. In the present study, a 2nd order upwind difference scheme is applied on the free-surface to obtain the time and spatial derivatives

$$\frac{\partial^2 \varphi_u}{\partial x^2}(\mathbf{x}_i) = \frac{1}{\Delta x^2}\left(\begin{array}{l} \frac{1}{4}\varphi_u(\mathbf{x}_{i+4}) - 2\varphi_u(\mathbf{x}_{i+3}) + \\ \frac{11}{2}\varphi_u(\mathbf{x}_{i+2}) - 6\varphi_u(\mathbf{x}_{i+1}) + \frac{9}{4}\varphi_u(\mathbf{x}_i) \end{array}\right) \tag{13}$$

According to Bunnik (1999) and Kim et al. (2005), EQ. (12) can be satisfied consequently by applying EQ. (13). Once the unknown potential φ_u is solved, the steady pressure distributed over the ship hull can be obtained from the linearized Bernoulli's equation

$$p = -\rho\left[\frac{\partial \varphi_u}{\partial t} - U\frac{\partial \varphi_u}{\partial x}\right] \tag{14}$$

the integral of the pressure over the hull surface, the forces (or moments) can be obtained by

$$F_i = \iint_S p n_i ds \ , \ i = 1, 2, \ldots, 6 \tag{15}$$

where

$$n_i = \begin{cases} \mathbf{n}, & i = 1,2,3 \\ \mathbf{x} \times \mathbf{n}, & i = 4,5,6 \end{cases} \tag{16}$$

The wave elevation on the free-surface can be obtained from the dynamic free-surface boundary condition in EQ. (6) in the form

$$\zeta = \frac{U}{g}\frac{\partial \varphi_u}{\partial x} - \frac{\partial \varphi_u}{\partial t} \tag{17}$$

3.2 THE MODIFIED BOUNDARY VALUE PROBLEM FOR SHIP-LOCK INTERACTION PROBLEM

It has been concluded by Toxopeus and Bhawsinka (2016) that the ordinary BVP in Section 3.1 could not be used to predict the ship-lock interaction problem, as shown in Figure 2. A modified BVP must be proposed to account for the complex flow around the ship while entering a lock.

When a ship enters or leaves a lock with a closed end, a so-called piston effect will be provoked due to the translation waves trapped in the narrow lock between the ship and the lock door. Meanwhile, as the water is accumulating or evacuating in a lock with closed end, a return flow will be generated.

Assuming a ship enters a lock with a constant forward speed U, the water volume in the lock increases by

$$\Delta V = UA_s(t) \cdot \Delta t \tag{18}$$

where A_s is the cross sectional area of the ship at moment t. This increased water volume will result in a return flow, which takes the same amount of water leakage through the narrow clearance. As the distance between the ship bow and the lock door decreases, the return flow velocity $v(\mathbf{x}, t)$ increases. Assuming the return flow in front of the vessel is uniform, the effect of return flow can be accounted into the body surface boundary condition in the form of an additional speed $v(t)$. Then the modified body surface condition can be rewritten as

$$\frac{\partial \varphi_u}{\partial n} = \left(U + v(t)\right) n_1 \tag{19}$$

The simplified $v(t)$ can be defined as

$$v(t) = \begin{cases} 0, & \text{at } t \le t_e \\ \kappa \frac{\delta}{l} \cdot (t - t_e), & \text{at } t_e < t \le t_c \end{cases} \tag{20}$$

where δ is block coefficient of the lock, which is defined as the ratio of the wetted cross sectional area of ship to the wetted cross sectional area of the lock. l is the length of the lock. t_e is the moment when the ship bow reaches the lock entrance and t_c is the moment when the ship is completely in the lock. The effect of the term $\kappa\delta/l$ in EQ. (20) is equivalent to an acceleration and κ is therefore referred to as the acceleration coefficient. At $t > t_c$, the total amount of water volume in the lock stays constant. The return flow mainly comes from the volume change in the space between the bow and the door. As the distance between bow and door decreases, the rate of volume change increases. The return flow velocity can still be determined by an acceleration coefficient. However, this acceleration coefficient will be smaller than κ. The change of the acceleration coefficient should be smooth. An empirical iteration method is introduced to estimate the return flow velocity after the ship has finished advancing in the lock, which is written as

$$v(t_n) = v(t_{n-1}) + \kappa \frac{\delta}{l} \cdot \frac{U\Delta t}{\left[v(t_{n-1}) - v(t_c)\right] + U}, \quad \text{at } t > t_c \qquad (21)$$

The initial condition for (21) is $v(t_1) = v(t_c)$, where $v(t_c)$ is calculated by EQ. (20).

By solving the boundary value problem in EQ. (3), (9), (19), (11) and (12) at each time step, the velocity potential φ_u can be obtained. A 2nd order upwind difference scheme is applied to obtain the time derivatives

$$\frac{\partial \varphi_u}{\partial t}(t_n) = \frac{1}{\Delta t}\left(\frac{3}{2}\varphi_u(t_n) - 2\varphi_u(t_{n-1}) + \frac{1}{2}\varphi_u(t_{n-2})\right) \qquad (22)$$

The unsteady pressure distributed over the ship hull can then be determined by

$$p = -\rho\left[\frac{\partial \varphi_u}{\partial t} - (U+v)\frac{\partial \varphi_u}{\partial x}\right] \qquad (23)$$

The forces (or moments) can be calculated by EQ. (15). The wave elevation on the free-surface can be obtained from the dynamic free-surface boundary condition in EQ. (6) in the form

$$\zeta(t) = -\frac{1}{g}\left[\frac{\partial \varphi_u}{\partial t} - (U+v)\frac{\partial \varphi_u}{\partial x}\right] \qquad (24)$$

4 RESULTS AND DISCUSSIONS

4.1 SHIP MODEL AND TEST MATRIX

Captive model tests were carried out by Vantorre et al. (2012) in FHR. The ship model used in the ship-lock problem is a bulk carrier, with main particulars listed in Table 1 in model scale with a scale factor of 1/75. The lock configuration is shown in Figure 3 with a space-fixed coordinate system *O-XY*. To minimize the computational domain, the long transition channel used for model test is truncated and only the part where $X > 0$ is retained for the numerical calculations. The initial position ($t = 0$) in the numerical simulation starts at $X = 0$. All the forces and moments are calculated in the body-fixed frame, as shown in Figure 3. Test G is selected as the validation case, where water depth to draft ratio $d/T = 1.2$, speed $U = 0.15$ *m/s*, and the model is towed on the centerline of the lock ($Y = 0$).

Table 1. Main particulars of bulk carrier

Length (*L*) (*m*)	3.533
Breadth (*B*) (*m*)	0.573
Draft Amidships (*T*) (*m*)	0.231
Block coefficient (C_B)	0.854

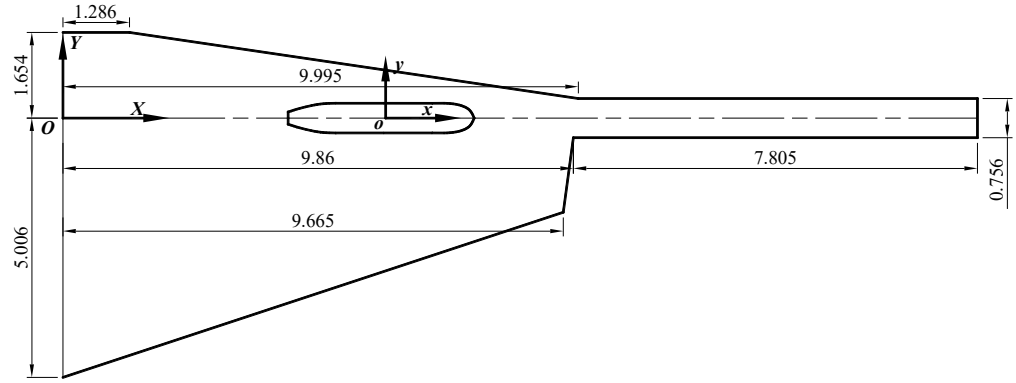

Figure 3. Configuration of the lock for captive model tests.

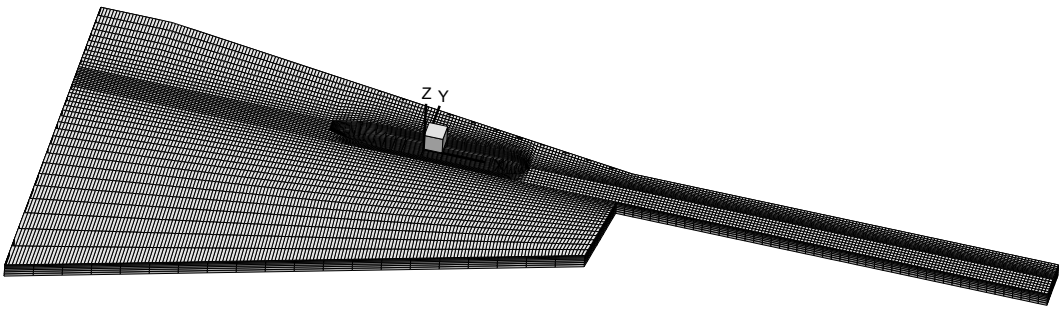

Figure 4. Panel distribution on the computational domain of Test G. There are 11,346 panels distributed on the entire computational domain: 960 on the wetted body surface, 9,874 on the free-surface, and 1,472 on the side walls.

4.2 RESULTS AND VALIDATIONS

The computational domain and mesh distribution of the present study is shown in Figure 4. A dynamic meshing technique is used, which enables an automatic update of the computational domain and mesh distribution at each time step when the ship is approaching the lock. The mesh is uniform longitudinally. Non-uniform mesh is applied only in the transverse direction due to the changes of banks and the lock walls. The results of the forces in *x*-, *y*-, and the moment in *x*-*o*-y directions are presented in Figure 5. It should be noted that all the positive directions are consistent with the body-fixed frame shown in Figure 3. The time step Δt in the numerical calculations is 0.39*s*.

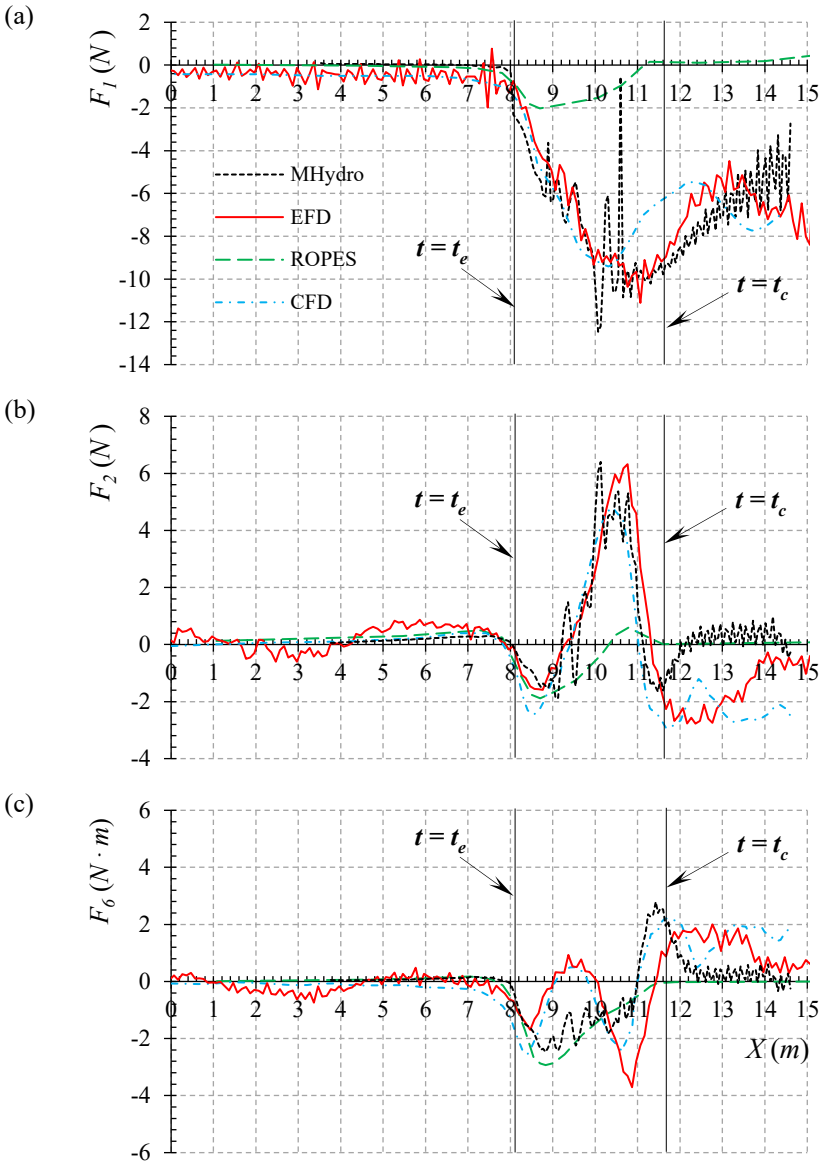

Figure 5. Validation of forces (or moments). (a) Resistance; (b) lateral force; (c) yaw moment. EFD results are provided by Vantorre et al. (2012). CFD results are published by Toxopeus and Bhawsinka (2016) by using viscous-flow code ReFRESCO. Free-surface effect is neglected in ReFRESCO. In the present MHydro program, the acceleration coefficient $\kappa = 0.2$.

Figure 5 (a) shows the resistance. Before the ship enters the lock ($t < t_e$), the resistance predicted by both ROPES and MHydro is very small ($F_1 \approx 0$). This is different from the CFD and EFD results. The discrepancies are due to the viscous contribution, which is more significant at model scale than at full scale. The negative values at $t < t_e$ obtained by CFD and EFD represent the drag force contributed by viscous effects. In the present case study, the ship's speed is very low ($F_r = 0.026$). According to Schultz (2007), at low to moderate speeds ($F_r < 0.25$), the frictional resistance is the largest component of the total drag. However, when the ship starts entering the lock, the contribution of different resistance components changes. The frictional resistance is no longer the largest component. The increased return flow velocity would cause an increase in the frictional resistance leading to higher total resistance. But this increase is not significant. As shown in Figure 5 (a), the resistance increases dramatically, which is mainly

caused by pressure integration due to the wave-making contribution. According to EQ. (23), the velocity potential gradient $(\partial\varphi_w/\partial t)$ plays a dominant role since the return flow speed and computational domain are changing at each time speed. Therefore, if a proper acceleration coefficient κ is specified in EQ. (20) to estimate the return flow velocity, the predictions by the present potential flow solver is still satisfactory (even better than CFD solutions). When the ship is completely in the lock ($t > t_c$), the total water volume will not increase, and the return flow is not as pronounced as that at $t < t_c$. As a result, the total resistance decreases. However, as the distance between the ship bow and the lock door becomes small, the water will accumulate in the gap and a complex wave phenomenon will occur. In the CFD modelling, the free-surface effect is neglected (Toxopeus and Bhawsinka, 2016) and its predictions at $t > t_c$ are not reliable. The present potential flow solver MHydro only keeps the steady terms in the free-surface condition in EQ. (8). As the clearance between the ship bow and the lock door decreases, MHydro underestimates the resistance. As the ship gets closer to the door, the generated unsteady waves will be reflected by the door and thereafter interact with the ship, leading to an increase of resistance. Both CFD and MHydro fail to predict this piston effect by neglecting unsteady free-surface effect. A similar conclusion can also be drawn on the lateral force F_2. As shown in Figure 5 (b), the modified potential flow solver can predict the lateral force very well at $t < t_c$. After the ship is completely in the lock, the flow becomes symmetrical very quickly if the unsteady terms are neglected on the free-surface. As a result, the lateral forces calculated by the present potential flow solver reduce to zero shortly after the ship completely enters the lock. The results in Figure 5 (c) indicate that the present potential flow method fails to predict the yaw moment when a ship is entering a lock. This is mainly due to the flow separation which occurs at the sharp corner of the lock entrance, as well as at the ship stern. The results by Toxopeus and Bhawsinka (2016) show the importance of eddies generated at sharp corners due to flow separation, as shown in Figure 6. This violates the irrotational assumption adopted in the potential flow method. The sign of yaw moment is determined by the asymmetry of the lock configuration, while the amplitude is determined by the entering speed and blockage coefficient. As the yaw moment is critical for a ship's maneuvering in the lock area, a symmetrical lock design could help to avoid the yaw moment, as well as the lateral force.

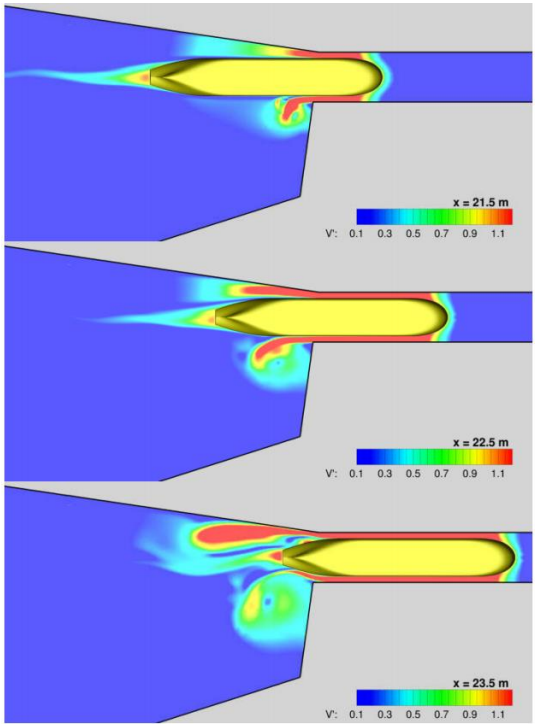

Figure 6. Visualization of the total velocity field on the free-surface by Toxopeus and Bhawsinka (2016). The *x*-coordinates presented in the figure can be transformed into the present space-fixed frame (as shown in Figure 3) by subtracting 12.335*m*.

As discussed above, the accuracy of the present calculation is highly dependent on the estimation of the return flow velocity. Figure 7 shows the return flow velocity calculated by empirical formulae in EQ. (20) and (21) with different acceleration coefficient κ. It should be noted that the return flow is assumed to be uniform. But in reality, the flow field is more complex. Numerical tests indicate the acceleration coefficient κ should range from 0.1 to 0.3. The corresponding results are shown in Figure 8. The resistance is more sensitive to the coefficient κ.

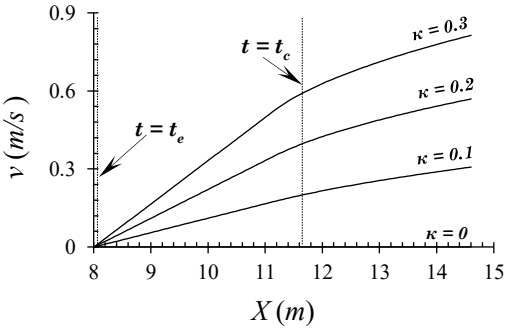

Figure 7. Return flow velocity with different acceleration coefficient κ.

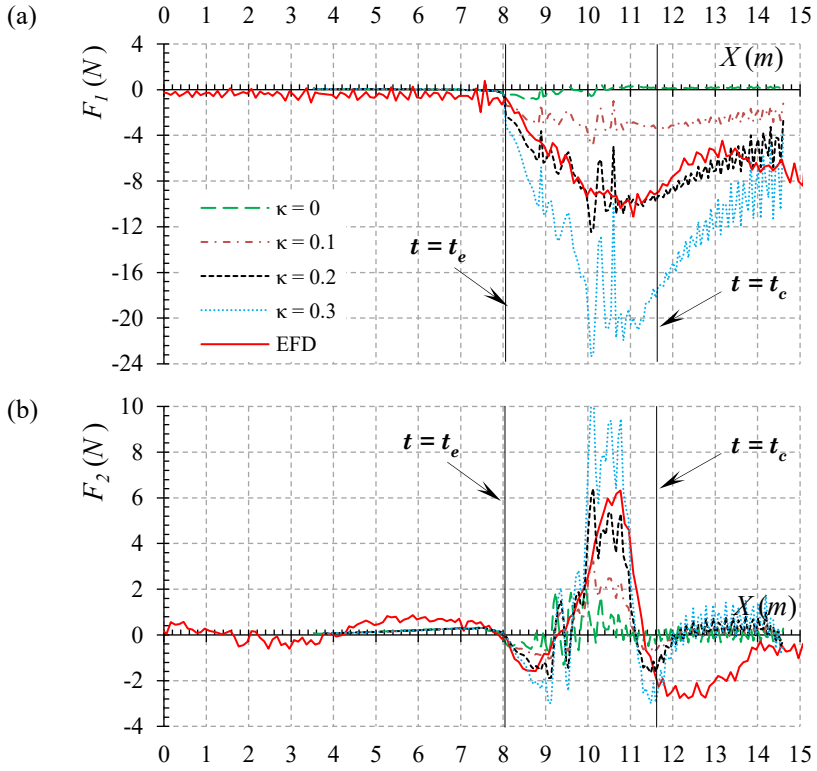

Figure 8. Comparison of forces with different acceleration coefficient κ.

4.3 DISCUSSIONS

The operability of a ship when it enters a lock is affected by a number of factors, including the width and water depth of the lock, ship size, entering speed, drift angle, the distance between ship bow and the lock door, and the eccentricity. In this section, we investigate the effect of water depth and eccentricity to see how these two factors influence the ship's manoeuvrability. The other parameters are remaining the same. By talking about the manoeuvrability of a ship when entering into a lock, the forces in all 6-DoFs should be analysed. The results in Figure 5 show that the forces (moments) in sway and yaw experience some fluctuations at $t_e < t < t_c$. Considering the hydrodynamic derivatives in sway and yaw are very large, the interaction forces (moments) in sway and yaw are not likely to make the ship deviate from its original course. The surge force, however, has larger magnitude, while the surge hydrodynamic derivative is relatively small. As a results, in the field observation, it is usually found that the vessel's speed decreases as it approach the lock door. In some cases, the vessel even stops due to the increase resistance. For this reason, it would be interesting to investigate the surge force induced by the ship-lock interaction. On the other hand, when the under keel clearance (UKC) is small, the risk of grounding should also be taken into account, and it will be interesting to investigate the vessel's sinkage during lock-entering manoeuver.

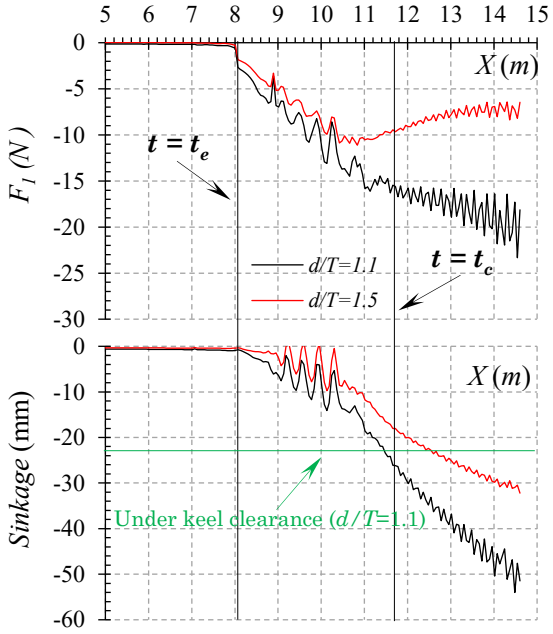

Figure 9. The resistance and sinkage of a bulk carrier when it enters a lock with different water depths. The sinkage is calculated by $F_3/\rho g A_w$, where Aw is the water plane area, which is taken as 1.9 m^2. The entering speed is 0.15m/s, and the acceleration coefficient κ=0.2.

The results of the resistance and sinkage in different water depths are shown in Figure 9. It can be seen that both the resistance and sinkage increase when the ship gradually enters the lock. As the ship is completely in the lock ($t > t_c$), the resistance experiences a decrease at large UKC

(d/T=1.5) when it approaches the door. It is confirmed by the experimental measurement, as mentioned before. However, as the UKC becomes very small (d/T=1.1), the resistance keeps an increasing trend, which may stop the vessel if no additional propelling actions are taken. On the other hand, the sinkage also experiences a significant increase when the UKC is very small. In particularly, just before the ship is completely in the lock, the sinkage becomes larger than the UKC (23.1 mm at d/T=1.1). The grounding occurs even without take the trim into account. To make normal progress, the entering speed should keep very low. Fortunately, the ship losses speed due to the increased resistance. Therefore, the speed lost (or increased resistance) by nature will prevent the ship from grounding.

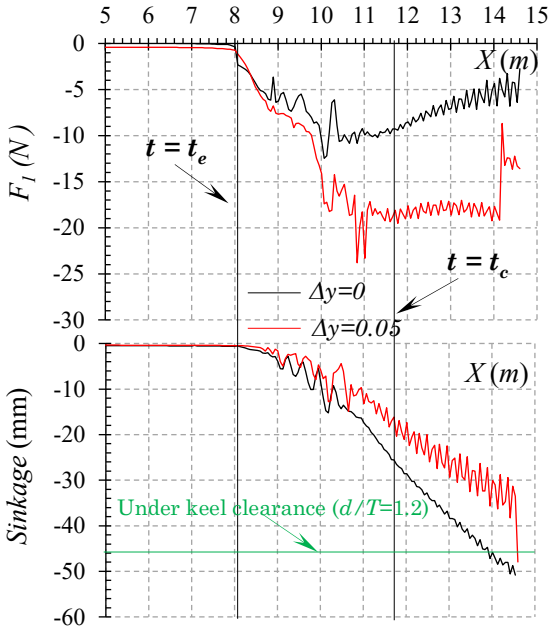

Figure 10. The resistance and sinkage of a bulk carrier when it enters a lock at different eccentricities. The sinkage is calculated by $F_3/\rho g A_w$, where Aw is the water plane area, which is taken as 1.9 m^2. The entering speed is 0.15m/s, and the acceleration coefficient κ=0.2.

The results of the resistance and sinkage in different eccentricities are shown in Figure 10. It is interesting to find that the resistance increases, while the sinkage decreases when a ship approaches the lock with an eccentricity of 50 mm. The eccentricity here refers to the lateral position of the ship model with respect to the lock's centre line. The difference in resistance and sinkage is induced by the different flow characteristics surrounding the vessel. It indicates that for the same blockage coefficient, there is a big difference in operability when a ship enters the lock in different courses. It can be concluded from Figure 9 and Figure 10 that both the water depth of lock and the eccentricity of the course have a significant influence on ship's manoeuvrability in lock entering process.

5 CONCLUSIONS

In the present study, a modified potential flow method is proposed to predict the hydrodynamic forces on a ships while entering a lock. The body surface boundary condition was modified in order to account for the return flow, which could not be captured by the potential flow theory. An empirical formula is introduced in the present study to estimate the return flow velocity. Through the comparisons to the benchmark data, as well as CFD calculations, it can be concluded that by complementing this return flow velocity with the boundary value problem, the modified potential flow solver could predict the resistance and lateral forces very well. However, it fails to predict the yaw moment due to the flow separation at the lock entrance and ship stern. It indicates the unsteady free-surface effects are very important in predicting the resistance and lateral force, while the viscous effect is less important. But the viscous effects are essential for the prediction of yaw moment. Neglecting the unsteady free-surface effects, the return flow and complex wave phenomenon cannot be captured. It should be noted that the present method is based on a reasonable estimation of the acceleration coefficient κ. This empirical coefficient may vary with ship model. Therefore, more benchmark data for various ship models are demanded, in order to establish a database to estimate suitable values of κ.

6 REFERENCES

Bunnik, T., 1999. Seakeeping calculations for ships, taking into account the non-linear steady waves, PhD thesis. Delft University of Technology, The Netherlands.

De Loor, A., Van Der Hout, J., Weiler, O.M., Kortlever, W.C.D., 2013. The use and validation of OpenFOAM to determine the lateral and longitudinal forces exerted on a vessel in the lock and in the lock approach, 3rd International Conference on Ship Manoeuvring in Shallow and Confined Water, Ghent, Belgium.

Henn, R., 2013. Real-time simulation of ships manoeuvring in locks, 3rd International Conference on Ship Manoeuvring in Shallow and Confined Water, Ghent, Belgium.

Kim, Y., Yue, D.K.P., Connell, B.S.H., 2005. Numerical dispersion and damping on steady waves with forward speed. Applied Ocean Research 27 (2), 107-125.

Lindberg, O., Glimberg, S.L., Bingham, H.B., Engsig-Karup, A.P., Schjeldahl, P.J., 2013. Real-Time Simulation of Ship-Structure and Ship-Ship Interaction, 3rd International Conference on Ship Manoeuvring in Shallow and Confined Water, Ghent, Belgium.

Meng, Q., Wan, D., 2016. URANS simulations of complex flows around a ship entering a lock with different speeds. International Journal of Offshore and Polar Engineering 26 (2), 161-168.

Schultz, M.P., 2007. Effects of coating roughness and biofouling on ship resistance and powering. Biofouling 23 (5-6), 331-341.

Toxopeus, S., Bhawsinka, K., 2016. Calculation of Hydrodynamic Interaction Forces on A Ship Entering A Lock Using CFD 4th International Conference on Ship Manoeuvring in Shallow and Confined Water, Hamburg, Germany.

Vantorre, M., Delefortrie, G., Mostaert, F., 2012. Behaviour of ships approaching and leaving locks: Open model test data for validation purposes. Version 3_0. WL Rapporten, WL2012R815_08e. Flanders Hydraulics Research and Ghent University - Division of Maritime Technology: Antwerp, Belgium.

Vergote, T., Eloot, K., Vantorre, M., Verwillingen, J., 2013. Hydrodynamics of a ship while entering a lock, 3rd International Conference on Ship Manoeuvring in Shallow and Confined Water, Ghent, Belgium.

Vrijburcht, A., 1988. Calculations of wave height and ship speed when entering a lock. Delft Hydraulics Publication

Wang, H.-Z., Zou, Z.-J., 2014. Numerical study on hydrodynamic interaction between a berthed ship and a ship passing through a lock. Ocean Engineering 88 (0), 409-425.

Yuan, Z.-M., Incecik, A., Jia, L., 2014. A new radiation condition for ships travelling with very low forward speed. Ocean Engineering 88, 298-309.

Yuan, Z.M., Incecik, A., 2016. Investigation of ship-bank, ship-bottom and ship-ship interactions by using potential flow method, 4th International Conference on Ship Manoeuvring in Shallow and Confined Water, Hamburg, Germany.

7 AUTHORS BIOGRAPHY

Zhi-Ming Yuan holds the current position of lecturer in hydrodynamics at University of Strathclyde. His research interests mainly lie in the theoretical and numerical analysis of the hydrodynamic performance of the ship and offshore structures.

ESTIMATION OF THE CENTRE OF ROTATION FOR A SHIP IN REAL SEA STATE ENVIRONMENT

Chen Zhang,
University of Oldenburg, and Jade University of Applied Science, Germany

Alexander Härting,
Jade University of Applied Science, Germany

Butteur Ntamba Ntamba,
Cape Peninsula University of Technology, Cape Town, South Africa

Bernhard Schwarz-Röhr,
Ghent University, Belgium, and Jade University of Applied Science, Germany

ESTIMATION OF THE CENTRE OF ROTATION FOR A SHIP IN REAL SEA STATE ENVIRONMENT

Chen Zhang, University of Oldenburg, and Jade University of Applied Science, Germany
Alexander Härting, Jade University of Applied Science, Germany
Butteur Ntamba Ntamba, Cape Peninsula University of Technology, Cape Town, South Africa
Bernhard Schwarz-Röhr, Ghent University, Belgium, and Jade University of Applied Science, Germany

SUMMARY

Wave induced ship motions are composed of translations and rotations, but there is no unique pivot point. In this paper it is suggested to define a centre of rotation (CR) as the point where the linear accelerations experienced by a sensor are not affected by the rotations. Based on trials in a real sea state environment, a method is investigated to estimate the CR, which may not coincide with the centre of gravity. The angles are determined by high-pass filtering and integration of the measured angular rates. The linear accelerations are then transformed from the body-fixed frame to the horizontal inertial frame, the transformation including an initially unknown offset vector between the CR and the sensor, which is estimated by a Kalman filter. The results indicate that the CR position can indeed be determined uniquely. Its dependence on the relative motion of the vessel in the wave system carries useful information for wave spectrum analysis.

NOMENCLATURE

CR	Ship centre of rotation
s	State vector
s_k	State vector at time k
s_{k-1}	State vector at time k-1
F_k	State transition model
P_k	Error covariance matrix at time k
Q_k	Covariance of process noise
H_k	Observation model
K_k	Kalman gain
u	Observation vector
u_k	Observation vector at time k
R_k	Covariance of observation noise
$\hat{s}_k$	Updated state vector at time k
$\hat{P}_k$	Updated error covariance at time k
I	Unitary matrix
ax_n	Surge acceleration at CR (m/s^2)
ay_n	Sway acceleration at CR (m/s^2)
az_n	Heave acceleration at CR (m/s^2)
r_x	Offset in x direction (m)
r_y	Offset in y direction (m)
r_z	Offset in z direction (m)
ax_{sensor}	Surge acceleration from sensor (m/s^2)
ay_{sensor}	Sway acceleration from sensor (m/s^2)
az_{sensor}	Heave acceleration from sensor (m/s^2)
ϕ	Roll angle (rad)
θ	Pitch angle (rad)
ψ	Yaw angle (rad)
$\ddot{\phi}$	Roll angular acceleration (rad/s^2)
$\ddot{\theta}$	Pitch angular acceleration (rad/s^2)
$\ddot{\psi}$	Yaw angular acceleration (rad/s^2)
R_n^b	Transformation matrix from earth-fixed frame to ship body-fixed frame
R_ϕ^T	Transformation matrix of roll angle
R_θ^T	Transformation matrix of pitch angle
R_ψ^T	Transformation matrix of yaw angle
ax_{off}	Acceleration caused by offset in x axis (m/s^2)
ay_{off}	Acceleration caused by offset in y axis (m/s^2)
az_{off}	Acceleration caused by offset in z axis (m/s^2)
DP	Dynamic positioning

1 INTRODUCTION

This work is part of a larger project that aims at determining the directional wave spectrum from ship motion measurements in deep and shallow water. Ship motions appear in translational (surge, sway and heave) and rotational (roll, pitch and yaw) degrees of freedom. The centre of rotation (CR) can be defined as the point where the linear accelerations are not affected by the rotations. The so defined CR cannot be expected to be rigidly fixed in the ship's body frame. However, its average can be determined and its displacement from the centre of gravity can be analysed in terms of parameters such as ship speed and wave incidence angle. It is expected that the position of the CR carries information on the sea state which can be exploited in the estimation of the directional wave spectrum.

In this paper a Kalman filter is presented that estimates the averaged CR position from motion measurements at an arbitrary point of the vessel. Sea trials on two vessels were performed to test the algorithm. Low cost sensors were used to measure linear accelerations and rotational rates.
In the long term it is intended to use such a system routinely to provide motion data for the determination of the exciting sea state.

2 VESSELS & EXPERIMENTAL CONDITIONS

2.1 AGULHAS II

Agulhas II is a South African icebreaking Polar Supply and Research Vessel (PSRV), with its overall length of 134.2m, breadth of 22m, and under 7.65m draught. There were two sensor boxes with low-cost gyros and accelerometers installed on-board. One was placed on the observation deck above the navigation bridge recording both, linear accelerations and angular rates in three degrees-of-freedom at a rate of 8Hz. It was connected to a GPS receiver to provide accurate position and time. The other sensor was set up in the engine control room within a few metres of the ship's centre of mass. This sensor was producing all three linear accelerations but only roll and pitch angular rates at a frequency of 10Hz.

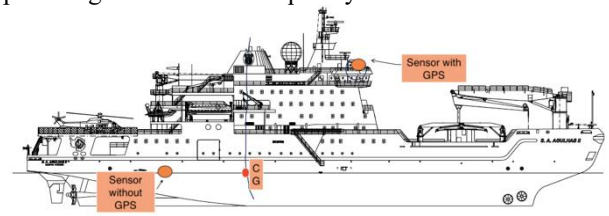

Figure 1. Agulhas II with sensor boxes on-board
(Bekker and Omer, 2018, legends added by author)

The experiment was conducted on a voyage Cape Town-Antarctica- Cape Town from 28th June 2017 to 12th July 2017. To keep file sizes manageable, the sensors were operated for intervals of 2 to 5 hours at a time. Naturally, the recording intervals could not be identic for both sensors. After synchronising the sensor without GPS by using correlation, the angular rates showed a nearly perfect match. Then, the linear accelerations could be pre-processed with exactly corresponding time intervals. Finally, the estimation algorithm was applied independently to the motion of both sensors.

2.2 SIMON STEVIN

The Belgian vessel Simon Stevin was deployed for off-shore research and also as a training platform in the Southern North Sea and the eastern part of the English Channel. The overall length of Simon Stevin is 36m, with its breadth of 9.4m, and draught is 3.5m. There was a sensor box with low-cost gyros and accelerometers all in three dimensions on-board deployed, the recorded data was autonomously saved to a SD card, owned by Jade University of Applied Science.
The experiments were performed at 6-8 November 2017 in Belgian waters close to Ostend. The average water depth there was generally larger than 20m, but near a few sandbanks it was only 12m. The experiment consisted of a number of dedicated trial runs, each lasting for about 30 minutes at a specific speed with a constant heading, and then repeated at different parameter settings.

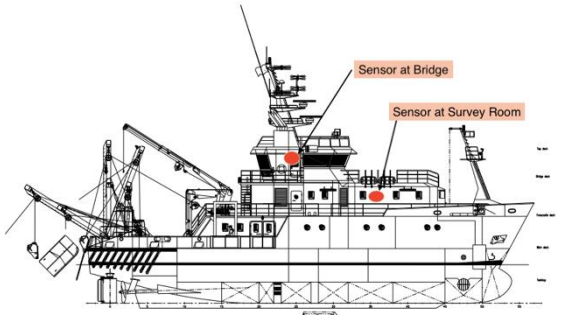

Figure 2. Simon Stevin with sensor boxes on-board
(Damen shipyard, legends added by author)

3 MATHEMATIC MODEL

3.1 KALMAN FILTER

The Kalman filter is an algorithm which uses a series of measurements and produces the estimation of required variables under consideration of statistic uncertainties such that the result is more precise than based on a single measurement. The algorithm can be separated into a prediction and a correction part. In the prediction part, the required variables forming the state vector, here the linear accelerations at CR and the components of the offset vector $s=[ax_n, ay_n, az_n, r_x, r_y, r_z]$, are propagated in time from k-1 to k with the transition matrix F and the error covariance matrix P, as given in equations (1) and (2).

$$s_k = F_k s_{k-1} \quad (1)$$
$$P_k = F_k P_{k-1} F_k^T + Q_k \quad (2)$$

In the correction part, the predicted state vector s_k is adjusted based on the difference between the actual measurements, here $u=[ax_{sensor}, ay_{sensor}, az_{sensor}]$, and the expected observations $H_k s_s$. For that purpose, the Kalman gain matrix K is computed, which is then also used to update the error covariance matrix P. The required calculation steps are shown in equations (3) to (5).

$$K_k = P_k H_k^T (R_k + H_k P_k H_k^T) \quad (3)$$
$$\hat{s}_k = s_k + K_k (u_k - H_k s_k) \quad (4)$$
$$\hat{P}_k = (I - K_k H_k) P_k (I - K_k H_k)^T + K_k R_k K_k^T \quad (5)$$

3.2 EULER TRANSFORMATION

From the sensor boxes on-board, three dimensional linear accelerations are acquired in the ship body-fixed frame. Nevertheless, the ship linear motions at CR are needed in the earth-fixed inertial frame. By integrating and high-pass filtering the measured angular rates, the angles could be determined independently. Then the three Euler angles roll, pitch and yaw can be utilized to transform from the earth-fixed frame to the ship body-fixed frame by applying the transformation matrix R_n^b, as described in equation (6). The individual rotation matrices R_ϕ^T, R_θ^T, R_ψ^T are formed from the Euler angles as shown in equations (7) to (9).

$$R_n^b = R_\phi^T \cdot R_\theta^T \cdot R_\psi^T \quad (6)$$

$$R_\phi^T = \begin{pmatrix} 1 & 0 & 0 \\ 0 & cos\phi & sin\phi \\ 0 & -sin\phi & cos\phi \end{pmatrix} \quad (7)$$

$$R_\theta^T = \begin{pmatrix} cos\theta & 0 & -sin\theta \\ 0 & 1 & 0 \\ sin\theta & 0 & cos\theta \end{pmatrix} \quad (8)$$

$$R_\psi^T = \begin{pmatrix} cos\psi & sin\psi & 0 \\ -sin\psi & cos\psi & 0 \\ 0 & 0 & 1 \end{pmatrix} \quad (9)$$

The accelerations at the offset point produced by the rotations can be expressed by equation (10).

$$\begin{pmatrix} ax_{off} \\ ay_{off} \\ az_{off} \end{pmatrix} = \begin{pmatrix} \ddot{\phi} \\ \ddot{\theta} \\ \ddot{\psi} \end{pmatrix} \times \begin{pmatrix} r_x \\ r_y \\ r_z \end{pmatrix} = \begin{pmatrix} \ddot{\theta} r_z - \ddot{\psi} r_y \\ \ddot{\psi} r_x - \ddot{\phi} r_z \\ \ddot{\phi} r_y - \ddot{\theta} r_x \end{pmatrix} \quad (10)$$

Thus after combing equations (6) to (10), the total acceleration at the sensor is given by equation (11).

$$\begin{pmatrix} ax_{sensor} \\ ay_{sensor} \\ az_{sensor} \end{pmatrix} = \left(R_n^b \cdot \begin{pmatrix} ax_n \\ ay_n \\ az_n + g \end{pmatrix} + \begin{pmatrix} ax_{off} \\ ay_{off} \\ az_{off} \end{pmatrix} \right) =$$

$$\begin{pmatrix} ax_n cos\theta cos\psi + ay_n cos\theta sin\psi - az_n sin\theta - g sin\theta + r_z\ddot{\theta} \\ ax_n(sin\phi sin\theta cos\psi - cos\phi sin\psi) + ay_n(sin\phi sin\theta sin\psi + cos\phi cos\psi) + az_n sin\phi cos\theta + g sin\phi cos\theta - r_z\ddot{\phi} \\ ax_n(cos\phi sin\theta cos\psi + sin\phi sin\psi) + ay_n(cos\phi sin\theta sin\psi - sin\phi cos\psi) + az_n cos\phi cos\theta + g cos\phi cos\theta + r_y\ddot{\phi} - r_x\ddot{\theta} \end{pmatrix} \quad (11)$$

4 RESULTS

4.1 RESULTS OF AGULHAS II

In the following, the origin of the ship coordinate system is placed in the centre of gravity as given by the loading computer. According to the right-hand rule, the three axes are pointing to bow, port and upward. For a rigid body the estimated CR position should not depend on the position of the sensor. For testing two sensors at different positions were used on the Agulhas II. Sensor I was placed in the engine control room without GPS, somewhat behind the centre of gravity. Its coordinates in the ship frame were estimated as (-8m, 0, 0), the x-position being rather uncertain. Sensor II was on the observation deck with GPS calibration, and its position in the ship frame could fairly accurately be measured to be (12.7m, 0m, 22.3m). For analysis, data sets were selected, where the ship was at a constant heading for several hours and the exciting wave system was dominated by a long-crested swell. The results for the estimated CR positions are shown in Table 1. As the CR may depend on the environmental conditions, the positions may be different for each data set. However, both sensors should yield consistent results.

Table 1. Results of selected Agulhas II sea trials

Data Set	Relative Angle [°]	Ship Speed [kn]	CR by Sensor I [m]			CR by Sensor II [m]		
			x	y	z	x	y	z
25&118	130 Port	0 (DP)	-6.7	-8.3	12.4	-10.7	-9.8	20.7
28&121	135 Port	7.5	-13.8	-13.1	2.5	-15.6	-10.6	9.9
38&135	130 Port	9.9	-15.4	-5.3	2.6	-16.4	-3.7	9.8
57&160	30 Port	13.5	-15	-13.9	-3.3	-13.2	-10.9	10.3
59&162	20 Port	13	-14.2	-13.4	-1.4	-11.7	-10.6	12.5

To assist analysis and interpretation of the results, Figure 3-10 have been prepared. Data set 25&118 has been omitted because the ship was in dynamic positioning mode and the thruster activity may have altered the dynamic behaviour. For each of the other data sets there are two figures. The first shows a small section of the time series for the linear accelerations, the other shows the estimated sensor offset from the CR for the full measurement period of several hours.

As for the linear accelerations, the labels I sensor and II senor represent the measurements directly at the sensor boxes, while labels I filtered and II filtered are defined to be the linear accelerations estimated by the Kalman filter. These are supposed to be the linear accelerations at the ships's CR and, therefore, these two lines should be identical.

As can be seen from Figure 3, 5, 7 and 9, the agreement varies from fair to nearly perfect. In heave the match is always good, while in surge and sway some discrepancies

appear in Figure 7 and 9. Note, however, that in the latter cases the absolute amplitude is small, the ship travels at high speed almost into the waves, while, in Figure 3 and 5, wave incidence is more broadside.

Looking at the estimated CR-offsets from the sensors (Figure 4, 6, 8 and 10) it can be said that the Kalman filter arrives at more or less stable, but not really constant values. Variations appear with a time characteristic of several minutes and a standard deviation of typically 2 m. It should be pointed out that the shape of the curves agrees very closely between the two sensors. The average values, after the Kalman filter has reached a settled state, are then subtracted from the sensor positions to give the CR-positions listed in table 1. The analysis indicates that, internally, the filter results are unique, which is corroborated by studying the covariance. Yet, the difference between the results achieved by the two sensors cannot be completely explained by the remaining statistic uncertainty.

The CR as defined in this paper is not a rigidly fixed point in the ship. There will be rapid variations within a wave period or an eigen period of the ship motion. In a wave slope reaching the ship inclined to starboard or port, the instantaneous CR will not be the same. For the average CR a characteristic dependence on the ship speed and the wave incidence angle can be expected.

Looking at the data sets in Table 1 as can be seen that, with waves coming from port, the CR is always deplaced to starboard from the midship plane, which would intuitively seem plausible. Unfortunately, there were no suitable data sets available with waves coming from starboard.

Comparing the columns in Table 1, the x- and y-coordinates of the estimated CR-position agree rather well between the two sensors. However, there is a systematic discrepancy in the z-coordinate. The values reached by sensor II seem to be too high by a considerable amount.

A preliminary analysis indicates that the reason may lie in small errors in the angles entering the transformation (chapter 3.2). The comparatively large gravitational acceleration g could easily corrupt the lateral accelerations, on which the estimated z-coordinate critically depends. Sensor I, being closer to the CR, is affected much less. More detailed investigations into this problem are under way.

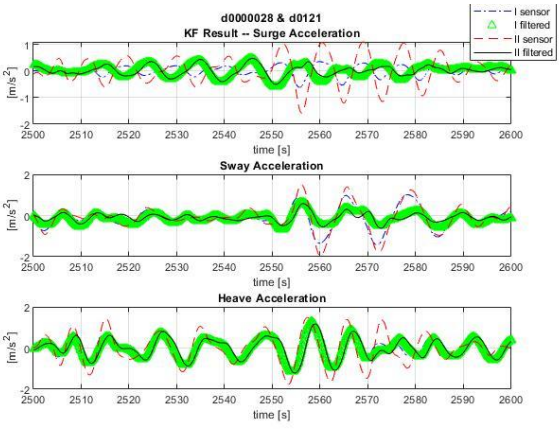

Figure 3. Linear motion of 28&121

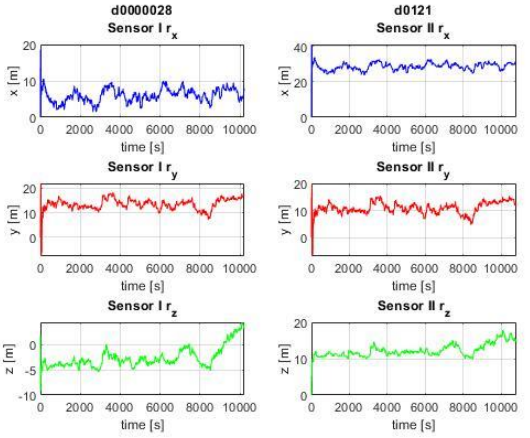

Figure 4. Offset estimation of 28&121

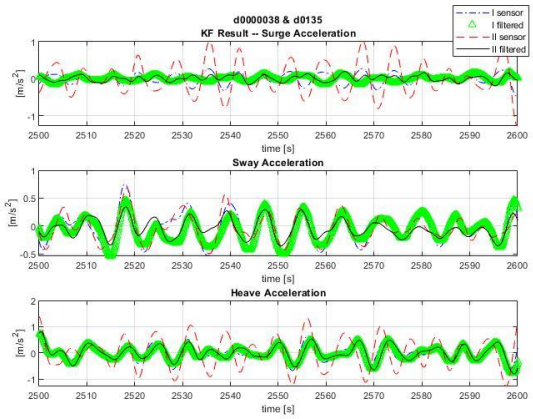

Figure 5. Linear motion of 38&135

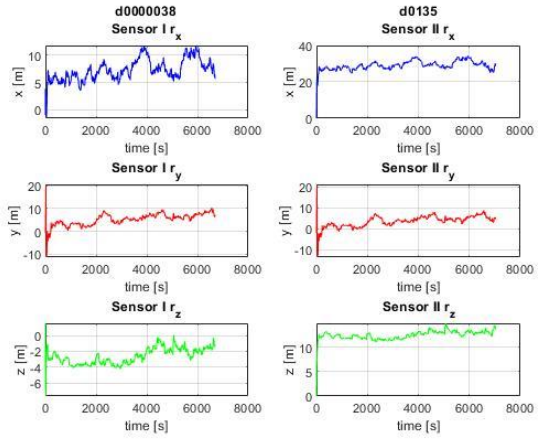

Figure 6. Offset estimation of 38&135

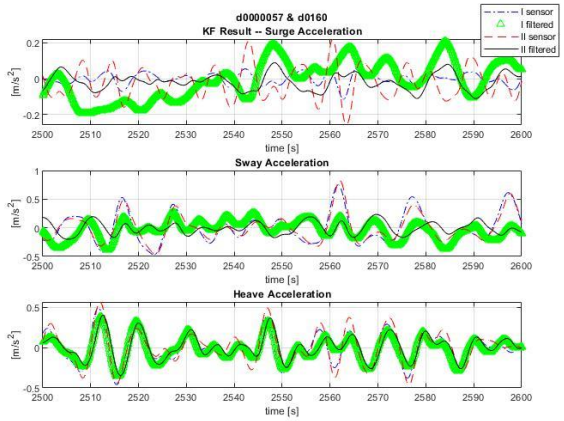

Figure 7. Linear motion of 57&160

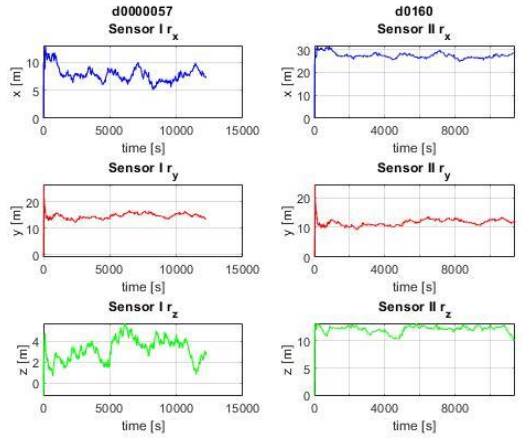

Figure 8. Offset estimation of 57&160

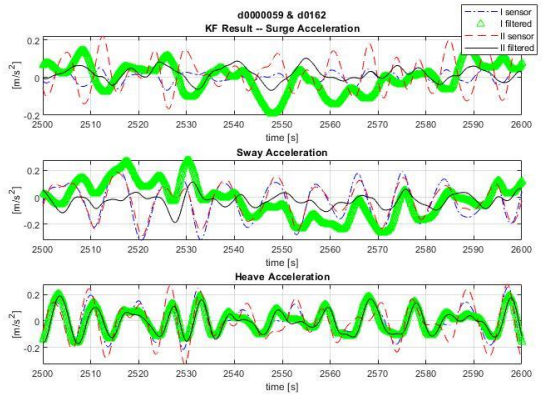

Figure 9. Linear motion of 59&162

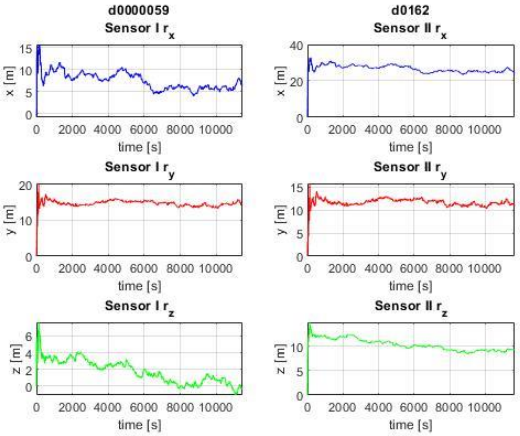

Figure 10. Offset estimation of 59&162

4.2 RESULTS OF SIMON STEVIN

There were two sensor boxes installed on Simon Stevin, as shown in the arrangement plan (chapter 2.2). As with the Agulhas II, the origin of the ship coordinate system is placed in the centre of gravity and the three axes are pointing to bow, port and upward. Up to now, only data from the sensor on the bridge have been analysed. Its position in the ship frame was determined to be (0.21m, 3.15m, 8.29m).

In Figure 11 and 12, the estimation of the offset vectors is presented for two data sets. The settling time until the filter reaches constant values is similar to the Agulhas samples, noting the much shorter duration of an individual trial run. After the adjusting period small oscillations can be observed with standard deviations of typically 0.1m, in fair agreement with the filter covariance. The results indicate that the offset vector between the sensor and the CR has been found uniquely for all of the investigated data sets.

The estimated CR positions for Simon Stevin are displayed in Table 2. The data set numbers, representing the sequence of sea trials, have been arranged by wave incidence angles. The numbers in last column of Table 2 are obtained by averaging the offsets after settling and then transforming them to the ship coordinated system. The estimated CR position appears to be quite stable when comparing data sets taken under similar external conditions, as for example data sets 21 and 23. In Table 2, the x-components of the CR position are always in front of the CG with rather constant values, except for the last two rows.

Looking at data sets 10 and 14 as another example, there are practically symmetric conditions between port and starboard. As expected, the y-component of the CR position changes sign, but the absolute values are significantly different. Also from the other data sets a general tendency to port can be identified. Investigating the z-component, data sets 4, 13 and 9, 18 are examples with port/starboard symmetry. In data sets 9, 18 the resulting value is lower, but there, also, the ship speed is much slower than in data sets 4, 13. Throughout the data

sets the z-component is in a reasonable range, except for data sets 2 and 3.

Variations in the estimated CR positions are certainly produced by different ship speed and wave conditions. However, not all of the variations in Table 2 can be explained by simple arguments. It must be noted that, in Table 2, wave characterization was reduced to the peak incidence angle. The actual wave spectra encountered in the area of the experiment was much more complex with a wide spread in angles and frequencies. Rudder action by the autopilot may have had an influence, especially on a small ship like the Simon Stevin. Finally, residual errors in the angle transformation may have led to errors in the estimation of the z-component of the CR position. At least some of these questions may be answered by the ongoing analysis of data from the second sensor in the survey room.

The results so far indicate that the CR position varies according to external factors, such as wave length, period and direction and the ship's seakeeping behaviour. Nevertheless, for an individual trial run with nearly constant conditions, a unique CR location can be produced.

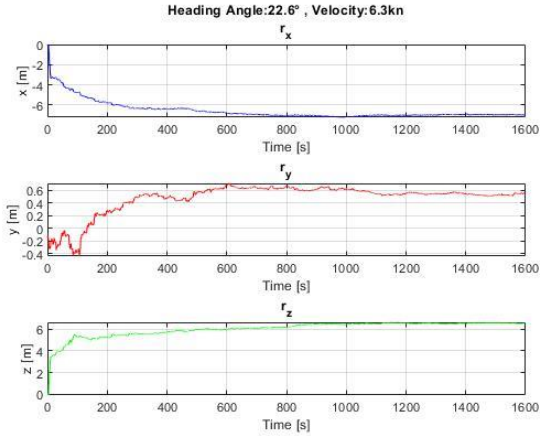

Figure 11. Offset estimation of data 21

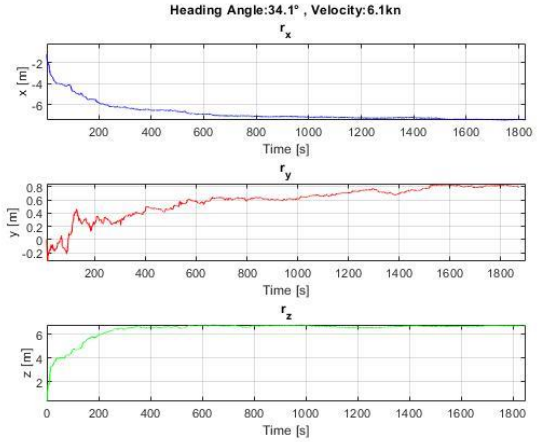

Figure 12. Offset estimation of data 23

Table 2. Results of selected Simon Stevin sea trials

Data Set	Relative Angle		Ship Speed	CR in ship frame		
	[°]		[kn]	[m]		
				x	y	z
1	142	Port	6.1	7.04	2.69	2.05
12	130	Port	4.2	7.46	2.55	1.73
4	167	Port	6.1	7.91	2.16	0.51
13	165	Port	9.5	8.03	2.77	0.88
15	176	Port	3.7	8.23	1.98	1.31
21	152	Port	6.3	7.39	2.63	1.7
23	155	Port	6.1	7.4	2.41	1.66
3	44	Port	5.8	9.44	4.37	-2.3
10	48	Port	3.8	7.03	3.78	1.18
9	167	Starboard	3.8	10.36	0.59	-0.5
18	165	Starboard	3.8	9.86	0.31	-1.05
2	45	Starboard	6.7	14.9	-1.45	-2.62
14	51	Starboard	3.8	11.26	-0.47	-1.64

5 CONCLUSIONS

The Kalman filter algorithm, coping with the influence of geometrical offsets and with the assistance of Euler transformation can be utilized to determine the ship's CR position. From data of all investigated sea trials, it is safe to conclude that the algorithm as such is proven. The results appear to be quite sensitive to variations of ship velocity and incident wave characteristics. It is therefore worthwhile to develop a mathematical model for the dependence of the CR position on the various influence parameters. Then, for estimating the directional wave spectrum from ship motions, the CR position can provide additional information, e.g. for port-starboard ambiguity resolution.

6 ACKNOWLEDGEMENTS

The authors are grateful to the crews of Agulhas II and Simon Stevin for their great help and pleasant cooperation.

7 REFERENCES

Abankwa, Nana O., et al, 2015. Ship motion measurement using an inertial measurement unit, in: the 2nd World Forum on Internet of Things. Milan, Italy. https://ieeexplore.ieee.org/document/7389083

Bekker, A., Omer, H., 2018. Human responses to wave slamming vibration on a polar supply and research vessel. Applied Ergonomics 67. 71-82 https://doi.org/10.1016/j.apergo.2017.09.008

Fossen Thor I., 2011, Kinematics, in: Handbook of Marine Craft Hydrodynamics and Motion Control. pp. 15–33. https://onlinelibrary.wiley.com/doi/book/10.1002/9781119994138.

Kalman, R., E., 1960. A new approach to linear filtering and prediction problems. Journal of Basic Engineering. 35-45. http://fluidsengineering.asmedigitalcollection.asme.org/article.aspx?articleid=1430402.

Soal, K., Bienert, J., Bekker, A., 2015. Operational modal analysis on the polar supply and research vessel the S.A. Agulhas II, in: the 6th International Operational Modal Analysis Conference. Gijon, Spain. https://www.researchgate.net/publication/280445237_Operational_Modal_Analysis_on_the_Polar_Supply_and_Research_Vessel_the_SA_Agulhas_II.

Linder J., Enqvist, M., Fossen, T. I., Johansen, T. A., Gustafsson, F., 2015. Online estimation of ship's mass and centre of mass using inertial measurements, in: the 10th IFAC Conference on Manoeuvring and Control of Marine Craft. Copenhagen, Denmark. pp. 134-139. https://www.sciencedirect.com/science/article/pii/S2405896315021618.

Pascoal, R., Guedes Soares, C., 2009. Kalman filtering of vessel motions for ocean wave directional spectrum estimation. Journal of Ocean Engineering. 477-488. https://www.sciencedirect.com/science/article/pii/S0029801809000183

Product Sheet of Fishery Research Vessel 3609 Simon Stevin, https://products.damen.com/en/ranges/fishery-research-vessel/frv-3609.

Triantafyllou, M. S., Bodson, M., Athans, M., 1983. Real Time estimation of ship motions using Kalman filtering techniques. IEEE Journal of Oceanic Engineering. 9-20. https://ieeexplore.ieee.org/document/1145542

8 AUTHORS BIOGRAPHY

Chen Zhang received her bachelor and master degree from Northwestern Polytechnical University, China in 2010 and 2013 respectively. Now she is a PhD candidate in the Department of Computer Science, Carl von Ossietzky University of Oldenburg, Germany. Her research interests contain measurement and analysis of ship movements at sea states, also including motion control.

Alexander Härting is a professor in Department of Maritime Studies, Jade University of Applied Science, Germany. His research interests include measurement and analysis of dynamic ship movements in seaway, integration of different navigation sensors, and measurement of the squat of seagoing vessels in narrow fairways.

Butteur Ntamba Ntamba hold a bachelor degree in mechanical engineering from University of Lubumbashi, Democratic Republic of Congo and a master degree from Cape Peninsula University of Technology (CPUT), South Africa. He is now a lecturer in the Faculty of Engineering and a PhD candidate with CPUT. His research work is on ship response in waves.

Bernhard Schwarz-Röhr holds his diploma degree of physics, and now he is a PhD candidate in Faculty of Engineering and Architecture, Ghent University, Belgium. He is responsible for wave estimation, sea state analysis, and measurement of ship movements.

SHALLOW WATER EFFECTS ON SHIP-GENERATED WAVES

Qingsong Zeng, Cornel Thill, and **Robert Hekkenberg**,
Maritime and Transport Technology, Delft University of Technology, the Netherlands

SHALLOW WATER EFFECTS ON SHIP-GENERATED WAVES

Qingsong Zeng, Cornel Thill, and **Robert Hekkenberg,** Maritime and Transport Technology, Delft University of Technology, the Netherlands

SUMMARY

Understanding the characteristics of the waves generated by a ship can improve the prediction of ship's wave resistance. Such waves generated in deep water have been studied in detail whereas in shallow water, the existing methods, mostly derived from inviscid flow, are not fully coping with physical phenomena. In this study, the changes in the height and length of ship-generated waves in shallow water are explored as well as the effects of waterbed friction. A Computational Fluid Dynamics (CFD) approach is selected as the main tool and a Wigley hull is chosen due to the availability of validating data. It is found that the wave cut analysis will slightly underestimate the wave resistance. The effects of bottom friction are perceivable and should be considered if a highly accurate prediction is required. This study, which improves the understanding of ship-generated waves, is expected to contribute to the prediction of ship's wave resistance in shallow water.

NOMENCLATURE

a	Wave amplitude (m)
B	Beam of ship (m)
CFD	Computational Fluid Dynamics
C_f	Coefficient of frictional resistance
C_{fb}	Coefficient of water bottom friction
C_r	Coefficient of residual resistance
C_t	Coefficient of total resistance
C_v	Coefficient of viscous resistance
c	Wave speed (m/s)
$E(m)$	Complete elliptic integral of the second kind
E_D	Energy dissipated on water bottom (J/m)
E_k	Kinetic energy per wavelength (J/m)
E_p	Potential energy per wavelength (J/m)
E_T	Total energy per wavelength (J/m)
Fr	Froude number
Fr_h	Depth Froude number
g	Acceleration of gravity (m/s^2)
H	Wave height (m)
h	Water depth (m)
$K(m)$	Complete elliptic integral of the first kind
k	Wavenumber (1/m)
L	The length of a ship (m)
m	Elliptic parameter
N	Number of grid points per wavelength
n	Number of wave along a ship hull
Re	Reynolds number
S	Wetted surface (m^2)
T	Draft of ship (m)
t	Time (s)
u	Horizontal velocity (m/s)
V_h	Velocity at water bottom (m/s)
w	Vertical velocity (m/s)
$y+$	y plus, a non-dimensional wall distance
ε	Percentage of energy dissipation
η	Free surface elevation (m)
λ	Wavelength (m)
ρ	Water density (kg/m^3)
τ	Shear stress (N/m^2)
ϕ	Velocity potential (m^2/s)
ω	Wave frequency (1/s)

1 INTRODUCTION

Investigating the properties of water waves is valuable to determine ships' wave resistance. In the existing theories of wave resistance prediction, one well-known method is wave pattern analysis, which based on the investigations of the relation between wave energy and water pattern (Eggers et al., 1967; Havelock, 1932; Michell, 1898). With the assistance of velocity potential, the velocity field and pressure field can be solved both analytically and numerically (Raven, 1996). However, wave pattern analysis does not always provide plausible results in shallow water, and the wave resistance obtained by linearized wave pattern analysis is usually larger than the measurements (Insel and Doctors, 1995; Sharma, 1963).

The problem mentioned above may be due to different properties of waves that are caused by a limited water depth. For small amplitude waves in deep water, the movements of water particles are linear and harmonic, and the trajectory is circular with its amplitude damping exponentially to the water depth (Airy, 1841). However, when the water is sufficient shallow, water particles can no longer move freely and the oscillating movements adjacent to the bottom will be affected by the bottom friction, as shown in **Figure 1.** An oscillatory boundary layer is formed above the bottom and a part of wave energy is dissipated in the boundary layer (Schlichting, 1979).

According to the studies in the past, changes of the characteristics of waves are observed in shallow water, e.g. the height (Putnam and Johson, 1949), velocity (Lamb, 1932) and length (McSullea et al., 2018). Therefore, the mechanism of wave propagation is different and the theory used to describe shallow water waves should not be limited to

the linear wave theory. According to Chakrabarti (1987), there are many theories, each with their own application ranges. Additionally, if the viscosity, e.g., effects of bottom friction (Jonsson, 1967), is considered, the problem will become much more complex.

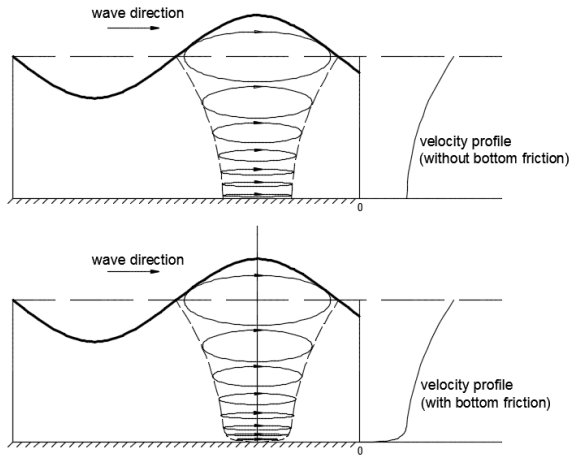

Figure 1. The sketch for movements and the maximum velocity profile in shallow water (top: without bottom friction; bottom: with bottom friction)

In model tests, a pervasive assumption is that the coefficient of wave resistance is solely a function of Froude number (Froude assumption) and stays the same for full-scale ships and its geometrically similar models (ITTC, 2011). As the full-scale Reynolds number and the Froude number cannot be achieved simultaneously in model tests, it is conventional to keep the Froude numbers identical during model tests on ship resistance. However, this study will validate with a novel approach that the wave resistance is also depending on Reynolds number, which helps to explain errors in model test-based resistance predictions of ships.

In this study, the changes in the height and the length of ship-generated waves in shallow water are first explored. Afterward, the energy dissipation on the water bottom is studied with different wave theories. The effects of the bottom friction on wave resistance are also discussed.

This article is built up as follows: In part 2, three wave theories that are applied in this study are described followed by verification and validation of the CFD code. Part 3 studies the shallow water effects on inviscid ship waves and part 4 discusses the influence of viscosity. Conclusions are given in part 5.

2 METHOD

This part introduces the basic characteristics of three waves theories, both linear and nonlinear, and they will be used for further analysis of wave profiles in part 3 and bottom friction in part 4. Afterward, the commercial CFD code by which the main results are generated is verified and validated for ship waves computation.

2.1 LINEAR AND NON-LINEAR WAVE THEORIES

In this section, the well-known Airy wave theory (Airy, 1841), a cnoidal wave theory (Benjamin et al., 1972), and the Stokes 2nd wave theory (Stokes, 1847) are introduced in sequence. Many details of those methods have been omitted and only the expressions of the governing equations, wave elevation, and bottom oscillating velocity are presented.

These wave theories are fundamental for analyzing the properties of waves in shallow water. Based on the linear wave theory, increments of wave length in inviscid shallow water will be described analytically (Part 3). The expressions of bottom oscillating velocity are essential for the analysis of bottom energy dissipation (Part 4).

2.1 (a) Airy wave theory

The Airy wave theory, or the so-called linear wave theory, assumes small amplitude waves and inviscid fluid. With the concept of velocity potential (ϕ), the kinematic and dynamic conditions on free surface can be derived:

$$\frac{\partial \eta}{\partial t} - w = 0, \tag{0}$$

$$\frac{\partial \phi}{\partial t} + g\eta = 0, \tag{0}$$

where η is the free surface elevation, w the velocity at the vertical direction, t the time and g the acceleration of gravity.

The solution of wave elevation and velocity potential can be given as

$$\eta(x,t) = a\cos(kx - \omega t), \tag{0}$$

$$\phi(x,z,t) = \frac{a\omega}{k} \cdot \frac{\cosh[k(z+h)]}{\sinh(kh)} \cdot \sin(kx - \omega t), \tag{0}$$

where a is the wave amplitude, k the wave number, ω the wave frequency, and h the water depth.

Based on the linear wave theory, the velocity of water particles at the bottom (V_h) is shown as follows:

$$V_h = \frac{a\omega}{\sinh(kh)} \cos(kx - \omega t) \cdot \tag{0}$$

2.1 (b) BBM wave theory (cnoidal wave)

In some cases, such as relatively large amplitude waves in shallow water, the items of the velocity and/or elevation derivatives on the free surface are no longer negligible. Therefore, the boundary conditions become

$$\frac{\partial \eta}{\partial t} + u\frac{\partial \eta}{\partial x} - w = 0, \tag{0}$$

$$\frac{\partial \phi}{\partial t} + \frac{1}{2}(u^2 + w^2) + g\eta = 0 \cdot \tag{0}$$

Then Boussinesq equations (Boussinesq, 1872) can be derived:

$$\frac{\partial^2\eta}{\partial t^2} = gh\frac{\partial^2\eta}{\partial x^2} + gh\frac{\partial^2}{\partial x^2}\left(\frac{3}{2}\frac{\eta^2}{h} + \frac{h^2}{3}\frac{\partial^2\eta}{\partial x^2}\right), \quad (0)$$

where the arguments have the same meaning as the linear theory. Cnoidal wave theory is needed to solve the equations. With some additional assumptions (more details are omitted), the Korteweg and De Vries (1895) equation (KdV equation) and Benjamin et al. (1972) equation (BBM equation) were achieved for unidirectional waves in shallow water.

As the BBM equation, or is also called the regularized long wave (RLW), is assumed to be more appropriate to describe long waves in nonlinear dispersive systems than KdV equation (Benjamin et al., 1972), the BBM wave is chosen as a representative of cnoidal waves.

Based on the assumption that the wave is permanent, i.e. independent of time, Dingemans (1997) provided the periodic solution for the BBM equation:

$$\eta(x,t) = -a_t + H\,\mathrm{cn}^2\left(2K(m)\frac{x-ct}{\lambda}\middle| m\right), \quad (0)$$

$$\lambda = \sqrt{\frac{16h^3}{3H}m}\frac{c}{\sqrt{gh}}\cdot K(m),$$

$$a_c = \frac{H}{m}\left(1-\frac{E}{K}\right), \quad a_t = H - a_c,$$

$$c = \left[1-\frac{1}{2}\frac{H}{h}+\frac{1}{m}\frac{H}{h}\left(1-\frac{3}{2}\frac{E}{K}\right)\right]\sqrt{gh},$$

$$T = \lambda / c,$$

where a_c and a_t are absolute values that the crest and the trough deviate the mean water level, H is the wave height, λ the wavelength, c the wave speed, and T the wave period. m is the elliptic parameter, $K(m)$ is the complete elliptic integral of the first kind, and $E(m)$ is the complete elliptic integral of the second kind. The velocity on water bottom is demonstrated as

$$V_h = u + \frac{1}{6}\cdot\frac{d^2u}{dx^2}, \quad (0)$$

where

$$u = \frac{c\eta}{h+\eta}.$$

2.1 (c) Stokes 2nd wave theory

Higher orders of Stokes waves were first introduced by Stokes (1847) using perturbation theory to achieve practical solutions for non-linear waves. By considering a different number of items in the Stokes expansion, different orders of Stokes waves can be obtained.

The most frequently used wave theories are from the second order to the fifth order, and this section briefly discusses the solution of the second order which is more appropriate than other orders to decribe ship-generated waves. According to the study of Dingemans (1994), the solution of the second-order Stokes wave on a limited even water depth is given:

$$\eta(x,t) = a\left[\cos\theta + ka\frac{3-\sigma^2}{4\sigma^3}\cos 2\theta\right], \quad (0)$$

$$\phi(x,z,t) = \frac{aw_0}{k\sinh(kh)}[\cosh[k(z+h)]\sin\theta + \frac{3ka}{8\sinh 3(kh)}\cosh[2k(z+h)]\sin 2\theta], \quad (0)$$

$$\omega = \omega_0\left[1 + k^2a^2\frac{9-10\sigma^2+9\sigma^4}{16\sigma^4}\right],$$

$$\theta = kx - \omega t,$$

$$\sigma = \tanh(kh),$$

$$\omega_0^2 = gk\cdot\tanh(kh).$$

The symbols again have the same meaning as used in linear wave theory. The velocity on water bottom of Stokes 2nd wave theory can be derived as

$$V_h = \frac{aw_0}{\sinh(kh)}\cdot\left[\cos(kx) + \frac{3ka}{4\sinh^3(kh)}\cos(2kx)\right]. \quad (0)$$

2.2 CODE VERIFICATION AND VALIDATION

The results of free surface elevation and ship resistance will be achieved through a commercial RANS solver: ANSYS(TM) Fluent (version 18.1). In this section, a Wigley hull sailing in deep water is applied to verify the code with a mesh study and validate the code with existing experiments.

2.2 (a) Ship model

The well-known Wigley hull, of which a large amount of experimental data is available, is applied. One corresponding governing equation of the hull surface is shown as follows:

$$y = \frac{B}{L}\left(1-\left(\frac{2x}{L}\right)^2\right)\left(1-\left(\frac{z}{T}\right)^2\right), \quad (0)$$

where B is the beam, L the length, and x, y, z are the values on the three directions of the ship-based coordinate system. The x is positive forward, y is positive port, z is positive upwards. The origin locates at the intersection of ship's midsection, ship center line, and the plane of still water surface. The detailed parameters are shown in **Table 1**.

Table 1. The main dimension of a Wigley hull model

	unit	Value
L*	m	2.500
B	m	0.250
T	m	0.156
S	m^2	0.930

(*L: length; B: beam; T: draft; S: wetted surface)

In this study, the trim and sinkage are not considered since shallow water effects are obvious already even for a fixed ship (as shown in the following parts). The trim and sinkage, which are certainly also important, will be subject to further investigation at a later time.

2.2 (b) Verification

To obtain accurate and relatively sharp wave profiles, enough grid points should be used within one wavelength. This subsection gives a comparison of various setups for choosing an appropriate number. Since the value of $y+$, a non-dimensional wall distance, can affect the results of ship resistance, a comparison of various $y+$ values is given as well.

In the numerical calculations, a structured mesh is applied and SST k-ω model is chosen as the turbulence model. The scheme of the pressure-velocity coupling is "Coupled" and the discretization of gradient is "Least Squares Cell-Based". "PRESTO!" is used for the discretization of pressure, and "Second Order Upwind" is applied for the discretization of momentum, turbulent kinetic energy, as well as specific dissipation rate.

The selection of the number of grid points per wavelength is based on linear wave theory, in which the number of the ship-generated waves along the hull (n) is a function of Froude number (Fr):

$$n = \frac{1}{2\pi Fr^2}. \quad (0)$$

Equation (0) makes it possible to estimate the wavelength before calculations. In **Table 2**, a different number of grid points per wavelength (N) are listed. Numerical results of the coefficients of frictional resistance (C_f) and total resistance (C_t) are also shown.

Table 2. The chosen number of grid points per wavelength and the results of resistance for Fr = 0.316 in deep water

Case	N	C_f (×10³)	C_t (×10³)
1	100	3.566	5.281
2	80	3.574	5.286
3	60	3.590	5.302
4	40	3.617	5.331
5	30	3.592	5.303
6	20	3.572	5.333

From **Table 2**, the differences of both the C_f and C_t for each case are within 2%, which indicates that the number of grid points per wave has a minor influence on the calculation of resistance. However, a different conclusion has to be made for the sharpness of free surface elevation. As shown in **Figure 2**, a wave-cut at y = 2B is depicted for each case in the range of x = -1.5L~0.8L.

Some remarks can be made based on **Figure 2**:

- When N = 20, the wave profile is not sharp enough for further analysis. The lowest acceptable number is 30;
- In the range of N = 30~60, the sharpness of wave profile increases with a refinement of the mesh, but the changes are becoming smaller when N is approaching 60;
- When $N \geq 60$, the refinement of the mesh only makes small contributions to the wave sharpness.

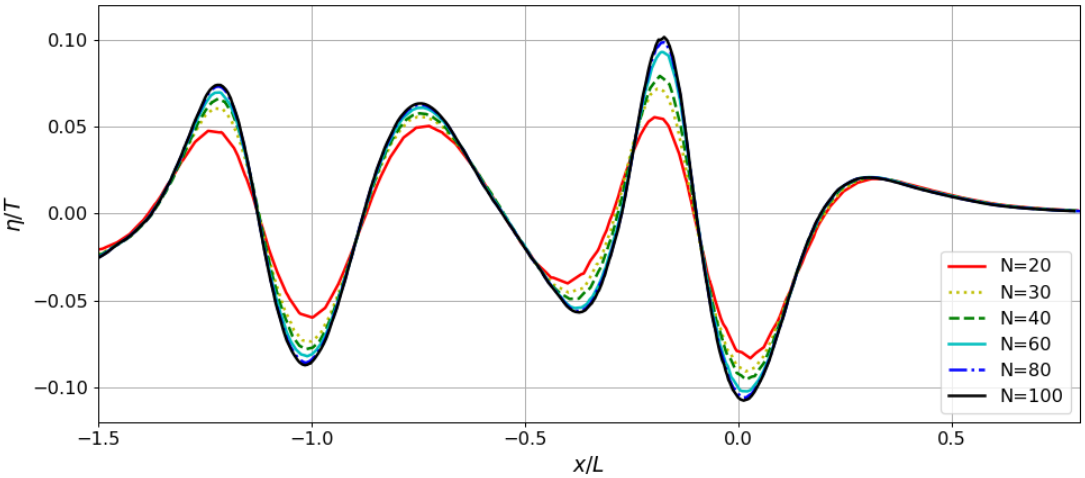

Figure 2. The wave cut at y = 2B for different cases in the range of x = -1.5L~0.8L (the hull locates at x = -0.5L~0.5L with the bow at 0.5L)

Table 3. The selected *y*+ and the corresponding location in the boundary layer

No.	Location	y+
1	viscous sublayer	0.5
2	viscous sublayer	1.25
3	viscous sublayer	2
4	viscous sublayer	4
5	buffer layer	6
6	buffer layer	10
7	buffer layer	15
8	buffer layer	25
9	log-law region	50
10	log-law region	100
11	log-law region	150
12	outer layer	250

The purpose of this mesh study is to find an acceptable setup instead of searching for the largest possible number of grid cells, i.e. a balance between accuracy and computing time. Therefore, an $N \geq 30$ is guaranteed for all cases and an $N \geq 60$ is applied when a sharp wave profile is required.

The value of $y+$ is another factor which can play a role in the accuracy of ship resistance computation. To choose an appropriate $y+$ for this study, various $y+$ values, which are listed in **Table 3**, are used to test the performance of the code.

The results of the coefficient of frictional resistance (C_f) and the residual resistance ($C_r = C_t - C_f$) in deep water are demonstrated in **Figure 3**. The ITTC57 correlation line for ship friction is also shown for comparison.

From **Figure 3**, it can be seen that

- The values of C_f show wiggles with $y+$ and the largest deviation from ITTC57 line is about 6%;
- When $y+ \approx 6$ and $y+ \approx 100$, the numerical results of C_f have a satisfactory agreement with ITTC57 line;
- The results of C_r are not sensitive to $y+$.

The wiggles of C_f are caused by different wall treatments with the value of $y+$, which is set within the selected ω-equation applied in the code. A low-Reynolds number model is used in the viscous sublayer. The wall function approach is switched on in the logarithmic layer. In the buffer layer, a method by blending the low-Re formulation and wall functions is applied to ensure a reasonable result. In the outer layer, the boundary layer is still resolved with wall functions and errors will be certainly generated. As stated by the code provider (ANSYS, 2017), the results should be "$y+$ insensitive", but perceptible errors can be found based on Figure 3. However, such errors are not significant (<6%) and are practically acceptable.

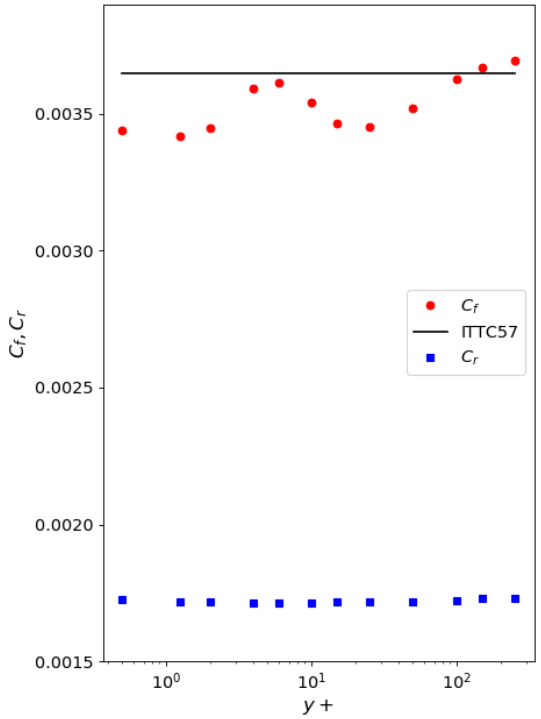

Figure 3. The friction coefficient C_f and the residual resistance coefficient C_r of a Wigley hull against *y*+ (deep water)

In practice, the value of C_f which coincides better with the ITTC57 line is assumed to be more accurate. Accordingly, the $y+$ around 6 or 100 is arbitrarily selected for all further calculations and the decision of the value will be made for each specific case. No $y+$ study was applied in shallow water as once the code was verified for $y+$ in deep water case, the results can be used to predict the behavior of the code in shallow water based on the corresponding values of $y+$.

2.2 (c) Validation

The validation is to make sure the code can have comparable results with a real physical model. In this subsection, the CFD results of free surface elevation along the Wigley hull in deep water is compared with the experiment performed by Kajitani et al. (1983).

Results of the wave profile along the ship hull for the case $N = 60$ and $y+ = 4$ are shown in **Figure 4**. In **Table 4**, the CFD results of frictional resistance coefficient are also compared with the ITTC57 correlation line (ITTC, 1957), and the total resistance coefficient is compared with the data of Kajitani et al. The model is fixed to the carriage and moves at $Fr = 0.316$, which has the same setup as the experiment.

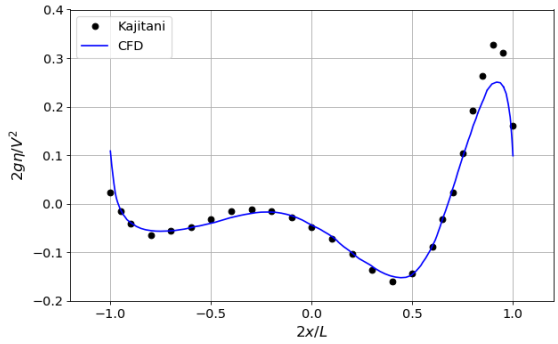

Figure 4. The validation of the free surface elevation along the Wigley hull (the bow is at $2x/L$ = 1.0; Fr = 0.316)

Table 4. Comparison of total resistance coefficient C_t

C_f–CFD (×10³)	C_f–ITTC (×10³)	Error- C_f
3.590	3.647	-1.56%
C_t -CFD(×10³)	C_t - Kajitani(×10³)	Error- C_t
5.302	5.149	2.97%

Based on **Figure 4** and **Table 4**, it can be derived that

- The CFD results of free surface elevation have a good agreement with experiments. Minor differences are observed except for the area close to the bow. It might be caused by a higher pressure gradient near the bow and a finer mesh can be a solution to fill the gap. However, the error is located in a narrow range and its influence is not significant.
- The errors of C_f and C_t are -1.56% and 2.97%, respectively, which lay within a practically acceptable range.

Therefore, the chosen code with the settings decided in this study is able to generate acceptable results of both ship resistance and wave profile.

3 SHALLOW WATER EFFECTS ON INVISCID SHIP WAVES

Compare to deep water, ship waves develop less freely in shallow water. The wave properties, such as wave height and wavelength, are altered due to limited water depth (Lamb, 1932). In this part, shallow water effects on the height and the superposition of ship-generated waves are explored in inviscid water. The effects of viscosity will be further discussed in part 4.

3.1 WAVE HEIGHT

Shallow water effects on wave height are relatively easy to be observed. In **Figure 5**, the free surface elevations of the stern waves and the bow waves at the center line are depicted, respectively, for the Wigley hull sailing at the same speed but with various water depths.

Some remarks can be made based on **Figure 5:**

- The height of the bow wave is larger when the water is shallower. Since a smaller under-keel clearance provides less room for the water to pass, more kinetic energy of the water will be transferred into potential energy resulting in higher bow waves;
- The changes are different for the stern waves. When $h/T \geq 2.0$, the height of the stern wave is increasing with a decreasing water depth. However, at a certain point when $h/T < 2.0$, the height of the stern wave drops immediately and then continue increasing with a decreasing water depth. The corresponding Fr_h of this turning point is about 1.0. This is probably caused by the disappearance of the transverse waves.

The changes in the height of ship-generated waves can alter the pressure distribution at the bow and the stern. Ship designers should take them into account to avoid possible negative effects.

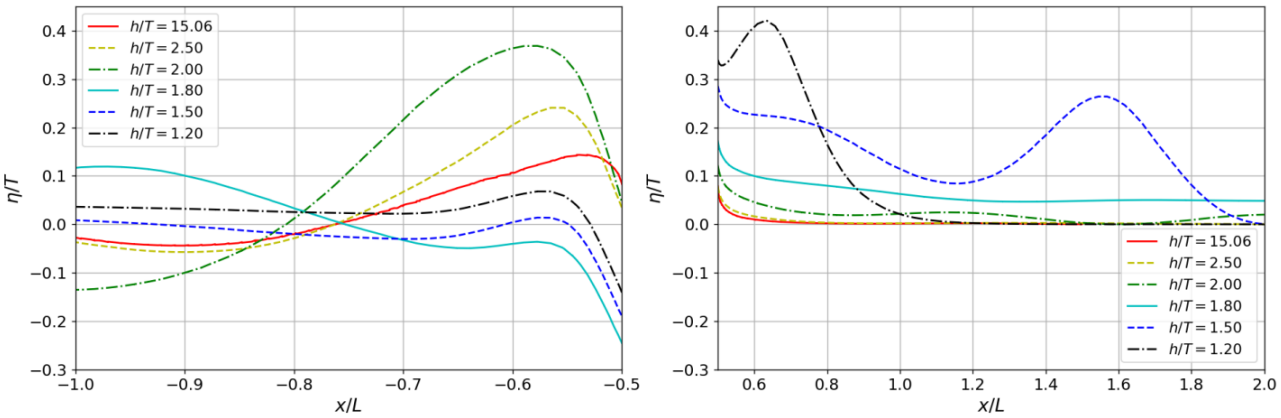

Figure 5. Stern waves (left) and bow waves (right) of a Wigley hull at various water depths (y = 0; Fr = 0.316; water comes from right to left; the bow is at x = 0.5L and stern is at x = -0.5L)

3.2 WAVELENGTH AND WAVE SUPER-POSITION

Another property of ship-generated waves affected by water depth is wavelength. If the linear wave theory is applied, the changes at wavelength can be given explicitly and theoretically. In the linear theory, the phase velocity (c) can be written as

$$c = \sqrt{\frac{g\lambda}{2\pi}\tanh\left(\frac{2\pi h}{\lambda}\right)}, \qquad (0)$$

where the λ is the wavelength, and h is the water depth. For well-developed waves generated by a ship, the phase speed of the water is equivalent to ship's velocity, which means that the phase speed of ship-generated waves is independent of water depth. Based on this, the relation of wavelength in deep and shallow water can be achieved as follows.

$$\frac{\lambda_s}{\lambda_d} = 1/\tanh\left(\frac{2\pi h_s}{\lambda_s}\right), \qquad (0)$$

where the subscripts s and d indicate shallow and deep water, respectively. This relation is visualized in **Figure 6**.

From **Figure 6,** it can be seen:

- When $\lambda_s/h_s \leq 3$, shallow water effects on wavelength are negligible;
- When $\lambda_s/h_s > 3$, the increase of wavelength in shallow water is approximately linear to λ_s/h_s.

However, the linear wave theory does not apply when the water is shallow, as the points ($Fr = 0.315$) shown in **Figure 6**. To directly study the changes of wavelength in shallow water, numerical results of the wave profile behind the stern of a Wigley hull are demonstrated in **Figure 7**.

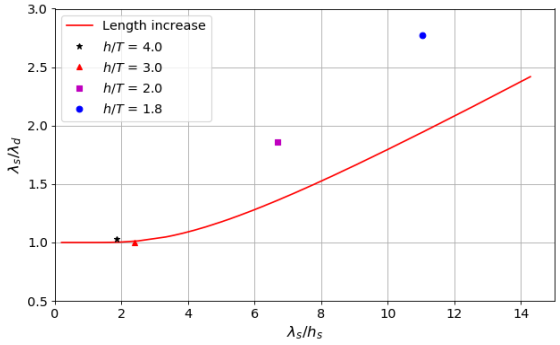

Figure 6. The ratio of wavelengths in shallow and deep water against the ratio of wavelength and water depth based on linear wave theory

When $h/T > 2$ (**Figure 7** left), of which $Fr_h < 1.0$, the wavelength is stretched slightly but such stretch becomes severe when $h/T < 2$ (**Figure 7** right). Such change is nonlinear and cannot be simply explained by the linear wave theory. For $h/T = 1.2$, the wavelength is even larger than three times the ship length. Therefore, when the water is shallow enough, the length of the wave will become infinite and this can be an explanation of the disappearance of the transverse wave system.

The wave superposition behind the stern is influenced by the changes of wavelength. The waves generated by the bow will arrive at the stern earlier, but a crest is always generated at the aft. Therefore, a good design for the wave superposition in deep water can be inappropriate for certain water depths.

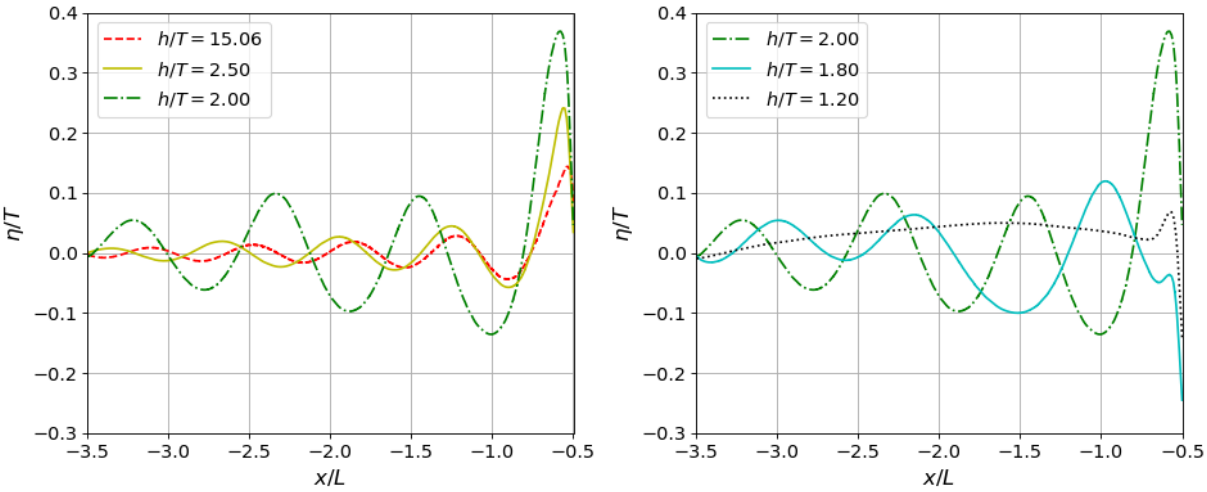

Figure 7. The wave profile after the stern of a Wigley hull ($y = 0$; $Fr = 0.316$; waters comes from right to left; the stern is at $x = -0.5L$; left: $h/T = 15.06$, 2.50, and 2.00; right: $h/T = 2.00$, 1.80, and 1.20)

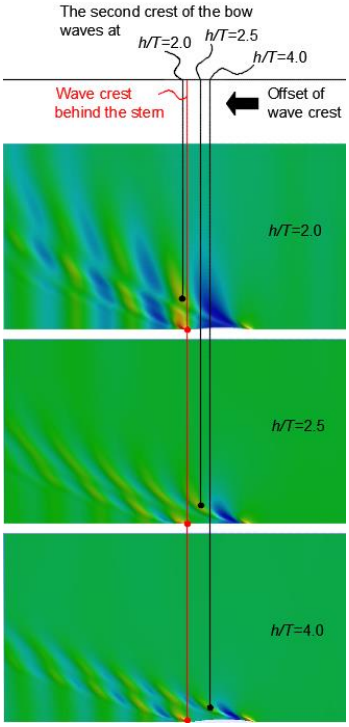

Figure 8. The wave pattern of a Wigley hull with various water depths (Fr = 0.316)

An example is given in **Figure 8**, in which the same velocity but different water depths are applied. It can be seen that the second crest of the bow wave system moves further aft for shallower water, which will surely have different superposition with the waves generated by the stern.

4 EFFECTS OF VISCOSITY ON SHIP WAVES

In the previous part, the properties of ship waves in inviscid shallow water already show significant differences from deep water. If the viscosity is considered, wave profiles will be further affected and the bottom friction of the waterway begins to play a role. In this part, the effects of viscosity on ship waves are studied followed by a discussion of the influence of bottom friction on ship wave resistance.

4.1 EFFECTS OF VISCOSITY ON WAVE HEIGHT

The viscosity of water acts as damping for ship-generated waves. Part of energy the waves contain will be dissipated due to the shear stress between water particles. Such dissipation will be accumulated with the propagation of waves, and the movements of water particles will be reduced obviously when they are far enough behind the ship. In **Figure 9**, wave profiles of a Wigley hull in inviscid flow and viscous flow are compared. When $Fr_h = 0.63$, the wave profiles are highly overlapped for $x \geq -L$, which means the influence of viscosity is not significant close to the ship hull. However, for the range $x < -L$, the wave height in viscous flow is apparently lower than that in inviscid flow.

Nevertheless, if a ship sails at a much higher speed, where the wave resistance dominates the total resistance, the effects of viscosity are too small to be considered, as shown for $Fr_h = 1.15$ in **Figure 9.**

The wave cut analysis is one of the well-known methods to estimate wave resistance. This theory is built on the wave pattern analysis which ignores the effects of viscosity. For example, the transverse wave cut needs to pick two transverse sections behind the stern to measure the free surface elevation. According to **Figure 9**, if $Fr_h = 0.63$ and one of or both of the two sections are located behind $x = -L$, the result derived from the transverse cut method will underestimate the wave resistance. However, if $Fr_h = 1.15$, the corresponding error is negligible.

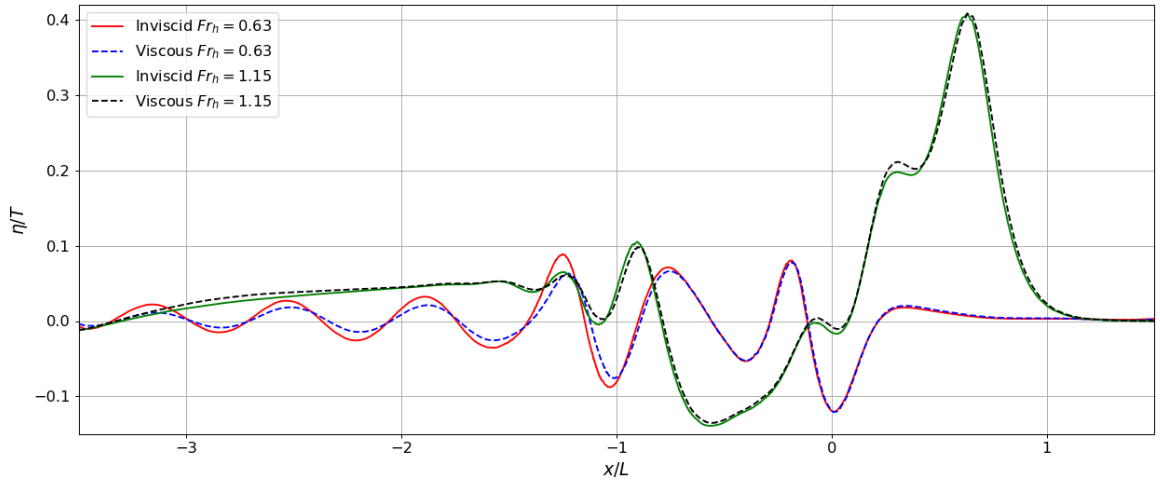

Figure 9. Comparison of longitudinal wave cuts of a Wigley hull in inviscid flow and viscous flow (wave cut at y = 2B; the stern is at x = -0.5L and the bow is at x = 0.5L)

Therefore, the effects of viscosity on wave resistance are important for low-Fr_h vessels and become minor when the Fr_h is high enough. An assessment of the influence of viscosity should be considered before applying wave pattern analysis.

4.2 EFFECTS OF BOTTOM FRICTION

The friction at the bottom of a waterway can be another factor affecting wave resistance. For viscous flow, the movements of water particles on the water bottom are stopped by bottom friction and the corresponding kinetic energy is dissipated. Such dissipation (E_D) can be estimated by integrating all instantaneous dissipation over one wavelength:

$$E_D = \int_0^{\lambda} \tau \cdot |V_h| \, dx, \qquad (0)$$

where λ is wavelength, and V_h is the oscillating velocity of water particles at water bottom when the viscosity is ignored. The τ is the shear stress which can be obtained by

$$\tau = C_{fb} \cdot \frac{1}{2} \rho V_h^2, \qquad (0)$$

where the C_{fb} is the coefficient of bottom friction.

To explore the significance of the energy dissipation on the water bottom, the percentage (ε) it takes in total wave energy (E_T) per wavelength is calculated:

$$\varepsilon = \frac{E_D}{E_T}, \qquad (0)$$

and the total energy can be achieved by

$$E_T = E_k + E_p, \qquad (0)$$

where the E_k and E_p are kinetic energy and potential energy pre wavelength, respectively, and they are obtained by

$$E_k = \frac{\rho}{2\lambda} \int_0^{\lambda} \int_{-h}^{\eta} \left(u^2 + w^2\right) dz dx, \qquad (0)$$

$$E_p = \frac{\rho}{2\lambda} \int_0^{\lambda} \eta^2 dx, \qquad (0)$$

where η is the elevation of the free surface, h the water depth, u and w are the velocities at the x and the z direction, respectively.

If equation (0) is used to estimate bottom energy dissipation, the choice of a wave theory can make a difference. Chakrabarti (1987) provided a graph to show the ranges of the suitability of different wave theories. The CFD results of stern waves in shallow water are presented in the graph, as shown in **Figure 10.**

Based on **Figure 10**, most cases are located in the range of the Stokes 2nd wave theory, and the Airy theory and the Cnoidal theory are slightly involved. To give a straightforward feeling about the energy dissipation on water bottom with different wave theories, an example is given in which specific values are assigned.

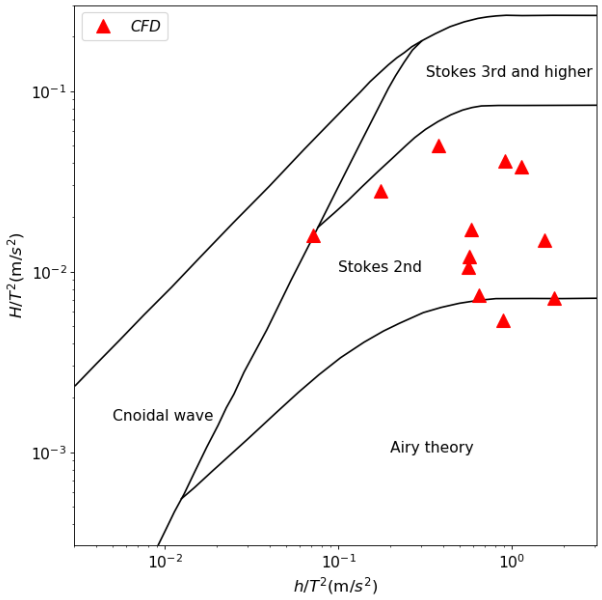

Figure10. The ranges of wave theories for ship waves in shallow water

From the CFD results in this study, it is found that the ratio between wavelength and water depth (λ/h) is always under 15. Therefore, a typical value of 10 is assigned. The material on the water bottom is assumed to be evenly distributed and the coefficient of bottom friction (C_{fb}), therefore, can be seen as a constant. According to Hardisty (1990), a typical value of C_{fb} is 0.1. As a result, the percentage of energy dissipation (ε) is calculated and shown in **Figure 11**.

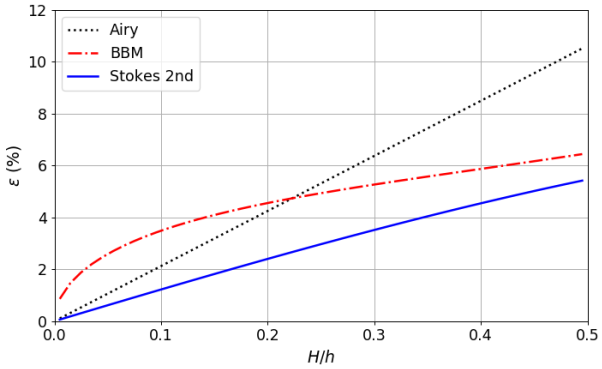

Figure 11.Energy dissipation on the bottom over one wavelength (ε) against wave height-water depth ratio (*H/h*) for three wave theories (C_{fb} = 0.1, λ/h =10)

Some comments can be made based on **Figure 11**:

- The percentage of energy dissipation is small (ε < 11%) for all three wave theories when $H/h \leq 0.5$;
- The Airy wave theory gives a higher estimation than the BBM theory and Stokes 2nd order theory;
- For ship-generated waves, where the H/h is usually less than 0.1, the ε < 4%.

Therefore, from the energy point of view, the effects of bottom friction are minor, but it is already enough to show that the wave resistance no longer depends on Froude number only (Froude assumption), but also depends on Reynolds number in shallow water. To explicitly show the effects of bottom friction on ship's wave resistance, numerical results of total resistance coefficient (C_t) and frictional resistance coefficient (C_f) are compared for considering (non-slip bottom) and not considering bottom friction, as shown in **Figure 12**.

A curve of the coefficient of viscous resistance ($C_v = C_t - C_w$) proposed by Zeng et al. (2019) is also shown for comparison. By subtracting the C_v from the C_t, values of C_w can be estimated.

Based on **Figure 12,** at least for lg(Re) = 6.05~6.4:

- The C_t considering bottom friction is larger than that when the bottom friction is ignored;
- Compare with the results of C_f, of which much smaller errors are observed, the wave resistance is more sensitive to the friction of water bottom;
- Whether or not the bottom friction is considered makes about 3% difference for the total resistance.

Therefore, a physical understanding has been obtained for how and to which extent the viscosity affects the wave resistance. Since the influence is small, the deviation of C_t caused by bottom friction is practically negligible, but it should be reconsidered if a strict prediction is required.

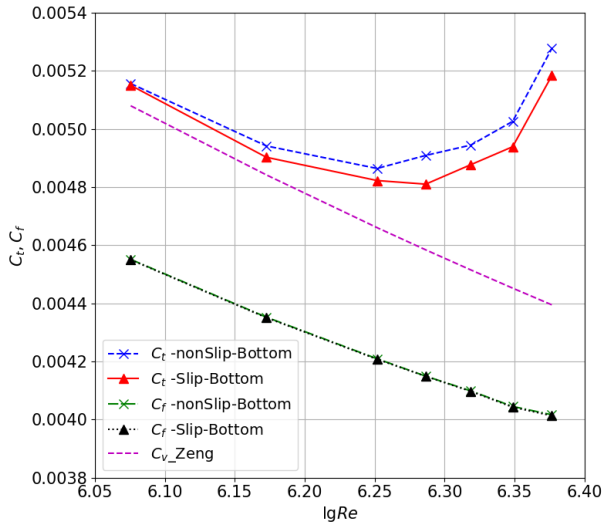

Figure 12. The results of C_t and C_f with non-slip water bottom and slip water bottom

5 CONCLUSIONS

In this study, shallow water effects on ship-generated waves are investigated in both inviscid flow and viscous flow. The CFD method was verified and validated for the calculations of ship waves. The effects of bottom friction were studied specifically. Based on the results, some concluded remarks can be made:

In inviscid flow:

- The bow wave is higher when the water is shallower, which leads to a higher resistance;
- For stern waves, when $Fr_h < 1.0$, the height of the first crest of stern waves is increasing with a decreasing water depth. When $Fr_h > 1.0$, the height drops immediately and then continue increasing with a decreasing water depth;
- Ship-generated waves become longer in shallow water for the same navigating speed. When $Fr_h > 1.0$, the wavelength increases dramatically and approximate infinity which leads to the disappearance of the transverse wave system.
- The waves generated by the bow will arrive earlier to the stern, which changes the wave superposition behind the stern.

In viscous flow:

- The viscosity of the water will lower the wave height behind the stern by which errors will be caused for wave cut analysis;
- The effect of viscosity on wave resistance is important for low-Fr_h vessels and becomes minor when the Fr_h is high enough. Since the wave resistance is a minority for low-speed vessels, the influence of viscosity on wave resistance at whole velocity range is practically unimportant;
- The effect of bottom friction is minor on wave resistance, but it is enough to reveal that the wave resistance does not merely depend on Froude number (Froude assumption), but the Reynolds number will also play a role in shallow water.

Consequently, in practice, the methods of wave resistance prediction in shallow water derived from inviscid flow are still valid since minor errors are caused by viscosity (≈ 3%) at relatively low Reynolds number. When the accuracy of wave resistance is strictly required, the effects of viscosity should be considered.

6 ACKNOWLEDGMENT

This research is funded by the China Scholarship Council (CSC).

7 REFERENCES

Airy, G.B., 1841. Tides and waves. Encyclopaedia Metropolitana (1817–1845), Mixed Sciences vol. 3.

ANSYS, 2017. ANSYS® Academic Research, Release 18.1, Help System, Fluent Theory Guide. Ansys Inc
.

Benjamin, T.B., Bona, J.L., Mahony, J.J., 1972. Model equations for long waves in nonlinear dispersive systems. Phil. Trans. R. Soc. Lond. A 272 (1220), 47-78.

Boussinesq, J., 1872. Theorie des ondes et des remous qui se propagent le long d'un canal rectangulaire horizontal, en communiquant an liquide contenu dans ce canal de vitesses sensiblement pareilles de la surface anfond, Liouvilles. J. Math. 17, 55-108.

Chakrabarti, S.K., 1987. Hydrodynamics of offshore structures. WIT press.

Dingemans, M.W., 1994. Water Wave Propagation Over Uneven Bottoms. Delft University of Technology.

Dingemans, M.W., 1997. Water Wave Propagation Over Uneven Bottoms: Part 2. World Scientific.

Eggers, K., Sharma, S., Ward, L., 1967. An assessment of some experimental methods for determining the wave-making characteristics of a ship form. Trans. of SNAME 75, 112-157.

Hardisty, J., 1990. Beaches: form and process. Springer Science & Business Media.

Havelock, T.H., 1932. The theory of Wave Resistance. Proc. R. Soc. Lond. A 138, 339-348.

Insel, M., Doctors, L.J., 1995. Wave-pattern prediction of Monohulls and Catamarans in a shallow water canal by Linearised Theory. Proceedings of 12th AFMC, University of Sidney, Sidney, 10-15.

ITTC, 1957. 8th International Towing Tank Conference, Madrid, Spanish.

ITTC, 2011. The Resistance Committee: Final Report and Recommendations, 26th International Towing Tank Conference, pp. 1-50.

Jonsson, I.G., 1967. Wave boundary layers and friction factors, Coastal Engineering 1966, pp. 127-148.

Kajitani, H., Miyata, H., Ikehata, M., Tanaka, H., Adachi, H., Namimatsu, M., Ogiwara, S., 1983. The summary of the cooperative experiment on Wigley parabolic model in Japan. TOKYO UNIV (JAPAN).

Korteweg, D.J., De Vries, G., 1895. XLI. On the change of form of long waves advancing in a rectangular canal, and on a new type of long stationary waves. The London, Edinburgh, and Dublin Philosophical Magazine and Journal of Science 39 (240), 422-443.

Lamb, H., 1932. Hydrodynamics. Cambridge university press.

McSullea, G., Rodrigues, J., Soares, C.G., 2018. Wake of a catamaran navigating in restricted waters, Progress in Maritime Technology and Engineering: Proceedings of the 4th International Conference on Maritime Technology and Engineering (MARTECH 2018), May 7-9, 2018, Lisbon, Portugal. CRC Press, p. 175.

Michell, J.H., 1898. XI. The wave-resistance of a ship. The London, Edinburgh, and Dublin Philosophical Magazine and Journal of Science 45 (272), 106-123.

Putnam, J., Johson, J., 1949. The dissipation of wave energy by bottom friction. Eos, Transactions American Geophysical Union 30 (1), 67-74.

Raven, H., 1996. A Solution Method for the Nonlinear Ship Wave Resistance Problem', Doctor's Thesis, Delft Univ. Techn., Delft, Netherlands.

Schlichting, H., 1979. Boundary Layer Theory 7th ed. McGRAW HILL BOOK COMPANY, New York.

Sharma, S.D., 1963. A comparison of the calculated and measured free-wave spectrum of an Inuid in steady motion, International Seminar on Theoretical Wave-Resistance.

Stokes, G., 1847. On the theory of oscillatory waves. Transactions of the Cambridge Philosophical Society VIII, 197-229.

Zeng, Q., Hekkenberg, R., Thill, C., 2019. On the viscous resistance of ships sailing in shallow water, Manuscript submitted for publication.

8 AUTHORS BIOGRAPHY

Qingsong Zeng holds the current position of a PhD candidate at Delft University of Technology (DUT). His previous experience includes CFD and ship resistance in shallow water.

Cornel Thill holds the position of the senior researcher and lecturer at DUT and is lecturer at the University of Duisburg-Essen in Germany, where he before joining DUT in 2015 held the position of the head of the hydrodynamic department of the *Development Centre for Ship technology and Transport systems* (DST). He gained further relevant experience in previous EU projects such as CREATING, SMOOTH (coordinator), STREAMLINE and MoVe IT!

Robert Hekkenberg holds the current position of an associate professor and Director of Studies BSc Marine Technology at DUT. He got his PhD at DUT in 2013 on "*Inland Ships for Efficient Transport Chains*". As a researcher at DUT, he was a partner in many inland shipping related EU projects such as CREATING and MoVe IT! His research fields are design optimization and maneuvering of inland ships as well as autonomous vessels.

Flanders
Hydraulics Research

Flanders
State of the Art

MARITIME TECHNOLOGY
GHENT UNIVERSITY

GHENT
UNIVERSITY